PROCEEDINGS

OF THE

PHYSICAL SOCIETY

JULY TO DECEMBER 1960

VOLUME 76

Published by
THE INSTITUTE OF PHYSICS AND THE PHYSICAL SOCIETY
1 Lowther Gardens, Prince Consort Road,
London S.W. 7

OFFICERS AND MEMBERS OF THE FIRST COUNCIL

PRESIDENT

Sir JOHN COCKCROFT, O.M., K.C.B., C.B.E., M.A., D.Sc., F.Inst.P., F.R.S.

IMMEDIATE PAST PRESIDENTS OF THE INSTITUTE AND OF THE SOCIETY

Sir GEORGE THOMSON, M.A., LL.D., Sc.D., Hon.F.Inst.P., F.R.S.
J. A. RATCLIFFE, C.B.E., M.A., F.R.S.

VICE-PRESIDENTS

Prof. R. W. DITCHBURN, B.Sc., M.A., Ph.D., F.Inst.P.
A. J. PHILPOT, C.B.E., B.Sc., M.A., F.Inst.P.
W. H. TAYLOR, M.A., D.Sc., F.Inst.P.
J. TOPPING, M.Sc., Ph.D., F.Inst.P.

HONORARY TREASURER

J. TAYLOR, M.B.E., D.Sc., F.R.I.C., F.Inst.P.

HONORARY SECRETARY

C. G. WYNNE, B.A., Ph.D., F.Inst.P.

ORDINARY MEMBERS OF THE COUNCIL

Prof. B. BLEANEY, M.A., D.Phil., F.R.S.
E. R. DAVIES, O.B.E., B.Sc., F.Inst.P.
Prof. B. H. FLOWERS, M.A., D.Sc.
J. M. A. LENIHAN, M.Sc. Ph.D. A.M.I.E.E., F.Inst.P.
G. R. NOAKES, M.A., F.Inst.P.
Prof. C. F. POWELL, M.A., Sc.D., F.R.S.
F. A. VICK, O.B.E., Ph.D., A.M.I.E.E., F.Inst.P.
Prof. D. A. WRIGHT, D.Sc., F.R.A.S., F.Inst.P.

REPRESENTING BRANCHES

M. R. HOPKINS, M.Sc., Ph.D., F.Inst.P.
Prof. H. LIPSON, M.A., D.Sc., F.Inst.P., F.R.S.

EXECUTIVE OFFICERS

Secretary:

H. R. LANG, B.Sc., Ph.D., A.R.C.S., F.Inst.P.

Deputy Secretary:

N. CLARKE, B.Sc., F.Inst.P.

Editor and Deputy Secretary:

A. C. STICKLAND, M.Sc., Ph.D.

CONTENTS

Part 1 *July* 1960

PAGE

Dr. H. R. Allan, Dr. R. F. Beamish, Dr. D. A. Bryant, Dr. H. Kasha and Mr. R. D. Wills. An investigation of extensive air showers, using Cerenkov detectors 1

Dr. A. S. Kaufman, Mr. T. P. Hughes and Mr. R. V. Williams. SCEPTRE III —An intense source of the spectra of highly ionized atoms. 17

The late Prof. E. G. Richardson. The transmission of sound through a wake . 25

Prof. L. M. Garrido. Perturbations in classical mechanics 33

Dr. D. W. Swan. Interpretation of ion mobility measurements in argon and helium liquids 36

Dr. A. Dalgarno and Dr. A. L. Stewart. The Lamb shift of helium . . 49

Mr. B. E. F. Macefield and Dr. J. H. Towle. Energy levels of ^{29}P, ^{33}Cl and ^{41}Sc from (d, n) reactions. 56

Mr. J. M. Reid and Dr. B. Lalovic. The high energy photodisintegration of helium, nitrogen and neon 65

Dr. R. W. Morriss. Observations of sudden ionospheric disturbances . . 79

Mr. A. Branwood and Dr. R. H. Tredgold. The electrical conductivity of barium titanate single crystals 93

Mr. W. B. Nash and Dr. K. J. Standley. The wall effect in ferrimagnetic resonance experiments 99

Mr. E. Thornton. Viscosity and thermal conductivity of binary gas mixtures: xenon–krypton, xenon–argon, xenon–neon and xenon–helium 104

Dr. P. A. Walker. The thermal conductivity and thermoelectric power of bismuth telluride at low temperatures 113

Dr. E. W. Billington. Some measurements of the elastic and viscous properties of thixotropic fluids 127

Mr. P. H. G. Dickinson and Prof. J. Sayers. Ion charge exchange reactions in oxygen afterglows 137

Dr. G. W. Greenlees and Dr. J. Lowe. The elastic and inelastic scattering of 19·6 MeV deuterons by Mg 149

Research Notes:

Mr. J. E. A. Lys and Mr. W. A. Runciman. The luminescence of uranium-activated fluorides 158

Dr. D. J. Craik and Dr. E. D. Isaac. Magnetic interaction domains . . 160

Letters to the Editor:

Dr. D. T. J. Hurle and Mr. S. Weintroub. The electrical resistivity of monocrystalline and liquid bismuth 163

Dr. A. J. F. Boyle, Dr. D. St. P. Bunbury, Mr. C. Edwards and Dr. H. E. Hall. A thermal red shift of the recoilless γ-emission of $^{119}Sn^{m}$ . . 165

Corrigendum: Mr. R. V. Williams and Dr. S. Kaufman 168

Reviews of Books 168

Part 2 *August* 1960

Mr. I. G. Austin. Infra-red Faraday rotation and free carrier absorption in Bi_2Te_3 169

Dr. R. Heastie and Mr. C. Lefebvre. Phase equilibria in condensed mixtures of argon and xenon 180

Dr. M. el-Nadi and Mr. M. Wafik. The direct inelastic scattering of deuterons . 185

PAGE

Dr. I. C. Percival. A variational principle for scattering phases 206

Dr. E. M. Reeves, Prof. R. W. Nicholls and Dr. D. A. Bromley. Optical excitation of N_2 by 0·5 to 1·5 Mev hydrogenic ions 217

Mr. A. N. Prasad and Prof. J. D. Craggs. Measurement of ionization and attachment coefficients in humid air in uniform fields and the mechanism of breakdown 223

Mr. D. E. Weston. Underwater explosions as acoustic sources 233

Mr. M. G. Haines. The Joule heating of a stable pinched plasma 250

Mr. J. F. Barnes and Dr. R. H. Tredgold. Field dependent electron mobility in ionic crystals 261

Mr. J. Sobhanadri. Calculations on ionic character and hybridization from dipole moments for AsF_3 and $AsCl_3$ 267

Dr. J. C. Anderson. Internal ferromagnetic resonance and magnetostatic modes in nickel–iron alloys 273

Mr. N. H. Saunders and Dr. R. S. Tebble. Magnetothermal effects in silicon–iron alloys 282

Research Notes:

Mr. S. K. Joshi and Dr. S. S. Mitra. Debye characteristic temperature of solids 295

Dr. K. W. Ogilvie. The half-value period of radium C′ 299

Mr. C. P. Flynn and Dr. E. F. W. Seymour. Knight shift of the nuclear magnetic resonance in liquid indium 301

Dr. P. H. E. Meijer. Note on the behaviour of a vapour–liquid system above and below the critical point 303

Letters to the Editor:

Prof. W. Low. Paramagnetic resonance spectrum of dysprosium in the cubic field of calcium fluoride 307

Dr. R. F. Pearson and Dr. R. W. Teale. Magnetic resonance and magnetocrystalline anisotropy in ytterbium iron garnet 308

Reviews of Books 311

Mr. R. A. Padmanabhan and Dr. E. L. Heasell. Ultrasonic relaxation in triethylamine 321

Dr. I. C. Percival. Waves in a conducting sheet situated in a strong magnetic field 329

Dr. P. K. Carroll and Dr. H. E. Rubalcava. Rotational analysis of the 5–1 band of the B′–B system of N_2 337

Dr. B. Dejon and Dr. K. Smith. Shadow effect in the scattering of Gev pions and nucleons by deuterons 346

Mr. B. R. Joshi and Dr. G. M. Lewis. On the measurement of orbital electron capture with particular reference to ^{131}Cs 349

Dr. D. M. Finlayson, Dr. I. S. Robertson, Dr. T. Smith and Dr. R. W. H. Stevenson. The optical absorption in manganese–zinc fluoride single crystals near the Néel temperature 355

Mr. M. S. Bhalla and Prof. J. D. Craggs. Measurement of ionization and attachment coefficients in carbon dioxide in uniform fields 369

Dr. J. M. Cowley and Mr. A. F. Moodie. Fourier images IV: the phase grating 378

Dr. P. D. Southgate. Internal friction in germanium and silicon I: electron and impurity relaxation 385

Part 3 (*cont.*) *September* 1960

PAGE

Dr. P. D. Southgate. Internal friction in germanium and silicon II: oxygen movement and dislocation damping 398

Research Notes:

Dr. A. R. Johnston and Prof. K. G. Emeleus. Note on a pinch effect in a low-pressure arc 409

Dr. E. W. Lee and Dr. R. R. Birss. The magnetostriction of lithium–chromium ferrite in the neighbourhood of its compensation point 411

Dr. G. S. Verma. Second dislocation relaxation peak in aluminium at low temperatures 412

Dr. C. Hilsum. Polar scattering in III–V compounds 414

Mr. S. B. Karmohapatro. Charge exchange between argon ions and atoms . 416

Prof. A. G. McLellan. Selection rules for spin–orbit matrix elements for the configuration f^n 419

Dr. A. Dalgarno. The stopping powers of atoms 422

Prof. E. Wolf. Correlation between photons in partially polarized light beams 424

Dr. J. G. Rutherglen. Asymmetry in scattering of 90–140 Mev polarized protons from nuclear emulsion material 427

Dr. J. G. Rutherglen and Mr. J. K. Walker. The photoproduction of charged pions from deuterium 430

Dr. H. S. Perlman. Relativistic K shell stopping power theory 433

Letters to the Editor:

Dr. Gy. Gergely. On the Ehrenberg–Franks experiment relating to the penetration of electrons into luminescent material 437

Mr. D. I. Porat and Mr. K. Ramavataram. A proposed method for measuring ranges of heavy ions in solids 438

Dr. M. S. Sodha. Estimation of inelastic collision cross section from electron mobility measurements 439

Reviews of Books 442

Part 4 *October* 1960

Dr. P. J. Eccles. Singly scattered delayed electrons in extensive cosmic ray air showers 449

Dr. S. Simons. Resistance anisotropy at low temperatures 458

Mr. A. C. Prior. A reversed carrier transport effect in germanium 465

Dr. C. B. Wilson. A phenomenological theory of the characteristic energy losses of fast electrons in metals. 481

Dr. H. C. Newns. On the stripping of two nucleons. 489

Miss C. Rhys-Roberts and Dr. R. H. Tredgold. A note on the theory of space charge limited currents 497

Dr. R. R. Birss and Dr. E. W. Lee. The saturation magnetostriction constants of nickel within the temperature range −196° to 365°C 502

Dr. I. H. Khan. On the polymorphism of the thallium halides. 507

Mr. P. V. K. Porgess and Dr. H. Wilman. Surface re-orientation, friction and wear, in the unidirectional abrasion of graphite 513

Mr. C. P. Flynn and Dr. E. F. W. Seymour. Nuclear quadrupole coupling with conduction electrons in cubic alloys 526

Mr. T. L. John. The numerical solution of the exchange equations for slow electron collisions with hydrogen atoms 532

PAGE

Mr. D. W. L. Sprung and Dr. J. B. Willis. The spin–orbit potential in proton–proton scattering 539

Dr. S. Hinds and Dr. R. Middleton. A study of the $^{27}Al(^{3}He, d)^{28}Si$ reaction . 545

Dr. S. Hinds and Dr. R. Middleton. The energy levels of ^{24}Mg and ^{32}Si . . 553

Dr. K. Smith, Dr. W. F. Miller and Mr. A. J. P. Mumford. The elastic and inelastic scattering of electrons and positrons from the s-states of atomic hydrogen 559

Research Notes:

Dr. T. S. Moss and Mr. T. D. H. Hawkins. Interband photoconductivity in germanium 565

Mr. R. Carey. Measurements of optimum domain widths in silicon–iron . 567

Mr. R. Beer and Dr. L. Bovey. The hyperfine structure of some uranium and americium lines in the 1·6–2·1 micron region 569

Dr. B. Donovan. Note on the treatment of impurity scattering in optical absorption in semiconductors 574

Dr. C. J. Batty. Total and absorption cross section for high energy pions . 577

Letters to the Editor:

Prof. E. A. Guggenheim. The equilibrium distribution of N atoms on N sites (or in N cells) 580

Reviews of Books. 582

Mr. C. J. Powell. The origin of the characteristic electron energy losses in ten elements 593

Mr. B. A. Robson and Mr. D. Robson. Spin–orbit effects in the inelastic scattering of 12 MeV neutrons in carbon 611

Dr. H. S. Perlman. The relativistic theory of K ionization by electrons . . 623

Dr. W. N. Asaad. Relativistic K electron wave functions by the variational principle 641

Mr. N. R. Ranganathan and Dr. R. Vasudevan. The stochastic problem of electron–photon cascades including polarization 650

Mr. S. K. Majumdar. Electrodynamics of a charged particle moving through a plasma without magnetic field 657

Dr. P. J. Dean, Dr. P. J. Kennedy and Dr. J. E. Ralph. Particle excited luminescence in diamond 670

Dr. J. E. Ralph. Radiation induced changes in the cathodoluminescence spectra of natural diamonds 688

Mr. J. H. Pace, Mr. D. F. Sampson and Dr. J. S. Thorp. Spin–lattice relaxation times in ruby at 34·6 Gc/s 697

Dr. O. Klemperer and Dr. A. Thetford (with a note by Dr. F. Lenz). Transmission of slow electrons through thin films 705

Dr. C. J. L. Booker and Dr. J. L. Wood. Further electrical effects of the adsorption of water vapour by anodized aluminium 721

Dr. B. F. Figgins. The specific heats of solid argon and an equimolar argon–krypton mixture 732

Dr. I. S. Grant. Radiative transitions in ^{8}Be 737

Dr. C. F. Barnaby and Dr. J. C. Barton. Performance of large area scintillation counters 745

PAGE

Prof. L. F. Bates and Mr. R. Carey. Domain patterns on 'cube-textured' silicon–iron sheet 754

Dr. B. S. Sood. Multipolarity and character of 961 kev resonance and 840 kev fluorescence radiation in ^{152}Sm 759

Dr. R. M. Glaister and Dr. H. F. Kay. An investigation of the cubic–hexagonal transition in barium titanate 763

Research Notes :

Mr. H. J. Wintle. The effect of attenuation on the acoustic resonant frequencies of gases in tubes 772

Dr. G. S. Verma and Mr. S. K. Joshi. Nuclear resonance absorption of ultrasound in KI and KBr 776

Dr. B. Dayal and Mr. S. P. Singh. Correct enumeration of vibration frequencies in the Brillouin zone 777

Dr. A. E. D. Heylen. Calculated electron mobility in hydrogen 779

Dr. H. K. Henisch and Dr. B. R. Marathe. A note on electroluminescence due to carrier accumulation 782

Dr. R. H. Jones. Hall coefficient and electrical conductivity measurements on lead selenide single crystals grown from the vapour 783

Dr. R. J. Elliott. Speculation on the centres formed by nitrogen in diamond 787

Dr. C. Curry and Mr. D. J. McNeill. Soft x-ray emission spectra of some transition and noble metals 791

Dr. Y. P. Varshni and Mr. R. C. Shukla. On Pauling's theory of alkali halide molecules 794

Dr. E. Fatuzzo. Switching properties of tetramethylammonium-trichloromercurate 797

Letters to the Editor :

Mr. N. K. Nayyar and Mr. G. S. Murty. The stability of an infinitive gravitating cylinder of paramagnetic material in the presence of magnetic field . 800

Dr. E. H. Putley. Impurity photoconductivity in n-type InSb 802

Dr. S. Doniach. Catalytic magnetization of atomic hydrogen? 806

Corrigendum:

Mr. N. Anderson. Compression waves in a plasma in a magnetic field . 808

Reviews of Books 809

Dr. R. Cooper, Mr. R. M. Higgin and Dr. W. A. Smith. The influence of ionic conductivity on the electric strength of KCl and NaCl 817

Dr. W. E. Spear. The hole mobility in selenium 826

Dr. Anne Pery-Thorne and Dr. W. R. S. Garton. Absorption of Krypton in the extreme ultra-violet 833

Mr. D. S. Pešić. Isotope effect in band spectra of magnesium oxide . . 844

Mr. H. J. Pain and Mr. P. R. Smy. Magnetic field interactions with shock ionized argon 849

Mr. J. L. Robins and Dr. J. B. Swan. Characteristic electron energy loss spectra of the transition metals, Ti to Cu 857

Dr. E. H. Linfoot. Wave-theoretic and ray-theoretic contrast transmission functions 870

PAGE

Mr. W. B. Bonnor. The field of an electric current in general relativity . . 891

Dr. D. L. Greenaway. Infra-red investigation of the acceptor levels formed by copper in germanium 900

Dr. R. Englman. The discontinuities in the solutions of the transport equation and the variational principle 909

Dr. A. A. Jaffe, Dr. F. de S. Barros, Dr. P. D. Forsyth, Dr. J. Muto, Dr. I. J. Taylor and Mrs. S. Ramavataram. Some (t, p) reactions in light nuclei . 914

Dr. J. C. Lisle and Dr. P. F. D. Shaw. Gamma radiation following resonant proton capture by chlorine 929

Mr. S. J. Fray, Dr. F. A. Johnson and Dr. R. H. Jones. Lattice absorption bands in indium antimonide 939

Miss Daphne F. Jackson. Form factors of the nucleus ^{6}Li. 949

Dr. R. B. Banerji. Anisotropy in ionospheric diffraction and its effect on drift measurement 959

Mr. W. S. Carter. The specific heats of two polymorphic forms of manganous sulphide, and the inferred possibility of antiferromagnetic ordering in stacking faults 969

Mr. J. S. M. Harvey, Dr. R. A. Kamper and Dr. K. R. Lea. Paramagnetic resonance absorption in bromine and chlorine 979

Research Notes:

Dr. G. L. Sewell. Electric conduction in antiferromagnetics . . . 985

Dr. B. H. Bransden and Mr. R. A. H. Hamilton. The elastic scattering of ^{3}He by ^{3}He 987

Dr. W. G. Henry. The Knight shift in alloys 989

Dr. R. C. Newman. The identification of precipitate particles in single crystals of silicon by reflection electron diffraction 993

Mr. G. D. Jones and Dr. W. A. Runciman. The infra-red absorption spectra of potassium manganicyanide and vanadium corundum . . . 996

Dr. D. R. Sweetman. The lifetime of the He^- Ion 998

Letters to the Editor:

Dr. B. V. Rollin and Mr. J. M. Rowell. Hot carriers in germanium . 1001

Corrigendum: Mr. D. W. L. Sprung and Dr. J. B. Willis 1002

Reviews of Books 1003

Subject Index, Vol. 76 1009

Index to Authors (with Titles), Vol. 76 1015

Index to Reviews of Books, Vol. 76 1022

PROCEEDINGS OF
THE PHYSICAL SOCIETY

VOL. 76, PART 1 — 1 July 1960 — No. 487

An Investigation of Extensive Air Showers, using Cerenkov Detectors

BY H. R. ALLAN, R. F. BEAMISH, D. A. BRYANT, H. KASHA† AND R. D. WILLS

Imperial College, London, S.W.7

MS. received 12th January 1960

Abstract. A method for studying extensive air showers is described, in which four detectors are used to record the Cerenkov light produced by the shower particles in tanks of water 20 cm deep. The size spectrum has been measured for shower sizes between 7×10^5 and 2×10^7 particles, and the results are in good agreement with those of other workers. The lateral distribution function appropriate to the Cerenkov detectors has been determined and found to be consistent, in the range $10\,\text{m} < r < 200\,\text{m}$, with the predictions of electron–photon cascade theory.

§ 1. INTRODUCTION

EXPERIMENTS carried out at the Massachusetts Institute of Technology (Clark *et al.* 1957) and Harwell (Cranshaw *et al.* 1958) have established that extensive air showers containing as many as 10^8 or 10^9 particles can arrive at sea level. The integral shower size spectrum, giving the flux of showers containing more than N particles, is of the form $KN^{-\gamma}$, where $\gamma \sim 1{\cdot}5$ to 2 over the range $N \sim 10^5$ to 10^8 particles, and this size spectrum can be related to the energy spectrum of the primary cosmic ray particles incident upon the earth's atmosphere. Estimates of the relation between primary energy and shower size at sea level give $E_{\text{primary}} \sim N \times 10^{10}$ ev to within a factor of 3 (Galbraith 1958); but this is true only on average, and large fluctuations may occur for individual showers (Oda 1960, Zatsepin 1960). Before the relation between primary energy and shower size can be found accurately, further knowledge of the details of shower structure is required.

From the astrophysical point of view, there is great interest in the detailed shape of the primary cosmic ray energy spectrum in the region 10^{15} ev to 10^{18} ev, since it is thought that primary particles of energy lower than 10^{15} or 10^{16} ev are produced within the galaxy while particles of higher energy may have an extra-galactic origin. One aim of experimental work is to detect the presence of a cut-off, or any irregularity in the primary energy spectrum, by measuring the size spectrum of extensive air showers with adequate precision.

The present paper describes some preliminary experiments towards this end. One difficulty in studying very large air showers is their low flux, and the corresponding need for large collecting areas. Showers containing more than 10^8 particles, for example, fall on an area of one square kilometre only once in two days, and the steep slope of the spectrum calls for a rapid increase in collecting area with increase in the shower size to be recorded. For the present experiment,

† Now at Technion, Israel Institute of Technology, Haifa.

a very modest collecting area of about 10^4 square metres only was used, a suitable site being conveniently accessible at the Imperial College Field Station, Silwood Park, Berkshire. Accordingly, the shower size spectrum has been examined in the region of N between 10^6 and 10^7 particles.

Accurate size measurement is essential for a detailed study of the spectrum: in the present experiment each shower size is measured to within 20%. This precision is obtained with a detecting array consisting of only four detectors. Each detector, moreover, is of very simple and economical construction. The same method of shower measurement could, therefore, be used to cover a very much larger collecting area without the cost becoming prohibitive.

Each detector consists essentially of a tank of water, the amount of Cerenkov light produced by the shower particles in the water being detected by a photomultiplier tube and recorded photographically as a pulse on a cathode ray oscilloscope. Such Cerenkov detectors are cheap in comparison with scintillator slabs or hodoscoped Geiger counter trays, and they have some merits of their own. Because of the detector thickness, the Cerenkov light output differs for different kinds of particles falling on the detector and for different particle energies. Cerenkov detectors thus do not measure the same characteristics of the shower as do Geiger counters or thin scintillator slabs. This is particularly the case at large distances from the shower axis, where the Cerenkov light output depends more upon the flux of incident photons than upon the electrons (§ 4.3). Since the photons are more numerous and carry more of the energy, this is a clear advantage in the measurement of shower size.

The Cerenkov detectors used in the present experiment have a depth of 20 cm of water. This depth is the minimum that allows a single particle traversing the detector to produce a measurable light signal at the photomultiplier: even so, the detector signal depends significantly upon incident particle energy. For electrons and μ-mesons, the energy must exceed 40 MeV to penetrate this depth, therefore particles of lower energy will not contribute their full quota of Cerenkov light. Each high energy photon may give 30% as much light as a fast μ-meson, through pair creation and Compton recoils. High energy electrons may contribute appreciably more light than μ-mesons, through the subsequent conversion of bremsstrahlung.

It follows from the above that the light produced in the detectors, and the voltage pulses delivered by them, are not proportional to the density of charged particles incident upon them. In most experiments on extensive air showers, however, it is just this density Δ which has been measured. The lateral distribution of the charged particle density is known to follow closely the function $f(r)$ calculated by Nishimura and Kamata (1950, 1951, 1952, Kamata and Nishimura 1958) for pure photon–electron cascades, with the age parameter s equal to 1·3 (Khristiansen 1956, Antonov *et al.* 1957, Rossi 1960). Thus

$$\Delta = Nf(r) \qquad \ldots\ldots (1)$$

where N is the shower size, i.e. the total number of charged particles at the level of observation.

For the Cerenkov detectors, equation (1) must be replaced by one describing the lateral distribution of the amount of Cerenkov light λ produced in 20 cm depth of water. We put

$$\lambda = Ng(r) \qquad \ldots\ldots (2)$$

where λ is regarded as a characteristic feature of the shower structure in its own right, and the function $g(r)$ is expected to be similar to, but not identical with, the Nishimura–Kamata function $f(r)$. It seems reasonable to assume that $g(r)$, like $f(r)$, is essentially independent of N: in other words that the energy spectra and relative numbers of the different shower components do not change with shower size. If they do change, the shower size spectrum obtained with Cerenkov detectors will differ from the spectrum obtained with a Geiger counter array: it would then be necessary to decide which distribution was a better guide to the energy spectrum of the primary particles.

The principles of operation of the array, some experimental details, and the results obtained, are described in subsequent sections. It is shown that the present method of shower detection gives the same shower size spectrum as was obtained by previous workers. It is also shown that the response of the Cerenkov detectors to shower particles is in general agreement with what would be expected from the calculations of Kamata and Nishimura (1958) on the lateral distribution of energy flow in pure electron-photon cascades.

§ 2. Principles of Operation of the Array

2.1. *Array Geometry*

The array consists of four Cerenkov detectors arranged as shown in figure 1. An array of the same geometrical pattern was used by Williams (1948) in an experiment employing ionization chambers. The advantage of this geometry

Figure 1. The detector array.

is that the showers recorded can be readily assigned to a definite collecting area (§ 2.5). The measurements reported in the present paper were obtained using detector spacings (i.e. the distance d in figure 1) of 30 m and 100 m.

2.2. *Shower Axis Location and Determination of $g(r)$*

The signals received from the detectors in the form of pulses are corrected for the different relative gains of the signal channels so that the signal S from each detector bears the same relation to the amount of Cerenkov light λ produced in the detector by shower particles. Writing $S=k\lambda$ in equation (2) we have

$$S=kNg(r). \qquad \ldots\ldots (3)$$

The determination of the relative gains of the signal channels, and the value of k, is described in §§ 3.3 and 4.2. If the function $g(r)$ is known, the four signals produced by each shower may be used to locate the shower axis.

For this purpose the assumption is made that showers fall vertically on the array, so that the distances r of equation (3) are measured along the ground, in the plane of the detectors. The validity of the assumption is considered in § 2.7. The signal ratio S_1/S_2 may now be used to construct a locus along which the axis of the shower must lie. A second signal ratio S_1/S_3 determines a second locus which in general intersects the first at two points. The signal from the fourth detector provides a further signal ratio, e.g. S_1/S_4, which is then used to remove the ambiguity in axis location. It also provides an indispensable check on the validity of the function $g(r)$ used in the analysis since, in the absence of statistical fluctuations in the recorded signals, the third locus should pass through one of the points of intersection of the other two. In practice, it is necessary to determine whether, on average, a failure of the three loci to intersect is due to statistical fluctuations, or to the inapplicability of $g(r)$.

2.3. *Shower Size Determination*

Once the shower axis is located, the shower size follows directly from equation (3) and any one of the recorded signals. It will be seen that only three signal measurements are used quantitatively in any one size measurement: consequently it is appropriate that the triggering condition for the array, which must be fulfilled before a shower is recorded, is that at least three of the detectors should register a signal greater than the smallest signal acceptable for use in the analysis. The criterion which determines the size of this trigger signal is discussed in the next section.

2.4. *The Trigger Signal*

It is clearly necessary that the signals from the detectors should be produced by a sufficiently large sample of the shower particles to have a statistical weight adequate for the determination of the shower size. Excessive statistical fluctuations will produce a distortion in the shape of the observed shower size spectrum, to an extent depending upon the statistical weight of the signals and the shape of the incident size spectrum. It can be shown that appreciable distortion is avoided if the size of individual showers is measured with an error of less than about 25%. To achieve this the errors in at least three signal measurements are required to be less than 20%. As the detectors respond not only to shower electrons but also, to some extent, to the accompanying photons (see § 4.3), the number of independent events producing each signal is larger than the number of incident electrons. For the 30 m array the trigger signal was set equal to the signal produced by the incidence of 20 electrons per detector and their accompanying photons; for the 100 m array it was set equal to the signal produced by the incidence of only 10 electrons per detector and their accompanying photons.

2.5. *Collecting Area*

In order to measure the flux of showers it is necessary to define a collecting area. The collecting area of the present array is the triangular area enclosed by the perpendicular bisectors of the lines joining the outer detectors to the

central one (see figure 1): its area is $1{\cdot}3d^2$, where d is the detector spacing. Showers whose axes fall within this area may be readily selected from the data by requiring the central detector to record a larger signal than any of the others. Limiting the collecting area in this way is not wholly arbitrary. The intersections of the loci which determine the position of the shower axis become oblique outside the triangle, producing large uncertainties in shower axis location and in size determination for small uncertainties in observed signal ratios. It does mean, however, that about one-half of the showers which are recorded by the array are rejected subsequently because their sizes cannot be measured sufficiently well. (In the present experiment, some account has been taken of the showers whose axes fall in the area between the collecting triangle and a circle of radius equal to the array spacing drawn about the central detector.)

In an array covering a much larger detecting area, a considerably smaller fraction of the showers would be rejected in this way. In such an array there

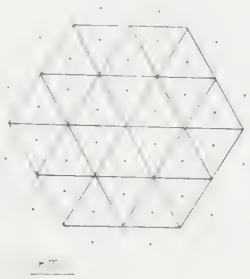

Figure 2. Proposed large array.

would be many detectors (figure 2) and each group of four would constitute a unit cell and define its own collecting triangle. Showers whose axes fell just outside the collecting triangle defined by one cell would generally be within the collecting triangle of an adjacent cell.

2.6. *Efficient Showers*

Only those showers which are able to satisfy the triggering condition imposed by the array wherever their axes fall within the collecting area can be used for a measurement of incident shower flux. Showers larger than a certain critical size N_0, which just meets this requirement, are referred to as 'efficient showers'. A shower has most difficulty in meeting the triggering requirements when its axis falls at one of the three positions M in figure 1. If S_0 is the trigger signal, the critical shower size is given from equation (3) by

$$kN_0 = \frac{S_0}{g(1{\cdot}3d)} \qquad \ldots\ldots(4)$$

where $1{\cdot}3d$ is the distance from M to the two furthest detectors. Showers smaller than N_0 may be able to trigger the array when their axes fall in preferred positions, but they are rejected in the course of the analysis.

Equation (4) determines the minimum shower size for which a flux can be measured in the two arrays with $d=30$ metres and $d=100$ metres. These minimum sizes are 7×10^5 and 5×10^6 particles respectively.

2.7. *Zenith Angle Effect*

The measurements of Clark (1957) show a zenith angle intensity distribution of the form $I(\theta)\,d\Omega = I(0)\cos^n\theta\,d\Omega$ where $n \simeq 10$. For such a distribution, the most probable zenith angle is 17·5°, and this means that distances measured in a horizontal plane are on average about 6% greater than the true radial distances from the shower axis. Furthermore, there will be a distribution in azimuthal angle, and this too will lead to distortions in the apparent lateral distribution if vertical incidence is assumed.

Although, in an experiment designed to examine the average behaviour of showers, the distribution of zenith angle can be allowed for on an average basis, it is clear that a study of the properties of individual showers would require the arrival direction of each shower to be recorded. One method of measuring the arrival direction is to record the time of arrival of the shower front at each of the detectors (Clark *et al.* 1957). The method of analysis described in the present paper can readily be adapted to use this additional information.

§ 3. Apparatus and Experimental Details

3.1. *The Cerenkov Detectors*

A scale drawing of a detector is shown in figure 3. The detector consists of a white 'Darvic' cylindrical tank, 20 cm deep and 0·6 m² in cross-sectional area, filled with water. A 2-inch diameter photomultiplier tube (E.M.I. 6097)

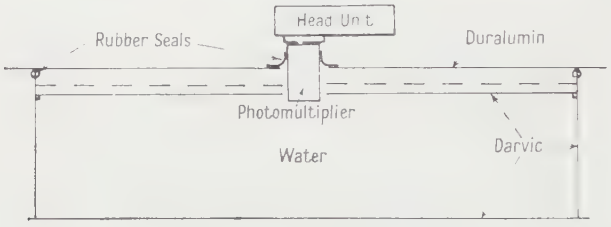

Figure 3. Cerenkov detector.

and its associated circuits record the Cerenkov light produced in the water by shower particles. The material used for the walls of the tank must have the property of diffusing light with a high coefficient of reflection in order that the light incident on the photomultiplier should be proportional to the total amount of Cerenkov light produced in the detector. It must also be chemically inert if the water is to remain clean over periods of months. The use of Darvic was suggested by Porter (1956, private communication). A duralumin disc and rubber seals prevent the escape of water vapour which might otherwise condense on circuit components. Each detector is enclosed by a thin metal box and housed with auxiliary apparatus in a small trailer.

3.2. *The Recording System*

Figure 4 shows a block diagram of the recording system. The output pulse from each photomultiplier head unit is transmitted to a central recording station where it is shaped to a rectangular pulse of 1 μsec duration by a shorted line consisting of 100 yards of coaxial cable. In order to provide an overall factor of 100 in pulse height measurement two oscilloscopes are used with different

gains. Each pulse is delayed before being displayed by the oscilloscopes so that the four pulses appear side by side on the screens. The oscilloscope traces are triggered by a master pulse and photographed with Shackman 35 mm cameras. A discriminator and coincidence unit receives the pulses from the detectors

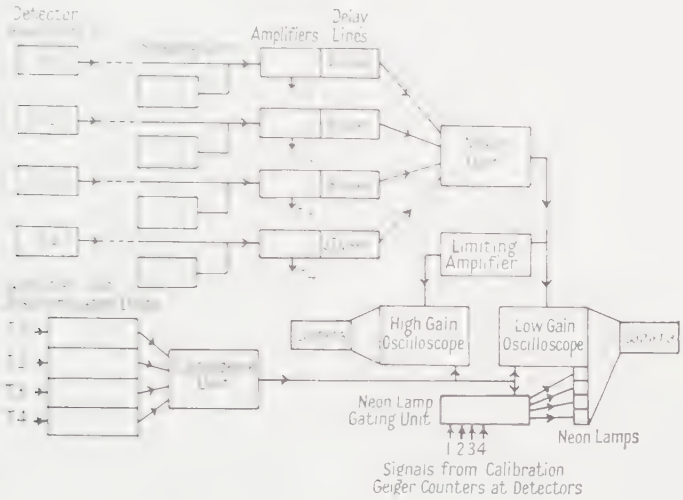

Figure 4. The recording system.

without delays. The master trigger pulse is produced when pulses greater than the trigger signal S_0 arrive simultaneously from the central detector (C1) and two others.

3.3. *Calibration Apparatus*

At each detector there is a calibration unit, consisting of two Geiger counter trays, each of area 180 cm², and a coincidence unit. When a Geiger counter coincidence occurs at the same time as a shower is recorded, the coincidence unit sends a pulse through a gate operated by the master trigger pulse, and so causes a neon indicator lamp to light up in the field of view of one of the cameras.

The probability of obtaining a two-fold coincidence in the Geiger counters when a flux of charged particles, density Δ, falls upon them is

$$P(\Delta) = (1 - e^{-a\Delta})^2 \qquad \ldots\ldots (5)$$

where a is the area of each counter tray. During the course of the experiment, data were accumulated on the relative frequency (i.e. the probability) with which the Geiger coincidences occur, as a function of the pulse height produced in the Cerenkov detector. By matching the observed distribution of probability against pulse height with the probability against density relation of equation (5) the relation between pulse height and particle density is obtained. To the extent that the lateral distribution functions of particle density and Cerenkov detector signal, $f(r)$ and $g(r)$, are different functions of r, this calibration is only an average one, appropriate to a particular range of r. It is shown in §4.2 how this calibration, which provides immediately the relative gains of the detectors, is used to determine the value of k in equation (3).

3.4. *Tests on the Cerenkov Detectors*

A μ-meson telescope, consisting of two 5-inch diameter scintillator slabs with photomultipliers, and a lead absorber 15 cm thick, was used to select single μ-mesons which penetrated the detector. The pulse height distribution produced by these particles was found to be broad, corresponding to the emission of between 1 and 2 photoelectrons at the photocathode on average. This number is rather small and must contribute to the statistical errors in the density measurements, but the effect is not serious. The use of a 5-inch diameter photomultiplier, or a deeper tank, would make the effect negligible. The mean pulse height from the detector varied by less than a factor of 2 as the μ-meson telescope was moved from near the centre of the tank to the circumference.

In a preliminary experiment with an array spacing of only 2 m, a pulse height distribution was obtained from each detector which showed excellent agreement with the density spectrum of small air showers obtained by Norman (1956) and other workers. By removing one of the detectors to a point 30 m from the other three, and requiring the distant detector to record the largest signal, it was possible to examine the signals produced in the group of detectors by showers whose axes fell at least 15 m from them. Under these conditions, where the particle density at the group of detectors was known to be sensibly uniform, the fluctuations in the recorded signals were consistent with those expected from the statistical weight of the signals.

In addition to giving confidence in the performance of the detectors, these measurements also provided a check on their relative gains, so that the main experiment could begin with approximately correct settings of the gain controls in the different signal channels.

3.5. *Operation of the Array*

406 showers were recorded on the array at a spacing of 30 m, and 256 showers were recorded at a spacing of 100 m. The measurements were taken intermittently between January and August 1959. Careful watch was kept on the stability of the amplifiers during this time with the aid of a pulse signal generator, and the overall gain in each channel was checked by looking for drifts in the Geiger counter calibration (particle density per unit pulse height). At the conclusion of the measurements, enough Geiger counter data were available to provide both the relative gains of the detectors and the absolute calibration in terms of particle density with an error of the order of 10%.

§ 4. Results and Discussion

4.1. *Lateral Distribution*

As has already been stated in § 1, the lateral distribution function $g(r)$ appropriate to the signals from the Cerenkov detectors is a characteristic feature of shower structure, which may be different from the distribution function for particle density $f(r)$. The function $f(r)$ is known to be given, to a close approximation, by the Nishimura–Kamata function for an age $s=1{\cdot}3$; the function $g(r)$ must be determined empirically from the experimental array data.

A method of finding the approximate form for $g(r)$, due to one of us (D. A. B.), is outlined in the Appendix: the function so determined was used as a trial function in equation (3):

$$S=kNg(r).$$

For each shower, the procedure of § 2.2 yielded a best estimate of the position of the shower axis, and the signal amplitudes in the four detectors then provided four estimates of kN, the shower size in arbitrary units. The mean $k\overline{N}$ was taken as the most probable value, and the ratios $S/k\overline{N}$ were plotted for comparison with $g(r)$.

Empirical adjustments were made to the shape of the trial function $g(r)$ until a satisfactory statistical scatter of the points about the line was obtained (figure 5 (*a*)). The function so determined has the analytical form

$$g(r) \propto r^{-(1{\cdot}85+6{\cdot}1\times 10^{-6}r^2)} \qquad \ldots\ldots (6)$$

where r is in metres, and the expression is valid over a range of r from 10 metres to 200 metres. Values of $g(r)$ found for smaller values of r are liable to error

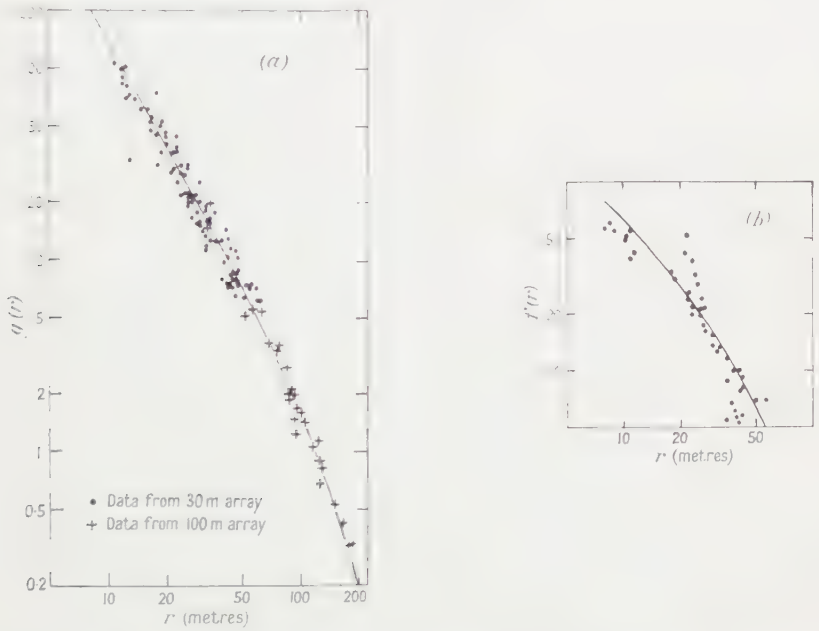

Figure 5. (*a*) Experimental verification of the function $g(r)$; (*b*) comparison of experimental data from the 30 m array with the Nishimura–Kamata function for $s = 1{\cdot}3$.

since, as an effect of statistical fluctuations, the position at which a shower axis is located tends to be systematically too far away from a detector when the true position is in fact very close.

The function $g(r)$ has a shape very similar to that of the particle density distribution $f(r)$ when r is greater than 40 metres, as can be seen from figure 6. For smaller r the difference is quite significant. In figure 5 (*b*) the shower data from the 30 metre array have been analysed on the assumption that the correct form for $g(r)$ is the Nishimura–Kamata function for $s = 1{\cdot}3$; the scatter of the points is much greater than in figure 5 (*a*).

The interpretation to be placed upon the shape of $g(r)$ is discussed in § 4.3.

4.2. *Shower Sizes*

The analysis of the lateral distribution (§ 4.1) provides relative shower sizes $k\overline{N}$ only. To determine the value of k, use was made of the Geiger counter calibration (§ 3.3). In this calibration, pulse heights from the Cerenkov

detectors are matched against probabilities of discharging a Geiger counter array. The matching depends particularly on the pulses for which the corresponding Geiger discharge probabilities lie between 0·2 and 0·8. The distances between shower axis and detector for such pulses (as determined in § 4.1) fall in a narrow range (90–120 metres for the 100 m array); accordingly the calibration gives $\Delta_1 S$ at a distance of 105 metres from the shower axis. Thus from a comparison of equation (1) and equation (3)—in which $f(r)$ is the Nishimura–Kamata function —the value of k was obtained. The accuracy depends mainly upon the accumulation of statistics, and in the present work was about 15%.

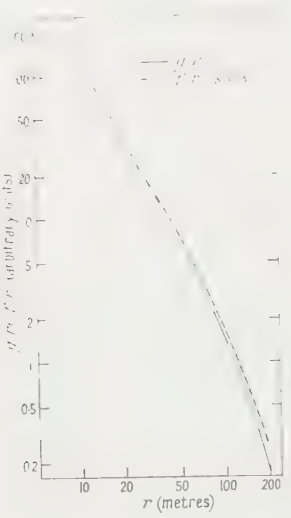

Figure 6. Comparison of the empirical structure function $g(r)$ with the Nishimura–Kamata particle density distribution $f(r)$ for $s = 1{\cdot}3$.

Figure 7. The integral size spectrum.

The accuracy of shower axis location was within about 4 metres for the 30 metre array and 6 metres for the 100 metre array. The numbers do not change in proportion, because of the shape of $g(r)$. The overall accuracy in kN for an individual shower measurement was within 20% Checks were made which confirmed that the 'efficient' showers (§ 2.6) fell uniformly over the collecting area.

The experimental results give only the number of showers above a given size per unit area per unit time. The zenith angle distribution measured by Clark (1957) was used to determine the effective solid angle for collection, which was 0·56 steradian. The size spectrum could therefore be plotted in the conventional manner, vertical flux per unit solid angle.

The integral size spectrum derived by combining the results from the two arrays is shown in figure 7, where each of the points plotted is independent and the total number of showers represented is 102. It is given by

$$k(\geqslant N) = (6{\cdot}8 \pm 0{\cdot}4)10^{-5}(N \times 10^{-6})^{-1{\cdot}83 \pm 0{\cdot}18}\ \mathrm{m^{-2}\,h^{-1}\,sterad^{-1}} \qquad \ldots\ldots (7)$$

over the range of N from 7×10^5 to 2×10^7 particles. Over this range it is in excellent agreement with the measurements of other workers (Clark *et al.* 1957,

Cranshaw *et al.* 1958, Rossi 1960) despite the differences in measuring technique. Since the measurements are essentially measurements of different components in the shower structure, this agreement helps to confirm the assumption that the average shower structure is independent of shower size. Tests with detectors considerably thicker would be valuable to check this point further. The chief conclusion to be drawn, however, is that the Cerenkov detector array provides a reliable, as well as a simple, way of measuring the shower size spectrum.

4.3. *Detector Characteristics: Shower Particle Energies*

It was pointed out in § 1 that the output from a Cerenkov detector depends upon both the nature of the incident particle and its energy. While both electrons and photons may participate in cascade multiplication, a μ-meson (if its energy exceeds 40 Mev) will simply pass straight through and contribute 20 cm of track length to the sources of Cerenkov light. We take the light output per μ-meson as the unit with which to measure the sensitivity of the detectors to other particles.

Measurements were made of the signal produced when single μ-mesons passed through the detector: the technique is described in § 3 in connection with tests of the optical properties of the detector. Although the statistical spread was considerable, it was possible to obtain a value for the average detector signal per μ-meson.

Now the Geiger counter calibration provides a value for S/Δ at distance r_0, S being the detector signal when the density of shower particles is Δ as measured by the Geiger counters (§ 4.2). We can thus compare the detector signal per incident electron with the pulse height per μ-meson. This ratio we call $n(r)$: it is shown in figure 8. The dependence of $n(r)$ upon r is clearly given by the ratio of the two distribution functions $g(r)\,f(r)$: the importance of the μ-meson

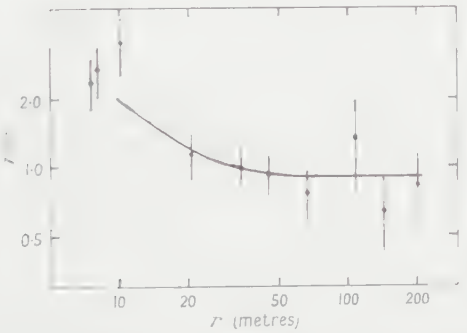

Figure 8. The function $n(r)=f(r)/g(r)$. The full line is determined from figure 6. The points are derived from those of figure 10.

calibration is that it gives the absolute magnitude of $n(r)$. It is difficult to determine $n(r)$ with precision, since not only is the observed $g(r)$ subject to error, but so is $f(r)$, which corresponds, according to different authors (Clark *et al.* 1957, Cranshaw *et al.* 1957, Antonov *et al.* 1957, Rossi 1960) to Nishimura and Kamata age parameters between $s=1{\cdot}25$ and $s=1{\cdot}4$. A value of $s=1{\cdot}3$ has been used in what follows.

It will be seen that $n(r)\simeq 1$ for large r, but is appreciably greater than 1 for $r<20$ metres. Similar effects have been observed by Brennan *et al.* (1958), Wallace (1960) and Oda (1960), when using scintillator slabs of 5–10 cm thickness.

The following considerations show how this could arise. We begin by considering the region of large r (~ 100 metres), where $n(r) \simeq 1$. In a comprehensive paper on photon–electron cascades, Kamata and Nishimura (1958) have suggested that the electrons at considerable distances from the shower axis ($\geqslant 100$ metres) are of low energy and do not radiate. These electrons are produced (mainly by the Compton process) from relatively low energy photons which have travelled from an origin close to the shower core. Suppose, then, that we are dealing, both in the detector and in the atmosphere above it, with straightforward photon absorption; then, since air and water are similar in absorption characteristics, we may assume that the 'beam' is attenuated uniformly through both with its characteristic absorption length x_0.

A value of $x_0 = 60\,\mathrm{g\,cm^{-2}}$ is appropriate to a fairly wide range of photon energies and represents the minimum absorption. If we write E as the energy carried into the detector by the photon beam, and ϵ the ionization loss of the secondary electrons per unit track length, then the energy absorbed in thickness $dx\,\mathrm{g\,cm^{-2}}$ of either air or water is $E\,dx/x_0$ and the resulting electron track length is $(E/\epsilon)(dx/x_0)$. The number of individual electrons which must traverse the thickness dx to produce this track length is $E/\epsilon x_0$, and this therefore is the electron flux that would be measured by, for instance, thin-walled Geiger counters. (If there is appreciable obliquity of the electron tracks to the direction of the beam, the number of electrons will be smaller. However, Compton recoil angles are mostly less than 10° for photon energies greater than a few MeV, so that the effect is not likely to exceed 1%.) In a thickness of detector x small enough for the decrease in E with depth to be negligible ($x \ll x_0$), the total track length produced by the photons is $(E/\epsilon)(x/x_0)$. But x is now the track length per μ-meson; accordingly the equivalent number of μ-meson tracks is $E/\epsilon x_0$, which is just the same as the electron flux. Thus $n(r) = 1$. With a detector of thickness $20\,\mathrm{g\,cm^{-2}}$, as in the present experiment, a straightforward correction leads to an expected value for $n(r)$ of 0·9, which is consistent with the experimental data of figure 8.

We conclude that the experimental value of $n(r)$ is in accord with the theory of Kamata and Nishimura and that in the region about 100 metres from the core the electron component is wholly secondary to the photons. The electron and photon quantum energies cannot exceed a few tens of MeV. It follows immediately that the number of photons is greater than the number of electrons, in the ratio of their path lengths. This too is reflected in Kamata and Nishimura's calculations of energy flux, which give more than ten times the energy of the electrons to the photon component. Evidence for the large number of photons comes in the present experiment from the relative smallness of the fluctuations in the detector signal measurements (§ 4.1), even with the 100 metre array, where the trigger signal was as low as ten electrons per detector. It is clear that the Cerenkov detector outputs depend on a much larger number of independent events than would be counted by a Geiger tray.

Having thus found an interpretation of the value of $n(r)$ shown in figure 8 for large values of r, we turn to the region $r \sim 10$ metres to 20 metres, where $n(r) \sim 1{\cdot}5$ to 2. Here we must suppose that cascade processes are dominant. In simple cascade theory (Approximation A, and very high energies) one expects the number of photons to exceed the number of electrons in the ratio 9/7. In a more realistic approximation Kamata and Nishimura (1958) calculate the relative flux of energy in the photon and electron components as a function of r.

At $r \sim 10$ metres they find the average electron energy to be about 100 Mev and the corresponding flux of energy in the photon component to be 1·6 times larger. This ratio is the same as the photon-electron number ratio calculated by Richards and Nordheim (1948) for energies in excess of 100 Mev, and we may make a rough picture by supposing that the electron and photon energies at approximately 10 metres from the axis are both 100 Mev, and that there are 1·6 photons per electron.

The electron track length produced by such an incident flux was estimated on the basis of cascade calculations by Arley (1938). The radiation length in water is $38\,\mathrm{g\,cm^{-2}}$, so the depth of the detector is about half a radiation length. In this length, high energy photons give about 0·3 times the track length produced by a μ-meson. An electron of a few hundred Mev gives about 1·1 track lengths. It is thus expected that the total track length per electron incident upon the detector should be approximately 1·5, but not much larger.

The calculations accordingly predict that $n(r)$ should equal about 1·5 for values of r less than about 10 metres. Between 10 metres and 100 metres, $n(r)$ should fall smoothly to a value of about 0·9, and for larger values of r it should remain constant. The experimental data (figure 8) are broadly in agreement with these predictions, but the range of variation in $n(r)$ is rather greater than expected, and values of $n(r)$ greater than 2 are found for $r \leqslant 10$ metres. The discrepancy may possibly be attributed to experimental errors in the determination of $g(r)$, but if so the errors are larger than expected. It was mentioned in § 4.1 that, for small values of r, shower locations are subject to a systematic error, which would have the effect of increasing both the apparent $g(r)$ and the $n(r)$ derived from it. However, the systematic error is thought to be small for r greater than 8 metres. An alternative explanation of the discrepancy is that the function $f(r)$—the Nishimura–Kamata function for $s = 1{\cdot}3$—does not correctly describe the particle density distribution function at $r \sim 10$ metres. An age parameter $s = 1{\cdot}2$ would give $n(r) = 1{\cdot}5$ at $r = 10$ metres, which is quite satisfactory. An age parameter, $s = 1{\cdot}4$, much used at one time, requires $n(r) = 2{\cdot}7$ at $r = 10$ metres, and is certainly inconsistent with the present results.

4.4. *General Comments*

The values of $n(r)$ calculated above relate to Cerenkov detectors in which the shower particles have to traverse 20 cm of water. For counters of different thickness, the trend in $n(r)$ will be similar, but the limiting values for small and large r will be different. Whatever the thickness, however, $n(r)$ will be a constant for r greater than 100 metres, and for such distances the detector will give a lateral distribution function $g(r)$ of the same shape as the true particle density function $f(r)$. For smaller values of r, $g(r)$ will become progressively steeper than $f(r)$ as the detector thickness is increased. The limit will be reached when the detector is thick enough to be essentially a detector of energy flux: according to Kamata and Nishimura $g(r)$ is then roughly one power of r steeper than $f(r)$.

These considerations hold for scintillation detectors as well as for Cerenkov detectors, in so far as their response is proportional to electron track length in the scintillator material. They serve to explain why the M.I.T. group (Rossi 1960) obtain what are essentially particle density distributions when using 10 cm thick scintillator slabs at large distances from the shower axis, whereas both Oda (1960) and Wallace (1960) find discrepancies between the indications of

scintillation counters and Geiger counters close to the shower axis. Wallace points out that the nucleonic component may be partly responsible for his effects, but this cannot be the explanation in the case of Cerenkov detectors.

The μ-meson component in extensive air showers is sufficiently penetrating to pass through several metres of water without attenuation: for μ-mesons $n(r)$ is therefore equal to 1. A Cerenkov detector much thicker than the photon absorption length of 60 cm water, can have $n(r)$ for the electron–photon component much less than 1, say about 0·5 for a depth of about 1 metre. Accordingly, such a detector will have an output which depends preferentially on the μ-meson component. This feature could be useful in tracing the lateral distribution function of the μ-mesons and in determining the proportion of μ-mesons in showers as a function of shower size.

Acknowledgments

The authors wish to thank Professor P. M. S. Blackett, in whose laboratories this work was carried out, for his continuing interest and support. They are most grateful to Dr. H. Elliot, who suggested the experiment, for many helpful discussions. Much of the preparatory work was done in conjunction with Dr. A. Goodings.

The authors owe special thanks to Mr. G. Cescotti for his help with the design and maintenance of the electronic equipment. The staff of the Imperial College Field Station at Silwood Park have been unfailingly generous in providing the necessary facilities.

R. F. B. and R. D. W. owe thanks to the Department of Scientific and Industrial Research for maintenance grants; H. K. wishes to thank the British Council for a Scholarship which enabled him to participate in the experiment.

APPENDIX

Determination of the Empirical Structure Function $g(r)$

We are presented with the problem of finding a function $g(r)$ which will give consistency between the Cerenkov detector signals S_1, S_2, S_3 and S_4 it being assumed that the output signals S (adjusted to equal gains in the four channels) are given by equation (3)

$$S = kNg(r). \qquad \ldots\ldots (3)$$

Merely by assuming that the function $g(r)$ is a monotonically decreasing function of r, we can use inequalities of the type $S_1 > S_2$, $S_3 > S_4$ etc. to locate each shower axis within the collecting triangle in one of the six subsidiary triangles shown in figure 9. Since the array is symmetric with respect to the detectors C2, C3 and C4, one can then relabel the S's and locate the axes of equivalent showers in just one of these areas (A) with $S_1 > S_2 > S_3 > S_4$.

Now consider the distribution of the ratio S_2/S_1 among different showers. Shower axis positions which yield a particular value for S_2/S_1 will all lie on a certain locus within the small triangle; all showers on that side of the locus nearer to the central detector (recording S_1) will yield a smaller ratio, while all those further away will yield a larger ratio. For the small range of distances involved on a given locus one can assume that S_2/S_1 is a function of r_2/r_1 so that a locus which has r_2/r_1 constant is also a locus for a fixed ratio S_2/S_1. Showers whose axes fall on the particular locus $r_2/r_1 = x$ such that one-half of all the shower axes fall to one side of this locus and half to the other, must therefore be

responsible for the median value in the distribution of the values of S_2/S_1. If the analysis is limited to the efficient showers (§ 2.6), we know that equal areas in the triangle contain equal numbers of the axes of recorded showers.

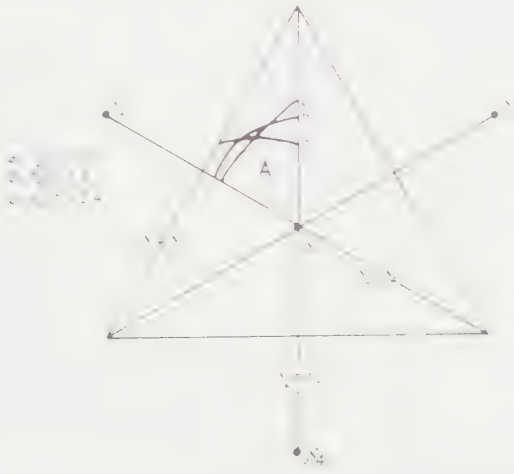

Figure 9. Determination of trial function for $g(r)$. The loci $r_2/r_1 = 1{\cdot}5$ etc. each divide the subsidiary triangle A into two equal areas. (The line marked $S_2 = S_4$ *should read* $S_3 = S_1$.)

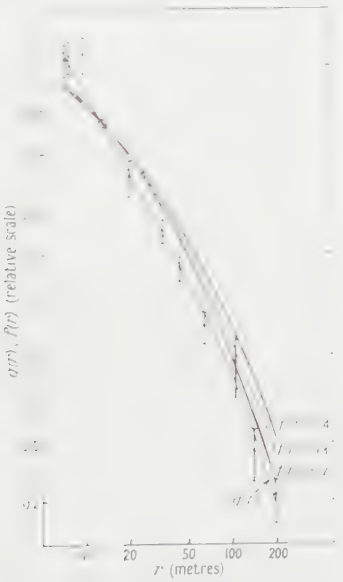

Figure 10. Experimental points obtained by the method described in the Appendix compared with $g(r)$ and with the Nishimura–Kamata functions for $s = 1{\cdot}2$, $1{\cdot}3$ and $1{\cdot}4$, referred to an arbitrary value at 13·5 metres.

Consequently, for efficient showers, the locus $r_2/r_1 = x$ which bisects the area of the small triangle defines the value of r_2/r_1 which yields the median value of S_2/S_1 in the distribution.

If we write $\bar{r}_1$ for the mean value of r_1 along the locus $r_2/r_1 = x$ inside the small triangle, we have

$$\frac{g(x\bar{r}_1)}{g(\bar{r}_1)} = \frac{S_2}{S_1}.$$

In a similar manner the distributions of S_3/S_1 and S_4/S_1, and partition values other than the median may be used to obtain further information about $g(r)$, and so a complete trial function may be constructed. Using this $g(r)$ the shower axes can all be located and kN determined for each.

If all the recorded showers are used for the above procedure it will be found that they do not fall uniformly over the area of the small triangle, since nothing has been done to eliminate those showers which are not 'efficient'. But rough estimates of shower size kN are nevertheless obtained and the smaller showers may then be removed from the data leaving only the efficient showers for which the above analysis is valid. The analysis may then be repeated to obtain a better approximation to $g(r)$.

In figure 10 the points indicate the information about $g(r)$ obtained by this method. It will be seen that it gives a close fit to the function finally adopted, and so can greatly reduce the labour which would be involved in finding the correct function purely by trial and error.

References

Antonov, I. N., Vavilov, I. N., Zatsepin, G. T., Kutuzov, A. A., Skvortzov, I. V., and Khristiansen, G. B., 1957, *Zh. Eksp. Teor. Fiz.*, **32,** 227.

Arley, N., 1938, *Proc. Roy. Soc.* A, **168,** 519.

Brennan, M. H., Millar, D. D., Rathgeber, M. H., and Wallace, C. S., 1958, *Nature, Lond.*, **182,** 1053.

Clark, G., 1957, Massachusetts Institute of Technology preprint, *Arrival Directions of Extensive Air Showers.*

Clark, G., Earl, J., Kraushaar, W., Linsley, J., Rossi, B., and Scherb, F., 1957, *Nature, Lond.*, **180,** 353, 406.

Cranshaw, T. E., de Beer, J. F., Galbraith, W., and Porter, N. A., 1958, *Phil. Mag.*, **3,** 277.

Cranshaw, T. E., Galbraith, W., and Porter, N. A., 1957, *Phil. Mag.*, **2,** 891.

Galbraith, W., 1958, *Extensive Air Showers* (London: Butterworth's Scientific Publications), p. 115.

Kamata, K., and Nishimura, J., 1958, *Suppl. Progr. Theor. Phys. Japan.*, **6,** 93.

Khristiansen, G. B., 1956, *Proc. Oxford Conf. Extensive Air Showers* (Harwell : Atomic Energy Research Establishment), p. 11.

Nishimura, J., and Kamata, K., 1950, *Progr. Theor. Phys., Japan,* **5,** 899.

—— 1951, *Ibid.*, **6,** 628.

—— 1952, *Ibid.*, **7,** 185.

Norman, R. J., 1956, *Proc. Phys. Soc.* A, **69,** 804.

Oda, M., 1960, *Proc. Moscow Cosmic Ray Conf. U.S.S.R.* (Moscow: I.U.P.A.P.), **2,** 30.

Richards, J. A., and Nordheim, L. W., 1948, *Phys. Rev.*, **74,** 1106.

Rossi, B., 1960, *Proc. Moscow Cosmic Ray Conf. U.S.S.R.* (Moscow: I.U.P.A.P.), **2,** 18.

Wallace, C. S., 1960, *Proc. Moscow Cosmic Ray Conf. U.S.S.R.* (Moscow: I.U.P.A.P.), **2,** 316.

Willliams, R. W., 1948, *Phys. Rev.*, **74,** 1689.

Zatsepin, G. T., 1960, *Proc. Moscow Cosmic Ray Conf. U.S.S.R.* (Moscow: I.U.P.A.P.), **2,** 192.

SCEPTRE III—An Intense Source of the Spectra of Highly Ionized Atoms

By A. S. KAUFMAN†, T. P. HUGHES AND R. V. WILLIAMS
Research Laboratory, Associated Electrical Industries Limited, Aldermaston, Berkshire

Communicated by A. A. Ware; MS. received 21st December 1959, in final form 22nd February 1960

Abstract. The present investigation draws attention to the potentialities of the high-current toroidal discharge assembly, SCEPTRE, as an intense source of the higher spectra. By way of illustration, several new classified lines of Ne IV, V and VI which have been observed in the range 2200 Å to 2300 Å are reported, thus permitting some revision of, and extension to, the analyses of these spectra. The complete F VI triplet $3s^3S–3p^3P^0$ has also been observed for the first time. Two new experimental methods of differentiating between the stages of ionization are given. With SCEPTRE, in contrast to conventional sources of spark spectra, gaseous samples are easily introduced into the deuterium plasma. Thus, such a discharge apparatus will be of value in exciting the spectra of the rare gases.

Experimental evidence is presented to show that the contribution of the Stark effect to the large observed widths of O V and F VI lines is very small. Consideration is also given to the detection of the coronal lines with SCEPTRE and to their value in studying ion motion within the plasma.

§ 1. INTRODUCTION

THE volumes of the *Atomic Energy Levels* (Moore 1949, 1952, 1958) testify to the achievement of many workers in the elucidation of atomic structure through the observation and classification of spectral lines. Yet even today many of the spectra of highly ionized atoms of the lighter elements have been inadequately analysed (for example, Ne VI) and some have not been analysed at all (for example, Ne VII) as the latest survey shows (Meggers 1959). Certain omissions are conspicuous in connection with the great interest in high-current discharges for thermonuclear research and, in particular, with the problem of proving the existence of high temperatures in these discharges (Hughes and Kaufman 1959). This problem can in principle be resolved by measuring the Doppler broadening of spectral lines for ions of different mass. However, in the spectral range above 2000 A the chief difficulty in attempting to apply this method in practice is the lack of suitable classified lines of ions with the requisite degree of ionization. Thus, there exists a practical need as well as an academic desire to add to our knowledge of the structure of highly ionized atoms.

† In former publications S. Kaufman; now at Department of Physics, The Hebrew University of Jerusalem, Israel.

The ring discharge has long been known as a spectroscopic source (Thomson 1891). It is the object of this paper to draw attention to the potentialities of high-current toroidal discharges as intense sources of the higher spectra. Working with the apparatus SCEPTRE III (Allen *et al.* 1958), some spectral lines hitherto only feebly excited have now been observed to be intensely bright, while several new lines of the Ne IV, V and VI and F VI spectra in the near ultra-violet region have been observed and classified. An account is also given of the experimental methods which may be used to differentiate between the stages of ionization.

§ 2. The Spectral Source

Following the observation of the excitation in SCEPTRE III of the O V triplet at 2781 Å and, to a lesser extent, of the C V triplet at 2271 Å, it was found that other highly ionized atoms could be excited. Certain impurities are easily introduced into the deuterium plasma in the form of a gas or vapour. Table 1 shows which elements have thus far been deliberately introduced and in what form. If the proportion of impurity to deuterium is excessive, the electron temperature may be lowered and the spectrum to be analysed will be weak or

Table 1. Elements introduced into the Plasma of SCEPTRE III

Element	Compound
Helium	
Boron	Boron trifluoride (BF_3)
	Diborane (B_2H_6)
Carbon	Methane (CH_4)
Fluorine	Boron trifluoride
Neon	
Argon	
Xenon	

completely absent. This effect was observed when too much boron trifluoride was added to the deuterium. The experience gained thus far indicates that a concentration of impurity *atoms* up to about 10% of that of deuterium is satisfactory. When the impurity-gas supply is turned off, the intensity of the corresponding spectral lines generally falls to one tenth of the original value after about 100 subsequent discharges. However, certain lines, such as the resonance lines of B III, are known to persist feebly for many more discharges.

§ 3. Identification of the Stage of Ionization

In conventional spectroscopic sources, such as vacuum sparks and Geissler tubes, spectra from different stages of ionization can be distinguished by altering the characteristics of the electrical circuit. It should be possible to do likewise with SCEPTRE III, for example, by reducing the quantity of energy supplied to the gas, but this has not yet been tried. However, two other methods can be employed.

In the first method the excitation of the spectral line, both temporally during the current pulse and spatially within the torus, is examined. In the present arrangement the line is selected by a Hilger quartz monochromator (focal ratio f/7) with a photomultiplier attachment. Oscillographic traces from ten successive

discharges are usually recorded superimposed on one photographic plate in order to average fluctuations in the luminous intensity. The spatial intensity distribution of the line across a section perpendicular to the torus axis is determined by scanning the vertical viewing window of SCEPTRE (Allen *et al.* 1958) with a narrow aperture and then applying the Abel integral equation to the intensity distribution obtained in this manner (Meek and Craggs 1953). Circular symmetry, assumed in the application of this equation, can be checked by similarly viewing the discharge through the horizontal window also mounted perpendicular to the torus axis. The determination of the spatial intensity distribution by graphical integration is tedious and a programme for the solution of the Abel integral equation by digital computer is now under consideration by Bockasten (private communication).

Figure 1 (Plate) shows that the Hα line makes its appearance early during the current pulse while the O v line, typical of highly ionized atoms, appears later and does not reach its peak intensity until the current is approximately at its maximum value. Comparison of spatial intensity distributions provides a further and more sensitive test of the stage of ionization. As shown in figure 2, the distribution for the O IV ion (ionization potential 77·4 eV) is quite different from that for the O V ion (ionization potential 113·9 eV). Variations in electron temperature for different discharge conditions can also be studied qualitatively in this manner by observing the relative strengths of spectral emission in different stages of ionization.

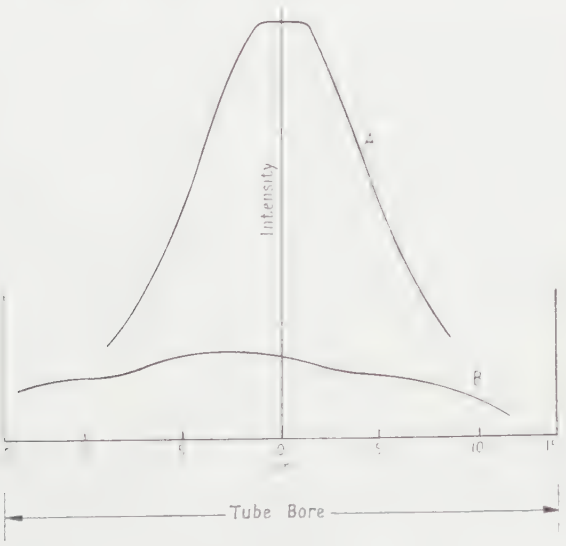

Figure 2. Spatial intensity distribution of O V and O IV lines. A: O V, 2781 Å, B: O IV, 3381 Å.

The second method of distinguishing between lines arising from atoms in different stages of ionization depends on comparisons of Doppler broadening. The dispersion of the Hilger medium quartz spectrograph (focal ratio approximately f·12) is adequate to permit measurement of the broadening of lines like the O V triplet. Exposure times of about one hour, corresponding to 1000 discharges at a repetition rate of twenty per minute, are sufficient to record the

O v triplet as intense lines. The photographic record represents the integrated light detected by the plate during the entire period of the current pulse.

It is found with SCEPTRE III that ions of the same element but in different stages of ionization possess different Doppler half-intensity widths. This dependence on ionization potential appears to be related to the spatial and temporal distributions of the emitting ions: the largest broadening is observed for those ions (for example, O v and B IV) which are predominantly excited on the torus axis and at a time when the current is at its maximum value. To cite one example: the Doppler half-widths of O v (2781 Å) and O IV (3072 Å) on the same spectrogram are 0·59 Å and 0·41 Å respectively after allowing for instrumental broadening.

§ 4. The Ne IV, V and VI and F VI Spectra

We now consider the classification of some of the new lines recorded with SCEPTRE III. Within the short range of about 100 Å between 2200 Å and 2300 Å new lines of Ne IV, V and VI were observed. The newly identified multiplets are presented to illustrate the potentialities of SCEPTRE as an intense source of the higher spectra and are not the only new neon multiplets detected in the spectral region above 2000 Å.

4.1. *Wavelength Measurement*

The spectral lines, recorded on Q3 photographic plates (by Ilford Limited), were scanned by a modified Hilger recording microphotometer fitted with an accurate micrometer screw. Almost all the wavelength standards were lines of Cu II and I (Shenstone 1936, 1949) produced by the discharge itself which was contaminated by copper and aluminium vapours from arc formation (Craston *et al.* 1958). Wavelengths, the means of triple readings, were measured with an accuracy to $\pm 0{\cdot}02$ Å (standard error) or better, except where stated in tables 3 and 4. The line of sight of the spectrograph was normal to the direction of the gas current, so that wavelength displacements observed for tangential viewing (Hughes and Kaufman 1959) were not anticipated. Confirmation was obtained from measurement of the C v line at 2271 Å (table 5).

4.2. *Ne IV*

The spectrogram displaying the new lines of Ne IV, V and VI was obtained from 300 discharges under the following conditions—deuterium at a partial pressure of 1·8 millitorr with neon at a partial pressure of about 0·2 millitorr, the capacitor bank charged to 25 kv, turns ratio 16 : 1, initial toroidal magnetic field of 500 oersteds and peak gas current of $7{\cdot}5 \times 10^4$ amp. The neon lines were recognized by comparison with other spectrograms obtained without the introduction of neon.

The terms relating to the Ne IV quartet $3s^4P$–$3p^4P^0$ are known from measurements in the vacuum ultra-violet region (Paul and Polster 1941). Two lines of this quartet were observed (table 2), thus confirming the term scheme and increasing the accuracy slightly. The full multiplet should be observed for a longer exposure time as was the case with the iso-electronic F III quartet. The observed Ne IV lines were distinctly broader than Ne III lines in close proximity.

Table 2. Ne IV Spectrum. Classified Lines and Revised Term Values

Int.	λ (air)	ν	Classification	Remarks
1	2220·81	45014·6	$2s^22p^2(^3P)3s\,^4P_{2\frac{1}{2}}$–$2s^22p^2(^3P)3p\,^4P_{1\frac{1}{2}}{}^0$	
2	2203·88	45360·3	$^4P_{2\frac{1}{2}}$– $^4P_{2\frac{1}{2}}{}^0$	dB

Desig.	J	Level	Interval
$3p\,^4P^0$	$1\frac{1}{2}$	*524666*	345
	$2\frac{1}{2}$	*525011*	

dB: observed by de Bruin (1932).

Table 3. Ne V Spectrum. Classified Lines and Extended Analysis

Int.	λ (air)	ν	Classification	Remarks
1	2306·6	43340	$2s^22p(^2P^0)3s^3P_2{}^0$–$2s^22p(^2P^0)3p^3D_2$	blend In II; E_1
1	2282·61	43796	$^3P_1{}^0$– $^3D_1$	E_2
6	2265·71	44123	$^3P_2{}^0$– $^3D_3$	blend Cu II; E_2
	[2263·6]	44164	$^3P_0{}^0$– $^3D_1$	blend Cu II
3	2259·57	44242·5	$^3P_1{}^0$– $^3D_2$	
0	2236·1	44707	$2s2p^2(^4P)3s^5P_1$–$2s2p^2(^4P)3p^5D_1{}^0$	blend Cu I; E_1
4	2232·41	44780·7	$^5P_3$– $^5D_4{}^0$	

Desig.	J	Level	Interval
$3s^3P^0$	0	[*596258*]	[368]
	1	*596626*	902
	2	*597528*	
$3p^3D$	1	640422	446
	2	640868	783
	3	641651	
$3p^5D^0$	0		
	1	*742214* + *x*	
	2		
	3		
	4	*743293* + *x*	

[ ], calculated. E_1, estimated error in wavelength of ±0·1 Å.
E_2, estimated error in wavelength of ±0·05 Å.

4.3. *Ne V*

The identification of the Ne V triplet $3s^3P^0$–$3p^3D$ (table 3) is fairly certain. The wavelengths agree with those obtained by extrapolation along the iso-electronic sequence. Also, the line widths were greater than those of Ne IV and the iso-electronic F IV triplet was strongly excited for similar discharge conditions. The intervals of the ^3P term fit the iso-electronic sequence better than the values derived by Paul and Polster (1941) while those of the ^3D term are also consistent with extrapolation along the sequence. However, no further check of the ^3D term is at present possible since the other multiplets related to it are expected at wavelengths less than 2000 Å.

Only two members of the Ne V quintet are identified (table 3). However, the identification appears to be fairly certain judging by the line widths and wavelength extrapolation along the C I sequence. The relative intensities of

the newly observed triplet and quintet also agreed with those of F IV for similar discharge conditions. The unobserved member $^5P_2$–$^5D_3{}^0$ was most probably obscured by the line Cu I 2227·775 Å. From the present data no improvement to the ^5P term (Moore 1949) is possible.

4.4. *Ne VI*

Three very broad lines are attributed to the Ne VI quartet $3s^4P^0$–$3p^4D$ (table 4). The identification is satisfactory in that their relative intensities are approximately in agreement with those of the iso-electronic F V lines and that there is a good fit

Table 4. Ne VI Spectrum. Classified Lines and Extended Analysis

Int.	λ (air)	ν	Classification	Remarks
[6]	2293·6	43586	$2s2p(^3P^0)3s\,^4P_{2\frac{1}{2}}{}^0$–$2s2p(^3P^0)3p\,^4D_{2\frac{1}{2}}$	blend Cu I; E_1
10	2258·02	44272·8	$^4P_{2\frac{1}{2}}{}^0$– $^4D_{3\frac{1}{2}}$	
7	2253·17	44368·1	$^4P_{1\frac{1}{2},\frac{1}{2}}{}^0$– $^4D_{2\frac{1}{2},1\frac{1}{2}}$	blend, Ne ?

Desig.	J	Level	Interval
$3s^4P^0$	$\frac{1}{2}$		
	$1\frac{1}{2}$	*833331*+*x*	782
	$2\frac{1}{2}$	*834113*+*x*	
$3p\,^4D$	$\frac{1}{2}$		
	$1\frac{1}{2}$		
	$2\frac{1}{2}$	877699+*x*	687
	$3\frac{1}{2}$	878386+*x*	

[ ], estimated. E_1, estimated error in wavelength of ±0·1 Å.

with extrapolation along the B I sequence. However, confirmation is required from further observations of lines related to these terms. The other strong members of the quartet were apparently obscured by interfering lines.

4.5. *Unclassified Neon Lines*

A number of additional neon lines are listed in table 5. The stage of ionization was estimated from their line widths.

Table 5. Additional Lines in the Range 2200 Å to 2300 Å

Int.	λ (air)	ν	Identification	Remarks
7	2285·79	43735·0	Ne IV	dB
6	2273·58	43969·9	Ne III	dB, KR
5	2270·89	44021·9	C V $2s^3S_1$–$2p^3P_2{}^0$	E
9	2264·54	44145·4	Ne IV or V	
9	2262·10	44193·0	Ne V or VI	

dB, observed by de Bruin (1932).
KR, recorded by Kayser and Ritschl (1939) as Ne III.
E, 2270·91 Å by Edlén (1952).

4.6. *F VI*

The complete F VI triplet $3s^3S-3p^3P^0$ (table 6) was observed for discharge conditions similar to those used for the observation of the neon lines.

Table 6. F VI Spectrum. Classified Lines and Extended Analysis

Int.	λ (air) (present)	ν	λ (air) (Edlén 1935)	Classification	
5	2327·28	42955·4	not observed	$2s(^2S)3s^3S_1-2s(^2S)3p^3P_0^0$	
7	2323·31	43028·8	2323·35	$^3S_1-$	$^3P_1^0$
9	2315·37	43176·3	2315·39	$^3S_1-$	$^3P_2^0$

Desig.	J	Level	Interval
$3p^3P^0$	0	790253	74
	1	790327	

It has been suggested that the broadening of lines like F VI and O V may be due to extraordinarily large electric fields present in the plasma and not to ion motion. If it is accepted that such fields could exist, then according to the theory of the Stark effect, such lines should be displaced from their zero-field position and the line widths of each member of the triplet should be different. In addition, the broadening of the O V triplet should be greater than that of the F VI triplet. The contrary was true. Edlén's values for the F VI wavelengths were confirmed. The half-intensity widths within the members of the triplets were practically identical and the F VI lines were broader than the O V lines.

§ 5. Discussion

In the earlier work on the spectra of highly ionized atoms, a spectroscopic source like a vacuum spark favoured the excitation of elements in solid form. Thus, it was possible to produce the Na VIII and Mg IX spectra but not the isoelectronic Ne VII spectrum which has a lower ionization potential. With SCEPTRE III the roles are reversed since the element is easily introduced as a gas or vapour. Hence, SCEPTRE is well suited to the excitation of the higher spectra of the rare gases.

Although SCEPTRE III is an intense source of even the weaker lines of the higher spectra, the presence of impurity lines impairs the accuracy of wavelength measurement because of the frequent occurrence of blends. This is particularly troublesome because of the large Doppler broadening present, which reduces the effective resolution on a spectrogram. The Doppler broadening in itself does not reduce the accuracy of measurement; the line profiles are symmetrical and their centres can be accurately determined on the microphotometer chart. Many of the impurity lines are of copper and aluminium in the first stages of ionization. Thus, their intensity should be reduced by recording the light emitted during the period about maximum gas current. It may also be possible to reduce the degree of Doppler broadening by a suitable selection of discharge conditions, without affecting the degree of ionization.

Should the electron temperature in SCEPTRE rise to about 7×10^5 deg K attempts could be made to record the strongest of the coronal lines with a large-aperture spectrograph. The detection of some forbidden lines from high-current

discharges has already been considered (Kaufman 1957). For the more highly ionized atoms, such as A XI, the spontaneous transition probability is relatively large, so that a chance to detect the forbidden lines exists. The detection of these lines is not only of great astrophysical interest. The forbidden lines arising from transitions in the ground configuration of an ion occur at comparatively long wavelengths. Thus, when the electron temperature is very high and all the strong spectral lines occur in the soft x-ray region, ion motion could still be easily studied by measuring the Doppler broadening of the forbidden lines.

§ 6. Conclusion

The observation and identification of new lines in the neon and fluorine spectra illustrate the potentialities of high-current toroidal discharges as intense sources of the spectra of highly ionized atoms. With such sources the opportunity now exists of extending the study of the atomic structure of ions which have an ionization potential below about 200 ev.

Acknowledgments

We gratefully acknowledge the assistance of Mr. A. C. Richardson, Miss M. R. Painter and Mr. R. P. de Ste. Croix with the microphotometry and of Mr. R. F. Hemmings, Mr. J. E. Read and other members of the Engineering Subsection in the operation of SCEPTRE III. The work was supported in part by the Atomic Energy Research Establishment and is published with the permission of Dr. T. E. Allibone, Director of the Laboratory.

References

Allen, N. L. *et al.*, 1958, *Nature, Lond.*, **181,** 222, 384.

de Bruin, T. L., 1932, *Z. Phys.*, **77,** 514.

Craston, J. L., Hancox, R., Robson, A. E., Kaufman, S., Miles, H. T., Ware, A. A., and Wesson, J. A., 1958, *Proc. 2nd U.N. Int. Conf. on the Peaceful Uses of Atomic Energy, Geneva*, Vol. **32**, p. 418.

Edlén, B., 1935, *Z. Phys.*, **94,** 56.

—— 1952, *Ark. Fys.*, **4,** 442.

Hughes, T. P., and Kaufman, S., 1959, *Nature, Lond.*, **183,** 7.

Kaufman, S., 1957, *Nature, Lond.*, **180,** 1345.

Kayser, H., and Ritschl, R., 1939, *Tabelle der Hauptlinien der Linienspektren aller Elemente*, 2nd edn (Berlin: Springer).

Meek, J. M., and Craggs, J. D., 1953, *Electrical Breakdown of Gases* (Oxford : Clarendon Press), p. 400.

Meggers, W. F., 1959, *Rev. Univ. Min.*, **15,** 233.

Moore, C. E., 1949, 1952, 1958, *Atomic Energy Levels*, Vols. 1, 2, 3 (Washington, D.C.: National Bureau of Standards).

Paul, F. W., and Polster, H. D., 1941, *Phys. Rev.*, **59,** 424.

Shenstone, A. G., 1936, *Phil. Trans.* A, **235,** 195.

—— 1949, *Ibid.*, **241,** 297.

Thomson, J. J., 1891, *Phil. Mag.*, (5) **32,** 335.

The Transmission of Sound through a Wake

By the late E. G. RICHARDSON
King's College, Newcastle-upon-Tyne

MS. received 28*th October* 1959, *in revised form* 30*th December* 1959

Abstract. Measurements are made of the signal picked up by a microphone in the ultrasonic beam launched across a fluid in a region containing the wake of a cylinder. Because of the disposition of vortices in the wake there is a difference of phase in sound rays reaching different parts of the microphone and the signal fluctuates periodically. These modulations of the ultrasonic signal are related to fluctuations in the velocity in the wake. The experiments are carried out (*a*) in water using a towed cylinder, (*b*) in air behind a cylinder fixed in a wind tunnel.

§ 1. Introduction

Considerable interest has been evinced recently in the transmission of sound through a turbulent region and in the sound originating in the turbulence itself. The author has been making experiments in the open air and in a wind tunnel in which he has sought to compare the diffraction or scattering of the sound in the turbulent boundary layers formed near the ground with that near the tunnel walls.

Experiments are also desirable in which the interaction between the sound and discrete vortices can be investigated, for in this way the theory can be tested under the simple conditions in which it is framed, i.e. unique values of wavelength, eddy size and sound velocity.

A flow system that suggests itself for this purpose is that of the eddying wake behind a cylinder when the regular and equi-spaced Benard–Karman vortices are proceeding downstream with constant velocity. In air this regular system is overlaid with other disturbances at a Reynolds number greater than 300 so that with a cylinder in a wind tunnel, very low velocities must be used to give rise to vortices of a reasonable diameter. If, however, a cylinder held at one end is towed through water then, as the author has shown, the cylinder is set in strong vibration at its natural (cantilever) frequency over a range of speeds, and in doing so throws off a regular street of vortices at this frequency up to velocities much higher than a limitation to a Reynolds number of 300 would suggest (Richardson 1958).

§ 2. Exploration of Wake of Cylinder towed in Water

The water experiments were carried out in the towing tank of the Naval Architecture Department of King's College, Newcastle. The cylinders were brass tubes $1\frac{1}{2}$ in. and 1 in. in diameter D, clamped in a vertical position to the carriage. They projected about 3 ft below the surface of the water. In their motion they occulted the horizontal beam of ultrasonics passing between two facing quartz 2 Mc/s transducers 20 cm apart mounted on a frame with heavy

base resting on the floor of the tank. The wavelength in water at this frequency is about 0·75 mm. The beam was at a depth of 18 in. below the water level. The transducers were in watertight holders, secured to the frame by screws which allowed them to be adjusted in azimuth to give the maximum signal.

One quartz was operated as source either in 'pulses' or continuously, while the other served as detector. The signal picked up by it was, after passing through a tuned amplifier, fed to a cathode-ray oscillograph and photographed. The passage of the cylinder itself occulted the beam. Thereafter, as the vortex filaments in the wake behind the cylinder intercepted the beam, a change in the amplitude of signal was recorded (figure 1, Plate). These fluctuations are due to the diffraction of the beam by the passing vortex, and are partly amplitude and partly phase modulations of the original signal.

In the interpretation of the records certain precautionary tests are necessary:

(i) The cylinder in vibrating sets up a dipole pressure field, which might be picked up by the receiver. This is eliminated from the record by using high frequency transducers and tuned detectors.

(ii) Pressures may be set up by the disturbance of the water surface level as the cylinder passes. However, vigorous stirring of the surface water had no effect on the magnitude of the signal. It was verified, by using a short cylinder penetrating only 9 in. below the surface, that no fluctuation of the signal occurred unless the end of the cylinder cut the ultrasonic beam in its passage.

Since, in the above treatment of the problem, the differences in magnitude of signal result from differences of phase over the surface of the crystal, it is necessary to establish a relationship between these quantities. This is done by keeping the two transducers at a fixed distance apart in still water and turning the sender. Results of this test are shown in figure 2 and indicate a near-linear relation between

Figure 2. Effect on signal of yawing the receiver in still fluid.

½ and 3 degrees of yaw; beyond this setting the signal begins to rise and fall in a series of diminishing peaks as the diffraction wings pass across the face of the receiver. In the experiments to be described there was no difficulty in holding the signal within the linear region.

(iii) One factor of importance is the width of the ultrasonic beam or aperture of the crystals. Ideally, for the sake of calculation, the ultrasonic beam should be a parallel one. In fact there is some spreading of the beam although the

quartz crystals were wide (2·5 cm) compared with the ultrasonic wavelengths in water. The sender must not be 'stopped' down too much or the radiated beam will spread: the relevant factor is $\gamma = 2\pi a/\lambda$ where acoustically a is the radius of the transducer and λ the wavelength of the sound in the medium (cf. the corresponding Rayleigh equation in optics). A typical value of γ for the full width of the crystals in water was 80 for the 2 Mc/s source. In air, values of γ will be 4·5 times greater than in water. There is however a limitation on the size of eddy which may be detected, if the source is too wide. In order to test this, the full width of the beam was occulted in turn with opaque objects (match sticks and wires) moved athwart it. It was found that the 'limit of resolution' was reached when the obstacle was about one-third the width of the crystal detector, i.e. it failed then to be detected in its passage. When measurements were being made on the wake of the cylinder in water this limitation was of no account, but it did set a limit to the frequency which could be detected in the more turbulent wakes of the cylinder at higher Reynolds numbers (see below). Some masking of the crystals and consequent reduction of signal amplitude can be tolerated, but the change of signal with phase is thereby also reduced.

An alternative method of operation was tried for the narrow beam because of the naturally small fluctuation which resulted using the above system of detection circuit. This involved comparing the *mean* phase at the detector with a sample derived from the source. As the transverse flow in the vortex street varied throughout the period (see below) so did the phase difference between the signal as launched and that which arrived at the pick-up and this was duly recorded on the oscillograph.

§ 3. Velocity in the Wake

We take the formulae for component velocity v (across) and u along the stream (undisturbed velocity U) for a vortex street as originally propounded by Karman and Rubach (1912), that is

$$u = \frac{K}{2l}\left[\frac{\sinh(2\pi/l)(y+\frac{1}{2}h)}{\cosh(2\pi/l)(y+\frac{1}{2}h) - \cos(2\pi/l)(x+\frac{1}{4}l)} - \frac{\sinh(2\pi/l)(y-\frac{1}{2}h)}{\cosh(2\pi/l)(y-\frac{1}{2}h) - \cos(2\pi/l)(x-\frac{1}{4}l)}\right]$$

$$v = \frac{K}{2l}\left[\frac{\sin(2\pi/l)(x+\frac{1}{4}l)}{\cosh(2\pi/l)(y+\frac{1}{2}h) - \cos(2\pi/l)(x+\frac{1}{4}l)} + \frac{\sin(2\pi/l)(x-\frac{1}{4}l)}{\cosh(2\pi/l)(y-\frac{1}{2}h) - \cos(2\pi/l)(x-\frac{1}{4}l)}\right].$$

Here K is the circulation in a vortex, l is the distance between eddies in line, h that across the stream; x is measured downstream from a plane halfway between a pair of vortices and y from a plane bisecting the system. Across any section the integral of u should be constant since it represents the general flux following the cylinder after it has passed.

The integral of v however varies from section to section, thus

$$\int_{-\infty}^{+\infty} v\,dy = 2K\tan^{-1}\left[\tan\left(\frac{\pi}{4} - \frac{\pi x}{l}\right) + \tan\left(\frac{3\pi}{4} - \frac{\pi x}{l}\right)\right]$$

so that the accretion per unit of path to the velocity of the sound cast athwart the wake varies periodically from section to section, being zero when x is an even multiple of $l/4$—in line of a vortex centre where the stream lines are parallel to Ox—to $\pm \frac{1}{2}\pi K$ (alternately) at the odd multiples.

Provided the beam is narrow compared with the eddy spacing, then as indicated on figure 3, the difference in the times of passage of sound rays at the extreme sides will be zero when the beam straddles a vortex core rising to a maximum halfway between these positions in approximately sinusoidal fashion, as the above formula indicates. The signal should fluctuate in magnitude in a similar fashion, except that the receiver does not distinguish between positive

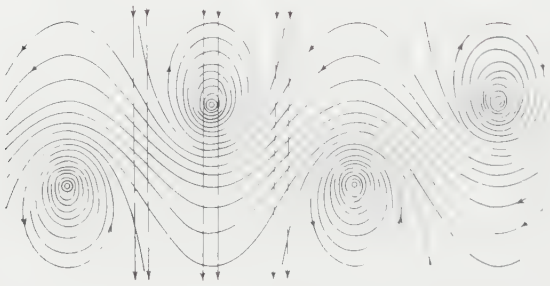

Figure 3. Vortex street with parallel rays delimiting beam (assumed collimated) launched at various locations relative to vortices.

and negative differences. The variation of extreme phase difference will become distorted from this form as the beam is made wider in relation to the eddy spacing.

When one considers that the velocity variations in the wake are of the order $1\,\mathrm{m\,sec^{-1}}$ and the velocity of sound in water $1500\,\mathrm{m\,sec^{-1}}$ (Mach number 0·007!) it is perhaps surprising that the signal is affected by the motion at all. The general diffraction amounts in fact to an angle whose tangent is 10^{-4}. The variation in time of passage of neighbouring rays of the beam however results in a difference of phase on arrival at the receiver which may be appreciable compared with the ultrasonic time period ($\sim 10^{-6}$ sec). These conclusions are borne out by the form of records such as those reproduced in figure 1 (a, b, c).

The signal from the unmasked crystal fell by about 40% of its undisturbed value per degree of yaw and to zero in $2\frac{1}{2}°$. The fluctuations in signal for the $1\frac{1}{2}$ in. rod at 6·5 ft sec $^{-1}$ (figure 1 (a, b)) were about 25% (just behind the cylinder), amounting to an extreme difference in the path of $\frac{1}{4}$ mm or a difference of velocity at these extremes of $3\,\mathrm{m\,sec^{-1}}$ (assuming an effective wake width of 10 cm and a sound velocity of $4350\,\mathrm{ft\,sec^{-1}}$). For two traverses taken with a beam $l/10$ in width (figure 3) this would correspond to a system of vortices with $K = 1{\cdot}25\,\mathrm{ft^2\,sec^{-1}}$.

Two other features of the films may be noted: (i) the decay of the vortex circulation with distance behind the cylinder, (ii) the existence of 'overtones' in the signal from the wake behind the cylinder when the latter is vibrating at large amplitude (figure 1(c)). These overtones seem to be rapidly damped and the system then settles down to a simple periodic one. It was not expected that in these cases the vortex system would correspond to the simple one observed behind a *rigid* cylinder.

For example, if the decay of circulation in the fundamental vortex frequency is represented by an exponential function $\ln K_0 K = \alpha x$, the value of α for figure 1 (*a*) is 10^{-3} per ft when the rod scarcely vibrates, but may be considerably greater at first when the rod has a large amplitude of vibration. Such estimates, readily obtained with this method, could only be derived from hot-wire results at the expense of great complexity and tedium.

§ 4. The Upstream Effects

If the cylinder were steady in its forward movement, no effect would be felt by the sound beam passing afore, to the extent that the detachment of the vortices does not affect the flow in advance, but if the cylinder vibrates it pushes the fluid to and fro in front of it and this causes the integral of $v dy$ across this area to fluctuate and with it the phase, which is what one observes (figure 1(*c*)).

It is possible to derive the streamlines for a cylinder vibrating sinusoidally and hence the phase variation in the signal as it passes just aft of the cylinder. The variation is not very different from that astern.

§ 5. Wake behind a Rigid Cylinder in a Wind Tunnel

A wooden cylinder (2 in. diameter) is set up in a 2 ft 6 in. wind tunnel which it spans. The probing ultrasonic beam passes between two transducers set behind holes in the vertical walls behind the cylinder, mounted on rubber supports. Typical records of the signal at Reynolds numbers of about 5000 are shown in figure 1(*d*).

Sources of 300 kc/s and 1 Mc/s have been used, operated in continuous fashion, the use of pulses in air being precluded by the long 'ringing time' of the crystals. The fluctuation of the signal in the receiver is led to a cathode-ray oscillograph and there recorded.

In an attempt to discover the sensitivity of the method and to supply a standard against which it could be assessed, a 1 cm cylinder was moved at 8 cm sec^{-1} in air between the two 1 Mc/s crystals, so as to probe the wake at a Reynolds number of 55, which corresponds to Kovasnay's detailed hot-wire measurements. This proved to be just at the limit of sensitivity for this set-up and a high amplification has to be used which was beginning to make the electronic 'noise' troublesome. Within these limits traverses such as those plotted on figure 3 corresponded adequately to the sound-probe measurements.

§ 6. Analysis of Records obtained with Cylinder in Wind Tunnel

A length of the film record is analysed as to power spectrum of the modulation by the method of computation described in the appendix.

In the absence of the cylinder the turbulence in the tunnel gives rise to a modulation spectrum with amplitude falling approximately with rising frequency as $(1+f^2)^{-1}$ (figure 4, curve *a*). With the cylinder vertical and the probing beam horizontal the octave of the fundamental Strouhal frequency (given by $fD/U = 0{\cdot}2$) and, at somewhat smaller amplitude, the second harmonic of this is clearly distinguished from the background (figure 4, curves *b*, *c*). The curves of figure 5 show the decay of fundamental and overtones as the wake proceeds downstream. The harmonics seem to be due to distortions of the flow near the confines of the wake, already apparent weakly in Kovasnay's (1949) and Roshko's (1953) hot-wire measurements at a Reynolds number of 180 and more strongly between 300 and 10 000.

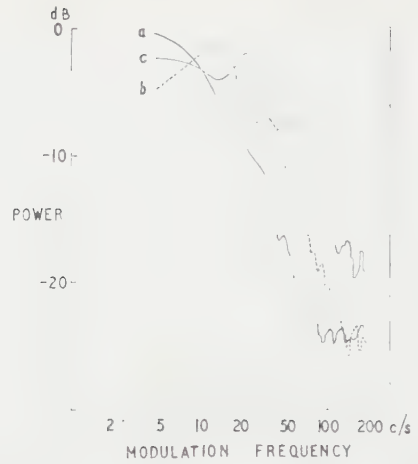

Figure 4. Analysis of signals in wind tunnel; *a*, in absence of cylinder; *b*, *c*, with vertical cylinder, 2 in. downstream and speeds 2·0 and 3·2 m sec^{-1}.

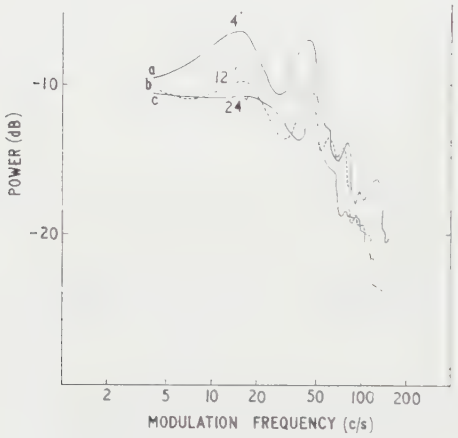

Figure 5. Signals at speed 2·2 m sec^{-1} and various distances downstream of vertical cylinder.

§ 7. Conclusions

Measurements such as these can be regarded from two aspects. Either one considers the ultrasonic beam as a probe for the wake, giving an integration of the transverse component of velocity in the path of the beam and so leading to a method of studying wakes and turbulent regions alternative to hot-wire and visual methods, or one can study the fluctuations in the sound signal as a stochastic process for its own sake.

The author has considered his work from both aspects, but he is more interested in obtaining a correlation between known vortex systems and the fluctuations in the sound beam, because he proposes to use this as a basis to analyse similar variations in the signal from a beam launched through a boundary layer or a jet, both model ones set up in a laboratory and those due to natural turbulence in the atmosphere and in the ocean.

From whichever aspect the work is regarded, the effect on the sound beam can be calculated from a velocity integral along the path, provided the wavelength of the sound is short compared with the diameter of the eddies encountered by it. When we expect to detect eddies comparable in size with the wavelength we enter the Rayleigh–Gans scattering region of optical theory and we may also meet apparatus limitations.

ACKNOWLEDGMENTS

The author wishes to thank the Directors of the Naval Architecture Department of King's College, Newcastle-upon-Tyne and of the Chemical Defence Experimental Establishment, Porton, for permitting the use of facilities and Mr. A. Rakowski and the Staff of the University of Durham Computing Laboratory for carrying out the analyses of records.

APPENDIX

Calculation of the Spectral Density using the Autocorrelation Function

The programme was adopted to calculate the spectral density of amplitude modulation of an ultrasonic signal by turbulent flow. The mensuration of ordinates was done on film records (with average enlargement tenfold). The number of observations N in different examples was from 260 to 885. The time difference Δt between two nearest observations was in most cases 2·6 msec.

Calculation of the Autocorrelation Coefficients

If x_i is an element of data: $i=1, \ldots . N$, the normalized autocorrelation function is given by

$$\rho_k = \frac{(N-k)\sum_1^{N-k} x_i x_{i+k} - \sum_1^{N-k} x_i \sum_1^{N-k} x_{i+k}}{\left[\left\{(N-k)\sum_1^{N-k} x_i^2 - (\sum_1^{N-k} x_i)^2\right\}\left\{(N-k)\sum_1^{N-k} x_{i+k}^2 - (\sum_1^{N-k} x_{i+k})^2\right\}\right]^{1/2}}$$

where k is the phase lag.

In most cases computations were made for $k=1, \ldots . 40$ which sufficed for the analysis of the most important part of the spectrum.

Calculation of the Spectral Density

Given the autocorrelation coefficients ρ_k $(k=1 \ldots n)$ the spectral density function was computed using the relation

$$a_r = \frac{1}{n}\left[\tfrac{1}{2}\{1+(-1)^n \lambda_n \rho_n\} + \sum_1^{n-1} \lambda_k \rho_k \cos\frac{rk\pi}{n}\right]$$

where λ_k is a weighting factor. (In this case Bartlett's smoothed periodogram has been used in the form $\lambda_k = 1-k/n$.)

After computing a_r, the estimated spectral density at the frequency $r/2n\Delta t$ c/s is given by $(n\Delta t\sigma^2/\pi)a_r$, where σ is the standard deviation in the set of original data x_i. As $n\Delta t\sigma^2/\pi$ is constant, the spectral density is proportional to a_r.

When, as in the wind tunnel signals, the frequency spectrum of fundamental and harmonics is overlaid with background, the estimation of the peaks due to the former is not simple, especially when, due to attenuation, they do not protrude

far above that background. Mr. M. B. Priestley of Manchester University has indicated (in a private communication) his method of doing this, but it is not yet in the form of a computer programme. Our approximate method of testing this point is to re-compute the spectral density function with n equal to several different values, e.g. 10, 20, 40, and to see whether the peaks in which we are interested retain the same amplitude each time.

References

Karman, Th., and Rubach, H., 1912, *Phys. Z.*, **13,** 49.
Kovasnay, L. S. G., 1949, *Proc. Roy. Soc.* A, **198,** 174.
Richardson, E. G., 1958, *Appl. Sci. Res.* A, **7,** 341.
Roshko, A., 1953, *Nat. Advis. Comm. Aero. Tech. Note No.* 2913.

Perturbations in Classical Mechanics

By L. M. GARRIDO

Facultad de Ciencias, Universidad de Zaragoza, Zaragoza, Spain

MS. received 19*th January* 1960

Abstract. This paper describes a method of evaluating perturbations in classical mechanics which is similar to quantum mechanics time dependent perturbation theory.

§ 1. Introduction

In classical mechanics perturbation theory is usually dealt with in a much more complicated manner than in quantum mechanics. Fuess (1927), in a very detailed treatment, shows how true this is.

Therefore it would be convenient to develop a concise method to treat many problems, such as calculations of satellites' orbits, plasma stability, etc., in a simpler way. In this paper we try to achieve this aim.

§ 2. The S Operator

Let us call $F(q,p)$ a function of the canonical set of conjugate variables $q=q(t)$ and $p=p(t)$, which does not depend explicitly on time. So as not to make the exposition cumbersome, we restrict ourselves to two conjugate variables. If we designate by Ω the operator that generates the total time derivative at the time origin, Taylor's theorem is written as

$$F\{q(t),p(t)\}=e^{t\Omega}F(q_0,p_0)e^{-t\Omega} \qquad \ldots\ldots(1)$$

where we define

$$q_0=q(0), \qquad p_0=p(0). \qquad \ldots\ldots(2)$$

Since the dynamical time evolution is carried through by the time evolution of $q(t)$ and $p(t)$ we have

$$\Omega=\dot{q}\frac{\partial}{\partial q_0}+\dot{p}\frac{\partial}{\partial p_0}$$

where $\dot{q}$ and $\dot{p}$ are the time derivatives of q and p at $t=0$, and $\partial/\partial q_0$ and $\partial/\partial p_0$ are the operators defined by the commutators

$$\left[\frac{\partial}{\partial q_0},\ q_0\right]=1 \quad \text{and} \quad \left[\frac{\partial}{\partial p_0},\ p_0\right]=1.$$

If $H=H(q,p)$ is the Hamiltonian† of our system and we write

$$H_p\equiv\frac{\partial H}{\partial p}, \quad H_q=\frac{\partial H}{\partial q} \qquad \ldots\ldots(3)$$

with the help of Hamilton's equations we can write

$$\Omega=H_p(q_0,p_0)\frac{\partial}{\partial q_0}-H_q(q_0,p_0)\frac{\partial}{\partial p_0}. \qquad \ldots\ldots(4)$$

† The Hamiltonian is time independent.

Let us suppose that the Hamiltonian H can be decomposed into two parts

$$H = H^0 + H^1 \qquad \ldots\ldots (5)$$

and that the equations of the time evolution generated by H^0 have been solved exactly in such a way that, if H^1 is considered as the perturbation Hamiltonian the functions

$$q = q_0(t), \qquad p = p_0(t) \qquad \ldots\ldots (6)$$

are the solutions to the unperturbed motion with the boundary conditions

$$q_0 = q_0(0), \qquad p_0 = p_0(0)$$

identical to the perturbed motion boundary conditions. Consequently we write now

$$\Omega = \Omega^0 + \Omega^1$$

where

$$\left.\begin{aligned} \Omega^0 &= H_p{}^0(q_0, p_0)\frac{\partial}{\partial q_0} - H_q{}^0(q_0, p_0)\frac{\partial}{\partial p_0}, \\ \Omega^1 &= H_p{}^1(q_0, p_0)\frac{\partial}{\partial q_0} - H_q{}^1(q_0, p_0)\frac{\partial}{\partial p_0}. \end{aligned}\right\} \qquad \ldots\ldots (7)$$

However we suppose that the unperturbed motion is completely solved. This fact is represented operationally by

$$F(q_0(t), p_0(t)) = \exp(t\Omega^0) F(q_0, p_0) \exp(-t\Omega^0). \qquad \ldots\ldots (8)$$

In this expression we make use of the functions (6).

Therefore we obtain

$$F(q(t), p(t)) = S(t) F(q_0(t), p_0(t)) S^{-1}(t) \qquad \ldots\ldots (9)$$

where $S(t)$ represents the operator

$$S(t) = \exp(t\Omega) \exp(-t\Omega^0) \qquad \ldots\ldots (10)$$

that is the solution, with the boundary value $S(0) = 1$, of the differential equation

$$\frac{dS(t)}{dt} = S(t)\Omega^1(t) \qquad \ldots\ldots (11)$$

where $\Omega^1(t) = \exp(t\Omega^0)\Omega^1 \exp(-t\Omega^0)$. This satisfies the integral equation

$$S(t) = 1 + \int_0^t dt^1 S(t^1)\Omega^1(t^1) \qquad \ldots\ldots (12)$$

which we can now solve by iteration to obtain the different perturbation terms.

§ 3. Interpretation of $\Omega^1(t)$

We define above the operator $\Omega^1(t)$ by the relation

$$\Omega^1(t) \equiv \exp(t\Omega^0)\Omega^1 \exp(-t\Omega^0). \qquad \ldots\ldots (13)$$

For internal consistency we have to write

$$\left.\begin{aligned} \exp(t\Omega^0)\frac{\partial}{\partial q_0}\exp(-t\Omega^0) &= \frac{\partial}{\partial q_0(t)} \\ \exp(t\Omega^0)\frac{\partial}{\partial p_0}\exp(-t\Omega^0) &= \frac{\partial}{\partial p_0(t)} \end{aligned}\right\} \qquad \ldots\ldots (14)$$

in such a way that the operator $\Omega^1(t)$ becomes

$$\Omega^1(t) = H_p{}^1(q_0(t), p_0(t)) \frac{\partial}{\partial q_0(t)} - H_q{}^1(q_0(t), p_0(t)) \frac{\partial}{\partial p_0(t)}. \quad \ldots\ldots (15)$$

Our problem is completely solved if we approximate the canonical set of variables

$$\left.\begin{aligned} q(t) &= S(t) q_0(t) S^{-1}(t) \\ p(t) &= S(t) p_0(t) S^{-1}(t) \end{aligned}\right\} \quad \ldots\ldots (16)$$

since the time evolution of F is given by

$$F(q(t), p(t)) = F(S(t) q_0(t) S^{-1}(t), S(t) p_0(t) S^{-1}(t)).$$

In doing so we will have to evaluate quantities such as $\partial q_0(t)/\partial q_0(t^1)$, the partial derivative of a time function with respect to the value of the same function at another instant of time. To achieve this aim we write the unperturbed motion solutions as functions of the boundary values at $t = 0$:

$$q_0(t) = q_0(q_0, p_0, t), \qquad p_0(t) = p_0(q_0, p_0, t). \quad \ldots\ldots (17)$$

From here we obtain $q_0(t^1)$ and $p_0(t^1)$, and the corresponding expressions for $q_0(t)$ and $p_0(t)$ with the boundary values $q_0(t^1)$ and $p_0(t^1)$ at $t = t^1$

$$\left.\begin{aligned} q_0(t) &= q_0(q_0(t^1), p_0(t^1), t - t^1) \\ p_0(t) &= p_0(q_0(t^1), p_0(t^1), t - t^1) \end{aligned}\right\} \quad \ldots\ldots (18)$$

where we can now evaluate the partial derivatives with respect to $q_0(t^1)$ and $p_0(t^1)$.

As an example we will consider the case when the unperturbed motion corresponds to a harmonic oscillator whose Hamiltonian is $H^0 = \frac{1}{2}p^2 + \frac{1}{2}\omega^2 q^2$. Then

$$q_0(t) = q_0 \cos \omega t + \frac{p_0}{\omega} \sin \omega t$$

$$p_0(t) = -q_0 \omega \sin \omega t + p_0 \cos \omega t$$

and therefore

$$\frac{\partial q_0(t)}{\partial q_0(t^1)} = \cos \omega (t - t^1), \qquad \frac{\partial p_0(t)}{\partial q_0(t^1)} = -\omega \sin \omega (t - t^1)$$

$$\frac{\partial q_0(t)}{\partial p_0(t^1)} = \frac{1}{\omega} \sin \omega (t - t^1), \qquad \frac{\partial p_0(t)}{\partial p_0(t^1)} = \cos \omega (t - t^1).$$

With the help of these last expressions and using the iteration expansion of $S(t)$ we can evaluate the successive perturbations to the harmonic oscillator motion caused by any perturbing Hamiltonian H^1.

Generalization to any other case is quite evident.

Acknowledgment

The author would like to thank Dr. Galindo Tixaire for many helpful discussions.

Reference

Fuess, E., 1927, *Handbuch der Physik*, Vol. V, *Storungsrechnung* (Berlin: Springer).

Interpretation of Ion Mobility Measurements in Argon and Helium Liquids

By D. W. SWAN
Electrical Engineering Department, Queen Mary College, London

MS. received 27th May 1959, in revised form 9th January 1960

Abstract. Previous interpretations of ion mobility measurements in liquefied argon and helium in terms of gas kinetic theory have shown that these liquids do not behave as compressed gases. A more detailed analysis of the total ion energy shows that in some instances the results have been incorrectly interpreted, while in others it would appear that impurities caused the apparent failure of theory. The re-interpretation indicates that kinetic theory is applicable to these liquids, and that the collision cross sections for ions in argon and helium I are very nearly the same in both the gaseous and liquid phases. Polarization attraction is shown to be of great importance. In liquid helium II it is necessary to consider quantum effects, but the experimental data can still be explained adequately by gas kinetic equations.

§ 1. Introduction

Recent measurements by Williams (1957) of ion mobilities in argon and helium liquids have been interpreted in terms of classical kinetic theory, and the large discrepancy between the calculated cross sections and the corresponding gaseous cross sections was taken to indicate that these liquids definitely could not be considered as compressed gases. The kinetic theory employed gave an electron collision cross section for argon liquid which was about one hundredth of the gaseous cross section, and also predicted the existence of electrons with mean energies as high as 22 ev (i.e. considerably above the ionization energy). This interpretation confirmed the earlier measurements of Malkin and Schultz (1951) who obtained cross sections and electron energies of a similar magnitude. Positive ion mobility values for A^+ in argon liquid were similarly inexplicable, since in this case the predicted cross section was 10^5 times greater than the recognized gaseous cross section. The temperature and field dependent mobilities of both positive and negative ions in helium liquid only emphasized the apparent departure from gaseous kinetic theory in the condensed phase.

It will be shown, however, that the measurements for liquid argon by Malkin and Schultz and by Williams, and also Williams' data at 4·2 °K in helium liquid, are in accordance with the predictions of classical kinetic theory provided that equations are employed which are valid for the particular conditions of temperature and field concerned, and that the effects of impurities are considered. Some more recent measurements of ion mobilities in liquid helium by Meyer and Reif (1958) are also examined, and it is shown that even below the λ-point the gaesous kinetic equations can be used provided allowance is made for quantum effects. A survey is given of the relevant equations and the conditions under which they are applicable, and this shows that the equations employed by Williams were, in many cases, not valid.

§ 2. The Theory of Ion Mobility

An ion drifting in a gas under the influence of an applied field reaches a dynamic equilibrium in which energy gained from the field is lost in collisions between the ion and gas atoms. The field E superimposes on the random thermal motion of the ion a drift velocity V which is determined by the ion mobility μ according to the relationship $V=\mu E$. The ratio of E to the gas pressure p is a measure of the gain in ion energy from the applied field and μ is constant for low E/p. At higher values of E/p, depending on the nature of the gas and the ion, μ becomes a function of E.

In general, ion mobility may be evaluated on the basis of kinetic theory and satisfactory agreement with experiment is found, but in certain cases a quantum theory is necessary in order to account adequately for all the forces between an ion and an atom. This latter case arises only when the ionic and atomic cores are identical; and even then the kinetic theory equations can still be used provided certain modifications are introduced.

Three types of ion–atom interactions are known to be effective. These are (i) gas kinetic elastic collisions, (ii) polarization in which a passing ion induces a dipole moment in an atom which is then attracted to the ion, (iii) symmetry effects which include resonance attraction and repulsion and also charge transfer where the electron can pass back and forth between ion and atom during a collision.

In the earlier theory due to Langevin (1903) only (i) was considered. Ion–ion interaction was neglected and it was assumed that the thermal velocity of the ion was large compared with the gain in velocity from the field. The final equation, applicable therefore to low ion concentrations and low field strengths, is

$$\mu=\frac{0{\cdot}815\boldsymbol{e}\lambda}{mc}\left(\frac{M+m}{M}\right)^{1/2} \qquad \ldots\ldots(1)$$

in which λ is the mean free path, M the mass of the atoms, m the mass of the ion, c the thermal agitation velocity of the ion and $\boldsymbol{e}$ the electronic charge, assuming singly charged ions. This equation predicts that μ should be proportional to $\boldsymbol{e}$, λ and $T^{-1/2}$, and also should be independent of the dielectric constant of the gas, none of which are confirmed by experiment. It does, however, give the correct dependence on density.

Langevin (1905) sought to remedy the shortcomings of (1) by including the polarization scattering in the derivation. The forces due to the induced dipoles of the polarized atoms have the effect of increasing the number of collisions, and provide a means of momentum transfer without direct encounter. As in the earlier derivation the field energy must be small in comparison with the thermal energy. The original equation given by Langevin has been modified slightly by Hassé (1926) and can be written

$$\mu=\frac{A}{\{\rho(\epsilon_r-1)\}^{1/2}}\left(\frac{M+m}{m}\right)^{1/2} \qquad \ldots\ldots(2)$$

where ρ is the gas density and ϵ_r is the dielectric constant. A is a function of a parameter Z where

$$Z^2=\frac{8\pi S^4\rho\boldsymbol{k}T}{(\epsilon_r-1)\boldsymbol{e}^2M} \qquad \ldots\ldots(3)$$

in which S is the sum of the radii of the ion and the atom and $\boldsymbol{k}$ is Boltzmann's constant. The value of Z is a measure of the relative importance of elastic and polarization scattering. Large Z corresponds to negligible polarization effects

while as Z decreases these forces increase in importance until they completely predominate when Z is zero. With a suitable value of S, the constant Z may be determined and A computed (Hassé 1926, Loeb 1955). Clearly the value of S is critical in determining μ and in view of the unreliability of many measurements of atomic diameters care must be taken in deciding the most suitable value for the conditions concerned. In many cases diameters deduced from viscosity measurements have been used. Wannier (1954) has calculated the effective ion–atom cross section for rare gas positive ions in the parent gas from measurements of the drift velocity at high fields and symmetry effects are automatically included. With πS^2 set equal to these experimentally determined cross sections reasonable success for gases has been obtained by Hornbeck (1951) and Varney (1952, 1953). It will be interesting to apply the same procedure to ions in the liquid phase.

There are two further equations which involve mobility and which also apply in the low field range. Firstly, the macroscopic properties of the liquid or gas can be introduced through Stokes' law expressed in the form

$$\mu = \boldsymbol{e}/6\pi\eta a \qquad \ldots\ldots (4)$$

where η is the viscosity and a the radius of the diffusing particle. Secondly, there is the Einstein relationship

$$\mu = D\boldsymbol{e}/\boldsymbol{k}T \qquad \ldots\ldots (5)$$

in which D is the self-diffusion coefficient at the absolute temperature T. These relationships will be useful in comparing results derived from the various equations.

Equations (1) to (5) fail when the energy gain from the field per mean free path is no longer much smaller than the thermal energy, and a comprehensive theory based on Boltzmann's transport equation has been developed by Wannier (1953) for this high field situation. The effect of different mass ratios has been included so that the results are applicable to electrons as well as ions. Gas kinetic repulsion and symmetry effects are combined in a single elastic ion–atom cross section σ_{ia} which, as mentioned earlier, can be evaluated from drift velocity measurements. Only elastic collisions are assumed to take place. The theory leads to the general mobility equation for the high field range

$$\mu = \left(\frac{M+m}{mM^2}\right)^{1/4} \left(\frac{\boldsymbol{e}\lambda}{E}\right)^{1/2} \qquad \ldots\ldots (6)$$

which has been found to give good agreement with experiment both for ions in the parent gas and for electrons. In conjunction with this equation Wannier has shown that the total ion energy in a high field can be expressed in the form

$$\epsilon = \tfrac{1}{2}(m+M)V^2. \qquad \ldots\ldots (7)$$

The first term on the right-hand side of (7) represents the energy of drift motion, and the second term that of random motion. For electrons $m \ll M$ and $\epsilon = \frac{1}{2}MV^2$. It can be seen from (6) that if λ is assumed to be a slowly varying function of ion energy, the mobility is no longer independent of E, and, in fact, is proportional to $E^{-1/2}$. The equations (6) and (7) are well established for gaseous ions but with a single exception have never been applied to ions in liquids. Williams used similar equations to interpret his electron drift velocity measurements in argon liquid, but the results were most unsatisfactory and apparently

indicated that the liquid departed widely from a gas-like state. For the intermediate range where field and thermal energies are comparable, an approximate equation can also be derived from Wannier's work giving

$$\mu^2 = \left\{ \left(\frac{3kT}{2ME^2} \right)^2 + \left(\frac{M+m}{m} \right) \left(\frac{e}{\rho\sigma E} \right)^2 \right\}^{1/2} - \left(\frac{3kT}{2ME^2} \right) \qquad \ldots\ldots (8)$$

in which σ is the collision cross section. In the high field limit (8) reduces to (6), while for negligible field energy an approximate low field equation is given which differs from (1) by only 20% in the numerical factor.

Experimental determinations of mobility frequently involve measurements of drift velocity under definite conditions of field and temperature, and in using the theoretical equations to derive cross sections from these results, it is essential that the correct equation be employed. This applies particularly to experiments at low temperatures or those in which large temperature changes occur, since it is possible to pass from the low to the high field condition by a reduction in temperature at constant field as well as by an increase of field at constant temperature. In view of their low temperatures and therefore low thermal energies, the liquefied gases argon and helium are particularly interesting, and a careful analysis of the energies of ions in these liquids will show that previous interpretations of mobility measurements are not correct in many instances.

A useful criterion for determining whether high or low field conditions hold has been given by Wannier. If low field conditions are satisfied, then

$$\left(\frac{M}{m} + \frac{m}{M} \right) eE\lambda \ll kT \qquad \ldots\ldots (9)$$

and the reverse is true when high field equations are applicable. The factor $M/m + m/M$ is necessary when the mass ratio is very different from unity as in that case the energy transfer on collision is small and the ion can store energy over many collisions. Rearrangement of (9) into a more convenient form for application to liquids gives

$$E \ll \frac{\rho\sigma kT}{Me} \left(\frac{mM}{m^2 + M^2} \right).$$

For ions in the parent gas or liquid $M = m$ and

$$E \ll \frac{\rho\sigma kT}{2Me} \qquad \ldots\ldots (10)$$

while for electrons $m \ll M$ and

$$E \ll \frac{\rho\sigma kTm}{M^2 e}. \qquad \ldots\ldots (11)$$

Although not accurate, (10) and (11) determine the energy range involved and hence indicate the appropriate mobility equations.

§ 3. Ions in Argon Liquid

Application of (10) and (11) to ions in liquid argon at 90 K shows that high field conditions pertain to electrons for fields in excess of 2 v cm^{-1}, and low field conditions pertain to positive ions over the whole of Williams' experimental field range, which for positive ion measurements was from 24 kv cm^{-1} to 187 kv cm^{-1}.

3.1. *Positive Ions*

Williams used equation (1) for the interpretation of positive ion mobility in argon liquid and, obtaining the meaningless ionic mean free path of $2{\cdot}6 \times 10^{-14}$ cm, concluded that ordinary kinetic theory was not applicable. However, it now appears that this value was wrongly calculated since a further determination by the author using equation (1) gives a mean free path of $2{\cdot}4 \times 10^{-9}$ cm, which is reasonable.

Table 1 shows the mobilities of positive ions in liquid argon calculated from all the low field equations and compared with the measured values. The spread in experimental data is small and reasonably accurate comparison is therefore possible. The gaseous cross section which includes charge exchange ($9{\cdot}3 \times 10^{-15}$ cm^2) was used in all cases, and very little difference was obtained

Table 1. Mobilities of A^+ in Argon Liquid at 90°K and of He^+ in Helium Liquid at 4·2°K

Equation	(1)	(2)	(4)	(5)	Experimental
Argon ($cm^2\ v^{-1}\ sec^{-1} \times 10^3$)	6·0	3·24	1·5	2·86	2·8–3·2 (Williams)
Helium I ($cm^2\ v^{-1}\ sec^{-1} \times 10^2$)	24·0	3·4	16·0	—	3·6 (Meyer and Reif)

when the cross section deduced from x-ray diffraction was used instead (Eisenstein and Gingrich 1942, $\sigma = 6{\cdot}35 \times 10^{-15}$ cm^2). The simple Langevin theory (equation (1)) predicts a mobility which is too high by a factor of about two, but the inclusion of polarization (equation (2)) gives excellent agreement. The mobilities deduced from viscosity data through equation (4) ($\eta = 2{\cdot}5 \times 10^{-3}$ poise) and from the diffusion coefficient through equation (5) ($D = 2{\cdot}07 \times 10^{-5}$ cm^2 sec^{-1}, Corbett and Wang 1956) are also in reasonable agreement with experiment, but deviations are to be expected if polarization attraction and charge exchange are important since in measuring the self-diffusion and viscosity coefficients uncharged particles were used.

3.2. *Negative Ions*

The negative ion mobility must be examined in terms of equation (6) alone, since the ions are undoubtedly free electrons and high field conditions are always satisfied. The high drift velocity of these ions is direct evidence for the absence of electron trapping to form stable negative ions.

Williams modified equation (1) to take account of the field dependence of both the mean free path and the r.m.s. velocity of the ion, the final equation differing from (6) when $M \gg m$ by a numerical factor of about 0·9. Introducing the electron energy from (7) and the collision cross section σ into (6) gives

$$\sigma\epsilon = \left(\frac{M}{4m}\right)^{1/2} \boldsymbol{ek} T_g \left(\frac{E}{p}\right). \qquad \ldots\ldots (12)$$

This form is convenient for direct comparison with gas data recorded at a temperature T_g, and the equivalent pressure for the liquid must be derived from the relationship $p = \rho \boldsymbol{k} T_g / M$. The drift velocity of electrons in liquid argon is shown in figure 1 and from these results it is possible to calculate σ as

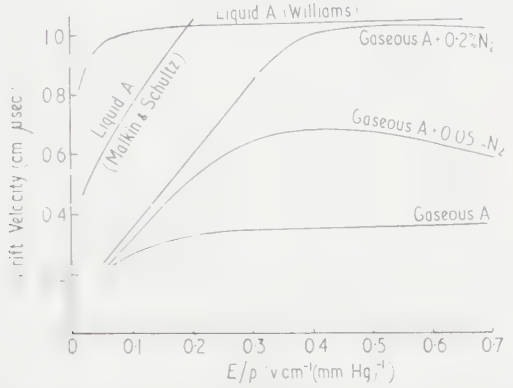

Figure 1. Drift velocity of electrons in liquid argon, gaseous argon, and argon–nitrogen mixtures.

a function of electron energy. The cross sections deduced in this way are seen to be about 100 times smaller than the gas cross section, and the mean energy appears to be about 20 ev, which is nearly twice the first excitation potential of argon and well in excess of the first ionization potential of 15·7 ev (figure 2).

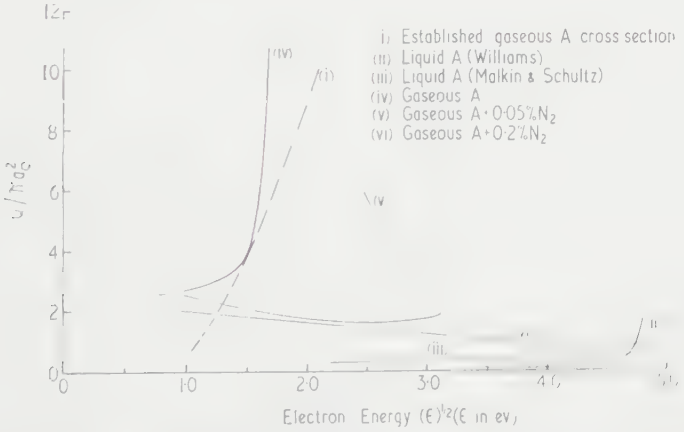

Figure 2. Collision cross sections for electrons in liquid and gaseous argon and in gaseous argon–nitrogen mixtures calculated from equation (12).

Williams suggested that the interaction of neighbouring atoms was responsible for the very small cross section in argon liquid, but this concept is artificial and unnecessary if the influence of likely impurities is considered. An examination of recent measurements of electron drift velocity in pure gaseous argon and in mixtures of gaseous argon and air, oxygen and nitrogen, shows that the presence of very small concentrations of molecular impurities can appreciably increase the drift velocity of electrons. Figure 1 shows measurements by Bortner, Hurst and Stone (1957) of the drift velocity of electrons in pure argon gas and in argon–nitrogen mixtures. These can be compared with the measured electron

drift velocities in argon liquid since they were taken at comparable conditions of E/p. The collision cross sections can be calculated for the pure gas and for the gas mixtures from equation (12) in the same way as for the liquid, and these are shown in figure 2. The cross section for the pure argon is in reasonable agreement with the recognized gaseous cross section (Massey and Burhop 1952, p. 116), confirming the validity of equation (12) for electrons at very low E/p, but the addition of nitrogen appears to reduce the cross section and increase the mean electron energy. The addition of small percentages of air or oxygen to argon has a similar effect.

Comparison of the estimated cross section for the liquid phase with that deduced from a mixture of argon and 0·2% nitrogen shows that they are of similar magnitude and energy dependence, which suggests that in fact the liquid argon used by Williams and by Malkin and Schultz contained a small percentage of dissolved molecular impurities. The very small collision cross sections calculated from kinetic theory must therefore not be considered as conclusive evidence that liquid argon does not behave as a compressed gas, and it will be necessary to redetermine the electron mobilities in liquid argon under carefully controlled conditions in order to show whether the transition from the gaseous to the liquid phase appreciably alters the elastic collision cross section.

Stacey (1959) has recently proposed that electron trapping by neutral argon atoms in the liquid is responsible for the field-independent electron drift velocity observed by Williams, and finds that good agreement is obtained between theory and experiment if the neutral argon atoms are assumed to have an electron affinity of 0·03 ev and a capture cross section of approximately 10^{-18} cm^2. However, the theory is seriously in error, as can be seen by consideration of the mean free path between trapping sites. The atomic number density in argon liquid is $2{\cdot}1 \times 10^{22}$ cm^{-3}, and if the cross section for trapping is of the order of 10^{-18} cm^2 then the mean free path between traps is of the order of 5×10^{-5} cm. In travelling this distance an electron will suffer many non-attaching elastic collisions with argon atoms, and since Stacey assumes that the elastic scattering cross section is not altered appreciably by the transition from the gaseous to the liquid phase normal mobility theory must be applied as expressed by equation (12). It is clearly incorrect to assume, as Stacey does, that the electron will accelerate over the whole mean free path as in a vacuum, and the mean energy of the electron between traps will therefore be given by $\frac{1}{2}MV^2$ and not $\frac{1}{2}mV^2$. If the mean kinetic energy of the electrons is about 2 ev (Stacey 1958), then the actual drift velocity between traps would not be approximately 8×10^7 cm sec^{-1} as envisaged by Stacey but only approximately 3×10^5 cm sec^{-1}. Since this latter value is less than the observed drift velocity by a factor of about three the trapping mechanism is obviously invalid.

A quantitative theory for the increase of electron drift velocity in argon gas containing small percentages of molecular impurities has been given by Klema and Allen (1950), but a simple explanation can be given by reference to the momentum transfer cross section for argon which will allow an estimate of the true electron energy to be made and which is quite adequate for the present purpose. In the pure argon gas at E/p of 0·5 v cm^{-1}(mm Hg)$^{-1}$ the electron drift velocity is found to be $3{\cdot}56 \times 10^5$ cm sec^{-1} corresponding to a mean energy of 2·76 ev, and at this energy the momentum transfer cross section is increasing rapidly with electron energy. Below the first excitation potential of argon there

are no inelastic losses, but if a very small quantity of nitrogen is added this will introduce inelastic scattering at energies as low as about 1 ev through the excitation of vibrational and rotational modes. The influence of this impurity, therefore, is to reduce the mean electron energy below that for pure argon, and with the lowering of energy there is an accompanying decrease of the momentum transfer cross section for the argon as a result of the Ramsauer effect. At a given value of E/p the drift velocity is inversely proportional to the momentum transfer cross section and to the square root of the mean energy, and since both are reduced as a result of the impurity there is an increase of the drift velocity. The concentration of molecular impurity must be small so that the majority of electron collisions are with the argon atoms. Thus, although the drift velocity measured by Williams indicates that ϵ is as high as 20 ev, the true mean energy is below that for electrons in pure argon. This erroneous deduction led Williams and Stacey (1957) to conclude that some electron multiplication was probably taking place in their liquid argon, whereas with the lower mean energy the probability of ionization is greatly reduced.

§ 4. Ions in Helium Liquid

Measurements of the mobilities of positive and negative ions in both liquid helium I and liquid helium II indicate that the negative ion is not a free electron but has an effective mass slightly in excess of the positive helium ion. The reports of the investigations in which these mobilities were measured do not give details of the purity of the helium employed, but some observations by Williams suggest that impurities were present which were particularly effective in the trapping of electrons to form low mobility negative ions, particularly as in one series of experiments the negative ion mobility was of the order of 15 $cm^2 v^{-1} sec^{-1}$, which could only be due to free electrons. Davidson and Larsh (1950) have shown that a very small concentration of dissolved oxygen in liquid argon is extremely efficient in removing free electrons by an attachment process, and since complete saturation of the helium liquid with air did not affect the measured mobilities it seems very likely that a similar process was also occurring in this liquid and that the observed ions were actually oxygen negative ions. Qualitatively this idea is supported by the fact that the negative ion mobility μ_- was always less than μ_+, which on a basis of mass difference is to be expected. Because of the lack of information concerning the effects of dissolved or suspended impurities in liquid helium it is not possible to consider this point further, but since variations of μ_- and μ_+ with temperature and with field are similar only the measurements of μ_- will be considered in detail. The nature of the ion is not certain but it is assumed to be the atomic ion He^+. The collision processes occurring in liquid helium II are very different from those occurring in a normal liquid, and for this reason it is necessary to consider separately measurements taken at temperatures above and below the λ-point.

4.1. *Helium I*

Equation (10) can be applied to He^+ in helium liquid at 4·2 °K and low field conditions are satisfied if $E \ll 3{\cdot}4 \times 10^{18}\,\sigma$. Since σ is not likely to be less than 10^{-15} cm^2, this requires that $E \ll 3$ kv cm^{-1}, and this is satisfied by the experimental conditions of the investigation by Meyer and Reif (1958). Measurements

by Williams at 4·2°K were taken at fields greater than 3 kv cm^{-1}, and consequently the higher mobility observed by him is to be expected.

It was shown in § 3 that good agreement can be obtained between experimentally determined positive ion mobility in liquid argon and kinetic theory if polarization attraction is considered, and the contribution of polarization to the scattering cross section is likely to be of importance in helium liquid also. The cross section necessary to give the value of μ_+ reported by Meyer and Reif (see table 1) can be calculated from equation (1), and is found to be $2{\cdot}5\times10^{-14}$ cm^2 at 4·2°K. This is very much larger than the cross section measured in the gaseous phase ($3{\cdot}8\times10^{-15}$ cm^2) which takes into account only elastic collisions and symmetry effects, suggesting that polarization effects are very important in the liquid. Putting πS^2 in equation (3) equal to $3{\cdot}8\times10^{-15}$ cm^2 we find $Z=0{\cdot}19$, showing that scattering due to polarization is indeed predominant, and from equation (2) the mobility of He^+ in liquid helium becomes $3{\cdot}4\times10^{-2}$ cm^{2}v^{-1}sec^{-1}. As for liquid argon, the agreement between theory and experiment is excellent when account is taken of the dielectric constant of the liquid. The mobilities of He^+ at 4·2°K as calculated from equations (1), (2) and (4) are shown in table 1 and the gaseous charge exchange cross section has been used in each case. Stokes' law (equation (4)) predicts μ_+ too large by a factor of ten, and this discrepancy can be attributed to the absence of charge exchange and polarization attraction on the viscosity of uncharged helium atoms.

It is of interest to consider briefly the magnitude of μ_- in helium liquid at 4·2°K. Recent measurements of the mobility of gaseous negative oxygen ions in the noble gases have been reported by McDaniel and Crane (1957), and assuming that mobility is inversely proportional to density the observed mobility at 0 °C and 760 mm Hg can be reduced to liquid helium densities. This predicts that the mobility of an oxygen negative ion in liquid helium would be $1{\cdot}67\times10^{-2}$ cm^{2}v^{-1}sec^{-1}, which is to be compared with the measured value of $1{\cdot}7\times10^{-2}$ cm^{2}v^{-1}sec^{-1}. Considering the extent of the extrapolation the agreement is remarkably good.

Williams measured μ_+ at 4·2°K using applied fields between 4 kv cm^{-1} and 130 kv cm^{-1}, and the inequality (10) indicates that low field equations must not be applied indiscriminately. It is apparent from the reported data that even at 4·2 °K the mobility was field dependent, and this implies that both field and thermal energies were of importance. For this condition equation (8) can be used to determine the ion–atom cross section, and since in the derivation of equation (8) only elastic collisions are considered, the cross section derived in this way is an effective hard-sphere cross section which will include an appreciable contribution from polarization attraction. At 23 kv cm^{-1} μ_+ was $7{\cdot}8\times10^{-2}$ cm^{2}v^{-1}sec^{-1}, and from equation (8) the effective cross section is $1{\cdot}4\times10^{-11}$ cm^2. The equivalent hard-sphere cross section calculated from low field data and equation (1) has been shown to be $2{\cdot}5\times10^{-14}$ cm^2, and since the contribution of polarization to the cross section is inversely proportional to the ion velocity a smaller total cross section at higher fields is to be expected.

The temperature dependence of μ_+ at a field of 23 kv cm^{-1} is shown in figure 3, and between 4·2°K and about 3°K the mobility decreases with decreasing temperature. If the cross section is assumed to be temperature independent, then equation (8) predicts a slight increase of μ_+ with decreasing temperature (figure 3); but equation (3), which gives an indication of the relative importance

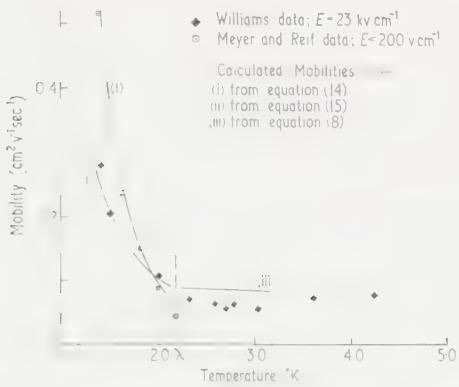

Figure 3. Mobility of positive ions in helium liquid as a function of temperature.

of polarization attraction even when the field and thermal energies are comparable, shows that the influence of polarization is increasing very rapidly in liquid helium as the temperature is lowered below 4·2 °K. (It is assumed that πS^2 is independent of temperature within this small range.) This results in an increase of the total effective cross section and therefore in an overall decrease of the mobility.

4.2. *Helium II*

In liquid helium II the ions do not collide with the superfluid liquid but only with the excitations, and above 1 °K, where the roton density is very much larger than the phonon density, the mobility is determined by ion–roton collisions alone. Recently Careri, Scaramuzzi and Thomson (1959) have confirmed the mobility measurements of Meyer and Reif and have shown that agreement between theory and experiment can be obtained by assuming only ion–roton collisions to be important. It appears that these collisions can be interpreted in terms of an elastic hard-sphere cross section. Since liquid helium II can be considered as a roton gas in a superfluid background liquid, it is of interest to apply the equations for ion mobility as derived from classical kinetic theory to the case of an ion moving in the roton gas. This is of particular interest in the case where the energy gain from the applied field is very much greater than the random thermal energy.

The number of rotons per cm³ at a temperature T is given by

$$N_r = \frac{2\mu_r^{1/2} P_0^2 (\boldsymbol{k}T)^{1/2}}{(2\pi)^{3/2}\hbar^3} \exp(-\Delta/\boldsymbol{k}T)$$

where μ_r is an effective mass, P_0 is a constant with dimensions of momentum, and Δ is the minimum energy required to excite a roton. The density of rotons is $N_r P_0^2 3\boldsymbol{k}T$ so that the effective roton mass for collisions between an ion and a roton is not μ_r but $P_0^2 3\boldsymbol{k}T$. Using the values of μ_r and P_0 given by Atkins (1959), the roton number density and effective roton mass m_r can be expressed as $N_r = 7{\cdot}3 \times 10^{22} T^{1/2} \exp(-\Delta/\boldsymbol{k}T)$ and $m_r = 16 m_{He}/T$, where m_{He} is the mass of a helium atom. The inequality (9), which indicates the limits of the low field equations gives

$$E \ll 4 \times 10^{17} \sigma_{ir} T^{5/2} \exp(-\Delta/\boldsymbol{k}T) \text{ v cm}^{-1},$$

where σ_{ir} is the ion–roton collision cross section (assumed independent of temperature). It has been suggested that $\sigma_{ir} \sim 10^{-13}\,\text{cm}^2$ and if $\Delta/k \sim 7^\circ\text{K}$, then at 2°K low field conditions are satisfied if $E \ll 7\,\text{kv cm}^{-1}$, while at $1{\cdot}2^\circ\text{K}$ $E \ll 180\,\text{v cm}^{-1}$. The field range employed by Meyer and Reif (50–$200\,\text{v cm}^{-1}$) is such that the thermal energy is predominant, but Williams' measurements were taken at fields as high as $50\,\text{kv cm}^{-1}$, and clearly the thermal energy will be only a small part of the total ion energy.

Consider first the low field equation (1). Substituting for N_r, and assuming m_r is much larger than the ionic mass we find

$$\mu = \frac{3{\cdot}38 \times 10^{-16}}{\sigma_{ir} T} \exp(\Delta/kT) \qquad \ldots\ldots (13)$$

where μ is in practical units.

Except for a small difference in the numerical factor this equation is the same as that applied by Careri, Scaramuzzi and Thomson to the data of Meyer and Reif, and from a plot of $\ln(\mu T)$ against $1/T$, Δ/k can be obtained and the cross section σ_{ir} can be estimated. The results are given in table 2.

Table 2. Δ/k and Ion–Roton Collision Cross Sections as deduced from Kinetic Theory

Equation	(1)	(2)	(6)
Δ/k (°K)	6·9	8·43	8·25
σ_{ir} (cm²)	6×10^{-14}	$\sim 10^{-15}$	2×10^{-13}

Equations (1) and (2) were compared with the low field data of Meyer and Reif, and equation (6) was compared with Williams' high field measurements.

The value of Δ/k deduced from equation (1) is very much lower than usually found experimentally, and it has been suggested that polarization may give rise to a local compression of the medium near the charge, and that as a consequence less energy is necessary to produce a roton at that point. It should be possible, therefore, to make use of equation (2), which includes the effects of polarization, and from this deduce a value of Δ/k which agrees more nearly with results obtained from experiments in which polarization is not important. If it is assumed that the density concerned in equations (2) and (3) is the density of the normal fluid, and that the dielectric constant is given by the Clausius–Mossotti relationship, then equation (2) can be written in the form

$$\mu = 2{\cdot}76 \times 10^{-3} A \exp(\Delta/kT) \qquad \ldots\ldots (14)$$

where μ is in practical units. From the experimental data of Meyer and Reif Δ/k can be calculated as $8{\cdot}43^\circ\text{K}$, which is in excellent agreement with values deduced from oscillating disc experiments. If it is assumed that polarization forces are completely dominant A can be replaced by 0·51, and μ_+ can be predicted as a function of temperature from equation (14). This is shown in figure 3. The agreement obtained is exceptionally good considering that the experimental data may be in error by as much as 50%.

If polarization forces are predominant, then Z as derived from equation (3) must be very small. Putting $Z \sim 10^{-2}$, $\pi S^2 \sim 2 \times 10^{-15} T^{-1}\,\text{cm}^2$, and this shows that the physical dimensions of a roton are comparable with the interatomic spacing.

Williams has measured μ_+ as a function of temperature at a constant field of 23 kv cm^{-1} and as a function of field at a constant temperature of 1·45 °K, and in both cases the field energy is considerably in excess of the thermal energy. Equation (6) must therefore be modified for the case of ion–roton collisions. Substituting for N_r and m_r gives

$$\mu^2 = \frac{8{\cdot}2 \times 10^{-3}}{E\sigma_{ir}} \exp(\Delta/\boldsymbol{k}T) \qquad \ldots\ldots(15)$$

where E is the applied field. Both E and μ are in practical units.

Using equation (15) and Williams measured data (figure 3), $\Delta/\boldsymbol{k}$ and σ_{ir} can be obtained and are given in table 2. The value of $\Delta\,\boldsymbol{k}$ is most satisfactory, and the very large cross section indicates that polarization attraction is still important in the high field range. At 23 kv cm^{-1} the thermal energy is not entirely negligible, and ideally equation (8) should be used. However, there is very little error in using (15), the cross section obtained from (8) being about 10% smaller than that predicted by equation (15).

Using the values of σ_{ir} and $\Delta\,\boldsymbol{k}$ deduced from the temperature variation at constant field, the variation of μ_+ with field may be obtained from equation (15). This is shown in figure 4, and the agreement with Williams' data is reasonable. A closer fit can be obtained if the thermal energy is considered by using equation (8).

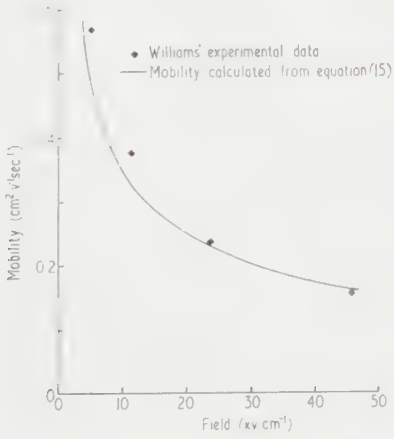

Figure 4. Mobility of positive ions in helium liquid at 1·45 °K.

§ 5. Conclusions

It has been shown that it is possible to explain both ionic and electronic mobilities in argon and helium liquids by kinetic theory provided that the correct equations are used and likely impurities are considered. In argon liquid and liquid helium I the collision cross section for positive ions is the same as found in the corresponding gas phase, with polarization scattering of extreme importance. It would appear that for the explanation of ion mobilities these liquids may be considered as compressed gases. The collision cross section found for electrons in argon liquid is shown to be in accordance with that expected if some molecular impurity were present in a very small concentration. In liquid helium II, where

ion–roton scattering is predominant, kinetic theory may be used to predict the mobilities, and very satisfactory agreement is obtained both for high field and for low field data. Again polarization is of great importnce.

Acknowledgments

The author wishes to thank Professor M. W. Humphrey Davies for facilities provided, and the Department of Scientific and Industrial Research for a maintenance allowance. He is particularly grateful to Dr. T. J. Lewis for his encouragement and helpful discussions.

References

Atkins, K. R., 1959, *Liquid Helium* (Cambridge: University Press).
Bortner, T. E., Hurst, G. S., and Stone, W. G., 1957, *Rev. Sci. Instrum.*, **28,** 103.
Careri, G., Scaramuzzi, F., and Thomson, J. O., 1959, *Nuovo Cim.*, **13,** 186.
Corbett, J. W., and Wang, J. H., 1956, *J. Chem. Phys.*, **25,** 422.
Davidson, N., and Larsh, A. E., 1950, *Phys. Rev.*, **77,** 707.
Eisenstein, A., and Gingrich, N. S., 1942, *Phys. Rev.*, **62,** 261.
Hassé, H. R., 1926, *Phil. Mag.*, **1,** 139.
Hornbeck, J. A., 1951, *Phys. Rev.*, **84,** 615.
Klema, E. D., and Allen, J. S., 1950, *Phys. Rev.*, **77,** 661.
Langevin, P., 1903, *Annales de Chimie* (*et de Physique*), (Series 7), **28,** 289.
—— 1905, *Ibid.*, (Series 8), **5,** 245.
Loeb, L. B., 1955, *Basic Processes of Gaseous Electronics* (University of California Press), p. 65.
McDaniel, E. W., and Crane, H. R., 1957, *Rev. Sci. Instrum.*, **28,** 684.
Malkin, M. S., and Schultz, H. L., 1951, *Phys. Rev.*, **83,** 1051.
Massey, H. S. W., and Burhop, E. H. S., 1952, *Electronic and Ionic Impact Phenomena* (Oxford: Clarendon Press).
Meyer, L., and Reif, F., 1958, *Phys. Rev.*, **110,** 279.
Stacey, F. D., 1958, *Aust. J. Phys.*, **11,** 158.
—— 1959, *Ibid.*, **12,** 105.
Varney, R. N., 1952, *Phys. Rev.*, **88,** 362.
—— 1953, *Ibid.*, **89,** 708.
Wannier, G., 1953, *Bell Syst. Tech. J.*, **32,** 170.
—— 1954, *Phys. Rev.*, **96,** 831.
Williams, R. L., 1957, *Canad. J. Phys.*, **35,** 134.
Williams, R. L., and Stacey, F. D., 1957, *Canad. J. Phys.*, **35,** 928.

The Lamb Shift of Helium

By A. DALGARNO† and A. L. STEWART‡

† Department of Applied Mathematics, ‡ Department of Physics,
The Queen's University of Belfast

MS. received 12th January 1960

Abstract. Using carefully selected oscillator strengths the logarithm of the average excitation energy, measured in rydbergs, appropriate to the Lamb shift is computed to be $4{\cdot}37 \pm 0{\cdot}03$. Taken together with recent calculations by Pekeris, the theoretical value of the ionization potential of helium is $198310{\cdot}674 \pm 0{\cdot}025\ \mathrm{cm}^{-1}$ compared with $198310{\cdot}8_2 \pm 0{\cdot}15\ \mathrm{cm}^{-1}$, the experimental value.

§ 1. Introduction

The major uncertainty in the theoretical value of the ionization potential of helium arises in the evaluation of the average excitation energy k_0 appropriate to the Lamb shift. According to Bethe (1947) k_0 is defined by the equation

$$\ln k_0 = \frac{\sum_n f_n (E_0 - E_n)^2 \ln (E_0 - E_n)}{\sum_n f_n (E_0 - E_n)^2} \qquad \ldots\ldots (1)$$

where f_n is the oscillator strength of the electric dipole transition from the ground state with binding energy E_0 to the nth excited state with binding energy E_n, the summations including integrations over all the continua. Clearly most of the contribution to k_0 comes from transitions corresponding to photo-ionization.

The first estimate of k_0 was given by Dalgarno and Lynn (1957), who used oscillator strengths with an asymptotic form determined to ensure that four sum rules are satisfied. A much improved estimate was then presented by Kabir and Salpeter (1957) who used oscillator strengths with the correct asymptotic form, which, however, satisfied only one sum rule. A combination of the two investigations should result in greater precision. In any event, a re-investigation is desirable since the contributions to k_0 from transitions to doubly excited states according to Dalgarno and Lynn and according to Kabir and Salpeter are very different.

§ 2. Sum Rules

If $\mathbf{r}_1$ and $\mathbf{r}_2$ are the position vectors of the two electrons referred to the nucleus and $\psi_0(\mathbf{r}_1, \mathbf{r}_2)$ and $\psi_n(\mathbf{r}_1, \mathbf{r}_2)$ are the wave functions of the ground and nth excited states respectively,

$$f_n = \tfrac{1}{3}(E_0 - E_n)|(\psi_0, [\mathbf{r}_1 + \mathbf{r}_2]\psi_n)|^2, \qquad \ldots\ldots (2)$$

E_0 and E_n being measured in rydbergs and distance in units of $a_0 = 5{\cdot}292 \times 10^{-9}$ cm. The oscillator strengths satisfy the sum rules (cf. Dalgarno and Lynn 1957)

(i) $$S_2 = \sum_n f_n (E_0 - E_n)^2 = \frac{32\pi}{3} (\psi_0, [\delta(\mathbf{r}_1) + \delta(\mathbf{r}_2)]\psi_0)$$

where $\delta(\mathbf{r})$ is the three-dimensional Dirac δ-function.

(ii) $$S_1 = \sum_n f_n (E_0 - E_n) = 4\{E_0 + 2(\psi_0, \mathbf{p}_1 \cdot \mathbf{p}_2 \psi_0)\}/3$$

where $\mathbf{p}_i$ is the momentum of the ith electron in atomic units.

(iii) $$S_0 = \sum_n f_n = 2,$$

(iv) $$S_{-1} = \sum_n f_n/(E_0 - E_n) = (\psi_0, [\mathbf{r}_1 + \mathbf{r}_2]^2 \psi_0)/3,$$

(v) $$S_{-2} = \sum_n f_n/(E_0 - E_n)^2 = \alpha/4,$$

where α is the dipole polarizability in units of a_0^3.

(vi) $$S_{-4} = \sum_n f_n/(E_0 - E_n)^4 = \beta$$

where β can be determined from experimental data on the refractive index and from experimental data on the Verdet constant.

We adopt the values for S_k given in table 1. S_2, S_1 and S_{-1} are taken from Pekeris (1959), S_{-2} from Essen (1953) and S_{-4} from Dalgarno and Lynn (1957).

Table 1. Values of Sum Rules

	Direct, theory or experiment	Derived from oscillator strengths
$\Sigma_n f_n (E_0 - E_n)^2 \ln (E_0 - E_n)$	—	530·2
S_2	121·3	121·3
S_1	8·17	8·17
S_0	2	2
S_{-1}	0·7525	0·7525
S_{-2}	$0{\cdot}349 \pm 0{\cdot}003$	0·346
S_{-4}	$0{\cdot}098_0$	0·0963

The accuracy of the experimental value of S_{-4} is uncertain.

§ 3. Asymptotic Forms

The transition matrix element may be written in the length, the velocity or the acceleration forms. The arguments of Dalgarno and Lewis (1956) suggest that for high energy transitions, the acceleration matrix element is the least sensitive to the wave functions adopted. The oscillator strength for a transition into the continuum described by an electron of energy ϵ rydbergs moving in the field of a helium ion $He^+(1s)$ in its ground state is accordingly written in the form

$$\frac{df}{d\epsilon} = \frac{1}{3}(I + \epsilon) \left\{ \frac{2}{(I+\epsilon)^2} \left| \left(\psi_0, \left[\frac{4\mathbf{r}_1}{r_1^3} + \frac{4\mathbf{r}_2}{r_2^3} \right] \psi_n \right) \right| \right\}^2 \quad \ldots\ldots (3)$$

where I is the first ionization potential of helium.

For large values of ϵ, we may replace $\psi_n(\mathbf{r}_1, \mathbf{r}_2)$ by

$$\psi_n(\mathbf{r}_1, \mathbf{r}_2) = \frac{1}{2\pi} \left(\frac{k}{2} \right)^{1/2} \{ u_0(\mathbf{r}_1) \exp(i\mathbf{k} \cdot \mathbf{r}_2) + u_0(\mathbf{r}_2) \exp(i\mathbf{k} \cdot \mathbf{r}_1) \} \quad \ldots\ldots (4)$$

where $u_0(\mathbf{r}_1)$ is the wave function of $He^+(1s)$ and $\mathbf{k}$ is the momentum of the ejected electron such that $k^2=\epsilon$. Then using the identities

$$\frac{i\mathbf{r}}{r^3}=\frac{1}{2\pi^2}\int\frac{d\mathbf{k}'}{k'^2}\,\mathbf{k}'\exp(i\mathbf{k}'.\mathbf{r})$$

$$\delta(\mathbf{r})=\frac{1}{8\pi^3}\int d\mathbf{k}'\exp(i\mathbf{k}'.\mathbf{r}),$$

it follows from (3) that for large values of ϵ

$$\frac{df}{d\epsilon}\sim C\epsilon^{-7/2}$$

where

$$C=\frac{512}{3}\left|\int\psi_0(\mathbf{r}_1,0)u_0(\mathbf{r}_1)d\mathbf{r}_1\right|^2. \qquad \ldots\ldots(5)$$

Expression (5) has been obtained previously by Kabir and Salpeter (1957), using an apparently new method. They evaluate the leading term of the velocity matrix element in momentum space after carrying out a certain transformation. However their transformation is equivalent to that which transforms the velocity matrix element to the acceleration matrix element in coordinate space. Kabir and Salpeter demonstrate by explicit calculation that C is insensitive to the choice of $\psi_0(\mathbf{r}_1,\mathbf{r}_2)$, their recommended value of C being 286. The method used by Kabir and Salpeter does not provide any estimate of the energy at which (5) is a satisfactory approximation to the oscillator strength and our purpose in presenting an alternative is to demonstrate that (5) is merely the leading term of (3), which may, of course, be evaluated without making the approximations involved in obtaining (5).

§ 4. Oscillator Strengths

4.1. *Singly Excited Discrete Transitions*

Calculations of discrete oscillator strengths up to 1957 have been briefly reviewed by Dalgarno and Lynn (1957). Since then, Low and Stewart (unpublished) have computed further values and they conclude that the use of the length matrix element leads to the most reliable results (see also Stewart and Wilkinson 1960). The results of Low and Stewart based upon the six-parameter Hylleraas (1929) representation of ψ_0 and a modified hydrogenic wave function for ψ_n are reproduced in table 2. The value for the resonance transition agrees closely with that recommended by Miller and Platzman (1957).

There are no reliable experimental values.

Table 2. Values of the Oscillator Strengths for the $(1s^2)^1S-(1s,np)^1P$ transitions in Helium

n	2	3	4	5	6
f_n	0·275	0·0746	0·0304	0·0153	0·00878

4.2. *Singly Ionized Transitions*

Oscillator strengths for singly ionized transitions have been computed by Huang (1948) using the six-parameter Hylleraas representation of ψ_0 and a hydrogenic approximation for the continuum in the length, velocity and acceleration formulations. Dalgarno and Lynn (1957) suggested that his velocity matrix

element is too large at the spectral head, and this has been confirmed recently by Stewart and Wilkinson (1960) who used a Hartree-Fock representation of the continuum state. We adopt the values recommended by Stewart and Wilkinson for energies ϵ up to 1 rydberg and Huang's acceleration values (extended to higher energies) for ϵ greater than 1 rydberg. This choice differs from that of Kabir and Salpeter (1957), who adopted Huang's velocity values for all ϵ, but is justified by the demonstration in § 3.

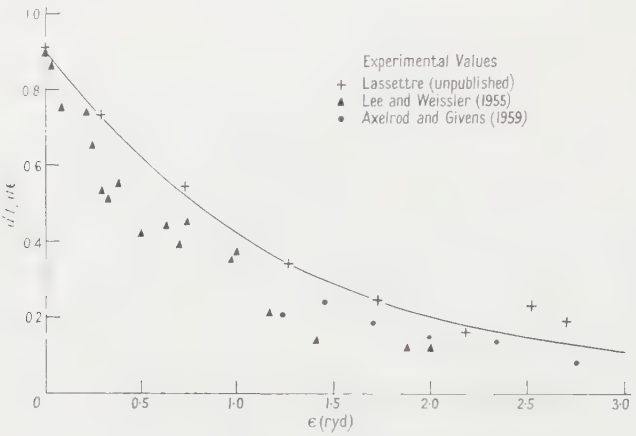

The oscillator strengths for single ionization of helium as a function of the energy ϵ rydbergs of the ejected electron. The full line is the adopted theoretical curve; the points are experimental values. To convert the oscillator strengths to photo-ionization cross sections, multiply $df/d\epsilon$ by $8{\cdot}07 \times 10^{-16}$ and to convert the energy scale to wavelength λ in Å, use the relation $\lambda = 911{\cdot}3/(1{\cdot}807 + \epsilon)$.

The selected values are illustrated in the figure, which shows also experimental values due to Lee and Weissler (1955), to Axelrod and Givens (1959) and to Lassettre (unpublished). In addition, Dershem and Shein (1931) have reported a value for $df/d\epsilon$ at 44·6 Å of 0·0030 compared with our theoretical value of 0·0022.

It may be noted that the adopted values for the singly excited and singly ionized transitions satisfy the continuity requirement at the spectral head (Hartree 1928, Hargreaves 1929).

4.3. *Simultaneously Excited and Ionized Transitions*

Because of the large energies involved, contributions to the Lamb shift of transitions in which the final state of the He^+ ion is excited are relatively important.

We can estimate the asymptotic contribution accurately by using the appropriate modification of (5). Thus for the $He(1s^2)$–$He(ns,\epsilon p)$ transition, $df/d\epsilon \sim C_{ns}\epsilon^{-7/2}$ where

$$C_{ns} = \frac{512}{3}\left| \int \psi_0(\mathbf{r}_1, 0) u(ns|\mathbf{r}_1) d\mathbf{r}_1 \right|^2,$$

$u(ns|\mathbf{r}_1)$ being the wave function describing $He^+(ns)$. We find that

$$C_{1s} : C_{2s} : C_{3s} = 1 : 0{\cdot}0487 : 0{\cdot}0066.$$

The total contribution for all states of He^+ can also be readily obtained. For

$$\sum_{ns} C_{ns} = \frac{512}{3} \sum_{n} \int \psi_0(\mathbf{r}_1, 0) u(ns|\mathbf{r}_1) d\mathbf{r}_1 \int \psi_0(\mathbf{r}_1', 0) u(ns|\mathbf{r}_1') d\mathbf{r}_1'$$
$$= \frac{512}{3} \int\int \delta(\mathbf{r}_1 - \mathbf{r}_1') \psi_0(\mathbf{r}_1, 0) \psi_0(\mathbf{r}_1', 0) d\mathbf{r}_1 d\mathbf{r}_1'$$
$$= \frac{512}{3} \int \left| \psi_0(\mathbf{r}_1, 0) \right|^2 d\mathbf{r}_1$$

with the result that the sum of the ratios for all states is 1·079. It is to be noted that the sum includes the contribution from double ionization.

For transitions such as $(1s)^2 - (np, \epsilon s)$, C vanishes and the leading term in the asymptotic formula falls off as $\epsilon^{-9/2}$. The contribution to the Lamb shift is therefore comparatively small.

To obtain estimates at lower energies, we assume that $\psi_0(\mathbf{r}_1, \mathbf{r}_2)$ can be written in the separable form $f(\mathbf{r}_1) f(\mathbf{r}_2)$, the function $f(r)$ being the Hartree approximation. Then writing

$$\psi(ns|\mathbf{r}_1, \mathbf{r}_2) = \frac{1}{\sqrt{2}} \{ u(ns|\mathbf{r}_1) F(\epsilon p|\mathbf{r}_2) + u(ns|\mathbf{r}_2) F(\epsilon p|\mathbf{r}_1) \},$$

where $F(\epsilon p|\mathbf{r})$ is the properly normalized Coulomb wave function, and using the length form of the matrix element, it follows that

$$\frac{df(1s^2 - 1s, \epsilon p)}{df(1s^2 - 1s, \epsilon p)} = \frac{(I_n + \epsilon)}{(I - \epsilon)} \frac{\left| \int f(\mathbf{r}) u(ns|\mathbf{r}) d\mathbf{r} \right|^2}{\left| \int f(\mathbf{r}) u 1s(|\mathbf{r}) d\mathbf{r} \right|^2}$$

where I_n is the nth ionization potential given by $I_n = I + 4 - 4/n^2$. At the spectral heads, the ratios for final 1s, 2s and 3s states are 1 : 0·0618 : 0·0079. These ratios are not too different from the asymptotic ratios and we shall assume initially that we may use the asymptotic ratios for all values of ϵ.

4.4. *Doubly Excited Discrete Transitions*

To provide a guide to the oscillator strengths of doubly excited discrete transitions, we assume that the spectral head continuity rule applies to all the discrete transitions. Together with the results of § 4.3, this gives for transitions to the (2s, np) and (3s, np) states the values listed in table 3. For transitions to the (2s, 2p) and (3s, 3p) states, the values may be compared with those of Vinti (1932) who obtained 0·011 and 0·0008 respectively.

Table 3. Values of the Oscillator Strengths for the $(1s^2)^1S - (2s, np)^1P$ and $(1s^2)^1S - (3s, np)^1P$ Transitions in Helium

n	$f(2s, np)$	$f(3s, np)$
2	0·0109	0·00148
3	0·00324	0·000439
4	0·00137	0·000186
5	0·000701	0·0000950
6	0·000405	0·0000549
7	0·000255	0·0000346
8	0·000171	0·0000232
9	0·000120	0·0000163
10	0·0000877	0·0000119

Apart from the $(2s, 2p)^1P$ and $(2s, 3p)^1P$ states, the energies of which probably lie 4·41 and 4·67 rydbergs respectively above the ground level, the locations of the doubly excited states are uncertain (cf. Bransden and Dalgarno 1953). We suppose that for the $(2s, np)^1P$ series, $E_0 - E_n = 4{\cdot}81 - 1{\cdot}58/n^2$ rydbergs with similar formulae for other doubly excited series.

§ 5. Calculations and Results

The oscillator strengths described in the previous section are in reasonable but not exact agreement with the sum rule requirements of § 2. We have modified them so that they conform to the sum rules S_2, S_1, S_0 and S_{-1} more precisely, the method of modification being largely arbitrary except that the constants describing the asymptotic behaviour are held fixed at the theoretical values given in §§ 4·2 and 4·3. The values of the sum rules derived using the modified oscillator strengths are given in the third column of table 1. The harmony of the computed and measured values of S_{-2} and S_{-4} lends further support to the accuracy of the derived oscillator strengths.

The individual contributions to the numerator and denominator of (1) are compared in table 4 with those obtained by Kabir and Salpeter (1957). Despite the considerable differences between the individual contributions, the actual values for the Lamb shift are very close; for $\ln k_0$ we obtain 4·37 and Kabir and Salpeter obtain 4·39.

Table 4. Contributions to the Numerator and Denominator of expression (1) in units of 121·28 ryd²

	Numerator		Denominator	
	K & S	D & S	K & S	D & S
Discrete single excitation	0·0048	0·0045	0·0098	0·0092
Discrete double excitation	0·0051	0·0073	0·0032	0·0049
Single ionization				
$\epsilon =$ 0–10 ryd	0·3478	0·3149	0·1981	0·1874
$\epsilon =$ 10–400 ryd	2·3470	1·9367	0·5743	0·4721
$\epsilon =$ 400–∞ ryd	1·7812†	1·6930	0·2370	0·2084
Simultaneous excitation and ionization	—	0·4132	—	0·1180
Sum	4·4859	4·3696	1·0224	1·0000

K & S: Kabir and Salpeter; D & S: Dalgarno and Stewart.

† This value is not consistent with the assertion by Kabir and Salpeter that for $\epsilon > 400$ ryd the asymptotic form of Huang's velocity formula was used. This would yield a value of 1·8896.

Kabir and Salpeter state that their possible error most probably lies between $\pm 0{\cdot}2$ and almost certainly between $-0{\cdot}2$ and $+0{\cdot}6$. We believe that our possible error most probably lies between $\pm 0{\cdot}03$ and almost certainly between $\pm 0{\cdot}1$, although these limits are not rigorously established.

The radiation corrections to $O(\alpha^3)$, α being the fine-structure constant, may be written for helium as

$$\Delta I_{\mathrm{L}} = E_{\mathrm{L},1} - E_{\mathrm{L},2} - E'_{\mathrm{L},2} - E''_{\mathrm{L},2}$$

(Kabir and Salpeter 1957, Araki 1957, Sucher 1958) where

$$E_{\mathrm{L},1} = 3{\cdot}534\,\mathrm{cm}^{-1} \quad \text{(Kabir and Salpeter 1957)},$$

$$E_{\mathrm{L},2} = \frac{32}{3}\,(\psi_0, \delta(r_1)\psi_0)(-2\ln\alpha - \ln k_0 + 19/30)\alpha^3 ryd,$$

$$E'_{\mathrm{L},2} = -0{\cdot}208\,\mathrm{cm}^{-1} \quad \text{(Pekeris 1959)}$$

and

$$E''_{\mathrm{L},2} = 0{\cdot}068_5\,\mathrm{cm}^{-1} \quad \text{(Dalgarno and Stewart 1960)}.$$

Using the expectation value of $\delta(\mathbf{r}_1)$ computed by Pekeris,

$$E_{\mathrm{L},2} = (5{\cdot}026 - 0{\cdot}823\delta)\,\mathrm{cm}^{-1}.$$

Hence

$$\Delta I_{\mathrm{L}} = (-1{\cdot}352 - 0{\cdot}823\delta)\,\mathrm{cm}^{-1}.$$

The sum of the non-relativistic ionization potential, the mass polarization and the relativistic corrections is given by Pekeris (1959) as $198312{\cdot}026\,\mathrm{cm}^{-1}$ so that

$$I = (198310{\cdot}674 - 0{\cdot}823\delta)\,\mathrm{cm}^{-1}.$$

Since δ is probably between $\pm 0{\cdot}03$, the probable theoretical value is

$$198310{\cdot}674 \pm 0{\cdot}025\ \mathrm{cm}^{-1}$$

compared with the experimental value of

$$198310{\cdot}8_2 \pm 0{\cdot}15\ \mathrm{cm}^{-1}$$

(Herzberg 1958). The estimated error in the theoretical value of I does not take account of the possible error of $E''_{\mathrm{L},2}$.

Acknowledgment

Dr. N. Lynn was of considerable assistance to us in the early stages of the calculations.

References

Araki, H., 1957, *Progr. Theor. Phys.*, **17**, 619.
Axelrod, N. N., and Givens, M. P., 1959, *Phys. Rev.*, **115**, 97.
Bethe, H. A., 1947, *Phys. Rev.*, **72**, 339.
Bransden, B. H., and Dalgarno, A., 1953, *Proc. Phys. Soc.* A, **66**, 911.
Dalgarno, A., and Lewis, J. T., 1956, *Proc. Phys. Soc.* A, **69**, 285.
Dalgarno, A., and Lynn, N., 1957, *Proc. Phys. Soc.* A, **70**, 802.
Dalgarno, A., and Stewart, A. L., 1960, *Proc. Phys. Soc.*, **75**, 441.
Dershem, E., and Shein, M., 1931, *Phys. Rev.*, **37**, 1238.
Essen, L., 1953, *Proc. Phys. Soc.* B, **66**, 189.
Hargreaves, J., 1929, *Proc. Camb. Phil. Soc.*, **25**, 75.
Hartree, D. R., 1928, *Proc. Camb. Phil. Soc.*, **24**, 426.
Herzberg, G., 1958, *Proc. Roy. Soc.* A, **248**, 309.
Huang, S. S., 1948, *Astrophys. J.*, **108**, 354.
Hylleraas, E. A., 1929, *Z. Phys.*, **54**, 347.
Kabir, P. K., and Salpeter, E. E., 1957, *Phys. Rev.*, **108**, 1256.
Lee, P., and Weissler, G. L., 1955, *Phys. Rev.*, **99**, 540.
Miller, W. F., and Platzman, R. L., 1957, *Proc. Phys. Soc.* A, **70**, 299.
Pekeris, C. L., 1959, *Phys. Rev.*, **115**, 1216.
Stewart, A. L., and Wilkinson, W. J., 1960, *Proc. Phys. Soc.*, **75**, 796.
Sucher, J., 1958, *Phys. Rev.*, **109**, 110.
Vinti, J. P., 1932, *Phys. Rev.*, **42**, 632.

Energy Levels of ^{29}P, ^{33}Cl and ^{41}Sc from (d, n) Reactions

By B. E. F. MACEFIELD and J. H. TOWLE
Atomic Weapons Research Establishment, Aldermaston, Berks.

MS. received 21*st December* 1959

Abstract. The time-of-flight technique has been used to study the neutron spectra from the reactions ^{28}Si(d, n)^{29}P, ^{32}S(d, n)^{33}Cl and ^{40}Ca(d,n)^{41}Sc. Weak neutron groups have now been resolved which correspond to levels in ^{29}P at $2{\cdot}42 \pm 0{\cdot}04$ and $3{\cdot}13 \pm 0{\cdot}03$ MeV, and in ^{33}Cl at $2{\cdot}11 \pm 0{\cdot}06$ and $2{\cdot}53 \pm 0{\cdot}06$ MeV. Only one group could be definitely attributed to the ^{40}Ca(d, n)^{41}Sc reaction, and this denotes a level Q-value of $-2{\cdot}86 \pm 0{\cdot}02$ MeV.

§ 1. Introduction

The (d, p) reactions on the target nuclei ^{28}Si, ^{32}S and ^{40}Ca have been studied with good resolution, and levels in ^{29}Si, ^{33}S and ^{41}Ca have been accurately located. The levels of ^{29}Si and ^{33}S have also been confirmed using (d, α) reactions. Information on the levels of the mirror nuclei ^{29}P, ^{33}Cl and ^{41}Sc is much less complete. Data have been obtained from the (p, γ) and (d, n) reactions, but those afforded by the former reaction are very restricted, while the latter requires the difficult techniques of neutron spectrometry.

In ^{29}Si there are well confirmed levels at 1·28, 2·03, 2·43, 3·07 and 3·62 MeV (Endt and Braams 1957). In the ^{28}Si(d, p)^{29}Si reaction with 8·2 MeV deuterons the third and fourth levels are only weakly excited (Holt and Marsham 1953).

The neutron spectrum from ^{28}Si(d, n)^{29}P has been studied with 9 MeV deuterons by Calvert *et al.* (1957), using a scintillation recoil spectrometer. Neutron groups were observed corresponding to levels in ^{29}P at 1·3, 1·9 and 3·5 MeV. Green (1955) obtained similar results with 8·5 MeV deuterons and using nuclear emulsions, but in addition found some unresolved neutrons which may be due to levels in ^{29}P at about 2·5 and 2·9 MeV.

A resonance in the yield of the ^{28}Si(p, γ)^{29}P reaction has been found at $0{\cdot}367 \pm 0{\cdot}002$ MeV, corresponding to a level in ^{29}P at $3{\cdot}078 \pm 0{\cdot}009$ MeV. This resonance level decays via excited states at $1{\cdot}380 \pm 0{\cdot}02$ and $1{\cdot}935 \pm 0{\cdot}02$ MeV (Van Oostrum *et al.* 1958).

In ^{33}S the first six levels are known to be at 0·841, 1·96, 2·31, 2·87, 2·94 and 2·97 MeV (Endt and Braams 1957). The proton groups leading to the levels at 1·96 and 2·31 MeV were very weak in the ^{32}S(d, p) reaction with 8·2 MeV deuterons (Holt and Marsham 1953).

The ^{32}S(d, n)^{33}Cl reaction has been studied by Middleton *et al.* (1953) using nuclear emulsions and 8 MeV deuterons. Levels in ^{33}Cl were found at $0{\cdot}76 \pm 0{\cdot}07$, $2{\cdot}84 \pm 0{\cdot}06$ and $4{\cdot}22 \pm 0{\cdot}08$ MeV, while at certain angles a weak group was observed corresponding to a possible level at 1·89 MeV. A study of the ^{32}S(p, γ)^{33}Cl reaction has revealed the doublet nature of the level at 2·84 MeV (van der Leun and Endt 1958). Resonances occur at 0·580 and 0·587 MeV, corresponding to levels at $2{\cdot}85 \pm 0{\cdot}02$ and $2{\cdot}86 \pm 0{\cdot}02$ MeV. The latter decays in part via the first excited state at $0{\cdot}806 \pm 0{\cdot}004$ MeV.

Plendl and Steigert (1959) using nuclear emulsions and 4 MeV deuterons have observed neutron groups from $^{40}Ca(d, n)^{41}Sc$. Q-values of $-0{\cdot}57$, $(-1{\cdot}13)$, $(-1{\cdot}41)$, $-2{\cdot}43$ and $-2{\cdot}54$ MeV were reported, corresponding to the ground state and levels of ^{41}Sc at (0·56), (0·84), 1·86 and 1·97 MeV. The data in brackets may be due to impurities. Butler (1959) has reported the presence of a resonance at 0·650 MeV in the yield of the $^{40}Ca(p, \gamma)^{41}Sc$ reaction.

In view of the importance of the concept of charge independence of nuclear forces, we have re-examined these (d, n) reactions with improved energy resolution with a particular interest in locating the levels expected in ^{29}P at about 2·4 MeV, and in ^{33}Cl at about 2·0 and 2·3 MeV, corresponding to levels in their mirror nuclei. By analogy with the corresponding (d, p) reactions, the neutron groups leading to these levels are expected to be of low intensity. Similarly, the $^{40}Ca(d, n)^{41}Sc$ reaction warranted further investigation. The bombarding energy was chosen to be approximately 4 MeV in these experiments, since this is sufficient to excite the levels of interest, and is compatible with good energy resolution.

The aim of this work was to obtain Q-values, and differential cross sections were not measured. Although it would be of interest to measure the angular distributions of the new neutron groups we have observed, their low intensity has precluded this. The angular distributions of the more intense groups have already been obtained by previous workers, at higher deuteron energies, and information on level spins has been deduced using stripping theory. Similar measurements with 4 MeV deuterons were therefore eschewed.

At low energies the time-of-flight technique affords better energy resolution than nuclear emulsions or the scintillation spectrometer. Neutron energies of 1 MeV or less can be measured with an uncertainty of $\pm 0{\cdot}02$ MeV. However this uncertainty increases in proportion to $E_n^{3/2}$, and thus for reasonably accurate measurements the technique strongly favours reactions of low Q-value. The reactions we have studied have ground-state Q-values of approximately zero, and thus the neutrons had energies not greater than 4 MeV, the bombarding energy. It will be seen in tables 1 and 2 that the most negative Q-values were measured with the greatest accuracy.

§ 2. Experimental Details

The time-of-flight spectrometer used in these experiments has been described previously (Batchelor and Towle 1959). Owing to the high background flux of neutrons due to the incidence of 20 μA of 4 MeV deuterons on the deflector plates, it was necessary to house the detector inside a larger shield than mentioned previously. This was a water tank 4 ft in diameter × 4 ft deep. The collimating channel and the detector housing were surrounded by a 2-inch thickness of lead in order to attenuate capture γ-rays produced in the tank. A comparison with a long counter showed that the neutron counting efficiency of the detector was constant within 10% over the energy range 0·6 to 4·0 MeV. The shield was mounted on a turntable allowing the angle of observation to be varied. The time to pulse-height converter was adjusted so that each channel of the 100-channel analyser corresponded to approximately 2 nsec (mμsec.)

The sulphur targets were prepared by vacuum evaporation of natural Sb_2S_3, and for one run CdS (98·7% ^{32}S) obtained from the Atomic Energy Research Establishment, Harwell. The silicon targets were similarly prepared from natural silicon, and natural silica was used as an oxygen target for background runs.

The calcium target was made by evaporation of natural calcium *in situ*, to minimize oxidation. Contamination of the targets by oxygen proved a serious hindrance, since the $^{16}O(d, n)^{17}F$ reaction is very prolific and has Q-values close to those of the reactions being studied. Target thicknesses of 200–300 $\mu g\,cm^{-2}$ were used, these producing an energy loss of approximately 25 kev to 4 Mev deuterons. The target backings were made of gold foil of thickness 0·005 in. Background measurements were made using clean gold backings as targets. The only structure observed in the time spectra of these background runs was due to slight deposits of carbon and oxygen.

§ 3. Results

3.1. $^{28}Si(d, n)^{29}P$

Figure 1(*a*) shows a time spectrum measured at 88° for a natural silicon target. The neutron groups have been assigned to levels in the residual nuclei, and are labelled correspondingly. In all the spectra the two peaks due to $^{16}O(d, n)^{17}F$ are present. Figure 1(*b*) is the spectrum obtained with a SiO_2 target under the same conditions, showing relatively few neutrons from ^{28}Si. A comparison of the relative heights of the two ^{17}F groups in figures 1 (*a*) and (*b*) shows that besides the five resolved groups due to ^{28}Si seen in 1(*a*), another, $^{29}P_3$ is situated beneath the ^{17}F ground state group.

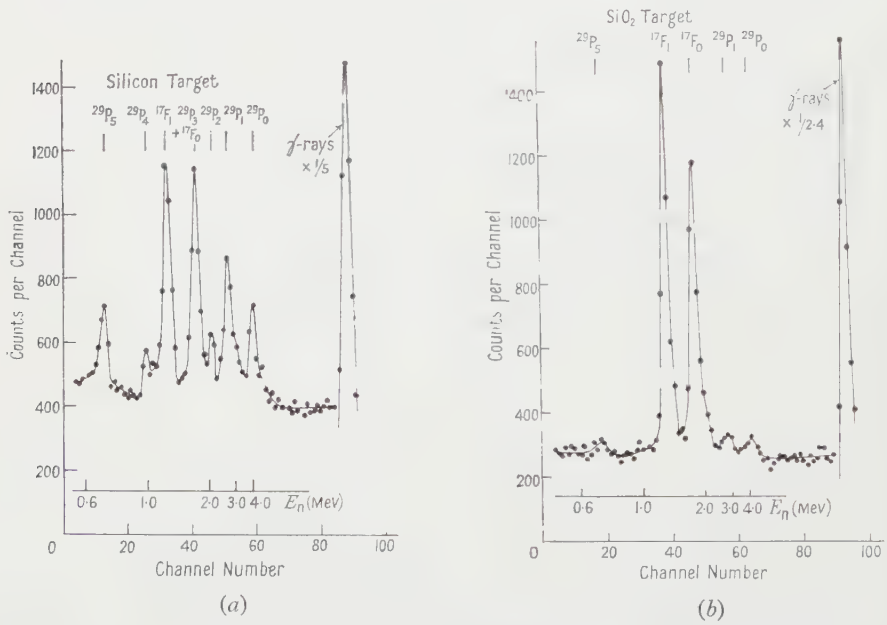

Figure 1 (*a*), (*b*). Time spectra of neutrons at 88° with $E_d = 3{\cdot}955$ Mev and a flight path of 181 cm.

At 30°, figure 2(*a*), the ^{17}F groups have moved to a slightly higher energy relative to the ^{29}P groups owing to centre-of-mass motion, and the group $^{29}P_3$ can be seen as a bump on the low energy side of $^{17}F_0$. A group $^{13}N_0$ has appeared due to ^{12}C contamination, and figure 2(*b*) shows for comparison the spectrum obtained with a carbon target of thickness 50 $\mu g\,cm^{-2}$, the ^{17}F groups being observed also.

The data collected from six runs on Si are shown in table 1. The Q-values for the various neutron groups are tabulated, and from the mean values the corresponding levels of ^{29}P are deduced.

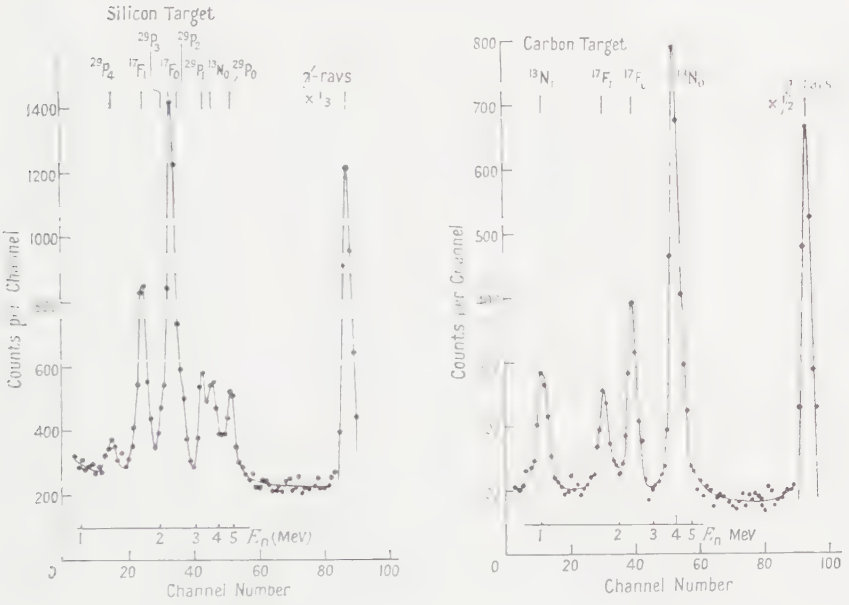

Figure 2 (*a*), (*b*). Time spectra obtained at 30° with $E_d = 3{\cdot}955$ MeV and a flight path of 231 cm.

3.2. $^{32}S(d, n)^{33}Cl$

Figure 3(*a*) shows the time spectrum obtained at 30° with an Sb_2S_3 target. Five groups due to ^{32}S are observed. A spectrum obtained under similar conditions with a carbon target of thickness 50 μg cm^{-2} is shown in figure 3(*b*).

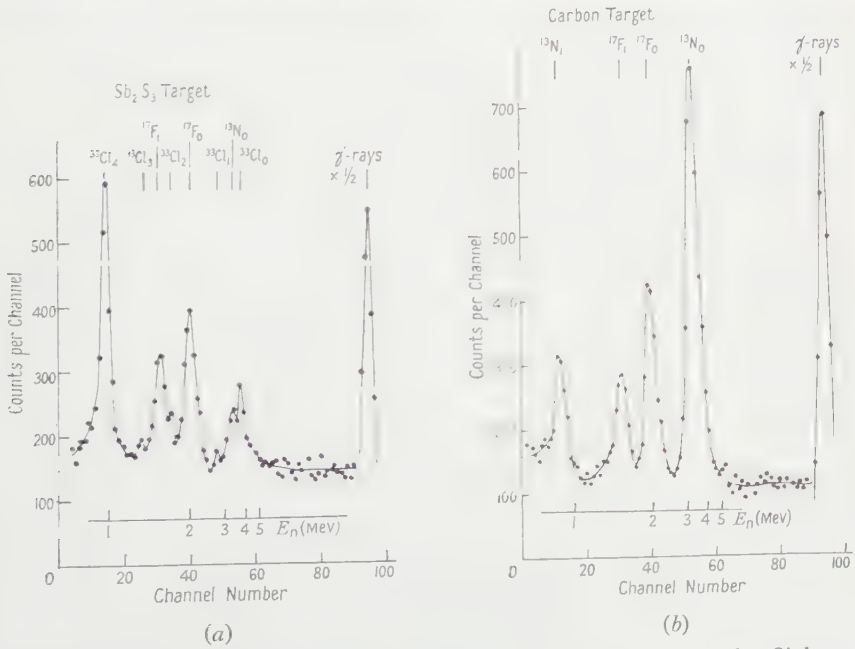

Figure 3 (*a*), (*b*). Time spectra obtained at 30° with $E_d = 3{\cdot}917$ MeV and a flight path of 231 cm.

Table 1. Q-values for Reaction ^{28}Si (d, n) ^{29}P

Energy (MeV)	Angle (deg)	Q-value (MeV)					
		0	1	2	3	4	5
3·955	75	+0·57 ± 0·10	−0·86 ± 0·07	−1·44 ± 0·06	—	−2·58 ± 0·02	−2·93 ± 0·02
3·955	88	+0·57 ± 0·10	−0·84 ± 0·07	−1·43 ± 0·06	−1·87 ± 0·04	−2·59 ± 0·02	−2·93 ± 0·02
3·955	30	+0·61 ± 0·10	−0·80 ± 0·07	—	−1·88 ± 0·04	−2·55 ± 0·02	—
3·384	88	+0·69 ± 0·07	−0·78 ± 0·04	−1·40 ± 0·03	—	—	—
3·955	88	+0·64 ± 0·10	−0·83 ± 0·07	−1·40 ± 0·06	−1·85 ± 0·04	−2·58 ± 0·02	—
3·955	88	+0·68 ± 0·10	−0·79 ± 0·07	−1·35 ± 0·06	−1·84 ± 0·04	−2·56 ± 0·02	—
Mean Q-values		+0·63 ± 0·06	−0·82 ± 0·03	−1·40 ± 0·03	−1·86 ± 0·02	−2·57 ± 0·01	−2·93 ± 0·01
†Levels ^{29}P		G.S.	1·38 ± 0·04	1·96 ± 0·04	2·42 ± 0·04	3·13 ± 0·03	3·49 ± 0·03

† Using Q (ground state) = 0·56 ± 0·03 MeV, see § 4.

The width of the fifth group $^{33}Cl_4$ is 80 kev at half height, which is consistent with the excitation of a single level at 2·82 Mev since the spread due to timing uncertainty is 75 kev, and the target thickness is 30 kev. The width is also consistent with the excitation of a doublet level of 7 kev splitting as observed by van der Leun and Endt (see §1). The doublet splitting would have to be 30 kev or more in order to increase significantly the observed width of the group.

In table 2 we present the reaction Q-values and corresponding levels of ^{33}Cl obtained from four runs, that at 35° being done with a target enriched in ^{32}S to 98·7%.

Table 2. Q-values for Reaction $^{32}S(d, n)^{33}Cl$

Energy (Mev)	Angle (deg)	Q-value (Mev)				
		0	1	2	3	4
3·917	30	+0·13 ± 0·09	−0·84 ± 0·06	−2·03 ± 0·03	−2·42 ± 0·02	−2·74 ± 0·02
3·505	15	+0·09 ± 0·09	−0·73 ± 0·07	−1·99 ± 0·03	−2·43 ± 0·02	−2·67 ± 0·02
3·505	35	+0·09 ± 0·09	−0·77 ± 0·07	−2·02 ± 0·03	−2·38 ± 0·02	−2·76 ± 0·02
4·221	45	—	—	−1·98 ± 0·04	−2·47 ± 0·03	−2·72 ± 0·02
Mean Q-values		+0·10 ± 0·05	−0·78 ± 0·05	−2·01 ± 0·02	−2·43 ± 0·03	−2·72 ± 0·03
Levels ^{33}Cl		G.S.	0·88 ± 0·07	2·11 ± 0·06	2·53 ± 0·06	2·82 ± 0·06

3.3. $^{40}Ca\ (d, n)^{41}Sc$

A time spectrum obtained at 30° from a natural calcium (97%^{40}Ca) target is shown in figure 4. Comparing this with a run on carbon under similar conditions, figure 2(*b*), we note that the intense group at 1 Mev coincides with the group $^{13}N_1$ from carbon contamination, but the latter supplies not more than 10% of the counts in this peak. In four runs (results in table 3) this group is the only one we can reliably attribute to ^{40}Ca. The width of the group (75 kev) is as we expect

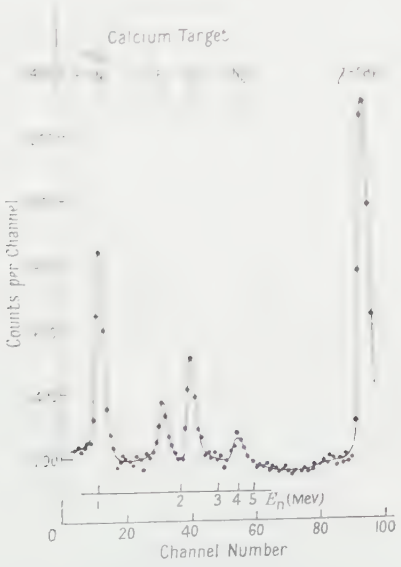

Figure 4. Time spectrum of neutrons at 30° from a calcium target. $E_d = 3{\cdot}955$ Mev and flight path = 231 cm.

for the excitation of a single level in ^{41}Sc. In table 3 the Q-values for the neutron groups from ^{16}O and ^{12}C contamination in the calcium targets are given for comparison.

Table 3. Q-values for ^{40}Ca(d, n)^{41}Sc

Energy (MeV)	Angle (deg)	Reaction				
		^{40}Ca(d, n)^{41}Sc	^{16}O(d, n)^{17}F		^{12}C(d, n)^{13}N	
3·515	15	$-2·89 \pm 0·02$	$-1·61 \pm 0·03$	$-2·08 \pm 0·02$	$-0·18 \pm 0·08$	$-2·68 \pm 0·02$
3·955	30	$-2·85 \pm 0·02$	$-1·61 \pm 0·04$	$-2·11 \pm 0·03$	—	—
3·955	45	$-2·83 \pm 0·02$	$-1·60 \pm 0·04$	$-2·10 \pm 0·02$	—	—
4·247	35	$-2·87 \pm 0·02$	$-1·63 \pm 0·06$	$-2·04 \pm 0·04$	—	—
Mean Q-values		$-2·86 \pm 0·02$†	$-1·61 \pm 0·02$	$-2·08 \pm 0·02$	$-0·18 \pm 0·08$	$-2·68 \pm 0·02$

† Corresponds to a level in ^{41}Sc at 1·72 MeV.

§ 4. Discussion

The ground-state Q-value of the ^{28}Si(d, n)^{29}P reaction has been reported as $-0·80 \pm 0·10$ MeV by Peck (1948), and as $0·29 \pm 0·04$ MeV by Mandeville *et al.* (1952), both measurements being made using nuclear emulsions. Calvert *et al.* (1957) and Green (1955) report $0·6 \pm 0·1$ and $0·74 \pm 0·1$ MeV respectively. To these we add our value of $0·63 \pm 0·06$ MeV. The first two levels of ^{29}P have recently been located at $1·386 \pm 0·01$ and $1·96 \pm 0·01$ MeV, using the ^{28}Si(^{3}He, d)^{29}P reaction (Hinds and Middleton, private communication, 1959). Using these data together with our excited state Q-values in table 1, a more accurate ground-state Q-value of $0·563 \pm 0·03$ MeV is obtained. The value obtained from atomic masses is $0·499 \pm 0·014$ MeV (Endt and Braams 1957).

Since the ^{29}P data were obtained using targets of natural silicon (4·7% ^{29}Si, 3·1% ^{30}Si), the possibility that the less intense neutron groups are due to the rare isotopes cannot be ruled out. Groups 3 and 4 (table 1) could conceivably be due to excitation of levels in ^{30}P at 5·2 and 5·9 MeV, or in ^{31}P at 7·0 and 7·7 MeV. This is unlikely, however, since there is no evidence in the spectra for groups leading to the many lower levels in these nuclei. Runs with separated Si isotopes were not made since they are available only as SiO_2, and the weaker neutron groups from Si are difficult to observe in the presence of the prolific groups from ^{16}O.

Middleton *et al.* (1953) have reported the ground-state Q-value for ^{32}S(d, n)^{33}Cl as 0·25MeV. This is to be compared with our measurement of $0·10 \pm 0·05$ MeV and the value from atomic masses of $0·060 \pm 0·013$ MeV (Endt and Braams 1957).

In the ^{40}Ca(d, n)^{41}Sc reaction, we have observed one intense group with a corresponding Q-value of $-2·86 \pm 0·02$ MeV. Plendl and Steigert (1959) report groups with Q-values of $-0·57$ MeV (ground state), $-2·43$ and $-2·54$ MeV. The ground-state Q-value obtained from the atomic masses of ^{40}Ca and ^{41}Ca, and the β^+ end point of the decay of ^{41}Sc (Elliot and King 1941) is $-0·60 \pm 0·08$ MeV with which Plendl and Steigert are in agreement. We have not observed the ground state group, presumably because of its low intensity. This is not surprising, since by analogy with the mirror reaction ^{40}Ca(d, p)^{41}Ca, the ground state is expected to be formed by f-wave proton capture. Proceeding with the analogy,

however, the first excited state of ^{41}Sc should be formed by capture of p-wave protons, and hence the corresponding neutron group should be relatively intense at forward angles. The group we observed was in fact more intense, by an order of magnitude, than any group of higher energy which could have been present in this reaction. It is difficult, therefore, to reconcile our results with those of Plendl and Steigert. The present measurements are, however, consistent with those of Butler (1959), on the $^{40}Ca(p, \gamma)^{41}Sc$ reaction. The resonance he observes at 0·650 MeV, corresponds to a level in ^{41}Sc at $Q(p, \gamma) + 0{\cdot}635$ MeV, which is equal to our value of $Q_0(d, n) + 2{\cdot}86$ MeV, since $Q(p, \gamma) \equiv Q_0(d, n) + 2{\cdot}225$ MeV.

Hinds and Middleton (private communication, 1959) have recently measured the Q-value of the $^{40}Ca(^3He, d)^{41}Sc$ reaction to be $-4{\cdot}410 \pm 0{\cdot}015$ MeV (preliminary result). Using this result, and the known masses of the neutron, deuteron and ^3He particle, the ground-state Q-value of the $^{40}Ca(d, n)^{41}Sc$ reaction is calculated to be $-1{\cdot}14 \pm 0{\cdot}02$ MeV, which disagrees considerably with previous values. Taking this value as the correct one, the neutron group we have observed corresponds to a level in ^{41}Sc at 1·72 MeV. Since the intensity of the group is high, it is then plausible to assume that this level is the first excited state of ^{41}Sc, corresponding to the 1·95 MeV state in the mirror nucleus ^{41}Ca. Thus the new Q-value leads to a very plausible explanation of our results, and is also in disagreement with earlier work on the $^{40}Ca(d, n)^{41}Sc$ reaction.

Figure 5 shows the level schemes of the mirror pairs of mass 29 and 33. The level energies of the nuclei in both pairs are remarkably close, thus furthering the confirmation of charge symmetry of nuclear forces.

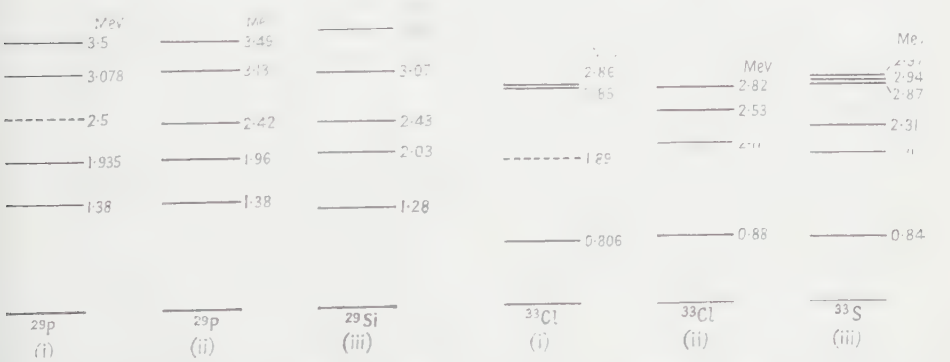

Figure 5 (*a*). Energy levels of ^{29}P and ^{29}Si. (i) Previously reported. (ii) Present work. (iii) After Endt and Braams (1957).

Figure 5 (*b*). Energy levels of ^{33}Cl and ^{33}S. (i) Previously reported. (ii) Present work. (iii) After Endt and Braams (1957).

In the course of this work, many measurements have been made of the Q-values of the ground and first excited groups from $^{12}C(d, n)^{13}N$ and $^{16}O(d, n)^{17}F$ at angles ranging from 15° to 88°. The mean Q-values are: ^{12}C, $-0{\cdot}257 \pm 0{\cdot}060$ and $-2{\cdot}648 \pm 0{\cdot}017$ MeV; and ^{16}O, $-1{\cdot}616 \pm 0{\cdot}03$ and $-2{\cdot}106 \pm 0{\cdot}025$ MeV. The first excited states of ^{13}N and ^{17}F are thus at $2{\cdot}39 \pm 0{\cdot}06$ and $0{\cdot}49 \pm 0{\cdot}04$ MeV. These results are in excellent agreement with previous work (Ajzenberg-Selove and Lauritsen 1959), and give confidence in the energy calibration of our spectrometer.

Acknowledgments

We are indebted to Dr. K. W. Allen and Mr. R. Batchelor for their interest and helpful comments, also to Dr. S. Hinds and Dr. R. Middleton for communicating their results prior to publication.

References

Ajzenberg-Selove, F., and Lauritsen, T., 1959, *Nucl. Phys.*, **11**, 1.
Batchelor, R., and Towle, J. H., 1959, *Proc. Phys. Soc.* A, **73**, 193 and A.W.R.E. Report NR/P–12/58 (unclassified).
Butler, J. W., 1959, *Nuclear Data Tables* 1959, (Ed. K. Way), United States Atomic Energy Commission.
Calvert, J. M., Jaffe, A. A., and Maslin, E. E., 1957, *Proc. Phys. Soc.* A, **70**, 78.
Elliot, D. R., and King, L. D. P., 1941, *Phys. Rev.*, **60**, 489.
Endt, P. M., and Braams, C. M., 1957, *Rev. Mod. Phys.*, **29**, 683.
Green, T. S., 1955, *Thesis*, University of Liverpool.
Holt, J. R., and Marsham, T. N., 1953, *Proc. Phys. Soc.* A, **66**, 467.
van der Leun, C., and Endt, P. M., 1958, *Physica*, **24**, 1095.
Mandeville, C. E., Swann, C. P., Chatterjee, S. D., and Van Patter, D. M., 1952, *Phys. Rev.*, **85**, 193.
Middleton, R., El-Bedewi, F. A., and Tai, C. T., 1953, *Proc. Phys. Soc.* A, **66**, 95.
Peck, R. A., 1948, *Phys. Rev.*, **73**, 947.
Plendl, H. S., and Steigert, R. E., 1959, *Bull. Amer. Phys. Soc.* II, **4**, 18.
Van Oostrum, K. J., Alster, J., Hazewindus, N., and Wapstra, A. H., 1958, *Physica*, **24**, 1051.

Note added in proof. Using pulse shape discrimination against the random background of γ-rays it has now proved possible to observe the ground state group of the reaction ^{40}Ca(d, n)^{41}Sc. The Q-valve has been measured as $-1{\cdot}140 \pm 0{\cdot}020$ MeV. An angular distribution at $E_d = 4.0$ MeV indicates $l = 3$ for the captured proton.

The High Energy Photodisintegration of Helium, Nitrogen and Neon

By J. M. REID and B. LALOVIC†
Department of Natural Philosophy, University of Glasgow

MS. received 2nd *November* 1959, *in final form* 19th *April* 1960

Abstract. A fast expansion cloud chamber, triggered by three proton telescopes was used to investigate photonuclear reactions in helium, nitrogen and neon. Various reactions yielding from one up to seven charged fragments involving the emission of a 100 MeV proton were observed in nitrogen and neon. The results basically agree with the model of photon absorption by p–n pairs in the complex nucleus, but an unexpectedly large number of events was found in which the residual nucleus disintegrated. The assumption that in $(50 \pm 15)\%$ of the cases in which the photon is absorbed by a (p, n) pair, the residual nucleus is sufficiently excited to disintegrate, brings the results into line with previous scintillation counter experiments in which p–n coincidences were studied.

A small number of (γ, p) events was found at energies substantially above the giant resonance. It was also found that 5–10% of the events occurring involved the emission of two fast protons.

§ 1. Introduction

Recent experimental investigations have produced convincing support for the theory of Levinger (1951) that, in some and perhaps in all cases of high energy photodisintegration of complex nuclei, the incident γ-ray interacts with a p–n pair, the so-called 'quasi-deuteron', giving rise to the simultaneous emission of a proton and neutron. The simple picture of the emitted nucleons having energies and angles of emission as for a free deuteron is however complicated by three considerations. Firstly the quasi-deuterons are not stationary but have a certain momentum distribution inside nuclei. Secondly the proton and neutron both have a certain probability of interacting with other nucleons on their way to the nuclear surface. Finally the remainder of the nucleus may be left in a state other than its ground state and this will modify the energy distribution. These factors introduce considerable complications both in the experimental and theoretical study of this process.

Extensive experimental investigations of the cross section and kinematics of quasi-deuteron photodisintegration have been undertaken at the Massachusetts Institute of Technology by Wattenberg *et al.* (1956) and at Illinois by Barton and Smith (1958). Both groups used scintillation counters to detect protons within a certain energy range emitted in a specified direction in coincidence with neutrons emitted in a second specified direction. The neutrons were also detected in scintillation counters. Their energies were known only in that they had to exceed a certain minimum value in order to trigger the coincidence circuits. By altering the angular position of the neutron counter it was found that the neutrons were

† Now at the Boris Kidric Institute, Belgrade.

spread in angular direction about that unique direction in which they would have travelled had the target nucleus been a stationary deuteron. This angular spread of the neutrons was attributed to the motion of the quasi-deuterons within the nucleus; the width of the spread was used to deduce the average internal momenta of quasi-deuterons in the case of He, Li, Be, C, O and A.

It has been suggested that all high energy photonucleons might originate from the disintegration of quasi-deuterons. The experimental test of this hypothesis by counter experiments involves correcting for the somewhat uncertain efficiency of the neutron counter for an unknown neutron energy spectrum and, perhaps with greater uncertainty, making an estimate of the effects and importance of internal scattering and absorption of the neutrons on their way out of the nucleus. While it now seems established that the main process responsible for the emission of high energy nucleons is the photodisintegration of the quasi-deuterons the possibility remains that up to about 25% of the high energy disintegrations might be arising from different disintegration processes. Two such processes might be direct single nucleon ejection, which is known to occur at lower energies, and the absorption of the γ-ray into nuclear substructures other than p–n pairs. Cross sections for these processes may be estimated but direct experimental evidence is at present lacking. The investigation to be described provides some information on these questions. In principle the method here used might, with much better statistics than at present attained, enable estimates to be made of cross sections of less likely processes such as reabsorption of real mesons in the nucleus of their origin or the formation even at high energies of a compound nucleus capable of evaporating one high energy proton.

The apparatus used in the present investigation consisted of a cloud chamber which, when triggered by proton scintillation telescopes, selectively photographed γ-ray disintegrations in which at least one proton of energy 80 to 120 MeV was emitted. This technique not only enables the proton angle in space to be measured with precision for each event but also permits the study of the track of the recoiling residual nucleus or the tracks of the charged fragments arising should the residual nucleus disintegrate.

In the case of events in which the residual nucleus does not disintegrate, the following items of information, which cannot be obtained from a counter experiment alone, become available :

(*a*) The triggering proton can be seen to be the sole ejected particle or to be one member of a p–n pair depending on whether or not the recoil is coplanar with the proton and the γ-ray beam. In the case of coplanar events, assuming that the mass of the target nucleus is known, a measurement of the directions of proton and recoil enables an energy and momentum balance to be made. From this the γ-ray energy and energies of recoil and proton may be obtained. The recoil range provides confirmation of the correctness of the interpretation and is a check on the range–energy relation; the proton energy is a useful check on the calibration of the scintillation telescopes.

(*b*) In the case of the (γ, pn) reactions, i.e. non-coplanar events, the neutron direction and energy may be calculated by balancing energy and momentum using the data of recoil range and direction. The energy of the initiating γ-ray is also obtained in these cases.

(*c*) If the quasi-deuteron model is valid for these (γ, pn) events, the observed residual nucleus must be recoiling with momentum exactly opposite to that of the

quasi-deuteron which absorbed the quantum. Hence the range distribution of the recoils represents directly the internal momentum distribution of the quasi-deuterons. It should be further noted that the quasi-deuteron internal momentum is known for each particular event. Consequently, the possibility exists of deriving the angular distribution corrected for deuteron internal momentum with the certainty that events in which the outgoing nucleons are seriously scattered have been excluded. Unfortunately, the number of events recorded is not large enough to produce statistically significant angular distributions.

§ 2. Experimental Details

2.1. *The Cloud Chamber*

The cloud chamber, through which the γ-ray beam from the 330 Mev electron synchrotron was passed (Atkinson *et al.* 1957) and which was triggered by the passage of higher energy protons through the scintillation counters described below, is shown diagrammatically in figure 1. It was a conventional expansion chamber of the rubber diaphragm type, volume defined, having a sensitive volume 30 cm × 30 cm × 15 cm. It was designed for operation at a compressed pressure of approximately 1·5 atm.

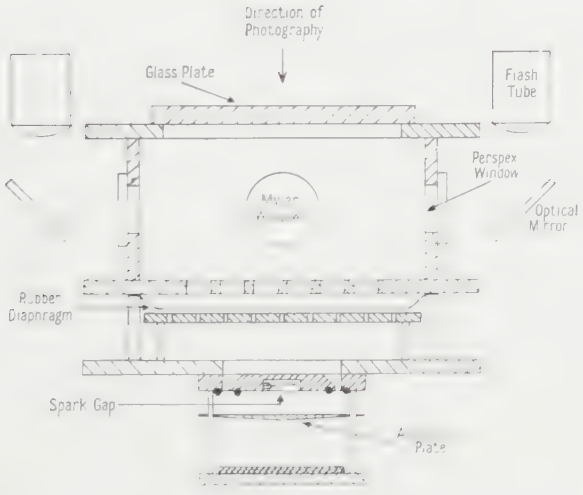

Figure 1.

A clearing field was applied between two wire grids 10 cm apart, one grid being connected to +400 v, the other to −400 v with respect to the earthed aluminium walls of the chamber. The high value of clearing field was found necessary to sweep away the ions from one burst of quanta before the arrival of the next burst $\frac{1}{5}$ second later. It was thus found possible to allow the synchrotron to pulse regularly at a recurrence frequency of 5 per second until such time as a proton was emitted of such an energy and in such a direction as to trigger the chamber. To prevent the electrostatic clearing field 'drawing' the tracks on the occurrence of an expansion, an electronic switch was designed to earth both grids 5 msec before the beginning of each synchrotron output pulse and to restore the voltage 20 msec after the end of the output pulse.

2.2. *The Cloud Chamber Expansion Valve*

The chamber expansion was achieved by means of a spark valve of the simple construction described by Meyer and Stodiek (1953). The pressure below the rubber diaphragm p_2 and the pressure in the spark cavity p_1 were such that atmospheric pressure on the underface sealed an aluminium plate against two concentric O-rings. The discharge of a 50 μF condenser charged to 2·5 kv through the spark gap disturbed the pressure balance and the aluminium plate blew off with great violence. The pressures p_1 and p_2 were set automatically in the following way. An electrical contact in a mercury manometer measuring the pressure p_2 was used to operate an electromagnetic valve in an air pressure line. A similar manometer contact operated a second valve on a rough vacuum line and thus set p_1. By adjusting these manometer contacts the state of balance of the aluminium disc could be made very critical.

The speed of complete opening of the spark valve was found, by timing the aluminium disc by a light beam and photocell, to be 3 msec. With such an opening speed and a filling of 1·5 atm of nitrogen with an alcohol–water mixture in the chamber the width of fast proton tracks, as measured from the photographs, was about 0·5 mm. Stereoscopic photographs were taken using three cameras. For analysis the films were reprojected through the camera optical systems.

2.3. *Scintillation Counter Telescopes*

The high energy photoprotons were detected by scintillation counter telescopes of the type commonly used for the detection of high energy particles. Each telescope consisted of two plastic scintillation counters set in coincidence. The scintillators were all of the same size, 10 cm × 7·5 cm × 1·25 cm. Pulses from each photomultiplier, after being amplified in fast I.D.L. amplifiers, were selected by integral discriminators and sent to coincidence circuits of 0·2 μsec resolving time. The output of this circuit was gated to accept only pulses coincident with the synchrotron beam in order to eliminate coincidences produced by cosmic rays or spurious pulses originating in the synchrotron circuits.

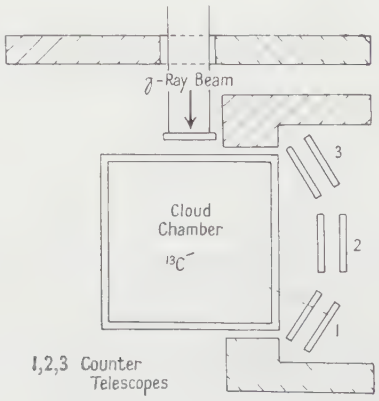

Figure 2.

Three identical telescopes were used, placed with respect to the γ-ray beam as shown in figure 2. The total solid angle subtended by the telescopes was approximately $4\pi/50$. Records were made of counts from each telescope separately.

In the analysis of the photographs a knowledge of which telescope triggered the chamber facilitated the finding of the triggering particle and at the same time reduced the chance of misidentification.

The discriminator biases of the front counters were set above the value corresponding to mesons in order that only protons should be detected. The back counters were biased to accept only protons which nearly stopped in this scintillator. In practice it was found necessary to have the proton energy spread from 80 MeV to 120 MeV in order that there should be a reasonable number of coincidences (and hence photographs) per hour.

In the later part of the investigation with neon as the gas in the chamber, a more elaborate method was devised whereby pulses from both front and back counters were photographed on an oscilloscope when a coincidence occurred. In this way, the particle energy was known more precisely without restricting the accepted energy spread. Also by plotting one pulse height against the other ($dE\,dx$ against E), we were able to confirm that the particles detected were protons.

2.4. *γ-ray Monitor*

For the purpose of cross-section measurements it was necessary to know the total number of quanta which passed through the cloud chamber in the course of the experiment. This was measured by passing the beam which emerged, through a thin window, from the cloud chamber into an ionization chamber which was connected to an integrating circuit. This arrangement had previously been calibrated in terms of equivalent quanta. From the records taken the number of equivalent quanta passing through the chamber between each triggering event was known.

§ 3. Experimental Results

Three gases, helium, nitrogen and neon, were used in the course of the present investigation and the results are separately analysed below. In the case of the helium and nitrogen experiments the bremsstrahlung spectrum had a maximum energy of 330 MeV; in the case of the neon experiment machine conditions necessitated a reduction to a maximum of 240 MeV.

3.1. *Helium*

The experiment with helium in the cloud chamber proved specially difficult for three reasons. Firstly the high energy photodisintegration cross section for a nucleus containing only four nucleons was expected to be and proved to be small. Added to this the monatomic nature of the gas meant that fewer nuclei were present than for a diatomic gas like nitrogen under the same conditions. An increase in the helium pressure would have necessitated redesigning the spark valve. The rate of occurrence of helium events was, therefore, comparatively unfavourable. Secondly the use of an alcohol–water mixture was necessary to achieve satisfactory track quality. This involved the presence of a significant number of nuclei of higher atomic weight having larger photodisintegration cross sections than helium. Thus on an appreciable number of occasions the chamber was triggered by a proton originating in an oxygen or carbon nucleus. Finally, because of the low stopping power of the chamber mixture in this experiment a 100 MeV proton proved difficult to observe against the background of drops caused by secondary electrons arising from the γ-ray beam.

Despite these difficulties a limited experiment with helium was undertaken since at the time in question there was little experimental information on the high energy photodisintegration of this nucleus. The helium results were also important for the following technical reason. In order to lighten the heavy core of ionization produced by secondary electrons in the γ-ray beam when nitrogen and neon were introduced into the chamber, the stopping power was reduced by diluting the heavier gases with helium. In this way the total pressure was kept high enough for satisfactory spark valve operation, while a stopping power was achieved which enabled events to be observed in the core. It was important to have some direct knowledge of the extent to which the helium content contributed to the material obtained in the nitrogen and neon experiments.

A total of 57 events was obtained in which the triggering particle was identified.

A group of 23 of these events involved three or more prongs. Assuming that meson production is not involved, no mode of disintegration of helium can lead to more than two prongs. These 23 events, therefore, were attributed to the nuclei of carbon and oxygen in the alcohol (pressure 2·2 cm Hg) and water vapour (pressure 0·9 cm Hg) and to a contamination of nitrogen found by mass spectrometry to amount to 5·2% of the helium content.

Among 28 two-prong non-coplanar events, to be interpreted as (γ, pn) reactions, were four in which the recoil tracks were distinctively thick and short. These were also attributed to the heavier nuclei. The two one-prong tracks found were believed to be of similar origin, the recoils being too short to distinguish against the drop background.

After this subtraction the events attributed to helium amounted to (i) four two-prong coplanar events and (ii) 24 two-prong non-coplanar events.

In the case of the events in group (i), using only the observed track directions and on the assumption that the reaction was ^{4}He(γ, p)^{3}H the energies of γ-ray and proton were calculated. For three of the events the results lay within satisfactory limits, the γ-ray energies being 135, 152 and 173 Mev and proton energies 89, 100 and 113 Mev. No fit was possible in the case of the fourth event which is discussed below.

Events in group (ii) were interpreted as examples of the reactions ^{4}He (γ, pn)^{2}H and ^{4}He(γ, p2n)^{1}H. As protons and deuterons were not distinguishable by track appearance it was not possible to separate the reactions. In two cases the recoiling particle stopped in the chamber. Assuming it to be a deuteron in both cases and taking the triggering proton energy to be 80 Mev an energy and momentum balance led to γ-ray energies of 243 and 175 Mev and neutron energies of 136 and 67 Mev, the neutron–proton kinematics being almost as for a deuteron photodisintegration.

Although in the remainder of the events in group (ii) the recoils passed into the walls of the chamber, they clearly fell into two sets. In 17 of them the recoil track was appreciably denser than that of the triggering proton and had the appearance of a lower energy proton or deuteron. In 5 of the events, however, the recoil and triggering particles were of very similar appearance. In all of these 5 events the angle between the two fast particles exceeded 125° and the two particles were within 10° of coplanarity with the γ-ray beam. The coplanar event which did not fit the ^{4}He(γ, p)^{3}H process was believed to be of this type. Events involving two fast protons were also observed in the case of the heavier nuclei and are discussed later. The 17 events of the former kind may be examples of quasi-deuteron

absorption in which the recoil is the 'spectator' deuteron or the proton arising from its subsequent disintegration.

The cross section calculated from the number of equivalent quanta through the chamber, for the production of protons going into the forward telescope (67 + 13°) was $0{\cdot}7 \pm 0{\cdot}2 \times 10^{-31}$ cm^2 Mev^{-1} Q^{-1} sterad^{-1}. The protons into the front (mean angle 67°), the middle (90°) and back (113°) telescopes were 12 : 10 : 2.

3.2. *Nitrogen*

A total of 166 events in which the triggering particle could be observed was obtained with a nitrogen–helium plus alcohol–water vapour mixture in the chamber. The events associated with helium were readily distinguished. The numbers of events of the main types to be attributed to C and O nuclei were estimated from a consideration of the numbers of events due to C, O and a known number of N nuclei in the helium experiment, a simple allowance being made for the A dependence of the cross sections.

The numbers of events are listed in table 1 according to the nucleus disintegrated and the number of charged prongs produced, one of the charged prongs always being the high energy triggering proton.

Table 1

	I	II	III	IV	V	VI	VII	Total
No. of prongs	1	2c	2nc	3	4	5	6	
Nitrogen	5	3	26	38	51	13	1	137
Helium		1	11					12
Carbon and Oxygen			3	2	5	2		12†
Unidentified		5						5
Total	5	9	40	40	56	15	1	166

c = coplanar; nc = non-coplanar.

† Separated statistically from 149 events involving nuclei heavier than helium.

Column I. Events in column I were attributed, as in the helium experiment, to (γ, pn) events in the heavier nuclei in which the recoil energy was so small that the recoil was not observed. For statistical purposes they were included in the group in column III (two-prong non-coplanar).

Column II. The events in column II were so divided after momentum and energy balance tests. The five labelled unidentified did not pass these tests and were not simple (γ, p) events.

Column III. The events in column III were assumed to be examples of the $^{14}N(\gamma, pn)^{12}C$ reaction. In thirteen cases the range of the ^{12}C recoil was measurable with an accuracy which justified an energy and momentum balance. For these cases the neutron energies were calculated taking the proton energy to be 100 Mev. Three of the neutrons have energies greater than 100 Mev, two energies between 80 and 100 Mev, three energies between 40 and 60 Mev, three energies between 20 and 40 Mev and two energies less than 20 Mev.

The distribution of ranges of all recoils of the (γ, pn) events in conjunction with the ^{12}C range–energy relations of Lillie (1952) led to the distribution of recoil energies in table 2. On the assumption that this energy is arising solely from internal momentum equal and opposite to that of the quasi-deuteron, then the corresponding quasi-deuteron energies will be obtained by multiplying by 6.

Table 2

Recoil energy (MeV)	0–1	1–2	2–3	3–8
Number of events	13	5	5	8

Column IV. The events in column IV were further grouped as in table 3.

Table 3

Triggering particle together with		
2 heavy tracks	1 heavy, 1 light	1 heavy, 1 very light
22	8	8

In 8 of the 22 cases in the first group the heavy tracks were of so similar an appearance as to suggest a symmetrical splitting of the ^{12}C recoil. They were interpreted as examples of $^{14}N(\gamma, pn)2^{6}Li$. In four of the cases both heavy particles terminated in the chamber gas and complete solution was possible. These led to values of γ-ray energies 228, 210, 210 and 170 MeV with neutron energies 72, 59, 68 and 40 MeV assuming the triggering protons to have energies of 100 MeV.

The remaining 14 events in this group were ascribed, on the basis of length and density of tracks, to the reaction $^{14}N(\gamma, pn)(^{9}Be + {}^{2}He)$.

The events in the second and third columns of table 3 probably correspond to reactions in which ^{12}C split into $^{11}B + {}^{1}H$ and $^{10}B + {}^{2}H$.

It was remarkable that in all events in the third column of table 3 the fast particle (which, if a proton, would, judging from track density, have energy in excess of 40 MeV) was almost coplanar with the triggering proton and γ-ray beam.

Column V. The four-prong events also divided into characteristic sub-groups as shown in table 4.

Table 4

Triggering particle together with			
3 heavy	2 heavy, 1 light	1 heavy, 2 light	2 heavy, 1 very light
26	13	6	6

In the case of almost all events in the first column all three heavy fragments were of comparable track thickness. It is very probable that they represent the reaction $^{14}N(\gamma, pn)3^{4}He$. In seven cases all heavy tracks terminated in the gas permitting an energy and momentum balance. This led to γ-ray energies ranging from 120 MeV to 230 MeV with neutron energies ranging from 1 MeV to 103 MeV. The energies of excitation left on the excited ^{12}C from which the three α-particles were assumed to have emerged were also calculated: the results ranged from 14·4 MeV to 27·1 MeV. In the other cases in which one or more of the fragments went to the chamber walls only a lower limit could be put on the ^{12}C excitation. This lower limit was mostly around 25 MeV, though in three cases at least 45 MeV was involved.

In the case of the events in the last column of table 4 the very energetic particles were again nearly coplanar with the triggering particles and the γ-ray beam. Their angles of emission corresponded roughly to the angle expected from a two body (p–p) disintegration.

Columns VI, VII. The events with 5 or 6 prongs could not be identified with particular reactions. The minimum energy required to produce an event with as many as six prongs was estimated to represent a recoil excitation of about 40 MeV. In addition, in most cases the fragments were estimated to have a total kinetic energy of more than 20 MeV. In four of these events a very fast particle was included and in one case it was almost in the plane of the triggering proton and γ-ray beam.

The events listed in table 1 as 'unidentified', which were coplanar to within 2°, involved angles of triggering proton and recoil with respect to the γ-ray beam which were not consistent with a (γ, p) reaction caused by a quantum of energy less than 330 MeV, the limit of the machine spectrum. It was concluded that a neutron was involved in each case but it is remarkable that all three products and the γ-ray happen to be in the same plane.

The cross section for photoproduction of protons of energy 100 MeV at an angle of $52 \pm 12°$ was found to be $0{\cdot}4 \times 10^{-30}$ cm^2 MeV^{-1} Q^{-1} sterad^{-1} in nitrogen.

The counts in the front (mean angle 52°), middle (90°) and back telescopes (138°) were 73 : 46 : 18.

3.3. *Neon*

At the time of performance of this experiment the machine energy, for technical reasons, was limited to 240 MeV. It proved possible in the course of this experiment to photograph the pulses from the scintillation counters on an oscilloscope and thus be more certain about triggering proton energies.

185 events were successfully associated with triggering particles. The effect of the helium, which had to be introduced to reduce the stopping power, and of the alcohol water vapour was separated out as before and the results are presented in table 5.

Table 5

	I	II	III	IV	V	VI	VII	Total
No. of prongs	2c	2nc	3	4	5	6	7	
Ne	4	32	60	25	17	11	1	150
C + O + He		16	4	8	3			31
Unidentified	4							4
Total	8	48	64	33	20	11	1	185

c = coplanar; nc = non-coplanar.

There were five events in which only the triggering particle was seen (1-prong). As in the case of nitrogen these were included in the 2-prong non-coplanar group.

Column I. The events in column I were checked by energy and momentum balance. The four which agreed with the assignment ^{20}Ne$(\gamma, p)^{19}$F arose from γ-rays of energies 145, 130, 123 and 115 MeV giving triggering proton energies of 118, 112, 104 and 96 MeV; this calculation is based on observed directions alone. There were four events which did not come close to a fit of this kind and, as in nitrogen, these were left as 'unidentified'.

Column II. Events in column II correspond to $^{20}Ne(\gamma, pn)^{18}F$. Twelve involved recoil ranges greater than 4 mm and these were, as in nitrogen, solved for energy of γ-ray and energy and direction of neutron. One neutron had energy greater than 100 MeV, two energies 80–100 MeV, one 60–80 MeV, four 40–60 MeV, one 20–40 MeV and three less than 20 MeV, the calculated energy of γ-ray being less than 240 MeV in each case.

Table 6 presents the energy distribution of all ^{18}F recoils.

Table 6

Recoil energy (MeV)	0–1	1–2	2–3	3–5
Number of events	14	9	4	5

Column III. The three-prong events in column III are presented in sub-groups in table 7.

Table 7

Triggering particle together with		
2 heavy	1 heavy, 1 light	1 heavy, 1 very light
44	14	2

In the case of twelve events in the first group in table 7 the heavy fragments were of similar appearance and length. They may represent reactions in which ^{18}F splits into $^{12}C + {}^{6}Li$ and $^{11}C + {}^{7}Li$. In other events in this group one of the fragments is of considerably longer range than the other having the appearance expected from the break-up of ^{18}F into $^{14}N + {}^{4}He$. In these events the kinetic energies of the fragments were not high, lying between 10 and 20 MeV. The binding energy of ^{4}He in ^{18}F being 4·4 MeV means that the energy of excitation of the ^{18}F recoil was 15–25 MeV.

In the case of the events with more than three prongs the possible reactions are so numerous that no particular interpretations are possible. The kinetic energy carried off by the charged fragments in most events exceeded 20 MeV. In the case of eight of the multiprong events there was a very fast particle emitted of energy comparable with that of the triggering proton and almost coplanar with it and the γ-ray beam.

The cross section for the photoproduction of 100 MeV protons at an angle of $65 \pm 15°$ in the case of neon was found to be $0{\cdot}4 \times 10^{-30}$ cm^2 MeV^{-1} Q^{-1} sterad^{-1}. The counts in the front (mean angle 65°), middle (90°) and back telescopes (115°) were 78 : 54 : 18.

§ 4. Internal Scattering of Photonucleons

In order to discuss our results on the basis of the quasi-deuteron model it is necessary to have an estimate of the percentage of the fast neutrons and protons which will undergo scattering on their way out. Such scattering will give rise to events more complex than (γ, pn).

Following Serber (1947) and Gottfried (1958), we write for the probability that both proton and neutron escape from the nucleus f_1 where

$$f_1 = \frac{1}{V_0}\int \exp\left(-\frac{x}{\Lambda_p}\right)\exp\left(-\frac{y}{\Lambda_n}\right)dV_0,$$

V_0 being the volume of the nucleus, x and y the distances travelled by the proton and neutron respectively from their point of origin to the nuclear surface and Λ_p and Λ_n the proton and neutron mean free paths.

The probability that the proton will escape and the neutron be scattered is written f_2 where

$$f_2 = \frac{1}{V_0}\int \exp\left(-\frac{x}{\Lambda_p}\right)\left\{1-\exp\left(-\frac{y}{\Lambda_n}\right)\right\}dV_0.$$

In our experiment two-prong non-coplanar events are related to f_1 and, on the assumption that no processes other than quasi-deuteron absorption are involved, all multiprong events are related to f_2. The ratio of these two types of events is then to be compared with the calculated values of f_2/f_1.

Λ_p was found for an average proton energy of 100 MeV (120 MeV inside the nucleus with a 30 MeV deep potential well), taking effective values for σ_{np} and σ_{pp} for nucleon scattering inside the nucleus from the formula

$$\sigma_{eff} = \sigma_{free}\left(1-\frac{7}{5}\frac{p_f^2}{p_i^2}\right)$$

where p_f and p_i are the maximum momentum of the Fermi gas (taken to be 200 MeV **c**) and the initial nucleon momentum. This reduction of cross section, which is due to the Pauli exclusion principle, was about 23%. The value of Λ_p was found to be $2{\cdot}94\times10^{-13}$ cm.

While the proton energy, under the conditions of the experiment, was fixed at 100 MeV, the neutron energy depended on the energy of the γ-ray and internal momentum of the (p, n) pair. Therefore, in calculating Λ_n one should integrate over the neutron energy spectrum. However, since we detected protons in a broad angular range such a calculation would be very involved. Instead of performing an exact integration we calculated the average neutron energy corresponding to the proton angles related to the centres of the middle and front telescopes. Assuming a $1/E$ bremsstrahlung spectrum and a Gaussian momentum distribution with $1/e = 15$ MeV the results were as follows:

	E_p (MeV)	θ_p(°)	$(E_\gamma)_{max}$(MeV)	$\bar{E}_n$(MeV)	$\Lambda_n(10^{-13}$cm)
Nitrogen	100	90	330	110	3·28
	100	50	330	72	2·5
Neon	100	90	240	75	2·56
	100	65	240	60	2·46

With these values for Λ_p and Λ_n, assuming the neutron and proton to be emitted in opposite directions and taking the nuclear radius $= A^{1/3}\times1{\cdot}3\times10^{-13}$ cm we evaluated f_1 and f_2 as follows:

	θ_p(°)	f_1	f_2	f_2/f_1
Nitrogen	90	0·27	0·24	0·89
	50	0·20	0·30	1·50
Neon	90	0·17	0·30	1·76
	65	0·16	0·30	1·93

Following Barton and Smith (1958) we define an absorption factor α, as the probability that a nucleon will suffer a collision on its way out of the nucleus. Then

$$\alpha_p = 1 - f_1 - f_2 \quad \text{and} \quad \alpha_n = f_2/(f_1 + f_2).$$

The calculated values of f_1 and f_2 give values of α_n which in nitrogen range from 0·60 for a 72 MeV neutron to 0·47 for a 110 MeV neutron and in neon range from 0·65 for a 60 MeV neutron to 0·53 for a 100 MeV neutron.

§ 5. Discussion of Experimental Results

5.1. (γ, pn) *Events and Multiprong Stars*

The experimental ratios of multiprong events to two-prong non-coplanar events for all counters were $3{\cdot}3 \pm 0{\cdot}6$ for nitrogen and $3{\cdot}6 \pm 0{\cdot}7$ for neon, in both cases significantly greater than the calculated f_2/f_1 values. The experimental figures correspond to α_n values of 0·77 and 0·78.

It is to be noted that a certain proportion of the two-prong non-coplanar events are in fact multiprong stars involving a neutron as the evaporated particle. We can estimate approximately the number of three-prong events in which an evaporated proton appears. (We assume that deuterons and tritons, which would have a similar appearance to protons are rare enough to be neglected for the purpose of this correction). Assuming that there will be at least the same number of neutron three-prong events we find the adjusted f_2/f_1 value to be approximately 8 for nitrogen and approximately 7 for neon giving α_n values of 0·89 and 0·87. We have probably over-corrected in ignoring the occurrence of events in which both a proton and a neutron are evaporated.

The experimental results thus lead to f_2/f_1 ratios much higher than those calculated. In this our results are at variance with those obtained less directly by counter experiments. For example, Weil and McDaniel (1953) obtained for carbon a value of $\alpha_n = 0{\cdot}45$ (i.e. $f_2/f_1 = 0{\cdot}8$).

We suggest that the explanation of the high experimental values in the present investigation is that, while the basic process is quasi-deuteron absorption, in many cases the rest of the nucleus is at the instant of photon absorption in an excited configuration. In these cases a multiprong event results although the photonucleons may be unscattered. This residual excitation would not affect the counter experiments but clearly prevents us equating multiprong stars with 'scattering' events. Our results, however, can be brought into line with the results of the counter experiments if it be assumed that in $(50 \pm 15)\%$ of the cases in which the photon is absorbed by a (p, n) pair the residual nucleus is sufficiently excited to disintegrate. In making this estimate we have taken $\alpha_n = 0{\cdot}65$ and the error corresponds to a value of the ratio of multiprong events to two-prong events varying from 3·6, which was the experimentally found ratio, to 7·0, which allows for neutron evaporation.

It is to be noted that, if this explanation is correct the excitation energy concerned is quite high. The lowest thresholds for reactions in ^{12}C and ^{18}F are 7·2 MeV and 4·3 MeV respectively. To these we must add the kinetic energies of the fragments, found in events of this type in both nitrogen and neon to be at least 15 MeV. Thus the minimum excitation energy is of the order of 20 MeV, the average certainly being much higher considering that the energy of neutrons emitted has not been allowed for in the above minimum estimation.

5.2. (γ, p) *Events*

A (γ, p) event involving a 100 MeV proton may, within the framework of the quasi-deuteron model, be thought of as involving the disintegration of a (p, n) pair of about 400 MeV/**c** internal momentum (i.e. kinetic energy of 40 MeV) in the direction of the emitted proton. Under these conditions the neutron would acquire very little energy and might remain bound within the residual nucleus.

A simple calculation assuming a Gaussian momentum distribution ($1/e = 15$ MeV) and a $1/E$ bremsstrahlung spectrum suggests that less than 1% of the total number of events triggering the front telescope should be of this type. This is lower than the experimental result.

At lower photon energies the (γ, p) process was treated by Courant (1951) on the basis of direct proton ejection. His formula, extended to the high energies involved here, on the assumption of a Fermi momentum distribution with $T_{max} = 22$ MeV and a potential well of depth 30 MeV, gives values for the cross section for nitrogen and neon an order of magnitude smaller than the values obtained in the experiment.

Thus although the statistics are poor, they do indicate that the (γ, p) cross section at γ-ray energy of 100 MeV may be larger than predicted by the simple models.

5.3. (γ, pp) *Events*

In about 10% of the nitrogen events and about 7% of the neon events a second fast particle of appearance similar to the triggering proton was emitted. This particle was never far from the plane of the γ-ray and triggering proton. A possible mechanism for such events is the electric quadrupole absorption of a photon by a (p, p) pair. They would also arise from head-on collisions between the outgoing neutron and a proton in the residual nucleus. A third explanation might lie in the production of π^+ mesons which are reabsorbed by a (p, n) pair. In this connection it may be noted that two events were found involving two fast particles in addition to the triggering proton, all three particles being almost coplanar. It is difficult to explain these events on the basis of neutron scattering or nuclear evaporation but they would be the type of event expected from π absorption into a group of two protons and a neutron.

In view of lack of statistics we make no attempt to evaluate the relative importance of these three possible processes.

Acknowledgments

The authors desire to thank Professor P. I. Dee for his support and interest throughout this investigation, Dr. W. McFarlane and the synchrotron operators for their collaboration in operating the electron accelerator and Mr. R. M. Turnbull for assistance in the operation of the cloud chamber and associated equipment.

We also wish to acknowledge the award to one of us (B.L.) of a Fellowship of the European Organisation for Nuclear Research (CERN) held during the period of the investigation.

References

Atkinson, J. R., McFarlane, W., Reid, J. M., and Swinbank, P., 1957, *Nucl. Instrum.*, **1,** 152.
Barton, M. Q., and Smith, J. H., 1958, *Phys. Rev.*, **110,** 1143.
Courant, E. D., 1951, *Phys. Rev.*, **82,** 703.
Gottfried, K., 1958, *Nucl. Phys.*, **5,** 557.
Levinger, J. S., 1951, *Phys. Rev.*, **84,** 43.
Lillie, A. B., 1952, *Phys. Rev.*, **87,** 716.
Meyer, B., and Stodiek, W., 1953, *Rev. Sci. Instrum.*, **24,** 76.
Serber, R., 1947, *Phys. Rev.*, **72,** 1114.
Wattenberg, A., Odian, A. C., Stein, P. C., Wilson, H., and Weinstein, R., 1956, *Phys. Rev.*, **104,** 1710.
Weil, J. W., and McDaniel, B. D., 1953, *Phys. Rev.*, **92,** 391.

Observations of Sudden Ionospheric Disturbances

By R. W. MORRISS
Cavendish Laboratory, Cambridge

Communicated by J. A. Ratcliffe; MS. received 7th December 1959

Abstract. Observations were made of the effect of sudden ionospheric disturbances on radio waves reflected from, and transmitted through, the ionosphere. The results of simultaneous measurements of the phase changes on waves of frequency 2–6 Mc/s are shown to indicate that they are due to an increase in the electron density which extends to above the maximum of the E layer, and possibly up to 150 km. Simultaneous measurements of the increases in absorption of waves in the frequency range 2 to 24 Mc/s (which include measurements of cosmic radio noise) show that there is usually an important increase in absorption in the lowest regions of the ionosphere where the electronic collision frequency is 10^7 or even 10^8 sec $^{-1}$. These conclusions are consistent with the observations of other workers. The above mentioned phenomena were also compared with phase changes observed on very long waves, but since there was found to be a large variation in the individual aspects of different sudden ionospheric disturbances it was not possible to draw any detailed conclusions.

§ 1. Introduction

It is well known that a sudden ionospheric disturbance is characterized by several phenomena observable on radio waves propagated via the ionosphere. Among these are: (i) for waves of frequency greater than about 1Mc/s an increase in the absorption is experienced in passing through the ionosphere, (ii) on all frequencies reflected from the ionosphere a decrease in phase path is observed.

Although these effects are usually attributed to a sudden increase of the electron density in the lower parts of the ionosphere, there is at present no evidence about the height distribution of this extra ionization.

In the experiments described in this paper the increase of absorption was measured on a number of frequencies reflected in the ionosphere and also on cosmic radio noise propagated through the ionosphere. Simultaneous measurements were made, during many sudden ionospheric disturbances, of the phase changes observed on the reflected waves. The results are used in discussing some features of the height distribution of the extra electrons present during the disturbance.

Attempts have often been made to compare the magnitudes of different phenomena associated with sudden ionospheric disturbances by measuring each of them on a series of disturbances, and comparing the means. Unfortunately, individual disturbances differ in detail from each other so much that this procedure can be misleading, particularly when, as has usually been the case, the mean values are determined from measurements on different series of disturbances. In this paper, therefore, attempts have been made, as far as possible, to compare different phenomena measured during the same disturbance.

§ 2. Principles of the Experimental Methods

2.1. *Phase and Group Paths*

Both the phase and group paths of a radio wave reflected in the ionosphere depend on (*a*) the height of reflection, (*b*) the magnitude and distribution of the electron density at all heights up to the reflection level. Suppose first that the heights of reflection of waves of different frequency used in an experiment remain constant. Then, if there is an increase in the electron density below the reflection levels at places where the refractive index is not very different from unity and where the electron collision frequency ν is small compared with the effective angular wave frequency $\omega+\omega_L$, the changes in phase path for the different frequencies will be in a simple ratio (Appendix I). In particular the changes in phase path ΔP and group path $\Delta P'$ will be equal in magnitude and opposite in sign (Appendix II). Findlay (1951) has shown how the changes in phase path on two nearby frequencies may be used to calculate the change in group path at the average frequency.

The results of the experiments described in § 4.1 show that, in general, the changes of phase path on different frequencies are not in the simple theoretical ratio deduced in Appendix I, and it is concluded that the assumption that the reflection levels remain constant is incorrect. This result is reinforced by the fact that for waves reflected from the E region the changes of phase and group path on a given frequency are not always equal in magnitude, or even opposite in sign (§ 4.2).

2.2. *Absorption*

If the electron concentration is increased only at some level below the reflection point, where the refractive index is nearly unity and above the level where $\nu \simeq \omega+\omega_L$, the extra absorption produced is of the 'non-deviative' type for which it is well known that

$$-\log \rho \propto (\omega+\omega_L)^{-2}. \qquad \ldots\ldots (1)$$

The observed increase in absorption on three frequencies reflected in the ionosphere, and on cosmic noise transmitted through the ionosphere on two relatively high frequencies, are discussed in § 5 and it is shown that the 'non-deviative' law (1) is seldom obeyed. A detailed discussion of the results leads to the conclusion that there is usually an important increase in the electron density at levels where $\nu \simeq \omega+\omega_L$ where $\omega/2\pi$ is of order 4 Mc/s; and in some cases the law fails to be obeyed even when $\omega/2\pi \simeq 16$ Mc/s.

2.3. *Phase Changes on Very Long Waves*

The magnitudes of sudden phase anomalies recorded on very long waves are compared with the simultaneous increases in cosmic noise absorption in § 6. The results show that such anomalies with a wide range of sizes can be associated with a given increase in absorption. It thus appears that there is a wide variation in the individual aspects of different sudden ionospheric disturbances. Firm conclusions cannot, however, be drawn from these results until there is available a better theory of the reflection of very long waves, of a kind which can relate the observed sudden phase anomalies to the change of electron distribution causing it.

§ 3. Experimental Arrangements

3.1. *Sudden Phase Anomaly Measurements*

The magnitude of the sudden phase anomaly was determined from routine records of the type described by Bracewell and Straker (1949) using one or other of the Post Office Senders GBR (16 kc/s) and GBZ (19·6 kc/s) situated at distances of 90 and 220 km respectively.

3.2. *Waves Reflected in the Ionosphere*

Measurements were made, using the pulse reflection technique, on waves of four frequencies reflected in the ionosphere. Two frequencies were chosen to be reflected in the E region (these were approximately 2·0 and 2·4 Mc/s in winter and 2·4 and 2·8 Mc/s in summer); and two in the F region (approximately 4·0 and 6·0 Mc/s). The exact frequencies had to be chosen to avoid interference from other senders. The changes of phase path for all four frequencies and the amplitude for the three highest frequencies were recorded continuously by the methods described by Findlay (1951).

3.3. *Cosmic Radio Noise Absorption*

Cosmic radio noise power was measured on waves of frequencies approximately 16·5 and 24·3 Mc/s which traversed the whole ionosphere. These frequencies were chosen to be as low as possible so that the increase in absorption would be appreciable, yet they had to be relatively free from interference by commercial senders.

The cosmic noise radiation on 24·3 Mc/s was received on a broadside array of five full-wave dipoles situated $\lambda/4$ above a reflecting screen of parallel wires. The receiver followed the design developed by Machin, Ryle and Vonberg (1952). The capacity switch of the original design was replaced by a circuit using germanium diodes to switch the receiver input between the aerial and a noise signal generator. The receiver bandwidth was about 3 kc/s, and to avoid the effect of interference from commercial senders the received frequency was swept back and forth continuously over a range of about 100 kc/s (Laffineur 1956). The smallest output recorded in the gaps between the interfering signals was taken to represent the cosmic noise power. It was usually obvious if the interference became so strong that the output failed to fall to the background level of cosmic noise.

The interference on 16·5 Mc/s was greater, but this was offset by the fact that the increase in absorption during a sudden ionospheric disturbance was also greater; and it was possible to obtain useful results, slightly less accurate than on 24·3 Mc/s, by using a single half-wave dipole connected to a standard communications receiver with a bandwidth of 1 kc/s. The receiver gain was checked half-hourly by switching the input to a noise signal generator.

In order to infer from the observations the absorption of a wave travelling vertically through the ionosphere, it is necessary to take account of the effects of the finite beamwidth of the aerial and the distribution of radio brightness over the sky. In making allowance for these effects it was assumed that (i) the absorption at any angle of incidence i depended on the length of path in the relevant portion of the ionosphere and hence was proportional to sec i, (ii) the

aerial polar diagram had the form expected from theoretical calculations, and (iii) for the higher frequency it was assumed that the radio brightness was distributed over the sky as found by Baldwin (1955) on 80 Mc/s.

With these assumptions it was possible to calculate the total power received in terms of the absorption for a vertically incident wave. By assuming that the night-time absorption was negligible it was then possible to determine the dependence of radio brightness on sidereal time. The distribution determined in this way for a frequency of 24·3 Mc/s agreed satisfactorily with the measurements of Baldwin on 80 Mc/s.

§ 4. Experimental Results: Phase Measurements

4.1. *Measurements of Changes of Phase Path*

The temporal variations of phase path for radio waves of five frequencies (including 19·6 kc/s) are shown for a period containing a sudden ionospheric disturbance in figure 1. It will be seen that even in the periods before and after the disturbance there are some 'random' changes of phase so that there is some uncertainty in estimating the effect of the disturbance. Since the random changes are rather larger (or slower) for waves reflected in the F region there is generally a greater uncertainty in the estimate of ΔP for the F region than for the E region. The uncertainties are of the order 0·4 km for the F region and 0·2 km for the E region.

Now suppose that, during a sudden ionospheric disturbance, the electron density N at a level where $\mu \simeq 1$ is increased by an amount ΔN; then since $\mu \simeq 1$ it is permissible to use the quasi-longitudinal approximation to the magneto-ionic

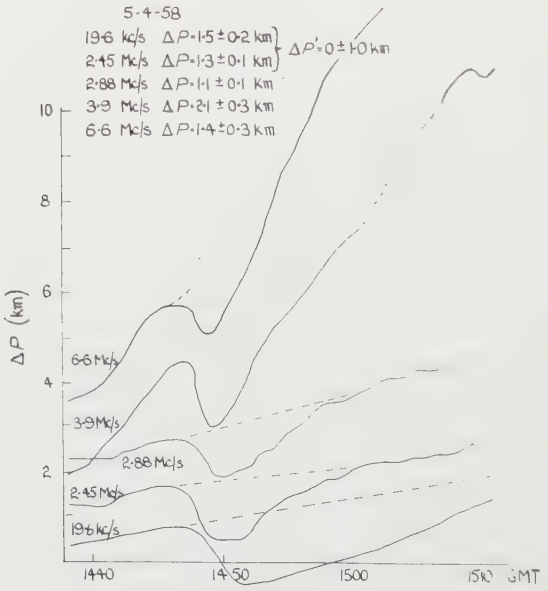

Figure 1. Changes of phase path associated with the sudden ionospheric disturbance on 5th April 1958 observed on five frequencies.

equation. Under these conditions it is shown in Appendix 1 that a stratum of thickness dh will contribute an increment dP to the phase path given by

$$dP = \left\{1 - \frac{4\pi e^2 N}{\epsilon_0 m\omega\{\omega + \omega_L + \nu^2/(\omega + \omega_L)\}}\right\} dh \qquad \ldots\ldots (2)$$

and the extra increment during a disturbance is

$$d(\Delta P) = -\frac{4\pi e^2 \Delta N}{\epsilon_0 m\omega\{\omega + \omega_L + \nu^2/(\omega + \omega_L)\}} dh\,. \qquad \ldots\ldots (3)$$

It follows from equation (3) that if $\nu^2 \ll (\omega - \omega_L)^2$ for all heights for which ΔN is appreciable, then a quantity Q defined by

$$Q = -\omega(\omega + \omega_L)\Delta P \qquad \ldots\ldots (4)$$

will be independent of ω. On the other hand if $\nu^2 \gg (\omega - \omega_L)^2$ the corresponding quantity Q', independent of ω, will be defined by

$$Q' = \{-\omega/(\omega + \omega_L)\}\Delta P. \qquad \ldots\ldots (5)$$

We may note that in either case (and for any intermediate case for which $\nu \simeq \omega + \omega_L$) the value of $-\Delta P$ should decrease with increasing frequency.

In table 1 the results for the sudden ionospheric disturbance shown in figure 1 are given together with the values of Q and Q' at the various frequencies. The fact that neither Q nor Q' is constant, and that $-\Delta P$ does not decrease with

Table 1

f (Mc/s)	$-\Delta P$ (km)	$Q \times 10^{-2}$	Q'
6·6	1·4 ± 0·3	28·3 ± 6·1	1·19 ± 0·25
3·9	2·1 ± 0·3	16·3 ± 2·3	1·62 ± 0·23
2·88	1·1 ± 0·1	5·04 ± 0·5	0·786 ± 0·07
2·45	1·3 ± 0·1	4·52 ± 0·35	0·885 ± 0·07

increase of frequency, shows that, for this particular disturbance, the phase changes cannot be explained by the injection of ionization well below the lowest reflection height.

The results are, therefore, taken to indicate that important ionization is injected during the sudden ionospheric disturbance at least up to the maximum of the E layer. Although the uncertainty is rather large it seems probable that the value of Q is not the same for the two higher frequencies so that it is likely that the increase of ionization extends at least up to the reflection level for waves of frequency 3·9 Mc/s (about 150 km).†

In order to investigate whether this conclusion is true generally for sudden ionospheric disturbances, the value of Q was determined, for each of a series of disturbances, on two frequencies; one reflected in the E region and the other in the F region (usually the higher of the two E region frequencies and the lower of the two F region frequencies were chosen). A histogram of the more accurate

† The fact that Q is not the same for the two higher frequencies is taken to imply that there is a change in the distribution of N near the reflection level of one of them at least. The fact that the results on the lower frequencies indicate extra ionization at least to 110 km makes it plausible that there are also changes at 150 km; though if this be accepted the data give no information about changes at the height of reflection of 6·6 Mc/s.

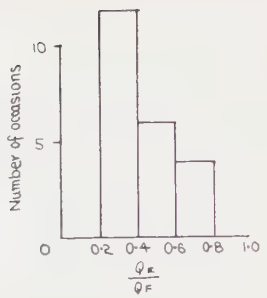

Figure 2. Histogram of values of Q_E/Q_F (equation (4)) for a number of sudden ionospheric disturbances. (If equation (4) were valid Q_E/Q_F would be unity and if equation (5) were correct it would be 0·6.)

values of Q_E/Q_F is shown in figure 2. If the conditions were appropriate to equation (4), Q_E/Q_F would be unity, whereas figure 2 shows that this ratio is always less than unity. If the assumption $\nu^2 \gg (\omega+\omega_L)^2$ appropriate to equation (5) were valid, then Q_E/Q_F would be about 0·6. Figure 2 shows that on more than half the occasions Q_E/Q_F was less than this value also. Thus these results support the conclusion that in most cases important ionization was introduced at least up to the peak of the E layer.

Because of the greater uncertainty in the estimates of ΔP for the frequencies reflected in the F region, it was not often possible to compare the results on two frequencies reflected from that region with adequate precision; but whenever the accuracy was sufficient the comparison supported the result deduced from table 1 that there was a change in the distribution of ionization at least in the lower F region.

4.2. *Changes of Phase and Group Path*

In his study of the effects of sudden ionospheric disturbances Findlay (1951) used methods almost the same as those used in the present work; and from his measurements of the phase changes on two nearby frequencies reflected in the E region he concluded that the changes of phase and group paths were equal and opposite. He therefore inferred that there was no change in conditions at the reflection level.

Since Findlay's conclusions are contrary to those expressed in the previous section, it is useful to apply his analysis to the present results by studying the change of group path of waves reflected from region E. The changes of group path were calculated from the expression

$$\Delta P' = \Delta P + \left(\frac{f}{\delta f}\right)\left\{\Delta P_{f+\delta f} - \Delta P_f\right\} \qquad \ldots\ldots (6)$$

given by Findlay. The magnitudes of the ratio $\Delta P'/\Delta P$ deduced from the results, on a mean frequency of about 2·4 Mc/s, were very variable. All the results of reasonable accuracy are shown in figure 3 in which the magnitude of the ratio is plotted against cos χ.†

† There seems to be a variation of the ratio with cos χ although the data are not accurate enough to establish such a variation with certainty, and $\Delta P'/\Delta P$ appears to be negative for cos $\chi > 0{\cdot}5$.

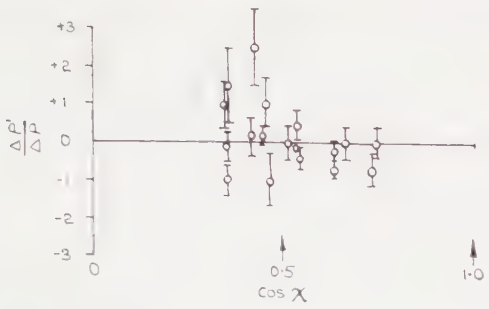

Figure 3. Values of $\Delta P'/\Delta P$ for waves reflected in region E plotted as a function of cos χ.

It will be seen that they do not support Findlay's statement that $\Delta P'/\Delta P = -1$. In this connection, however, it is worthy of notice that Findlay remarks that for the 30 sudden ionospheric disturbances which he studied $\Delta P'/\Delta P$ was always negative but on several occasions it was numerically less than unity. Although there is a discrepancy between the two sets of results we are satisfied that our accuracy was sufficient to establish the fact that $\Delta P'/\Delta P$ can be of either sign, and that, in general $|\Delta P'/\Delta P| < 1$.

§ 5. Measurements of Absorption

A typical record of the amplitude of the signal observed on three frequencies for a period containing a sudden ionospheric disturbance is shown in figure 4. To estimate the increase in absorption, the median value of the fading signal was estimated by eye before, during, and after the disturbance, and the normal course of the absorption in the absence of the disturbance was interpolated between the data before and after the event. The uncertainty in the estimate of the excess absorption for waves reflected in the ionosphere was normally less than 2 dB.

For the cosmic noise measurements the fading was much less pronounced and the uncertainty in the estimated absorption was only about 0·2 dB unless interference from commercial senders was unusually severe.

Under conditions for which the quasi-longitudinal approximation to the magneto-ionic equation can be applied it is well known that the absorption coefficient may be expressed in the form

$$\kappa = \frac{1}{2c\mu}\frac{4\pi e^2}{\epsilon_0 m}\frac{N\nu}{(\omega \pm \omega_L)^2 + \nu^2} \qquad \ldots\ldots(7)$$

where the upper sign refers to the Ordinary magneto-ionic component.

If the electron density is increased by ΔN at levels where $\mu \simeq 1$ the change in the effective reflection coefficient ρ for the Ordinary wave may be written

$$\Delta(-\log\rho) = \frac{4\pi e^2}{\epsilon_0 mc}\int \frac{\Delta N \nu dh}{(\omega+\omega_L)^2+\nu^2}. \qquad \ldots\ldots(8)$$

This equation should be appropriate for waves reflected from the ionosphere since measurements were made on the Ordinary wave only. The cosmic radio waves passed through the ionosphere once only and the total power in both

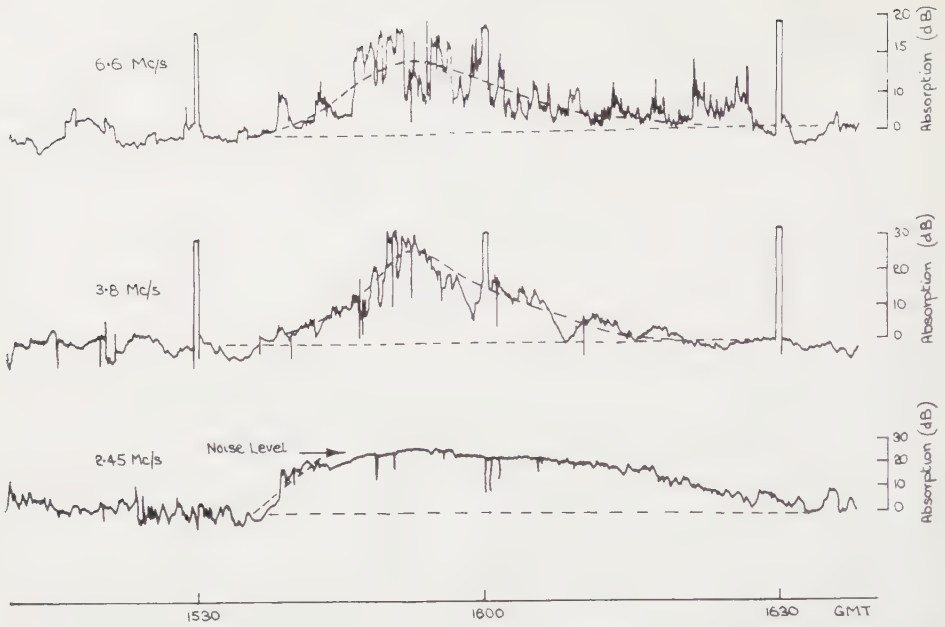

Figure 4. Amplitude of the reflected signals on three frequencies 1500–1630 h. on 27th March 1958 showing a sudden ionospheric disturbance between 1536–1620.

magneto-ionic components was measured. It may be shown (Appendix III) that when $\omega \gg \omega_L$ the effective reflection coefficient for these conditions may be written

$$\Delta(-\log \rho) = \frac{2\pi e^2}{\epsilon_0 mc} \int \frac{\Delta N \nu \, dh}{\omega^2 + \nu^2}. \qquad \ldots\ldots (9)$$

For waves reflected from the ionosphere there is some evidence (Whitehead 1957) that the normal absorption occurs partly in a region where $(\omega + \omega_L)^2 \gg \nu^2$ or $\mu \simeq 1$ and partly near the level of reflection. Despite the results inferred in the previous section, it may well be true that during a sudden ionospheric disturbance the main change in absorption is due to ionization well below the reflection level in a place where ν is large, but still small compared with $\omega + \omega_L$: so that it might be expected, during a disturbance, that

$$\Delta(-\log \rho) \propto (\omega + \omega_L)^{-2}. \qquad \ldots\ldots (10)$$

To test these hypotheses results were therefore examined by plotting observed values of $[\Delta(-\log \rho)]^{-1/2}$ against $\omega + \omega_L$ for reflected waves, and $[2\Delta(-\log \rho)]^{-1/2}$ against ω on the same scale for cosmic noise waves. Typical plots of the results are shown in figure 5. On some occasions, as in figure 5 (*a*), the results agreed quite well with the theoretical relation, but more frequently the points departed from the expected line like those of figures 5 (*b*) or 5 (*c*) in which there is a progressive discrepancy towards lower frequencies.

In general the results for the two highest frequencies, corresponding to the absorption of cosmic noise, were in agreement with the theoretical prediction within the experimental error; thus the expected ratio of $\Delta(-\log \rho)$ on 16·5 Mc/s to that on 24·3 Mc/s is 2·17 while the mean value of this ratio for 35 sudden ionospheric disturbances was $2{\cdot}13 \pm 0{\cdot}15$.

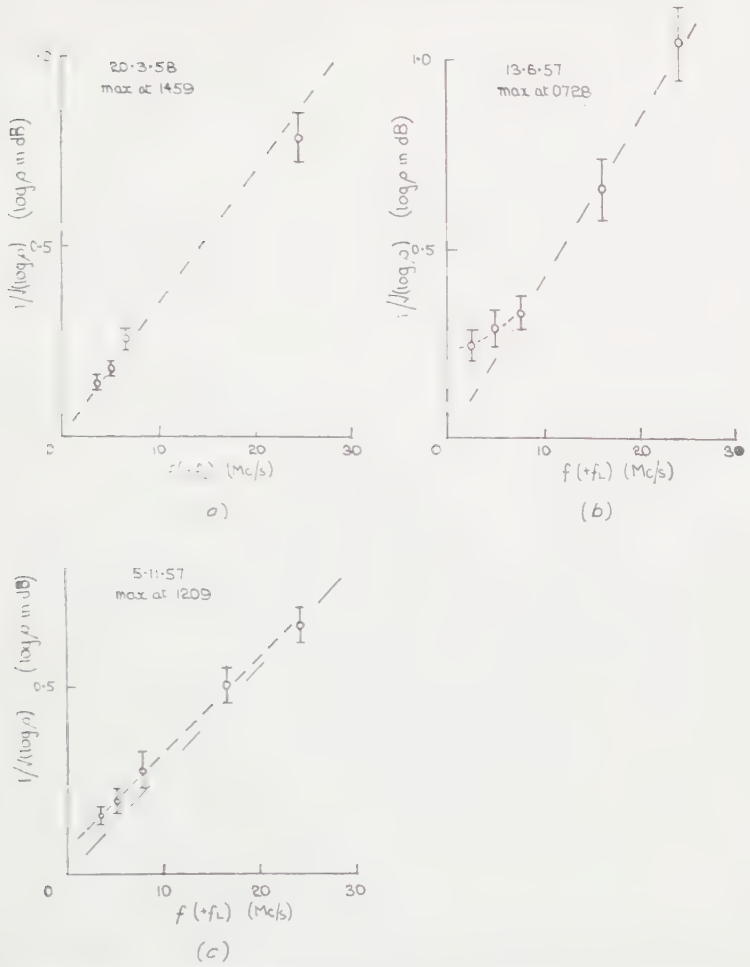

Figure 5. Frequency variation of the excess absorption during three sudden ionospheric disturbances showing the departure from the expected relation on the hypothesis $\nu \ll \omega + \omega_L$.

For the largest disturbances, however, the expected relation did not hold even on the two highest frequencies. For example, throughout one very large disturbance it was possible to study in detail the ratio of the absorption on the two cosmic noise frequencies: the results are shown in figure 6, from which it is obvious that the ratio decreased appreciably as the absorption on 24·3 Mc/s increased. To test whether the ratio was always smaller when the absorption on 24·3 Mc/s was high the mean value of the ratio was found for sudden ionospheric disturbances grouped according to the absorption on 24·3 Mc/s. The results of this comparison are shown in table 2.

Table 2

Absorption on 24·3 Mc/s (dB)	<1	between 1 and 2	>2
Ratio $\dfrac{\Delta(-\log \rho)_{16\cdot5}}{\Delta(-\log \rho)_{24\cdot3}}$	2·4	2·0	1·8
Deviation	0·1	0·2	0·1

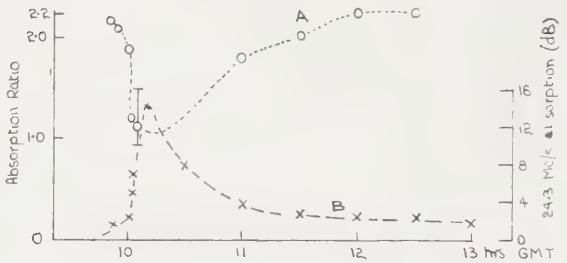

Figure 6. The ratio of excess absorption on 16·5 Mc/s to that on 24·3 Mc/s during the sudden ionospheric disturbance of 23rd March 1958, and the absorption excess recorded on 24·3 Mc/s.

A simple interpretation of these results seems to be available in equation (9) if it is supposed that the extra ionization was not all injected at a level where $\omega^2 \gg \nu^2$. Suppose, for example, in an extreme case that all the electrons were injected at one level, then for the two cosmic noise frequencies ω_1 or ω_2 (both $\gg \omega_L$) we should have

$$\frac{\Delta(-\log \rho_1)}{\Delta(-\log \rho_2)} = \frac{\omega_2^2 + \nu^2}{\omega_1^2 + \nu^2}. \qquad \ldots\ldots (11)$$

This ratio would lie between ω_2^2/ω_1^2, if both frequencies were large compared with ν, and unity, if both frequencies were small compared with ν. Thus the experimental results can be explained by supposing that at least some of the extra electrons were injected near the level where $\nu/2\pi = 16{\cdot}5$ Mc/s or $\nu = 10^8$ sec^{-1}.

This conclusion can be extended to explain the way in which, in figure 5, the points corresponding to the lower (reflected) frequencies depart from the expected straight line. This departure is in a sense which implies that the absorption is relatively less at the lower frequencies, so that it is consistent with the idea that $\nu \simeq \omega + \omega_L$ for the lower frequencies but $\nu \ll \omega$ at the higher frequencies.

The departures from the expected linear relation could also be explained by supposing that the deviative absorption was decreased on all the reflected frequencies during the sudden ionospheric disturbance, for example by an increase in the gradient of electron density at all the reflection heights. But in view of the results for large disturbances it seems more probable that the alternative explanation is correct.

To illustrate further how results from low frequencies depart from the law of equation (10) we may note that the absorption $\Delta(-\log \rho_1)$ on a low frequency ω_1 may be calculated from that measured on a high (cosmic noise) frequency ω_2 from the expression

$$\Delta(-\log \rho_1) = \frac{2\omega_2^2}{(\omega_1 + \omega_L)^2} \Delta(-\log \rho_2). \qquad \ldots\ldots (12)$$

Figure 7 is a histogram of the ratio R of the observed increases in absorption on 2·4 Mc/s to those given by equation (12) with $\omega_2 = 24{\cdot}3$ Mc/s. The fact

that the observed absorption is usually less than that expected is consistent with the hypothesis that the increase in absorption is partly due to extra ionization at a height where ν is large ($\sim 10^7$ sec^{-1}).

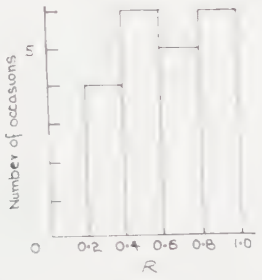

Figure 7. Histogram of the ratio of the excess absorption on 2·4 Mc/s to that calculated, by means of equation (12), from the observations on 24·3 Mc/s.

§ 6. High Frequency Absorption and Very Long Wave Phase

It has been suggested by Shain and Mitra (1953) that there is a simple linear relation between the increase in absorption of cosmic noise and the magnitude of the decrease in phase height of very long waves (sudden phase anomaly).

The results of a number of measurements of the size of the phase anomaly on 16 kc s or 19·6 kc/s and the corresponding increases in cosmic noise absorption are shown in figure 8 together with the linear relation suggested by Shain and Mitra. It is clear that although there is some correlation between the magnitudes of the two events there is considerable variability in the results. In particular small increases in absorption may be accompanied by large sudden phase anomalies.

A detailed discussion of the relation between these two quantities must await a full wave theory of the reflection of very long waves, since there is at present no simple known way of relating the magnitude of a sudden phase anomaly to the increase of electron density producing it.

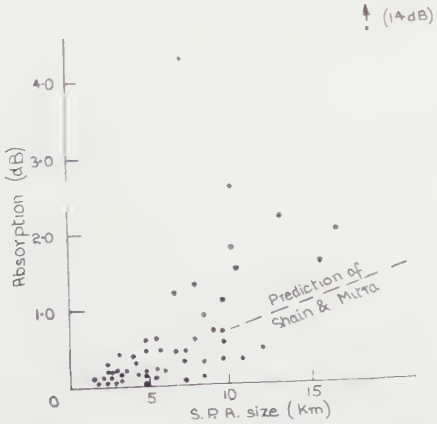

Figure 8. A comparison of the magnitude of the sudden phase anomaly and the excess absorption on 24·3 Mc/s. The straight line corresponds to the relation given by Shain and Mitra (1953).

§ 7. Conclusions

The experiments described in this paper have led to the conclusion that during a sudden ionospheric disturbance the major part of the extra ionization is injected in the E-region up to the E layer peak and probably appreciably above it. This result is in agreement with the observations of Bibl (1951) and Taubenheim (1957) who found that there was always a short-wave fade-out whenever the critical frequency f_0E increased suddenly by more than 0·2 Mc/s.

The main extra absorption of radio waves during a sudden ionospheric disturbance appears nevertheless to take place very low in the ionosphere, and important absorption frequently takes place where $\nu = 10^7$ sec^{-1} (at a height of about 65 km) and at times extends down to levels where $\nu = 10^8$ sec^{-1} (at a height of about 50 km). This conclusion is consistent with the observations of Friedman *et al.* (1958) that in sudden ionospheric disturbances there is appreciable flux of x-rays of wavelength near 1–2 Å.

APPENDIX I

It is well known that, under conditions in which the quasi-longitudinal approximation is valid, the expression for the refractive index in the magneto-ionic theory reduces to

$$\mu^2 = 1 - \frac{4\pi Ne^2}{\epsilon_0 m\omega\{\omega \pm \omega_L + \nu^2/(\omega \pm \omega_L)\}}$$

where the upper signs in the denominator are appropriate to the Ordinary wave.

Now when $\mu \simeq 1$, then $1-\mu^2 = 2(1-\mu)$. Thus the contribution to the phase path $\int \mu\, dh$ from a stratum of thickness dh is, for the Ordinary wave,

$$dP = \left\{1 - \frac{4\pi e^2 N}{\epsilon_0 m\omega\{\omega + \omega_L + \nu^2/(\omega + \omega_L)\}}\right\} dh$$

for a double traversal and if $\nu \ll \omega + \omega_L$ we may write for the change ΔP in the total phase path produced by a change ΔN in N

$$-\Delta P = Q/\{\omega(\omega + \omega_L)\}$$

where Q is independent of the frequency.

If on the other hand ν approaches $\omega + \omega_L$, ΔP will vary more slowly with frequency.

APPENDIX II

The phase and group paths of a wave travelling vertically through a medium of refractive index μ varying with height and reflected at a height h are given by

$$P = 2\int_0^{h_m} \mu\, dh,$$

$$P' = 2\int_0^{h_m} \mu'\, dh,$$

where μ' is the group refractive index.

To find the order of magnitude of the changes to be expected from a small change in μ when μ is near unity we may use the approximate relation $\mu' = 1/\mu$ so that

$$P = 2\int_0^{h_m} \frac{dh}{\mu}.$$

If h_m decreases, $\Delta P'$ and ΔP would have the same sign since both integrands are positive, but if μ decreases, $\Delta P'$ and ΔP will have opposite signs, and for a small change in μ, near unity, they will be nearly equal in magnitude.

APPENDIX III

Since the cosmic noise radiation incident on the ionosphere is essentially unpolarized, the waves transmitted through the ionosphere in the two characteristic modes are phase incoherent. The apparatus measures the total cosmic noise power. If P_0 is the incident power and P_r the received power

$$P_r = \tfrac{1}{2}P_0 \exp\left\{-\frac{2\pi e^2}{\epsilon_0 mc}\int \frac{N\nu}{(\omega+\omega_L)^2+\nu^2}\,dh\right\} + \tfrac{1}{2}P_0 \exp\left\{-\frac{2\pi e^2}{\epsilon_0 mc}\int \frac{N\nu}{(\omega-\omega_L)^2+\nu^2}\,dh\right\}$$

and for frequencies which penetrate the ionosphere and for which $\omega^2 \gg \omega_L{}^2$ this leads to

$$P_r = P_0 \exp\left\{-\frac{2\pi e^2}{\epsilon_0 mc}\int \frac{N\nu}{\omega^2+\omega_L{}^2+\nu^2}\,dh\right\} \cosh\left\{\frac{2\pi e^2}{\epsilon_0 mc}\int \frac{N\nu\,\omega\omega_L}{(\omega^2+\omega_L{}^2+\nu^2)^2}\,dh\right\}$$

so that

$$-\log\left(\frac{P_r}{P_0}\right) = \frac{2\pi e^2}{\epsilon_0 mc}\int \frac{N\nu}{\omega^2+\omega_L{}^2+\nu^2}\,dh - \log\cosh\left\{\frac{4\pi e^2}{\epsilon_0 mc}\int \frac{N\nu\omega\omega_L}{(\omega^2+\omega_L{}^2+\nu^2)^2}\,dh\right\}.$$

If we ignore the variation of ω_L with altitude over the relevant range of height, and put

$$B = \frac{2\pi e^2}{\epsilon_0 mc}\int \frac{N\nu}{\omega^2+\omega_L{}^2+\nu^2}\,dh$$

the first approximation to $-\log\rho$, then

$$-\log\rho = B - \log\cosh\{(2\omega\omega_L B)/(\omega^2+\omega_L{}^2+\nu^2)\}.$$

Normally, in the absence of sudden ionospheric disturbances, B is less than 0·25 neper at 16·5 Mc/s and $2\omega_L\,\omega = 0{\cdot}14$ so that if $\nu^2 \ll \omega^2$ the second term in the expression for $-\log\rho$ is of order log cosh (0·035) $= 6 \times 10^{-4}$ neper which is less than the probable error of a measurement (0·025 neper).

During the largest sudden ionospheric disturbances observed, B was of order 2·4 nepers, and the correction term would be of order 0·06 neper which is still small compared with the measured absorption.

Thus for all cases considered here, we may write for the cosmic noise absorption

$$-\log\rho = \frac{2\pi e^2}{\epsilon_0 mc}\int \frac{N\nu}{\omega^2+\omega_L{}^2+\nu^2}\,dh.$$

Acknowledgments

This work formed part of the programme of the British National Committee for the International Geophysical Year. The author is indebted to that Committee for a grant; and also to the Department of Scientific and Industrial Research for the award of a maintenance grant.

Thanks are also due to Dr. F. G. Smith and to Dr. B. H. Briggs who supervised the work, to Mr. J. A. Ratcliffe, Dr. K. Weekes, and the other members of the Cavendish Laboratory for their encouragement and help, and to Mr. J. H. Burr for valuable assistance with the records and the maintenance of the equipment.

References

Baldwin, J., 1955, *Mon. Not. R. Astr. Soc.*, **115,** 684.
Bibl, K., 1951, *Ann. Geophys.*, **7,** 208.
Bracewell, R. N., and Straker, T. W., 1949, *Mon. Not. R. Astr. Soc.*, **109,** 28.
Findlay, J. W., 1951, *J. Atmos. Terr. Phys.*, **1,** 367.
Friedman, H, *et al.*, 1958, *Ann. Geophys.*, **14,** 232.
Laffineur, M., 1956, *J. Atmos. Terr. Phys.*, **9,** 347.
Machin, K. E., Ryle, M., and Vonberg, D. D., 1952, *Proc. Instn Elect. Engrs*, Pt. III, **99,** 127.
Shain, C. A., and Mitra, A. P., 1953, *J. Atmos. Terr. Phys.*, **4,** 204.
Taubenheim, J., 1957, *J. Atmos. Terr. Phys.*, **11,** 14.
Whitehead, J. D , 1957, *J. Atmos. Terr. Phys.*, **10** 12.

The Electrical Conductivity of Barium Titanate Single Crystals

By A. BRANWOOD and R. H. TREDGOLD
Department of Physics, University College of North Wales, Bangor, Caerns.

MS. received 18*th January* 1960, *in final form* 25*th February* 1960

Abstract. The conductivity of a number of barium titanate single crystals was measured as a function of temperature, applied field, electrode material, thickness and time. Typical results are given, and tentative theories put forward to account for the observed activation energies, the striking non-ohmic nature of the conductivity, and the influence of the electrode material. Results for some doped crystals are also briefly reported.

§ 1. Introduction

Barium titanate ($BaTiO_3$) is the prototype of the group of ferroelectric materials having the perovskite structure. Above 120°c it has cubic symmetry and is para-electric, below 120°c but above −5°c it has tetragonal symmetry (the tetragonal axis corresponds to the direction of electrification), and below −5°c two further phases exist which do not concern us here. It is characterized by having a very high intrinsic dielectric constant varying between values of several hundred and several thousand, depending on temperature and crystallographic direction (Merz 1949, 1953). Good thin flat single crystals can be grown using a method originated by Remeika (1954), and these crystals show negligible ionic conductivity (Hurd, Simpson and Tredgold 1959). Furthermore preliminary measurements made by Busch, Flury and Merz (1948) indicate that the energy gap between the Fermi surface and the conduction band is of the order 1 ev, and that thus the electrical conductivity at temperatures above 0°c is large enough to be measured with reasonable accuracy. These various properties render barium titanate a very suitable material in which to study the electrical conductivity mechanism of nearly ionic crystals.

This paper reports the variation of the conductivity of barium titanate crystals as a function of temperature, applied field, electrode material, impurities, direction of polarization and thickness. Tentative deductions are made from these results, but a full understanding of the subject awaits the completion of a number of related studies which are in progress and which will be given brief mention at the end of this paper.

§ 2. The Crystals

The crystals used were obtained from three different sources but were all grown by the Remeika (1954) method. In this method, powdered barium titanate is fused in potassium fluoride in a platinum crucible and the resulting melt is slow-cooled from 1180°c to about 800°c when the excess potassium fluoride is poured off and the residue is cooled to room temperature. The crystals are then extracted by boiling in hot water. The success of the method depends upon

the presence of a small quantity of iron in the melt. The amount of iron which finally enters the crystals is so small as to be difficult to detect by chemical means. Nevertheless paramagnetic resonance studies (Hornig, Rempel and Weaver 1958, 1959) appear to indicate that iron does enter the $BaTiO_3$ lattice in detectable quantities (but see also Low and Shaltiel 1958).

The crystals used were between about 0·03 and 0·01 cm thick and were large enough to allow circular electrodes of diameters ranging from 0·25 to 0·50 cm, to be deposited on them. Carbon tetrachloride, followed by dilute nitric acid, was used to clean the specimens, and metal electrodes were then evaporated on to the crystals *in vacuo*. A travelling microscope was used to measure the electrode diameters, while the crystal thickness was measured using a micrometer.

§ 3. Method of Measurement

The crystal was placed in a suitable electric furnace, the electrodes being held by spring loaded contacts. A thermocouple was used to measure the temperature, and preliminary measurements were carried out to ensure that the whole of the specimen and the thermocouple were at the same temperature to within 1 °C throughout the temperature range of interest. The applied potential was obtained from h.t. batteries, and the current was measured by a Leeds–Northrop d.c. current amplifier. The most sensitive range of this instrument corresponds to a full-scale deflection of 10^{-9} amp, so that if time was allowed for the instrument to settle down and appropriate screening precautions were taken, the current could be estimated to 10^{-11} amp. The input impedance of this amplifier was sufficiently small compared with the specimen resistance that it could be neglected for all but the highest temperature readings made.

§ 4. Preliminary Investigations

Initially a study was made, using various electrode patterns, to ensure that the surface layer did not tend to short-circuit the main conduction path. A satisfactory negative result was obtained. This experiment also served as a check on the cleaning methods.

A study of conductivity as a function of crystal direction was next made. It is well known (von Hippel and Matthias 1948) that the use of polarized light allows one to distinguish between *c* and *a* domains. Thus a crystal having regions with the tetragonal axis normal to the surface (*c* domains), and other regions with the tetragonal axis in the surface (*a* domains) can easily be studied using monochromatic light and a polarizing microscope. By suitable rotation of the analyser one set of domains can be made to appear dark, and the other set light. Furthermore suitable application of an alternating field to a crystal, allows one to rearrange the domain pattern and hence the ratio of *c* domain to *a* domain in it. In this experiment, sodium light was used in conjunction with very thin gold electrodes which were sufficiently transparent to this light. The polarizing microscope used was fitted with a high temperature stage and a camera. Provision was made for measuring the conductivity and temperature of a crystal, while the domain pattern was recorded photographically for each value of field and temperature. The experiment was repeated on several different crystals. For each crystal, several different domain patterns were employed in turn. Within the experimental error ($\pm 2\%$ at these low temperatures < 120 °C), it was impossible to detect any

variation of conductivity with orientation (i.e. with different ratios of *a* domain area to *c* domain area). Subsequent experiments were thus carried out, without the inconvenience and temperature limitations of the optical system.

§ 5. Electrode Materials

In the experiment just described, it was noticed that experimental points were not exactly repeatable, and that the currents measured using gold electrodes tended to increase slowly with time. It was thus decided to make a study of current as a function of time for a number of electrode materials. Two sets of experiments were made, one at 102 °C and the other at 160 °C. In either case, measurements were made on crystals held in glass covered specimen holders, immersed in temperature controlled silicone oil baths, and a field of 4000 volts cm^{-1} was employed. The following electrode materials were studied: Au, Ag, Cu, Cr, Al, Zn. Copper electrodes deteriorated rapidly with time and it is impossible to make any general statement about their behaviour. The crystals with chromium, aluminium and zinc electrodes showed no change with time, and all had about the same specific conductivity with similar fields and temperatures. The crystals with gold and silver electrodes, however, showed a marked increase of conductivity with time. A typical result is shown in figure 1. It seemed likely that this increase of conductivity was caused by the diffusion of electrode material into the barium titanate lattice under the influence of the applied field. This theory was supported by the results of the following experiments.

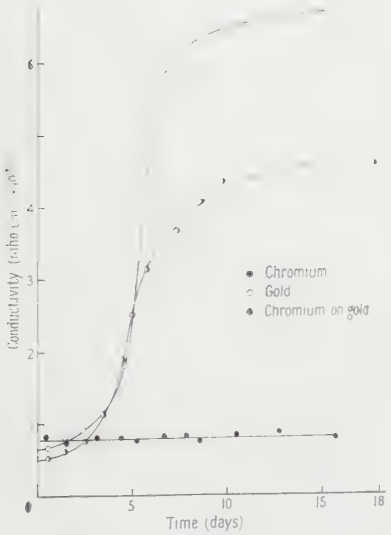

Figure 1. Conductivity plotted against time at 102°c with fields of approximately 4000 volts cm^{-1} for different electrode materials.

Figure 2. Natural logarithm of conductivity plotted against inverse of absolute temperature.

Two similar crystals were chosen and each had a gold electrode deposited on one side and a chromium electrode deposited on the other. One was connected in a circuit in which the gold acted as the anode, and the other in which the gold acted as the cathode. The crystal having a gold anode showed an increase in conductivity with time, and the other did not. A possible explanation of the behaviour of the two groups of electrode materials was the suggestion that gold and silver readily allow the diffusion of oxygen through the electrodes, while chromium etc. do not. To investigate this hypothesis, a crystal was prepared with gold electrodes on both sides and slightly larger chromium electrodes on top of these. This crystal behaved like one which had simple gold electrodes thus disposing of the hypothesis based on different gaseous diffusion rates. Finally, a crystal which had a gold anode and had had current passing through it for about three weeks was taken and the anode was removed. The crystal was cleaned chemically, and new chromium electrodes were deposited. The measured conductivity was uninfluenced by the change of electrodes indicating that gold must have entered the $BaTiO_3$ lattice.

The quantity of gold which enters the lattice and the depth of penetration cannot be deduced from the above facts and hence a full explanation of the results described cannot be given as yet. Work is in progress to clarify these points by means of radioactive tracer techniques. In the work described in the remainder of the paper chromium electrodes were employed.

§ 6. Conductivity Measurements

The conductivity of a number of single crystals was measured using fields of up to 10^4 volts cm^{-1}, in the temperature range 15°C to 480°C. Results for a typical crystal are shown in figure 2. The general features of the curves shown in this figure are well reproduced from crystal to crystal. There was however a scatter in the absolute value of the conductivity of about $\pm 15\%$ from the mean. The peak in conductivity in the region of the Curie temperature corresponds to a peak

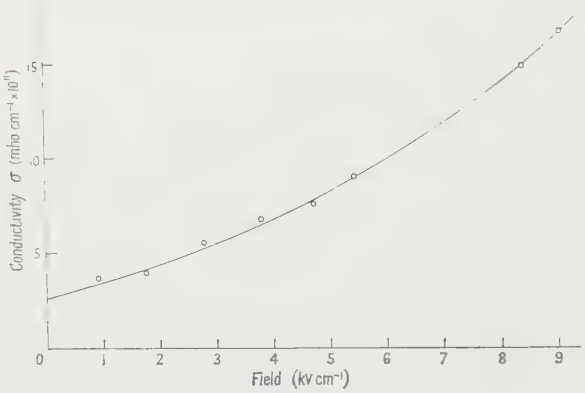

Figure 3. Variation of conductivity with applied field at 220°C.

in intrinsic dielectric constant reported by Merz (1949). Unfortunately it tells us little about the conduction process as all the models so far proposed, predict such a peak. Above the Curie temperature the slope of the ($\ln \sigma$, $1/T$) curve (T in °K) corresponds to an activation energy of $0{\cdot}84 \pm 0{\cdot}02$ ev and a value of $\sigma_0 \sim 0{\cdot}1$

(where σ_0 is the intercept on the σ axis). Above about 270°c there is a fairly sharp transition to a slope of $1{\cdot}22 \pm 0{\cdot}22$ ev with $\sigma_0 \sim 200$. The variation of conductivity with field for a fixed temperature is implied in figure 2 and shown explicitly in figure 3.

§ 7. Doped Crystals

Crystals containing small quantities of Zn and Pb were also studied. The percentages of these impurities are not known accurately but are probably less than 0·1%. The Zn doped specimen had a conductivity of from 30 to 40 times greater than that of the pure material throughout the temperature range. The form of the $(\ln \sigma, 1/T)$ curve was similar but the Curie temperature was reduced to about 70 °c and the lower and higher activation energies were 0·65 ev and 1·15 ev respectively. Similar results were obtained for the lead doped specimen.

§ 8. Discussion

According to Mott and Gurney (1940a) the conductivity of a semiconductor is given by

$$\sigma = 2e\mu \left(\frac{N}{V}\right)^{1/2} \left(\frac{2\pi mkT}{h^2}\right)^{3/4} \exp\left(-\frac{E}{2kT}\right) \qquad \ldots\ldots(1)$$

where e is the electronic charge, μ the mobility, N/V the density of donors, E is the energy gap, and the other symbols have their usual meanings. If we attempt to fit this expression to the high temperature results and assume that they correspond to intrinsic conduction we find that $E = 2{\cdot}44 \pm 0{\cdot}04$ ev and μ must be about 1 $cm^2 v^{-1} sec^{-1}$. Now according to Horie, Kawabe and Sawada (1954) the intrinsic energy gap as measured by optical means is approximately 3 ev and thus allowing for the Frank–Condon principle, the value 2·44 ev obtained from thermal data is quite satisfactory. The value for μ is also credible.

Below 270 °c the behaviour could be explained as impurity semiconduction with about 10^{14} donors per cm^3 and an energy gap of 1·7 ev. If this explanation is correct, the donors are likely to be oxygen vacancies rather than impurities, as the absolute conductivity in this region only varies by a small amount between one batch of crystals and another, even though all of the crystals were not obtained from the same source. It is unlikely that the impurities are Fe^{3+} as other evidence exists (Hurd, Simpson and Tredgold 1959) that iron goes into $BaTiO_3$ as Fe^{2+}.

The striking non-ohmic nature of the conductivity still requires an explanation. Four possible explanations of this suggest themselves, and we will discuss them in turn.

(i) Space charge limitation of the current enhanced by trapping. Suppose the crystal contains a fairly high density of electron traps of depth $E \gg kT$ and that most of the current is caused by the presence of *excess* electrons which have entered from the cathode. It may then be shown (Mott and Gurney 1940b, Suits 1957) that the current will be given by

$$i = AU^2/L^3 \qquad \ldots\ldots(2)$$

where L is the thickness of the crystal, and U is the applied potential.

This mechanism does not appear to apply in this case for the following reasons. The theory is not consistent with the fact that most of the current in the region above 270 °c appears to come from intrinsic semiconduction. (The behaviour is

still non-ohmic in this temperature region.) Furthermore the variation of current as the inverse *cube* of the thickness of the crystal should be easily detectable. We have carried out careful measurements in an attempt to detect this effect and have obtained negative results.

It should be pointed out that the form of space-charge limitation discussed by Rose and Smith (1955) and Lampert (1956) will not apply in this case. They consider a material in which the density of excess electrons is comparable with the density of traps, and show that the current will increase very rapidly with applied field (a fourth power, or even higher power law results from this work). For $BaTiO_3$ we obtain something approaching a square law.

(ii) Kanzig (1955) has shown that $BaTiO_3$ has a surface exhaustion layer about 10^3 Å thick which probably contains numerous oxygen vacancies which could act as traps. Thus one would have a trapping layer having a thickness independent of crystal thickness. One thus might identify the energy 1·7 ev with these traps and the energy 2·44 ev with intrinsic conduction in the main body of the crystal. Unfortunately this model does not predict non-ohmic behaviour in the region above 270°c.

(iii) It can be shown that the interaction of the applied field, and the field due to the electrical image of an electron in the cathode will lead to non-ohmic conduction in a dielectric. In the case in question however, the applied fields are not large enough to produce the required effect.

(iv) It is possible that the actual electron mobility is field dependent. The work of Fröhlich (1937) on dielectric break down, indicates that the mobility of a conduction electron in an ionic crystal should increase with applied field. How big this effect should be is difficult to ascertain without detailed calculations. Work in this department is in progress on this problem.

§ 9. Future Work

To obtain a full insight into the electric conduction mechanism in $BaTiO_3$, one requires information on Hall mobility, drift mobility, and the diffusion of the electrode material into the lattice. Work on these topics in this department is projected or in hand.

References

Busch, G., Flury, H., and Merz, W., 1948, *Helv. Phys. Acta*, **21**, 212.
Fröhlich, H., 1937, *Proc. Roy. Soc.* A, **160**, 230.
von Hippel, A., and Matthias, B., 1948, *Phys. Rev.*, **73**, 268.
Horie, T., Kawabe, K., and Sawada, S., 1954, *J. Phys. Soc. Japan*, **9**, 823.
Hornig, A. W., Rempel, R. C., and Weaver, H. E., 1958, *Phys. Rev. Letters*, **8**, 284.
—— 1959, *J. Phys. Chem. Solids*, **10**, 1.
Hurd, J. D., Simpson, A. W., and Tredgold, R. H., 1959, *Proc. Phys. Soc.*, **73**, 448.
Kanzig, W., 1955, *Phys. Rev.*, **98**, 549.
Lampert, M. A., 1956, *Phys. Rev.*, **103**, 1648.
Low, W., and Shaltiel, D., 1958, *Phys. Rev. Letters*, **1**, 51.
Merz, W., 1949, *Phys. Rev.*, **76**, 1221.
—— 1953, *Ibid.*, **91**, 513.
Mott, N. F., and Gurney, R. W., 1940, *Electronic Processes in Ionic Crystals* (Oxford: University Press), a, p. 158; b, p. 171.
Remeika, J. P., 1954, *J. Amer. Chem. Soc.*, **76**, 940.
Rose, A., and Smith, R. W., 1955, *Phys. Rev.*, **97**, 1531.
Suits, G. H., 1957, *J. Appl. phys.*, **28**, 454.

The Wall Effect in Ferrimagnetic Resonance Experiments

By W. B. NASH† and K. J. STANDLEY
Department of Physics, University of Nottingham

MS. received 27th January 1960, in final form 22nd February 1960

Abstract. Measurements have been made of the shift in the applied magnetic field for resonance, caused by the presence of a conducting wall. Small spheres of nickel ferrite and magnesium manganese ferrite were used at wavelengths of 0·87, 1·25 and 3·12 cm and of yttrium iron garnet at a wavelength of 3·12 cm only. The shift was always to lower fields and was independent of frequency within experimental error. Its magnitude at room temperature was 135 and 100 oersteds in nickel and magnesium manganese ferrites respectively. In the garnet, the shift was found to be dependent upon the orientation of the steady field with respect to the conducting plane. A simple explanation is presented which gives agreement with the experimental data in order of magnitude.

§ 1. Introduction

The disturbing influence of a nearby electrical conductor upon the apparent high frequency magnetic properties of a ferrimagnetic material was first reported by Spencer and Le Craw (1955). In a microwave resonance experiment, it is found that the position of the resonance line of a ferrimagnetic sample is affected by the close proximity of a conductor to the specimen; a brief indication of the magnitude of this 'wall shift' was given by Snieder (1958).

During a recent series of resonance measurements, the magnitude and sign of the wall shift were determined at wavelengths of 0·87, 1·25 and 3·12 cm and at temperatures in the range 20° c to about 300° c. Samples used were spheres of polycrystalline nickel ferrite and magnesium manganese ferrite (both of porosity about 5%), ranging in diameter from 0·2 to 0·8 mm. The absorption curves for these samples varied in width from about 80 to 500 oersteds in the temperature and frequency range investigated. Well established resonance techniques were employed (Standley and Reich 1955), using cavities resonating in H_{11n} modes. The spheres were set off from the end wall of the cavity on thin sheets of mica of measured thicknesses.

Measurements were also made on spheres of yttrium iron garnet, both single and polycrystals, at a wavelength of 3·12 cm at room temperature. The garnet absorption line is sufficiently strong and narrow to permit observation in a non-resonant waveguide and the signal reflected from a short circuit was detected and displayed on an oscillograph, using a simple 50 c/s field modulation system. The effect of moving the conducting wall towards the garnet sphere could be seen and measured directly; the two configurations with the steady field parallel and perpendicular to the conducting wall were used, and the effect of moving the sphere across the wall, i.e. varying the radio-frequency field strength, was studied.

† Now at Signals Research and Development Establishment, Ministry of Aviation, Christchurch, Hants.

A subsidiary experiment confirmed that the metal wall was the cause of the shift. A ferrite sphere mounted on the end wall of the 3 cm cavity showed peak absorption in an applied magnetic field H_w. The sphere was then mounted on a quartz rod and was moved several millimetres from the wall into the cavity. The resonance field was now H_r and was unaltered by further movement of the rod into the cavity. The specimen was then placed on a thin (0·0005 in.) sheet of copper foil about 2 mm square on top of the quartz rod which was again inserted right into the cavity. The resonance field was found to be H_w.

§ 2. Experimental Results

Referring first to the ferrite measurements, the experimental data may be summarized as follows: (i) H_r was always greater than H_w. (ii) For a given material and temperature $H_r - H_w$ was independent of wavelength and sphere size within the experimental error of ± 10 oersteds at 3·12 cm and ± 30 oersteds at 0·87 cm. (iii) For a given material $H_r - H_w$ diminished as the temperature was raised, becoming negligibly small in the region of the Curie point. This fact only can be stated with certainty for the magnesium manganese ferrite, with a Curie temperature of about 300°c. (iv) A small decrease in H_w, only slightly greater than the experimental uncertainty, was observed as the specimen was moved from the centre of the end wall towards the circumference. (v) The line width observed when the sphere was in contact with the end wall appeared in general to be about 5% greater than that found when the sphere was well removed from any conductor. This may have been due to the excitation of unresolved magnetostatic modes. Such an explanation is supported by the garnet measurements (figure 2, Plate).

In nickel ferrite, the mean values of $H_r - H_w$ at the three wavelengths amount to 135, 115 and 100 oersteds at 20, 100 and 200°c. In the magnesium manganese ferrite, at the same temperatures, the shifts were 100, 90 and 45 oersteds respectively.

The measurements with the yttrium iron garnet specimens confirmed (i) above. They were used also to establish the form of the dependence of the resonance field upon the distance of the specimen from the reflecting wall. The results shown in figure 1 refer to a sphere, 0·31 mm in diameter, in which only the uniform precessional mode (Kittel 1948, Dillon 1958) was generally excited. Included also in this figure are data obtained with a magnesium manganese ferrite sphere, 0·62 mm diameter, in the resonant cavity at a wavelength of 3·12 cm. The oscillograms shown in figure 2 refer to a garnet sample and indicate the extent of the shift; the gain, sweep and steady field were kept constant during the measurements. The decrease in the Kittel mode and the increased excitation of a second mode are obvious. The second mode shifts slightly to lower fields as the wall is approached. This mode is also excited strongly when the conducting wall is $\lambda_g/4$ from the specimen.

At room temperature and a wavelength of 3·12 cm, the value of $H_r - H_w$ for yttrium iron garnet was 45 oersteds. Within the experimental error of ± 5 oersteds, no change in this value was observed when the conductivity of the reflecting surface was decreased. (The original silver reflecting plate was replaced by brass which was then coated with graphite.) These data were obtained with the arrangement of figure 3 (*a*), with the steady field parallel with

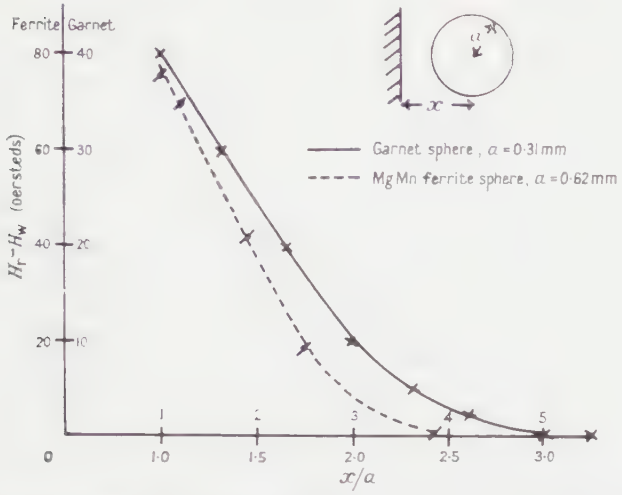

Figure 1. The variation of observed shift with separation of the sphere from the conductor.

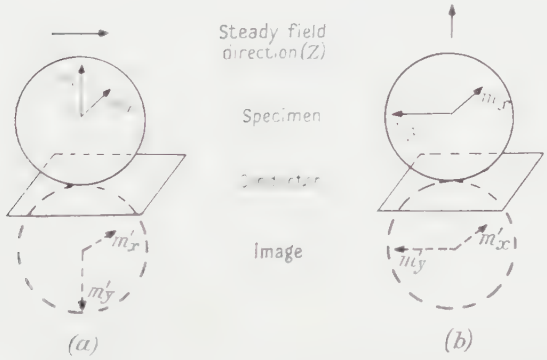

Figure 3. The relative orientations of steady field, radio-frequency moments and conducting wall, and the assumed image. In case (*a*) the steady field is parallel with the wall, and in case (*b*) it is perpendicular to the wall. In each case the x component of the moment is directed into the plane of the paper.

the conducting wall. When the steady field was perpendicular to the wall (figure 3 (*b*)) the shift was about 75 oersteds. These data obtained with single crystal specimens were confirmed by measurements on polycrystalline spheres, although the broader resonance lines decreased the accuracy of the measurements.

§ 3. Discussion

The above experimental results establish two facts. Firstly, the 'wall shift' occurs through the presence of a nearby conducting surface; if the specimen is moved λ_g 2 from the conducting wall so that it is identically placed with respect to the standing wave system, yet well removed from any conductor, the shift is zero. Secondly the shift does not appear to occur solely through the suppression of the uniform precessional mode and the excitation of higher order modes in the sample. When observations were made using a larger diameter (0·8 mm)

slightly non-spherical garnet sphere, other modes were excited even when the specimen was well removed from the wall. Certainly, as the wall was approached, some modes were enhanced and others reduced, but there was also seen a gradual shift of the uniform precessional mode to lower resonance fields.

We are thus led to ask what the effect of the nearby conducting surface can be. Assuming first that the wall is planar and a perfect conductor, the electromagnetic boundary conditions require that the normal component of the magnetic induction and the tangential component of electric field are zero. Both conditions can be satisfied by replacing the conductor by an exact image of the ferrimagnetic sphere, mirrored in the conductor. Alternatively we can suppose that the magnetic field due to the precessing moment of the sphere sets up eddy currents in the conductor which create fields acting back upon the moment equivalent to those from an exact magnetic image. This model requires that the steady component of the magnetization will have a similar steady image, which is not acceptable: the reason is the assumption of perfect conductivity. With an imperfect conductor such as we must have in practice, there will be no image of the steady component of the magnetization, but it would seem to be a reasonable approximation to suppose that an image of the rotating component of the moment will persist.

If we assume that the total moment m of the sample of radius a is located at its centre, then the image contributes to the x component of the magnetic field there an amount $-m_x/(2a)^3$, in both configurations of figure 3. The y-component contribution is $-2m_y/(2a)^3$ in configuration (a), and $-m_y/(2a)^3$ in configuration (b). If we add these fields to the values of H_x and H_y used in Kittel's (1948) derivation, the resonance conditions become

$$\omega^2/\gamma^2 = H_r^2 = \left(H_{wa} + \frac{m}{(2a)^3}\right)\left(H_{wa} + \frac{2m}{(2a)^3}\right)$$

..... (figure 3(a)) ..... (1)

$$\omega^2/\gamma^2 = H_r^2 = \left(H_{wb} + \frac{m}{(2a)^3}\right)^2$$

..... (figure 3 (b)) ..... (2)

where ω is the angular frequency and γ is the magneto-mechanical ratio. Now $m/(2a)^3 = \pi M/6$ where M is the saturation magnetization, and so long as the wall shift is small compared with H_r, equations (1) and (2) yield

$$H_r - H_{wa} \simeq \pi M/4$$

$$H_r - H_{wb} = \pi M/6.$$

Wall shifts calculated from these expressions are compared with experimental data, at room temperature, in the table.

	Wall shift (oersteds)	
	Calculated	Observed
Nickel ferrite	160	135
MgMn ferrite	115	100
Yttrium iron garnet, case (a)	105	45
Yttrium iron garnet, case (b)	70	75

Thus the simple model predicts wall shifts which are correct in sign and order of magnitude, but the observed shifts are usually smaller than those calculated and the relative magnitudes for the two cases (*a*) and (*b*) are predicted wrongly. A more realistic model, which assumes the image to be smaller in magnitude than the object and also takes into account the phase difference between the direct and image fields at the centre of the specimen, does not alter the relative magnitudes of the two cases. On this model, the wall shift should fall off as $1/x^3$ (figure 1) where x is the distance between the conductor and the sphere centre, and should be proportional to the saturation magnetization. The latter dependence is qualitatively followed, but the observed shift does not accurately follow a $1/x^3$ law.

In the above, the radio-frequency permeability of the sample has been assumed to be unity, which is clearly a good approximation to the true condition but may not be exact.

We have not carried these calculations further since most features of the observed shift have been simulated. Further, we doubt whether the experimental arrangement is correctly represented just by an image which is reduced in size, since in a superficially similar problem Mascart and Joubert (1883) had to introduce an infinite distribution of images in the form of two magnetic ribbon helices extending from the position of the geometrical image to infinity.

Recently, Hauser and Brown (1959) have published brief details of a calculation which includes an estimate of the wall shift. Apparently considering our case (*a*) they find the shift is equal to $\frac{1}{3}\pi M(a/x)^3$, using the symbols defined above. This formula is identical in form with ours, differing only in the numerical constant; referring to the table, it will give calculated shifts 4/3 of those shown, in less satisfactory agreement with experiment.

Acknowledgments

The authors wish to express their thanks to Professor K. W. H. Stevens for many valuable discussions and to Professor L. F. Bates for his continued interest and advice. The work described forms part of an investigation carried out for the Admiralty, to whom acknowledgment is made for permission to publish this paper.

References

Dillon, J. F., 1958, *Phys. Rev.*, **112**, 59.
Hauser, W., and Brown, L., 1959, *J. Appl. Phys.*, **30**, 1460.
Kittel, C., 1948, *Phys. Rev.*, **73**, 155.
Mascart, E., and Joubert, J., 1883, *Electricity and Magnetism*, Vol. 1 (London : De la Rue), pp. 556–573.
Snieder, J., 1958, *Appl. Sci. Res.* B, **7**, 185.
Spencer, E. G., and Le Craw, R. L., 1955, *J. Appl. Phys.*, **26**, 250.
Standley, K. J., and Reich, K. H., 1955, *Proc. Phys. Soc.* B, **68**, 713.

Viscosity and Thermal Conductivity of Binary Gas Mixtures: Xenon–Krypton, Xenon–Argon, Xenon–Neon and Xenon–Helium†

By E. THORNTON‡

Battersea College of Technology, London

Communicated by L. R. B. Elton; MS. received 26th October 1959, in final form 16th February 1960

Abstract. The coefficients of viscosity and thermal conductivity of binary mixtures of xenon with krypton, argon, neon and helium have been determined experimentally over the full range of composition of each mixture at a pressure of 70 cm of mercury and at a temperature in the range 18·0 to 18·3°c. Values of the dimensionless quantity $f=\lambda/\eta c_v$ have been obtained for each mixture. The experimental values are compared with theoretical values based on the Lennard-Jones (6–12) potential of interaction between molecules, using force constants derived from viscosity data. Agreement between the experimental and theoretical results is not complete. It is suggested that the discrepancies may be due principally to deficiencies in the empirical rule recommended in the literature for determining the force constant, ϵ_{12}/k, for interactions between unlike molecules.

§ 1. Introduction

The shortage of experimental data for the transport properties of mixtures of monatomic gases led to the setting up of a programme at Battersea College of Technology, London, for the systematic investigation of the variation of viscosity and thermal conductivity of binary mixtures of the gases xenon, krypton, argon, neon and helium over the full range of composition of each mixture. It was decided that measurements would be made at a pressure of 70 cm of mercury and at a temperature in the range 18·0 to 18·3°c.

Binary mixtures of argon, neon and helium were studied by Baker (1955), who compared his experimental results with values calculated from formulae given by Chapman and Cowling (1952) for molecules assumed to be point-centres of repulsion; satisfactory agreement between the theoretical and experimental values was obtained.

Measurements with the binary mixtures of krypton with argon, neon and helium were made by Gordon (unpublished).

This paper deals with binary mixtures of xenon with krypton, argon, neon and helium. It gives details of the apparatus and techniques employed, and presents the experimental results obtained. These measured values are compared with theoretical values based on the Lennard-Jones (6-12) potential of interaction between molecules.

† Part of the work described in this paper forms the essence of the author's M.Sc. Thesis, University of London, 1959.

‡ Now at the Gas Council, London Research Station, Watson House, London, S.W.6.

§ 2. Experimental

Viscosity was determined by means of a modified Rankine viscometer, as described by Heath (1953). For mixtures Heath used only a single mercury pellet in his experiments; in the present work a split pellet was used for all measurements, so that the correction for the effect of surface tension on the time of fall of the pellet given by Rankine and Smith (1921) could be employed. Nitrogen was used as the calibrating gas; the viscosity of nitrogen was taken as $174{\cdot}0\,g\,cm^{-1}\,sec^{-1}$ at 18°c from the measurements of Trautz and Baumann (1929) and Rigden (1938).

Thermal conductivity was determined by means of a Shakespear katharometer. The use of the katharometer for this type of measurement has been described by Ibbs and Hirst (1929). The two platinum coils of the katharometer were mounted in glass tubes. One tube was sealed, and contained dry air; the other was open so that any gas could be introduced into it. The coils formed two arms in a bridge circuit, and the out-of-balance current was measured by means of a sensitive microammeter. The design of the bridge circuit was based on the analysis given by Daynes (1933). The katharometer was calibrated by observing the deflection of the microammeter for gases of known thermal conductivity; the pure rare gases were used for this purpose, and the values of thermal conductivity were obtained by interpolation from the measurements of Kannuluik and Carman (1952).

The gas mixtures were prepared in a burette in which a fixed volume was defined by an index to which the mercury level could be raised; the volumetric proportions of the mixtures were obtained by measuring partial pressures in this fixed volume.

Purity of component gases.

The purities of the component gases were stated by the manufacturer to be as follows:

Helium and neon	spectrally pure
Argon	impurities not exceeding 0·2%
Krypton	99–100%, balance xenon
Xenon	99–100%, balance krypton

Experimental accuracy.

As each mixture in a series was prepared from the preceding one, errors in the mixture proportions due to errors in the pressure measurements were cumulative; the maximum error in the composition of the ninth mixture of a series due to this cause was estimated to be $\pm 0{\cdot}3\%$, and the errors in preceding mixtures were correspondingly smaller.

The error in the viscosity measurements was estimated to be not greater than $\pm 1{\cdot}0\%$.

The accuracy of the thermal conductivity measurements decreased as the thermal conductivity of the gas increased. It was estimated that the maximum error in low values of the thermal conductivity was approximately $\pm 2{\cdot}2\%$, and that for high values the maximum error rose to approximately $\pm 4{\cdot}0\%$. These estimates take no account of any differences between the results of Kannuluik and Carman and those of other workers.

§ 3. Results

The experimental values of viscosity and thermal conductivity of the four gas mixtures, as measured at 70·0 cm of mercury and at a temperature in the range 18·0–18·3 °C, are given as a function of mixture composition in table 1.

Table 1. Viscosity, Thermal Conductivity and Values of $f=\lambda/\eta c_v$: Experimental and Theoretical Values

(1)	(2)	(3)		(4)		(5)	
		(*a*)	(*b*)	(*a*)	(*b*)	(*a*)	(*b*)
Xe–Kr	100	225	225	132†	127	2·58	2·50
	89·6	228	227	138	135	2·57	2·52
	78·6	229	229	145	142	2·59	2·52
	69·3	233	231	152	149	2·58	2·53
	59·5	233	233	160	158	2·61	2·55
	49·1	237	235	168	166	2·59	2·54
	39·7	238	237	178	175	2·63	2·54
	29·6	240	239	187	185	2·62	2·54
	20·1	243	241	197	195	2·61	2·53
	11·5	245	243	207	205	2·61	2·52
	0	247	246	220†	218	2·60	2·50
Xe–A	100	225	225	132†	127	2·58	2·50
	90·5	226	226	145	142	2·64	2·59
	79·2	228	227	163	159	2·69	2·64
	70·1	229	228	180	177	2·74	2·71
	59·8	229	229	202	199	2·80	2·76
	49·8	230	229	226	223	2·82	2·79
	40·5	229	229	251	248	2·83	2·80
	30·0	229	228	280	281	2·76	2·79
	21·3	228	227	311	313	2·72	2·75
	10·9	224	225	358	357	2·68	2·66
	0	221	221	416†	412	2·52	2·50
Xe–Ne	100	224	225	132†	127	2·59	2·50
	90·3	232	231	166	162	2·88	2·84
	79·4	240	240	213	208	3·20	3·15
	67·3			277	269		
	59·4	258	257	327	316	3·61	3·56
	50·4	268	265	398	378	3·72	3·65
	39·3	278	276	500	473	3·76	3·67
	28·5	291	288	624	590	3·63	3·56
	19·9	299	297	752	710	3·46	3·39
	10·3	306	305	925	883	3·10	3·07
	0	310	309	1160†	1141	2·44	2·50
Xe–He	100	224	225	132†	127	2·59	2·50
	89·8	229	229	232	227	4·02	3·94
	79·2	232	233	356	349	5·40	5·27
	68·7	237	238	518	494	6·70	6·37
	59·4	242	243	680	651	7·51	7·16
	49·4	245	248	905	857	8·28	7·76
	40·1	249	253	1110	1098	8·22	8·02
	30·4	252	257	1440	1423	8·19	7·94
	20·1	252	258	1800	1894	7·09	7·29
	13·9	248	253	2180	2273	6·42	6·54
	6·3	232	235	2708	2894	4·83	4·97
	0	194	194	3560†	3614	2·46	2·50

† Calibration points for katharometer.

(1) Gas mixture; (2) %Xe; (3) Viscosity (10^{-6} g cm^{-1} sec^{-1}); (4) thermal conductivity (10^{-7} cal cm^{-1} sec^{-1} deg^{-1}); (5) $f=\lambda/\eta\, c_v$; (*a*) experimental; (*b*) theoretical.

From these observations, calculations were made of the values of the dimensionless quantity f defined by the equation

$$\lambda = f\eta c_v$$

where λ = thermal conductivity, η = viscosity, c_v = specific heat at constant volume.

Values of c_v for argon and helium were obtained from Partington and Shilling (1924); values for neon, krypton and xenon were calculated from the equation

$$c_v = \frac{R}{M(\gamma - 1)}$$

where $R = 1{\cdot}986$ cal deg^{-1} mol^{-1}, M = molecular weight, $\gamma = c_p/c_v$.

The values of γ used for these gases were taken from Kaye and Laby (1956). The specific heat of each mixture was assumed to be equal to the sum of the products of the specific heat and mass fraction of each component of the mixture. The experimental values of f for each mixture are given in table 1.

§ 4. Theoretical Values

The theoretical values of the first approximations to the viscosity and thermal conductivity for these pure gases and gas mixtures were calculated from the formulae for dilute gases given by Hirschfelder, Curtiss and Bird (1954). The calculations are based on the Lennard-Jones (6–12) potential of interaction between molecules, that is the potential ϕ for a distance of separation r is given by

$$\phi = 4\epsilon\left[\left(\frac{\sigma}{r}\right)^{12} - \left(\frac{\sigma}{r}\right)^{6}\right]$$

where ϵ and σ are the force constants. Values of the force constants used for the pure gases, shown in table 2, are given by Hirschfelder, Curtiss and Bird (1954) as derived from viscosity data. All calculations were made for a temperature of 18·0°c.

Table 2. Force Constants for Pure Gases

	Xe	Kr	A	Ne	He
σ(Å)	4·055	3·61	3·418	2·789	2·576
ϵ/k (°K)	229	190	124	35·7	10·22

For mixtures, the force constants for the interactions between unlike molecules were obtained from the empirical 'combining laws'

$$\sigma_{12} = \tfrac{1}{2}(\sigma_1 + \sigma_2), \quad \epsilon_{12} = (\epsilon_1\epsilon_2)^{1/2}.$$

The formulae for binary mixtures express composition in terms of mole fractions; it has been assumed that the gases are ideal, so that mole fractions could be taken as equal to volume fractions, thus enabling a direct comparison between calculated and experimental values to be made.

The calculated values of viscosity and thermal conductivity of the four mixtures are given in table 1.

Theoretical values of the first approximation to the dimensionless quantity f for each mixture were obtained from the calculated viscosities and thermal conductivities; the specific heats of the pure gases were taken as equal to $3R/2$, i.e. 2·98 cal deg^{-1} mol^{-1}. The calculated values of f are given in table 1.

§ 5. Discussion

To facilitate comparison of the results, the experimental points and theoretical curves for viscosity and thermal conductivity are shown plotted in the figure.

5.1. *Viscosity*

The validity of this method of measuring viscosity is indicated by the agreement to within one per cent of the values for viscosity of the pure gases obtained by this method and the values obtained, by interpolation to 18°c, from the results quoted for the same gases by other workers (Rankine 1910, Nasini and Rossi 1928, Trautz and Binkele 1930, Trautz and Heberling 1934, Johnston and Grilly 1942, Landolt–Börnstein 1955).

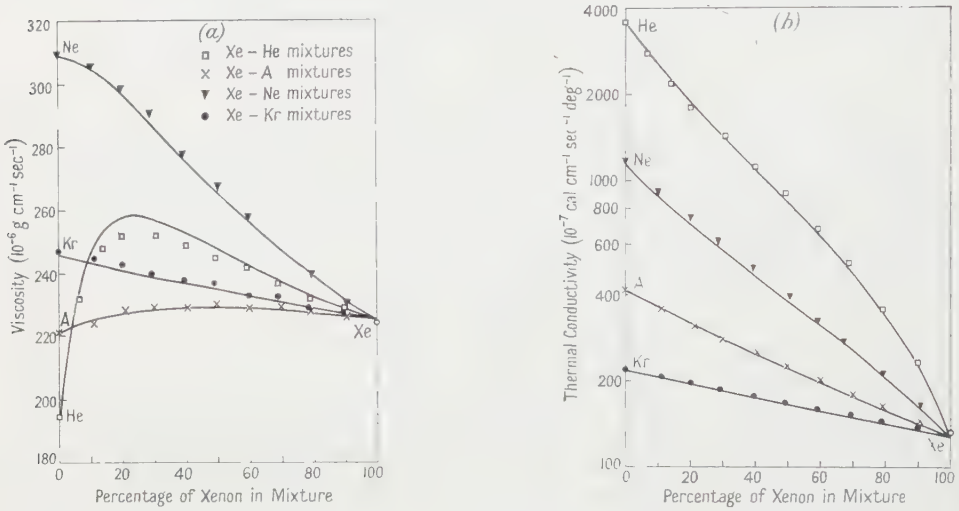

Viscosity and thermal conductivity of gas mixtures. Experimental results are shown by points; the curves show calculated values.

The only published results found with which the present experimental values for mixtures could be compared were those for binary mixtures of xenon and helium, reported by Trautz and Heberling (1934). These workers carried out their measurements at 20, 127, 227 and 277°c; their results at 20°c are approximately one per cent higher than the values for this mixture found during the present work, and the maximum value of the mixture viscosity occurs at approximately the same mixture composition. This represents quite satisfactory agreement.

For the binary mixtures xenon–krypton, xenon–argon and xenon–neon, the differences between the experimental and theoretical values lie within the estimated limits of the experimental error, so that agreement between theory and experiment is satisfactory. For xenon–helium mixtures, however, the calculated values lie well beyond the range of the experimental error, and clearly some modification of the theoretical formula is required.

The theoretical value of viscosity of a pure gas is quite sensitive to a change in the value of the force constant ϵ/k, so that it is not possible to seek a better theoretical result by changing the force constants for the pure gases. This

suggests that the differences between theoretical and experimental values for mixtures may result from the use of the empirical rules for determining the force constants for interactions between unlike molecules.

It was found empirically that closer agreement between the experimental and theoretical values for the xenon–helium mixtures could be obtained by using a value for the force constant ϵ_{12}/k of 65, which is approximately 35% greater than the value given by the empirical rule. These results are given in table 3.

Table 3. Viscosity of Xenon–Helium Mixtures: $\epsilon_{12}/k = 65°K$

	Viscosity (10^{-6} g cm^{-1} sec^{-1})	
% Xe	Experimental	Theoretical ($\epsilon_{12}/k = 65$)
100	224	225
89·8	229	228
79·2	232	232
68·7	237	236
59·4	242	240
49·4	245	245
40·1	249	249
30·4	252	252
20·1	252	252
13·9	248	248
6·3	232	231
0	194	194

As the calculated viscosity for a mixture is quite sensitive to changes in ϵ_{12}/k, however, it is not possible to secure better general agreement by an arbitrary increase in the values of ϵ_{12}/k for all the mixtures.

This discussion suggests that the discrepancy between the experimental and theoretical values of the viscosities of xenon–helium mixtures is due to the inadequacy of the empirical rule for determining ϵ_{12}. The rule is least satisfactory when the difference in mass of the molecules is greatest; some allowance appears necessary for this, and further theoretical work on the interaction between unlike molecules is clearly required.

Two other possible explanations of the discrepancy must also be considered. The first is that the differences may be due to quantum effects, which would be more important for helium than for the other gases. The second is that the Lennard-Jones (6–12) model does not give a sufficiently close approximation to the actual interaction potential between molecules; this view receives support from work on thermal diffusion by Grew, Johnson and Neal (1954) and by Amdur and Schatzki (1957), where it was shown that calculated values for the thermal diffusion factor based on the Lennard-Jones (6–12) model could not be fitted to the experimental results.

Mason and Rice (1954a) have shown that the experimental values for the viscosity of helium are more closely reproduced by the exp-six potential than by the Lennard-Jones (6–12) potential; it has also been shown (Mason and Rice 1954b) that for the transport properties of xenon, krypton, argon and neon the exp-six potential and the Lennard-Jones (6–12) potential are about equally successful in reproducing the experimental results.

Mason (1955) has examined the agreement between some experimental results for the viscosities of binary mixtures and values calculated for the exp-six potential, using semi-empirical combination rules for interactions between unlike molecules; agreement for mixtures containing krypton and xenon was poor, and it was suggested that this was due rather to the failure of the exp-six model for krypton and xenon than to the inadequacy of the combination rules for these two gases. The same data were used by Srivastava (1958), but with modified combination rules; agreement between calculated and observed values of viscosity was reported as satisfactory except for mixtures containing xenon.

Thus the exp-six potential, which is considered to be physically more realistic, appears to have a weakness similar to that shown here by the Lennard-Jones (6–12) model; whether this is due to the inadequacy of these potentials or to an incomplete understanding of interactions between unlike molecules remains unresolved.

5.2. *Thermal Conductivity*

Saxena (1957) has reported values of thermal conductivity at 38°C for the binary mixtures xenon–argon and xenon–helium. When Saxena's results for the pure gases are compared with those obtained by interpolating the results of Kannuluik and Carman (1952) to 38°C it is found that for argon and helium there is close agreement, but for xenon Saxena's value is 4% lower.

When allowance is made for the change in thermal conductivity with temperature and for the difference in the experimental values for pure xenon, there is satisfactory agreement between Saxena's results for mixtures and those reported here.

For krypton, argon, neon and helium agreement between theory and experiment is satisfactory, especially in view of the relatively wide range of absolute values quoted by various workers, but the theoretical value for xenon is 4% lower than the experimental value. Better agreement for all mixtures with a high percentage of xenon would result from a lower experimental value for pure xenon; such a value is given by Saxena (1957).

Close agreement between calculated and experimental results for the binary mixtures xenon–argon, xenon–helium and argon–helium have been reported by Saxena (1957), using the Lennard-Jones (6–12) model. The present work shows satisfactory agreement for the mixtures xenon–krypton and xenon–argon, but for the mixtures xenon–neon and xenon–helium some of the calculated values lie outside the range of the estimated experimental error.

However, Mason and Saxena (1959) have shown that more accurate theoretical values for the conductivity of mixtures, and specifically for equimolar mixtures of xenon–argon and xenon–helium at 38°C, may be obtained from the slight modification of a formula due to Muckenfuss and Curtiss (1958). The present results need to be compared with values calculated from this more recent formula.

5.3. *The Dimensionless Quantity* $f=\lambda/\eta c_v$

For monatomic gases with smooth spherically symmetrical molecules the theoretical value of the first approximation to f is 2·5. It has been shown that the values of f for the inert gases lie between 2·4 and 2·6 (see Chapman and Cowling 1952, Kannuluik and Carman 1952), and the present work confirms this. For mixtures, however, the values of f tend to display a maximum value, approximately

in the middle of the range of composition, and the value of this maximum increases as the difference in molecular weights of the component gases becomes greater. Agreement between the experimental and calculated values is satisfactory.

Corresponding to the high maximum value of f for mixtures of a light and a heavy gas, the Prandtl number will show a minimum for approximately the same composition.

§ 6. Conclusions

Comparison of the calculated and experimental values shows that agreement between theory and experiment is not complete. This lack of agreement is most marked for mixtures of a heavy gas with a light gas. The discrepancies appear to be due principally to unsuitable values for some of the force constants, ϵ_{12}/k, representing interactions between unlike molecules. This suggests that further work is required so that the force constants for interactions between unlike molecules may be calculated from relationships more generally applicable than the empirical rules recommended in the literature; interaction potentials more general than the Lennard-Jones (6–12) model may need to be considered.

Acknowledgments

The writer would like to record his indebtedness to the late Dr. H. R. Heath, who instituted the research programme of which this work forms a part, for his generous help and guidance.

Thanks are due Dr. L. R. B. Elton for helpful discussions and valuable suggestions in preparing the manuscript.

Grateful acknowledgment is made to the North Thames Gas Board for facilities afforded in carrying out the work, and to the University of London for permission to publish the results.

References

Amdur, I., and Schatzki, T. F., 1957, *J. Chem. Phys.*, **27,** 1049.
Baker, W. A. D., 1955, *M.Sc.Thesis*, University of London.
Chapman, S., and Cowling, T. G., 1952, *The Mathematical Theory of Non-Uniform Gases* (Cambridge: University Press).
Daynes, H. A., 1933, *Gas Analysis by Measurement of Thermal Conductivity* (Cambridge: University Press).
Grew, K. E., Johnson, F. A., and Neal, W. E. J., 1954, *Proc. Roy. Soc.* A, **224,** 513.
Heath, H. R., 1953, *Proc. Phys. Soc.* B, **66,** 362.
Hirschfelder, J. O., Curtiss, C. F., and Bird, R. B., 1954, *Molecular Theory of Gases and Liquids* (London: Chapman and Hall).
Ibbs, T. L., and Hirst, A. A., 1929, *Proc. Roy. Soc.* A, **123,** 134.
Johnston, H. L., and Grilly, E. R., 1942, *J. Phys. Chem.*, **46,** 948.
Kannuluik, W. G., and Carman, E. H., 1952, *Proc. Phys. Soc.* B, **65,** 701.
Kaye, G. W. C., and Laby, T. H., 1956, *Tables of Physical and Chemical Constants* (London: Longmans).
Landolt–Börnstein, 1955, *Physikalish Chemische Tabellen*, Vol. 4, Part 1 (Berlin: Springer).
Mason, E. A., 1955, *J. Chem. Phys.*, **23,** 49.
Mason, E. A., and Rice, W. E., 1954 a, *J. Chem. Phys.*, **22,** 522.
——1954 b, *Ibid.*, **22,** 843.
Mason, E. A., and Saxena, S. C., 1959, *J. Chem. Phys.*, **31,** 511.
Muckenfuss, C., and Curtiss, C. F., 1958, *J. Chem. Phys.*, **29,** 1273.

Nasini, A. G., and Rossi, C., 1928, *Gazz. Chim. Ital.*, **58,** 433.
Partington, J. R., and Shilling, W. G., 1924, *The Specific Heats of Gases* (London: Ernest Benn).
Rankine, A. O., 1910, *Proc. Roy. Soc.* A, **83,** 265.
Rankine, A. O., and Smith, C. J., 1921, *Phil. Mag.*, **42,** 603.
Rigden, P. J., 1938, *Phil. Mag.*, **25,** 961.
Saxena, S. C., 1957, *Indian J. Phys.*, **31,** 597.
Srivastava, K. P., 1958, *J. Chem. Phys.*, **28,** 543.
Trautz, M., and Baumann, P. B., 1929, *Ann. Phys., Lpz.*, **2,** 733.
Trautz, M., and Binkele, H. E., 1930, *Ann. Phys., Lpz.*, **5,** 561.
Trautz, M., and Heberling, R., 1934, *Ann. Phys., Lpz.*, **20,** 118.

The Thermal Conductivity and Thermoelectric Power of Bismuth Telluride at Low Temperatures

By P. A. WALKER

Communication from the Staff of the Research Laboratories of The General Electric Company Limited, Wembley, England

MS. received 17*th September* 1959, *in revised form* 12*th January* 1960

Abstract. Measurements have been made of the thermal conductivity and thermoelectric power of a range of single crystal samples of p- and n-type Bi_2Te_3 between 6 and 200 K. The observed lattice conductivity could be interpreted in terms of scattering by the tellurium isotopes. Measurements on the iodine doped samples showed the existence of appreciable impurity scattering. Interpretation of the thermoelectric power results suggests a multiband structure for Bi_2Te_3.

§ 1. Introduction

In recent years the transport properties of bismuth telluride have been measured by a number of workers. Most of this work has been confined to the temperature range above 77 °K and it is only recently that these measurements have been extended down to liquid helium temperatures. The interest in this temperature range is two-fold. Firstly it enables a critical appraisal to be made of conventional theory as applied to this material and secondly it enables a study to be made of the interaction of imperfections in the material with the charge carriers and with the lattice vibrations.

Previous measurements of the Hall coefficient and electrical conductivity down to liquid helium temperatures reported by Yates (1959) have revealed discrepancies with simple semiconductor theory. This paper describes measurements that have been made of the thermal conductivity and thermoelectric power of a range of p- and n-type material between 6 and 200 K. Interpretation of the observed thermal conductivities gives information on the phonon mean free path and on the scattering of the phonons by the iodine atoms. Comparison of the thermoelectric power with conventional theory leads to certain conclusions regarding the effective mass of the charge carriers and suggests a possible band structure.

§ 2. Experimental

The cryostat used for the measurements was originally designed for optical absorption studies on semiconductors between 4 and 300 K. Based on the design of Roberts (1955) it consisted of a nitrogen chamber, a helium chamber and a working chamber, and their associated radiation shields. The whole assembly was surrounded by a common vacuum space which during the measurements was maintained at a pressure less than 5×10^{-5} mm Hg.

The working chamber was cooled initially by a circulating stream of helium gas and finally by the condensation of helium into it. A heater wound round the chamber enabled its temperature to be raised above that of the surrounding

radiation shield and maintained automatically at any temperature between 4 and 300°K. A platinum resistance thermometer attached to the chamber monitored the temperature and actuated the control of the heater current.

The specimen chamber which was contained within the working chamber is shown in detail in figure 1. For the thermal measurements the windows on the ends of the chamber were replaced by copper discs E and were held in place by

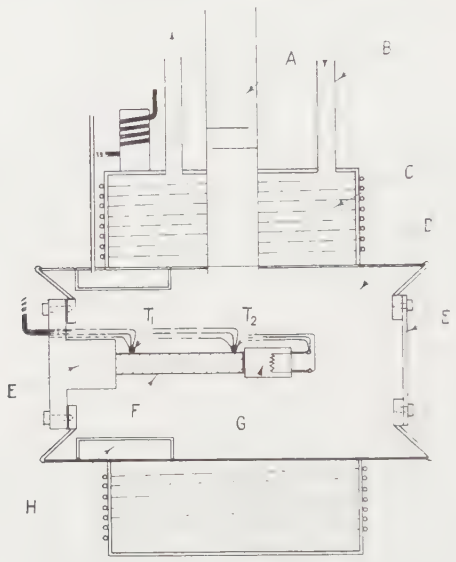

Figure 1. The specimen chamber. A: pumping tube; B: filling tube; C: working chamber; D: specimen chamber; E: copper disc; F: specimen; G: specimen heater; H: gas thermometer bulb.

six screws, a layer of grease being put on the mating surfaces to ensure thermal contact. The specimen F was soldered to one of the discs, which acted as a sink for the thermal conductivity measurements, and to the heater G. All electrical leads were thermally anchored to the nitrogen, helium and working chambers before passing to the specimen. The length of the wire between the final anchoring point and the specimen was made as long as possible (24 cm) so as to reduce the heat flow along them.

Temperature measurements in the range 4 to 30°K were made by means of a thermocouple composed of copper against copper plus 0·006% tin (cf. Dauphinee, MacDonald and Pearson 1953). Between 30 and 300 K copper-eureka thermocouples were used. The two types of thermocouples were combined into a common three-lead junction, the copper lead being common to both couples. Before use the thermocouples were calibrated against a low temperature gas thermometer of the type described by Mendelssohn (1931). The thermocouples were attached to the side of the specimens via two short lengths of 20 s.w.g. copper wire and were approximately 2 cm apart.

The measurements were all made on specimens cut from along the length of single crystal ingots of bismuth telluride prepared by A. R. Sheard. As shown in table 1, the specimens differed by the amount of iodine added to the stoichiometric composition. Subsequent chemical analysis, by H. J. Cluley and P. M. C. Proffitt of the Chemistry Department, showed that the final iodine content was

less than the amount added; the difference is seen by comparing columns (2) and (3) and arises from volatilization of iodine during the preparation of the single crystal ingots. Before the specimens were mounted in the cryostat, their cross sectional area was determined using a travelling microscope. The effective

Table 1. Samples Measured

(1)	(2)	(3)	(4)	(5)†
SBTC 18	Undoped	—	p	30·4
SBTC 19	0·055% I	0·027%	p	25·3
SBTC 27	0·06% I	0·037%	n	30·0
SBTC 16	0·07% I	0·046%	n	24·0
SBTC 15	0·09% I	0·059%	n	52·8
SBTC 10	0·20% I	0·124%	n	34·0

(1) Specimen; (2) added iodine‡; (3) final iodine concentration‡; (4) type; (5) form factor (cm^{-1}). The symbols used to indicate the various specimens are given in figure 6.

† Form factor $= \dfrac{\text{length}}{\text{cross sectional area}}$

‡ by weight.

separation between the thermocouples was determined from the resistivity of the material by measuring the electrical resistance between them. All contacts to the specimen were nickel plated and then tinned with low melting point solder.

The thermal conductivity and thermoelectric power of the specimens were measured simultaneously, the temperature gradient being established along the cleavage planes. Corrections were applied to the measured conductivity to take into account the heat loss resulting from conduction along the specimen leads and radiation between the specimen and the surrounding walls. The magnitude of this correction was determined experimentally and although at low temperatures it amounted to only a small percentage of the total, at higher temperatures, where the radiation losses predominated, it became of the same order of magnitude as the heat conducted through the specimen. This made it necessary to limit the thermal conductivity measurements to the range $T < 150°\text{K}$. Over this temperature range the observed values were thought to be subject to a maximum random error of $\pm 5\%$.

The thermoelectric voltage appearing across the specimen as a result of the applied temperature gradient was measured with respect to the copper thermocouple leads. Comparison of these leads with a sample of lead (cf. Jan, Pearson and Templeton 1958) enabled absolute values of the thermoelectric power of Bi_2Te_3 to be derived from the measured voltage. The measured values were thought to be subject to a random error of less than $\pm 2\%$.

§ 3. Thermal Conductivity

3.1. *Lattice Component*

The thermal conductivity of a solid is composed of a component K_L due to the conduction of heat by the atomic lattice and a component K_E due to the conduction of heat by the free charge carriers (electrons or holes in the case of semiconductors) present in the solid. Thus

$$K = K_L + K_E. \qquad \ldots\ldots (1)$$

The electronic component K_E may be calculated from the electrical conductivity σ using the equation

$$K_E = \sigma(k/e)^2 TL \qquad \ldots\ldots (2)$$

where $L(k/e)^2$ is the Lorenz number and has the value $2{\cdot}5 \times 10^{-8}$ ($v^2\,deg^{-2}$) for a completely degenerate conductor. For a semiconductor the value of L is dependent upon the position of the Fermi level with respect to the band edge and on the scattering law of the charge carriers (cf. Bowley, Delves and Goldsmid 1958).

The lattice component of the thermal conductivity in Bi_2Te_3 was derived from the smoothed experimental values by subtracting the electronic component which at $80°K \simeq 0{\cdot}15K_L$. Values of K_E were calculated from (2) using the measured electrical conductivity of the samples and values of L derived from the equations given by Bowley, Delves and Goldsmid (1958). In evaluating L, it was assumed that acoustic lattice vibrations were the predominant scattering mechanism, and the position of the Fermi level was derived from the measured thermoelectric power. At low temperatures where this procedure could be in error due to increasing amounts of impurity scattering, L approximates to the degenerate value, and the relative importance of K_E decreases, i.e. $K_E \simeq 0{\cdot}02K_L$.

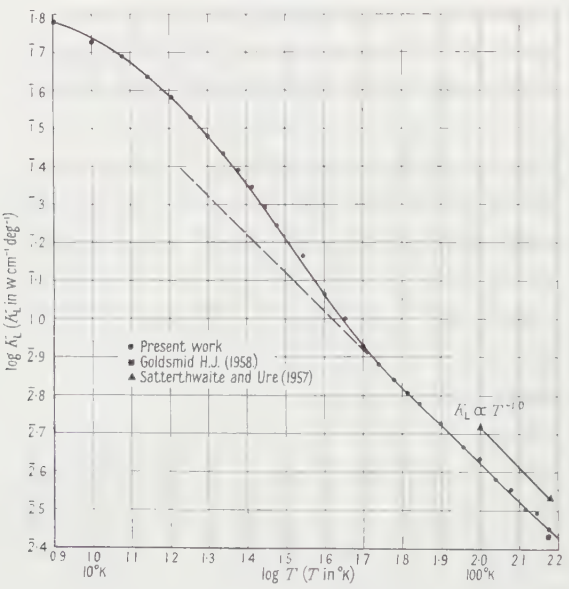

Figure 2. Lattice conductivity of stoichiometric Bi_2Te_3.

Values of the lattice component of the thermal conductivity of stoichiometric Bi_2Te_3 obtained in this way are plotted against temperature in figure 2. Also shown are the values of Goldsmid (1958 b) and of Satterthwaite and Ure (1957) for tellurium doped Bi_2Te_3. Over the temperature range $50 < T°K < 150$, the temperature variation of the lattice component was found to be

$$K_L = 4{\cdot}3T^{-1{\cdot}0}\ w\,cm^{-1}\,deg^{-1} \qquad \ldots\ldots (3)$$

which may be compared with

$$K_L = 5{\cdot}1T^{-1{\cdot}0}\ w\,cm^{-1}\,deg^{-1}$$

obtained by Satterthwaite and Ure (1957)†. For $25 < T^{\circ}\text{K} < 50$ the experimental points rise above the straight line given by equation (3) and have a temperature dependance of $T^{-1\cdot48}$.

The phonon mean free path l may be derived from the lattice conductivity by means of the equation

$$K_L = \tfrac{1}{3} C_V l v \qquad \ldots\ldots (4)$$

where C_V is the specific heat and v is the phonon velocity. R. W. Hill and C. A. Bailey of the Clarendon Laboratory, Oxford, have measured the specific heat of Bi_2Te_3 between 1 and 20 K. They find (private communication) that the Debye temperature $\theta_0 \simeq 145$ K. In actual fact the Debye T^3 law is only followed below 2°K and at higher temperatures, where the specific heat follows a T^2 law, it is necessary to assume that θ_0 decreases to a minimum of 116 K at 9 K and then increases to 142°K at 20°K. Assuming that the phonon velocity in Bi_2Te_3 is similar to that in bismuth and has the value $v = 2 \times 10^5$ cm sec^{-1}, the variation of phonon mean free path with temperature is shown in figure 3.

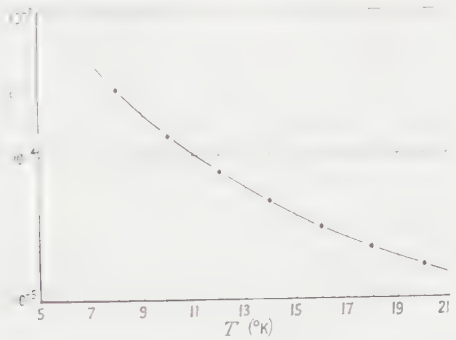

Figure 3. Phonon mean free path. l is in centimetres.

The experimental values for the mean free path may be compared with those predicted by theory. It has been shown by Leibfried and Schlömann (1954) that in the presence of three-phonon interactions in which the wave vector is not conserved (Umklapp processes) the phonon mean free path is given by

$$l_U = 0{\cdot}06 \frac{k}{\hbar^2} \frac{\theta_0 \bar{m}^2}{\gamma^2 \rho} f\left(\frac{T}{\theta_0}\right) \qquad \ldots\ldots (5)$$

where

$$f\left(\frac{T}{\theta_0}\right) \simeq \frac{\theta_0}{T} \text{ for } T > \theta_0 \qquad \ldots\ldots (6)$$

and is of the form

$$\left(\frac{T}{\theta_0}\right)^3 \exp\left(\frac{\theta_0}{bT}\right) \text{ for } T < \theta_0 \qquad \ldots\ldots (7)$$

$\bar{m}$ is the mean atomic mass, ρ is the density, γ Gruneisen's constant $\simeq 2$ and b a constant $\simeq 2$. Considerable uncertainty exists about the precise nature of the low temperature form of this equation, and equation (7) is not a very reliable means of assessing the mean free path in this region. With decreasing temperature we know that in the presence of 'Umklapp' scattering the mean free path rises sharply above the values given by equations (5) and (6). At 40 K ($\theta_0/3{\cdot}6$), these equations predict a value for l_U which is about four times as large as that obtained

† Actual equation given by Satterthwaite and Ure is in error by a factor of 10^2.

by extrapolating the curve of figure 3. This means that the 'Umklapp' mean free path must be considerably greater than the experimental values and consequently that this scattering process may be neglected at the lower temperatures.

The only other scattering process which can give a T^{-1} variation of thermal conductivity is that due to point imperfections. Since there is no reason for believing that the specimens contain any appreciable impurity it must be assumed that the scattering is caused by the tellurium isotopes. Various estimates of the isotope scattering effect have been given. Ziman (1956) using a variational method has derived the following equation for the mean free path l_i in the presence of a small proportion x_i of a single isotope of mass m_i:

$$l_i = 3{\cdot}493 \times 10^{-5} \frac{a}{x_i} \frac{\bar{m}^2}{(m_i - \bar{m})^2} \left(\frac{\theta_0}{T} \right)^4 \qquad \ldots\ldots (8)$$

where a is the average atomic spacing. Although this equation only gives a minimum mean free path, it may be used for small isotope concentrations. Since Bi_2Te_3 contains a comparatively large concentration of isotopes (e.g. 0·089% ^{120}Te, 2·46% ^{122}Te, 0·87% ^{123}Te, 4·61% ^{124}Te, 6·99% ^{125}Te, 18·71% ^{126}Te, 31·79% ^{128}Te and 34·47% ^{130}Te) it is necessary to use the recent equation of Berman *et al.* (1959) for the mean free path in the presence of large isotope concentrations. This equation has the form

$$l = 0{\cdot}042 (l_i^0 l_0)^{1/2} \left(\frac{\theta_0}{T} \right)^{9/2} \qquad \ldots\ldots (9)$$

where

$$l_0 = \frac{k}{\hbar^2} \frac{\theta_0 \bar{M}}{N\gamma^2} \qquad \ldots\ldots (10)$$

$$l_i^0 = 3{\cdot}493 \times 10^{-5} \frac{a\bar{M}^2}{\Sigma x_i (M_i - \bar{M})^2} \qquad \ldots\ldots (11)$$

and $\bar{M}$ is the average mass per atom (= 160·2 for Bi_2Te_3), N the number of atoms per cm^3, Gruneisen's constant $\gamma \simeq 2$, a^3 the volume per atom and x_i the concentration of isotope of mass M_i.

Although this equation has been found to be in good agreement with the experimental results on LiF and many other materials, the calculated mean free path for Bi_2Te_3 is approximately 20 times larger than the observed values. As may be seen from equation (9) l is extremely dependent upon the value taken for θ_0. Using the experimental values for the mean free path, it is found that agreement may be obtained between theory and experiment if the θ_0' values given in table 2 are used. At first sight the temperature variation of θ_0' is disturbing.

Table 2

T(°K)	θ_0' (°K)	θ_0 (°K)	θ_0'/θ_0
10	71·6	117	0·613
15	79·3	127·5	0·622
20	88·5	142	0·622
25	95·3		
30	98·2		

Debye temperature: θ_0', derived from thermal conductivity results and θ_0, derived from specific heat results.

However, if these values are compared with θ_0 derived from the specific heat results one finds that the ratio θ_0'/θ_0 is independent of temperature. The constancy of this ratio is interesting since θ_0 and θ_0' represent different average properties of the vibrational spectrum and might be expected to be different in the case of a highly anisotropic material like Bi_2Te_3.

Assuming a T^3 variation of the specific heat, the theory of Berman *et al.* (1959) predicts a conductivity

$$K \propto (l_0 l_1^0)^{1/2} T^{-3/2}. \qquad \ldots\ldots (12)$$

Although this compares favourably with the observed temperature variation of $T^{-1.45}$ between 25 and 50 K, it must be pointed out that the experimentally observed T^2 dependence of the specific heat would lead to a $T^{-5/2}$ relation for the thermal conductivity.

At lower temperatures the thermal conductivity tends to flatten out suggesting the existence of a maximum at about 6°K. This is confirmed by the thermal conductivity measurements of MacDonald *et al.* (1959) between 2 and 20°K. In view of the large size of the samples compared with the phonon mean free path boundary scattering may be neglected. It seems likely therefore that the maximum in the conductivity must be caused by the presence of dislocations in the material. This conclusion is supported by considerable evidence from other sources (cf. Wright 1959) which suggests that Bi_2Te_3 contains a large concentration of dislocations.

3.2. *Impurity Scattering*

The thermal conductivity measurements on iodine-doped Bi_2Te_3 have shown the existence of considerable phonon scattering at the iodine atoms. As may be seen from figure 4, the lattice resistivity increases with the amount of iodine added, the relative change increasing with decreasing temperature.

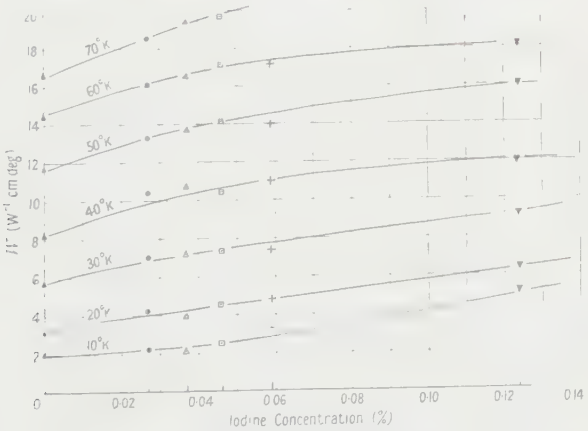

Figure 4. Variation of thermal resistivity with iodine doping. For symbols see figure 6.

Using the equations of Berman *et al.* (1959) it is possible to calculate the expected variation of thermal resistivity with iodine content. In making these calculations it is assumed that the change in the elastic properties of the lattice resulting from the inclusion of the iodine atoms may be neglected and that the phonon scattering is a consequence of the mass difference between the iodine

atoms and the mean atomic mass of the lattice. In this respect it is necessary to consider the case of interstitial and substitutional atoms separately. For interstitial atoms the mass difference must be considered to be the mass of the iodine atom (126·9 a.m.u.) while for substitutional atoms it is the deviation from the mean atomic mass, i.e. (160·2 − 126·9) = 33·3 a.m.u.

Using equation (11) and the iodine contents given in table 1, the mean free path parameter l_I^0 due to the iodine atoms may be calculated. This must be combined with l_i^0 for isotope scattering to give the total mean free path l_c

$$l_c = l_0\left[\frac{l^0_{I+i}}{l_i^0}\right]^{1/2} \qquad \ldots\ldots(13)$$

where

$$\frac{1}{l^0_{I+i}} = \frac{1}{l_I^0} + \frac{1}{l_i^0}$$

assuming l_0 and θ_0 do not vary with iodine concentration. Evaluation of equation (13) using the modified θ_0' and assuming $T = 20$ K leads to mean free path values which, when substituted in equation (4), give the thermal resistivities shown in figure 5. Comparison with the experimental points shows that the iodine atoms

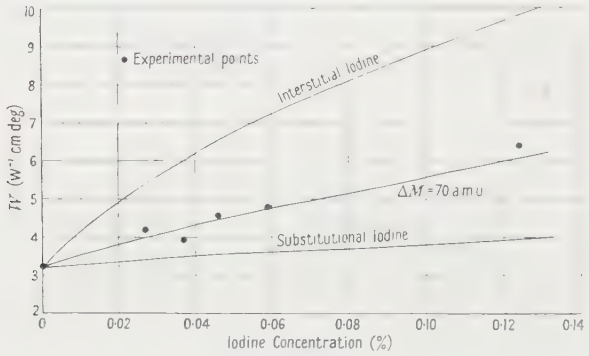

Figure 5. Thermal resistivity at 20°K.

are somewhere between interstitial and substitutional atoms and have an effective mass difference of about 70 a.m.u. This mass difference would be obtained if $\frac{1}{4}$ of the iodine atoms went into the lattice interstitially while the remaining $\frac{3}{4}$ went in substitutionally.

§ 4. Thermoelectric Power

4.1. *Theoretical*

Assuming a scattering law such that the relaxation time τ may be related to energy by the equation

$$\tau = E^\lambda \qquad \ldots\ldots(14)$$

the general expression for the thermoelectric power of a single-band semiconductor is

$$\alpha = \frac{k}{e}\left(\frac{1}{kT}\frac{K_2}{K_1} - \eta\right) \qquad \ldots\ldots(15)$$

where

$$K_n = \text{const.}\left((n+\tfrac{1}{2}+\lambda)kT^{n+1/2+\lambda}\int_0^\infty \frac{E^{n-\frac{1}{2}+\lambda}}{1+\exp(E-\eta)}\,dE\right) \qquad \ldots\ldots(16)$$

and η is the reduced Fermi level with respect to the band edge.

For a degenerate material in which $\eta > 3$, equation (15) may be approximated (to within 10%) by

$$\alpha = \frac{k}{e}\left[\frac{1}{\eta}\frac{\pi^2}{3}(1{\cdot}5+\lambda)\right]. \qquad \ldots\ldots(17)$$

Using the degenerate expression for the Fermi level in terms of the effective mass m and the carrier density $\mathfrak{n}$, this equation becomes

$$\begin{aligned}\alpha &= \frac{k}{e}\left[\frac{\pi^2}{3}(1{\cdot}5+\lambda)\frac{2mk}{h^2}\left(\frac{4\pi}{1{\cdot}5\mathfrak{n}}\right)^{2/3}T\right] \\ &= \frac{k}{e}\left[\frac{\pi^2}{3}(1{\cdot}5+\lambda)\frac{2mk}{h^2}\left(\frac{4\pi}{1{\cdot}5}\frac{R_{\mathrm{H}}e}{r}\right)^{2/3}T\right] \qquad \ldots\ldots(18)\end{aligned}$$

where the factor r appearing in the expression for the Hall coefficient R_{H} is dependent on the position of the Fermi level, the scattering law and on the anisotropy of the band structure.

For non-degenerate material in which $\eta < -0{\cdot}5$ equation (15) may be approximated by (to within 10%)

$$\begin{aligned}\alpha &= \frac{k}{e}\left[\frac{5}{2}+\lambda-\eta\right] \\ &= \frac{k}{e}\left[\frac{5}{2}+\lambda+\ln\frac{2(2\pi k)^{3/2}}{h^3}+\ln\frac{R_{\mathrm{H}}e}{r}+\frac{3}{2}\ln mT\right]. \qquad \ldots\ldots(19)\end{aligned}$$

4.2. *Experimental*

As shown in figure 6, the thermoelectric power of the two p-type and four n-type specimens of bismuth telluride increases monotonically with temperature between 6 and 200 K. Above 200 K the thermoelectric power of the near intrinsic specimen SBTC 27 starts to decrease due to the influence of the minority carriers. From an examination of these curves it is concluded that there is no appreciable contribution to the thermoelectric power due to the phonon drag effect. This interaction between the phonons and the charge carriers determines the behaviour of some high purity semiconductors at low temperatures (cf. Herring 1954). Its absence in bismuth telluride is thought to be a consequence of the low thermal conductivity and high impurity content of the material.

The plateau and slight increase of thermoelectric power shown by the specimens at the lowest temperatures is in general agreement with the recent observations of MacDonald *et al.* (1959), and seems likely to be due to a change in scattering law with decreasing temperature. At very low temperatures impurities cause appreciable scattering of the charge carriers. With decreasing temperature therefore λ rises and the thermoelectric power (cf. equation (17)) tends to increase. To extend the interpretation of the results further, it is necessary to take into account the carrier density which in the case of a one-band model may be derived from the Hall coefficient. The measurements of Yates (1959) have shown that there is little change in the Hall coefficient between 4·2 and 200 K. The change that does occur however is anomalous and has to be interpreted on the basis of a multiband model. It seems most meaningful therefore to derive the carrier density from the residual Hall coefficient measured at 4·2°K.

Consider the low temperature, i.e. degenerate, region represented by equation (18). The full curves on the $\alpha/R_{\mathrm{H}}{}^{2/3}$ against temperature diagram shown in figure 7 correspond to the degenerate region where $\eta > 3$ while the broken curves

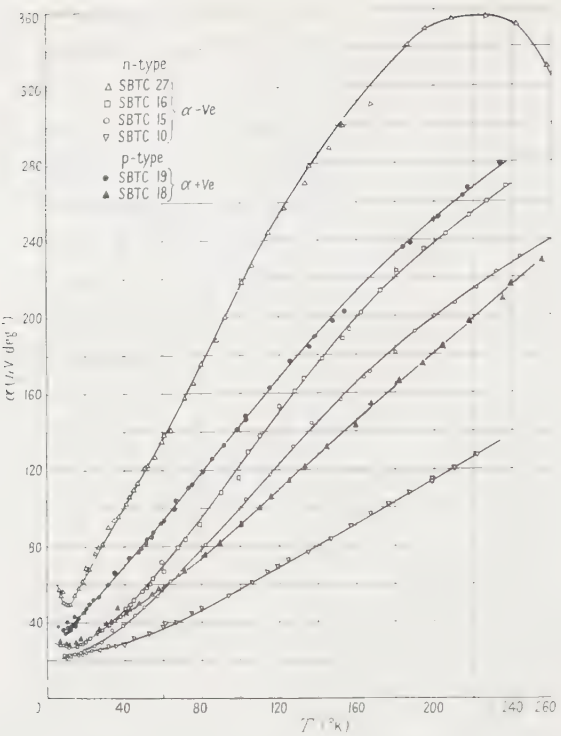

Figure 6. Variation of thermoelectric power with temperature.

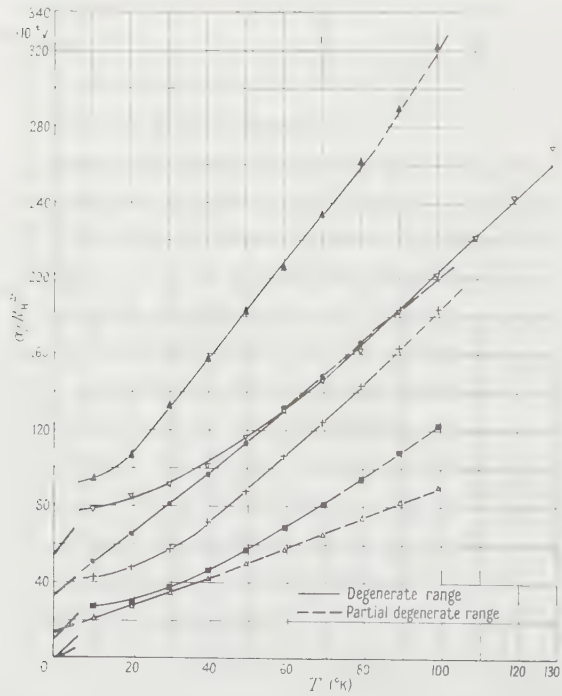

Figure 7. $\alpha/R_H^{2/3}$ plotted against T in degenerate region.

represent the region of partial degeneracy where $\eta < 3$. All the curves have a linear region, the gradient of which (cf. equation (18)) is determined by λ, m and r. The change in gradient from specimen to specimen is shown in figure 8 and implies that these parameters must be dependent on the iodine doping.

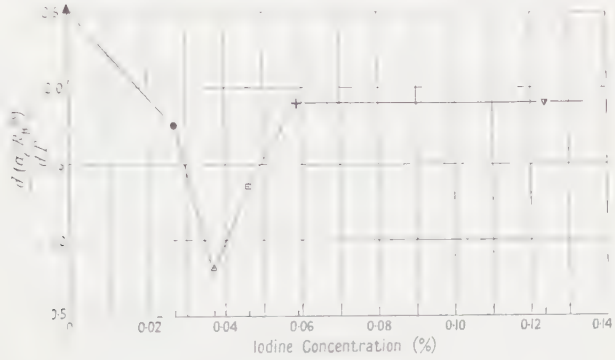

Figure 8. $d(\alpha/R_H^{2/3})/dT$ plotted against iodine doping.

On the basis of equation (18), one would expect the extrapolated linear regions of the curves of figure 7 to pass through the origin. Although this is the case for two of the specimens, the others have a finite intercept on the $T = 0$ K axis. This has been observed for other semiconductors and Kolamoets (1958) has shown that for a strongly degenerate electron gas, the thermoelectric power would be expected to have the form

$$\alpha = \beta T + \alpha_0 \qquad \ldots\ldots (20)$$

where α_0 and β are determined by the concentration of imperfections (impuritites – defects) and by the scattering law. From figure 7 it is seen that the value of the intercept α_0 decreases as the iodine doping increases, becomes zero at 0·046% iodine, and then increases at 0·124% iodine. In a qualitative manner this suggests the filling up of lattice vacancies followed by the introduction of interstitial impurities.

At the higher temperatures, the specimens approach the non-degenerate region and the results may be analysed by means of equation (19). In figure 9 the experimental values are plotted in the form $(\alpha e/k - \ln R_H)$ against $\ln T$. The solid curves represent the region of non-degeneracy where $\eta < -0{\cdot}5$ and equation (19) would be expected to hold. According to this equation, the linear portion of the curves should have a slope of 1·5. The observed variation of slope with iodine doping is shown in figure 10. Goldsmid (1958a) observed a similar deviation for polycrystalline material. Examination of (19) shows that the discrepancy could be caused by m or r being dependent on temperature and on the iodine content.

It has been shown by Delves (1959) that scattering of the carriers by optical mode vibrations of the lattice gives large values for the slope $d\alpha/d\ln T$ ($= 2{\cdot}25$ for non-degenerate material). The observed change of slope with doping could be accounted for by a change in the relative amounts of optical and acoustic mode scattering.

4.3. *Discussion*

Although it has not proved possible to draw many firm conclusions from these measurments, they have emphasized the discrepancies which exist between

the observed behaviour of Bi_2Te_3 and that predicted by simple theory. Interpretation of the results on the basis of a simple one-band model assuming

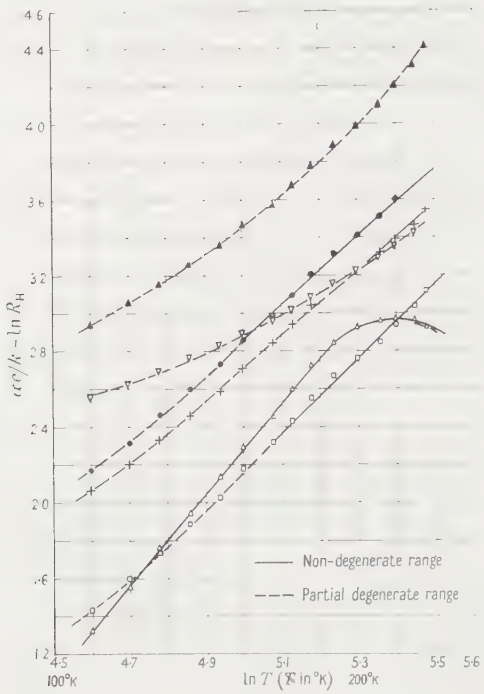

Figure 9. $\alpha e/k - \ln R_H$ plotted against $\ln T$ in non-degenerate region.

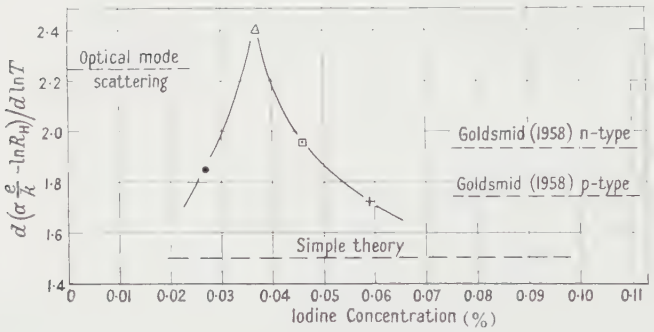

Figure 10. $d(\alpha e/k - \ln R_H)/d \ln T$ plotted against iodine doping.

spherical energy surfaces and an energy dependent relaxation time leads to the conclusion that λ, m or r or any combination of them is dependent on temperature and on the iodine content of the material.

The scattering law is known to be dependent on impurity content for many materials. Evidence from the electrical measurements on Bi_2Te_3, suggests however that impurity scattering only becomes appreciable at the very lowest temperatures.

An effective mass dependent upon impurity content can be a consequence of a very low density of states band. With the rapid filling up of such a band, the effective mass, which is a measure of the curvature of the band, could be expected to vary. A more likely reason for a varying effective mass is a multiband

structure. Such a band structure has been proposed for Bi_2Te_3 by Mooser and Pearson (1958). Their model which consists of a low density of states, low effective mass conduction band overlapping the normal valence and conduction bands would result in a variation of effective mass with doping. However, this model does not explain the variation of R_H at low temperatures observed by Yates (1959). In order to account for these measurements Yates proposed a four-band model. It would be possible to explain a variation of effective mass with doping if we assumed that the charge carriers in the different bands had different effective masses.

The factor r which appears in the expression for the Hall coefficient is dependent upon the degree of degeneracy, the scattering law, and the anisotropy of the band structure. This anisotropy may be expressed in terms of the effective mass components along three principal directions (cf. Drabble 1958). Thus a dependence of λ or m on iodine content would result in a corresponding dependence of r.

In conclusion we consider whether there is any *a priori* reason for expecting bismuth telluride to have a multiband structure. As pointed out by Drabble and Goodman (1958) it is necessary, when considering the structure of Bi_2Te_3, to distinguish between two types of differently bonded tellurium atoms. Thus the atoms are arranged in the sequence $Te^{(1)}$–Bi–$Te^{(2)}$–Bi–$Te^{(1)}$. It has been suggested by Drabble and Goodman that the bonding between the $Te^{(1)}$ $Te^{(1)}$ atoms is covalent whilst that between the Bi $Te^{(1)}$ and Bi–$Te^{(2)}$ atoms is a mixture of covalent and ionic bonding. It is believed that the bonds between the bismuth and tellurium atoms are fully saturated and that there is a difference between the Bi Te^{1} bonds and the Bi Te^{2} bonds. This difference is reflected in the shorter bond length of Bi Te^{1} (3·12 A) compared with that of Bi–$Te^{(2)}$ (3·22 A).

The energy gap in a semiconductor is determined by the weakest bond, i.e. largest bond length, which in the case of Bi_2Te_3 is Bi $Te^{(2)}$. However, since there is only a 3% difference in the bond lengths it is to be expected that there will be a second pair of bands having a slightly greater energy gap. This picture of the chemical bonds in Bi_2Te_3 thus leads to a dual valence band and a dual conduction band (Wright 1959). As far as transport properties are concerned, these bands may be considered to act in parallel. They may therefore be identified, in a qualitative manner, with the four-band model proposed by Yates (1959).

Acknowledgments

I wish to thank Dr. J. M. Ziman and Mr. F. W. Sheard for helpful discussions in connection with the interpretation of the thermal conductivity results and also for letting me see their paper prior to its publication.

References

Berman, R., Nettley, P. T., Spencer, A. N., Stevenson, R. W. H., Sheard, F. W., and Ziman, J. M., 1959, *Proc. Roy. Soc.* A, **253,** 403.

Bowley, A. E., Delves, R., and Goldsmid, H. J., 1958, *Proc. Phys. Soc.*, **72,** 401.

Dauphinee, T. M., MacDonald, D. K. C., and Pearson, W. B., 1953, *J. Sci. Instrum.*, **30,** 399.

Delves, R., 1959, *Proc. Phys. Soc.*, **73,** 572.

Drabble, J. R., 1958, *Proc. Phys. Soc.*, **72,** 380.

Drabble, J. R., and Goodman, C. H. L., 1958, *J. Phys. Chem. Solids*, **5,** 142.

Goldsmid, H. J., 1958 a, *Proc. Phys. Soc.*, **71,** 633.
—— 1958 b, *Proc. Phys. Soc.*, **72,** 17.
Herring, C., 1954, *Phys. Rev.*, **96,** 1163.
Jan, J. P., Pearson, W. B., and Templeton, I. M., 1958, *Canad. J. Phys.*, **36,** 627.
Kolamoets, N. V., 1958, *Zhur. Tekh. Fiz.*, **28,** 936.
Leibfried, G., and Schlömann, E., 1954, *Nachr. Acad. Wiss. Göttingen,* **2a,** 71.
MacDonald, D. K. C., Mooser, E., Pearson, W. B., Templeton, I. M., and Woods, S. B., 1959, *Phil. Mag.* **4,** 433.
Mendelssohn, K., 1931, *Z. Phys.*, **73,** 482.
Mooser, E., and Pearson, W. B., 1958, *J. Phys. Chem. Solids,* **7,** 65.
Roberts, V., 1955, *J. Sci. Instrum.*, **32,** 294.
Satterthwaite, S. B., and Ure, R. W., 1957, *Phys. Rev.*, **108,** 1164.
Wright, D. A., 1959, *Research,* **12,** 300.
Yates, B., 1959, *J. Electronics and Control,* **6,** 26.
Ziman, J. M., 1956, *Proc. Roy. Soc.* A, **237,** 344.

Some Measurements of the Elastic and Viscous Properties of Thixotropic Fluids

By E. W. BILLINGTON
Admiralty Oil Laboratory, Brentford, Middlesex

MS. received 12*th October* 1959, *in final form* 1*st March* 1960

Abstract. A coaxial cylinder viscometer is described which was designed to measure the elastic and viscous properties of fluids which exhibit thixotropic behaviour, in particular of natural 'wax-containing' oils. A constant torque is applied to the inner cylinder which is free to rotate, while the outer cylinder is kept stationary. The change in the rate of shear with time for which the stress is applied can be measured. The shape of the resulting 'rate of shear, time' graph can be interpreted so as to distinguish and measure the elastic and viscous properties. An example is given of the behaviour of a typical 'wax-containing' oil together with a suggested quantitative interpretation of the results.

§ 1. Introduction

Certain fluids are known to possess a quasi-rigid structure and it is possible for such systems to exhibit an elastic response to changes of stress similar to that observed in a solid. The visco-elastic properties of a fluid having a non-zero yield value can be examined by simple recoil experiments in which the outer cylinder of a coaxial cylinder viscometer is kept fixed and a constant stress is applied to the inner cylinder. The rate and degree of rotation of the inner cylinder, and the subsequent recovery on removing the applied stress, is measured. An extension of the simple static recoil experiment is to subject the outer cylinder to sinusoidal oscillations and measure the amplitude of rotation of the inner cylinder (Oldroyd, Strawbridge and Toms 1951).

Fluids which exhibit the phenomena of thixotropy possess an internal structure which produces a resistance to flow. Thixotropy is defined as the reversible time-dependent decrease of the resistance to flow accompanying the application of a shearing stress. The visco-elastic properties of this class of fluid cannot adequately be examined by simple recoil experiments owing to the time dependence of the internal structure. In order to examine the effects due to a system of elastic elements in a fluid exhibiting thixotropic behaviour it is preferable that the viscosity measurements be made under conditions of constant applied stress, the change in the rate of shear with time being measured. Viscosity measurements have been made on natural 'wax-containing' residual oils using a coaxial cylinder viscometer of the type described by Mooney and Ewart (1934), in which a constant stress is applied to the inner cylinder which is free to rotate, the outer cylinder being kept stationary. The thixotropic behaviour of the wax-containing oils is attributed to the presence of individual wax crystallites in a Newtonian base oil. The individual wax crystallites, in a system maintained free of stress and in thermal equilibrium, coalesce to form an internal structure of crystal aggregates. The crystal aggregates can be considered as deformable particles of time-dependent particle size, which produce an increase in the resistance to flow depending on the time of storage. Thus, there will be a limiting value of

the applied shearing stress below which flow does not occur; this value of the applied stress will be referred to as the yield stress, or yield value, p_y (Billington 1960). Continuous shearing of the fluid causes breakdown of the aggregates into individual particles which are the smallest particles of breakdown. After an infinite time of shearing the system has been completely transformed from the 'near solid state' to a liquid consisting of the individual particles dispersed in the Newtonian base liquid. At any given time of shearing the system consisting of the remaining fraction of individual particles dispersed in the base liquid will be referred to as the residual liquid. The viscosity of the residual liquid, assumed to be Newtonian, is related to the shear stress $p_R(t)$ by the equation

$$p_R(t) = \eta_R \dot{S}_t \qquad \ldots\ldots (1)$$

where η_R is the residual viscosity and $\dot{S}_t$ is the measured rate of shear at time t.

A complete rheological examination of a fluid exhibiting thixotropic behaviour under conditions of constant applied stress, is dependent on obtaining measurements of how the rate of shear changes with time for various values of the applied stress. The essential conditions of the experiment are that a separate sample is used for each value of the applied stress, and that at the commencement of each experiment all the samples are in the same rheological condition. The method which has been developed requires the use of a minimum of three identical viscometers which are filled with the test material and stored under identical conditions for a period of time sufficiently long to ensure that the three samples are in the same state at the commencement of each measurement. In this way measurements are obtained at three different applied stresses on samples which are known to be uniform throughout, and which have not been disturbed by unnecessary shearing prior to the measurements.

§ 2. Experimental

2.1. *The Viscometer Cylinders*

A coaxial cylinder viscometer similar to that described by Lee and Warren (1940) has been used to obtain the dependence of the rate of shear on the time of shearing. The design of the main assembly is shown in figure 1. The lower ends of both inner and outer cylinders are tapered to form cones which meet in a common apex. The apex of the cone section of the inner rotating cylinder forms part of the lower bearing. The bearing point of the inner cylinder fits into a cup recessed into one end of a hardened steel screw which forms part of the apex of the outer cone. The inner cylinder can be raised clear of the outer cone section by adjusting the position of the cup bearing. The coaxial cylinder unit is mounted centrally, between three pillars which support the pulley system, on a base plate provided with levelling screws. A known torque is applied to the inner cylinder by means of weights via a torque shaft and clutch mechanism. The torque shaft and clutch together with the associated pulley system are mounted on a separate triangular plate which is held in position on top of the three supports. The angular rotation is measured by a pointer attached to the torque shaft which moves over a circular scale graduated in degrees. Mounted on the free end of the torque shaft is a mirror for use with a lamp and scale to enable small deflections to be observed. The viscosity of the Newtonian and non-Newtonian oils has been measured using cylinders made from brass, Perspex, and duralumin; the results for both types of oil were found to be independent of the moment of inertia of the inner cylinder.

To keep the weight of the instruments as small as possible the viscometers were made from duralumin.

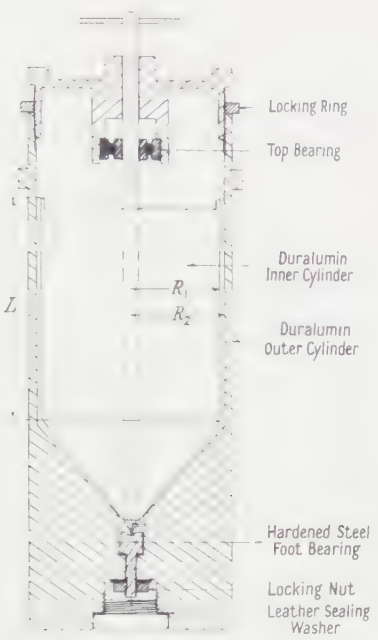

Figure 1. The viscometer cylinders.

The mean value of the shearing stress p at a cylinder of effective radius R_0 terminated by a cone of half-apex angle θ_0 is given by the relation (Mooney and Ewart 1934)

$$p = \frac{G}{2\pi R_0^2 L}\left(1 + \frac{R_0}{3L\sin\theta_0}\right)^{-1} \qquad \ldots\ldots(2)$$

where G is the applied torque and L is the mean length of the cylindrical sections. The square of the effective radius is given by $R_0^2 = 2R_1^2R_2^2/(R_1^2 + R_2^2)$ where R_1 and R_2 are the radii of the inner and outer cylinders respectively. The rate of shear $\dot{S}$ is given by equation (3)

$$\dot{S} = \Omega(R_2^2 + R_1^2)/(R_2^2 - R_1^2) \qquad \ldots\ldots(3)$$

where Ω is the angular velocity. In equation (2) the applied torque G is given by the relation

$$G = (W_1 + W_2 + m)gr \qquad \ldots\ldots(4)$$

where g is the gravitational constant, W_1 and W_2 are two applied weights, r is the radius of the torque shaft and m is an experimental correction made to the calculated shearing stress to allow for frictional losses in the instrument. The range of shearing stresses available, using viscometer cylinders having $L = 10$ cm, $R_1 = 4{\cdot}077$ cm, $R_2 = 4{\cdot}366$ cm and half-apex angle $\theta_0 = 40{\cdot}4$ extends from 10 dyn cm^{-2}, to 1200 dyn cm^{-2}, for a torque shaft radius $r = 0{\cdot}515$ cm.

The instruments were calibrated over a wide temperature range using oils which had previously been calibrated at the National Physical Laboratory, Teddington. The correction m is obtained from the graph $(1/t', W)$ where t'

is the time for one complete revolution of the inner cylinder for an applied load W. The relation between $1/t'$ and W for a Newtonian liquid is linear, and the intercept on the abscissa when $1/t'$ is zero is taken as the value of the correction m, usually of the order of 20 g. The use of weights to apply the torque G to the inner cylinder imposes a limitation to the length of time for which the system can be continuously sheared without having to adjust the level of the weights. The momentary removal of the applied stress for the purpose of adjusting the level of the weights has no detectable effect on the 'rate of shear, time' curve.

2.2. *Sample Preparation*

The viscometers are filled with the material under test in the 'as-received' condition and placed in a constant temperature water bath. The working volume of the viscometer bath was approximately a metre in length by 40 cm deep and 30 cm wide. The large volume of the bath required to accommodate the viscometers, and the conduction of heat along the exposed parts of the viscometers, made the use of a temperature controlled chamber essential. A non-homogeneous internal structure frequently occurs in samples of small volume, such as the sample contained between the cylinders of the viscometer, if subjected to sudden shock-chilling to the test temperature. The reduction of the temperature of the sample from the 'as-received' temperature (usually room temperature) to the test temperature at a controlled rate during the initial stage of the storage period has been found to produce a homogeneous sample. The temperature of the chamber was automatically reduced at the rate of 1 °C a day from the 'as-received' temperature to the test temperature of 3 °C. The temperature of the viscometer bath was continuously monitored by twelve thermocouples distributed over the volume of the bath; the temperature just inside the top of the outer cylinder of each instrument was also recorded using thermocouples. The readings of all thermocouples including the control system for the constant temperature chamber were continuously recorded outside the chamber. The presence of the operator in the chamber produces initially a small fluctuation in the temperature of the chamber, but no corresponding change in the temperature of the viscometer bath could be detected. The temperature of the oil samples could be controlled to within $\pm 0{\cdot}05$ °C. The viscometers were stored for three days at the test temperature; measurements of the change in the rate of shear with time were made at three different applied stresses.

2.3. *U-tube Experiments*

A possible method of measuring the yield value, based on the viscous flow of a fluid in a cylindrical tube, has been examined. The yield stress is defined for the purposes of this experiment as the critical value of the applied stress at which flow can just be detected in a cylindrical tube. The shear stress per unit area p at the wall of a tube of radius R and length L is given by the relation

$$\Delta P \pi R^2 = p 2\pi RL$$
$$p = \Delta PR/2L \qquad \ldots\ldots (5)$$

where ΔP is the pressure drop across the tube. The flow tube used in these experiments is in the form of a U-tube made from stainless steel tubing

$1{\cdot}5 \pm 0{\cdot}2$ mm internal diameter and $2{\cdot}1 \pm 0{\cdot}2$ mm external diameter, and of such a length that the length to internal diameter ratio is 300 ± 5. The appropriate length of steel tubing is bent into a U, 35 ± 2 mm wide, and with a smooth curve at the bottom. Each end of the U-tube is brazed into a short brass sleeve 12 mm long and approximately 7 mm in external diameter and the open end of the U bridged with a horizontal brass strip 7 mm wide and 2 mm thick. The U-tubes are fitted with small lengths of rubber tubing approximately 3 cm in length and filled with the test fluid to the top of each piece of rubber tubing. The excess fluid in the rubber tubing allows for contraction on cooling. At the time of test the rubber tubing together with the excess fluid is removed to leave a flat surface at both ends of the U-tube. A known pressure is applied to one end of the U-tube and the time for the fluid to emerge from the free end is measured. The movement of the fluid is observed by means of a travelling microscope. An inherent difficulty is to assess at what stage the deformation of the fluid to produce a leading profile gives way to the critical velocity profile necessary for viscous flow to occur. The movement of the whole profile was continuously observed and the first movement at the wall of the tube was taken as the criterion for the onset of viscous flow. Ten U-tubes are mounted side by side in a constant temperature bath. At the end of a given time of storage a different pressure is applied to each tube in turn. Invariably one or more tubes have to be discarded due possibly to uneven gelling, or partial filling. Measurements have not been extended beyond a storage period of three days. The time interval from the instant at which the pressure is applied to the formation of the critical velocity profile will be referred to as the 'initial response time β'. In these preliminary experiments no provision was made for a controlled rate of cooling.

§ 3. Results

The graph $(p, 1/\beta)$ in figure 2 shows how the initial response time β depends on the shearing stress at the wall of a U-tube for three different oils. The apparent linear relationship between p and $1/\beta$ can be expressed by a relation of the form

$$(p - p_y)\beta = \text{const.} \qquad \ldots\ldots(6)$$

where the ordinate intercept p_y, corresponding to infinite response time, is identified with the yield value defined in § 2.3.

Figure 3 shows how the rate of shear obtained from the viscometer measurements on sample D, depends on the time measured from the instant the torque is applied to the inner cylinder of the viscometer for three different applied stresses. The removal of the applied stress for the short time taken to adjust the height of the weights is seen to have no detectable effect on the 'rate of shear, time' curve. The time interval τ elapsing between the application of the stress p and the onset of viscous flow is obtained by extrapolating the rate of shear, time curve to zero rate of shear; this is shown in figure 4 for sample D. The controlling mechanism by which the velocity profile is produced in the U-tube experiment is assumed to be the same for the initial deformation of the fluid in the viscometer, and the time interval between applying the stress and the onset of viscous flow will therefore be referred to as the initial response time τ. The relation between applied stress p and response time τ for sample D is shown in the graph $(p, 1/\tau)$ of figure 5. As in the case of the U-tube experiments the linear relation of equation (6) holds

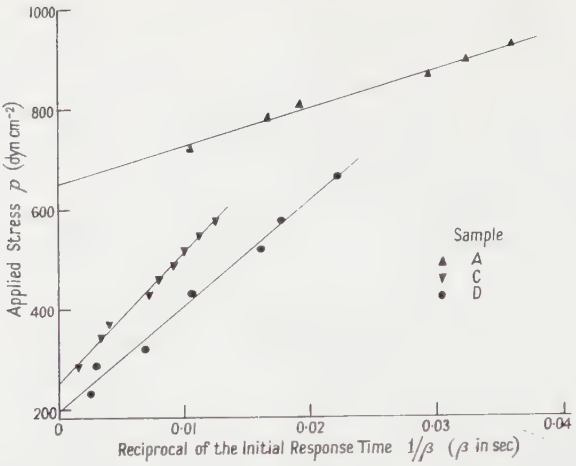

Figure 2. Dependence of the initial response time β on the applied stress p.

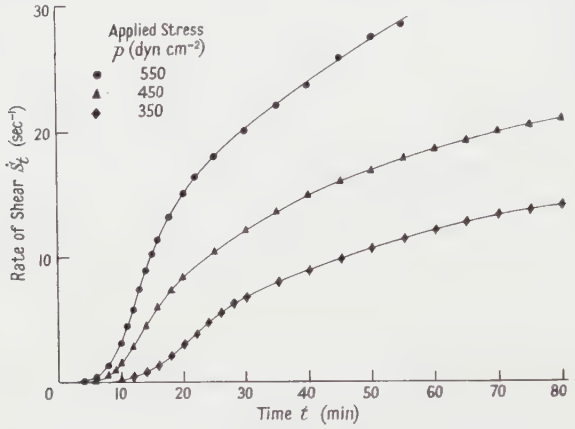

Figure 3. Variation of the observed rate of shear $\dot{S}_t$ with time.

for the initial deformation process in the viscometer. For sample D the initial yield value is 210 dyn cm^{-2} as compared with approximately 195 dyn cm^{-2} obtained from the U-tube experiment.

After an infinite time of shearing it is assumed that the system has been completely reduced to the residual liquid consisting of the individual wax crystallites dispersed in the Newtonian base liquid. It is further assumed that the residual liquid also exhibits Newtonian behaviour such that the viscosity η_R of the residual liquid is given by the relation

$$p = \eta_R \dot{S}_R \qquad (t = \infty) \qquad \ldots\ldots (7)$$

where p is the applied stress and $\dot{S}_R$ is the limiting value of the rate of shear corresponding to an infinite time of shearing. The residual viscosity cannot be evaluated from viscosity measurements at constant applied stress, and recourse must be made to measurements at constant rate of shear (Billington 1960). For sample D a value of 2·8 poise at 3 °C has been obtained. Using this value of η_R the rate of shear $\dot{S}_R$ can be calculated. Defining a new variable χ by the relation

$$\chi = \frac{t - \tau}{t_i - \tau} \qquad (0 \leqslant \chi \leqslant \infty) \qquad \ldots\ldots (8)$$

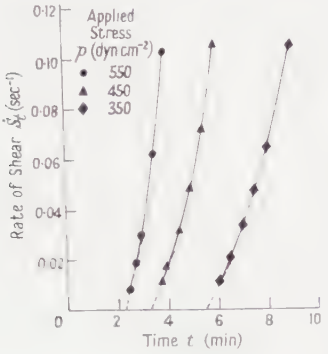

Figure 4. Determination of the response time τ from the rate of shear, time curve.

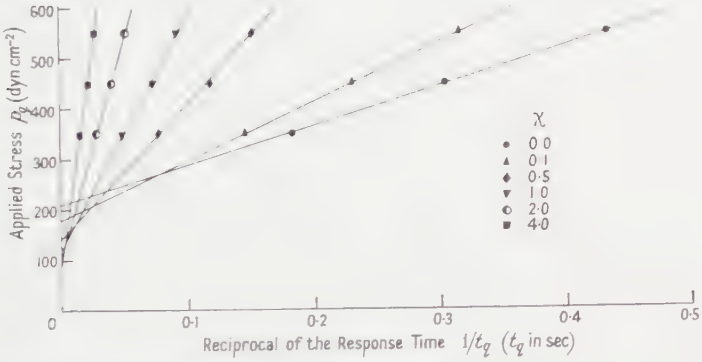

Figure 5. Dependence of the reciprocal of the response time t_q on the applied stress p_q (for $\chi=0$, $t_q=\tau$).

where t_i is the time corresponding to the point of inflection on the rate of shear, time curve $(\dot{S}, t)$ and introducing the normalized rate of shear ϕ defined by the relation

$$\phi = \frac{\dot{S}_t - \dot{S}_\tau}{\dot{S}_R - \dot{S}_\tau} \quad (0 < \phi < 1) \qquad \ldots\ldots (9)$$

where $\dot{S}_\tau$ is the rate of shear corresponding to the initial velocity profile at time τ. In this way the three $(\dot{S}, t)$ curves of figure 3 compound into a single curve. The independent measurements of ϕ and χ corresponding to the three applied stresses, reduce to a mean value which can be measured with an accuracy to $\pm 10\%$ as shown in the graph (ϕ, χ) in figure 6.

§ 4. Discussion

A method of correlating the present measurements at constant applied stress with the earlier measurements at constant rate of shear is considered in this section.

The condition for which χ is zero corresponds to zero time of shearing measured from the instant at which viscous flow first occurs. The internal structure of the thixotropic fluid breaks down with continuous shearing, that is the yield value decreases with increasing time of shearing. It is assumed that the strength of the internal structure at any given instant, that is the yield value, is a characteristic

property of the thixotropic fluid, dependent only on the concentration and size of the deformable particles. The (ϕ, χ) curve is independent of the applied stress and is assumed to be directly related to the breakdown of the internal structure with continuous shearing, that is to the yield value. For a given value

Figure 6. Variation of ϕ with χ.

of χ there are three values of the time t corresponding to the three applied stresses. Let the values of the applied stresses p for the different viscometers be $(p_1, p_2, \ldots p_q)$ and let the corresponding values of the time for a given value of χ be $(t_1, t_2, \ldots t_q)$ where the response time t_q is obtained from the relation

$$t_q = [(t_i - \tau)\chi + \tau]_q. \qquad \ldots\ldots (10)$$

The relation between the applied stress p_q and the reciprocal of the response time t_q is shown in the graph $(p_q, 1/t_q)$ of figure 5 for various values of χ. The linear relationship may be expressed by an equation of the form

$$\{p_q - p_y(\chi)\}t_q = \text{const.} \qquad \ldots\ldots (11)$$

where the ordinate intercept $p_y(\chi)$ is assumed to be the yield value corresponding to a given value of χ. Equation (6) is seen to be a special case of (11) since for $\chi = 0$, $t_q = \tau$ from (10) and $p_y(\chi) = p_y(0)$ which is the initial yield value. The change in the yield value with increasing χ is shown in the graph (ψ, χ) of figure 7 where ψ is defined by the relation

$$\psi = p_y(\chi)/p_y(0) \quad (0 \leqslant \psi \leqslant 1). \qquad \ldots\ldots (12)$$

If elastic effects exist after viscous flow has commenced it is assumed that the elastic and viscous effects are mutually exclusive. That is the applied stress may be considered as the superposition of two independent stress systems given by the relation

$$p = p_v(t) + p_\epsilon(t) \qquad \ldots\ldots (13)$$

where $p_v(t) = p_R(t) + p_y(t)$ is the stress system producing viscous flow, and $p_\epsilon(t)$ the stress system producing elastic effects. The shear stress $p_R(t)$ producing viscous flow of the residual liquid for a given applied stress can be evaluated for all values of t, using the experimental values of the rate of shear and the value of η_R obtained from experiments at constant rate of shear, using equation (1). Combining equations (1) and (7) we obtain the relation

$$p_R(t) = p\dot{S}_t/\dot{S}_R$$

and using this relation in (13) we obtain for the stress $p_\epsilon(t)$ the relation

$$p_\epsilon(t)=p(1-\dot{S}_t/\dot{S}_R)-p_y(t) \qquad \ldots\ldots(14)$$

and

$$p_\epsilon(t)-p_\epsilon(\tau)=p_y(0)-p_y(t)-p(\dot{S}_t-\dot{S}_\tau)/\dot{S}_R.$$

Since $\dot{S}_R \gg \dot{S}_\tau$ the term $(\dot{S}_t-\dot{S}_\tau)/\dot{S}_R$ may be set equal to ϕ and the expression then reduces to

$$p_\epsilon(t)-p_\epsilon(\tau)=p_y(0)(1-\psi)-p\phi. \qquad \ldots\ldots(15)$$

Defining a new variable μ by the relation

$$\left.\begin{aligned} \mu &= \frac{p_\epsilon(t)-p_\epsilon(\tau)}{p_\epsilon(\mathrm{i})-p_\epsilon(\tau)} \quad \begin{pmatrix} \tau \leqslant t \leqslant t_\mathrm{i} \\ 0 \leqslant \mu \leqslant 1 \end{pmatrix} \\ \mu &= \frac{p_\epsilon(t)}{p_\epsilon(\mathrm{i})} \quad \begin{pmatrix} t_\mathrm{i} \leqslant t < \infty \\ 1 \geqslant \mu \geqslant 0 \end{pmatrix} \end{aligned}\right\} \qquad \ldots\ldots(16)$$

where $p_\epsilon(\mathrm{i})$ is the value for $t=t_\mathrm{i}$ corresponding to the point of inflection on the (S_t, t) curve. In this way the three independent stress systems $p_\epsilon(t)$ corresponding to the three values of the applied stress compound into a single curve as shown in the graph (μ, χ) in figure 7.

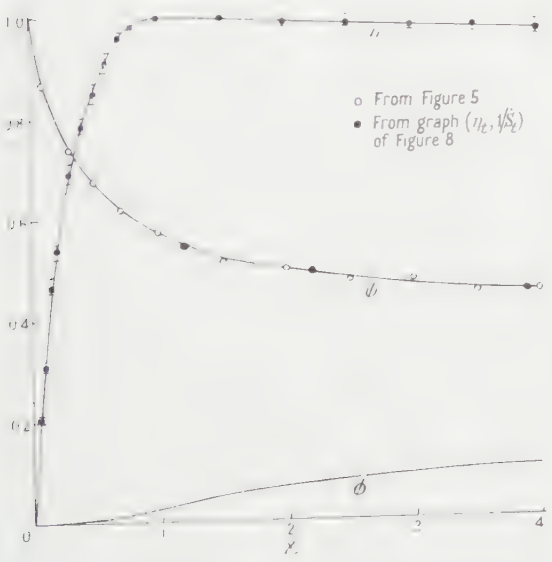

Figure 7. Variation of ϕ, ψ and μ with χ.

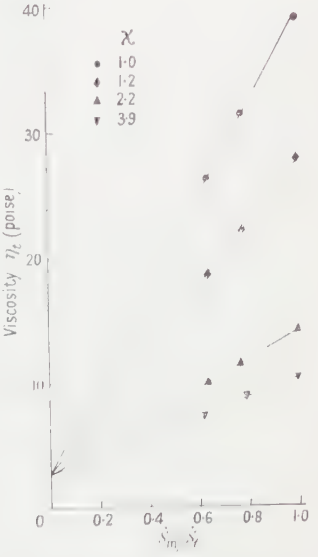

Figure 8. Dependence of the viscosity η_t on the reciprocal rate of shear.

The viscosity for a given value of χ is obtained from the relation

$$\eta_t=\frac{p-p_\epsilon(t)}{\dot{S}_t}. \qquad \ldots\ldots(17)$$

The dependence of the viscosity on the reciprocal rate of shear is shown in figure 8 for four values of χ; the rate of shear $\dot{S}_m$ is the value corresponding to the smallest applied stress. The linear relationship between η_t and $1/\dot{S}_t$ implies a relation of the form

$$(\eta_t-\eta_R)\dot{S}_t=p_y(t) \qquad \ldots\ldots(18)$$

which is the same as the equation obtained for the viscosity measurements at constant rate of shear. The value of the residual viscosity η_R obtained from the ordinate intercept for four values of χ is 2·8 poise. Several values of the viscosity η_R in the region of 2·8 were examined but the misalignment of the three independent (ϕ, χ) curves was found to be a minimum for $\eta_R = 2{\cdot}8$ poise. The yield value has been obtained from the slope of the graph $(\eta, 1/\dot{S}_t)$ for several values of χ and are shown on the graph (ψ, χ) in figure 7 to be in agreement with the values obtained from the graph $(p_q, 1/t_q)$ of figure 5.

It is assumed that during the time interval τ the applied stress is partitioned in such a way that the initial yield stress $p_y(0)$ produces the necessary relative movement of the internal structure which must occur during the deformation of the system to produce a leading profile. At time τ the leading profile attains the critical value corresponding to the initial velocity profile and viscous flow occurs. The yield value decreases with continuous shearing and the stress $p_\epsilon(t)$ increases during the time interval $t_i - \tau$ due to the relatively slow rate of increase of the shear stress $p_R(t)$. For times of shearing in excess of t_i the stress $p_R(t)$ increases rapidly due to the increase in the rate of shear, but the decay of the yield value is insufficient to compensate for the increase in $p_R(t)$ which can therefore only occur if $p_\epsilon(t)$ decreases.

Acknowledgment

Acknowledgment is made to the Admiralty for permission to submit this paper for publication.

References

Billington, E. W., 1960, *Proc. Phys. Soc.*, **75,** 40.
Lee, A. R., and Warren, J. B., 1940, *J. Sci. Instrum.*, **17,** 63.
Oldroyd, J. G., Strawbridge, D. J., and Toms, B. A., 1951, *Proc. Phys. Soc.* B, **64,** 44.
Mooney, M., and Ewart, R. H., 1934, *Physics*, **5,** 350.

Ion Charge Exchange Reactions in Oxygen Afterglows

By P. H. G. DICKINSON and J. SAYERS
Department of Electron Physics, University of Birmingham

MS. received 29th December 1959, in final form 24th February 1960

Abstract. A method is described for measuring cross sections for ion charge exchange at mean ion energies corresponding to gas temperatures of the order of 300 °K.

The measurements are made in afterglows following pulsed radio-frequency gas discharges, using a mass spectrometer to identify the ions present, and to observe their relative rates of change of population.

The reaction cross section for the process

$$O^+ + O_2 \rightarrow O_2^+ + O$$

has been deduced from the measured population decay rate of the O^+ ion, at gas temperatures from 200 °K to 300 °K.

The apparent variation of the cross section with gas temperature is not considered to indicate a systematic temperature dependence.

The cross section was found to be $3{\cdot}2 \pm 0{\cdot}5 \times 10^{-16}\,cm^2$, corresponding to a rate coefficient of $2{\cdot}5 \pm 0{\cdot}4 \times 10^{-11}\,cm^3\,sec^{-1}$, for the process.

The relevance of this result to upper ionospheric studies is briefly discussed.

§ 1. Introduction

Measurement of cross sections for charge exchange between ions and neutral particles has hitherto been made by methods using either the attenuation of a monoenergetic ion beam, or the ionization produced in the neutral gas through which the beam has passed (e.g. Ziegler 1953, de Heer, Huizenga and Kistemaker 1955, Hasted and Gilbody 1957, Ghosh and Sheridan 1957). Ion beams have been used over an energy range from several hundred electron volts down to about one electron volt. Below this energy the use of ion beams for this type of experiment becomes technically very difficult.

Cross sections at energies of less than one electron volt are, however, of great interest, since the gas temperatures found in the ionosphere and in laboratory afterglow studies correspond to mean energies between 0·5 and 0·04 ev. For this reason, in the work reported here, measurements have been made in afterglows following pulsed gas discharges. The range of temperatures obtainable with the apparatus used was from 200 °K to 300 °K. A time resolving mass spectrometer was used to identify the ions present and to measure their relative rates of population change.

Since the cross section for charge exchange may be expected to be a function of the relative velocity of the particles concerned, the true parameter measured is a rate coefficient, which is the cross section integrated over the velocity distribution.

§ 2. Method

The reaction studied in the present investigation is

$$O^+ + O_2 \rightarrow O_2^+ + O \qquad \ldots\ldots (1)$$

and the parameter measured is k_1, the rate coefficient for this process.

Process (1) may result from either of two mechanisms, namely charge transfer,

$$X^+ + YZ \rightarrow X + YZ^+ \qquad \ldots\ldots (2)$$

or ion exchange,

$$X^+ + YZ \rightarrow XY^+ + Z. \qquad \ldots\ldots (3)$$

In the case of process (1) the two forms are indistinguishable, but ion exchange is expected, on theoretical grounds, to have a much greater cross section (Bates 1955), and if this is the case it should be the dominant process. In this paper, however, process (1) will be referred to by using the general name, charge exchange.

If $[O^+]$ represents the concentration of atomic oxygen ions and $[O_2]$ represents the concentration of molecular oxygen, then

$$\frac{d[O^+]}{dt} = \frac{d[O_2]}{dt} = -v\sigma_1(v)[O^+][O_2] \qquad \ldots\ldots (4)$$

where $\sigma_1(v)$ is the cross section for process (1) when the relative velocity of the colliding particles is v. When the particles have a relative velocity distribution defined by a normalized function $f(v)$, the term $v\sigma_1(v)$ in equation (4) must be replaced by k_1, where

$$k_1 = \int_0^\infty v\sigma_1(v)f(v)dv. \qquad \ldots\ldots (5)$$

Since $[O_2]$ is large compared with $[O^+]$, the fractional change in $[O_2]$ caused by the decay may be neglected, and $[O_2]$ regarded as constant. Hence integrating equation (4) gives

$$\ln [O^+] = -\lambda_e t + \text{const.} \qquad \ldots\ldots (6)$$

where

$$\lambda_e = k_1[O_2] \qquad \ldots\ldots (7)$$

is the logarithmic decay coefficient.

Therefore for process (1) an exponential decay of $[O^+]$ is expected from equation (6), with a decay coefficient which is proportional to $[O_2]$, as predicted by equation (7). k_1 can thus be obtained directly from a single measurement of λ, at a known value of $[O_2]$, assuming that process (1) is the only effective O^+ loss mechanism.

In this work λ is measured over a range of $[O_2]$ values, allowing both a verification of the predicted proportionality of λ to $[O_2]$, and a mean value of k_1 to be obtained.

§ 3. Apparatus

3.1. *The Discharge and Pulsed Power Source*

The afterglows, in which the measurements were made, followed gas discharges which were produced by 100 kw pulses of radio-frequency power of 7 Mc/s. The pulses were of approximately 20 microseconds duration, with a repetition frequency of 50 per second. The discharges were generated in a glass tube, at gas pressures of the order 1 mm Hg. The radio-frequency power was applied between two electrodes E (see figure 1), each consisting of an external copper sleeve connected to an internal molybdenum disc.

The vacuum system involved greased taps and joints, and liquid air traps were used to prevent hydrocarbon vapours from reaching the discharge and mass spectrometer, M.S. (figure 1). The system could be evacuated to a pressure below 5×10^{-6} mm Hg.

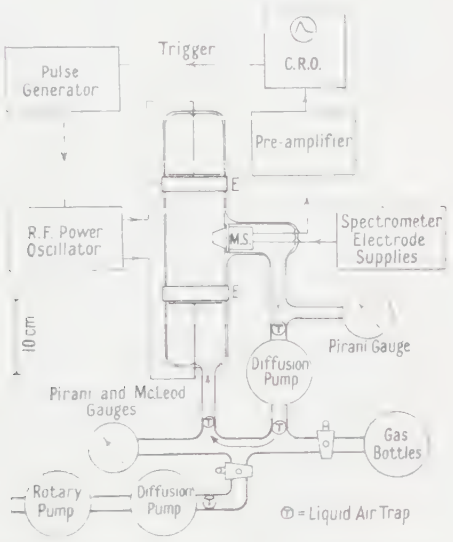

Figure 1. The apparatus, schematic diagram.

The gas pressure in the discharge tube could be measured by both the McLeod and Pirani gauges.

3.2. *The Mass Spectrometer*

3.2.1. *General.*

The mass spectrometer, developed and built by L. W. Kerr (1953), was of the radio-frequency linear accelerator type, similar to that described by Boyd and Morris (1955). This type has the advantage, for this work, of having no external magnetic field to disturb the afterglow. The instrument was used to show the variation of the ion concentration with time in the afterglow, as a display on an oscillograph. Positive or negative ions having masses between 1 and 250 a.m.u. could be selected for study. The charge to mass ratio of any single ion type could be determined with an accuracy to about 5%, while ions differing in mass by 15% or more could be resolved.

3.2.2. *Description.*

Apart from differences in constructional design, the instrument differed from that built by Boyd and Morris in two main respects. Firstly an 18-stage linear accelerator was used in place of the 12 stages of their model. This was done without increasing the ion path length, which remained less than 3 cm. Secondly the ion current, of about 10^{-9} amp, passed from the collector along a rod, inside an earthed coaxial nickel tube, and through the grid resistor of the first stage of a highly screened a.c. coupled pre-amplifier. The ion current was, in fact, completely screened between the collector and the oscillograph input, and this

prevented pick-up of mains hum, or of the radio-frequency linear accelerator voltage or the discharge pulse. As further precautions against pick-up, the power supplies to the pre-amplifier were screened and filtered, and the heater current to the valves was supplied from screened batteries.

The high-frequency response of the pre-amplifier was limited by the time constant of the input circuit, which was approximately 50 microseconds, depending upon the value of the grid resistor used. This allowed the rapid changes in ion current during the afterglow to be linearly amplified and displayed on an oscillograph as a function of time.

3.2.3. *Performance.*

It is necessary that the variation of the ion current with time, as measured from the oscillograph should be directly proportional to the variation of the ion density in the afterglow. This would not be so if any of the d.c. electrode potentials varied during the afterglow, or if the ion current amplification was not linear. Neither of these effects was detected, and no further reason was found to indicate any time dependence of the mass spectrometer sensitivity.

Due to inadequacy of existing theories of ion collection by probes, absolute ion densities in the afterglow could not be deduced using the mass spectrometer.

The ratio of the population densities of different ion types having like charges could be estimated, after correction for the effect of the difference in diffusion coefficients.

The ratio of the positive ion collection efficiency of the mass spectrometer to that for negative ions could not be accurately ascertained. This was because of the possible different behaviours of positive and negative ions in the ion sheath at the orifice. Hence the ratio of the population densities of ion types having unlike charges could not be estimated with accuracy.

These limitations did not affect the oxygen charge exchange measurements.

§ 4. Experimental Procedure

4.1. *Cleaning*

Clean discharge conditions were obtained by repeatedly running discharges in helium or in oxygen–helium mixtures, and flushing with clean gas.

The purity of the discharge conditions was tested by using the mass spectrometer to detect ionized impurities.

4.2. *Absorption Loss of Oxygen*

It was found that after the discharge tube had been cleaned by discharges in helium alone, the pressure in a subsequent oxygen discharge dropped rapidly due to 'clean-up' on to the internal electrodes and glass walls. This effect only occurred when the discharge was running. It was much reduced if oxygen had first been adsorbed by running the discharge in an oxygen–helium mixture (see figure 2). It was important that the partial pressure of oxygen during the decay rate measurements should be known as accurately as possible. However, because a comparatively large pressure of helium was used as a passive recoil agent, any change in oxygen partial pressure due to 'clean-up' during measurements could not be directly observed.

For these reasons, immediately before any charge exchange measurements were made, the discharge was run for a few minutes in an oxygen-helium mixture. Oxygen loss by 'clean-up' was further reduced by limiting the time for which the discharge was on to less than 40 seconds. All the mass spectrometer adjustments were made, and photographs taken in this time.

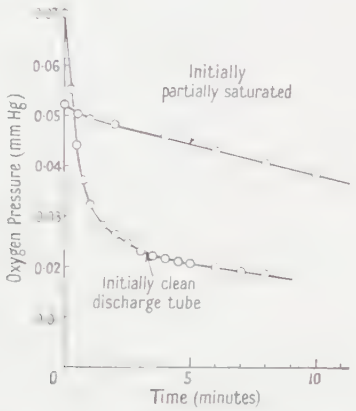

Figure 2. Oxygen loss by 'clean-up'.

If, in spite of these precautions, the partial pressure of oxygen did change significantly during the time taken to record the decay, a second photograph would tend to record a slower decay than the first. No systematic trend of this type was observed.

4.3. *Measurement*

The measurements were made in afterglows with oxygen partial pressures varying from the lowest accurately measurable pressure of about 0·002 mm Hg up to 0·025 mm Hg, at which pressure the O^- ions decayed too fast for reliable measurement, and the O_2^+ ion concentration became comparable with that of O^+.

Helium at a pressure of about 1 mm Hg (see § 5.1.2) was used as a passive recoil agent to prevent loss of O^- ions by diffusion to the walls of the discharge tube. Gas temperatures between 200 and 300 K were used, the variation being obtained by external cooling of the discharge tube. The gas temperature was measured using the change in pressure of a fixed mass of gas in the system, that is, using the system as a gas thermometer.

When no ions were being accelerated by the mass spectrometer, the oscilloscope showed a deflection of the trace due to transient effects following the discharge. The true ion current was superimposed upon this background. Photographs were taken of both traces by double exposure on 35 mm film. Two pairs of exposures were taken of each gas filling, to ensure that 'clean-up' (see § 4·2) was not causing any serious error.

The time scale was obtained from time markers superimposed on the traces. These were recorded on each photograph, so that any distortions due to curvature of the screen, time-base non-linearity, and photographic distortion, would have no effect on the time calibration.

The difference between the two traces, as a function of time in the afterglow, was measured from enlargements of the films, and the logarithm of the deflection plotted against time. These semi-logarithmic graphs were expected to be straight lines (see § 2), the slopes of which would give logarithmic decay coefficients of O^+ at particular pressures. The coefficients could then be plotted as a function of oxygen partial pressure at fixed gas temperatures. Each of these graphs was expected to be a straight line, from the slope of which the rate coefficient could be calculated at the appropriate temperature.

§ 5. Results

5.1. *Preliminary Results*

5.1.1. *Impurities.*

The ions detected in helium discharges were Cl^-, N^+, mass 18^+ and 18^- (± 1 a.m.u.). With the exception of Cl^-, the currents due to these impurity ions were scarcely detectable above the amplifier noise level.

Under normal working conditions, in helium–oxygen mixtures, only O^- and Cl^- were observed, in addition to the O^+ ions being studied. The O^- concentration was scarcely detectable, and was short lived in the afterglow, while the Cl^- concentration was larger and more persistent. It is not possible to give a quantitative estimate of the ratio of the O^+ and Cl^- concentrations in the afterglow (see § 3.2.3).

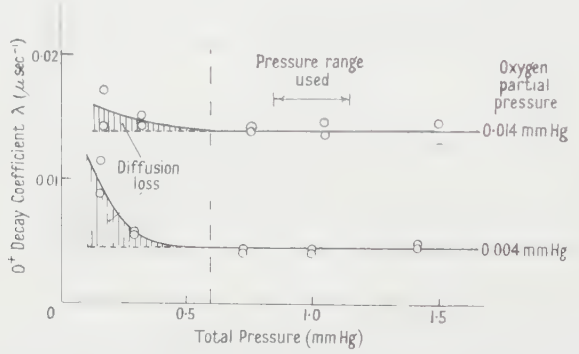

Figure 3. Suppression of diffusion by passive recoil gas (helium). The charge exchange decay is independent of total pressure.

The chlorine gas is thought to originate in the glass walls of the discharge tube, because a chloride flux was used in the manufacture of the glass.

For discussion of these results see § 6.1.

5.1.2. *Diffusion.*

As diffusion loss is a function of gas pressure, the O^+ ion decay rate at various passive recoil gas pressures was investigated (see figure 3). As the total pressure was reduced, while keeping the oxygen partial pressure constant, the O^+ decay coefficient was found to be constant down to a total pressure of about 0·6 mm Hg. For total pressures below this, a sharp rise in decay coefficient occurred, as diffusion loss began to augment the loss by charge exchange, the latter being

dependent only on the oxygen partial pressure. The helium pressure was varied for two partial pressures of oxygen. After consideration of these graphs the total pressure used in the following measurements was therefore $1 \pm 0{\cdot}15$ mm Hg.

5.2. *Decay Rate Measurements*

Altogether 66 different sets of afterglow conditions were investigated: 26 at 300 °K, 15 at 276 °K, 11 at 263 °K and 14 at 204 °K.

The graphs of ln $[O^-]$ against t, which were expected to be linear from equation (6), §2, showed a tendency to curvature at early times, up to about 300 microseconds, in the afterglow, but at later times they became linear (see figure 4, discussed in §6.3). The slope of the linear part of the semi-logarithmic graph was considered to be λ, the coefficient for O^- decay by charge exchange.

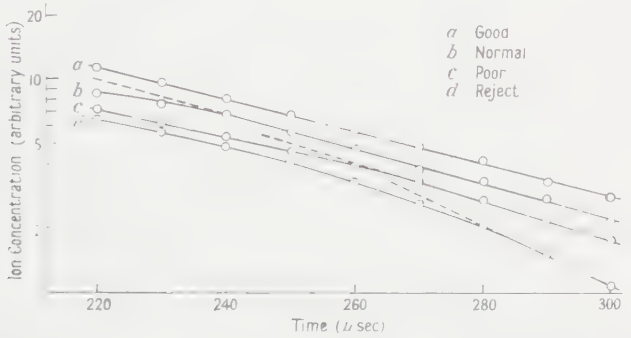

Figure 4. Typical ln (ion concentration) decay curves.

The variation of O^+ decay coefficient with oxygen partial pressure is shown in figure 5 for various gas temperatures. These graphs show a general proportionality of decay coefficient to partial pressure, between pressures of 0·005 and 0·020 mm Hg, but outside these limits deviations occur. The spread at high pressure is due to the experimental accuracy being reduced because the O^- ion currents were small, and the decays rapid. At pressures below 0·004 mm Hg the decay coefficients tend to be larger than predicted by extrapolation of the graph to the origin. No explanation can be given for this effect, which, however, has little influence on the final value of the rate coefficient.

5.3. *Rate Coefficient Derivation*

The mean slope of each graph shown in figure 5 was found by averaging the values of λ/P for all the points. The most probable error was also found from these values.

From the average value of λ/P the rate coefficient could be found directly:

$$k_1 = 7{\cdot}18 \times 10^{-20} T\lambda/P \text{ cm}^3 \text{ sec}^{-1}, \qquad \ldots\ldots (8)$$

where $\lambda = O^+$ decay coefficient $= 1/$(time to fall to half density) (sec^{-1}), $P =$ oxygen partial pressure (mm Hg), $T =$ gas temperature (°K).

The rate coefficients obtained at the temperatures used are shown graphically in figure 6. It will be seen that no systematic variation with temperature can be suggested from these results, although the spread is greater than the probable errors of the individual values, which were repeatable.

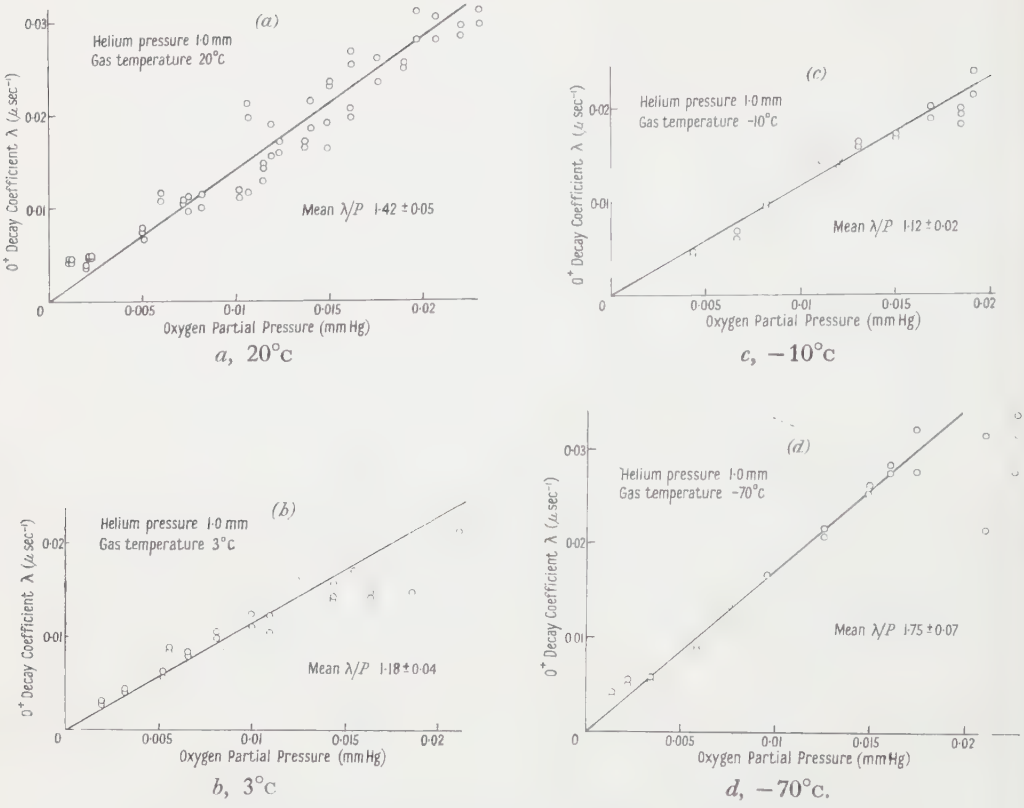

Figure 5. Dependence of O^+ decay coefficient on oxygen pressure.

The value of the rate coefficient quoted is the mean of the four values found, which were weighted according to the reciprocals of the respective percentage probable errors.

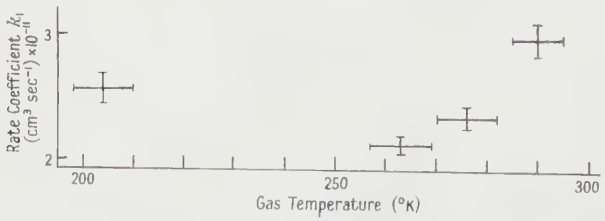

Figure 6. Variation of oxygen charge exchange rate coefficient with gas temperature.

The error quoted takes into account the spread of results at the different temperatures.

The value obtained for the rate coefficient for oxygen charge exchange is

$$k_1 = 2{\cdot}5 \pm 0{\cdot}4 \times 10^{-11}\,\mathrm{cm^3 sec^{-1}}$$

corresponding to a cross section of

$$\sigma_1 = 3{\cdot}2 \pm 0{\cdot}5 \times 10^{-16}\,\mathrm{cm^2}.$$

§ 6. Discussion of Results

The value of the rate coefficient obtained in § 5.3 was arrived at on the assumption that oxygen charge exchange (process (1), § 2) was the only effective O^+ loss mechanism in the afterglows examined. The reasons for neglecting other possible loss processes will now be discussed.

6.1. *Recombination*

The question of loss of O^+ ions by recombination with negatively charged particles will be considered. One possibility is ion–ion recombination, for example

$$O^+ + O^- \rightarrow O' + O'. \qquad \ldots\ldots (9)$$

Now, using the same terminology as in § 2,

$$\frac{d[O^-]}{dt} = \frac{d[O^+]}{dt} = -v\sigma_9(v)[O^-][O^+]. \qquad \ldots\ldots (10)$$

The ratio $[O^-]/[O^-]$ could not be accurately ascertained (see § 3.2.3), but it is certain that $[O^-]$ was not greater than $[O^+]$. This is because, in the absence of other positive ions, a surplus negative charge would have resulted. Let us take the most unfavourable value of the ratio by putting $[O^-] = [O^+]$. Integrating equation (10) then gives the well-known recombination law

$$[O^+] \propto \frac{1}{t}; \quad \frac{d[O^+]}{dt} \propto -\frac{1}{t^2}. \qquad \ldots\ldots (11)$$

The logarithmic decay coefficient at time t is

$$\lambda(t) = -\frac{1}{[O^-]}\frac{d[O^-]}{dt} \propto \frac{1}{t}. \qquad \ldots\ldots (12)$$

Hence the slope of a graph of $\ln[O^-]$ against t would decrease with time, and the graph would be convex downwards. If $[O^-]$ was less than $[O^+]$, this curvature would be accentuated. However, within experimental error, the semi-logarithmic graphs were not found to be convex downwards.

Similar argument also eliminates the possibility of recombination with Cl^- ions or electrons being significant. Also, electron recombination is expected, on theoretical grounds, to have a small recombination coefficient at these pressures.

The fast decay of the small O^- concentration is considered to be by electron transfer to chlorine, which has a high electron affinity. This is borne out by the observed slow decay and larger concentration of Cl^-.

6.2. *Diffusion*

The following precautions were taken to ensure that any loss of O^+ ions by diffusion to the walls of the discharge would be of negligible proportions.

The discharge tube electrode system was designed to give as uniform a plasma as possible in the region where observations were made.

The radial distribution of the ionization was a function of the frequency of the radio-frequency power, which was chosen to give a uniform central plasma of about 3 cm radius. This distribution was ascertained by means of a movable Langmuir probe. Loss of O^- ions by diffusion was further reduced by using a passive recoil gas (see § 5.1.2).

6.3. O^+ *Decay Law*

The decay of the O^+ ion population was expected to be exponential (see § 2), and the observed decays were exponential at late times. Sometimes, however, the decays were slower at early times in the afterglow (see § 5.2 and figure 4). This effect would be explained if an O^+ ion production process was occurring. Since no other positive ions were observed to be decaying early in the afterglow, this process was thought to be ionization of oxygen by collision with metastable helium atoms. The energy available from a metastable atom is sufficient both to ionize an oxygen molecule and to dissociate the excited ion so formed. Thus

$$He_m + O_2 \rightarrow O_2^{+\prime} + He + e^- \quad \ldots\ldots (13)$$

followed after a very short time by

$$O_2^{+\prime} \rightarrow O^+ + O \quad \ldots\ldots (14)$$

leaving an energy surplus of 1·1 ev.

The examples of O^+ ion decays given in figure 4 show clearly the curvature described above. It should be pointed out that the oxygen partial pressures were not the same from graph to graph in these examples, so that they would not be expected to show the same gradient.

The time, for which the deviation from an exponential decay lasted, varied with the discharge conditions, possibly because it was a function of the initial metastable concentration. In some cases (e.g. figure 4 (*d*)) the curvature persisted until the O^+ ion current was too small for accurate observation of the linear part of the graph. These decays obviously could not be used in the charge exchange measurements, and were rejected. This was only necessary for about 4% of the observed decays. One third of all the decays showed no curvature (as figure 4 (*a*)), and half showed only slight curvature at early times (figure 4 (*b*)).

6.4. *Summary*

For the above reasons it is considered that during the exponential O^+ ion decays, the only effective process for production or loss of O^+ ions was charge exchange.

As further justification for this view it was found that, within the usable range of pressures the logarithmic decay coefficient was directly proportional to the oxygen partial pressure, as expected (§ 2).

The present experimental value for the charge exchange rate coefficient is not inconsistent with a theoretical estimate by Bates (1955) based on an ion exchange mechanism. He concludes that the rate coefficient for ion exchange could be as high as 10^{-10} cm^3 sec^{-1}.

§ 7. Charge Exchange in the Ionosphere

It is generally accepted that the main positive ions in the upper ionosphere, particularly in the F2 layer, are atomic in form. This conclusion is supported by recent rocket and satellite measurements which identify the positive ions as O^+, and by the conclusion (Penndorf 1950) that photo-chemical dissociation of molecular oxygen should be nearly complete at these altitudes. Since there can be few negative ions in the F2 layer (Bates and Massey 1946, 1947) the only single stage loss mechanism for the O^+ ions is recombination with free electrons, and the cross section for this process is so small that the rate of destruction of O^+

and of electrons would be very slow, much slower than has in fact been observed (Ratcliffe *et al.* 1956). Similar considerations to the above led Bates and Massey (1946) to suggest that the loss process for ionization in the F2 region, and possibly also in the rather lower F1 layer, is a two stage process, thus:

(*a*) Charge exchange collisions between O^+ ions and oxygen molecules (process 1, § 2), it being supposed that the latter are present as a very small fraction of the total gas.

(*b*) Fast recombination of the resultant O_2^+ ions with free electrons, by the dissociation process

$$O_2^+ + e^- \rightarrow O' + O'. \qquad \ldots\ldots (15)$$

The existence of the small proportions of O_2, necessary for the above processes, can be accepted on the basis of predictions by Nicolet and Mange (1954) that diffusion and turbulence would produce a detectable molecular concentration at F layer altitudes. Confirmation of this has been obtained by rocket measurements of the absorption by molecular oxygen of solar ultra-violet light (Byram Chubb and Friedman 1955).

In the case where the molecular oxygen concentration is low, and particularly in the F2 layer, the average life of the O^+ ion may be quite long compared with the life of the O_2^+ ions, which are lost by the rapid process of dissociative recombination with the free electrons. The O^+ ions will thus be the main ion type, and the loss rate for electrons will therefore be determined by the charge exchange rate for the atomic positive ions.

Ratcliffe and others (1956) have measured the electron loss rate in the F2 layer, and have summarized their results in the formula

$$\alpha(\mathrm{F2}) = \frac{10^{-4}}{n_e} \exp\left(\frac{300 - z}{50}\right) \mathrm{cm^3\,sec^{-1}} \qquad \ldots\ldots (16)$$

where $\alpha(\mathrm{F2})$ is the effective recombination coefficient for the height z (km), and n_e is the electron concentration.

If we take a typical value of $n_e = 8 \times 10^5\,\mathrm{cm^{-3}}$ at an altitude of 300 km, we obtain

$$\alpha(\mathrm{F2}) = 1{\cdot}2 \pm 0{\cdot}4 \times 10^{-10}\,\mathrm{cm^3\,sec^{-1}}.$$

If, however, the decay of electrons is limited by charge exchange we may write

$$\alpha(\mathrm{F2}) = \frac{k_1[\mathrm{O_2}]}{n_e}\,\mathrm{cm^3\,sec^{-1}}, \qquad \ldots\ldots (17)$$

where k_1 is the rate coefficient for charge exchange (§ 2).

If the value of k_1 measured experimentally in this work, is combined with Ratcliffe's value above for $\alpha(\mathrm{F2})$, it is possible to calculate the molecular oxygen concentration as $3{\cdot}8 \pm 1{\cdot}4 \times 10^6\,\mathrm{cm^{-3}}$ at 300 km. This value is obtained on the assumption that k_1 is approximately the same at 300 K (laboratory) as at 1100 K (probable gas temperature in the F2 layer). This point might be clarified by interpolation if ion beam measurements of k_1 at higher energies were available.

Another value of $[O_2]$ is found to be of the order $3{\cdot}8 \times 10^6\,\mathrm{cm^{-3}}$, from a model atmosphere extrapolated to high altitudes, using tentative mass spectrographic results from Aerobee rockets, combined with some theoretical predictions (Hulburt 1955).

These two predictions of the molecular oxygen concentration are thus in close agreement.

§ 8. Conclusion

The rate coefficient for the reaction

$$O^+ + O_2 \rightarrow O_2^+ + O$$

is found to be $2{\cdot}5 \pm 0{\cdot}4 \times 10^{-11}\,cm^3\,sec^{-1}$, at gas temperatures of approximately 300°K, corresponding to a cross section of $3{\cdot}2 \pm 0{\cdot}5 \times 10^{-16}\,cm^2$.

This value confirms the view that dissociative recombination with molecular oxygen ions produced by the above charge exchange reaction could be the primary electron loss process in the F2 layer, and the molecular oxygen concentration at F2 altitudes is predicted to be $3{\cdot}8 \pm 1{\cdot}4 \times 10^6\,cm^{-3}$, in close agreement with a model atmosphere drawn up in 1955.

Acknowledgments

The authors wish to thank Dr. L. W. Kerr, who developed and built the mass spectrometer, and Dr. G. R. Court, who gave valuable assistance with the experimental work. One of us (P. H. G. D.) is grateful to the Department of Scientific and Industrial Research for a Research Studentship.

References

Bates, D. R., 1955, *Proc. Phys. Soc.* A, **68,** 344.
Bates, D. R., and Massey, H. S. W., 1946, *Proc. Roy. Soc.* A, **187,** 261.
—— 1947, *Ibid.*, **192,** 1.
Boyd, R. L. F., and Morris, D., 1955, *Proc. Phys. Soc.* A, **68,** 1.
Byram, E. T., Chubb, T. A., and Friedman, H., 1955, *Phys. Rev.*, **98,** 1594.
Ghosh, S N., and Sheridan, W. F., 1957, *J. Chem. Phys.*, **26,** 480.
Hasted, J. B., and Gilbody, H. B., 1957, *Proc. Roy. Soc.* A, **238,** 334.
de Heer, F. J., Huizenga, W., and Kistemaker, J., 1955, *Appl. Sci. Res.*, **5B,** 337.
Hulburt, E. O., 1955, *Advances in the Physics of the Upper Air since* 1950 (Washington, D.C.: Naval Research Lab.).
Kerr, L. W., 1953, *Ph. D. Thesis*, Queen's University of Belfast.
Nicolet, M., and Mange, P., 1954, *J. Geophys. Res.*, **59,** 15.
Penndorf, R., 1950, *Phys. Rev.*, **77,** 561.
Ratcliffe, J. A., Schmerling, E. R., Setty, C. S. G. K., and Thomas, J. O., 1956, *Phil. Trans. Roy. Soc.* A, **248,** 609.
Ziegler, B., 1953, *Z. Phys.*, **136,** 108.

The Elastic and Inelastic Scattering of 19·6 MeV Deuterons by Mg

By G. W. GREENLEES and J. LOWE
Physics Department, University of Birmingham

MS. received 21*st January* 1960, *in final form* 29*th February* 1960

Abstract. Absolute differential cross sections are presented for the inelastic scattering of 19·6 MeV deuterons by ^{24}Mg leading to the first excited state at 1·37 MeV, in the angular range 15°–120° (c.m.). The angular distribution shows a sharp rise at forward angles ($\theta_{c.m.} < 40°$) and a rather weak oscillation at more backward angles. It is concluded from an analysis of the results that the electric contribution to the scattering is smaller than has been previously assumed, and that a distorted wave treatment is essential if a satisfactory fit is to be achieved. Absolute differential cross sections are also presented for the elastic scattering of 19·6 MeV deuterons by Mg.

§ 1. Introduction

The inelastic scattering of deuterons by nuclei has been observed by several authors (Greenlees, Kempton and Rhoderick 1949, Greenlees 1955, Holt and Young 1949, Haffner 1956, Hinds, Middleton and Parry 1957 and others) in the energy range 5–15 MeV. The analysis of these results has generally been in terms of two theoretical treatments of inelastic deuteron scattering, based on two alternative assumptions as to the reaction mechanism. In the first (Huby and Newns 1951), the scattering is assumed to take place through the interaction of one nucleon of the deuteron with the surface of the target nucleus, the other nucleon remaining too far from the target nucleus to interact with it. This approach is suggested by the success of stripping theories based on the same assumption (e.g. Butler 1951, Friedman and Tobocman 1953). The second theory is that of Mullin and Guth (1951) in which it is assumed that the scattering results from the electric interaction between the deuteron and the target nucleus.

Hinds, Middleton and Parry (1957), using 8·9 MeV deuterons, obtained an angular distribution for the ^{24}Mg(d,d′)^{24}Mg* (1·37 MeV) reaction which showed moderate agreement with the theory of Huby and Newns (1951) using an interaction radius of 7×10^{-13} cm. Haffner (1956) analysed his results for the inelastic scattering of 15·1 MeV deuterons by several nuclei, including ^{24}Mg, in terms of the two theoretical treatments but was unable to obtain a satisfactory fit with either theory. He found that, in general, the angular distributions rose too sharply at forward angles to fit the nuclear interaction theory (i.e. that of Huby and Newns) alone. This sharp forward rise is more characteristic of the electric interaction theory, but this theory did not fit the angular distributions at backward angles, nor could it reasonably account for the absolute magnitude of the observed cross sections. Haffner therefore concluded that both electric and nuclear interactions are of comparable importance in inelastic deuteron scattering.

Following Haffner's work, Mamasakhlisov and Kopaleishvili (1958) have calculated the differential cross sections using both electric and nuclear terms in the deuteron–nucleus interaction. In the present paper, an investigation of the inelastic scattering of 19·6 Mev deuterons by ^{24}Mg is described and the results are compared with the theory of Mamasakhlisov and Kopaleishvili.

The success of the optical model in the analysis of elastic proton scattering by nuclei (cf. Feshbach 1958) has led many workers to investigate the elastic scattering of composite particles to determine whether the model can provide an equally simple description in this case also. Some success has been achieved in the case of α-particles (Igo and Thaler 1957, Cheston and Glassgold 1957), and the parameters of the complex well used are of interest since they reflect some features of the interaction of the α-particle with the nucleus. In the case of elastic deuteron scattering, the experimental information is not yet extensive, although several angular distributions have been obtained at 21·6 Mev by Yntema (1959). The problem is of interest, since the composite structure of the deuteron is known to be important in its interaction with nuclei (e.g. from the large observed stripping cross sections), whereas this composite structure is not included explicitly in the optical model. In the present paper, a determination of the differential cross section for elastic deuteron scattering by natural Mg is described.

Experimental studies of deuteron scattering are complicated by the high, positive Q-value and large cross section of the (d, p) reactions. Detection of deuterons in the presence of protons from this reaction was achieved in the present experiment by means of a $(dE\ dx, E)$ particle selecting system, described in § 2 of this paper.

§ 2. Experimental Method

The 19·7 Mev external deuteron beam of the Nuffield cyclotron at Birmingham University was collimated, passed through a target at the centre of a 12 in. scattering chamber, collected in a Faraday cup and integrated. Particles scattered by the target were detected by a CsI(Tl) scintillation counter system mounted on the rotable lid of the scattering chamber.

The apparatus and experimental method were identical with those described by Greenlees *et al.* (1957 a, b) except that in the present experiment the detection system comprised two scintillation counters in series in the path of scattered particles. In the first, the phosphor was a $\frac{1}{2}$ mm thick CsI(Tl) crystal, and light collected from the side of this crystal was detected by a Dumont 6292 photomultiplier. The stopping power of the crystal was equivalent to about 100 mg cm^{-2} of Al. Since this is small compared with the range of protons or deuterons at the energies of interest, the counter measured essentially the specific energy loss dE/dx of a particle passing through it. The second counter was sufficiently thick to stop all particles entering the detection system, and therefore measured the residual energy E. This counter has already been described by Greenlees *et al.* (1957 a).

Signals from the two counters were amplified, shaped and applied to the X and Y plates respectively of a cathode-ray tube whose beam was brightened by a coincidence signal from the two counters. When a particle entered the detection system, therefore, a bright spot was produced on the cathode-ray tube screen,

lying on a line on the screen representing a graph of dE/dx against E. Since such a graph depends on the charge and mass of the particle, spots corresponding to protons and deuterons lay at different regions of the cathode-ray tube screen.

This is demonstrated in figure 1 (Plate), which shows a time exposure photograph of the cathode-ray tube screen when both protons and deuterons were entering the counter. As can be seen from figure 1, the proton and deuteron traces can easily be distinguished on the screen, and to examine the spectrum of scattered deuterons, the screen was masked so that only the deuteron curve was visible, and a photomultiplier was mounted in front of the cathode-ray tube. Pulses from this photomultiplier were used to gate a 100 channel Hutchinson–Scarrott pulse height analyser, which was arranged to analyse the pulses from the E counter.

With a 4·5 mg cm^{-2} Mg target in position, the deuteron spectra obtained on the pulse height analyser showed groups which were attributed to deuterons elastically scattered by ^{24,25,26}Mg, and to inelastically scattered deuterons leading to the first excited state in ^{24}Mg at 1·37 MeV. Spectra were recorded at scattering angles between 15° and 110° and angular distributions for the two groups were obtained. Since the coincidence efficiency and effective solid angle of the detection system were not known, accurate absolute cross sections could not be determined directly.

§ 3. Results

Four typical spectra obtained on the pulse height analyser are shown in figure 2. The principal difficulty in extracting cross sections from the experimental spectra was the incomplete separation of the two groups. The 33° spectrum

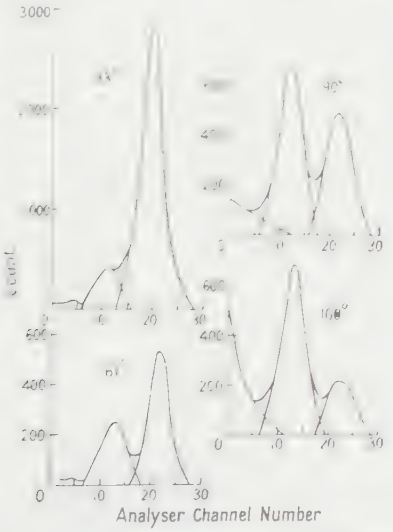

Figure 2. Four pulse height spectra for 33°, 61°, 90° and 100° (c.m. system) respectively. Bias was used in the pulse height analyser in each case so that the zeros of the energy scales are not shown.

shows a case where this difficulty was particularly severe, whereas in the spectrum for 61° the separation is comparatively good. The spectra for 90° and 100° show how difficulties arose at backward angles from the presence of background due to inelastic scattering by ^{25}Mg, and to gamma ray pulses admitted by random

coincidences between the two counters. In no case did significant errors arise from proton contamination of the spectra.

Determination of the absolute values of the differential cross sections obtained from the spectra was carried out in two ways:

(i) A single elastic cross section measurement was made at 33° using the single counter system described by Greenlees *et al.* (1957 a, b). This system measures absolute differential cross sections, but cannot distinguish protons from deuterons in the detection system, and subtraction of the proton background from the elastic deuteron peak was therefore necessary. The accuracy of this method is limited by this background subtraction to $\pm 15\%$.

(ii) A preliminary optical model analysis of the elastic scattering results (Hodgson, private communication: cf. § 4.2) showed that, for a range of reasonable parameters for the complex well, the cross sections at forward angles ($\theta_{\text{c.m.}} < 30°$) is nearly independent of the well parameters. The analysis was also applied to the results of Yntema (1959) for the elastic scattering of 21·6 Mev deuterons by Mg. Although a perfect fit to either set of results was not achieved, the independence of the calculated cross sections of the well shape suggests that the ratio of the cross sections for 19·6 Mev and 21·6 Mev at small angles should be given reliably by the calculations. Normalization of the elastic angular distribution to the value computed from Yntema's results at forward angles using the optical model calculations therefore provides absolute scales for both elastic and inelastic cross sections. The absolute values obtained by this method were 20% higher than those given by (i) above. It was felt that this method was more reliable than method (i); however, there is no real discrepancy in view of the limited accuracy of either method.

The results for inelastic and elastic scattering are shown in figures 3 and 4 respectively. The elastic scattering results are presented as the ratio of the observed to the Rutherford cross sections. The errors shown in these figures

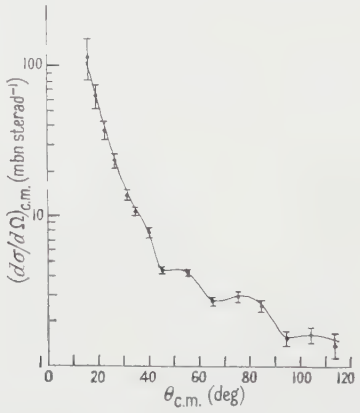

Figure 3. Inelastic scattering of 19·6 Mev deuterons by ^{24}Mg ($Q = -1{\cdot}37$ Mev).

are relative (at different scattering angles) only. For the inelastic scattering, they arise principally from uncertainties in the graphical separation of the two groups from each other and from the background, the statistical uncertainty being less than 3% in general. For the elastic scattering, an additional relative error, significant at small angles, arises from errors in the computed Rutherford cross sections due to uncertainties in the scattering angles.

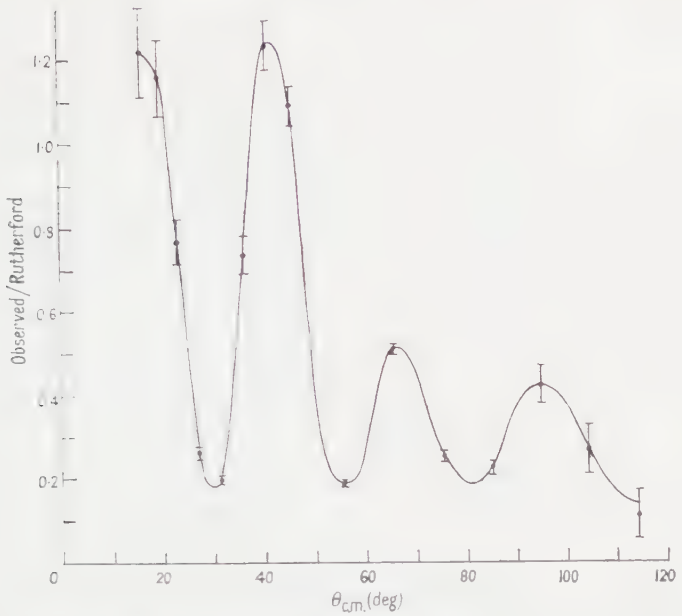

Figure 4. Ratio of observed to Rutherford cross sections for the elastic scattering of 19·6 MeV deuterons by Mg.

All cross sections in figures 3 and 4 are subject to an additional absolute error. As discussed above, this error is difficult to determine, but is estimated at $\pm 10\%$. All scattering angles are accurate to $\pm 0{\cdot}2°$. The incident beam energy at the centre of the target was $(19{\cdot}6 \pm 0{\cdot}2)$ MeV. Numerical values for the observed cross sections are given in tables 1 and 2.

Table 1. Elastic Scattering of Deuterons by Mg

$\theta_{c.m.}$ (deg)	$(d\sigma/d\Omega)_{c.m.}$ (mbn sterad^{-1})	Observed cross section / Rutherford cross section
16·2	1820 ± 110	1·26 ± 0·11
19·5	810 ± 40	1·19 ± 0·09
22·8	296 ± 15	0·79 ± 0·06
26·8	54·1 ± 2·7	0·274 ± 0·016
31·2	22·8 ± 1·1	0·208 ± 0·012
35·8	48·6 ± 2·5	0·75 ± 0·05
40·6	50·3 ± 2·5	1·26 ± 0·06
45·5	28·8 ± 1·1	1·12 ± 0·05
55·3	2·40 ± 0·10	0·195 ± 0·007
65·3	3·57 ± 0·11	0·530 ± 0·016
75·3	1·03 ± 0·05	0·264 ± 0·013
85·1	0·646 ± 0·052	0·236 ± 0·018
94·7	0·86 ± 0·10	0·44 ± 0·05
104·3	0·43 ± 0·10	0·28 ± 0·06
113·9	0·140 ± 0·070	0·119 ± 0·06

Incident deuteron energy (lab. system) = $(19{\cdot}6 \pm 0{\cdot}2)$ MeV.

Error in $\theta = \pm 0{\cdot}2°$.

Errors in columns 2 and 3 are relative (at different scattering angles) only, and all values in these columns are subject to an absolute error of $\pm 10\%$.

Quoted errors in column 3 include the uncertainty in the computed Rutherford cross section arising from the angular error.

Table 2. Inelastic Scattering of Deuterons by ^{24}Mg ($Q = 1{\cdot}37$ MeV)

$\theta_{\text{c.m.}}$ (deg)	$(d\sigma/d\Omega)_{\text{c.m.}}$ (mbn sterad^{-1})
16·3	113 ± 34
19·5	63 ± 11
22·9	36 ± 5
26·9	23 ± 2·5
31·3	13·4 ± 1·0
35·9	10·3 ± 0·6
40·7	7·65 ± 0·45
45·7	4·26 ± 0·26
55·5	4·13 ± 0·26
65·5	2·66 ± 0·18
75·4	2·86 ± 0·23
85·3	2·55 ± 0·26
95·0	1·54 ± 0·17
104·5	1·61 ± 0·21
114·0	1·38 ± 0·27

Incident deuteron energy (lab. system) = (19·6 ± 0·2) MeV.
Error in $\theta = \pm 0{\cdot}2°$.
Quoted errors in the cross sections are relative (at different scattering angles) only, and all values in column 2 are subject to an absolute error of ± 10%.

§ 4. Discussion

4.1. *Inelastic Scattering*

The present results show some similarity to those of Haffner (1956) at 15·1 MeV in that the angular distribution exhibits a rather weak oscillation at angles greater than about 40°, and rises sharply at more forward angles. These features were interpreted by Haffner as being due to the nuclear and the electric scattering respectively. The calculation of Mamasakhlisov and Kopaleishvili, which includes both electric and nuclear terms in the deuteron–nucleus interaction, should therefore be appropriate for an analysis of the present results.

In this calculation, scattering by a deformed nucleus is considered. This is relevant to ^{24}Mg, which is known to have a deformation of $\beta = 0{\cdot}63$, and a quadrupole moment of ten times the single particle value (Rakavy 1957). The nuclear interaction is assumed to be localized at the nuclear surface, and the calculation is carried out in Born approximation, using plane waves, with a cut-off at the nuclear surface, for the deuteron translational wave functions. These approximations are similar to those used by many workers (e.g. Austern, Butler and McManus 1953, Butler 1957) for inelastic proton and α-particle scattering, and are known to yield reasonable agreement with experiment, in general, at incident energies above about 15 MeV. Further approximations are made by Mamasakhlisov and Kopaleishvili which amount to neglect of the finite size of the deuteron at certain points in the calculation.

Mamasakhlisov and Kopaleishvili take the nuclear charge distribution radius R to be equal to the cut-off radius for nuclear interaction R_0. This is a bad

approximation in the present case since the cut-off radius is found to be much larger than the known charge radius (Rakavy 1957). The charge radius R enters the calculation of Mamasakhlisov and Kopaleishvili only as $ZR^2\beta$ which is $\frac{1}{3}(5\pi)^{1/2}$ times the intrinsic quadrupole moment Q_0. In the present case Q_0 is known, so that explicit values of R and β are not required. The cut-off radius occurring in the electric interaction term (the r_0 of Mamasakhlisov and Kopaleishvili) would be expected to be approximately equal to R_0 the cut-off radius for the nuclear interaction. In fact the calculated cross section is insensitive to the precise value chosen for r_0, and in the present analysis it was set equal to R_0.

With the above modifications, the expression for the angular distribution for a $0^+ \rightarrow 2^+$ transition becomes

$$\frac{d\sigma}{d\Omega} = \frac{\mu^2}{\pi\hbar^4}\left(1 \pm \frac{Q}{E}\right)^{1/2}\left[\frac{\pm\alpha}{q}\tan^{-1}\left(\frac{q}{\pm\alpha}\right)\right]^2 \times\left\{\pm 2V_0R_0^2\beta j_2(qR_0) + 0{\cdot}2(5\pi)^{1/2}Q_0e^2\frac{j_1(qR_0)}{qR_0}\right\}^2$$

where μ is the reduced mass, E is the incident energy, $(E+Q)$ the outgoing energy, and $1/\alpha = 4{\cdot}31\times10^{-13}$ cm is the deuteron 'size'. The parameter q is $\hbar$ times the momentum transfer, Q_0 is the intrinsic quadrupole moment ($-0{\cdot}66$ barn, see Rakavy 1957) and V_0 is the strength parameter for the nuclear interaction. The first and second terms in the braces correspond respectively to scattering by the nuclear and electric terms in the interaction.

For any realistic choice of parameters, only the nuclear term is appreciable at angles greater than 30°, and R_0 has been determined from the angular distribution in this region. The value of V_0 for a best fit is somewhat arbitrary.

A comparison of the theoretical prediction with the present results is shown in figure 5. Theoretical curves are presented for both positive and negative values of V_0, since the sign cannot be deduced from the experimental results. Three conclusions follow immediately from the comparison:

(i) The interaction radius is large; a value of $R_0 = 6{\cdot}8\times10^{-13}$ $(=2{\cdot}36A^{1/3})$ cm was used to fit the results. It is well known that large nuclear radii are required to fit direct interaction calculations, especially where composite incident particles are involved (cf. Butler 1957). However the radius found here is larger than is usually required for reactions such as (p, p′), (p, α), (α, α′) and (d, p); for example, a value of $5{\cdot}5\times10^{-13}$ cm was used by Butler in the analysis of ^{24}Mg (α, α′) exciting the same level as in the present experiment, and a value $5{\cdot}2\times10^{-13}$ cm was used by Hinds, Middleton and Parry (1958) in the analysis of a number of ^{24}Mg (d, p) reactions.

The large radius presumably reflects the high probability of break-up of the deuteron in nuclear matter.

(ii) The contribution from electric scattering is small, and is negligible at angles greater than 30°. In particular, it cannot account for the sharply rising cross section at forward angles.

(iii) The zeros in the theoretical curve at angles greater than 30° are not observed experimentally. This is a well-known effect and has been discussed by Butler (1957). It arises from failure of the approximation of a well-defined interaction radius. The effect is normally found only at energies below about 15 MeV, where it is usually attributed to an appreciable penetration of the incident

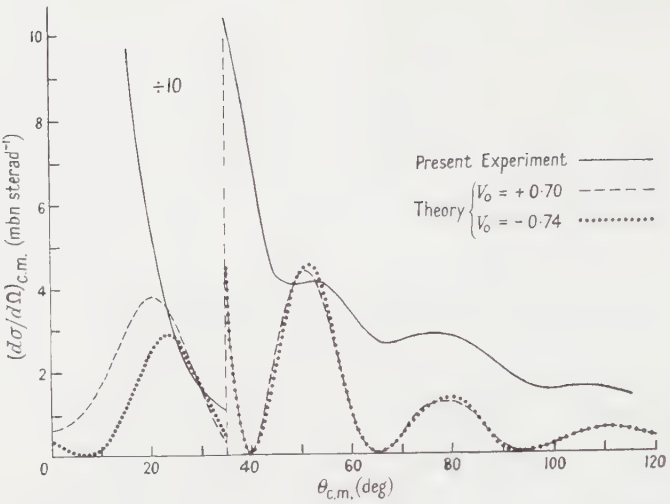

Figure 5. A comparison of the present inelastic scattering results with the theoretical predictions. The ordinates have been reduced by a factor of 10 in the region below 35°.

wave into the nucleus. However, the large interaction radius found renders this interpretation untenable in the present case.

The absence of the theoretical zeros is not the result of an appreciable compound nucleus contribution, since a crude estimate indicates that this contribution is at least an order of magnitude smaller than the observed cross sections. Direct empirical evidence for the smallness of the compound nucleus contribution comes from the work of Freemantle, Gibson and Rotblat (1954) who were unable to detect deuterons from the reaction ^{12}C (d, d') ^{12}C* ($Q = -7{\cdot}65$ MeV) at 19·1 MeV. Scattering to this state is forbidden because it does not arise from a single particle excitation of the ground state configuration, a selection rule which applies to direct interaction but not to compound nucleus scattering.

It is apparent from (ii) above that an alternative explanation of the sharply rising forward cross section must be found. This cannot be an effect of the finite size of the deuteron, since Mamasakhlisov and Kopaleishvili's result can be modified to include finite size effects correctly, giving an angular distribution essentially identical with that shown in figure 5. The work of Levinson and Banerjee (1958) has shown that a similar forward rise observed in inelastic proton scattering can be explained if distorted waves rather than plane waves with a sharp cut-off, are used for the translational wave functions in the calculation of the matrix element. The use of a distorted wave calculation to fit the present results would also be essential if a satisfactory fit is to be achieved in the backward angle region, since in such a calculation, the approximation of a well-defined interaction radius is not used. No distorted wave treatment has been published for deuteron scattering, but for certain choices of parameters, the proton calculations of Levinson and Banerjee show considerable similarity to the present results. Since the finite size of the deuteron does not appreciably affect the angular distribution it seems likely that a satisfactory fit can be achieved by this means. Recently, Tobocman (1959) has obtained improved fits to (d, p) angular distributions using a distorted wave treatment.

4.2. *Elastic Scattering*

The present results show a general similarity to many results for the elastic scattering of intermediate energy protons by nuclei, in that the angular distributions show maxima and minima characteristic of a diffraction pattern, as would be expected if they are to be interpreted in terms of scattering by a complex potential. Also, the present results show a strong similarity to those of Yntema (1959) for the elastic scattering of 21·6 MeV deuterons by Mg. This is again consistent with an optical model interpretation, since the scattering by a complex potential cannot change appreciably in an energy interval small compared with its imaginary part. Of course, the two sets of results were normalized to agree at forward angles; however, the similarity extends throughout the entire angular range studied.

A preliminary optical model analysis has been attempted (P. E. Hodgson, private communication). However, no results are given here, since more data, especially at backward angles, are required to enable meaningful and unambiguous values of the optical model parameters to be deduced from the analysis.

Acknowledgments

The authors wish to thank all members of the Cyclotron Scattering Group for help in recording the results. They are also grateful to Dr. P. E. Hodgson for work on the optical model analysis of the elastic scattering results. One of us (J. L.) also wishes to thank the Department of Scientific and Industrial Research for financial support.

References

Austern, N., Butler, S. T., and McManus, H., 1953, *Phys. Rev.*, **92,** 350.
Butler, S. T., 1951, *Proc. Roy. Soc.* A, **208,** 559.
—— 1957, *Phys. Rev.*, **106,** 272.
Cheston, W. B., and Glassgold, A. E., 1957, *Phys. Rev.*, **106,** 1215.
Feshbach, H., 1958, *Ann. Rev. Nucl. Sci.*, **8,** 49.
Freemantle, R. G., Gibson, W. M., and Rotblat, J., 1954, *Phil. Mag.*, **45,** 1200.
Friedman, F. L., and Tobocman, W., 1953, *Phys. Rev.*, **92,** 93.
Greenlees, G. W., 1955, *Proc. Phys. Soc.* A, **68,** 97.
Greenlees, G. W., Haywood, B. C., Kuo, L. G., and Petravic, M., 1957 a, *Proc. Phys. Soc.* A, **70,** 331.
Greenlees, G. W., Kempton, A. E., and Rhoderick, E. H., 1949, *Nature, Lond.*, **164,** 663.
Greenlees, G. W., Kuo, L. G., and Petravic, M., 1957 b, *Proc. Roy. Soc.* A, **243,** 206.
Haffner, J. W., 1956, *Phys. Rev.*, **103,** 1398.
Hinds, S., Middleton, R., and Parry, G., 1957, *Proc. Phys. Soc.* A, **70,** 900.
—— 1958, *Proc. Phys. Soc.*, **71,** 49.
Holt, J. R., and Young, C. T., 1949, *Nature, Lond.*, **164,** 1000.
Huby, R., and Newns, H. C., 1951, *Phil. Mag.*, **42,** 1442.
Ico, G., and Thaler, R. M., 1957, *Phys. Rev.*, **106,** 126.
Levinson, C. A., and Banerjee, M. K., 1958, *Annals of Physics*, **3,** 67.
Mamasakhlisov, V. I., and Kopaleishvili, T. I., 1958, *Soviet Physics, J.E.T.P.*, **34, (7),** 809.
Mullin, C. J., and Guth, E., 1951, *Phys. Rev.*, **82,** 141.
Rakavy, G., 1957, *Nucl. Phys.*, **4,** 375.
Tobocman, W., 1959, *Phys. Rev.*, **115,** 98.
Yntema, J. L., 1959, *Phys. Rev.*, **113,** 261.

RESEARCH NOTES

The Luminescence of Uranium-activated Fluorides

By J. E. A. LYS and W. A. RUNCIMAN
University of Canterbury, Christchurch, New Zealand

MS. received 8th February 1960

Powder samples of a number of metal fluorides activated with uranium were prepared, and their low-temperature luminescence spectra upon irradiation with ultra-violet light were examined on a spectrograph.

The following uranium-activated fluorides showed fairly sharp line spectra at 77°K: LiF, NaF, KF, MgF_2, ZnF_2 (weak). The following gave spectra showing a band structure, not resolved into lines : CsF, CaF_2, SrF_2, BaF_2 (weak). CdF_2 gave a weak continuous spectrum. CeF_3 and AlF_3 showed no luminescence.

The luminescence of MgF_2(U), a strong green in colour at 77°K, but weak at room temperature, has not been reported previously. It had been found (Slattery 1929) to be inert at room temperature and at liquid air temperature. The spectrum shows an easily recognizable pattern, with a repetition frequency of 804 cm $^{-1}$. The main lines are listed in table 1, measured using a Hilger large glass spectrograph. The intensities of the lines are given as weak (w), medium (m), or strong (s). Letters have been assigned to some of the lines to show the repetitive nature of the spectrum.

Table 1. Luminescence Lines, MgF_2(U)

Intensity	Wavelength in air (Å)	Wave number *in vacuo* (cm^{-1})	Designation
m	5275·1	18952	
s	5315·7	18807	E_0
m	5332·6	18747	
s	5414·8	18463	D_1
s	5445·4	18359	C_1
m	5501·1	18173	
s	5528·1	18084	A_1
m	5539·2	18048	F_1
s	5553·5	18002	E_1
m	5663·4	17652	D_2
m	5695·0	17554	C_2
m	5729·3	17449	B_2
s	5785·6	17280	A_2
m	5797·6	17244	F_2
m	5813·3	17197	E_2
w	6004·9	16648	B_3
m	6067·7	16476	A_3
w	6079·7	16443	F_3
w	6099·2	16391	E_3
w	6308·7	15847	B_4
w	6378·0	15673	A_4

The fine structure in the luminescence spectra may be attributed to the normal vibrations of the luminescent centres, the latter being regarded, to a certain degree of approximation, as a molecular group. The vibrational energy levels of the centre are superimposed upon the electronic energy levels. The low-temperature luminescence spectrum arises from transitions from a common excited state level, or perhaps from a small number of excited state levels, to a variety of vibrational levels of the electronic ground state.

Magnesium fluoride, MgF_2, has the rutile structure, in which each Mg^{2+} ion has six neighbouring F^- ions, four of which, at the corners of a square, are slightly closer than the other two. If a hexavalent uranium ion U^{6+} replaces a Mg^{2+} ion in the crystal lattice, charge compensation could be satisfied most simply by replacement of the four nearest F^- ions by O^{2-} ions from the air. This replacement of F^- ions by O^{2-} ions has been shown to occur in the formation of NaF(U) (Runciman 1956).

Thus the luminescent centre in MgF_2(U) could be a (UO_4F_2) group, probably in the form of a slightly distorted octahedron, with the four O^{2-} ions at the corners of a square. Then the 504 cm^{-1} repetition frequency would correspond to a normal vibrational mode of this centre, treated as a separate molecular group.

The absorption spectrum of MgF_2(U) at 77° K was also found to be a line spectrum, but without any recognizable pattern. The main absorption lines are listed in table 2.

Table 2. Absorption Lines, MgF_2(U)

Intensity	Wavelength in air (Å)	Wave number *in vacuo* (cm^{-1})
m	5018·3	19922
w	5141·9	19443
m	5159·8	19375
w	5193·2	19251
w	5199·1	19229
m	5272·8	18960
w	5315·4	18808 (E_0)

The line E_0 at 5315·7 Å appears to be the fundamental line of the luminescence spectrum, and is a resonance line. Observations at lower temperatures would be necessary to see whether luminescence lines at higher energies than E_0 disappear and whether absorption at E_0 persists at these temperatures. If so, then E_0 would correspond to a transition between the lowest (zero) vibrational levels of the two electronic states concerned

The absorption spectra of NaF(U) and LiF(U) were also examined. Improved spectra were obtained for these phosphors by using clear crystal-like samples rather than powder samples. They were prepared by heating powder samples to a temperature above the melting-point of the fluoride and cooling slowly. These samples cut down exposure times considerably, and gave fewer complicating emission lines.

In a detailed interpretation of the NaF(U) luminescence spectrum that has been made (Runciman 1956), it was suggested that the line at 5636 Å was a

resonance line. However, no sign of absorption at this wavelength was found in this work. There may be a resonance line that appears only very weakly in the spectra, being forbidden by selection rules. Such a possible resonance line has been found, at 5603 Å. Observations at lower temperatures could serve as a check on this suggestion; the line should still appear in both spectra at lower temperatures.

References

Runciman, W. A., 1956, *Proc. Roy. Soc.* A, **237**, 39.
Slattery, M. K., 1929, *J. Opt. Soc. Amer.*, **19**, 175.

Magnetic Interaction Domains

By D. J. Craik and E. D. Isaac

Physics Department, University of Nottingham

Communicated by L. F. Bates; MS. received 4th March 1960

§ 1. Introduction

It is generally accepted that in alloys of the Alcomax type, the high coercivity is connected with the growth, during tempering, of fine, elongated precipate particles. These particles are too small to contain domain boundaries and hence their magnetization cannot be reversed by wall motion, but must rotate in response to a demagnetizing field: in spherical particles this rotation takes place against the magnetocrystalline anisotropy. Calculations by Néel (1947) and by Stoner and Wohlfarth (1948) predicted that for elongated single domain particles, high coercivities should arise due to the shape anisotropy of the particles, and the high coercivity of Alcomax is customarily explained in this way.

However, Bitter figure studies by various workers, notably Nesbitt and Williams (1950) and Andrä (1956), have shown that apparently normal domain structures are still present even in specimens possessing the optimum magnetic properties. It was tentatively suggested by these authors that the patterns they obtained represented magnetically coherent regions in which the smaller oriented particles are uniformly magnetized in the same direction, and evidence to support this idea has recently been produced in this laboratory.

The observation of these large scale structures on magnetically hard Alcomax does not, on its own, exclude the possibility that they are normal domains, since the structure and constitution of this material is not precisely known. Although the precipitate structure is apparently necessary for high coercivities, the respective contributions of the matrix and the precipitate to the magnetism of the material as a whole are not yet clear, and domain walls could conceivably run through both components. It seemed that this important topic could be resolved by examination of a better defined material.

Such a material has recently been developed by the General Electric Company. It consists simply of elongated single domain iron particles embedded in a non-magnetic matrix. These particles are approximately 150 Å in diameter and have very large elongation factors. They are aligned in a magnetic field and compacted

in a matrix of mercury. The iron particles are coated by a thin layer of tin, the purpose of this non-magnetic coating being to prevent direct contact which would lead to loss of coercivity due to fanning etc. (Jacobs and Bean 1955).

§ 2. Experimental Procedure

The elongated single domain iron particle specimen described here was a rectangular block of dimensions 0·05 in. × 0·25 in. × 0·5 in. It had a coercivity of 720 Oe, a remanence of 8910 gauss and a $(BH)_{max}$ of $4{\cdot}08 \times 10^6$ gauss Oe. The wide surface was polished on graded diamond powders and although a bright metallic surface could be obtained with care, it was not found possible to eliminate all the scratches. The direction of polishing was normal to the long ('easy') axis. Bitter figures were studied in the conventional manner with the specimen between the pole-pieces of an electromagnet. In the demagnetized condition some patterns formed on many parts of the surface and the behaviour of the patterns on one such region is described.

Figure 1† represents saturation, the bands of colloid running normally to the easy direction being due to surface undulations. As the applied field was reduced, a very faint zigzag boundary was observed to originate at a fault in the surface and move rapidly across the field of view. This is shown by the arrows in figure 2. After these patterns had completely disappeared, the specimen remained in the condition represented by figure 1. When the applied field was reduced further and reversed, the patterns shown in figures 3 and 4 were observed. In figure 3 are seen indistinct structures of the same form as the normal spike domains seen on uniaxial materials and the growth of these structures as demagnetization proceeds is again similar to growth of spikes.

§ 3. Discussion

Two quite different and distinct processes have been observed. The first, the formation and movement of the zigzag boundaries, is assumed to have no direct relation with the elongated single domain material, but to represent the demagnetization and resaturation of a thin magnetic film on the surface of the specimen. This film, presumably consisting of iron or an iron alloy with the matrix material, is thought to have been produced by the effects of polishing, i.e. it is a Beilby layer. Zigzag boundaries running normally to the easy direction have frequently been observed in thin films of iron; see, for example, Williams and Sherwood (1957). These boundaries could not, in this case, represent the magnetic structure of the specimen as a whole since they had completely disappeared before the reversal of the externally applied field.

The second process observed was the growth of structures during demagnetization of the specimen as a whole which, as noted above, resembles closely the domain processes occurring in a normal uniaxial material. However, it is clear that large scale domains, i.e. regions of uniform magnetization in which all the atomic moments are aligned, cannot exist in these magnetically discontinuous elongated single domain materials. Thus the regions indicated by the powder patterns here must consist of assemblies of the fine iron particles, the magnetic moments of which are all aligned. The shape of each individual particle defines

† For all figures see Plate.

the pair of possible directions of magnetization in it (Stoner and Wohlfarth 1948) but the arrangement of the particles into assemblies must be governed by magnetostatic interaction, and hence it is proposed that these assemblies be termed magnetic interaction domains.

Although it has been shown that the interaction domains behave similarly to Weiss domains, there must be important differences in detail, particularly in the nature and properties of the domain divisions which are of overriding importance in the magnetization process, and further work is being directed towards the estimation of the width and energy of these divisions, and to the elucidation of their structure. It may be noted, for example, that the energy associated with the division is presumably low, since the interaction domains seen are very long and narrow as compared with normal domains in a magnetically similar material, and more precise information of this nature should be obtained in the future.

Acknowledgments

This work has been part of a wider study of permanent magnet materials under the guidance of Professor L. F. Bates. The elongated single domain magnets were kindly supplied by Dr. F. E. Luborsky and T. O. Paine. One of the authors (E.D.I.) thanks the Electrical Research Association for a maintenance grant and for permission to publish.

References

Andrä, W., 1956, *Ann. Phys., Lpz.*, **19,** 10.
Jacobs, I. S., and Bean, C. P., 1955, *Phys. Rev.*, **100,** 1060.
Néel, L., 1947, *C.R. Acad. Sci., Paris*, **224,** 1488, 1550.
Nesbitt, E. A., and Williams, H. J., 1950, *Phys. Rev.*, **80,** 112.
Stoner, E .C., and Wohlfarth, E. P., 1948, *Phil. Trans. Roy. Soc.* A, **240,** 599.
Williams, H. J., and Sherwood, R. C., 1957, *J. Appl. Phys.*, **28,** 548.

LETTERS TO THE EDITOR

The Electrical Resistivity of Monocrystalline and Liquid Bismuth

In recent years the electronic properties of bismuth at low temperatures have been extensively studied and, arising from this work, models for the band structure of the semi-metal have been proposed (see Lax 1958 for a review). Published data for the high temperature resistivity are, however, not in good agreement with one another. Anomalous temperature dependence of the resistivity of both mono- and polycrystalline specimens, including a negative temperature coefficient just below the melting point (so-called 'anticipation of melting'), have been reported which have often been ascribed to phase changes in the bismuth lattice (see for example Pietenpol and Miley 1929). Further, the sensitive dependence of the resistivity on purity, structural perfection and crystallographic direction have not always been appreciated. The results reported here were obtained from measurements on single crystals of high structural perfection and purity and of known orientation.

The bismuth, initially of 99·99% purity was zone refined *in vacuo*. The techniques employed to produce single crystals of the refined material, in the form of rods accurately $\frac{1}{4}$ in. in diameter and approximately 5 in. long, are described elsewhere (Hurle 1959). The orientations of the crystals were determined using a combined optical/x-ray technique (Hurle and Weintroub 1959).

The crystal rod, placed in a specially designed holder of bore equal to the diameter of the rod, was maintained *in vacuo* within a furnace. The resistivity of the rod was deduced from measurements of the potential across two probes which made electrical contact with the rod at a fixed distance apart, when a constant current of 200 mA was passed axially through the rod. The current was supplied through a spring-loaded graphite plug at each end of the rod. When the crystal melted and therefore contracted (approximately 3·4%), the plugs moved under the action of the springs and ensured that the molten bismuth accurately filled the bore of the holder. The resistivity measurements could therefore be continued into the liquid phase. The temperature of the furnace was servo-controlled to rise linearly at 9 deg h^{-1} and the temperature of the rod was measured by two thermocouples embedded in the holder. The thermocouple and probe voltages were continuously recorded on two potentiometric recorders and were very accurately measured at periodic intervals with a Diesselhorst potentiometer.

The variation with temperature T of the electrical resistivity ρ of five single crystals of bismuth and of liquid bismuth is shown graphically in the figure. The range of temperature covered was from approximately 20 °C, through the melting point (271·0 °C), and up to 300 °C. The orientation ϕ of the crystals is the angle between the axis of measurement and the trigonal axis. An equipment failure during the measurement of the $\phi = 67·5°$ crystal prevented the recording of values of ρ between 150° and 200 °C for this crystal. ρ varied linearly with

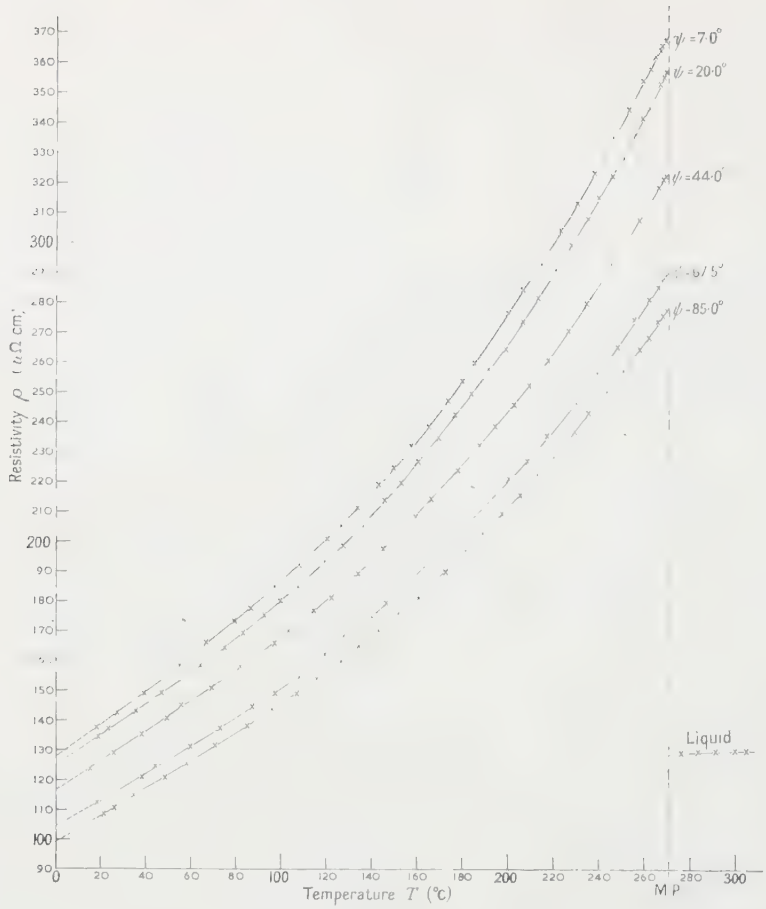

The variation of resistivity ρ with temperature T (experimental results).

$\cos^2\psi$ at constant temperature in agreement with the Voigt–Thomson law. Values of ρ for crystals of $\psi = 0$ and 90° were extrapolated from the $\rho/\cos^2\psi$ plot and are given, together with the estimated errors of measurement, in the table.

The Variation of Resistivity ρ with Temperature T for Crystals of $\psi = 0$ and 90

Resistivity ρ ($\mu\Omega$ cm)		Temperature T (°c)
$\psi = 0$	$\psi = 90$	
$128{\cdot}5 \pm 2{\cdot}4$	$98{\cdot}5 \pm 2{\cdot}2$	0 (Extrapolated)
$138{\cdot}4 \pm 1{\cdot}7$	$108{\cdot}0 \pm 1{\cdot}4$	20
$186{\cdot}1 \pm 2{\cdot}0$	$144{\cdot}6 \pm 1{\cdot}7$	100
$273{\cdot}7 \pm 2{\cdot}6$	$209{\cdot}5 \pm 2{\cdot}2$	200
$366{\cdot}8 \pm 3{\cdot}2$	$274{\cdot}1 \pm 2{\cdot}6$	271

The anisotropy of the resistivity (ρ_0/ρ_{90}) increased very slightly with increasing temperature from 1·28 at room temperature to 1·34 at the melting point. The mean temperature coefficient of resistivity between 0 and 100°c was 448 and $468 \times 10^{-5}\,\mathrm{deg}^{-1}$ for $\psi = 0$ and 90° respectively. The resistivity of liquid bismuth at 271·0°c was $128{\cdot}05 \pm 0{\cdot}80\,\mu\Omega\,\mathrm{cm}$. The change in the resistivity on melting ($\rho_{\mathrm{liq}}/\rho_{\mathrm{sol}}$) was therefore $0{\cdot}349 \pm 0{\cdot}005$ and $0{\cdot}467 \pm 0{\cdot}007$ for $\psi = 0$ and 90°

respectively. Spectrographic analysis of one of the crystals after resistivity measurements had been made on it, showed the only detectable impurities to be 5 parts in 10^6 of tin and 2 parts in 10^6 of copper.

The significant difference between the present results and those of previous authors is the complete absence, in the present work, of any of the reported anomalies ascribed to the existence of phase transformations, 'anticipation of melting' etc. Contrary to the observations of Donat and Stierstadt (1933), ρ_0/ρ_{90} increased steadily right up to the melting point. The value for the resistivity of liquid bismuth at 271 c is about 2% lower than that obtained recently by Roll and Motz (1957). The change on melting is larger (i.e. a smaller value of ρ_{liq}/ρ_{sol}) than that reported by Donat and Stierstadt in 1933: their crystals showed a decrease in ρ just before melting.

The authors wish to thank Messrs. Mining and Chemical Products Ltd. for the gift of the bismuth and for carrying out the spectrographic analysis.

Physical Laboratory,
University of Southampton.
29th February 1960, in final form 31st March 1960.

D. T. J. Hurle.†
S. Weintroub.

Donat, E., and Stierstadt, O., 1933, *Ann. Phys., Lpz.*, **17**, 897.
Hurle, D. T. J., 1959, *Ph.D. Thesis*, University of Southampton.
Hurle, D. T. J., and Weintroub, S., 1959, *Brit. J. Appl. Phys.*, **10**, 336.
Lax, B., 1958, *Rev. Mod. Phys.*, **30**, 122.
Pietenpol, W. B., and Miley, H. A., 1929, *Phys. Rev.*, **34**, 1588.
Roll, A., and Motz, H., 1957, *Z. Metallkunde*, **48**, 272.

† Now at the Royal Radar Establishment, Great Malvern, Worcestershire.

A Thermal Red Shift of the Recoilless γ-Emission of $^{119}Sn^m$

The purpose of this note is to report some measurements of a temperature dependent red shift in the frequency of the recoilless γ-emission discovered by Mössbauer (1958); the existence of this effect was predicted by Josephson (1960), and since this work was started Pound and Rebka (1960a) have independently discovered the effect in ^{57}Fe. The effect may be of importance in the interpretation of experiments designed to measure the gravitational red shift (Pound and Rebka 1959, Cranshaw *et al.* 1960, Pound and Rebka 1960b).

The effect arises as follows. When a nucleus emits a γ-ray its mass decreases by an amount $\delta M = E_\gamma/c^2$, and for a nucleus in a crystal this causes a small rise in all the lattice vibration frequencies. For the recoilless γ-ray discovered by Mössbauer the lattice is in the same quantum state before and after emission (Lamb 1939); the internal energy of the lattice will therefore be greater after emission. This extra lattice energy must be provided by the nuclear transition, so that the energy of the emitted γ-ray is reduced.

If the mass of one atom in a lattice of N identical atoms of mass M is decreased by δM the frequency rise of a given lattice vibration depends on how the position of the atom concerned is related to the pattern of nodes and antinodes of the given vibration. However, the *average* fractional rise in frequency for all lattice modes

is $\delta M/2NM$, provided that $\delta M \ll M$ (Montroll and Potts 1955). Hence the reduction in energy of a γ-ray due to the mass change of the emitting atom is given by

$$\delta E = \frac{E_\gamma}{2NMc^2} U, \qquad \ldots\ldots(1)$$

where U is the contribution to the internal energy of the crystal from lattice vibrations, including zero point energy. The energy shift depends on temperature through the temperature dependence of U, and therefore full resonance absorption will only be obtained if the temperatures T_S, T_A of source and absorber are equal. If the temperatures are unequal full resonance absorption can be restored by moving the source away from the absorber with a velocity v which, from equation (1), is given by

$$\delta v = \frac{1}{2c} \int_{T_S}^{T_A} C_v \, dT, \qquad \ldots\ldots(2)$$

where C_v is the specific heat per unit mass of the material of source and absorber. The velocity δv is a convenient measure of the thermal red shift of the absorber relative to the source.

The source used in the present experiments was $^{119}Sn^{m}$, which emits a 24 kev γ-ray in the process of its decay to the ground state; the low energy of the γ-ray results in an appreciable fraction of recoilless transitions even at room temperature. The source was driven with uniform velocity alternately towards and away from the absorber at a frequency of about 2 c/s. Scalers counting pulses from a scintillation counter and from a standard oscillator were gated for about 80% of the sweep in each direction. The gates could be adjusted accurately to ensure that the scalers counted over the same part of the sweep for the two directions of motion; any residual instrumental asymmetry was eliminated by alternating the phase of the gates and associated scalers relative to the direction of motion.

The absorber foil was contained in an evacuated enclosure and could be cooled or heated by conduction along a copper rod, whereas the source was maintained at room temperature (about 25°C) throughout. For each absorber temperature the counting rate for both directions of motion was measured at two velocities, chosen to correspond to the steep and nearly linear part of the resonance absorption curve (about $2{\cdot}6 \times 10^{-2}$ cm sec^{-1}, whereas the half-width was about $4{\cdot}5 \times 10^{-2}$ cm sec^{-1}). In these circumstances the thermal shift (provided that it is small compared with the line width) is given by

$$\delta v = \tfrac{1}{2}(v_1 - v_2)\left(\frac{n_+ - n_-}{n_1 - n_2}\right) \qquad \ldots\ldots(3)$$

where n_+ and n_- are the counting rates for motion towards and away from the absorber respectively, for one speed, and n_1 and n_2 are the counting rates at speeds v_1 and v_2 respectively, for one direction of motion. In evaluating the results mean values of $n_+ - n_-$ for the two speeds and of $n_1 - n_2$ for the two directions of motion were used. The experimental values of thermal red shift relative to room temperature are shown in the figure as a function of absorber temperature, together with a theoretical curve calculated from equation (2). The errors shown on the points are purely statistical. It can be seen from the figure that experiment and theory are in quantitative agreement within the statistical accuracy.

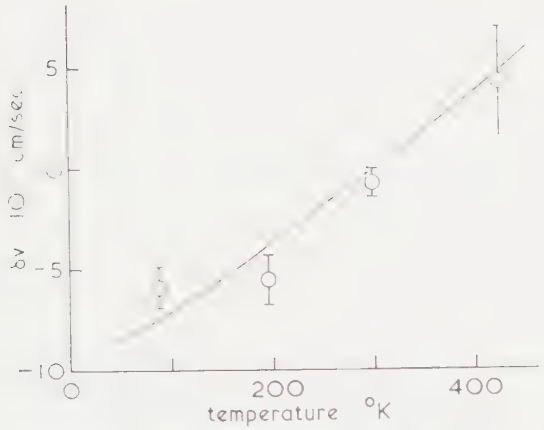

The thermal red shift relative to room temperature; the curve is theoretical (equation (2)).

Equation (2) shows that the effect described above may be very important for experiments designed to measure the gravitational red shift; the importance of accurate temperature control in such experiments may be visualized by noting that if the source were heated by dropping it from a height h, a thermal shift equal to the gravitational shift for height $\frac{1}{2}h$ would be produced. Thus, in a typical experiment with ^{57}Fe a temperature difference of 1 °K between source and absorber would produce an effect equal to the gravitational one (Pound and Rebka 1960 b). For the ^{67}Zn experiment in preparation at Manchester a 1 °K temperature difference would produce about three times the gravitational shift at 20 °K, but only about 2% of the gravitational shift at 4 °K, because of the T^3 variation of the specific heat of zinc in this region. It thus seems that ^{67}Zn at 4 °K gives the best hope of sufficient temperature stability for an accurate measurement of the gravitational red shift.

We should like to thank Dr. D. Shoenberg for bringing Mr. B. D. Josephson's prediction to our notice, and thereby stimulating our thoughts on this subject. We are also grateful to the isotopes division of the Atomic Energy Research Establishment, Harwell, for supplying the ^{119}Sn^{m}.

One of us (C. E.) is indebted to the Department of Scientific and Industrial Research for financial support.

The Physical Laboratories,
University of Manchester.
8th April 1960.

A. J. F. Boyle.
D. St. P. Bunbury.
C. Edwards.
H. E. Hall.

Cranshaw, T. E., Schiffer, J. P., and Whitehead, A. B., 1960, *Phys. Rev. Lett.*, **4**, 163.
Josephson, B. D., 1960, *Phys. Rev. Lett.*, **4**, 341.
Lamb, W. E., 1939, *Phys. Rev.* **55**, 190.
Montroll, E. W., and Potts, R. B., 1955, *Phys. Rev.*, **100**, 525.
Mössbauer, R. J., 1958, *Z. Phys.*, **151**, 124.
Pound, R. V., and Rebka, G. A., 1959, *Phys. Rev. Lett.*, **3**, 439.
—— 1960 a, *Ibid.*, **4**, 274.
—— 1960 b, *Ibid.*, **4**, 337.

CORRIGENDUM

The Measurement of Electron Temperature in High Temperature Plasmas, by R. V. Williams and S. Kaufman (now A. S. Kaufman) (*Proc. Phys. Soc.*, 1960, **75**, 329).

In figure 1 the units along the abscissa *should read*: 0·0, 0·5, 1·0, and not 0, 5, 10.

On page 331, 3rd line from the bottom, table 1 *should read* table 2.

REVIEWS OF BOOKS

Der Raman Effekt, by F. Matossi. Pp. iv + 84. (Brunswick: Friedrich Vieweg und Sohn, 1959.)

Dr. Matossi's monograph on the Raman effect provides a useful introduction into the experimental techniques of Raman spectroscopy and the interpretation of the observed spectra. An opening section on Rayleigh scattering, fluorescence and Raman effect is followed by a detailed account of the spectroscopic methods and the theory of molecular and crystal vibrations which give rise to the Raman spectra. The symmetry characters of the normally occurring symmetry classes are appended in a table. The selection rules for the fundamental and overtones can be derived from it in a simple manner which is fully explained in the text. Examples are given of the elucidation of molecular and crystal structure, in particular in the case of organic molecules for which Raman spectroscopy has provided a wealth of data. The book does not contain a bibliography but references are given in footnotes. L. KELLNER.

Photopiles au Sélénium, by G. Blet. Pp. xiii + 150. (Paris: Dunod, 1958.) 1100 fr.

Hydrodynamics, by D. H. Wilson. Pp. viii + 149. (London: Edward Arnold, 1959.) 30*s*.

Functions of Complex Variables, by P. Franklin. Pp. ix + 246. (London: Pitman, 1959.) 25*s*.

Electromagnetism and Relativity, by E. G. Cullwick. Pp. xxiii + 291. (London: Longmans, Green 1959.) 63*s*.

Absolute Analysis, by F. and R. Nevanlinna. Pp. viii + 259. (Berlin, Göttingen, Heidelberg: Springer, 1959.) DM. 39.

Algebra, by B. L. van der Waerden. Pp. x + 275. (Berlin, Göttingen, Heidelberg: Springer, 1959.) DM. 29.60.

International Journal of Air Pollution, Vol. 1, Nos. 1/2. October, 1958. Pp. ii + 154. (London, New York, Paris, Los Angeles: Pergamon Press.) £6 per volume.

Infra-red Faraday Rotation and Free Carrier Absorption in Bi_2Te_3

By I. G. AUSTIN†

Communication from the Staff of the Research Laboratories of The General Electric Company Limited, Wembley, England

MS. received 5th January 1960, in final form 25th February 1960

Abstract. The Faraday rotation at wavelengths in the range 8–15 μ has been measured on several n- and p-type single crystals of Bi_2Te_3 using a magnetic field of 17 koersteds. The results are interpreted as the sum of rotations arising from free carriers and interband transitions. The latter appear to be sensitive to the impurity content. An attempt has been made to separate the components and use the free carrier rotation to estimate the effective mass parameters.

Free carrier absorption measurements in the range 8–20 μ are also reported. These lead to an independent estimate of the same effective mass parameters, showing fair agreement with the Faraday measurements.

The results are discussed in the light of recent galvanomagnetic measurements on some of the crystals.

§ 1. Introduction

Recent work has shown that useful information concerning the effective mass parameters in semiconductors may be gained from a study of the Faraday rotation associated with free carriers (Mitchell 1955, Moss 1959, Stephen and Lidiard 1959, Austin 1959). According to the Drude–Zener theory, the rotation at infra-red frequencies, for carriers in a simple isotropic energy band, is given by the expression

$$\theta = 1{\cdot}52 \times 10^{-11} \frac{N\lambda^2 B}{n(m^*)^2} \text{ deg metre}^{-1} \text{ (m.k.s. units)} \quad \ldots\ldots (1)$$

where N is the carrier concentration, λ is the wavelength, B the magnetic induction, n the refractive index and m^* the effective mass. Reliable estimates of m^* may be obtained by combining measurements of θ with a knowledge of the carrier concentration from Hall data, as shown by Moss, Smith and Taylor (1959) and Moss and Walton (1959) for InSb and GaAs.

For a complex energy band structure consisting of ellipsoidal energy surfaces in **k**-space the effective mass in (1) is interpreted as an average, depending on the shape and orientation of the ellipsoids. Stephen and Lidiard (1959) have discussed this situation for cubic crystals and Walton and Moss (1959) have verified the theory accurately for n-type Ge.

A corresponding generalization for uniaxial crystals has been given by the present author (Austin 1959, to be referred to as I). An equation similar to (1) was shown to apply for propagation down the optic axis and used to discuss preliminary measurements on Bi_2Te_3. This material is an anisotropic semiconductor (class $R\bar{3}m$), with a small energy gap (0·13 ev), and unusually high refractive index (9·2) (Austin 1958). Galvanomagnetic studies by Drabble, Groves and Wolfe

† Now at The National Physical Laboratory, Teddington, Middlesex.

(1958) and Drabble (1958) suggest that the energy surfaces of the conduction and valence bands are of the many-valley kind.

Detailed measurements of the Faraday rotation as a function of wavelength on a number of single crystals are reported here. The interpretation is complicated by a relatively strong rotation near the absorption edge, presumably associated with the effect of interband transitions. This rotation shows an unexpected change of sign in samples which are heavily compensated with iodine. An attempt has been made to separate the free carrier contribution and calculate the effective mass parameters.

Measurements of the free carrier absorption are also reported and used to estimate effective mass parameters. These compare favourably with the values obtained from the Faraday measurements.

The results are discussed in the light of previous galvanomagnetic measurements on some of the ingots.

§ 2. Faraday Rotation Measurements

2.1. *Experimental Procedure*

To observe Faraday rotation light must be propagated through the crystal along the direction of the applied magnetic field. The appropriate beam geometry was obtained by means of two small mirrors placed between the poles of an electromagnet. It was then possible to use a small pole gap, and achieve a field of 17 k oersteds with a relatively small magnet. All measurements were made in a liquid nitrogen cryostat, since the transmission of Bi_2Te_3 is greatly improved on cooling (see § 3).

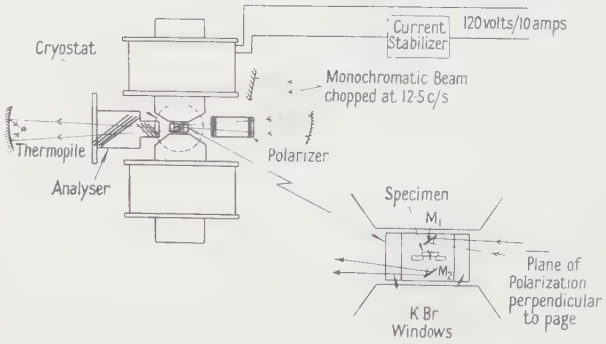

Figure 1. Faraday effect apparatus.

A schematic diagram of the apparatus is shown in figure 1. Radiation from a prism monochromator was focused between the poles of a magnet (Newport Type A) using reflection optics. The gap between the poles was $\frac{1}{2}$ in. and accommodated the lower part of a demountable vacuum cryostat. This part of the cryostat was made from square section brass tube and incorporated two small mirrors, M_1 and M_2 (aluminized glass), to turn the light in a direction parallel to the magnetic field. Strain-free polished KBr windows were provided on either side. The specimen occupied a position between the mirrors, and was mounted on a thin copper strip sealed into a glass vessel, which formed the upper half of the cryostat and contained liquid nitrogen.

The polarizer and analyser were constructed from sheets of silver chloride stacked at the Brewster angle, eight sheets being used for each. In the analyser the sheets were stacked two ways, as described by Makas and Shurcliff (1955), to counteract lateral deviation of the beam. The analyser assembly was mounted on a rotating microscope stage graduated in degrees.

Monochromatic radiation was provided by means of a double prism spectrometer using KBr prisms, and detected using a high gain linear amplifier tuned to 12·5 c s. A transistor stabilizer, based on a design by Wenham (1959), was used to stabilize the magnetic current against supply fluctuations and thermal drift. This effectively eliminated noise in the amplifier arising from field fluctuations.

Faraday rotations were measured in the following way. The field was applied in one direction and the maximum and minimum transmission determined by rotating the analyser. The analyser was then set to a position corresponding to the mean transmission and the angular reading noted. The same process was repeated with the field reversed and the rotation taken as half the difference between the two settings.

Observations without a specimen showed that no detectable rotation was introduced by reflections (Kerr effect) at the mirrors M_1 and M_2. A test set of measurements on several n-type samples of InSb showed good agreement with results by Moss, Smith and Taylor (1959), using an alternative method. Other measurements on n-type InAs and InP covering the range 2–20 μ, accurately fitted equation (1). In particular, measurements of θ as a function of B showed that rotations up to approximately 50° could be measured without serious errors arising from depolarizing effects at the exit mirror M_2. Measurements were generally reproducible to approximately 1°.

2.2. *The Specimens*

The single crystals were prepared by Mr. A. R. Sheard using a zone-melting process and are listed in table 1. Ingots prepared from stoichiometric quantities of elements were always p-type; intrinsic and n-type material was produced by compensation with iodine.

Table 1. Electrical Data on Samples

(1)	(2)	(3)	(4)
14P	0·17	$1·5 \times 10^{19}$	165
23P	0·20	$1·3 \times 10^{19}$	150
19P	0·68	$3·8 \times 10^{18}$	200
27N	12·2	$1·7 \times 10^{17}$	Intrinsic
16N	1·2	$1·7 \times 10^{18}$	480
25N	1·0	$2·1 \times 10^{18}$	470
6N	0·62	$3·5 \times 10^{18}$	450

(1) Ingot number and type; (2) Hall constant at 4°K ($cm^3\ coul^{-1}$); (3) carrier concentration at 4°K (cm^{-3})†; (4) Hall mobility at 20°C ($cm^2\ v^{-1}\ sec^{-1}$) ‡.

† Calculated from the expression $N=(\alpha_3'/\alpha_1^2)/Re$ where (α_3'/α_1^2) is the anisotropy factor given in table 2, column 4.

‡ Data from Yates (1959).

Also shown in this table are Hall coefficients measured on adjacent slices at 4·2°K. Bismuth telluride has two principal Hall coefficients (Drabble, Groves

and Wolfe 1958, Drabble 1958). The present measurements relate to crystals with the magnetic field directed along the principal (3-fold) axis. The corresponding carrier concentrations are indicated in column (3). These have been calculated using equation (4) in § 2.5. The evidence from electrical measurements (Goldsmid 1958) indicates that the free carrier concentration is constant in all these samples up to room temperature, except for 27N which becomes intrinsic.

Thin sections, suitable for optical measurements, were readily obtained using the excellent cleavage of this material parallel to the (0001) plane. In all the measurements the radiation was directed normally on to the cleavage surface, thus giving transmission down the optic axis.

2.3. *Theory*

Before discussing the results it is convenient to summarize the theoretical expectations.

The free carrier Faraday rotation for a uniaxial crystal with simple, many-valley energy surfaces of the form

$$E = \frac{\hbar^2}{2m_0}\,\alpha_{ij}k_ik_j$$

has been discussed in I. Here E is the energy, $\mathbf{k}$ the wave vector, and α_{ij} the reciprocal effective mass tensor. It was shown that an equation of the form (1) applied for propagation down the optic axis, where m^* is replaced by a parameter $(\alpha_3')^{-1/2}$, which represents the appropriate effective mass average. For a general arrangement of valleys

$$\alpha_3' = \alpha_{11}\alpha_{22} - \alpha_{12}^2 \qquad \ldots\ldots(2)$$

where the α_{ij} refer to any one valley, the 3 axis being chosen parallel to the principal symmetry axis.

The rotation near the absorption edge associated with the effect of interband transitions has received little attention so far in the literature. Classical theory applied to a Lorentz oscillator (Darwin and Watson 1927, Moss 1959) gives the approximate expression

$$\theta \propto \frac{B\omega^2}{(\omega^2 - \omega_0^2)^2} \qquad \ldots\ldots(3)$$

where ω_0 is the resonant frequency. Stephen and Lidiard (1959), using a quantum treatment, but giving no details, have proposed a similar expression. Small rotations of this form have been reported by Ramaseshan (1946) for diamond, and by Kimmel (1957) for several semiconductors. Although the classical theory predicts a positive rotation, Smith, Moss and Taylor (1959) have recently reported a negative interband rotation for InSb, suggesting that the detailed band structure plays a part in determining the sign.

2.4. *Results*

Figure 2 shows the rotation plotted against the square of the wavelength for several n- and p-type specimens. The rotation is taken as positive when it is clockwise for radiation propagated along the direction of the magnetic field towards the observer. All measurements were made at $-195\,^\circ$C, using a field of 17 k oersteds. The samples ranged in thickness from approximately 30 to 150 microns, but for convenience all the measurements have been normalized to a

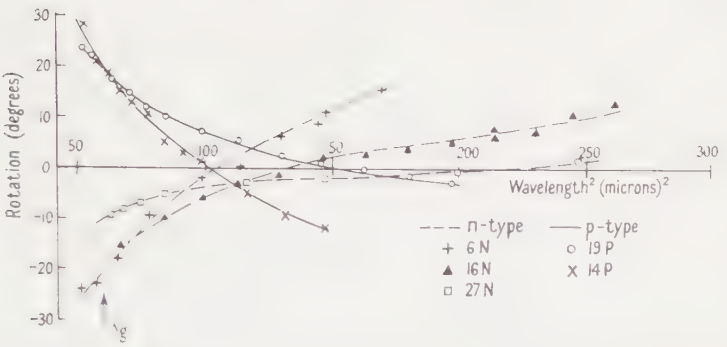

Figure 2. Faraday rotation in n- and p-type Bi_2Te_3. All measurements are normalized to a sample thickness of 75 microns. Field 17 k oersteds; temperature −195°c.

thickness of 75 microns. Also shown is λ_g, the wavelength corresponding roughly to the energy gap. At long wavelengths measurements were limited mainly by the large reflectivity loss.

2.5. *Discussion*

At wavelengths greater than approximately 12μ the rotation increases with wavelength, though not following a λ^2 law. The rotation increases in magnitude with rising carrier concentration and is positive for n-type samples and negative for p-type, as expected for free electrons and free holes. We assume therefore that the main effect at these wavelengths is due to free carriers.

Near the absorption edge the magnitude of the rotation decreases rapidly with increasing wavelength in all the samples. The behaviour up to approximately 10μ is similar to that predicted by equation (3), suggesting that interband transitions are the main influence in this region. However, the sign of the rotation near the edge is different for n- and p-type specimens. This result is unexpected, since the rotation due to interband transitions is essentially an intrinsic property of the crystal.

The n-type specimens used in this work were heavily compensated with iodine. A comparison between the results for the n- and p-type specimens suggests that the rotation due to interband transitions becomes progressively more negative with increasing iodine concentration. The impurity states in these crystals are merged with the band edges, corresponding to overlapping impurity bands (Goldsmid 1958). Since the sign of the interband rotation probably depends on detailed assumptions concerning the band structure, we may speculate that the change in sign in Bi_2Te_3 is associated with the perturbing influence of the impurity levels. At present there is no theoretical treatment of this problem.

In order to separate the free carrier rotation we will assume that the contribution at long wavelengths arising from interband transitions can be estimated for each sample using equation (3) fitted to points near the absorption edge. The theoretical basis for this treatment is not strong, but it will be shown that a reasonably consistent analysis can be made on these lines.

Figure 3 shows the free carrier rotations obtained after correction in this manner. In fitting equation (3) to points near the absorption edge some allowance has been made for the free carrier component in this region, by a method of successive approximations. For the p-type samples the interband component is especially

large. As a check on the method the difference between the measured rotations for 14P (undoped) and 19P at wavelengths beyond about 12μ is given in figure 3. Since the iodine content of 19P is small this difference may be attributed to the difference in free hole concentrations.

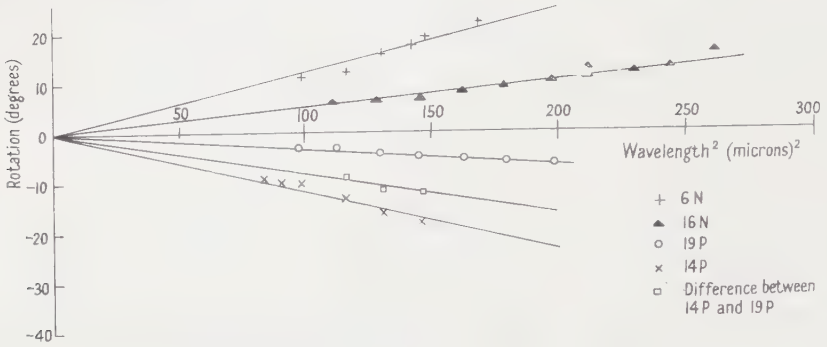

Figure 3. Free carrier Faraday rotation in Bi_2Te_3. Field 17 koersteds; temperature $-195°$C.

The corrected rotations show reasonable agreement with the λ^2 law of equation (1), and for the subsequent discussion it will be assumed that this expression may be applied.

Now the Hall constant expression for the model discussed in I, for the magnetic field along the three-fold axis, is given by

$$R=\left[\frac{\alpha_3'}{\alpha_1^2}\right]\frac{\langle\tau^2\rangle}{\langle\tau\rangle^2}\frac{1}{Ne} \qquad \ldots\ldots(4)$$

where N is the total free carrier concentration, α_3'/α_1^2 is a dimensionless quantity and

$$\alpha_1=(\alpha_{11}+\alpha_{22})/2. \qquad \ldots\ldots(5)$$

The factor involving the relaxation time averaged over the electron distribution will be taken as one since all the samples were highly degenerate at 4·2°K.

Eliminating the carrier concentration in (1), using (4), we obtain an expression containing the parameter $(\alpha_1/\alpha_3')^2$, which represents the square of an effective mass average. The values obtained for this effective mass average are shown in table 2, column 2.

Table 2. Effective Mass Parameters in Bi_2Te_3

(1)	(2)	(3)	(4)	(5)
14P	0·26		0·32†	0·09
23P		0·35	0·32	
19P	0·25	0·28	0·48†	0·12
14 and 19P combined results	0·27		0·40 (av.)	0·11
16N	0·15	0·15	0·33	0·050
25N		0·16	0·33	
6N	0·14	0·13	0·33†	0·046

(1) Ingot number and type; (2) α_1/α_3' from Faraday measurements; (3) α_1/α_3' from free carrier absorption; (4) Hall effect anisotropy factor (α_3'/α_1^2); (5) 'conductivity' effective mass in (0001) plane: $(\alpha_1/\alpha_3')(\alpha_3'/\alpha_1^2)$.

† Values obtained by Drabble, Groves and Wolfe (1958) and Drabble (1958). Other values assumed.

It is difficult to assess the reliability of this interpretation. The main uncertainty arises from the correction due to interband transitions. However, since $\alpha_1 \alpha_3'$ depends on the square root of the rotation, the effect of errors in θ is somewhat reduced. The results in table 2 are reasonably self-consistent, and as shown in the next section are supported by independent measurements of the free carrier absorption.

§ 3. Free Carrier Absorption Measurements

3.1. *Experimental Method*

Free carrier absorption measurements were made at wavelengths in the range 8-20μ on cleavage sections of a number of the samples listed in table 1. Measurements were made at room temperature and -190° C in a vacuum cryostat with KBr windows. A bellows arrangement allowed the specimen to be moved in and out of the beam. Absorption coefficients K were calculated from the usual transmission equation (Fan and Becker 1951)

$$T = (1-R)^2[\exp KL - R^2 \exp(-KL)]^{-1}$$

which allows for internal reflection. R is the reflectivity and L the thickness.

Values of R were calculated from refractive index data given elsewhere (Austin 1958). As a check, R was also estimated from transmission data using samples of different thickness to eliminate the absorption loss. The value found in this way ($R = 0{\cdot}67$) compares favourably with the calculated figure ($R = 0{\cdot}64$) and confirms the unusually high figure of 9·2 for the refractive index.

3.2. *Results*

In figures 4 and 5, values of K as a function of wavelength, at room temperature and -190° C, have been plotted on logarithmic scales. At room temperature the variation of K with wavelength can be described by a simple power law of the form λ^s where s is slightly greater than two. Values of s are shown in figure 4.

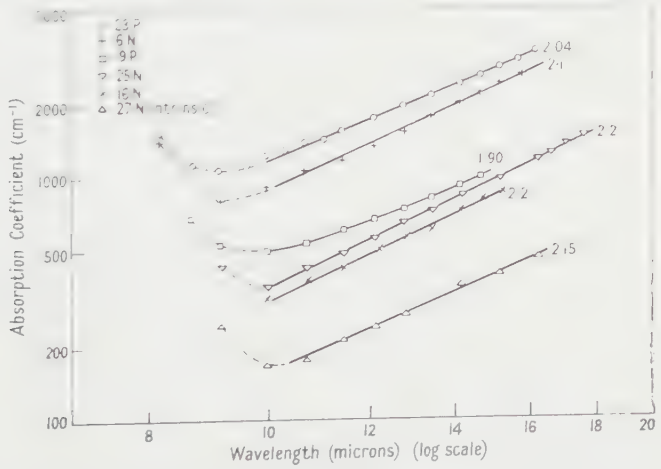

Figure 4. Free carrier absorption in Bi_2Te_3 at room temperature. Values of s are shown against curves.

On cooling to -190° C the absorption in all samples shows a substantial decrease, by a factor of about 4. In some samples a simple power law applies only

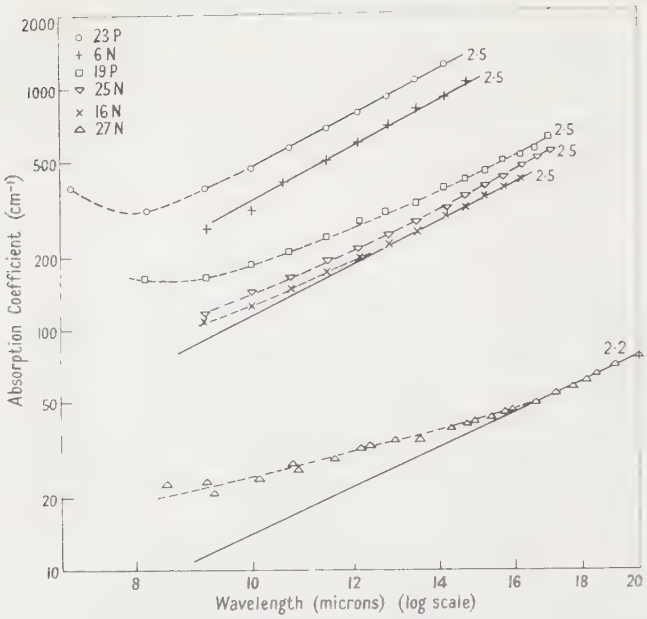

Figure 5. Free carrier absorption in Bi_2Te_3 at $-190°$C. Values of s are shown against curves.

at longer wavelengths, with $s \simeq 2{\cdot}5$, and extrapolation to shorter wavelengths indicates a small overlying absorption. This is most clearly shown in the sample with the lowest carrier concentration (27N).

3.3. *Discussion*

The wavelength dependence at room temperature is close to the λ^2 law predicted by the Drude–Zener theory (cf. Mott and Jones 1936). More rigorous quantum treatments by Meyer (1958) and Rosenberg and Lax (1958) lead to substantially the same wavelength dependence, where the carriers are scattered by phonons. These theories, however, require a detailed knowledge of the deformation potential constants and lattice vibration spectrum of the crystal. Although the Drude Zener theory contains somewhat drastic approximations, Moss (1954) and Spitzer and Fan (1957) have shown that reasonable results are obtained under conditions where lattice scattering predominates and the quantum energy of the radiation is of the order of kT. These conditions are approximately satisfied in Bi_2Te_3 at room temperature and approximately 15μ ($h\nu \simeq 4kT$). Goldsmid (1958) has shown that acoustic mode scattering predominates at this temperature in spite of the large impurity content, presumably because of the large dielectric constant.

For the model discussed in I the Drude–Zener theory gives the result

$$K_{\parallel} = 0{\cdot}53 \times 10^{-12} \frac{N\lambda^2 \alpha_3'}{\mu_H n} \langle \tau \rangle \langle \tau^{-1} \rangle \quad \text{(m.k.s. units)} \quad \ldots\ldots (6)$$

where $K_{\parallel}$ is the free carrier absorption coefficient for the electric vector in the (0001) plane. μ_H is the Hall mobility defined by the product of R in equation (4) and the d.c. conductivity in the same plane.

Table 1 shows values of μ_H determined from results by Yates (1959) using similar specimens. The product in equation (6) involving the relaxation time

averaged over the electron distribution lies between 1·1 and 1·3 for these samples. This may be shown using data on the energy dependence of the relaxation time by Goldsmid (1958), and Fermi levels given elsewhere (Austin 1958).

Using the Hall constant in equation (4) to eliminate the carrier concentration in equation (6) we obtain an expression involving the parameter $(\alpha_1'\alpha_3')^2$ as before. It is interesting to note that the two methods lead to the same effective mass average. This result is independent of the arrangement of valleys and would also occur for a cubic crystal. The values of $\alpha_1'\alpha_3'$ calculated in this way from the free carrier absorption data are shown in table 2, column (3). The figures compare favourably with the estimates in column (2), if we assume there is no substantial variation of the effective mass with temperature.

The results at −190° C cannot be analysed in this fashion. The higher values for s are consistent with the presence of impurity scattering (Fan, Spitzer and Collins 1956), and this is indicated by the mobility data (Yates 1959). On cooling to −190° C the mobility in these samples increases by a factor of the order of 9. Since the carrier concentration remains constant, a corresponding decrease in absorption would be expected on the basis of equation (6). However, the measured decrease is by a factor of the order of 4 only.

§ 4. Comparison with Galvanomagnetic Data

The effective mass parameters $\alpha_1'\alpha_3'$ estimated by the two methods above are in reasonable agreement. It is of interest therefore to combine these results with detailed galvanomagnetic measurements by Drabble, Groves and Wolfe (1958) to see what further deductions can be made concerning the band stucture.

In the models proposed by these authors six valleys are centred on reflection planes in k-space, in both n- and p-type material. For this arrangement the only non-zero α_{ij} parameters are those listed below, and it follows that

$$\alpha_1/\alpha_3' \equiv \tfrac{1}{2}(\alpha_{11}^{-1}+\alpha_{22}^{-1}).$$

The relative magnitudes of the various α_{ij} have been obtained by Drabble, Groves and Wolfe (1958), on samples from two of the ingots used in this work (19P and 6N). Combining these data with the values of α_1/α_3' in table 2, column (2), we obtain the absolute α_{ij} values in table 3.

Table 3

Sample	α_{11}	α_{22}	α_{33}	α_{13}	$\Delta^{-1/3}$	$S^{2/3}\Delta^{-1/3}$	S (number of valleys)
19P	2·15	13·1	2·73	0·66	0·24	0·51	3·1
6N	40	3·9	5·4	0·89	0·12	0·35	5·1

Also shown is the density of states effective mass per ellipsoid, which is given by $\Delta^{-1/3}$, where Δ is the determinant of the α_{ij}. A comparison with the density of states effective mass, $S^{2/3}\Delta^{-1/3}$, from thermoelectric measurements (Drabble, private communication) gives an estimate of S, the number of valleys. The results indicate that a six-valley model is appropriate for n-type material and a three-valley model for p-type. This implies that the valence band maxima are situated at the extremities of the Brillouin zone.

Finally, it is of interest to note that the inertial effective mass for conduction in the cleavage plane, which is given by α_1^{-1} (see I), is easily obtained by multiplying the effective mass average obtained in the present measurements α_1/α_3', by the anisotropy factor α_3'/α_1^2 in the Hall coefficient. The values obtained in this way are shown in table 2, column (5), and indicate inertial effective masses of approximately one tenth and one twentieth of the free electron mass for holes and electrons respectively.

§ 5. Conclusions

The present discussion of the Faraday measurements rests partly on an empirical basis. However, the two estimates of the effective mass parameters are in reasonable agreement and this lends some support to the interpretation. Measurements at longer wavelengths would give a more reliable estimate of the free carrier rotation, but in this material the large reflectivity loss introduces a severe limitation.

The rotational behaviour near the absorption edge requires further elucidation. At present there is little experimental or theoretical evidence on this problem in semiconductors. In Bi_2Te_3, the magnitude of this rotation is much larger than in other materials, such as Ge and InP (Kimmel 1957). Classical theory predicts a rotation proportional to the dispersion (Becquerel 1897). Near the absorption edge in Bi_2Te_3 the dispersion is large, being associated with a large refractive index.

A simple interpretation of the free carrier absorption at room temperature has been given, using the Drude–Zener theory. At low temperatures this is not possible, and a detailed interpretation has not been attempted. There is a lack of agreement between existing theories of the free carrier absorption in the presence of impurity scattering (Rosenberg and Lax 1958). A closer study of crystals with a low free carrier concentration would be of interest to establish whether the extra absorption at shorter wavelengths is an impurity effect or an intrinsic property of the crystal. Such measurements might throw light on the suggestion by Mooser and Pearson (1958) that the forbidden gap in this material is bridged by a band with a small density of states.

References

Austin, I. G., 1958, *Proc. Phys. Soc.*, **72,** 545.

—— 1959, *J. Electron. and Control*, **6,** 271.

Becquerel, H., 1897, *C.R. Acad. Sci., Paris*, **125,** 679.

Darwin, C. G., and Watson, W. H., 1927, *Proc. Roy. Soc.* A, **114,** 474.

Drabble, J. R., 1958, *Proc. Phys. Soc.*, **72,** 380.

Drabble, J. R., Groves, R., and Wolfe, R., 1958, *Proc. Phys. Soc.*, **71,** 430.

Fan, H. Y., and Becker, M., 1951, *Semiconductor Materials, Reading Conference* (London: Butterworths Scientific Publications).

Fan, H. Y., Spitzer, W., and Collins, R. J., 1956, *Phys. Rev.*, **101,** 566.

Goldsmid, H. J., 1958, *Proc. Phys. Soc.*, **71,** 633.

Kimmel, H., 1957, *Z. Naturf.*, **12a,** 1016.

Makas, A. S., and Shurcliff, W. A., 1955, *J. Opt. Soc. Amer.*, **45,** 998.

Meyer, H. J. G., 1958, *Phys. Rev.*, **112,** 298.

Mitchell, E. W. J., 1955, *Proc. Phys. Soc.* B, **68,** 973.

Mooser, E., and Pearson, W. B., 1958, *J. Phys. Chem. Solids*, **7,** 65.

Moss, T. S., 1954, *Proc. Phys. Soc.* B, **67,** 775.

—— 1959, *Optical Properties of Semiconductors* (London: Butterworths Scientific Publications).

Moss, T. S., Smith, S. D., and Taylor, K. W., 1959, *J. Phys. Chem. Solids*, **8,** 323.

Moss, T. S., and Walton, A. K., 1959, *Proc. Phys. Soc.*, **74,** 131.
Mott, N. F., and Jones, H., 1936, *Properties of Metals and Alloys* (Oxford: University Press).
Ramaseshan, S., 1946, *Proc. Ind. Acad. Sciences*, **24A,** 104.
Rosenberg, R., and Lax, M., 1958, *Phys. Rev.*, **112,** 843.
Smith, S. D., Moss, T. S., and Taylor, K. W., 1959, *J. Phys. Chem. Solids*, **11,** 131.
Spitzer, W. G., and Fan, H. Y., 1957, *Phys. Rev.*, **106,** 882.
Stephen, M. J., and Lidiard, A. B., 1959, *J. Phys. Chem. Solids*, **9,** 43.
Walton, A. K., and Moss, T. S., 1959, *J. Appl. Phys.*, **30,** 951.
Wenham, D. G., 1959, *Proc. Instn Elect. Engrs* B, **106,** 1384.
Yates, B., 1959, *J. Electron. and Control*, **6,** 26.

Phase Equilibria in Condensed Mixtures of Argon and Xenon

By R. HEASTIE and C. LEFEBVRE
Department of Physics, Queen Mary College, London

MS. received 15*th February* 1960

Abstract. The solid–liquid phase equilibrium diagram of argon and xenon has been determined within a limited composition range. A eutectic point exists at a temperature $1\frac{1}{2}$° below the triple-point temperature of argon and at a composition of 23 mole per cent of xenon. At this temperature, argon and xenon are insoluble in the solid state over the composition range 2·7–62 mole per cent xenon. The results are consistent with the predictions of the cell theory of solutions.

The vapour pressure of solid xenon and triple-point data of xenon are reported.

§ 1. Introduction

Recently a number of investigations of the properties of binary solutions of the inert gases, argon, krypton and xenon have been reported. Interest in these solutions has arisen because of the spherical symmetry and the lack of internal motions of the component molecules.

Measurements of the vapour pressure of solid solutions of argon and krypton (Walling and Halsey 1958, Heastie 1959) and of krypton and xenon (Freeman and Halsey 1956) have been reported. The magnitude of the excess free energy of the solutions calculated from these results is in good agreement with that predicted by the cell theory (Prigogine 1957). However, no *measurements* of the limits of solubility of the inert gases in the solid state nor of the critical solution temperatures T_c have been reported.

The values of T_c may be estimated, (*a*) from experimental data of the pure components, using the cell theory of solutions or (*b*) from measured values of the vapour pressure of the solutions (at temperatures greater than T_c) with the assumptions of the strictly regular solution theory. Using an approximate equation for T_c (Prigogine 1957, eqn 12.8.1) we have calculated the values of the critical solution temperatures in two cases. These values of T_c, reduced by 25% to make allowance for the assumption in the theory of random mixing, are: argon–krypton 44° K, krypton–xenon 89 K. From the experimental data of the solid solutions, values of T_c have been estimated to be: argon–krypton 56 ± 8 K (Walling and Halsey 1958) and krypton–xenon 91 ± 2 K (Freeman and Halsey 1956).

In the case of argon krypton mixtures the lowest temperatures at which the vapour pressure has been measured are 70·0° K (Walling and Halsey 1958) and about 60 K (Heastie 1959). Measurements of the specific heat of solid mixtures of argon and krypton containing (*a*) 59·5 mole per cent krypton over the range 12–58° K (Eucken and Veith 1936) and (*b*) 50 mole per cent krypton from 10–77° K (Figgins, unpublished) have been made. In none of these experiments has a solid–solid phase change been evident.

The lowest temperature employed by Freeman and Halsey in their investigation of krypton–xenon mixtures was 87·2°K and no phase separation was observed. More recently, vapour pressure measurements (Heastie 1959†) of krypton–xenon mixtures have shown indications of the formation of two solid phases when gas mixtures (within a certain concentration range) have been condensed into solid at a number of temperatures between 65° and 110°K. The results of these experiments showed that the solid mixtures were not in thermodynamic equilibrium and consequently the limits of solid solubility could not be determined.

The estimated values of T_c suggest that in a number of the experiments described above, the temperatures employed were less than the true values of the critical solution temperatures. It seems probable that phase separation was not observed in these experiments because of a small diffusion rate in the solid mixtures. The rate of diffusion in argon–xenon mixtures would, because of the greater dissimilarity of the two components, be expected to be greater than in the case of the two other mixtures considered here, and, consequently, one might hope to *observe* solid–solid phase transitions in these mixtures. For this reason the present investigation of argon–xenon mixtures has been undertaken.

§ 2. Method

The method employed has been described in detail elsewhere (Heastie 1959). The two components were mixed in known proportions in the gaseous state and then condensed as solid into a calorimeter contained in an evacuated cryostat surrounded by liquid oxygen. The calorimeter was allowed to warm at a controlled rate and the vapour pressure of the mixture and the temperature of the calorimeter were measured at convenient time intervals. The phase-transition temperatures and pressures were inferred either from the discontinuities in slope of the pressure, temperature curves or by the method of thermal analysis.

The experimental uncertainties in the measurements are estimated to be : temperature $\pm 0{\cdot}03$°K, pressure $\pm 0{\cdot}1$ cm Hg, composition not greater than 1% in the mole fraction of either component.

§ 3. Results

In figure 1 are shown the vapour pressure measurements of (i) pure argon (crosses) and (ii) a mixture of argon and xenon containing 2·7 mole per cent of xenon (points). In the case of argon, the points lie on two curves EA and FA intersecting at the triple point of argon, A. The phases present in the mixture are: along DB, two solid phases (designated by S_1 and S_2 in figure 1) and vapour; along BG, one solid phase (S_1), liquid and vapour; and along GH, liquid and vapour. The phase-transition points of this mixture may be determined from the discontinuities in slope of the curve DBGH at the points B (the 'melting' point) and G (the 'freezing' point).

From a study of the (P, T) curves of a number of such mixtures of different compositions the phase boundary lines on the phase-equilibrium diagram may be inferred. The phase boundaries are the three 3-phase lines (shown in figure 1 by full lines), AB, CB and DB. These lines intersect in a quadruple point (the eutectic point) at B.

† Contribution to *Symposium uber Thermodynamik, Fritzens-Wattens, Tyrol* (to be published).

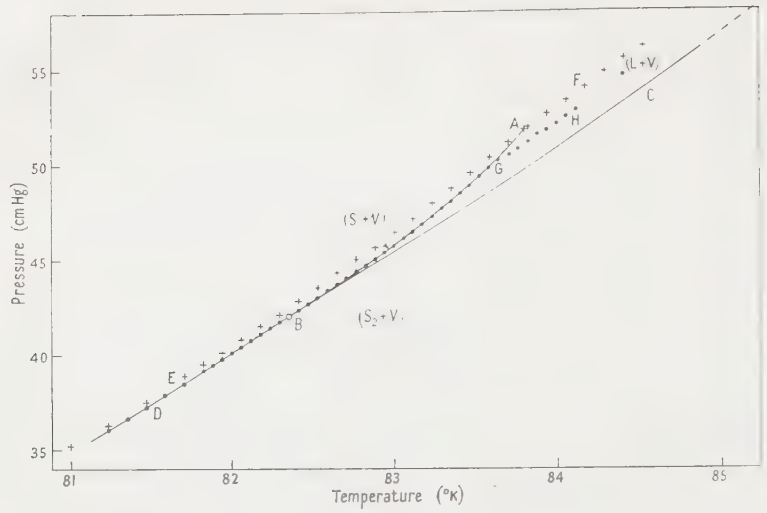

Figure 1. The pressure, temperature phase-equilibrium diagram of argon and xenon. Actual results are shown for (i) argon (crosses) and (ii) a mixture containing 2·7% mole% of xenon (points). The phase boundaries (full lines) are inferred from the results for a number of mixtures. S_1 and S_2 represent solid solutions of two different compositions; L, liquid solution; V, vapour. The three 3-phase boundary lines AB, CB and DB intersect in the eutectic point, B, at which S_1, S_2, L and V are in thermodynamic equilibrium.

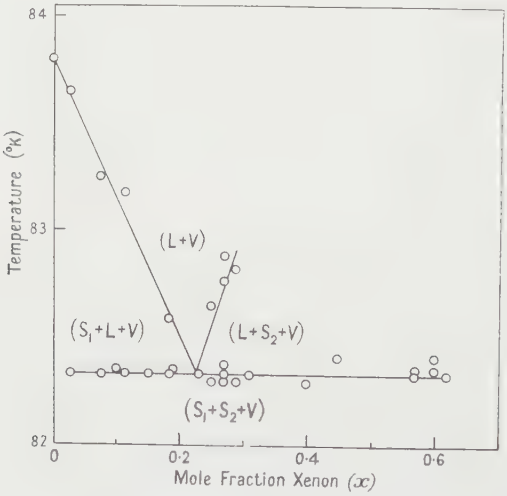

Figure 2. The temperature, composition phase-equilibrium diagram of argon and xenon.

The temperature, composition phase-equilibrium diagram shown in figure 2 has been deduced from the above data.

The vapour pressure of xenon has been measured within the temperature range 126–161·38 °K and the data are given in table 1. The values determined for the triple-point temperature 161·38 °K and pressure $61{\cdot}2_5$ cm Hg are compared with previously reported values in table 2.

Table 1. Vapour Pressure of Solid Xenon

T (°K)	125·26	132·56	137·11	141·01	145·33	148·50
P (cm Hg)	2·29	4·98	7·97	11·65	17·13	22·51
T (°K)	152·39	156·14	158·10	160·42	161·38	
P (cm Hg)	30·88	41·63	48·31	57·27	61·25	

Table 2. Triple-point Data of Xenon

Triple-point temperature (°K)	Triple-point pressure (cm Hg)	Reference
$161{\cdot}38 \pm 0{\cdot}03$	$61{\cdot}2_5 \pm 0{\cdot}1$	Present investigation
$160{\cdot}5_6$	$57{\cdot}5_6$	Freeman and Halsey 1956
$161{\cdot}36 \pm 0{\cdot}03$	$61{\cdot}22 \pm 0{\cdot}02$	Clusius 1941
161·3	$61{\cdot}1 \pm 0{\cdot}15$	Clusius and Riccoboni 1937

§ 4. Discussion

The impurities present in the argon used were estimated by the suppliers, British Oxygen Co. Ltd., to be not greater than 0·001 mole per cent. Air Reduction Sales Co., who supplied the xenon, estimate the impurities to be 0·02 mole per cent of krypton and 0·01 mole per cent of nitrogen.

The method of determining the 'freezing points' from the vapour pressure measurements was found to be unsuitable for the reasons given below. Figure 1 shows a discernible change in slope in the pressure, temperature graph for the mixture, $x = 0{\cdot}027$, at the point G; (x is the mole fraction of xenon). For this mixture the freezing point G could be reliably inferred by this method. For mixtures richer in xenon, however, this change in slope was too small for the certain detection of the freezing points. Consequently, most of the liquidus points on figure 2 were determined by thermal analysis. This latter method was successful within the range $0 < x < 0{\cdot}25$. As the mole fraction of xenon was increased above 0·23 the discontinuities in slopes of these temperature, time curves became increasingly less distinct. For this reason one branch of the liquidus could be determined over a very short range of temperature only.

The three-phase curve BC of figure 1 has been determined over as large a temperature range as the apparatus permitted. The limitation was set by the maximum pressure that could be measured with the manometer used. The measurements show that the slope of the curve, BC, increases steadily from the eutectic temperature to 96·00 K, at which temperature the vapour pressure is 160·0 cm Hg.

From figure 2 it may be seen that all the phase-transition points that have been determined lie within a small temperature range of $1\frac{1}{2}°$. Under these circumstances care is needed, in the deduction of the (T,x) phase-equilibrium diagram, in order to distinguish between a solidus curve with continuous slope and a eutectic line. We have examined the results of experiments with some twenty mixtures and conclude that argon and xenon form a eutectic mixture from the following observations: (*a*) all the mixtures investigated in the composition range $0{\cdot}027 < x < 0{\cdot}620$ have, within experimental error, a common vapour pressure curve (DB in figure 1) over the temperature range of about 71 82·30 K, (*b*) within this composition range thermal analysis indicated a phase change in all mixtures at a temperature of $82{\cdot}30 \pm 0{\cdot}06$ K, and (*c*) the three-phase curve, ABC (in figure 1),

inferred from the investigations of many mixtures has a discontinuity in slope at the point B. At this point, the eutectic point, $P = 41{\cdot}76 \pm 0{\cdot}01$ cm Hg, $T = 82{\cdot}30 \pm 0{\cdot}06$°K and $x = 0{\cdot}23_5 \pm 0{\cdot}005$.

§ 5. Conclusion

In the determination of the critical solution temperature by the cell theory of solutions a knowledge of certain properties of one component (in the solid state) is required *at the critical solution temperature*. The theory shows that the predicted value of T_c, in the case of argon–xenon mixtures, is considerably greater than the triple-point temperature of argon. Extrapolation of the experimental solid state data into a temperature range in which the solid does not exist, is therefore required. For this reason no realistic estimate of the actual value of the critial solution temperature of argon and xenon mixtures can be made.

The results of the experimental investigation show that argon and xenon are insoluble, in the solid state, within the range $0{\cdot}027 < x < 0{\cdot}62$ and that the critical solution temperature is greater than 82·30°K (the eutectic temperature). The solid–solid phase boundaries on the (T, x) phase-equilibrium diagram have not been determined but it is clear from figure 2 that one of these boundaries lies entirely within the region $0 > x > 0{\cdot}027$ and is consequently very steep. The prediction by the cell theory of a high value of the critical solution temperature for these solutions is certainly consistent with these results.

Acknowledgments

We are grateful for facilities provided by Professor G. O. Jones. One of us (C.L.) wishes to acknowledge a grant from l'Institut pour l'Encouragement de la Recherche Scientifique dans l'Industrie et l'Agriculture, Bruxelles. We thank Dr. B. Figgins for communicating results to us before publication.

References

Clusius, K., 1941, *Z. Phys. Chem.* B, **50,** 403.
Clusius, K., and Riccoboni, L., 1937, *Z. Phys. Chem.* B, **38,** 81.
Eucken, A., and Veith, H., 1936, *Z. Phys. Chem.* B, **34,** 275.
Freeman, M. P., and Halsey, G. D., 1956, *J. Phys. Chem.*, **60,** 1119.
Heastie, R., 1959, *Proc. Phys. Soc.*, **73,** 490.
Prigogine, I., 1957, *The Molecular Theory of Solutions* (Amsterdam: North Holland).
Walling, J. F., and Halsey, G. D., 1958, *J. Phys. Chem.*, **62,** 752.

The Direct Inelastic Scattering of Deuterons†

By M. EL-NADI and M. WAFIK‡
Faculty of Science, Cairo University, Egypt, U.A.R.

MS. received 13*th January* 1959, *in final form* 26*th November* 1959

Abstract. A general expression for the differential cross section of inelastically scattered deuterons is derived by assuming the complete antisymmetrization of the total wave functions of the system. This is found to give rise to different possible mechanisms: (i) the direct surface scattering in which the incident deuteron itself forms the scattered particle, (ii) the nucleon exchange stripping in which one of the constituents of the deuteron is exchanged by a similar one from the target nucleus, (iii) the target nucleus stripping in which a deuteron from the target nucleus is ejected, while the rest is captured by the incident particle, and (iv) the knock-on process in which the incident deuteron knocks out a deuteron from the target nucleus and is then itself absorbed. Comparison is made between the theory and experimental data; good agreement with experiments is obtained.

§ 1. Introduction

Recent experimental data (Vogelsang and McGruer 1958, Van Heerden 1958, Hinds, Middleton and Parry 1957, Haffner 1956) on the angular distribution of inelastically scattered deuterons show some characteristics which could not be explained according to the compound nucleus theory. The differential cross section for the scattered deuterons shows a maximum in the region of small angles. The forward peaking of the angular distribution can in many cases be fitted well by a theoretical curve calculated from the theory developed by Huby and Newns (1951). They assumed that only one of the constituents of the incoming deuteron interacts with the target nucleus, the other nucleon remaining outside the nucleus. The interacting nucleon exciting the nucleus will then bounce off and the deuteron emerges as a whole, forming the outgoing particle. The differential cross section will display angular distributions similar to those for the well-known deuteron stripping distributions.

In other cases (Haffner 1956), angular distributions were observed, which could not be fitted to the Huby Newns formula. Moreover, additional peaks were found at large angles. The fact that an appreciable intensity of the outgoing deuterons takes place at intermediate and backward angles may suggest mechanisms other than that introduced by Huby and Newns.

Recently Sawicki (1958) and others (Matsunobu and Yoshida 1958) have proposed direct interaction theory for the inelastic scattering of deuterons for strongly deformed nuclei, using the strong coupling approximation of the unified nuclear model. Another approach to the inelastic scattering processes was suggested by Blair and Henley (1959), who assumed the α-particle model for ^{9}Be and studied the inelastic cross sections for excitation of rotational, vibrational and single particle states. These models show some of the characteristics found experimentally in the inelastic scattering processes.

† Work performed under the auspices of the U.A.R. Atomic Energy Commission.

‡ Now at Department of Mathematical Physics, University of Birmingham.

The purpose of the present work is to consider some other mechanisms, which seem physically possible, and then derive general expressions for the angular distribution of the scattered deuterons. The following possibilities are assumed: (i) the incident deuteron is merely scattered at the nuclear surface, and itself forms the outgoing particle, (ii) a nucleon in the incident deuteron may be exchanged by a similar nucleon from the target nucleus, (iii) the outgoing deuteron may have come from the target nucleus, while the incident particle is absorbed.

These processes can be considered as implied by the complete antisymmetrization of the wave functions involved in the collision process. Each of these three possibilities will be studied separately, and corresponding formulae will be derived.

Finally, comparisons are made between experimental and theoretical angular distributions for a number of (d, d′) reactions. It will be seen that good agreement between the predictions of theory and experiment has been generally obtained.

§ 2. General Expression for the (d, d′) Cross Section

Consider a beam of deuterons bombarding a target nucleus T. The target nucleus can be pictured as consisting of a core c together with an extra proton–neutron pair labelled p′ and n′ respectively. The incident deuteron d consists of a neutron n, plus the associated proton p. The scattering amplitude determining the differential cross section for the direct (d, d′) reaction is given by

$$\mathrm{T} = (2\pi\hbar^2)^{-1} m_{\mathrm{d}}^{*} \langle \Psi_{\mathrm{f}} | V | \Psi_{\mathrm{i}} \rangle \qquad \ldots\ldots (1)$$

where Ψ_{i} and Ψ_{f} are the initial and final state wave functions of the system, V represents the perturbation potential, and m_{d}^{*} denotes the reduced mass of the deuteron.

The differential cross section for a beam of unpolarized deuterons is given by

$$\frac{d\sigma}{d\Omega} = \frac{v_{\mathrm{d}}}{v_{\mathrm{d}}} \sum_{\mathrm{av}} |\mathrm{T}|^2 \qquad \ldots\ldots (2)$$

where v_{d} and $v_{\mathrm{d}'}$ are the velocities of the incident and ejected deuterons respectively. The summation is carried over the final states, and averaged over the initial states.

Adopting the Born approximation, the total initial wave function Ψ_{i} can be written in the form

$$\psi_{\mathrm{i}}(\mathbf{p}\mathbf{n};\, \mathbf{p}'\mathbf{n}'\mathbf{c}) = \psi_{\mathrm{d}}(\mathbf{p}\mathbf{n}) \exp\left\{\frac{i\mathbf{k}_{\mathrm{d}}}{2}(\mathbf{r}_{\mathrm{p}} + \mathbf{r}_{\mathrm{n}})\right\} \psi_{\mathrm{T}}(\mathbf{p}'\mathbf{n}'\mathbf{c}) \exp\left\{i\mathbf{k}_{\mathrm{T}}\left[\frac{m_{\mathrm{d}}}{2m_{\mathrm{T}}}(\mathbf{r}_{\mathrm{p}'} + \mathbf{r}_{\mathrm{n}'}) + \frac{m_{\mathrm{c}}}{m_{\mathrm{T}}}\mathbf{r}_{\mathrm{c}}\right]\right\} \qquad \ldots\ldots (3)$$

where $\mathbf{k}_{\mathrm{d}}$ and $\mathbf{k}_{\mathrm{T}}$ are respectively the incident deuteron and target nucleus wave vectors relative to the centre of mass ($\mathbf{k}_{\mathrm{T}} = -\mathbf{k}_{\mathrm{d}}$); $\mathbf{r}_{\mathrm{p}}$ and $\mathbf{r}_{\mathrm{n}}$ represent the position vectors of the proton p and neutron n contained in the incident deuteron d; $\mathbf{r}_{\mathrm{p}'}$, $\mathbf{r}_{\mathrm{n}'}$, and $\mathbf{r}_{\mathrm{c}}$ are the position vectors of the proton p′, the neutron n′, and the core c of the target nucleus; m_{d}, m_{c}, and m_{T} are the masses of the deuteron, core and target nucleus. The vectors $\mathbf{p}$, $\mathbf{n}$, $\mathbf{p}'$, $\mathbf{n}'$, and $\mathbf{c}$ represent all the coordinates (positional and spin) of these particles.

Since it is impossible to distinguish the origin of the nucleons constituting the outgoing deuteron, it is necessary to antisymmetrize (French 1957) the total wave function describing the final† state of the outgoing deuteron plus the residual nucleus with respect to interchange of similar nucleons. Therefore in the centre-of-mass system the final configuration is represented by the wave function

$$\begin{aligned}\psi_{\mathrm{f}}(\mathbf{pn};\mathbf{p'n'c}) &= \psi_{\mathrm{d'}}(\mathbf{pn})\exp\left\{\frac{i\mathbf{k}_{\mathrm{d}}}{2}(\mathbf{r}_{\mathrm{p}}-\mathbf{r}_{\mathrm{n}})\right\}\psi_{\mathrm{R}}(\mathbf{p'n'c})\exp\left\{i\mathbf{k}_{\mathrm{R}}\left[\frac{m_{\mathrm{d}}}{2m_{\mathrm{T}}}(\mathbf{r}_{\mathrm{p'}}+\mathbf{r}_{\mathrm{n'}})+\frac{m_{\mathrm{c}}}{m_{\mathrm{T}}}\mathbf{r}_{\mathrm{c}}\right]\right\}\\
&+\psi_{\mathrm{d}}(\mathbf{p'n'})\exp\left\{\frac{i\mathbf{k}_{\mathrm{d'}}}{2}(\mathbf{r}_{\mathrm{p}}+\mathbf{r}_{\mathrm{n'}})\right\}\psi_{\mathrm{R}}(\mathbf{pnc})\exp\left\{i\mathbf{k}_{\mathrm{R}}\left[\frac{m_{\mathrm{d}}}{2m_{\mathrm{T}}}(\mathbf{r}_{\mathrm{p}}+\mathbf{r}_{\mathrm{n}})+\frac{m_{\mathrm{c}}}{m_{\mathrm{T}}}\mathbf{r}_{\mathrm{c}}\right]\right\}\\
&-\psi_{\mathrm{d}}(\mathbf{pn'})\exp\left\{\frac{i\mathbf{k}_{\mathrm{d'}}}{2}(\mathbf{r}_{\mathrm{p}}-\mathbf{r}_{\mathrm{n'}})\right\}\psi_{\mathrm{R}}(\mathbf{p'nc})\exp\left\{i\mathbf{k}_{\mathrm{R}}\left[\frac{m_{\mathrm{d}}}{2m_{\mathrm{T}}}(\mathbf{r}_{\mathrm{p'}}+\mathbf{r}_{\mathrm{n}})+\frac{m_{\mathrm{c}}}{m_{\mathrm{T}}}\mathbf{r}_{\mathrm{c}}\right]\right\}\\
&-\psi_{\mathrm{d}}(\mathbf{p'n})\exp\left\{\frac{i\mathbf{k}_{\mathrm{d'}}}{2}(\mathbf{r}_{\mathrm{p'}}+\mathbf{r}_{\mathrm{n}})\right\}\psi_{\mathrm{R}}(\mathbf{pn'c})\exp\left\{i\mathbf{k}_{\mathrm{R}}\left[\frac{m_{\mathrm{d}}}{2m_{\mathrm{T}}}(\mathbf{r}_{\mathrm{p}}+\mathbf{r}_{\mathrm{n'}})+\frac{m_{\mathrm{c}}}{m_{\mathrm{T}}}\mathbf{r}_{\mathrm{c}}\right]\right\}\end{aligned}\qquad\ldots\ldots(4)$$

where $\mathbf{k}_{\mathrm{d'}}$ and $\mathbf{k}_{\mathrm{R}}$ are respectively the emitted deuteron and residual nucleus wave vectors relative to the centre of mass ($\mathbf{k}_{\mathrm{R}}=-\mathbf{k}_{\mathrm{d'}}$).

The scattering amplitude formed by equations (3) and (4) will therefore consist of four terms, corresponding to the respective terms in equation (4). The last two terms in equation (4) give identical contributions to the scattering amplitude (neglecting the Coulomb interaction).

Thus the matrix element determining the differential cross section will give rise to three separate terms:

$$\langle\Psi_{\mathrm{f}}|V|\Psi_{\mathrm{i}}\rangle=F+G+H.\qquad\ldots\ldots(5)$$

F describes the direct surface scattering, in which the incident deuteron itself forms the scattered particle, and is given by

$$\begin{aligned}F=a_0\int\psi_{\mathrm{d'}}{}^*(\mathbf{pn})\exp\left\{\frac{-i\mathbf{k}_{\mathrm{d'}}}{2}(\mathbf{r}_{\mathrm{p}}+\mathbf{r}_{\mathrm{n}})\right\}\psi_{\mathrm{R}}{}^*(\mathbf{p'n'c})\\
\times\exp\left\{-i\mathbf{k}_{\mathrm{R}}\left[\frac{m_{\mathrm{d}}}{2m_{\mathrm{T}}}(\mathbf{r}_{\mathrm{p'}}+\mathbf{r}_{\mathrm{n'}})+\frac{m_{\mathrm{c}}}{m_{\mathrm{T}}}\mathbf{r}_{\mathrm{c}}\right]\right\}V\\
\times\psi_{\mathrm{d}}(\mathbf{pn})\exp\left\{\frac{i\mathbf{k}_{\mathrm{d}}}{2}(\mathbf{r}_{\mathrm{p}}+\mathbf{r}_{\mathrm{n}})\right\}\psi_{\mathrm{T}}(\mathbf{p'n'c})\exp\left\{i\mathbf{k}_{\mathrm{T}}\left[\frac{m_{\mathrm{d}}}{2m_{\mathrm{T}}}(\mathbf{r}_{\mathrm{p'}}+\mathbf{r}_{\mathrm{n'}})+\frac{m_{\mathrm{c}}}{m_{\mathrm{T}}}\mathbf{r}_{\mathrm{c}}\right]\right\}d\tau.\end{aligned}\qquad\ldots\ldots(6)$$

The second term G represents the nucleon exchange stripping term, in which a proton from the incident deuteron is exchanged by another proton from the target nucleus; it is given by

$$\begin{aligned}G=a_1\int\psi_{\mathrm{d'}}{}^*(\mathbf{p'n})\exp\left\{\frac{-i\mathbf{k}_{\mathrm{d'}}}{2}(\mathbf{r}_{\mathrm{p'}}+\mathbf{r}_{\mathrm{n}})\right\}\psi_{\mathrm{R}}{}^*(\mathbf{pn'c})\\
\times\exp\left\{-i\mathbf{k}_{\mathrm{R}}\left[\frac{m_{\mathrm{d}}}{2m_{\mathrm{T}}}(\mathbf{r}_{\mathrm{p}}+\mathbf{r}_{\mathrm{n'}})+\frac{m_{\mathrm{c}}}{m_{\mathrm{T}}}\mathbf{r}_{\mathrm{c}}\right]\right\}V\\
\times\psi_{\mathrm{d}}(\mathbf{pn})\exp\left\{\frac{i\mathbf{k}_{\mathrm{d}}}{2}(\mathbf{r}_{\mathrm{p}}+\mathbf{r}_{\mathrm{n}})\right\}\psi_{\mathrm{T}}(\mathbf{p'n'c})\exp\left\{i\mathbf{k}_{\mathrm{T}}\left[\frac{m_{\mathrm{d}}}{2m_{\mathrm{T}}}(\mathbf{r}_{\mathrm{p'}}+\mathbf{r}_{\mathrm{n'}})+\frac{m_{\mathrm{c}}}{m_{\mathrm{T}}}\mathbf{r}_{\mathrm{c}}\right]\right\}d\tau.\end{aligned}\qquad\ldots\ldots(7)$$

† Since it can be shown that it is unnecessary to antisymmetrize the initial wave function.

The last term H corresponds to the target nucleus stripping and knock-on process in which the outgoing deuteron is ejected from the target nucleus, it can be expressed in the form

$$H = a_2 \int \psi_{d'}^*(\mathbf{p'n'}) \exp\left\{\frac{-i\mathbf{k}_{d'}}{2}(\mathbf{r}_{p'}+\mathbf{r}_{n'})\right\}\psi_R^*(\mathbf{pnc}) \times \exp\left\{-i\mathbf{k}_R\left[\frac{m_d}{2m_T}(\mathbf{r}_p+\mathbf{r}_n)+\frac{m_c}{m_T}\mathbf{r}_c\right]\right\} V \times \psi_d(\mathbf{pn}) \exp\left\{\frac{i\mathbf{k}_d}{2}(\mathbf{r}_p+\mathbf{r}_n)\right\}\psi_T(\mathbf{p'n'c}) \exp\left\{i\mathbf{k}_T\left[\frac{m_d}{2m_T}(\mathbf{r}_{p'}+\mathbf{r}_{n'})+\frac{m_c}{m_T}\mathbf{r}_c\right]\right\} d\tau. \quad \ldots\ldots (8)$$

Before proceeding to calculate these three terms separately in the centre-of-mass system we shall study first the interaction potentials which can give rise to these different processes.

§ 3. Interaction Potentials

The complete Hamiltonian for the (d, d') reaction can be written in the form

$$H = H_0 + V \quad \ldots\ldots (9)$$

where H_0 is the unperturbed Hamiltonian representing the initial state of the system when the incident deuteron and the target nucleus are at infinite separation, and V represents a 'perturbation'. These operators depend on all the variables of the system described above and can be written explicitly as

$$H_0 = H_T + T_n + T_p + V_{np} \quad \ldots\ldots (10)$$

$$V = V_{pT} + V_{nT} \quad \ldots\ldots (11)$$

$$= V_{dc} + V_{dd'} \quad \ldots\ldots (12)$$

with

$$V_{pT} = V_{pp'} + V_{pn'} + V_{pc} \quad \ldots\ldots (13)$$

$$V_{nT} = V_{np'} + V_{nn'} + V_{nc} \quad \ldots\ldots (14)$$

$$V_{dc} = V_{pc} + V_{nc} \quad \ldots\ldots (15)$$

$$V_{d'd} = V_{pp'} + V_{p'n} + V_{np'} + V_{nn'}. \quad \ldots\ldots (16)$$

In the above expressions H_T represents the Hamiltonian of the target nucleus, T_n and T_p refer to the kinetic energy operators of the neutron and proton forming the incident deuteron, and V_{ij} is the interaction between the two particles i and j.

The perturbing potential V consists of different parts which can give rise to various mechanisms. If in the amplitude (6) we use the form V_{pT} or V_{nT} for the interaction potential V, then we get immediately the Huby–Newns formula. Similarly if we use instead of these the potential $V_{dd'}$ in the same amplitude (6) we get a formula of the Austern–Butler–McManus (1953) type. In the present work, however, we shall study the effect of a four-body potential of the form

$$V_F = V_0\delta(\mathbf{r}_p - \mathbf{r}_{p'})\delta(\mathbf{r}_n - \mathbf{r}_{n'}) \quad \ldots\ldots (17)$$

which represents the simultaneous collision of the incident deuteron with the extra neutron–proton pair surrounding the core.

If on the other hand we use the potential $V_{pp'}$ for V in the exchange amplitude (7) then we get for the intensity of the scattered beam a formula of the Huby–Newns type.

If now, the expression (12) for the potential U is used in the amplitude (8), then we get two terms. The first corresponds to the target nucleus stripping of the type discussed by Madansky and Owen (1955). The second term represents the knock-on process.

§ 4. Direct Surface Scattering

In this process the incident deuteron undergoes surface scattering, after simultaneous collision with the extra neutron proton pair surrounding the core, and is itself the out-going deuteron.

We shall assume that the interaction V_F is of the form

$$V_F = V_0 \delta(\mathbf{r}_p - \mathbf{r}_{p'}) \delta(\mathbf{r}_n - \mathbf{r}_{n'}). \qquad \ldots\ldots (18)$$

The total wave functions of the system describing the initial and final state configurations will be expressed in terms of eigenfunctions of the constituent sub-systems, using spin–orbit coupling.

The explicit expression of the total wave function representing the initial state configuration in the centre-of-mass system can be written

$$\begin{aligned}
&\psi_i(\mathbf{pn};\ \mathbf{p'n'c}) \\
&= \sum_{\sigma_p \sigma_n} C(\tfrac{1}{2}\tfrac{1}{2}1;\ \sigma_p \sigma_n) \chi_{\frac{1}{2}}^{\sigma_p}(\mathbf{s}_p) \chi_{\frac{1}{2}}^{\sigma_n}(\mathbf{s}_n) \phi_d(|\mathbf{r}_p - \mathbf{r}_n|) \sum_{\lambda_{p'} \lambda_c \lambda_{p'c} \lambda_{n'} \lambda_T \sigma_{p'} \sigma_c \sigma_{p'c} \sigma_{n'} \sigma_T} \\
&\quad C(l_{p'} l_c l_{p'c};\ \lambda_{p'} \lambda_c) C(l_{p'c} l_{n'} l_T;\ \lambda_{p'c} \lambda_{n'}) C(\tfrac{1}{2} s_c s_{p'c};\ \sigma_{p'} \sigma_c) C(s_{p'c} \tfrac{1}{2} s_T;\ \sigma_{p'c} \sigma_{n'}) \\
&\quad \times C(l_T s_T J_T;\ \lambda_T \sigma_T) \chi_{\frac{1}{2}}^{\sigma_{p'}}(\mathbf{s}_{p'}) \chi_{\frac{1}{2}}^{\sigma_{n'}}(\mathbf{s}_{n'}) \chi_{s_c}^{\sigma_c}(\mathbf{s}) \psi_{l_{p'}}^{\lambda_{p'}}(\mathbf{r}_{p'} - \mathbf{r}_c) \psi_{l_{n'}}^{\lambda_{n'}}(\mathbf{r}_{n'} - \mathbf{r}_c) \psi_{l_c}^{\lambda_c}(\xi) \\
&\quad \times \exp\left\{ i\mathbf{k}_d \left[\tfrac{1}{2}(\mathbf{r}_p + \mathbf{r}_n) - \frac{m_d}{2m_T}(\mathbf{r}_{p'} + \mathbf{r}_{n'}) - \frac{m_c}{m_T} \mathbf{r}_c \right] \right\} \qquad \ldots\ldots (19)
\end{aligned}$$

where $C(J_1 J_2 J_3;\ m_1 m_2)$ represents the Clebsch Gordan vector coupling coefficient, χ_s^{σ} the spin wave function for a particle of spin s and its projection σ; $\phi_d(|\mathbf{r}_p - \mathbf{r}_n|)$ the spatial part of the internal wave function of the deuteron; ξ represents the internal coordinates of the nuclear core; and the rest of the symbols have their conventional meaning.

Similarly we have for the final state configuration the following expression

$$\begin{aligned}
&\psi_f(\mathbf{pn};\ \mathbf{p'n'c}) \\
&= \sum_{\sigma'_p \sigma'_n} C(\tfrac{1}{2}\tfrac{1}{2}1;\ \sigma'_p \sigma'_n) \chi_{\frac{1}{2}}^{\sigma'_p}(\mathbf{s}_p) \chi_{\frac{1}{2}}^{\sigma'_n}(\mathbf{s}_n) \phi_{d'}(|\mathbf{r}_p - \mathbf{r}_n|) \sum_{\lambda'_{p'} \lambda'_c \lambda'_{p'c} \lambda'_{n'} \lambda_R \sigma'_{p'} \sigma'_c \sigma'_{p'c} \sigma'_{n'} \sigma_R} \\
&\quad C(l'_{p'} l'_c l'_{p'c};\ \lambda'_{p'} \lambda'_c) C(l'_{p'c} l'_{n'} l_R;\ \lambda'_{p'c} \lambda'_{n'}) C(\tfrac{1}{2} s'_c s'_{p'c};\ \sigma'_{p'} \sigma'_c) \\
&\quad \times C(s'_{p'c} \tfrac{1}{2} s_R;\ \sigma'_{p'c} \sigma'_{n'}) C(l_R s_R J_R;\ \lambda_R \sigma_R) \\
&\quad \times \chi_{\frac{1}{2}}^{\sigma'_{p'}}(\mathbf{s}_{p'}) \chi_{s'_c}^{\sigma'_c}(\mathbf{s}) \chi_{\frac{1}{2}}^{\sigma'_{n'}}(\mathbf{s}_{n'}) \psi_{l'_{p'}}^{\lambda'_{p'}}(\mathbf{r}_{p'} - \mathbf{r}_c) \psi_{l'_{n'}}^{\lambda'_{n'}}(\mathbf{r}_{n'} - \mathbf{r}_c) \psi_{l'_c}^{\lambda'_c}(\xi) \\
&\quad \times \exp\left\{ i\mathbf{k}_{d'} \left[\tfrac{1}{2}(\mathbf{r}_p + \mathbf{r}_n) - \frac{m_d}{2m_T}(\mathbf{r}_{p'} + \mathbf{r}_{n'}) - \frac{m_c}{m} \mathbf{r}_c \right] \right\}. \qquad \ldots\ldots (20)
\end{aligned}$$

Using equations (19) and (20) in (6) together with (18) and applying the orthonormality relations between the spin wave functions we get

$$F=\sum_{\lambda_{p'}\lambda_c\lambda_{p'c}\lambda_{n'}\lambda_T\lambda'_{p'}\lambda'_{p'c}\lambda'_{n'}\lambda_R\sigma_p\sigma_n\sigma_{p'}\sigma_c\sigma_{p'c}\sigma_{n'}\sigma_T} C^2(\tfrac{1}{2}\tfrac{1}{2}1;\ \sigma_p\sigma_n)C^2(\tfrac{1}{2}s_cs_{p'c};\ \sigma_{p'}\sigma_c)$$
$$\times C^2(s_{p'c}\tfrac{1}{2}s_T;\ \sigma_{p'c}\sigma_{n'})C(l_pl_cl_{p'c};\ \lambda_{p'}\lambda_c)C(l_{p'c}l_{n'}l_T;\ \lambda_{p'c}\lambda_{n'})C(l_Ts_TJ_T;\ \lambda_T\sigma_T)$$
$$\times C(l'_{p'}l_cl'_{p'c};\ \lambda'_{p'}\lambda_c)C(l'_{p'c}l'_{n'}l_R;\ \lambda'_{p'c}\lambda'_{n'})C(l_Rs_RJ_R;\ \lambda_R\sigma_R)V_0$$
$$\times\int|\phi(|\boldsymbol{\rho}_p-\boldsymbol{\rho}_n|)|^2\psi^*_{l'_{p'}}{}^{\lambda'_{p'}}(\boldsymbol{\rho}_p)\psi^*_{l'_{n'}}{}^{\lambda'_{n'}}(\boldsymbol{\rho}_n)\psi_{l_{p'}}{}^{\lambda_{p'}}(\boldsymbol{\rho}_p)\psi_{l_{n'}}{}^{\lambda_{n'}}(\boldsymbol{\rho}_n)$$
$$\times\exp\{i\mathbf{f}(\boldsymbol{\rho}_p+\boldsymbol{\rho}_n)\}d\boldsymbol{\rho}_pd\boldsymbol{\rho}_n \qquad (21)$$

where we have taken the centre of mass of the core as a new origin, and denoted by $\boldsymbol{\rho}_p$ and $\boldsymbol{\rho}_n$ the new coordinates as shown in figure 1, so that

$$\boldsymbol{\rho}_i=\mathbf{r}_i-\mathbf{r}_c \text{ with i=p, n respectively} \qquad \ldots\ldots(22)$$

and

$$\exp\left\{i\frac{m_c}{m_T}\mathbf{Q}[\tfrac{1}{2}(\mathbf{r}_p+\mathbf{r}_n)-\mathbf{r}_c]\right\}=\exp\{i\mathbf{f}(\boldsymbol{\rho}_p+\boldsymbol{\rho}_n)\} \qquad \ldots\ldots(23)$$

where

$$\mathbf{f}=\tfrac{1}{2}\frac{m_c}{m_T}\mathbf{Q} \qquad \ldots\ldots(24)$$

and

$$\mathbf{Q}=\mathbf{k}_d-\mathbf{k}_{d'}. \qquad \ldots\ldots(25)$$

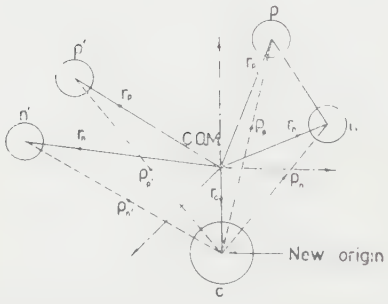

Figure 1. The initial configuration coordinate system, referred to the centre of mass of the entire system as origin. The transformation in coordinates necessary to make the centre of mass of the core the new origin is also shown.

We shall take for the internal wave function of the deuteron the Gaussian form

$$\phi_d(|\boldsymbol{\rho}_p-\boldsymbol{\rho}_n|)\propto\exp\{-\gamma^2(\rho_p{}^2+\rho_n{}^2)\}\{\rho_p\rho_n\}^{\frac{1}{2}}\sum_{l\lambda}I_{l+\frac{1}{2}}(2\gamma^2\rho_p\rho_n)Y^*_l{}^{\lambda}(\Omega_p)Y_l{}^{\lambda}(\Omega_n). \qquad \ldots\ldots(26)$$

$I_{l+\frac{1}{2}}(2\gamma^2\rho_p\rho_n)$ is the modified Bessel function, and $Y_l{}^{\lambda}(\Omega)$ is the conventional spherical harmonic. On choosing the direction of the vector $\mathbf{f}=\frac{1}{2}(m_c/m_T)\mathbf{Q}$ as the polar axis with respect to which the angles Ω_p and Ω_n are defined, the two plane waves given by equation (23) can be expanded along this direction and we get

$$\exp\{i\,\mathbf{f}(\boldsymbol{\rho}_p+\boldsymbol{\rho}_n)\}=\sum_{LL'}4\pi[L]^{\frac{1}{2}}[L']^{\frac{1}{2}}i^{L+L'}J_L(f\rho_p)J_{L'}(f\rho_n)Y_L{}^0(\Omega_p)Y_{L'}{}^0(\Omega_n) \qquad \ldots\ldots(27)$$

where $J_L(f\rho)$ is the spherical Bessel function (Watson 1944), and the symbol $[z]$ will be used to denote the quantity $2z+1$.

We shall now use equations (26) and (27) in equation (21) and form the spherical harmonic expansion of the proton and neutron wave functions (taking only the single values $l_{n'}$ and $l_{p'}$ according to the shell model concept). We then express the products of spherical harmonics of the same argument as a linear superposition of single spherical harmonics, carry out the angular integrations over Ω_p and Ω_n, and take the Bessel functions outside the integral since they are slowly varying functions. The remaining integral will be a function of R_0, and will be denoted simply by $\Lambda(R_0, l_{p'}, l_{n'}, l'_{p'}; l'_{n'})$.

The scattering amplitude is then given by

$$F = A \sum_{\lambda_{p'}\lambda_{c}\lambda_{p'c}\lambda_{n'}\lambda_{T}\lambda'_{p'}\lambda'_{p'c}\lambda'_{n'}\lambda_{R}\sigma_{p}\sigma_{n}\sigma_{p'}\sigma_{c}\sigma_{p'c}\sigma_{n'}\sigma_{T}} \left\{\prod_{i=1}^{12} C_i^F\right\} \sum_{lLL'L_pL_n} (-)^{\lambda+\lambda_{p'}+\lambda'_{p'}} i^{L_p+L_n}$$
$$\times [l_{p'}]^{\frac{1}{2}}[l_{n'}]^{\frac{1}{2}}[l'_{p'}]^{\frac{1}{2}}[l'_{n'}]^{\frac{1}{2}}$$
$$\times [l]\left\{\prod_{i=13}^{20} C_i^F\right\} I_{l+\frac{1}{2}}(4\gamma^2 R_0^2) J_{L_p}(fR_0) J_{L_n}(fR_0) \Lambda(R_0, l_{p'}, l_{n'}, l'_{p'}, l'_{n'}) \quad \ldots\ldots (28)$$

where $\prod_{i=1}^{12} C_i^F$ denotes the product of 12 Clebsch–Gordan coefficients in (21), and

$$\prod_{i=13}^{20} C_i^F = C(l_{p'} l'_{p'} L;\ 00) C(LlL_p;\ 00) C(l_{n'} l'_{n'} L';\ 00) C(L'lL_n;\ 00)$$
$$\times C(l_{p'} l'_{p'} L;\ \lambda_{p'} - \lambda'_{p'}) C(LlL_p;\ -\lambda\lambda) C(l_{n'} l'_{n'} L';\ \lambda_{n'} - \lambda'_{n'}) C(L'lL_n;\ \lambda - \lambda). \quad \ldots\ldots (29)$$

The various sums occurring in equation (28) can be simplified by vector coupling methods (Biedenharn, Blatt and Rose 1952).

On squaring (28) summing and averaging over final and initial spin states, we find the intensity of the outgoing deuterons due to direct surface scattering to be

$$|F|^2 = A' \sum_f [f]^{-1} W^2(l_T J_T l_R J_R;\ s_T f)$$
$$\times \Big| \sum_{lLL'L_pL_n g} i^{+L+L'} [l][g][L]^{-\frac{1}{2}} Z(l_{p'} l_{p'c} l'_{p'} l'_{p'c};\ l_c L)$$
$$\times Z(L_p L L_n L';\ lf) Z(l_{n'} f l_n L;\ gL') W(l_R l_{p'c} L l'_{n'};\ g l'_{p'c}) W(l_{n'} l_{p'c} f l_R;\ l_T g)$$
$$\times C(L'lL_n;\ 00) C(LlL_p;\ 00) I_{l+\frac{1}{2}}(4\gamma^2 R_0^2) J_{L_p}(fR_0) J_{L_n}(fR_0)\Big|^2 \quad \ldots\ldots (30)$$

where the quantum numbers f and g are given by

$$\mathbf{f} = \mathbf{L} + \mathbf{L}' \quad \ldots\ldots (31)$$

$$\mathbf{g} = \mathbf{L} + \mathbf{l}'_{n'}. \quad \ldots\ldots (32)$$

The function W is the Racah coefficient. The associated coefficient Z is related to W by

$$Z(l_1 J_1 l_2 J_2;\ sL) = i^{L-l_1-l_2} \{[l_1][l_2][J_1][J_2]\}^{1/2} W(l_1 J_1 l_2 J_2;\ sL) C(l_1 l_2 L;\ 00). \quad \ldots\ldots (33)$$

We shall now show that this expression can be simplified greatly by using the properties of the Clebsch–Gordan and Racah coefficients.

The sum over l extends from 0 to ∞; however, due to the modified Bessel function $I_{l+1/2}(4\gamma^2 R_0^2)$, most of the contribution comes from the first few terms.

The quantum number L assumes the values $|l_{p'} - l'_{p'}|$ to $l_{p'} + l'_{p'}$. The other quantum number L_p assumes the values $|L - l|$ to $L + l$. The allowed values of L' and L_n are given by similar inequalities.

Conservation of total angular momentum requires the following selection rule

$$\mathbf{J}_R - \mathbf{J}_T = \mathbf{f} = \mathbf{L} + \mathbf{L}'. \qquad \ldots\ldots (34)$$

This follows from the various triangle conditions under which the Z's and W's are non-zero.

In addition conservation of parity demands that the quantum number f be even if the parity of the residual and target nuclei are the same, and odd if they are opposite.

§ 5. Nucleon Exchange Stripping

We now consider the inelastic scattering of deuterons in which a nucleon in the incident deuteron may be exchanged with a similar nucleon inside the target nucleus. We have assumed, for definiteness, that the single exchangeable nucleon in the target nucleus is the proton p'. Let c' refer to the remainder of the target nucleus. The internal wave function of the target nucleus can be written as $\psi_T(\mathbf{p'c'})$. Also the internal wave function of the residual nucleus takes the form $\psi_R(\mathbf{p'c'})$.

We shall choose the potential $V_{pp'}$ to be of the form

$$V_{pp'} = V_1 \delta(\mathbf{r}_p - \mathbf{r}_{p'}). \qquad \ldots\ldots (35)$$

We now expand the wave functions for the initial and final configurations in terms of the complete set of simultaneous eigenfunctions of the total angular momenta and their projections for the constituents of these configurations. We therefore write

$$\begin{aligned}
&\psi_i(\mathbf{pn}\,;\ \mathbf{p'c}) \\
&= \sum_{\sigma_p \sigma_n} C(\tfrac{1}{2}\tfrac{1}{2}1\,;\ \sigma_p \sigma_n) \chi_{\frac{1}{2}}^{\sigma_p}(\mathbf{s}_p) \chi_{\frac{1}{2}}^{\sigma_n}(\mathbf{s}_n) \phi_d(|\mathbf{r}_p - \mathbf{r}_n|) \sum_{\lambda_{p'} \lambda_{c'} \lambda_T \sigma_{p'} \sigma_{c'} \sigma_T} C(l_{p'} l_{c'} l_T\,;\ \lambda_{p'} \lambda_{c'}) \\
&\quad \times C(\tfrac{1}{2} s_{c'} s_T\,;\ \sigma_{p'} \sigma_{c'}) C(l_T s_T J_T\,;\ \lambda_T \sigma_T) \chi_{\frac{1}{2}}^{\sigma_{p'}}(\mathbf{s}_{p'}) \chi_{s_{c'}}^{\sigma_{c'}}(\mathbf{s'}) \psi_{l_{p'}}^{\lambda_{p'}}(\mathbf{r}_{p'} - \mathbf{r}_c) \psi_{l_{c'}}^{\lambda_{c'}}(\xi') \\
&\quad \times \exp\left\{ i\mathbf{k}_d \left[\tfrac{1}{2}(\mathbf{r}_p + \mathbf{r}_n) - \frac{m_d}{2m_T} \mathbf{r}_{p'} - \frac{m_{c'}}{m_T} \mathbf{r}_{c'} \right] \right\}. \qquad \ldots\ldots (36)
\end{aligned}$$

We also have for the final configuration the following expression:

$$\begin{aligned}
&\psi_f(\mathbf{p'n}\,;\ \mathbf{pc'}) \\
&= \sum_{\sigma'_{p'} \sigma'_n} C(\tfrac{1}{2}\tfrac{1}{2}1\,;\ \sigma'_{p'} \sigma'_n) \chi_{\frac{1}{2}}^{\sigma'_{p'}}(\mathbf{s}_{p'}) \chi_{\frac{1}{2}}^{\sigma'_n}(\mathbf{s}_n) \phi_{d'}(|\mathbf{r}_{p'} - \mathbf{r}_n) \\
&\quad \times \sum_{\lambda_p \lambda'_{c'} \lambda_R \sigma'_p \sigma'_{c'} \sigma_R} C(l_p l'_{c'} l_R\,;\ \lambda_p \lambda'_{c'}) C(\tfrac{1}{2} s'_{c'} s_R\,;\ \sigma'_p \sigma'_{c'}) C(l_R s_R J_R\,;\ \lambda_R \sigma_R) \\
&\quad \times \chi_{\frac{1}{2}}^{\sigma'_p}(\mathbf{s}_p) \chi_{s'_{c'}}^{\sigma'_{c'}}(\mathbf{s'}) \psi_{l_p}^{\lambda_p}(\mathbf{r}_p - \mathbf{r}_{c'}) \psi_{l'_{c'}}^{\lambda'_{c'}}(\xi') \\
&\quad \times \exp\left\{ i\mathbf{k}_{d'} \left[\tfrac{1}{2}(\mathbf{r}_{p'} + \mathbf{r}_n) - \frac{m_d}{2m_T} \mathbf{r}_p - \frac{m_{c'}}{m_T} \mathbf{r}_{c'} \right] \right\}. \qquad \ldots\ldots (37)
\end{aligned}$$

Using the above expansions in equation (7) and applying the orthonormality relations between the spin wave functions, together with equation (35) we get

$$\begin{aligned}
G = &\sum_{\lambda_p \lambda_{p'} \lambda_{c'} \lambda_T \lambda_R \sigma_p \sigma_n \sigma_{p'} \sigma_{c'} \sigma_T \sigma_R} C(\tfrac{1}{2}\tfrac{1}{2}1\,;\ \sigma_p \sigma_n) C(l_{p'} l_{c'} l_T\,;\ \lambda_{p'} \lambda_{c'}) C(\tfrac{1}{2} s_{c'} s_T\,;\ \sigma_{p'} \sigma_{c'}) \\
&\times C(l_T s_T J_T\,;\ \lambda_T \sigma_T) C(\tfrac{1}{2}\tfrac{1}{2}1\,;\ \sigma_{p'} \sigma_n) C(l_p l_{c'} l_R\,;\ \lambda_p \lambda_{c'}) C(\tfrac{1}{2} s_{c'} s_R\,;\ \sigma_p \sigma_{c'}) \\
&\times C(l_R s_R J_R\,;\ \lambda_R \sigma_R) V_1 \int |\phi_d(|\boldsymbol{\rho}|)|^2 \psi^*_{l_p}{}^{\lambda_p}(\boldsymbol{\rho}_p) \psi_{l_{p'}}{}^{\lambda_{p'}}(\boldsymbol{\rho}_p) \\
&\times \exp\{ i\mathbf{g}(\boldsymbol{\rho} + \alpha \boldsymbol{\rho}_p) \} d\boldsymbol{\rho}_p d\boldsymbol{\rho} \qquad \ldots\ldots (38)
\end{aligned}$$

where

$$\mathbf{g} = \tfrac{1}{2}(\mathbf{k}_d - \mathbf{k}_{d'}) \qquad \ldots\ldots (39)$$

$$\boldsymbol{\rho}_\nu = \mathbf{r}_\nu - \mathbf{r}_c \qquad \nu = p, n$$

$$\boldsymbol{\rho} = \boldsymbol{\rho}_n - \boldsymbol{\rho}_p \qquad \ldots\ldots (40)$$

$$\alpha = 2 - m_d/m_T. \qquad \ldots\ldots (41)$$

We introduce the Gaussian form for $\phi_d(|\boldsymbol{\rho}|)$:

$$\phi_d(|\boldsymbol{\rho}|) \propto \exp(-\gamma^2\rho^2). \qquad \ldots\ldots (42)$$

The centre of coordinates in equation (38) is transformed to the centre of the 'core' c'; $\boldsymbol{\rho}_p$ and $\boldsymbol{\rho}_n$ indicate position vectors of the proton and the neutron respectively referred to the new origin. This transformation in coordinates is shown in figure 2.

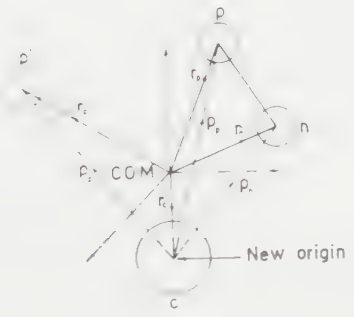

Figure 2. The initial configuration coordinate system, referred to the centre of mass of the entire system as origin. The transformation in coordinates necessary to make the centre of mass of the core the new origin is also shown.

We can also expand the two plane waves along the direction of the wave vector **g** defined above:

$$\exp\{i\mathbf{g}(\boldsymbol{\rho} + \alpha\boldsymbol{\rho}_p)\} = \sum_{LL'} 4\pi[L]^{\frac{1}{2}}[L']^{\frac{1}{2}} i^{L-L'} J_{L'}(g\rho) J_L(\alpha g\rho_p) Y_{L'}^{0}(\Omega) Y_L^{0}(\Omega_p). \qquad \ldots\ldots (43)$$

We shall now use equations (42) and (43) in equation (38), denote the product of the eight Clebsch Gordan coefficients by the symbol $\prod_{i=1}^{8} C_i^G$ and carry out the integration over the solid angles Ω and Ω_p. We assume that the proton exchange process takes place on the surface of a sphere of interaction of radius R_1. The Bessel functions will be taken outside the integral (at R_1). The values of the integral on the proton wave functions will depend on R_1, and will be denoted by $\Lambda(R_1, l_p, l_{p'})$. The scattering amplitude is thus given by

$$G = A\exp(-g^2/8\gamma^2) \sum_{\lambda_p\lambda_{p'}\lambda_{c'}\lambda_T\lambda_R\sigma_p\sigma_n\sigma_{p'}\sigma_{c'}\sigma_T\sigma_R} \sum_L (-)^{\lambda_p} i^L [l_p]^{\frac{1}{2}}[l_{p'}]^{\frac{1}{2}} \left\{\prod_{i=1}^{8} C_i^G\right\}$$
$$\times C(l_p l_{p'} L; 00) C(l_p l_{p'} L; -\lambda_p\lambda_p) J_L(\alpha g R_1) \Lambda(R_1, l_p, l_{p'}). \qquad \ldots\ldots (44)$$

The various sums occurring in equation (44) can be reduced by the usual vector coupling methods: squaring, summing over the final and averaging over the initial states we get for the intensity of the deuterons inelastically scattered by proton exchange process:

$$|G|^2 = A' \exp(-g^2/4\gamma^2) \sum_L \sum_{fg} [f][g] W^2(s_T \tfrac{1}{2} s_R \tfrac{1}{2};\ s_{c'} f) W^2(f \tfrac{1}{2} 1 \tfrac{1}{2};\ \tfrac{1}{2} 1)$$
$$\times W^2(f s_R J_T l_T;\ s_T g) W^2(L l_R g s_R;\ l_T J_R) Z^2(l_p l_R l_{p'} l_T;\ l_{c'} L) J_L^2(\alpha g R_1) \quad \ldots\ldots (45)$$

where the quantum numbers f and g are given by:

$$\mathbf{f} = \mathbf{s}_T + \mathbf{s}_R$$
$$\mathbf{g} = l_T + \mathbf{s}_R. \quad \ldots\ldots (46)$$

The conservation of the total angular momentum of the system restricts the values of L to those given by

$$|\mathbf{J}_R + \mathbf{J}_T + \mathbf{1}|_{\min} \leqslant L \leqslant J_R + J_T + 1 \quad \ldots\ldots (47)$$

where

$$\mathbf{L} = \mathbf{l}_p + \mathbf{l}_{p'}.$$

Moreoever, conservation of parity implies that L should be odd or even according to whether or not there is a change of parity.

§ 6. Target Nucleus Stripping and Knock-on Interaction

We now admit the possibility that the outgoing deuteron may be ejected entirely from the target nucleus. This can occur in two ways: (i) The incident deuteron captures the core of the target nucleus, while the extra proton–neutron pair outside the nuclear core is emitted forming the outgoing deuteron. This mechanism may be called target nucleus stripping; (ii) the incident deuteron replaces the outer proton–neutron pair which forms the emitted deuteron. This process is called knock on-interaction.

These two mechanisms arise from the interaction potential V which can be written as

$$V = V_H + V_K \equiv V_{dc} + V_{dd'}$$

where $V_H \equiv V_{dc}$ represents the interaction between the incident deuteron and the core of the target nucleus which is to be captured. $V_K \equiv V_{dd'}$ is the interaction between the incident deuteron and the proton–neutron pair outside the nuclear core. These two potentials respectively are responsible for the target nucleus stripping and the knock-on interaction. We shall consider these two mechanisms separately.

6.1. *Target Nucleus Stripping*

In this mechanism the incident deuteron captures the core of the target nucleus while the outer proton neutron pair in the latter is emitted forming the outgoing deuteron. The scattering amplitude H corresponding to the target nucleus stripping is given by equation (8).

The perturbation potential V_H is taken as an interaction between the incident deuteron and the captured core. Thus we can write V in the form

$$V_H = V_2 \delta(|\mathbf{r}_c - \mathbf{r}_d| - R_2). \quad \ldots\ldots (48)$$

We can expand the total wave functions of the initial and final configurations in terms of the simultaneous eigenfunctions of the component parts of the system. The initial and final states can be written in the centre-of-mass system as

$$\psi_i(\mathbf{pn};\ \mathbf{p'n'c}) = \sum_{\sigma_p\sigma_n} C(\tfrac{1}{2}\tfrac{1}{2}1;\ \sigma_p\sigma_n)\chi_{\frac{1}{2}}^{\sigma_p}(\mathbf{s}_p)\chi_{\frac{1}{2}}^{\sigma_n}(\mathbf{s}_n))\phi_d(|\mathbf{r}_p-\mathbf{r}_n|)$$
$$\times \sum_{[illegible]} C(l_{p'}l_n l_{p'n'};\ \lambda_{p'}\lambda_{n'})$$
$$\cdot C(\tfrac{1}{2}\tfrac{1}{2}s_{[illegible]};\ \sigma_{[illegible]})C(s_{[illegible]}s_c s_{[illegible]};\ \sigma_{[illegible]})C(l_{[illegible]}s_T J_T;\ \lambda_{pn}\sigma_T)$$
$$\times \chi_{\frac{1}{2}}^{\sigma_{p'}}(\mathbf{s}_{p'})\chi_{\frac{1}{2}}^{\sigma_{n'}}(\mathbf{s}_{n'})\chi_{s_c}^{\sigma_c}(\mathbf{s})\psi_{l_{p'}}^{\lambda_{p'}}(\mathbf{r}_{p'}-\mathbf{r}_c)\psi_{l_{n'}}^{\lambda_{n'}}(\mathbf{r}_{n'}-\mathbf{r}_c)$$
$$\cdot \exp\left\{i\mathbf{k}_d\left[\tfrac{1}{2}(\mathbf{r}_{[illegible]}-\mathbf{r}_{[illegible]})-\frac{m_d}{2m_T}(\mathbf{r}_{[illegible]}+\mathbf{r}_n)-\frac{m_c}{m_T}\mathbf{r}_c\right]\right\}, \qquad \ldots\ldots(49)$$

where we have considered the core as a single particle and ignored its internal structure, and hence we have only the two orbital angular momenta $l_{p'}$ and $l_{n'}$, and

$$\psi_f(\mathbf{p'n'};\ \mathbf{pnc})$$
$$= \sum_{\sigma'_{p'}\sigma'_{n'}} C(\tfrac{1}{2}\tfrac{1}{2}1;\ \sigma'_{p'}\sigma'_{n'})\chi_{\frac{1}{2}}^{\sigma'_{p'}}(\mathbf{s}_{p'})\chi_{\frac{1}{2}}^{\sigma'_{n'}}(\mathbf{s}_{n'})\phi_{d'}(|\mathbf{r}_{p'}-\mathbf{r}_{n'}|)$$
$$\times \sum_{\sigma_p\sigma_n\sigma_{pn}\sigma'_c\sigma_R\lambda'_c} C(\tfrac{1}{2}\tfrac{1}{2}s_{pn};\ \sigma'_p\sigma'_n)C(s_{pn}s'_c s_R;\ \sigma_{pn}\sigma'_c)C(l'_c s_R J_R;\ \lambda'_c\sigma_R)$$
$$\times \chi_{\frac{1}{2}}^{\sigma'_p}(\mathbf{s}_p)\chi_{\frac{1}{2}}^{\sigma'_n}(\mathbf{s}_n)\chi_{s'_c}^{\sigma'_c}(\mathbf{s})\psi_{l'_c}^{\lambda'_c}(\mathbf{r}_c-\mathbf{r}_d)\phi_d(|\mathbf{r}_p-\mathbf{r}_n|)$$
$$\times \exp\left\{i\mathbf{k}'_d\left[\tfrac{1}{2}(\mathbf{r}_{p'}+\mathbf{r}_{n'})-\frac{m_d}{2m_T}(\mathbf{r}_p+\mathbf{r}_n)-\frac{m_c}{m_T}\mathbf{r}_c\right]\right\}. \qquad \ldots\ldots(50)$$

In the above equation the deuteron is in an S-state, and hence l'_c is the only orbital angular momentum involved in combining the core and the deuteron to form the residual nucleus.

On choosing the centre of mass of the incident deuteron as origin, with respect to which the new coordinates $\boldsymbol{\rho}_i$ are referred, and using equations (49) and (50) in equation (8) together with the orthonormality relations for the spin wave functions, we obtain

$$H = \sum_{\lambda_{p'}\lambda_{n'}\lambda'_c\sigma_{p'}\sigma_{n'}\sigma'_{p'}\sigma'_{n'}\sigma'_c\sigma_R} C(\tfrac{1}{2}\tfrac{1}{2}1;\ \sigma_p\sigma_n)C(l_{p'}l_n l_{p'n'};\ \lambda_{p'}\lambda_{n'})$$
$$\times C(\tfrac{1}{2}\tfrac{1}{2}s_{p'n'},\ \sigma_{p'}\sigma_{n'})C(s_{p'n'}s_c s_T;\ \sigma_{p'n'}\sigma_c)C(l_{p'n'}s_T J_T;\ \lambda_{p'n'}\sigma_T)$$
$$\times C(\tfrac{1}{2}\tfrac{1}{2}1;\ \sigma_{p'}\sigma_{n'})C(\tfrac{1}{2}\tfrac{1}{2}s_{pn};\ \sigma'_p\sigma'_n)C(s_{pn}s_c s_R;\ \sigma_{pn}\sigma_c)C(l'_c s_R J_R;\ \lambda'_c\sigma_R)$$
$$\times \int \psi^*_{lc'}{}^{\lambda_{c'}}(\boldsymbol{\rho}_c)\exp(i\mathbf{h}_c\boldsymbol{\rho}_c)V_H d\boldsymbol{\rho}_c$$
$$\times \int \phi^*_d(|\boldsymbol{\rho}_p-\boldsymbol{\rho}_n|)\phi_d(|\boldsymbol{\rho}_p-\boldsymbol{\rho}_n|)d\boldsymbol{\rho}_p d\boldsymbol{\rho}_n$$
$$\times \int \phi_d(|\boldsymbol{\rho}_{p'}-\boldsymbol{\rho}_{n'}|)\exp\{i\mathbf{h}(\boldsymbol{\rho}_{p'}+\boldsymbol{\rho}_{n'})\}\psi_{l_{p'}}^{\lambda_{p'}}(\boldsymbol{\rho}_{p'})\psi_{l_{n'}}^{\lambda_{n'}}(\boldsymbol{\rho}_{n'})d\boldsymbol{\rho}_{p'}d\boldsymbol{\rho}_{n'}$$
$$\ldots\ldots(51)$$

where the momentum transfer vectors $\mathbf{h}_c$ and $\mathbf{h}$ are given by

$$\mathbf{h}_c = -\mathbf{k}_d - \frac{m_d}{m_T}\mathbf{k}_{d'} \qquad \ldots\ldots(52)$$

$$\mathbf{h} = -\tfrac{1}{2}\mathbf{k}_{d'} - \frac{m_d}{2m_T}\mathbf{k}_d. \qquad \ldots\ldots(53)$$

This shift in coordinates is shown in figure 3 with the notation

$$\boldsymbol{\rho}_i = \mathbf{r}_i - \mathbf{r}_d \quad \text{with} \quad i = p, n \text{ and } c. \qquad \ldots\ldots (54)$$

$$\boldsymbol{\rho}_j = \mathbf{r}_c - \mathbf{r}_j \quad \text{with} \quad j = p' \text{ and } n'. \qquad \ldots\ldots (55)$$

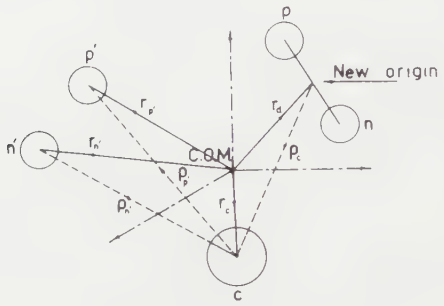

Figure 3. The initial configuration coordinate system, referred to the centre of mass of the entire system as origin. The transformation in coordinates necessary to make the centre of mass of the incident deuteron the new origin is also shown.

If we choose the direction of the momentum transfer vector $\mathbf{h}$ as the axis of quantization,we get for the expansions of the plane waves occurring in equation (51) the following:

$$\exp(i\mathbf{h}_c \cdot \boldsymbol{\rho}_c) = \sum_{l'_c \lambda'_c} 4\pi i^{l'_c} J_{l'_c}(h_c \rho_c) Y_{l'_c}^{\lambda'_c}(\Omega_c) Y^*_{l'_c}{}^{\lambda'_c}(\mathbf{h}_c, \mathbf{h}) \qquad \ldots\ldots (56)$$

where $(\mathbf{h}_c, \mathbf{h})$ is the angle between $\mathbf{h}_c$ and $\mathbf{h}$,

$$\exp\{i\mathbf{h}(\boldsymbol{\rho}_{p'} + \boldsymbol{\rho}_{n'})\} = \sum_{L_{p'} L_{n'}} 4\pi [L_{p'}]^{\frac{1}{2}} [L_{n'}]^{\frac{1}{2}} i^{L_{p'} + L_{n'}} J_{L_{p'}}(h\rho_{p'}) J_{L_{n'}}(h\rho_{n'})$$
$$\times Y^0_{L_{p'}}(\Omega_{p'}) Y^0_{L_{n'}}(\Omega_{n'}). \qquad \ldots\ldots (57)$$

For the internal wave function $\phi_d(|\boldsymbol{\rho}_p - \boldsymbol{\rho}_n|)$ we use the Gaussian function

$$\phi_{d'}(|\boldsymbol{\rho}_{p'} - \boldsymbol{\rho}_{n'}|) \propto \exp\{-\gamma^2(\rho_{p'}{}^2 + \rho_{n'}{}^2)\}(\rho_p \rho_n)^{-\frac{1}{2}}$$
$$\times \sum_{l\lambda} I_{l+\frac{1}{2}}(2\gamma^2 \rho_{p'} \rho_{n'}) Y^*_l{}^{\lambda}(\Omega_{p'}) Y_l^{\lambda}(\Omega_{n'}). \qquad \ldots\ldots (58)$$

We substitute these expansions in equation (51) and form the spherical harmonic expansion of the wave functions of the particles p', n' and c; we then express the products of the spherical harmonics of the same argument in equation (59) as a linear combination of single spherical harmonics, perform the angular integrations over $\Omega_{p'}$, $\Omega_{n'}$ and Ω_c and, as before, take the spherical Bessel functions outside the integral at R_2. The remaining integral will be denoted by $\Lambda(R_2, l_{p'}, l_{n'}, l'_c)$.

Then the scattering amplitude becomes

$$H = A \sum_{\lambda_{p'} \lambda_{n'} \lambda_{p'n'} \lambda'_c \sigma_p \sigma_n \sigma_{pn} \sigma_{p'} \sigma_{n'} \sigma_{p'n'} \sigma_c \sigma_T \sigma_R} \left\{ \prod_{i=1}^{9} C_i^H \right\}$$
$$\times \sum_{l \lambda l'_c \lambda'_c L_{p'} L_{n'}} (-)^{\lambda} i^{l'_c + L_{p'} + L_{n'}} [l]^{\frac{1}{2}} [l_{p'}]^{\frac{1}{2}} [l_{n'}]^{\frac{1}{2}} Y^*_{l_{c'}}{}^{\lambda'_c}(\mathbf{h}_c, \mathbf{h}) \left\{ \prod_{i=10}^{13} C_i^H \right\}$$
$$\times I_{l+\frac{1}{2}}(2\gamma^2 R_2{}^2) J_{l_{c'}}(h_c R_2) J_{L_{p'}}(hR_2) J_{L_{n'}}(hR_2) \Lambda(R_2, l_{p'}, l_{n'}, l'_c) \qquad \ldots\ldots (59)$$

where $\prod_{i=1}^{9} C_i^H$ denotes the product of nine Clebsch-Gordan coefficients occurring in equation (51), and

$$\prod_{i=10}^{13} C_i^H = C(ll_{p'}L_{p'};\ -\lambda\lambda)C(ll_nL_{n'};\ \lambda-\lambda)C(ll_{p'}L_{p'};\ 00)C(ll_{n'}L_{n'};\ 00). \quad \ldots\ldots(60)$$

The intensity of the scattered beam is derived from equation (59) by summing and averaging over the final and initial states respectively. Using Racah algebra, this can be evaluated in a closed form:

$$\begin{aligned}|H|^2 = \sum_{f g h \lambda' c} & [f][g][h]W^2(1s_c,J_Tl_{p'n};\ s_Tf)W^2(1s_c,J_Rl'_c;\ s_Rg)W^2(fl_{p'n'}gl'_c;\ s_ch)\\ & \times \Big|\sum_{l'_c L_{p'} L_{n'}} (-)^{l+l'_c} i^{l'_c}[l]^{\frac{1}{2}} Z(L_n ll_{p'n}l_{p'};\ l_n L_{p'})C(l_{p'n'}l'_c h;\ 0\lambda'_c)\\ & \times C(ll_{p'}L_{p'};\ 00)C(ll_{n'}L_{n'};\ 00)\mathrm{Y}^*_{l'_c}{}^{\lambda'_c}(\mathbf{h}_c,\mathbf{h})\mathrm{J}_{l'_c}(h_cR_2)\mathrm{I}_{l+\frac{1}{2}}(2\gamma^2R_2^2)\\ & \times \mathrm{J}_{L_{p'}}(hR_2)\mathrm{J}_{L_{n'}}(hR_2)\Big|^2. \quad \ldots\ldots(61)\end{aligned}$$

The selection rule governing the value of the capture angular momentum $l_{c'}$ is

$$\mathbf{J}_R = \mathbf{s}_c + \mathbf{l}'_c + \mathbf{1} \quad \ldots\ldots(62)$$

where s is the intrinsic spin of the core. We have also the additional rule

$$\mathbf{J}_R - \mathbf{J}_T = \mathbf{l}_{p'} + \mathbf{l}_{n'} + \mathbf{1} + \mathbf{1}. \quad \ldots\ldots(63)$$

6.2. *Knock-on Interaction*

In this process the incident deuteron knocks out a deuteron from the target nucleus, and is then captured. The scattering amplitude K corresponding to the knock-on interaction is also given by equation (8) where V in this case stands for the interaction between the incident deuteron and the extra proton neutron pair outside the core of the target nucleus. The explicit expression of this potential is given by

$$V_{dd'} = V_{pp'} + V_{pn'} + V_{np'} + V_{nn'}. \quad \ldots\ldots(64)$$

The scattering amplitude formed by equations (8) and (64) will therefore consist of four terms, corresponding to the respective potentials in equation (64). These four terms give similar contributions, and for the purpose of calculation we shall choose only the potential $V_{pp'}$ which will be of the form

$$V_{pp'} = V_2\delta(\mathbf{r}_p - \mathbf{r}_{p'}). \quad \ldots\ldots(65)$$

We now expand the total wave functions representing the initial and final state configurations in terms of eigenfunctions of the constituent sub-systems.

We therefore write

$$\begin{aligned}&\psi_i(\mathbf{pn};\ \mathbf{p'n'c})\\ &= \sum_{\sigma_p\sigma_n} C(\tfrac{1}{2}\tfrac{1}{2}1;\ \sigma_p\sigma_n)\chi_{\frac{1}{2}}{}^{\sigma_p}(\mathbf{s}_p)\chi_{\frac{1}{2}}{}^{\sigma_n}(\mathbf{s}_n)\phi_d(|\mathbf{r}_p-\mathbf{r}_n|)\\ &\quad \times \sum_{\lambda_{p'}\lambda_{n'}\lambda_{p'n'}\lambda_c\lambda_T\sigma_{p'}\sigma_{n'}\sigma_{p'n'}\sigma_c\sigma_T} C(l_{p'}l_{n'}l_{p'n'};\ \lambda_{p'}\lambda_{n'})C(l_{p'n'}l_cl_T;\ \lambda_{p'n'}\lambda_c)\\ &\quad \times C(\tfrac{1}{2}\tfrac{1}{2}s_{p'n'};\ \sigma_{p'}\sigma_{n'})C(s_{p'n'}s_cs_T;\ \sigma_{p'n'}\sigma_c)C(l_Ts_TJ_T;\ \lambda_T\sigma_T)\\ &\quad \times \chi_{\frac{1}{2}}{}^{\sigma_{p'}}(\mathbf{s}_{p'})\chi_{\frac{1}{2}}{}^{\sigma_{n'}}(\mathbf{s}_{n'})\chi_{s_c}{}^{\sigma_c}(\mathbf{s})\psi_{l_{p'}}{}^{\lambda_{p'}}(\mathbf{r}_{p'}-\mathbf{r}_c)\psi_{l_{n'}}{}^{\lambda_{n'}}(\mathbf{r}_{n'}-\mathbf{r}_c)\psi_{l_c}{}^{\lambda_c}(\xi)\\ &\quad \times \exp\left\{i\mathbf{k}_d\left[\tfrac{1}{2}(\mathbf{r}_p+\mathbf{r}_n) - \frac{m_d}{2m_T}(\mathbf{r}_{p'}+\mathbf{r}_{n'}) - \frac{m_c}{m_T}\mathbf{r}_c\right]\right\}. \quad \ldots\ldots(66)\end{aligned}$$

We also have for the final configuration the following expression:

$$\psi_f(\mathbf{p'n'};\ \mathbf{pnc}) = \sum_{\sigma'_{p'}\sigma'_{n'}} C(\tfrac{1}{2}\tfrac{1}{2}1;\ \sigma'_{p'}\sigma'_{n'})\chi_{\frac{1}{2}}^{\sigma'_{p'}}(\mathbf{s}_{p'})\chi_{\frac{1}{2}}^{\sigma'_{n'}}(\mathbf{s}_{n'})\phi_{d'}(|\mathbf{r}_{p'}-\mathbf{r}_{n'}|)$$
$$\times \sum_{\lambda_p\lambda_n\lambda_{pn}\lambda'_c\lambda_R\sigma'_p\sigma'_n\sigma'_{pn}\sigma'_c\sigma_R} C(l_p l_n l_{pn};\ \lambda_p\lambda_n)C(l_{pn}l'_c l_R;\ \lambda_{pn}\lambda_c)$$
$$\times C(\tfrac{1}{2}\tfrac{1}{2}s_{pn};\ \sigma'_p\sigma'_n)C(s_{pn}s'_c s_R;\ \sigma_{pn}\sigma'_c)$$
$$\times C(l_R s_R J_R;\ \lambda_R\sigma_R)\chi_{\frac{1}{2}}^{\sigma'_p}(\mathbf{s}_p)\chi_{\frac{1}{2}}^{\sigma'_n}(\mathbf{s}_n)\chi_{s'_c}^{\sigma'_c}(\mathbf{s})\psi_{l_p}^{\lambda_p}(\mathbf{r}_p-\mathbf{r}_c)$$
$$\times \psi_{l_n}^{\lambda_n}(\mathbf{r}_n-\mathbf{r}_c)\psi_{l'_c}^{\lambda'_c}(\xi)$$
$$\times \exp\left\{i\mathbf{k}_{d'}\left[\tfrac{1}{2}(\mathbf{r}_{p'}+\mathbf{r}_{n'})-\frac{m_d}{2m_T}(\mathbf{r}_p+\mathbf{r}_n)-\frac{m_c}{m_T}\mathbf{r}_c\right]\right\}. \quad \ldots\ldots(67)$$

Using the above expansion in equation (8) and applying the orthonormality relations between the spin wave functions, together with equation (65) we get:

$$K = \sum_{\substack{\lambda_{p'}\lambda_{n'}\lambda_{p'n'}\lambda_c\lambda_T\lambda_p\lambda_n\lambda_{pn}\lambda_R \\ \sigma_{p'}\sigma_{n'}\sigma_{p'n'}\sigma_c\sigma_T\sigma_p\sigma_n\sigma_{pn}\sigma_R}} C(\tfrac{1}{2}\tfrac{1}{2}1;\ \sigma_p\sigma_n)C(l_{p'}l_{n'}l_{p'n'};\ \lambda_{p'}\lambda_{n'})C(l_{p'n'}l_c l_T;\ \lambda_{p'n'}\lambda_c)$$
$$\times C(\tfrac{1}{2}\tfrac{1}{2}s_{p'n'};\ \sigma_{p'}\sigma_{n'})C(s_{p'n'}s_c s_T;\ \sigma_{p'n'}\sigma_c)C(l_T s_T J_T;\ \lambda_T\sigma_T)$$
$$\times C(\tfrac{1}{2}\tfrac{1}{2}1;\ \sigma_{p'}\sigma_{n'})C(l_p l_n l_{pn};\ \lambda_p\lambda_n)C(l_{pn}l_c l_R;\ \lambda_{pn}\lambda_c)$$
$$\times C(\tfrac{1}{2}\tfrac{1}{2}s_{pn};\ \sigma_p\sigma_n)C(s_{pn}s_c s_R;\ \sigma_{pn}\sigma_c)C(l_R s_R J_R;\ \lambda_R\sigma_R)$$
$$\times V_2\int \phi^*_{d'}(|\boldsymbol{\rho}_{p'}-\boldsymbol{\rho}_{n'}|)\psi^*_{l_p}{}^{\lambda_p}(\boldsymbol{\rho}_p)\psi^*_{l_n}{}^{\lambda_n}(\boldsymbol{\rho}_n)\psi_{l_{p'}}{}^{\lambda_{p'}}(\boldsymbol{\rho}_p)\psi_{l_{n'}}{}^{\lambda_{n'}}(\boldsymbol{\rho}_{n'})$$
$$\times \phi_d(|\boldsymbol{\rho}_p-\boldsymbol{\rho}_n|)\exp\{i[\mathbf{k}_p\cdot\boldsymbol{\rho}_p+\mathbf{k}_n\cdot\boldsymbol{\rho}_n+\mathbf{k}_{n'}\cdot\boldsymbol{\rho}_{n'}]\}d\boldsymbol{\rho}_p d\boldsymbol{\rho}_n d\boldsymbol{\rho}_{n'} \quad \ldots\ldots(68)$$

where

$$\mathbf{k}_p = \frac{m_c}{2m_T}(\mathbf{k}_d - \mathbf{k}_{d'}) \quad \ldots\ldots(69)$$

$$\mathbf{k}_n = \tfrac{1}{2}\mathbf{k}_d + \frac{m_d}{2m_T}\mathbf{k}_{d'} \quad \ldots\ldots(70)$$

$$\mathbf{k}_{n'} = -\frac{m_d}{2m_T}\mathbf{k}_d - \tfrac{1}{2}\mathbf{k}_{d'}. \quad \ldots\ldots(71)$$

In the derivation of equation (68) we have transformed the coordinates to the centre of the nuclear core c, where the position vector $\boldsymbol{\rho}_i$ denotes the new coordinates as shown in figure 3, so that

$$\boldsymbol{\rho}_i = \mathbf{r}_i - \mathbf{r}_c \text{ with i = p, n and n' respectively.} \quad \ldots\ldots(72)$$

We shall use the Gaussian form for the internal wave function of the deuteron. We can also expand the three plane waves along the direction of the momentum transfer vector $\mathbf{k}_p$ defined above:

$$\exp(i\mathbf{k}_p\cdot\mathbf{p}_p) = \sum_{\mathscr{L}_p} 2\pi^{1/2}(\mathscr{L}_p)^{1/2}i^{\mathscr{L}_p}J_{\mathscr{L}_p}(k_p\rho_p)Y^0_{\mathscr{L}_p}(\Omega_p) \quad \ldots\ldots(73)$$

$$\exp(i\mathbf{k}_n\cdot\boldsymbol{\rho}_n) = \sum_{L_n\Lambda_n} 4\pi i^{L_n}J_{L_n}(k_n\rho_n)Y^*_{L_n}{}^{\Lambda_n}(\Omega_n)Y_{L_n}{}^{\Lambda_n}(\mathbf{k}_p,\mathbf{k}_n) \quad \ldots\ldots(74)$$

$$\exp(i\mathbf{k}_{n'}\cdot\boldsymbol{\rho}_{n'}) = \sum_{L_{n'}\Lambda_{n'}} 4\pi i^{L_{n'}}J_{L_{n'}}(k_{n'}\rho_{n'})Y^*_{L_{n'}}{}^{\Lambda_{n'}}(\Omega_{n'})Y_{L_{n'}}{}^{\Lambda_{n'}}(\mathbf{k}_p,\mathbf{k}_{n'}). \quad \ldots\ldots(75)$$

We can substitute these expansions in equation (68), and form the spherical harmonic expansion of the wave functions of the particles involved in the scattering amplitude; we then carry out the angular integrations, and take the Bessel functions outside the integral at R_2. The value of the remaining integral will depend on R_2 and will be denoted by $\Lambda(R_2, l_\mathrm{p}, l_\mathrm{n}, l_{\mathrm{p}'}, l_{\mathrm{n}'})$. The scattering amplitude is thus given by

$$K = A \sum_{\lambda_\mathrm{n}\lambda_{\mathrm{n}'}\lambda_\mathrm{p}\lambda_{\mathrm{p}'}\lambda\lambda'} \sum_{l_\mathrm{n}l_{\mathrm{n}'}l_\mathrm{p}l_{\mathrm{p}'}L_\mathrm{n}L_{\mathrm{n}'}L_\mathrm{p}L_{\mathrm{p}'}\mathscr{L}_\mathrm{n}\mathscr{L}_\mathrm{p}} \left\{\prod_{i=1}^{12} C_i^K\right\} \sum_{l\lambda l'\lambda' L_\mathrm{p}L_{\mathrm{p}'}\mathscr{L}_\mathrm{p}L_\mathrm{n}L_{\mathrm{n}'}\mathscr{L}_\mathrm{n}m'}$$
$$\times (-)^{\lambda_\mathrm{p}+\lambda+\lambda'+\lambda_\mathrm{n}} i^{L_\mathrm{p}+L_\mathrm{n}+L_{\mathrm{n}'}} [l][l'][l_\mathrm{n}]^{\frac{1}{2}}[l_\mathrm{p}]^{\frac{1}{2}}[l_{\mathrm{n}'}]^{\frac{1}{2}}[l_{\mathrm{p}'}]^{\frac{1}{2}}[L_\mathrm{n}]^{-\frac{1}{2}}[L_{\mathrm{n}'}]^{-\frac{1}{2}}$$
$$Y_{\mathscr{L}_\mathrm{n}}^{m'}(\mathbf{k}_\mathrm{n}, \mathbf{k}_{\mathrm{n}'})$$
$$\cdot \left\{\prod_{i=13}^{23} C_i^K\right\} \mathrm{I}_{l+\frac{1}{2}}(2\gamma^2 R_2^2)\mathrm{I}_{l'+\frac{1}{2}}(2\gamma^2 R_2^2)\mathrm{J}_{\mathscr{L}_\mathrm{p}}(k_\mathrm{p}R_2)\mathrm{J}_{L_\mathrm{n}}(k_\mathrm{n}R_2)\mathrm{J}_{L_{\mathrm{n}'}}(k_{\mathrm{n}'}R_2)$$
$$\times \Lambda(R_2, l_\mathrm{p}, l_\mathrm{n}, l_{\mathrm{p}'}, l_{\mathrm{n}'}), \qquad \ldots\ldots (76)$$

where $\prod_{i=1}^{12} C_i^K$ denotes the product of the twelve Clebsch-Gordan coefficients occurring in equation (68), and

$$\prod_{i=13}^{23} C_i^K = C(ll_\mathrm{p}L_\mathrm{p};\ -\lambda\lambda_\mathrm{p})C(l'l_{\mathrm{p}'}L_{\mathrm{p}'};\ -\lambda'\lambda_{\mathrm{p}'})C(L_\mathrm{p}L_{\mathrm{p}'}\mathscr{L}_\mathrm{p};\ \Lambda_\mathrm{p}\Lambda_{\mathrm{p}'})C(ll_\mathrm{n}L_\mathrm{n};\ \lambda-\lambda_\mathrm{n})$$
$$\cdot C(l'l_{\mathrm{n}'}L_{\mathrm{n}'};\ \lambda'\Lambda_{\mathrm{n}'})C(L_\mathrm{n}L_{\mathrm{n}'}\mathscr{L}_\mathrm{n};\ \Lambda_\mathrm{n}\Lambda_{\mathrm{n}'})C(ll_\mathrm{p}L_\mathrm{p};\ 00)C(l'l_{\mathrm{p}'}L_{\mathrm{p}'};\ 00)$$
$$\times C(L_\mathrm{p}L_{\mathrm{p}'}\mathscr{L}_\mathrm{p};\ 00)C(ll_\mathrm{n}L_\mathrm{n};\ 00)C(l'l_{\mathrm{n}'}L_{\mathrm{n}'};\ 00). \qquad \ldots\ldots (77)$$

The intensity of the ejected deuterons by knock-on interaction is derived from equation (76) by squaring, and summing over the final and averaging over the initial states. The various sums can be reduced by using the usual vector coupling methods. Then the intensity becomes

$$|K|^2 = A' \sum_{ghkm} [h][k]W^2(gl_\mathrm{pn}l_\mathrm{T}l_\mathrm{c};\ l_{\mathrm{p}'\mathrm{n}'}l_\mathrm{R})W^2(1s_\mathrm{c}J_\mathrm{T}l_\mathrm{T};\ s_\mathrm{T}h)W^2(1s_\mathrm{c}J_\mathrm{R}l_\mathrm{R};\ s_\mathrm{R}k)$$
$$\times W^2(hs_\mathrm{c}gl_\mathrm{R};\ l_\mathrm{T}k)\Big| \sum_{ll'L_\mathrm{p}L_{\mathrm{p}'}\mathscr{L}_\mathrm{p}L_\mathrm{n}L_{\mathrm{n}'}\mathscr{L}_\mathrm{n}} (-)^{\mathscr{L}_\mathrm{n}-\mathscr{L}_\mathrm{p}l-l'}$$
$$\times \mathrm{Y}_{\mathscr{L}_\mathrm{n}}^{m}(\mathbf{k}_\mathrm{n}, \mathbf{k}_{\mathrm{n}'})[l]^{\frac{1}{2}}[l']^{\frac{1}{2}}[\mathscr{L}_\mathrm{p}]^{\frac{1}{2}}[\mathscr{L}_\mathrm{n}]^{\frac{1}{2}}Z(L_\mathrm{n}L_\mathrm{p}l_\mathrm{n}l_\mathrm{p};\ l_\mathrm{pn}l)$$
$$\times Z(L_{\mathrm{n}'}L_{\mathrm{p}'}l_{\mathrm{n}'}l_{\mathrm{p}'};\ l_{\mathrm{p}'\mathrm{n}'}l')X(\mathscr{L}_\mathrm{n}L_{\mathrm{n}'}L_\mathrm{n};\ \mathscr{L}_\mathrm{p}L_{\mathrm{p}'}L_\mathrm{p};\ gl_{\mathrm{p}'\mathrm{n}'}l_\mathrm{pn})$$
$$\times C(ll_\mathrm{p}L_\mathrm{p};\ 00)C(l'l_{\mathrm{p}'}L_{\mathrm{p}'};\ 00)C(L_\mathrm{p}L_{\mathrm{p}'}\mathscr{L}_\mathrm{p};\ 00)C(\mathscr{L}_\mathrm{n}\mathscr{L}_\mathrm{p}g;\ m0)$$
$$\times \mathrm{I}_{l+\frac{1}{2}}(2\gamma^2R_2^2)\mathrm{I}_{l'+\frac{1}{2}}(2\gamma^2R_2^2)\mathrm{J}_{\mathscr{L}_\mathrm{p}}(k_\mathrm{p}R_2)\mathrm{J}_{L_\mathrm{n}}(k_\mathrm{n}R_2)\mathrm{J}_{L_{\mathrm{n}'}}(k_{\mathrm{n}'}R_2)|^2 \quad \ldots\ldots (78)$$

where the quantum numbers g, h and k are given by

$$\mathbf{g} = \mathbf{l}_{\mathrm{p}'\mathrm{n}'} + \mathbf{l}_\mathrm{pn}; \quad \mathbf{h} = \mathbf{s}_\mathrm{c} + \mathbf{l}_\mathrm{T}; \quad \mathbf{k} = \mathbf{s}_\mathrm{c} + \mathbf{l}_\mathrm{R}. \qquad \ldots\ldots (79)$$

The function X is the $9j$ Wigner coefficient.

Conservation of the total angular momentum requires

$$\mathbf{J}_\mathrm{R} - \mathbf{J}_\mathrm{T} = \mathbf{g} + \mathbf{1} + \mathbf{1} \qquad \ldots\ldots (80)$$

where

$$\mathbf{g} = \mathbf{l}_\mathrm{p} + \mathbf{l}_\mathrm{n} + \mathbf{l}_{\mathrm{p}'} + \mathbf{l}_{\mathrm{n}'}.$$

In addition, conservation of parity implies that g should be odd or even according to whether or not there is a change of parity.

§ 7. Comparisons with Experiment and Discussion

Equations (30), (45), (61) and (78) together with their associated selection rules provide a basis for computing the differential cross section for a specified reaction. The predictions of the theory developed in the preceding sections have been compared with the experimental angular distributions for some typical (d, d′) reactions.

As can be seen from figures 4 to 15, there is a common contribution to the (d, d′) reaction from the nucleon exchange mechanism whose amplitude is given by G. Table 1 gives some data concerning the nuclear states involved in the considered reactions, together with the allowed values of the quantum number

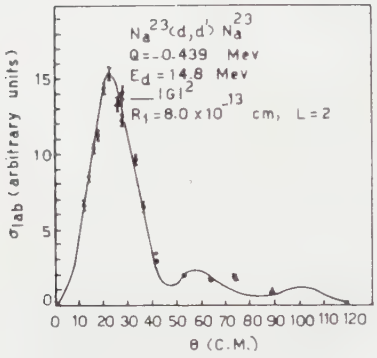

Figure 4. Comparison of theory and experiment for the reaction ^{23}Na(d, d′)^{23}Na proceeding to the first state (Van Heerden 1958).

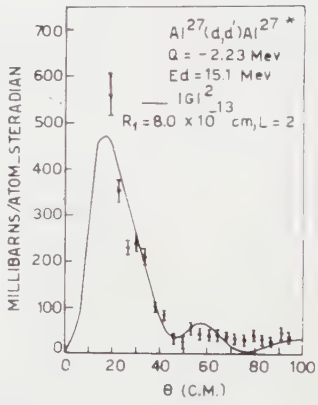

Figure 5. Comparison of theory and experiment for the reaction ^{27}Al(d, d′)^{27}Al* proceeding to the first state (Haffner 1956).

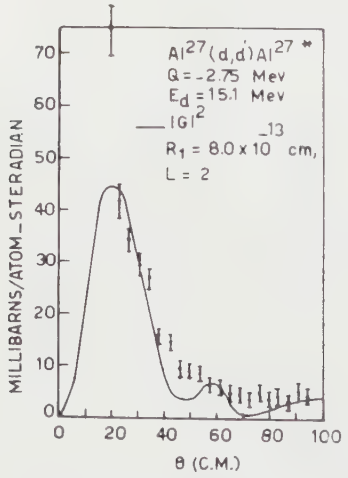

Figure 6. Comparison of theory and experiment for the reaction ^{27}Al(d, d′)^{27}Al* proceeding to the second state (Haffner 1956).

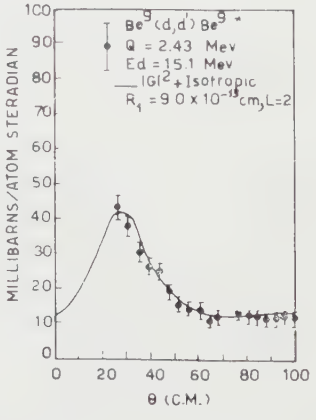

Figure 7. Comparison of theory and experiment for the reaction ^{9}Be(d, d′)^{9}Be* proceeding to the first state (Haffner 1956).

Table 1. Parameters Characterizing the Nucleon Exchange Differential Cross Section

E_d	Nucleus	J_T^π	Q	J_R^π	Orbit of p′	L	R_1 (10^{-13} cm)	$\frac{\sigma_c}{\sigma_e+\sigma_c}$	Ref.
15·0	^{6}Li	1^+	−2·19	3^+	$p_{\frac{3}{2}}$	2	8·4		4
15·1	^{9}Be	$\frac{3}{2}^-$	−2·43	$\frac{5}{2}^-$	$p_{\frac{3}{2}}$	2	9·0	30%	4
15·0	^{12}C	0^+	−4·43	2^+	$p_{\frac{3}{2}}$	2	7·7		4
8·7	^{20}Ne	0^+	−1·63	2^+	$d_{\frac{5}{2}}$	2	8·0	32%	3
14·8	^{23}Na	$\frac{3}{2}^+$	−0·44	$\frac{5}{2}^+$	$d_{\frac{5}{2}}$	2	8·0	—	1
15·1	^{24}Mg	0^+	−1·37	2^+	$d_{\frac{5}{2}}$	2	8·0	13%	4
8·9	^{24}Mg	0^+	−1·37	2^+	$d_{\frac{5}{2}}$	2	8·0	39%	2
15·1	^{27}Al	$\frac{5}{2}^+$	−2·23	$\frac{3}{2}^+$	$d_{\frac{5}{2}}$	2	8·0	—	4
15·1	^{27}Al	$\frac{5}{2}^+$	−2·75	$\frac{5}{2}^+$	$d_{\frac{5}{2}}$	2	8·0	—	4
8·9	^{28}Si	0^+	−1·78	2^+	$d_{\frac{5}{2}}$	2	8·0	50%	2

References: 1, Vogelsang and McGruer (1958), 2 Hinds, Middleton and Parry (1957), 3, Van Heerden (1958) 4, Huffner (1956).

L for the nucleon exchange amplitude G. Numerical calculations for the nucleon exchange intensity show some resemblance with the Huby Newns theoretical curve. This might be expected, since in fact, the Huby–Newns model is a special case of the nucleon exchange mechanism, since the stripped particle is itself recaptured again by its partner.

In figures 4 to 6 the experimental data are compared with the angular distributions predicted by (+5) only. The fact that excellent agreement between the theoretical and experimental angular distributions is observed provides strong support for the proton exchange stripping mechanism. These figures represent examples of reactions proceeding via pure exchange process.

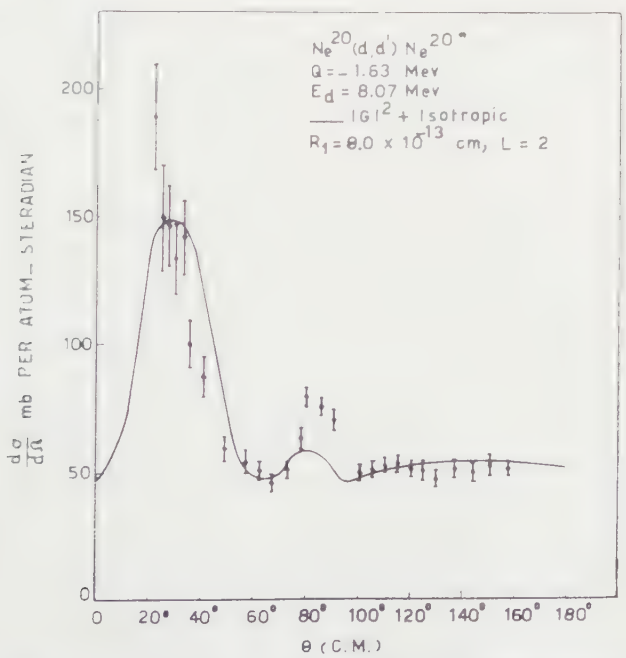

Figure 8. Comparison of theory and experiment for the reaction ^{20}Ne(d, d′)^{20}Ne* proceeding to the first state (Vogelsang and McGruer 1958).

In figures 7 to 11 the experimental points can be adequately represented if the pure exchange intensity is added to an isotropic background representing contributions from compound nucleus formations. Also shown in table 1 are the ratio of $\sigma_{comp}/(\sigma_{exch}+\sigma_{comp})$ measured at the first peak together with the values of the interaction radius R_1. The values of R_1 are chosen to give best fitting.

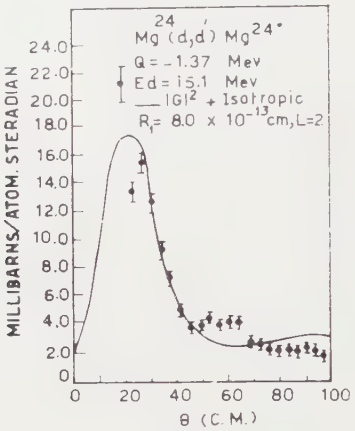

Figure 9. Comparison of theory and experiment for the reaction ^{24}Mg(d, d')^{24}Mg* proceeding to the first state (Haffner 1956).

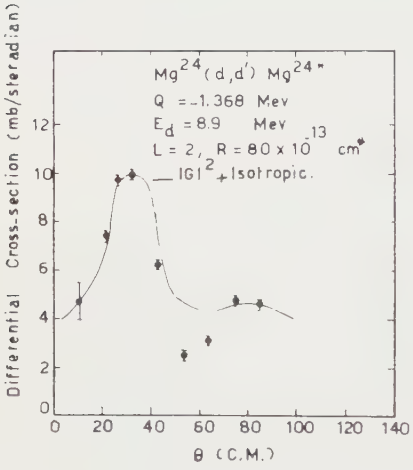

Figure 10. Comparison of theory and experiment for the reaction ^{24}Mg(d, d')^{24}Mg* proceeding to the first state (Hinds *et al.* 1957).

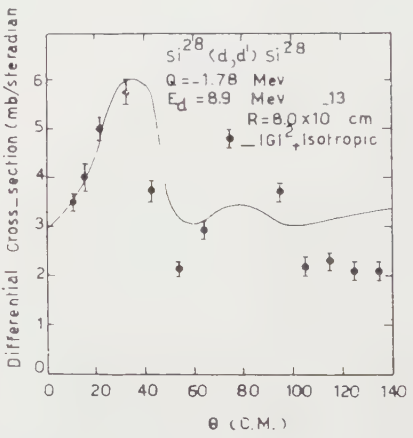

Figure 11. Comparison of theory and experiment for the reaction ^{28}Si(d, d')^{28}Si* proceeding to the first state (Hinds *et al.* 1957).

Figures 12 and 13 show the angular distributions of deuterons inelastically scattered from ^{6}Li and ^{12}C nuclei respectively. These two reactions are interesting in that the experimental data for the differential cross section show a comparable secondary peak at large angles. This may suggest an additional contribution from other mechanisms such as F or H to the usual nucleon exchange process G.

In these two figures the experimental points are compared with the theoretical curves obtained from $|G+H|^2$. In figure 12 the allowed values of the capture angular momentum l'_c are limited to even values by the parity rule, given by (61). The value $l'_c=0$ was found to give best fit. However, this choice of $l'_c(=0)$ leads to the value of 2 for the total angular momentum of the ^{4}He core, which is different from that of the free α-particle. We take for $l_{p'}$ and $l_{n'}$ the value 1 as this is the expected value according to the shell model. In figure 13 the value of l'_c is also taken to be zero, which leads to the value 1 for the total angular momentum of the ^{10}B core. This is again different from that of the free core. The values of $l_{p'}$ and $l_{n'}$ are taken as unity in accordance with the predictions of the shell model. In these two cases, inteference terms between the nucleon exchange and target nucleus stripping intensities are found to play a significant role.

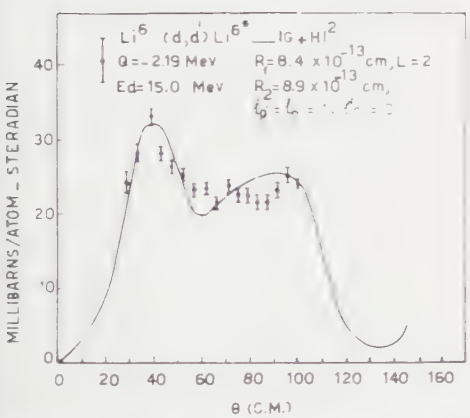

Figure 12. Comparison of theory and experiment for the reaction ^{6}Li(d, d')^{6}Li* proceeding to the first state (Haffner 1956).

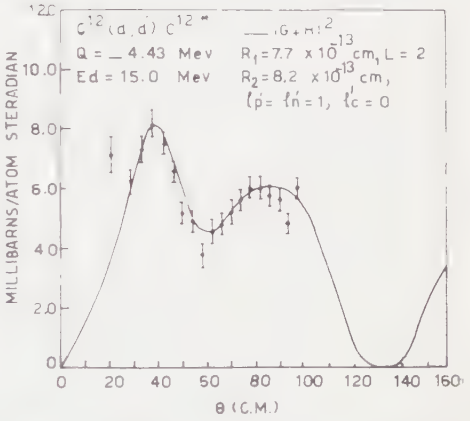

Figure 13. Comparison of theory and experiment for the reaction ^{12}C(d, d')^{12}C* proceeding to the first state (Haffner 1956).

This characteristic secondary peaking in the angular distribution of the scattered deuterons in these two reactions may also suggest the possibility that they arise from a combination of F and G. In figures 14 and 15 are shown the theoretical curves obtained from $|F|^2+|G|^2$ for the nuclei ^{6}Li and ^{12}C respectively. Table 2 gives information about the allowed values of the quantum numbers and nuclear interaction radii required to fit the experimental data. For these two reactions no interference terms exist between the two mechanisms F and G since there is a phase difference of $\frac{1}{2}\pi$ between the two amplitudes.

Table 2. Parameters Characterizing the Direct Scattering and Target Stripping Differential Cross Sections

	F			*H*					
Nucleus	$l'_{p'}$	$l'_{n'}$	R_0 $\times10^{-13}$ cm	$l_{p'}$	$l_{n'}$	l'_c	J'_c	J_c	R_2 $\times10^{-13}$ cm
^{6}Li	1	1	8·3	1	1	0	2+	0+	8·9
^{12}C	1	1	7·0	1	1	0	1+	3+	8·2

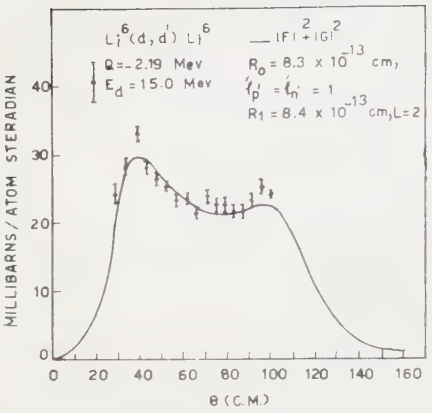

Figure 14. Comparison of theory and experiment for the reaction ^{6}Li(d, d')^{6}Li proceeding to the first state (Haffner 1956).

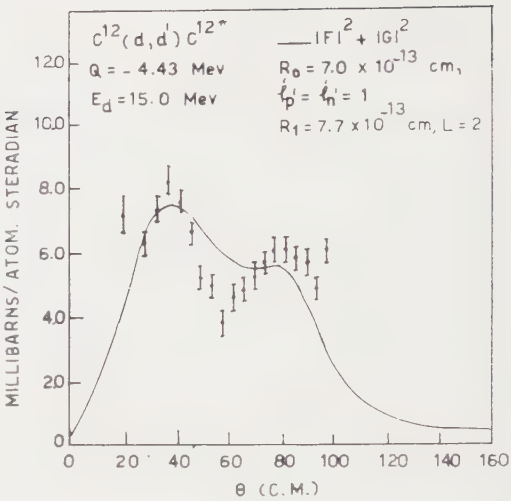

Figure 15. Comparison of theory and experiment for the reaction ^{12}C(d, d')^{12}C* proceeding to the first state (Haffner 1956).

Comparison of figures 12 to 15 shows that a better fit is obtained with the first combination $|G+H|^2$ for the ^{12}C nucleus and with the second combination $|F|^2+|G|^2$ for the ^{6}Li nucleus.

Unfortunately, the calculation of the differential cross section for the knock-out process is more difficult than the other cases, owing to the existence of several summation quantum numbers. For the purpose of illustrating the nature of the differential cross section, the angular distribution is calculated for the case when $l_p=l_n=l_{p'}=l_{n'}=0$. This can be realized by a reaction of the form ^{30}P (d, d') ^{30}P to the 0·7 Mev excited state. In this case $J_T{}^{\pi}=J_R{}^{\pi}=1^+$. The expected behaviour of the differential cross section is shown in figure 16. Apart from the rise in intensity at $\theta=0°$, the resulting curve is similar to that obtained by the exchange or Huby process with angular momentum transfer of value 2.

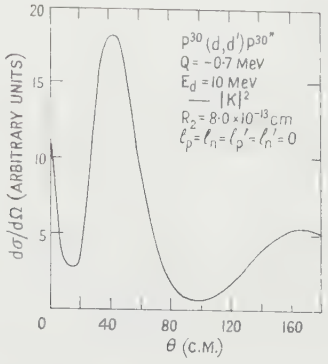

Figure 16. Knock-on interaction angular distribution appropriate for the first excited state reaction ^{30}P(d, d')^{30}P with $E_d=10$ Mev (lab.).

Acknowledgments

The authors would like to express their gratitude to the referees for their valuable comments, and to Mr. El-Khishin for his helpful discussions concerning this manuscript.

References

Austern, N., Butler, S. T., and McManus, H., 1953, *Phys. Rev.*, **92,** 350.
Biedenharn, L. C., Blatt, J. M., and Rose, M. E., 1952, *Rev. Mod. Phys.*, **24,** 249.
Blair, J. S., and Henley, E. M., 1959, *Phys. Rev.*, **112,** 2029.
French, A. P., 1957, *Phys. Rev.*, **107,** 1655.
Haffner, J. W., 1956, *Phys. Rev.*, **103,** 1398.
Hinds, S., Middleton, R., and Parry, G., 1957, *Proc. Phys. Soc.* A, **70,** 900.
Huby, R., and Newns, H. C., 1951, *Phil. Mag.*, **42,** 1442.
Madanksy, L., and Owen, G. E., 1955, *Phys. Rev.*, **99,** 1608.
Matsunobu, H., and Yoshida, S., 1958, *Progr. Theor. Phys.*, **19,** 599.
Sawicki, J., 1958, *Nucl. Phys.*, **7,** 50.
Van Heerden, I. J., 1958, *Nucl. Phys.*, **6,** 55.
Vogelsang, W. F., and McGruer, J. N., 1958, *Phys. Rev.*, **109,** 1663.
Watson, G. N., 1944, *A Treatise on The Theory of Bessel Functions* (Cambridge : University Press).

A Variational Principle for Scattering Phases

By I. C. PERCIVAL
Physics Department, University College London

MS. received 16*th December* 1959

Abstract. A first-order variational principle for a stationary scattering phase is obtained by keeping constant the energy normalization for permitted variations of the wave function. The principle is used to derive (i) a variational correction to the phase obtained from given approximate wave functions, (ii) a first-order perturbation theory, (iii) a first Born approximation and (iv) a variational method for obtaining approximate wave functions analogous to that of Kohn. (i), (ii) and (iii) are more generally applicable than the corresponding expressions for $\tan\delta_l$ and $\sin\delta_l$, where δ_l is the phase, and simple models suggest that they are more accurate than for $\tan\delta_l$, but an example indicates that (iv) may be worse than Kohn's variational method. A possible explanation is given.

The theory is generalized to many channels. Many complications arise which are absent or trivial for one channel, and the generalization is not complete, since we are unable to define a stationary phase matrix, and the range of application is more limited.

§ 1. Introduction

The variational principle for the energy is an important property of those solutions of the time-independent Schrödinger equation which represent bound states, and may be used to derive variational corrections to the energy, a perturbation theory, and a variational method for approximate wave functions. The normalization of the wave function plays an important role, and a generalization to states with one free channel may be made through energy normalization. This leads directly to a first-order variational principle for a stationary scattering phase. This principle has already been obtained by Demkov (1958), and we here compare it with other variational principles, and extend the theory to many channels.

§ 2. Normalization for Single-channel Scattering

When obtaining the variational principle for the energy of bound states, there are two equivalent methods of treating the normalization. The energy E may be defined as

$$E=\int d\tau\psi^*H\psi/N, \qquad \ldots\ldots(1)$$

where ψ is the wave function, H the Hamiltonian and N the normalization integrel

$$N=\int d\tau\psi^*\psi. \qquad \ldots\ldots(2)$$

Variations of the wave functions are then restricted to well-behaved functions for which N is finite. Alternatively N may be omitted from the definition of E, and ψ further restricted to those functions for which $N=1$. In either case E is stationary for the appropriate variations about an exact solution of the Schrödinger equation.

When obtaining the variational principle for the phase we shall treat the normalization by a method analogous to the second alternative. The variational principle itself is not affected by this choice of method.

The wave function which represents scattering in a single channel is of the form

$$\Psi_E(X,r)_{r\to\infty} \psi(X)\, F_E(r)/r, \qquad \ldots\ldots(3)$$

where r is the channel coordinate, and X represents all other coordinates. $\psi(X)$ may be chosen normalized to unity and is a solution of the equation

$$[H(X)-E_0]\psi(X)=0. \qquad \ldots\ldots(4)$$

The Hamiltonian of the whole system is

$$H=H(X)+V(X,r)-\frac{\hbar^2}{2m}\left[\frac{1}{r}\frac{d^2}{dr^2}r-\frac{l(l+1)}{r^2}\right], \qquad \ldots\ldots(5)$$

where m is the channel mass. We shall suppose that $V(X,r)$ is real and tends to zero at least as fast as $1/r^2$ as $r\to\infty$. In the asymptotic region where r is large F_E has the form

$$F_E(r)\sim A\sin(kr-\tfrac{1}{2}l\pi+\delta_l), \qquad \ldots\ldots(6)$$

where l is the orbital angular momentum quantum number of relative motion,

$$\hbar^2k^2=2m(E-E_0)=m^2v^2, \qquad \ldots\ldots(7)$$

v is the channel velocity and δ_l is the scattering phase. The partial cross section Q_l for elastic scattering in the channel is

$$Q_l=\frac{4\pi}{k^2}(2l+1)\sin^2\delta_l. \qquad \ldots\ldots(8)$$

The normalization constant A is so far arbitrary, but in order to obtain a variational principle for the scattering problem, A must be specified both for the exact wave function and for any variations in that wave function that may be considered. We consider only variations in which Ψ_E is well behaved, F_E has the asymptotic form (6), E is constant, and in which the scattering phase δ_l is real. For the exact wave function the last condition follows from the conservation of probability during the collision.

Corresponding to the normalization condition for bound states we have an energy normalization condition

$$\int\int dX r^2 dr\, \Psi_{E^{(1)}}{}^*(X,r)\,\Psi_{E^{(2)}}(X,r)=\delta(E^{(1)}-E^{(2)}), \qquad \ldots\ldots(9)$$

where $\delta(x)$ is the Dirac delta-function, from which

$$A=2^{1/2}/(\pi v)^{1/2}, \qquad \ldots\ldots(10)$$

apart from an arbitrary phase factor; v is the channel velocity, and all integrals cover the full range of the variables. The normalization is independent of the detailed form of the function near $r=0$. Apart from a factor $2^{1/2}$ this normalization is exactly that obtained from the condition of unit inward (or outward) flux.

§ 3. Variational Principle for the Phase

We therefore consider finite variations $\Delta\Psi$ on the exact function Ψ subject to the condition

$$\left.\begin{aligned}\Psi' &= \Psi + \Delta\Psi \underset{r\to\infty}{\sim} \psi(X) 2^{1/2}(\pi v)^{-1/2} r^{-1} \sin(kr - \tfrac{1}{2} l\pi + \delta_l') \\ F' &= F + \Delta F \underset{r\to\infty}{\sim} 2^{1/2}(\pi v)^{-1/2} \sin(kr - \tfrac{1}{2} l\pi + \delta_l')\end{aligned}\right\} \quad \ldots\ldots (11)$$

where the approximate phase $\delta_l' = \delta_l + \Delta\delta_l$ is real; this limits us to variations for which the flux is held constant, by analogy with the bound state, where the integral over the probability density is held constant. The variational principle derived here thereby differs from the variational principle for $\tan \delta_l$ used in the methods of Hulthén (1944) and Kohn (1948), for which the flux varies according to the choice of $\Delta\Psi$.

Like Hulthén and Kohn we consider variations in the convergent integral

$$L = \frac{\pi}{\hbar} \int\int dX r^2\, dr\, \Psi_E^*(H - E)\Psi_E \quad \ldots\ldots (12)$$

which is zero when Ψ_E is a solution of the Schrödinger equation.

$$\frac{\hbar}{\pi}\Delta L = \int\int dX r^2 dr\, [\Delta\Psi_E^*(H-E)\Psi_E + \Psi_E^*(H-E)\Delta\Psi_E + \Delta\Psi_E^*(H-E)\Delta\Psi_E]. \quad \ldots\ldots (13)$$

For variations about the exact function the first term is zero, and by Green's theorem the second term is equal to

$$\lim_{r\to\infty} \frac{\hbar^2}{2m}\left(F' \frac{dF}{dr} - F\frac{dF'}{dr}\right). \quad \ldots\ldots (14)$$

Substituting the asymptotic forms of F and F' we obtain

$$\Delta L = \frac{\pi}{\hbar} \int\int dX r^2 dr\, \Delta\Psi_E^*(H-E)\Delta\Psi_E + \sin\Delta\delta_l \quad \ldots\ldots (15)$$

from which follows the first-order variational principle:

$$\Delta(\delta_l - L) = \mathrm{O}\,[(\Delta\Psi_E)^2] \quad \ldots\ldots (16)$$

for variations about a solution of the Schrödinger equation.

The functional η_l of Ψ_E defined by

$$\eta_l = \delta_l - L \quad \ldots\ldots (17)$$

is stationary for variations about the solution Ψ_E of the Schrödinger equation, where the variations are restricted to satisfy the conservation of probability and the normalization condition (11). For these solutions $L = 0$ and $\eta_l = \delta_l$, so that η_l is a stationary scattering phase.

As with bound states we may remove the normalization restriction on F_E by a re-definition, in this case of L: for

$$F \sim Q 2^{1/2}(\pi v)^{-1/2} \sin(kr - \tfrac{1}{2} l\pi + \delta_l), \quad \ldots\ldots (18)$$

where Q is independent of r, but may vary with F; L is defined to be

$$L = \frac{\pi}{\hbar |Q|^2} \int\int dX r^2\, dr\, \Psi_E^*\,(H-E)\,\Psi_E. \quad \ldots\ldots (19)$$

§ 4. Applications of the Variational Principle

(i) *Phase correction.* The principle is used to obtain, from an approximate solution of the Schrödinger equation, an estimate of the scattering phase which is correct to first order in the error. The approximate solution must have the

asymptotic form (6). After normalization to $A=2^{1/2}(\pi c)^{1/2}$ let the approximate solution be Ψ_E', and the exact solution Ψ_E. Then

$$\eta_l(\Psi_E')=\delta_l'-\frac{\pi}{\hbar}\int\int dX r^2 dr\,\Psi_E'^*(H-E)\Psi_E' \qquad \ldots\ldots(20)$$

$$=\eta_l(\Psi_E)-\Delta\eta_l(\Psi_E')$$

$$=\eta_l(\Psi_E)+O[(\Delta\Psi_E)^2] \qquad \ldots\ldots(21)$$

is correct to first order in $\Delta\Psi_E$.

(ii) *First-order perturbations.* Following from (i), let Ψ_E' be an exact solution of the approximate equation

$$(H'-E)\Psi_E'=0, \qquad \ldots\ldots(22)$$

where $H'=H-\Delta H$ and ΔH, which is usually a potential function, tends to zero at least as fast as $1/r^2$. Then

$$\eta_l(\Psi_E')=\delta_l'+\frac{\pi}{\hbar}\int\int dX r^2 dr\,\Psi_E'^*\Delta H\Psi_E'$$

$$=\eta_l(\Psi_E)+O[(\Delta\Psi_E)^2]. \qquad \ldots\ldots(23)$$

In sections (i) and (ii) the first equality indicates the method used in practice to obtain the stationary phase.

(iii) *The first Born approximation for the phase* (see Mott and Massey 1949, p. 28, Kohn 1954). If we choose

$$H'=H(X)-\frac{\hbar^2}{2m}\left[\frac{1}{r}\frac{d^2}{dr^2}r-\frac{l(l+1)}{r^2}\right], \quad \Delta H=-V(X,r) \qquad \ldots\ldots(24)$$

then $$\Psi_E'=\psi(X)m^{1/2}(\hbar r)^{-1/2}J_{l+1/2}(kr)$$

and $$\eta_l(\Psi_E')=\frac{-\pi m}{\hbar^2}\int_0^\infty dr\,|J_{l+1/2}(kr)|^2\,V(r)\,r \qquad \ldots\ldots(25)$$

where $$V(r)=\int dX\,|\psi(X)|^2\,V(X,r).$$

(iv) *A variational method analogous to that of Kohn* (1948) for obtaining approximate solutions of the Schrödinger equation by using restricted forms of Ψ_E'. Putting $\Psi_E'=G(c_0,\ldots,c_N;X,r)$ with $c_0=\delta_l'$, the equation $\partial\eta_l(\Psi_E')/\partial c_i=0$, with the normalization and the other c_i held constant, is sufficient to determine c_i and thus $\Psi_E'(X,r)$. The phase $\eta_l(\Psi_E')$ is correct to first order in $\Delta\Psi_E$.

§ 5. Comparison with other Variational Principles

The approximate wave functions obtained through variations permitted by the variational principle for $\tan\delta_l$ have their normalization determined by the condition that the coefficient of $\sin(kr-\frac{1}{2}l\pi)$ in the asymptotic region shall be held constant. The energy normalization and the flux are then different for different permitted approximate wave functions, and may even tend to infinity near singularities in $\tan\delta_l$. A similar variational principle may be derived for $\exp(2i\delta_l)$ (the S-matrix); for this principle the approximate wave functions may have different normalization, and also the inward and outward fluxes may differ, thus violating the conservation of probability.

By contrast the approximate wave functions in the variational principle for the scattering phase do not ever violate the conservation of probability, and the

principle is a natural generalization of the variational principle for the energy of bound states by virtue of its normalization condition.

The exact form of Born's approximation derived from a variational principle depends on the subsidiary conditions on the wave functions. The $\tan\delta_l$ variational principle gives equation (25) with $\tan\delta_l$ in place of η_l. In consequence it is impossible to obtain a phase of modulus greater than $\pi/2$. The usual derivation gives $\sin\delta_l$ in place of η_l, which violates the conservation of probability when the integral is greater in modulus than unity. The expression (25) suffers from neither of these limitations.

The practical advantage of these applications of the phase variational principle appears only when powers of δ_l or $\Delta\delta_l$ higher than the first are appreciable. δ_l' is zero in the first Born approximation, whose use when $\Delta\delta_l$ is large is to be avoided if possible, but frequently no better is available.

When $\Delta\delta_l$ is large compared with $\pi/2$ then the estimate of the partial cross section Q_l using the Born approximation to the phase is unlikely to be significantly better or worse than the choice of $Q_l = 2\pi(2l+1)k^{-2}$, which is one-half the maximum. But under these conditions a large number of partial waves will contribute to the total cross section $\Sigma_l Q_l$. When this number is very large, neither is likely to be very far from the correct value, on statistical grounds. However situations occur (Seaton 1955) in which the total cross section has significant contributions both from those Q_l for which δ_l is large and those for which δ_l is small compared with $\pi/2$. In such situations the phase Born approximation provides a method of including both contributions consistently.

Kohn (1954) has shown that the Born approximation for δ_l is preferable to that for $\tan\delta_l$ and $\sin\delta_l$ in the high energy limit. For further comparison the exact phases and the phases obtained from the Born approximations for δ_l, $\sin\delta_l$ and $\tan\delta_l$ are compared for model† potentials in figures 1 and 2.

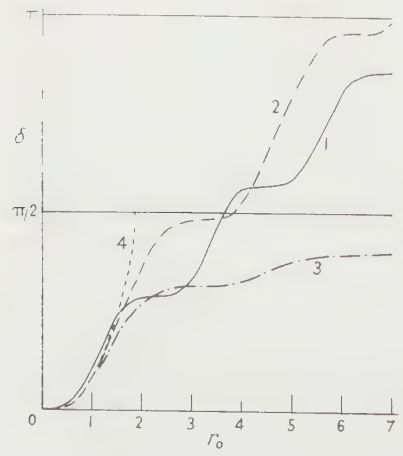

Figure 1. Scattering phases δ for square well potential as functions of r_0, the well breadth.

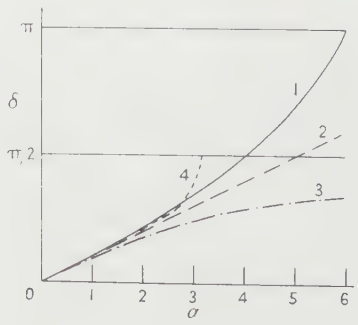

Figure 2. Scattering phases δ for centrifugal potential a/r^2.

1, Exact phase; 2, δ obtained from Born approximation for δ; 3, δ obtained from Born approximation for tan δ; 4, δ obtained from Born aproximation for sin δ.

† The author would like to thank Dr. M. J. Seaton for providing these examples.

In figure 1 the comparison is made for the equation

$$[d^2/dr^2 - u(r) + k^2]F(r) = 0 \qquad F(0) = 0 \qquad \ldots\ldots (26)$$

with the square well potential

$$\left.\begin{aligned} u(r) &= -a \qquad r < r_0 \\ u(r) &= 0 \qquad r > r_0. \end{aligned}\right\} \qquad \ldots\ldots (27)$$

The curve is plotted for $k = 1$, $a = 0{\cdot}96$ with $\delta - \delta_0$ as a function of the well breadth r_0. In figure 2 the comparison is made for the phase $\delta_l = \delta_2$ when

$$u(r) = \frac{l(l+1)}{r^2} - \frac{a}{r^2} \qquad \ldots\ldots (28)$$

with $l = 2$. The exact phase exists only for $4a \leqslant (2l+1)^2$ and all phases are independent of k. In both examples the phase obtained from sin δ exists only over a small range.

A first order variational method for obtaining scattering phases consists of two parts: (*a*) the derivation of an approximate wave function from a stationary functional (subject to certain subsidiary conditions), and (*b*) the first-order correction of the asymptotic phase of this approximate wave function, which may or may not be obtained from the same stationary functional. In the table the phase obtained by applying the correction (i) to the asymptotic phase of a wave function obtained by method (iv) is compared with the variational method of Kohn, which is based entirely on the variational principle for tan δ_l. The comparison is made for elastic potential scattering by the undistorted field of the ground state

Comparison of scattering phases. Numerical integration by McDougall (1932). The phase variational method results in a quadratic equation, and the root chosen, indicated by italics, is determined by the size of ΔL. The Kohn results of Massey and Moiseiwitsch (1951) were recalculated to give an additional decimal place

Phase	k 0·1	0·15	0·2	0·3	0·4	0·5	1·0
Numerical integration	0·730	—	0·9731	1·0458	—	1·0448	0·9057
Phase variation (1)	*0·7215*	*0·8834*	*0·9730*	1·0611	1·1171	1·1656	1·1452
Phase variation (2)	0·6482	0·8732	0·9702	*1·0444*	*1·0564*	*1·0435*	*0·9037*
Kohn	0·7215	0·8832	0·9719	1·0450	1·0564	1·0441	0·9042
Kohn wave functions, phase corrected.	0·7215	0·8832	0·9719	1·0451	1·0572	1·0446	0·9062

of the hydrogen atom, using the same form for the trial functions as Massey and Moiseiwitsch (1951). Evidently the phase variational method is slightly worse than the Kohn method. The main source of error is the poor approximate function obtained by method (iv) for part (*a*) of the variational method. The phase correction (i) applied to a Kohn approximate function in this case gives a phase more accurate than when either the tan δ_l (Kohn) or δ_l variational principle is used for parts (*a*) and (*b*).

The results of the last paragraph might be explained as follows. If a stationary quantity Q is to be obtained accurately from an approximate wave function F', it is desirable that Q should vary as little as possible about its value for the exact wave function F. But if the qauntity Q is to be used to obtain an approximate wave function by first-order variational method as accurately as possible then it should

be sensitive to small variations in the function. Since these two conditions are incompatible, it is no cause for surprise that the phase variational principle should be better than variational principles for $\tan \delta_l$ for obtaining phases from given approximate wave functions in applications (i), (ii) and (iii) but worse for obtaining approximate wave functions in application (iv).

§ 6. Many Channels

At a given energy E the N^2 elastic and inelastic processes associated with N coupled channels of a two-body collision may be considered together as constituent parts of a single N-channel scattering process, and represented mathematically by the N-dimensional linear space of solutions of the Schrödinger equation. Any particular pure state is represented by a function lying in this space. The single equation which determines the scattering in one channel goes over to a set of coupled differential equations, or one matrix differential equation, for N independent solutions. The commutation properties of the matrices introduce new features into the variational principles.

The diagonalization of the scattering matrix leads to eigenphases which are in some respects analogous to the scattering phase in one channel, but they do not determine the scattering cross sections completely: for this the coupling constants, or else the transformation matrix which diagonalizes the scattering matrix, is required. A variational principle for the eigenphases alone is not sufficient for most purposes.

We use the Hermitian phase matrix ξ, which is real when the representation for the bound states is chosen so that the reactance matrix is real, which completely determines the scattering cross sections and reduces to the phase δ_l in the case of a single channel. A variational principle for ξ is derived.

§ 7. Matrix Equations

The time-independent Schrödinger equation for an N-channel scattering process may be reduced to a set of N coupled equations of the form

$$-\frac{\hbar^2}{2m_i}\left[\frac{d^2}{dr_i^2}-\frac{l_i(l_i+1)}{r_i^2}+k_i^2\right]F_{ip}(r_i)+\sum_{j=1}^{N}V_{ij}F_{jp}(r_j)=0 \qquad \ldots\ldots(29)$$

$$(i,p=1,\ldots,N)$$

with boundary conditions at the origin

$$F_{ip}(r_i)=0, \quad (r_i=0) \qquad \ldots\ldots(30)$$

where i and j label the channels and p labels a set of N linearly independent solutions which span the solution space. For the channel i, m_i is the mass, r_i the channel coordinate and $\hbar^2k_i^2/m_i=2(E-E_i)$ is twice the kinetic energy in a centre-of-mass coordinate frame. E is the total energy of the whole system and E_i the residual energy of the reaction products. Equations (29) may be written in matrix form

$$(H-E)F\equiv -\tfrac{1}{2}\hbar^2m^{-1}[(d/dr)^2-l(l+1)r^{-2}+k^2]F+VF=0, \qquad \ldots\ldots(31)$$

where k, l, m and d/dr are diagonal matrices with elements $\boldsymbol{\delta}_{ij}k_i$, $\boldsymbol{\delta}_{ij}l_i$, $\boldsymbol{\delta}_{ij}m_i$ and $\boldsymbol{\delta}_{ij}d/dr_i$ respectively and $\boldsymbol{\delta}_{ij}$ is the Kronecker delta.

We shall suppose that V is a Hermitian operator, so that

$$\int_0^\infty F^\dagger dr VG=\int_0^\infty (VF)^\dagger dr G \qquad \ldots\ldots(32)$$

for well-behaved matrix functions $F(r)$ and $G(r)$ for which $F(0)=G(0)=0$. The order of the factors must be maintained because the matrices do not all commute.

The diagonal matrix $\int_0^\infty \dots dr \dots$ has elements $\int_0^\infty \dots \delta_{ij} dr_i \dots$

and operates as an integral on both sides of the symbol dr.

The explicit form of the operators V_{ij} will depend on the scattering problem. For elementary potential scattering

$$V_{ij}F_{jp}(r_j)=\int_0^\infty dr_j \delta(r_i-r_j)u_{ij}(r_j)F_{jp}(r_j) \qquad \dots\dots(33)$$

where $u_{ij}(r_j)$ are potential functions and $\delta(r)$ is the Dirac delta-function. Note that $V_{ij}F_{jp}(r_j)$ is a function of r_i. For other types of scattering the V_{ij} may be exchange operators or more complicated. We suppose V contains only short-range terms, so that F has the asymptotic form

$$F \underset{v\to\infty}{\sim} (2\pi v)^{-1/2}[e^{-ix}A - e^{ix}B] \qquad \dots\dots(34)$$

where v, the diagonal velocity matrix, and

$$x = kr - \tfrac{1}{2}l\pi \qquad \dots\dots(35)$$

are introduced for convenience. A and B are constant matrices independent of r.

§ 8. Conservation, Normalization and Standard Representation

The phase variational principle for one channel was derived in § 3 for approximate functions which satisfied the physical condition of conservation of probability, and the mathematical condition of constant normalization. For many channels the former condition imposes

$$A^\dagger A = B^\dagger B \qquad \dots\dots(36)$$

on the functions F of (34). The proof is exactly that for the unitary property of the S-matrix: The normalization condition takes the form

$$\int_0^\infty F_{E^{(1)}}{}^\dagger(r)dr F_{E^{(2)}}(r) = \delta(E^{(1)}-E^{(2)}) \cdot I \qquad \dots\dots(37)$$

which is equivalent to

$$A^\dagger A + B^\dagger B = 2I \qquad \dots\dots(38)$$

so that when both conditions are satisfied A and B are unitary matrices.

Any approximate function F satisfying the conservation law may be converted to certain standard forms by post-multiplication.

In the standard scattering representation the matrix functions have the asymptotic form

$$F^{(0)} \sim (2\pi r)^{-1/2}[e^{-ix} - e^{ix}S], \qquad \dots\dots(39)$$

where S is the unitary scattering matrix.

Each column of $F^{(0)}$ contains incoming waves in one channel only. Since S is unitary we may define a Hermitian phase matrix ξ such that

$$S = \exp(2i\xi). \qquad \dots\dots(40)$$

Postmultiplying $F^{(0)}$ by $ie^{-i\xi}$ we obtain a standing wave representation

$$F^{(1)} \sim (2\pi v)^{-1/2} i[e^{-ix}e^{-i\xi} - e^{ix}e^{i\xi}]. \quad \ldots\ldots(41)$$

This is not the same as the standing wave representation $F^{(2)}$ used in the definition of the eigenphases, although both $F^{(1)}$ and $F^{(2)}$ reduce to $2^{1/2}(\pi v)^{-1/2}\sin x$ for a single channel.

§ 9. Variational Principle for Many Channels

We consider the variation $\Delta\xi$ in the Hermitian phase matrix ξ. The derivation of the variational principle is the same as that for one channel, except for the lack of commutation. Using the representation $F^{(1)}$ for all exact and approximate functions, let

$$L = \frac{\pi}{\hbar}\int_0^\infty F^{(1)}\, dr(H-E)F^{(1)}. \quad \ldots\ldots(42)$$

Then since $F^{(1)\prime} = F^{(1)} + \Delta F$ and $(H-E)F^{(1)} = 0$, for the exact solution $F^{(1)}$ we have

$$\begin{aligned}\frac{\hbar}{\pi}\Delta L &= \int_0^\infty F^{(1)\prime\dagger} dr(H-E)F^{(1)\prime} - \int_0^\infty F^{(1)} dr^\dagger (H-E)F^{(1)} \\ &= \int_0^\infty \Delta F^{(1)\dagger} dr(H-E)\Delta F^{(1)} + \int_0^\infty F^{(1)\dagger} dr(H-E)\Delta F^{(1)} + \int_0^\infty \Delta F^{(1)\dagger} dr(H-E)F^{(1)} \\ &= \int_0^\infty \Delta F^{(1)\dagger} dr(H-E)\Delta F^{(1)} + \int_0^\infty F^{(1)\dagger} dr(H-E)F^{(1)\prime} \\ &\quad + \int_0^\infty [(H-E)F^{(1)}]^\dagger dr F^{(1)\prime}. \quad \ldots\ldots(43)\end{aligned}$$

But the potential operator, the centrifugal term and the constant E are all Hermitian so that only the derivative terms remain, and to first order in ΔF,

$$\begin{aligned}\frac{\hbar}{\pi}\Delta L &\simeq \int_0^\infty F^{(1)\dagger} dr[-\tfrac{1}{2}\hbar^2 m^{-1}(d/dr)^2]F^{(1)\prime} - \int_0^\infty [-\tfrac{1}{2}\hbar^2 m^{-1}(d/dr)^2 F^{(1)}]^\dagger dr F^{(1)\prime} \\ &= \tfrac{1}{2}\hbar^2 \lim_{r\to\infty}\{[m^{-1}(d/dr)F^{(1)}]^\dagger F^{(1)\prime} - F^{(1)\dagger} m^{-1}(d/dr)F^{(1)\prime}\} \quad \ldots\ldots(44)\end{aligned}$$

by Green's theorem. On substituting the asymptotic forms given by (41)

$$\begin{aligned}\frac{\hbar}{\pi}\Delta L &\simeq \tfrac{1}{2}\hbar^2 \lim_{r\to\infty}\{[e^{-ix}e^{-i\xi} + e^{ix}e^{i\xi}]^\dagger ik(2\pi v)^{-1} m^{-1}[e^{-ix}e^{-i\xi'} - e^{ix}e^{i\xi'}] \\ &\quad + [e^{-ix}e^{-i\xi} - e^{ix}e^{i\xi}]^\dagger ik(2\pi v)^{-1} m^{-1}[e^{-ix}e^{-i\xi'} + e^{ix}e^{i\xi'}]\} \\ &= i\hbar(2\pi)^{-1}[e^{i\xi}e^{-i\xi'} - e^{-i\xi}e^{i\xi'}]. \quad \ldots\ldots(45)\end{aligned}$$

By the perturbation theory of non-commuting operators, analogous to the perturbation theory of the time-dependent Schrödinger equation:

$$\begin{aligned}e^{i\xi'} = e^{i(\xi+\Delta\xi)} &= \lim_{s\to\infty}[e^{i\xi/s}(1 + i\Delta\xi/s)]^s \\ &= e^{i\xi} + i\int_0^1 d\alpha e^{i(1-\alpha)\xi}\Delta\xi e^{i\alpha\xi} + O[(\Delta\xi)^2], \quad \ldots\ldots(46)\end{aligned}$$

so that to first order in ΔF,

$$\Delta L \simeq \tfrac{1}{2}\int_0^1 d\alpha[e^{i\alpha\xi}\Delta\xi e^{-i\alpha\xi} + e^{-i\alpha\xi}\Delta\xi e^{i\alpha\xi}]. \quad \ldots\ldots(47)$$

In order to evaluate $\Delta\xi$ explicitly in terms of ΔL it is convenient to diagonalize ξ. Let U be a unitary matrix which performs this diagonalization. (This matrix also diagonalizes the S-matrix.) Then

$$[U^{-1}e^{i\alpha\xi}U]_{mn}=\delta_{mn}\exp(i\alpha\delta_m), \qquad \ldots\ldots(48)$$

where δ_m are the eigenphases of the scattering matrix and δ_{mn} is the Kronecker delta. Then if

$$\Delta L^{(2)}=U^{-1}\Delta L U, \quad \Delta\xi^{(2)}=U^{-1}\Delta\xi U, \qquad \ldots\ldots(49)$$

it may be shown by carrying out the integration that

$$\Delta\xi_{mn}{}^{(2)}=\frac{\delta_m-\delta_n}{\sin(\delta_m-\delta_n)}\Delta L_{mn}{}^{(2)}. \qquad \ldots\ldots(50)$$

This variational principle has a less elegant form than the principle for one channel. There is no stationary matrix corresponding to the stationary phase η.

The principle cannot be used in the above form when the exact matrix ξ is not known, and this is generally the case. However, a similar expression may be obtained by expanding $e^{i\xi}$ to first order in $\Delta\xi$, with ξ' constant.

$$\Delta L\simeq\tfrac{1}{2}\int_0^1 d\alpha[e^{i\alpha\xi'}\Delta\xi e^{-i\alpha\xi'}+e^{-i\alpha\xi'}\Delta\xi e^{i\alpha\xi'}]. \qquad \ldots\ldots(51)$$

If U' is the matrix which diagonalizes ξ', and

$$\Delta L^{(2')}=U'^{-1}\Delta L U', \quad \Delta\xi^{(2')}=U'^{-1}\Delta\xi U' \qquad \ldots\ldots(52)$$

then

$$\Delta\xi_{mn}{}^{(2')}=\frac{\delta_m'-\delta_n'}{\sin(\delta_m'-\delta_n')}\Delta L_{mn}{}^{(2')}. \qquad \ldots\ldots(53)$$

Evidently the singularities in the coefficient of ΔL will give trouble and the variational principle is worthless if the difference between any pair of eigenphases is near a non-zero multiple of π, unless the corresponding element of ΔL is negligible.

§ 10. The First Born Approximation for Many Channels

For this particular application of the variational principle, δ_m' are all equal to zero, and the difficulties mentioned in the previous section do not arise.

$$\Delta\xi\simeq\Delta L=L'$$

$$\Delta\xi\simeq-\frac{\pi}{\hbar}\int_0^\infty F^{(1)\prime\dagger}dr\,VF^{(1)\prime}. \qquad \ldots\ldots(54)$$

$$F^{(1)\prime}\sim 2^{1/2}(\pi v)^{-1/2}\sin(kr-\tfrac{1}{2}l\pi) \qquad \ldots\ldots(55)$$

is real and diagonal, so that

$$\left.\begin{aligned}\Delta\xi&=\pi\hbar^{-2}m^{1/2}\int_0^\infty r^{1/2}J_{l+1/2}(kr)dr\,Vr^{1/2}J_{l+1/2}(kr)m^{1/2}\\ \Delta\xi_{ij}&=\pi\hbar^{-2}m_i^{1/2}m_j^{1/2}\int_0^\infty r_i^{1/2}J_{l_i+1/2}(k_ir_i)dr_iV_{ij}r_j^{1/2}J_{l_j+1/2}(k_jr_j),\end{aligned}\right\} \qquad \ldots\ldots(56)$$

where it should be noted that $V_{ij}r_j^{1/2}J_{l_j+1/2}(k_jr_j)$ is a function of r_i. Using the Born approximation to the phase matrix, the S-matrix is

$$S=\exp(-2i\Delta\xi) \qquad \ldots\ldots(57)$$

and if V is Hermitian the conservation laws are never violated. In actual computation the S-matrix is best obtained through diagonalization of the $\Delta\xi$-matrix.

§ 11. Conclusion

For one channel the phase variational principle is applicable over a wider range than other first-order variational principles. The perturbation theory for the phase, including the Born approximation to the phase may be expected to give more accurate results than the corresponding approximations to tan δ_l. The phase variational method for obtaining approximate wave functions does not appear to be so satisfactory as the Kohn method, but the phase correction applied to a Kohn approximate wave function may be more satisfactory than the Kohn method used on its own.

For many channels the range of application of the variational principle is limited by singularities for the off-diagonal elements of the phase matrix, and so does not show such advantages over the R- and S-matrix variational principles as in the single-channel case. However, these singularities do not appear in the derivation of the Born approximation to the phase matrix, which consequently shows the same advantage over the other forms of the Born approximation as when there is only one channel.

The phase variational principle for free states is a natural generalization of the energy variational principle for bound states by virtue of its normalization condition.

Acknowledgments

I should like to thank Mr. L. Castillejo and Dr. M. J. Seaton for helpful discussions, and Mrs. J. B. G. Wallace for assistance with the computations.

References

Demkov, Yu. N., 1958, *Variational Principles in Collision Theory* (Moscow: State Publishing House for Physics and Mathematics). In Russian.

Hulthén, L., 1944, *Kungl. Fysiog. Sällk, Lund Förh*, **14**, 257.

Kohn, W., 1948, *Phys. Rev.*, **74**, 1763.

—— 1954, *Rev. Mod. Phys.*, **26**, 292.

McDougall, J., 1932, *Proc. Roy. Soc.* A, **136**, 549.

Massey, H. S. W., and Moiseiwitsch, B. L., 1951, *Proc. Roy. Soc.* A, **205**, 483.

Mott, N. F., and Massey, H. S. W., 1949, *Theory of Atomic Collisions* (Oxford: University Press).

Seaton, M. J., 1955, *Proc. Phys. Soc.* A, **68**, 457.

Optical Excitation of N_2 by 0·5 to 1·5 MeV Hydrogenic Ions

By E. M. REEVES†‡, R. W. NICHOLLS†§ and D. A. BROMLEY‖

† Department of Physics, University of Western Ontario, London, Ontario, Canada
‖ Atomic Energy of Canada, Ltd., Chalk River, Ontario

MS. received 15*th January* 1960

Abstract. Spectroscopic studies have been made upon the luminosities produced by 0·5 to 1·5 MeV beams of H^+, HH^+, HHH^+ in N_2 at pressures below 100 μ Hg. Photography and identification of spectra, measurement of the variation of intensities of spectral features with pressure, and spectroscopic temperature measurements confirm a primary mechanism of single collision ionization with excitation. Effects of secondary excitation processes by secondary electrons produced in the primary processes are discussed.

§ 1. Introduction

A previous spectroscopic survey of the luminosity arising from the passage of 0·5 and 1 MeV protons through nitrogen and oxygen at pressures between a few microns of mercury and atmospheric pressure (Nicholls, Reeves and Bromley 1959, to be referred to as I) has now been extended to include the molecular hydrogen ions HH^+ and HHH^+ (H_2^+ and H_3^+ respectively in mass-spectroscopic notation) in N_2 up to energies of 1·5 MeV. In addition to further spectroscopic identifications, quantitative measurements have been made on rotational temperatures and also on the variation of intensity of spectral features with pressure. These measurements point fairly conclusively to a set of excitation mechanisms discussed below.

§ 2. Experimental

In order to obtain higher beam intensities ($\sim 5\,\mu$A) than those used in the previous experiments (I, $\sim 0{\cdot}25\,\mu$A), a differential pumping system was used instead of a metallic window to separate the collision chamber from the accelerator vacuum system. Circular apertures, $\frac{1}{16}$ inch in diameter, served both to define and to collimate the atomic and molecular ion beams, and also as differential pumping baffles. A chamber pressure of 100 μ Hg was the highest which could be maintained with the available pumps while retaining adequate vacuum in the accelerator system. Nitrogen was introduced into the differentially pumped collision chamber through a needle valve and pressures were measured with calibrated Pirani gauges.

Atomic and molecular hydrogen ion beams from 0·5 to 5·0 μA were supplied by the Chalk River 3 MeV Van de Graaff accelerator. After traversing the bombardment chamber, the ion beam was collected by an insulated, oil cooled electrode, and integrated using a standard integrator circuit (Gingel and Bromley,

‡ Now at Department of Physics, Imperial College, London, S.W.7.
§ Temporarily on leave of absence at National Bureau of Standards, Washington, D.C.

in preparation). Luminosity produced in the target gas was viewed at 90° and at 15° to the incident beam direction through quartz and lucite windows in the chamber. Figure 1 (Plate I) is a photograph of the collision chamber; a double exposure was used to show the collision chamber and the luminosity of ion beam. A time exposure of a few minutes was used to record the ion beam, and a second (flash) exposure of about a millisecond was superimposed to record the chamber and surrounding equipment.

Simple condensing lenses were used to form images of the beam luminosity on the slits of three spectrographs and a spectrometer, all of which were used at different times during the experiment. They were: (*a*) an f/1·1 prism spectrograph (Reeves and Nicholls 1958), (*b*) a Hilger f/4 spectrograph, (*c*) a 1·5 metre Bausch and Lomb grating spectrograph, and (*d*) a photon counting grating spectrometer. The spectrometer employed a conventional collimator, plane grating and telescope system, together with a dry ice cooled RCA 1P28 photomultiplier which was set to count photons from the (0,1) 4278 Å band of the N_2^+ First Negative system. Output pulses from the photomultiplier, greater than a bias set to discriminate against photomultiplier and amplifier noise, were scaled for a predetermined total integrated beam charge delivered to the collecting electrode. The integrating system automatically eliminated the effect of small beam current fluctuations on the measurement of relative spectral intensity.

§ 3. Results

Three series of measurements were carried out: (*a*) photography and identification of spectra associated with each of the ion beams H^-, HH^-, and HHH^- in N_2 for a range of target gas pressures, (*b*) measurement of intensity distributions for rotational lines of the N_2^+ bands leading to a determination of the 'rotational temperature', and (*c*) measurement of the dependence upon gas pressure of several of the spectral features at each of three incident ion energies 0·5, 1·0 and 1·5 MeV respectively.

3.1. *Spectral Identifications*

The spectra from beams of the three types of ions in N_2 were photographed with the f/1·1 and f/4 spectrographs and were all very similar in appearance. The dominant features were bands of N_2^+ (First Negative and Meinel systems) accompanied by bands of N_2 (First and Second Positive systems) (I). Several lines of H I, N I, and N II were also observed in some cases.

As has been discussed previously (I) the First and Second Positive systems of N_2 were excited by secondary electrons (delta rays) within and outside the beam. Thus the resulting spectra showed features not only of the luminous beam, but also of the less luminous sheath surrounding it. Figure 2 (Plate II) is a spectrum of 1·0 MeV H^+ in N_2 at a pressure of 58 μ Hg photographed with the Hilger f/4 spectrograph using a one hour exposure of Kodak IN plate. The three N_2^+ Meinel bands are λ7850 Å (2, 0), λ8085 Å (3, 2) and λ8330 Å (4, 2). The N I feature near λ8700 Å consists of six lines between λ8680 Å and λ8718 Å of N I multiplet 1 (Moore 1945). A strong line of N I multiplet 2 also lies at λ8216 Å and may therefore partly overlap the Meinel (4, 2) band as the reciprocal dispersion of the spectrograph is 2000 Å mm^{-1} in this region. No lines of H I were observed for any proton beams in N_2 from 0·5 to 1·5 MeV (I).

For HH^+ and HHH^+ beams in N_2 the above N_2^+ and N_2 bands were observed accompanied by several weak lines of NI and NII as well as very weak H_γ and H_β. These lines are listed in table 1.

Table 1. Identifications of Atomic Lines excited by 1 MeV HHH^+ Beams in N_2

Wavelength (Å)	Identification†	Wavelength (Å)	Identification†
4041	NII (39)	4788, 4803	NII (20)
4099, 4110	NI (10)	4861	H_β
4340	H_γ very weak	4895	NII (1)
4432	NII (55)	4935	NI (9)
4530	NII (59)	5001–5005 (4 lines)	NII (4, 9, 64)
		5680	NII (3)

† Numbers in parentheses refer to multiplet numbers in the compilation of Moore (1945).

3.2. *Temperature Measurements*

Relative intensities of the rotational lines of the R-branch of the λ3914 Å (0, 0) band of the N_2^+ First Negative system were measured using photographic photometry. Spectra were photographed on 103a-0 film using a 30 μ slit and the 1·5 m grating spectrograph with exposures of 1–2 hours.

For the N_2^+ First Negative system ($^2\Sigma - ^2\Sigma$), the intensity $I_{K'K''}$ of a rotational line is given in standard notation (Herzberg 1950) by

$$I_{K'K''} = c\nu^4_{K'K''} K' \exp\left[-1{\cdot}44B'K'(K'+1)/T_{\mathrm{rot}}\right] \qquad \ldots\ldots(1)$$

for lines of the R-branch provided that thermal rotational equilibrium exists. The variation of the ν^4 term over a band is small in practice, and thus the rotational temperature may be determined from the slope $(-1{\cdot}44B'/T_{\mathrm{rot}})$ of the straight line obtained by plotting $\log(I_{K'K''}/K')$ against $K'(K'+1)$.

It is also possible to obtain an estimate of the rotational temperature by determining which line (K', K'') of the R-branch of the band has a maximum intensity, for which, from equation (1)

$$\begin{aligned} T_{\mathrm{rot}} &= 1{\cdot}44B'K'(2K'+1) \\ &= 1{\cdot}44B'(K''+1)(2K''+3). \end{aligned} \qquad \ldots\ldots(2)$$

Figure 3 shows a plot of $(\log I_{K'K''}/K')$ against $K'(K'+1)$ for the λ3914 Å N_2^+ band excited by 1·0 MeV protons in N_2 at 60 μ Hg. A temperature of 276 ± 10 K was inferred from the slope of the best 'least squares' straight line fitted to the experimental points. This agrees with the laboratory temperature to within 5 deg. A temperature of 301 ± 80 K was inferred from spectra excited by beams of 1·0 MeV HH^+ and 1·5 MeV HHH^+ in N_2 at the same pressure using equation (2).

Similar agreement has been obtained between laboratory temperature and rotational temperatures of N_2^+ bands excited by 3 keV protons (Carleton 1957) and 10 and 30 keV protons (Roesler *et al.* 1958). Our measurements which show agreement between gas kinetic and rotational temperatures at particle energies above 500 keV show that there is no appreciable interaction between the bombarding particle and the internal motion of the target molecule.

It is interesting to compare this conclusion for high energy particle beams with those drawn from similar spectroscopic temperature measurements made

on N_2^+ excited by 2–4 kev Li^+ ions where strong evidence has been obtained that the rotational motion is severely perturbed in the collision (Reeves and Nicholls, in preparation).

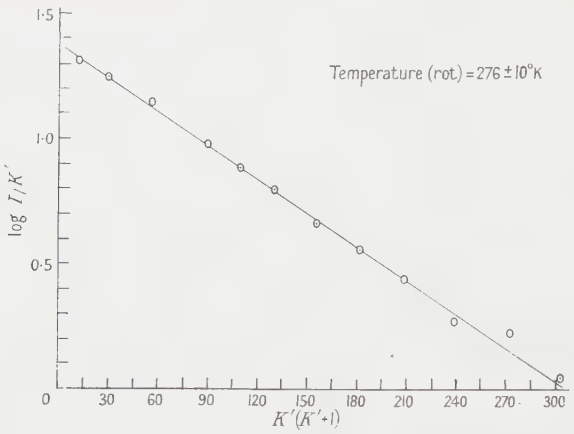

Figure 3. Plot of log I/K' against $K'(K'+1)$ for determination of rotational temperature.

3.3. *Pressure Dependence*

Figure 4 summarizes the results of measurements carried out to measure the variation with pressure of intensity of the λ 4278 Å (0, 1) band of the First Negative system of N_2^+ excited by 0·5 and 1·0 MeV protons using the photon counting spectrometer. In each case the linear segments at low gas pressures (0–60 μ) of the curves is evidence of single collision excitation processes (I). At higher pressures (60–100 μ) the curve rises steeply as would be expected when significant contributions to excitation arise from secondary processes.

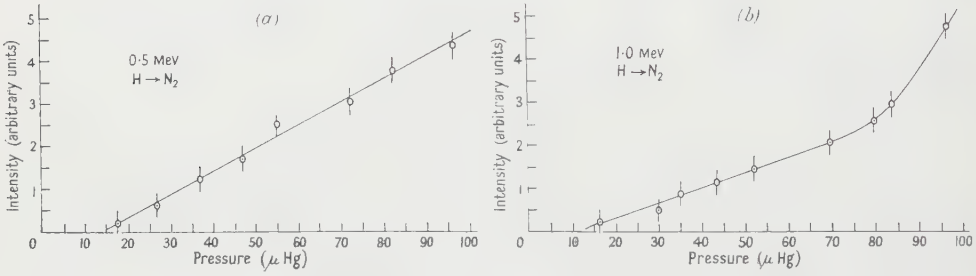

Figure 4. Variation of intensity of λ 4278 Å (0, 1) N_2^+ band with N_2 pressure (the ion beams used are H^+); (*a*) using 0·5 MeV protons; (*b*) using 1·0 MeV protons.

It will be noticed that the 0·5 MeV curve was linear over the complete range of pressure studied, while the 1·5 MeV curve was linear up to 85 μ Hg at which point, owing to the onset of secondary excitation mechanisms involving δ-rays, the curve rises steeply with pressure. As has been pointed out above, the linearity of the early regions of each curve is strongly indicative of the operation of single collision excitation processes. It is possible to discuss the variation of slope of the linear region with energy of particle beam as follows.

If, in the linear region, the total luminosity output L per cm^3 per second is proportional to gas density (or gas pressure P) and specific energy loss dE/dx, then

$$\left.\begin{aligned} L &= \text{const. } P\, dE/dx \\ \text{and} \qquad dL/dP &= \text{const. } dE/dx. \end{aligned}\right\} \qquad \ldots\ldots (3)$$

Thus the slope of the luminosity–pressure curves like figure 4 should vary with energy in the same way that dE/dx varies with energy, that is (Segrè 1953) as a monotonically decreasing function of increasing energy. A comparison between the measured slopes dL/dP and calculated values can be made using the data of Segrè (1953) for air scaled to the value of the observed slope for $\frac{1}{2}$ MeV protons. This comparison is shown in table 2.

Table 2. Comparison of Slopes

E(MeV)	0·5	1·0	1·5
Experimental slope	0·5	0·34	0·22
Calculated slope	(0·5)†	0·31	0·24‡

† Calculated slope scaled to experimental slope here.

‡ No curve is given for this case as difficulty was experienced with the detection and data near the break point were not reliable. In the linear region however the data were sufficient to provide an experimental value of slope.

§ 4. Discussion

The linear dependence of N_2^+ band intensity upon pressure up to at least 60 μ, and the absence of Balmer lines of hydrogen in the observed spectra strongly suggests that the most probable primary collision mechanism operating in proton beams passing through N_2 targets is a single collision involving ionization with excitation, namely

$$H^+ + N_2 \rightarrow H^+ + N_2^{+*} + e. \qquad \ldots\ldots (4)$$

Further the linearity of the intensity–pressure plot indicates that, except at higher pressures (above the break point in each case), the energetic secondary electrons (delta rays) produced in the ionizing collisions play little part in excitation of the N_2^+ bands. However, the fact that the N_2 Second Positive and First Positive band system increase in intensity with increasing gas pressure suggests that the secondary electrons are the dominant agents in exciting the N_2 band systems (which require a multiplicity change (I)).

Similar excitation mechanisms of N_2^+ bands are thought to hold in the case of HH^+ and HHH^+ beams, i.e.

$$\left.\begin{matrix} HH^+ \\ HHH^+ \end{matrix}\right\} + N_2 \rightarrow \left.\begin{matrix} HH^+ \\ HHH^+ \end{matrix}\right\} + N_2^{+*} + e. \qquad \ldots\ldots (5)$$

The weak lines of N I and N II excited in HH^+ and HHH^+ beams indicate the probable operation of dissociative collisions of the form

$$\left.\begin{matrix} HH^+ \\ HHH^+ \end{matrix}\right\} + N_2 \rightarrow \left.\begin{matrix} HH^+ \\ HHH^+ \end{matrix}\right\} + N^* + N^{+*} + e. \qquad \ldots\ldots (6)$$

The very weak H lines observed in HHH^+ beams in all probability arose from one of the possible dissociations of HHH^+, e.g.

$$HHH^+ + N_2 \rightarrow \left.\begin{matrix} H + H^+ \\ \\ HH^+ \end{matrix}\right\} + H^* + N_2^{+*} + e. \qquad \ldots\ldots (7)$$

Acknowledgments

Two of the authors (R. W. N. and E. M. R.) wish to acknowledge partial support of this work by contracts with the Air Force Cambridge Research Centre and the Air Force Office of Scientific Research and the Office of Naval Research and by research grants from the National Research Council of Canada. One of us (E. M. R.) gratefully acknowledges an Ontario Research Foundation Fellowship.

References

Carleton, N. P., 1957, *Phys. Rev.*, **107,** 110.
Herzberg, G., 1950, *Spectra of Diatomic Molecules* (New York : Van Nostrand).
Moore, C. E., 1945, *A Multiplet Table of Astrophysical Interest*, Princeton Observatory Contributions No. 20.
Nicholls, R. W., Reeves, E. M., and Bromley, D. A., 1959, *Proc. Phys. Soc.*, **74,** 89.
Reeves, E. M., and Nicholls, R. W., 1958, *J. Opt. Soc. Amer.*, **48,** 358.
Roesler, F. L., Fan, C. Y., and Chamberlain, J. W., 1958, *J. Atmos. Terr. Phys.*, **12,** 200.
Segrè, E., 1953, *Experimental Nuclear Physics* (New York : Wiley), Vol. 1, p. 166.

Measurement of Ionization and Attachment Coefficients in Humid Air in Uniform Fields and the Mechanism of Breakdown

By A. N. PRASAD and J. D. CRAGGS
Department of Electrical Engineering, The University of Liverpool

MS. received 22nd October 1959, in revised form 4th March 1960

Abstract. Measurement of pre-breakdown currents and breakdown potentials in humid air in the E/p range of 30 to 40 v cm^{-1} (mm Hg)$^{-1}$ at total pressures of 150 and 300 mm Hg with partial pressures of water vapour in the range 2·5 to 15 mm Hg indicate a pronounced increase in attachment compared with conditions in dry air. From the semi-logarithmic plots of current against electrode separation, Townsend's ionization coefficient α and an attachment coefficient η have been obtained for humid air employing the modified Townsend equations for the growth of current. From the measured breakdown potentials, values of Townsend's secondary coefficient γ have been calculated using the modified Townsend breakdown criterion. Further the percentage increase in breakdown potential in humid air has been plotted as a function of the partial pressure of water vapour.

From similar measurements in pure water vapour at pressures of 10 and 20 mm Hg in the E/p range of 30 to 50 v cm^{-1} (mm Hg)$^{-1}$, values of α/p and η/p have been obtained for water vapour. A mean cross section for attachment has been computed for various values of mean electron energies assuming a Maxwellian distribution and employing the earlier measurements of drift and agitation velocities.

§ 1. Introduction

This work was undertaken to study the influence of the presence of water vapour on ionization and attachment coefficients and uniform field breakdown in air. In the earlier work, on the measurement of these quantities in dry air (Harrison and Geballe 1953, Prasad 1959), it was shown that when electron attachment of the type

$$e + AB \rightarrow AB^- \text{ or } A + B^- \qquad \ldots\ldots(1)$$

occurs in the growth of the electron avalanche, the modified Townsend equation for the growth of pre-breakdown current in uniform fields and the criterion for breakdown are satisfactory to explain the uniform field breakdown at high pressures (of the order of one atmosphere). These equations are:

$$\frac{I}{I_0} = \left[\frac{\alpha}{\alpha-\eta}\exp(\alpha-\eta)d - \frac{\eta}{\alpha-\eta}\right] \qquad \ldots\ldots(2a)$$

$$\frac{I}{I_0} = \left[\frac{\alpha}{\alpha-\eta}\exp(\alpha-\eta)d - \frac{\eta}{\alpha-\eta}\right] \Big/ \left[1 - \frac{\gamma\alpha}{\alpha-\eta}\{\exp(\alpha-\eta)d - 1\}\right] \qquad \ldots\ldots(2b)$$

$$\frac{\gamma\alpha}{\alpha-\eta}[\exp(\alpha-\eta)d - 1] = 1 \qquad \ldots\ldots(3)$$

where α and γ are Townsend's primary and secondary coefficients respectively and η is an attachment coefficient, defined analogous to α as the mean number of attachments per electron per centimetre of drift in the field direction.

Whereas in dry air the negative ion formation is largely due to that in oxygen, since attachment in carbon dioxide is relatively small (Craggs and Tozer 1960), in humid air, however, negative ion formation in water vapour is also to be considered. While the experimental data in oxygen (and dry air) are satisfactory, this is not so for water vapour (and humid air) where no direct measurements of cross section for attachment are available. The earlier work in water vapour has been summarized in a review by Craggs and McDowell (1955) and the operative collision processes appear to be:

$$\left.\begin{array}{l}(a)\ e+H_2O\rightarrow OH+H^- \text{ with an appearance potential of } 5{\cdot}7 \text{ ev}\\ (b)\ e+H_2O\rightarrow 2H+O^- \text{ with an appearance potential of } 7{\cdot}3 \text{ ev}\\ (c)\ e+H_2O\rightarrow H_2O^{-*}\rightarrow 2H+O^-\\ (d)\ e+H_2O\rightarrow H+H^++O^-+e \text{ with an appearance potential of } 20{\cdot}8 \text{ ev}\\ (e)\ e+H_2O\rightarrow H^++H^-+O^-+2e \text{ with an appearance potential of } 34{\cdot}3 \text{ ev.}\end{array}\right\} \quad \ldots\ldots (4)$$

In a recent mass spectrometric study of negative ion formation in water vapour, Muschlitz and Bailey (1956) observe a further OH ion which they postulate is the result of a secondary ion molecular collision of the type

$$H^-+H_2O\rightarrow OH^-+H_2$$
$$\text{or}\quad O^-+H_2O\rightarrow OH^-+OH. \qquad \ldots\ldots (5)$$

Energy considerations in the present work (where mean energies are less than 10 ev) rule out the possibility of reactions 4(*d*) and 4(*e*) contributing to the negative ion formation to any appreciable degree. Thus considering the remaining reactions it is seen that the mechanism of negative ion formation is of the type $e+AB\rightarrow A+B^-$ in terms of the ultimate products of the reaction, and hence, ignoring secondary processes as an approximation in humid air a generalized attachment coefficient η can be defined for the entire gas which represents the combined rates of formation of negative ions in the constituent O_2 and H_2O due to the various reactions. Under these conditions therefore the growth of pre-breakdown current can be represented by the modified Townsend equation (cf. equation (2)) and uniform field breakdown in humid air can be explained on the basis of the Townsend build-up mechanisms.

The authors find that the measurements of pre-breakdown currents in air with varying degrees of water vapour content conform to the above theory. Further, measurements of pre-breakdown currents in pure H_2O justify the assumption of the mechanism of negative ion formation as indicated above. From the values of the attachment coefficient obtained in H_2O the mean cross section for attachment for the swarm has been computed assuming a Maxwellian distribution and employing the earlier measurements of drift and agitation velocities.

§ 2. Experimental Technique and Results

A detailed description of the apparatus and the accuracies of the measurements have been published earlier (Hopwood *et al.* 1956, Prasad 1959) and will not be

dealt with here. Two cathodes, one of dural and one of platinum, both of 15 cm overall diameter machined to a Rogowski profile, have been used in the present work. Pre-dried, compressed air, supplied in a cylinder by Messrs. B.O.G. Ltd., has been employed throughout the present work and in the earlier measurements on dry air (Prasad 1959). To check the dryness of air supplied the following technique was adopted. Pre-breakdown currents and breakdown potentials were measured using (*a*) cylinder air directly, (*b*) cylinder air dried in a liquid N_2 trap, (*c*) room air dried in a liquid N_2 trap. Results agreeing closely within the experimental error were obtained from all the three samples, thus justifying the use of cylinder air directly for this study. An auxiliary Pyrex glass vessel (~ 5 cm diameter) was connected to the chamber through appropriate taps such that it could be evacuated either by the main pumps via the chamber or directly by an auxiliary rotary pump in isolation. Pure distilled water, used throughout this study, was introduced into this vessel and frozen by arranging a liquid N_2 bath around the vessel. After the vessel had been evacuated to the limiting vacuum of the auxiliary pump, it was isolated from the pump and evacuated further by the main diffusion pump to 10^{-5} mm Hg. The total pressure of H_2O + dry air was set on the micromanometer (cf. Hopwood *et al.* 1956) to ± 1 mm Hg and water vapour was evaporated to the desired partial pressure (p_w mm Hg) into the chamber under vacuum, the pressure being measured on an oil manometer using silicone oil (to ± 1 mm oil) and the dry air from the cylinder was then leaked in until the total pressure equalled the preset total pressure on the micromanometer. Thus both the partial pressure of H_2O and the total pressure of the humid air could be measured to high accuracy. It was found however that on application of an appropriate voltage to the gap, large 'volume leakage' currents ($\sim 5 \times 10^{-11}$ to 10^{-10} A) were present in the gap even without the ultra-violet irradiation of the cathode. Though these currents did not vary appreciably with E/p (v cm^{-1} (mm Hg)$^{-1}$) no measurements could be made since they were of the same order of magnitude as the expected pre-breakdown currents. Since any leakage currents to earth on insulators can only 'shunt' the main gap and hence would not be recorded on the electrometer connected between the cathode and earth, it was felt that these currents originated in the gas itself. This was further confirmed by warming the insulators where accessible; this had no detectable effect on the currents. Since the air employed in these experiments was leaked into the chamber from a cylinder at a pressure of $1\frac{1}{2}$ to 2 atmospheres, it is possible that the expansion of the air to the low pressure of the chamber with the consequent reduction of temperature, caused condensation of the water to some extent. This reasoning was confirmed by preheating the air to about 100 °C as it was leaked into the chamber, which reduced the leakage currents to less than 5×10^{-11} A, the lowest detectable current on the electrometer. This additional procedure was therefore adopted throughout this study. Further, it was found that the photocurrent yield from the cathode was relatively poor, particularly after a breakdown run in air and hence the cathode was repeatedly 'cleaned' by running a low pressure (~ 1–2 mm Hg) glow discharge in hydrogen at a current of 5–10 mA for 15–30 minutes.

The measurements of pre-breakdown currents and breakdown potentials made in this study are summarized in table 1, together with the designation of individual runs for convenience. The runs hereafter will be referred to by

these designations. Further, pre-breakdown currents were measured in pure H_2O at 10 and 20 mm Hg over an E/p range of 30–50 v cm^{-1} (mm Hg)$^{-1}$.

Table 1

(1)	(2)	(3)	(4)	(5)
150	2·5	Platinum	30–40	150/2·5/Pt
	5	Dural	30–50	150/5/D
	9	Dural	30–50	150/9/D
	9	Platinum	—	150/9/Pt
	15	Dural	30–45	150/15/D
300	5	Platinum	30–40	300/5/Pt
	10	Platinum	30–40	300/10/Pt
	18	Dural	—	300/18/D
150	0	Platinum	30–40	150/Pt
	0	Dural	30–40	150/D

(1) Total pressure p (at 20°c); (2) partial pressure of H_2O p_w (at 20°c); (3) cathode material; (4) range of E/p (v cm^{-1} (mm Hg)$^{-1}$); (5) designation.

After the four runs with the dural cathode it was found that the I_0 yield from the cathode dropped very low ($\sim 10^{-13}$ to 10^{-12} A in vacuum) and the clean-up treatment did not produce any appreciable change. On examination it was found that the cathode was covered with a grey-white layer which could not be removed except by the use of abrasives. It was therefore decided to change to the platinum cathode. This was used advantageously to investigate the dependence of the breakdown potential on the cathode material. The difficulties experienced with the dural cathode regarding the photoelectric yield were not present with the platinum cathode, thus demonstrating its better surface stability.

In the case of measurement of pre-breakdown currents with pure H_2O, it was found that reproducibility became, particularly at high $E/p(>40)$, very poor unless the pressure was maintained to ± 1 mm oil (i.e. $\sim 80\mu$ Hg). This was achieved by letting the H_2O vapour stand in the chamber at approximately the desired pressure for a period of $1\frac{1}{2}$ to 2 hours and then leaking in the vapour needed. The need for this procedure is due to the presence of the nylon h.v. bushing, etc. in the chamber which presumably is partly hygroscopic and needs to come to equilibrium at the water vapour pressure. After the stated period, the results were always found to be reproducible to within the limits of the error of the experiment.

For the sake of brevity ($\log I, d$) plots of only two runs in humid air are given in figures 1 and 2. All these plots exhibit curvatures characteristic of equation (2), thus justifying the assumptions made regarding the mechanism of negative ion formation.

No upcurving or very slight upcurving was observed in all these plots at large values of d (i.e. $1 < d < 3$ cm), indicating very low secondary electron yields, contrary to runs in dry air. Therefore no extensive values of γ could be measured directly and hence it was decided to calculate values of γ employing the measured breakdown potentials and the values of α and η. From the ($\log I, d$) plots, the coefficients α and η were evaluated by a careful process of curve-fitting using equation (2*a*), such that the measured and calculated values of currents at any particular value of d agree to within 5% in the range $d = 0{\cdot}4$ to $3{\cdot}0$ cm; consequently the errors in α and η should in general not be greater than $\pm 5\%$. It

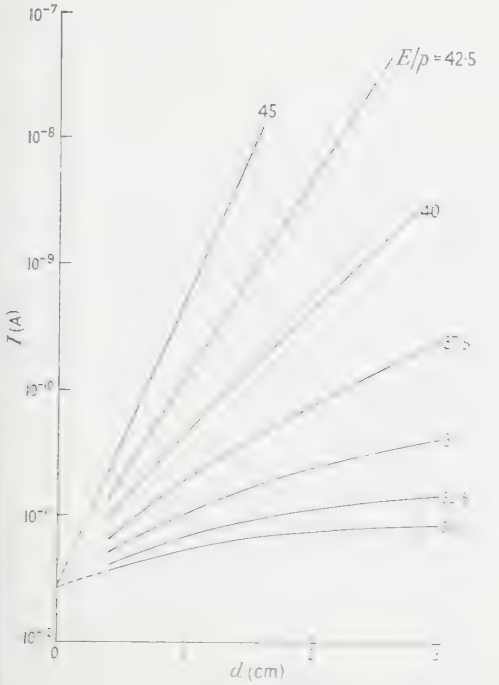

Figure 1. Ionization currents in humid air at 150/5/D for various constant values of the parameter E/p.

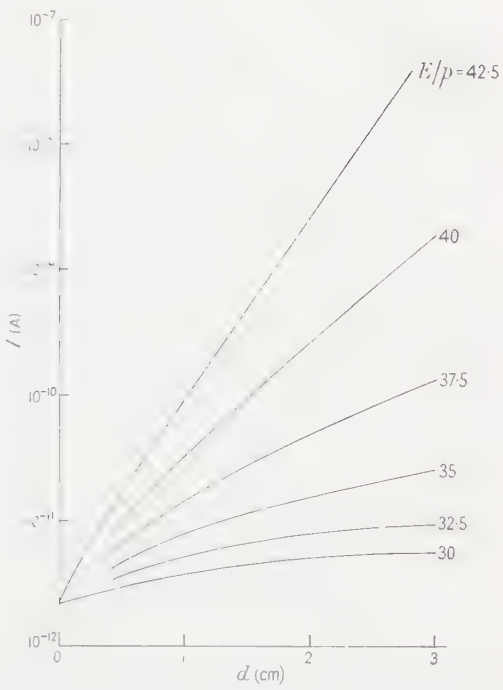

Figure 2. Ionization currents in humid air at 150/9/D for various constant values of the parameter E/p.

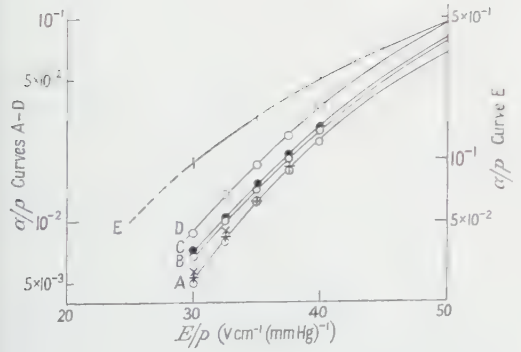

Figure 3. Values of α/p as a function of E/p in water vapour and in humid air for various values of p_w. Curve A, ○ ○, 150/2·5/Pt; + +, 300/5/Pt; curve B, 150/5/D: × ×, 300/10/Pt; curve C, 150/9/D; curve D, 150/15/D; curve E, water vapour.

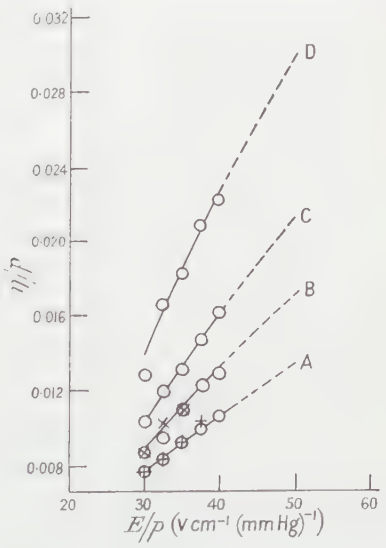

Figure 4. Values of η/p as a function of E/p in humid air for various values of p_w. Curve A, 150/2·5/Pt: + +, 300/5/Pt; curve B, 150/5/D: × ×, 300/10/Pt; curve C, 150/9/D; curve D, 150/15/D.

was found that in all the 150 mm Hg runs the curvatures of the $(\log I, d)$ plots for $E/p > 40$ were very slight, being confined to $d < 8$ mm to 10 mm and hence no measured values of α/p and η/p could be obtained for $E/p > 40$. However, as has been pointed out in an earlier publication (Prasad 1959), the mean slope of the $(\log I, d)$ plots under these conditions, where $\alpha/p \gg \eta/p$, was $(\alpha - \eta)/p$. Thus although the values of both α/p and η/p could not be determined individually for $E/p > 40$, the values of $(\alpha - \eta)/p$ could be obtained for $E/p \geqslant 45$. It was found that the values of $(\alpha - \eta)/p$ so obtained agreed to within 5% with the corresponding mean extrapolated values of $(\alpha - \eta)/p$ obtained from the runs conducted at $E/p < 40$ for the various compositions of the humid air, thus justifying the procedure adopted for the evaluations of γ in this study. The values of α/p and η/p obtained in this study are indicated in figures 3 and 4. It can be seen that the values of α/p and η/p obtained from the 300/5/Pt and the 300/10/Pt runs agree with those from 150/2·5/Pt and 150/5/D respectively.

Table 2. Values of Breakdown Potential in Humid Air (kv)

	Dural cathode					Platinum cathode				
pd	150/0 300/0	150/5	150/9	150/15	300/18	150/0 300/0	150/2·5	300/5	300/10	150/9
75	4·2	4·3	4·5	4·5	—	4·3	4·4	—	—	4·4
150	7·4	7·6	7·8	7·9	7·8	7·4	7·6	7·6	7·7	7·8
225	10·4	10·8	11·0	11·1	11	10·3	10·6	—	10·7	10·9
300	13·3	13·8	14·1	14·2	14·1	13·1	13·6	13·6	13·8	14·0
375	16·1	16·8	17·1	17·2	17·1	15·9	16·5	—	16·7	17·0
450	18·9	19·7	20·1	20·3	20·1	18·5	19·4	19·3	19·6	20·0
600	24·2	25·4	—	—	26·0	23·5	—	24·9	25·3	25·8
750	29·3	—	—	—	31·7	28·6	—	30·3	30·8	—
900	34·0	—	—	—	—	33·5	—	35·7	36·3	—
760	29·6	31·5†	—	32·4†	32·1	28·9	—	30·7	31·3	—

pd in mm Hg cm. † Extrapolated values.

Measured values of breakdown potentials from this study are summarized in table 2. Here again it can be seen that the breakdown potentials obtained from 300/5/Pt agree with those from 150/2·5/Pt and those from 300/18/D agree with those of 150/9/D. Further it can be seen that the dependence of breakdown potential on the cathode material is very small in the case of humid air, whereas it is pronounced for dry air. Figures 5 (*a*) and 5 (*b*) indicate the percentage variation in breakdown potential at a total pressure of 150 mm Hg as a function of the partial pressure of water vapour for the two cathode materials employed for different values of *pd* (mm Hg cm). Calculated values of γ using the measured breakdown potential values and mean extrapolated values of α/p and η/p, employing equation (3) are summarized in table 3 for both the dural and the platinum cathodes. It was found that at $E/p = 47{\cdot}5$ and 50, in the case of the 150/9/D runs where current measurements were extended to distances within 10–15% of the sparking distance, the measured and calculated values of γ were in agreement to within 15%, thus demonstrating the accuracy of the above calculations.

The pre-breakdown currents measured in pure H_2O vapour at 10 mm Hg are indicated in figure 6. It can be seen that here again the current plots exhibit curvatures characteristic of equation (2) and indicate the presence of very high

attachment rates. The values of α/p and η/p evaluated from these measurements at both the pressures are indicated in figures 3 (curve E) and 7 respectively, together with the measurements of η/p by Bailey and Duncanson as quoted by

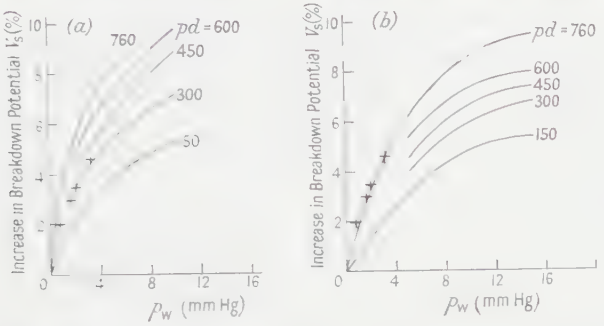

Figure 5. (*a*) Percentage increase in breakdown potential as a function of p_w at a total pressure of 150 mm Hg obtained with a platinum cathode for different values of pd. + +, calculated points from the observations of Allen and Phillips (1959). (*b*) Percentage increase in breakdown potential as a function of p_w at a total pressure of 150 mm Hg obtained with a dural cathode for different values of pd. + +, calculated points from the observations of Allen and Phillips (1959).

Healey and Reed (1941) and Kuffel (1959). Measured breakdown potentials in H_2O vapour are summarized in table 4. No measurements of γ were possible since no upcurving was observed in the ($\log I, d$) plots even at a value of E/p of

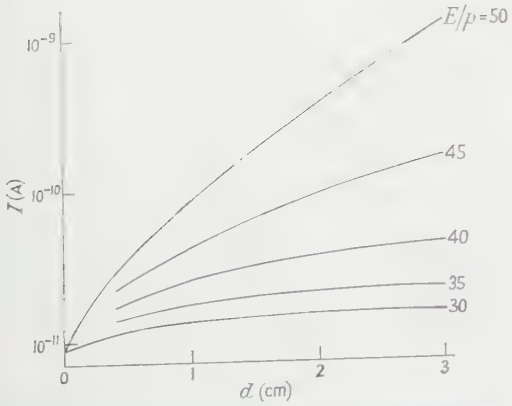

Figure 6. Ionization currents in H_2O vapour at 10 mm Hg for various constant values of the parameter E/p.

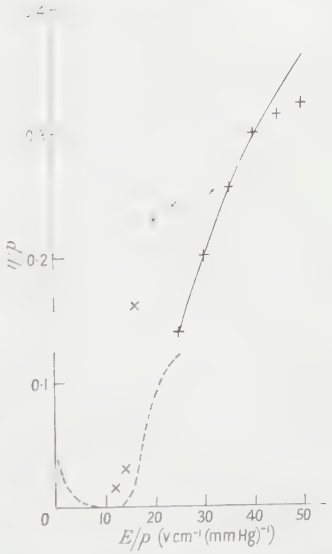

Figure 7. Values of η/p in H_2O vapour: + +, this study; × ×, Bailey and Duncanson (1930). The broken line is due to Kuffel (1959).

50 at 3 cm gaps. From the values of η/p, employing the drift and agitation velocity measurements of Bailey and Duncanson (Healey and Reed 1941) and assuming a Maxwellian distribution, mean cross sections for attachment in water vapour

Table 3. Calculated Values of γ in Humid Air

	γ : dural cathode				γ : platinum cathode			
E/p	150/0	150/5	150/9	150/15	150/0	150/2·5	300/10	150/9
40	$4{\cdot}4\times10^{-6}$	—	—	—	$3{\cdot}3\times10^{-5}$	$1{\cdot}1\times10^{-6}$	—	—
42·5	$1{\cdot}2\times10^{-5}$	$7{\cdot}6\times10^{-7}$	$7{\cdot}1\times10^{-8}$	—	$4{\cdot}7\times10^{-5}$	$7{\cdot}2\times10^{-6}$	$1{\cdot}5\times10^{-6}$	$3{\cdot}4\times10^{-7}$
45·0	$4{\cdot}0\times10^{-5}$	$2{\cdot}9\times10^{-6}$	$4{\cdot}4\times10^{-7}$	$7{\cdot}5\times10^{-8}$	$6{\cdot}9\times10^{-5}$	$2{\cdot}1\times10^{-5}$	$5{\cdot}2\times10^{-6}$	$9{\cdot}2\times10^{-7}$
47·5	$1{\cdot}8\times10^{-4}$	$9{\cdot}1\times10^{-6}$	$1{\cdot}7\times10^{-6}$	$3{\cdot}6\times10^{-7}$	$1{\cdot}6\times10^{-4}$	$5{\cdot}7\times10^{-5}$	$1{\cdot}6\times10^{-5}$	$3{\cdot}2\times10^{-6}$
50·0	$3{\cdot}5\times10^{-4}$	$1{\cdot}6\times10^{-5}$	$8{\cdot}9\times10^{-6}$	$1{\cdot}1\times10^{-6}$	$2{\cdot}2\times10^{-4}$	$8{\cdot}9\times10^{-5}$	$2{\cdot}6\times10^{-5}$	$1{\cdot}2\times10^{-5}$

Table 4. Values of Breakdown Potential in Water Vapour

pd (mm Hg cm)	10	20	30	40	50
Breakdown potential (v)†	1080	1600	2070	2530	2990

† Obtained with the platinum cathode.

have been computed for various values of mean energies using the equation

$$\sigma_w = \frac{1}{N_0}\frac{w}{U}\frac{\eta}{p}$$

where w and U are the drift and agitation velocities respectively and N_0 the number of molecules cm^{-3} at 0 °C and 1 mm Hg. These are indicated in figure 8.

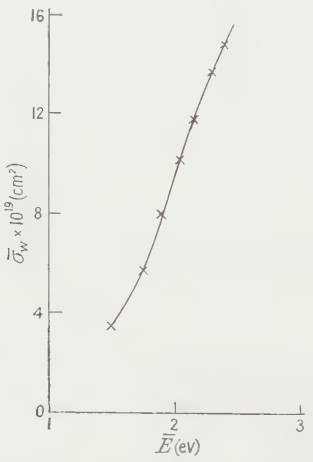

Figure 8. Values of mean cross sections for attachment in H_2O vapour for various mean energies.

§ 3. Discussion

The absence of any pressure effects in the measurements of η/p in both the humid air and water vapour, confirms the assumption of $e + AB \rightarrow AB^-$ or $A + B^-$ as the mode of negative ion formation in water vapour and there appears to be no evidence in the present work of any pressure dependent reactions, though no individual reactions can be specified in this technique of measurement, since mass spectrometric observations cannot, at present, be made. However in humid air there appears to be no simple relationship between the increase in η/p and the increase in the water vapour content, even though the values of η/p from 300/5/Pt and 300/10/Pt agree with those of 150/2·5/Pt and 150/5/D

indicating that the observed attachment depends on the volumetric composition of the mixture alone. The increase in η/p between 150·9 D and 150·15 D appears to follow a partial pressure law, though this may be fortuitous.

In humid air no appreciable rise in α/p occurs at any particular value of E/p until the partial pressure of water vapour is greater than 2·5 mm Hg, though there is a pronounced increase in the values of η/p. Thus there is a reduction in $(\alpha-\eta)/p$ with respect to the conditions in dry air. This, coupled with the very low values of γ (cf. table 3) as indicated by both the relatively poor photoelectric yields and by the absence of upcurving in the $(\log I, d)$ plots, accounts for the large increase in breakdown voltage of air with the increase in humidity. Meek (1959) has recently published a preliminary interpretation of the low secondary coefficients in terms of photon absorption, a mechanism suggested earlier by Köhrmann (1956) for humid air. Further there appears to be a pronounced dependence of the breakdown potential on the cathode material in the case of dry air, the breakdown potential with the dural cathode being higher than that with the platinum cathode. Further details of this effect as observed in other gases as well will be published elsewhere. This dependence however seems to be very small, though definite, in the case of humid air (cf. 150·9 D, 150·9 Pt in table 2). The breakdown potential with different degrees of water vapour content appears to depend purely on the partial pressure ratio of dry air to water vapour as evident in table 2. However figures 5 (*a*) and (*b*) indicate that the percentage increase in breakdown potential tends to 'saturate' with the increase in water vapour content p_w beyond a partial pressure of water vapour of 10 to 13 mm Hg. Further the percentage increase in V_S for any particular value of p_w seems to be dependent on the cathode material. Points calculated from the recent measurements of breakdown potential of humid air (Allen and Phillips 1959) obtained at a total pressure of 760 mm Hg and various values of p_w, employing brass electrodes at 1 cm separation, are also included in figures 5 (*a*) and (*b*). These points have been calculated for a total pressure of 150 mm Hg and pd of 760 on the basis of the ratio of partial pressure of dry air to that of water vapour and these agree well with the measurements obtained in this study with the dural cathode. Some recent observations in this laboratory by Leyn (unpublished) indicate that the values of breakdown potential obtained with dural and brass electrodes do not differ appreciably.

The appreciable difference between the measurements obtained in this study with the platinum cathode and those of Allen and Phillips (1959) is, it is suggested, due to the different cathode materials used in the two cases. Further, it is of interest to note that the data obtained at total pressure of 760 mm Hg can be correlated on the basis of partial pressures with that obtained at 150 mm Hg, thus demonstrating the validity of a partial pressure law in the values of V_S in humid air.

The η/p values in water vapour indicate a strong attachment (cf. figure 7). The values of η/p from the present study differ appreciably from those of Bailey and Duncanson (1930). This, it is suggested, is due to the very large increase in α/p at $E/p > 30$, which introduces a large error in the diffusion techniques of earlier workers. The agreement with the data of Kuffel (1959) however is satisfactory. Values of η/p obtained in this study for $E/p \geqslant 45$ have not been considered for the computation of the mean curve (figure 7), since at these high

values of E/p the accuracy of evaluation of η/p becomes poor (Prasad 1959). Since this paper was prepared, cross section data in water vapour obtained by Buchel'nikova (1958) have become available. The computation of attachment cross sections, i.e. in swarm conditions, from these results show marked disagreement with the present work. Thus, at mean electron energies of 2 and 3 ev respectively Buchel'nikova's data (see figure 8 for comparison) give attachment cross sections of $1{\cdot}75 \times 10^{-19}$ and 4×10^{-19} cm^2 respectively for a Maxwellian distribution. Since no published data are available on the drift and agitation velocities in humid air or on the effect of the presence of water vapour on the electron energy distribution in air, no correlation is possible between the data from humid air and that from water vapour regarding the cross section for attachment.

§ 4. Conclusions

The absence of pressure effects in the η/p values in this study, it is suggested, indicates that the negative ion formation in water vapour and humid air is of the form: $e + AB \rightarrow AB^-$ or $A + B^-$.

There appears to be a pronounced increase in attachment and in the breakdown potential in humid air as against dry air and this would, it is suggested, make comparison of data on air quite erroneous, particularly the data from the earlier measurements where no attempts were made to dry the air used, unless the humidity is specified. The pronounced dependence of the breakdown potential on the cathode material in both dry air and, to a lesser degree, in humid air, requires the specification of the cathode material as well, essential for purposes of comparison of data as obtained by different workers. Further the presence of water vapour appears to lower the secondary electron yields considerably and requires a detailed study. The dependence of the breakdown potential on the cathode material at these large values of pd confirms the view held by earlier workers (Llewellyn Jones and Parker 1952) that the Townsend build up mechanism is satisfactory to explain the uniform field breakdown in air.

Acknowledgments

One of the authors (A.N.P.) is grateful to the University of Liverpool for a Fellowship and to the Electrical Research Association for a subsidiary grant and for permission to publish this work. We are indebted to Professor J. M. Meek for discussions on these experiments.

References

Allen, K. R., and Phillips, K., 1959, *Nature, Lond.*, **183,** 174.
Bailey, V. A., and Duncanson, W. E., 1930, *Phil. Mag.*, **10,** 145.
Buchel'nikova, N. A., 1958, *Zh. Eksper. Teor. Fiz.*, **35,** 1119.
Craggs, J. D., and McDowell, C. A., 1955, *Rep. Progr. Phys.*, **18,** 375 (London: Physical Society).
Craggs, J. D., and Tozer, B. A., 1960, *Proc. Roy. Soc.* A, **254,** 229.
Harrison, M. A., and Geballe, R., 1953, *Phys. Rev.*, **91,** 1.
Healey, R. H., and Reed, J. W., 1941, *The Behaviour of Slow Electrons in Gases* (Sydney: Amalgamated Wireless (Australasia)).
Hopwood, W., Peacock, N. J., and Wilkes, A., 1956, *Proc. Roy. Soc.* A, **235,** 334.
Köhrmann, W., 1956, *Ann. Phys., Lpz.*, **18,** 379.
Kuffel, E., 1959, *Proc. Phys. Soc.*, **74,** 297.
Llewellyn Jones, F., and Parker, A. B., 1952, *Proc. Roy. Soc.* A, **213,** 185.
Meek, J. M., 1959, *Nature, Lond.*, **183,** 1805.
Muschlitz, E. E., and Bailey, T. L., 1956, *J. Phys. Chem.*, **60,** 681.
Prasad, A. N., 1959, *Proc. Phys. Soc.*, **74,** 33.

Underwater Explosions as Acoustic Sources

By D. E. WESTON
Admiralty Research Laboratory, Teddington, Middlesex

MS. received 19*th November* 1959, *in revised form* 30*th March* 1960

Abstract. The manner in which underwater explosions differ from low-amplitude point sources of sound is considered theoretically, especially effects due to cavitation near the sea surface. Some measured differences between the acoustic source levels of various size charges and some absolute charge source levels are given. These experimental results are presented for charge sizes between 0·002 and 50 lb, for charge depths from 7 to 60 fathoms, and for frequencies from 25 c/s to 6·4 kc/s. The results at a given depth are shown to obey a simple scaling law. Theoretical source levels are calculated by Fourier analysis of shot pressure–time curves reported by Arons. At high frequencies the theoretical spectral energies of the shock wave and the bubble pulses are simply added together, but at low frequencies it is necessary to take account of phase. In general there is very good agreement between the experimental and theoretical levels, and certain small discrepancies are explained in terms of bubble migration and related effects.

§ 1. Introduction

Underwater explosions have been used as acoustic or seismic sources in many connections: for example in geophysical prospecting, in radio-acoustic and pure acoustic navigation, for signalling including distress signalling, and for the investigation of underwater sound propagation. Explosions provide a pulse source of great power, so that measurements at long ranges may be made without costly generating equipment. In addition they contain energy in a wide range of frequencies and are not restricted in depth. They have some disadvantages as acoustic sources in research work, mainly due to finite-amplitude effects.

In the course of various sea trials organized by the Admiralty Research Laboratory, many explosive charges have been fired, and much experimental information accumulated. From this it has been possible to deduce absolute source levels for the various charge sizes, which are needed if transmission loss is to be found from measurements of received signal level. In addition there have been several special experiments to measure the energy differences between charges. A knowledge of these differences is necessary so that measurements of various workers with various charges may be reduced to a common standard. The present results are mainly for 1-lb charges of T.N.T. but some data are given for other charges from detonators up to 50 lb—a range of 1:25 000 in weight of explosive.

This paper considers first the special nature of the underwater explosion as an acoustic source, particularly effects due to surface cavitation, so that the experimental results may be processed having regard to these effects. The measured charge differences and free-field source levels are then reported, and discussed

first in the light of the simple theoretical scaling laws. The theoretical Fourier spectra for the shot pressure–time curve reported by Arons *et al.* (Arons 1948, 1954, Arons, Slifko and Carter 1948, Arons and Yennie 1948) are calculated and compared with experiment, and the modification due to such effects as bubble migration are examined. A generalization of some of the theoretical laws at low frequencies, together with its application to underground explosions and other disturbances, is given elsewhere (Weston 1960).

§ 2. The Underwater Explosion

The general character of underwater explosions is well established, and Cole (1948) may be given as a general reference. When a high explosive is detonated the detonation wave propagates through it and it is converted to incandescent gas at a very high pressure. A spherically symmetrical shock wave is radiated into the water. The pressure rise in the shock wave is practically instantaneous, and is followed by a decay which is initially exponential with time constant typically a fraction of a millisecond. By the time the gas bubble has expanded to its maximum radius the radiated pressure has become slightly negative. Due to the water inertia the bubble overshoots its equilibrium radius, so it begins next to contract, and then undergoes a damped radial oscillation. Observations of up to 10 oscillations have been reported, the actual number depending on how soon the bubble breaks up into smaller parts. At each bubble minimum a pressure pulse is radiated, of smaller amplitude but longer duration than the shock wave. The first bubble pulse has an impulse comparable with that of the shock wave. The radiated pressure–time curve is quantitatively described in § 7.

When the shock wave reaches the surface it is reflected as a tension wave, which may cause cavitation. This can sometimes be seen on cine records as a white flash just below the surface. If the water surface is initially fairly smooth a slight roughening of the same extent as the flash is visible, which is usually described as the 'black ring'. In addition, with a strong shock wave the area above the charge may rise into a dome of broken water, this spray dome having a diameter less than that of the black ring. The precise mechanism of the cavitation phenomenon is not certain, but it can best be understood in terms of the multiple layer theory of Wood, Lakey and Butterworth (1924). The reflected tension wave causes a fracture just below the water surface, and the momentum associated with the first part of the shock is trapped in the region above the fracture. The next part of the shock wave is reflected at the new surface and a second fracture formed. A series of layers will result, stopping when the amplitude in the tail of the shock is insufficient to cause cavitation. These layers will collide and break up to form the spray dome. The region with one layer only may be identified with the black ring. This picture is of course idealized, and in practice will be blurred by such effects as surface roughness. In addition the cavitation regions will probably not be voids with sharp boundaries, but more like layers of bubbles—so producing their white appearance.

The most spectacular surface effect is the plume, which may appear as a bush-like eruption or as a thin spout. The plume occurs later than the spray dome and is due to the oscillating bubble moving upwards under gravity and arriving at the surface. For the deeper charges the bubble breaks up before reaching the surface, and the plume is replaced by an upwelling of frothy water.

§ 3. Differences from a Low-amplitude Point Source

3.1

The underwater explosion differs from a fixed low-amplitude acoustic source both because of the high pressure generated, and because the source may move whilst it is still radiating. The most direct effect of the finite amplitudes is that the different parts of the shock wave travel with different velocities, and there is a Riemann broadening plus a continual sharpening of the pulse. The latter keeps the viscous energy loss at the shock front at a high level by continuously transferring some of the spectral energy to the higher frequencies. These effects are less important beyond about 100 yards and are discussed further in § 6. Very near the charge the velocity of propagation of the shock wave is supersonic, but the saving in transit time is typically only a small fraction of a millisecond.

3.2

If there is cavitation the tension wave reflected from the water surface will not be of full strength, and the signal propagated to a distance may be affected. This occurs mainly for the shock wave at the sea surface, but bubble pulses may also cause cavitation. Theoretically cavitation may still occur after an intermediate shock wave reflection at the sea bottom, or even at the bottom itself if there is sufficient gas there to make the boundary behave as a free surface.

The study of cavitation in this connection is too large a subject to be treated adequately in this paper, and therefore the brief account below concentrates on presenting the main results. It applies to shock wave cavitation at the sea surface, and assumes the charge is not so shallow that the explosion gases blow out through the surface on their first expansion.

There has been much controversy on the effective tensile strength of water, even when discussion is limited to results on cavitation above underwater explosions. The author has measured $7\frac{1}{2}$ fathoms as the critical depth for the appearance of the corrugations (or black ring) above a 1-lb charge, corresponding to 290 lb in $^{-2}$ for the sum of water breaking tension and the 15 lb in $^{-2}$ atmospheric pressure. The breaking tension is likely to vary with the shock wave duration and therefore with the charge size, but will here be assumed constant. Similarly the critical depth for the spray dome was measured as $4\frac{1}{2}$ fathoms, in close agreement with the results of Kolsky *et al.* (1949).

For shallower charges the theoretical horizontal extent of the surface cavitation is usually given simply by the slant range at which the shock pressure has fallen to the above figure (290 lb in $^{-2}$). In extreme cases there may be corrections due to the hydrostatic pressure gradient, the curvature of the cavitation surface, refraction, surface roughness etc. The 'cavitation angle' is a useful quantity, defined as the angle to the horizontal made by a line joining the source to the edge of the cavitated area. The cavitation effects are most likely to be serious for large shallow charges, e.g. 50 lb at 7 fathoms, which has a calculated cavitation angle of 14°.

To investigate the effect on a distant signal it is necessary to compare the cavitation angle with the various angles important in describing the undisturbed propagation. At high frequencies only the rays with small grazing angles at the surface are normally effective for propagation, since for larger angles there is a

change over from specular to diffuse reflection. Typically the cavitation angle is greater than the angles of the rays carrying the high-frequency energy, so cavitation is unimportant for the high frequencies. At low frequencies rays with angles greater than 14° may be effective, so that cavitation effects will sometimes be significant. This is especially true at very low frequencies, where the direct and surface reflected rays will normally tend to cancel one another out and produce a dipole spreading law. However it is shown later that the major contribution to the low-frequency energy comes from the first bubble pulse, so that overall the low-frequency effects are seldom important. For all the depths, sizes and frequencies discussed in this paper only marginal effects due to cavitation are to be expected.

3.3

Some of the energy lost on surface reflection is re-radiated as cavitation noise, and as noise due to the water in the spray dome falling back. There is also the falling-back of the water in the plume. Some of these noises may be observed at close range, but it is thought unlikely that they are significant at long range.

3.4

When a strong shock wave is reflected at a very small glancing angle from a free surface the reflection is irregular, and the separate pressure and tension waves are replaced by a single pulse of reduced magnitude, as discussed theoretically by Penney and Pike (1950) etc. In idealized conditions this irregular reflection will eventually occur near the surface for any charge weight and depth, and for a 50-lb charge at 7 fathoms the calculated range is 4600 ft. However, refraction and rough surface effects make its occurrence uncertain, and it is probably not important at all in the present connection.

3.5

Energy is radiated for as long as the bubble continues to oscillate; for the larger charges and shallower depths the bubble rises appreciably during one oscillation and some of the energy is radiated from a reduced source depth, so that surface image interference may be more serious. The worst case considered here is that of a 50-lb charge at 7 fathoms, where the vertical rise due to gravity in one oscillation is one quarter of the original source depth. This leads at very low frequencies to a decrease of $2\frac{1}{2}$ dB in the contribution of the first bubble pulse, the shock wave of course being unaffected. In addition it is with these very conditions of large shallow charges that migration makes the bubble pulse energy output relatively unimportant. Thus it appears that reduced radiation depth effects may usually be ignored in the present connection. Bubble migration is more important in its effect on the energy spectrum of the bubble pulse, as discussed in §8.2, which also presents more background information on migration generally.

All the effects considered in this section are marginal, and not too serious for the data presented here. A few other data have been rejected because of these effects. Note also that with a slight change of circumstances the effects could lead to considerable error, and it is necessary to bear the limits of all of them in mind.

§ 4. Measured Differences between Charges

4.1

There are surprisingly few charge comparisons in the literature, and most workers have corrected their results assuming energy is proportional to W (charge weight) or $W^{2/3}$, though neither is correct in general. Worzel and Ewing (1948) report some comparisons of pressure measured at a distance for various charges, and O'Brien (1960) gives a similar comparison for Admiralty Research Laboratory records of the low-frequency signals from 1-lb and 50-lb charges fired on the sea bed at about 20 fathoms (averaging 23 dB at about 10 c s). All these results agree roughly with those presented below. However the main need is for comparisons at one depth and in a series of reasonably narrow frequency bands, preferably for charges fired off the bottom and preferably of energy rather than pressure.

4.2

The measurements here and in § 5 are of the *energy flux density*, since this is the quantity for pulses which obeys the same transmission laws as *intensity* for continuous-wave sources. In practice the quantities actually measured in the two cases are $\int p^2\,dt$ and p^2, where p is acoustic pressure and t is time. The comparisons presented in table 1 were made on different occasions, typically with the explosions several miles distant and with the different sizes of charges fired in succession at the same position. The signals were received on a barium titanate hydrophone, amplified, and fed to a series of eight octave-filters (covering the range 25 c/s to 6·4 kc/s) each followed by a small analogue computer.

Table 1. Measured Differences from a 1-lb Charge

Measured octave-band energy differences in dB from a charge demolition S.C. 1 lb (T.N.T.)								
Frequency (c/s)	35	70	140	280	560	1100	2200	4500
Depth (fathoms)								
Detonator electric No. 79 Mark 1.N, corresponding to about 0·002 lb T.N.T.								
5	−34·0	−31·0	−30·7	−30·0	−28·0	−25·5	−23·5	−22·7
10	−35·0	−30·3	−30·0	−30·3	−27·3	−25·0	−20·0	−18·0
20	−35·0	−33·0	−31·6	−33·4	−31·2	−28·6	−22·0	−24·0
30	−46·0	−41·5	−35·5	−36·0	−30·9	−30·0	−28·7	−27·0
Charge demolition $1\frac{1}{4}$ lb T.N.T.								
7	+0·2	+0·3	+0·5	+0·1	+0·2	+0·0	−0·1	+0·1
Bundle $3 \times 1\frac{1}{4}$ lb T.N.T.								
7	+0·3	+1·5	+2·5	+1·7	+2·1	+2·1	+1·7	+1·5
Bundle 4×1 lb S.C. (T.N.T.)								
20	+4·5	+4·6	+4·7	+4·7	+4·7	+4·8	+4·7	—
Charge demolition 50 lb Mark 3 T.N.T.								
5	—	+19·0	+16·0	+15·0	+15·0	+15·0	+12·0	+11·0
7	+12·5	+14·6	+15·2	+16·2	+14·8	+13·7	+13·0	+12·5
20	—	+18·2	+16·5	+15·0	+14·5	+14·0	+14·0	+10·0
30	+14·5	+17·0	+17·5	+16·9	+15·4	+13·4	+10·0	+9·0
40	+14·6	+16·2	+16·2	+16·1	+14·8	+12·9	—	—

The computers or octave-energy units were specially designed six-valve assemblies consisting of a calibrated potentiometer, two-stage feedback amplifier, two-valve square-law device, Miller integrator, and output valve feeding a pen recorder. The square-law device was based on that of Tucker (1952), and comprised a phase-splitter feeding a double triode with output taken from the common cathode. The units could accept a wide range of input levels, frequencies and pulse durations. It was necessary that they should be simple and physically small since several had to be used simultaneously, sometimes on board ship, and they have been operated successfully over a number of years. In all work with charges the possibility of the shock wave causing overload has to be watched carefully, so that the wide-band level plus all the octave-energy unit levels were monitored for overload using thyratron triggers and neon indicators.

4.3

In addition to the results in table 1, comparisons of 5-lb charges (5 lb 60/40 R.D.X./T.N.T.) with four 1-lb charges have shown that the mean

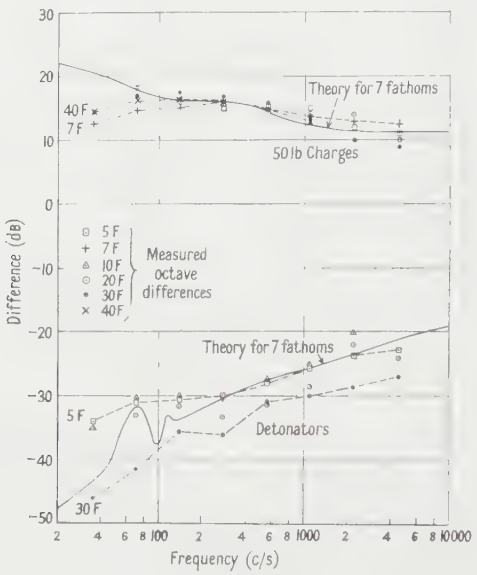

Figure 1. Differences from a 1-lb charge.

difference is less than 0·3 dB for frequencies between 113 c/s and 1740 c/s. The general accuracy of the table 1 comparisons is to about ± 1 dB, in a few cases it is a little worse but in several cases it is to about $\pm 0{\cdot}3$ dB. In particular the $1\frac{1}{4}$-lb figures and the 50-lb figures at 7 and 40 fathoms are reliable, being derived from a very large number of observations. Thus the small changes in the low-frequency figures for 50-lb charges between 7 and 40 fathoms are real, and the systematic low-frequency variation in the detonator figures is also real. The detonator and 50-lb results are illustrated in figure 1, in which the theoretical lines should be temporarily ignored since the actual values of the differences will be discussed in § 8. Many of the table 1 results are unexpected, for example the differences for the $1\frac{1}{4}$-lb, $3 \times 1\frac{1}{4}$-lb and some other charges are significantly

smaller than expected on any reasonable theory. This may be connected with the manner of detonation, and shows that it is unwise to rely on theoretical differences. The table 1 results were taken in water depths varying from a few tens of fathoms to several hundred fathoms, and there is no reliable evidence for any variation with measurement site.

4.4

During the firing of a long series of charges it is possible to obtain information on their constancy of acoustic output, provided there is no random variation due to the propagation through the medium. For 1-lb charges the scatter in the octave-energy levels is less than $\pm 0{\cdot}5$ dB, being greatest at the extreme high and low frequencies. The scatter for 50-lb charges is greater than this, possibly due to variable bubble migration, and for detonators greater still. The detonator variability at 35 c/s, of magnitude several decibels, is explained in §7 by the uncertain cancellation effect.

§ 5. Measured Charge Source Levels

5.1

From the shots fired at closer ranges it has been possible to deduce the absolute free-field source levels presented in table 2. The energy flux spectrum levels have been obtained by measuring $(1/\rho c)\int p^2\,dt$ for an octave band as described in §4, and dividing by the bandwidth. Here ρc is the acoustic impedance, and strictly the term 'energy flux' may only be applied if there is a plane wave front, e.g. near a free surface the true energy flux is not measured. There are some other difficulties in strictly defining charge acoustic source levels because of finite amplitude effects, but these effects are small beyond about 100 yards. The choice of 100 yards as the reference distance is also convenient because it is typical for the range from charge to first boundary reflection. Shots at distances between about 100 yards and several miles have been used, though the more distant shots are only suitable if the water is deep. At small ranges it may be assumed that attenuation and absorption are insignificant at the lower frequencies, so that there is cylindrical spreading for ranges greater than a few water depths. The transmission loss may then be calculated from a simplified theory based on

Table 2. Absolute Source Levels for a 1-lb Charge

Frequency (c/s)	35	70	140	280	560	1100	2200	4500
Free-field source spectrum levels of energy flux density for 60-fathom 1-lb charge, in dB w.r.t. 1 erg cm^{-2} $cycle^{-1}$ at 100 yards	+17·2	+12·8	+9·9	+5·4	+2·8	−0·5	−5·0	−13·9
Differences with charge depth								
60F–45F :	+5·1	−2·0	Expected to be small from theory and experiment, assumed zero					
60F–40F :	+4·4	+1·0						
60F–7F :	+0·4	0·0						

Weston (1959) if certain assumptions about the bottom reflection coefficient are made. At high frequencies there is spherical spreading out to appreciable ranges. The correction for transmission loss finally used is thus frequency dependent and takes account of many different factors, but it may be pointed out that at such close ranges the correction depends but little on the propagation mechanisms assumed. In addition for some shots separate measurements have been made of the energies of the arrivals following the different ray paths. Unfortunately the subject of propagation loss is too large to be discussed properly here, even with the restriction to close ranges.

5.2

Very large numbers of results have been used to obtain table 2 but the measurement of absolute levels is intrinsically more difficult than that of the table 1 differences. Thus at, and above, 140 c/s the results for all depths have been lumped together, which has both theoretical and experimental justification. In this frequency range the accuracy relative to neighbouring spectrum levels is to about ± 1 dB, but the absolute accuracy depends on additional factors such as hydrophone calibrations and is perhaps a little worse. At, and below, 70 c s the variation with depth is not in general accurately known, but the best estimate is entered. However the large variation from 60 to 45 fathoms is known to within $\pm 0{\cdot}5$ dB, so for the 35 c/s octave the enormous ratio of about 3 : 1 in energy is real, and presumably due to the changing bubble pulse time (see § 8.3).

5.3

To find the best source level values for any charge size and depth it is necessary to start with the 1-lb 60-fathom figures in table 2, convert to the required depth,

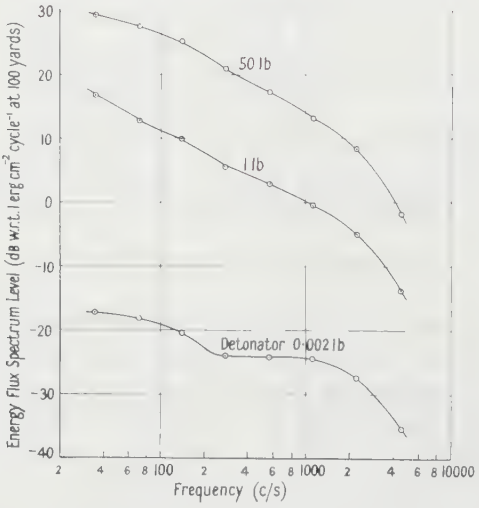

Figure 2. Measured absolute source levels for 7-fathom charges.

and then convert to the required size using smoothed table 1 differences. The results of this procedure are illustrated in figure 2 for various-sized charges at 7 fathoms.

§ 6. Scaling Law

For charges of different sizes fired at the *same depth* there is a simple scaling law. Identical pressure curves are obtained when plotted against a reduced time $t\ W^{1/3}$ and measured at corresponding values of reduced range $r\ W^{1/3}$. This applies rigorously to the shock and to the bubble pulses, but only if effects such as bubble migration and surface cavitation may be neglected. The various energy spectra may therefore be reduced to 1-lb charge equivalents, and this is illustrated in figure 3 for the 7-fathom results from figure 2. The reduction is carried out with the simplifying approximation that pressure is inversely proportional to range, and the errors arising are discussed at the end of §6.

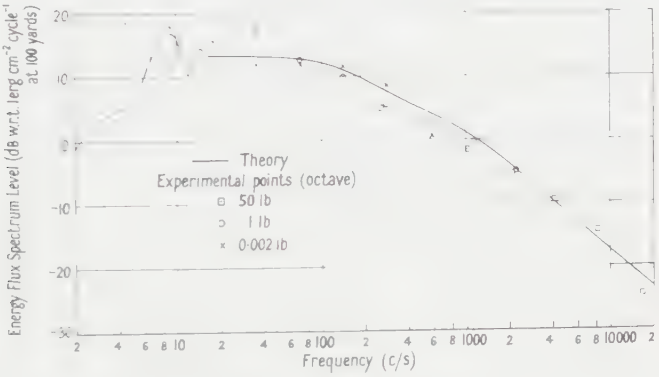

Figure 3. Source levels for 7-fathom charges scaled to 1 lb.

Table 3. Factors for Reduction of Spectrum Level to a 1-lb Charge Equivalent

W (lb)	0·002	50
$W^{1/3}$ or frequency factor	0·126	3·68
$W^{-4/3}$ (dB or level change)	+36	−22·7

The first step is multiplication of the frequency by $W^{1/3}$. Secondly, consider that the total charge energy is proportional to W (assuming spreading without attenuation), and also that the radiated energy per octave is proportional to W. Due to the frequency shift the octave bandwidth is proportional to $W^{1/3}$, so that the spectrum level or energy per cycle is proportional to $W^{4/3}$. Thus the second step in the reduction is multiplication of spectrum level by $W^{-4/3}$, which may be deduced alternatively from equations (5), (9) and (14) of §7. The conversion factors are given in table 3.

Disregarding temporarily the theoretical curve in figure 3, it may be seen that the experimental points lie fairly well on a single line. This is evidence for the correctness of both the source level spectrum shapes and the measured differences between charges. Consideration of the experimental spreading laws quoted in §7 shows that the rate of shock wave pressure decay is a little faster than the spherical spreading assumed above. However this means the scaling laws need slight modification only at the higher frequencies, such that the 50-lb results for reduced frequencies above 1 kc/s should be decreased an extra 1·5 dB.

The effect of bubble migration in lowering the 50-lb results in the middle frequencies is discussed in § 8.2, after the presentation of the Fourier analysis predictions.

§ 7. Fourier Analysis

7.1

The best data for the explosion pressure–time curves have been given by Arons *et al.*, both for bubble pulses (Arons, Slifko and Carter 1948, Arons 1948, Arons and Yennie 1948) and recently for the shock wave at long ranges (Arons 1954). Experimental curves for charges at 500 feet depth are given by Arons and Yennie, and using these Raitt (1952) has already carried out a numerical Fourier analysis. However it is desired here to obtain analytical expressions for the spectrum level, so that variation with charge size, depth etc. may be easily

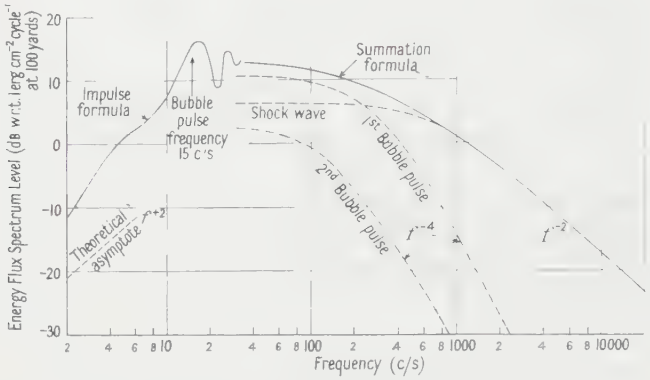

Figure 4. Theoretical source spectrum for 20-fathom 1-lb charge.

investigated. Thus a different approach has been followed, the spectrum being split into two parts and certain simplifying assumptions made. At the high frequencies the shock wave and bubble pulses have been analysed separately, and the resulting spectrum energies added. At low frequencies the shock wave and bubble pulses have been replaced by impulses and account taken of phase. In this section the results are illustrated by the numerical values for a 1-lb T.N.T. charge at 20 fathoms, as measured 100 yards away, and its theoretical spectrum is shown in figure 4.

7.2

According to Arons (1954) the shock wave values are:

Peak pressure

$$P_0 = 2{\cdot}16 \times 10^4 (W^{1/3}/r)^{1{\cdot}13} \text{ lb in}^{-2} \quad (W \text{ in lb, } r \text{ in ft})$$
$$= 2{\cdot}35 \times 10^6 \text{ dyn cm}^{-2} \text{ for 1 lb at 100 yards.} \qquad \ldots\ldots (1)$$

Positive impulse

$$I_0 = 1{\cdot}78 W^{1/3} (W^{1/3}/r)^{0{\cdot}94} \text{ lb sec in}^{-2}$$
$$= 576 \text{ dyn sec cm}^{-2}. \qquad \ldots\ldots (2)$$

Time constant

$$t_0 = 58 W^{1/3} (W^{1/3}/r)^{-0{\cdot}22} \mu\text{sec}$$
$$= 2{\cdot}03 \times 10^{-4} \text{ sec.} \qquad \ldots\ldots (3)$$

The above time constant describes the initial decay of the shock, after which the shock pressure drops more slowly. It is possible to define a slightly greater time constant which gives a better description for the lower frequency components:

$$t_0 = I_0/P_0 = 2{\cdot}44 \times 10^{-4} \text{ sec.} \qquad \ldots\ldots(4)$$

The Fourier analysis for the energy spectrum of an exponentially decaying pulse may easily be shown to be

$$E_0(f) = \frac{2P_0^2}{\rho c(1/t_0^2 + 4\pi^2 f^2)}, \qquad \ldots\ldots(5)$$

where f is frequency. This is a well-known result but in deriving it more than one worker has omitted the factor 2, a frequent and surprising cause of error in Fourier analysis using exponential functions being the neglect of the 'negative frequencies' (see also eqn (9)). In the plot in figure 4 the t_0 value from equation (4) is used, since it gives a better overall fit. At low frequencies the spectrum is flat, but changes over near $1/(2\pi t_0) = 653$ c/s (the '3-dB down point') to an f^{-2} or -6 dB per octave law. The rise time at the shock front is only a few microseconds, so that the -6-dB slope should hold up to a limit of several tens of kc/s (cf. Arons, Yennie and Cotter 1949, Arons and Wertheim, unpublished†).

7.3

Now the bubble pulses are fairly symmetrical, and their shape is well matched by an exponential rise followed by an exponential decay. From Arons (1948), for the first bubble,

Peak pressure
$$P_1 = 3450(W^{1/3}/r) \text{ lb in}^{-2}$$
$$= 0{\cdot}793 \times 10^6 \text{ dyn cm}^{-2}. \qquad \ldots\ldots(6)$$

Positive impulse
$$I_1 = 9{\cdot}58(W^{1/3}/r)d_0^{-1/6} \text{ lb sec in}^{-2}$$
$$= 953 \text{ dyn sec cm}^{-2}. \qquad \ldots\ldots(7)$$

Here d_0 is the depth in feet plus 33, and has been evaluated for a charge at 20 fathoms. A time constant for either side of the pulse may be defined in a manner similar to that of equation (4):

$$t_1 = I_1/2P_1 = 6{\cdot}01 \times 10^{-4} \text{ sec.} \qquad \ldots\ldots(8)$$

The energy spectrum for the double exponential pulse may easily be shown to be

$$E_1(f) = \frac{8}{\rho c}\left(\frac{P_1/t_1}{1/t_1^2 + 4\pi^2 f^2}\right)^2. \qquad \ldots\ldots(9)$$

This is also plotted in figure 4. At low frequencies the spectrum is flat like that for the shock waves, but changes over near $1/(2\pi t_1) = 265$ c/s ('6-dB point') to an f^{-4} or -12 dB per octave law. At high frequencies the predicted spectrum level will be too great, since the -12-dB spectrum slope corresponds to the discontinuity in pressure gradient at the peak of the simulated bubble pulse (see Weston 1960), which is not present in the real pulse. However at these frequencies the bubble contribution to the total spectrum energy is insignificant.

† 1950, Woods Hole Oceanographic Institution, ref. no. 50-32.

For the second bubble there are the approximate relationships

$$P_1/P_2 = 4{\cdot}72, \qquad P_2 = 0{\cdot}168 \times 10^6 \text{ dyn cm}^{-2} \qquad \ldots\ldots (10)$$

$$I_1/I_2 = 2{\cdot}47, \qquad I_2 = 386 \text{ dyn sec cm}^{-2} \qquad \ldots\ldots (11)$$

$$t_2 = I_2/2P_2 = 11{\cdot}5 \times 10^{-4} \text{ sec.} \qquad \ldots\ldots (12)$$

The spectrum follows from equation (9) and is also plotted in figure 4, with its '6-dB point' at 135 c/s. The contribution of further bubble pulses may be neglected with little error.

7.4

The total radiated energy spectrum shown in figure 4 is obtained by summing the energies due to the shock wave and the first two bubble pulses. It may be noted that according to Arons and Yennie (1948) rather more than half the total chemical energy of the charge is associated with the shock wave, but even including the bubble pulses rather less than half the total energy is eventually radiated as acoustic waves. Below about 230 c/s it may be seen that the major contribution to the spectrum energy comes from the first bubble pulse, and it is only above 230 c/s that the shock wave predominates. The summation spectrum shows no appreciable downward kink at this change over frequency, although it might under some conditions (the 7-fathom curve in figure 3 has such a tendency).

For bubbles far from a boundary the interval between the shock wave and the bubble pulse peak is

$$T_1 = 4{\cdot}36 W^{1/3} d_0^{-5/6} = 6{\cdot}59 \times 10^{-2} \text{ sec at 20 fathoms.} \qquad \ldots\ldots (13)$$

Thus the 'bubble pulse frequency' $1/T_1 = 15{\cdot}2$ c/s. The summation method of calculating spectrum level is valid only for frequencies much greater than $1/T_1$, typically for frequencies above, say 35 c/s.

7.5

At low frequencies the shock wave and bubble pulses may be replaced by their impulses I_0, I_1 and I_2 occurring at times 0, T_1, and $T_3 = T_1 + T_2$. The interval between the first and second bubble pulses $T_2 = 0{\cdot}72 T_1 = 4{\cdot}75 \times 10^{-2}$ sec. In addition, at low frequencies allowance must be made for the fact that the pressure goes negative between the pulses, so that the impulse over the whole pressure–time curve is zero. This is taken into account by adding a steady negative pressure of duration T_3. The energy spectrum for such a system may easily be shown to be

$$E_L(f) = (2/\rho c)[\{I_0 + I_1 \cos 2\pi f T_1 + I_2 \cos 2\pi f T_3 - N \sin 2\pi f T_3\}^2 + \{I_1 \sin 2\pi f T_1 + I_2 \sin 2\pi f T_3 - N(1 - \cos 2\pi f T_3)\}^2], \qquad \ldots\ldots (14)$$

where $N = (I_0 + I_1 + I_2)/(2\pi f T_3)$. This impulse formula for the spectrum level is valid for frequencies much less than $1/2\pi t_1 = 265$ c/s, or say less than 140 c/s. Thus it overlaps the summation curve by two octaves, in a region where the spectrum level curve forms a plateau. The impulse spectrum has a main maximum near 15 c/s (the bubble pulse frequency), with minor oscillations above this frequency.

Now since the total impulse is zero the spectrum level at very low frequencies must be proportional to f^2 (Weston 1959b), and on expansion the asymptotic form of equation (14) is found to be

$$E_L(f) = (2\pi^2 f^2/\rho c)\{I_1(T_1 - T_2) - (I_0 - I_2)T_3\}^2. \qquad \ldots\ldots (15)$$

For the usual range of depths the particular values of I and T are such that there is almost complete cancellation, and the coefficient of f^2 is very small. For example at 20 fathoms the asymptotic level becomes 24·4 dB higher if one puts $I_1 = I_2 = 0$, leaving only the shock impulse. Thus the spectrum slope predicted by equation (14) in the 1–10 c/s region is greater than the +6 dB per octave of equation (15), and the spectrum curve falls off sharply just below the bubble pulse frequency. With real charges, however, the bubble impulse is likely to vary from shot to shot (due to migration, turbulence, etc.), and the cancellation may not be so effective. Thus the average spectrum level is likely to be higher than that given by equation (15), and would be expected to vary greatly. The scatter in the measured 35 c s level for detonators is certainly larger than that for any other charge or frequency, and the mean level is higher than expected. It should be noted that cancellation does not affect the total energy output, but only changes the frequency distribution.

§ 8. Comparison of Measurements with Theory

8.1. *General Agreement*

A theoretical curve for 7 fathoms is shown in figure 3, again based on equations (5), (9) and (14). Different depths have deliberately been chosen for the theoretical curves discussed in § 7 and the present section, so that the theoretical change with depth may be seen. The major difference arises from the changed bubble pulse frequency, so that the 7-fathom curve of figure 3 shows a larger region with a flat spectrum than does the 20-fathom curve of figure 4. The 7-fathom depth was not chosen to illustrate the comparison of theory and experiment because agreement is particularly good there (it is in fact rather better at the other, greater, depths), but because it exhibits the special effects due to bubble migration. By applying the scaling laws of § 6 to the 7-fathom spectrum curve the theoretical 7-fathom difference curves shown in figure 1 may be derived.

The general agreement between measurements and theory in figures 1 and 3 is good, especially for the 1-lb results in figure 3. The existence of a maximum at the bubble pulse frequency is shown in the detonator results of both figures 1 and 3, though there is a smoothing out tendency since the measurements are all in octave bands. It may be noted that the humps in figures 1 and 3 may be shown to exist from independent measurements of detonator to 1-lb differences and by direct observations of the detonator source spectrum. The lowness of the theoretical prediction for detonators for frequencies below the bubble pulse frequency (figures 1 and 3) was explained at the end of § 7, and there is the possibility of a slight enhancement near the bubble pulse frequency due to the contribution of higher order pulses.

8.2. *Bubble Migration*

The only remaining significant discrepancy in figure 3 is the low experimental value for the low-frequency 50-lb results, amounting to about 5 dB at 35 c/s (or 130 c/s scaled). The sign and value of this source level discrepancy agree with those shown in figure 1 for the 50-lb–1-lb differences. It is thought to be due to bubble migration under gravity which, as already noted in § 3.5, is most important for large charges at shallow depths—so that in extreme cases there is virtually no bubble pulse at all. The phenomenon has been studied by Taylor

(1942), Bryant (1942), Kennard (1943), Friedman (1947) and others. Migration is also influenced by the nearness of boundaries, such that an oscillating bubble is repelled by a free surface and attracted towards a rigid surface, but this effect is only important for the smaller charges.

The explosion bubble moves very slowly when it is expanded, but may rise rapidly under gravity during its contracted phase. This is because the momentum is proportional to the time integral of the bubble buoyancy, which will produce a larger velocity when the associated bubble size is small. In considering migration effects it is useful to know the values of the maximum bubble radius a, and the vertical rise b between the initiation and the first bubble pulse. From, for example, Arons (1948),

$$a = 12{\cdot}6(W/d_0)^{1/3}\,\text{ft} = 3\,\text{ft for 1 lb at 7 fathoms.} \qquad \ldots\ldots(16)$$

Kennard (1943) gives the approximate formula

$$b \sim 4\sqrt{W/P_a}\,\text{ft} \sim 1{\cdot}7\,\text{ft for 1 lb at 7 fathoms,} \qquad \ldots\ldots(17)$$

where P_a is the hydrostatic pressure in atmospheres.

When there is migration some of the kinetic energy of radial motion is transferred upon contraction to kinetic energy of vertical motion. This factor rather than the gas pressure can then determine the minimum bubble radius, which is thereby increased. It may be noted that it is normally only about twice the original charge radius. The peak bubble pulse pressure may be much reduced, but in contrast the impulse is affected little. The main effect on the bubble pulse spectrum will be that of a bodily shift to lower frequencies, the '6 dB down' frequency being reduced in approximately the same ratio as the peak pressure. Migration also causes an increase in the bubble interval T_1.

According to Kennard the above reduction ratio depends on the value of b/a; for a 1-lb charge at 7 fathoms $b/a \sim 0{\cdot}6$ and the predicted reduction ratio is about 0·2. This should lead to an appreciable lowering of the spectrum level in the neighbourhood of 200 c/s, and though there is experimental support for this in figure 3 it is of doubtful significance, e.g. no reliable evidence of variation with depth was obtained for 140 c/s and above. However for a 50-lb charge at 7 fathoms the bubble radius a is 11 ft, and the calculated rise is about the same. Under these conditions the bubble pulse is of very little importance, and in fact the low-frequency 50-lb results are fitted extremely well by the shock wave theoretical spectrum alone. However, it might again be necessary to take account of the bubble pulse if the 50-lb measurements were extended to frequencies below about 10 c/s.

It is worthwhile calculating the depth at which such bubble migration effects become small. This may be arbitrarily defined as corresponding to $b/a = 0{\cdot}3$, with a predicted reduction ratio of about 0·7. From equations (16) and (17) for the critical depth

$$d_0 \sim 200W^{1/4}\,\text{ft.} \qquad \ldots\ldots(18)$$

This corresponds to about 1 fathom for a detonator, 30 fathoms for a 1-lb charge, and 80 fathoms for a 50-lb charge.

Now the explosion bubble must eventually break up when it stops oscillating, and the break-up is likely to be accelerated when it is rising rapidly under gravity. It may be noted that a bubble is unstable in form when it is contracting (Taylor

1942), and the shape may be distorted at the minimum radius—where the speed of rise is a maximum. This suggests that the bubble pulse may be virtually eliminated when the migration is serious. Experiments by other workers have shown that the bubble distortion is indeed greatest for shallow charges (and also when the original charge is not spherically symmetrical), and that bubble pulses are missing for large shallow charges (quite apart from catastrophic effects such as blow-out at the surface). This also suggests the possibility of a systematic variation of source level with firing area etc., due to changes in the sea turbulence conditions. There is however no reliable evidence for this, e.g. no significant changes in the measured differences with site.

8.3. *Variation with Depth*

The variation of charge-source level with depth is obviously of general interest, because charge sources are used on various occasions at a variety of depths. There is also a particular interest because charges may be fired at different depths at the same position, perhaps to investigate mode excitation functions in shallow water. It is necessary to be able to separate variation due to the source from that due to propagation. There is little source variation at high frequencies since the shock wave corresponds to a high impedance source, but at low frequencies there is considerable variation.

Now the shock wave is unaffected by depth, as noted above. The bubble pulse peak pressures are also unaffected for the range of depths used (provided the bubble is stationary), and their impulses vary only very slowly—with $d_0^{-1/6}$. The only parameter changing rapidly with depth for non-migratory bubbles is the bubble interval T_1 proportional to $d_0^{-5/6}$. Thus, on going from 7 to 60 fathoms there is a four-fold increase in the bubble-pulse frequency. Some of these effects have already been seen when comparing figures 3 and 4 (see also figure 5), and there are also the special effects which do not obey the simple scaling laws —e.g. gravity migration.

Consider now the experimental results, and first the detonator to 1-lb differences in figure 1 where there are large real differences with depth. On going from 5 to 30 fathoms the calculated detonator bubble-pulse frequency moves up from about 60 to 160 c/s, and this is evident in the results. This moving up is also responsible for the decreasing (algebraic) difference at the lowest frequencies as depth is increased, but a quantitative theory is difficult because of the variable cancellation effect discussed in §7. Changes in the 1-lb spectrum should have a relatively small effect on these differences.

The 50-lb–1-lb differences in figure 1 show less depth variation, because the bubble-pulse frequencies tend to lie below the range of interest though there should be marginal effects due to the 1-lb 40-fathom charges. The most obvious depth effects are for the lowest frequencies at 7 fathoms, due to the 50-lb charge migration already discussed in §8.2. A small variation may be expected at the middle frequencies too, because of the $d_0^{-1/6}$ impulse law plus small bubble migration effects on both the 1-lb and 50-lb charges. However this is swamped by the experimental scatter, even though the latter is surprisingly small.

The absolute charge source levels shown in table 2 exhibit appreciable depth variations only for frequencies at, or below, about 70 c s. The 35 c/s and 70 c/s values are plotted in figure 5 and compared with the theoretical curve for a single frequency at the octave centre. The experimental and theoretical levels agree

in mean level, the magnitude of the depth variations is correct, but detailed agreement is completely lacking. This cannot be wholly ascribed to the width of the measurements band, and it may be yet another phenomenon in which bubble migration plays a part.

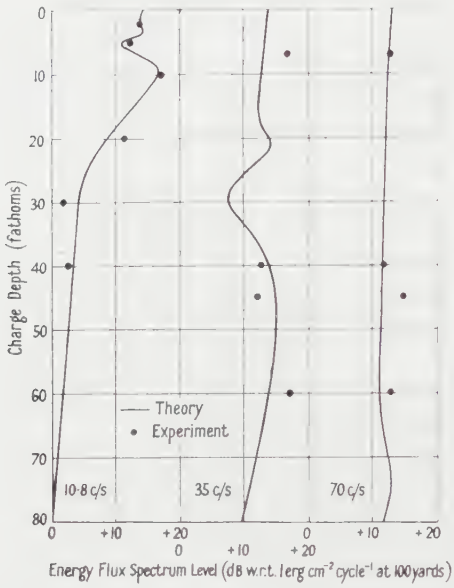

Figure 5. Dependence of 1-lb source levels on charge depth. Experimental points: arbitrary reference for 10·8 c/s, absolute for 35 c/s and 70 c/s.

Figure 5 also shows experimental data for the narrow bandwidth at 10·8 c/s, based on unpublished ground-wave measurements by W. W. Reay in the area off Perranporth, Cornwall, described by Merriweather (1958). The considerable depth dependence measured there was due both to the source variation and the mode excitation function, and it was necessary to correct for the latter by assuming a sinusoidal form with a maximum at 25 fathoms in water 45 fathoms deep. The general level has been adjusted to give the best fit to the theoretical line but is known to be approximately correct; the agreement in shape is excellent.

§ 9. Conclusions

Surface cavitation and the change of source position due to bubble migration are shown to have only a small effect on the acoustic signal received at a distance. The measured differences between charges (table 1) and the absolute charge source levels (table 2) obey the simple scaling laws, and agree well with the predictions from Fourier analysis. For the larger and shallower charges it is also necessary to allow for the effect of migration in reducing the contribution of the bubble pulses.

Many minor problems remain, especially some connected with the finite-amplitude propagation discussed in § 3. In general it is still desirable to use

experimental rather than theoretical values for charge differences and source levels, especially when migration makes accurate prediction difficult. Thus the most important part of this paper is the presentation of the experimental results in tables 1 and 2, with accuracy generally to about ± 1 dB.

Acknowledgments

Thanks are due to the Captains and Ships' Companies of R.R.S. *Discovery II* and many of H.M. Ships for their patient help during arduous trials. The author is also grateful to many colleagues, some of whose results have been included, and especially to W. W. Reay, A. S. Merriweather and A. A. Horrigan.

References †

Arons, A. B., 1948, *J. Acoust. Soc. Amer.*, **20**, 277 (U.E.R. II, 481).
—— 1954, *J. Acoust. Soc. Amer.*, **26**, 343.
Arons, A. B., Slifko, J. P., and Carter, A., 1948, *J. Acoust. Soc. Amer.*, **20**, 271 (U.E.R. II, 475).
Arons, A. B., and Yennie, D. R., 1948, *Rev. Mod. Phys.*, **20**, 519 (U.E.R. I, 1137).
Arons, A. B., Yennie, D. R., and Cotter, T. P., 1949, *Nav. Ord. Rep.*, 478 (U.E.R. I, 1473).
Bryant, A. R., 1942, *Road Research Laboratory Report*—Index 10 (U.E.R. II, 163).
Cole, R. H., 1948, *Underwater Explosions* (Princeton: University Press).
Friedman, B., 1947, *Inst. for Math. and Mech., N.Y.U.*, Rep. 166 (U.E.R. II, 329).
Kennard, E. H., 1943, *David Taylor Model Basin Report* (U.E.R. II, 377).
Kolsky, H., Lewis, J. P., Sampson, M. T., Shearman, A. C., and Snow, C. I., 1949, *Proc. Roy. Soc.* A, **196**, 379.
Merriweather, A. S., 1958, *Geophys. J.*, **1**, 73.
O'Brien, P. N. S., 1960, *Geophys. J.*, **3**, 29.
Penney, W. G., and Pike, H. H. M., 1950, *Rep. Progr. Phys.*, **13**, 46.
Raitt, R. W., 1952, *Oceanographic Instrumentation* (N.A.S.–N.R.C. Publ. 309), **70**.
Taylor, G. I., 1942, *Min. Home Security*, S.W.19 (U.E.R. II, 131).
Tucker, M. J., 1952, *Electronic Engng*, **24**, 466.
Weston, D. E., 1959, *Proc. Phys. Soc.*, **73**, 365.
—— 1960, *Geophys. J.*, **3**, 191.
Wood, A. B., Lakey, R. H., and Butterworth, S., 1924, A.R.L./S/12 (U.E.R. I, 497).
Worzel, J. L., and Ewing, M., 1948, *Geol. Soc. Amer. Mem.*, 27.

† Many of the papers cited have been reprinted in a joint Anglo-American compendium of reports published in 1950 by the Office of Naval Research and entitled *Underwater Explosion Research* (shortened here to U.E.R.).

The Joule Heating of a Stable Pinched Plasma

By M. G. HAINES

Physics Department, Imperial College of Science and Technology, London

Communicated by R. Latham; *MS. received* 10*th December* 1959, *in revised form* 9*th March* 1960

Abstract. The hydromagnetic equations are employed to obtain the conditions necessary for a pressure balance in a pinched discharge in ionized deuterium. The time dependent energy equation is integrated to give the time taken to heat the plasma by Joule heating with bremsstrahlung radiation losses only, and with a pressure balance maintained at all time. This heating time is shown to depend on the radius, line density, and final temperature of the plasma. The current density distribution during the heating process is calculated, showing only a small divergence from uniformity. The condition for no run-away electrons to be present at any time during the heating process is shown to place a restriction only on the minimum line density of the particles. The effect of an unbalance of pressure, causing a change in the outside radius of the plasma during the heating process, is discussed. Finally, the utilization of a transient energy source and its relation to discharge parameters is considered.

§ 1. Introduction

The aim of this paper is to present scaling relations which will be useful to those working on electrical pinched discharges in ionized hydrogen or deuterium, where Joule heating is the predominant heating mechanism. A few relations such as the well known Bennett relation have been derived before, but the heating time scale, the current density distribution in the plasma during heating, and the relation of discharge parameters to run-away electrons and circuit parameters have not previously been published.

Essentially the heating process considered in this paper is the second stage in a pinched discharge. The first stage is the initial ionization and compression of the gas so that at the end of this stage the plasma is pinched to a radius a, and, when viewed in cylindrical geometry, carries an axial current $\mathcal{I}_0$ and is at a uniform temperature T_0. In the second stage, it is assumed that a pressure balance is required at all times so that the plasma, being pinched and isolated from the walls, does not alter its dimensions during the heating process. Under this condition, as the temperature rises due to Joule heating by the current, so the current must rise to maintain the pressure balance. The time scale is thus the same for the rise of temperature and current. The exact current and temperature profile with time is found when bremsstrahlung radiation is the only heat loss. Heat losses due to cyclotron radiation and heat conduction are not considered here. Also, the plasma is assumed to be stable throughout the heating process and to be cylindrically symmetrical. It is unfortunate that this condition is difficult to achieve, for a physical system as described is likely to be essentially unstable. On the other hand, the calculations on stability have been made with models which are not good

approximations compared with actual expected conditions, and experimental work has not been very extensive. With further investigations conditions may in fact be found, perhaps using carefully programmed magnetic fields, that will extend the duration of the pinched discharge long enough to cover the heating times calculated here. In any event, it is interesting to follow the consequences of the heating process under the assumption of stability.

During the heating process the total axial current and the electrical conductivity (which is a function of the temperature) change with time. The current density distribution will not therefore be uniform across the radius, but it will be shown in § 4 that the distribution is, in fact, close enough to uniformity not to alter the general calculations which will be made assuming uniform current density.

Whilst the plasma is under pressure balance, the electric field varies inversely with the temperature. During the heating process it therefore falls from a maximum to a minimum value. However, this electric field must at all times be much smaller than the critical electric field at which the electrons run away, otherwise the energy will entirely be expended on run-away electrons instead of being transferred by Joule heating to the ions. A condition for this will be calculated in § 5.

If the applied electric field does not follow the theoretical profile with time, then the current also will begin to diverge from its correct value and cause an unbalance in the radial pressure. This will result in a radial acceleration of the plasma and an alteration in the outside radius of the plasma. It will be shown in § 6 that this change eventually results in a restoration of the total current to its proper value for pressure balance which is independent of this outside radius. The electric field thus controls the radius of the plasma column, and this affects the time scale for Joule heating.

Finally, the relations between a transient energy source for heating the plasma and the dimensions, density and peak temperature of the plasma are derived. It is hoped that these formulae will be helpful to those designing experimental pinched discharge devices.

§ 2. The Steady State

The relevant hydromagnetic equations for a stationary plasma possessing cylindrical symmetry and carrying an axial current are

$$\frac{1}{r}\frac{\partial}{\partial r}(rB_\phi)=\mu i_z \qquad \ldots\ldots(1)$$

$$i_z=\sigma E_z \qquad \ldots\ldots(2)$$

$$\frac{\partial p}{\partial r}=-i_z B_\phi . \qquad \ldots\ldots(3)$$

It will be assumed that, during the heating process under pressure balance conditions, the current density i_z and electric field E_z are uniform over the radius. This assumption will be examined in detail in § 4. The pressure balance condition in the radial direction is given in equation (3).

Since over most of the discharge the electrical conductivity depends only on temperature, uniform electric field and uniform current imply uniform temperature. This implication is further enhanced by the high thermal conductivity of the plasma and its radial isolation outside its radius a from the walls of the containing vessel.

In fully ionized hydrogen or deuterium, if the electron and ion temperatures are the same, the pressure p and internal energy U can be written as

$$p = 2nkT \qquad \ldots\ldots(4)$$

$$U = 3nkT \qquad \ldots\ldots(5)$$

where n is the number density of electrons or ions and is related to the line density N by

$$N = \int_0^a 2\pi n r dr \qquad \ldots\ldots(6)$$

where a is the outside radius of the plasma.

Similarly the total axial current $\mathscr{I}$ is related to the current density i_z by

$$\mathscr{I} = \int_0^a 2\pi i_z r dr . \qquad \ldots\ldots(7)$$

Using the condition that $n = 0$ for $r \geqslant a$, equations (1), (3) and (4) yield, on integration,

$$n = \frac{\mu \mathscr{I}^2}{8\pi^2 a^2 kT}\left[1 - \frac{r^2}{a^2}\right] \text{ for } r \leqslant a . \qquad \ldots\ldots(8)$$

Then, applying equation (6) one can obtain the relation, first derived by Bennett (1934) between axial current, temperature and line density

$$16\pi NkT = \mu \mathscr{I}^2, \qquad \ldots\ldots(9)$$

and the distribution of number density in the form

$$n = \frac{2N}{\pi a^2}\left[1 - \frac{r^2}{a^2}\right] \text{ for } r \leqslant a . \qquad \ldots\ldots(10)$$

The time dependent energy equation for the axially symmetrical plasma where Joule heating, and losses by bremsstrahlung radiation and radial thermal conduction, occur, can be written as

$$\frac{\partial U}{\partial t} - \frac{1}{r}\frac{\partial}{\partial r}\left[\lambda r \frac{\partial T}{\partial r}\right] = i_z E_z - \beta n^2 T^{1/2} \qquad \ldots\ldots(11)$$

where λ is the thermal conduction coefficient and β is the bremsstrahlung radiation coefficient. Any effect of electrodes, if they be present, is ignored in this paper. An estimate of the heat losses to electrodes has been made by Haines (1960) for the steady state when Joule heating is balanced by bremsstrahlung radiation losses and axial heat conduction and diffusion.

The integration of equation (11) over the radius eliminates the heat conduction term, because the heat flux vector is zero for $r \geqslant a$. Also, in this integration, the radial dependence of the number density is assumed to be given by equation (10) during the heating process: this again depends on the current density and temperature being uniform and a pressure balance being maintained always. Then equation (11) becomes

$$\frac{dT}{dt} = \phi T^{-1/2} - \psi T^{1/2} \qquad \ldots\ldots(12)$$

where the electrical conductivity is given by

$$\sigma = \alpha T^{3/2} \qquad \ldots\ldots(13)$$

(see, for example, Spitzer 1956), and

$$\phi = \frac{16}{3\alpha\mu a^2} \quad \text{and} \quad \psi = \frac{4\beta N}{9\pi a^2 k}. \qquad \ldots\ldots(14)$$

ϕ and ψ can be treated as constants during the heating process, and so equation (12) is the simplified time dependent energy equation.

The maximum possible temperature T_m occurs when Joule heating is balanced by bremsstrahlung radiation losses, that is, steady state is reached and dT/dt is zero. Then

$$T_m = \frac{\phi}{\psi} = \frac{12\pi k}{\alpha\mu\beta N}$$

$$\text{or } NT_m = 2{\cdot}65 \times 10^{27} \qquad \ldots\ldots (15)$$

where α and β have values of $1{\cdot}1 \times 10^{-3}$ and $1{\cdot}42 \times 10^{-40}$ in m.k.s. units for hydrogen or deuterium. At this temperature, the maximum current I_m then flows, and from equations (9) and (15) is given by

$$I_m = \frac{8\sqrt{3}\pi k}{\mu(\alpha\beta)^{1/2}} = 1{\cdot}2 \times 10^6 \text{ amp.} \qquad \ldots\ldots (16)$$

It is to be noted that this maximum current is a constant, independent of the line density, temperature, and radius of the plasma. This result has been derived by Pease (1957).

§ 3. The Heating Time Scale

Under pressure balance conditions, the energy equation (12) can be integrated from time $t=0$ to t when the temperature rises from T_0 to T, to yield

$$t = \frac{3\alpha\mu a^2 T_m^{3/2}}{8}\left[\frac{1}{2}\ln\left(\frac{\sqrt{T_m}+\sqrt{T}}{\sqrt{T_m}-\sqrt{T}}\right) - \frac{\sqrt{T}}{\sqrt{T_m}}\right.$$

$$\left. - \frac{1}{2}\ln\left(\frac{\sqrt{T_m}+\sqrt{T_0}}{\sqrt{T_m}-\sqrt{T_0}}\right) + \frac{\sqrt{T_0}}{\sqrt{T_m}}\right]. \qquad \ldots\ldots (17)$$

This equation can be expanded in the form

$$t = \frac{3\alpha\mu a^2 T_m^{3/2}}{8}\left[\frac{1}{3}(\zeta^3 - \zeta_0^3) + \frac{1}{5}(\zeta^5 - \zeta_0^5)\right.$$

$$\left. + \frac{1}{7}(\zeta^7 - \zeta_0^7) + \ldots.\right] \qquad \ldots\ldots (18)$$

where $\zeta = \sqrt{T}/\sqrt{T_m}$ and $\zeta_0 = \sqrt{T_0}/\sqrt{T_m}$.

From equation (17), it can be seen that it takes an infinite time to reach T_m, but in order to obtain a time scale for the heating process, the time τ_η taken to reach a fraction η^2 of T_m can be found, where $T_0 \ll T$, as below:

$$\tau_\eta = \frac{3\alpha\mu a^2 T_m^{3/2}}{8}\left[\frac{1}{2}\ln\left(\frac{1+\eta}{1-\eta}\right) - \eta\right]. \qquad \ldots\ldots (19)$$

For example, if $\eta = 0{\cdot}9$

$$\tau_{0{\cdot}9} = 3{\cdot}25 \times 10^{-10} a^2 T_m^{3/2}. \qquad \ldots\ldots (20)$$

For the case when bremsstrahlung radiation is zero, equation (18) reduces to

$$t = \frac{1}{8}\alpha\mu a^2 T^{3/2} = 1{\cdot}89 \times 10^{-10} a^2 T^{3/2} \qquad \ldots\ldots (21)$$

where again $T_0 \ll T$.

The relation between current and time during the heating process under pressure balance can be obtained from equations (9) and (17). In fact, I/I_m and I_0/I_m simply can be written for ζ and ζ_0 respectively in equation (18), because the current is proportional to the square root of the temperature.

Similarly the relation between the applied electric field and time can be obtained as follows from equations (2), (9) and (13)

$$E_z = \frac{i_z}{\sigma} = \frac{\mathscr{I}}{\pi a^2 \alpha T^{3/2}}$$
$$= \left[\left(\frac{16k}{\pi\mu\alpha^2}\right)\right]^{1/2} \frac{\sqrt{N}}{a^2 T} \qquad \ldots\ldots (22)$$
$$= 6{\cdot}86 \times 10^{-6} \frac{\sqrt{N}}{a^2 T}$$

for ionized hydrogen or deuterium. This means that, since the electric field is inversely proportional to the temperature, it falls from a maximum initial value E_0 at temperature T_0 to a minimum final value of $E_{\min}$ at temperature T_m. The actual time dependence of the electric field can be seen by writing $\sqrt{E_{\min}}/\sqrt{E}$ and $\sqrt{E_{\min}}/\sqrt{E_0}$ for ζ and ζ_0 respectively in equation (18).

The radius of the plasma a is not governed directly by the total current which flows but by the applied electric field. This can be seen from equations (9) and (22), the former showing the current depending on the temperature and line density only, and the latter showing that the electric field depends also on the radius of the plasma. The time scale for heating, however, is also affected by the radius of the plasma. A discussion on this will be found in §§ 6 and 7.

§ 4. Current Density Distribution

The theory in the previous sections depends for its validity essentially on the current density being uniform across the radius of the plasma during the heating process. The actual current density distribution can be calculated where the total axial current $\mathscr{I}$, the electrical conductivity σ and the outside radius of the plasma are known functions of time, using the theory by Haines (1959). The current density i_z was found in this theory using a Laplace transform of $\mathscr{I}$ and the appropriate Fourier–Mellin inversion theorem, as shown:

$$i_z(x, y) = \frac{1}{2\pi i} \lim_{\eta\to\infty} \int_{\xi-i\eta}^{\xi+i\eta} \frac{e^{yp}\sqrt{p}I_0(\sqrt{p}x)}{2\pi a^2 I_1(\sqrt{p})} \int_0^\infty \mathscr{I}(q)e^{-pq}dqdp \qquad \ldots\ldots (23)$$

where $x = \frac{r}{a}$ and $y = \int_0^t \frac{dt}{\mu\sigma(t)a^2(t)}$, $\qquad \ldots\ldots (24)$

q is a dummy variable equivalent to y, and I_0 and I_1 are Bessel's imaginary functions of zero and first order respectively.

In this particular problem, in order to avoid a rather complex calculation, the current distributions are calculated during the Joule heating of the plasma under pressure balance for the case when bremsstrahlung radiation is put to zero. The axial current $\mathscr{I}$ then rises steeply all the time; in fact, always more steeply than with radiation losses present, so that the distribution of current obtained from this will be the worst possible divergence from uniformity.

Equation (12) in this case becomes

$$\frac{dT}{dt} = \phi T^{-1/2} \qquad \ldots\ldots (25)$$

ϕ being given by equation (14).

For the application of this general transform theory, the total axial current and the current density everywhere must be zero at $t = 0$. However, in this

problem of the second stage of a pinched discharge the initial current has a value of $\mathscr{I}_0$ and the temperature T_0 is related to this by equation (9):

$$\mathscr{I}_0=\left[\frac{16\pi Nk}{\mu}\right]^{1/2}T_0^{1/2}. \qquad \ldots\ldots(26)$$

The total axial current which must be used for the transform theory is therefore $\mathscr{I}'$, given by

$$\mathscr{I}'=\mathscr{I}-\mathscr{I}_0=\left[\frac{16\pi Nk}{\mu}\right]^{1,2}(T^{1/2}-T_0^{1/2}). \qquad \ldots\ldots(27)$$

Similarly, the current density i_z will be given by

$$\left.\begin{aligned} i_z'&=i_z-i_{z0}\\ \text{where}\quad i_{z0}&=\mathscr{I}_0/\pi a^2. \end{aligned}\right\} \qquad \ldots\ldots(28)$$

From equations (13), (24) and (25) a relation between y and T can be obtained

$$\begin{aligned} y&=\int_{T_0}^{T}\frac{1}{\mu\varkappa a^2}\frac{dt}{dT}\frac{dT}{T^{3/2}}\\ &=\frac{3}{16}\ln\frac{T}{T_0}. \end{aligned} \qquad \ldots\ldots(29)$$

Then, writing $(T_0/T)^{3p/16}$ for e^{-py} from this equation, the Laplace transform of $\mathscr{I}'$ becomes

$$\begin{aligned} \int_0^\infty \mathscr{I}'(q)\,e^{-pq}dq&=\left[\frac{16\pi Nk}{\mu}\right]^{1,2}\int_{T_0}^{\infty}(T^{1,2}-T_0^{1/2})\left(\frac{T_0}{T}\right)^{3p/16}\frac{16dT}{3T}\\ &=\mathscr{I}_0\left(\frac{1}{p-8/3}-\frac{1}{p}\right). \end{aligned} \qquad \ldots\ldots(30)$$

Inserting this into equation (23), the current density distribution is

$$i_z'=\frac{1}{2\pi i}\lim_{\eta\to\infty}\int_{\xi-i\eta}^{\xi+i\eta}\frac{e^{py}\,pI_0(\sqrt{p}\,r/a)\mathscr{I}_0}{2\pi a^2 I_1(\sqrt{p})}\left(\frac{1}{p-8/3}-\frac{1}{p}\right)dp. \qquad \ldots\ldots(31)$$

It can be shown on expansion that the integrand is a single valued function of p with poles of $\bar{i}_z'(x,p)$ occurring at $p=0$, $p=8/3$ and $p=-\gamma_n^2$, where γ_n, $n=1,2\ldots$ are the non-zero roots of the equation

$$J_1(\gamma_n)=0.$$

From an evaluation of the residues at these poles one obtains, using equation (28),

$$\begin{aligned} i_z(x,y)=\frac{\mathscr{I}_0}{2\pi a^2}\exp\left(\frac{8}{3}y\right)&\frac{\left\{\sqrt{\frac{8}{3}}I_0\left(\sqrt{\frac{8}{3}}x\right)\right\}}{I_1\left(\sqrt{\frac{8}{3}}\right)}\\ &-\sum_{n=1,2\ldots}^{\infty}\frac{\mathscr{I}_0\exp(-\gamma_n^2 y)\gamma_n^2 J_0(\gamma_n x)}{\pi a^2 J_0(\gamma_n)}\left(\frac{1}{\gamma_n^2}-\frac{1}{\gamma_n^2+\frac{8}{3}}\right) \end{aligned} \qquad \ldots\ldots(32)$$

where y is given by equation (29).

In this result for current density distribution, the first term is seen to be the particular integral of the differential equation for current density

$$\frac{1}{x}\frac{\partial}{\partial x}\left(x\frac{\partial i_z}{\partial x}\right)-\frac{\partial i_z}{\partial y}=0 \qquad \ldots\ldots(33)$$

where

$$\frac{\partial i_z}{\partial y}=\frac{8}{3}i_z. \qquad \ldots\ldots(34)$$

This is the long time term, giving a current density distribution not far from uniform; in fact the current density at the surface of the plasma is 1·79 times that at the centre.

The transient terms (the infinite summation term) give a more pronounced skin effect at the start of the current profile, but these decay as the temperature increases because

$$e^{-\gamma_1^2 y} = \left(\frac{T_0}{T}\right)^{3\gamma_1^2/16} = \left(\frac{T_0}{T}\right)^{2\cdot753}.$$

In fact, these transient terms die away to 1/e of their original value when $T = 1{\cdot}72T_0$, and to 1% of their original value when $T = 5{\cdot}32T_0$. This characteristic time τ for decay is very much smaller than the heating time $\tau_{0\cdot9}$; in fact

$$\frac{\tau}{\tau_{0\cdot9}} = 0{\cdot}42\left(\frac{T_0}{T_m}\right)^{3/2}.$$

Thus it can be concluded that the current density is not very far from uniform during the heating process under pressure balance.

However, the divergence from uniformity will have an effect on the energy equation (25) tending to modify ϕ. Fortunately, the Bennett relation (equation (9)) is unaffected by the distribution of current when there is a pressure balance and uniform temperature across the radius: this can be seen as follows:

$$2NkT = \int_0^a 2\pi r p\,dr$$
$$= \left[\pi r^2 p\right]_0^a - \pi\int_0^a r^2\frac{\partial p}{\partial r}\,dr.$$

From the condition that $p = 0$ at $r = a$, and from equations (1) and (3), this becomes

$$2NkT = \mu\pi\int_0^a r i_z\left[\int_0^r r i_z\,dr\right]dr$$
$$= \frac{\mu\pi}{2}\left[\int_0^a r i_z\,dr\right]^2.$$

Then by equation (7) the Bennett relation (9) is obtained.

The modification to ϕ for the long time term only will be found. This modification is independent of time because the relative distribution of current over the radius given by this term is a constant with time, namely $I_0(\sqrt{(8/3)}x)$. However, the current distribution will be modified again by the changed ϕ. Therefore, the current density used will be the first term in equation (32) with $\sqrt{(8/3)}$ replaced by ξ which then has to be found. This is

$$i_z(x, y) = \frac{\mathscr{I}_0}{2\pi a^2}\exp(\xi^2 y)\frac{\xi I_0(\xi x)}{I_1(\xi)} \qquad \ldots\ldots(35)$$

and is the particular solution of equation (33) with equation (34) as

$$\frac{\partial i_z}{\partial y} = \xi^2 i_z. \qquad \ldots\ldots(36)$$

Since the current distribution is constant, one can write on integration

$$\frac{d\mathscr{I}}{dy} = \xi^2\mathscr{I} \qquad \ldots\ldots(37)$$

or

$$\mathscr{I} = \mathscr{I}_0\exp(\xi^2 y). \qquad \ldots\ldots(38)$$

On integrating equation (11) it can be seen that

$$3Nk\frac{dT}{dt} = \frac{2\pi a^2}{\sigma}\int_0^1 i_z^2 x dx \qquad \ldots\ldots(39)$$

for the case when no radiation losses occur.

Using equation (35) and the relation

$$2\int_0^1 \mathrm{I}_0^2(\xi x)x dx = \mathrm{I}_0^2(\xi) - \mathrm{I}_1^2(\xi)$$

equation (39) becomes

$$3Nk\frac{dT}{dt} = \frac{\pi a^2}{\sigma}\frac{\mathscr{I}_0^2}{4\pi^2 a^4}\exp(2\xi^2 y)\frac{\xi^2[\mathrm{I}_0^2(\xi) - \mathrm{I}_1^2(\xi)]}{\mathrm{I}_1^2(\xi)}. \qquad \ldots\ldots(40)$$

Using equations (9), (24) and (37), this becomes

$$\frac{d\mathscr{I}}{dy} = \xi^2\mathscr{I}\frac{2}{3}\frac{\mathrm{I}_0^2(\xi) - \mathrm{I}_1^2(\xi)}{\mathrm{I}_1^2(\xi)}. \qquad \ldots\ldots(41)$$

Comparing equation (41) with equation (37), we can see that ξ is the root of the equation

$$\mathrm{I}_0^2(\xi) = \frac{5}{2}\mathrm{I}_1^2(\xi) \qquad \ldots\ldots(42)$$

giving a value of $\xi = 1{\cdot}656$ (compared with its unmodified value of $\sqrt{(8/3)} = 1{\cdot}633$).

To obtain the modified ϕ, equations (9), (13), (37) and (42) are used in equation (40) to give

$$\frac{dT}{dt} = \frac{2\xi^2}{\mu\chi a^2}T^{1/2}. \qquad \ldots\ldots(43)$$

ϕ is thus modified to $5{\cdot}485/\chi\mu a^2$ (as compared with $5{\cdot}333/\chi\mu a^2$).

In equation (21), the time taken to heat up to a temperature $T(\gg T_0)$ is modified to $1{\cdot}68\times10^{-10}a^2T^{3/2}$.

In conclusion it can be stated that the current distribution during heating is nearly uniform and only slightly affects the previous calculations.

§ 5. The Effect of Run-away Electrons

The critical electric field, above which electrons run away and Joule heating is considerably reduced, is given by Dreicer (1958) (in m.k.s. units) as

$$E_c = 1{\cdot}51\times10^{-12}\left(\frac{\ln\Omega}{10}\right)\frac{n}{T}\ \mathrm{vm}^{-1} \qquad \ldots\ldots(44)$$

where n is the number of electrons per centimetre. To be consistent with Dreicer's formulation of $\ln\Omega$, Spitzer's (1956) formulation for electrical conductivity will be used in this section. This is

$$\sigma = 1{\cdot}53\times10^{-3}\left(\frac{10}{\ln\Omega}\right)T^{3/2}. \qquad \ldots\ldots(45)$$

To prevent run-away electrons in the heating process described in previous sections, it is essential that the applied electric field E_z is always much less than E_c, otherwise the theory does not hold and the plasma is not efficiently heated.

E_z is given by

$$E_z = \frac{i_z}{\sigma} = \left(\frac{\ln\Omega}{10}\right)\frac{1}{1{\cdot}53\times10^{-3}T^{3/2}}\frac{\mathscr{I}}{\pi a^2} \qquad \ldots\ldots(46)$$

using equation (45).

Then, from equations (44) and (46),

$$\frac{E_z}{E_c} = 1{\cdot}38 \times 10^{14} \frac{\mathscr{I}}{a^2 n T^{1/2}}. \qquad \ldots\ldots (47)$$

If there is a pressure balance at all time, equation (9) can be used together with

$$N \simeq \pi a^2 n \qquad \ldots\ldots (48)$$

to give

$$\frac{E_z}{E_c} \simeq \frac{10^7}{N^{1/2}}. \qquad \ldots\ldots (49)$$

In order that electrons in the high energy tail of the Maxwellian distribution do not grow by collisions into the run-away velocity region over a reasonable period of time, it is necessary that $E_z/E_c \leqslant 1/100$.

Therefore it can be seen from equation (49) that the condition for no run-away electrons is that the line density N is greater than 10^{15} electrons per metre. This is a sufficient condition, when the plasma is under pressure balance, to prevent run-away electrons, and it is to be noted that the ratio E_z/E_c as given by equation (49) is a constant during the heating process.

The number density n actually goes to zero at the surface of the plasma (see equation (10)), and the approximation made in equation (48) is not strictly applicable. Thus it is difficult to avoid a few run-away electrons occurring at the surface of the plasma.

§ 6. Upset of Pressure Balance

The equation of motion for the plasma in the radial direction can be written as

$$\rho \frac{dv_r}{dt} = -i_z B_\phi - \frac{\partial p}{\partial r} \qquad \ldots\ldots (50)$$

where ρ is the density of the plasma. When the acceleration is zero, there is a pressure balance given by the Bennett relation, equation (9), where the temperature is assumed to be uniform over the radius.

Ohm's law for a radially moving plasma can be written as

$$i_z = \sigma (E_z + v_r B_\phi). \qquad \ldots\ldots (51)$$

During the heating process outlined in § 3, the electric field should follow equation (22) in order that a pressure balance should be kept. If, however, E_z diverges from this value, it will cause a corresponding change in the current density i_z as seen in equation (51). This in turn causes an unbalance in equation (3), and as can be seen in equation (50), a radial acceleration is produced. The resulting radial velocity modifies equation (51) so as to tend to restore the original value of current density. Soon, the acceleration is stopped and equations (3) and (4) are restored. The outside radius of the plasma, the current density and pressure gradient are altered from what they would have been if E_z had not diverged, but the total current flowing does not depend on the outside radius of the plasma and this is restored to the same value as it would have been.

Thus it can be generally summarized that the electric field governs the outside radius of the plasma (see equation (22)): any divergence in pressure balance due to a change in electric field results eventually only in a change of radius, the total axial current flowing, when the pressure balance is restored, being the same as it would have been if there had been no change in the electric field.

In particular, if during the steady state when the current is $\mathscr{I}_m = 1{\cdot}2 \times 10^6$ amp; the electric field is increased so as to increase the total current beyond $\mathscr{I}_m$, the radius of the plasma column decreases until the resistance of the plasma column is increased so as to reduce the current back to $\mathscr{I}_m$. The maximum temperature T_m in this steady state does not depend on the plasma radius but only on the line density (see equation (15)).

If the electric field is not carefully programmed with time so as to preserve a pressure balance at all time, that is, the outside radius a of the plasma varies with time, then, if this variation of a is small and slow, it can be included in the preceding theory, § 3, on the heating time scale, as follows. Equation (12) can be modified to give

$$dT/dy = \phi' T^{-1/2} - \psi' T^{1/2}$$

where

$$y = \int_0^t \frac{dt}{a^2(t)}, \quad \phi' = \frac{16}{3\varkappa\mu} \quad \text{and} \quad \psi' = \frac{4\beta N}{9\pi k}.$$

Equations (17), (18) and (19) can be similarly altered to give modified time scales if $a(t)$ is known. The results of § 4 on current distributions are unaltered by these small variations with time of the outside radius.

§ 7. Utilization of a Transient Energy Source

If the source of electrical energy, for supplying the axial current to heat the plasma and to create the pinching force, is a bank of condensers, then it is required to know how to utilize this so as to reach the required peak temperature T_p in the plasma when the current pulse is at its peak value $\mathscr{I}_p$.

A quantity $\mathscr{E}$ is now defined as being the total energy available as Joule heating for the plasma in the discharge tube up till the time when the current is at its peak value. It is assumed that the current and electric field vary with time as given in § 3 so as to maintain a pressure balance always.

Then,
$$\mathscr{E} = \int_0^{\tau_\eta} V\mathscr{I}\, dt \qquad \ldots\ldots (52)$$

where τ_η is given by equation (19), and V is the total voltage across the plasma, and is equivalent to zE, z being the length of the plasma column.

Using equations (2), (9) and (12) it can be seen that

$$\mathscr{E} = \frac{16kzN}{\mu\varkappa a^2} \int_{T_0}^{\eta^2 T_m} \frac{dT}{\phi - \psi T}$$

which by equation (14) becomes

$$\mathscr{E} = \frac{36\pi k^2}{\mu\varkappa\beta} z \ln\left(\frac{1}{1-\eta^2}\right) \qquad \ldots\ldots (53)$$

$$= 1{\cdot}1 \times 10^3 z \ln\left(\frac{1}{1-\eta^2}\right)$$

η being defined as

$$\eta = \frac{\mathscr{I}_p}{\mathscr{I}_m} = \frac{\mathscr{I}_p}{1{\cdot}2 \times 10^6} \qquad \ldots\ldots (54)$$

or
$$\eta = \frac{T_p^2}{T_m^2} \quad \text{(see § 3).} \qquad \ldots\ldots (55)$$

Thus, from equation (53) it can be seen that the energy per unit length of discharge determines the fraction η or the peak current obtained. Depending on the line density N used, this also fixes the peak temperature acquired in this idealized model.

The equations which relate the circuit parameters, $\mathscr{E}$, $\mathscr{I}_p$, τ_p to the plasma parameters, a, z, N and T_p are (15), (19), (53) using (54) and (55). They are summarized below in a suitable form.

$$NT_p = \sqrt{\eta} \times 2{\cdot}65 \times 10^{27}$$

$$\tau_\eta = 5{\cdot}2 \times 10^{-10} \frac{a^2 T_p^{3/2}}{\eta^{3/4}} \left[\frac{1}{2} \ln \left(\frac{1+\eta}{1-\eta} \right) - \eta \right]$$

$$\mathscr{E} = 1{\cdot}1 \times 10^5 z \ln \left(\frac{1}{1-\eta^2} \right)$$

where $\eta = 8{\cdot}3 \times 10^{-7} \mathscr{I}_p < 1$, $\mathscr{I}_p$ is the peak current in amps, T_p the peak temperature in °K, τ_η the time taken to reach peak temperature in seconds, $\mathscr{E}$ the energy in joules dissipated in the plasma in time τ_η, N the line density of ions or electrons per metre length, a the radius of plasma column in metres and z the length of plasma column in metres.

For example, if one has a condenser bank which can dissipate $\mathscr{E}$ joules in a time τ_η sec by which time the current has a peak value of $\mathscr{I}_p$ amp, then, by choosing a required peak temperature T_p, one can estimate from these equations the radius a and length z of the plasma column and its line density N.

Alternatively, if one requires a plasma of radius a, length z, line density N and peak temperature T_p, one can estimate the size and characteristics of the energy source.

Acknowledgments

The author would like to thank Dr. Latham and members of the High Temperature Physics Group of Imperial College for encouragement and discussion on this work, which was done whilst in receipt of a maintenance grant from the Department of Scientific and Industrial Research.

References

Bennett, W. H., 1934, *Phys. Rev.*, **45**, 890.

Dreicer, H., 1958, *Proceedings of the Second International Conference on the Peaceful Uses of Atomic Energy*, **31**, 57 (Geneva: United Nations).

Haines, M. G., 1959, *Proc. Phys. Soc.*, **74**, 576.

—— 1960, *Ibid.*, in the press.

Pease, R. S., 1957, *Proc. Phys. Soc.* B, **70**, 11.

Spitzer, L., 1956, *Physics of Fully Ionized Gases* (New York : Interscience Publishers.)

Field Dependent Electron Mobility in Ionic Crystals

By J. F. BARNES and R. H. TREDGOLD
Physics Department, University College of North Wales, Bangor

MS. received 26th February 1960, in final form 17th March 1960

Abstract. The Boltzmann equation for electronic conduction in an ionic crystal is set up and an approximate solution is obtained through terms in the cube of the field. Explicit results are obtained for values of $h\omega_0$ of $2kT$ and $\frac{1}{2}kT$ where ω_0 is the angular frequency of longitudinal optical modes. It is shown that for fields less than the known breakdown fields the mobility decreases with increasing field. The non-ohmic effects will always be negligible for fields less than 10^5 v cm^{-1}.

§ 1. Introduction

Ionic crystals divide themselves roughly into two groups in so far as their electronic conductivity is concerned.

The first group includes PbS, PbSe and PbTe and its members behave in many ways like conventional covalent semiconductors. The intrinsic energy gap is much less than 1 ev and thus at ordinary temperatures the conductivity is quite high and it may be necessary to use Fermi Dirac statistics in discussing the behaviour of the electrons in the conduction band.

The second group includes many materials used as dielectrics, such as Al_2O_3 and $BaTiO_3$, such technically important materials as CdS, and also the alkali halides. In this group the apparent energy gap is much more than 1 ev and an observable electronic current can only be obtained by the application of a field which is, in any case, greater than 10^3 v cm^{-1}, and in some cases may need to be much greater. The conductivity observed in this group usually departs considerably from a simple ohmic behaviour. The extreme example of non-ohmic behaviour is, of course, the rapid increase of current with applied field which immediately precedes dielectric breakdown.

In order to understand the non-ohmic behaviour of these materials, one must attempt to disentangle trapping, space charge and field emission effects on the one hand, from a genuine field dependence of mobility on the other hand. In this paper we study the field dependence of mobility of electrons in a simple model for an ionic crystal. The study can be considered as complementary to the work of Howarth and Sondheimer (1953). They studied the low field behaviour of ionic materials in which degeneracy must be taken into account. We treat the case in which degeneracy may be ignored but in which the mobility starts to become field dependent. We assume that the fields under consideration will not be enough to have a serious influence on the electronic effective mass and thus any non-ohmic term will arise via the field dependence of the scattering of the electron by the ionic vibrations. The results obtained can only be semi-quantitative in nature as, in the interest of simplicity we make two important

simplifications: (i) the polaron effect is ignored (Fröhlich 1954, Allcock 1956); (ii) it is assumed that the effective mass of the electron is the free mass. We feel that the major error is likely to arise through approximation (ii) and a separate study of effective mass in NaCl is being carried out as a check on these assumptions.

§ 2. Interaction between a Conduction Electron and the Lattice Vibrations

We consider one electron in the conduction band interacting with the vibrating ions. The electron will suffer collisions with the vibrating ions, and will either gain or lose energy in the process. It may be shown (Fröhlich 1937, Howarth and Sondheimer 1953) that the longitudinal 'optical' modes are by far the most effective in scattering electrons and we will thus only consider these.

We treat the crystal as a continuous medium, with the masses and charges of each type of ion uniformly distributed throughout the crystal. In the linear approximation, all the longitudinal 'optical' modes will have approximately the same angular frequency ω_0, given by

$$\omega_0^2 = \frac{4\pi n_+ e^2}{M} \qquad \ldots\ldots(1)$$

where n_+ is the density of positive ions in the crystal and

$$\frac{1}{M} = \frac{1}{M^+} + \frac{1}{M^-} \qquad \ldots\ldots(2)$$

where M^+ and M^- are the masses of the positive and negative ions respectively. This result follows if the Coulomb forces predominate as compared with the nearest neighbour forces, and we can then treat the system as a plasma (Tonks and Langmuir 1929).

In order to determine the collision probability between an electron and a phonon we need to write down the complete Hamiltonian of the system

$$H = H_{\mathrm{el}} + H_{\mathrm{osc}} + H_{\mathrm{int}}. \qquad \ldots\ldots(3)$$

H_{el} is the Hamiltonian of the electron

$$H_{\mathrm{el}} = \frac{\hbar^2 \mathbf{k}^2}{2m} \qquad \ldots\ldots(4)$$

where $\mathbf{k}$ is the wave vector, and m is the mass of the electron. H_{osc} is the sum of the Hamiltonians of all the oscillators

$$H_{\mathrm{osc}} = \frac{\omega_0^2 M}{2} \sum_{\mathbf{K}} \left[-\frac{\hbar^2}{\omega_0^2 M} \left(\frac{\partial^2}{\partial q_{\mathrm{c}}^2} + \frac{\partial^2}{\partial q_{\mathrm{s}}^2} \right) + q_{\mathrm{c}}^2 + q_{\mathrm{s}}^2 \right] \qquad \ldots\ldots(5)$$

the sum is taken over a hemisphere in $\mathbf{K}$ space, and q_{c} and q_{s} are cosine and sine normal mode coordinates.

As in the Debye model of specific heats, we assume that the wave number $\mathbf{K}$ has all values up to a 'cut-off' value $\mathbf{K}_{\max}$ chosen so that the number of normal modes corresponds to the number of positive ions in the crystal.

H_{int} is the interaction Hamiltonian between the electron and the lattice vibrations

$$H_{\mathrm{int}} = -e \left(\frac{8\pi M}{V} \right)^{1/2} \omega_0 \sum_{\mathbf{K}} \left[-\frac{q_{\mathrm{s}}}{K} \cos \mathbf{K} \cdot \mathbf{r} + \frac{q_{\mathrm{c}}}{K} \sin \mathbf{K} \cdot \mathbf{r} \right] \qquad \ldots\ldots(6)$$

where V is the volume of the crystal.

H_{el} and H_{osc} lead to wave functions for the electron and the lattice vibrations. We assume that if H_{int} is treated as a perturbation we will obtain collision probabilities which are at least of the right order of magnitude and qualitatively of the correct form.

The total energy U of the system in the absence of H_{int} is

$$U = \sum_{\mathbf{K}} (n(\mathbf{K}) + \tfrac{1}{2})\hbar\omega_0 + \frac{\hbar^2\mathbf{k}^2}{2m} \qquad \ldots\ldots(7)$$

where $n(\mathbf{K})$ are the quantum numbers of the lattice oscillators.

The probability per second W that the electron will make a transition from the state $\mathbf{k}$ to the state $\mathbf{k}'$, coupled with a transition of the oscillator from n to n' may now be calculated using perturbation theory.

For the case of emission of energy by the electron, the probability is only non-zero when

$$\mathbf{k}' = \mathbf{k} - \mathbf{K} \qquad \ldots\ldots(8)$$

$$W(\mathbf{k}, \mathbf{k} - \mathbf{K}) = \frac{8\pi(N+1)\omega_0 e^2}{V\hbar K^2} \frac{\partial}{\partial t}\left(\frac{\sin^2 \xi t}{\xi^2}\right) \qquad \ldots\ldots(9)$$

where

$$\hbar\xi = E_{\mathbf{k}'} - E_{\mathbf{k}} + \hbar\omega_0. \qquad \ldots\ldots(10)$$

For the case of absorption of energy by the electron, the probability is only non-zero when

$$\mathbf{k}' = \mathbf{k} + \mathbf{K} \qquad \ldots\ldots(11)$$

$$W(\mathbf{k}, \mathbf{k}+\mathbf{K}) = \frac{8\pi N\omega_0 e^2}{V\hbar K^2} \frac{\partial}{\partial t}\left(\frac{\sin^2 \xi t}{\xi^2}\right) \qquad \ldots\ldots(12)$$

where

$$\hbar\xi = E_{\mathbf{k}'} - E_{\mathbf{k}} - \hbar\omega_0. \qquad \ldots\ldots(13)$$

Here N is the statistical mean of the quantum number n of a lattice oscillator and is given by

$$N = \frac{1}{\exp(\hbar\omega_0/kT) - 1}. \qquad \ldots\ldots(14)$$

Hence the probabilities per second are only large when $\xi = 0$, i.e. conservation of energy, and only those transitions are possible in which momentum is conserved ((8) and (11)).

We have now to determine the distribution $F(\mathbf{k})$ of electrons in $\mathbf{k}$ space when a field is applied along the z axis of the crystal.

The distribution of electrons must satisfy Boltzmann's equation

$$-\frac{eE}{\hbar}\frac{\partial F(\mathbf{k})}{\partial k_z} = b - a. \qquad \ldots\ldots(15)$$

The left-hand term gives the rate at which electrons are accelerated out of the state $\mathbf{k}$ by the applied field E.

a is the rate at which electrons are scattered out of the state $\mathbf{k}$ by collision with lattice waves:

$$a = F(\mathbf{k})\frac{V}{8\pi^3}\left[\int W(\mathbf{k}, \mathbf{k}+\mathbf{K})d^3\mathbf{K} + \int W(\mathbf{k}, \mathbf{k}-\mathbf{K})d^3\mathbf{K}\right]. \qquad \ldots\ldots(16)$$

b is the rate at which electrons are scattered into the state $\mathbf{k}$ by collision with lattice waves:

$$b = \frac{V}{8\pi^3}\int\left[W(\mathbf{k}-\mathbf{K},\,\mathbf{k})F(\mathbf{k}-\mathbf{K}) + W(\mathbf{k}+\mathbf{K},\,\mathbf{k})F(\mathbf{k}+\mathbf{K})\right]d^3\mathbf{K}. \quad \ldots\ldots(17)$$

As there are only a few electrons in the conduction band, the exclusion principle may be ignored, and in the case where there is no applied field acting on the crystal, it is obvious that the electron distribution is a Maxwell–Boltzmann distribution

$$\text{i.e.} \quad F(\mathbf{k}) = A\exp\left(-\hbar^2\mathbf{k}^2/2mkT\right) \quad \ldots\ldots(18)$$

where A is a constant.

§ 3. Determination of the Distribution Function

As the distribution function is a Maxwell–Boltzmann function in the case of no applied field, we will assume, that when there is an applied field the distribution will be a modified form of Maxwell–Boltzmann function displaced in the k_z direction

$$F(\mathbf{k}) = \exp\left(-\alpha^2(\mathbf{k}-\mathbf{k}_0)^2\right) \quad \ldots\ldots(19)$$

where $\alpha^2 = \hbar^2/2mkT$ and $\mathbf{k}_0$ is in the k_z direction. The integration for a is easily performed, but in the case of b it is necessary to expand $F(\mathbf{k})$ in ascending powers of k_0, and terms up to ${k_0}^3$ are retained in our approximation. Thus we obtain

$$\begin{aligned}
b-a &= N\beta\exp\left(-\alpha^2(k^2+{k_0}^2)\right)\left\{\left[2\alpha^2k_0\cos\theta + 2\alpha^6{k_0}^3\left(k^2+\frac{2m\omega_0}{\hbar}\right)\sin^2\theta\cos\theta\right]\right.\\
&\quad\times\left[\tfrac{1}{2}k(2+\lambda)I_1 - 2\pi(1+\lambda)^{1/2}\right]\\
&+\alpha^4{k_0}^2\left[(3\cos^2\theta-1)\left(\frac{k^2}{4}(2+\lambda)^2I_1 - \pi k(1+\lambda)^{1/2}(2+\lambda)\right) + \left(k^2+\frac{2m\omega_0}{\hbar}\right)I_1\sin^2\theta\right]\\
&\left.+\tfrac{2}{3}\alpha^6{k_0}^3(5\cos^3\theta-3\cos\theta)\left[\frac{k^3}{8}(2+\lambda)^3I_1 - \frac{\pi k^2}{6}(1+\lambda)^{1/2}(4+\lambda)(4+3\lambda)\right]\right\}\\
&+(N+1)\beta\exp\left(-\alpha^2(k^2+{k_0}^2)\right)\left\{\left[2\alpha^2k_0\cos\theta + 2\alpha^6{k_0}^3\left(k^2-\frac{2m\omega_0}{\hbar}\right)\sin^2\theta\cos\theta\right]\right.\\
&\quad\times\left[\tfrac{1}{2}k(2-\lambda)I_2 - 2\pi(1-\lambda)^{1/2}\right]\\
&+\alpha^4{k_0}^2\left[(3\cos^2\theta-1)\left(\frac{k^2}{4}(2-\lambda)^2I_2 - \pi k(1-\lambda)^{1/2}(2-\lambda)\right) + \left(k^2-\frac{2m\omega_0}{\hbar}\right)I_2\sin^2\theta\right]\\
&\left.+\tfrac{2}{3}\alpha^6{k_0}^3(5\cos^3\theta-3\cos\theta)\left[\frac{k^3}{8}(2-\lambda)^3I_2 - \frac{\pi k^2}{6}(1-\lambda)^{1/2}(4-\lambda)(4-3\lambda)\right]\right\}
\end{aligned} \quad \ldots\ldots(20)$$

where

$$\beta = \frac{\omega_0 e^2 m}{2\pi\hbar^2} \quad \ldots\ldots(21)$$

$$\lambda = \frac{2m\omega_0}{\hbar k^2} \quad \ldots\ldots(22)$$

$$I_1 = \frac{2\pi}{k}\log\left|\frac{1+(1+\lambda)^{1/2}}{1-(1+\lambda)^{1/2}}\right| \quad \ldots\ldots(23)$$

$$I_2 = \frac{2\pi}{k}\log\left|\frac{1+(1-\lambda)^{1/2}}{1-(1-\lambda)^{1/2}}\right| \quad \ldots\ldots(24)$$

θ is the angle between $\mathbf{k}$ and the k_z direction. We now proceed to choose k_0 such

that $F(\mathbf{k})$ is the best solution to (20), chosen in the sense of least squares. We thus obtain

$$\frac{\partial}{\partial k_0}\int\left[\frac{eE}{\hbar}\frac{\partial F(\mathbf{k})}{\partial k_z}+b-a\right]^2 d^3k=0 \qquad \ldots\ldots(25)$$

as an equation in k_0.

In order to obtain an explicit form for (25) it is necessary to evaluate a number of definite integrals, only a few of which can be obtained in terms of known functions. The remainder (25 in all) have been evaluated numerically for values of the parameter $\hbar\omega_0/kT$ of 2 and $\frac{1}{2}$. In the former case, we obtain

$$-3{\cdot}9\,\beta\frac{eE}{\hbar}+5{\cdot}8p\beta^2k_0+40p^2\beta\frac{eE}{\hbar}k_0^2=0 \qquad \ldots\ldots(26)$$

and in the latter

$$-15{\cdot}8\beta\frac{eE}{\hbar}+282p\beta^2k_0+23{\cdot}2p^2\beta\frac{eE}{\hbar}k_0^2=0. \qquad \ldots\ldots(27)$$

Here $p=(\hbar/2m\omega_0)^{1/2}$. We thus find that

$$k_0=\frac{5{\cdot}8\beta}{80peE/\hbar}\left[\left(1+18{\cdot}5\frac{e^2E^2}{\beta^2\hbar^2}\right)^{1/2}-1\right]$$
$$=0{\cdot}67\frac{eE}{p\beta\hbar}\left[1-4{\cdot}6\frac{e^2E^2}{\beta^2\hbar^2}\ \ldots\right] \qquad \ldots\ldots(28)$$

corresponding to (26), and

$$k_0=\frac{6{\cdot}13}{peE/\hbar}\left[\left(1-\frac{1}{54{\cdot}2}\frac{e^2E^2}{\beta^2\hbar^2}\right)^{1/2}-1\right]$$
$$=0{\cdot}056\frac{eE}{p\beta\hbar}\left[1-\frac{1}{217}\frac{e^2E^2}{\beta^2\hbar^2}\ \ldots\right] \qquad \ldots\ldots(29)$$

corresponding to (27).

§ 4. Discussion

Since the above calculation depends on choosing an $F(\mathbf{k})$ of the same shape as that corresponding to zero field, and since we have been obliged to expand

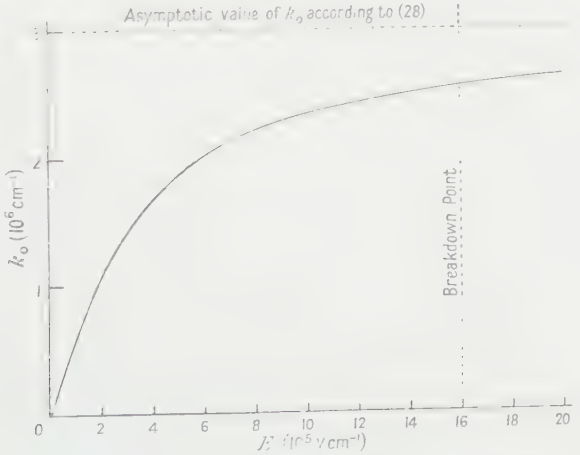

Variation of k_0 with field for NaCl with $\hbar\omega_0=2kT$.

$F(\mathbf{k})$ through the third power of k_0 only, it is unlikely that our results (28), (29) will be valid for very large values of E. In the figure we show k_0, (which is

proportional to the current) as a function of field. For $\hbar\omega_0 = 2kT$ (which is about correct for the alkali halides at 200°K) the conductivity is still decreasing with field at the breakdown point.

Now qualitative considerations based on the scattering mechanism studied here, lead one to suppose that the 'plasma boundary' connected with dielectric breakdown in von Hippel's theory (1940) should correspond to the condition

$$\frac{\hbar^2 k_0^2}{2m} = \hbar\omega_0 \qquad \ldots\ldots (30)$$

and it is evident that breakdown actually occurs with k_0 very much less than the value given by equation (30). Now supposing the approximations used here are valid, it is evident that the 'plasma boundary' has nothing to do with dielectric breakdown.

It may also be deduced from the above results that the mobility must be sensibly independent of field for fields less than 10^5 V cm^{-1} for any realistic values of kT and $\hbar\omega_0$. For low fields and $\hbar\omega_0 = 2kT$ we find the mobility $\mu = 6{\cdot}8$ cm^2 V^{-1} sec^{-1}. This result may be compared with that given by the approximation of Howarth and Sondheimer, namely $\mu = 4{\cdot}0$ cm^2 V^{-1} sec^{-1}.

Acknowledgment

One of us (J. F. B.) wishes to acknowledge the financial assistance given by the Department of Scientific and Industrial Research.

References

Allcock, G. R., 1956, *Advanc. Phys.*, **5**, 412.
Fröhlich, H., 1937, *Proc. Roy. Soc.* A, **160**, 230.
—— 1954, *Advanc. Phys.*, **3**, 325.
von Hippel, A., 1940, *J. Chem. Phys.*, **8**, 605.
Howarth, D. J., and Sondheimer, E. H., 1953, *Proc. Roy. Soc.* A, **219**, 53.
Tonks, L., and Langmuir, I., 1929, *Phys. Rev.*, **33**, 195.

Calculations on Ionic Character and Hybridization from Dipole Moments for AsF_3 and $AsCl_3$

By J. SOBHANADRI
Physics Department, Andhra University, Waltair, India

Communicated by D. Premaswarup; MS. received 30th December 1959, in final form 22nd March 1960

Abstract. From theoretical calculations carried out for the two trihalides AsF_3 and $AsCl_3$ using the molecular orbital method, estimates of hybridization and ionic character in the bond orbital have been obtained using the observed values of the dipole moments. These are compared with corresponding data from quadrupole coupling constants.

§ 1. Introduction

In continuation of the work in this laboratory by Narasimha Rao (1957, 1959) dealing with calculations on dipole moments using wave mechanical methods, the present work is undertaken on the trihalides, AsF_3 and $AsCl_3$; the observed dipole moments for the molecules are used to obtain estimates of the respective hybridization and ionic character parameters. The important previous work on the subject was mentioned in the references above. The method adopted for the present calculations is that developed by Pople (1950) and Duncan and Pople (1953) based on the molecular orbital theory.

The halides of group V elements seem to offer an advantage in calculations of this nature. Studying the variation of the ratio of the observed dipole moment of these molecules to the product of the electro-negativity difference and inter-nuclear distance, Kisliuk (1954) has found the ratio to be constant for each group V nucleus and increasing steadily from the lighter to the heavier ones. This suggests, as he has remarked, that the dipole moments can be explained in terms of the hybridization of the bonding orbitals rather than in terms of the relative size of the atoms, the polarization of the core electrons etc.

The molecule AsF_3 is particularly chosen since its quadrupole coupling data unambiguously indicate the presence of sp-hybridization only. This inference was drawn by Dailey (1953) from a consideration of the sign and the large magnitude of the coupling constant of arsenic in AsF_3. He points out that this large coupling constant definitely indicates that the bonding orbitals are not pure p-orbitals, but some sort of hybrid orbitals. If the hybrid bonds are considered as constructed from a set of p-orbitals and directed along the molecular axis, then a defect of electrons might be expected along that direction. If, however, these are constructed using s-orbitals of the valence shell, the two non-bonding electrons of the valence shell would be promoted to the hybrid orbital which would not be true if any other (say d or f) orbital were to be used for hybridization. An excess of p electrons therefore results along the molecular axis since the non-bonding orbital contains two electrons while the bonding orbital on the average

contains only one, and this excess is evident from the sign of the coupling constant. A similar feature may be expected in $AsCl_3$, its quadrupole coupling constant (Kisliuk and Townes 1951) being similar in sign and magnitude. Further, in these molecules hybridization occurs on the apical atom alone and not on the halogen since, as a general rule, the dipole moment would tend to sustain hybridization on the positive atom and to quench it on the negative atom (Gordy 1955). That the apical atom alone is concerned was also pointed out by Kisliuk in his interpretation of the nature of the chemical bond in group V trihalides from microwave spectroscopic measurements.

§ 2. Calculations on AsF_3

The electron configurations of the arsenic atom in its ground state is represented as $1s^2 2s^2 2p^6 3s^2 3p^6 3d^{10} 4s^2 4p^3$, while for the fluorine atom it is written as $1s^2 2s^2 2p^5$, and the As–F bond is regarded as arising from the pairing of $As(4p)_\sigma$ and $F(2p)_\sigma$ orbitals. The atomic orbital approximation of perfect pairing of electron spins is assumed, so that the bonds are treated as localized. The bonding orbital of arsenic is assumed to be a mixture of s- and p-orbitals. The wave functions for the bonding and non-bonding orbitals are written approximately as linear combinations of atomic orbitals, as in the case of NH_3; the non-bonding orbital being directed along the molecular symmetry axis. The three equivalent bond orbitals are

$$\psi_{b1} = \lambda\{\cos\epsilon_b\,\phi(\mathrm{As}, 4s) + \sin\epsilon_b\,\phi(\mathrm{As}, 4p_{b1})\} + \mu\,\phi(\mathrm{F}_1, 2p)$$
$$\psi_{b2} = \lambda\{\cos\epsilon_b\,\phi(\mathrm{As}, 4s) + \sin\epsilon_b\,\phi(\mathrm{As}, 4p_{b2})\} + \mu\,\phi(\mathrm{F}_2, 2p)$$
$$\psi_{b3} = \lambda\{\cos\epsilon_b\,\phi(\mathrm{As}, 4s) + \sin\epsilon_b\,\phi(\mathrm{As}, 4p_{b3})\} + \mu\,\phi(\mathrm{F}_3, 2p)$$

where $\cos\epsilon_b$ and $\sin\epsilon_b$ are hybridization parameters, while λ and μ are ionic character parameters. $4p_{b1}, 4p_{b2}, 4p_{b3}$ are the $4p_\sigma$ atomic orbitals of the As atom directed along the three bond directions. $(F_1, 2p)$, $(F_2, 2p)$, $(F_3, 2p)$ are the $2p_\sigma$ orbitals of the three F atoms.

The wave function for the lone-pair orbital is written as

$$\psi_L = \cos\epsilon_L\,\phi(\mathrm{As}, 4s) + \sin\epsilon_L\,\phi(\mathrm{As}, 4p_L)$$

$4p_L$ being the $4p_\sigma$ atomic orbital of the arsenic atom directed along the symmetry axis.

The unknown parameters in the equations are evaluated by making use of the orthogonality conditions between the bonding orbitals and the bond and lone-pair orbitals as was done by Duncan and Pople for NH_3. The individual values of λ and μ are obtained from the normalization condition for ψ_b, when λ/μ is known from the orthogonality condition. The orthogonality conditions give

$$\lambda^2(\cos^2\epsilon_b + \sin^2\epsilon_b\cos\alpha) + 2\lambda\mu(S_1\cos\epsilon_b + S_2\sin\epsilon_b\cos\alpha) + \mu^2 S_3 = 0$$

and

$$\frac{\lambda}{\mu} = -\frac{(\cos\epsilon_L S_1 + \sin\epsilon_L\cos\gamma\, S_2)}{\cos\epsilon_b\cos\epsilon_L + \sin\epsilon_b\sin\epsilon_L\cos\gamma}$$

in which α is bond angle and γ is the angle between a bond and the lone-pair direction; S_1, S_2, S_3 are the three overlap integrals defined as

$$S_1 = \int \phi(\mathrm{As}, 4s)\phi(\mathrm{F}, 2p)\,d\tau$$
$$S_2 = \int \phi(\mathrm{As}, 4p)\phi(\mathrm{F}, 2p)\,d\tau$$
$$S_3 = \int \phi(\mathrm{F}_1, 2p)\phi(\mathrm{F}_2, 2p)\,d\tau.$$

The normalization condition for the bonding orbital gives

$$\lambda^2 + 2\lambda\mu(S_1 \cos\epsilon_b + S_2 \sin\epsilon_b) + \mu^2 = 1.$$

If we locate the origin of the coordinate system at the As atom, the dipole moment due to the bonding electrons is given as $m_b = 2e(\xi - d/2)$ where ξ is the coordinate of the centre of negative charge and may be obtained from

$$\xi = \int \psi_{b_1}^2 \xi \, d\tau \Big/ \int \psi_{b_1}^2 \, d\tau$$

and d is the internuclear distance. The contribution of the bonding electrons to the total moment is $M_b = 3\, m_b \cos\gamma$. The dipole moment contribution of the non-bonding electrons is $M_L = -2e\, \bar{\xi}_L$ in which $\bar{\xi}_L$ is obtained from

$$\bar{\xi}_L = \int \psi_L^2 \xi_L \, d\tau \Big/ \int \psi_L^2 \, d\tau.$$

However, since the wave functions are normalized, $\int \psi_{b_1}^2 \, d\tau = 1$ and $\int \psi_L^2 \, d\tau = 1$. The total moment M is equal to $M_b + M_L$, the sum of the contributions of the bonds and of the single-pair.

The necessary integrals are evaluated by taking a value of 1·712 Å for the internuclear distance and 102° for the bond angle from microwave measurements (Kisliuk and Geschwind 1953). The atomic wave functions used are hydrogen-like and values of the effective nuclear charge are adopted from Pauling and Sherman (1932). These are $Z_p = 7{\cdot}72$, $Z_s = 10{\cdot}14$ for the As atom and $Z_p = 4{\cdot}84$ for the F atom.

Table 1

λ/μ	λ	μ	$\cos\epsilon_b$	$\cos\epsilon_L$	M_b	M_L	M
∞	1	0	0·415	0·696	−3·312	−6·714	−10·026
1·00	0·6801	0·6801	0·400	0·694	+3·637	−6·709	−3·072
0·60	0·4971	0·8284	0·388	0·691	+6·764	−6·706	+0·058
0·40	0·3616	0·9038	0·379	0·688	+8·594	−6·704	+1·890
0·36	0·3342	0·9283	0·372	0·684	+9·514	−6·703	+2·811
0·30	0·2816	0·9410	0·369	0·681	+9·922	−6·702	+3·220

The results of the calculations are given in table 1. By suitably varying the values of λ and μ, different values are obtained for the hybridization parameters and the dipole moments. The experimental value of the dipole moment for AsF_3 as obtained from microwave measurements by Shulman, Dailey and Townes (1950) is 2·815 Debye units. This value, it may be observed from the above table, is derived when λ/μ, which is a measure of the polarity of the bond orbital, is equal to 0·36. The corresponding value of $\cos\epsilon_b$ is 0·372 which amounts to about 14% for the s-character. The contribution of the non-bonding electrons (given by M_L) to the total dipole moments is considerable and is almost independent of the polarity of the bond orbital. The same feature was observed in the case of NH_3 by Duncan and Pople (1953).

The amount of hybridization deduced above may be expected in view of the large value of the coupling constant for As in this molecule (−235 Mc/s). From a study of the quadrupole coupling constant, Dailey assigned 15% s-hybridization agreeing very closely with the value derived from the dipole moment in this

investigation. It may be of interest to note that the value of s-hybridization derived from the bond angle (s-character $= \cos\alpha/(\cos\alpha - 1)$ (Townes and Schawlow 1955, p. 238)) comes to about 17% which is in fair agreement with the above values. Gordy's estimate (Gordy, Smith and Trambarulo 1953) of 8% for the s-character may perhaps be low, in view of the 9% s-character for the As bond orbital in AsH_3 which has a much lower coupling constant than AsF_3.

The ionic character (equal to $\mu^2 - \lambda^2$) of As–F bond derived in this investigation is about 70%. This value is consistent with the large electro-negativity difference between the As and F atoms (2·0). Pauling's graph (Pauling 1940) of ionic character plotted against electro-negativity difference indicates about 60% while the revised estimate of Townes and Dailey (1950) gives somewhat more ionic character for AsF_3.

§ 3. Calculations on $AsCl_3$

Similar calculations are carried out for $AsCl_3$. Values of 2·161 Å for the bond length and 98°25′ for the bond angle are adopted from microwave data (Kisliuk and Townes 1950), and an effective nuclear charge of 7·42 is taken for the Cl atom. The results are shown in table 2.

Table 2

λ/μ	λ	μ	$\cos\epsilon_b$	$\cos\epsilon_L$	M_b	M_L	M
∞	1	0	0·357	0·785	−5·757	−6·682	−12·439
1·00	0·6070	0·6070	0·310	0·780	+4·354	−6·680	−2·326
0·90	0·5794	0·6439	0·296	0·779	+5·503	−6·677	−1·174
0·80	0·5429	0·6785	0·292	0·776	+6·723	−6·676	+0·047
0·68	0·4987	0·7214	0·279	0·770	+8·641	−6·671	+1·970
0·60	0·4521	0·7535	0·274	0·768	+9·763	−6·670	+3·093

The observed value (Townes and Schawlow 1955, p. 614) of 1·97 Debye units is obtained when λ/μ is equal to 0·68 and $\cos\epsilon_b$ is equal to 0·279. This amounts to about 8% s-character for the bonding orbital which is in agreement with the value of 10% assigned by Townes and Schawlow (1955, p. 242) from the quadrupole coupling constant, while the Cl–As–Cl bond angle yields about 12–13%. A lower value of the s-character for $AsCl_3$ than for AsF_3 may be expected because of the lower coupling in $AsCl_3$.

The ionic character for the As–Cl bond comes to about 28% which is consistent with the value of 22 to 25% expected from the Pauling graph, the electro-negativity difference between the two atoms being 1·0. The S-shaped curve of Townes and Dailey (1955) however indicates a larger value, about 40%, for the ionic character.

§ 4. Conclusions

The molecular orbital theory calculations carried out for the two molecules $AsCl_3$ and AsF_3 indicate that the non-bonding electrons make a substantial contribution to the total dipole moment. The estimates of ionic character and hybridization obtained in this investigation are consistent with approximate deductions from other data and may be considered fairly reliable as full orthogonality conditions have been used in this derivation. $AsCl_3$ indicates less

s-character in the bonding orbitals than AsF_3. It should be pointed out also that in the present calculations the effect of inner core electrons has been neglected for reasons stated earlier and also elsewhere (Narasimha Rao 1959).

In the above calculations, hydrogen-like wave functions are used. In order to see how far these results may be sensitive to the choice of the wave functions, calculations are also carried out for one molecule AsF_3 using Slater type functions. For $n=4$, the Slater function involves fractional powers, and the computation of the overlap integrals in this case cannot be simply evaluated. For this reason Craig *et al.* (1954) corrected the fraction to the nearest integer and then evaluated the integrals, while Jaffe and Doak (1954) obtained the integral values as averages of the corresponding overlap integrals for $n=3$ and $n=5$. The author has adopted this latter method for evaluating the integrals for AsF_3.

The results are given in table 3.

Table 3

λ/μ	λ	μ	$\cos\epsilon_b$	$\cos\epsilon_L$	M_b	M_L	M
∞	1	0	0·415	0·696	−4·252	−6·634	−10·886
1·00	0·6359	0·6359	0·380	0·691	+2·962	−6·630	−3·668
0·80	0·5633	0·7042	0·372	0·689	+4·324	−6·626	−2·302
0·60	0·4684	0·7805	0·359	0·685	+5·962	−6·622	−0·660
0·40	0·3446	0·8616	0·338	0·679	+7·785	−6·618	+1·167
0·23	0·2135	0·9283	0·329	0·650	+9·366	−6·547	+2·819
0·20	0·1879	0·9396	0·344	0·643	+9·616	−6·536	+3·080

The value of $\cos\epsilon_b = 0{\cdot}329$ corresponds to about 11% s-character, slightly lower than the 14% obtained previously, while the amount of ionic character in the As–F bond, given as $\mu^2-\lambda^2$, is observed to be 80% which is slightly higher than the 70% derived from table 1. The qualitative features, however, have not altered. This feature was pointed out by Schatz (1954) from calculations on HCl using Slater type, hydrogen-like, and modified hydrogen-like wave functions.

Acknowledgments

The author is deeply indebted to Professor K. R. Rao for his invaluable guidance throughout the progress of the work. His grateful thanks are also due to the Government of India for the award of a Senior Research Scholarship. He is grateful to Dr. D. Premaswarup for many helpful suggestions.

References

Craig, D. P., *et al.*, 1954, *J. Chem. Soc.*, 354.
Dailey, B. P., 1953, *J. Phys. Chem.*, **57**, 490.
Duncan, A. B. F., and Pople, J. A., 1953, *Trans. Faraday Soc.*, **49**, 217.
Gordy, W., 1955, *Disc. Faraday Soc.*, **19**, 14.
Gordy, W., Smith, W. V., and Trambarulo, R. F., 1953, *Microwave Spectroscopy* (New York: John Wiley).
Jaffe, H. H., and Doak, G. O., 1954, *J. Chem. Phys.*, **22**, 196.
Kisliuk, P., 1954, *J. Chem. Phys.*, **22**, 86.
Kisliuk, P., and Geschwind, S., 1953, *J. Chem. Phys.*, **21**, 828.
Kisliuk, P., and Townes, C. H., 1950, *J. Chem. Phys.*, **18**, 1109.
—— 1951, *Phys. Rev.*, **83**, 210A.

Pauling, L., 1940, *The Nature of Chemical Bond* (London: Oxford University Press).
Pauling, L., and Sherman, J., 1932, *Z. Krist.*, **81,** 1.
Pople, J. A., 1950, *Proc. Roy. Soc.* A, **202,** 323.
Rao, D. V. G. L. Narasimha, 1957, *Trans. Faraday Soc.*, **53,** 1160.
—— 1959, *Ibid.*, **58,** 19.
Schatz, P. N., 1954, *J. Chem. Phys.*, **22,** 695.
Shulman, R. G., Dailey, B. P., and Townes, C. H., 1950, *Phys. Rev.*, **78,** 145.
Townes, C. H., and Dailey, B. P., 1950, *Phys. Rev.*, **78,** 346A.
—— 1955, *J. Chem. Phys.*, **23,** 118.
Townes, C. H., and Schawlow, A. L., 1955, *Microwave Spectroscopy* (New York, London: McGraw-Hill).

Internal Ferromagnetic Resonance and Magnetostatic Modes in Nickel–Iron Alloys

By J. C. ANDERSON†
University of Witwatersrand, Johannesburg

MS. received 17*th February* 1960, *in final form* 4*th March* 1960

Abstract. Experiments are described in which colloidal suspensions of nickel iron alloys in paraffin-wax have been prepared for the purpose of measuring, by internal ferromagnetic resonance, the total internal magneto-crystalline anisotropy field as a function of alloy composition. Determination of the internal resonance frequency is by measurement of the complex permeability of the particles over a range of frequencies. The variation of internal field with composition is found to be in agreement with previous qualitative observations by Anderson and Donovan employing a different technique and the total anisotropy is found to pass through a minimum in the region of 65% nickel. Values for the anisotropy constants K_1 and K_2 are calculated from the results and are compared with published values.

Multiple peaks in the permeability against frequency curves are interpreted as magnetostatic resonance modes of different order as predicted by Walker from theoretical considerations.

§ 1. Introduction

In an earlier paper (Anderson 1960, to be referred to as I) internal resonance measurements on small cobalt particles precipitated in a copper matrix were reported. It was shown that the value of the internal field which represents the magneto-crystalline anisotropy, determined from the variation with frequency of the complex permeability, was in good agreement with that calculated from anisotropy constants measured by static methods. This work is considered to validate the experimental method used to determine the anisotropy field, in which small particles of the ferromagnetic material are placed in a high frequency alternating field and their permeability measured as a function of frequency. The same method as was described in I has been used in the present work. This differs from the standard ferromagnetic resonance type of measurement described, for instance, by Reich (1956).

The internal field, calculated from the observed resonant frequency by simple spin-resonance theory, is found to fall rapidly from the value for pure nickel as iron is added, reaching a marked minimum at 65% nickel; thereafter the field increases again, but at a much slower rate. The results indicate that the total anisotropy energy of the specimens used never actually reaches zero in the alloy series.

§ 2. Experimental Details

2.1. *Preparation of Specimens*

The colloidal-sized particles were produced from an ingot of the desired composition by a 'breeding arc' in an atmosphere of dry hydrogen (see, for instance, Svedberg 1928 and Bagguley 1955).

† Now at Royal Holloway College, University of London, Englefield Green, Surrey.

A 10 kw induction heater was modified by replacing the normal work coil by two electrodes. The non-earthed side of the tank circuit feeding the normal work coil was connected to a copper tube, of $\frac{1}{8}$ in. diameter, through which the normal flow of cooling water was carried, the water circuit being completed by a length of rubber tube. This electrode was bent so that it fitted inside a 2 in. diameter Pyrex glass tube into which it was sealed by leading it through a cork. Through a cork at the other end of the glass tube was led a stainless steel tube which was coupled to the spindle of a light electric motor. The arrangement was such that the stainless steel electrode, which was earthed, rotated close to the cooled copper electrode.

The alloy was produced by melting a suitable mixture of carbonyl nickel and iron powders in a furnace through which dry hydrogen was streamed. The resulting ingots were rolled to strip of approximately $\frac{1}{4}$ in. width by $\frac{1}{32}$ in. thick. The strip was annealed at 1000°c for one hour, followed by furnace cooling for ten hours. Short lengths of it were wrapped round the two electrodes so that the high-frequency arc was struck between them.

Before starting the arc, the inside of the Pyrex tube was given a thin coating of paraffin wax so that particles flying out of the arc would adhere to the walls of the tube. It was found necessary to blow cold air over the tube whilst the arc was burning. A suitable concentration of alloy in the wax was obtained by running the arc for approximately half an hour.

The wax carrying the particles was removed from the tube by dismounting and warming it. To ensure the removal of the maximum amount of material the tube was washed through with molten wax.

Particles of all sizes, up to as much as 2 mm in diameter, are obtained from the arc. Some particles, generally the smallest, arise from condensation as droplets from metal vapour. Others are torn out of the electrodes explosively and are in the majority. To limit the range of particle sizes, and to eliminate larger particles, the melted wax was centrifuged at 3000 rev/min until it hardened. Photographs of typical particles are shown in figure 1 (Plate). The range of sizes obtained was from about 1 to approximately 25 microns in diameter, with a majority in the range 5 to 10 microns. Spherical particles were found to be relatively rare, indicating that the most important mechanism of production is that of explosive disruption of the electrodes. Many of the particles produced by the latter process show signs of cubic symmetry.

The specimen was formed as a rod of length approximately 4 cm and diameter 0·5 cm. A blank specimen was also produced which had the same dimensions and was composed of the same wax, but did not contain any metal particles.

2.2. *Measurement of Permeability*

The apparatus used has been briefly described in an earlier paper (Anderson and Donovan 1959). The full detail and theory has been given recently (Anderson 1960b).

A modified Foster–Seeley discriminator is used to measure the complex permeability of the test specimen. It is inserted in the test coils of the discriminator and the change in magnitude and phase of the secondary induced voltage is observed. The effects of the wax, and certain artifacts of the apparatus, are eliminated by taking similar measurements on the blank specimen. Frequencies

in the range 16 to 240 Mc s were used. Resonance is revealed by an increased absorption of power in the specimen, characterized by a peak in the curve of the imaginary part μ_2 of permeability plotted against frequency, and by a phase shift of the induced signal, characterized by a deviation in the curve for the real part μ_1 of permeability plotted against frequency.

§ 3. Results

3.1. *Complex Permeability and Resonance Frequencies*

In figure 2 are shown the real and imaginary parts of permeability plotted against frequency for the 90% Ni-10% Fe alloy. The dotted curve shows the results obtained for a specimen prepared from the wax as extracted from the

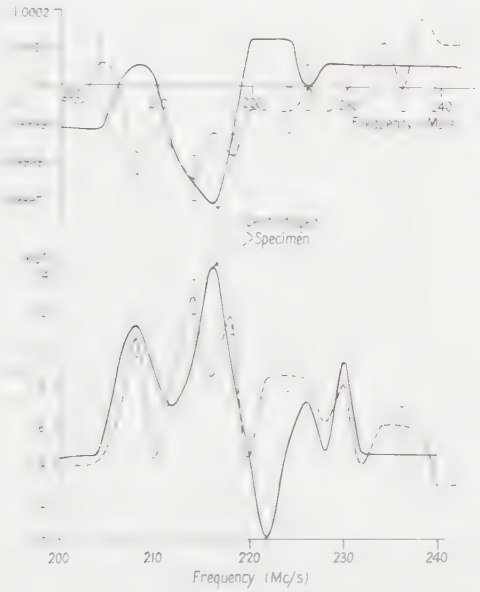

Figure 2. Complex permeability of 90% Ni–10% Fe alloy.

breeding arc The solid line shows the results obtained after centrifuging, when the multiple peaks appear to 'condense' into two main, double peaks. Multiple peaks were found in every case, as is exemplified by figure 3 showing the curve for the centrifuged 75% nickel specimen.

The larger of the first pair of peaks is taken as representing the resonance frequency, for reasons which will be discussed later. In figure 4 is shown the variation with composition of the resonance frequency for the colloidal specimens; this is compared with the curve obtained from a series of polycrystalline alloys examined by transmission line technique, described in an earlier paper (Anderson and Donovan 1957). No quantitative significance can be attached to the polycrystalline results.

It has been pointed out by Kittel (1946) that permeability has little but formal significance at high frequencies, so that the absolute magnitudes calculated for the real and imaginary parts of permeability can have little meaning attached to them. For this reason the accuracy with which they are determined is not

of interest. The measurement technique is aimed at the observation of variation of permeability with frequency. The limits of detectable change in permeability are 1% in μ_1 and 0·05% in μ_2. These are the limits of error and are shown by vertical lines in figure 2.

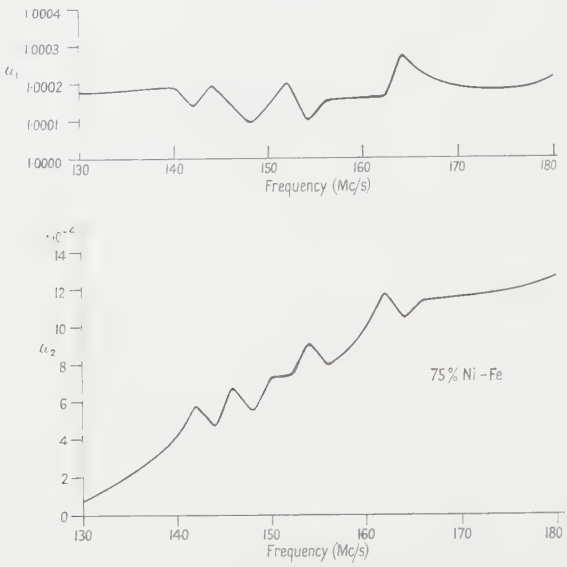

Figure 3. Complex permeability of 75% Ni–25% Fe alloy.

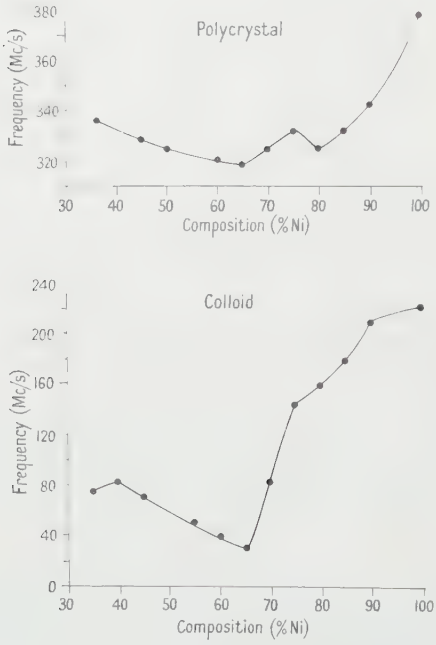

Figure 4. Variation of internal resonance frequency with composition for polycrystalline and colloidal Ni–Fe alloys.

3.2. *Anisotropy Constants and Internal Field*

The equations giving the anisotropy fields for the three easy directions of magnetization occurring in the Ni–Fe alloy series are given below:

$$\langle 100 \rangle \quad H_k = \frac{2K_1}{M_s} \qquad \ldots\ldots (1)$$

$$\langle 110 \rangle \quad H_k = -\frac{1}{2M_s}(K_1 - \tfrac{1}{2}K_2) \qquad \ldots\ldots (2)$$

$$\langle 111 \rangle \quad H_k = -\frac{4}{3M_s}(K_1 + \tfrac{1}{3}K_2) \qquad \ldots\ldots (3)$$

where M_s is the saturation magnetization and K_1, K_2 are the anisotropy constants.

Alloys containing 35, 40 and 45% nickel have a $\langle 100 \rangle$ easy direction and the internal field has been calculated from equation (1) using the values for K_1 given by Hall (1939). The results are compared with those obtained from the resonance frequency using the simple spin–resonance formula $f_0 = \gamma H_k$, in table 1. It

Table 1. Anisotropy Constants for Ni–Fe Alloys

(1)	(2)	(3)	(4)	(5)	(6)	(7)	(8)
35	+3	—	1·93	3·9	27·8	+21·5	—
40	+5	—	1·84	6·8	29·3	+20·8	—
45	+4	—	1·75	5·75	25	+17·4	—
55	0	−150	1·58	29·45	18	—	−91·6
60	−2·5	−120	1·50	23·8	14	—	−66·8
65	−6	−70	1·37	16·7	20·7	—	−47·4
70	−11	−17	1·23	22·7	28·5	—	−30·9
75	−30	−18	1·1	53·4	50·7	—	−12·5
80	−13	−20	1·03	31·0	56·8	—	−69·4
85	−17·5	−23	0·95	39·0	63·6	—	−66
90	−24·5	−23	0·81	63·4	77·1	—	−39·5
100	−56	+53	0·60	101	78·5	—	+78·75

(1) Alloy (% Ni); (2) K_1 (10^3 erg cm^{-3}); (3) K_2 (10^3 erg cm^{-3}); (4) M_S (μ_B); (5) H_k calc. (Oe); (6) H_k meas. (Oe); (7) K_1 calc. (10^3 erg cm^{-3}); (8) K_2 calc. (10^3 erg cm^{-3}).

will be seen that agreement between the calculated and measured values is not good. Using the experimental value of the field, values for K_1 have been calculated and are shown. It is pointed out that these compare more favourably with the values given by Bozorth (1952) which for 35, 40 and 45% nickel are 16, 21 and 20×10^3 erg cm^{-3} respectively.

The 55, 60 and 65% nickel alloys have been shown by Kleiss (1936) to have a $\langle 110 \rangle$ easy direction. In this case the internal field is given by equation (2) and involves K_2. The values of the latter shown in table 1 are those given by Bozorth (1951) and have been used, together with Hall's values for K_1, to calculate values for the internal field. Again the agreement with experiment is poor. It is generally acknowledged that the accurate measurement of K_2 is difficult and so the results have been used to yield values for K_2. These are shown in the table.

Because of the relatively slow cooling treatment given to the alloys it is thought that their anisotropy should correspond more closely to the values given by Hall for an ordered specimen; the slightly raised resonance frequency at the composition

75% nickel could be interpreted as the result of a degree of long-range order, which is known to occur at the composition $FeNi_3$ in slowly cooled alloys. Since the majority of particles are explosively produced they would probably retain any ordering present in the original electrodes. Using the ordered values for K_1 and equation (3) the values of H_K calculated for the alloys 70, 75, 80, 85 and 90% nickel are shown in table 1. Agreement between these and the experimental values is slightly better in these cases, especially for the compositions 70 and 75% nickel. The results have again been used to yield values for K_2, which are shown.

It is known that the anisotropy constants are extremely sensitive to the state of strain of the specimen for the compositions with finite magnetostriction. As a result of the method of production the particles might be expected to contain large strains. It is therefore doubtful if the values obtained from torque measurements on carefully prepared, strain-relieved specimens can be applied in this case.

§ 4. Magnetostatic Modes

It has been shown by Walker (1957) that, when the wavelength of the applied radio-frequency field is much larger than the physical dimensions of the sample, propagation effects may be ignored. Further, the exchange field is given approximately by $10^{-8}/\lambda^2$Oe where λ is the radio-frequency wavelength, and in the present experiments this is negligibly small. The forces concerned in the equation of motion are, under these circumstances, purely magnetostatic, each spin moving in the steady field present. Walker shows that the solution of the equation provides a series of modes of oscillation higher in frequency than the fundamental spin-resonance mode.

These modes will only be excited if the radio-frequency field is non-uniform. From the configuration of the test coils in the apparatus used it is clear that this is the case in the present experiments.

When the separation between the fundamental resonance frequency and the higher mode is small, Walker gives the formula

$$\Omega \simeq \left(\frac{(1-z^2)\alpha^2 \Omega_H}{(1-z^2)\alpha^2 + z^2} \right)^{1/2}.$$

In this, z is the value of the argument of the associated Legendre function $P_n^m(z)$ for which the function has the value zero. Ω is given by $\omega/4\pi\gamma M_S$ where ω is the angular frequency of the mode; Ω_H is given by $H_K/4\pi M_S$; α is the ratio of the axes of the particle, assumed spheroidal. The ratio is taken such that the numerator of it is the length of the axis in the direction of the magnetization. Values of the argument z for which the associated Legendre function is zero have been calculated for various values of m and n, and are shown in table 2.

In his treatment Walker assumes the particle to be magnetized to saturation as a whole. This is not the case in the present instance, since no external field is applied. The eccentricity factor α will not, therefore, be given by the macroscopic dimensions of the particle. The particles in the present experiments are all multi-domain and it is not unreasonable to suppose that, for a given alloy composition, the size and shape of surface domains will be much the same for most of the particles. It is suggested that α should be a domain eccentricity factor determined by the length and width of the domain, and by the skin depth of the

Table 2. Squares of Values of Argument $|z|$ for which $P_n^m(z)=0$

n	$m=0$	$m=1$	$m=2$	$m=3$	$m=4$
1					
2	0·25				
3	0·6	0·2			
4	0·742	0·429	0·143		
5	0·82	0·587	0·333	0·111	
6	0·86	0·680	0·483	0·409	0·136
7	0·89				
8	0·91				
9	0·925				
10	0·935				
11	0·942				
12	0·946				
13	0·949				

$$P_n^m(z)=0=\frac{d^n+m_1z^2-1)^n}{d^n+m_2}$$

Table 3. Skin Depths for Nickel–Iron Alloys

Alloy (% Ni)	ρ (ohm metres $\times 10^{-8}$)	f_0 (Mc/s)	Skin depth (metres $\times 10^{-8}$)
100	9	220	1·14
90	15	208	1·53
85	20	178	1·87
80	21·8	158	2·05
75	24·5	142	2·35
70	27·5	82	3·25
65	30	30	5·64
60	34·5	39	5·3
55	41	50	5·05
45	65	70	5·43
40	74·5	82	5·38
35	81·5	78	5·77

Figures for resistivity from Yensen (1920).

alloy at the frequency concerned, the domain being considered as an approximation to an ellipsoid.

It would be expected that α will vary from alloy to alloy. The variation of skin depth with composition has been calculated on the assumption, based on the experimental results, that

$$\mu_R=(\mu_1{}^2+\mu_2{}^2)^{1/2}+\mu_2\simeq 1$$

and is given in table 3. It will be seen that the skin depth increases with decreasing nickel content and passes through a maximum at the composition corresponding to the lowest anisotropy energy. Examination of the alloy strips from which the electrodes were formed, by the Bitter technique, has shown that the domain sizes vary in a similar way with composition. The conclusion, therefore, is that α may not vary by very much over the composition range.

Values of α have been estimated from the domain dimensions in the strips examined and the values subsequently adjusted, by trial and error, to obtain a fit between the calculated modes and the experimentally observed resonance peaks. The results are shown in figure 5, and it will be seen that reasonable agreement can be obtained between theory and experiment.

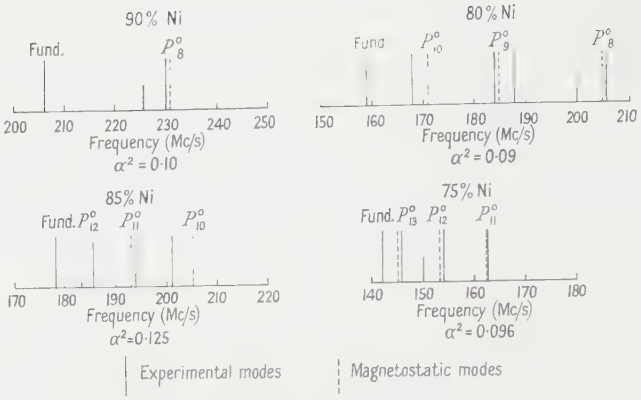

Figure 5. Magnetostatic modes in Ni–Fe alloys.

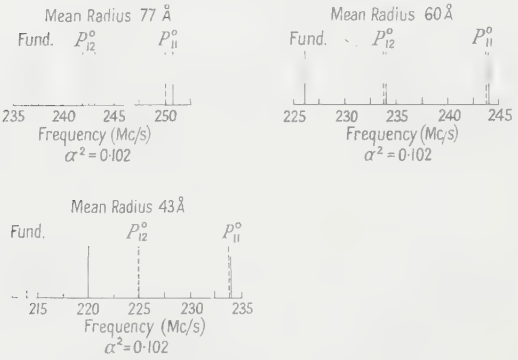

Figure 6. Magnetostatic modes in small cubic cobalt particles.

Similar multiple peaks were obtained in some cases in the experiments on cobalt particles reported in I. These higher resonance frequencies have been fitted to calculated magnetostatic modes in the same way, and the results are shown in figure 6. Again it will be seen that reasonable agreement can be obtained.

§ 5. Discussion

As in previous internal ferromagnetic resonance experiments, the narrow line-widths obtained indicate that the mechanism is not affected by the shape of the particles. If shape anisotropy had an influence the wide range of particle sizes and shapes would result in a continuous spectrum of resonance frequencies, different for each particle, and it would be impossible to obtain clear resonance peaks.

A feature common to all results obtained has been the splitting of the fundamental resonance peak, a subsidiary peak appearing at a frequency below, and close to, the fundamental one. Artman (1957) has shown that, in the case of standard ferromagnetic resonance in an applied field, it is possible to obtain two resonance frequencies. This is based upon the supposition of multi-domain structure in the specimen. He postulates a dynamic demagnetizing factor, determined by α, for the domains and shows that one resonant frequency will be obtained when the field is perpendicular to the domain walls, and another, lower one, when the field is parallel to the domain walls. The detail of his

calculation depends, however, on the presence of an applied field, and it is not obvious how this should be amended to apply to the internal ferromagnetic case. The proposed mechanism could, however, operate in the present work, and would account for the doublet peaks observed experimentally.

In connection with the magnetostatic modes it is pointed out that there are many possible combinations of values of x and z which could provide modes agreeing, more or less, with the experimentally observed peaks. The spacing, in frequency, of the experimental peaks follows no obviously regular law; the Kittel spin wave modes, observed by Seavey and Tannenwald (1959) in thin films, would provide a frequency spacing proportional to the squares of integers, and the present results do not conform to this. It is considered that the Walker solution is the most likely mechanism in the present work.

§ 6. Conclusion

Evidence of internal ferromagnetic resonance in nickel-iron alloys has been obtained and some correlation has been found with the known variation of anisotropy energy with composition. The total anisotropy has been found to be a minimum in the region of 65% nickel, and some indication of long-range ordering in the region of $FeNi_3$ has been obtained. The results provide some support for the existence of magnetostatic spin-wave resonance modes when propagation and exchange effects can be neglected.

Acknowledgments

This work was carried out in the Physics Department of the University of the Witwatersrand, Johannesburg, under Professor F. R. N. Nabarro. Drs. B. Donovan and E. P. Wohlfarth have contributed useful suggestions. Mrs. M. Brown drew the diagrams.

References

Anderson, J. C., 1960 a, *Proc. Phys. Soc.*, **75,** 33.
—— 1960 b, *J. Brit. Instn Radio Engrs*, **20,** 219.
Anderson, J. C., and Donovan, B., 1957, *Proc. Phys. Soc.* B, **70,** 186.
—— 1959, *Ibid.*, **73,** 593.
Artman, J. O., 1957, *Phys. Rev.*, **105,** 62.
Bagguley, D. M. S., 1955, *Proc. Roy. Soc.* A, **228,** 549.
Bozorth, R. M., 1951, *Ferromagnetism* (New York: Van Nostrand).
Hall, R. C., 1939, *J. Appl. Phys.*, **30,** 816.
Kittel, C., 1946, *Phys. Rev.*, **70,** 281.
Kleiss, I. D., 1936, *Phys. Rev.*, **50.,** 1178.
Reich, K. H., 1956, *Phys. Rev.*, **101,** 1647.
Seavey, M. H., and Tannenwald, P. E., 1959, *J. Phys. Radium*, **20,** 323.
Svedberg, T., 1928, *Colloid Chemistry* (New York: Rumbold).
Walker, L. R., 1957, *Phys. Rev.*, **105,** 390.
Yensen, T. D., 1920, *J. Amer. Inst. Elect. Engrs*, **39,** 396.

Magnetothermal Effects in Silicon–Iron Alloys

By N. H. SAUNDERS†§ and R. S. TEBBLE‡

† Department of Physics, University of Leeds
‡ Department of Physics, University of Sheffield

MS. received 21*st December* 1959, *in revised form* 24*th February* 1960

Abstract. Measurements are recorded of the reversible magnetothermal effect in two alloys of silicon–iron. Analysis of the measurements by the method of Stoner and Rhodes, though hindered by the absence of reliable data on the basic magnetic constants of the materials, shows that over the field range studied the experimental coefficient b'' is nowhere constant but tends to the 'rotational' value $b=(T/K_1)(\partial K_1/\partial T)$ as the field increases. The possibility is considered that the variation is associated with changes in a 'spike' domain structure. It is concluded that such a structure may be involved but cannot by itself account for the details of the observations.

§ 1. Introduction

A good deal of attention has been paid in recent years to the problem of interpreting bulk magnetization changes in ferromagnetics in terms of elementary domain mechanisms. A number of techniques have emerged, involving for example pure magnetic measurements, magnetoresistance measurements, and magnetothermal measurements. The latter in particular has yielded interesting and significant results for a wide range of materials and consists essentially of measuring the small temperature changes which occur in a specimen as it is taken step by step round a magnetization cycle under adiabatic conditions. It has been clearly recognized that the theory in terms of which such measurements are analysed (Stoner and Rhodes 1949, Teale and Rowlands 1957) can be precisely developed only in relation to reversible magnetization changes and experimental methods have developed with this in mind. In one of them (Bates and Sherry 1955), small forward and reverse field changes are applied to a specimen at various points along the cycle. The forward step yields a 'total' heat measurement, i.e. it includes contributions from both reversible and irreversible changes in domain configuration, whilst ideally the reverse step, if it is small enough, yields only the reversible part. In another method, used by Tebble, Wood and Florentin (1952), Tebble and Teale (1957) and also in the work reported here, direct measurement of the small temperature changes themselves is avoided, and measurements are in effect made of $(\partial I/\partial T)_H$ thermodynamically related to $(\partial T/\partial H)_S$; small changes in temperature ΔT are imposed on the specimen at various points of the cycle and the resulting magnetization changes ΔI are measured. The maximum ΔT consistent with a reversible ΔI is found by experiment.

The three domain processes which can occur during magnetization changes are domain boundary movement, domain vector rotation and change in intrinsic magnetization I_0. The contribution to the observed thermal effects from the

§ Now at the Research Laboratories of the Associated Electrical Industries (Rugby) Ltd.

last process can usually be calculated independently, leaving the remainder to be considered in relation to the many possible mechanisms involving boundary movements and rotations. The general outcome of several such analyses can be well illustrated by reference to the investigation by Tebble and Teale (1957) on polycrystalline annealed nickel. The method will be explained in detail in § 2 but it may be mentioned here that it involves the calculation of a coefficient b'' at various field values. If only one domain mechanism other than change in I_0 is involved in magnetization changes, then the value of b'' should be independent of field and characteristic of that mechanism; above about ± 100 Oe b'' was found to be constant at a value characteristic of the mechanism of domain vectors rotating against crystal anisotropy forces. The work reported in this paper forms a continuation of this work and is concerned with the silicon–iron alloys. The behaviour of these well-known and widely used soft magnetic alloys was expected to be strongly influenced by boundary movements in low and moderate fields and an investigation of the reversible magnetothermal effects in these fields afforded a chance of studying this basic process.

Previous work on polycrystalline Si–Fe (0·5% and 4%) has been reported by Bates and Marshall (1953). Only total heat data were obtained, making an analysis in the hysteresis region impossible by the Stoner and Rhodes method. In higher fields, however, its application is justifiable, and three of the four sets of data yielded b'' results which were unusual in some respects. Either rapid variation in high fields was found or b'' was positive when it is normally expected to be a negative quantity.

More recently, Bates and Sansom (1959) have made reversible measurements on a polycrystalline iron specimen, a single crystal of 2·7% Si–Fe and a 0·5% polycrystalline specimen. Except in fields below about 100 Oe b'' was found to be sensibly independent of H for each specimen, the actual values being associated with $(T/K_1)(\partial K_1/\partial T)$ and therefore suggesting rotations against magneto-crystalline forces. Fields up to 1000 Oe were employed but no evidence of the unusual b'' behaviour observed by Bates and Marshall was found. The present investigation is effectively complementary to Bates and Sansom's work in that attention is confined here to the low and moderate field region where boundary movement effects may arise.

Mention should also be made of one other relevant investigation (Bates, Christoffel, Clow and Davis 1957). The specimen was a single crystal of 2% Si–Fe having a 'rooftop' orientation, i.e. its long axis was [001] and surface (110). Total and reversible magnetothermal measurements were made in the field range -600 Oe to $+600$ Oe. From 150 Oe to 600 Oe change in I_0 alone accounted for the observations; below 150 Oe b'' was calculated as a function of field but a constant value was not found. Rotations could not explain the results but powder pattern observations on the specimen suggested that boundary movements in the form of growing Néel (i.e. transverse) and reverse spike domains played a large part.

§ 2. The Theory of the Method

For a reversible adiabatic change in magnetization involving only change in I_0 and rotations against crystal anisotropy forces, Stoner and Rhodes (1949) have

shown that the change in heat content $\Delta Q'$ per unit volume, can be written

$$\Delta Q' = ad(IH) + bHdI \qquad \ldots\ldots(1)$$

where $$a \equiv -(T/I_0)(\partial I_0/\partial T) \quad \text{and} \quad b \equiv (T/K_1)(\partial K_1/\partial T). \qquad \ldots\ldots(2)$$

I and H denote the magnetization and effective field respectively; K_1 is the modulus of the first anisotropy constant and T is the absolute temperature. The first term in equation (1) is the contribution to $\Delta Q'$ from change in I_0 whilst the second term is the contribution from the rotational mechanism. The equation is often written in the differential form

$$(\partial Q'/\partial H)_S = a(I + H\kappa_r) + bH\kappa_r \qquad \ldots\ldots(3)$$

with $\kappa_r = (\partial I/\partial H)_T$, the reversible susceptibility. As mentioned in the Introduction, it is $(\partial I/\partial T)_H$ which is measured, the connection with $(\partial Q'/\partial H)_S$ being given by

$$(\partial Q'/\partial H)_S = -T(\partial I/\partial T)_H. \qquad \ldots\ldots(4)$$

The other measurements are I and κ_r as functions of H and their analysis proceeds by the calculation at various values of H of a quantity b'' defined by

$$b'' = \frac{-T(\partial I/\partial T)_H + a(1 + H\kappa_r)}{H\kappa_r}. \qquad \ldots\ldots(5)$$

A glance at equation (3) now shows that b'' equals the constant b when the model to which (3) applies is appropriate to the magnetization changes in the specimen under investigation. Some examples of this were noted in the Introduction.

Teale and Rowlands (1957) have shown from a consideration of the free magnetic energy that an expression similar to (5) is obtained for all single mechanism systems, i.e. those in which only one domain mechanism other than change in I_0 occurs during magnetization changes. The quantity b'' will take on the constant value appropriate to the mechanism involved. Expressions analogous to equation (2) were given for several well-known mechanisms.

When b'' is found to depend on field, the occurrence of several mechanisms is indicated. This situation also, has been discussed by Teale and Rowlands (1957) but it was not possible to give a perfectly general and at the same time useful method of analysis. However, in the case where the relative magnetization I/I_0 could be expressed in terms of a single variable (domain vector orientation or boundary position for example), it was shown that (cf. eqn (3))

$$(\partial Q'/\partial H)_S = a(I + H\kappa_r) + \kappa_r \sum_{n=1}^{n} S_n v_n \qquad \ldots\ldots(6)$$

where $$v_n = (\partial F_n/\partial I)_T \qquad \ldots\ldots(7a)$$

with $$F_n = A_n f_n I/I_0 \qquad \ldots\ldots(7b)$$

and $$\sum v_n = \sum_{n=1}^{n} (\partial F_n/\partial I)_T = H. \qquad \ldots\ldots(7c)$$

The summation extends over the 'n' participating mechanisms (other than change in I_0 which is represented by the first term in eqn (6)). The quantities F_n are the contributions to the free magnetic energy from these mechanisms and are assumed to have the form shown in equation (7b) with $f_n(I/I_0)$ being some

function of $I\,I_0$. The coefficients S_n are characteristic of the mechanisms (b in eqns (1) and (2) is an example) and are related to the A_n by

$$S_n=(T/A_n)(\partial A_n/\partial T). \qquad \ldots\ldots(8)$$

The conditions under which equation (6) is valid would seem to limit its application at most to the analysis of magnetization changes involving either the rotation process or the boundary movement process but not both together. Several free energy contributions may still be associated with each process of course (i.e. several domain mechanisms may participate) and possible ways of using equation (6) have therefore been considered.

Direct and detailed application of the equation to experimental data is prohibited by the fact that the v_n are not in general experimentally measurable; only their sum is fixed by condition (7*c*). A more tentative and qualitative approach is therefore necessary. The following purely formal argument was suggested by the fact that many experimental (b'', H) curves in low and moderate fields resemble a branch of a rectangular hyperbola. Now from equations (3) and (6) we have

$$b''H=\sum_{n=1}^{n} S_n v_n. \qquad \ldots\ldots(9)$$

Separating one element of the sum in (9) and making use of equation (7*c*), it is easily seen that

$$(b''-S_1)H=\sum_{n=2}^{n}(S_n-S_1)v_n. \qquad \ldots\ldots(10)$$

If it could be assumed that the right-hand side of (10) was independent of H then a hyperbolic relation between b'' and H would follow with b'' tending to the constant value S_1 as H increases. It would clearly be necessary for all but one of the v_n to be independent of H which would imply that the corresponding expressions for F_n must be linear functions of $I\,I_0$. In general, a detailed examination of many domain structures would be needed to decide the circumstances under which a mechanism could be so represented and perhaps the most effective practical procedure is to plot b'' against $1/H$ for particular sets of data and then, if straight lines are obtained, to consider possible domain models in the light of any particular features of the data or known characteristics of the materials concerned. An attempt to develop this method of analysis using the present results is made in § 5.

One special application of the above general expressions is worth mentioning. If only two mechanisms, apart from change in I_0, occur during magnetization then equations (7*c*) and (9) can be solved simultaneously for v_1 and v_2, to give

$$v_1=H(b''-S_2)/(S_1-S_2) \quad \text{and} \quad v_2=H(S_1-b'')/(S_1-S_2). \qquad \ldots\ldots(11)$$

Substituting these expressions into equation (6) yields

$$(\partial Q'/\partial H)_S=a(I+H\kappa_r)+H\kappa_r S_1(b''-S_2)/(S_1-S_2)+H\kappa_r S_2(S_1-b'')(S_1-S_2). \qquad \ldots\ldots(12)$$

In this special case therefore, a complete separation of the measured $(\partial Q'/\partial H)_S$ into its constituent parts is possible at any value of H in terms of b'' and the values of S_1 and S_2 for the two mechanisms involved. This may be applicable to data for specimens having relatively simple magnetic structures, such as single crystals.

§ 3. Experimental Technique

In its general design the apparatus followed that described by Tebble and Teale (1957) to which reference should be made for details. Some modifications were introduced however to improve the mechanical stability of that arrangement, the main one consisting of mounting the magnetizing coil, its balancing partner and the astatic magnetometer on a heavy brick pier resting on anti-vibration matting. The advantages resulting from the effective elimination of spurious magnetometer deflections due to mechanical vibrations were partly offset however by the effects of stray magnetic fields on the silicon–iron specimens. The random changes of magnetization produced in the specimens led to significant magnetometer disturbance and consequently to difficulties in obtaining reliable $(\partial I/\partial T)_H$ measurements. The effects were particularly severe for the 4% specimen in low fields and no data are reported below for this region.

For the determination of $(\partial I/\partial T)_H$, each ellipsoidal specimen was provided with a copper–constantan thermocouple to measure the change in temperature ΔT caused by passing a heated stream of oil over it; the resulting magnetization change ΔI was obtained from the deflection of the magnetometer, calibrated as described in the above reference. The sensitivity was usually about 10^{-2} e.m.u. mm^{-1} at 1 metre and the maximum ΔT for reversibility varied from about 1°C to 5°C.

The reversibility susceptibility κ_r in the highest fields was obtained from the slope of the magnetization curve; elsewhere the a.c. bridge method of Tebble and Corner (1950) was used. An interesting feature of these latter measurements was the observation of anomalous eddy current effects in both specimens (cf. Aspden 1957); the measured susceptibility decreased with increasing bridge frequency at a faster rate than predicted by the usual eddy current treatment, though the discrepancy became less marked the higher the field. In these circumstances the required κ_r data were obtained by extrapolation from readings at several frequencies.

The (I, H) measurements were obtained by the usual search coil and ballistic galvanometer method, the galvanometer being calibrated by a standardized mutual inductometer.

§ 4. Details of the Specimens and Results

Two polycrystalline specimens were examined, one a 4% alloy and the other containing 0·288% silicon (by weight) according to the manufacturer's analysis. Each was turned into ellipsoidal form and the measurements reported here refer to the unannealed state.

(i) 4% specimen: length 37·05 cm, diameter 0·366 cm, $H_c = 0{\cdot}17$ Oe, $I_r = 480$ e.m.u., demagnetizing factor $N = 0{\cdot}00529$.

(ii) 0·288% specimen: length 39·9 cm, diameter 0·400 cm, $H_c = 1{\cdot}56$ Oe, $I_r = 680$ e.m.u., $N = 0{\cdot}00543$.

The experimental results are presented below in both graphical and tabular form (tables 1 and 2), the latter having been taken from the best curves drawn through the experimental points. In all cases H denotes the effective field and the measurements have been corrected for demagnetizing effects where necessary.

Table 1. 4% Si–Fe, Unannealed; Values of Measured Quantities taken from Smooth Curves drawn through Experimental Points

Average Temperature 20°C

$-H$	$-I$	$+\kappa_T$	$-(\partial Q'/\partial H)_S$	$+H$	$+I$	$+\kappa_T$	$+(\partial Q'/\partial H)_S$
160	1456	—	33·7	30	1268	3·10	44·9
150	1448	0·78	32·3	40	1297	2·49	42·0
140	1440	0·83	31·1	50	1320	2·08	39·7
130	1432	0·90	30·3	60	1339	1·79	37·7
120	1422	0·99	30·6	70	1356	1·60	36·0
110	1412	1·09	31·3	80	1372	1·46	34·6
100	1400	1·19	32·2	90	1386	1·32	33·3
90	1388	1·31	33·4	100	1399	1·21	32·3
80	1374	1·43	34·6	110	1411	1·09	31·3
70	1359	1·57	35·8	120	1421	1·00	30·6
60	1342	1·77	37·3	130	1431	0·93	30·6
50	1324	2·10	39·0	140	1440	0·87	31·15
40	1300	2·51	41·0	150	1448	0·83	32·2
30	1270	3·17	44·3	160	1456	—	33·6

Table 2. 0·288% Si–Fe, Unannealed; Values of Measured Quantities taken from Smooth Curves drawn through Experimental Points

Average Temperature 19°C

$-H$	$-I$	$+\kappa_T$	$-(\partial Q'/\partial H)_S$	$+H$	$+I$	$+\kappa_S$	$+(\partial Q'/\partial H)_S$
160	1465	0·78	30·3	5	730	11·1	10
150	1455	0·81	31·2	10	955	7·1	23·7
140	1444	0·85	32·3	20	1135	3·65	33·2
130	1434	0·90	33·3	30	1215	2·45	37·8
120	1423	0·95	34·3	40	1263	1·98	39·8
110	1410	1·00	35·3	50	1295	1·72	39·4
100	1397	1·06	36·3	60	1321	1·53	38·7
90	1381	1·12	37·5	70	1343	1·39	38·0
80	1365	1·19	38·8	80	1361	1·26	37·3
70	1349	1·27	40·1	90	1377	1·16	36·6
60	1330	1·39	41·4	100	1393	1·07	35·8
50	1308	1·56	42·8	110	1408	1·00	35·1
40	1283	1·74	44·0	120	1421	0·95	34·4
30	1250	2·10	48	130	1433	0·90	33·6
20	1206	2·81	50	140	1444	0·85	32·95
10	1115	6·3	45	150	1455	0·81	32·2
5	1015	9·6	30	160	1465	0·78	31·5

In figure 1, the portion of the curve between -40 Oe and $+5$ Oe is shown as a broken line because experimental conditions made it difficult to obtain reliable and reproducible measurements. The relatively large scatter of the points in the range -40 Oe to -10 Oe is particularly evident and may indicate some complicated changes in domain structure; irreversible effects, which provide the most natural explanation, were not noticed during the measurements.

It has been found that a close correspondence exists between the (I, H) data in fields greater than about 20 Oe for the present 4% specimen and specimen 1 (4% untreated) investigated by Bates and Marshall (1953). The 'total Q'' data for their specimen are therefore compared in figure 2 with values of

$$\int_{-160}^{H} (\partial Q'/\partial H)_S dH,$$

calculated from the present results. Such a comparison is to some extent justified by the fact that the magnetization changes in the field range considered appear to be mainly reversible judging from the hysteresis loop.

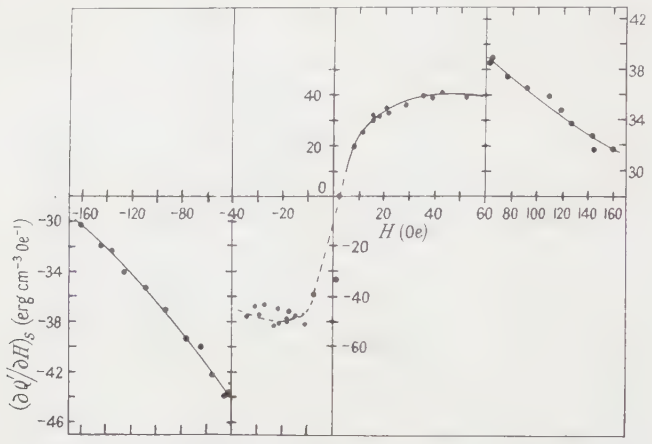

Figure 1. Reversible $(\partial Q'/\partial H)_S$; 0·288% silicon–iron (note change of scale).

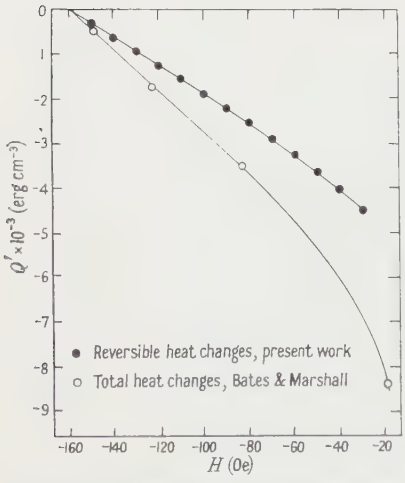

Figure 2. Reversible Q'; 4% silicon–iron.

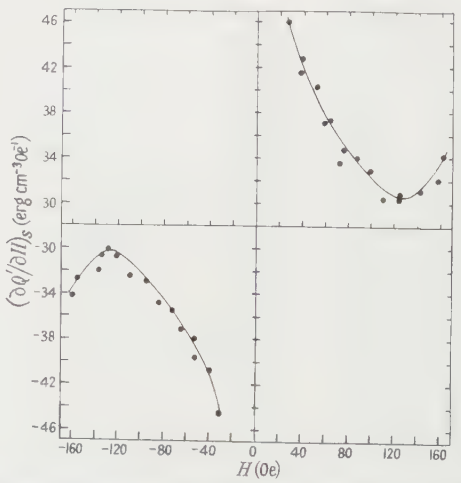

Figure 3. Reversible $(\partial Q'/\partial H)_S$; 4% silicon–iron.

§ 5. Discussion

Although the comparison just referred to is limited in field range by the fact that the $(\partial Q'/\partial H)_S$ results, given in figure 3, can only be integrated down to about -30 Oe it can be seen that a measure of agreement is obtained which is satisfactory when it is considered that two sets of data were obtained by different experimental methods and the earlier set were 'total Q'' results. This correspondence between basic measurements is of some consequence here since the calculation of the derived quantity b'' involves a knowledge of the values of the coefficients a (see eqn (2)) which has only recently become available for the silicon–iron alloys. Bates and Marshall (1953), on the basis of the information then obtainable, estimated for the 4% Si–Fe a value $a = 3{\cdot}51 \times 10^{-2}$ and for

the 0·5% alloy $3{\cdot}4 \times 10^{-2}$ at 290 K. The information on which these estimates were made has been re-examined and with the results of more recent measurements these are given in table 3. They maybe in error by about ±5% and

Table 3. Values of the Coefficient $a = -(T/I_0)(\partial I_0/\partial T)$ at Room Temperature for some Alloys of Silicon–Iron

Weight (% Si)	0	0·288	0·5	2·7	3·55	4·0	4·98
$a \times 10^2$	3·6[a], 3·9[b], 3·3[c]	4·0[e]	4·3[b]	4·6[b]	5·0[d]	5·2[e]	5·8[d]

a, Weiss and Forrer (1929); b, Bates and Sansom (1959); c, Crangle (1959, private communication); d, Parsons (1957); e, by interpolation.

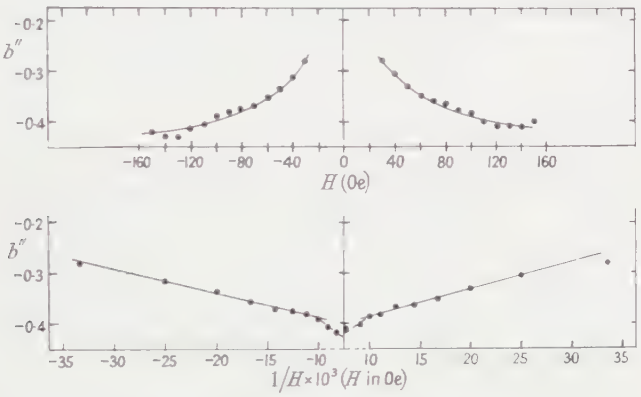

Figure 4. b'' analysis; 4% silicon–iron.

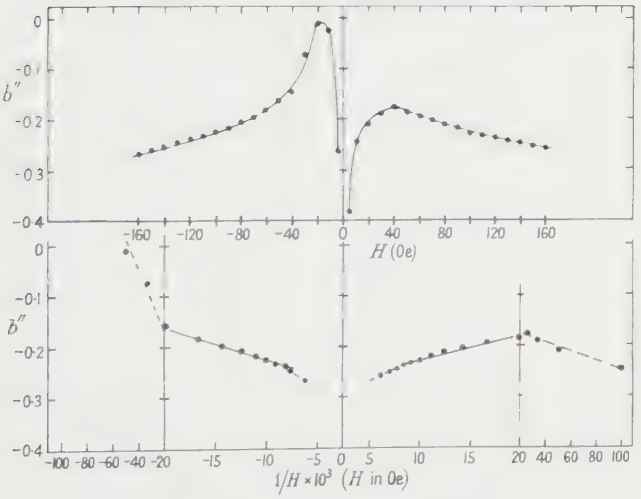

Figure 5. b'' analysis; 0·288% silicon–iron (note change of scale).

some uncertainty therefore attaches to the quantitative b'' results in figures 4 and 5. However, the general conclusions should be unaffected.

Before proceeding with the analysis, it is interesting to note the changes which are brought about in the b'' results of Bates and Marshall if new estimates of a

are used. The re-calculated values of b'' shown in figure 6 are now negative in all cases over a reasonably wide range of field except in the 4% alloy, where the unusual behaviour of b'' is still present in high fields.

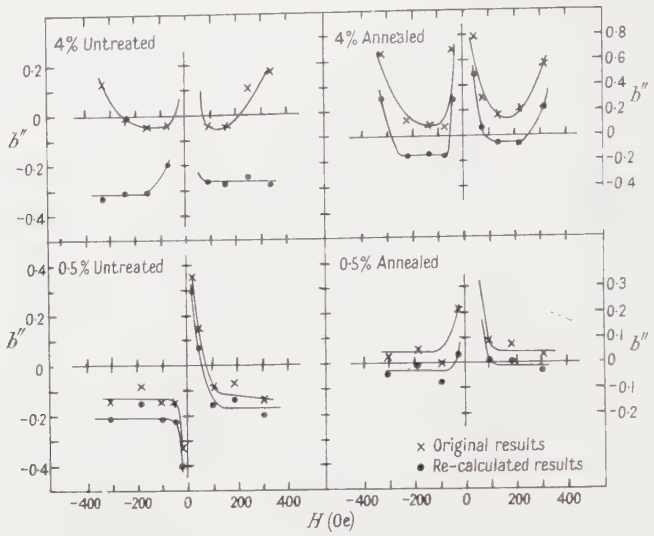

Figure 6. Re-calculation of Bates and Marshall (1953) data using new values of $a=-(T/I_0)(\partial I_0/\partial T)$. Original results: $a=3{\cdot}51\times10^{-2}$ for 4% Si–Fe and $a=3{\cdot}4\times10^{-2}$ for 0·5% Si–Fe; re-calculated results: $a=5{\cdot}2\times10^{-2}$ for 4% Si–Fe and $a=4\times10^{-2}$ for 0·5% Si–Fe.

Perhaps the first noteworthy feature of the results of the present measurements, shown in the upper parts of figures 4 and 5, is that b'' is nowhere constant in the field range covered. The simultaneous occurrence of several domain mechanisms is therefore indicated even in fields which can be regarded as 'moderate to high' compared with the coercivities of the specimens. For both specimens it can be seen that b'' seems to tend to a constant value as H increases, i.e. about $-0{\cdot}42$ for the 4% specimen (cf. the re-calculated value $-0{\cdot}3$ for the Bates and Marshall 4% untreated specimen) and about $-0{\cdot}29$ for the 0·288% specimen. The limits of accuracy are to about $\pm5\%$ on the average. Compared with the primary ferromagnetics, there are relatively few reliable data here which enable these values to be unambiguously linked with any particular mechanism, especially the usual rotation mechanism specified by $(T/K_1)(\partial K_1/\partial T)$.

The values of this coefficient given in table 4 are estimated from results given by Bates and Sansom (1959) for 2·7% Si–Fe and by Graham (1959, private communication) for 3·1% and 5·1% Si–Fe. The experimental value of

Table 4. Values of $b=(T/K_1)(\partial K_1/\partial T)$ for Silicon–Iron at Room Temperature

% Si	2·7	3·1	5·1
$(T/K_1)(\partial K_1/\partial T)$	−0·37	−0·38	−0·46

$b''=-0{\cdot}42$ for the 4% alloy clearly fits reasonably into this scheme and it therefore seems likely that b'' tends to $(T/K_1)(\partial K_1/\partial T)$ as H increases. A similar conclusion is probable in the case of the 0·288% specimen ($b''=-0{\cdot}29$);

in support of this Bates and Sansom find $b'' = -0{\cdot}29$ for iron and $-0{\cdot}37$ for 0·5% silicon–iron.

For both specimens then, b'' appears to tend to a value of the order of b as H increases. It can also be seen from figures 4 and 5 that, other than in the lowest fields, b'' increases numerically with H. This general behaviour is similar to that reported for many other specimens (for example see figures 7 and 8 for nickel and cobalt) and the problem is to discover the combination of domain mechanisms

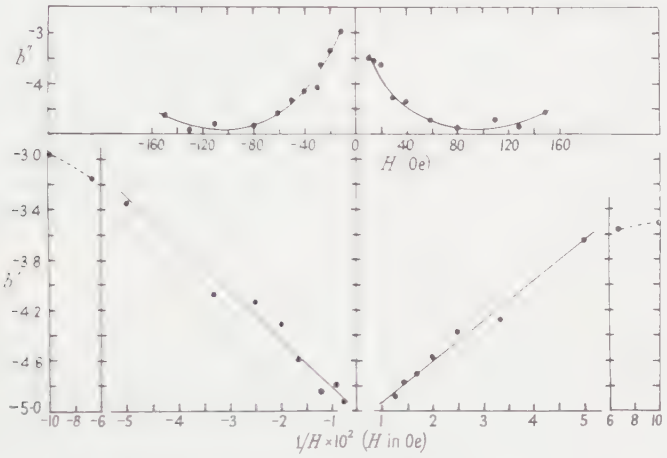

Figure 7. b'' analysis; annealed nickel data from Tebble and Teale (1957).

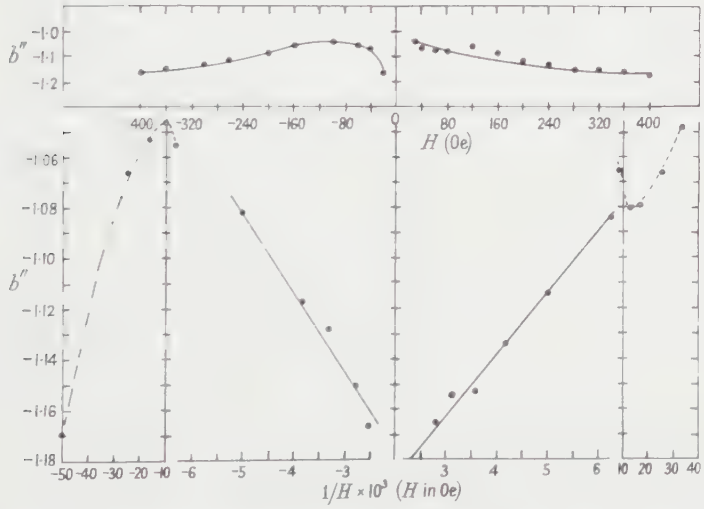

Figure 8. b'' analysis; annealed cobalt data from Tebble and Teale (1957).

responsible for it in each case. Assuming that the effect $b'' \propto (T/K_1)(\partial K_1/\partial T)$ as H increases signifies ordinary rotations, it could be simply asserted, probably correctly, that the observed variation follows from the additional occurrence of one or more reversible boundary movement mechanisms. In the absence of the necessary comprehensive theory, there remains the possibility of examining likely models which are amenable to discussion in terms of the existing theory.

The following is mainly concerned with the spike domain model, considered for example by Bates *et al.* (1957). These domains, initially magnetized transversely to the surrounding material, were found to feature largely in the demagnetization of their single crystal specimen of silicon–iron. The domains nucleated at imperfections, including the surfaces and grain boundaries. It has been shown that, because of the μ^* effect, the mechanism of redistribution of free poles on the spike surfaces as H varies can be characterized by $b=(T/K_1)(\partial K_1/\partial T)$ rather than the usual $2(T/I_0)(\partial I_0/\partial T)$ (see Teale and Rowlands 1957). The mechanism of change in boundary area also occurs in this spike structure and a simple two-mechanism model (free poles and boundary energy) thus emerges as a possible means of accounting more fully for the observed b'' results. It must be assumed that all the change in magnetization can be associated with the growth of the spikes. The coefficient appropriate to the boundary area mechanism is $(T/\gamma)(\partial\gamma/\partial T)$ where γ is the boundary energy per unit area; in value, $(T/\gamma)(\partial\gamma/\partial T)$ is approximately $\frac{1}{2}b$ (e.g. Rowlands 1956).

Now equation (2), restricted to $n=2$, can be written

$$b''-S_1=(S_2-S_1)(v_2/H) \qquad \ldots\ldots(13)$$

and over a field range in which v_2 is sensibly independent of H, b'' should be linear in $1/H$. That this is approximately the case for the 4% specimen can be seen from figure 4 which also shows, what is perhaps most important, that $(S_2-S_1)v_2$ should be positive (confining attention to positive fields for convenience). The same result holds for the 0·288% specimen in fields greater than about 50 Oe. Since the value of b'' appears to tend to b in high fields, it is reasonable to set $S_1=b$ and $S_2=\frac{1}{2}b$ in equation (13), from which it then follows that $v_2=(\partial F_\gamma/\partial I)_T$ must be positive and sensibly constant (F_γ is the free energy associated with the spike surface area). Now whilst it can be constant, it is clear that $(\partial F_\gamma/\partial I)_T$ cannot be positive since the spike domains decrease in size as the magnetization increases. Even setting $S_1=\frac{1}{2}b$ and $S_2=b$, contrary to the experimental indications, does not resolve the difficulty since for any reasonable shape of a spike $(\partial F_\sigma/\partial I)_T$, (where F_σ is the free energy contribution from the free pole mechanism) is positive when it is required to be negative.

Several variations on the spike domain model have been examined in this way with the same general results, and it would seem that it cannot by itself account for the observed numerical decrease of b'' as H decreases. It should perhaps be remembered that its dominance has only been demonstrated in specially orientated single crystals whereas the present specimens are in polycrystalline form. On the other hand, the occurrence of a spike structure in the specimens is qualitatively consistent with several aspects of the magnetic measurements; thus, the highest values of I reached, 1456 e.m.u. for the 4% specimen and 1465 e.m.u. for the 0·288% specimen, are well below the saturation values of 1570 e.m.u. and 1705 e.m.u. respectively. Following Bates *et al.* this may be explained by the presence of a relatively large number of transverse spikes even above the knee of the magnetization curve; and may be associated with the process of nucleation spikes.

In figures 7 and 8, the $(b'', 1/H)$ procedure is applied to the results of Tebble and Teale (1957) for annealed nickel and cobalt. Over the range of field in which b'' varies significantly it can be seen that the plots obtained are similar to those

shown in figures 3 and 5 for the present specimens. An attempted interpretation of the results in terms of equation (13) meets with the same kind of difficulties as described above; in essence, a suitable mechanism specified by S_2, cannot be found which makes the quantity $(S_2 - S_1)c_2$ positive in positive fields. It is probably too much to expect a simple two-mechanism model to account for the behaviour of polycrystalline specimens such as these.

It may be appropriate to add a note about a modified definition of b'' used by Bates *et al.* (1957). As stated earlier, b'' calculated in the normal way was not found to be constant in the field range of interest, $|H| < 150$ Oe. However, the empirical use of $H - H_c$ instead of H in the calculations resulted in a constant value $-0{\cdot}43$ which was linked with the coefficient b ($-0{\cdot}47$ for the specimen) as evidence for the spike structure discussed above. The interesting feature of this in the present context is that the substitution of $H - H_c$ for H to yield a constant quantity, b_m'' say, implies a hyperbolic relation between b'' and H. The significance of H_c is, however, not clear.

§ 6. Conclusion

The present investigation has been concerned with the measurement and interpretation of reversible magnetothermal effects in the silicon iron alloys. Two polycrystalline alloys were examined firstly a 4% alloy and then a 0·288% alloy.

Within the limits imposed by lack of knowledge of the basic magnetic parameters of the materials, it seems that b'' in each specimen tends to the value $b \equiv (T/K_1)(\partial K_1/\partial T)$ as H increases. The effect of 'spike' domains is discussed and it seems that this model cannot account by itself for the decrease in the numerical value of b'' as H decreases. It is likely that other processes, such as the usual rotational mechanism (also specified by b), also occur but the theory is not yet sufficiently developed to enable a separation of the usual effects to be made. The formal $(b'', 1/H)$ procedure may be of use in other investigations and its application has therefore been illustrated.

Fair agreement is found between the thermal measurements for the present 4% specimen and the 4% untreated specimen of Bates and Marshall. The unusual b'' results for the specimens investigated by these authors have been briefly considered and it is clear that the explanation lies in the fact that the values of a then available were incorrect. With revised estimates of a, most, but not all, of the irregularities are removed.

Acknowledgments

The authors would like to thank Professor E. C. Stoner under whose direction this work was begun and Professor W. Sucksmith for making available the facilities of the Physics Department of the University of Sheffield during the later stages of the investigation. We are indebted to Messrs G. K. N. Ltd., for samples of silicon–iron material, to the Department of Scientific and Industrial Research for a maintenance grant (N.H.S.) and finally to Dr. J. Crangle, Dr. D. Parsons and Dr. C. K. Graham who kindly made available to us the results of their measurements.

References

Aspden, H., 1957, *Proc. Instn Elect. Engrs* C, **104,** 2.
Bates, L. F., Christoffel, D. A., Clow, H., and Davies, P. F., 1957, *Proc. Roy. Soc.* A, **243,** 160.
Bates, L. F., and Marshall, G., 1953, *Rev. Mod. Phys.*, **25,** 17.
Bates, L. F., and Sansom, D. J., 1959, *Proc. Phys. Soc.*, **74,** 53.
Bates, L. F., and Sherry, N. P. R., 1955, *Proc. Phys. Soc.* B, **68,** 642.
Parsons, D., 1957, *Thesis*, University of Sheffield.
Rowlands, G., 1956, *Thesis*, University of Leeds.
Stoner, E. C., and Rhodes, P., 1949, *Phil. Mag.*, **40,** 481.
Teale, R. W., and Rowlands, G., 1957, *Proc. Phys. Soc.* B, **70,** 1123.
Tebble, R. S., and Corner, W. D., 1950, *Proc. Phys. Soc.* B, **63,** 1005.
Tebble, R. S., and Teale, R. W., 1957, *Proc. Phys. Soc.* B, **70,** 51.
Tebble, R. S., Wood, J. E., and Florentin, J. J., 1952, *Proc. Phys. Soc.* B, **65,** 858.
Weiss, P., and Forrer, R., 1929, *Ann. Phys., Paris*, **12,** 279.

RESEARCH NOTES

Debye Characteristic Temperature of Solids

By S. K. JOSHI and S. S. MITRA
Physics Department, Allahabad University, India

MS. received 10th March 1960

Abstract. Debye characteristic temperatures for a number of solids belonging to cubic, hexagonal, tetragonal and trigonal crystal systems are calculated from their elastic constants using series expansion and numerical methods.

§ 1. Introduction

The Debye characteristic temperature Θ enters into a large number of solid state problems such as electrical resistivity, thermal conductivity, temperature dependence of the intensity of x-ray reflections and the scattering of thermal neutrons, because of its inherent relationship with lattice vibrations. It is roughly below this temperature that the quantum effects come into play. The importance of this parameter and the scarcity of the available data have prompted this effort to calculate and tabulate the Debye temperature of some solids utilizing the values of elastic constants measured in recent years.

§ 2. Determination of Θ

At very low temperatures only the lattice waves of nearly infinite wavelengths contribute to the specific heat and $\Theta(0)$ values derived from elastic constants are equal to those derived from specific heat data, where $\Theta(0)$ is given by

$$\Theta(0) = \frac{\boldsymbol{h}}{\boldsymbol{k}}\left(\frac{9N}{4\pi IV}\right)^{1/3}.$$

Here

$$I = \int_0^{4\pi} \sum_i \frac{1}{v_i^3}\frac{d\Omega}{4\pi},$$

$\boldsymbol{h}$ is Planck's constant, $\boldsymbol{k}$ is Boltzmann's constant, N is the number of vibrating units in volume V of the specimen and v_i are the velocities of propagation for low frequency vibrations and as such are functions of direction. The subscript i numbers the solutions to the Christoffel equation for plane wave motion. The problem of estimation of Θ for an anisotropic substance is thus really reduced to that of averaging of the inverse cube of each of the elastic velocities over all directions. Two methods are available:

(i) Numerical integration method. For a few cubic crystals the tables prepared by de Launay (1956) may be used, but the scope of the tables is limited to only those cubic crystals whose elastic constants satisfy certain conditions. Independent numerical integration for individual substances involves tedious calculations.

(ii) Series expansion method. Hopf and Lechner's (1914) method modified by Quimby and Sutton (1953) and Houston's method developed by Betts *et al.* (1956a, b) may be used. This extended Houston's method is easy and all-embracing and well suited to treat the whole vibration spectrum. It can therefore be used to calculate Θ values at non-zero temperatures for any particular model of atomic forces (Horton and Schiff 1959, Horton 1959).

Debye Characteristic Temperatures and Elastic Constants for some Crystals

(i) Cubic system

Formula	Substance	Elastic constants (in units of 10^{11} dyn cm^{-2}) c_{11}	c_{44}	c_{12}	Source	Debye temperature (°K) Calc.	Exptl†
AgBr	Silver bromide	5·63	0·720	3·3	Huntington 1958	135	144
AgCl	Silver chloride	6·01	0·625	3·62	Huntington 1958	143	183
$C_6H_{12}N_4$	Hexamine	1·5	0·70	0·30	Ramchandran and Wooster 1951	130	
CaF_2	Fluorspar	16·44	3·47	5·02	Huntington 1958	500	474
CsBr	Caesium bromide	3·00	0·756	0·78	Bolef and Menes 1959	136	
CsI	Caesium iodide	2·46	0·624	0·67	Bolef and Menes 1959	115	
FeS_2	Pyrites	36·2	10·4	−4·4	Huntington 1958	703	645
		37·7	10·9	3·2	Prasad and Wooster 1956	710	
GaAs	Gallium arsenide	11·88	5·38	0·594	Bateman *et al.* 1959	314	
GaSb	Gallium antimonide	8·85	4·33	4·04	Huntington 1958	233	
						230 (de Launay)	
NaBr	Sodium bromide	3·87	0·97	0·97	Huntington 1958	211	
NaI	Sodium iodide	2·93	0·737	0·782	Eros and Reitz 1958	156	
NH_4Br	Ammonium bromide	2·96	0·53	0·59	Huntington 1958	177	
NH_4Cl	Ammonium chloride	3·90	0·68	0·72	Huntington 1958	270	
PbS	Galena	10·2	2·5	3·8	Huntington 1958	229	
RbBr	Rubidium bromide	3·17	0·388	0·42	Bolef and Menes 1959	129	
RbI	Rubidium iodide	2·56	0·287	0·31	Bolef and Menes 1959	102	100–118
TlBr	Thallium bromide	3·78	0·756	1·48	Huntington 1958	114	
TlCl	Thallium chloride	4·01	0·76	1·53	Huntington 1958	125	
V	Vanadium	19·6	6·7	13·5	Sándor and Wooster 1959	397	338
						394 (de Launay)	
ZnS	Zinc sulphide	10·0	3·4	6·5	Prince and Wooster 1959	309	

(ii) Hexagonal system

Formula	Substance	Elastic constants (in units of 10^{11} dyn cm^{-2})					Source	Debye temperature (°K)	
		c_{11}	c_{33}	c_{11}	c_{12}	c_{13}		Calc.	Exptl†
Be	Beryllium	30·8	35·7	11·0	−5·8	8·7	Gold 1950	1376	1160

(iii) Tetragonal system

		c_{11}	c_{33}	c_{44}	c_{66}	c_{12}	c_{13}			
In	Indium	4·45	4·44	0·655	1·22	3·95	4·05	Huntington 1958	78	109
$(NH_4)H_2PO_4$	Ammonium di-hydrogen phosphate	6·85	3·24	0·861	0·602	−0·18	1·78	Hearmon 1952	262	
KH_2PO_4	Potassium di-hydrogen phosphate	7·23	6·18	1·28	0·618	0·439	1·98	Hearmon 1952	237	
		7·35	8·7	2·2	2·265	2·34	2·8	Huntington 1958	196	
Sn	Tin	8·6	13·3	4·9	5·3	3·5	3·0	Prasad and Wooster 1955	258	195
		8·39	9·67	1·75	0·741	4·87	2·81	Huntington 1958	163	
TiO_2	Rutile	28·0	46·0	12·0	16·0	18·0	14·0	Vick *et al.* 1959	1184	

(iv) Trigonal system

		c_{11}	c_{33}	c_{44}	c_{66}	c_{13}	c_{14}			
$C_{14}H_{10}O_2$	Benzil	1·12	0·295	0·416	0·598	−0·098	−0·146	Chakraborty and Sen 1959	90	
$CaCO_3$	Calcite	13·74	8·01	3·42	4·67	4·50	−2·03	Huntington 1958	487	
$NaNO_3$	Sodium nitrate	8·67	3·74	2·13	3·52	1·60	0·82	Huntington 1958	453	

† Experimental Θ values are taken from *American Institute of Physics Handbook*, 1957 (New York: McGraw-Hill), pp. 4–47, 48.

§ 3. Results

The values of Θ and the elastic constants from which they have been calculated for a number of substances belonging to the various symmetry classes are presented in the table. The experimental Θ values derived from specific heat measurements are also shown wherever available.

§ 4. Discussion

In most of the cases Θ is calculated after the method of Betts *et al.* (1956 a, b). In some suitable cases, as indicated in the table, Θ has also been calculated from de Launay tables. For an accurate evaluation of Θ the values of elastic constants measured at about 0°K should have been used (Alers and Neighbours 1959). But in the absence of such data we have used elastic constants measured at ordinary temperatures which yield an approximate value of Θ.

Acknowledgments

The authors are deeply indebted to Professor K. Banerjee for his interest in the investigation and are thankful to Dr. A. B. Bhatia for helpful correspondence. One of the authors (S. S. M.) wishes to acknowledge the award of a senior research fellowship by University Grants Commission, Government of India.

References

Alers, G. A., and Neighbours, J. R., 1959, *Rev. Mod. Phys.*, **31**, 675.
Bateman, T. B., McSkimin, H. J., and Whelan, J. M., 1959, *J. Appl. Phys.*, **30**, 544.
Betts, D. D., Bhatia, A. B., and Horton, G. K., 1956 a, *Phys. Rev.*, **104**, 43.
Betts, D. D., Bhatia, A. B., and Wyman, M., 1956 b, *Phys. Rev.*, **104**, 37.
Bolef, D. I., and Menes, M., 1959, *Bull. Amer. Phys. Soc.*, **4**, 427.
Chakraborty, S. C., and Sen, R. K., 1959, *Bull. Nat. Inst. Sci.* (*India*), No. 14, 20.
Eros, S., and Reitz, J. R., 1958, *J. Appl. Phys.*, **29**, 683.
Gold, L., 1950, *Phys. Rev.*, **77**, 390.
Hearmon, R. F. S., 1952, *Brit. J. Appl. Phys.*, **3**, 120.
Hopf, L., and Lechner, G., 1914, *Verh. dtsch. phys. Ges.*, **16**, 643.
Horton, G. K., 1959, *Proc. Roy. Soc.* A, **252**, 551.
Horton, G. K., and Schiff, H., 1959, *Proc. Roy. Soc.* A, **250**, 248.
Huntington, H. B., 1958, *Solid State Physics* (New York : Academic Press), Vol. **7**, p. 213.
de Launay, J., 1956, *Solid State Physics* (New York : Academic Press), Vol. **2**, p. 286.
Prasad, S. C., and Wooster, W. A., 1955, *Acta Cryst.*, **8**, 682.
—— 1956, *Ibid.*, **9**, 169.
Prince, E., and Wooster, W. A., 1951, *Acta Cryst.*, **4**, 191.
Quimby, S. L., and Sutton, P. M., 1953, *Phys. Rev.*, **91**, 1122.
Ramchandran, G. N., and Wooster, W. A., 1951, *Acta Cryst.*, **4**, 431.
Sándor, E., and Wooster, W. A., 1959, *Acta Cryst.*, **12**, 332.
Vick, G. L., Hollander, L. E., and Brown, A. E., 1959, *Bull. Amer. Phys. Soc.*, **4**, 463.

The Half-value Period of Radium C′

By K. W. OGILVIE
University of Edinburgh†

Communicated by N. Feather; MS. received 29th January 1960, in final form 30th May 1960

§ 1. Introduction

In current lists of radioactive constants the half-value period of RaC′ is given as $163{\cdot}7 \pm 0{\cdot}1\,\mu$sec. This value is based upon a single accurate determination by von Dardel (1950a, b). Previously however, several experiments of lower accuracy had indicated a value of about $150 \pm 5\,\mu$sec. Both the 'integral' method of coincidence counting, in which the resolving time of the mixer circuit is varied, and the 'differential' or delayed coincidence method, were used. Information about these earlier experiments is set out in the table.

Author	Date	Method	Half-value period (μ sec)
Dunworth	1939	Integral β coincidence	150 ± 20
Rotblat	1941	Integral β coincidence	145 ± 5
Rotblat	1941	Integral γ coincidence	155 ± 20
Ward	1942	Integral (one counter)	148 ± 6
Jacobsen and Sigurgiesson	1943	Differential coincidence	155 ± 5

Von Dardel used an elaboration of the method of delayed coincidences whereby coincidence rates were recorded simultaneously for twenty different delays of the leading pulse, in this case that from the β-particle counter.

The investigation here described was carried out in Edinburgh during 1951 in order to find out whether the obvious discrepancy could be due to a small systematic error in the older determinations. A new experiment was performed by the integral method, paying careful attention to the electronic technique. It has been thought worth while to report briefly on this experiment, even after this lapse of time, chiefly because no other 'check' experiment of comparable accuracy has been described in the meantime. The result of the experiment was to confirm von Dardel's value.

§ 2. Description of the Experiment

Coincidences were detected between β-particles from RaC and α-particles from RaC′ using a simple arrangement of Geiger counters. The resolving time of the coincidence circuit was varied by altering the duration of the pulses fed to the mixer from the β-particle counter, the pulses in each channel being formed by trigger circuits. A paralysis circuit connected to each counter was adjusted so that the paralysis time introduced was long compared with the greatest pulse duration used in that channel. This was found to be of some importance, as

† Now at the F.B.S. Falkiner Nuclear Research Laboratory, Department of Physics, University of Sydney.

irregular firing of the trigger circuits could not then occur, and all pulses fed to the coincidence mixer were of the proper duration. The source, radium active deposit on an aluminium foil of thickness 11 mg cm^{-2}, was arranged in such a way that α-particles could not enter the β-particle counter.

If N atoms of RaC′ are formed per second, and the resolving time is $T(=T_\alpha+T_\beta)$, the genuine coincidence rate with such an arrangement is

$$N\epsilon_\beta\epsilon_\alpha\{1-\exp(-\lambda T_\beta)\}.$$

The efficiencies of the two counters, ϵ_β and ϵ_α, are supposed to include the solid angle factors, and T_β and T_α are the pulse durations in β and α channels respectively. If the possibility of emission by the source of two radiations in 'prompt' coincidence is included, and if for these radiations the efficiencies of the counters are ϵ_β', ϵ_α' respectively, the total coincidence rate becomes

$$R=(Nm\epsilon_\beta'\epsilon_\alpha'+N\epsilon_\beta\epsilon_\alpha)-N\epsilon_\beta\epsilon_\alpha\exp(\lambda T_\alpha)\exp(-\lambda T), \quad \ldots\ldots(1)$$

having the form $R=A-B\exp(-\lambda T)$. The quantity m is the number of prompt coincidences per disintegration of RaC′, and we discuss the meaning of $\epsilon_\beta'\epsilon_\alpha'$ below.

The experiment consisted of varying T_β, determining in a subsidiary experiment the resulting resolving time using two separate sources of β-particles, and fitting the coincidence rates observed with the radium source to an expression of the form given.

After the data from seven separate experimental runs had been combined and corrected for source decay the best fit to equation (1) was

$$R=\{4{\cdot}12-3{\cdot}60\exp(-4{\cdot}35\times10^3T)\}\times10^4.$$

The result for the half-value period is accordingly $t_{1/2}=159{\cdot}5\pm3\,\mu$sec.

The most likely small systematic error in the earlier experiments occurs in the generation of delays and resolving times by trigger circuits In the absence of paralysis of sufficient duration, two input pulses separated by less than the characteristic time of the circuit lead to the production of short output pulses, and this effect is in the correct direction to explain the discrepancy. If too few counts were recorded at the nominally larger resolving times during experiments by the integral method, the curve of coincidence rate against resolving time becomes distorted, since the maximum value N_0 corresponding to a large nominal resolving time, is reduced. The form of equation (1) is not then strictly appropriate, but in an experiment of moderate accuracy the best fit using such an expression leads to a value of λ which is too large.

The origin of the observed prompt coincidences must now be considered; they can hardly arise in the disintegration RaC→RaC′.

In the decay of RaB ($^{214}_{82}$Pb) three intense γ-rays are emitted from the excited ^{214}Bi nucleus, having energies 242, 295 and 352 kev. The total proportion of internal conversion electrons from these rays is (Nielson, Nielson and Waggoner 1956) $23\pm2\%$, of which 19% are K conversions. Instantaneous coincidences can be detected between the β-particles from RaB and photoelectrons or K x-rays as well as between photoelectrons and K x-rays themselves. Because a total thickness of 18 mg cm^{-2} Al had to be traversed in order to reach the β-particle counter few photoelectrons could be counted there. Most of the instantaneous

coincidences were therefore due to β-particles detected in the β counter and photoelectrons or K x-rays detected in the α counter; or K x-rays detected in the β counter and photo-electrons or β-particles in the α counter.

The number of instantaneous coincidences is thus given by the expression

$$Nm(\epsilon_{\beta\beta}'\epsilon_{\alpha p}'+\epsilon_{\alpha K}'\epsilon_{\beta\beta}'+\epsilon_{\alpha\beta}'\epsilon_{\beta K}'),$$

where $\epsilon_{\alpha p}'$, for example, means the efficiency of detecting photoelectrons in the α counter. Since $\epsilon_{\beta\beta}'=\epsilon_{\alpha\beta}'=\epsilon_\beta$ and also $\epsilon_{\alpha p}'\simeq\epsilon_\alpha$, we obtain

$$Nm\left[\epsilon_\alpha\epsilon_\beta\left\{1+\frac{\epsilon_{\alpha K}'+\epsilon_{\beta K}'}{\epsilon_\alpha}\right\}\right].$$

The terms inside the square bracket must be identified with $\epsilon_\beta'\epsilon_\alpha'$ in equation (1) so that

$$\frac{A}{B}-1=0{\cdot}14=m\left\{1+\frac{\epsilon_{\alpha K}'+\epsilon_{\beta K}'}{\epsilon_\alpha}\right\}$$

using the experimental results. As the ratio of efficiencies must be considerably less than unity, this lends support to the high values of internal conversion coefficient ascribed to the γ-rays emitted by RaB.

References

von Dardel, G., 1950 a, *Ark. Fys.*, **2**, 32, 337.

—— 1950 b, *Phys. Rev.*, **79**, 734.

Dunworth, J. V., 1939, *Nature, Lond.*, **144**, 152.

Jacobsen, J. C., and Sigurgiesson, T., 1943, *Det. K. Danske Vidensk. Selsk. Nat-Fys.*, **20**, 11.

Nielson, K. O., Nielson, O. B., and Waggoner, M. A., 1956, *Nucl. Phys.*, **2**, 476.

Rotblat, J., 1941, *Proc. Roy. Soc.* A, **177**, 260.

Ward, A. G., 1942, *Proc. Roy. Soc.* A, **181**, 183.

Knight Shift of the Nuclear Magnetic Resonance in Liquid Indium

By C. P. Flynn and E. F. W. Seymour

Department of Physics, University of Leeds

MS. received 12th April 1960, in final form 27th April 1960

Using a Pound–Watkins type of spectrometer and a conventional phase-sensitive detection system the nuclear magnetic resonances of ^{113}In and ^{115}In have been observed at a frequency of 5·50 Mc/s in finely divided liquid indium of purity 99·9%. The particle size was of the order of 40 μ, which is less than the skin depth under the conditions used. The resonances were detected both above the melting point (156°c) and in the supercooled state, but not in the solid metal. The peak-to-peak width of the derivative of the ^{115}In resonance was 2·3 gauss and that of ^{113}In was approximately the same. The signal amplitudes were about 200 and 10 times noise, respectively, in rough agreement with the isotopic abundances of 95·84% and 4·16%.

As was observed in an investigation of bismuth (Flynn and Seymour 1959) the amplitude of the resonance signal exhibited a thermal hysteresis below the melting point, the signal being observable in the range 125°c to 156°c only

while cooling from above the melting point. This corresponds to a supercooling which is a fairly general phenomenon among metals in finely divided states (Turnbull 1950). The fact that the range of supercooling observed here, expressed as a fraction of the melting temperature, was smaller than that (0·18 to 0·25) observed by Turnbull for any of the metals he investigated is unexplained. The fact that no resonance was observed in the solid is doubtless due to the existence in the solid of an electric quadrupole coupling amounting to about 45 Mc/s (Hewitt and Knight 1959).

The ratio of the frequencies of the ^{113}In and ^{115}In resonances at the same magnetic field was found to be $\nu(^{115}\text{In})/\nu(^{113}\text{In}) = 1{\cdot}00216 \pm 0{\cdot}00004$. This is in agreement with the ratio found in aqueous solutions of the nitrate and chlorate (Ting and Williams 1953, Rice and Pound 1957). The frequency of the ^{115}In resonance was compared with that of protons in glycerine in the same magnetic field. The ratio of these frequencies varied with temperature as shown in the table.

Sample	Temp. (°C)	$\nu(^{115}\text{In})/\nu(^{1}\text{H})$	Reference
$In(NO_3)_3$ solution	20	$0{\cdot}219101 \pm 0{\cdot}000013$	Ting and Williams (1953)
$In_2(SO_4)_3$ solution	20	$0{\cdot}219128 \pm 0{\cdot}000008$	This research
Indium metal	170	$0{\cdot}220850 \pm 0{\cdot}000007$	This research
Indium metal	223	$0{\cdot}220830 \pm 0{\cdot}000009$	This research
Indium metal	360	$0{\cdot}220797 \pm 0{\cdot}000012$	This research

Also shown in the table is the corresponding ratio found by Ting and Williams (1953) for an aqueous solution of indium nitrate. Partly in order to guard against possible systematic errors arising from differences in apparatus, and partly to check that any chemical shift in the nitrate solution is not untypical, measurements of the ^{113}In and ^{115}In resonances were made in solutions of indium sulphate. Although the width of the ^{115}In resonance was concentration dependent, being 3·2 gauss for a 10% molar solution and 7·8 gauss for a 20% solution, the frequency of the resonance appeared to be independent of concentration. (No useful measurements of the width of the weaker ^{113}In resonance could be made.) Proctor and Yu (1951) observed a similar change of width with concentration for a solution of the nitrate and attributed the effect to a changing degree of dissociation.

The shift of the resonance in the liquid metal with respect to that in the sulphate solution is $[0{\cdot}786 \pm 0{\cdot}007 - (14 \pm 3) \times 10^{-5}(T - 170)]$ per cent in the range $170°\text{C} < T < 360°\text{C}$. This is assumed to be mainly a conduction electron shift (Knight 1956), but there is a possibility of a contribution due to a chemical shift in the solution. Any such chemical shift may well be a small effect since it appears insensitive to degree of dissociation and to change of chemical composition. The conduction electron shift is comparable with those observed for metals with similar atomic numbers. The temperature dependence, which is similar to that for liquid gallium and caesium (Gutowsky and McGarvey 1953), may be attributed to the effects of thermal expansion on the spin susceptibility of the conduction electrons, and on the probability density at the nucleus of the conduction electrons at the Fermi surface, both of which quantitites appear as factors in the theoretical expression for the Knight shift. The sign and order of magnitude of the temperature coefficient are accounted for if the spin

susceptibility is proportional to (volume)$^{2/3}$, as it would be for free electrons, and if the probability density depends on volume solely through the requirement of normalization of the conduction electron wave function.

Acknowledgments

We wish to thank the Royal Society for a grant which assisted this work. One of us (C. P. F.) wishes to thank the Department of Scientific and Industrial Research for a maintenance allowance.

References

Flynn, C. P., and Seymour, E. F. W., 1959, *Proc. Phys. Soc.*, **73**, 945.
Gutowsky, H. S., and McGarvey, B. R., 1953, *J. Chem. Phys.*, **21**, 2114.
Hewitt, R. R., and Knight, W. D., 1959, *Phys. Rev. Letters*, **3**, 18.
Knight, W. D., 1956, *Solid State Physics*, **2**, 93.
Proctor, W. G., and Yu, F. C., 1951, *Phys. Rev.*, **81**, 20.
Rice, M., and Pound, R. V., 1957, *Phys. Rev.*, **106**, 953.
Ting, Y., and Williams, D., 1953, *Phys. Rev.*, **89**, 595.
Turnbull, D., 1950, *J. Appl. Phys.*, **21**, 1022.

Note on the behaviour of a Vapour–Liquid System above and below the Critical Point†

By P. H. E. Meijer

Physics Department, Catholic University of America, Washington, D.C.

MS. received 1st *February* 1960, *in revised form* 5th *April* 1960

Abstract. On the basis of the van der Waals equation we show that the maxima in the specific heat at constant pressure (infinite below the critical point and finite above) lie on one continuous line through the critical point. Experimental data fit the curve, above as well as below the critical point, although the van der Waals equation is known to be not entirely correct. The calculation is based on the rules of Ehrenfest for higher order transitions and does not make use of the caloric properties of the substance.

The persistence of a kind of transition above the critical point, experimentally confirmed by Jones and Walker (1956) as a large maximum in the specific heat at constant pressure, is considered on the basis of the van der Waals equation. It is shown that this phenomenon lies on a line that is a 'smooth' extension of the vapour–liquid line in the (pressure, temperature) diagram below the critical point, i.e. the curve has no discontinuity in its derivative at the critical point.

The equation of state of van der Waals is

$$\{P+(N^2a/V^2)\}(V-Nb)=N\boldsymbol{k}T \qquad \ldots\ldots(1)$$

† This research was supported by the U.S. Air Force through the Air Force Office of Scientific Research, Air Research and Development Command.

where N is the number of molecules per mole, b and a are two constants. The first is the volume occupied by the atoms. (One supposes that the force law has a hard core.) The second is related to the attractive part of the potential as pointed out for instance, by Hill (1948, 1951).

We may characterize, according to Smoluchowski (1908), the critical point as the point for which we have an inflection point with horizontal tangent

$$\left(\frac{\partial P}{\partial V}\right)_{T=T_c} = 0 \quad \ldots\ldots (2); \qquad \left(\frac{\partial^2 P}{\partial V^2}\right)_{T=T_c} = 0 \quad \ldots\ldots (3)$$

although the connection with the disappearance of the meniscus is lost in this way. If we introduce

$$\tau = \frac{T - T_c}{T_c} \; ; \; \pi = \frac{P - P_c}{P_c} \; ; \; x = \frac{V - V_c}{V_c} \qquad \ldots\ldots (4)$$

we have for the equation of state

$$3x^3 + \pi(1+x)^2(2+3x) - 8\tau(1+x)^2 = 0. \qquad \ldots\ldots (5)$$

(*a*). *The region below the critical point.*

This equation has three different real roots for x only if π and τ are both negative. In order to determine the vapour–liquid line $P = P(T)$ we have to apply Maxwell's rule (see, for instance, Hirschfelder, Curtiss and Bird 1954). One characteristic of $x^3 = 0$, i.e. $(V - V_c)^3 = 0$ is its antisymmetry and this property will be preserved for values of the parameters π and τ in the neighbourhood of zero†. In order to bring this out, we lower the origin by substituting $\pi = \pi' + \pi_1$. We find the curve (that is, the value of the parameter τ) which goes through this point by assuming that *one* of the roots is still approximately zero

$$x = 0 \rightarrow \pi_1 = 4\tau, \qquad \text{i.e. } \pi = \pi' + 4\tau;$$

substituting this in (5) we find in the neighbourhood of the critical point (π' and τ small permits one to disregard the higher powers of x in these terms)

$$2\pi' = 2\pi - 8\tau = -3x^3 - 12\tau x. \qquad \ldots\ldots (6)$$

It is obvious that the horizontal line prescribed by the principle of Maxwell is

$$\pi' = 0 \quad \text{or} \quad \pi = 4\tau \qquad \text{(both negative)}. \qquad \ldots\ldots (7)$$

This determines the slope of the vapour–liquid curve in the critical point.

(*b*). *Above the critical point.*

We first discuss the criterion used to determine the 'continuation of the vapour–liquid curve'. From experimental data, the maximum of C_p could be used as a criterion, but this cannot be derived from the equation of state unless an additional assumption about C_v is made, i.e. C_v has a monotonic behaviour.

It seems more natural to base our considerations on the Gibbs function $G = G(T, P)$. The equation of state is one of the results derived from this function. Below the critical point the two first derivatives are discontinuous (a transition of the first order in Ehrenfest's (1933) formulation).

Above the critical point the result mentioned above can be formulated as a 'strong variation in the third derivative' or a 'smoothed-out third-order transition'. However, these statements contribute more to semantics than to

† Careful analysis of the experimental data of isotherms near the critical point shows that the power is actually closer to 4 than to 3 (Widom and Rice 1955).

physics. On the other hand the importance of the Ehrenfest classification is that if *one* of the nth derivatives undergoes a strong variation, all the other thermodynamic quantities which are derivatives of G of the same order will behave similarly.

From the experiments of Jones and Walker (1956) we see that C_p has a sharp peak as a function of T at certain temperatures and pressures above the critical point. We want to consider this as a peak of

$$\frac{C_p}{T} = \left(\frac{\partial S}{\partial T}\right)_P = -\left(\frac{\partial^2 G}{\partial T^2}\right)_P, \qquad \ldots\ldots(8)$$

instead of C_p, since this is connected with the derivative of a thermodynamic property. We will characterize the locus of points $P = P(T)$ above the critical point by stating that $(\partial^3 G/\partial T^3)_P$ undergoes a strong variation (although not really a discontinuity), i.e. in the Ehrenfest terminology we would have a smoothed out transition of the third order. This implies that the other derivatives

$$\frac{\partial^3 G}{\partial P \partial T^2} = \left(\frac{\partial^2 V}{\partial T^2}\right)_P; \quad \frac{\partial^3 G}{\partial P^2 \partial T} = \left(\frac{\partial^2 V}{\partial P \partial T}\right)_{P,T} \text{ and } \frac{\partial^3 G}{\partial P^3} = \left(\frac{\partial^2 V}{\partial P^2}\right)_T, \qquad \ldots\ldots(9)$$

undergo similar variations. The third derivative of G with respect to T can only be found if the caloric equation is known, which is usually not the case, but the previous three depend on the equation of state only. The maxima in $C_p - C_v$ are also expressible in the equation of state but this needs the *assumption* that C_v behaves uneventfully in the neighbourhood of these points in the (P, T) plane in order to draw conclusions about C_p.

If we consider $\partial^2 V/\partial P^2$ we find from (6):

$$\left(\frac{\partial^2 x}{\partial \pi^2}\right)_\tau = -8[3(3x^2 + 4\tau)^3]^{-1} \qquad \ldots\ldots(10)$$

which for $\tau \to 0$ has a discontinuity of type x^{-1} at $x = 0$. Substitution of $x = 0$ into (7) gives

$$\pi = 4\tau \qquad \ldots\ldots(11)$$

which gives us the slope of the locus. If we consider this 'transition' as continuation of the ordinary phase transition below the critical point, we find that the locus is continuous, i.e. has no kink, in accordance with the experimental results.

The three derivatives (9) can be obtained from (5) directly and a rather tedious calculation shows that they all have a sharp maximum near $x = -2\tau$. Substituting this approximation in the equation of state we find that the locus in second approximation is given by

$$\pi = 4\tau(1 + 3\tau) \qquad \ldots\ldots(12)$$

which represents the experimental curve of Jones and Walker satisfactorily. The second approximation is an important check since the previous result (11) could have been purely accidental.

We would like to make a final remark on the criterion used for the extension of the phase transition above the critical point. Since the critical point is usually characterized by equations (2) and (3), which imply that $\partial^2 V/\partial P^2 = 0$, we tried to use the latter to characterize the locus; this does not give the right result in higher approximation, neither did the generalizations of $\partial V/\partial T = 0$ as proposed by Rice (1955). The correct result is obtained by looking at points where the

expression undergoes large 'variations', which comes closer to the idea of transitions than demanding that either one or the other of the above expressions be equal to zero.

References

Ehrenfest, P., 1933, *Proc. Kon. Akad., Amsterdam,* **36,** 153.
Hill, T., 1948, *J. Chem. Educ.*, **25,** 347.
—— 1951, *J. Chem. Phys.*, **19,** 261.
Hirschfelder, J. O., Curtiss, C. F., and Bird, R. B., 1954, *Molecular Theory of Gases and Liquids* (New York : J. Wiley) p. 364.
Jones, G. O., and Walker, P. A., 1956, *Proc. Phys. Soc.* B, **69,** 1348.
Rice, O. K., 1955, *Thermodynamics and Physics of Matter,* Ed. F. D. Rossini (Princeton: University Press), § E, p. 445.
Smoluchowski, M. V., 1908, *Ann. Phys., Lpz.*, **25,** 205.
Widom, B., and Rice, O. K., 1955, *J. Chem. Phys.*, **23,** 1250.

LETTERS TO THE EDITOR

Paramagnetic Resonance Spectrum of Dysprosium in the Cubic Field of Calcium Fluoride

Bleaney (1959) has recently suggested that some rare earth ions with an odd number of electrons and ground state $J \geq 5/2$ may have as their lowest level a fourfold degenerate Γ_8 state in a cubic crystal field. In an external magnetic field the Γ_8 state splits into four levels which, in general, are not equidistant. This suggests that these ions may be suitable for a three level Bloembergen type maser (Bloembergen 1956). Bleaney suggested ions such as Ce^{3+}, Nd^{3+} and Dy^{3+}.

We have recently measured the spectrum of Ce^{3+} in a single crystal of calcium fluoride (Dvir and Low 1960). We have shown that indeed the lowest level is the Γ_8 state and that it behaves essentially like the $J=5/2$ level in which the initial splitting between the quartet and doublet is larger than the Zeeman splitting. We have also tried to measure the spectrum of Nd^{3+} in calcium fluoride and have observed a number of new lines. However, in the main our crystals contained ions situated in a crystal field of axial symmetry.

We should like to report here the spectrum of dysprosium in calcium fluoride. The spectrum was measured at 20°K and at a frequency of 8766·7 Mc/s. One isotropic line was observed with half-width of about 30 gauss with $g = 7{\cdot}47 \pm 0{\cdot}03$. There is some indication that the line is broadened by spin–lattice relaxation. The large line width and the poor signal-to-noise ratio did not permit an accurate measurement of the hyperfine components. Some of these, principally isotope ^{163}Dy, were detected.

The ground state of dysprosium is $^6H_{15/2}$. In the cubic field of calcium fluoride these levels split up into three quartets (Γ_8) and two doublets (Γ_6 and Γ_7) (Judd 1957). The experimental g-factor can be fitted to that of the Γ_7 doublet. This doublet can be approximated by

$$\alpha\Psi(J=\frac{15}{2},J_z\ldots)+(1-\alpha)\Psi(J=\frac{13}{2},J_z\ldots)$$

where

$$\Psi(J=\frac{15}{2},J_z\ldots)=\left(\frac{77}{192}\right)^{+1/2}|J_z=\pm\frac{13}{2}\rangle-\left(\frac{65}{192}\right)^{+1/2}|J_z=\pm\frac{5}{2}\rangle$$
$$-\left(\frac{39}{192}\right)^{+1/2}|J_z=\mp\frac{3}{2}\rangle+\left(\frac{11}{192}\right)^{+1/2}|J_z=\mp\frac{11}{2}\rangle$$

and $\Psi(J=13/2,J_z)$ has the same form.

The admixture from the next higher levels is caused by intermediate coupling. If breakdown of Russell–Saunders coupling is neglected ($\alpha=1$) the computed g-factor is 17/3 Λ or 7·555. The deviation of the g-factor by about 1% is probably caused by the intermediate coupling from the $J=13/2$ level which is only about 3000 cm^{-1} above the $J=15/2$ level.

The signal-to-noise ratio of better than 15 : 1 indicates that most of the dysprosium ions are situated at cubic lattice sites. It also indicates that the next Γ_8 level must be removed by at least 50°K from the Γ_7 level. Contrary to the suggestion by Bleaney this ion is, therefore, not suitable for a Bloembergen type maser.

This work was supported in part by the United States Air Force, Research and Development Command, through its European Office.

W. Low.

Department of Physics,
Hebrew University,
Israel.
25th February 1960.

Bleaney, B., 1959, *Proc. Phys. Soc.*, **73**, 937.
Bloembergen, N., 1956, *Phys. Rev.*, **104**, 324.
Dvir, M., and Low, W., 1960, *Proc. Phys. Soc.*, **75**, 136.
Judd, B. R., 1957, *Proc. Phys. Soc.* B, **70**, 880.

Magnetic Resonance and Magnetocrystalline Anisotropy in Ytterbium Iron Garnet

This letter reports anomalous effects which have been noted in measurements on ytterbium iron garnet, $Yb_3Fe_5O_{12}$. The single crystals used were grown by the flux method by Mr. J. Page of these laboratories.

Ferrimagnetic samples exhibit resonant absorption of microwave energy with a maximum, as a function of applied static magnetic field, at H_r. Figure 1 shows the variation of H_r with temperature for a small, polished, spherical, single crystal specimen of ytterbium iron garnet with H_r applied in a [100] crystallographic direction and in a [111] direction. The frequency concerned was 9400 Mc/s. Below 220°K there is a sharp drop in H_r [111] whereas H_r [100] varies only slowly. Curves relating to other directions in a (110) plane lie between the curves illustrated.

Similar measurements using a microwave frequency of 17 000 Mc/s gave qualitatively similar results. Above about 220°K the difference,

$$H_r[100] - H_r[111],$$

is the same at the two frequencies, but below this temperature the difference at the higher frequency becomes greater, rising to 2160 oersteds at 140°K.

According to the normal interpretation of microwave resonance at a single frequency $H_r[111] - H_r[100] = 10\,K_1/3M$ where all but the first-order magnetic anisotropy constant are neglected. The g-factor can then be determined from $\omega/\gamma = H_r[100] + 2\,K_1/M$ where $\gamma = ge/2mc$. Values for K_1 for ytterbium iron garnet derived in this way have been reported (Jones, Rodrigue and Wolf 1958).

Such an interpretation of the measurements reported here leads to a rapid rise in the magnitude of K_1 (as in Jones *et al.* 1958) and g below 220°K. Also the values for these two parameters calculated from the measurements at 9400 Mc/s diverge below this temperature from the values deduced from the 17 000 Mc/s measurements.

K_1 has also been measured by one of us (R.F.P.) by the static torque method. The values are in agreement with those obtained as described only above 220 K. Below this temperature the rapid increase in the magnitude of K_1 is not observed. Throughout the temperature range covered by figure 1, K_1 increases roughly linearly with reducing temperature and at 130 K K_1/M is only -160 oersteds,

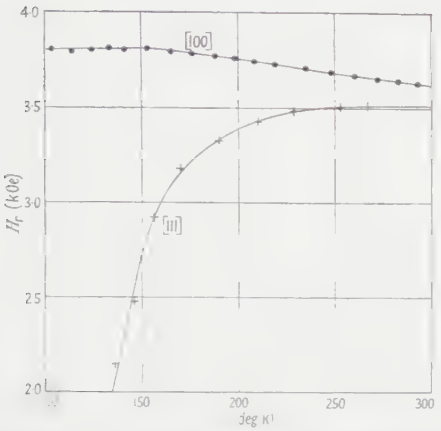

Figure 1. H_r plotted against T. Frequency 9400 Mc/s.

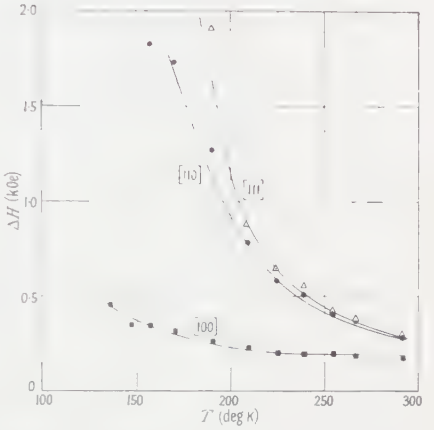

Figure 2. ΔH plotted against T. Frequency 9400 Mc/s.

compared with -600 oersteds and -810 oersteds deduced by the conventional method from the measurements at 9400 Mc s and 17 000 Mc/s respectively.

This suggests that the rapid fall in H_r [111] (and all directions other than [100]) below 220 K is not due to anisotropy in the magnetocrystalline energy but to some other effect associated with the microwave resonance phenomenon.

Figure 2 shows values of the magnetic resonance line width ΔH measured at 9400 Mc s, as a function of temperature. ΔH becomes increasingly anisotropic as the temperature is reduced, with ΔH [100] much narrower than for other crystallographic directions. It seems reasonable to suggest that the effect which causes the reduction in H_r in directions other than [100] is also associated with the broadening of the resonance line in these directions.

It has been shown (Kittel 1959) that when the rare earth sub-lattice is heavily damped H_r can be increased considerably in the rare earth garnets; the increase being greater as the temperature is reduced from room temperature. If, as is reasonable, it is assumed that in ytterbium iron garnet the effect of the rare earth sub-lattice upon resonance is greatest in directions other than [100], the reduction of H_r in these directions reported here is contrary to the effect produced by the mechanism treated by Kittel.

If the resonance properties observed in the [100] direction are assumed to be normal and those in other directions anomalous, the g-factor can be deduced from H_r [100] at the two frequencies, using the relationship $\omega = \gamma(H_r + H_e)$ where $H_e = 2K_1/M$. The g-factor deduced is $1{\cdot}87 \pm 0{\cdot}02$ with no significant variation with temperature throughout the range 300°K to 130°K. Values for K_1/M deduced from H_e are in reasonable agreement with those measured by the static method throughout this temperature range. For the [111] direction a similar comparison does not show any such agreement, thus confirming the assumptions stated at

the beginning of this paragraph. Hence the present measurements show that K_1 for ytterbium iron garnet is much smaller than previously reported below 200°K.

The authors believe that the anomalous anisotropic resonance behaviour of ytterbium iron garnet is novel. The effect may be associated with the anisotropy in the exchange interaction between the ytterbium and iron sub-lattices already noted (Wickersheim and White 1960).

A more detailed description of the phenomenon will be published shortly.

Mullard Research Laboratory,
Cross Oak Lane,
Salfords, Nr. Redhill,
Surrey.
6th May 1960.

R. F. Pearson.
R. W. Teale.

Jones, R. V., Rodrigue, G. P., and Wolf, W. P., 1958, *J. Appl. Phys.*, **29**, 434.
Kittel, C., 1959, *Phys. Rev.*, **115**, 1587.
Wickersheim, K. A., and White, R. L., 1960, *Phys. Rev. Lett.*, **4**, 123.

REVIEWS OF BOOKS

Theory of Elementary Particles, by J. HAMILTON. Pp. xii + 482. (Oxford: Clarendon Press, 1959.) 75*s*.

This book deals with a branch of theoretical physics that has grown up from small beginnings since the end of the war. One who remembers the state of the subject in pre-war days is struck first by the sheer mass of this work. According to the author the book is intended to give an account of 'the basic methods and concepts' of high-energy physics and indeed, the many and extensive footnotes bear witness to the fact that this is a condensation of even more extensive material. Thus the research student, for whom the volume is primarily intended, will almost certainly find either a detailed treatment or a most adequate set of references to any subject of enquiry, except for developments too recent to have been included. To the reviewer's knowledge there is no other single volume on the subject—and the literature is by now becoming quite extensive—in which so much is covered.

The book opens with an introductory chapter on classical fields, as is customary, but the content of this chapter is notably different from the conventional in including physically oriented sections on the propagation of high energy particles through matter (optical disc and sphere). The following chapters II–IV deal with the quantization of boson fields, the Dirac equation, and the quantization of fermion fields. Each of these chapters goes rather further than one might expect from its title. Thus among other things one finds a full treatment of the problems connected with low-energy photons in chapter II, a discussion of parity violation, two component theory etc. in chapter III, and accounts of both perturbation and Tamm–Dancoff methods in chapter IV. Chapter V is devoted to a treatment of S-matrix and renormalization theories and is followed by chapter VI on 'Heisenberg operators and pion–nucleon scattering', in which Chew–Low techniques are given prominence. This chapter also introduces one to the concept and use of dispersion relations. Here above all, the author cannot escape the consequences of writing on a subject undergoing spectacular development. No doubt these sections will look very different in any future edition of the book.

The following chapter is headed 'Selection rules', and discusses the important role of symmetry relations such as time reversal, CTP theorem etc. This is also the point at which the reader is first introduced to strange particles in general.

Perhaps the outstanding single feature of this work is the next chapter on 'Polarization analysis'. Here the author has succeeded in presenting in a most clear and systematic manner all the basic formulae on polarization which are so essential for the analysis of experiments. To the reviewer's knowledge no comparable account has been published hitherto.

The concluding chapter has the title 'Foundations of field quantization' and discusses in some detail the Schwinger and Feynmann principles. It is followed by an appendix on Green's functions and invariant functions.

Although the graduate student would be brave to sit down and attempt to master the contents of this book in one attack, it is a work that both he and the more senior worker will doubtless have many an occasion to turn to for a good few years to come.

N. KEMMER.

Theory of Relativity, by W. PAULI. Translated by G. FIELD. Pp. xiv + 241. (London, New York, Paris, Los Angeles: Pergamon Press, 1958.) 35*s*.

It is an outstanding tribute to Pauli's eminence in theoretical physics that his article published in German in 1921 should now appear in English translation. It is also a wry comment on the lack of any major progress in the subject in 38 years.

In the part dealing with the special theory the lapse of time has made hardly any difference. Pauli's brilliant mathematical treatment is combined with a discussion of the physical foundations of the theory which is, to the advantage of the book, much fuller than most present-day writers would regard as necessary.

Although the treatment of the general theory is of a like level of distinction, the subtle change in attitude that has occurred in the 38 years since it was written robs this part of some of its freshness. Naturally the great effort that has gone into quantization is not mentioned in the body of the book, but it is disappointing that the supplementary notes do not discuss it either. Similarly, neither gravitational waves nor gravitational energy is now considered to be the simple subject the reader of this book might be led to believe. The supplementary note on the equations of motion is so brief as to be disappointing. Against these disadvantages must be put a clarity of understanding of the foundations that can be looked for in vain in most more recent presentations of the theory. The cardinal role of the principle of equivalence and the comparatively minor significance of the general principle of covariance are so well brought out that it is a joy to read the book for these parts alone.

Dr. G. Field's translation is outstandingly good. H. BONDI.

Theoretical Elasticity, by CARL E. PEARSON. Pp. xii + 218. (Harvard: University Press; London: Oxford University Press, 1959.) 48*s*.

The aim of the author of this book is to provide " a compact and convenient summary of methods and results in the field of theoretical elasticity." Chapters 1 and 2 introduce vectors and Cartesian tensors, which are then used in a detailed treatment of the elementary theory of stress (chapter 3) and deformation (chapter 4). With increasing speed the author next outlines the basic theory of elastic solids (chapter 5) and the methods of obtaining general solutions associated with the names of Betti, Kelvin, Boussinesq, Galerkin and others (chapter 6). Chapter 7 deals in an abstract way with variational methods and chapter 8 with the elastic constants when temperature change is taken into consideration. The book closes with brief chapters on time-dependent problems and non-linear elasticity.

The book is very uneven in treatment, with much space devoted to topics foreign to its subject while important results needed in the argument are merely quoted or verified. In the mathematics there are many careless or inadequate statements. The author's habit of giving a general argument, without pointing out its purpose, physical significance, or any application, makes for hard reading. In general the references are few and insufficient.

But much of the material is of great interest and previously not to be found in book form. Although the book cannot be recommended to the beginner, a reader with knowledge of the subject will find it stimulating.

E. R. LAPWOOD.

Topics in Electromagnetic Theory, by DEAN A. WATKINS. Pp. ix + 118. (New York: John Wiley; London: Chapman and Hall, 1958.) 120*s*.

The major part of this short book is concerned with the electromagnetic field problems which arise in the theory of microwave valves. Its principal merit is that it gives an excellent account of the properties of the periodic structures which play such an important part in travelling wave tubes, backward wave oscillators, etc. The treatment is at the level appropriate to a student with some knowledge of electromagnetic theory beginning a study of this subject. The mathematical details are elegantly presented and are illustrated by physical arguments where appropriate. The second chapter on the properties of the helix is particularly useful in that it gives a simple, yet comprehensive, account of this widely used structure.

A second objective of the book is to emphasize the essential similarity of the theoretical treatments of diverse branches of microwave engineering. In this, the author is much less successful, the discussion of, for example, the helical aerial being much less complete than one would desire. The last chapter on ferrites and their microwave applications is also rather sketchy and can be regarded as no more than a very brief introduction.

The first three-quarters of the book, in which the author is dealing with his own special subject are excellent and can be strongly recommended as an introduction to the theory of microwave valves. J. BROWN.

Radiation Biology and Medicine, edited by W. D. CLAUS. Pp. xx + 941. (Reading, Massachusetts: Addison-Wesley; London: Pergamon Press, 1958.) 87*s*.

This encyclopaedic survey, prepared for the United States Atomic Energy Commission, deals firstly with the biological effects of radiation and secondly with the uses of radiation in medical, agricultural and biochemical research.

Radiation (taken here to comprise x-rays, γ-rays and sub-atomic particles) is unique among physical agencies in the variety of its effects at every level of biological organization from the single molecule to the entire species. These effects are discussed in eighteen chapters which make up roughly half of the book. R. L. Platzman's lucid account of the basic processes in the interaction of radiation with living matter provides a foundation for other contributors who discuss the responses of cells, tissues and organs. H. J. Muller introduces a group of essays on the genetic effects of radiation, with particular reference to human populations. A great deal of information is expertly summarized, though no attempt is made at any numerical assessment of the hazards resulting from fall-out, hospital x-rays or other man-made radiations. Injuries to the individual from internal or external radiation sources are discussed in some detail and four chapters are devoted to the control of radiation hazards.

The second half of the book begins with a short and useful review (by D. J. Rosenthal and J. H. Lawrence) of the uses of radioactive isotopes in the study and treatment of disease. M. Brucer discusses the value of ^{60}Co and other long-lived γ-emitters in the treatment of cancer and L. E. Farr writes briefly on the medical uses of nuclear reactors, describing several American projects still at early stages of development. The role of high-energy accelerators in medical and biological research is also explained.

The many important and fruitful applications of isotope techniques in biochemistry receive proper attention. These topics are heavy going for the physicist, though the historical intermissions help to make the picture clearer. Applications in soil science and in entomology provide interesting chapters of less specialized nature.

Most of the 56 contributors write in a plain style, making their points clearly without recourse to jargon. Nearly every chapter is followed by a long bibliography. Many scientists now have a personal or professional interest in the biological effects of radiation; they will find this book useful both for occasional reference and for leisurely study. J. M. A. LENIHAN.

Progress in Nuclear Physics, Vol. 7, edited by O. R. FRISCH. Pp. vii + 326. (London, New York, Paris, Los Angeles: Pergamon Press, 1959.) 84*s*.

This is the most recent in a series of annual volumes that come out about every eighteen months. The series meets a need. The need is for articles written by professionals in nuclear physics to explain their branch to professionals in other branches of nuclear physics. Too often review articles are intra- rather than inter-branch; written by thundering virtuosi they exhaust the subject and the reader alike, they synthesize and extrapolate and are submitted in support of candidature for academic renown. But they do not persuade that physics is interesting. Frisch from the beginning of his series has insisted that his authors inform without blinding and excite without prestidigitation. By and large he and they succeed in this volume as in its predecessors.

D. V. Bugg writes a useful article to show how rapidly the bubble chamber is expanding. (Not so useful in his remark, having just discussed deuterium, that helium is the lightest atom of $T=0$.) F. R. Metzger writes an excellent article on the theory and techniques of resonance fluorescence. B. G. Harvey broadens the scope with an almost persuasive article on spallation, a subject so complicated that only chemists venture to tackle it. A. E. Glassgold's article on the optical model is indeed a model: starting, as all best guides, with ' un peu d'histoire ' it takes us to the present state of the art quickly and in almost narrative form—a feat all but concealing that the number of the parameters exceeds the number of papers written. Finally, two parity-violating articles: ' Measurement of Helicity ' by L. Grodzins and ' Weak Interactions ' by J. J. Sakurai; they have been well correlated and their overlap is small and unexceptionable. The first of the pair is concerned with techniques for measuring the screw-sense of electrons and photons. It will be of the greatest usefulness and is very timely. Let us note sadly that left-circularly polarized gamma rays and right-circularly polarized optical photons have identical definitions—clearly one or other of them should be observed only in a mirror and/or the front of the other (or the one) should be labelled ' back ' (to avoid confusion). The second of the pair is a fascinating review of the recent exciting developments culminating in the striking success of universal V–A. (By dramatic chance additions in proof just catch $\pi \rightarrow e + \nu$.) This article is happily and humanely composed: it refers to the eastern tradition, etymology, snails, the old days, poverty, legend, garbage, innocence, Lord Kelvin and God.

The volume is well balanced and well produced. For this editor and publishers deserve credit. But neither will get any for the shocking puff ' The Leading International Review Series in Nuclear Physics ' that claims the middle of the dust jacket. We are not buying toothpaste. D. H. WILKINSON.

Handbuch der Physik, Vol. XXXVIII 2, *Neutrons and Related Gamma Ray Problems*, edited by S. FLÜGGE. Pp. vi+868. (Berlin: Springer, 1959.) DM. 178.

The juggernaut continues. This volume contains two articles the first of which, 'The Production and Slowing Down of Neutrons' by E. Amaldi, is a large book of 660 pages; the second, 'Penetration and Diffusion of X-Rays' by V. Fano, L. V. Spencer and M. J. Berger is a mere lengthy monograph.

It must be said at once that Amaldi's article is astonishingly readable. The subject does not look very promising and could be—indeed has been—written up with excruciating dullness, but Amaldi has struck a happy blend of detail and narrative, experiment and theory that make the search for information in it a pleasure, even though one may succeed in putting it down before getting to the end. An introductory section has the right balance between history and later exactness, and in fact is within itself an excellent short monograph that would be of considerable use in, say, undergraduate teaching, if available separately. It is, alas, lost. Later sections deal with: Reactions with emission of neutrons and neutron sources; The slowing down of neutrons of energy larger than a few ev; Slowing down and diffusion of neutrons in the chemical region, i.e. E less than or of the order of 1 ev; The diffusion of thermal neutrons. Amaldi's over all approach is experimental but there is considerable theoretical detail in the sections on slowing down and diffusion—no sophisticated problems but an excellent grounding for someone moving into reactor physics. It is very fitting that this considerable work should have come from a member of the great Rome team of the early 30's and should have been written from Rome.

The penetration and diffusion of x-rays is an exceedingly complex problem. In the analogous problem for neutrons one is helped by one's ignorance of the fine details of the elementary cross sections and so may justifiably use approximations. With x-rays however, at least those of low energy, one believes that the fundamental processes are well understood and so all that stands in the way of an exact solution is mortality. The situation is aggravated by the fact that the solutions to the elementary processes themselves, although exact, are frequently not analytic or at least not tractably so. Fano and his group at the Bureau of Standards in Washington have for many years hammered dedicatedly at this problem or nest of problems. This article describes how, though the problem has not been broken, it has been beaten, into shape. Successive sections discuss: Elementary processes; General theory; Calculation of flux distributions in infinite homogeneous media; Effects of boundaries and inhomogeneities; Experimental aspects. For so complex a subject the writing is very clear. This article contains very little light relief but it is surely appropriate that a work with so grim and forbidding a title as 'A million random digit numbers with 100000 normal deviates' should be published from a place called Glencoe. (Back in 1692 there were only about 200 normal deviates.) D. H. WILKINSON.

Die Methoden der Molekülphysik und ihre Anwendungs Bereiche, by H. PREUSS. Pp. vi+167. (Berlin: Akademie-Verlag, 1959.) DM.22.

This book sets out to describe all the main methods used in the application of wave mechanics to the calculation of the electronic structure and other properties of molecules. There is an enormous amount of material, dealing with both σ and π bonds, but in order to compress it within 167 pages,

Dr. Preuss has found it necessary to omit much of the detailed analysis. He also starts by presupposing a basic knowledge of the wave equation and its main principles. As a result the book is not easy reading. But it contains a good deal of material not yet found in other similar textbooks. Thus Moffitt's method of atoms-in-molecules, the theory of the density matrix, the free-electron model, and Löwdin's natural spin orbitals are all described and illustrated. In nearly every case tables of numerical magnitudes are given to show the degree of success obtained by the particular technique being considered. In this respect the book is likely to prove very useful, particularly to those who already have some knowledge in this field. It would have been even more useful if it had been provided with an index. C. A. COULSON.

Physics and Philosophy, by W. HEISENBERG. Pp. 176. (London: Allen and Unwin, 1958.) 15*s*.

Although we are still very much engaged in the making of modern physics and realize at each successive step that the development which began roughly with this century shows no sign of slackening, we are already interested in its history. A survey of achievement so far, and of its philosophical implications, by one of the main architects of the—admittedly unfinished—edifice is bound to command attention.

The present volume contains the substance of the Gifford Lectures delivered by Professor Heisenberg in St. Andrews in 1955–56. The great successes gained by physics in the past half century permit the author the luxury of being clear without being dogmatic, a most refreshing combination which the full-time philosopher can nowadays rarely afford. In most of the chapters Heisenberg simply thinks aloud, taking sides here and there, giving his reasons for doing so, but never being too sure that his opinion is final. Sometimes, as in the chapters on the Copenhagen interpretation of the quantum theory, he is personally involved and he lets his reader know it whereas in others, as for instance in that on relativity, he adopts a critically descriptive attitude. Throughout the book one has the impression that Heisenberg is making up his own mind on the philosophical problems presented by physics and this, for the reader, is a most fascinating process. Instead of being presented with the results of enquiry and their carefully prepared derivation, we are taken into the author's confidence when he is trying to arrive at conclusions in a forest thickly planted with doubt and reservations. The fact that we are made to see and appreciate these is in itself a tribute to the author's clarity.

This is neither a textbook nor a philosophical thesis and it would be both misleading and presumptious to give a precis of its contents. The approach chosen by Heisenberg is clearly set out on the first page when he says: " every tool carries with it the spirit by which it has been created ", and it is the definition rather than the analysis of this spirit with which he is mainly concerned. However, in the last chapter he discusses, again in an undogmatic manner, the impact of modern physics on human affairs and the change which this has made to the position of the physicist in society.

Those who hope that this book will fill the blank space reserved for modern science in their philosophy classes will be disappointed. Far from having his thinking done for him by the author, the reader must realize that, in this series of stimulating lectures, Heisenberg is making him think. Anyone who is willing to do so will find this book most rewarding. K. MENDELSSOHN.

Elektronen- und Ionenprozesse in Ionenkristallen, by O. Stasiw. Pp. viii + 307. (Berlin, Göttingen, Heidelberg : Springer, 1959.) DM. 66.

Professor Stasiw is well known in the field of colour centres and imperfections in ionic crystals and his book on this topic will be read widely.

The first half is concerned (i) with the statistics of lattice defects and applications to the study of ionic conductivity, diffusion and dielectric loss phenomena, (ii) with optical absorption by perfect crystals and by crystals both additively coloured and containing deliberate additions of foreign ions, and (iii) with the statistics of electrons liberated thermally and optically and the related semiconductive and photoconductive effects. This development is logical and detailed and prepares the way for the review of photochemical processes which occupies much of the second half of the book (subtitled " with consideration of photochemical processes "). Topics here include the formation and aggregation of colour centres in pure and additively coloured crystals and in crystals containing additions of sensitizing foreign ions (e.g. KCl + KH and AgBr + Ag_2S) and also the influence of mechanical deformation on photochemical processes. The last two chapters of the book deal with the application of nuclear resonance techniques to the study of the structure of imperfect crystals and with the quantum theory of the absorption of light by crystals. This last chapter contains a full account of the interactions of electrons and lattice vibrations, necessary for the understanding of the shape and width of colour centre absorption bands.

A rather surprising omission is the absence of a full discussion of paramagnetic resonance methods. These methods yield information about the electronic and atomic structure of colour centres in a way that is often breath-taking. The technique provided the first direct information about the disposition of the wave function of the F-centre electron and so confirmed the vacancy model: it has subsequently yielded a wealth of information on various hole (V) centres and impurity centres—information which seems quite unattainable by more classic methods. It is also surprising that there is not a fuller mention of the polarization of luminescence radiation and the dichroism which can be induced in some crystals (otherwise isotropic); these studies in principle also give direct information about the symmetry, and thus the atomic configuration, of colour centres. These points apart, however, the book is a most pleasant and useful review of the field, and we welcome it. A. B. LIDIARD.

Dendritic Crystallization, by D. D. Saratovkin. Translated by J. E. S. Bradley from the Russian. Pp. iv + 126. (New York : Consultants Bureau ; London : Chapman and Hall, 1959.) 50*s*.

The enormous variety of forms shown by growing crystals has been the subject of study almost before scientific crystallography began. Among the most fascinating, as well as the most complicated, are the dendrites, or tree-like forms, to which we are accustomed since children in the hoar frost on the window-panes. They have accumulated enormous literature, most of which is purely descriptive.

Of recent years, however, the study of dendrites has become of great importance in applied physics and technology, since the growth of crystals, particularly of pure crystals for electronic purposes, has become a technique in its own right. That is why we can welcome the translation of Saratovkin's book on *Dendritic Crystallization* which is one of the few devoted entirely to this subject.

The reading of the book indicates that the problems of dendritic growth are now emerging from the descriptive into the truly scientific phase with controlled experiments, but that still the very complexity of the phenomena baffles any single theory to account for them all. It is evident that dendrites only occur when crystallization is relatively rapid, and consequently inevitably in conditions where different parts of the same dendrite are in different physical states. This puts a premium on careful observation and makes a rigid theory of dendrite formation extremely difficult. As this book shows, much work has been done on dendrites in the Soviet Union, work which is little, if at all, known to English speaking scientists, and Saratovkin's book is particularly valuable in this respect introducing us to literature with which we are unfamiliar. Here are given a summary of researches on dendrites, some extremely extensive, beginning with the pioneer work of Chernov in the last century and going on to that of Bochvar and Lemmlein at the present day.

The author also shows a very considerable acquaintance with both German and British contributions, including the more recent work on function of dislocations.

The value of the book is enhanced by the author's very good stereo-microscopic photographs of dendrites, and in general by a very readable presentation of the subject. Certain interesting points are made, namely the control of the dendritic axes by impurities, the distinction between dendritic and skeleton crystals, and the mode of formation of honeycomb and foliated dendrites.

The book should be of particular interest to metallurgists on account of the discussion on the crystallization of eutectics and the experiments on the crystallization of eutectics from mixture of metals well below their melting points.

At a time when we are still unclear on the mode of growth under equilibrium conditions, it is premature to expect a complete theory of dendrites, but the phenomena reported in this book should certainly offer a lead to those wishing to undertake research in this fascinating field. J. D. BERNAL.

Methods of Experimental Physics, Vol. 1, *Classical Methods*, edited by I. ESTERMANN. Pp. xii + 596. (New York, London: Academic Press, 1959.) $12.60.

There is no traditional way of writing books on experimental methods, so that a reviewer must devote much of his space to defining the general scheme of a book bearing such a title as the present. The volume follows the lines of the great German *Handbücher*; it aims at covering its topics in an encyclopaedic way, often starting from elementary and fundamental considerations; it is not very critical nor eminently readable, but it does direct the reader's attention to a great variety of facts and makes available to him a great number of references. The references are brought up to 1957, in some places to 1958.

The eight sections deal with evaluation of results, fundamental units, mechanics of solids and of fluids, vibrations and sound, heat and thermodynamics, optics, electricity and magnetism. The section on errors and statistics contains very valuable material but is in places so condensed as to be obscure. The sections on units and on the statics, kinematics of solids and fluids are useful since they contain in compact form information which may be needed by working physicists and which may have been omitted from a physics course. But in a

work of this kind it is surely wrong to leave the impression that viscous flow is Newtonian in all important cases: 'thixotropy' does not appear in the index nor in the text. The subsection on vacuum phenomena could mislead the student by failing to discuss adequately the important cases which are dominated by the gases given off from surfaces and the techniques of 'outgassing'. The thermodynamics is of a formal and even philosophical cast which is unexpected in the context. The heat section deals with thermometry, calorimetry and heat flow, the optics with geometrical and wave optics, spectroscopy and the detection of radiation.

These sections are overburdened with hurried résumés of material which is easily accessible in textbooks known to every physicist: notable omissions are the practically important, and frequently neglected considerations of intensity and brightness in optical systems, and any mention of the modern 'spatial frequency filter' treatment of optical resolution.

The sections on electricity and magnetism are valuable summaries of theory and experimental methods, but appear to perpetuate the regrettable division which exists, in textbooks but not in practice, between 'electronic' and other methods. Electronic instruments are certainly mentioned and their characteristics are sketched, but there is no discussion of their principles and no circuit details are given.

The principal value of the book seems to lie in reminding the physicist of 'classical' work which may have been crowded out of physics teaching: the reviewer hopes to use it as a check list and source of references when planning experimental work or lecture courses, but he feels that it sits a little uncomfortably between textbook and encyclopaedia. H. J. J. BRADDICK.

Mathematics in Physics and Engineering, by J. IRVING and N. MULLINEUX. Pp. xvii + 883. (New York, London: Academic Press, 1959.) $11.50.

Here is the latest addition to the already swollen ranks of bumper maths books for scientists and engineers. There are long chapters on differential equations, Bessel and Legendre functions, transform theory, matrices, dynamics, calculus of variations, complex variable theory, numerical methods, and integral equations, as well as appendices covering a variety of topics, such as the convergence of series and of integrals, elliptic integrals, and vector analysis. The book is evidently intended for postgraduate students of physics and engineering, although it includes some material which would normally appear in undergraduate courses. A good knowledge of calculus is the only obvious prerequisite, but the abruptness with which the various topics are introduced would suggest that an undergraduate course of mathematics for physicists and engineers is assumed.

The standard of rigour is not high, and, in spite of the length of the work, the treatment is sometimes irritatingly abbreviated. For example, although twelve pages are devoted to isoperimetric problems in the calculus of variations, the most difficult point in the basic problem is dismissed in the statement: "Hence it is necessary to introduce the Lagrangian multiplier . . ." (the first time Lagrangian multipliers have been mentioned in the text).

A feature of the book is the large number of worked examples drawn from many branches of applied mathematics. These are undoubtedly interesting, and should be useful to teachers of applicable mathematics. For the students

themselves, however, they may be rather a mixed blessing. Is it necessary for a structural engineer to concern himself with detailed solutions of Schrödinger's equation, or an atomic physicist with problems on the bending of beams and the buckling of plates? Need either bother about aerofoils moving at supersonic speeds? It must be realized that, at postgraduate level, specialization has inevitably begun. Although it is possible that at some time a physicist or an engineer may be called upon to solve a problem which lies within the other's domain, it is impossible to prepare in advance for every eventuality. In any case, this book fails to prepare for some very probable eventualities. For example, group theory, which is in everyday use by theoretical physicists, is not even mentioned.

A book which attempts to be as catholic as this must inevitably resemble the curate's egg, and there is no reason why anyone, physicist or engineer, should be obliged to accept the bad with the good, the unwanted with the wanted. Before producing such weighty tomes publishers would do well to consider whether or not a series of small monographs, of which the present work would furnish half a dozen or so, might be of greater value. S. RAIMES.

Fundamental Aspects of Reactor Shielding, by H. GOLDSTEIN. Pp. xvi + 416. (Massachusetts: Addison-Wesley; London: Pergamon Press, 1959.) $9.50.

The calculation of the penetration of radiation into matter is not a problem which can be solved by carrying over the tried and tested methods of reactor core physics; it is a field of study in its own right which demands a knowledge of techniques which only specialists can provide. For such people, and for those about to enter the field, this book is of vital importance and will surely become an essential part of their equipment.

As the title implies, the emphasis throughout is on the fundamentals of the subject and the early chapters deal very adequately with such topics as the definition of biological and physical dose, permissible levels of exposure and the sources of radiation in reactors. The discussion on dose definition is particularly valuable in view of the confusion which often surrounds the subject.

After a useful, but somewhat digressive, chapter on experimental shielding facilities, the rest of the book is devoted to its principal objective, the penetration of gamma rays and neutrons into matter with a review of the methods of calculation available. The section on gamma radiation is excellent and is difficult to fault, containing as it does, an authoritive account of the ' method of moments ' which has by now come to be universally accepted as the basic technique for the problem and with which Dr. Goldstein has himself been closely connected.

The final chapter on neutrons gives a very good account of this difficult and still developing subject, but suffers from the disadvantage that, although fast neutron penetration is dealt with, not much help is given on the problem of calculating the thermal flux in a multi-region shield (an important requirement for design purposes).

It is not intended to be a practical handbook of shield design (nothing is given on radiation streaming in ducts, nuclear heating or activation of coolants) but, on its own terms, as a fundamental account of the subject, it is first class and an invaluable aid to understanding. The style is lucid throughout and no textual errors have been found. K. T. SPINNEY.

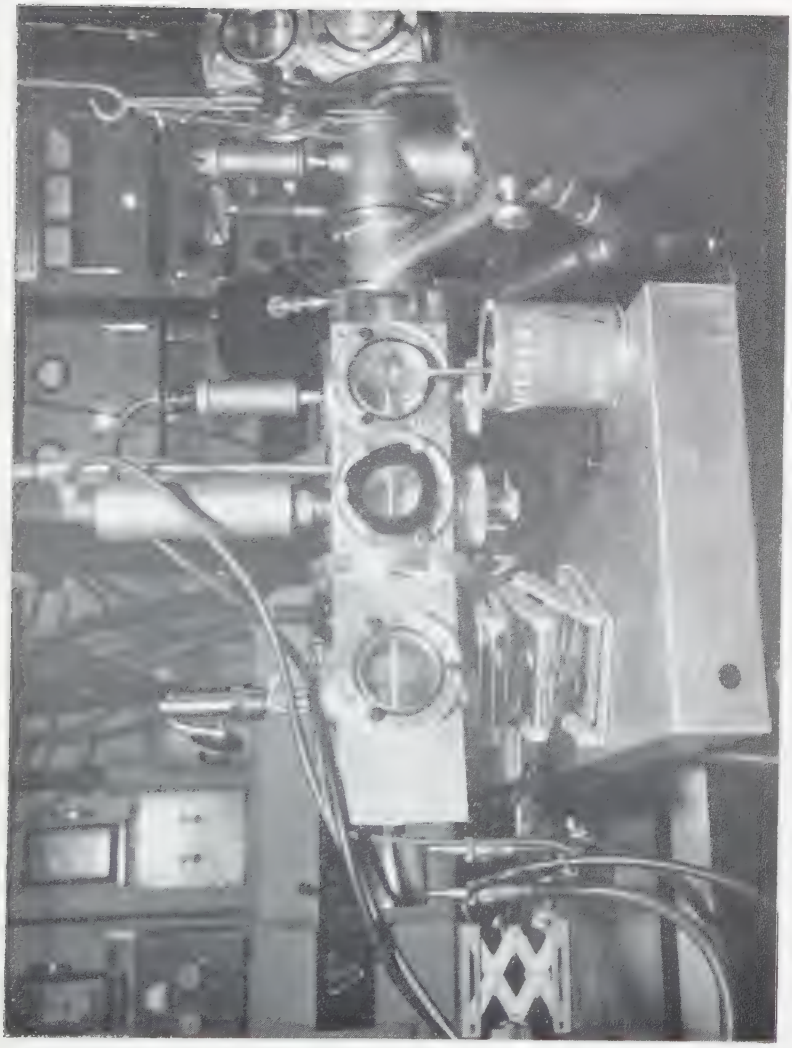

Figure 1. Collision chamber and luminous ion beam.

Plate I

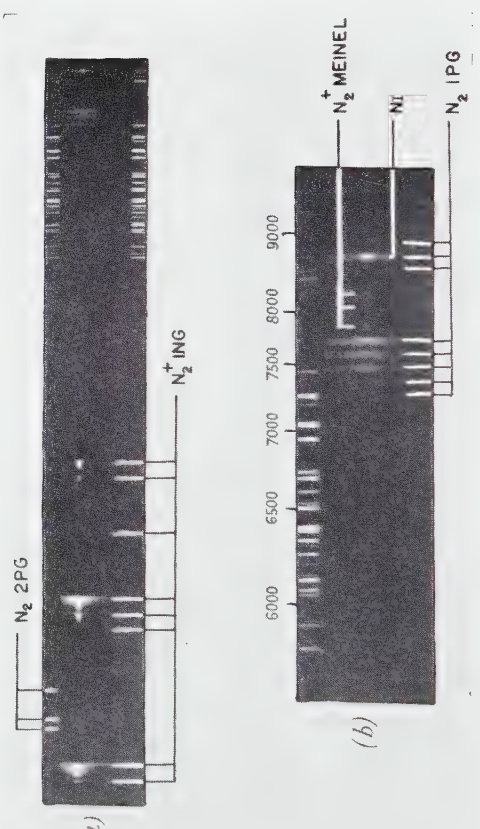

Figure 2. 1 MEV proton induced spectrum in N_2 at 58 μ Hg. (*a*) The spectrum between 3500 Å and 9000 Å; (*b*) the spectrum between 7000 Å and 9000 Å.

Plate II

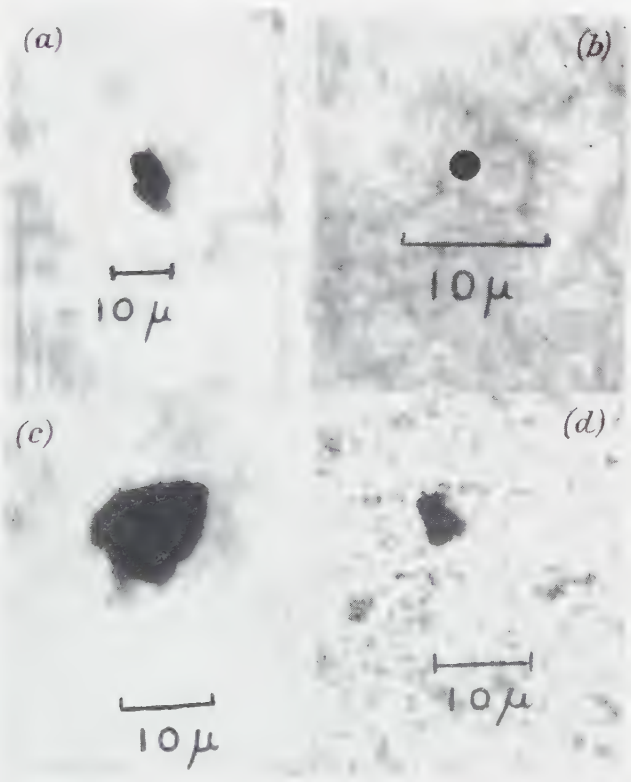

Figure 1. Typical particles of alloy. (*a*), 90% Ni; (*b*), 70% Ni; (*c*), 55% Ni; (*d*), 35% Ni.

Ultrasonic Relaxation in Triethylamine

By R. A. PADMANABHAN† and E. L. HEASELL
Electrical Engineering Department, Imperial College, London

MS. received 15*th February* 1960

Abstract. The absorption of ultrasonic waves in triethylamine has been studied at temperatures between −50 °c and 25 °c, at frequencies between 10 and 100 Mc/s. These measurements supplement those reported in 1956 by Heasell and Lamb and permit a more detailed analysis. To explain the complete set of results it is necessary to assume the existence of a temperature-dependent entropy of activation. Physical reasons as to why this is a plausible explanation are advanced.

§ 1. Introduction

A previous study of ultrasonic absorption in triethylamine has shown that it exhibits anomalous absorption in the temperature range 25° to 75°c, at frequencies between 20 and 200 Mc/s (Heasell and Lamb 1956). This behaviour has been interpreted in terms of the perturbation of a postulated equilibrium between the different rotational isomers of this liquid.

Litovitz and Carnevale (1958) have studied the ultrasonic absorption in triethylamine as a function of pressure, between atmospheric pressure and 3500 lb/in². These measurements were made at 0°c and thus could not be compared directly with the previous observations.

§ 2. Experimental Procedure

As previous investigation had shown, no further purification of the liquid obtained from the suppliers was necessary. The samples obtained for the present work were initially measured without further treatment. Measurements were made at frequencies of 10·87, 30·3, 50·1 and 111·5 Mc/s, and between temperatures of −50 °c and 25 °c. A description of the measuring procedure may be found in Andreae, Bass, Heasell and Lamb (1958).

Preliminary analysis of the results showed that they did not follow the expected pattern and that the region of apparent discrepancy occurred around 0 °c. Two further sets of measurements were made at frequencies of 50·1 and 10·2 Mc/s. These frequencies were chosen as being more significant for the analysis of the data around 0°c.

A sample of the liquid was allowed to stand over quicklime for 48 hours being occasionally shaken; it was then fractionally distilled, only the middle fraction of the distillate being retained. The boiling point was 89·3°c.

The measuring system was enclosed in a large polythene bag, the electrical connections being brought out through small holes and tightly bound with adhesive tape. The bag could be inflated with dry nitrogen and maintained at a pressure slightly above atmospheric.

†Mr. Padmanabhan carried out this work whilst on leave from the National Physical Laboratory of India, New Delhi.

A sample of the distilled liquid was transferred into the measuring chamber and the bag tightly closed. After allowing some minutes for the nitrogen to completely displace the air from the system the cooling process was started. No condensation was observed at any stage of the cooling process, even at the lowest temperatures reached, $-60°$c.

§ 3. Experimental Results

The plots of α/f^2 against temperature are shown in figure 1. At 50 Mc/s the check measurements agree precisely with the original ones. At the lower frequencies, 10·87 and 10·2 Mc/s, direct comparison is not possible. However, using the parameters of the relaxation, A, B and f_c, determined from the original measurements, the values of α/f^2 were calculated for the check measurements.

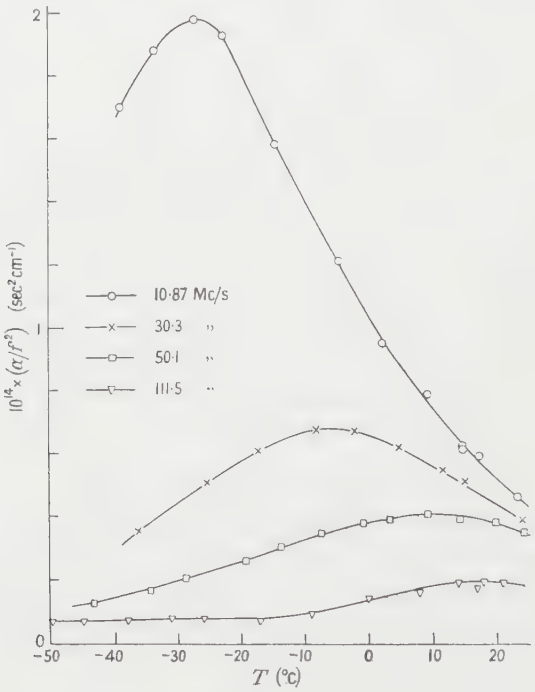

Figure 1. α/f^2 plotted against temperature.

The two sets of values agree well down to $-20°$c, and below that temperature the divergence is less than 4%. The values in the table represent the best fit to the experimental data of the relation

$$\alpha/f^2 = A/[1+(f/f_c)^2] + B. \qquad \ldots\ldots(1)$$

At the lowest temperature greatest weight has been given to the 10·87, 30·3 and 111·5 Mc/s results, at the higher temperatures the 10·87, 50·1 and 111·5 Mc/s data have been used. The results at -10, -5, 0, 5 and 10°c have been computed from both combinations to show that they give satisfactory continuity. The table gives the values of A, B, f_c and μ_{max} obtained from the experimental data. The double entries in the table show the values of the parameters obtained from the alternative sets of data.

In the analysis of the data the use of equation (1) implies that a single relaxation time is sufficient to describe the process observed. The agreement between the values re-computed from the above parameters and those derived by experiment is within $\pm 4\%$ down to $-20°$c, and within $\pm 6\%$ below this temperature.

T(°c)	−40	−35	−30	−25	−20	−15	−10	−5
$10^{17}A$ (sec^2 cm^{-1})	6600	5375	4360	3560	2825	2170	1735	1395
							1738	1404
$10^{17}B$ (sec^2 cm^{-1})	56	—	42	—	34	—	29	—
(f_c) (Mc/s)	6·07	7·67	9·60	11·8	14·7	18·6	23·0	28·1
							22·9	27·3
$10^2\,\mu_{max}$	2·84	2·87	2·86	2·83	2·77	2·63	2·55	2·47
							2·54	2·41
T(°c)	0	5	10	15	20	25		
$10^{17}A$ (sec^2 cm^{-1})	1112	902	740	605	503	442		
	1052	903						
$10^{17}B$ (sec^2 cm^{-1})	40	—	66	—	78	—		
f_c (Mc/s)	34·3	39·6	47·9	59·5	74·2	98·1		
	34·9	40·0						
$10^2\,\mu_{max}$	2·36	2·17	2·11	2·10	2·14	2·45		
	2·27	2·19						

The dilatation of triethylamine has been calculated from the density data quoted by Timmermans (1950). The values quoted cover the temperature range 0° c to 85° c, and within this range the dilatation is constant. It has been assumed that the dilatation remains constant over the rest of the temperature range.

The specific heat of the liquid was measured by Phipps (see Heasell and Lamb, 1956) in the temperature range 25° c to 60° c. Within that range the specific heat may be expressed by the relation

$$C_p = 0{\cdot}5039 + 0{\cdot}00017t + 0{\cdot}0000064t^2 \text{ cal g}^{-1} \text{ deg}^{-1}.$$

If a direct extrapolation is made to −60° c the resulting values show a minimum at −12·5° c arising from the presence of the third term. If the latter is neglected and a linear extrapolation made from Phipps' results, then the specific heat varies between 0·5039 and 0·4937 cal g^{-1} deg^{-1} in the range 0° c to −60° c, a variation of only 2·1%.

The sound velocity has been measured from −65° c to 25° c and is found to follow a linear extrapolation from the original measurements:

$$v = 1253 - 4{\cdot}47t \text{°c}.$$

At no temperature was the dispersion of velocity greater than 1%.

§ 4. Molecular Interpretation

The molecular interpretation has been previously discussed (Heasell and Lamb 1956). It was proposed that the triethylamine molecule can assume any one of three possible geometrical configurations (figure 2). The anomalous absorption is attributed to the perturbation of the equilibrium between two of these three possible states.

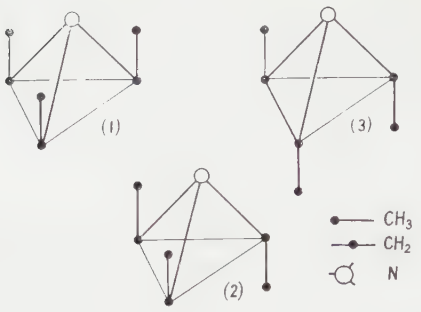

Figure 2. Rotational isomers of triethylamine.

§ 5. Analysis of Experimental Data

We shall follow the original analysis by assuming that an equilibrium between only two states is involved and may be described by a first-order reaction

$$\text{(lower energy state) } A_1 \rightleftharpoons A_2 \text{ (higher energy state).} \qquad \ldots\ldots (2)$$

Since the velocity dispersion may be neglected the static and infinite frequency adiabatic compressibilities may be assumed equal. In this case (Meixner 1953) there is no need to distinguish between the experimental relaxation time τ_m and the adiabatic–isobaric relaxation time τ_{ps}.

If k_{12} and k_{21} are the forward and reverse rate constants, and if we assume that $k_{12} \ll k_{21}$, then following the notation of the previous paper

$$f_c = (\boldsymbol{k}T/2\pi h) \exp(\Delta S_2^{\ddagger}/R) \exp(-\Delta H_2^{\ddagger}/RT). \qquad \ldots\ldots (3)$$

where $\Delta H_2^{\ddagger}$ and $\Delta S_2^{\ddagger}$ are the enthalpy and entropy changes occurring in the reverse reaction (2)→(1), between state (2) and the top of the barrier separating these states. Thus a plot of $\ln(f_c/T)$ against $1/T$ should be a straight line of slope $\Delta H_2^{\ddagger}/R$. It has been shown (Meixner 1952, Davies and Jones 1953) that for a thermal relaxation process

$$\frac{\Delta\beta_s}{\beta_s} = (\gamma - 1)\frac{\Delta C_p}{C_p}\left(\frac{\Delta V}{\Delta H}\frac{1}{V}\frac{C_p}{\theta} - 1\right)^2 \qquad \ldots\ldots (4)$$

expresses the fractional change in adiabatic compressibility. If it is assumed that the volume change of reaction is negligible, and that ΔG, the free energy difference between states (1) and (2), is greater than $3RT$, then, as shown previously, the maximum value of sound absorption per wavelength μ_{max} is given by

$$\mu_{max} = \frac{\pi}{2C_p}(\gamma - 1)R\left(\frac{\Delta E}{RT}\right)^2 \exp\left(-\frac{\Delta E}{RT}\right)\exp\left(\frac{\Delta S}{R}\right). \qquad \ldots\ldots (5)$$

Now

$$\gamma = v^2\theta^2 T/(JC_p 10^7) \qquad \ldots\ldots (6)$$

thus

$$\mu_{max} = \frac{\pi v^2\theta^2 T}{2JC_p^2 10^7} R\left(\frac{\Delta E}{RT}\right)^2 \exp\left(-\frac{\Delta E}{RT}\right)\exp\left(\frac{\Delta S}{R}\right). \qquad \ldots\ldots (7)$$

We have assumed that θ is constant, thus a plot of $\ln(\mu_{max} T C_p^2/v^2)$ against $1/T$ should be a straight line of slope $\Delta E/R$.

The two relevant plots obtained from the experimental data are shown in figures 3 and 4. Figure 3 has the appearance of consisting of two straight portions, whilst figure 4 looks as if it might extrapolate to form two parallel lines, joined by a smooth curve.

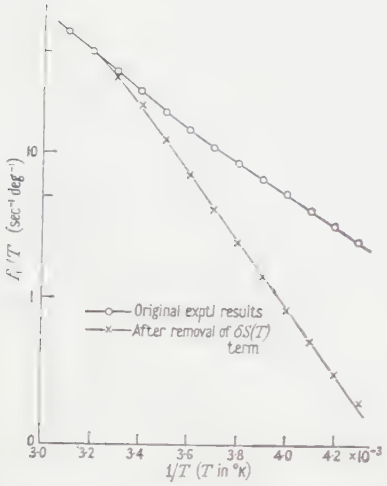

Figure 3. Log_{10} (f_c/T) plotted against $1/T$.

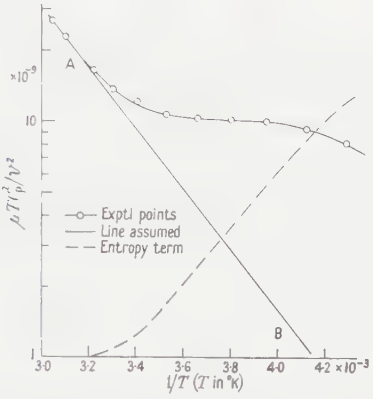

Figure 4. Log_{10} $(\mu TC_p^2/v^2)$ plotted against $1/T$.

In arriving at the two graphs presented a number of assumptions have been made; we have neglected the velocity dispersion that must accompany a relaxation process. The latter is certainly less than one per cent throughout the present temperature range, as evidenced by our own experimental results. We have assumed that the change of volume occurring between the two isomers involved is negligibly small. Litovitz and Carnevale (1958) have studied the pressure dependence of the relaxation at pressures up to 3500 kg cm $^{-2}$. It was found that f_c was independent of pressure within this range at 0 °C. This supports our assumption that the volume change is negligibly small. We have also extrapolated the specific heat results beyond their intended range. However, the net variation in specific heat is small and in any case would only affect the graph proposed for the evaluation of ΔE. Finally, we have assumed that the relaxation may be analysed in terms of a single relaxation time. Whilst theoretical treatments of the behaviour of more complex relaxing systems have been given (Meixner 1954, Davies 1956) there is no evidence, within the present accuracy of measurement, that more than one set of parameters need be used.

§ 6. Interpretation of the Observations

One of the usual assumptions made in the analysis of ultrasonic data is that the various activation energies and entropy differences are temperature-independent. In the present case it seems worth considering further the assumption concerning the entropy changes.

In the original analysis of the data on triethylamine it was remarked that the entropy changes then deduced were reasonable, insofar as the molecule possesses methyl groups which are probably free to rotate in some configurations but not

in others. Increasing the size of these groups will produce further hindrance to rotation. In a study of tri-*n*-butylamine (Krebs and Lamb 1958) it was found that the entropy difference was small and in fact negative.

We have assumed that the entropy terms may be divided

$$\Delta S_2^{\ddagger} = \Delta S_2^{\ddagger} \pm \delta S(T)$$

$$\Delta S = \Delta S \pm \delta S(T)$$

the temperature-dependent term being the same for both entropy differences. Figures 4 and 5 show the results of assuming that the straight lines, AB and A′B′ respectively, represent the temperature-independent entropy and energy differences, deviations from these lines being due to the effect of the term $\delta S(T)$ above. Inspection of figure 5 shows that in this case it is necessary to divide the corresponding data by exp $[\delta S(T)/R]$, whilst the corresponding data of figure 4 must be multiplied. The results of this procedure are shown in figure 3 and figure 6 respectively.

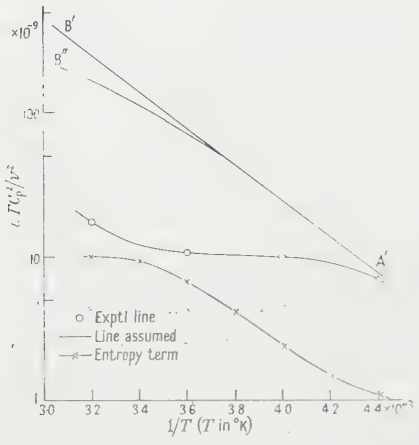

Figure 5. Log_{10} $(\mu TC_p^2/v^2)$ plotted against $1/T$.

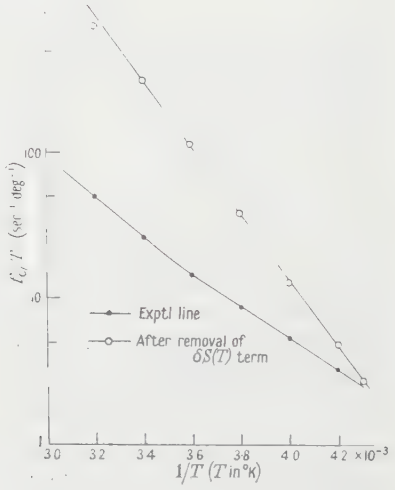

Figure 6. Log_{10} (f_c/T) plotted against $1/T$.

It is necessary to observe that whilst along line AB, figure 4, the assumption $\Delta G > 3RT$ remains true (ΔG lies between 3·5 and 4·5), this assumption is not true along line A′B′, figure 5. The theoretical line which would be obtained, even for temperature-independent values of the parameters is that shown as A′B″. However, the term exp$[\delta S(T)/R]$ becomes small at the higher temperatures, of the order of 0·1, and thus the evaluation of $\delta S(T)$ may still be made by measuring the ratio of the experimental value and that given by A′B′.

Inspection of figures 3 and 6 show that the recalculated data are now more nearly a linear plot than were the original results. The linearity found using the values deduced from figure 5 is rather better than that obtained using figure 4. In both cases the accuracies to be attached to the parameters obtained from the linearized plots cannot be high, say ±10%.

The reaction parameters obtained are as follows:

	figure 4	figure 5	
$\Delta H_2^{\ddagger}$	10·8	10·1	kcal mol^{-1}
$\Delta S_2^{\ddagger}$	17	19	cal mol^{-1} deg^{-1}
ΔE	5·9	5·9	kcal mol^{-1}
ΔS	11	16	cal mol^{-1} deg^{-1}

The temperature-dependent terms are shown graphically in figures 4 and 5. It is possible to evaluate an activation energy to be associated with the change of entropy, since the predicted variation is monotonic and nearly linear on our plots. In each case the energy obtained is approximately the same, 5·6 kcal mol^{-1}. This value is especially reasonable since it corresponds to the energy difference between the terminal states listed above. If it is considered that the barrier, between the two isomeric forms postulated, is due to the steric hindrance occurring when one methyl group passes over another, then the energy involved when one of these groups tries to rotate about the central C–N bond, or to rotate about the outer C–C bond might be expected to be of the same order.

Ultrasonic data alone give only values for the difference in energy or entropy between two states, thus it is not possible to distinguish between the two sets of values given above using ultrasonic data alone.

In the case of figure 4, we see that the entropy difference between final states decreases with increasing temperature. This might be expected to correspond to a relative increase of the ground state entropy. However, the ground state parameters do not enter into the expression for f_c. The f_c data also indicate that the calculated entropy difference decreases with temperature increase. The latter would correspond to a relative increase in the entropy of the higher energy stable state. These two conclusions are not immediately compatible and would involve a relative shift of two of the states, the change in the ground state being twice as great as that of the higher state.

In the case of the data obtained in conjunction with figure 5, a simpler explanation is possible: both entropy changes would be compatible with a decrease in the entropy of the higher energy state with decreasing temperature.

Since the interpretation associated with figure 5 is both simpler and more physically reasonable it is proposed that this be adopted as the correct explanation.

The similarity between the two activation energies, that for the whole reaction, and that obtained from the temperature-dependent entropy term, supports the idea that the observed relaxation is associated with the restricted rotation of one of the ethyl groups about the central C–N bond. Since the entropy difference is always positive, then, in accordance with the work of Krebs and Lamb (1958) it is concluded that state (1), figure 2, corresponds to the ground state. If a third isomeric configuration is possible then it must be separated from the other two by a large barrier, since we do not observe any effects due to it in the present temperatures–frequency range.

Acknowledgments

One of us (R.A.P.) wishes to thank the Assam Oil Company Ltd., for financial support during this work; we would both like to express our thanks to Dr. Lamb for his advice and assistance. The authors gratefully acknowledge the financial assistance provided by the Worshipful Company of Clothworkers during this work.

References

Andrea, J., Bass, R., Heasell, E. L., and Lamb, J., 1958, *Acustica*, **8,** 131.
Davies, R. O., 1956, *Rep. Progr. Phys.*, **19,** 350 (London: Physical Society).
Davies, R. O., and Jones, G. O., 1953, *Advanc. Phys.*, **2,** 370.
Heasell, E. L., and Lamb, J., 1956, *Proc. Roy. Soc.* A, **237,** 233.
Krebs, K., and Lamb, J., 1958, *Proc. Roy. Soc.* A, **244,** 558.
Litovitz, T. A., and Carnevale, E. H., 1958, *J. Acoust. Soc. Amer.*, **30,** 134.
Meixner, J., 1952, *Acustica*, **2,** 101.
—— 1953, Offprints from *Kolloid Z.*, **134,** 3.
—— 1954, *Z. Phys.*, **139,** 30.
Timmermans, J., 1950, *Physico Chemical Constants of Pure Organic Compounds* (Amsterdam: Elsevier).

Waves in a Conducting Sheet situated in a Strong Magnetic Field

By I. C. PERCIVAL

Physics Department, University College, London

MS. received 16*th December* 1959, *in revised form* 19*th February* 1960

Abstract. The hydromagnetic approximation is applied to the elementary linear theory of transverse waves in a thin uniform plane conducting sheet, in which the inertia is provided by the sheet, and the restoring forces by strong vacuum magnetic fields on either side of the sheet.

The dispersion relation and damping are obtained. The waves should be observable in the laboratory.

§ 1. Introduction

A hydromagnetic wave is a propagating oscillation in which the inertia is provided by a conducting fluid and the restoring force by a magnetic field. Generally the magnetic field confined within the fluid plays a dominant role. Such waves were first considered by Alfvén (1950) and have since then received very extensive theoretical treatment. They have also been demonstrated experimentally in mercury by Lundquist (1949), in liquid sodium by Lehnert (1954) and in gaseous plasmas by Bostick and Levine (1955), by Allen *et al.* (1959), by Sawyer, Scott and Stratton (1959) and by Jephcott (1959).

We consider the elementary theory of those magnetomechanical waves in which the inertia is provided by a uniform conducting sheet and the restoring forces are provided by vacuum magnetic fields situated on either side of this sheet. It is supposed that the thickness of the sheet is small in comparison with the wavelength of the wave, and that the internal elastic and magnetic stresses within the sheet are small compared with the forces exerted by the external magnetic fields, except in so far as they serve to transmit these external forces to the material of the sheet. This material may be solid, liquid or gaseous.

A sheet of gaseous plasma confined by magnetic fields tends to broaden owing to diffusion across the lines of force, and the theory presented applies to this case only during the period in which the thickness is small compared with the wavelength.

We shall suppose that the waves are of small amplitude so that a linear theory is applicable. The viscosity of the medium will be neglected, and it will be supposed that its intrinsic magnetic permeability is unity.

The basic equations for the vacuum are

$$\nabla . \mathbf{B} = 0, \qquad \nabla \times \mathbf{B} = 0 \qquad \ldots\ldots (1)$$

and at the boundary the magnetic induction $\mathbf{B}$ is continuous if the resistivity η is finite. Stewartson (1957) has shown that a necessary condition for $\mathbf{B}$ to be

discontinuous at the boundary of a perfectly conducting fluid for any length of time is that the normal component of $\mathbf{B}$ at the boundary should be zero. We shall suppose the normal component of $\mathbf{B}$ to be zero if the sheet is a perfect conductor.

§ 2. Waves in a Plane Conducting Sheet

Consider an infinite plane conducting sheet of volume density ρ and thickness h whose mid-plane is the $y=0$ plane of a chosen coordinate system. Using the notation of Kruskal and Schwartzschild (1954) let the magnetic fields in the regions $\mathscr{R}^{\pm}$ defined by $y>+h/2$ and $y<-h/2$ be $\tilde{\mathbf{B}}^{\pm}$. This is the unperturbed system and, for equilibrium to exist, $\tilde{B}^{+}=\tilde{B}^{-}$. When oscillations displace the sheet from the plane, $\mathscr{R}^{+}$ and $\mathscr{R}^{-}$ will refer to the regions on either side of the sheet.

The displacements of the sheet will be denoted by $y_{\mathrm{S}}(x)$ and the consequent changes in the field by $\tilde{\mathbf{B}}^{\pm}$.

In this section we shall suppose that the sheet is a perfect conductor of negligible thickness, that the unperturbed fields on either side of the sheet are in the same direction, and that waves propagate in that direction, which will be chosen to be the direction of the x axis, unit vector $\mathbf{e}_x$. Then

$$\tilde{\mathbf{B}}^{+}=\tilde{B}\mathbf{e}_x=\tilde{\mathbf{B}}^{-}, \qquad \mathbf{k}=k\mathbf{e}_x \qquad \ldots\ldots (2)$$

where $l=2\pi/k$ is the wavelength of a monochromatic wave. Consider standing waves of the form

$$y_{\mathrm{S}}=A\sin kx \qquad \ldots\ldots (3)$$

where A is a function of time.

It is reasonable to impose the boundary condition that the magnetic disturbance remains in the region of the sheet, so that

$$\lim_{y\to\pm\infty} \mathbf{B}^{\pm}=\tilde{B}\mathbf{e}_x. \qquad \ldots\ldots (4)$$

The whole perturbed system is periodic of period $l=2\pi/k$ in the x direction, so that

$$\mathbf{B}=\tilde{B}[1\pm a\mathrm{e}^{\mp ky}\sin(kx+\phi)]\mathbf{e}_x+\tilde{B}a\mathrm{e}^{\mp ky}\cos(kx+\phi)\mathbf{e}_y. \qquad \ldots\ldots (5)$$

Higher harmonics are due to non-linearity and may be neglected.

The boundary condition at the sheet is $\mathbf{B}.\mathbf{n}=0$ where $\mathbf{n}$ is the normal to $y=A\sin kx$ and so to first order in Ak:

$$\phi=0, \qquad a=Ak. \qquad \ldots\ldots (6)$$

We also need the magnetic field at the sheet

$$(B^{\pm})^2=\tilde{B}^2(1\pm 2ky_{\mathrm{S}}), \qquad \ldots\ldots (7)$$

ignoring terms of order $(Ak)^2$.

Consider the motion of an element of the sheet of unit length in the z direction and of length δx in the x direction. To first order in Ak, it follows from Newton's law of motion that

$$\rho h\delta x\,\frac{\partial^2 y_{\mathrm{S}}}{\partial t^2}=(p^{-}-p^{+})\delta x, \qquad \ldots\ldots (8)$$

where p^{-} and p^{+} are the magnetic pressures on either side of the sheet. The

magnetic pressures (Spitzer 1956, p. 25) are $p^{\pm}=(B^{\pm})^2/8\pi$ and by equation (7)

$$\left.\begin{aligned}\rho h\frac{\partial^2 y_S}{\partial t^2} &= -\frac{\tilde{B}^2}{8\pi}4ky_S\\ \frac{\partial^2 y_S}{\partial t^2}+\omega^2 y_S &= 0,\end{aligned}\right\} \quad \ldots\ldots (9)$$

where

$$\omega^2=\frac{k}{h}\frac{\tilde{B}^2}{2\pi\rho}. \quad \ldots\ldots (10)$$

Since ω is the angular frequency of oscillation, the phase velocity of progressive waves is

$$V_S^2=\frac{\omega^2}{k^2}=\frac{2}{kh}\frac{\tilde{B}^2}{4\pi\rho}=\frac{2}{kh}V_A^2, \quad \ldots\ldots (11)$$

where V_A is the velocity of Alfvén waves in a infinite medium of the same material as the sheet, permeated by a uniform field of magnitude $\tilde{B}$. The group velocity of the sheet waves is one half their phase velocity and both velocities are higher than the Alfvén wave velocity.

A rough physical argument provides a link between the two types of waves. In the sheet wave the energy in the distortion of the field falls off as $\exp(-2ky)$. The effective depth of the distortion in the y direction is $2\times\int_0^\infty \exp(-2ky)\,dy=k^{-1}$, where the factor 2 comes from the magnetic field on both sides of the sheet. The amount of material contained in this depth corresponds to a uniform distribution of density ρkh throughout space, and one would expect the phase velocity of the waves to be the same as for Alfvén waves with such a density, that is

$$V_S'^2=\frac{1}{kh}V_A^2.$$

There is a discrepancy of a factor 2 which can be explained as follows. The true Alfvén waves have a perturbation field which is entirely orthogonal to the unperturbed field, whereas the sheet waves have one half their magnetic energy in a field component parallel to the unperturbed field.

§ 3. Derivation by Energy Equation

The dispersion relation (11) can be derived by equating the maximum kinetic and potential (or magnetic) energies of a standing wave. This method of derivation will enable us to generalize more easily to the case in which the fields $\tilde{\mathbf{B}}^-$ and $\tilde{\mathbf{B}}$ and the phase velocity are all in different directions, and to treat the damping when the sheet is an imperfect conductor.

Consider standing waves of the form

$$y_S=A_0\sin kx\sin\omega t. \quad \ldots\ldots (12)$$

Then

$$\frac{\partial y_S}{\partial t}=A_0\sin kx\,\omega\cos\omega t. \quad \ldots\ldots (13)$$

The potential energy is zero when $y_S=0$ so that $\sin\omega t=0$ and $\cos\omega t=\pm 1$. All the energy of the wave is then in kinetic form. The mean energy E per unit area in the (x,y) plane is obtained to second order in A_0 by averaging over one complete cycle in the x direction. Then

$$E=\oint d(kx)\tfrac{1}{2}\rho h v^2\Big/\oint d(kx)=\tfrac{1}{4}A_0^2\omega^2\rho h, \quad \ldots\ldots (14)$$

where the integration is over one cycle.

The kinetic energy is zero when $\partial y_S/\partial t = 0$, and all the energy of the wave is then in potential form, that is magnetic field energy. Here, as in corresponding derivations in stability theory, some care is required.

The magnetic energy per unit area due to the presence of the wave is

$$E = \oint d(kx) \int_{-\infty}^{\infty} dy \left[\frac{B^2}{8\pi} - \frac{\tilde{B}^2}{8\pi}\right] \Big/ \oint d(kx) \qquad \ldots\ldots (15)$$

and if the perturbation field is $\hat{\mathbf{B}} = \mathbf{B} - \tilde{\mathbf{B}}$, then

$$16\pi^2 E = \oint d(kx) \int_{-\infty}^{\infty} dy 2\tilde{\mathbf{B}} . \hat{\mathbf{B}} + \oint d(kx) \int_{-\infty}^{\infty} dy |\hat{\mathbf{B}}|^2. \qquad \ldots\ldots (16)$$

The first term must be zero for equilibrium to exist. It may be shown to be zero identically by magnetic flux conservation. The second term is correct to second order when $\hat{\mathbf{B}}$ is correct to first order, and will be used to compute the magnetic energy due to the wave.

From equation (5)

$$\hat{\mathbf{B}}^{\pm} = \tilde{B} A_0 k e^{\mp ky} (\pm \sin(kx)\mathbf{e}_x + \cos(kx)\mathbf{e}_y)$$

$$\begin{aligned} 16\pi^2 E &= \oint d(kx) \left[\int_{-\infty}^{A_0 \sin kx} dy |\hat{\mathbf{B}}|^2 + \int_{A_0 \sin kx}^{\infty} dy |\hat{\mathbf{B}}|^2\right] \\ &= \oint d(kx) \frac{(\tilde{B} A_0 k)^2}{2k} [\exp(2A_0 k \sin kx) + \exp(-2A_0 k \sin kx)] \\ &\simeq 2\pi \tilde{B}^2 A_0^2 k \qquad \ldots\ldots (17) \end{aligned}$$

to second order in A_0. To this approximation

$$E = \tilde{B}^2 A_0^2 k/8\pi. \qquad \ldots\ldots (18)$$

Equating (14) and (18) we obtain (10) and the dispersion relation (11).

§ 4. Waves and Fields at Different Angles

Let the phase velocity of the wave be in the x direction and the unperturbed fields on either side of the sheet be

$$\tilde{\mathbf{B}}^{\pm} = \tilde{B}_x{}^{\pm}\mathbf{e}_x + \tilde{B}_z{}^{\pm}\mathbf{e}_z. \qquad \ldots\ldots (19)$$

For equilibrium to exist the magnetic pressures in the regions $\mathscr{R}^+$ and $\mathscr{R}^-$ must be equal:

$$(\tilde{B}_x{}^+)^2 + (\tilde{B}_z{}^+)^2 = (\tilde{B}_x{}^-)^2 + (\tilde{B}_z{}^-)^2.$$

When the potential energy is zero, the kinetic energy per unit area is given by equation (14). The z components of the magnetic field are unchanged by the perturbation and make no contribution to the potential energy of the wave. Therefore when the kinetic energy is zero, the mean energy per unit area is

$$E = \tfrac{1}{2}[(\tilde{B}_x{}^+)^2 + (\tilde{B}_x{}^-)^2] A_0^2 k/8\pi. \qquad \ldots\ldots (20)$$

Equating the two expressions for the energy, the phase velocity is given by

$$V_S{}^2 = \frac{1}{kh} \frac{(\tilde{B}_x{}^+)^2 + (\tilde{B}_x{}^-)^2}{4\pi\rho} \qquad \ldots\ldots (21)$$

and the group velocity is

$$\begin{aligned} \mathbf{V}_G &= \partial\omega/\partial\mathbf{k} \\ &= \left[\frac{(\tilde{B}_x{}^+)^2 + (\tilde{B}_x{}^-)^2}{16\pi\rho kh}\right]^{1/2} \left[\mathbf{e}_x + 2\frac{\tilde{B}_x{}^+\tilde{B}_z{}^+ + \tilde{B}_x{}^-\tilde{B}_z{}^-}{(\tilde{B}_x{}^+)^2 + (\tilde{B}_x{}^-)^2} \mathbf{e}_z\right]. \qquad \ldots\ldots (22) \end{aligned}$$

§ 5. Damping due to Finite Resistivity

In the case of Alfvén waves the damping due to finite resistivity makes the waves difficult to observe in the laboratory; it is important to obtain some estimate of the corresponding damping of the sheet waves. This damping is due to the diffusion of the oscillating magnetic field into the sheet where its energy is dissipated by ohmic loss. All damping due to the mechanical properties of the sheet will be neglected.

We shall suppose that the sheet consists of material whose electrical resistivity is so low that the energy loss per cycle is small compared with the total energy of the wave. Also we shall neglect the thickness h of the sheet and the amplitude A_0 of the waves in comparison with the wavelength $l=2\pi/k$. Only the simple case in which the magnetic fields on either side of the sheet are in the direction of the propagation of the wave will be considered.

The field within the sheet is required. For small oscillations the sheet is nearly flat, and the velocity of motion is small, so it should be possible to obtain the field for a region small compared with the wavelength as if it were a stationary planar slab of thickness h with oscillating boundary conditions, obtained by neglecting the effect of finite resistivity on the field outside the sheet.

This assumption may be justified from the basic equations and it is found to be valid when the effect of internal motions within the sheet can be neglected, and η is so small that powers of η higher than the first can also be neglected.

We use the coordinate system $O'x'y'z'$ illustrated in the figure, for which $z'=z$ and the $y=0$ surface is the mid-surface of the sheet, whose boundaries lie at $y'=\pm h/2$. x' represents distance along the sheet perpendicular to Oz. These coordinates are approximately rectangular over regions in the (x,y) plane of a size small compared with the wavelength.

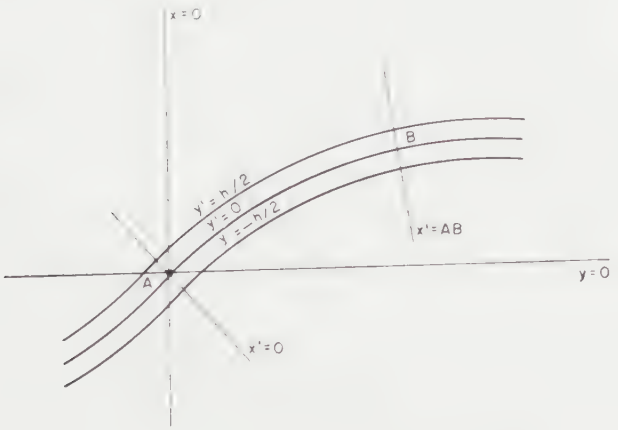

The primed system of coordinates ($z'=z$). The thickness of the sheet and the y scale have been exaggerated. AB is the distance along $y'=0$ from A to B.

In this coordinate system (dropping the primes, which are implied throughout the rest of this section):

$$\frac{\partial \mathbf{B}}{\partial t} = \frac{\eta}{4\pi} \nabla^2 \mathbf{B}, \qquad \ldots\ldots (23)$$

and the boundary conditions at $y = \pm h/2$ may be obtained from equations (7) and (12). They are

$$\begin{aligned}\mathbf{B}^{\pm} &= \tilde{B}(1 \pm y_S k)\mathbf{e}_x \\ &= \tilde{B}(1 \pm A_0 k \sin kx \sin \omega t)\mathbf{e}_x \qquad (y = \pm h/2). \qquad \ldots\ldots (24)\end{aligned}$$

Evidently $\mathbf{B} = B\mathbf{e}_x$ throughout the sheet, for the variations in the y direction are of order $(kh)^{-2}$ larger than those in the x direction, which may therefore be neglected:

$$\frac{\partial B}{\partial t} = \frac{\eta}{4\pi} \frac{\partial^2 B}{\partial y^2}. \qquad \ldots\ldots (25)$$

Let

$$C = \tilde{B} A_0 k \sin kx. \qquad \ldots\ldots (26)$$

The standard derivation of the radio frequency skin effect then shows that if the skin depth is

$$d = \left(\frac{\eta}{2\pi\omega}\right)^{1/2} \qquad \ldots\ldots (27)$$

(see for instance Spitzer 1956, p. 52), and $\chi = (1+i)/d$, then

$$B = Ce^{i\omega t} \sinh(\chi y)/\sinh(\chi h/2). \qquad \ldots\ldots (28)$$

The power dissipated per unit area of sheet

$$\begin{aligned}\epsilon_d &= \frac{\eta C}{(4\pi)^2} \left| \frac{\chi}{\sinh(\chi h/2)} \right|^2 \int_{-h/2}^{h/2} dy \cosh(\chi y) \cosh(\chi^* y) \\ &= \frac{2\eta}{d} \left(\frac{C}{4\pi}\right)^2 T(h/d), \qquad \ldots\ldots (29)\end{aligned}$$

where the function

$$T(X) = \frac{\sinh X + \sin X}{\cosh X - \cos X}. \qquad \ldots\ldots (30)$$

Note that C is a function of x, defined by equation (26).

We require the power dissipated per unit area by the magnetic field averaged over one cycle in space and time, which is

$$\begin{aligned}-\frac{\partial E}{\partial t} &= \oint d(kx) \frac{\epsilon_d}{2} \Big/ \oint d(kx) \\ &= \frac{1}{2\pi} \frac{\eta}{d} \left(\frac{\tilde{B}}{4\pi}\right)^2 (A_0 k)^2 \oint d(kx) \sin^2(kx) T(h/d) \\ &= \frac{\eta}{2d} \left(\frac{\tilde{B}^2 A_0 k}{4\pi}\right)^2 T(h/d). \qquad \ldots\ldots (31)\end{aligned}$$

From equation (18) for the mean energy of the wave per unit area:

$$-\frac{\tilde{B} A_0 k}{4\pi} \frac{\partial A_0}{\partial t} = \frac{\eta}{2d} \left(\frac{\tilde{B} A_0 k}{4\pi}\right)^2 T(h/d), \qquad \ldots\ldots (32)$$

where the amplitude A_0 is now a function of time which varies slowly in comparison with the wave oscillations :

$$A_0(t) = \exp(-\nu t), \qquad \ldots\ldots (33)$$

$$\nu = \frac{\eta}{4ld} T(h/d), \qquad \ldots\ldots (34)$$

where $l=2\pi/k$ is the wavelength. Asymptotic forms for the function $T(X)$ are

$$\left.\begin{aligned} T(X)&\simeq 2/X \quad X^{-1}\gg 1\\ T(X)&\simeq 1 \qquad X\gg 1\end{aligned}\right\} \qquad \ldots\ldots(35)$$

and a formula for the damping exponent valid in the two asymptotic regions is

$$\nu\simeq \frac{\eta}{l}\left(\frac{1}{d}+\frac{2}{h}\right) \qquad (h\gg d \text{ or } h\ll d). \qquad \ldots\ldots(36)$$

The time for e-fold decay of the amplitude of the wave is approximately the time for the magnetic field to diffuse a distance $(lq)^{1/2}$ where q is the lesser of the skin depth and the thickness of the membrane.

The theory does not enable us to obtain any slow phase changes in the wave that are of order unity over a period of the order ν^{-1}, if any such phase changes are present.

The possibility of detecting these waves depends on the number of oscillations which take place before they are damped below the limits of observation. A useful measure is the 'quality' or Q of the wave analogous to the quantity used for coils and resonant cavities.

$$\begin{aligned} Q&=\frac{\text{energy stored in the wave}}{\text{energy lost per radian of oscillation}}\\ &=\frac{\omega}{2\nu}. \end{aligned} \qquad \ldots\ldots(37)$$

Using the definition (27) of d, the quality of the sheet wave is

$$Q_{\mathrm{S}}=\frac{2}{k\,dT(h/d)} \qquad \ldots\ldots(38)$$

$$=\frac{4}{\omega^2 h\,dT(h/d)}\frac{\bar{B}^2}{4\pi\rho}. \qquad \ldots\ldots(39)$$

The quality of an Alfvén wave in a continuous uniform medium of the same material as the sheet is

$$Q_{\mathrm{A}}=\frac{2}{k^2d^2}=\frac{2}{\omega^2d^2}\frac{\bar{B}^2}{4\pi\rho}. \qquad \ldots\ldots(40)$$

We compare the quality of the sheet waves and Alfvén waves of the same frequency for two extreme cases, using the asymptotic formulae (35) for $T(X)$.

When

$$h\gg d \qquad T(h/d)\simeq 1$$

and

$$Q_{\mathrm{S}}/Q_{\mathrm{A}}\simeq 2d/h\ll 1. \qquad \ldots\ldots(41)$$

The sheet waves damp much more rapidly than the Alfvén waves.

When

$$h\ll d \qquad T(h/d)\simeq 2d/h$$

and

$$Q_{\mathrm{S}}/Q_{\mathrm{A}}\simeq 1. \qquad \ldots\ldots(42)$$

The two types of waves damp at the same rate.

When the damping of the sheet waves is comparable with that of Alfvén waves, the former should be observable in copper and mercury. The mechanical

stresses in the copper sheet could be reduced by splitting it into thin strips at right angles to the lines of magnetic force and suspending these strips very loosely.

For a gaseous plasma the hydromagnetic approximation may not be valid. In particular if the wavelength c/f_p of radiation in free space at the plasma frequency f_p is long compared with the skin depth d then the inertia of the electrons cannot be neglected (Spitzer 1956, p. 52).

§ 6. Conclusion

A plane uniform sheet of conducting material situated in a uniform vacuum magnetic field can support transverse magnetomechanical waves similar to the Alfvén waves in a three-dimensional continuum of the conducting material. The dispersion relation is given by equation (11), where h is the thickness of the sheet, and other symbols have their usual meanings. The phase velocity is dependent on frequency and is greater than for the corresponding Alfvén waves.

When the skin depth is much greater than the sheet thickness the sheet waves are damped at the same rate as the corresponding Alfvén waves. The sheet waves should be observable under laboratory conditions in mercury and copper.

References

Alfvén, H., 1950, *Cosmical Electrodynamics* (Oxford: Clarendon Press).

Allen, T. K., Baker, W. R., Pyle, R. V., and Wilcox, J. M., 1959, *Phys. Rev. Letters*, **2**, 383.

Bostick, W. H., and Levine, M. A., 1955, *Phys. Rev.*, **97**, 13.

Jephcott, D. F., 1959, *Nature, Lond.*, **183**, 1652.

Kruskal, M., and Schwartzschild, M., 1954, *Proc. Roy. Soc.* A, **223**, 348.

Lehnert, B., 1954, *Phys. Rev.*, **94**, 815.

Lundquist, S., 1949, *Phys. Rev.*, **76**, 1805.

Sawyer, G. A., Scott, P. L., and Stratton, T. E., 1959, *Phys. of Fluids*, **2**, 47.

Spitzer, L., Jr., 1956, *Physics of Fully Ionized Gases* (Interscience Tracts on Physics and Astronomy, No. 3) (New York, London: Interscience).

Stewartson, K., 1957, *Proc. Camb. Phil. Soc.*, **53**, 544.

Rotational Analysis of the 5–1 Band of the B′–B System of N_2

By P. K. CARROLL† and H. E. RUBALCAVA‡

† Physics Department, University College, Dublin
‡ Chemistry Department, University College, Dublin

MS. received 22*nd February* 1960, *in final form* 18*th March* 1960

Abstract. The 5–1 band of the recently discovered B′→B system of N_2 has been photographed under large dispersion and a rotational analysis has been made. The upper state has been shown to be of species $^3\Sigma_u^-$ and the lower state has been confirmed to be $B^3\Pi_g$. The rotational constants derived from the analysis are $B' = 1{\cdot}381_6\,\mathrm{cm}^{-1}$, $D' = 4{\cdot}6 \times 10^{-6}\,\mathrm{cm}^{-1}$, $B'' = 1{\cdot}610_4\,\mathrm{cm}^{-1}$, $D'' = 5{\cdot}4 \times 10^{-6}\,\mathrm{cm}^{-1}$. The spin structure of the $^3\Sigma_u^-$ state has been determined and a discrepancy between theory and experiment noted.

§ 1. Introduction

Recent spectroscopic studies of nitrogen discharges and afterglows have shown the presence of a new system of bands in the near infra-red. The first band of the system was discovered in a discharge tube source by Carroll and Sayers (1953) who gave measurements of the four strongest heads at 8265·5, 8283·8, 8293·3 and 8310·6 Å. The band was degraded to longer wavelengths but otherwise was very similar in structure to the First Positive bands. Only one band of the new transition was observed due to the high intensity of the First Positive system in the same spectral region.

More recently Kistiakowsky and Warneck (1957), while investigating the spectrum of the Lewis–Rayleigh afterglow under low dispersion, observed some poorly resolved features at 6934, 7823, 8949 and 10434 Å which they were unable to assign satisfactorily. There was no obvious relationship between these bands and the band at 8265·5 Å. Later however, more extensive measurements of the system giving head structure were made by LeBlanc, Tanaka and Jursa (1958) who studied the afterglow emission of nitrogen–argon mixtures at low temperatures. These workers identified the lower state as $B^3\Pi_g$ but were unable to establish the character or vibrational numbering of the upper state. It was evident from this work that the 8265·5 band was the $(n+1)$–1 band of the afterglow system, where n is the unknown integer used by LeBlanc, Tanaka and Jursa in their vibrational analysis. An investigation of the isotope effect has shown that $n = 4$ so that the band discussed in the present work is in fact the 5–1 band.

The new transition is of importance not only because of its appearance in the nitrogen afterglow but also because two bands of the system have been reported in the spectrum of the night sky by Khvostikov and Megrelishvili (1959). Furthermore the electronic character of any new state of N_2 is of considerable interest for comparison with the extensive and detailed data on the theoretically

predicted levels which have been given by Mulliken (1957). The work described below was therefore undertaken with a view to establishing the nature of the B′ state† and determining its rotational constants. A brief preliminary report of the results has already been given (Carroll and Rubalcava 1959).

§ 2. Experimental

The source employed was essentially the same as that described by Carroll and Sayers (1953), i.e. a conventional transformer discharge through nitrogen. The conditions necessary for the appearance of the new transition were (*a*) that the N_2 should be quite pure and in particular free from O_2 and (*b*) that the discharge tube should be very clean. The pressure of N_2 was varied from 0·2 to 3·5 mm and within this range no noticeable change in the intensity of the transition occurred. Low current densities were used in the experiments in order to keep the rotational temperature low. This procedure facilitated the analysis as it rendered the heads of the new band more obvious under large dispersion and reduced the overlapping by the higher rotational lines of the First Positive bands. It should be recalled that the new band lies in the middle of the $\Delta v = 1$ sequence of the First Positive system and it is only because there is a local minimum in the intensity of the latter system that the new band can be observed at all. The spectrum was photographed in the second order of the 21 ft grating in the Physics Department of University College, Dublin, on hypersensitized Kodak II N plates. Second, third and fourth order iron arc lines were used as reference spectra. In addition to the structure of the B′–B band many lines of the 3–2 First Positive band were measured in the same region. A comparison of these measurements with those given by Carroll (1952) (to be referred to as I) in the analysis of the 3–2 band suggests that the wave numbers in both cases are correct to about 0·02 cm^{-1}, although weak or blended lines will be in error by amounts greater than this.

§ 3. Analysis

Under large dispersion the band appeared fairly weak and it was also overlapped to some extent by First Positive structure, especially at higher J values. Nevertheless a number of branches were picked out by inspection. At this stage the knowledge that the lower level was $v = 1$ of the $B\,^3\Pi_g$ state considerably facilitated the analysis. By using the data in I for this level and by applying the combination principle it was possible to identify branches, calculate others and assign N values. In this way three components were found in the new band, each consisting of a fairly strong P, Q and R branch. The presence of well developed Q branches showed that the upper state was not of species $^3\Pi$ while the absence of Λ-doubling eliminated the possibility that it might be of species $^3\Delta$. The observations were however consistent with the upper state being $^3\Sigma$. This was verified by the identification of a number of satellite branches from which the fine structure in the B′ state was shown to be typical of a $^3\Sigma$ state.

†The designation B′ for the new state has been used by Wilkinson (1959); Kistiakowsky and Warneck referred to their afterglow bands as the 'Y bands'.

The lower state is of g-symmetry; therefore according to the selection rule of $g \leftrightarrow\!\!\!\!\!\!+\!\!\!\!\!\!\rightarrow g$, the upper state must be of u-symmetry. Furthermore, the 2:1 intensity alternation in the rotational structure characteristic of N_2 is observed and in all cases the lines from levels with even N are found to be the stronger. Hence the upper state must be $^3\Sigma_u^-$.

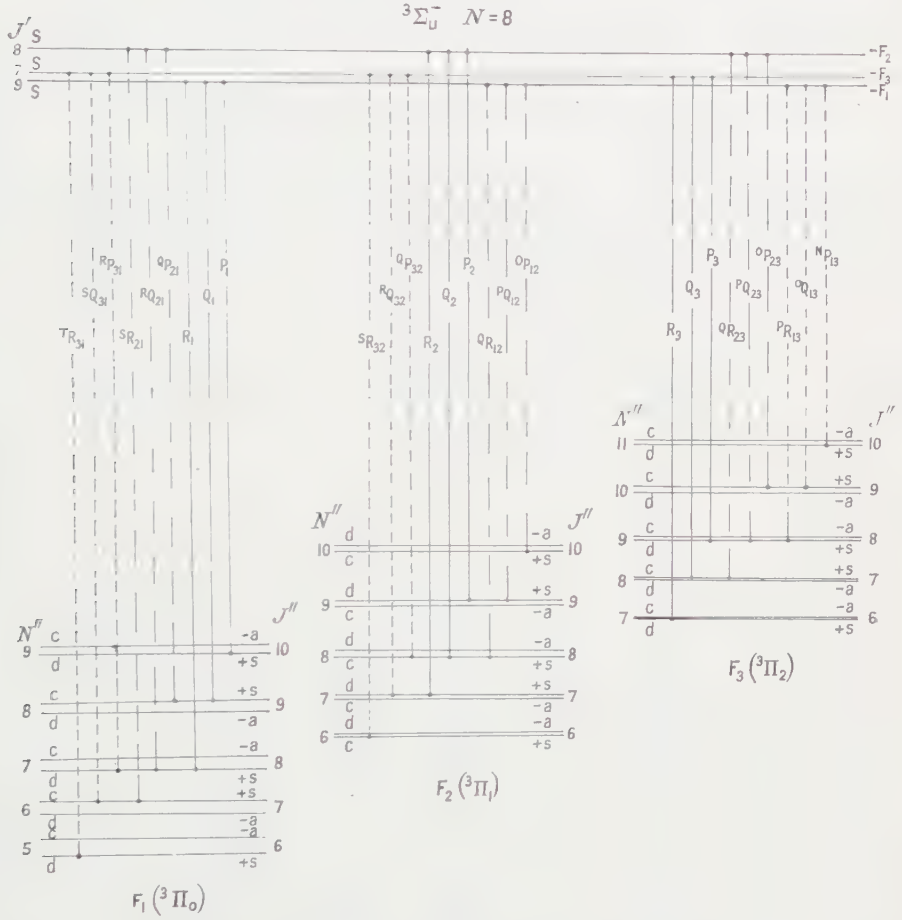

Figure 1. Energy level diagram for a $^3\Sigma_u^- \rightarrow {}^3\Pi_g$ transition.

An energy level diagram for a $^3\Sigma_u^- \rightarrow {}^3\Pi_g$ (case *a*) transition is shown in figure 1. Twenty-seven branches are theoretically predicted for such a transition and in the present analysis at least some structure was found for twenty-four of the expected branches. The two satellite branches, $^RP_{31}$ and $^PR_{13}$, which are associated with the two main branches R_1 and P_3 respectively were not resolved because of the very small splitting between the F_1 and F_3 levels in the $^3\Sigma_u^-$ state (see below); the $^QP_{32}$ and $^QR_{12}$ branches were unresolved from one another for the same reason. The results of the analysis are given in table 1. Figure 2 (Plates I and II) shows a reproduction of part of the band together with the identification of the branches.

The $B\,^3\Pi_g$ *state.*

As the lower state of the new system is known to be $B\,^3\Pi_g$ the combination differences for the lower level determined from the present analysis should agree with those obtained for the upper level of the 1–0 First Positive band. The latter were got from the rotational analysis given in I and were found to agree very well with the values derived from the present work. As a typical example, table 2 gives the $\Delta_2 F_{2d}(J)$ values, as obtained from both sets of data.

The rotational constants B and D for the lower level were computed by a procedure similar to that described in I. The results are given in table 3 which also gives the constants determined from the analysis of the 1–0 First Positive band. The latter values are to be considered the more accurate as they are based on more extensive data.

The Λ-type doubling for the $^3\Pi$ state was determined from the analysis by the usual methods. The results are not given here as more extensive data for the Λ-doubling are already available in I.

Table 1. Wave Numbers and Line Assignments for the 5–1 Band of the B′–B System

J	R_1	Q_1	P_1	$^SR_{21}$	$^RQ_{21}$	$^QP_{21}$	$^TR_{31}$	$^SQ_{31}$
0	12106·49			12107·86				
1	106·39	12101·62		110·37			12121·02	
2	106·01	098·40	12098·06	112·73	12106·49		125·98	
3	105·36	94·91	91·65	114·84	105·94	12095·46	130·86	12114·12
4	104·46	91·25	85·12	116·76	105·08	91·86	135·52	116·14
5	103·30	87·39	78·44	118·38	103·89	87·99		117·70
6	101·85	83·19	71·44	119·81	102·46	83·85		119·16
7	100·11	78·77	64·22	120·83	100·76	79·41		120·16
8	98·06	74·06	56·66	121·69	98·73	74·70		121·02
9	95·74	69·06	48·81	122·19	96·37	69·70		121·54
10	93·08	63·69	40·64	122·49	93·75	64·47		121·84
11	90·11	58·01	32·09	122·19	90·74	58·67		121·54
12	86·77	51·95	23·29	121·69	87·50	52·59		121·02
13	83·05	45·60	14·07	120·83	83·85	46·30		120·16
14	78·98	38·83	04·52	119·51	79·68	39·44		118·86
15	74·51	31·69	11994·58	117·88	75·23	32·27		117·26
16	69·70	24·13	84·20	115·92	70·36	24·74		
17	64·47	16·22	73·46	113·33	65·14	16·86		
18	58·82	07·88	62·32	110·37	59·54	08·62		
19	52·72	11999·14	50·81	107·13	53·48	11999·87		
20		89·94	38·84			90·71		
21		80·38	26·49			81·13		
22		70·38	13·70			71·11		
23		59·93	00·50			60·69		
24		49·05	886·90			49·83		
25		37·78	72·90			38·54		
26		26·15	58·50					
27		14·03						
		01·58						

Table 1 (*continued*)

J	$^{Q}R_{12}$	$^{P}Q_{12}$	$^{O}P_{12}$	R_2	Q_2	P_2	$^{S}R_{32}$	$^{R}Q_{32}$
0								
1								
2				12069·96			12081·62	12069·28
3	12059·92			71·64	12060·68		86·14	70·97
4	58·67	12047·47		72·88	59·22	12047·64	90·27	72·18
5	56·56	42·76	12031·45	73·55	57·19	43·37	93·75	72·88
6	54·00	37·45	23·84	73·79	54·64	38·02	96·97	73·09
7	51·04	31·45	15·26	73·55	51·74	32·09	99·38	72·88
8	47·67	25·24	06·27	72·88	48·32	25·82	101·26	72·18
9	43·77	18·51	11996·85	71·64	44·45	19·17	102·95	70·97
10	39·44	11·41	87·00	69·96	40·09	12·00		69·28
11	34·58	03·70	76·68	67·84	35·32	04·38		67·19
12	29·30	11995·62	65·83	65·26	29·97	11996·25		64·63
13	23·55	87·00	54·57	62·18	24·21	87·71		61·55
14	17·35	77·97	42·73	58·67	17·98	78·65		58·01
15	10·54	68·50		54·64	11·26	69·14		54·00
16	03·40	58·55		50·24	04·08	59·18		49·59
17	11995·90	48·04		45·26	11996·44	48·77		44·65
18	87·71	37·15		39·81	88·33	37·83		39·17
19		25·75		33·97	79·74	26·49		
20		13·84		27·62	70·68	14·63		
21		01·70		20·81	61·17	02·39		
22				13·60	51·19	11889·65		
23				05·86	40·79	76·45		
24				11997·62	29·84	62·81		
25				88·80	18·47	48·71		
26					06·67			

J	$^{O}Q_{13}$	$^{N}P_{13}$	$^{Q}R_{23}$	$^{P}Q_{23}$	$^{O}P_{23}$	R_3	Q_3	P_3
0								
1								
2						12045·05		
3			12035·41			48·32	12034·77	
4				12021·14		50·89	34·33	12020·59
5	12003·09		33·97	17·54	12003·70	52·79	33·39	16·86
6	11996·00	11982·45	32·54	13·25	11996·69	54·00	31·87	12·56
7	88·33	71·75	30·39	08·31	88·99	54·64	29·70	07·64
8	80·17	60·69	27·59	02·78	80·72	54·64	26·94	02·10
9	71·11	49·05	24·13	11996·69	71·75	54·00	23·55	11996·00
10	61·72	36·76	20·22	89·94	62·32	52·79	19·60	89·33
11		23·97	15·77	82·71	52·23	51·04	15·08	82·01
12		10·75	10·54	74·86	41·55	48·70	09·99	74·19
13		896·82	04·80	66·47	30·51	45·84	04·38	65·83
14		82·43	11998·74	57·68	18·89	42·54	11998·23	56·98
15		67·52	92·21	48·16	06·76	38·54	91·57	47·54
16				38·24		34·14	84·38	37·62
17				27·86		29·20	76·68	27·20
18				16·92		23·77	68·50	16·30
19				05·56		17·84	59·83	04·88
20						11·41	50·62	11892·97
21						04·52	40·95	80·59
22						11997·13	30·82	67·73
23						89·26	20·17	54·37
24						80·85	09·08	40·52
25						72·02	11897·50	
26						62·67	85·51	
27						52·84	73·10	

Table 2. $\Delta_2F_{2d}(J)$ Values for the $v=1$ Level of the $B\,^3\Pi$ State determined from the Present Analysis and also from the Analysis of the 1–0 First Positive Band

J	$\Delta_2F_{2d}(J)$ Present work	$\Delta_2F_{2d}(J)$ First Positive system	J	$\Delta_2F_{2d}(J)$ Present work	$\Delta_2F_{2d}(J)$ First Positive system
0			12	86·61	86·58
1			13	93·04	93·03
2	22·02	22·09	14	99·49	99·49
3	28·27	28·63	15	105·87	105·89
4	34·86	35·09	16	112·41	112·30
5	41·46	41·52	17	118·77	118·71
6	47·97	47·96	18	125·18	125·12
7	54·38	54·38	19	131·58	131·56
8	60·88	60·85	20	138·03	137·92
9	67·26	67·28	21	144·36	144·33
10	73·71	73·74	22	150·79	150·72
11	80·13	80·17	23	157·15	157·08

Table 3

	$B'\,^3\Sigma_u^-$, $v=5$	$B\,^3\Pi_g$, $v=1$	
		Present work	First Positive system (I)
B (cm^{-1})	$1{\cdot}381_6$	$1{\cdot}610_4$	1·6108
D (cm^{-1})	$4{\cdot}6\times10^{-6}$	$5{\cdot}4\times10^{-6}$	$5{\cdot}93\times10^{-6}$

The $B'\,^3\Sigma_u^-$ state.

In any $^3\Sigma$ state, on account of the triplet fine structure, three sets of combination differences, $\Delta_2F_1(N)$, $\Delta_2F_2(N)$ and $\Delta_2F_3(N)$ can be formed. In the present case for N greater than about 5, the spin splitting in the $B'\,^3\Sigma_u^-$ state is almost independent of N (see below) and hence the $\Delta_2F(N)$ values as determined from the three components are almost the same for a given value of N. To determine the rotational constants B and D therefore, the three sets of $\Delta_2F(N)$ values were averaged and treated in the usual graphical manner as described by Herzberg (1950). The constants obtained are given in table 3.

The dependence of B_v on v is given by the well-known equation

$$B_v = B_e - \alpha_e(v+\tfrac{1}{2}). \qquad \ldots\ldots(1)$$

As only one vibrational level was studied in the present work it was not possible to determine α_e and B_e directly. However Pekeris (1934) has shown that if a Morse potential function is used to describe an electronic state the following relationship holds

$$\alpha_e = \frac{6\,(\omega_e x_e B_e^3)^{1/2}}{\omega_e} - \frac{6B_e^2}{\omega_e}. \qquad \ldots\ldots(2)$$

As the vibrational constants were known for the $^3\Sigma_u$ state, equations (1) and (2) were solved for α_e and B_e. The results obtained were $\alpha_e = 0{\cdot}0156\,\text{cm}^{-1}$, $B_e = 1{\cdot}467\,\text{cm}^{-1}$ and $r_e = 1{\cdot}281$ Å.

The spin splitting in the B' state can readily be determined from wave number differences of the type

$$\delta_{12}(N) = {}^RQ_{21}(N-1) - R_1(N-1)$$
$$\delta_{32}(N) = {}^PQ_{23}(N+1) - P_3(N+1)$$

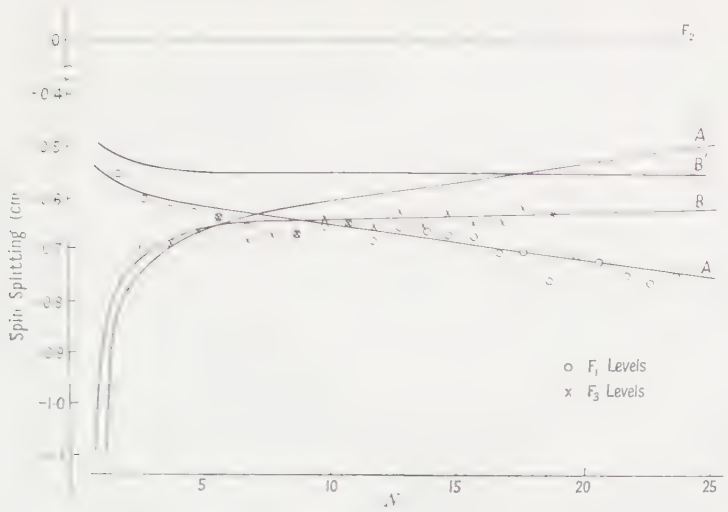

Figure 3. Observed and calculated spin splitting in the $^3\Sigma_u^-$ state. Curves A and A′ are the δ_{12} and δ_{32} splittings respectively as calculated from the observed δ_{12} values using Schlapp's formula; curves B′ and B are the same splittings calculated from the observed δ_{32} data.

where $\delta_{12}(N)$ and $\delta_{32}(N)$ measure the separation of the $F_1(N)$ and $F_3(N)$ levels respectively from the $F_2(N)$ level. The average values of these quantities are given in table 4 and shown graphically in figure 3.

Table 4. Spin Splitting in the $v=5$ Level of the B′ $^3\Sigma_u^-$ State

N	$-\delta_{12}$	$-\delta_{32}$	N	$-\delta_{12}$	$-\delta_{32}$
1			13	0·66	0·63
2	0·55		14	0·67	0·66
3	0·60	0·69	15	0·68	0·63
4	0·62	0·69	16	0·68	0·65
5	0·63	0·66	17	0·71	0·65
6	0·64	0·64	18	0·71	0·62
7	0·66	0·68	19	0·77	0·64
8	0·62	0·67	20	0·72	
9	0·67	0·67	21	0·73	
10	0·65	0·64	22	0·76	
11	0·65	0·65	23	0·78	
12	0·69	0·66	24	0·76	

According to Schlapp (1937), in a $^3\Sigma$ state the $F_2(N)$ component follows the simple rotator formula while the splittings of the other two components from this are given by

$$\delta_{12}(N)=(2N+3)B_v-\{(2N+3)^2B_v^2+\lambda^2-2\lambda B_v\}^{1/2}+\gamma(N+1)-\lambda \quad \ldots\ldots(3)$$

$$\delta_{32}(N)=-(2N-1)B_v+\{(2N-1)^2B_v^2+\lambda^2-2\lambda B_v\}^{1/2}-\gamma N-\lambda \quad \ldots\ldots(4)$$

where λ and γ are constants. On expanding these expressions in powers of λ/B and on rejecting squares and higher powers of this quantity, one finds that the

splittings given by (3) and (4) reduce to the values given by Kramers' (1929) formula

$$\delta_{12}(N) = -\frac{2\lambda(N+1)}{2N+3} + \gamma(N+1), \qquad \ldots\ldots(5)$$

$$\delta_{32}(N) = -\frac{2\lambda N}{2N-1} - \gamma N. \qquad \ldots\ldots(6)$$

With the present data it was found that the differences in the spin splittings calculated by both Schlapp's and Kramer's formulae were well within the limits of accuracy of our measurements except at the lowest N values where the former was slightly better. Kramers' expressions (5) and (6) were therefore used to determine λ and γ as they lend themselves to simple graphical treatment. The values obtained were: from (5) $\lambda = 0{\cdot}63\,\mathrm{cm}^{-1}$, $\gamma = -0{\cdot}0052\,\mathrm{cm}^{-1}$ and from (6) $\lambda = 0{\cdot}60\,\mathrm{cm}^{-1}$, $\gamma = 0{\cdot}0014\,\mathrm{cm}^{-1}$. The values of λ and γ should of course be the same; however, the discrepancy in both quantities is outside the limits of experimental error. The effect is illustrated in figure 3 which shows together with the experimental data the theoretical curves calculated from both sets of data. It is seen that each pair of λ and γ values represents satisfactorily the splitting from which they were determined but not the other splitting. Furthermore for both Kramers' and Schlapp's formulae the sum $\delta_{12}(N-1)+\delta_{32}(N+1)$ should be constant and equal to $-(2\lambda+\gamma)$, whereas with the present data this sum shows a small but definite linear dependence on N. In connection with this anomaly it is of interest to note that another small but real discrepancy between theory and experiment has been reported in I for the $A\,^3\Sigma_u^+$ state of N_2.

§ 4. Conclusion

Mulliken (1957) has recently prepared a detailed table of the experimentally observed levels of N_2 together with the estimated positions and other properties of additional states whose existence is theoretically predicted. Among the latter are two, a $^3\Delta_u$ and a $^3\Sigma_u^-$ state, both of which arise from the electron configuration $KK(\sigma_g 2s)^2(\sigma_u 2s)^2(\pi_u 2p)^3(\sigma_g 2p)^2(\pi_g 2p)$ and which should lie between the well-known $B\,^3\Pi_g$ and $C\,^3\Pi_u$ states. The predicted energy and constants for the states are

	T_{00}	ω_e	r_e(Å)
$^3\Delta_u$	60500	1490	1·28
$^3\Sigma_u^-$	70700	1530	1·27

The values of T_{00} and ω_e for the B′ state as determined from the R_2 head measurements of Le Blanc, Tanaka and Jursa (1958) are $65874\,\mathrm{cm}^{-1}$ and $1513{\cdot}1\,\mathrm{cm}^{-1}$ respectively and lie roughly midway between the values for the $^3\Delta_u$ and $^3\Sigma_u^-$ states of Mulliken so that, on these data alone, it was not possible to identify the B′ state. In fact Le Blanc, Tanaka and Jursa (1958) favoured $^3\Delta_u$ as the upper state of the infra-red bands. The present analysis shows that the B′ state must be identified with the predicted $^3\Sigma_u^-$ state. In view of the uncertainties inherent in the theoretical work the agreement between the experimental and theoretical data for the $^3\Sigma_u^-$ state can be considered very good.

Wilkinson (1959) has reported several forbidden transitions in the absorption spectrum of N_2 in the vacuum ultra-violet. One of these is identified as the B′←X transition. In his most recent work on the fine structure of these bands Wilkinson (private communication) from a comparison of the experimental and calculated intensity distribution has concluded that the transition is of the type $^3\Sigma_u^- \leftarrow {}^1\Sigma_g^+$. Thus the present results and the work of Wilkinson are in excellent agreement.

A few final points may be made about the new system. An examination of the potential curves for the B and B′ states shows that the strongest bands of the system lie quite far in the infra-red. In particular the most intense transition from $v' = 0$ should be the 0–1 band at 20 400 Å. Indeed in this region the B′→B bands may well be as strong as the First Positive system. Furthermore the right-hand limbs of the potential curves for the two states cross at about 72 000 cm^{-1} so that in principle at least the transition could change from B′→B to B→B′ for some of the infra-red bands. Again the $^3\Delta_u$ state is predicted to lie below the B′ $^3\Sigma_u^-$ state so that the allowed $^3\Delta_u \rightarrow B\,^3\Pi_g$ system should have its most intense bands at even longer wavelengths than the B′→B system. The study of electronic spectra in the infra-red beyond the photographic limit has been largely neglected; in the case of N_2 at least it is a field which might well repay investigation.

Acknowledgments

In conclusion we should like to thank Professor R. S. Mulliken and Dr. P. G. Wilkinson for their correspondence in the course of this work and for informing us of their results prior to publication.

References

Carroll, P. K., 1952, *Proc. Roy. Irish Acad.* A, **54,** 369.
Carroll, P. K., and Rubalcava, H. E., 1959, *Nature, Lond.*, **184,** 119.
Carroll, P. K., and Sayers, N. D., 1953, *Proc. Phys. Soc.* A, **66,** 1138.
Herzberg, G., 1950, *Spectra of Diatomic Molecules* (New York: Van Nostrand).
Khvostikov, I. A., and Megrelishvili, T. G., 1959, *Nature, Lond.*, **183,** 811.
Kistiakowsky, G. B., and Warneck, P., 1957, *J. Chem. Phys.*, **27,** 1417.
Kramers, H. A., 1929, *Z. Phys.*, **53,** 422.
LeBlanc, F., Tanaka, J., and Jursa, A., 1958, *J. Chem. Phys.*, **28,** 979.
Mulliken, R. S., 1957, *The Threshold of Space* (London: Pergamon Press), p. 169.
Pekeris, C. L., 1934, *Phys. Rev.*, **45,** 98.
Schlapp, R., 1937, *Phys. Rev.*, **51,** 342.
Wilkinson, P. G., 1959, *J. Chem. Phys.*, **30,** 773.

Shadow Effect in the Scattering of GeV Pions and Nucleons by Deuterons†

By B. DEJON‡ and K. SMITH§

‡ Brookhaven National Laboratory, Upton, New York
§ Argonne National Laboratory, Lemont, Illinois

MS. received 7th December 1959, *in revised form 25th January* 1960

Abstract. The experimental total cross sections for the individual pion–nucleon and nucleon–nucleon processes have been used to deduce the pion–deuteron and nucleon–deuteron total cross sections using a geometrical optic model

§ 1. Introduction

It is known, experimentally (see Chen, Leavitt and Shapiro 1954, Cool, Piccioni and Clark 1956 and Coor *et al.* 1955), that the cross section for the scattering of high energy (~ 1 GeV) pions and nucleons by deuterons is less than the sum of the corresponding neutron and proton cross sections, measured separately.

Glauber (1955) has shown that the non-additivity of the free-particle cross sections can be largely explained by 'eclipses', in which either the neutron or the proton lies in the shadow cast by the other. Glauber obtained cross section defects, of the magnitude observed, by using the diffraction approximation in the calculation of the scattering amplitudes and assuming black sphere interactions. Sitenko (1959) used the same approximation, but assumed a different individual nucleon–pion scattering function. Both authors performed their calculations only at a single incident energy.

Since there are more experimental data available now, we shall compute the π–d cross sections over an energy range from 0·55 to 1·5 GeV. Furthermore, since in this energy range the wavelength of the incoming particle is small compared with the range of nuclear interactions (2×10^{-13} cm), the interaction will not vary appreciably in distances comparable with this wavelength and so we would expect the incident particle to follow its classical path. Thus it seems justified to try to account for the observed cross section 'defect' on the basis of a classical model.

§ 2. Geometrical Optic Model for the Scattering Process

We assume that the regions of interaction of the constituent nucleons of the deuteron with the incoming particles are spheres with sharp boundaries. The radii r are given by the formula $\sigma = \pi r^2$, where σ is the experimental total cross section of the nucleon under consideration. We do not use black spheres, since we allow for scattering as well as purely absorptive interactions.

The deuteron is taken to be two such spheres, whose centres are a distance R apart. The polar and azimuthal angles of the vector **R** relative to the Z axis (the direction of the incident beam) are θ and ϕ. The cross section of the deuteron, for a given (R, θ, ϕ), is taken to be the area presented by the two spheres to an

† Work performed under the auspices of the U.S. Atomic Energy Commission.

observer at infinity. To obtain the true deuteron cross section we average over all possible positions of the two components of the deuteron in three space.

For a given R, a uniform probability distribution is assumed over the directions (θ, ϕ). Thus, an average deuteron cross section for a fixed R is obtained, which is then weighted according to the square of the radial wave function of the deuteron. Hence the deuteron cross section is given by

$$\sigma(r_1, r_2) = \sigma_1 + \sigma_2 - \left(\int_0^\infty |\psi(R)|^2 dR \right)^{-1} \int_0^\infty dR\, |\psi(R)|^2 \frac{1}{4\pi R^2} \int_0^\pi \int_0^{2\pi} R d\theta \times R \sin\theta d\phi X(r_1, r_2, R, \theta) \quad \ldots\ldots (2.1)$$

where $\psi(R)\ R$ is the deuteron radial wave function, and X is the region of overlap of the two areas, which is

$$X(r_1, r_2, R, \theta) = \sum_{i=1}^{2} r_i^2 (\alpha_i - \cos\alpha_i \sin\alpha_i), \quad \ldots\ldots (2.2)$$

with

$$\cos\alpha_i = \frac{r_i^2 - r_j^2 + R^2 \sin^2\theta}{2 r_i R \sin\theta}\ ; \quad \begin{matrix} i,j = 1,2, \\ i \neq j, \end{matrix} \quad \ldots\ldots (2.3)$$

provided the two spheres really overlap. If they do not overlap X is set equal to zero, and if one sphere is completely behind or in front of the other (i.e. $r_i + R \leqslant r_j$), then X is set equal to the cross sectional area of the smaller sphere.

The model does not take into account the fact that the kinetic energy of the incoming particle may not be equal to its collision energy, due to the internal motion of the nucleons in the deuteron. However, the error in the collision energy thus introduced is only of the order of ~ 30 Mev. In regions where there is no sharp resonance in the experimental cross sections, the values of σ should not be influenced much by this error in the collision energy, especially as these errors can be expected partially to cancel each other in those regions where the dependence of the nucleon cross sections on the energy is monotonic.

§ 3. Results

The calculation was begun using Burke's (1956) Hulthén wave function and then Moravcsik's (1958) analytic approximations to the Gartenhaus functions. Some deuteron cross sections were also obtained using the Gaussian S-state wave function of Burke and Robertson (1957) and the Gaussian deuteron function of Bransden, Smith and Tate (1958), which contains a d-state component.

The calculation of the cross section, given in equation (2.1), was performed on an IBM-704 digital computing machine. The time taken to compute a cross section was about four minutes.

For 0·8 Gev pions and 1·4 Gev nucleons on deuterons, using the same input cross sections as Glauber (1955), and Moravcsik's (1958) deuteron wave function, the present model gave the following cross section defects:

π–d : 3·6 to 4·2 mbn (experiment : 4 to 6 mbn; Glauber : 1 to 3 mbn)

n–d : 8·8 to 10·1 mbn (experiment: 6 to 9 mbn; Glauber : 4·5 to 7·2 mbn).

It is noted that the results are in quite good agreement with the experimental results quoted by Glauber.

Additional pion–deuteron cross sections were calculated using the π^-–p and π^+–p measurements of Cool, Piccioni and Clark (1956). The unpublished Saclay and M.I.T. data on the π –p total cross sections have also been used, together with the Cool, Piccioni and Clark (1956) π^+–p data, to calculate pion–deuteron cross sections. The Saclay data were not corrected for μ^- and e^- contamination, which is expected to be about 6% at the lower energies and about 2% at higher energies. The results, again using Moravcsik's functions, are presented in the table.

π–d Total Cross Sections in mbn

The 'shadow', in mbn, is given in parenthesis.

Energy (Gev)	Calculated $\sigma_{\pi-d}$, using the data from: Cool *et al.* (1956)	Saclay	M.I.T.	Expt π–d Cool *et al.* (1956)
0·55	50·4 (3·9)	37·1 (2·0)		48·6 (4·9)
0·67		41·7 (2·3)	45·0 (2·5)	
0·76	61·2 (4·4)	55·1 (3·9)	57·0 (4·0)	60·9–62·2 (3·4–4·7)
1·02	64·3 (5·2)	71·5 (6·0)	62·5 (5·0)	67·2 (2·3)
1·26	62·5 (5·5)	65·7 (6·1)	68·5 (6·8)	62·5 (5·5)
1·38	66·1 (6·1)			60·3–64·1 (11·9–8·1)
1·5	60·1 (5·2)			57·0 (8·3)

§ 4. Discussion

It is noted that the model yields numbers of the observed magnitude, even over the quite wide energy range of the table. The large difference (~ 10 mbn) between the calculated values at 0·55 Gev and 1·02 Gev, is due to the different positions of the maxima in the π^-–p data taken from the three sources.

The several wave functions used gave about the same results, with the exception of the Gaussian function of Bransden, Smith and Tate (1958), which consistently gave too large a deuteron cross section.

Acknowledgments

We should like to thank Dr. Luke Yuan for giving to us the Saclay and M.I.T. data in advance of publication and Dr. P. G. Burke for sending to us his unpublished parameters for the Hulthén function.

References

Bransden, B. H., Smith, K., and Tate, C., 1958, *Proc. Roy. Soc.* A, **247,** 73.
Burke, P. G., 1956, Ph.D. Thesis, University of London.
Burke, P. G., and Robertson, H. H., 1957, *Proc. Phys. Soc.* A, **70,** 777.
Chen, F. F., Leavitt, C. P., and Shapiro, A. M., 1954, *Phys. Rev.*, **95,** 663 (A).
Cool, R., Piccioni, O., and Clark, D., 1956, *Phys. Rev.*, **103,** 1082.
Coor, T., Hill, D. A., Hornyak, W. F., Smith, L. W., and Snow, G., 1955, *Phys. Rev.*, **98,** 1369.
Glauber, R. J., 1955, *Phys. Rev.*, **100,** 242.
Moravcsik, M. J., 1958, *Nucl. Phys.*, **7,** 113.
Sitenko, A. G., 1959, *J. Exper. Theor. Phys. U.S.S.R.*, **36,** 1419.

On the Measurement of Orbital Electron Capture with particular reference to ^{131}Cs

By B. R. JOSHI and G. M. LEWIS
Department of Natural Philosophy, University of Glasgow

MS. received 1st *March* 1960

Abstract. A scintillation counter method, which eliminates the need for escape corrections, has been developed for the measurement of L/K capture ratio for intermediate and high Z nuclei. With this method the L/K capture ratio has been determined for ^{131}Cs at $0{\cdot}153 \pm 0{\cdot}008$. The computed value for this simple allowed transition, of known energy, is 0·145, which lies only marginally lower.

§ 1. Introduction

Considerable interest has been shown in recent years in the determination of the relative probabilities of L- and K-electron capture. In general the L/K capture ratio can be expected to depend on both the nuclear and the electron structure of the atom. For an allowed transition, however, this ratio should always be independent of the nuclear matrix elements; and should be a function of the decay energy, and electron distributions only Very approximately then

$$\left(\frac{\mathrm{L}}{\mathrm{K}}\right)_{\text{ratio}} \simeq \frac{(E-\epsilon_{\mathrm{L}})^2}{(E-\epsilon_{\mathrm{K}})^2}\frac{g_{\mathrm{L_I}}{}^2+f_{\mathrm{L_{II}}}{}^2}{g_{\mathrm{K}}{}^2} \simeq \frac{(E-\epsilon_{\mathrm{L}})^2}{(E-\epsilon_{\mathrm{K}})^2}\frac{1}{8}.$$

Here ϵ_{L}, ϵ_{K} are the electron binding energies, $E-\epsilon_{\mathrm{K}}$ is the energy given to the neutrino in K capture, g and f relate to the electron wave functions at the nucleus; $f_{\mathrm{L_{II}}}{}^2$ is small and g^2 can be expected to vary as $1/n^3$ where n is the principal quantum number. The theoretical computations originated by Marshak (1942) and by Rose and Jackson (1949), have been extended by Brysk and Rose (1958). Further amendments have been made by Odiot and Daudel (1956), which lead to larger theoretical values, but the magnitude of the correction falls off rapidly with rising Z and becomes insignificant above $Z \sim 17$.

When the transition energy is known an L/K ratio assignment affords an important check on the validity of the basic theory. The available experimental results have been reviewed by Radvanyi (1955) and Fink (1958). The results are not numerous and, except for a few cases, they are not precise enough to provide a satisfactory comparison with the relevant theory. The number of suitable nuclei is quite small. Among the few more accurate experimental results discrepancies of order 10–20% with prediction obtain. This state of affairs stems largely from the technical difficulties encountered in the exact measurement of the very soft L x and Auger radiations emitted, and from K x-ray escape. For the investigation of low Z gaseous sources a proportional counter method has been utilized by Drever and Moljk (1957), which eliminates escape corrections.

It seemed desirable therefore to study the electron capture process further; and particularly for an intermediate Z nucleus. For such nuclei L/K values are very scarce. ^{131}Cs is of particular interest because the transition energy is known from the inner bremmstrahlung spectrum end-point to be 355 ± 10 kev (Saraf 1954). The transition is allowed; for $\log ft = 5{\cdot}3$, and the shell model predicts a $5/2 \rightarrow 3/2$ transition with no change in parity. The decay, furthermore, is a simple one as shown in figure 1. The intensities of the L and K x-rays have been studied by Fink (1955). The predicted value for the L/K electron capture ratio for ^{131}Cs, based on the calculations of Brysk and Rose, is 0·145. To determine the L/K capture ratio for this nucleus an improved scintillation method of internal source spectroscopy has been developed here, which eliminates all escape corrections in the L/K capture measurements.

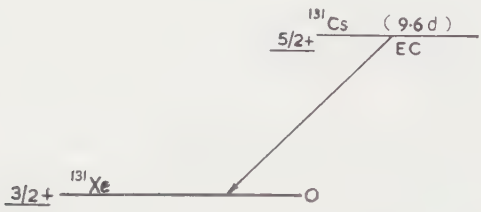

Figure 1. Decay scheme of ^{131}Cs.

The aggregate energy released by successive ionizing radiations can in principle be faithfully recorded by embedding the source in a scintillation crystal (cf. Bannerman, Lewis and Curran 1951, Scharff-Goldhaber, der Mateosian, Johnson and McKeon 1951).

The present method is illustrated in figure 2. Firstly an inner activated sodium iodide crystal was grown with a trace of the source. There is then no

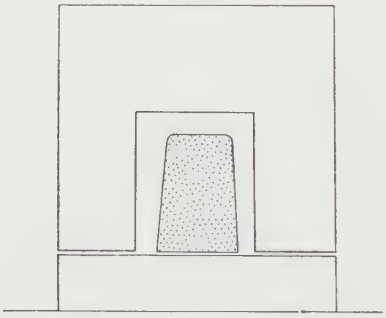

Figure 2. Well type method—the source is dispersed in the inner NaI(Tl) crystal, and this latter is itself completely surrounded by NaI(Tl).

self absorption in this dispersed source. For a moderately sized crystal the L radiations are absorbed, and the K x-rays too unless they are liberated near the surface (cf. Compton and Allison 1936, Appendix IX). This K escape, though small (a few per cent of the K's for a crystal of size 1 cm^3), is of critical importance, since a K α escape is fallaciously registered in the counter as an L-capture event. To eliminate these K surface escape effects, the crystal in which the source was buried was itself wholly entombed in an outer well type crystal, fitted with a lid

of the same material. With this arrangement the K-capture radiation from the source was wholly absorbed, and registered as a K-capture event. This method has proved to be simple, and effective, in operation.

§ 2. Experimental Procedure

The ^{131}Cs was supplied by the Amersham Radiochemical Centre, in chloride form. It has been obtained by chemical separation as the daughter nucleus of ^{131}Ba. A preliminary search was made for any γ-radiations emitted by a thin external source of the ^{131}Cs, with a 2 in. × 2 in. diameter NaI (Tl) Harshaw scintillator, and a multichannel pulse analyser. Calibration was effected by RaD (46·5 kev), and other external sources. Except for the very prominent K x-ray peak at approximately 30 kev no line radiations were obtained in the range of 10 kev–1 Mev, indicating that the source was very pure.

A trace of the ^{131}Cs source was added to a few grammes of Harshaw NaI (Tl) chippings; and these were inserted into a vessel of satin-surfaced fused silica, which was slightly heated, evacuated, and then sealed. Single crystals were readily grown by the Bridgman (1925) method, up to 1 cm^3 in size.

The half-life of the source was found by measuring the K peak from one of these crystals over a period of several half-lives. It was found to decay with $T_{1/2} = 9{\cdot}6$ days in agreement with the results of Yaffe *et al.* (1949).

For the well type application a single crystal, approximately 5 mm^3, was cut and cleaned. This was inserted in the well type crystal of Harshaw NaI (Tl) which had an external size 1¼ cm^3, the walls of this latter were approximately 3 mm thick and the lid approximately 2 mm thick. The crystal system was immersed in liquid paraffin and surrounded by an aluminized mylar reflector. An aluminium container with a thin mylar window was used, since this type of container showed no phosphorescence effects. The photomultiplier used in the main work was an E.M.I. 9514S tube, selected for its low noise and good resolution. The tube had been kept in the dark for a long period, and was not exposed at all during the experiments. Arrangements could be made for cooling the tube when necessary. The system was surrounded by 2 in. thick lead screening to minimize background effects. The pulses were amplified in a non-overloading amplifier (type NE 5202), and were displayed on a CDC multichannel pulse height analyser.

§ 3. Results

A sharp peak was observed at 35 kev due to K capture. The gain of the amplifier could be increased by a factor of 10 and a broad distinct peak due to L capture (~5 kev) was found. Typical K and L peaks are shown in figure 3. This figure shows one of several runs in which the crystal and photomultiplier system had been cooled for several hours, in a cooling jacket, with freezing brine (−15 c). Data concerning the last 15 channels in the figure 3 (*b*) were obtained in a subsidiary run. A background run was made with the well type crystal alone, under similar conditions. The thermal noise of the tube was also measured similarly for comparison. Above 2 kev the background curve differed little from the thermal noise curve.

In the region of the K peak background effects were small, and figure 3 (*a*) gives immediately the measure of K capture. Figure 3 (*b*) shows the L capture region and the broken curve shows the L peak after background effects have

been allowed for. Apart from the low energy rise this curve accords approximately with the distribution that could be expected from statistical considerations (cf. W. B. Lewis 1942), taking the K peak as a standard. The rise at low energy was found to be unaltered when the paralysis time of the kicksorter (35–200 μsec) was increased, externally, to 1 msec. Moreover a run on the L/K ratio taken

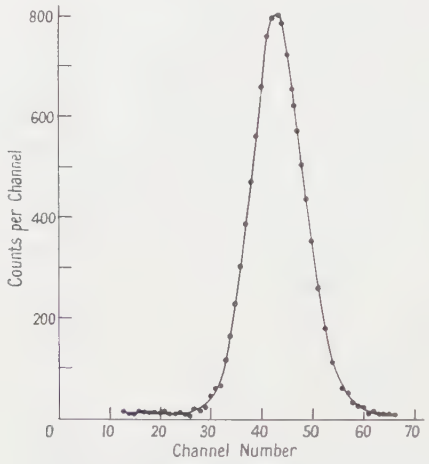

Figure 3 (*a*). ^{131}Cs K peak at 35 kev obtained with the arrangement of figure 2; with cooling (5 min run).

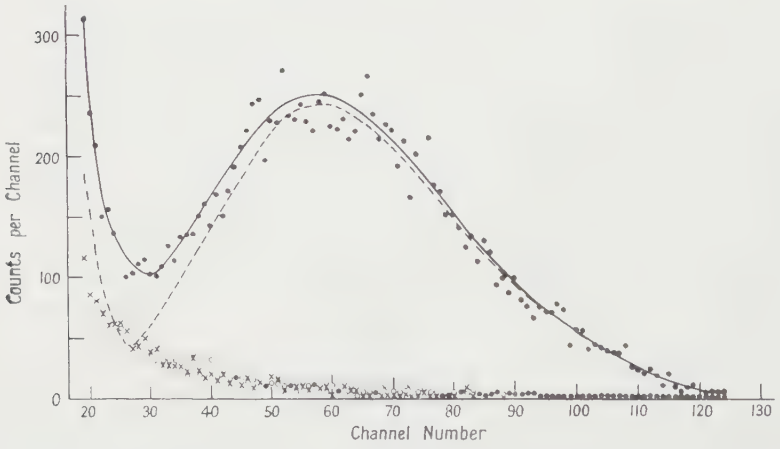

Figure 3 (*b*). ^{131}Cs L peak at approximately 5 kev similarly (30 min run). Crosses denote background run, taken with the well type crystal of NaI(Tl), with no inner source crystal, under similar conditions; circles, thermal noise of the tube, similarly; the broken curve shows the curve obtained by allowing for the background.

after the crystals had been several days in the dark showed no essential change from figure 3, when allowance was made for the loss of source strength over that time. The rise, in a region associated with single electron emission from the photocathode, seemed to be induced by the L and K radiations which had already recorded properly in the L and K peaks. It could be due to delayed emission, for instance, induced by phosphoresence in the crystal and by glow in the multiplier. Such effects could be expected from the work of Harrison (1954),

and Bernstein, Bjerknes and Steele (1958), for example. Further confirmation was obtained by wrapping a ^{131}Cs source of comparable strength in 5/1000 in. silver foil to stop the L x-rays and placing this in the well. The K peak occurred, no L peak of course, but still, quantitatively, the characteristic rise at low energy; indicating that the rise should be dissociated from the L-capture peak. In conclusion, it should be stated that M capture, which would give a broad peak of 1 kev, could be contributing, at least partially, at the trough of the broken curve.

§ 4. Analysis and Conclusion

L and K peaks were analysed by measuring the relative areas under the respective peaks. Dead-time corrections for the kicksorter have been applied—these were generally less than 1%. Measurements were done repeatedly over several half-lives with similar results. The crystal was cleaned on many occasions by absolute alcohol and its size altered appreciably, the consistency of the results indicated that the source was distributed throughout the crystal. This was further confirmed by measurement of the amount of K-escape radiation, by surrounding the radioactive crystal with aluminium foil. The mean value obtained for the L/K ratio was $0{\cdot}153 \pm 0{\cdot}008$, and the error limits are mostly associated with the assessment of the lower energy end of the L peak. It should be further stated, that if there is M capture present, in amounts predicted by theory, that the L/K value will tend towards the lower limit.

It should be mentioned finally that a complete series of experiments had previously been made here with single active crystals, without the well type device. These had been made with a different ^{131}Cs source specimen. In these the K x-ray escape was measured experimentally, and also found to be in agreement with assessments based on a uniform source distribution. For a crystal $1\,cm \times 0{\cdot}6\,cm$ diameter this K x-ray escape was approximately 5%. After correcting for this escape the L/K capture ratio could be deduced. This method gave values for the L/K capture ratio of approximately 16% in accord with the more precise value $0{\cdot}153 \pm 0{\cdot}008$ given above.

The computed value of 0·145 for this intermediate Z nucleus is seen to be only marginally lower.

Acknowledgments

We would like to thank Professor P. I. Dee for his interest in the work, and we are grateful to Dr. R. W. P. Drever for helpful discussions.

References

Bannerman, R. C., Lewis, G. M., and Curran, S. C., 1951, *Phil Mag.*, **40**, 1097.
Bernstein, W., Bjerknes, C., and Steele, R., 1958, *Liquid Scintillation Counting* (London, Paris, New York: Pergamon Press), p. 74.
Bridgman, P. W., 1925, *Proc. Amer. Acad. Arts Sci.*, **60**, 350.
Brysk, H., and Rose, M. E., 1958, *Rev. Mod. Phys.*, **30**, 1169.
Compton, A. H., and Allison, S. K., 1936, *x-rays in Theory and Experiment*, 2nd Edn, (London: Macmillan), Appendix IX.
Drever, R. W. P., and Moljk, A., 1957, *Phil Mag.*, **16**, 427.
Fink, R. W., 1955, *Phys. Rev.*, **98**, 1293.
—— 1958, Atomic Energy Commission Report ORO–173.
Harrison, F. B., 1954, *Nucleonics*, **12**, 24.

Lewis, W. B., 1942, *Electrical Counting* (Cambridge: University Press), p. 116.
Marshak, R. E., 1942, *Phys. Rev.*, **61,** 431.
Odiot, S., and Daudel, R., 1956, *J. Phys. Rad.*, **17,** 60.
Radvanyi, P., 1955, *J. Phys. Rad.*, **16,** 509.
Rose, M. E., and Jackson, J. L., 1949, *Phys. Rev.*, **76,** 1540.
Saraf, B., 1954, *Phys. Rev.*, **94,** 642.
Scharff-Goldhaber, G., der Mateosian, E., Johnson, G. W., and McKeown, M., 1951, *Phys. Rev.*, **83,** 480.
Yaffe, L., Kirsch, M., Standil, S., and Grunlund, J. M., 1949, *Phys. Rev.*, **75,** 699.

The Optical Absorption in Manganese Zinc Fluoride Single Crystals near the Néel Temperature

By D. M. FINLAYSON, I. S. ROBERTSON†, T. SMITH and R. W. H. STEVENSON

Department of Natural Philosophy, University of Aberdeen

MS. received 8*th December* 1959, *in revised form* 21*st March* 1960

Abstract. The visible and ultra-violet absorption spectra of single crystals of manganese fluoride, and of two manganese zinc fluoride mixtures, have been measured down to 62°K.

The sharp lines arising from the level complexes $\{^4E_g{}^4A_{1g}\}(^4G)$ and $^4E_g(^4D)$, which are insensitive to the magnitude of the crystalline electrostatic field, show a non-linear shift with temperature, which varies with composition, and is correlated with the temperatures at which long-range antiferromagnetic order becomes appreciable.

A separation of the exchange interaction effect from that due to the thermal expansion of the lattice can be made with some certainty in the material of medium dilution, except in the immediate neighbourhood of the ordering temperature where effects due to the lattice expansion anomaly may be appreciable.

The magnitude of the antiferromagnetic interaction shift aids the identification of the transitions, and is interpreted as giving a measure of the variation of short-range spin order with temperature.

Measurements of line width and oscillator strength have been made for several absorption lines, and the data for the magnetically dilute materials can be interpreted on simple vibrational models, but for pure manganese fluoride these models seem less satisfactory.

§ 1. Introduction

Many measurements have been made on the optical absorption of magnetically dilute materials, particularly the compounds containing hydrated ions of the first transition group. The levels have been related to those of the free ion by considering the effect of a crystalline electrostatic field of the appropriate symmetry. Various smaller perturbations, such as those due to the vibrational modes of the complex ions, and the spin–orbit, spin–spin and covalency effects can be included (Koide and Pryce 1958).

In antiferromagnetic materials, exchange interaction may substantially modify the energy levels, and an attempt has been made to detect such effects in manganese fluoride. This has a number of absorption bands in the visible and near ultra-violet, and some of these have relatively small half widths and well-defined maxima, so that the small line shift with temperature can be followed with fair accuracy.

This shift would be expected to arise from the change in crystalline field strength D_q with lattice dimensions, and also from the splittings of the ground state and excited states produced by the exchange interaction. The latter should vary (along with the spin ordering temperature) with change in the concentration

†Now at the Department of Physics, The University, Hull.

of the magnetic ion and it should therefore be possible to separate the two effects by measurements on manganese fluoride diluted with a suitable non-magnetic ion. Zinc fluoride was chosen because it is of the same crystal structure with approximately the same lattice parameters as manganese fluoride, and it was found that mixed crystals could be grown over a wide range of compositions.

Since the experimental work described in this paper was completed, a report on the optical absorption of MnF_2 has been made by Stout (1959), and comparison with his results will be made where possible.

§ 2. Specimen Preparation

The crystals were grown in graphite crucibles by the Stockbarger technique. Evaporation was reduced by maintaining a pressure of about 2 cm of oxygen-free nitrogen in the furnace during the growth period. The manganese fluoride was obtained by repeated crystallizations of selected materials, when green manganous oxide separated out as an impurity. The commercial zinc fluoride powder appeared to be of an even lower purity. A very considerable quantity of water was removed by heating *in vacuo*, but the residue was a stone-like white mass containing a large proportion of zinc oxide. However, by setting the crucible rather high in the furnace heater, zinc fluoride could be distilled on to the lid, leaving the relatively refractory oxide in the crucible. The evaporated material, after further crystallizations, gave a clear colourless product.

The mixed crystals were prepared by mixing the appropriate quantities of pure crystallized manganese fluoride and zinc fluoride, melting down at a temperature of about 950°C, and growing at a rate of 2 mm per hour. Cone-ended crucibles of $\frac{1}{4}$ in. to $\frac{3}{8}$ in. diameter and length 3 in. were used. If a single crystal was not obtained the product invariably shattered during cooling as a result of the differential thermal expansion. In a few runs, however, homogeneous single crystals up to 1 in. in length were obtained, and it was noted that in such instances the *c* axis of the tetragonal cell was aligned approximately along the axis of the crucible.

The crystal compositions were determined by volumetric analysis, using E.D.T.A. as titrant, and masking the zinc with cyanide (Flaschka and Armin 1953).

Manganese fluoride does not cleave well, so that suitably oriented plates were sawn from the crystal, and the surfaces ground and polished.

§ 3. Optical Absorption

3.1. *Method of Measurement*

A Hilger Uvispek spectrophotometer with quartz prism was used in conjunction with a vacuum cryostat fitted with lithium fluoride windows. The specimen crystal was mounted within a copper block attached to a liquid air reservoir, and could be rotated into the beam when required. The reservoir could be pumped to extend the range to 62°K. Temperatures were measured by a copper–constantan thermocouple attached to the specimen mount.

Hydrogen lines were used for calibration and it was found that drift occurred during a run even though the temperature of the room was thermostatically controlled. To permit a wavelength check between each low temperature reading, a manganese fluoride plate, with optic axis perpendicular to the surface,

was inserted in the beam. This plate remained at room temperature and the maximum of a suitable absorption line was used as a reference point. Thus the line shift was obtained as the difference of two readings taken within a short time interval.

Absorption readings in polarized light were obtained by interposing a polaroid sheet between the exit slit of the monochromator and the cryostat. This reduced the light intensity, but by over-running the filament lamp source it was possible to examine the absorption down to 3200 Å.

Pure manganese fluoride was found to give an orange-red fluorescence at low temperatures, particularly when excited by wavelengths corresponding to absorption peaks in the ultra-violet. In the crystals containing zinc, the fluorescence was much less intense. As the detector gives a measure of the integrated incident light irrespective of wavelength, the measurements were checked with a filter interposed between the cryostat and the detector, which absorbed the fluorescent radiation but passed the main beam. The difference between the two sets of results was well within the experimental error in the original absorption readings.

3.2. *Energy Level Interpretation of the Absorption Spectrum*

The transmission curve for pure MnF_2 at room temperature and at 63°K is shown in figure 1 and the values for the wave numbers corresponding to line maxima in the absorption spectrum are given in table 1. All measurements

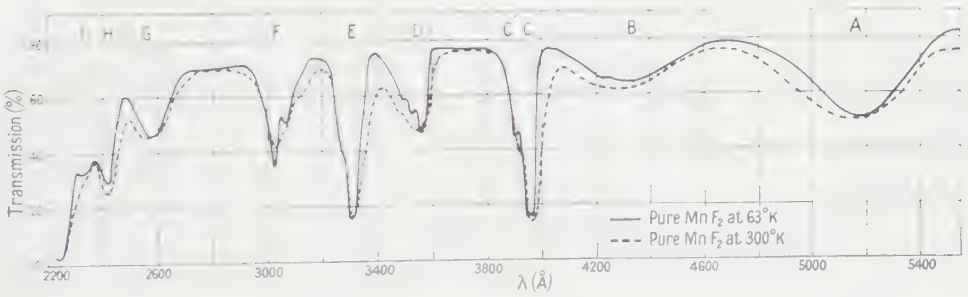

Figure 1. Transmission curve for pure MnF_2 at room temperature and at 63°K.

Table 1. Line Wave Numbers for MnF_2 at Room Temperature
Calculated values correspond to $B=671$, $C=3710$ and $D_q=820\,cm^{-1}$

Line	Transition	$10^{-3}\nu$ (cm^{-1}) Measured	Calculated
A	$^6A_{1g} \rightarrow {}^4T_{1g}({}^4G)$	19·50	19·50
B	$^6A_{1g} \rightarrow {}^4T_{2g}({}^4G)$	23·41	22·56
C	$^6A_{1g} \rightarrow \{{}^4E_g {}^4A_{1g}\}({}^4G)$	25·21	25·23
		25·32	
C′		25·50	
D	$^6A_{1g} \rightarrow {}^4T_{2g}({}^4D)$	28·15	28·40
E	$^6A_{1g} \rightarrow {}^4E_g({}^4D)$	30·17	29·90
		30·22	
F	$^6A_{1g} \rightarrow {}^4T_{1g}({}^4P)$	33·08	35·40
G	$^6A_{1g} \rightarrow {}^4A_{2g}({}^4F)$	39·01	40·66
H	$^6A_{1g} \rightarrow {}^4T_{1g}({}^4F)$	41·34	42·00
I	$^6A_{1g} \rightarrow {}^4T_{2g}({}^4F)$	43·20	44·72

refer to room temperature with the exception of line I which is not resolved at room temperature. The wave number for this line is therefore given at 90 °K. For the lines measured by Stout (1959), the agreement with the present data is satisfactory.

Manganese fluoride has a rutile structure and the symmetry of the manganese site is rhombic, but the identification of the transitions corresponding to the different lines can be made on the assumption of a cubic electrostatic field, as it is known that there are only slight differences between the absorption in manganese fluoride and in the cubic material K MnF_3 (Hrostowski and Kaiser 1959). The similarity also extends to the details of the different line profiles. Thus the variation in the extinction coefficient through the line corresponding to the transition between the ground state and the $\{^4A_{1g}{}^4E_g\}$ complex in a cubic field, as given by Heidt, Koster and Johnson (1959) is very similar to the line C for MnF_2.

Using the cubic field approximation, two procedures can be followed. Either the Racah parameters B and C together with the electrostatic field parameters D_q can be treated as adjustable parameters and the best fit with the experimental results obtained (Heidt, Koster and Johnson 1959), or the values of B and C appropriate to the free ion can be used, and D_q and a covalency parameter ϵ adjusted to fit the experimental data. A modified version of the first technique has been used. The values of B and C found to give the best fit by Heidt have been adopted as being more nearly correct than the free ion values, and a D_q of 820 cm^{-1} has been found to give the best fit in MnF_2. The predicted wave numbers are given in table 1.

When the free ion values of $B=950$ and $C=3280$ are used and a covalency factor is introduced, the best fit was obtained by Stout with $D_q=780\,cm^{-1}$ and $\epsilon=0{\cdot}064$. The levels are again identified as in table 1, but the $^4E_g(^4G)$ and $^4A_{1g}(^4G)$ levels are now separated and Stout suggests that the two lines at 25·21 and 25·32 cm^{-1} are due to transitions to the $^4A_{1g}$ level, and the 25·50 cm^{-1} line to the ^4E_g levels. This assignment is not certain because spin–orbit and spin–spin interactions, together with the orthorhombic component in the crystal field all produce changes in the separation of these levels (Koide and Pryce 1958).

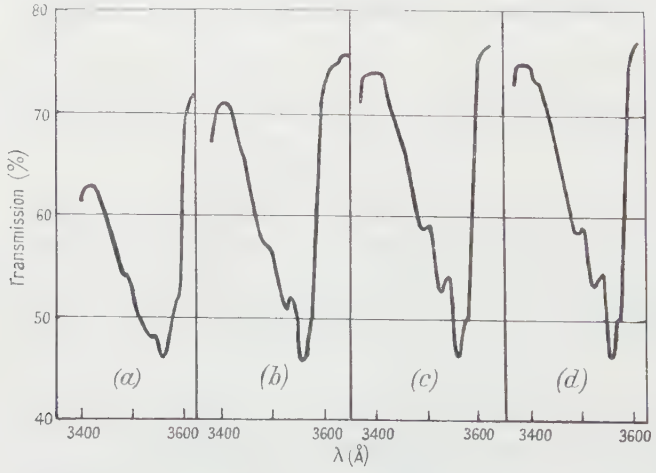

Figure 2. Transmission curve for line D in pure MnF_2 at (*a*) 300°K, (*b*) 150°K, (*c*) 90°K and (*d*) 63°K. The line does not depend upon the polarization of the light.

However, it is supported by the results on line shift with temperature discussed in § 3.3.

It may be noted that at the lower temperature fine structure corresponding to vibrational effects was observed in some of the lines. Thus the line D, which is produced by transitions to $^4T_{2g}$ levels, shows a resolution into four peaks, at least one of which must be associated with vibrational excitation (figure 2).

3.3. *Temperature Shifts for Sharp Lines*

The temperature shifts of the sharp lines C and E (which arise from levels which are independent of the crystalline field parameter D_q in the cubic case) can be measured with fair precision, and it is from these that the magnitude of the exchange interaction effects has been inferred.

The shifts of the two main components of the line C for the three compositions are shown in figure 3. The separation of the components was facilitated by the use of polarized light, for it was found that the component of higher frequency was strongly absorbed for light with electric vector perpendicular to the optic axis, whereas the lower frequency component was strongly absorbed when the light was polarized parallel to the axis (figure 10).

For the most dilute material ($Mn_{0.10}Zn_{0.90}F_2$) there are small linear line shifts at a rate of about $10\,cm^{-1}/(100\,^\circ C)$. In the intermediate crystal ($Mn_{0.62}Zn_{0.38}F_2$) the line shift at room temperature is again linear with the same slope as above, but as the temperature falls below 100°K the slope progressively increases. For pure MnF_2 the slope at room temperature is rather greater than for the diluted crystals, and the upswing at lower temperatures is also more pronounced.

Similar behaviour is shown by the sharp line E (figure 4).

It is suggested that this sequence is correlated with the increasing importance of exchange interaction with the increasing manganese concentration, and therefore with the increasing deviations from a linear inverse susceptibility–temperature plot. In $Mn_{0.10}Zn_{0.90}F_2$ the plot is linear down to 6°K, in $Mn_{0.62}Zn_{0.38}F_2$ the departure from linearity occurs at about 50°K, while in MnF_2 the Néel point minimum is at about 68°K (Finlayson *et al.*, to be published). Before the interaction effect can be discussed quantitatively, however, it is necessary to separate out the line shifts with temperature caused by the variation in lattice dimensions. This can be obtained from the most magnetically dilute material where interaction effects are negligible (figure 3). In $Mn_{0.62}Zn_{0.38}F_2$ the same rate of shift is obtained at higher temperatures so that the difference between the extrapolation of this linear section and the curve at lower temperatures (figure 3) gives the net interaction shift (figure 5). The interaction shifts for the two components of the sharp line E were obtained by a similar procedure and are also shown in figure 5. These shifts are the combined result of the direct effect of the interaction on the energy levels of the manganese ion, and of the change in crystal field resulting from the expansion anomaly near the ordering temperature. The relative magnitudes of the two mechanisms are difficult to estimate, and Stout (1959) has suggested that the crystal field change is important. However, in MnF_2 the anomalous fractional lattice changes $\Delta a/a$ and $\Delta c/c$ are less than 10^{-3} (Gibbons 1959). This probably causes a shift of the order of 1 cm^{-1}, as the shifts of the sharp lines C and E are less than 25 cm^{-1} when the fractional lattice changes, as a result of varying composition, are more than 3×10^{-2} (figure 8). Therefore,

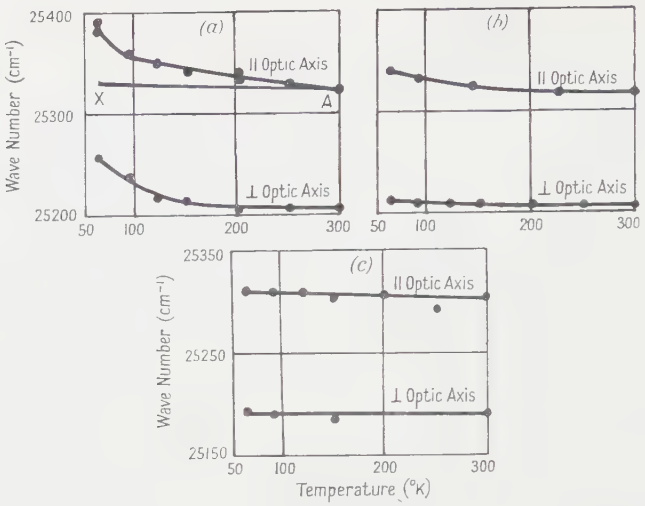

Figure 3. Change of line frequency with temperature for line C using polarized light travelling perpendicular to the optic axis. (*a*) Pure MnF_2, (*b*) $Mn_{0.62}Zn_{0.38}F_2$, (*c*) $Mn_{0.10}Zn_{0.90}F_2$.

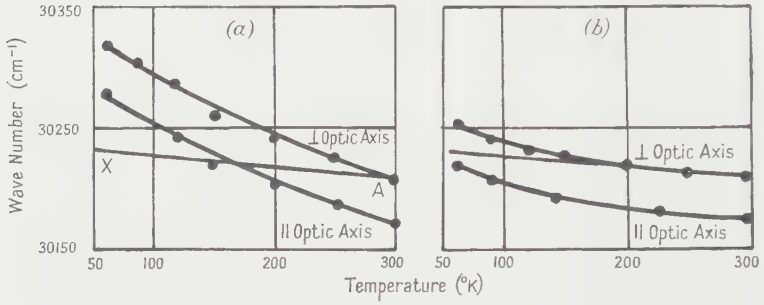

Figure 4. Change of line frequency with temperature for line E using polarized light travelling perpendicular to the optic axis. (*a*) Pure MnF_2; XA is a line with slope equal to the wave number change with lattice dilation; (*b*) $Mn_{0.62}Zn_{0.38}F_2$.

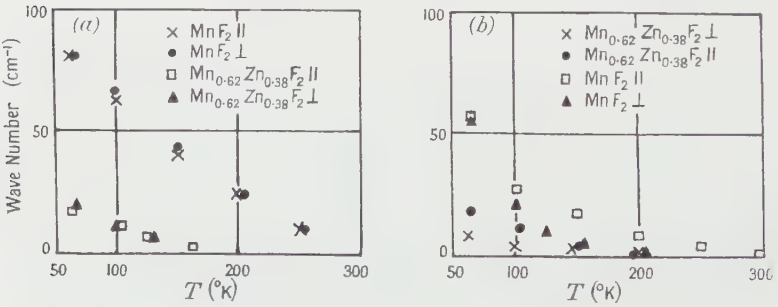

Figure 5. Interaction shift of lines E (*a*) and C (*b*) for $Mn_{0.62}Zn_{0.38}F_2$ and increased shift above that at room temperature in MnF_2 for the same lines.

in this discussion, the complete interaction shift will be attributed to direct exchange effects.

For pure MnF_2 the interaction effect appears to be important already at room temperature, because the wave-number–temperature slope of both C and E is considerably greater than the common room-temperature slope of the two diluted materials. An extension of the measurements to higher temperatures is being undertaken to test the interaction origin of the increased slope at room temperature. Until such data are avilable it is only possible to obtain a provisional lower limit to the interaction shift. Thus, if a line XA is drawn (figure 3) with the slope due to thermal expansion obtained from the magnetically dilute materials, then the divergence between line and curve now gives the increase in interaction shift over that value which pertains at room temperature (point A). The interaction shifts obtained in these ways are shown in figure 5 for C and E. For both lines the lower limit to the interaction shift is much greater with pure MnF_2 than with $Mn_{0\cdot62}Zn_{0\cdot38}F_2$. It must be emphasized that the interaction shifts for MnF_2 must be regarded as less certain than the shifts in the magnetically dilute material as a direct extrapolation from a linear section was not possible.

The lowering of the ground state energy of the ith manganese ion in the ordered antiferromagnetic state is given by $-M_i\Sigma 2J_{ij}M_j$. Here M_i and M_j are the components of the spin angular momenta along the antiferromagnetic axis, and J_{ij} is the exchange integral. Interaction splitting also occurs in the excited levels as is shown by the different interaction shifts for lines C and E. The relative magnitudes of the splitting in different levels can be estimated by a method suggested by Kanamori (Stout 1959). The super-exchange mechanism takes place through the overlap of the d orbitals with neighbouring fluorine atoms. As the manganese ion is octahedrally surrounded by fluorine ions, the overlap will be greatest for the dγ orbitals. It is therefore assumed that the exchange integrals are proportional to the fractional occupancy of dγ orbitals by the component of spin along the c axis. The fractional occupancy of the dγ orbitals in the different states is obtained from the wave functions for maximum spin quantum number ϵ_s (Koide and Pryce 1958) and is found to be $\frac{1}{2}$ for the $^6A_{1g}$ ground state, $\frac{25}{175}$ for $^4A_{1g}(^4G)$, $\frac{4}{21}$ for $^4E_g(^4G)$ and $\frac{1}{7}$ for $^4E_g(^4D)$. The corresponding energy changes are proportional to the product of M_i and J_{ij} and are thus in the ratios $(\frac{5}{2}\cdot\frac{1}{5}):(\frac{5}{2}\cdot\frac{25}{175}):(\frac{5}{2}\cdot\frac{4}{21}):(\frac{5}{2}\cdot\frac{1}{7})$. These four levels, together with the transitions between them, are shown in figure 6. Two simplifications have been made: first, all the ions have been shown in the lowest ground state before excitation; secondly, only the transitions associated with small changes in ϵ_s have been indicated, as the more nearly ϵ_s is a good quantum number, the more nearly will the selection rules reduce to $\Delta\epsilon_s = \pm 1,0$. Under these conditions, it follows that the interaction shifts for transitions from the ground state to the lowest ϵ_s levels arising from $^4A_{1g}(^4G)$, $^4E_g(^4G)$ and $^4E_g(^4D)$ are in the ratios $(\frac{1}{2}-\frac{1}{5}):(\frac{1}{2}-\frac{25}{175}):(\frac{1}{2}-\frac{4}{21})$, i.e. 1·05 : 0·75 : 1. Even for complete order some transitions for which $\Delta\epsilon_s \neq \pm 1,0$ will take place and lead to a broadening of the line, and this broadening will become more marked as the temperature rises. However, the ratio of the interaction shifts will remain unaltered for the transitions considered above as the fractional occupancy of dγ orbitals does not depend upon ϵ_s, which will therefore represent the relative interaction shifts for an important fraction of the transitions even at temperatures where there is an appreciable population in

higher ϵ_S levels. The ratios of the shifts of the centres of gravity of the lines would be more satisfactory for comparison with experiment, but this cannot be computed until more is known of the relative intensities of transitions between different ϵ_S levels.

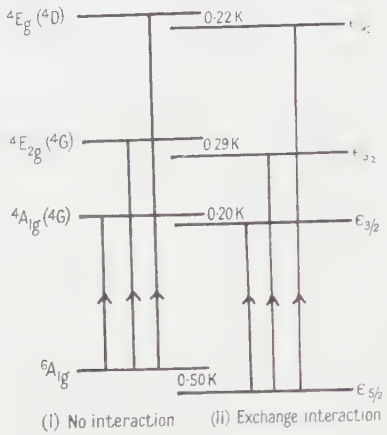

Figure 6. Schematic representation of transitions between ground state and excited levels (i) with no exchange interaction, (ii) with exchange interaction.

Figure 5 shows that for pure MnF_2 the ratio of the interaction shifts for lines E and C is always greater than 1, with a value of 2·8 at 100°K. In $Mn_{0.62}Zn_{0.38}F_2$, where the experimental measurements have a greater fractional error but where the extrapolation is more certain, the ratio is $1{\cdot}0 \pm 0{\cdot}3$. Thus the experimental results are not sufficiently accurate to decide with certainty if the C line should be associated with a transition to a $^4A_{1g}(^4G)$ or a $^4E_g(^4G)$ level, but the shifts are more consistent with the $^4A_{1g}$ assignment. It should be noted that also Stout gives the line as arising from a transition to a $^4A_{1g}$ level.

In $Mn_{0.62}Zn_{0.38}F_2$ the interaction shift is proportional to ΣS_j, and the shapes for all four components of C and E are of the general character to be expected from nearest neighbour short range order (Kaufmann and Onsager 1949). Unfortunately no detailed treatment is available for short-range order with $S = \frac{5}{2}$.

For MnF_2 only the change in interaction shift over the temperature range is known. However, it is clear that the interaction shift is much more important at higher temperatures than in the dilute material. This is still true if the reduced temperatures T/T_{ordering} are used for making the comparison. Again no detailed theory is available for $S = \frac{5}{2}$, but the quasi-chemical theory applied to $S = \frac{1}{2}$ would give this qualitative change with the decreased number of nearest neighbours in the magnetically dilute material (Elcock 1956).

Other work on the influence of exchange interaction on optical properties is that of Newman and Chrenko (1959 a, b) on NiO and CoF_2, and Pratt and Coelho (1959) on MnO and CoO. With the exception of Stout's article the most relevant work to the present investigation is that on $MnCl_2.4H_2O$ and $MnBr_2.4H_2O$ by Tsujikawa and Kanda (1958). Their measurements were made on lines which corresponded to our line C, and showed a rather smaller shift to higher frequency near the Néel temperatures. However, these

temperatures are low, between 1·6°K and 2·2°K, and so even a short-range order interaction would be restricted to a very narrow temperature range. The data do not appear to permit a differentiation between the direct effect of short-range order on the levels and the effect of a lattice anomaly.

3.4. *Broad Line Temperature Shifts*

The temperature shifts of the broad lines in MnF_2 are shown in figure 7. No dependence on the polarization of the light has been detected. The broad lines arise from energy levels, which are dependent upon the crystalline field parameter D_q, so that relatively large thermal expansion shifts, correlated in direction and magnitude with the slope of the level in the Orgel diagram (Tanabe and Sugano 1954), will be superimposed upon the interaction shift.

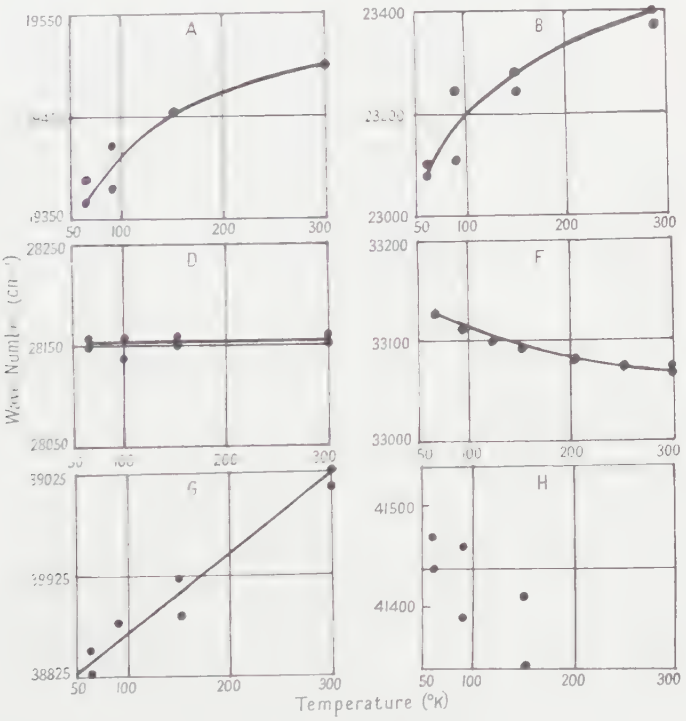

Figure 7. Changes in line frequency with temperature for lines A, B, D, F, G and H in MnF_2.

Thus the movement of lines A and B to lower frequencies as the temperature decreases corresponds to the negative slope of the $^4T_{1g}(^4G)$ and $^4T_{2g}(^4G)$ levels with increasing D_q, while the upward movement of line F corresponds to the positive slope of the $^4T_{1g}(^4P)$ level. Line D shows little shift with temperature, as expected from the small slope of the $^4T_{2g}(^4D)$ level. However, line G is broad and moves to lower frequency, whereas from its assignment to $^4A_{2g}(^4F)$, one would expect G to be a fairly stationary sharp line showing mainly interaction effects.

3.5. *Line Shift with Composition*

The line shifts with composition at room temperature are shown in figure 8. For lines A, B and D the position of maximum absorption appears to be independent of the direction of polarization, whereas for lines F, G and H this could not be checked. The frequencies of lines D, F and H do not vary appreciably, whereas the lines A and G decrease in frequency with dilution and line B increases. Dilution with zinc corresponds to a decrease in both lattice parameters and presumably to an increase in D_q. Hence the opposite motions of lines A and B are not accounted for, because these lines involve levels both of which have a negative slope in the Orgel diagram.

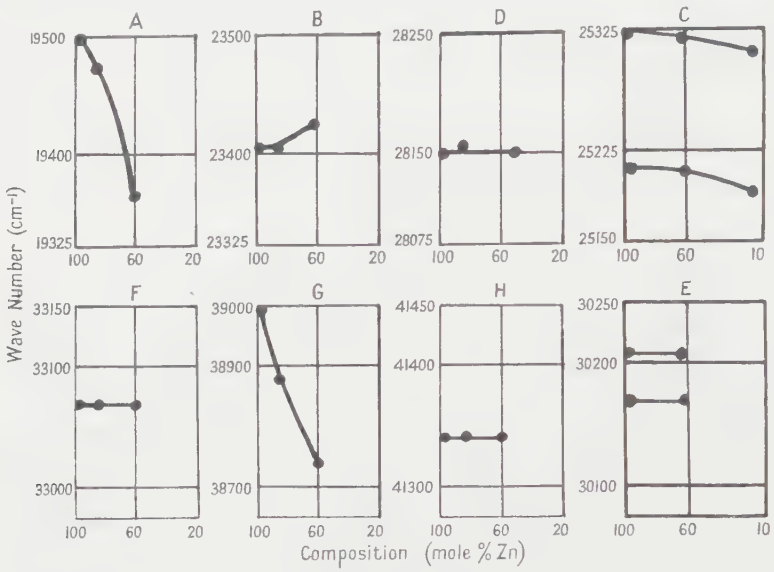

Figure 8. Change in line wave number with sample composition. Measurements with unpolarized light.

§ 4. Line Width

The variation of line width with temperature has been measured for lines A to F. The following treatment is similar to that given by Klick and Schulman (1952) in their analysis of Mn^{2+} in $ZnSiO_4$. The configurational energy of both ground and excited states is represented by parabolae and the half line width ΔE is then proportional to the square root of an effective temperature T_{eff} given by

$$T_{\text{eff}} = \frac{h\nu_g}{2k} \coth\left(\frac{h\nu_g}{2kT}\right)$$

where ν_g is the vibrational frequency in the ground state (Williams and Hebb 1951). It follows that the rate of variation of line width with the square root of the absolute temperature should show a falling off at low temperatures, the form of the curve depending upon ν_g. The data for $Mn_{0.62}Zn_{0.38}F_2$ are shown in table 2, and in figure 9 (*a*). The variation for all lines is similar, and can be fitted to a $\sqrt{T_{\text{eff}}}$ curve by using a value ν_g of approximately $9 \times 10^{12}\,\text{sec}^{-1}$. A vibrational frequency of the same order ($10^{13}\,\text{sec}^{-1}$) was used by Klick and Schulman in the paper quoted above.

The corresponding line widths for pure MnF_2 are given in table 3 and plotted in figure 9 (*b*).

Here, however, the curves (figure 9 (*b*)) show no levelling and display a range of slopes, i.e. there is no evidence of $\sqrt{T_{\text{eff}}}$ variation with constant ν_g. It must be concluded that the simple vibrational model is unsatisfactory for the pure MnF_2, in spite of its applicability to the diluted material.

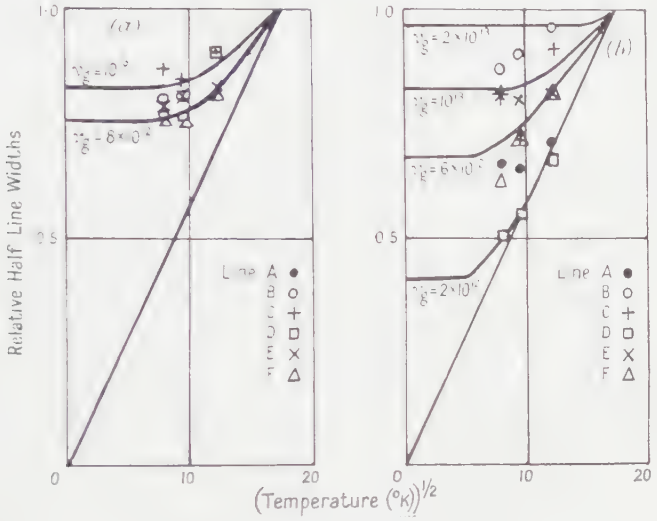

Figure 9. Relative half line widths plotted against $T^{1/2}$, (*a*) for $Mn_{0.62}Zn_{0.38}F_2$, (*b*) for pure MnF_2. The lines corresponding to different vibrational frequencies are as predicted from a T_{eff} law.

Table 2. Half Line Widths for Unpolarized Light for $Mn_{0.62}Zn_{0.38}F_2$

	Half line width (cm^{-1}) at			
Line	300°K	150°K	90°K	63°K
A	925	770	765	755
B	1245	1020	1015	1015
C	160	145	135	140
D	595	540	455	460
E	275	230	225	215
F	610	495	460	460

Table 3. Half Line Width for Unpolarized Light for MnF_2

	Half line width (cm^{-1}) at			
Line	300°K	150°K	90°K	63°K
A	1030	730	670	680
B	1010	975	935	880
C	160	145	115	130
D	795	548	440	400
E	290	235	230	237
F	650	525	465	410

§ 5. Polarization Effects

The profiles of the lines E and C depend upon the polarization of the incident light, so that it is possible to test whether the transitions involved are of a magnetic

dipole or electric multipole type. In figure 10 the line profiles for C are shown for the three different orientations in the polarized beam. If the transition were of magnetic type, then orientations (*b*) and (*c*) would be equivalent. However, it is found that (*a*) and (*c*) are equivalent, so that the transition is of electric multipole type. This is in agreement with the assumption made in previous discussions (Tanabe and Sugano 1954, Koide and Pryce 1958, Stout 1959).

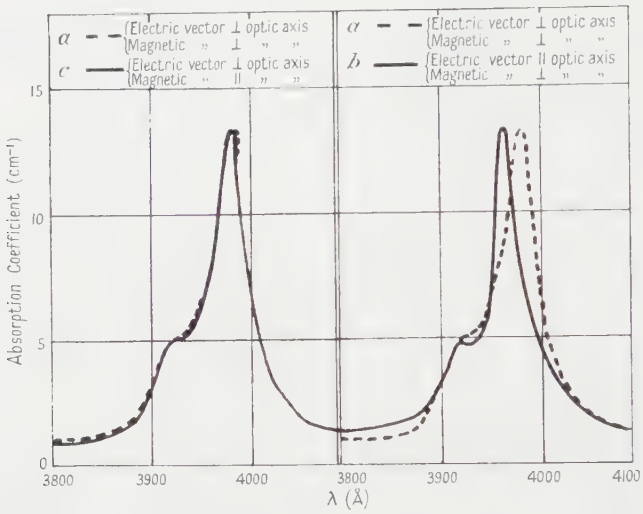

Figure 10. Absorption coefficient against wavelength for line C.

§ 6. Intensities

The theoretical prediction of oscillator strength requires a knowledge of the vibrational modes of the lattice (Koide and Pryce 1958). In the absence of these data, the simplified treatment of Holmes and McClure (1957) has been used. The oscillator strength is related to the ground state vibrations which remove the centre of symmetry of the surroundings of the manganese ion, and the vibrational levels are assumed to be equally spaced, with separation $k\theta$.

The oscillator strength f is then given by $f=f_0\{1+\exp(-\theta/T)\}$ where f_0 is the oscillator strength at 0°K. Holmes and McClure found that they could represent the behaviour of two bands in $NiSO_4.7H_2O$ with a single value of θ.

Here the variation of oscillator strength for the lines A and B in pure MnF_2 and for $Mn_{0.62}Zn_{0.38}F_2$ is given in table 4.

Table 4. Variation of Oscillator Strength with Temperature for Lines A and B

Line	300°K	150°K	90°K	63°K
	MnF_2			
A	3.77×10^{-7}	3.07×10^{-7}	2.97×10^{-7}	2.88×10^{-7}
B	3·62	2·94	2·95	2·95
	$Mn_{0.62}Zn_{0.38}F_2$			
A	2.50×10^{-7}	1.97×10^{-7}	1.89×10^{-7}	1.75×10^{-7}
B	1·86	1·53	1·51	1·45

The corresponding graphs (figures 11 and 12) include curves for θ values 500°, 440° and 370°K. For both materials line A is best fitted by $\theta = 370$°K and line B by $\theta = 500$°K, the agreement being more satisfactory in the magnetically dilute material. Thus, unlike $NiSO_4.7H_2O$, the same θ value will not serve for both lines. However the two θ values correspond to frequencies of 8×10^{12} and 10^{13} sec^{-1}, which are of the same order as the value $\nu_g = 9 \times 10^{12}$ sec^{-1} derived from line width measurement on $Mn_{0.62}Zn_{0.38}F_2$.

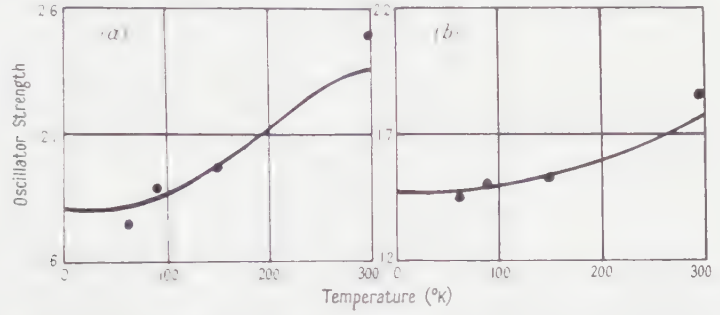

Figure 11. Measured variation in oscillator strength with temperature for $Mn_{0.62}Zn_{0.38}F_2$. (*a*) Data for line A together with variation corresponding to $f_0 = 1.81 \times 10^{-7}$ and $\theta = 370$°, (*b*) data for line B together with variation corresponding to $f_0 = 1.81 \times 10^{-7}$ and $\theta = 500$°.

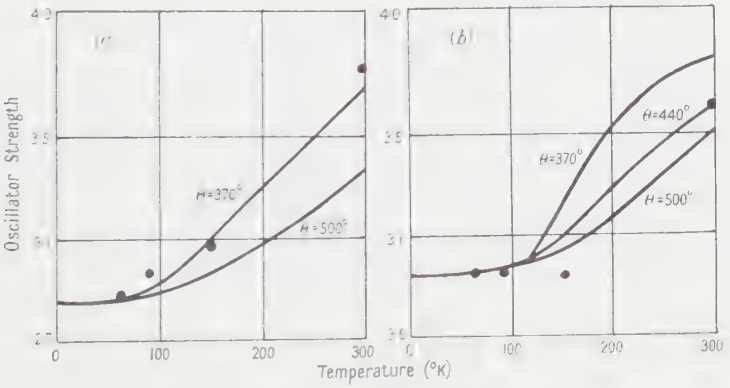

Figure 12. Measured variation of oscillator strength with temperature for MnF_2. (*a*) Data for line A together with variation corresponding to $f_0 = 2.85 \times 10^{-7}$, $\theta = 370$° and $\theta = 500$°, (*b*) data for line B together with variation corresponding to $f_0 = 2.94 \times 10^{-7}$, $\theta = 370$°, 440° and 500°.

The difference in θ values for A and B may indicate a difference in the vibrational frequencies in the upper and ground states, which are assumed to be the same in the Holmes and McClure treatment. It may be noted that in the magnetically dilute material the oscillator strengths for lines A and B are always less than in the pure MnF_2. Thus the value of f_0 for lines A and B is 1.81×10^{-7} and 1.47×10^{-7} while in pure manganese fluoride the strengths are 2.85×10^{-7} and 2.94×10^{-7}. It was originally expected that dilution with zinc would lead to an increase in the oscillator strength, as in the mixed crystal the manganese ion is surrounded by some manganese and some zinc ions, and so in the magnetically dilute material the manganese ion is in general in a less symmetrical position.

Conclusions

There are absorption spectrum changes, particularly line shifts, which are associated with the Néel temperature. These effects extend upwards over a considerable temperature range, through part of which, the portion of the shift caused by the direct interaction effect can be separated from that due to lattice contraction.

The super-exchange interaction splitting of the manganese levels follows short-range rather than long-range spin order, and it would seem that optical measurements are likely to provide information not readily available by other methods.

In the magnetically dilute material a simple vibrational model provides a reasonably satisfactory account of the variation of line width and oscillator strength with temperature. The model fails for pure MnF_2.

Acknowledgments

We should like to express our thanks to Professor R. V. Jones for the provision of laboratory facilities, to Mr. T. Wratten who constructed the cryostat, to Mr. W. Mitchell who assisted in the crystal growing, and to Dr. S. Davidson who carried out the chemical analysis.

The spectrophotometer was purchased from a grant from the Department of Scientific and Industrial Research.

References

Elcock, E. W., 1956, *Order–Disorder Phenomena* (London: Methuen).
Flaschka, H., and Armin, A. M., 1953, *Mikrochim. Acta*, 414.
Gibbons, D. F., 1959, *Phys. Rev.*, **115**, 1194.
Heidt, L. J., Koster, G. F., and Johnson, A. M., 1959, *J. Amer. Chem. Soc.*, **80**, 6471.
Holmes, O. G., and McClure, D. S., 1957, *J. Chem. Phys.*, **26**, 1686.
Kaufman, B., and Onsager, L., 1949, *Phys. Rev.*, **76**, 1244.
Hrostowski, H. J., and Kaiser, R. H., 1959, *Bull. Amer. Phys. Soc.*, **4**, 167.
Klick, C. C., and Schulman, J. H., 1952, *J. Opt. Soc. Amer.*, **42**, 910.
Koide, S., and Pryce, M. H. L., 1958, *Phil. Mag.*, **3**, 607.
Newman, R., and Chrenko, R. M., 1959 a, *Phys. Rev.*, **114**, 1507.
—— 1959 b, *Phys. Rev.*, **115**, 1147.
Pratt, G. W., and Coelho, R., 1959, *Bull. Amer. Phys. Soc.*, **4**, 53.
Stout, J. W., 1959, *J. Chem. Phys.*, **31**, 709.
Tanabe, Y., and Sugano, S., 1954, *J. Phys. Soc. Japan*, **9**, 766.
Tsujikawa, I., and Kanda, E., 1958, *Colloque International du Magnetisme de Grenoble* (Paris: C.N.R.S.).
Williams, F. E., and Hebb, M. H., 1951, *Phys. Rev.*, **84**, 1181.

Measurement of Ionization and Attachment Coefficients in Carbon Dioxide in Uniform Fields

By M. S. BHALLA and J. D. CRAGGS

Department of Electrical Engineering, University of Liverpool

MS. received 25th January 1960, in final form 10th March 1960

Abstract. The growth of pre-breakdown currents in uniform field conditions has been studied in carbon dioxide at different pressures in the E/p range of 1200 to 26 v cm^{-1} (mm Hg)$^{-1}$. Experimental measurements of the Townsend ionization coefficient α show good agreement with the earlier measurements in the E/p range of 1200 to 100 v cm^{-1} (mm Hg)$^{-1}$ and with the recent measurements in the E/p range of 70 to 50 v cm^{-1} (mm Hg)$^{-1}$. The results show that earlier measurements neglecting attachment may be in error below $E/p = 50$ v cm^{-1}(mm Hg)$^{-1}$. It is suggested that the mechanism of negative ion formation is due to dissociative attachment, consequently the growth of current at constant E/p can be represented by the appropriate modification of the Townsend equation. Employing this equation, values of α and the dimensionally equivalent attachment coefficient η have been computed. Further, static breakdown potentials have been measured up to pd (pressure × gap length) ~ 1500 mm Hg cm and the values of secondary coefficient γ have been calculated using the modified Townsend breakdown criterion.

From the the mean values of α/p and η/p, the mean cross sections for ionization and attachment have been calculated for various electron mean energies and compared with the values computed from low pressure single collision data, by assuming either a Maxwellian or a Druyvesteyn distribution of electron energies. It is concluded that neither of these distributions explains the results.

§ 1. Introduction

The formation of negative ions by electron attachment to various common diatomic and triatomic inorganic molecules was studied by earlier workers but no electron attachment was observed in carbon dioxide (Loeb 1956, Bradbury and Tatel 1934). However, recent work of Craggs and Tozer (1960) in these laboratories, using a Lozier apparatus to study collision processes in carbon dioxide, demonstrated for the first time the production of negative ions in that gas. The process was interpreted as

$$CO_2 + e \rightarrow CO + O^-. \qquad \ldots\ldots (1)$$

It therefore seemed desirable to study attachment in carbon dioxide in swarm conditions and to measure the attachment coefficients for various values of the parameter E/p (E is the field strength, p the gas pressure) in uniform fields. Since this necessarily involved the measurement of ionization coefficients an opportunity was taken to measure the latter over a wide range of the parameter E/p and to

compare them with the results of the previous workers. The work is of interest also in that, as in CO, NO, etc., the negative ions formed are principally O^-, the study of which is relevant to attachment studies in dry and moist air (Prasad 1959, Prasad and Craggs 1960).

It has been shown (Harrison and Geballe 1953, Geballe and Reeves 1953) that when electron attachment of the type

$$AB + e \rightarrow AB^- \quad \text{or} \quad A + B^- \qquad \ldots\ldots (2)$$

occurs in the growth of the electron avalanche the equation for the current flowing in a uniform field gap is given by

$$\frac{I}{I_0} = \left[\frac{\alpha}{\alpha-\eta} e^{(\alpha-\eta)d} - \frac{\eta}{\alpha-\eta}\right] \Big/ \left[1 - \frac{\gamma\alpha}{\alpha-\eta}(e^{(\alpha-\eta)d} - 1)\right] \qquad \ldots (3)$$

where α is Townsend's primary coefficient, η the attachment coefficient, γ the secondary coefficient, d the electrode separation and I_0 the initial electron current at the cathode.

It follows from equation (3) that the criterion for breakdown at which the current I becomes self-maintained and independent of I_0 is

$$\frac{\gamma\alpha}{\alpha-\eta}(e^{(\alpha-\eta)d_s} - 1) = 1 \qquad \ldots\ldots (4)$$

where d_s is the breakdown sparking distance (cm).

Provided only those current measurements are considered in which contributions due to secondary processes are negligible then equation (3) is reduced to

$$\frac{I}{I_0} = \left[\frac{\alpha}{\alpha-\eta} e^{(\alpha-\eta)d} - \frac{\eta}{\alpha-\eta}\right]. \qquad \ldots\ldots (5)$$

Equation (5) indicates that the semi-logarithmic plot of $(I/I_0, d)$ is not linear and that curve fitting techniques are necessary to evaluate α and η accurately.

Consequently values of α, η and γ have been calculated in carbon dioxide by employing equations (3), (4) and (5) and the authors find that the measurements of pre-breakdown currents conform to the above theory over a wide range of pressures.

From the mean values of α/p and η/p so obtained, the ionization and attachment cross sections have been calculated for various electron mean energies and an attempt has been made to compare these values of cross sections with the values computed from Craggs and Tozer's (1960) single collision data by assuming either a Maxwellian or a Druyvesteyn distribution.

§ 2. Experimental Procedure

The apparatus used in the present study has been fully described by Hopwood, Peacock and Wilkes (1956) except for a few modifications, which have been made to improve its performance and accuracy. The ionization chamber has been fitted with an auxiliary inlet so that either spectroscopically pure gas in Pyrex glass containers or compressed gas in a cylinder can be introduced. The chamber can be evacuated to 5×10^{-6} mm Hg with an apparent leak of $0{\cdot}4\mu\,h^{-1}$. The aluminium-alloy cathode used previously with an overall diameter of 15 cm,

machined and polished to a Rogowski profile, has been electroplated with platinum to provide better surface stability. A quartz envelope photocell of type QVA–39 has been incorporated in the low pressure mercury discharge lamp assembly to monitor the ultra-violet radiation used to provide the initial photoelectric currents from the cathode.

The gas pressures are measured (corrected to 20°c) either on an oil manometer using silicone oil of specific gravity 1·09 to within $\pm 0{\cdot}05$ mm Hg or a micro-manometer using metal bellows as a pressure sensitive element to within $\pm 0{\cdot}5$ mm Hg at the higher pressures. The electrode separation is measured to within $\pm 0{\cdot}005$ mm by means of a rigidly supported micrometer. A new potential divider of improved design has been incorporated in the high-voltage supply to provide the ionization chamber with continuously variable voltage (0·2 volt steps) from 0 to 50 kv, known with an absolute accuracy to 0·3%.

The ionization currents are measured by determining the voltage drop across a set of high stability resistances in the range 10^7 to 10^{11} ohms using an extremely stable feedback electrometer amplifier (Allenden 1958). The values of these resistances were carefully measured to an accuracy better than 1%. The departures from linearity in the amplifier were found to be within the permitted values of the precision indicating meter (Sangamo Weston d.c. microammeter, model 882) used. Measurement of an ionization current was made by using two different resistances, whenever the magnitude of the current was such that good accuracy could be obtained for both readings. This procedure provided a frequent check on the relative values of the resistances and throughout the investigation no changes in the values were detected. Thus the ionization currents could be determined with an absolute accuracy to 1·5%, and relatively they could be measured more accurately than this. The overall accuracy in the measurement of α/p should therefore be not greater than 3%. It is more difficult to assess the errors in η/p, since they depend on curve fitting but it is estimated that in the most favourable conditions (medium values of E/p) they are about $\pm 3\%$, increasing to perhaps $\pm 10\%$ for low and high values of E/p.

Care was taken that no dissociation occurred in carbon dioxide due to photolysis. Chapman, Chadwick and Ramsbottom (1907), Coehn and Sieper (1916) and Coehn and Spitta (1930) observed that in the presence of water vapour carbon dioxide can be dissociated by irradiation with ultra-violet light depending upon the water vapour concentration. However, Coehn and May (1934) have shown the inability of ultra-violet light to cause a decomposition in extremely dry carbon dioxide. Therefore, special care was taken to dry the carbon dioxide.

The gas used in the experiments at pressures up to 100 mm Hg was spectroscopically pure and supplied by the B.O.G. Ltd., but preliminary measurements up to 100 mm Hg and the final measurements at higher pressures were made in cylinder gas (97% carbon dioxide, 2% nitrogen, oxygen less than 1%) obtained from the Distillers Co. Ltd. Each gas filling from the cylinder was passed very slowly through a trap, maintained at -50 c by using a mixture of solid carbon dioxide and acetone.

To confirm that no dissociation occurred due to photolysis, the light from the ultra-violet lamp was allowed to fall on the cathode (in the usual manner) for 24 hours after taking one set of measurements for a particular gas filling. The measurements were then repeated and in all cases the results calculated

from the two sets of measurements agreed within experimental limits and never showed any systematic error. As a precaution, whenever the cathode was 'cleaned' by running a low pressure glow discharge in an atmosphere of oxygen-free hydrogen in the chamber, the chamber was subsequently evacuated, filled with carbon dioxide and the cathode then stabilized by irradiating it with ultra-violet light. This procedure helped to stabilize the cathode in approximately 15 minutes.

§ 3. Data and Results

The experiments were conducted over a pressure range of 0·5 to 700 mm Hg (corrected to 20°c) and a range of E/p from 26 to 1200 v cm^{-1} (mm Hg)$^{-1}$. Typical results obtained at 100 and 25 mm Hg are shown in figure 1 where the natural logarithm of the currents is shown plotted as a function of the gap distance. All these plots exhibit curvatures characteristic of equation (5), thus justifying the assumptions made regarding the mechanism of negative ion formation. It was observed, however, that beyond a particular value of E/p, for each pressure the curvature of these plots ceased to be apparent and the latter become linear.

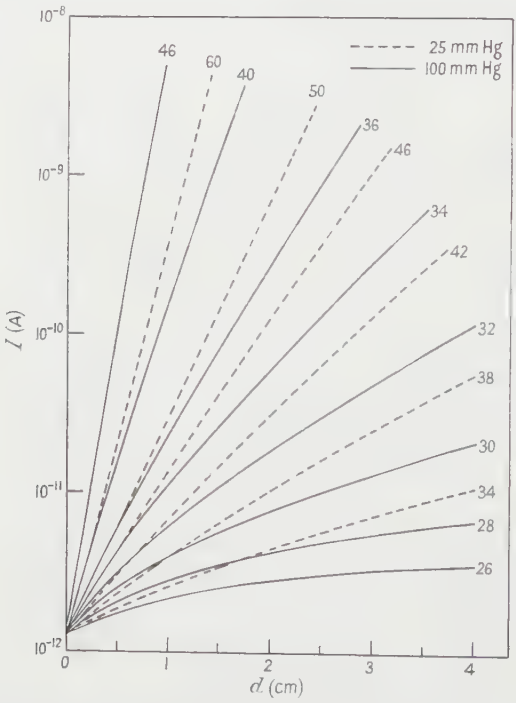

Figure 1. Ionization currents in carbon dioxide at 100 and 25 mm Hg pressure for various constant values of the parameter E/p (v cm^{-1} (mm Hg)$^{-1}$).

The absence of appreciable upcurving in all these plots at large values of d indicates very low secondary electron yields except at very low pressures (0·5 and 1 mm Hg), where the contributions due to secondary processes were taken into account while calculating α. Consequently it was impracticable to measure values of γ directly and hence γ's were calculated employing the measured breakdown potentials and the values of α and η. However, in experiments conducted at a

pressure of 25 mm Hg where a few values of γ ($\sim 10^{-6}$) were directly measurable over a small range $55 < E/p < 70$ v cm^{-1} (mm Hg)$^{-1}$, it was found that the observed values of γ were in agreement with the calculated values to within 10%, thus justifying the use of Townsend's breakdown criterion for the evaluation of γ.

3.1. *Evaluation of α and η*

The values of α and η have been computed from the above mentioned curves by a careful process of curve fitting employing equation (5). The values of α/p and η/p thus obtained in the range of E/p from 26 to 50 v cm^{-1} (mm Hg)$^{-1}$ at 100 and 25 mm Hg pressures are given in table 1 and the values of η/p have been plotted as a function of E/p in figure 2, which also includes data taken in this laboratory by Chatterton with a Bradbury filter. The values of α/p and η/p

Table 1. Values of α/p and η/p for CO_2 at 100 and 25 mm Hg Pressure

	100 mm Hg		25 mm Hg	
E/p	α/p	η/p	α/p	η/p
26	0·0072	0·0096	—	—
30	0·0160	0·0120	0·0160	0·0120
32	0·0233	0·0144	0·0232	0·0144
34	0·031	0·0155	0·031	0·0156
36	0·040	0·0160	0 040	0·0160
38	0·051	0·0182	0·051	0·0180
40	0·063	0·0188	0·063	0·0188
42	0·074	0·0172	0·074	0·0172
44	0·088	0·0168	0·088	0·0160
46	0·100	0·0135	0·102	0·0144
48	—	—	0·115	0·0104
50	0·122	—	0·124	—

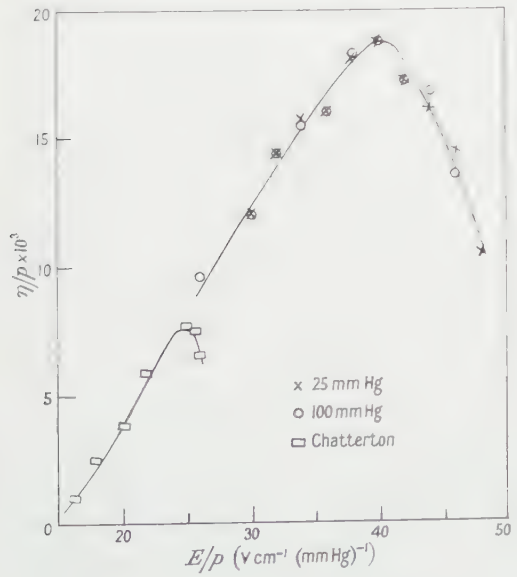

Figure 2. Values of η/p as a function of E/p in carbon dioxide.

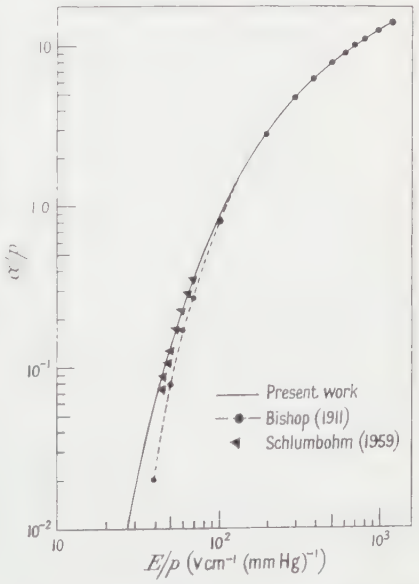

Figure 3. Values of α/p as a function of E/p in carbon dioxide for comparison with previously published data.

obtained at pressures of 300 and 700 mm Hg have not been included, since they are considered only to be of sufficient accuracy to estimate γ from the measured breakdown potentials because of impurities present in the gas (cylinder gas).

The values of α/p for the parameter $E/p > 50$ have been calculated from the linear plots of $(\log I, d)$ on the assumption that attachment is negligible.

The mean values of α/p obtained in the present study for various values of E/p have been plotted as a function of E/p in figure 3, for purposes of comparison with the results of Bishop (1911) and Schlumbohm (1959).

3.2. *Breakdown Measurements and* γ

Breakdown potentials V_s were measured over a pressure range of 1 to 700 mm Hg (corrected to 20°c) up to $pd \sim 1500$ mm Hg cm and are plotted as a function of pd in figure 4. Results showed no pressure dependence (within 2%) for any particular value of pd, thus indicating that Paschen's law is obeyed in this region.

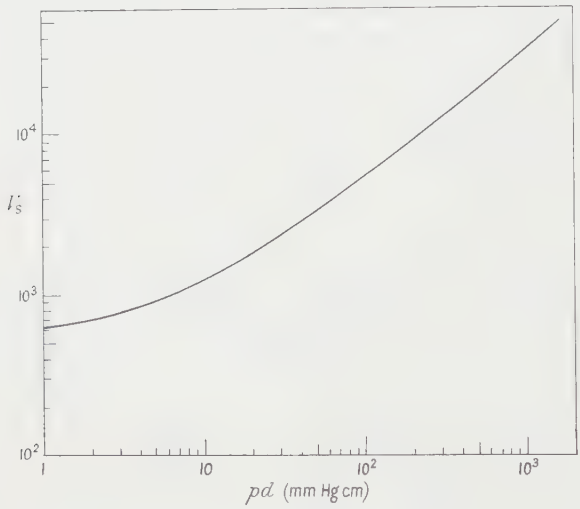

Figure 4. Observed breakdown potentials in carbon dioxide as a function of pd.

As mentioned earlier, no measurements of γ were possible since no upcurving was observed in the $(\log I, d)$ plots. Calculated values of γ using the breakdown sparking distances d_s for various values of E/p (calculated from the breakdown potentials at different pressures) and mean extrapolated values of α/p and η/p, employing equation (4) are summarized in table 2.

Table 2. Calculated Values of γ in CO_2 with Pt Cathode and Relative Sparking Distances pd_s

p (mm Hg)	5 (spec. pure)				25 (spec. pure)				100 (spec. pure)					
E/p	200	150	120	100	70	65	60	55	60	55	50	46	42	40
pd_s	4·2	6·6	9·8$_5$	14·6	36·3	46·3	60·0	82·8	62	84	118	169	260	342
$\gamma \times 10^7$	72	69	55	51	31	20	13	7·2	11·5	6·8	5·6	5·2	4·5	3·7

p (mm Hg)	300 (cylinder)					700 (cylinder)		
E/p	42	40	38	36	34	36	34	32
pd_s	255	321	426	600	930	616	917	1484
$\gamma \times 10^7$	4·5	2·8	2·0	1·14	0·5	1·02	0·67	0·43

§ 4. Correlation of Results with Low Pressure Experiments

Calculated values of mean cross sections for ionization $\overline{\sigma^+}$ and for attachment $\overline{\sigma^-}$ employing the cross section data from low pressure experiments in carbon dioxide (Craggs and Tozer 1960) are compared with the data from the present study for the Maxwellian and Druyvesteyn distributions.

The earlier work of Deas and Emeléus (1949), Tozer, Thorburn and Craggs (1958) and Thompson (1959) shows that the mean cross section for any particular collision process for the mean energy $\bar{E}$ of a given energy distribution is given by the equation:

$$\overline{\sigma_{\bar{E}}} = \int \sigma_E v_E dN_E \Big/ \int v_E dN_E \qquad \ldots\ldots (6)$$

where σ_E is the cross section for this process for electrons of energy E ev and v_E is the velocity of, and dN_E the number of electrons in the energy range E to $E+\delta E$ of the distribution in the swarm. Further, swarm constants α/p and η/p can be converted into a mean cross section for any particular value of E/p from the knowledge of the drift velocity W, the mean velocity of agitation U and mean energy $\bar{E}$ of the electrons as functions of E/p by using the equation

$$\overline{\sigma_{\bar{E}}} = \left(\frac{1}{N}\right)\left(\frac{W}{U}\right)\left(\frac{\theta}{p}\right) \qquad \ldots\ldots (7)$$

where N is the number of molecules per cm^3 at 1 mm Hg at the appropriate temperature and θ represents α or η. However it is to be noted that when employing the data from the diffusion experiments (see Healey and Reed 1941) the various quantities should be corrected for the different energy distributions assumed (Healey and Reed 1941, Huxley and Zaazou 1949).

The $\overline{\sigma^+}$ and $\overline{\sigma^-}$ values thus obtained by using the ionization and attachment cross sections from Craggs and Tozer's (1960) low pressure data employing equation (6) and the mean values of α/p and η/p from the present measurements employing equation (7) are represented for both the Maxwellian and the Druyvesteyn distributions in figures 5 and 6. Skinker's (1922) values of the drift and agitation velocities have been used in the latter calculations.

§ 5. Discussion of Results

From the double sets of values at 25 and 100 mm Hg pressure given in table 1 it can be seen that the measured values of α/p and η/p for different gas fillings are consistent. Further the values of α/p obtained at different pressures in the range E/p where the results overlap, also showed good agreement within the experimental limits ($\pm 2\%$). These considerations suggest that α/p and η/p are not pressure dependent and are therefore functions of E/p. However no accurate measurements of α/p and η/p could be made at pressures higher than 100 mm Hg because the quantities of spectroscopically pure gas required were large. The values of α/p and η/p do not depend on the ionization current. This is shown by a careful consideration of the experimental data such as those, for example, plotted in figure 1.

The values of α/p over a wide range of the parameter E/p plotted in figure 3 show good agreement with the earlier measurements of Bishop (1911) in the

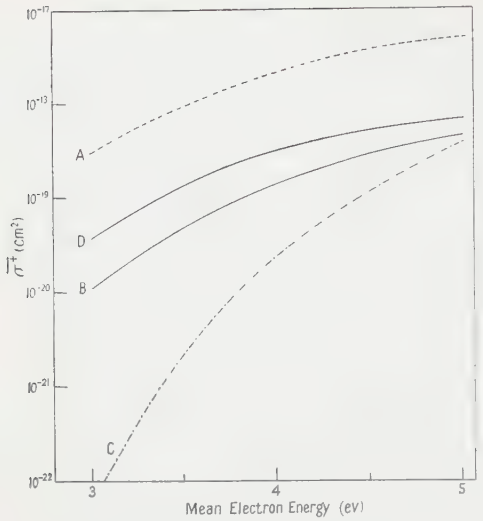

Figure 5. Ionization cross sections in carbon dioxide as a function of mean energy. A, calculated from Craggs and Tozer's low pressure data, for a Maxwellian distribution of electron energies; B, calculated with the data from the present study, for a Maxwellian distribution of electron energies; C, as for A but with a Druyvesteyn distribution; D, as for B but with a Druyvesteyn distribution.

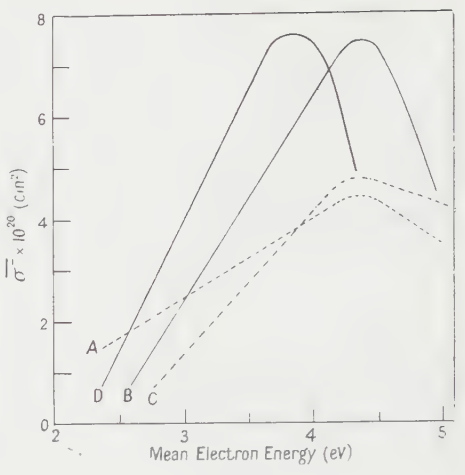

Figure 6. Attachment cross sections in carbon dioxide as a function of mean energy. A, B, C, D, as in figure 5.

E/p range of 1200 to 100 v cm^{-1} (mm Hg)$^{-1}$ (even though the pressure measurements at 0·5 and 1 mm Hg are not very satisfactory) and with the recent measurements of Schlumbohm (1959) in the E/p range of 70 to 50v cm ^{1}(mm Hg)$^{-1}$. The values of α/p for $E/p < 50$ v cm^{-1} (mm Hg)$^{-1}$ differ appreciably from the previous measurements of Schlumbohm because attachment processes ignored by Schlumbohm considerably influence the computed values of α below this value of E/p.

Figures 5 and 6 show, respectively for ionization and attachment, the comparisons between mean cross sections for the swarms deduced from α and η measurements, and from the low pressure single collision work of Craggs and Tozer (1960) assuming either a Maxwellian or a Druyvesteyn distribution. It is apparent that, neither for ionization nor attachment processes in the present conditions, do these distributions apply. Thus it seems from figure 6 that the attachment data give a better general agreement between themselves than the ionization data, which would be expected, since the calculations of α from collision cross sections involve an accurate knowledge of the tail shape for the distribution, a quantity notoriously difficult to calculate accurately (Lewis 1958) whilst the attachment data refer largely to the lower energy part of the distribution and hence are somewhat insensitive to the type of energy distribution function employed.

The values of γ (table 2) are of interest. They are considerably less than corresponding values for dry air (Prasad 1959) where, for example, $\gamma \sim 10^{-5}$

for $E\,p = 38$–40 at 700 mm Hg, a value about 100 times higher than that for comparable conditions in CO_2 (see table 2). The γ values for humid air (Prasad and Craggs 1960) overlap the CO_2 values. It has been suggested by Köhrmann (1956) and in more detail by Meek (1959) that the abnormally low γ's for humid air may be due to a high absorption of the photons responsible for photoelectric emission at the cathode. In the case of CO_2, the published data for absorption coefficients are similar in their general trend with wavelength and magnitude, so the same reason for the low γ's may apply.

§ 6. Conclusions

Measurements of Townsend's first ionization coefficient were made in carbon dioxide and assuming Townsend's breakdown criterion to apply, calculations of the γ coefficient were made. However, contrary to statements in the literature, allowance must be made for electron attachment which, in fact, is greater than that in dry air in comparable conditions, and consequently is easily measurable. The electron energy distribution in the present experiments must differ appreciably from the Maxwellian or Druyvesteyn forms. This departure is more marked than is usually the case with the commonly investigated gases.

Acknowledgments

One of us (M.S.B.) is indebted to the Electrical Research Association for financial support and for permission to publish this paper. We are grateful to Mr. A. N. Prasad for many discussions and advice.

References

Allenden, D., 1958, *Electron. Engng*, **30**, 31.
Bishop, E. S., 1911, *Phys. Rev.*, **33**, 325.
Bradbury, N. E., and Tatel, H. E., 1934, *J. Chem. Phys.*, **2**, 835.
Chapman, D. L., Chadwick, S., and Ramsbottom, J. E., 1907, *J. Chem. Soc.*, **91**, 942.
Coehn, A., and May, B. W., 1934, *Z. Phys. Chem.* B, **26**, 117.
Coehn, A., and Sieper, G., 1916, *Z. Phys. Chem.*, **91**, 347.
Coehn, A., and Spitta, T., 1930, *Z. Phys. Chem.* B, **9**, 401.
Craggs, J. D., and Tozer, B. A., 1960, *Proc. Roy. Soc.* A, **254**, 229.
Deas, H. D., and Emeléus, K. G., 1949, *Phil. Mag.*, **40**, 460.
Geballe, R., and Reeves, M. L., 1953, *Phys. Rev.*, **92**, 867.
Harrison, M. A., and Geballe, R., 1953, *Phys. Rev.*, **91**, 1.
Healey, R. H., and Reed, J. W., 1941, *The Behaviour of Slow Electrons in Gases* (Sydney Amalgamated Wireless (Australasia)).
Hopwood, W., Peacock, N. J., and Wilkes, A., 1956, *Proc. Roy. Soc.* A, **235**, 334.
Huxley, L. G. H., and Zaazou, A. A., 1949, *Proc. Roy. Soc.* A, **196**, 402.
Köhrmann, W., 1956, *Ann. Phys., Lpz.*, **18**, 379.
Lewis, T. J., 1958, *Proc. Roy. Soc.* A, **244**, 166.
Loeb, L. B., 1956, *Handbuch der Physik* (Berlin: Springer) **21**, 460.
Meek, J. M., 1959, *Nature, Lond.*, **183**, 1805.
Prasad, A. N., 1959, *Proc. Phys. Soc.*, **74**, 33.
Prasad, A. N., and Craggs, J. D., 1960, *Proc. Phys. Soc.*, in the press.
Schlumbohm, H., 1959, *Z. angew. Phys.*, **11**, 156.
Skinker, M. F., 1922, *Phil. Mag.*, **44**, 994.
Thompson, J. B., 1959, *Proc. Phys. Soc.*, **73**, 821.
Tozer, B. A., Thorburn, R., and Craggs, J. D., 1958, *Proc. Phys. Soc.*, **72**, 1081.

Fourier Images IV : The Phase Grating

By J. M. COWLEY and A. F. MOODIE

Division of Chemical Physics, C.S.I.R.O., Chemical Research Laboratories, Melbourne, Australia

Communicated by A. L. G. Rees; *MS. received* 1st *February* 1960

Abstract. The nature of the Fourier images obtained from phase objects is investigated theoretically both for the particular case of the sinusoidal grating and also for the general two-dimensional periodic object. The results are verified experimentally with light optics using a two-dimensional phase grating of 50 μ periodicity.

A detailed investigation is made of the intensity distribution on planes mid-way between, and in the immediate neighbourhood of Fourier image planes. While there is no contrast on the Fourier image planes themselves, it is shown that a simple relationship (equation (3.4)) exists between the pattern on neighbouring planes and the phase distribution in the general two-dimensional object. It is shown that there will be no moiré effect at full aperture for phase gratings effectively in contact.

Analogies with the scattering of electrons by thin crystals are pointed out and it is indicated that under certain conditions a representation of the charge distribution will be obtained with modern electron microscopes. Full consideration of this point is deferred.

§ 1. Introduction

In previous publications (Cowley and Moodie 1957 a, b, c, to be referred to as I, II, III) various aspects of Fourier images were discussed. Although the theory applied to complex objects the detailed results were confined to amplitude objects. It is the purpose of this communication to extend the detailed treatment to phase gratings.

In previous communications some early references were overlooked. These include an account by Talbot (1836) of fringes observed near a grating irradiated with a parallel beam of light, and an approximate theory for a sinusoidal lattice by Rayleigh (1881) who obtained a focusing condition. Weisel (1910) and Wolfke (1913) refined and extended both the theoretical and experimental treatment and gave a simplied account of some of the symmetrical out-of-focus patterns obtained from one-dimensional amplitude gratings. The phenomenon has recently been observed in ultrasonic cells (e.g. Hiedemann and Breazeale 1959).

While the optical phase grating is itself of considerable interest our main purpose will be to obtain results which can be applied to the imaging of crystal lattices by means of electrons. The conditions under which there is correspondence between the scattering of electrons by a crystal lattice and the scattering of light by a phase object has been discussed in some detail (for instance Cowley and

Moodie 1957 d). It is sufficient to remark here that under conditions quite frequently encountered in the practice of electron microscopy and electron diffraction the correspondence will be almost complete; light optical analogues may therefore be conveniently employed to check the simpler results. This will be done in the present paper and the application to the imaging of lattices merely indicated at several points. Detailed discussion of the electron case will be published separately. It may be noted that Lenz and Scheffels (1958) have made a limited application of standard Fresnel diffraction theory to the calculation of out-of-focus electron microscope images and obtained qualitative agreement with observations on some biological material with a periodic structure.

§ 2. The Sinusoidal Lattice

The sinusoidal lattice will be considered separately because of its immediate practical importance and because of its simplicity. The crystal is described by

$$q_1(x) = \exp\{iC_1\sigma \sin(2\pi x/a)\} = \sum_{h=-\infty}^{\infty} \mathrm{J}_h(C_1\sigma) \exp\{2\pi i h x/a\}, \qquad \ldots\ldots (2.1)$$

where, for light σ is given by $-2\pi/\lambda_0$ and for electrons by $2\pi m\lambda_0/h^2$, λ_0 being the wavelength *in vacuo* and C_1 a constant depending on the thickness and refractive index of the object.

If this object is illuminated by a point source placed at a distance R_q from it, then, as is shown in II, the wave function on a plane at a distance R is given by

$$\psi(x) = \sum_{-\infty}^{\infty} \mathrm{J}_h(C_1\sigma) \exp\{2\pi i \mu h^2\} \exp\{2\pi i h x/Ma\}, \qquad \ldots\ldots (2.2)$$

where

$$\mu = \tfrac{1}{2} \frac{\lambda_0}{a^2} \frac{RR_q}{R - R_q}.$$

Hence, when μ is integral or half integral a series of Fourier images is formed, but these have zero contrast. On all other planes, however, the contrast is finite. In particular, for the planes $\mu = (2n+1)/4$, that is, for those mid-way between Fourier images,

$$\psi(\tfrac{1}{4}) = \sum_{-\infty}^{\infty} \mathrm{J}_{2h}(C_1\sigma) \exp\left\{2\pi i \frac{2hx}{Ma}\right\} - i \sum_{-\infty}^{\infty} \mathrm{J}_{2h+1}(C_1\sigma) \exp\left\{2\pi i \frac{(2h+1)x}{Ma}\right\}$$

$$= \mathrm{J}_0(C_1\sigma) + 2\sum_{1}^{\infty} \mathrm{J}_{2h}(C_1\sigma) \cos\left\{2\pi \frac{2hx}{Ma}\right\} + 2\sum_{0}^{\infty} \mathrm{J}_{2h+1}(C_1\sigma) \sin\left\{2\pi \frac{(2h+1)x}{Ma}\right\},$$

whence

$$I(\tfrac{1}{4}) = 1 + \sin\{2C_1\sigma \sin(2\pi x/Ma)\}. \qquad \ldots\ldots (2.3)$$

Hence, for sufficiently small values of $C_1\sigma$ a clear representation of the phase distribution will be obtained on the $(2n+1)/4$ planes. This result holds only for the sinusoidal lattice. Further the range of validity of equation (2.3) for electrons includes values of C_1 sufficiently large to make severe distortion, or even halving of the fringe spacing possible. Discussion of these results, which have application to the interpretation of various images recently observed in the electron microscope will be deferred till § 5.

§ 3. The General Two-dimensional Lattice

The lattice is described by

$$\phi'(x,y)=\exp\{i\sigma\phi(x,y)\}=\exp\left[i\sigma\sum_h\sum_k E_{hk}\exp\left\{2\pi i\left(h\frac{x}{a}+k\frac{y}{b}\right)\right\}\right],$$

with

$$\mathscr{F}\phi(x,y)=E_{hk},\quad \mathscr{F}\phi'(x,y)=E_{hk}'=\int_{-\infty}^{\infty}\int_{-\infty}^{\infty}\phi'(x,y)\exp\{2\pi i(ux+vy)\}\,dx\,dy.$$

Here $\phi(x,y)$ is to be understood as a projection of the refracting material or the potential, that is

$$\phi(x,y)=\int_{-\infty}^{\infty}\phi(x,y,z)\,dz.$$

Hence, if $a=b$, the wave function on an arbitrary plane of observation is given by

$$\psi(x,y)=\sum_h\sum_k E_{hk}'\exp\{i\theta\}\exp\{2\pi i\mu(h^2+k^2)\},$$

where

$$\theta=\frac{2\pi}{Ma}(hx+ky).$$

For the case $\mu=\frac{1}{4}$,

$$\psi(\tfrac{1}{4})=\sum_{h\,\text{even}}\sum_{k\,\text{even}}E_{hk}'\exp\{i\theta\}-\sum_{h\,\text{odd}}\sum_{k\,\text{odd}}E_{hk}'\exp\{i\theta\}$$
$$+i\sum_{h\,\text{odd}}\sum_{k\,\text{even}}E_{hk}'\exp\{i\theta\}+i\sum_{h\,\text{even}}\sum_{k\,\text{odd}}E_{hk}'\exp\{i\theta\}. \quad \ldots\ldots(3.1)$$

Now

$$\phi'(x,y)=1+i\sigma\phi(x,y)+\{i\sigma\phi(x,y)\}^2/2!+\{i\sigma\phi(x,y)\}^3/3!+\ldots.$$

Hence

$$E_{hk}'=\delta(h,k)+i\sigma E_{hk}-\frac{\sigma^2}{2!}\sum_{h_1}\sum_{k_1}E_{h_1k_1}E_{h-h_1,k-k_1}$$
$$-\frac{i\sigma^3}{3!}\sum_{h_1}\sum_{k_1}\sum_{h_2}\sum_{k_2}E_{h_1k_1}E_{h_2k_2}E_{h-h_1-h_2,\,k-k_1-k_2}+\ldots.$$

Therefore

$$\sum_{h\,\text{even}}\sum_{k\,\text{even}}E_{hk}'\exp\{i\theta\}=\sum_{h\,\text{even}}\sum_{k\,\text{even}}\delta(h,k)\exp\{i\theta\}+i\sigma\sum_{h\,\text{even}}\sum_{k\,\text{even}}E_{hk}\exp\{i\theta\}$$
$$-\frac{\sigma^2}{2!}\sum_{h\,\text{even}}\sum_{k\,\text{even}}\sum_{h_1}\sum_{k_1}E_{h_1k_1}E_{h-h_1,\,k-k_1}\exp\{i\theta\}-\ldots.$$

The summations can be evaluated in terms of the functions ϕ_{ee}, ϕ_{oo}, ϕ_{eo}, ϕ_{oe}, where, typically,

$$\phi_{oe}=\sum_{h\,\text{odd}}\sum_{k\,\text{even}}E_{hk}\exp\{i\theta\}.$$

There results

$$\sum_{h\,\text{even}}\sum_{k\,\text{even}}E_{hk}'\exp\{i\theta\}=1+i\sigma\phi_{ee}-\frac{\sigma^2}{2!}(\phi_{ee}^2+\phi_{eo}^2+\phi_{oe}^2+\phi_{oo}^2)$$
$$-\frac{i\sigma^3}{3!}(\phi_{ee}^3+3\phi_{oo}^2\phi_{ee}+3\phi_{eo}^2\phi_{ee}+3\phi_{oe}^2\phi_{ee}+6\phi_{eo}\phi_{oe}\phi_{oo})+\ldots.$$

The other terms of (3.1) may be evaluated by similar means to give

$$\psi(\tfrac{1}{4}) = 1 - i\sigma(\phi_{ee}-\phi_{oo}) - \frac{i^2\sigma^2}{2!}\{(\phi_{ee}-\phi_{oo})^2 - (\phi_{eo}-\phi_{oe})^2\}$$

$$+ \frac{i^3\sigma^3}{3!}\{(\phi_{ee}-\phi_{oo})^3 + 3(\phi_{ee}-\phi_{oo})(\phi_{eo}-\phi_{oe})^2\} + \dots$$

$$+ i\Big[\, i\sigma(\phi_{eo}+\phi_{oe}) + i^2\sigma^2(\phi_{ee}+\phi_{oo})(\phi_{eo}+\phi_{oe}) + \dots$$

$$- \frac{i^3\sigma^3}{3!}\{(\phi_{eo}+\phi_{oe})^3 + 3(\phi_{ee}+\phi_{oo})^2(\phi_{eo}+\phi_{oe})\} + \dots \Big]$$

$$= \exp\{i\sigma(\phi_{ee}-\phi_{oo})\}\cos\sigma(\phi_{eo}-\phi_{oe}) - \exp\{i\sigma(\phi_{ee}+\phi_{oo})\}\sin\sigma(\phi_{eo}+\phi_{oe})$$

$$= \exp\{i\sigma(\phi_{ee}+\phi_{oo})\}[\cos 2\sigma\phi_{oo}\cos\sigma(\phi_{eo}-\phi_{oe}) - \sin\sigma(\phi_{eo}+\phi_{oe})$$

$$- i\{\sin 2\sigma\phi_{oo}\cos\sigma(\phi_{eo}-\phi_{oe})\}].$$

Therefore

$$I(\tfrac{1}{4}) = 1 + \sin 2\sigma\phi_{oe}\sin 2\sigma\phi_{eo} - \cos 2\sigma\phi_{oo}(\sin 2\sigma\phi_{eo} + \sin 2\sigma\phi_{oe}). \quad \dots\dots (3.2)$$

$$I(-\tfrac{1}{4}) = 1 + \sin 2\sigma\phi_{oe}\sin 2\sigma\phi_{eo} + \cos 2\sigma\phi_{oo}(\sin 2\sigma\phi_{eo} + \sin 2\sigma\phi_{oe}). \quad \dots\dots (3.3)$$

Results for other values of μ may be obtained in the same way, although the form of the distribution will in general be more complicated than that of equation (3.2). Analogous results are also readily obtained for one-dimensional distributions. Thus for a one-dimensional distribution,

$$I(\tfrac{1}{4}) = 1 + \sin 2\sigma\phi_o,$$

where

$$\phi_o = \sum_{h\ \mathrm{odd}} E_h \exp\{i\theta\}.$$

As in the case of the amplitude grating the out-of-focus patterns are in general sharp and detailed. Even in the limit of small phase change, however, the patterns are completely different. Thus equation (3.2) takes the form

$$I(\tfrac{1}{4}) = (1 - 2\sigma\phi_{oe})(1 - 2\sigma\phi_{eo})$$

for small phase change while, for an amplitude object,

$$I(\tfrac{1}{4}) = (\phi_{ee}-\phi_{oo})^2 + (\phi_{eo}+\phi_{oe})^2.$$

Some of the implications and applications of equations of the above type to electron microscopy will be considered in §5. The point of immediate interest, however, is that such equations offer no direct means of reconstructing the equivalent amplitude object. Nor are the standard devices of light optics applicable. For instance, in the classical wave descriptions of phase-contrast systems the approximation is made that the maximum phase change through the object is small, a condition that will scarcely ever be satisfied by an electron beam and a real crystal. Further, as Linfoot (1955) points out, even for the phase object of small phase change the appearance inside and outside focus on an ordinary microscope bears no simple relation to the equivalent amplitude object.

Consider, however, a plane near a Fourier-image plane defined by $\mu = n + \epsilon$, where n is an integer and ϵ satisfies $\epsilon(h^2+k^2) \ll 1$ for all reciprocal lattice coordinates. Then

$$\begin{aligned}\psi(x,y) &= \sum_h \sum_k E_{hk}' \exp\{i\theta\} \exp\{2\pi i\epsilon(h^2+k^2)\} \\ &\simeq \sum_h \sum_k E_{hk}' \exp\{i\theta\}[1+2\pi i\epsilon(h^2+k^2)] \\ &= \phi'\left(\frac{x}{M}, \frac{y}{M}\right) - i\frac{M^2a^2}{2\pi}\epsilon\nabla^2\phi'\left(\frac{x}{M}, \frac{y}{M}\right) \\ &= \phi'\left[1+\epsilon\frac{M\sigma a^2}{2\pi}\left\{\nabla^2\phi + \frac{i\sigma}{M}\left(\left(\frac{\partial\phi}{\partial x}\right)^2 + \left(\frac{\partial\phi}{\partial y}\right)^2\right)\right\}\right].\end{aligned}$$

Hence the intensity distribution correct to the first order in ϵ is given by

$$I = 1 + \tfrac{1}{2}\frac{l\sigma\lambda}{\pi}\nabla^2\phi(x,y), \qquad \ldots\ldots (3.4)$$

where l is the distance from the Fourier-image plane.

For the electron optical case $\nabla^2\phi = 4\pi\rho(x,y)$, where $\rho(x,y)$ is the projected charge distribution, so that

$$I = 1 + 2l\sigma\lambda\rho(x,y). \qquad \ldots\ldots (3.5)$$

Thus in the neighbourhood of every Fourier-image plane of the general two-dimensional periodic object a magnified image of the charge distribution in the crystal will be formed.

Equations (3.4) and (3.5) will also apply to non-periodic objects provided that l is now taken to be the distance from the Gaussian focus.

These results can be applied to a special case in the wave theory of the moiré effect. In general defect-of-focus patterns will be quite complex (Cowley and Moodie 1959). However it is possible to show that under certain fairly restrictive conditions two crystals may be regarded effectively as being 'in contact'. Suppose those conditions to be satisfied so that

$$\phi_{12}' = \phi_1'\phi_2' = \exp\{i(\sigma_1\phi_1 + \sigma_2\phi_2)\}.$$

ϕ' in the above formulae can now be replaced directly by ϕ_{12}' so that

$$I = 1 + 2l\lambda(\sigma_1\rho_1 + \sigma_2\rho_2).$$

Thus, at full aperture and when the crystals are effectively in contact, there will be no contrast on Fourier-image planes, and on neighbouring planes the sum of the charge distributions will be observed. That is, at full aperture, all moiré effect disappears.

§ 4. Light Optics Experiments

Experiments using light were made both to test the theoretical predictions and also to gain some experience in the analogous technique for interpreting electron micrographs where the *a priori* information will in general be very much less.

The experimental arrangements were the same as those described in I, the object being a phase grating prepared by Mr. Hayes of the Defence Standards Laboratories. The unit cell was square with $a = 50{\cdot}9 \pm 0{\cdot}1\,\mu$; the pattern was known to be approximately that of a grid with a mark-to-space ratio of about

0·14, and the maximum phase change was thought to be of the order of one wavelength. The diffraction pattern obtained from this grating is shown in figure 1†.

Structure factors for an ideal amplitude grating of the above mark-to-space ratio were calculated and multiplied by an artificial temperature factor of the conventional form, $\exp\{-c(h^2+k^2)\}$. The half-width was chosen so as to make the calculated intensitites approach zero in the same range of reciprocal space as those of the phase grating. The assumption was thus made that the errors in the grating had a normal distribution, and the best fit on this assumption was obtained for a half-width of about 2μ. In other words the mean grating consisted of the ideal grating convoluted with a Gaussian of 2μ half-width. The summation of the modified structure factors is shown in figure 2.

This should be a fairly accurate representation of the average shape of the grid. The value of the phase change was then determined by evaluating equation (3.3) as a function of σ for the points (0, 0), (0, $\frac{1}{4}$), ($\frac{1}{4}$, $\frac{1}{4}$). A comparison of these sets of values with the intensities at the corresponding points on the pattern obtained experimentally eliminated all but a few values of σ. More extensive calculations for each of these values then showed that $\sigma=\pi$. This determination was made to an accuracy of $\pm 18^\circ$ corresponding to ± 250 Å pathlength difference in air.

More extensive calculation might have improved on this but the accuracy at this point is determined largely by imperfections in the grating which make the recognition of detail difficult. Comparison of figures 3 and 4 shows that equation (3.3) describes the observed pattern to within experimental error. In particular the pronounced maximum on the orgin, the faint streaks along the axis centred on ($\frac{1}{4}$, 0), and the slight depression round ($\frac{1}{2}$, $\frac{1}{2}$) are characteristic of $I(-\frac{1}{4})$ for this grating.

Equation (3.4) was then tested by calculating $\nabla^2\phi$ and comparing this distribution with that obtained experimentally in the neighbourhood of a Fourier-image plane. Figures 5 and 6 indicate that the agreement is satisfactory. The minimum at the origin together with the faint diagonal minima constitute a sensitive test.

§ 5. Some Applications to Electron Microscopy

It was shown in III that for the very unfavourable case of illumination by an incoherent Gaussian source, the least resolvable distance is given by

$$\Delta=\sigma R/(R+R_q)$$

where σ is the half-width of the source. In some modern electron microscopes the effective source of illumination can be less than 10μ so that, with a beam convergence of 10^{-2} to 10^{-3} radians Δ can be of the order of 10 A. The general considerations of this paper may then apply if certain conditions are satisfied. It should be noted that under the above conditions all Fourier images will have unit magnification.

In order to apply the above results to practical cases in electron microscopy considerable additional calculation is required. In particular the rather involved effects resulting from limited objective apertures prove to be of importance.

† All figures are Plates.

As indicated in § 1 these calculations will be given elsewhere and we limit ourselves here to pointing out the importance of recognizing that crystals in the electron microscope behave, at their simplest, as phase objects. Under heavily restrictive conditions certain very simple systems can yield results in apparent agreement with calculations assuming amplitude scattering and this has led to confusion in much of the recent literature. Even in these systems, however, more detailed examination of the patterns shows the hypothesis of scattering by an amplitude object to be inadmissible.

Again, the complexity of even apparently simple systems is much greater than appears, from published work, to be generally recognized. This arises in large part from the absence of a sharp focal plane in the Gaussian sense and the tendency to select patterns of maximum contrast. These in general will bear little direct relation to even a simple lattice as an inspection of equation (3.2) shows.

The above remarks apply only to conventional methods of electron microscopy where the magnification of the Fourier images will be unity. It can be seen that the methods briefly remarked on in III for obtaining higher magnification by means of Fourier images remain applicable provided that the patterns are suitably interpreted.

References

Cowley, J. M., and Moodie, A. F., 1957 a, *Proc. Phys. Soc.* B, **70,** 486.
—— 1957 b, *Ibid.*, **70,** 497.
—— 1957 c, *Ibid.*, **70,** 505.
—— 1957 d, *Acta Cryst. Camb.*, **10,** 609.
—— 1959, *Ibid.*, **12,** 423.
Hiedemann, E. A., and Breazeale, M. A., 1959, *J. Opt. Soc. Amer.*, **49,** 372.
Lenz, F., and Scheffels, W., 1958, *Z. Naturf.*, **139,** 226.
Linfoot, E. H., 1955, *Recent Advances in Optics* (Oxford: Clarendon Press).
Rayleigh, Lord, 1881, *Phil. Mag.*, **11,** 196.
Talbot, F., 1836, *Phil. Mag.*, **9,** 401.
Weisel, H., 1910, *Ann. Phys., Lpz.*, **33,** 995.
Wolfke, M., 1913, *Ann. Phys., Lpz.*, **40,** 194.

Internal Friction in Germanium and Silicon I: Electron and Impurity Relaxation

By P. D. SOUTHGATE†
Mullard Research Laboratories, Redhill, Surrey

MS. received 16*th July* 1959, *in revised form* 4*th March* 1960

Abstract. The internal friction of single crystal silicon and germanium at 100 kc/s shows a relaxation peak near 0·56 of the melting temperature. The peak is electronic in origin and the relaxation time is the carrier lifetime. At the peak temperature, in many of the specimens measured, intrinsic recombination and intrinsic conduction are the dominant mechanisms, and the peak height at any given frequency depends only upon specimen orientation. If impurities are introduced so that the extrinsic lifetime becomes less than the intrinsic lifetime at the peak temperature, then the peak height is reduced. From the shape of the electronic peak and from its shift with frequency, the temperature variation of both intrinsic and extrinsic lifetime may be deduced. The activation energy of recombination of carriers in silicon appears to be 1·45 ev and in germanium about 1·15 ev, although it is difficult to reconcile these values with existing theories. The height of the peak gives the deformation potential constant; in silicon it is 2·3 ev and in germanium 6·5 ev per unit dilatational strain, which values are of the same order as those derived from hydrostatic measurements.

In silicon crystals containing oxygen, having a [111] vibration axis, an internal friction peak appears at 1030°c (100 kc/s). The peak is not present if the silicon is oxygen free or has a [100] axis, and can be attributed to the movement of dissolved oxygen. The activation energy is 2·55 ev. The peak height varies, but in most crystals grown from silica crucibles the maximum logarithmic decrement is of the order 3×10^{-4}. In germanium a small peak appears in some specimens at 770°c (100 kc/s). No reduction of its height has been observed on annealing, and its shape is consistent with that of impurity relaxation.

§ 1. Introduction

In metals a considerable volume of information has been accumulated on impurity diffusion and electronic relaxation by the analysis of internal friction data. In semiconductors, however, this type of information has not been obtained from investigations prior to that reported here. Kessler (1957) has published a thorough set of measurements on the internal friction of germanium in the 40–120 kc s range. A relaxation peak appeared which can now be recognized as an electronic relaxation peak, although experimental artefacts prevented its correct analysis at the time. Other investigations have been carried out in the megacycle range by McSkimin (1953), Truell and Bronzo (1953), Granato and Truell (1956), Teutonico, Granato and Truell (1956) and Lamb, Redwood and Shteinshleifer (1959). At these frequencies one would not expect impurity

† Now at Armour Research Foundation, Chicago, Illinois, U.S.A.

or electronic relaxation, and no such analysis of these results has been reported. Previous publications of the author (Southgate 1957, 1958) have described a relaxation peak due to impurity oxygen in silicon.

This paper refers to measurements made at 100 kc/s (and occasionally 300 kc/s) on silicon and germanium, at temperatures covering much of the range between room temperature and the melting point. In both materials an electronic relaxation peak appears at 0·56 of the melting temperature, which is described by the theory of Weinreich (1956). The relatively large relaxation peak due to impurity oxygen appears, in silicon, at higher temperatures. The analysis method employed for the electronic peak in both silicon and germanium will be described first, followed by presentation of more detailed results. A further paper (Southgate 1960, to be referred to as Part II) will give details of dislocation damping and the behaviour of dissolved oxygen during heat treatment. The value of internal friction will be denoted by the logarithmic decrement Δ.

§ 2. Electronic Relaxation Peak Analysis

Weinreich's theory of the electro-acoustic effect depends on the fact that elastic strains in a semiconductor can change the band gap, and hence the intrinsic charge carrier density, without producing large electric fields, thermal excitation giving equal numbers of carriers of opposite sign. Thus relaxation effects can occur having periods long compared with the 'electron diffusion' relaxation time. The theory, when applied to an intrinsic semiconductor, gives

$$\Delta = \frac{\pi q^2 n}{2\boldsymbol{k}T} \frac{(1+\omega_i/\omega^2\tau)\omega_i/\omega}{(1+\omega_i/\omega^2\tau)^2+\omega_i^2/\omega^2},$$

q being the 'acoustic charge' of the carriers, τ the carrier recombination time, and n the carrier density. The frequency ω_i is such that the associated wavelength is close to the charge carrier diffusion distance, and is of the order 10^{11} sec $^{-1}$. The geometry used in deriving this formula is that of a dilatational wave travelling in an infinite medium; and for the case of longitudinal oscillation of a thin bar, it is necessary to modify the expression to account for Poisson's ratio strain. The conduction band will be taken to be such that the band shift depends only on dilatation of the material and not on shear. If now the strain axis is one of greater than two-fold symmetry, Poisson's ratio will have a unique value, and a simple calculation shows that q in the above formula may be replaced by the expression

$$V_1(1-2\nu)E^{-1/2} \qquad \ldots\ldots(1)$$

V_1 being the deformation potential constant of the band gap per unit dilatation, ν Poisson's ratio, and E Young's modulus in the direction of strain. Measurements reported here are made at frequencies small compared with ω_i, and so

$$\Delta = \frac{\pi q^2 n}{2\boldsymbol{k}T} \frac{\omega\tau}{1+\omega^2\tau^2}. \qquad \ldots\ldots(2)$$

There are two components to the lifetime, one due to recombination across the band gap (intrinsic recombination) and the other to recombination via a lattice imperfection level (extrinsic recombination). Direct measurements of lifetime have not yet been reported at elevated temperatures, but it is postulated here that in the region of the peak, intrinsic recombination is of the order of 1 μsec. In material having sufficiently high lifetime at room temperature, it

seems likely that intrinsic recombination alone determines the magnitude of the internal friction. The form of intrinsic lifetime variation is tentatively taken as

$$\tau_i = \tau_0 \exp(E_r/\boldsymbol{k}T) \qquad \ldots\ldots (3)$$

where the energy E_r is of the order of the band gap, and τ_0 is constant. In silicon this form will be seen to fit the highest extrinsic lifetime specimens well. In germanium extrinsic recombination complicates the results to a greater extent, and the assumption of the form is more of a conjecture. The two materials are, nevertheless, felt to be sufficiently analogous to justify the assumption, which will be retained through the remainder of the analysis.

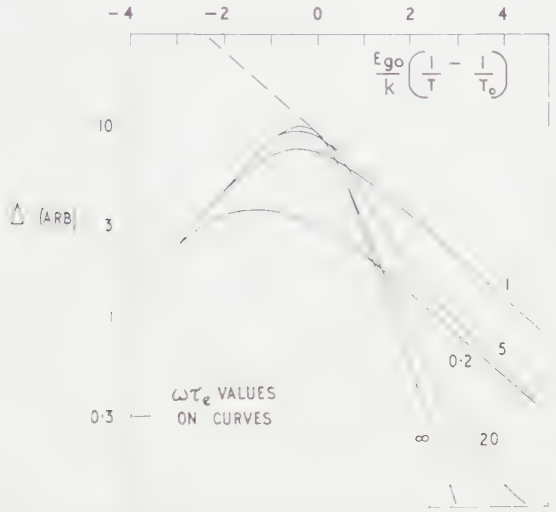

Figure 1. General form of electronic relaxation peak for combined intrinsic and extrinsic recombination, the extrinsic lifetime being temperature independent

The total carrier lifetime is formed by reciprocal summation

$$\frac{1}{\tau} = \frac{1}{\tau_i} + \frac{1}{\tau_e}. \qquad \ldots\ldots (4)$$

On the basis of the Shockley–Read (1952) theory it is supposed that extrinsic lifetime τ_e does not vary rapidly with temperature. Thus τ_e will be important at the lower temperatures where τ_i, as given by (3), becomes large in comparison. Figure 1 shows a set of curves calculated from equations (2) and (3) for the ideal case of a constant extrinsic lifetime, the frequency remaining constant. The curves have been normalized, E_{go} being the band gap extrapolated to zero temperature. The general form of the curves should apply equally well to germanium or to silicon, although the exact shapes in figure 1 are for silicon. For $\omega\tau_e > 1$ the temperature at which the peak appears does not depend on τ_e, although it depends on frequency. On the other hand, if $\omega\tau_e < 1$ a peak will still be observed whose location and magnitude change with τ_e. This will not be a true relaxation peak as the condition $\omega\tau = 1$ will never be satisfied, and no shift of peak temperature with frequency will be observed. In materials having different values of τ_e,

the slope† of the lower temperature shoulder of the peaks will vary between $E_r + \frac{1}{2}E_{g0} + \frac{1}{2}kT$ and $\frac{1}{2}E_{g0} + \frac{1}{2}kT$, whereas the slope of the upper temperature shoulder will remain approximately constant. As the measurement frequency is increased, the peak of those curves for which $\omega\tau_e > 2$ will occur at a higher temperature and move along the dotted line, which is of slope $\frac{1}{2}E_{g0} + \frac{1}{2}kT$ and represents approximately the change of carrier concentration. The activation energy E_r may be obtained directly from the magnitude of the temperature shift.

Thus, the general shape and temperature behaviour of the peak shows whether it is a true relaxation peak, and hence whether the deformation potential can be calculated from the peak height by the use of the relations (1) and (2). Deviations from the curves shown in figure 1 will occur if the extrinsic lifetime is sensibly temperature dependent. In this case, in the region where extrinsic recombination is dominant, the difference between $\frac{1}{2}E_{g0} + \frac{1}{2}kT$ and the lower temperature shoulder slope will indicate the temperature dependence of extrinsic lifetime.

§ 3. Experimental Details

A detailed description has been given elsewhere (Southgate 1959) of the apparatus, which employs electrostatic drive and frequency modulation detection of specimen oscillation. The specimen resonates longitudinally at 100 kc/s, and is suspended about its nodal plane by fine tungsten wires. It is held in a high vacuum during measurement, and is heated by a molybdenum tube furnace. After being set into oscillation, the drive is switched off and the decay curve recorded on a pen recorder.

The electrostatic drive method has the advantage that losses into the drive and measurement systems are very small. None of the curves presented has been corrected for this loss. Some of the decay curves observed were not true exponentials. This amplitude dependence is thought to be entirely due to loss at the support wires (Southgate 1959) and there is no indication that the true internal friction ever shows amplitude dependence over the range of vibration amplitude measured here, i.e. up to a strain amplitude of 10^{-5}. Experimental points exhibiting this mounting loss are characterized by their sporadic appearance in the temperature characteristic.

Specimens were cut approximately to shape by a diamond wheel, and the damaged surface layer removed by subsequent hand-grinding on a glass plate using BM302 and 303½ abrasive. It was found that a parallelism of the specimen sides to within 0·05 mm could be achieved in this way. Immediately before being mounted in the apparatus, the specimen was etched in a nitric–hydrochloric acid mixture, washed in de-ionized water, and dried on filter paper. Specimen cross sections vary from 4 to 6 mm square; the length depends on the axial orientation, being 42 mm for silicon and 25 mm for germanium in [111].

Unless otherwise stated, all specimens referred to in the remainder of the paper are single crystal, and were measured with their axes of vibration in [111]. All were grown in an argon atmosphere, the germanium by pulling from a graphite crucible and the silicon either by pulling from a silica crucible or by the floating-zone technique. Room temperature resistivities were in the range 10–50Ω cm for all specimens except two which were doped with aluminium to 2·7Ω cm.

† The term ' slope ' of an internal friction plot will be taken to mean the slope of a $(\ln \Delta, 1/kT)$ plot, i.e. the activation energy if Δ obeys a simple Arrhenius equation.

§ 4. Results

4.1. *Analysis of Silicon Results*

Nearly all silicon specimens measured showed a clearly defined electronic loss peak, although analysis of the peak shape is complicated by the fact that above the peak temperature there are usually comparable contributions to Δ from both electronic and oxygen relaxation mechanisms. Separation has been effected by assuming that the high temperature shoulder of the electronic peak and the low temperature shoulder of the oxygen peak, on a ($\ln \Delta$, $1/T$) plot, are both straight lines, and together form the total loss in this region. This method was found adequate to determine the lines uniquely in most cases.

All twelve specimens measured showed curves of a shape and location consistent in every way with the description of § 2, assuming various concentrations of recombination centres. The accuracy with which the experimental points may be fitted by theoretical curves can be judged from figure 2, which refers to a specimen having a room temperature lifetime of 30 μsec. The continuous curve is synthesized from three components: the electronic peak, the oxygen peak, and a constant mounting loss of 10^{-7}. The good fit between the experimental points and the theoretical electronic peak, indicates that extrinsic lifetime does not change much between room temperature and 600°c. The fitting of the oxygen peak at $1000/T = 0{\cdot}77$ will be discussed shortly.

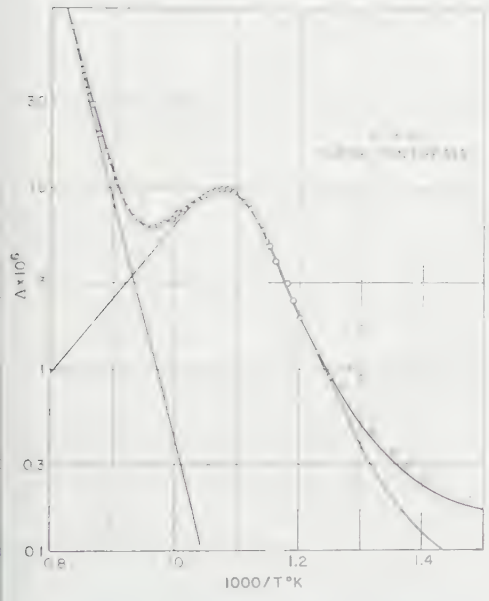

Figure 2. Fit of synthesized theoretical curve to measurements.

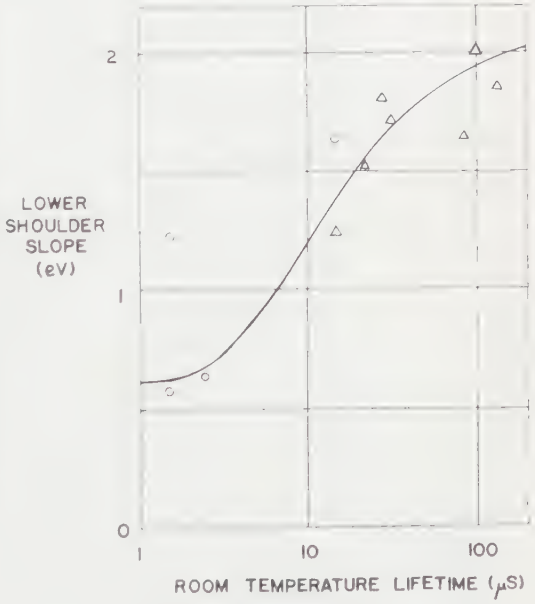

Figure 3. Silicon: Lower shoulder slope energy against room temperature lifetime.

As the specimens were taken through successive thermal cycles, the contamination increased, despite the cleaning precautions taken; and the lower temperature shoulder of the curve became less steeply sloped. Figure 3 shows the approximate slope of the measured low temperature shoulder plotted against the room

temperature lifetime.† A continuous curve derived from the theory of § 2, on the assumption of temperature independent extrinsic lifetime, is also shown. The lower end of the theoretical curve is fixed at an energy $\frac{1}{2}E_{g0}+\frac{1}{2}kT=0{\cdot}65$ ev, while the position of the upper end is determined by the type of detailed curve fitting shown in figure 2. In view of the experimental errors, and the possible changes of extrinsic lifetime between room temperature and the peak temperature, the approximate agreement between the scattered experimental points and the curve is regarded as reasonably good. As the contamination progresses the room temperature lifetime becomes too short for convenient measurement but in all specimens measured the slope of the shoulder approached approximately 0·65 ev when this occurred. As expected the peak magnitude decreased at this point.

The energy E_r associated with intrinsic recombination used in figures 2 and 3 is 1·45 ev. The spread of values of the upper temperature shoulder slope, which should remain unaffected by recombination centres, indicates an error in E_r of $\pm 0{\cdot}1$ ev. The slope of the higher temperature shoulder is best measured when the oxygen peak is small or absent; this occurred in the one specimen in [100], and two specimens grown by the floating-zone method, one in [111] and one 6° off [112].

Average values obtained for specimens in [111] exhibiting predominantly intrinsic recombination are $9{\cdot}8\times10^{-6}$ for the peak height and 655°c for the peak temperature. The shift of peak temperature with a 3:1 frequency change, measured on two specimens, was $1/T=6{\cdot}8\times10^{-5}$, yielding an energy E_r of 1·4 ev which compares well with the value derived from the peak shape. Measurements on a polycrystalline specimen of mean grain diameter 1 mm showed an electronic peak of similar height and location to those in single crystal specimens, the derived extrinsic lifetime being about 3 μsec.

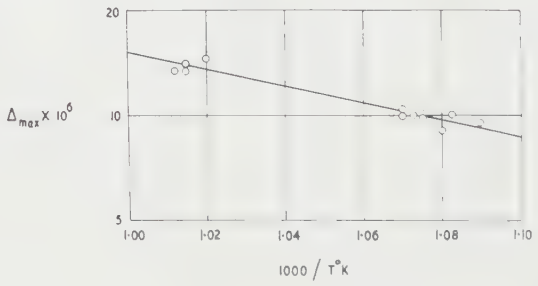

Figure 4. Silicon: (Δ_m,$1000/T_m$). At 100 kc/s, initial measurements only are plotted.

A change of peak temperature consequent on a change of measuring frequency will alter the peak height. Figure 4 shows a peak height against peak temperature plot; the straight line represents the change of carrier concentration as given by Morin and Maita (1954a), and, as expected, the experimental points lie scattered about this line. Points are only shown for which the intrinsic recombination is dominant at the peak temperature.

† The author is indebted to Dr. B. K. Ridley for making these measurements. The lifetime quoted is the 'short' lifetime, longer trapping times being ignored, although evidently present in many specimens.

The oxygen peak has been taken to obey the Snoek formula

$$\Delta = \Delta_0 \frac{\omega\tau}{1+\omega^2\tau^2} \qquad \ldots\ldots(5)$$

Δ_0 being approximately temperature independent and τ being the thermally activated atomic jump time. The shapes of the various peaks measured all follow this formula approximately, although the magnitudes of Δ_0 vary considerably. A single activation energy only is involved, and figure 5 shows the fit between the experimental points and a solid curve obeying equation (5). This curve has been taken to have an activation energy of 2·6 ev. The average, taken from the lower temperature shoulder slope for 16 curves, is 2·55 ev, although the higher temperature shoulder slope seems to be more variable and averages 2·95 ev. Equation (5) indicates that the slopes should be equal. It is suggested in Part II that precipitation of oxygen during measurement causes this inequality, and that the lower temperature shoulder slope should give the true activation energy. The average peak temperature is 1030°c.

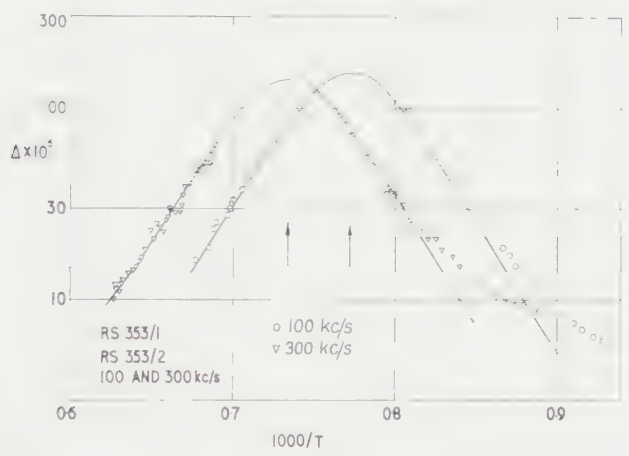

Figure 5. Oxygen peak in silicon.

Two specimens were grown under identical ambient conditions, one having an axis in [111], and the other in [100]. The oxygen peak appears in the first, but not the second, demonstrating that the sites between which oxygen can diffuse are identically located with respect to a [100] axis but not with respect to [111]. Of the floating-zone grown specimens measured, one has been previously floating-zone refined *in vacuo* and has a barely discernable oxygen peak, although its axis is [111]. The other had no previous vacuum refinement, and the peak height showed that the dissolved oxygen concentration was about 2% of that in crystals pulled from silica crucibles.

Confirmation of the activation energy value is obtained from the magnitude of the peak shift with frequency. Figure 5 shows experimental points at 100 kc/s and 300 kc s, the high temperature shoulder at 100 kc/s being taken from a parallel specimen which exhibits identical low temperature behaviour. The duplicate was used to avoid the possibility of anneal affecting the second set of values measured. The temperature shift between the two maxima is

$\delta(1/T) = 3{\cdot}8 \times 10^{-5}$, corresponding to an energy of 2·52 ev, which is in excellent agreement with that derived from the peak shape. Deviation between theoretical and experimental curves at low temperature end is due to electronic loss. At 300 kc/s, points having the highest Δ cannot be measured owing to insensitivity of the apparatus.

4.2. *Analysis of Germanium Results*

In germanium, the shape of the electronic peak is more variable than in silicon, since it appears that impurities which reduce the extrinsic lifetime are more readily introduced by heat treatment near the electronic peak temperature. Even those specimens having the greatest maximum Δ cannot be fitted by curves based on intrinsic recombination only, and it seems that extrinsic recombination has never been negligible below the peak temperature in any of the specimens measured. As a consequence, the results show that the lower temperature shoulder slope tends to be in the region of $\frac{1}{2}E_{g0} + \frac{1}{2}\boldsymbol{k}T = 0{\cdot}42$ ev, and for such specimens the peak value is frequently below the maximum observed, so that the curve looks like the $\omega\tau_e = 0{\cdot}2$ curve in figure 1. Several peaks have been measured, however, which do not fit the simple theoretical curve, since the higher temperature shoulder slope is too low. The reason for the misfit has not been determined, although it could be explained by a sufficiently erratic behaviour of extrinsic lifetime. On the basis of the larger values of higher temperature slope, which are usually more clearly defined, one can derive an activation energy E_r of approximately 1·15 ev for the intrinsic lifetime. Specimens have been measured in [111], [110] and [100]. Peak magnitudes range from 3×10^{-6} to 28×10^{-6}, and peak temperatures from 375°c to 460°c. The average of the eight peaks having the highest maxima gives a peak temperature of 395°c, with a relatively small scatter between the peaks.

Measurements of Electronic Peak at 100 kc/s: Germanium, Specimen T 675
Chronological order

Frequency (kc/s)	Shoulder Energies (ev) Higher temp.	Lower temp.	$\Delta_{max} \times 10^6$	$1000/T_{max}$
300	0·82	0·33	18	1·42
100	0·58	0·28	8·0	1·47
300	0·72	0·31	17	1·38
100	0·58	—	18	1·57
300	0·72	—	25	1·45

If the specimen is doped with a sufficient concentration of known impurity, the effect of the accidentally introduced impurities can be swamped. In a specimen containing about 5×10^{14} gold atoms per cm^3, thermal cycling produces relatively little change in the characteristic. The specimen has been compensated with antimony so that it is an intrinsic semiconductor at room temperature. The general shape of the curve is that to be expected from a specimen with a recombination level 0·1 ev from the centre of the band and a room temperature lifetime of about 0·8 μsec. Photoconductive measurements are in agreement with such a low value, giving a room temperature lifetime below 1 μsec.

Care must be taken in determining the shift of peak temperature with frequency, as significant recombination centre diffusion can take place between successive measurements of curves. Results are given in the table for T675† at 100 and 300 kc s, measurements of the last two pairs of peaks being taken alternately at either frequency. A significant change of maximum Δ has occurred between successive heatings, although the specimen was only taken to 700 c and cooled again over a period of about half-an-hour while measurements were taken. The extrinsic lifetime must have increased over this period, so that the last pair of peaks are more nearly true relaxation peaks than the previous pair. The larger temperature shift between the last pair agrees with this interpretation. An energy of about 0·8 ev may be derived from this shift, but there is not enough evidence to indicate whether this is near the true activation energy for recombination.

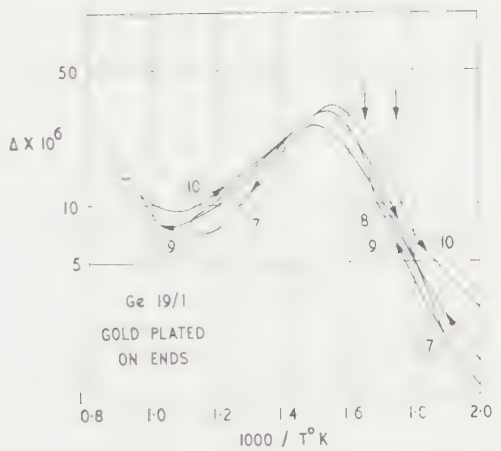

Figure 6 Germanium: Specimen 19/1 with a 0·1 μ gold film on the ends. Numbers indicate sequence of heating.

Attempts have been made to remove impurities from a specimen by using gold as a getter. A thin film of gold at the specimen surface should form a molten gold-germanium alloy at higher temperatures and act as a sink for the impurity, thus increasing extrinsic lifetime and reducing the variation of peak shape between specimens. An initial experiment showed that if a film 0·1 μ thick is evaporated along the specimen sides, Δ increases to 10^{-3} at higher temperatures. Subsequently, care was taken to evaporate the gold onto the specimen ends only, where it cannot affect Δ directly. Figure 6 shows the effect of thermal cycling on a specimen with a 0·1 μ gold film on the ends. This specimen had a history of several heats with etched surfaces and also one heat with a gold film on the sides, which may have effected a preliminary gettering. Reproducibility is much better than observed previously with the same specimen and the peak height exceeds that of any unplated specimens. The slope of the lower temperature shoulder is sufficiently different from $\frac{1}{2}E_{g0} + \frac{1}{2}kT$ to indicate that intrinsic recombination is dominant at the peak and hence that the peak height may be

† The author is grateful to Dr. J. O. Kessler of R.C.A. Laboratories, for supplying this crystal. Some measurements on it have already been described (Kessler 1957).

used to calculate the deformation potential. Small kinks in the curves, indicated by the arrows, occur near the gold-germanium eutectic, and it is reasonable to suppose that these are due to the melting of alloy which has diffused along the specimen sides. An estimate of kink amplitude indicates a contribution of 3×10^{-6} to Δ from the diffused layer, this accounting for the difference between the first heat (7) and the cooling (8).

In some specimens a small peak appears at 770°c, and this region is shown in figure 7 for three specimens. Annealing of 1/1 for 90 minutes at 890°c, and of T675 for 120 minutes at 780°c and 45 minutes at 890°c produces no change of peak height. Analysis of the peak shapes after subtraction of those components

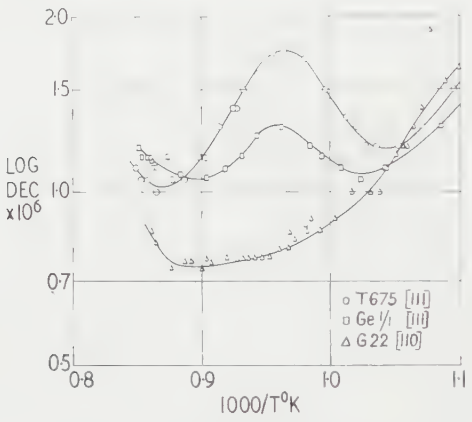

Figure 7. Peak at 770°c in germanium.

of the loss thought to be due to the high temperature rise mechanism (see Part II) and the electronic mechanism indicates an activation energy of about 1·8 ev. The 100–300 kc/s shift of the peak in T675 is $\delta(1/T) = 3 \times 10^{-5}$, corresponding to an energy of about 3 ev; the error in this measurement is, however, large, and the real value of the activation energy remains somewhat indeterminate.

§ 5. Discussion

5.1. *Electronic Relaxation*

It is as well first to summarize the reasons for believing the peak at 0·56 of the melting temperatures to be electronic in origin. They are more evident in silicon.

(i) The peak height is independent of dislocation density over a wide range and hence the peak is most unlikely to be due to dislocation relaxation (see Part II).

(ii) The peak height and location is independent of type and concentration of impurities, except in low-lifetime material. Furthermore, if attempts are made to fit a simple Snoek-type formula to the location and frequency-shift relationship, the pre-exponential factor associated with relaxation time differs from that usually found for point defect relaxation.

(iii) As the frequency is changed, the temperature dependence of peak height is approximately the same as that of charge carrier density.

From the analysis of the results in the previous section, it is evident that the theory of Weinreich can be given a complete account of the electronic losses.

The only uncertainty remaining is the exact form of the temperature dependence of the carrier lifetime. In silicon, the contributions from intrinsic and extrinsic recombination can be separated with a fair degree of certainty, yielding 1·45 ev for E_r. There are dangers, however, in associating this value with an activation energy, since it has been obtained by curve-fitting over a fairly small temperature range. Equally well, one could have chosen a temperature-dependent pre-exponential term. Thus, inserting a T^{-3} factor in equation (3) shows that the experimental curves for silicon can be fitted by an intrinsic lifetime which varies as the inverse square of the carrier concentration. In germanium the energy of 1·15 ev is too high to be broken down in this manner. However, it is quite possible that the curves having lower values of high temperature shoulder slope give the true indication of the intrinsic recombination. In this case E_r would be only of the order of 0·95 ev, corresponding to the temperature variation of the inverse square of the carrier concentration (Morin and Maita 1954a).

The carrier recombination theories of van Roosbroeck and Shockley (1954) and of Dumke (1957), which latter uses the more complex band model now known to apply to silicon, give an activation energy of intrinsic lifetime in intrinsic semiconductors of only about half the band gap. These theories evidently do not apply to silicon in the region of the relaxation peak since such a small energy could not be fitted to the curves. Beattie and Landsberg (1959) have more recently put forward a theory involving Auger effects, and show that the intrinsic lifetime governed by this mechanism has an activation energy of $(1+2\mu)E_g/(1+\mu)$ where μ is the ratio of hole to electron effective masses. In silicon, using the average effective masses quoted by Conwell (1958), an energy of 2 ev is predicted, which is significantly higher than the experimentally determined value. In germanium the theory predicts 1·25 ev, which is not too far from the larger of the experimentally suggested values, 1·15 ev. It is evident, however, that further measurements on specimens of carefully controlled purity will be needed to check this possible agreement. The general conclusion at present seems to be that no single theory explains the intrinsic lifetime behaviour of both germanium and silicon, and that there is no direct theoretical support for the suggestion that the lifetime varies essentially as the inverse square of the carrier density.

From the height of the electronic peak, the deformation potential may be estimated. A complicating factor arises from the many-valley structure of the silicon and germanium bands, since here the band gap will depend on both the dilatational strain and the shear strain, and in the Weinreich theory depends only on dilatation. In general, pure shear will raise some valleys and lower others (relative to the valence band). For small displacements, however, the population of any one valley is a linear function of the change in energy, and the total change of electron population is thus a function of the average displacement of the valleys relative to the valence band. No sudden change of slope of this average displacement can occur, and hence, by the symmetry argument of Shockley (1950) the electron population depends only on the dilatational strain. The formalism of §2 is therefore applicable.

Calculation of the deformation potential from equations (1) and (2), using the measured electronic peak height, involves a knowledge of Poisson's ratio ν and Young's modulus E, both of which are orientation dependent. Averaged values of elastic constants have been taken from the literature (McSkimin 1953, Bond

et al. 1950, Fine 1953) and ν values calculated using the relations of Voigt (1928). Values of carrier density obtained by Morin and Maita (1954a, b) are used. From these are derived deformation potentials, per unit dilatational strain, of magnitude 2·3 ev in silicon and 6·5 ev in germanium. These results are in fair agreement with those of Slykhouse and Drickamer (1958) who found values of 1·9 ev for silicon and 6·0 ev for germanium from absorption edge shift measurements, and with those of Paul and Brooks (1954) whose measurements of piezoresistance gave 2·0 ev in silicon and 4·2 ev in germanium. Differences in the values may well arise from the higher temperatures at which the acoustic measurements have been made.

The orientation dependence of peak heights is approximately as expected: the ratios of the heights in [111] and [100] in silicon should, according to equations (1) and (2), be 1·59 : 1 which compares with the measured values of 1·51 : 1. In germanium no check can be made as it is not clear whether peaks for specimens in directions differing from [111] are true relaxation peaks.

5.2. *Oxygen Relaxation*

The discussion in this section will be confined solely to oxygen in silicon, as there is insufficient evidence to confirm analogous behaviour in germanium.

Wert and Zener (1949) have shown that if the relaxation process consists of elementary diffusion steps, having an activation energy H, the relaxation time

$$\tau = (z\nu_0 e^{S/k})^{-1} e^{H/kT},$$

S being the entropy of diffusion, ν_0 the atomic mean vibration frequency and z the number of nearest neighbour positions. The driving force for diffusion is the Gibbs free energy $H - TS$. An approximate value of S is given by

$$\beta H \frac{d}{dt}(\ln G),$$

G being the mean elastic shear modulus and β a constant near unity. On the 'ideal gas' approximation ν_0 should be approximately kT/h. Inserting the value 2·55 ev for H gives $\nu_0 = 7 \times 10^{13}$, which is gratifyingly near $kT/h = 3 \times 10^{13}$. This activation energy value is also in agreement with the direct diffusion measurements of Logan and Peters (1957) from which may be derived an approximate value of 3·1 ev.

Infra-red studies indicate that oxygen is interstitially held in undistorted ('as-grown') silicon, the Si–O–Si bond angle being 100° as in quartz. Features of this oxygen location have been discussed by Kaiser, Keck and Lange (1956) and by Hrostowski and Kaiser (1957), and consideration of the simple geometry of the location shows that relaxation will give an internal friction peak in [111] but not in [100]. However, the strain field around the oxygen has not been sufficiently well mapped out to allow derivation of the oxygen concentration from the height of the internal friction peak. Heat treatment of the silicon will change the location of some of the oxygen, allowing it to diffuse to sites where it does not affect the internal friction, and the use of internal friction measurements to study this diffusion will be described in Part II.

Acknowledgments

Contributions to this work from many sources, in addition to those already indicated, are gratefully acknowledged. Specimens were supplied by the crystal

growing departments of the Mullard Laboratories and the Philips Laboratories, Eindhoven. The assistance of Mr. J. Cantrell in making many of the measurements has been particularly valuable, while useful discussions have been held with Dr. F. A. Kroger, Dr. B. K. Ridley, Mr. K. Tweedale and Dr. J. Wilks. Continuous progress of the investigation has been assured by the encouragement of Dr. K. Hoselitz and the support of the Mullard Research Laboratories.

References

Beattie, A. R., and Landsberg, P. T., 1959, *Proc. Roy. Soc.* A, **249,** 16.
Bond, W., Mason, W. P., McSkimin, H. J., Olsen, K. M., and Teal, G. K., 1950, *Phys. Rev.*, **78,** 176.
Conwell, E. M., 1958, *Proc. Inst. Radio Engrs, N.Y.*, **46,** 1282.
Dumke, W. P., 1957, *Phys. Rev.*, **105,** 139.
Fine, M. E., 1953, *J. Appl. Phys.*, **24,** 338.
Granato, A., and Truell, R., 1956, *J. Appl. Phys.*, **27,** 1219.
Hrostowski, H. J., and Kaiser, R. H., 1957, *Phys. Rev.*, **107,** 966.
Kaiser, W., Keck, P. H., and Lange, C. F., 1956, *Phys. Rev.*, **101,** 1264.
Kessler, J. O., 1957, *Phys. Rev.*, **106,** 646.
Lamb, J., Redwood, M., and Shteinshleifer, Z., 1959, *Phys. Rev. Letters*, **3,** 28.
Logan, E. A., and Peters, A. J., 1957, *J. Appl. Phys.*, **28,** 819.
McSkimin, H. J., 1953, *J. Appl. Phys.*, **24,** 988.
Morin, F. J., and Maita, J. P., 1954 a, *Phys. Rev.*, **94,** 28.
—— 1954 b, *Ibid.*, **96,** 1128.
Paul, W., and Brooks, H., 1954, *Phys. Rev.*, **94,** 1128.
van Roosbroeck, W., and Shockley, W., 1954, *Phys. Rev.*, **94,** 1558.
Shockley, W., 1950, *Electrons and Holes in Semiconductors* (New York: van Nostrand), p. 522.
Shockley, W., and Read, W. T., 1952, *Phys. Rev.*, **87,** 835.
Slykhouse, T. E., and Drickamer, H. G., 1958, *J. Phys. Chem. Solids*, **7,** 210.
Southgate, P. D., 1957, *Proc. Phys. Soc.* B, **70,** 804.
—— 1958, *Physics of Solid State: Proceedings of Brussels Conference* (New York: Academic Press), vol. **1**, p. 240 (1960).
—— 1959, *J. Sci. Instrum.*, **36,** 284.
—— 1960, *Proc. Phys. Soc.*, **76,** 398.
Teutonico, L. J., Granato, A., and Truell, R., 1956, *Phys. Rev.*, **103,** 832.
Truell, R., and Bronzo, J., 1953, *Phys. Rev.*, **90,** 152.
Voigt, W., 1928, *Lehrbuch der Kristallphysik* (Leipzig: Teubner), p. 589.
Weinreich, G., 1956, *Phys. Rev.*, **104,** 321.
Wert, C., and Zener, C., 1949, *Phys. Rev.*, **76,** 1169.

Internal Friction in Germanium and Silicon II: Oxygen Movement and Dislocation Damping

By P. D. SOUTHGATE†
Mullard Research Laboratories, Redhill, Surrey

MS. received 16*th July* 1959, *in revised form* 4*th March* 1960

Abstract. Measurements of the magnitude of electronic and oxygen impurity relaxation peaks in single crystal silicon yield values for the extrinsic carrier lifetime and the relative oxygen concentration, respectively. This method is used to study the production of recombination centres associated with oxygen impurity, and the internal precipitation of oxygen. Recombination centres are induced when oxygen-containing silicon is cooled rapidly from above 1000°c to 650°c, reducing the lifetime to less than 0·35 μsec, which then recovers at a rate which increases with successive heat treatments. Precipitation onto internal particles at 1025°c occurs in the order of 3 hours for 2·7 Ω cm aluminium-doped silicon, and considerably longer for a purer sample, indicating that aluminium acts as an efficient precipitation nucleus. A 2% plastic deformation of the aluminium-doped specimen does not greatly reduce the precipitation time. Analysis of the precipitation curve form indicates that stresses around the precipitate particles may be important in determining the precipitation rate.

Dislocation relaxation produces a rise in internal friction at elevated temperatures, an activation energy of 1·1 ev in germanium and 1·5 ev in silicon being associated with the rise. In silicon and germanium specimens which have been plastically deformed by about 2% the process becomes dominant above 0·6 of the melting temperature. Undistorted ('as-grown') specimens show a rise at higher temperatures, which varies in magnitude between specimens, and which could be due to the same process as that in deformed specimens. Oxygen in silicon appears to inhibit the loss process. Experimental results are discussed in the light of three possible theories, and it is concluded that there is insufficient evidence to indicate which one is applicable.

§ 1. Introduction

In a previous paper (Southgate 1960, to be referred to as Part I) the analysis of internal friction data obtained at 100 kc/s in germanium and silicon has been described. It was shown how the shape of a relaxation peak at 0·56 of the melting temperature was determined by the charge carrier recombination centre density, and how the magnitude of a peak in silicon at 1030°c depended on the density of interstitially dissolved oxygen. The present paper will describe the use of these relationships to study the production and annealing of recombination centres in silicon containing oxygen, and the internal precipitation of oxygen. The analysis of Part I will be assumed to be correct throughout this paper. If the height of the oxygen peak diminishes, it will be assumed that a proportionate amount of oxygen has been internally precipitated onto particles, although it is

† Now at Armour Research Foundation, Chicago, Illinois, U.S.A.

possible that it has moved to an alternative site which does not produce internal friction. If the height of the electronic peak diminishes, it will be assumed that recombination centres have been introduced, although again there may be another explanation.

At higher temperatures, in deformed material, a large rise of internal friction occurs. This effect was first observed by Kessler (1957 a), who interpreted it as dislocation damping. Further measurements in both silicon and germanium will be described here.

The magnitude of the internal friction will be denoted by the logarithmic decrement Δ.

§ 2. Experimental Details

Internal friction is measured by observing the decay of 100 kc/s longitudinal oscillations of a nodally supported half-wave bar. Details of measuring techniques and specimen preparation have been indicated in Part I and elsewhere (Southgate 1959) and will not be repeated here.

Plastically deformed specimens were produced by three methods: (i) the germanium specimen was extended in argon at about 500 °c, (ii) silicon specimens were twisted at about 1000 °c in a simple apparatus containing a nitrogen–hydrogen mixture and (iii) silicon specimens were twisted, under constant strain, after reduction to circular section, at about 1000 °c *in vacuo*. In case (iii) a strain–time record showed that the specimens entered the work-hardened region of slip at a surface shear strain of about 2%. In all cases, the strain appeared to be uniform along the sample axis and deformation occurred without any visible cracking. Before straining, the centre portion of each sample was reduced to a smaller circular cross section by grinding, and after straining, the remaining square-section end-pieces were cut off.

All specimens discussed are single crystal and most have an axis of vibration in [111]. They have been zone-refined and have resistivities of the order of 10 Ω cm, although all silicon specimens not grown by the floating-zone method contain oxygen in concentrations of the order of 1 in 10^5.

§ 3. Oxygen in Silicon

3.1. *Oxygen Precipitation*

The kinetics of oxygen precipitation were studied in a distorted specimen, and its 'as-grown' twin. Both these specimens were cut from aluminium-doped crystals of 2·7 Ω cm room-temperature resistivity. It is assumed that during precipitation, contributions to Δ other than that of dissolved oxygen remain constant. The fraction still to be precipitated is then

$$\beta = \frac{c - c_f}{c_0 - c_f} = \frac{\Delta_m - \Delta_{mf}}{\Delta_{m0} - \Delta_{mf}}$$

where c and Δ_m are the concentration and maximum Δ, and subscripts 0 and f denote initial and final stages. Annealing near the peak temperature of 1030 °c was carried out while the specimen was mounted in the apparatus, peak height measurements being made at intervals, and the results are shown in figure 1. Precipitation can be seen to take a period of some hours at 1030 °c. Restoration of the original peak occurs after 10 minutes' anneal at 1280 °c. Precipitation

is about three times as fast after this re-solution treatment, and is slower at lower temperatures, but the introduction of dislocations by plastic deformation affects the precipitation rate to only a small extent. If one shifts the time axis

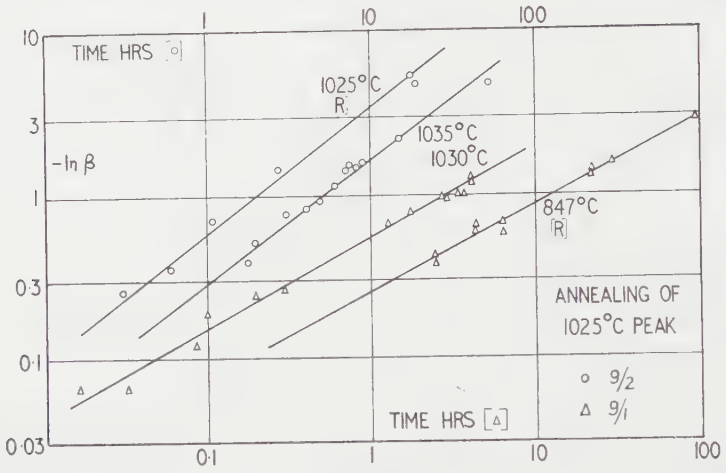

Figure 1. Precipitation of oxygen in ' as-grown ' 9/2 and twisted 9/1. Precipitation temperatures on curves. R: after re-solution at 1280°C. β is the fraction still to be precipitated.

of the 1030°C precipitation of the deformed specimen by a factor 3 to account for an imaginary reprecipitation, and compares this line with the 847°C reprecipitation, an activation energy of 1·7 ev is obtained. The accuracy and significance of this value are, however, not very well defined.

Further measurements of oxygen precipitation have been made on a specimen with a room-temperature resistivity of 27 Ω cm. From the few accurate points available, it is evident that the precipitation rate is considerably lower than for the aluminium-doped specimens, Δ_m only falling from 3×10^{-5} to $2{\cdot}2 \times 10^{-5}$ in 20 hours. It seems likely that the difference is due to the presence of aluminium in the more rapidly precipitating specimens.

3.2. *Oxygen Recombination Centres*

In oxygen-containing silicon, heating above 1000°C for about 10 minutes, followed by a radiation cooling (quenching) to 650°C, causes a considerable reduction of electronic peak height. Brief reports of the effect have already been published (Southgate 1957). It can be associated with oxygen, since it does not occur in the most oxygen-free floating-zone-grown specimen (or in germanium, which contains very little oxygen). The effect is due to the introduction of recombination centres which produce an extrinsic recombination time of less than $1/\omega$ at the peak, although a detailed demonstration of this introduction by checking the $(\Delta, 1/T)$ curve is difficult since annealing occurs during measurement. Such recombination centres will be referred to as thermal traps.

Table 1. Reduction of Electronic Peak Height after Radiation Cool to 650°C

Anneal temperature (°C)	800	1050	1060	1060
Duration (min)	3	5	12	18
$\Delta \times 10^6$	9	6·5	3·2	2·2
τ_e (μsec)	5	1	0·3	0·2

The extent of the reduction following quenching is a function of the time and temperature of the pre-quench heat treatment, and table 1 shows the variation for specimen 15 1. It can be seen that over the range covered, a greater Δ reduction occurs for an increase in either time or temperature of the heat treatment. If Δ at the intrinsic peak temperature is reduced to a fraction r of its intrinsic value, it is easily shown from the theory of Part I that

$$\tau_e^{-1} = [\sqrt{(1-r^2)} + 1 - r]r^{-1}, \qquad \ldots\ldots (1)$$

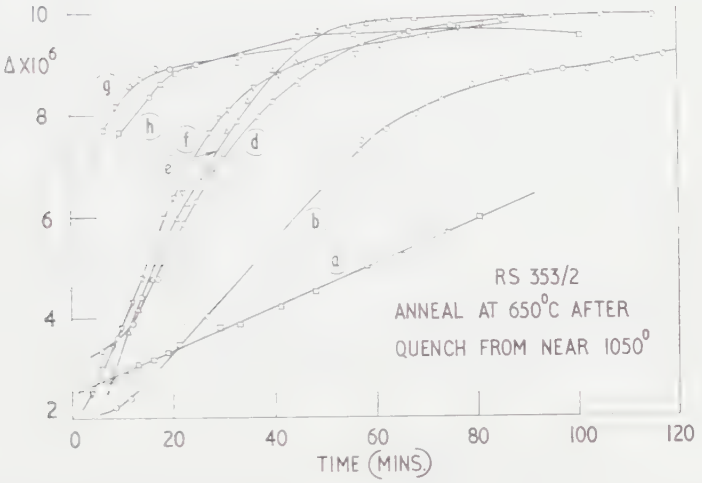

Figure 2. Annealing of Si 353/2 near 650°c following successive quenches from near 1050°c.

Figure 3. Decay of thermal traps: τ_e values derived from height of electronic peak.

where τ_e is the extrinsic lifetime and ω is the circular frequency of oscillation. The last column in table 1 shows the calculated extrinsic lifetime immediately after quenching.

The peak height reduction is only temporary, and recovery takes place in the order of one hour at 650°c. After a further heating to above 1000°c and anneal at 650°c, a more rapid recovery occurs. Figure 2 shows a sequence of anneals on a specimen grown from a silica crucible, the intermediate heatings being from 5 to 25 minutes at about 1050°c. The rate of recovery does not appear to depend primarily on the duration of the preceding intermediate heat, but rather on the total history of the specimen. Curves g and h of figure 2 were taken after a ten-minute treatment at 1250°c in order to see the effect of a re-solution of oxygen which may have been precipitated. No return to the original curve form is seen. After heating at 1000°c for more than 100 hours a permanent reduction of electronic height occurs, even if the oxygen is redissolved. It is probable that the permanent reduction is due to fast diffusers entering the specimen.

The number of recombination centres is proportional to $1/\tau_e$, which can be obtained from equation (1). Figure 3 shows a plot of $1/\tau_e$ against time, thus giving a direct indication of the decay of thermal traps. The specimen of figure 2 is shown together with 15/1, of similar origin, and KC 1/2, which contains about 50 times less oxygen. Rather surprisingly, the last specimen gives a similar curve to the other two.

§ 4. High Temperature Rise

In silicon having no oxygen peak, and in germanium, for which no large oxygen peak has been observed, a further rise of Δ takes place towards the melting temperature. This high-temperature rise is greatly enhanced by plastic deformation, and appears to be due to a dislocation mechanism.

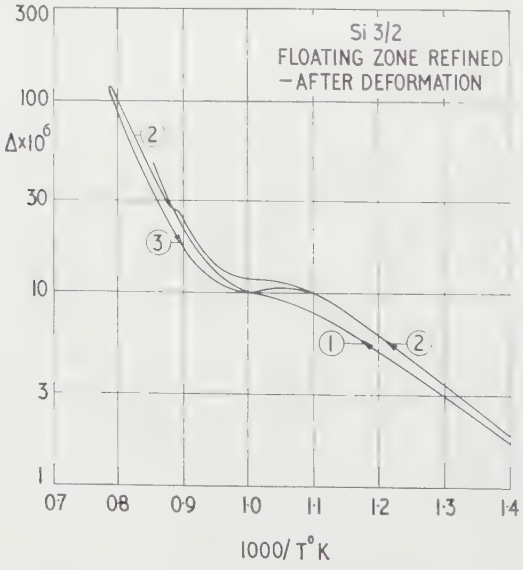

Figure 4. Oxygen-free deformed silicon crystal.

In 'as-grown' crystals of germanium, the rise is only small, and is often only discernable close to the melting temperature. However, in a specimen having a [110] axis, which was extended† by 1·6% at 500°c, the magnitude of the high temperature rise was a factor of 3000 greater than that of a similar 'as-grown' specimen. Curves for these specimens have been given in a previous paper (Southgate 1958). The activation energy of the rise is 1·1 ev. In silicon, the energy is higher, and figure 4 shows the magnitude of the rise in an oxygen-free silicon specimen which has been twisted *in vacuo*, the surface shear strain being about 2%. Some annealing occurs during measurements. In a similarly twisted specimen containing oxygen in concentrations of the order 10^{-5}, however, no rise is seen. It therefore appears that oxygen can inhibit the loss mechanism, since simple masking of the rise by the oxygen peak would not be sufficient to completely conceal it. Silicon specimens deformed in a nitrogen–hydrogen atmosphere show a rather large loss in the 700°–900°c region, which reduces on anneal. Introduction of hydrogen from the atmosphere in which deformation took place, and its subsequent evaporation, may be the cause of these changes; the effect is complicated by the partial precipitation of oxygen during the high temperature anneal.

Table 2. High Temperature Rise in Silicon
Successive measurements on the same specimens indicate that annealing is occurring

Specimen	359/1	3/1		3/2		KC 1/2
Activation energy (ev)	1·4	— 1·48		— 1·58		2·0
$\Delta(1000/T=0{\cdot}7)\times 10^6$	9	5	2	650	520	8·5

The magnitudes and activation energies of the high temperature rise in some silicon specimens are given in table 2. The energy of the rise in 'as-grown' oxygen-free 3/1 is close to that in its deformed twin 3/2, although the magnitudes are very different. Specimen 359/1 contains about 1 in 10^5 of oxygen, but in this case the rise is not masked by an oxygen peak since no peak appears for this specimen orientation, [100]. The magnitude of the rise in 'as-grown' crystals is of the same order in oxygen-containing and oxygen-free specimens, indicating that oxygen does not inhibit the rise occurring in 'as-grown' specimens, in contrast to deformed specimens. A higher activation energy is seen in KC 1/2, which contains an oxygen concentration only 2% of that in 359/1, but the origin of the difference of energy is not clear. There were indications of a higher activation energy in an earlier measurement of 3/1, but since annealing was occurring during measurement, no definite value could be assigned. Figure 5 shows the experimental curve for KC 1/2 divided into its components, electronic peak, oxygen peak, and high temperature rise.

It seems clear that the high-temperature rise behaviour of silicon and germanium is essentially the same in deformed specimens. However, in 'as-grown' specimens, the variability is rather too great to feel confident of the similarity of behaviour. In particular, the annealing behaviour varies, and both increases and decreases of high-temperature rise with time can be seen in silicon and germanium specimens.

† This extended specimen was kindly supplied by Dr. H. G. van Bueren.

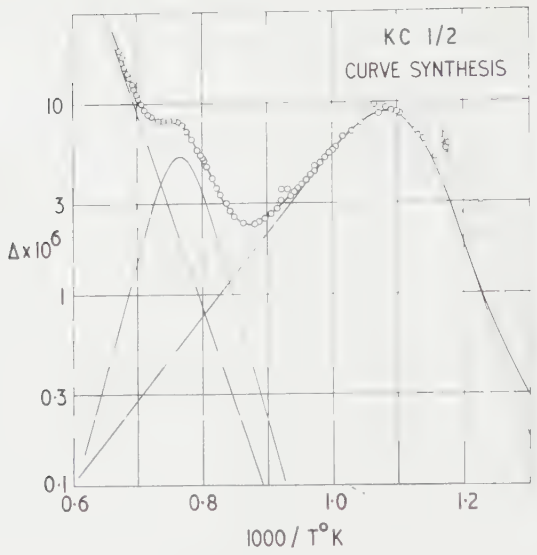

Figure 5. Floating-zone-grown KC 1/2, showing high-temperature rise in 'as-grown' specimen.

§ 5. Discussion

5.1. *Oxygen Precipitation and Recombination Centres*

Diffusion-limited precipitation processes can usually be fitted by the formula

$$\beta = \exp(-t/t_0)^m,$$

β being the fraction of solute still to be precipitated and t_0 a characteristic time of precipitation. It has frequently been supposed that the index m indicates the shape of the precipitation particles. Subsequent calculations by Ham (1958) have, however, shown that in strictly diffusion-limited precipitation this is not the case; and that m should in general be near unity, except in the early stages of precipitation. The data for precipitation in specimens 9/1 and 9/2 given in figure 1 show that here the index m is 0·54 and 0·69, respectively. Thus, there is some additional limitation on precipitation rate. It seems likely that this is due to a modification of diffusion rate by stresses built up around the growing particles, which according to the Rayleigh scattering observations of Kaiser (1957) are spheres of silica. If it is supposed that oxygen diffuses interstitially through the bulk, then growth of the spheres would entail a build-up of material in the region and a consequent reduction of precipitation rate. Conversely, substitutional diffusion would produce a tension in the medium immediately surrounding the precipitate particles and hence increase the diffusion rate in this region, since formation of silica from a substitutionally held oxygen atom releases a vacancy. The postulated decrease of diffusion rate thus indicates that oxygen diffuses interstitially.

Lederhandler and Patel (1957) have measured the rate of oxygen precipitation near 1050°c using infra-red absorption as an index of oxygen content, and

obtained precipitation times in undeformed specimens significantly longer than those of 9/2, although deformed specimens showed precipitation times of the same order as those in the twisted 9/1. It seems most probable that the aluminium in 9/1 and 9/2 is forming the predominant nucleation centres; there are 5×10^{15} atoms per cm^3 as compared with about 10^{11} atom sites per cm^3 along the dislocations in the deformed material.

The introduction of thermal traps and their annealing is evidently a complex phenomenon. In discussing the effect three forms of oxygen will be considered: Form I, present in a majority over the temperature range 700°–1300°c, which produces a mechanical relaxation but does not act as a recombination centre; Form II, representing a small fraction of the total above 1000°c (in quasi-equilibrium) which is the thermal trap; and Form III, forming an increasingly large percentage of the total above 1100°c, which does not produce a mechanical relaxation. The existence of the last form is not certain, and it has been suggested merely to explain the fact that Δ on the high temperature side of the oxygen peak often drops more rapidly than expected from the activation energy of the peak (see Part I). Forms II and III could possibly be the same. It should be pointed out that none of these necessarily involves the SiO_4 group discussed by Fuller and Logan (1957) which is concerned in effects occurring below 500°c.

The transition II I takes place more rapidly with successive anneals at 650 c. It seems reasonable to suppose on this evidence that further defects, such as impurities or vacancies, which can change the rate of transition, are present in variable quantities. Proximity and oxygen aggregation effects are unlikely since the introduction of thermal traps is studied here in crystals which have suffered only short-period high-temperature anneal and in which the general precipitation evidence indicates that very few of the oxygen atoms have had time to aggregate. In Part I the location of Form I is discussed. It is probably interstitial so that 2·55 ev, the relaxation activation energy, is the energy of bulk diffusion. Thermal traps could then be formed if II were substitutional, and possibly the varying decay time reflects the varying anneal rates of excess vacancies frozen in by the quench from 1050 c to 650 c. Excess vacancies would tend to maintain a higher concentration of II, although there is no obvious reason for a variation of a vacancy anneal rate. An alternative explanation for the curves of figure 3 could be that the heating introduces three kinds of traps, one decaying at the rate given by a, a second decaying at approximately the rate given by c, and a third kind which does not anneal rapidly. The variation of total rate could then be due to the initial introduction of different ratios of the three kinds of traps, curve b for instance being due to a 10 : 1 ratio of the second kind to the first kind. However, it is felt that at present there is insufficient evidence from this study to permit more positive identification of the processes or forms of oxygen involved.

It is notable that the electronic peak height is affected to only a small extent by deformation in all cases for both silicon and germanium, indicating that the component of extrinsic lifetime due to dislocations is greater than 1·5 μsec. The density of dislocations is probably in the range 10^8 to 10^9 cm^{-2}, at least this is the observed etch-pit density, and at room temperature the results of Wertheim and Pearson (1957) indicate that the lifetime due to this density would be about an order of magnitude less than 1·5 μsec. Hence it seems likely that the capture cross section of the dislocations must reduce markedly with temperature increase.

5.2. *Dislocation Motion*

The association of plastic deformation with the high-temperature rise suggests that dislocation motion may be responsible for the loss. As mentioned previously, it has not been established that the rises in 'as-grown' and deformed specimens are of the same nature; however, in this section dislocation loss mechanisms which could apply to either feature will be discussed. It is also possible that the loss may be due to vacancy pair relaxation, since large numbers of vacancy pairs are generated during plastic deformation. In germanium, the activation energy for divacancy diffusion is suggested by Seeger (1958) to be 1·6 ev, and very tentatively by Letaw (1956) to be 2·2 ev. These energies are considerably higher than the observed 1·1 ev, and consideration of the annealing behaviour of the high-temperature rise does not support the possibility that a variation of divacancy concentration with temperature adds to the energy. Similarly, in silicon one would anticipate energies of divacancy diffusion higher than the 1·5 ev observed for the high-temperature rise in deformed material. Hence divacancy motion is not thought to be responsible.

Existing theories which could be applied to the high temperature rise are: (i) the Bordoni peak theory of Seeger, Donth and Pfaff (1957) referred to here as the SDP theory, (ii) the impurity field damping theory of Weertman (1955, 1957), (iii) the vacancy drag theory of Kessler (1957 b). Theories of hysteretic loss due to dislocation break-away will not be considered as they lead to a larger amplitude variation of Δ than actually observed.

Theories (i), (ii) and (iii) will all give a loss which depends on the distribution of the dislocation pinning points. This dependence is covered by the general theory of Granato and Lucke (1956). If the pinning is mainly by point defects whose distribution along the dislocation lines remains constant as the dislocation density is increased, say by plastic deformation, then Δ will be proportional to the dislocation density. If, on the other hand, pinning is predominantly at dislocation intersections, then Δ will be approximately independent of dislocation density. In general, both types of pinning are probably significant, and thus, as has been observed, the loss does not increase with plastic deformation as much as does the dislocation density. The observed decrease of Δ with annealing does not help to distinguish which mechanism fits best, as in each case a condensation of a greater number of pinning points during annealing would have the same effect. The lack of any large effect of deformation on the rise in oxygen-containing samples can be adequately explained in each case by assuming that oxygen can pin the dislocations. Each mechanism will now be considered in turn.

(i) In many metals the Bordoni peak occurs in the kilocycle region, at temperatures between 10°K and 100°K. The SDP theory, which assumes the peak is due to a thermally activated motion of dislocations from one potential well to the next by the lateral motion of kinks in the dislocations, shows that the peak temperature increases with increasing Peierls force of the dislocation. Hence in germanium and silicon, where the Peierls force is anticipated to be larger than in metals due to greater bond strength, and to greater localization of the dislocation, a considerably higher Bordoni peak temperature may be expected. The high-temperature rise could thus be part of a Bordoni peak which appears near or above the melting point. If this is so, an estimate of the expected

activation energy can be obtained from the SDP theory. The value of the pre-exponential frequency factor is found (SDP equations (4.5) and (4.5 *a*)), assuming the formulae for the mass and energy per unit length of the dislocation given in the paper to apply. It then appears that, for a peak in silicon near 1400°c at 100 kc/s, the 'activation energy' of the process which would be derived on the simple formula (SDP equation (2.1)) is about 2·6 ev. Stress amplitudes of vibration are assumed low compared with the Peierls stress. It thus seems unlikely that this dislocation mechanism is responsible for the high-temperature rise in 'as-grown' crystals, either in silicon or, by a similar argument, in germanium. In deformed crystals, it is possible there is a peak just above the maximum temperature of measurement, and in this case an energy of about 1·9 ev would be expected in silicon. Such a value is, however, still significantly larger than that measured.

(ii) According to the solution hardening theory of Mott and Nabarro, a certain length of dislocation is taken to move coherently through the crystal when stress is applied, the stress field of impurities producing resistance to dislocation motion without actually pinning it. Weertman (1955, 1957) uses this concept to calculate internal friction, assuming that the potential wells are regularly spaced rather than random, and applying standard rate theory to determine their velocity. It should be noted that the temperature is assumed here to be sufficiently high for rapid interchange between the potential wells formed by the lattice planes which are used in the SDP theory, so that these wells do not resist dislocation motion.

If the atomic fraction of impurity is between 10^{-2} and 10^{-7}, approximations can be made to Weertman's formula, from which it seems that the activation energy H derived from the temperature increase of Δ is almost independent of impurity concentration. The formula is then

$$H = A\epsilon^{2/3}\tfrac{1}{2}Gb^3$$

where A is close to unity, ϵ is the impurity misfit factor (fractional difference in atomic size), and the remaining factor is equal to the stress energy of the dislocation per unit atom length. Substitution of misfit factors of the order 0·05 will give activation energies equal to those observed. Since the nature of the impurities is not known—they need not be electrically active little further correlation can be made between theory and experiment.

(iii) Vacancies are more mobile than impurity atoms and will move in the stress field of dislocations at higher temperatures. The phase lag between the dislocation movement and the vacancy movement produces a loss. Kessler (1957 b) has made detailed calculations of this loss, assuming that the dislocation is surrounded by a vacancy atmosphere. If the atmosphere and the general vacancy concentration are in thermal equilibrium, then as the temperature increases (*a*) the Cottrell atmosphere of vacancies disperses, (*b*) the vacancy jumps become quicker and (*c*) the equilibrium concentration of vacancies increases. Associating energies Q, H and K with these processes leads to an effective energy of the rise equal to $Q+H-K$. Again, an assessment of this value is difficult to make since none of the component values is known accurately, but in germanium, the values of H and K estimated by Letaw (1956) require a value of Q equal to 2·1 ev. This should be the binding energy of a vacancy at

its distance of closest approach, and the value derived is higher than that given by the Cottrell (1953) formula, at least on the basis of the values assumed by Kessler for closest approach distance. The discrepancy is not sufficiently large to discount the theory, which in other respects agrees as well with experiment as does the Weertman theory.

It can thus be seen that the number of undetermined parameters involved in these three theories is large, and until further experimental studies have been carried out on annealing of the high-temperature rise and the effect of varying impurity content, it will not be possible to determine whether the Kessler or the Weertman mechanism, or any other, is dominant in the high-temperature rise region.

Acknowledgments

Many vital contributions to the investigation in the form of provision of materials and of helpful discussions by members of Mullard Research Laboratories and of Philips Laboratories, Eindhoven, are gratefully acknowledged. A large proportion of the measurements reported were carried out by Mr. J. Cantrell, while progress of the work has been assured by the encouragement of Dr. K. Hoselitz and the support of the Mullard Research Laboratories.

References

Cottrell, A. H., 1953, *Dislocations and Plastic Flow in Crystals* (Oxford: University Press), p. 57.

Fuller, C. S., and Logan, R. A., 1957, *J. Appl. Phys.*, **28,** 1427.

Granato, A., and Lucke, K., 1956, *J. Appl. Phys.*, **27,** 583.

Ham, F. S., 1958, *J. Phys. Chem. Solids*, **6,** 335.

Kaiser, W., 1957, *Phys. Rev.*, **105,** 1751.

Kessler, J. O., 1957 a, *Phys. Rev.*, **106,** 646.

—— 1957 b, *Ibid.*, **106,** 654.

Lederhandler, S., and Patel, J. R., 1957, *Phys. Rev.*, **108,** 239.

Letaw, H., 1956, *J. Phys. Chem. Solids*, **1,** 100.

Seeger, A., 1958, *Solid State Physics: Proceedings of Brussels Conference* (New York: Academic Press), vol. **1**, p. 61 (1960).

Seeger, A., Donth, H., and Pfaff, F., 1957, *Disc. Farad. Soc.*, No. 23, p. 16.

Southgate, P. D., 1957, *Proc. Phys. Soc.* B, **70,** 804.

—— 1958, *Solid State Physics: Proceedings of the Brussels Conference* (New York: Academic Press), vol. **1,** p. 240 (1960).

—— 1959, *J. Sci. Instrum.*, **36,** 284.

—— 1960, *Proc. Phys. Soc.*, **76,** 385.

Weertman, J., 1955, *J. Appl. Phys.*, **26,** 202.

—— 1957, *J. Appl. Phys.*, **28,** 193.

Wertheim, G. K., and Pearson, G. L., 1957, *Phys. Rev.*, **107,** 694.

RESEARCH NOTES

Note on a Pinch Effect in a Low-pressure Arc

By A. R. JOHNSTON† and K. G. EMELEUS
Physics Department, Queen's University, Belfast

MS. received 19*th April* 1960

The constriction of a discharge under the action of its own magnetic field is well known to be of importance in some of the heavy current devices which have been used in attempts to bring about thermonuclear reactions in hot plasmas. Similar effects, controlled magnetic constriction of an ordinary low-pressure arc column, and the converse effect, magnetic expansion, have been studied experimentally by one of us (Johnston 1955) with Langmuir probe techniques. The constriction of the column was produced by a magnetic field with lines in the same direction as those of the field of the arc, and the expansion by having the fields in opposite directions. The controlling field was produced by a current in a water-cooled cylindrical copper tube situated along the axis of the arc.

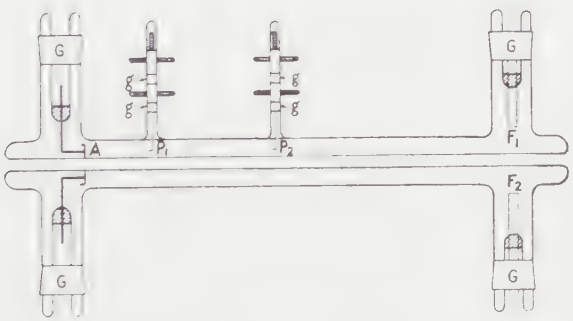

Mercury arc tube for demonstrating positive and negative pinch effects: A, anode; F_1 and F_2, cathodes; P_1 and P_2, Langmuir probes (cylindrical forms shown); G and g, ground joints. Details of the electrode leads and probe movements are not shown, and the pumping tube, at the anode end, is omitted.

The discharge tube, shown in the figure, was 60 cm long and 5·0 cm in outside diameter, the centre was occupied by an inner glass tube 8 mm in outer diameter, the whole being much like a Liebig condenser. The copper tube, which is not shown in the figure, fitted loosely in the inner tube and projected at both ends. The main electrodes were an annular nichrome anode A, and two straight wire hot cathodes F_1 and F_2 made of 200 μ thoriated tungsten. This arrangement of electrodes was chosen so as to help maintain the discharge uniform over the annular cross section of the tube. The positive column was investigated with

† Now at Queen's University, Kingston, Ontario, Canada.

two probes P_1 and P_2, each of which could be moved radially by a screw system—not shown in detail—mounted in a side tube and operated through ground joints. The tube contained mercury vapour at a pressure of 1 to 2 μ, and was used on the pumps. The discharge currents ranged from 40 to 160 mA, most measurements being carried out at 100 mA. The current through the copper tube was supplied by batteries and could be varied from 0 to 150 A. When the current through the copper was in the same direction as the arc current, the arc could be seen to contract around the inner glass tube. When the currents were in opposite directions the arc was pressed against the outer wall. The strongest magnetic field had only a slight effect otherwise on the macroscopic discharge parameters, reducing the anode current and increasing the potential difference across the tube each by about 6 to 10%. Within the range of magnetic fields used the arc did not exhibit any tendency to break up into striations or to assume a spiral form, except for the strongest field under expansion conditions, when there was a slight tendency to spiral. Noise increased from the zero additional magnetic field condition by only a factor of two for the strongest field.

A number of Langmuir probe measurements were made using a logarithmic oscillograph circuit (Johnston 1956). Although some doubt arises about the interpretation of the probe characteristics, because of the magnetic field (Spiwak and Reichrudel 1936, Bickerton and von Engel 1956), they indicated that the visible changes in the plasma were accompanied by changes in electron temperature, in addition to the expected changes in electron density. The electron temperature was apparently not constant across the positive column, in presence of the extra magnetic field. A negative radial temperature gradient was found in the contracted discharge, and a positive gradient in the expanded discharge. These gradients were found both with cylindrical probes placed parallel and normal to the field lines, and with plane probes normal to the field lines. The results for the various probes, although not agreeing in detail, showed similar radial variations of the electron temperature. The gradient increased with the current through the copper; typically, a change in temperature from 6×10^4 to 3×10^4 °K was found in a radial distance of 0·5 cm for a current of 150 A.

It is difficult to judge how reliable the electron temperature measurements are, but the temperature gradient recorded did reverse when the direction of the current through the copper was reversed, which would leave the magnitude of the radial gradient of the magnetic field due to the current through the copper unchanged. The temperature gradients are in the opposite directions to those predicted by transport theory for an infinite plasma (Ware 1954), and their existence and magnitude, if real, are probably considerably dependent on boundary conditions.

References

Bickerton, R. J., and von Engel, A., 1956, *Proc. Phys. Soc.* B, **69**, 46.
Johnston, A. R., 1955, *Thesis*, University of Belfast.
— 1956, *Brit. J. Appl. Phys.*, **7**, 266.
Spiwak, G., and Reichrudel, E., 1936, *Phys. Z. Sowet.*, **9**, 655.
Ware, A. A., 1954, *Proc. Phys. Soc.* A, **67**, 869.

The Magnetostriction of Lithium–Chromium Ferrite in the Neighbourhood of its Compensation Point

By E. W. LEE† and R. R. BIRSS‡

† Department of Physics, The University, Sheffield
‡ Imperial College, London

MS. received 12*th April* 1960

Certain antiferromagnetic substances exhibit rapid changes in Young's modulus as their temperature is varied just below their Néel temperatures (Street and Lewis 1951, Fine 1952). It has been suggested that this may be due to movement of antiferromagnetic domain walls brought about by the interaction between the applied stress and magnetostriction. This is the same explanation as that given to a similar occurrence in ferromagnetics and also accounts for the ΔE effect. With antiferromagnetics a difficulty arises because it is impossible to move the walls by the application of a magnetic field since the intra-domain magnetization is zero, so that even if single crystals are available it is not possible to measure the magnetostriction by normal means. At this stage it is perhaps worth while mentioning that the magnetostrictive strain which can be detected in very strong fields (Belov and Kevitin 1959) does not give the desired information. If a field is applied parallel to the antiferromagnetic axis it decreases the number of 'wrong' spins. If it is applied perpendicular to this axis it merely tilts the spin moments through a small angle towards the field direction. Both processes may give rise to a measurable magnetostriction but they are not necessarily related to the magnetostriction required to explain the Young's modulus anomaly which is an anisotropic strain depending on the direction of antiferromagnetic ordering with respect to the crystal axes.

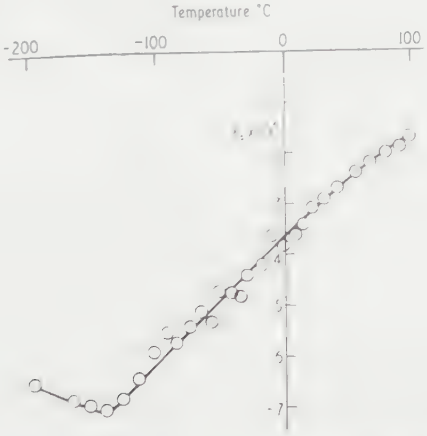

Polycrystalline magnetostriction constant λ_s of $Li_{0\cdot5}Fe_{0\cdot5}Cr_{1\cdot7}O_4$. The compensation point is at 20°C.

A ferrite at its compensation point has zero magnetic moment and hence behaves like an antiferromagnetic. Thus one can investigate the properties of a ferrite with a compensation point in its antiferromagnetic form by observation

of its behaviour on either side of the compensation point. In view of the apparent impossibility of measuring antiferromagnetic magnetostriction directly we have measured the magnetostriction of lithium–chromium ferrite of composition $Li_{0.5}Fe_{0.8}Cr_{1.7}O_4$ as a function of temperature. According to Gorter (1954) the compensation point is 20° c. The measurements were made by observing the strain in a polycrystalline disc as it was rotated in a saturating field of 5000 oersteds thereby eliminating any volume magnetostriction. The results are shown in the figure. It is evident that there is no anomalous behaviour at the compensation point and that the magnetostriction in the antiferromagnetic form is essentially the same as in the ferrimagnetic state. Thus we conclude that the magnetostriction is determined by the magnetic moment of the individual sub-lattices and not by the net moment.

This result suggests that the order of magnitude of the magnetostriction of ferromagnetics and antiferromagnetics may be very similar and that the explanation of the Young's modulus anomaly in terms of stress-induced domain wall movement is in order. In this connection it may be remarked that CoO exhibits a large change in Young's modulus and that cobalt ferrite has the largest magnetostriction yet observed.

Acknowledgments

This work was carried out whilst both authors were members of the Physics Department at Nottingham University and we should like to record our thanks to Professor L. F. Bates for allowing us the facilities of his laboratories and for his continual interest in this work.

We are indebted to Dr. E. W. Gorter for kindly supplying us with the sample of lithium–chromium ferrite.

References

Belov, K. P., and Kevitin, R. Z., 1959, *J. Exp. Theor. Phys.* (*U.S.S.R.*), **37,** 565, English Translation, 1960, *Soviet Physics, J.E.T.P.*, **10,** 400.
Fine, M. E., 1952, *Phys. Rev.*, **87,** 1143.
Gorter, E. W., 1954, *Philips Res. Reports*, **9,** 403.
Street, R., and Lewis, B., 1951, *Nature, Lond.*, **168,** 1036.

Second Dislocation Relaxation Peak in Aluminium at Low Temperatures

By G. S. VERMA
Department of Physics, University of Allahabad, Allahabad

MS. received 22nd April 1960

In aluminium Lax and Filson (1959) have observed a second low temperature dislocation relaxation peak which is considerably narrower than Bordoni (1954) peaks occurring at higher temperatures. The interesting thing to be observed is that the second dislocation relaxation peak is broader than the single relaxation spectrum at lower frequencies (figure 1 at 51 kc/s), but becomes narrower than the single relaxation spectrum at higher frequencies (figure 2 at 414 kc/s). According

to Zener's (1948) theory for a single relaxation time, the ratio of the damping Q^{-1} to its maximum value Q_m^{-1} is given by $Q^{-1}/Q_m^{-1} = \text{sech}\,(\ln \omega/\omega_m)$ where ω_m is the characteristic relaxation frequency for maximum damping. Using $\omega = \omega_A \exp[-W/\boldsymbol{k}T]$, where ω_A is the limiting frequency associated with the attenuation peak due to dislocations and W is the activation energy, and $\omega_m = \omega_A \exp[-W/\boldsymbol{k}T_m]$ where T_m is the temperature corresponding to maximum damping, we obtain the relation

$$\frac{Q^{-1}}{Q_m^{-1}} = \text{sech}\,\frac{W}{\boldsymbol{k}}\left(\frac{1}{T_m} - \frac{1}{T}\right).$$

Values of Q^{-1}/Q_m^{-1} have been calculated at different temperatures using the experimental values of W and compared with the experimental values of Q^{-1}/Q_m^{-1} as shown in figures 1 and 2.

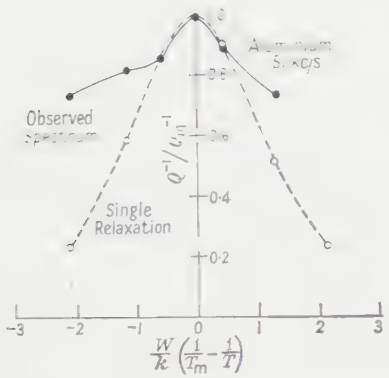

Figure 1. Second dislocation relaxation peak in aluminium at 51 kc/s compared with Zener's single relaxation curve $\frac{Q^{-1}}{Q_m^{-1}} = \text{sech}\,\frac{W}{\boldsymbol{k}}\left(\frac{1}{T_m} - \frac{1}{T}\right)$.

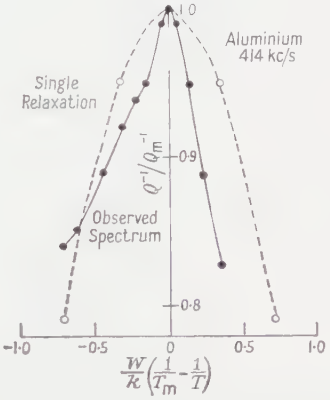

Figure 2. Second dislocation relaxation peak in aluminium at 414 kc/s compared with Zener's single relaxation curve $\frac{Q^{-1}}{Q_m^{-1}} = \text{sech}\,\frac{W}{\boldsymbol{k}}\left(\frac{1}{T_m} - \frac{1}{T}\right)$.

The frequency–temperature dependence of the second relaxation peak in aluminium gives an activation energy of 550 calories per mole, i.e. 0·024 ev. Values of the Peierls stress τ_p^0 can be obtained from the relation

$$W = \left(\frac{7b^3}{\pi^{3/2}}\right)\mu\left(\frac{\tau_p^0}{\mu}\right)^{1/2}$$

where b is the distance between the closest atoms in the glide direction of the dislocation and μ is shear modulus. In aluminium μ is $2{\cdot}5 \times 10^{11}$ dyn cm^{-2} and b is $2{\cdot}48 \times 10^{-8}$ cm. Hence using $W = 0{\cdot}024$ ev, we find $\tau_p^0/\mu = 6{\cdot}4 \times 10^{-5}$ which is less than the upper limit $3{\cdot}6 \times 10^{-4}$ found by Cottrell (1953). However, the ratio τ_p^0/μ can also be expressed as

$$\frac{\tau_p^0}{\mu} = \left(\frac{2\pi^3}{3\sqrt{3}}\right)\left(\frac{W_k^2}{\mu^2 b^6}\right)$$

where W_k is the energy of a kink of the dislocation. Lothe and Hirth (1959) have proposed a model for low temperature dislocation motion using the concept

of nucleation and growth of kinks in dislocations lying in Peierls potential troughs. According to their model the observed activation energy for the creep in the pure aluminium equals $2W_k$, i.e. $2W_k = 3400\,\text{cal mol}^{-1} = 0{\cdot}15\,\text{ev}$. Using this value of W_k, the ratio $\tau_p{}^0/\mu$ is found to be equal to $1{\cdot}144 \times 10^{-4}$ which is closer to Cottrell's upper limit of $\tau_p{}^0/\mu$.

References

Bordoni, P. G., 1954, *J. Acoust. Soc. Amer.*, **26**, 495.
Cottrell, A. H., 1953, *Dislocations and Plastic Flow in Crystals* (Oxford: Clarendon Press).
Lax, E., and Filson, D. H., 1959, *Phys. Rev.*, **114**, 1273.
—— 1959, *Tech. Report* No. XVI, Dept. of Physics, University of California, Los Angeles.
Lothe, J., and Hirth, J. P., 1959, *Phys. Rev.*, **115**, 543.
Zener, C., 1948, *Elasticity and Anelasticity of Metals*, 1st edn (Chicago: University Press).

Polar Scattering in III–V Compounds

By C. HILSUM

Services Electronics Research Laboratory, Baldock, Herts.

MS. received 9th April 1960

Ehrenreich (1959) has shown that the electron mobility in pure InSb is limited at room temperature by lattice optical mode scattering, and that acoustic modes are relatively unimportant. There is now sufficient information to make rough calculations for five other III V compounds, to see if similar conclusions can be drawn.

For zinc-blende crystals the mobility limit at 290 °K due to polar optical mode scattering is given by

$$\mu = 3 \times 10^{31} \left(\frac{e}{e_c{}^*}\right)^2 \left(\frac{m}{m^*}\right)^{3/2} FMa^3\nu \left(\exp\left[\frac{\boldsymbol{h}\nu}{\boldsymbol{k}T}\right] - 1\right) \text{cm}^2\text{v}^{-1}\text{sec}^{-1}$$

where $e_c{}^*$ is the effective charge defined by Callen (1949), M the reduced mass of the atoms, a the lattice constant and ν the longitudinal fundamental optical frequency. F is a slowly varying function of $\boldsymbol{h}\nu/\boldsymbol{k}T$ which at room temperature is approximately equal to 0·7 for all the compounds considered.

In the table we show results for InSb, InAs, InP, GaSb, GaAs and AlSb, using parameters deduced from far infra-red restrahlen spectra (Picus *et al.* 1959), refractive indices, dielectric constants and effective masses. Effective mass values measured by magneto-optical effects have been used where available. In the other cases we have taken the approximate values quoted in the literature, generally deduced from the dependence of mobility on impurity content in impure specimens. The simple relation given above must be modified for the case of electron mobility in InSb to allow for the non-parabolic conduction band, and the screening due to the large number of electrons present at room temperature.

Predicted and Measured Mobilities for III–V Compounds

(1)	(2)	(3)	(4)	(5)	(6)	(7)	(8)	(9)
InSb	Electron	0·013	0·13	5·5	260	200000	78000	10^{14}
	Hole	0·18				3600	750	
InAs	Electron	0·03	0·22	7	340	22000	33000	10^{16}
	Hole	0·41				500	450	
InP	Electron	0·07	0·24	10	480	6800	4800	5×10^{15}
	Hole	0·4				500	150	
GaSb	Electron	0·047	0·11	7	340	43000	5000	10^{17}
	Hole	0·5				1200	1000	
GaAs	Electron	0·072	0·17	8·5	400	11000	8000	5×10^{16}
	Hole	0·5				600	400	
AlSb		—	0·19	10	480	—		10^{17}
	Hole	0·4				800	460	

(1) Material; (2) carrier; (3) m^*/m; (4) e_c^*/e; (5) $\nu(10^{12}\ \mathrm{sec}^{-1})$; (6) $\hbar\nu/k(^\circ\mathrm{K})$; (7) calculated polar mobility ($\mathrm{cm^2\ v^{-1}\ sec^{-1}}$); (8) measured mobility ($\mathrm{cm^2\ v^{-1}\ sec^{-1}}$); (9) lowest total impurity content ($\mathrm{cm^{-3}}$).

We should expect that the measured mobilities will be less than those given solely by polar scattering, since other scattering mechanisms cannot be ignored. Impurity scattering is important in all the compounds except InSb, and some indication of the lowest total impurity contents achieved are given in the table. If the appropriate allowance is made for impurity scattering, in every case but three the predicted mobility is within a factor of two of that measured. For electrons in InSb we have no appreciable impurity scattering, but we must consider electron–hole scattering, which can be treated in a similar way. At room temperature, there are $1{\cdot}6 \times 10^{16}$ holes per $\mathrm{cm^3}$, and if the scattering due to them is combined with polar scattering, the mobility predicted (Ehrenreich 1959) is $110\,000\ \mathrm{cm^2\ v^{-1}\,sec^{-1}}$, in good agreement with the measured value.

For holes in InSb and electrons in GaSb we find that the mobilities calculated from combined polar scattering and impurity scattering are much higher than the values found in practice. There is conflicting evidence about the effective mass of holes in InSb. We have used $0{\cdot}18\,m$, the value obtained from cyclotron resonance (Dresselhaus *et al.* 1955), and a value of near $0{\cdot}5\,m$ would be needed to give a polar mobility equal to the measured mobility. If we calculate m_h from the equation

$$n_i^2 = 4(2\pi \boldsymbol{k} T/\boldsymbol{h}^2)^3 (m_e m_h/m^2)^{3/2} \exp(-E/\boldsymbol{k}T)$$

taking the energy gap as 0·17 ev, the intrinsic concentration as $1{\cdot}6 \times 10^{16}\ \mathrm{cm^{-3}}$ (Hilsum and Barrie 1958, Hrostowski *et al.* 1955), and the electron mass appropriate to this concentration (Moss, Smith and Taylor 1959) as $0{\cdot}016\,m$, we find that m_h is approximately $0{\cdot}5\,m$. Other electrical measurements may be used for finding m^*, but the answers obtained often depend on an implicit assumption that acoustic scattering is dominant. For example, the value for m_h of $0{\cdot}18\,m$ deduced by Weiss (1956) from thermoelectric effects is doubled if one assumes that the relaxation time is independent of energy. Since the cyclotron resonance value is not firmly established (Kip, private communication) we cannot come to any definite conclusions, but it is certainly possible that polar scattering is the limiting process here too.

There is no obvious reason for the discrepancy between the predicted and measured values of electron mobility in GaSb. We may illustrate this by comparing the parameters of GaSb with those of InAs since v, M and a are the same for both materials. GaSb is so much less polar than InAs that we must conclude that its carrier mobilities should be the larger.

There is always the possibility that acoustic scattering is in fact the dominant mechanism for GaSb, but if this were so we should then have to explain why this one compound should be the exception in this family of materials. Rough calculations of the mobility due to acoustic scattering can be made following the deformation potential method (Bardeen and Shockley 1950), and these give for GaSb a value of $3 \times 10^5 \text{ cm}^2 \text{ v}^{-1} \text{sec}^{-1}$.

Sagar (1959) has shown that the (000) minimum of the conduction band in GaSb is about 0·08 ev below the (111) minima. The effective mass appropriate to the (111) minima is about 0·22 m, and if we had used this value we would have obtained a polar mobility of 10 000 $\text{cm}^2 \text{ v}^{-1} \text{sec}^{-1}$. But if the band separation is as large as 0·08 ev the lower effective mass should be used for calculations on pure material at room temperature. It is possible that Sagar has overestimated the separation, but it seems more likely that the gallium antimonide available at present is very highly compensated, and gives little indication of the true potentialities of the material. Pure GaSb should have an electron mobility approaching that of InAs, if not InSb.

Acknowledgments

The author is grateful to Drs. O. Simpson, D. J. Oliver and A. C. Rose-Innes for valuable discussions, and to the Admiralty for permission to publish.

References

Bardeen, J., and Shockley, W., 1950, *Phys. Rev.*, **77,** 407.
Callen, H. B., 1949, *Phys. Rev.*, **76,** 1394.
Dresselhaus, G., Kip, A., Kittel, C., and Wagoner, G., 1955, *Phys. Rev.*, **98,** 556.
Ehrenreich, H., 1959, *J. Phys. Chem. Solids*, **9,** 129.
Hilsum, C., and Barrie, R., 1958, *Proc. Phys. Soc.*, **71,** 676.
Hrostowski, H., Morin, F., Geballe, T., and Wheatley, G., 1955, *Phys. Rev.*, **100,** 1672.
Moss, T. S., Smith, S. O., and Taylor, K. W., 1959, *J. Phys. Chem. Solids*, **8,** 323.
Picus, G., Burstein, E., Henvis, B., and Hass, M., 1959, *J. Phys. Chem. Solids*, **8,** 282.
Sagar, A., 1959, Westinghouse Research Report, 6–40602–3–R1.
Weiss, H., 1956, Z. *Naturf.*, **11a,** 131.

Charge Exchange between Argon Ions and Atoms

By S. B. KARMOHAPATRO

Saha Institute of Nuclear Physics, Calcutta, India

MS. received 15*th March* 1960, *in final form* 3*rd May* 1960

§ 1. Introduction

The experimental results of the measurement of cross sections of charge exchange by single electron capture of low energy argon ions in argon gas given by Hasted and Gilbody (1957) indicate a reaction with an energy difference $\Delta E = 0{\cdot}18$ ev between $^2P_{3/2}$ and $^2P_{1/2}$ states of the argon ions. Such

asymmetric behaviour of some symmetric reactions in the light of the adiabatic hypothesis gives more information about the nature of the reactions. In this work, we have calculated the cross section for the reaction

$$A^+ + A \rightarrow A + A^+ \qquad \ldots\ldots (1)$$

with $\Delta E = 0$ and 0·18 ev theoretically with the impact parameter method and compared the $(\sigma, (\text{ev})^{1\cdot2})$ curve with the experimental curve given by Hasted and Gilbody (1957).

§ 2. Method

The method used for calculating the charge exchange cross sections is similar to that used by Karmohapatro and Das (1958) with the difference that of the four terms of the analytical wave function for argon worked out by Löwdin and Appel (1956) only the first one instead of the first two has been used here. In short, the method consists of assuming the one-electron model of the atom and the relative motion of such slow collisions is considered classically.

With this model, the interaction potential

$$H' = \frac{1}{R} - \frac{1}{r_b} \qquad \ldots\ldots (2)$$

operated on

$$\psi_{i,f} = A_1 \exp(-a_1 r_{a,b}) \qquad \ldots\ldots (3)$$

for the initial and the final states, gives

$$H_{fi} = \frac{S(R)}{R} - J(R) \qquad \ldots\ldots (4)$$

where

$$S(R) = \langle a|b\rangle, \quad J(R) = \left\langle a\left|\frac{1}{r_b}\right|b\right\rangle$$

$$A_1 = -0{\cdot}81754, \quad a_1 = 1{\cdot}5080.$$

R is the distance between the nucleus of the argon ion and the atom and r_b is the distance between the nucleus of the argon ion and the electron of the atom, with suffixes a, b for the initial and final states, respectively.

The solution of the integrals $S(R)$ and $J(R)$ gives the probability of the reaction as

$$P(R_0) = \sin^2 \chi \qquad \ldots\ldots (5)$$

where

$$\chi = \sum_{\nu} \int_{-\infty}^{\infty} \frac{H_{fi}}{\hbar v} \cos\left(\frac{\Delta E x}{\hbar v}\right)^2 dx. \qquad \ldots\ldots (6)$$

ΔE is the internal energy involved in the reaction and v is the velocity of the ions.

The numerical value of χ is computed for different values of R_0, the closest distance of collision, and the cross section is obtained graphically from the integral

$$\sigma = 2\pi \int_0^{\infty} P(R_0) R_0 \, dR_0. \qquad \ldots\ldots (7)$$

This method, for the different values of v, gives the $(\sigma, (\text{ev})^{1\cdot2})$ curve.

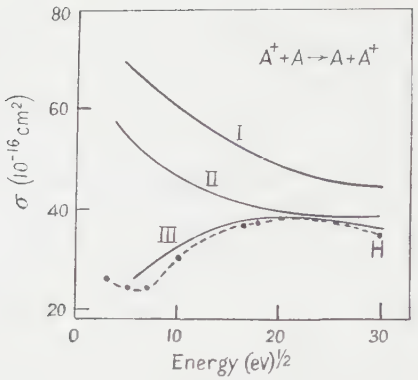

Comparison of the theoretical cross section velocity curves obtained by the impact parameter method using Slater's wave function (curve I) and the first term of Löwdin's wave function (curve II, $\Delta E = 0$ and curve III, $\Delta E = 0{\cdot}18$ ev), with the experimental curve (H) obtained by Hasted and Gilbody (1957).

§ 3. Results

$(\sigma, (\text{ev})^{1/2})$ curves in the energy range 25–900 ev for the reaction

$$A^+ + A \rightarrow A + A^+$$

are obtained by the above method for both types of reactions with $\Delta E = 0$ (curve II) and 0·18 ev (curve III). In the figure these curves are compared with the experimental curve given by Hasted and Gilbody (1957).

§ 4. Conclusion

It may be concluded that the one term approximation of such an analytical wave function gives more accurate results in the low energy range than the Slater nodeless wave function, even for a symmetric charge exchange reaction, as will be evident from the figure by comparing curve II with curve I, reproduced from Gurnee and Magee (1957).

From the figure it is evident that the theoretical curve II has a closer agreement with the experimental curve, given by Hasted and Gilbody (1957) showing the reaction as asymmetric with $\Delta E = 0{\cdot}18$ ev. However, in the light of previous conclusions (Karmohapatro 1959) regarding the dependence of the probability of such charge exchange upon the experimental conditions, it can be said that the reaction in equation (1) may happen in four ways:

$$\left.\begin{aligned}
&\text{(i)}\ A^+(^2P_{3/2}) + A \rightarrow A + A^+(^2P_{3/2}) \\
&\text{(ii)}\ A^+(^2P_{1/2}) + A \rightarrow A + A^+(^2P_{1/2}) \\
&\text{(iii)}\ A^+(^2P_{3/2}) + A \rightarrow A + A^+(^2P_{1/2}) - 0{\cdot}18\,\text{ev} \\
&\text{(iv)}\ A^+(^2P_{1/2}) + A \rightarrow A + A^+(^2P_{3/2}) + 0{\cdot}18\,\text{ev}.
\end{aligned}\right\} \quad \ldots\ldots (8)$$

The symmetric reactions (i), (ii) or the asymmetric ones (iii), (iv) cannot be distinguished by the above method. However, experiments under different conditions may show superposed effects of these types of reactions, happening in different fractions. Thus, the curve due to Hasted and Gilbody shows that most of the reactions are due to processes (iii) and (iv).

Cross sections for the argon ions with energy less than 25 ev are theoretically not calculated in the present work. The experimental curve has an inflection at the low energy end, which may be explained by assuming that the reactions (i), (ii) of equation (8) are more prominent in this lower energy region. However, the present method may be applied to the low energy ion–atom collisions with certain accuracy; or for energies near threshold where trajectories are not assumed to be straight, the approximation method described by Rosen (1958) may give good results. Dalgarno (1958) has calculated the charge exchange cross sections related to the mobility for A^+ in A. The discrepancy of these data with the experimental curve shows an apparent violation of the theory of dependence of mobility of ions in parent gases on the charge exchange cross sections as worked out by Massey and Mohr (1934). This discrepancy may be due to the asymmetric behaviour of the reactions as (iii) and (iv) in equation (8), which is similar to the case of ions in unlike gases.

The shape of the experimental curve may mean that the processes (iii) and (iv) play the dominant role throughout the energy range. However, on the low energy side, processes (i) and (ii) might be contributing a sizeable percentage in the total cross sections, producing the inflection in the experimental curve. The actual percentages may be estimated theoretically provided all the terms, to which the cross section is sensitive, are included in the calculations for each individual process.

Acknowledgments

The author is thankful to Professor B. D. Nag, Director of the Saha Institute of Nuclear Physics and Professor D. N. Kundu for their keen interest in this work.

References

Dalgarno, A., 1958, *Phil. Trans.* A, **250,** 426.
Gurnee, E. F., and Magee, J. L., 1957, *J. Chem. Phys.*, **26,** 1237.
Hasted, J. B., and Gilbody, H. B., 1957, *Proc. Roy. Soc.* A, **238,** 334.
Karmohapatro, S. B., 1959, *J. Chem. Phys.*, **30,** 538.
Karmohapatro, S. B., and Das, T. P., 1958, *J. Chem. Phys.*, **29,** 240.
Löwdin, P. O., and Appel, K., 1956, *Phys. Rev.*, **103,** 1746.
Massey, H. S. W., and Mohr, C. B. O., 1934, *Proc. Roy. Soc.* A, **144,** 188.
Rosen, P., 1958, *Phys. Rev.*, **109,** 348.

Selection Rules for Spin Orbit Matrix Elements for the Configuration f^n

By A. G. McLellan
University of Canterbury, Christchurch, New Zealand
MS. received 14*th March* 1960

Selection tables in W and U, the quantum numbers of Racah (1949), are derived for spin–orbit matrix elements between states of configuration f^n.

The space parts of the complete anti-symmetric wave function of an electronic configuration f^n, which is an eigenfunction of S^2, L^2, M_L and M_S are seven-dimensional tensors of rank n with a basis of $\phi_1(m_1)\phi_2(m_2)..\phi_n(m_n)$, where each

ϕ is a one-electron spatial wave function of angular momentum quantum number $l=3$. These tensors provide a basis for representations of the unitary group U_7 in seven dimensions and any of its sub-groups such as R_7, G_2 and R_3. Here R_7 and R_3 are the real orthogonal groups in seven and three dimensions, and G_2 is the group used by Racah (1949) to define the quantum number U, while R_7 defines the quantum number W. Further, such tensors form a basis for a representation of S_n, the symmetric group of permutations of the n electronic coordinates. Since this representation of S_n commutes with the above representations of U_7 and its sub-groups, tensors may be selected which transform irreducibly according to both U_7 and S_n in the following manner. The irreducible representations of S_n and U_7 in this tensor space are both defined by a partition of the integer n, i.e. $(n_1, n_2, n_3 \ldots)$, $n_1 \geqslant n_2 \geqslant n_3 \geqslant \ldots$ Corresponding to a certain partition, tensors may be chosen to form a rectangular array the number of rows and columns of which being the dimensions of the corresponding irreducible representations Γ and D say, of S_n and U_7 respectively. This rectangular array has the property that the rows transform irreducibly according to Γ while the columns transform irreducibly according to D (see e.g. van der Waerden 1932 and Weyl 1946). It is clear that the columns can be arranged according to the irreducible representations of U_7, R_7, G_2, R_3, and may thus be labelled by the set of numbers v, W, U, L, M_L. A further label α indicates the row of the rectangular array to which the basis tensor $|\alpha; vWULM_L\rangle$ belongs.

These tensors must be combined with spin wave functions $|\beta; SM_S\rangle$ which similarly transform irreducibly according to the representation Γ_a of S_n which is the associated representation of Γ, and to the representation, defined by S, of the unitary group in the two dimensional spin space. These functions may be chosen so that the representation matrix in Γ_a of an element P of S_n is δ_P times the matrix representing P in Γ, where δ_P is $+1$ or -1 as the permutation P is even or odd. In this case, since the representations Γ and Γ_a may be chosen to be unitary, it may be shown that the antisymmetric complete wave function is given by

$$|vWUSLM_LM_S\rangle = \sum_{\alpha} |\alpha; SM_S\rangle |\alpha; vWULM_L\rangle. \qquad \ldots\ldots (1)$$

Thus the matrix of the spin–orbit operator referred to these states is

$$\langle v'W'U'S'L'M_L'M_S' | \sum_{i=1}^{n} \mathbf{s}_i . \mathbf{l}_i | vWUSLM_LM_S\rangle$$

$$= \sum_{i,\alpha,\beta} \langle \alpha; S'M_S' | \mathbf{s}_i | \beta; SM_S\rangle . \langle \alpha; v'W'U'L'M_L' | \mathbf{l}_i | \beta; vWULM_L\rangle.$$

$\ldots\ldots (2)$

Racah (1949) has observed that tensors such as $\mathbf{l}_i$ which transform irreducibly according to the representation D_1 of R_3 transform according to the representation (110) of R_7 and (11) of G_2. Thus allowed matrix elements must be such that the product representations of R_7 and G_2, $(W') \times (110) \times (W)$ and $(U') \times (11) \times (U)$ respectively contain the identity representation of the respective group at least once. $c(WW'(110))$ and $c(UU'(11))$ the number of times the identity representations (000) and (00) of R_7 and G_2 occur in the above product representations have been calculated by methods similar to those employed by Judd (1959) and are tabulated below. Since the spin–orbit matrix element between the states

$|v'W'U'S'L'JJ_z\rangle$ and $|vWUSLJJ_z\rangle$ is linearly related to matrix elements of the above kind, the same selection rules in W and U will hold between these states as between the Russell–Saunders states.

The selection table for W is not useful for matrix elements between states of high multiplicity: no matrix elements between the states listed in table 2 of Elliott, Judd and Runciman (1957) are forbidden for W, which are allowed for other quantum numbers including the seniority number v. However it may be useful for states of lower multiplicity. The selection table for U has been verified and is proving useful in calculations of spin–orbit matrix elements for f^4, f^5 and f^6 which are now being made here. This table may also be verified by reference to the matrix elements for f^3 (Judd and Loudon 1959).

From the form of the spin–orbit matrix element in equation (2), it is easy to see that singlet–singlet spin–orbit matrix elements must be zero. Another known selection rule, that spin–orbit matrix elements are zero between different states of highest multiplicity for configuration l^n may be easily derived from the form (1) for the complete wave function. By using the identity

$$\sum_{i=1}^{n} \mathbf{s}_i . \mathbf{l}_i = \frac{1}{n} \mathbf{S} . \mathbf{L} + \frac{1}{n^2} \sum_{i,j,k=1}^{n} (\mathbf{s}_i - \mathbf{s}_j) . (\mathbf{l}_i - \mathbf{l}_k), \qquad \ldots\ldots (3)$$

and the fact that for $n \leqslant 2l+1$, the single space part of the wave function is anti-symmetric to interchange of the spatial coordinates of any pair of electrons, it is easy to show that the spin–orbit matrix element between such states is simply

$$\frac{1}{n} \langle SM_S' | \mathbf{S} | SM_S \rangle . \langle W'U'LM_L' | \mathbf{L} | WULM_L \rangle$$

for elements diagonal in SL and zero otherwise. Since matrix elements for $n+2l+1$ equivalent electrons are minus the corresponding elements for n equivalent electrons, this rule may be extended to $n \leqslant 4l+2$.

$c(WW'(110))$

	(000)	(100)	(110)	(200)	(111)	(210)	(211)	(220)	(221)	(222)
(000)	–	–	1	–	–	–	–	–	–	–
(100)	–	1	–		1	1	–		–	–
(110)	1	–	1	1	1	–	1	1	–	–
(200)	–	–	1	1	–	–	1	–	–	–
(111)	–	1	1	–	1	1	1	–	1	–
(210)	–	1	–	–	1	2	1	–	1	–
(211)	–	–	1	1	1	1	2	1	1	1
(220)	–	–	1	–	–	–	1	1	1	–
(221)	–	–	–	–	1	1	1	1	2	1
(222)	–	–	–	–	–	–	1	–	1	1

$c(UU'(11))$

	(00)	(10)	(11)	(20)	(21)	(30)	(22)	(31)	(40)
(00)	–	–	1	–	–	–	–	–	
(10)	–	1	–	1	1	–		–	–
(11)	1	–	1	1		1	1	–	–
(20)	–	1	1	1	1	1		1	–
(21)	–	1	–	1	2	1	–	1	1
(30)	–	–	1	1	1	1	1	1	1
(22)	–	–	1	–	–	1	1	1	–
(31)	–	–	–	1	1	1	1	2	1
(40)	–	–	–	–	1	1	–	1	1

References

Elliott, J. P., Judd, B. R., and Runciman, W. A., 1957, *Proc. Roy. Soc.* A, **240**, 509.
Judd, B. R., 1959, *Proc. Phys. Soc.*, **74**, 330.
Judd, B. R., and Loudon, R., 1959, *Proc. Roy. Soc.* A, **251**, 127.
Racah, G., 1949, *Phys. Rev.*, **76**, 1352.
van der Waerden, B. L., 1932, *Die Gruppentheoretische Methode in der Quantenmechanik* (Berlin: Springer).
Weyl, H., 1946, *Classical Groups* (Princeton: University Press).

Note added in proof.—Dr. B. R. Judd has recently brought to my attention the following additional selection rule:

(*a*) If $c(WW'\ (110))=1$ and $W=W'$, all matrix elements that are non-diagonal in U and L vanish;

(*b*) If $c(UU'\ (11))=1$ and $U=U'$, all matrix elements that are non-diagonal in L vanish.

The Stopping Powers of Atoms

By A. Dalgarno

Department of Applied Mathematics, The Queen's University of Belfast

MS. received 4th May 1960

§ 1. Introduction

The stopping powers of atoms towards fast particles can be expressed in terms of an average excitation energy I (cf. Livingstone and Bethe 1937). By a slight generalization of a formula given by Mott and Massey (1949), it may be shown that

$$\ln I=\sum_n f_n \ln (E_0-E_n)\Big/\sum_n f_n \qquad \ldots\ldots(1)$$

where f_n is the electric dipole oscillator strength of the transition from the ground state of the atom to the nth excited state, E_0-E_n is the energy of the transition and the summations include integrations over the continua. The evaluation of (1) by explicit summation is possible only for hydrogen and helium, and for heavier elements it has been supposed that I must be determined by analysis of the experimental data.

It is the purpose of this note to describe a purely theoretical method of computing I which is capable of yielding values correct to an uncertainty of the order of one per cent and which can be applied to any element.

§ 2. The Evaluation of I

We define a function

$$S(k)=\sum_n f_n(E_0-E_n)^k. \qquad \ldots\ldots(2)$$

Then (cf. Dalgarno and Lynn 1957)

$$S(2)=\frac{16\pi Z}{3}\sum_i \langle\delta(\mathbf{r}_i)\rangle \qquad \ldots\ldots(3)$$

where $\mathbf{r}_i$ is the position vector of the ith electron of the atom;

$$S(1)=\frac{4}{3}\left\{E_0+\frac{1}{2}\sum_{i\neq j}\langle\mathbf{p}_i\cdot\mathbf{p}_j\rangle\right\} \qquad \ldots\ldots(4)$$

where E_0 is the binding energy measured in rydbergs and $\mathbf{p}_i$ is the momentum of the ith electron;

$$S(0)=N \qquad \ldots\ldots(5)$$

where N is the number of electrons;

$$S(-1)=\frac{1}{3}\langle(\sum_i \mathbf{r}_i)^2\rangle\ ; \qquad \ldots\ldots(6)$$

$$S(-2)=\tfrac{1}{4}\alpha \qquad \ldots\ldots(7)$$

where α is the atomic dipole polarizability in units of a_0^3 ($a_0=5{\cdot}292\times10^{-9}$ cm). In addition it may be shown that S (2·5) tends logarithmically to infinity.

The general form of $S(k)$ suggests that a reliable analytic fit can be obtained according to

$$S(k)=\{a+bk+ck^2+d\ln(2{\cdot}5-k)\}^k S(0), \qquad \ldots\ldots(8)$$

a, b, c and d being determined so that the values of (3), (4), (6) and (7) are reproduced. Now

$$\ln I=\left[\frac{d}{dk}\ln S(k)\right]_{k=0} \qquad \ldots\ldots(9)$$

so that with (8)

$$I=(a+d\ln 2{\cdot}5)\text{ rydbergs.} \qquad \ldots\ldots(10)$$

We have applied the method to hydrogen, helium, lithium and beryllium using the most accurate available wave functions to calculate the expectation values and using the best estimates available for the polarizabilities. The derived values of I are given in the table. Comparison data are provided for H and He by direct summation of (1) and for Li and Be by analysis of experimental data (cf. Burkig and MacKenzie 1957) and the corresponding values of I are also given in the table.

	Values of I (ev)			
	H	He	Li	Be
Experimental†	15·$_0$	41·$_5$	39·$_0$	64·$_0$
Equation (10)	14·8	41·7	38·8	66·1

† The values for H and He are the results of explicit evaluations of (1).

The value for Be derived from (10) may be slightly too large since the Hartree–Fock wave functions employed probably overestimate both (3) and (4).

In any event, the experimental values may be in error by 2 or 3 ev, so that the two sets of results are in harmony. Thus the simple method proposed here is capable of yielding values of I to an accuracy at least comparable with that obtaining in the determination of I from experimental data.

A similar method has been proposed by Pekeris (1959) for the evaluation of the average excitation energy K associated with the Lamb shift but the probable error is very much larger.

References

Burkig, V. C., and MacKenzie, K. R., 1957, *Phys. Rev.*, **106,** 848.
Dalgarno, A., and Lynn, N., 1957, *Proc. Phys. Soc.* A, **70,** 802.
Livingstone, M. S., and Bethe, H. A., 1937, *Rev. Mod. Phys.*, **9,** 245.
Mott, N. F., and Massey, H. S. W., 1949, *Theory of Atomic Collisions* (Oxford: Clarendon Press).
Pekeris, C. L., 1959, *Phys. Rev.*, **115,** 1216.

Correlation between Photons in Partially Polarized Light Beams

By E. WOLF

Institute of Optics, University of Rochester, Rochester, N.Y., U.S.A.

MS. received 28th March 1960

In several important investigations, Hanbury Brown and Twiss (1956a, 1957a, b) demonstrated that the fluctuations in the current outputs from two photoelectric detectors illuminated by a coherent or partially coherent light beam are in general correlated. A clear explanation of this effect was given by Purcell (1956) and his analysis was extended by Mandel (1958). The Hanbury Brown–Twiss effect may be used to determine the *degree of coherence* between light vibrations at two points in space and has important applications in connection with the measurement of stellar diameters (Hanbury Brown and Twiss 1956b, 1958a, b).

The analyses published so far apply to light which is either linearly polarized or completely unpolarized. It is the purpose of this note to extend some of the results to partially polarized light and to show that the Hanbury Brown–Twiss effect can also be used to determine the *degree of polarization* of a light beam.

Consider first the fluctuations in the output of a single photoelectric detector, illuminated by a plane, quasi-monochromatic, partially polarized light wave. Let us resolve the electric vibrations in the incident wave into two mutually orthogonal components, at right angles to the direction of propagation. If only one of the components (x, say) were present, then, according to the calculations of Purcell and Mandel, the mean square fluctuation in the number of photoelectrons ejected in a time interval T averaged over a sequence of such intervals is given by

$$\overline{\Delta n_x^2} = \overline{n_x}\left(1 + \frac{\tau_0}{T}\overline{n_x}\right) \qquad \ldots\ldots(1)$$

where it is assumed that T is much greater than the coherence time τ_0 of the light. If only the other component (y, say) were present, one would of course have a strictly similar expression for the corresponding mean square fluctuation $\overline{\Delta n_y^2}$.

In a partially polarized beam the fluctuations of the light vibrations in the x- and y-components are correlated. Assuming that the emission of the photoelectrons is associated stochastically with the two polarization components one must expect that there is then also a non-vanishing correlation $\overline{\Delta n_x \Delta n_y}$ in the fluctuations of n_x and n_y. To determine $\overline{\Delta n_x \Delta n_y}$ we assume that the joint probability distribution for the two components of the electric vector in the incident beam is Gaussian (as may in general be assumed by an appeal to the central limit theorem of probability theory). Then it follows by a similar calculation as carried out by Mandel (1958) in connection with his formula (23) that

$$\overline{\Delta n_x \Delta n_y} = \overline{n_x}\,\overline{n_y}(\tau_0/T)|\mu_{xy}|^2, \qquad \ldots\ldots (2)$$

where μ_{xy} is the normalized complex correlation coefficient which characterizes the correlation between the components E_x, E_y of the incident electric vector, the components being represented by analytical signals (Born and Wolf 1959, Wolf 1959). Hence taking into account both polarization components, it follows from (1) and (2) that the mean square fluctuation in the number of photoelectrons emitted in intervals of duration T, when the detector is illuminated by a partially polarized beam is

$$\begin{aligned}\overline{\Delta n^2} &= \overline{\Delta n_x^2} + \overline{\Delta n_y^2} + 2\overline{\Delta n_x \Delta n_y} \\ &= \bar{n}[1 + \sigma(\tau_0/T)\bar{n}], \qquad \ldots\ldots (3)\end{aligned}$$

where

$$\bar{n} = \overline{n_x} + \overline{n_y}$$

and

$$\sigma = 1 - 2\left(\frac{\overline{n_x}\,\overline{n_y}}{\bar{n}^2}\right)(1 - |\mu_{xy}|^2). \qquad \ldots\ldots (4)$$

The formula (3) can only be physically meaningful if the right-hand side is independent of any particular choice of the x and y directions. To show that this is so and also to express $\overline{\Delta n^2}$ in terms of the degree of polarization of the light we introduce the coherency matrix $J_{ij} = \langle E_i E_j^* \rangle$, $(i,j = x,y)$, angular brackets denoting the time average. Then if α denotes the quantum sensitivity of the photoelectric detector, $\overline{n_x} = \frac{1}{2}\alpha T J_{xx}$, $\overline{n_y} = \frac{1}{2}\alpha T J_{yy}$. Also $|\mu_{xy}|^2 = J_{xy}J_{yx}/J_{xx}J_{yy}$, and (4) becomes

$$\sigma = 1 - \frac{2|J|}{(J_{xx} + J_{yy})^2}, \qquad \ldots\ldots (5)$$

where $|J| = J_{xx}J_{yy} - J_{xy}J_{yx}$ is the determinant of the coherency matrix. Since the right-hand side of (5) only involves the two rotational invariants of the coherency matrix, σ is independent of the particular choice of the x and y directions; so is evidently also $\bar{n}$ since $\overline{n_x} + \overline{n_y} = \frac{1}{2}\alpha T(J_{xx} + J_{yy})$. Moreover from (5) and formula (5.14) of Wolf (1959) it follows that

$$\sigma = \tfrac{1}{2}(1 + P^2), \qquad \ldots\ldots (6)$$

where P is the degree of polarization of the light. Hence the expression (3) finally becomes

$$\overline{\Delta n^2} = \bar{n}[1 + \tfrac{1}{2}(1+P^2)(\tau_0/T)\bar{n}]. \qquad \ldots\ldots (7)$$

The term $\frac{1}{2}(1+P^2)(\tau_0/T)\bar{n}$ represents an *excess fluctuation* in the counting rate over that given by classical particle statistics. In the special case when $P=1$ or $P=0$ (completely polarized or completely unpolarized light), (7) reduces to the expressions found by Purcell and Mandel.

It is now a simple matter to determine the correlation between the fluctuations in the output from two photoelectric detectors, illuminated by two portions of a partially polarized beam. If suffixes 1 or 2 refer to each of the two detectors, the mean square fluctuation in the count from each is given by an expression such as (7), with n_1 or n_2 written in place of n. If the two outputs are joined together, one reverts to the single channel experiment with $n=n_1+n_2$. Hence using the standard formula $\overline{\Delta n^2}=\overline{\Delta n_1{}^2}+\overline{\Delta n_2{}^2}+2\overline{\Delta n_1 \Delta n_2}$, it readily follows that the correlation in the fluctuations of the counts from the two detectors is given by

$$\overline{\Delta n_1 \Delta n_2} = \tfrac{1}{2}(1+P^2)(\tau_0/T)\bar{n}_1\bar{n}_2. \qquad \ldots\ldots (8)$$

Again, in the special cases when $P=0$ or $P=1$, and when the light is coherent this formula is in agreement with the results of Purcell and Mandel.

The relation (8) shows that the degree of polarization of a light beam may in principle be determined from measurements of the correlation in the outputs of two photoelectric detectors illuminated by two portions of the beam. This possibility is probably of no great practical interest at present, since the method requires carefully controlled experiments and much greater technical skill than is needed in measurements by conventional means; the method is, however, of considerable theoretical interest since it does not require the use of a polarizing or a compensating device. The principle could probably be more profitably used in connection with polarization measurements involving electromagnetic radiation of other regions of the spectrum, employing appropriate square law detectors.

Acknowledgment

This research was supported by the United States Air Force, under Contract No. AF 49 (638)—602, monitored by the AF Office of Scientific Research of the Air Research and Development Command.

References

Born, M., and Wolf, E., 1959, *Principles of Optics* (London, New York : Pergamon Press), §10.2.

Hanbury Brown, R., and Twiss, R. Q., 1956a, *Nature, Lond.*, **177,** 27.

—— 1956 b, *Ibid.*, **178,** 1046.

—— 1957 a, *Proc. Roy. Soc.* A, **242,** 399.

—— 1957 b, *Ibid.*, **243,** 291.

—— 1958 a, *Ibid.*, **248,** 199.

—— 1958 b, *Ibid.*, **248,** 222.

Mandel, L., 1958, *Proc. Phys. Soc.*, **72,** 1037.

Purcell, E. M., 1956, *Nature, Lond.*, **178,** 1449.

Wolf, E., 1959, *Nuovo Cim.*, **13,** 1165.

Asymmetry in Scattering of 90–140 Mev Polarized Protons from Nuclear Emulsion Material†

By J. G. RUTHERGLEN
Department of Natural Philosophy, University of Glasgow

MS. received 21*st April* 1960

Abstract. The polarization in proton scattering from nuclear emulsion material has been measured by a counter method at proton energies of 143, 115 and 91 Mev. The results are in good agreement with estimations based on previous results for the constituent elements of the material and provide a good calibration for experiments in which nuclear emulsions are used as a polarization analyser.

§ 1. Introduction

It has already been shown (Feld and Maglic 1958) that the measurement of the asymmetry in scattering of protons in nuclear emulsions promises to be a useful technique in the determination of the polarization of proton beams of low intensity at energies in the region of 150 Mev. It therefore seemed desirable to obtain data of improved statistical accuracy and to extend the measurements over a wider energy range. In order to achieve this in a reasonable time it was decided to use counter techniques rather than actual scanning of emulsions.

§ 2. Experimental Procedure

The external polarized beam from the Harwell cyclotron was used in these measurements. This beam is produced by scattering at about 8° from an internal carbon target and was known to have a polarization $P_1 = 0{\cdot}46 \pm 0{\cdot}01$. This beam passed axially through a solenoid which was capable of producing sufficient magnetic field to precess the proton spins through angles up to 120° in either sense with respect to their initial vertical direction. When this solenoid was correctly aligned, the movement of the beam due to the field was extremely small ($< 0{\cdot}1°$).

Targets were set up in this beam and scattered protons were detected by two scintillation counter telescopes, each consisting of two counters in coincidence, which were capable of rotating in a horizontal plane about a vertical axis through the target. The distances of the counters of each telescope from the target were 96 cm and 130 cm. The effective angles subtended by the counter telescope at the target were 0·8° in the horizontal plane and 1·8° in the vertical plane. The total width at half intensity of the angular resolution curve, measured by rotating the telescope through the direct beam, was 1·4°. Aluminium absorbers were placed between the two counters in each telescope to set a lower limit to the proton energy which could be detected. This lower limit was usually about 9 Mev below the mean proton energy.

† Work performed as a Vacation Consultant at Atomic Energy Research Establishment, Harwell.

The emulsion targets were made from stripped G5 emulsions, cut to a suitable size and cemented together. The majority of the measurements were made with a target of surface density 0·945 g cm^{-2}, but some of the measurements at large angles were made with a 1·6 g cm^{-2} target. Measurements were also made at some angles on carbon and silver, using targets of surface density 1·41 g cm^{-2} and 0·815 g cm^{-2} respectively.

The energy of the proton beam was measured by means of a range curve, using the aluminium absorbers between the counters. The energy of the beam at the centre of the emulsion target was found to be 143 MeV, with a spread of ± 4 MeV at half intensity. For measurements at lower energies, CH_2 absorbers were placed in the beam between the solenoid and the target, and a collimator was placed between the absorbers and the target to ensure that the beam width was not appreciably increased by multiple scattering in the absorber. This resulted in a reduction of beam intensity by a factor of about three at 115 MeV and about six at 91 MeV, relative to the intensity at 143 MeV. The proton beam was monitored by an ionization chamber placed in the beam at about 2 metres behind the target. The total charge was measured by means of a current integrator.

For each measurement the counts in the left and right telescopes were recorded for equal monitor counts with the solenoid field off and with the field required to precess the proton spins through 120°. Background runs were also made under both field conditions with the target removed and an equivalent thickness of aluminium added to the absorbers between the counters. Background counting rates were usually less than 10% of the rates with the target in place. Then if L and R are the counting rates, with background subtracted, we have

$$\epsilon = \left(\frac{L}{R}\right)_0 \times \left(\frac{R}{L}\right)_{120°} = \frac{1+P_1P_2}{1-P_1P_2} \times \frac{1+\frac{1}{2}P_1P_2}{1-\frac{1}{2}P_1P_2}$$

where P_1 is the polarization of the proton beam and P_2 the polarization produced by the target. Thus from the measured values of ϵ the values of P_2 were calculated. In this method all systematic errors are negligible, except that due to lateral movement of the beam direction resulting from changing the solenoid field. This movement was measured by exposing x-ray films in the beam at the target and at about 150 cm behind the target. The centre of gravity of the beam was then determined by scanning the films with a micro-densitometer. The shifts were of the order of 0·03° for one field direction and 0·08° for the other, with respect to the zero field direction. They varied slightly for different conditions of absorber and collimators, and were measured to an accuracy of about $\pm 0{\cdot}015$° for each condition under which runs were made. Corrections were then made to the value of ϵ, using these shift measurements combined with the measured variation of scattering cross section with angle for each target. In the first set of runs measurements were made with both field directions and the two values of $(R/L)_{120°}$ were corrected separately. These corrected values agreed well within the statistical errors and the mean value was taken for the evaluation of ϵ. In later runs measurements were only made with the field direction which gave the smaller shift ($\sim 0{\cdot}03$°). Under the most unfavourable conditions the uncertainty of $\pm 0{\cdot}015$° in the beam direction resulted in an uncertainty of the order of $\pm 0{\cdot}01$ in the final value of P_2.

§ 3. Results

The final results obtained for carbon, emulsion and silver are shown in the table. In calculating the errors shown in this table, all known sources of error

Energy (Mev)	θ (deg)	$\theta\sqrt{E}$ (deg Mev$^{1/2}$)	Polarization P_2 Carbon	Emulsion	Silver
143	6·45	77	0·457 ± 0·015	0·373 ± 0·010	
	7·0	84		0·399 ± 0·017	
	7·65	92	0·459 ± 0·015	0·440 ± 0·017	0·398 ± 0·026
	9·0	108		0·422 ± 0·015	0·402 ± 0·022
	10·5	126	0·530 ± 0·015	0·440 ± 0·030	0·376 ± 0·035
	12·0	144	0·586 ± 0·018	0·479 ± 0·030	0·365 ± 0·061
	14·0	167		0·454 ± 0·040	
	16·0	192		0·662 ± 0·050	
	20·0	239		0·680 ± 0·050	
	22·0	263	0·955 ± 0·045	0·699 ± 0·070	
115	6·7	72		0·226 ± 0·020	
	7·0	75	0·378 ± 0·026	0·276 ± 0·015	0·202 ± 0·015
	9·0	96·5	0·415 ± 0·028	0·295 ± 0·020	0·285 ± 0·040
	11·0	118	0·392 ± 0·036	0·322 ± 0·030	0·122 ± 0·070
	13·0	140	0·305 ± 0·050	0·230 ± 0·046	0·15 ± 0·10
	15·0	161	0·455 ± 0·070	0·364 ± 0·061	
91	7·5	71·5	0·292 ± 0·085	0·150 ± 0·030	0·178 ± 0·036
	10·0	95·5	0·287 ± 0·045	0·214 ± 0·032	0·130 ± 0·046
	12·5	119	0·335 ± 0·087	0·157 ± 0·046	0·107 ± 0·095
	15·0	143	0·272 ± 0·083	0·096 ± 0·076	
	17·5	167		0·21 ± 0·13	

have been included except that due to the uncertainty of the value of P_1, which has been taken to be 0·46. The value of the polarization from carbon at 7·65° is seen to be 0·459 ± 0·015, in good agreement with previous Harwell measurements. For the absolute values of P_2 it would therefore seem reasonable to take $P_1 = 0{\cdot}46 \pm 0{\cdot}008$, in which case an error of $\pm 0{\cdot}018 P_2$ should be added in quadrature with the errors shown in the table.

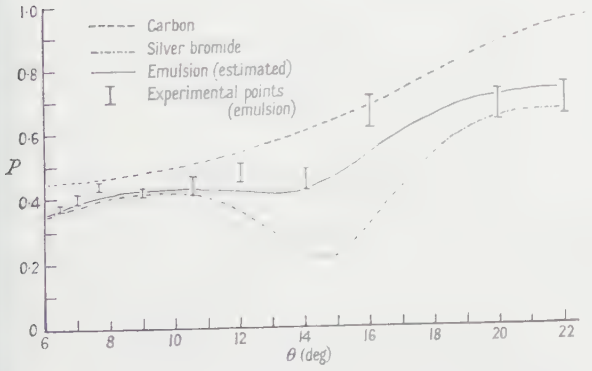

Figure 1. Polarization plotted against scattering angle, 143 Mev.

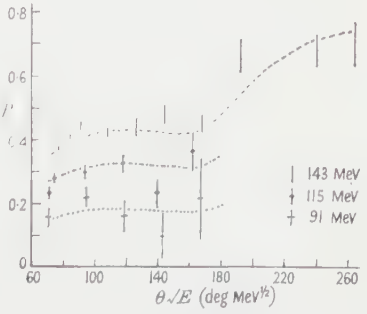

Figure 2. Polarization plotted against $\theta\sqrt{E}$.

The emulsion results at 143 Mev are also shown in figure 1. The bottom curve in figure 1 is an estimate for the polarization from AgBr based on the previous measurements for Ag (Dickson, Rose and Salter, unpublished). The top curve

is the polarization for carbon (Dickson and Salter 1957) and the middle curve is an estimate for emulsion, assuming that the contribution from the light elements is equal to that from the same mass of carbon. The ratio of the masses of light elements to that of AgBr in the emulsion was assumed to be 0·19. It will be seen that the measured polarization from emulsion agrees well with the estimated curve. The polarization at small angles is determined mainly by the AgBr but at angles near the diffraction minimum of AgBr the scattering from the light elements becomes comparable and consequently the polarization remains reasonably high.

The emulsion results at all three energies are shown in figure 2. The polarization is plotted against $\theta_{\backslash} E$, since one would expect the general shape of the curves to be similar on this scale. It will be seen that the polarization falls off fairly rapidly with decreasing proton energy. The weighted mean values for the average polarization for $70 < \theta_{\backslash} E < 170$ are $0{\cdot}412 \pm 0{\cdot}010$, $0{\cdot}275 \pm 0{\cdot}012$ and $0{\cdot}172 \pm 0{\cdot}020$ at 143, 115 and 91 Mev respectively. (The errors include the error in P_1.)

The mean value at 143 Mev is not in agreement with the results of Feld and Maglic (1958), who obtained an average value of $0{\cdot}60 \pm 0{\cdot}06$ at a mean proton energy of 135 Mev for scattering angles between 5° and 12°. At angles greater than 12° the results are in agreement, within the statistical errors. It may be significant that the region of disagreement is that in which the cross section is varying most rapidly with scattering angle and hence where the asymmetries are most sensitive to small angular errors. It seems possible that such false asymmetries may arise in the method used by Feld and Maglic, either due to distortion of the emulsion in processing or by the effects of multiple scattering.

Acknowledgments

The author would like to thank Mr. B. Rose, Mr. A. E. Taylor and Dr. D. Edwards for the use of their apparatus and for their advice and assistance, and the cyclotron crew for running the machine.

References

Dickson, J., and Salter, D. C., 1957, *Nuovo Cim.*, **6**, 238.
Feld, B. T., and Maglic, B. C., 1958, *Phys. Rev. Letters*, **1**, 376.

The Photoproduction of Charged Pions from Deuterium

By J. G. Rutherglen and J. K. Walker
Department of Natural Philosophy, University of Glasgow

MS. received 3rd May 1960

§ 1. Introduction

An experimental determination of the ratio of π^- to π^+ mesons photoproduced from deuterium is of considerable importance in the verification or otherwise of current theoretical predictions. The angular and energy dependence of the ratio has been studied by a number of workers and the results

have been discussed in some detail by Moravcsik (1957). The experiment reported here describes measurements of the ratio at a laboratory angle of 125 and gamma-ray energies in the range 190–240 MeV.

§ 2. Apparatus

A liquid target of effective thickness 0·238 g cm^{-2} of hydrogen or 0·575 g cm^{-2} of deuterium was exposed to the 240 MeV bremsstrahlung from the Glasgow electron synchrotron. Pions were detected by means of a scintillation counter telescope at a mean laboratory angle of 125° to the photon beam.

The telescope consisted of three scintillation counters. Particles which stopped in the second counter were defined by a 123 coincidence-anticoincidence. Mesons were separated from electrons and protons by means of their dE/dx and E pulse heights from counters 1 and 2.

These pulse heights were recorded by photographing a cathode-ray tube spot display, in which the coordinates of each spot were proportional to the pulse heights C_1 and C_2 from counters 1 and 2. Positive pions were identified by their characteristic $\pi^+ \rightarrow \mu^+$ decay in counter 2. The detection scheme required a coincidence between the meson signal and a delayed signal from the muon. A second cathode-ray tube spot display was used for recording C_1 and C_2 pulse heights which were accompanied by delayed coincidences. Typical spot pictures with a liquid hydrogen target are shown in figure 1, in which the

Figure 1. The three groups of spots correspond to electrons, mesons and protons from left to right respectively. The larger spots represent those events for which there has been a delayed coincidence.

'ordinary' and 'delayed coincidence' pictures have been superimposed, the latter being shown by heavy dots. It will be seen that about 50% of π^+ mesons were accompanied by recorded delayed coincidences. Thus the efficiency for recording a delayed coincidence was determined from the hydrogen runs and was used in the analysis of measurements on deuterium.

The counter thicknesses were such that pions stopping in counter 2 had an energy range at creation from about 18–28 MeV. For measurements of pions

of higher energy, absorbers of carbon were placed between the target and the telescope. Corrections were made for decay in flight, nuclear absorption and losses due to events in which π^- star products produce vetoes by entering the anticoincidence counter. The individual correction due to any one of these sources was never greater than 4%.

§ 3. Results

Four sets of data were taken with different absorbers to cover the pion energy range from 20–50 MeV from both the hydrogen and deuterium targets.

E (MeV)	θ_{lab} (deg)	E_γ (MeV)	π^-/π^+
17·8–27·8	125	190–209	$1{\cdot}45 \pm 0{\cdot}11$
28·8–36·6	125	210–226	$1{\cdot}27 \pm 0{\cdot}12$
37·1–44·0	125	227–240	$1{\cdot}43 \pm 0{\cdot}25$
45·2–51·5	125	—	$1{\cdot}83 \pm 0{\cdot}71$

The π^-/π^+ ratios for the four runs are shown in the table. It should be noted that the highest energy run is beyond the kinematic limit of 43·7 MeV for pion production at 125° from a free nucleon by 240 MeV bremsstrahlung gamma rays. Mesons are only produced in this energy region because of the finite momentum of the nucleons in the deuterium. The angular variation of the π^-/π^+ ratio from deuterium as a function of energy has been discussed in some detail by Moravcsik (1957). Figure 2 and 3 are reproduced from Moravcsik's paper with

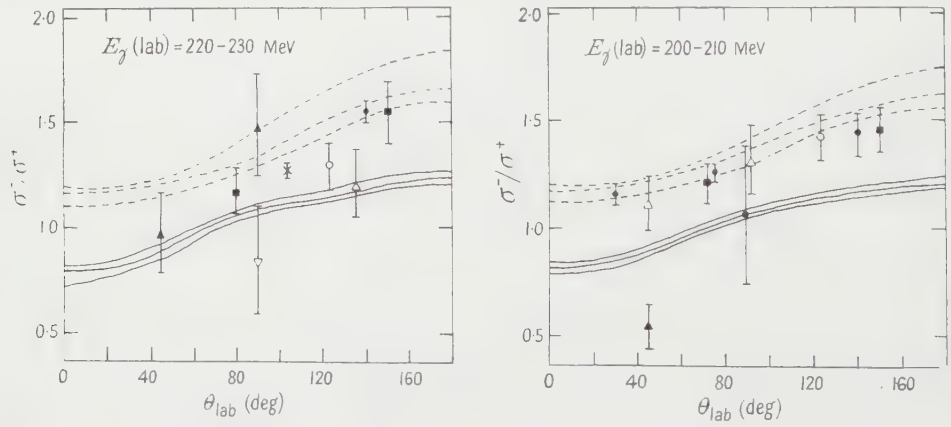

Figures 2 and 3. The angular distribution of the ratio of π^- to π^+ mesons photoproduced from deuterium. The solid and broken curves are the ordinary and 'adjusted' versions of the theory due to Moravcsik (1957), whose paper should be consulted for references to the previous experimental data. The present results are represented by open circles.

the addition of the present data in the form of open circles from the three lowest energy runs. The point in figure 2 is the weighted mean of the data from 210–240 MeV. It will be seen that the agreement with previous experimental data is good and gives further support to the 'adjusted' version of the theory.

The majority of the previous data was taken with bremsstrahlung end-point energies between 300 and 500 MeV. Thus the present results give a satisfactory confirmation that the previous results were not appreciably affected by contributions from gamma rays of energy much higher than that appropriate to the free nucleon case.

ACKNOWLEDGMENTS

The authors wish to thank Dr. W. McFarlane and the synchrotron technicians for their co-operation, Dr. W. Hogg for the provision of liquid targets and Professor P. I. Dee for the interest shown in the work. One of us (J. K. W.) expresses appreciation to the Department of Scientific and Industrial Research for a maintenance grant held during the course of this work.

REFERENCE

MORAVCSIK, M. J., 1957, *Phys. Rev.*, **105**, 267.

Relativistic K Shell Stopping Power Theory

BY H. S. PERLMAN

Physics Department, University of Melbourne

Communicated by P. Swan; *MS. received 29th March* 1960

Abstract. The contribution of the K shell to the stopping power of mercury for relativistic electrons is calculated using Dirac wave functions and the Møller interaction. The results are compared with those of approximately relativistic calculations.

---

§ 1. INTRODUCTION

ALTHOUGH theoretical estimates of the stopping power contributions of individual shells are not readily susceptible to empirical verification, one can, to some advantage, compare the individual contributions predicted by different theoretical treatments. To this end, we will quickly review the results of previous calculations.

By way of delineation, interest here is confined to the average energy lost per unit length traversed by the electrons, variations from the average, i.e. straggling, being ignored. Further, we are interested only in energy losses due to non-radiative collisions with isolated atoms. Accordingly density effect considerations are not relevant here.

The non-relativistic theory developed by Bethe (1930) employs the Born approximation and hydrogenic Schrödinger wave functions. For incident electrons it gives (cf. Bethe and Ashkin 1953),

$$-\left(\frac{dE}{dx}\right)_{\mathrm{K}} = \frac{4\pi e^4 N(1+f/2)}{m_0 v^2}\left\{\ln\left(\frac{m_0 v^2}{2I_{\mathrm{K}}}\sqrt{\frac{e}{2}}\right) + \text{correction terms } \mathrm{O}\left(\frac{I_{\mathrm{K}}}{E^0}\right)\right\} \quad \ldots\ldots(1.1)$$

where f denotes the total oscillator strength of all optical transitions from the two K states to all unoccupied states, N the number of atoms per unit volume and $\bar{I}_K$ the so-called mean ionization potential of the K shell, which together with f has been computed for different atoms.

The relativistic theory developed by Møller (1932) and Bethe (1933) using the Moller interaction, in Born approximation, with Darwin atomic wave functions and the assumption $Z\alpha \ll 1$, yields

$$-\left(\frac{dE}{dx}\right)_K = \frac{2\pi e^4 N}{m_0 v^2}(1+f/2)\left\{\ln\frac{2m_0\gamma^2 v^2(E^0-m_0c^2)}{\bar{I}_K{}^2} + \frac{1}{8}\left(\frac{\gamma-1}{\gamma}\right)^2 - \left[3-\left(\frac{\gamma-1}{\gamma}\right)^2\right]\ln 2 + \frac{1}{\gamma^2} + \text{correction terms } O\left(\frac{I_K}{E^0}\right)\right\} \quad \ldots\ldots (1.2)$$

where the parameters $\bar{I}_K$ and f are identical with those in (1.1).

A word of explanation is necessary regarding the source of equations (1.1) and (1.2). Both these results involve some modification of the usual expressions quoted in this connection (cf. Bethe and Ashkin 1953, pages 254–5, equations (51) and (52)).

In the first place, for electrons, the theory has hitherto been considered only for hydrogen and helium where $1+f\,2=2$, there being no higher occupied states, and further the higher order corrections have been ignored. But for heavy incident particles, both these effects, namely, the exclusion of transitions to occupied states and the higher order corrections, have been considered (Brown 1950, Walske 1952, 1956). The former effect can be incorporated plausibly into electron K stopping though the correction terms probably need some modification (hence (1.1)).

In the second place, both these effects have hitherto been considered explicitly only in non-relativistic work. Incorporation into relativistic electron K stopping theory is seemingly straightforward (hence (1.2)).

§ 2. Present Calculations

For heavy atoms, with many upper shells occupied, the probability of discrete excitation of a K electron is considerably diminished. This fact, together with the effect of the weighting by E^0-E^1, the energy loss of the incident electron, which is much larger for ionizing collisions, provides ample justification for the approximation to the total K shell stopping power $-(dE/dx)_K$.

$$-\left(\frac{dE}{dx}\right)_K = N\int\int(E^0-E^1)\Phi' dq dW \quad \ldots\ldots (2.1)$$

Φ' being the differential cross section for K ionization derived by Perlman (1960) using Dirac atomic wave functions and the Møller interaction.

The K shell stopping powers for mercury were computed from (2.1) employing the results for the Φ' implicit in Perlman (1960).

Just one point of difficulty need be mentioned. The E^0-E^1 factor weights the predominant contribution in the W integration somewhat towards larger W as compared with the total cross section calculation. But the values of p (and W) chosen for the evaluation of the Φ''s (i.e. ultimately the Dirac continuum wave functions) were such as to accommodate a total cross section calculation and

consequently there is a slight dearth of Φ' values in the upper W region. This was remedied by extrapolation, but it will be appreciated that the stopping powers are accordingly less accurate here than the corresponding total cross sections of Perlman (1960). Even so, the final error in the results (see figure) is probably less than 10%.

§ 3. Discussion

Comparing theoretical K stopping powers, one might expect that at high incident energies, where the unknown correction terms in (1.2) are negligible, the results entailed by (1.2) with $\bar{I}_K$ and f as given by non-relativistic considerations (see Bethe and Ashkin 1953, table 1) would agree quite well with the present relativistic calculations. Examination of the figure indicates that this is grossly untrue for heavy elements.

The reason for this is that in the derivation of (1.2) it is assumed both implicitly, through the use of Darwin wave functions, and also explicitly, that $Z\alpha \ll 1$, and of course this is not so for mercury.

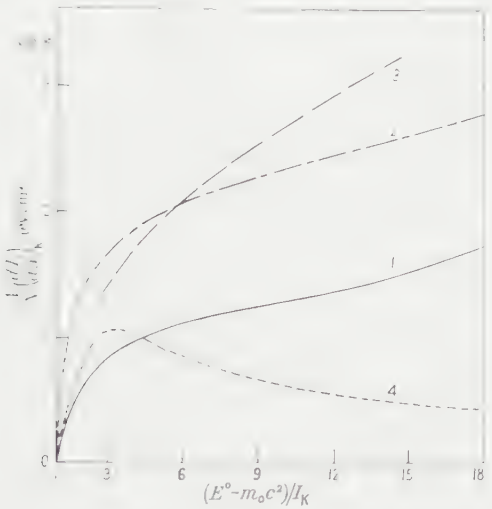

K stopping powers of Hg for electrons. 1, Exact relativistic (present work); 2, semi-relativistic (Bethe *et al.*, cf. eqn (1.2)) ; 3, †Darwin semi-relativistic (present work); 4, non-relativistic (Bethe *et al.*, cf. eqn (1.1)).

† The present ' Darwin semi-relativistic ' values differ from the Bethe ' semi-relativistic' in that the latter involve the additional explicit approximation $(Z\alpha)^2 \ll 1$.

Consequently, one cannot, with any justification, employ $\bar{I}_K$, as determined by Bethe and co-workers, together with (1.2), for the calculation of the K stopping of electrons by medium to heavy elements.

That this same kind of observation would also apply to heavy particle K stopping at relativistic incident energies (in excess of say 100 Mev for protons) is clear. But further, the calculations of Jamnik and Zupancic (1957) indicate that even for slow protons (1 Mev), the use of Dirac rather than Schrödinger wave functions for the K electrons of heavy elements affects the K ionization cross sections (and derivatively, K stopping powers) by factors of up to two.

It seems reasonable to conclude, therefore, that for the heavier elements, the K stopping power theory for heavy particles developed by Bethe, Brown and Walske is also in significant error at all incident energies in excess of a few times the K ionization energy. This is of course qualitatively just what one would expect, since their work ignores relativity completely. What is surprising, however, is the extent of the error that appears to be committed thereby even at low incident energies.

Acknowledgment

The author wishes to express his gratitude to Associate Professor C. B. O. Mohr for his continued encouragement and assistance.

References

Bethe, H., 1930, *Ann. Phys., Lpz.*, **5,** 325.
—— 1933, *Handb. d. Phys.*, **24,** 273 (Berlin: Springer).
Bethe, H., and Ashkin, J., 1953, *Experimental Nuclear Physics*, Vol. I, ed. E. Segrè (New York: John Wiley).
Brown, L., 1950, *Phys. Rev.*, **79,** 297.
Jamnik, D., and Zupancic, C., 1957, *Mat. Fys. Medd. Dan. Vid. Selsk*, **31,** No. 2.
Møller, C., 1932, *Ann. Phys., Lpz.*, **14,** 531.
Perlman, H. S., 1960, *Proc. Phys. Soc.*, **76,** in the press.
Walske, M., 1952, *Phys. Rev.*, **88,** 1283.
—— 1956, *Ibid.*, **101,** 940.

LETTERS TO THE EDITOR

On the Ehrenberg Franks Experiment relating to the Penetration of Electrons into Luminescent Material

Ehrenberg and Franks (1953) have examined the penetration of electrons into luminescent crystals by a microscopic method based on the luminous figure produced by a narrow bundle of electrons incident on the crystal. They suggested that the range–energy relation observed would be satisfied by a formula of the type $R = V^2/c + d$, where c and d are empirical constants; the magnitude of the zero-energy range d varies between 1·3 and 3·7 μ for the crystals investigated, and its occurrence is attributed to diffusion of slow electrons, excitons, or radiation. Recent measurements, according to a personal communication from Dr. Ehrenberg, have, however, indicated a very much smaller value of d, so that the values quoted must now be taken as upper limits.

The constant d can be interpreted by the ambipolar diffusion of released secondaries (electrons and holes). Broser and Broser-Warminsky (1958) estimate the upper limit of ambipolar diffusion length at 1 μ in CdS crystals. The diffusion length of excitons is considerably larger, having the magnitude of millimetres (Auth and Rideer 1959, Balkanski and Waldron 1958, Diemer *et al.* 1958).

Our recent studies on diffusion processes in cathodoluminescence have given 0·05–0·1 μ for the length of ambipolar diffusion in several types of luminescent crystals. These values were deduced from the voltage dependence of cathodoluminescence. The details of our studies will be published in a forthcoming paper.

The upper limit of the ambipolar diffusion length can be experimentally determined respectively estimated by the Ehrenberg–Franks experiment.

The author wishes to express his sincere thanks to Dr. W. Ehrenberg for valuable comments and for informing him of results recently obtained in his laboratory.

Research Institute for
Telecommunication,
Budapest, Hungary.

Gy. Gergely.

2nd May 1960.

Auth, V., and Rideer, R., 1959, *Ann. Phys., Lpz.*, **2**, 351.
Balkanski, M., and Waldron, R. D., 1958, *Phys. Rev.*, **112**, 123.
Broser, I., and Broser-Warminsky, R., 1958, *J. Phys. Chem. Solids*, **6**, 386.
Diemer, G., van Gurp, G. J., and Hoogenstraaten, W., 1958, *Philips Research Reports*, **13**, 458, and **14**, 11.
Ehrenberg, W., and Franks, J., 1953, *Proc. Phys. Soc.* B, **66**, 1057.

A Proposed Method for Measuring Ranges of Heavy Ions in Solids

Shallow ionization chambers (Holloway and Livingston 1938) or cloud chambers (Blackett and Lees 1932) are commonly used for the determination of ranges of heavy ions in gases. The ionization efficiency decreases sharply at the end of the range of the ion but is sufficient for consistent data of the extrapolated range to be obtained. In the case of solid absorbers one commonly reduces the energy of the ion by interposing a foil of measured surface density to absorb the greater part of the particle energy. The residual range is then measured with a shallow ionization chamber and is estimated by use of suitable conversion factors to convert the range in air to the range of the solid absorber in question. Another method is to use a multi-layer target to stop the heavy ions. The distribution of range is then determined by measuring the number of stopped ions in each of the target layers. This method is suitable for the range measurements of radioactive isotopes (Katcoff, Miskel and Stanley 1948) since sensitive tools, such as a radio-chemical analysis are required to establish the number of ions stopped in each layer. It is proposed to measure range–energy relations of heavy ions by the following method: A 'thick' target is bombarded with mono-energetic ions whose range–energy relation in the target material is to be established. The ions will come to rest inside the target at an average range R. The target is next bombarded with protons of energy E_1 to produce resonance reactions with the embedded ions. This energy is higher than the energy E_2 at which the particular resonance reaction would have taken place if the ion had not penetrated a thickness R into the target material. The range of the heavy ion is thus measured in terms of the rate of energy loss of protons in the target.

The feasibility of this method is illustrated by the following example: Suppose that the range of slow carbon ions in gold has to be measured. A gold target, thicker than the range of the ions, is bombarded with mono-energetic carbon ions of energy E_c. The ions will come to rest in the gold target at a mean range R_c. An ion current of 5μA for one hour will leave about 10^{17} carbon particles embedded in the gold target, corresponding to a carbon target of approximately $1\mu g\,cm^{-2}$ surface density. The target is then bombarded with protons of energy E_1 to produce known resonances in C, e.g. $C(p,p'\gamma)C$ with $E_\gamma = 4{\cdot}40$ MeV and $\sigma_{inel.} = 6{\cdot}8$ mbn sterad^{-1} (Maeder, Martin, Miller and Schneider 1954). A carbon foil is next introduced in the path of the protons to produce the resonance at the surface of the foil and thus at a lower proton energy E_2, say. Knowing the rate of energy loss of protons in gold we easily calculate the mean range R_c of the carbon ions

$$R_c(E_c) = \int_{E_1}^{E_2} \frac{dE}{(dE/dx)_{E_p}}$$

where $E_p = \frac{1}{2}(E_1 + E_2)$ with a good approximation. Assuming a normal distribution for the straggling of the range of ions we obtain

$$\Omega_c^2 = \Omega^2 - \Omega_p^2$$

where Ω_c^2 is the mean square deviation of the carbon ion range, Ω^2 the measured mean square deviation and Ω_p^2 represents the resonance width of the protons and its broadening due to the energy loss of the protons in the target material. The latter is a small quantity and, furthermore, can be calculated from theory.

The method has limitations in that suitable resonance reactions of sufficient cross section are required for this measurement. On the other hand there is no need for preparation of thin uniform foils which tend to rupture due to the high energy loss of the heavy ions per unit path length. Also there is no need to measure the thickness of the foil since the range is obtained in terms of the known rate of energy loss for protons. It should therefore be also suited to the measurements of ranges in chemically active targets which could then be evaporated *in situ*.

The Physical Laboratories,
The University,
Manchester.
6th May 1960.

D. I. Porat.
K. Ramavataram.

Blackett, P. M. S., and Lees, D. S., 1932, *Proc. Roy. Soc.* A, **134**, 658.
Holloway, M. G., and Livingston, M. S., 1938, *Phys. Rev.*, **54**, 18.
Katcoff, S., Miskel, J. A., and Stanley, C. W., 1948, *Phys. Rev.*, **74**, 631.
Maeder, D., Martin, M., Miller, R., and Schneider, H., 1954, *Helv. Phys. Acta*, **27**, 166.

Estimation of Inelastic Collision Cross Section from Electron Mobility Measurements†

A number of investigators have expressed the mobility of electrons at high electric fields in slightly ionized gases in terms of integrals involving the collision cross sections and the distribution function of electron velocities, which has to be obtained from a complex differential equation. The enormous complexity of these expressions, when inelastic collisions are also considered makes any estimation of the cross sections extremely difficult, if not impossible.

In this communication the author has used an approach similar to that used by Shockley (1951) and others in semiconductors, to develop a method for order of magnitude estimation of the inelastic collision cross sections from the mobility data.

To keep the analysis simple the following assumptions have been made: (i) The inelastic collisions in which the electron gains energy from the molecule are negligible. (ii) The cross sections for elastic collisions and inelastic collisions in which an electron loses an energy ϵ_j to the molecule are both proportional to v^n, where v is the electron velocity. This is a very restrictive assumption but should be satisfactory for order of magnitude determinations. (iii) The velocity distribution of electrons in the presence of an electric field is Maxwellian, corresponding to a temperature T, higher than the gas temperature T_0. Thus the number of electrons per unit volume having velocities between x and $x+dx$ is given by

$$N(x)dx = Ax^2 \exp(-x^2/\lambda)dx \qquad \ldots\ldots(1)$$

where $x = (m/2\boldsymbol{k}T_0)^{1/2}v$ is the dimensionless velocity, $\lambda = \Gamma/\Gamma_c$, m is the electronic mass, and $\boldsymbol{k}$ is Boltzmann's constant.

† Work supported by Armour Research Foundation, Chicago, U.S.A.

The collision frequency ν of an electron is given by

$$\nu = \nu_1 + \nu_2 \qquad \ldots\ldots (2)$$

where

$$\nu_1 = n_0 \sigma_1 v = a_1 x^n, \qquad \ldots\ldots (2a)$$

$$\left.\begin{aligned} \nu_2 &= n_0 \sigma_2 v = a_2 x^n, \quad \text{when } x > x_0, \\ \nu_2 &= n_0 \sigma_2 v = 0, \qquad \text{when } x < x_0, \end{aligned}\right\} \qquad \ldots\ldots (2b)$$

n_0 is the number of neutral molecules per unit volume, suffixes 1 and 2 refer to the elastic and inelastic collisions respectively, σ is the collision cross section,

$$a = n_0 \sigma (2\boldsymbol{k} T_0/m)^{n/2}/v^{n-1}$$

and

$$x_0^2 = m v_0^2/2\boldsymbol{k} T_0 = \epsilon_0/\boldsymbol{k} T_0.$$

The drift mobility of electrons, obeying Maxwellian distribution of velocities is given by

$$\mu = \frac{e}{m} \frac{\langle x^2/\nu \rangle}{\langle x^2 \rangle}, \qquad \ldots\ldots (3)$$

where e is the electronic charge.

Using equations (1), (2) and (3) we obtain

$$\mu = \frac{4e(a_1 + a_2)^{-1} \lambda^{-n/2}}{3m\pi^{1/2}} \left[\Pi\left(\frac{3-n}{2}\right) + \frac{a_2}{a_1} \int_0^{x_0^2/\lambda} y^{(3-n)/2} e^{-y} dy \right], \qquad \ldots\ldots (4)$$

where $$y = x^2/\lambda \quad \text{and} \quad \Pi(z) = \int_0^\infty y^z e^{-y} dy$$

is a tabulated function (Jahnke and Emde 1945). The average rate of energy loss by an electron due to collisions is given by

$$\left(\frac{\partial \epsilon}{\partial t}\right)_{\text{collision}} = \left\langle -\frac{2m}{M} \tfrac{1}{2} m v^2 \nu_1 \right\rangle + \left\langle -\epsilon_0 \nu_2 \right\rangle, \qquad \ldots\ldots (5)$$

since an energetic electron (at high electric field) loses a fraction $2m/M$ of its energy in an elastic collision with a molecule, where M is the mass of the neutral molecules.

In steady state the power gained by the electron from the electric field E should be equal to that lost by the electrons in collisions. Hence using equations (1), (2) and (5) we obtain

$$e\mu E^2 = \frac{4m\boldsymbol{k} T_0}{M\pi^{1/2}} a_1 \lambda^{(n+2)/2} \Pi\left(\frac{3+n}{2}\right) + \frac{2a_2 \epsilon_0 \lambda^{n/2}}{\pi^{1/2}} \left[\Pi\left(\frac{n+1}{2}\right) - \int_0^{x_0^2/\lambda} y^{(n+1)/2} e^{-y} dy \right]. \qquad \ldots\ldots (6)$$

At low electric fields, where the electrons are not energetic enough to have appreciable inelastic collisions, equations (4) and (6) reduce to

$$e\mu E^2 = \frac{4m\boldsymbol{k} T_0}{M\pi^{1/2}} a_1 \lambda^{(n+2)/2} \Pi\left(\frac{3+n}{2}\right) \qquad \ldots\ldots (6a)$$

and

$$\mu = \frac{4e\lambda^{-n/2}}{3m\pi^{1/2} a_1} \Pi\left(\frac{3-n}{2}\right). \qquad \ldots\ldots (4a)$$

Eliminating λ between equations (6 *a*) and (4 *a*) we get

$$\mu = \left\{\frac{4}{3\pi^{1/2}}\,\Pi\left(\frac{3-n}{2}\right)\right\}^{(n+2)/(2n+2)} \left\{\frac{4}{\pi^{1/2}}\,\Pi\left(\frac{3+n}{2}\right)\right\}^{n/(2n+2)} \frac{\boldsymbol{k}T_0}{M}\left(\frac{e}{ma_1}\right)^{2/n} E^{-n/(n+1)}. \quad \ldots\ldots (7\,a)$$

If we use the distribution function, obtained by Chapman and Cowling (1953), it may be easily shown that for the corresponding case

$$\mu = \frac{(3-n)}{3}\left\{\frac{(n-1)}{3}\right\}^{-n/(n+2)} \frac{\Pi[(1-3n)/(2n+2)]}{\Pi[(1-2n)/(2n+2)]} \frac{\boldsymbol{k}T_0}{M}\left(\frac{e}{ma_1}\right)^{2/n} E^{n/(n+1)}. \quad \ldots\ldots (7\,b)$$

It may be seen that equations (7 *a*) and (7 *b*) are very similar.

Equations (4) and (6) represent a simple parametric relationship between the mobility μ and the electric field E and may be used for the order of magnitude estimation of the inelastic collision cross sections, from the mobility data.

Physics Division,
Armour Research Foundation,
Chicago, Illinois, U.S.A.

M. S. Sodha.

6th May 1960.

Chapman, S., and Cowling, T. G., 1953, *The Mathematical Theory of Non-uniform Gases* (Cambridge: University Press), p. 350.

Jahnke, E., and Emde, F., 1945, *Tables of Functions* (New York : Dover Publications), 4th edition, p. 9.

Shockley, W., 1951, *Bell Syst. Tech. J.*, **30**, 990.

REVIEWS OF BOOKS

Radioisotopes for Industry, by R. S. Rochlin and W. W. Schultz. Pp. ix + 190. (New York: Reinhold, 1959.) 38*s*.

The authors aim to demonstrate the usefulness of radioisotope techniques to engineers and plant managers " with a minimum of unfamiliar jargon and highly technical discussion ". In the space of 152 pages of text, plus appendices, this is a formidable task, tackled with commendable brevity and plain speech. A wealth of examples is presented, sometimes rather too briefly, but with sufficient conviction to encourage industrial readers to follow up details through a widely chosen bibliography.

Economic advantages, entirely in America are stressed, using figures now thought by some to be rather conjectural. Details of training facilities, sources of supply and health regulations are also restricted to the U.S.A. and tend to localize a book which deserves to be more widely read. There is a natural tendency to select American applications, but many foreign advances are scrupulously acknowledged.

The scientific introduction is inadequate and the appendix on ' technical aspects of radioactivity ' helps but little, so the reader is still confronted, without warning, with such terms as deuterons, fast and thermal neutrons.

Provided he is not discouraged, however, the industrial reader as well as the applied scientist should find this little book stimulating and rewarding.

J. L. PUTMAN.

Acoustique Musicale, by Colloques Internationaux du Centre National de la Recherche Scientifique. Pp. 260. (Paris: Editions du Centre National de la Recherche Scientifique, 1959.) 3400 *fr*.

Acoustique Musicale is a handsomely produced report (in French) of the proceedings of an international conference on musical acoustics: it contains a series of papers dealing with the theory of consonance and dissonance, the origin of musical scales, and the physics of musical instruments.

The section on musical instruments deals particularly with those of the violin family, the organ, and other wind instruments. Recent work on the mechanism of sound production, harmonic content, and the role of transients is described, and there is yet another contribution to the search for the ' secret of the Stradivarius '. A paper from the U.S. Navy Electronics Laboratory deals with the typical inaccuracies of pitch to which instruments and instrumentalists are subject in performance.

In order to follow the discussions on consonance and dissonance, the reader will certainly need to be equipped with some knowledge of musical history and elementary harmony. It emerges very clearly that science cannot dictate to music, but can only help to describe and illuminate. Consonance in one context may become dissonance in another.

Music, moreover, embraces more than the work of the classical composers. At least one paper in this volume is devoted to scales in oriental music, and in the reported discussions we find a happy remark about the latest fashion in western music: " Je suis heureux d'apprendre que les musiciens ' concrets ' se

rendent compte de la nécessité de se donner des règles; je leur souhaite bonne chance ". H. R. ALLAN.

Experimental Nuclear Physics, Vol. III, edited by E. SEGRÈ. Pp. ix+811. (New York : John Wiley and Sons, 1959.) 184*s*.

The writer of a modern textbook on theoretical nuclear physics can develop his subject along well-defined lines. There exists for him an adequate framework of nuclear models and interactions and a wealth of experimental data from which he can select illustrative material. In undertaking the converse task of providing an expert survey of experimental methods and results, Professor Segrè and his collaborators have faced a more difficult problem. Not only is their subject extraordinarily large and diverse, but it also inevitably leans heavily on theory at many points. The authors have therefore been called on to display gifts of interpretation as well as of exposition and the main articles in the present concluding volume are consequently well-rounded monographs.

The particular volume under review may perhaps be described as a modern version of the classical work of Rutherford, Chadwick and Ellis. It is interesting to note that the traditional division of the subject of radioactivity into discussions of alpha, beta and gamma radiations is still thought to be the best mode of classification. The common features of radioactive decay, however, such as fluctuations and genetic relationships, are presented in a useful introductory article by E. Segrè. This is followed by the chapter on alpha radioactivity (G. C. Hanna) which provides a thorough coverage of the whole field. Early regularities of the subject, such as the Geiger–Nuttall rule, are set within the wider context of recent results and the important interpretations of systematics now offered by the nuclear shell model and the collective model are well brought out. The experimental techniques, including radiochemistry, are treated in adequate detail and there is a comprehensive table of alpha emitters. The following two articles, each written jointly by M. Deutsch and O. Kofoed-Hansen, are equally expert and comprehensive accounts of gamma rays and beta rays. The experimental methods are thoroughly discussed and many useful tables of data are given. The experimentalist is shown clearly not only how, and with what accuracy, measurements may be made, but also how they may be interpreted in terms of nuclear level schemes. The apparatus of interpretation naturally includes discussions of angular correlation theory and of transition probabilities. There is also a useful section on neutrinos, including a very clear account of the analysis of the results of both ' classical ' and modern beta-ray experiments in the light of parity non-conserving interactions. The helicity experiment of Goldhaber, Gradzins and Sunyar is included.

The last edition of the book of Rutherford, Chadwick and Ellis was published in 1930, just at the beginning of the age of nuclear machines. Professor Segrè's work in 1959 must inevitably supplement the classical divisions of the topic of radioactivity by an account of particle accelerators, and this is offered in a stimulating article by E. M. McMillan, who has himself contributed so much to the subject. This chapter admirably conveys the excitement of the development of new machines, and although the detailed illustrations are drawn mainly from the famous accelerators of the Berkeley laboratory, the achievements of other workers are adequately discussed. The article well shows that advance from the earliest accelerators to the alternating gradient synchrotron (beyond which the

author does not proceed) has been an organic growth of theory and practice.

Professor Segrè and his authors are to be congratulated on having made available a permanent record of the status of most of the main branches of experimental nuclear physics, excluding meson physics, in the period 1953–1958. Their work, which must of course be supplemented by regular periodical reviews, will remain a standard reference and a useful handbook for many years to come. The standard of presentation and typography in this volume, as in its predecessors, is excellent.

W. E. BURCHAM.

Introduction to Mathematical Physics, by WILLIAM BAND. Pp. xi + 326. (London, New York : Van Nostrand, 1959.) 54*s*. 6*d*.

This book sets out to cover the entire field of mathematical physics in a single volume of moderate size. It has seven chapters. introduction; the language of mathematical physics; the continuum theory of matter; the molecular theory of matter; the theory of fields; the theory of relativity; quantum theory.

The limitations of such an enterprise are obvious, but nevertheless the reviewer well remembers the use he himself made of the comparable book by Georg Joos. The preface says : " This text is designed for use in courses on theoretical physics, for college senior and graduate students ". Whatever its suitability for the American system, it is clearly not a book that any of our undergraduate courses could be based on since it attempts to cover topics that stretch over from the first to beyond the final year of our courses. It could however find a place in our libraries, particularly for the use of the student of above average ability who is intent on looking ahead of his course and for instance reading about, say relativity, while his compulsory study is still classical mechanics.

However, given the author's aims, to what extent does he achieve them ? In the first place one must note that the author chooses a presenation in which the whole of continuum mechanics is covered before a particle is even mentioned. Not everyone will agree with the author's justification of this plan. However, the book is certainly very readable and much of it is excellently presented. To pick one particular example arbitrarily, the short but clear statement of the nature of the allowed boundary conditions in problems of partial differential equations represents a piece of excellent condensed exposition. Every now and then, however, one encounters a point where one feels that condensation has gone too far. Thus early in chapter 2 one reads on vibrating strings, " the equation of motion is then easily shown to be . . . " and there follows the usual equation for the lateral displacement, including friction in a medium. There is no discussion in the text of the forces involved, merely a diagram with a three-line caption gives some indication how the equation is derived.

To give another example of a rather unusual approach, very early on the scalar product of two vectors is defined in terms of the bilinear sum of Cartesian components. Equation (2.5) then *defines* the angle between two vectors as the scalar product divided by the product of the absolute magnitudes. Then as an *exercise* we find the problem : " Prove that equation (2.5) agrees with the usual definition of angles between two vectors in Euclidean geometry ". Surely this is hardly good first reading for a student!

The book is well produced with many diagrams and sometimes quite extensive sets of exercises at the end of every section.

N. KEMMER.

Crystal Chemistry of Simple Compounds of Uranium, Thorium, Plutonium, Neptunium, by E. S. Makarov. Translated from Russian by E. B. Uvarov. Pp. iii + 145. (New York : Consultants Bureau; London: Chapman and Hall, 1959.) 42*s*.

This book is bound to be useful, even if only as a collection of facts. Two pleasantly brief introductory chapters on the classification of crystal structures into molecular, chain, layer and coordination types, on bond classification, and on intermetallic compound systematics start the book. Then comes a detailed chapter on the structure of the elements in all their phases, and the relationships between these. The compounds grouped according to the addition element, so that it is easy (provided a sixth sense guides one to the first pages of chapter 4) to find the literature reference and a brief statement of the compounds and their stability ranges for any addition. A chapter on ionic radii leads quickly to one on the duality in the chemistry of these elements occasioned by the close balance between 5f and 6d valence states.

It is thorough, up to 1958, and in cases of rival interpretations in the literature, usually gives a judgment as to which is to be preferred. It is not indexed, though it seems intended to a considerable extent to function as a guide to the original literature. A good index would have been a great help to those who want to use it as an occasional reference book. A useful, competent book, almost entirely about its title, but not beyond improvement. W. M. LOMER.

Proceedings of the International Conference on Nuclear Physics, Paris, 1958, edited by P. Gugenberger. Pp. xxiv + 950. (Paris : Dunod, 1959.) 9500 *fr*.

This book is the account of the International Conference on Nuclear Physics held in Paris 7th 12th July, 1958 which dealt with nuclear interactions at low energies and nuclear structure. The sub-headings are elastic scattering; nuclear forces and sizes; direct interaction; heavy ions; photonuclear reactions; independent particle model and connection with the collective model; collective model; structure of nuclear matter; weak interactions (theory and recent experimental results). Each of these topics was presented by one to three speakers following which there was discussion presented verbatim in this volume. The many dozen short prepared contributions that formed the second part of the conference are also given in full in this volume. It is impossible to summarize these proceedings or to do more than say that there were no major surprises and no contributions made for which this volume is likely to be a definitive reference. However, many of the contributions form interesting and valuable alternative presentations of matters already treated in the various review series.

D. H. WILKINSON.

Absorption and Dispersion of Ultrasonic Waves, by K. F. Herzfeld and T. A. Litovitz. (Pure and Applied Physics, Vol. 7.) Pp. xviii + 535. (New York, London: Academic Press, 1959.) $14.50.

The purpose of this book is well set out in the preface; it is to discuss the propagation of ultrasonic waves in fluids, with particular reference to the

mechanism of the absorption process and of the dispersion which usually accompanies absorption. While it avoids the subject of propagation in solids (a fact that might perhaps have been written into the title), it is nevertheless true that much of the theory under discussion may also be applied to solids; the book is therefore of general interest to those using ultrasonic techniques in their investigations.

At the start, there is a lengthy (22 page) introduction which contains a very full summary of the rest of the book. The term ' introduction ' here is not entirely happy; it will introduce a reader, who already has some familiarity with the subject, to what is to come, but the new research student would require some additional guidance from his supervisor before tackling it. One is sorry too that the authors start off in the very first paragraph by appearing to anticipate criticism. This seems unnecessary somehow; the search for the mechanism behind the process is essential to physics and there is no need to defend such searching.

The new research student (or other non-specialist) who omits the introduction and proceeds directly to page 25 will find that he has relatively plain sailing ahead. The book is very readable. All symbols used in the extensive mathematics are clearly defined in a list at the beginning of the book.

The first chapter deals, very rightly, with the Stokes–Navier equations of hydrodynamics (the reader is left to infer which these are) and with classical absorption theory. The next chapter introduces the reader kindly and lengthily to the relaxation process. A short discussion of scattering and high intensity effects complete the first one-third of the book.

The remaining two-thirds discuss the application of the theory to gases and to liquids, introducing additional theory where necessary. Experimental methods are mentioned only briefly, but experimental results are fully presented and discussed.

In the preface, the authors describe the book as half-way between a textbook and a handbook. This is a very fair description. Even although it is not comprehensive in its coverage and its arguments in places bear the authors' personal stamp, it fills most usefully a gap in the present literature and should be of value to all physicists and physical chemists interested in this field.

L. MACKINNON.

La Spectrographie Infrarouge et les Grandeurs Moleculaires, by LOUIS DE BROGLIE. Pp. 128. (Paris: Revue d'Optique Théorique et Instrumentale, 1958.) 1200 *fr.*

This little monograph contains a dozen brief articles by different authors. Their main concern is to outline theoretical methods which underlie the interpretation of infra-red spectra in terms of molecular structure and properties. The articles range from the Born–Oppenheimer approximation (Daudel and Bratoz) through force constants (Barchewitz and Lefebvre), absolute intensity of bands (Legay and Laforgue), chemical reactivity (Josien) to the intricacies of vibration rotation interaction in degenerate vibrations (Amat).

There are also two articles on far infra-red spectra (Lecomte and Hadni). As a thumb-nail sketch of some important aspects of infra-red spectroscopy, this is a useful addition to the literature.

G. B. B. M. SUTHERLAND.

La Théorie Physique au Sens de Boltzmann et ses Prolongements Modernes, by René Dugas. Pp. 308. (Paris : Dunod, 1959.) 3700 *fr.*

René Dugas is already well known as a general historian of mechanics as well as a writer on philosophical problems arising out of the work of the great 17th century scientists. The present book, completed just before his death in 1957 confirms the width of his scholarship and the depth of his understanding when handling the borderline problems of the history and philosophy of science. In it he breaks new ground; for curious though it may seem, the problems of 19th century science have received relatively scant attention on the part of historians, perhaps because of the closeness of that age to our own. Yet because of this it contains material which—as de Broglie points out in a specially written preface—has a moral to point for our own generation of physicists. Throughout his long life Boltzmann's atomistic viewpoint found itself assailed from the side of the school of energetics and other more phenomenologically orientated physicists, such as Mach, Ostwald, Duhem, Hertz. The author traces with fine insight both the physical and the philosophical components of this story which was to end, at a time when Boltzmann's faith was finally to be vindicated, in the latter's suicide in 1906. In our own day, as de Broglie writes, the struggle between the positivist and phenomenological orthodoxy of quantum mechanics and the more charitable proponents of a structural view-point are finding themselves in a similar situation. Boltzmann's researches into classical statistical mechanics, his attempts to reconcile the irreversibility involved in the Second Law with the reversible laws of classical mechanics; his influence on the earliest theories of Planck; and his impact on contemporary theory: all this is traced in meticulous detail without deteriorating into a merely chronological descriptive approach. It constantly retains a sense of direction: that of illuminating Boltzmann's fundamental ideas, and with them, the major tendencies in 19th century physics. This volume fills an important gap in the literature and should be read by all who have even the most marginal interest in the subject. GERD BUCHDAHL.

An Approach to Modern Physics, by E. N. da C. Andrade. Pp. x+254. (London: G. Bell and Sons, 1959.) 27*s.* 6*d.*

In these days when all newspapers have Science Correspondents, and the layman reads of the construction of large and extremely costly machines for studying particles which will never be seen by the human eye, it is fitting that a non-scientist should ask what the results mean, and should wish to follow the developments in theory and experiment which have led to current research. The rapidity of these developments is demonstrated by the necessity after only three years for a revised and expanded edition of this book, itself very different from Professor Andrade's original book *The Mechanism of Nature*, published in 1930. Professor Andrade has succeeded admirably in giving, without using a single mathematical symbol, a very readable and understandable account of the progress of physics from its classical origins to the present day. Chapter VI, about solids and liquids, is a particularly good introduction to this field; as Professor Andrade says, fashions change, and the solid state is now an expanding and fascinating study of great technological importance. The last chapter is a thought-provoking discussion of the possibilities and limitations of physical measurement and theory, and their bearing on causality and determinism. It is

perhaps arguable that some of the elegant results of modern physics, such as the Compton effect, the photoelectric effect and the Einstein relation between energy and mass are so simple to write down in the form of an equation that it is a pity to miss the opportunity of their dramatic effect. This loss is however balanced by the simple and elegant language and the wealth of analogies and illustrations which make Professor Andrade's book a pleasure to read. C. M. P. JOHNSON.

Introductory Nuclear Theory, by L. R. B. ELTON. Pp. ix + 286. (London : Pitman, 1959.) 40*s*.

One of the most popular introductory texts on nuclear physics is *Elementary Nuclear Theory* by Bethe and Morrison, and it is unavoidable that one makes a comparison between that well-known book and the new one by Dr. Elton. To start with they are very similar in scope although the material is handled in a somewhat different manner. Both start with the general properties of nuclei like radii and binding energies, and go on to discuss nuclear forces, the two-body problem, nuclear reactions, disintegration, and nuclear structure. The main difference is that Bethe and Morrison assume the reader to be familiar with the essentials of quantum mechanics, such as the elements of scattering theory and the usual results of first-order perturbation theory in the time-dependent formalism, whereas Elton does not and he therefore develops these points *ab initio*.

Both books concentrate on the physics of the problems posed; but Dr. Elton believes, and states in his preface, that the reader who does not work through the mathematics does not understand the physics; and no doubt that is true of many readers. Nevertheless, one wonders whether the reader who has to be shown explicitly how to remove the centre-of-mass motion in the two-body problem would make very much at this stage of his education of the sections on multipole radiative transitions and on the invariants of β-decay : perhaps there is some lack of balance here. Dr. Elton is probably the first textbook writer to have treated β-decay in terms of the newly established parity violation, and he is to be congratulated on having made a consistent job of it. However, it is alarming to see, in two quite distinct diagrams, the shape of the allowed β-spectrum drawn incorrectly at low energies. In his chapter on nuclear structure Dr. Elton does more justice to the shell model than Bethe and Morrison, and as much justice to the alpha-particle model as it deserves; but neither gives due weight to the collective model, Elton not even mentioning the rotational spectra, a surprising omission in a book that is, on the whole, so up-to-date. Both books end with a table of isotopes and their properties, but Elton's is much more useful, including the magnetic dipole and electric quadrupole moments in addition to the spins. His book also has instructive examples for the more earnest of his readers at the end of each chapter. The third year undergraduate and the first year post-graduate will find it very useful to have one or other of these two books, but perhaps not both. Of the two, Bethe and Morrison's is the more consistently elementary and physical, Elton's the more explicitly mathematical and difficult.

B. H. FLOWERS.

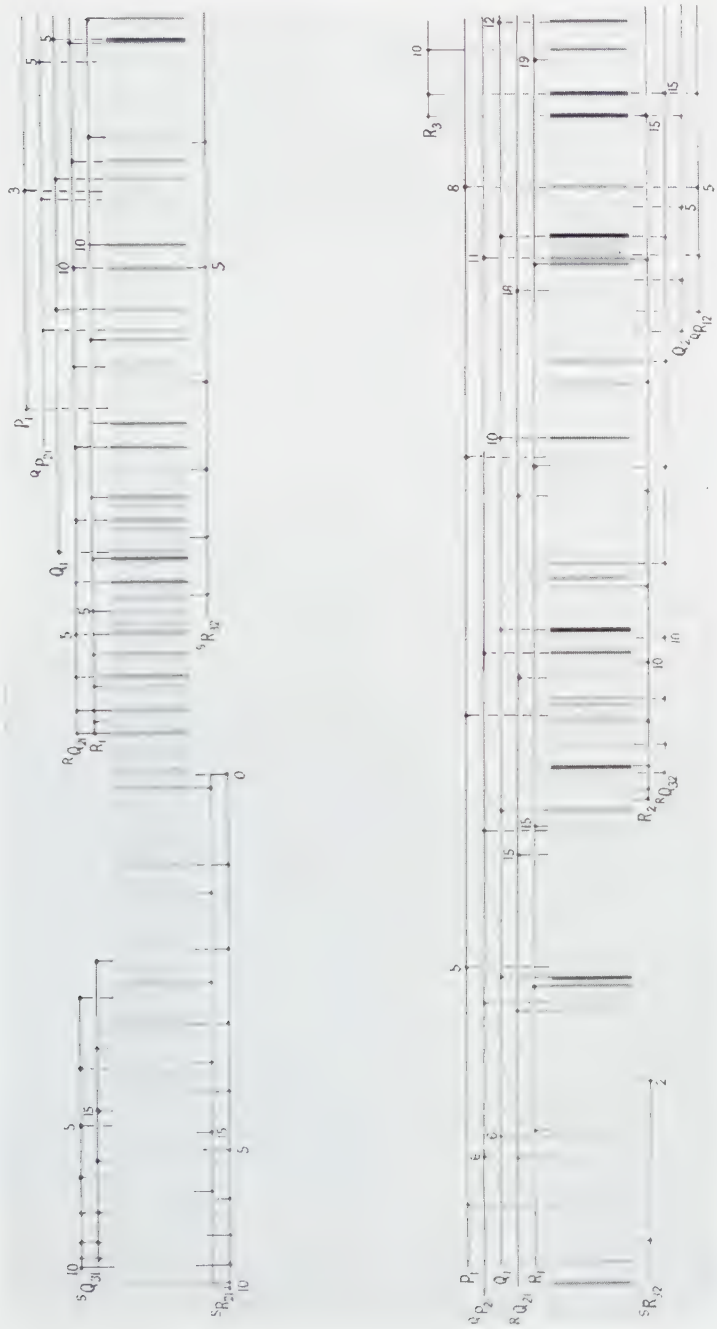

Figure 2. Reproduction of part of the 5-1 band of the B' -B system. The original spectrum was contact printed on to a high contrast plate and then enlarged. During enlargement the paper was moved parallel to the lines to improve the appearance of the spectrum. To avoid confusion the lower J lines of the head-forming branches are not shown except in the case of $^{S}R_{21}$ and $^{S}Q_{31}$.

Plate I

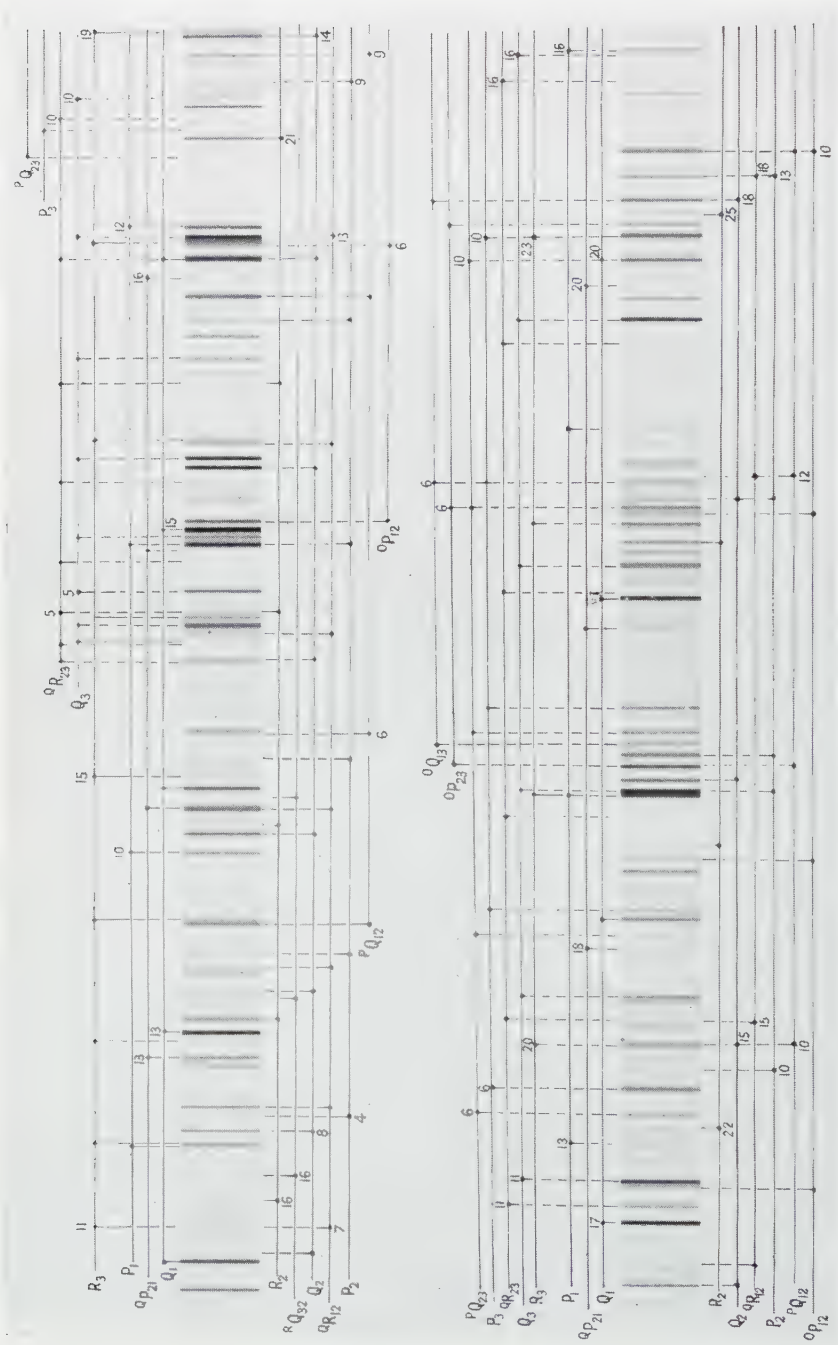

(Figure 2 *continued.*)

Plate II

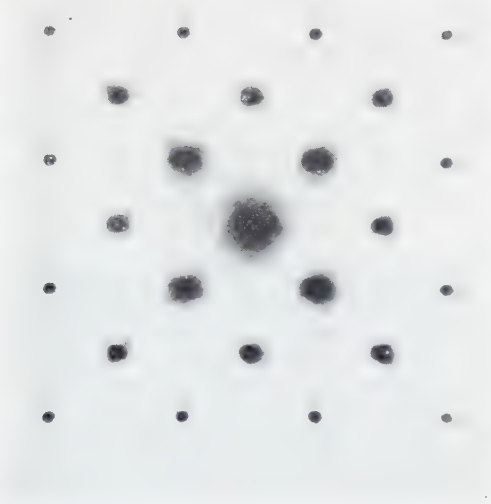

Figure 1. Diffraction pattern from phase grating.

Figure 2. Calculated average grid profile.

Figure 3. Fourier image $I\,(-\frac{1}{4})$.

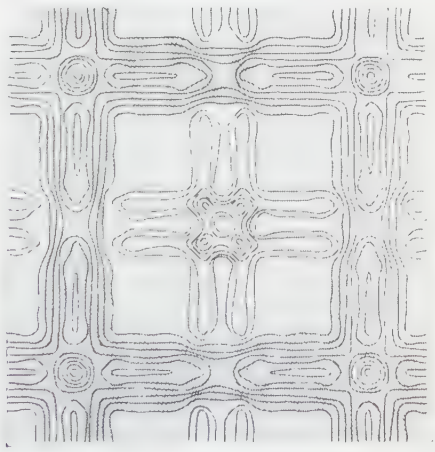

Figure 4. Calculated Fourier image $I\,(-\frac{1}{4})$ with $\sigma=\pi$.

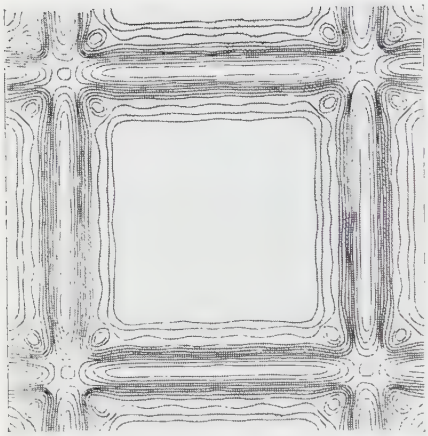

Figure 5. Calculated value of $\nabla^2\phi$.

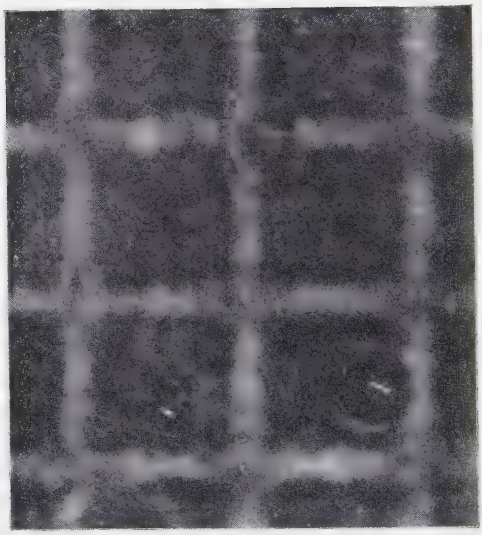

Figure 6. Pattern obtained 100 μ from a Fourier-image plane.

Singly Scattered Delayed Electrons in Extensive Cosmic Ray Air Showers

By P. J. ECCLES†
Department of Physics, University of Melbourne
MS. received 2nd March 1960, in final form 5th April 1960

Abstract. On the basis of population density and delay distribution the majority of the delayed particles detected by Jelley and Whitehouse associated with extensive air showers are shown not to be singly scattered shower electrons. The mean delay of such electrons is $2 \cdot 10^{-8}$ sec contrasting with the previously measured value of 14×10^{-8} sec. The detected delayed particles are probably μ-mesons.

§ 1. Introduction

Delayed particles have been detected associated with cosmic-ray air showers by several workers, e.g. Jelley and Whitehouse working at Harwell with a cylindrical liquid scintillator (1953) and Officer and Eccles with a tray of fast Geiger counters (1954). Using a hodoscope tracking device Officer and Eccles measured nine events in which the delay could have been caused by path differences when the delayed particle would have travelled at an angle to the shower axis, or by velocity differences when the timing equipment would have been set off by a photon, possibly from a burnt-out cascade, caused by the delayed particle in the 15 cm of lead absorber above the counters. In a later experiment (unpublished) in which the equipment of Officer and Eccles was adapted to operate under zero absorber, the fraction of shower particles found to be delayed was low compared with that found by Jelley and Whitehouse. This led to the numerical investigation of singly scattered shower electrons as the possible cause of this low rate, because, if the delayed particles arrive preferentially from a large zenith angle where the solid angle subtended by the Geiger counter tray has decreased, the rate may well be lower than that recorded by a vertical cylindrical detector whose solid angle has initially increased with zenith angle.

For this straightforward calculation the atmosphere up to 1 km above the detector is divided up into a graded series of levels $(1, \ldots t, \ldots 19)$ and a graded series of concentric cylinders, whose common axis is the path of the shower core, divides these layers into annuli. Further, because the detector is not necessarily at the core of a detected shower, a further set of concentric cylinders of radii $r_1, \ldots r_n, \ldots r_{10}$, identical to those about the core, is erected about the detector with its axis parallel to the first. Finally a set of core to detector distances $l_1 = 0, \ldots l_y, \ldots l_{10}$ is chosen and from the knowledge of the lateral distribution of shower particles (Cocconi 1958) and a numerical calculation involving intersecting annuli, the fraction of sea-level shower particles $f(n, y)$ in any annulus about the detector is found for any distance of it from the shower axis. Application of the Mott scattering cross section and the probability of survival of each

† Now at Massachusetts Institute of Technology, U.S.A.

electron or one of its secondaries to the detector, of 1 m^2 area, leads to the contribution in number from the general annulus to the delayed particles detected, and the geometrical position of the annulus gives the delay.

§ 2. Assumptions and Premises

The following assumptions and premises are made and are fully analysed in an unpublished thesis (Eccles 1959). (*a*) The lateral structure function is assumed cylindrically symmetric (Cocconi 1954), independent of shower size (Abrosimov *et al.* 1956, Cranshaw, Galbraith and Porter 1957, Clark *et al.* 1957 a and all shower groups reporting at the Varenna Conference 1958), and independent of altitude up to 1 km since the above experiments were performed at a variety of low altitudes. (*b*) The altitude dependence of the number of particles in a shower is taken from Clark *et al.* (1957 b). (*c*) The lateral distribution of shower particles at sea level is taken from Cocconi (1958) and is the same for all energies up to 300 Mev (Porter *et al.* 1958). (*d*) The integral energy spectrum is taken (Mitra and Rosser 1949) to be $N(E)=K(E+E_c)^{-1\cdot4}$ taking the shower age parameter $s=1\cdot4$ (Cocconi 1958). (*e*) All particles in the annulus (n, t) are assumed to be at the centre of gravity of its cross section. (*f*) All electrons are assumed to travel parallel to the shower axis prior to scattering. This approximation will be re-examined in the discussion. (*g*) The probability of arrival of the scattered electron or its secondaries is calculated from the results of Laughlin and Beattie (measured in water, 1951) for low energy electrons and cascade theory is included for the higher energy electrons. (*h*) Multiple scattering of the deflected electron is assumed to be negligible. It is expected that as many electrons from one annulus will be scattered away from the detector as are scattered towards it—to a first approximation at least. (*i*) The Mott formula is used for the scattering cross section. This is correct for $0\cdot5<E<300$ Mev—the entire energy range of interest. The radiative correction to the scattering formula is neglected as it is small at the angles contributing most heavily to the delayed particles, and for the same reason the ratio of the scattering cross section in air to that given by the approximate Mott formula is taken as unity (McKinley and Feshbach 1948). The formula applies equally to electrons and positrons (Elton and Parker 1953).

§ 3. The Fraction of Shower Particles that are Delayed Electrons

Excluding secondaries to other delayed particles, electrons can only be delayed by path differences. Their small rest mass ensures that their velocity is very nearly equal to that of light. As soon as it drops below this electrons begin to slow up rapidly and soon stop. Furthermore, after penetrating the material above the Harwell scintillator a 10 Mev electron produces a barely detectable pulse, thus eliminating any possible recorded delay due to velocity differences.

The fraction of the sea level shower particles which are single scattered electrons, of energy E at scattering, from the general annulus (n, t) that will reach the detector at distance l_y from the core is given by

$$U=\{(1-\sin^2\tfrac{1}{2}\theta)(\sin\tfrac{1}{2}\theta)^{-4}\omega(n,t)(X_t-X_{t-1})\exp[(X_t+X_{t-1})/2\lambda]\}$$
$$\times[P_E(n,t)f(n,y)(1/E^2)F(E)]\{(NZ^2/4A)(e^2/m_0c^2)^2(m_0c^2)^2\},$$

where $(NZ^2/4A)(e^2/m_0c^2)^2(m_0c^2/E)^2(1-\sin^2\tfrac{1}{2}\theta)(\sin\tfrac{1}{2}\theta)^{-4}$ is the Mott scattering cross section, $\omega(n, t)$ is the solid angle subtended by a detector similar to the

Harwell one but $1\,m^2$ horizontal cross section, $X_t - X_{t-1}$ is the thickness of the annulus in $kg\,m^{-2}$, $\exp[(X_t + X_{t-1})\,2\lambda]$ is the correction for the increase in the number of particles with height ($\lambda = 1750\,kg\,m^{-2}$), $P_E(n, t)$ is the probability of detecting the scattered electron and $F(E)$ is the fraction of the shower electrons within the energy band of mean energy E Mev.

U is the product of three functions. The first is independent of E and y, the second depends on the four variables E, n, t and y, and the last is a constant. The annuli contributing to delays less than 3×10^{-8} sec or greater than $1\,\mu$sec are neglected as these are outside the delay distribution measured by the Harwell team.

The first function is multiplied by $P_E(n, t)$ and then by $f(n, y)$ and an array for each y is produced for each energy considered. Summing each array over n and t and multiplying by $1/E^2$ gives the function designated $g(E, y)$. This is calculated only for three energy bands of mean energy 16, 40 and 85 Mev but, because of the similarity of the delay distributions from each of these energies (which will be obtained later and is displayed in the figure) and the monotonic variation with E of $g(E, y)$, values for other energies are found by interpolation and limited extrapolation with constant y.

For each detector position about the core, therefore, the density of shower particles that are delayed in the range 0·03 to 1·0 μsec is found by

$$\sum_E g(E,y)F(E)\{(NZ^2/4A)(e^2/m_0c^2)^2(m_0c^2)^2\}.$$

Therefore

$$\sum_y [\sum_E g(E,y)F(E)\{(NZ^2/4A)(e^2/m_0c^2)^2(m_0c^2)^2\}\pi(r_y^2 - r_{y-1}^2)] = \sum_y q(y) \text{ say.}$$

This is equal to 2% and is the fraction of shower particles that are actually delayed singly scattered electrons in the above range.

Table 1. Comparison of Populations of Delayed Electrons and Shower Particles as a Function of Distance from the Core

Distance of annulus to core (m)	0	15	30	50	70
$q(y)$	0·00007	0·00032	0·0015	0·0022	0·0018
$f(n, 1)$	0·123	0·112	0·172	0·116	0·083
Distance of annulus to core (m)	90	125	175	250	400
$q(y)$	0·0019	0·0036	0·0040	0·0024	0·0014
$f(n, 1)$	0·061	0·098	0·060	0·062	0·050

$q(y)$ and $f(n, 1)$ are compared in table 1 which shows that if, on the average, the delayed electrons are 2% of shower particles, this is not true at every position in the shower. For instance at the outskirts of the shower they are 5% while out to 20 metres from the core they are only 0·16% of shower particles. This confirms the observation of theoretical workers (see §6) that singly scattered electrons do not become a significant fraction of shower particles except at the outskirts of a shower.

§ 4. The Apparent Fraction of Shower Particles that are Detectable Delayed Electrons

Because the actual fraction of shower particles that are delayed electrons at any point is not constant, the apparent average fraction that are delayed particles, detected using a normal shower set, will be less than the 2% calculated above.

It can be proved (Eccles 1959) that the total number of showers whose cores hit an annulus of width δr distant r from a set of detectors at which detectable densities are produced is given by

$$T(r)\delta(r)=\left\{\int_0^\infty \rho^{-\gamma-1}[1-\exp(-S_1\rho)]^2[1-\exp(-S_2\rho)]d\rho\right\}2\pi Kr\phi(r)^\epsilon\delta r$$

where γ is the exponent of the integral shower density spectrum and is a slowly varying function of ρ. If assumed constant over the densities most frequently recorded by the Harwell shower set, its best value is 1·37 using Murdoch's (1958) expression for the shower density spectrum. S_1 and S_2 are the area of the delayed particle detector and the Geiger counter trays respectively. K is the constant in the differential shower number spectrum $S(N)\delta N=KN^{-\epsilon-1}\delta N\,\mathrm{m}^{-2}\,\mathrm{sec}^{-1}$, and $\rho(r)=N\phi(r)$ is Cocconi's expression for the shower density at a point distant r from a shower of total number N particles.

If each shower is assumed to have constant density over the detector set—a fair assumption for the Harwell 5 metre spaced set—it can be shown that $\gamma=\epsilon$ which is the exponent of the integral shower number spectrum.

Hence $T(r)=Q\int_0^\infty r\phi(r)^{1\cdot37}\,dr$ collecting the terms independent of r. Therefore

$$[q(y)/f(n,1)]\left\{\int_{r_{n-1}}^{r_n} r\phi(r)^{1\cdot37}\,dr\Big/\int_0^\infty r\phi(r)^{1\cdot37}\,dr\right\}=R(n)$$

is the fraction of shower particles in the nth ($=y$th) annulus about the core that would be detected as delayed by a normal shower set, since $q(y)/f(n,1)$ is the fraction of shower particles in the nth annulus that are delayed, and the quotient of the integrals is the fraction of occasions on which a shower is detected with its core distant r_n from the detectors.

Application of this formula to the experimental arrangement of Jelley and Whitehouse (1953) gives $\Sigma_n R(n)=1\%$ as the apparent fraction of shower particles that would be detected by the Harwell 5 metre spaced set if there was no energy limitation.

Finally, a minimum electron energy is required to enter the scintillator and give a detectable pulse so the apparent fraction that is detectable as delayed is even less than 1%.

This is given by $\Sigma_n R(n)\,W(n)=0\cdot38\%$ where $W(n)$ is the fraction of delayed electrons that is detectable in the nth annulus about the core.

We conclude that the Harwell group could have detected 0·38% of shower particles as delayed electrons.

§ 5. The Delay Distribution

As mentioned earlier (§ 3) the delay distribution is obtained separately for each energy. A separate delay distribution for each y is obtained from the set of arrays whose terms are

$$\{(1-\sin^2\tfrac{1}{2}\theta)(\sin\tfrac{1}{2}\theta)^{-4}\omega(n,t)(X_t-X_{t-1})\exp[(X_t+X_{t-1})/2\lambda]\}\,P_E(n,t)f(n,y)$$

by selecting a set of delay intervals and adding up the contribution to each. For each y in each energy the distributions are normalized to the same total number of particles and each adjusted term in the delay intervals is multiplied by

$R(n)W(n)$ where $y = n$. This weights the delays recorded by the detector depending on its distance from the core. For each energy the sum over y of the weighted terms in delay interval is shown as a point in the figure.

Also shown in the figure and normalized to the same value at 3×10^{-8} sec are the delay distribution if $W(n) = 1$, and the delay distributions actually measured by Jelley and Whitehouse (1953) and Eccles (to be published). It can be seen that the inclusion of the insensitivity of the Harwell scintillator changes the slope little but represses the long delays.

The mean delay of the electrons in showers is measured as $2{\cdot}0 \times 10^{-8}$ sec from the slope of the delay distribution near zero delay, whereas that of Eccles for the delayed shower particles is $12{\cdot}4 \times 10^{-8}$ sec and that of Jelley and Whitehouse is approximately $\simeq 14 \times 10^{-8}$ sec.

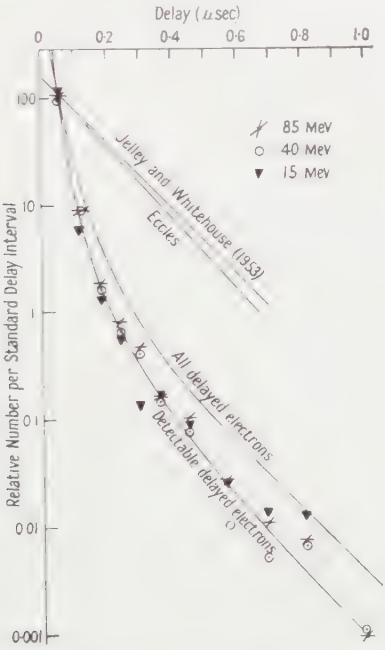

Delay distribution of singly scattered shower electrons detectable with the equipment of Jelley and Whitehouse (1953). Also shown for comparison are the same delay distribution with no energy limitation, and the measured delay distributions of Jelley and Whitehouse (1953) and Eccles to be published).

Jelley and Whitehouse detected delayed particles associated with 0·85% of extensive air showers and claimed that 0·85% of shower particles were delayed. The reason for the identity of these two percentages is not immediately obvious and was investigated by Eccles (1954) who showed after a detailed numerical investigation that the latter fraction was nearer 0·7% and that 0·53% had delays greater than 3×10^{-8} sec. This was only the apparent fraction of shower particles calculated by assuming that the lateral distribution of shower particles was the same as that of the delayed particles at every point in the shower. The actual fraction can only be calculated if the lateral distribution of the delayed particles in showers is known.

0·53% of shower particles which the Harwell team detected as delayed gave them 315 delayed events, therefore the 0·38% of shower particles which are calculated as detectable delayed electrons should have given them 228 events out of the 55 500 examined. Using the calculated delay distribution (see figure) and the experimentally deduced exponential delay distribution (Jelley and Whitehouse 1953) the expected number of delayed electrons and the experimentally deduced number of delayed particles in each interval is shown in table 2. A composite distribution extracted from these is also shown.

Table 2. Comparison of Calculated and Observed Events per Delay Interval

Centre of delay interval (μsec)	0·050	0·083	0·117	0·150	0·183	0·217	0·25	0·283
Calculated number of delayed electrons	174	37	11	4	1	1	0	0
Experimentally deduced number of delayed particles in each delay interval†	66	51	40	31	24	19	15	12
Total	240	88	51	35	25	20	15	12

† The actual observed numbers were respectively 66, 52, 41, 33, 35, 17, 10, 4.

Eccles (to be published) will show that the delayed particles, detected by himself and the Harwell group (1953) which have a mean delay of approximately 13×10^{-8} sec, are μ-mesons. Consequently no delayed singly scattered electrons were recorded as being separated from the delayed μ-mesons recorded by the Harwell group, since no sign of the steeply falling delay distribution appeared.

The Harwell group reported that their pulses were 10×10^{-8} sec wide at the base 'giving a limiting resolution of 3×10^{-8} sec'. On the occasions where the delayed pulse and the prompt shower pulse were not the same height the resolution would be poorer than the limiting value. Since the above calculation includes all electrons that can produce a barely detectable pulse, it is likely that most of the expected 174 occasions out of 55 500 in which the generally small scattered electron pulse should sit on top of the larger shower pulse were not observed. Very likely some delayed μ-meson events were also missed. In the same way, with pulses 10×10^{-8} sec long the small delayed electron pulse would still sit on the tail of the shower pulse for events in the second delay interval, and out of 90 possible delays perhaps 40 could be overlooked.

In the next delay interval beyond 10×10^{-8} sec, where the scintillator–scanner combination should have a high efficiency, the difference between 51 expected and 41 observed could be statistical.

It is deduced, therefore, that the bulk of the delayed particles detected by the Harwell group are not electrons and an experiment was designed (Eccles to be published) to detect μ-mesons and measure their energy spectrum. That the particles were protons was considered unlikely by Officer and Eccles (1954).

§ 6. The Lateral Distribution of Singly Scattered Electrons in Showers

Table 1 shows $q(y)$, the fraction of total shower particles which are delayed electrons in the yth annulus about the shower core. From this it can be shown

that the function $r\Delta(r)$ behaves as r^{-n} where n has the values shown in table 3, and $\Delta(r)$ is related to the density $D(r)$ of singly scattered electrons by the relation $N\Delta(r) = D(r)$ where N is the number of particles in the shower at sea level.

Table 3. The Behaviour of the Lateral Distribution Function of Delayed Electrons as r^{-n}

Metres from core at sea level	10	20	25	40	60	80	100	150	200	300	500
Value of n	−1·05	−1·05	−1·0	−0·61	−0·14	0·2	0·5	1·4	1·9	2·1	2·4

The values stated in table 3 for all delayed singly scattered electrons compare well with the results of previous theoretical workers (Molière 1946, Eyges1948, Poiani and Villi 1952) who agree that $rf(r)$ behaves as r^{-3} at large distances from the core. $rf(r)$, the lateral distribution of singly scattered electrons, is related to their density $S(r)$ by

$$f(r) = r_1^2 S(r) \, N$$

where r_1 is measured in shower units. One shower unit = 76 metres at sea level, and the values of n from table 3 for $r \gg 76$ metres tend to 3. These values could be closer to 3 if the considerable proportion of μ-mesons and their associated decay electrons at the outskirts of the shower were eliminated from the lateral distribution chosen as a basis for the calculation. These particles have a very flat lateral distribution with $0 < n < 0{\cdot}5$ (Porter, Cranshaw and Galbraith 1957) and are claimed to be about 50% of shower particles at 800 metres from the core (Antonov *et al.* 1957, Cranshaw *et al.* 1958). Hence the shower electron lateral distribution will have a larger value of n in this region than that given by Cocconi's expression for all shower particles and this will affect the singly scattered electron lateral distribution by increasing its value of n above that stated in table 3 at large distances from the core.

The value of $n = -1{\cdot}05$ at the core shows that the density of the delayed singly scattered particles increases up to 20 metres from the core simply because their most prolific source, the shower core, must be a given distance from the detector before measurable delays are recorded.

§ 7. Discussion

The upper and lower extrapolations of the functions $g(E, y)$ beyond the three energy values chosen can now be examined. Firstly the lower extrapolation is ignored in the calculated delay distribution because of the energy limitation discussed above and will only be of minor importance for the general case of a super-sensitive detector. Secondly the number of delayed particles and their delay distribution are insensitive to $g(E, y)$ for large E as the contribution from these only becomes important at distances greater than 90 metres from which only 40% of the delayed particles arrive and of which approximately 14% come from the doubtful region of $g(E, y)$. Hence only approximately 5% of shower particles are in this doubtful region and quite large changes in $g(E, y)$ will have little effect on the result. An even smaller fraction of the electrons have energies greater than 400 Mev and as the Mott formula is not valid here it is justifiable to neglect these completely.

Inclusion of the fact that electrons are not all travelling parallel to the shower (the inclusion of multiple scattering before single scattering) would increase the number of singly scattered electrons simply by reducing the angle θ they have to be scattered through in some cases, and a small reduction in θ means a large increase in $\mathrm{cosec}^4 \frac{1}{2}\theta$—the dominant term in the scattering formula. However, an examination of the arrays in the early part of the calculation shows that at every level the annulus with the smallest θ, and thus the one most affected by the multiple scattering, will contribute only to the first delay interval. The net result will be to steepen up the delay distribution which is already steep enough to prove that the particles Jelley and Whitehouse detected are not singly scattered electrons.

§ 8. Conclusions

We conclude on the basis of a numerical calculation that 2% of shower particles are delayed electrons with delays longer than 3×10^{-8} sec. Because of their lateral distribution and energy spectrum the apparatus of a previous experiment at Harwell could indicate that about 0·4% are delayed, if the results are analysed on the basis that the delayed particle density is proportional to the shower density at all points. Further, it has been shown that few of the delayed particles recorded by the Harwell team are in fact singly scattered delayed electrons. This is not inconsistent with possible inefficiencies in the method of detection used, since the very sharply exponential fall of the delay distribution (mean delay $= 2 \times 10^{-8}$ sec) encloses almost all of the events in the first two delay classes of the apparatus, where the generally small delayed pulse is actually on top of the prompt pulse.

The behaviour of the lateral distribution of these particles at large distances from the shower core is not inconsistent with previous calculations if allowance is made for the high proportion of μ-mesons and their decay electrons in the same region.

Acknowledgment

The author acknowledges the receipt of the Sir Thomas Lyle Research Fellowship in Physics while this work was in progress.

References

Abrosimov, A. T., Bedniakov, A. A., Zatsepin, V. I., Nechin, I. A., Solov'eva, V. I., Khristiansen, G. B., and Chikin, P. S., 1956, *Soviet Phys., J.E.T.P.*, **2,** 237 (English translation).

Antonov, Yu. N., Vavilov, Yu. N., Zatsepin, G. T., Kutuzov, A. A., Skvortsov, Yu. N., and Khristiansen, G. B., 1957, *Soviet Phys., J.E.T.P.*, **5,** 172 (English translation).

Clark, G., Earl, J., Kraushaar, W., Linsley, J., Rossi, B., and Scherb, F., 1957 a, *Nature, Lond.*, **180,** 353.

—— 1957 b, *Ibid.*, **180,** 406.

Cocconi, G., 1954, *Phys. Rev.*, **95,** 1705.

—— 1958, *Nuovo Cim., Suppl.*, **8,** 578.

Cranshaw, T. E., Galbraith, W., and Porter, N. A., 1957, *Phil Mag.*, **2,** 891.

Cranshaw, T. E., Galbraith, W., Porter, N. A., De Beer, J. F., and Hillas, M., 1958, *Nouvo Cim., Suppl.*, **8,** 578.

Eccles, P. J., 1954, *M.Sc. Thesis*, University of Melbourne.

—— 1959, *Ph.D. Thesis*, University of Melbourne.

Elton, L. R. B., and Parker, K. H., 1953, *Proc. Phys. Soc.* A, **66,** 428.
Eyges, L., 1948, *Phys. Rev.*, **74,** 1801.
Jelley, J. V., and Whitehouse, W. J., 1953, *Proc. Phys. Soc.* A, **66,** 454.
Laughlin, J. S., and Beattie, J. W., 1951, *Phys. Rev.*, **83,** 692.
McKinley, W. A. Jr, and Feshbach, H., 1948, *Phys. Rev.*, **74,** 1759.
Mitra, S. M., and Rosser, W. G. V., 1949, *Proc. Phys. Soc.* A, **62,** 364.
Molière, G., 1946, *Cosmic Radiation* (New York: Dover Publications).
Murdoch, H. S., 1958, *Nucl. Phys.*, **8,** 157.
Poiani, G., and Villi, C., 1952, *Nuovo Cim.*, **9,** 825.
Porter, N. A., Cranshaw, T. E., De Beer, J. F., Parham, A. C., and Sherwood, A. G., 1958, *Phil. Mag.*, **3,** 827.
Porter, N. A., Cranshaw, T. E., and Galbraith, W., 1957, *Phil. Mag.*, **2,** 900.
Officer, V. C., and Eccles, P. J., 1954, *Aust. J. Phys.*, **7,** 410.
Varenna Conference, 1958, *Nuovo Cim., Suppl.*, **8,** 560–700.

Resistance Anisotropy at Low Temperatures

By S. SIMONS
Queen Mary College, University of London

MS. received 22nd March 1960, in final form 5th May 1960

Abstract. We give a theoretical treatment, based on the variational principal, for the thermal conductivity tensor of dielectrics at low temperatures, where N-processes predominate. The general expression is developed in the case where U-processes are the only ones not conserving wave number, and the ratio of components of the conductivity tensor at very low temperatures is here shown to depend only on the geometry of the lattice unit cell. The results are applied to different crystal structures, and a satisfactory comparison is made with the somewhat meagre available experimental data on quartz and sapphire.

§ 1. Introduction

As the proportion of N-processes increases, corresponding to a decrease in temperature T, the solution of the Boltzmann equation tends towards a linear combination of the three independent resolutes of wave number, and in the limit as $T \to 0$ this becomes the exact solution. The undetermined coefficients in this combination may be obtained via the relevant variational principle, and this approach has been employed in detail for isotropic media by Ziman (1956) for impurity scatter, and by Leibfried and Schlömann (1954) and Simons (1957) for Umklapp resistance. In the latter case the result depends on an integral which cannot be accurately evaluated analytically.

In § 2 of this paper we extend the formal development of the theory to anisotropic dielectrics and obtain the thermal conductivity tensor σ_{ij} in terms of a tensor S_{ij} independent of the particle interactions and a tensor R_{ij} depending on the interaction mechanism. The tensor S_{ij} is investigated further in § 3, where it is shown that at low temperatures it becomes diagonal. In § 4 the tensor R_{ij} is considered for the case of U-processes, and it is shown that at very low temperatures $R_{ij} = \alpha C_{ij}$ where α involves the intractable integral referred to above and C_{ij} is a tensor depending only on the geometry of the unit cell of the lattice. Thus the ratio of the components of the conductivity tensor may be easily obtained from the crystal structure. In § 5 this ratio is considered for various lattices, and the results are compared with experiment for quartz and sapphire.

§ 2. The Conductivity Tensor when N-processes Predominate

For simplicity of exposition we shall suppose that we are concerned only with thermal conduction due to phonons; the extension to electrons and electrical conduction is trivial. The heat current vector J_i is given by

$$J_i = -(1/8\pi^3)\sum_m \int v_i^{(m)} E^{(m)} (\partial F^{(m)}/\partial E^{(m)}) \phi^{(m)} d\mathbf{k} \qquad \ldots\ldots (1)$$

where $v_i^{(m)}$, $E^{(m)}$ and $F^{(m)}$ are respectively the group velocity, energy, and Bose–Einstein equilibrium distribution function for a phonon of wave number $\mathbf{k}$, and polarization m; the sum is over all polarizations. $\phi^{(m)}$ measures the deviation from equilibrium, being defined by $f^{(m)} = F^{(m)} - (\partial F^{(m)}/\partial E^{(m)})\phi^{(m)}$, where $f^{(m)}$ is the existing non-equilibrium distribution function

It may be readily shown (Ziman 1956, Simons 1957) that the solutions of the various Boltzmann equations for the $\phi^{(m)}$'s are such as to minimize the expression

$$Z \equiv \sum_t L_t[\phi]_t^2 + 2T^{-1}(\partial T/\partial x_j)\sum_m \int E^{(m)}(\partial F^{(m)}/\partial E^{(m)})v_j^{(m)}\phi^{(m)}d\mathbf{k}, \quad \ldots\ldots(2)$$

where $[\phi]_t$ is the linear combination of ϕ's relevant to the tth type of collision process and L_t is the corresponding collision operator, which first multiplies by factors depending on the phonons taking part in the collision process, before integrating over all the wave numbers of these phonons; the t sum is over all types of collision process. $\partial T/\partial x_j$ is the temperature gradient in the x_j direction and the summation convention is employed for subscripts.

Now, as the temperature decreases and N-processes predominate, the solution $\phi^{(m)}$ tends towards

$$\phi^{(m)} = a_p k_p \quad \ldots\ldots(3)$$

where k_p is the resolute of $\mathbf{k}$ in the x_p direction and a_p is an undetermined constant, since this solution gives no contribution to the collision terms in (2) arising from N-processes. Substituting therefore the solution (3) into (2) gives

$$Z \equiv R_{pq}a_p a_q - 2(\partial T/\partial x_j)T^{-1}S_{pj}a_p$$

where

$$R_{pq} = \sum_t L_t[k_p]_t[k_q]_t \quad \ldots\ldots(4a)$$

$$S_{ij} = \sum_m \int E^{(m)}(\partial F^{(m)}/\partial E^{(m)})v_j^{(m)}k_i d\mathbf{k}. \quad \ldots\ldots(4b)$$

Minimizing Z with respect to a_p now yields

$$a_p = [R_{pq}]^{-1}S_{qj}(\partial T/\partial x_j)T^{-1}. \quad \ldots\ldots(5)$$

Further, substituting for $\phi^{(m)}$ from equations (3), (4*b*) and (5), into equation (1), we obtain

$$J_i = \sigma_{ij}(\partial T/\partial x_j),$$

where the conductivity tensor σ_{ij} is given by

$$8\pi^3 T\sigma_{ij} = [R_{pq}]^{-1}S_{pi}S_{qj}. \quad \ldots\ldots(6)$$

§ 3. Development of S_{ij}

To simplify further the second-order tensor S_{ij} defined in equation (4*b*), we introduce the third-order tensor

$$G_{pji}^{(m)} = \delta_{pj}k_i D(E^{(m)})$$

where

$$D(E^{(m)}) = \int_0^{E^{(m)}} \epsilon(\partial F/\partial\epsilon)d\epsilon. \quad \ldots\ldots(7)$$

Then

$$\begin{aligned}\partial G_{pji}^{(m)}/\partial k_p &= \delta_{pj}[\delta_{ip}D^{(m)} + k_i(\partial D^{(m)}/\partial E^{(m)})(\partial E^{(m)}/\partial k_p)] \\ &= \delta_{ij}D^{(m)} + \hbar k_i v_j^{(m)}E^{(m)}(\partial F^{(m)}/\partial E^{(m)}).\end{aligned}$$

Thus

$$\delta_{ij}\int D^{(m)}d\mathbf{k}+\hbar\int E^{(m)}(\partial F^{(m)}/\partial E^{(m)})k_i v_j^{(m)}d\mathbf{k}=\int(\partial G_{pji}^{(m)}/\partial k_p)d\mathbf{k}$$

$$=\int G_{pji}^{(m)}dA_p=\int k_i D^{(m)}dA_j, \qquad \ldots\ldots(8)$$

where $d\mathbf{A}$ is an element of the surface area of the volume of integration—the first Brillouin zone, and where the second step in equation (8) is the tensor generalization of the vector divergence theorem. Thus from equations (4*b*) and (8) we have

$$S_{ij}=-\hbar^{-1}\left\{\delta_{ij}\int D(E)\left[\sum_m W^{(m)}(E)\right]dE-\int k_i\left[\sum_m D(E^{(m)})\right]dA_j\right\} \qquad \ldots\ldots(9)$$

where $W^{(m)}(E)dE$ is the volume of $\mathbf{k}$ space in the range dE for polarization m. Now, at the low temperatures necessary for N-processes to predominate, the second integral in equation (9) may be neglected, since at the surface of the Brillouin zone the Bose–Einstein distribution will be negligibly small as compared with its average value throughout the zone.† Thus, at low temperatures the tensor S_{ij} will become diagonal, being given by $S_{ij}=g\delta_{ij}$, where

$$g=-\hbar^{-1}\int D(E)\left[\sum_m W^{(m)}(E)\right]dE.$$

Hence in this region, we see from equation (6) that

$$\sigma_{ij}=(g^2/8\pi^3 T)[R_{ij}]^{-1}. \qquad \ldots\ldots(10)$$

§ 4. Development of R_{ij}

For the majority of collision processes much too little is known of the anisotropy of the scattering for the tensor R_{ij} to be evaluated at all accurately; however, for U-processes we shall now show that considerable progress can be made. Let us suppose that there exist N sets of reciprocal lattice vectors $\mathbf{K}^{(uv)}$, where u denotes the set $(1\leqslant u\leqslant N)$, and v $(1\leqslant v\leqslant n_u)$ gives the n_u vectors required by symmetry (all of length $K^{(u)}$), within the set. Then the corresponding collision operators will be given by

$$L_l=L_{(\alpha)}^{(uv)}=Q_{(\alpha)}\delta([\mathbf{k}]_{(\alpha)}-\mathbf{K}^{(uv)}) \qquad \ldots\ldots(11)$$

where α specifies the number‡ and polarization of phonons taking part in the collision process, and equation (11) defines the operator $Q_{(\alpha)}$, which is independent of u and v. From equation (4*a*), we then have

$$R_{ij}=\sum_{\alpha uv}\{Q_{(\alpha)}\delta([\mathbf{k}]_{(\alpha)}-\mathbf{K}^{(uv)})\}K_i^{(uv)}K_j^{(uv)} \qquad \ldots\ldots(12)$$

making use of the substitution property of a δ-function. From the assumed symmetry it follows that the expression in braces in equation (12) is independent of v, and thus

$$R_{ij}=\sum_u\left(H^{(u)}\sum_v K_i^{(uv)}K_j^{(uv)}\right), \qquad \ldots\ldots(13)$$

† The same will be true of electrons if the Fermi surface does not cut the zone boundary.

‡ The results obtained will thus be correct for interactions involving an arbitrary number of phonons, corresponding to any order of perturbation theory. Hence our conclusions do not depend on the validity of first-order perturbation theory in this context.

where

$$H^{(u)} = \sum_{\alpha} Q_{(\alpha)} \delta([\mathbf{k}]_{\alpha} - \mathbf{K}^{(uv)}). \qquad \ldots\ldots(14)$$

Hence, from equation (10) it follows that

$$r_{ij} = \sigma_{ij}^{-1} = (8\pi^3 T/g^2) \sum_{u} \left(M^{(u)} \sum_{v} l_i^{(uv)} l_j^{(uv)} \right) \qquad \ldots\ldots(15)$$

where $M^{(u)} = K^{(u)2} H^{(u)}$ and $\boldsymbol{l}^{(uv)}$ is a unit vector in the direction of $\mathbf{K}^{(uv)}$.

Now, as mentioned in § 1, it is impracticable to evaluate at all accurately the collision integrals $H^{(u)}$, and therefore for the present purposes we shall suppose them to be unknown parameters. Equation (15) then gives relations between otherwise independent components of the conductivity tensor, as long as the number of such independent components is greater than N, the number of $H^{(u)}$ included in the u summation. Now, it may be shown (Leibfried and Schlömann 1954, Simons 1957) that at low temperatures

$$H^{(u)} \propto T^m \exp(-b/T) \qquad \ldots\ldots(16)$$

where m is constant and b depends on u, being smaller for shorter $K^{(u)}$. Thus, as the temperature decreases, fewer $H^{(u)}$ need be considered in order to attain the same degree of accuracy in evaluating r_{ij} from equation (15). Hence in the limit as $T \to 0$ we need retain only the shortest $K^{(u)}$†, to yield

$$r_{ij} = (8\pi^3 TM/g^2) \sum_{v} l_i^{(v)} l_j^{(v)}, \qquad \ldots\ldots(17)$$

where the u subscript has now been suppressed, corresponding to our considering only the predominant term in the u summation. We see from this result that $r_{ij} \propto \Sigma_v l_i^{(v)} l_j^{(v)}$ in the low temperature limit, and thus that we may obtain the ratio of components of the conductivity tensor from a knowledge of the geometry of the lattice unit cell alone; this limiting ratio is independent of temperature. At somewhat higher temperatures it will be necessary to take into account more than one $H^{(u)}$ in equation (15) in accordance with the above remarks, and if we consider those temperatures where two $H^{(u)}$ are sufficient, then it may be shown from equations (15) and (16) that the limiting ratio of components as given by equation (17) must be multiplied by a factor $[1 + \alpha \exp(-\beta/T)]$, where α and β are constants, provided that $\Sigma_v K_i^{(uv)} K_j^{(uv)}$ is non-zero for the shorter $K^{(u)}$.

§ 5. Application to Crystal Systems and Comparison with Experiment

We now consider the form taken by our previous results for the various primitive Bravais lattices. It is clear from equation (17) that if symmetry requires the existence of only two reciprocal lattice vectors ($\pm \mathbf{K}$) for the shortest $K^{(u)}$, then in the low temperature limit r_{ij} will be proportional to

$$\begin{pmatrix} 0 & 0 & 0 \\ 0 & 0 & 0 \\ 0 & 0 & 1 \end{pmatrix}$$

† By shortest $K^{(u)}$, we mean in this paper those $\mathbf{K}^{(u)}$ vectors which are such that the minimum frequency of a phonon undergoing a transition into two other phonons in a U-process, is less than the corresponding frequency for other $\mathbf{K}^{(u)}$. Neglecting dispersion effects, it may be readily shown that this corresponds to $v_l v_t K^{(u)}/(v_l + v_t)$ being a minimum, where v_l and v_t are the longitudinal and transverse sound velocities respectively along the direction of $\mathbf{K}^{(u)}$.

where the z axis is taken parallel to $\mathbf{K}$; that is, parallel to the direction of maximum interplanar spacing. This result, plausible on physical grounds, is relevant to triclinic, monoclinic and orthorhombic lattices. It also applies to tetragonal and hexagonal lattices if the direction of maximum interplanar spacing is parallel to the c axis. If, however, this direction is perpendicular to the c axis, then r_{ij} will be proportional to the tensor

$$\begin{pmatrix} 1 & 0 & 0 \\ 0 & 1 & 0 \\ 0 & 0 & 0 \end{pmatrix},$$

where the z axis is retained parallel to the c axis.

At higher temperatures, it is necessary to consider more sets of reciprocal lattice vectors for substitution into equation (15), and it is readily shown that for the orthorhombic, tetragonal and hexagonal lattices it is impossible to introduce sets of $\mathbf{K}$ vectors, fewer than the number of independent non-zero components of r_{ij}. Thus for these lattices our approach yields no new results. For the monoclinic Bravais lattice, the reciprocal lattice is also monoclinic, and we may choose the z direction along the diad axis of this lattice ($\mathbf{K}^{(1)}$). The x direction can then be chosen parallel to the shortest reciprocal lattice vector in the xy plane ($\mathbf{K}^{(2)}$), while the next shortest reciprocal lattice vector in this plane is taken as $\mathbf{K}^{(3)}$. It is known from symmetry considerations that for this lattice,

$$r_{ij} = \begin{pmatrix} r_{xx} & r_{xy} & 0 \\ r_{xy} & r_{yy} & 0 \\ 0 & 0 & r_{zz} \end{pmatrix},$$

and it is clear from equation (15) that using the above three vectors, r_{zz} will involve $M^{(1)}$, while r_{xx} will involve $M^{(2)}$ and $M^{(3)}$. However, r_{xy} and r_{yy} both involve only $M^{(3)}$, and it is thus readily seen that $(r_{xy}/r_{yy}) = \tan\theta$, where θ is the angle between $\mathbf{K}^{(3)}$ and the y axis.

For the triclinic Bravais lattice, the reciprocal lattice is also triclinic, and we take the three shortest non-coplanar reciprocal lattice vectors as $\mathbf{K}^{(1)}$, $\mathbf{K}^{(2)}$, $\mathbf{K}^{(3)}$, (with $K^{(1)} < K^{(2)} < K^{(3)}$). The z direction can then be chosen parallel to $\mathbf{K}^{(1)}$, while $\mathbf{K}^{(2)}$ is taken in the xz plane. For this lattice, all components of r_{ij} are in general non-zero, and it is clear from equation (15) that r_{xy}, r_{yy}, r_{yz} will involve only $M^{(3)}$ while r_{xz}, r_{xx} will involve $M^{(2)}$ and $M^{(3)}$, and r_{zz} will involve $M^{(1)}$, $M^{(2)}$ and $M^{(3)}$. Following this up in detail yields the following three relations between r_{ij}:

$$r_{xy} : r_{yy} : r_{zy} = \cos(3x) : \cos(3y) : \cos(3z)$$

and

$$\cos^2(3y)\,[\cos(2x)\,r_{xz} - \cos(2z)\,r_{xx}] = \cos(3x)\,r_{yy}\,[\cos(3z)\cos(2x) - \cos(2z)\cos(3x)],$$

where (ab) is the angle between $\mathbf{K}^{(a)}$ and the b axis.

Finally, we consider the case of a trigonal Bravais lattice, and suppose the rhombohedral unit cell to possess axes $\mathbf{a}$, $\mathbf{b}$, $\mathbf{c}$ each of length a, making an angle α with one another. Then the reciprocal lattice will also be trigonal, and its rhombohedral unit cell will have axes $\mathbf{a}'$, $\mathbf{b}'$, $\mathbf{c}'$ each being of length a' $[= a^{-1}\cot\tfrac{1}{2}\alpha/(4\cos^2\tfrac{1}{2}\alpha - 1)^{1/2}]$, making an angle α' $[= \cos^{-1}(\tfrac{1}{2}\sec^2\tfrac{1}{2}\alpha - 1)]$ with one another. Now, if we choose the z direction symmetrically with respect to $\mathbf{a}$, $\mathbf{b}$ and $\mathbf{c}$, it is known from symmetry considerations that the only non-zero r_{ij}

are r_{zz} and $r_{xx}=r_{yy}$. Thus in order to obtain any useful results, it is necessary to restrict ourselves to the low-temperature limit, employing only the single set of shortest reciprocal lattice vectors. Which set will be the shortest depends on α and the elastic constants; there are three possibilities: (i) the set of six vectors of the form $\mathbf{a}'-\mathbf{b}'$, with

$$K^{(1)}=2a'\sin\tfrac{1}{2}\alpha'=a^{-1}\operatorname{cosec}\tfrac{1}{2}\alpha;$$

(ii) the set of six vectors of the form $\mathbf{a}'$, with

$$K^{(2)}=a'=a^{-1}\cot\tfrac{1}{2}\alpha/(4\cos^2\tfrac{1}{2}\alpha-1)^{1/2};$$

(iii) the set of two vectors of the form $\mathbf{a}'+\mathbf{b}'+\mathbf{c}'$ with

$$K^{(3)}=[3(1+2\cos\alpha')]^{1/2}a'=3^{1/2}a^{-1}/(4\cos^2\tfrac{1}{2}\alpha-1)^{1/2}.$$

For given α and elastic constants, it is therefore necessary to calculate $\gamma^{(n)}K^{(n)}$ for $n=1$, 2, 3, where $\gamma^{(n)}=v_l v_t/(v_l+v_t)$, (see footnote just before equation (17)) and thus to decide which is the set of shortest reciprocal lattice vectors. If $\gamma^{(n)}$ is independent of n, then the shortest for $\alpha<60^\circ$ is $K^{(3)}$, for $60^\circ<\alpha<109^\circ 28'$ is $K^{(2)}$, and for $109^\circ 28'<\alpha<120^\circ$ is $K^{(1)}$. We see immediately from equation (17) that if $K^{(1)}$ is the shortest, then $r_{zz}=0$ and if $K^{(3)}$ is the shortest, $r_{xx}=r_{yy}=0$. With the aid of a little geometry, it is readily shown that if $K^{(2)}$ is the shortest, $r_{xx}/r_{zz}=(1-\cos\alpha')/(1+2\cos\alpha')=(1+2\cos\alpha)/(1-\cos\alpha)$.

Let us now apply these results to quartz, which possesses a trigonal unit cell with $\alpha=93^\circ 56'$. From the formulae given above, we obtain $K^{(1)}=1{\cdot}37a^{-1}$, $K^{(2)}=1{\cdot}01a^{-1}$, $K^{(3)}=1{\cdot}87a^{-1}$. Via the known elastic constants of quartz, we find $\gamma^{(n)}$ from the relevant secular equation for the sound velocities, and thus obtain

$$\gamma^{(1)}=\gamma,\quad \gamma^{(2)}=1{\cdot}05\gamma,\quad \gamma^{(3)}=1{\cdot}24\gamma.$$

This yields

$$\gamma^{(1)}K^{(1)}=1{\cdot}37\gamma a^{-1},\quad \gamma^{(2)}K^{(2)}=1{\cdot}06\gamma a^{-1},\quad \gamma^{(3)}K^{(3)}=2{\cdot}31\gamma a^{-1}.$$

Hence, at sufficiently low temperatures, only $K^{(2)}$ will be operative, giving $r_{xx}/r_{zz}=0{\cdot}81$. Since $\gamma^{(1)}K^{(1)}$ differs from $\gamma^{(2)}K^{(2)}$ by about 30%, we may expect this limiting ratio to be attained to within a few per cent for θ_D/T greater than about 20; that is, for T less than about 15°K. As the temperature rises above this value, r_{xx}/r_{zz} should increase, corresponding to the effect of $K^{(1)}$ becoming apparent.

Now, as far as experimental results are concerned, it would seem that the best measurements are those of Berman (1953 and private communication), which give $r_{xx}/r_{zz}=1{\cdot}23$ at 14°K, increasing to 1·58 at 28°K. The result at 14°K is certainly at variance with our theoretical value and the reason for this is not hard to find. It is due to the fact that the silicon in natural quartz possesses about 10% of isotope 'impurity', and the oxygen about 0·2%. Berman, Foster and Ziman (1956) have considered measurements of the absolute conductivity of quartz, and have shown that at $\theta_D/20$, they deviate substantially from the values expected for pure Umklapp scatter, due to phonon scatter by these isotopes. Thus, the discrepancy between theory and experiment at 14 K is readily understandable. As the temperature increases, the relative effect of isotope scatter decreases, and hence the theoretical increase in r_{xx}/r_{zz} for temperatures greater than $\theta_D/20$ is borne out by the experimental result at 28 K. It is clear that in order to effect a detailed comparison with theory, it is necessary to have

experimental results on quartz containing a single isotope of each element. Alternatively we might try to calculate the resistance anisotropy due to impurity scatter, but this will involve a detailed knowledge of the anisotropy of phonon velocity.

Finally, we consider the case of sapphire (Al_2O_3) which possesses a trigonal unit cell with $\alpha = 55° 6'$. Owing to the lack of data on the elastic constants, we are unable to determine the values of $\gamma^{(u)}$, and must therefore content ourselves with calculating $K^{(u)}$, when using the formulae given previously, we obtain $K^{(1)} = 2{\cdot}16a^{-1}$, $K^{(2)} = 1{\cdot}31a^{-1}$, $K^{(3)} = 1{\cdot}18a^{-1}$. Now, since $K^{(3)}$ is about 10% less than $K^{(2)}$, while $K^{(1)}$ is more than 60% greater than $K^{(2)}$, we would expect that when taking the γ factor into consideration, either $K^{(2)}$ or $K^{(3)}$ could turn out to be the shortest reciprocal lattice vector. From the previous results we then see that these correspond respectively to $r_{xx}/r_{zz} = 5{\cdot}01$ or zero in the low-temperature limit. Now, the very small difference between $K^{(2)}$ and $K^{(3)}$ means that the maximum temperature at which this limiting ratio will become apparent is almost certainly somewhat less than $\theta_D/30$, that is, less than about 30°K. However, the only low temperature measurements on the resistance anisotropy of sapphire are those of Berman (private communication) which give $r_{xx}/r_{zz} \simeq 1{\cdot}22$ in the range 65° to 90°K, the ratio being constant to within a few per cent. Since there is only a single isotope of aluminium, the effect of isotope 'impurity' will be much smaller for sapphire than for quartz. The experimental results, as considered by Berman, Foster and Ziman (1956), show that the relative isotope effect is probably less than about 10% for θ_D/T less than about 14; that is for T greater than about 70°K. In view of the remarks at the end of § 4, we can then understand the observed temperature independent anisotropy as being due to both $K^{(2)}$ and $K^{(3)}$ contributing to the resistance, since the temperature is still too high for the relative exponential decrease of the contribution of one of them to become apparent. On the other hand there is no contribution from $K^{(1)}$ since the temperature is low enough for this to have been 'frozen out'. Accepting the results of the previous theory, together with the experimental result, we can then calculate the ratio of $M^{(2)}$ to $M^{(3)}$ from equation (15). This yields

$$\frac{r_{zz}}{r_{xx}} = \frac{1-\cos\alpha}{1+2\cos\alpha} + \frac{M^{(3)}}{M^{(2)}}\frac{1+\cos\alpha}{1+2\cos\alpha},$$

whence we obtain $M^{(2)}/M^{(3)} = 1{\cdot}18$, and $H^{(2)}/H^{(3)} = 0{\cdot}96$. This result is plausible, since we would have expected $H^{(2)}$ and $H^{(3)}$ to be approximately equal. That they are equal to within 5% is presumably fortuitous, especially in view of our neglect of anisotropy due to isotope scatter.

It is clear that in order to obtain a detailed comparison with theory, it would be necessary to work at low temperatures with a substance containing only one isotope of each element, and with a crystal structure which yields a large relative difference between the two shortest reciprocal lattice vectors.

References

Berman, R., 1953, *Advanc. Phys.*, **2**, 103.

Berman, R., Foster, E. L., and Ziman, J. M., 1956, *Proc. Roy. Soc.* A, **237**, 344.

Leibfried, G., and Schlömann, E., 1954, *Nachr. Akad. Wiss. Göttingen, Math.-Phys. Kl.* 2a, **4**, 71.

Simons, S., 1957, *Thesis*, University of Cambridge.

Ziman, J. M., 1956, *Canad. J. Phys.*, **34**, 1256.

A Reversed Carrier Transport Effect in Germanium

By A. C. PRIOR

Royal Radar Establishment, Malvern, Worcs.

MS. received 30*th November* 1959, *in final form* 22*nd March* 1960

Abstract. The difference in the behaviour of electrons and holes in germanium in the degree of departure from linearity of their drift velocity–electric field relationships is shown theoretically and experimentally to influence substantially the motion of a density distribution in near intrinsic material at high fields. In n-type germanium the normal motion can be reversed. A consequence is that injection or extraction, depending on the nature of the contact, can occur from the negative end of an n-type specimen. Cross section variations can also act as sources of injection or extraction. An apparent negative resistance has been observed, and a tentative explanation is given. Changes in mobility ratio due to mechanical stress can have an appreciable effect at high fields, and it is shown that even at low fields interpretation of piezoresistance measurements could be influenced by these considerations.

§ 1. Introduction

The variation with electric field of the drift velocity of electrons in n-type (Ryder 1953, Gunn 1956), and of holes in *p*-type (Ryder 1953, Prior 1960) germanium has been published by several authors. These results show that while the mobility of both electrons and holes falls substantially with increasing field above about 1000 v cm $^{-1}$, the fall is greater for the electrons; that is, the ratio of the mobility of electrons to that of holes decreases as the field increases. The object of this paper is to point out several consequences of this mobility ratio variation with field on the motion of a carrier density distribution at high fields. In particular, under suitable conditions in n-type germanium, the velocity of this density distribution is reversed, leading to an effect which can be described as a stationary or backward travelling carrier density shock wave. Under such conditions both injection and extraction can occur from the negative end of an n-type germanium specimen, depending on the nature of the contacts. A further consequence is that, even in a specimen with uniform carrier and impurity concentration, the passage of a current through the specimen can cause changes of carrier density if the cross section varies. These effects have been demonstrated experimentally.

§ 2. Theory

2.1. *Injected Distribution*

The effects to be discussed concern the motion of a carrier density distribution in a semiconductor of uniform impurity concentration under the action of an

applied potential difference. This motion is determined by the detailed field configuration produced by a space charge distribution, which is itself determined by the carrier distribution, and which changes continuously with the latter. The movement of these space charges constitutes flow of current, but a simple calculation shows that, for the situations considered in this treatment, the currents are always small compared with the total current, which, for germanium at room temperature, exceeds the former by at least two orders of magnitude under the least favourable conditions of low impurity concentration and very high field. Thus, instead of detailed consideration of the space charge it is legitimate to substitute the assumption of current continuity, or, since the initial space charge will not be of concern, the slightly wider and more usual assumption of space charge neutrality.

As a further simplification, generation, recombination and diffusion of carriers are neglected, since inclusion of these phenomena would considerably complicate the treatment and add little to its illustrative value, while the qualitative effects of their inclusion are almost self-evident for the simple arrangement discussed.

With these assumptions, consider now a germanium bar of uniform cross section and impurity concentration. At a point x along the bar the number of electrons and holes per unit length are $p+N$ and p respectively, N being the excess of ionized donor over acceptor impurities. The current through the specimen is jX (electronic charge), and at the point x the drift velocity of the electrons is $-bv$ and that of the holes is $v(1+\epsilon)$; b is the normal low field mobility ratio, and the quantity ϵ, which is a function of the electric field, represents the fact that the relation between the drift velocity and field is not the same for the electrons as for the holes. The effects being discussed are due to the non-zero value of ϵ, which is positive for germanium. This is illustrated in figure 1, which shows the previously published (Gunn 1956, Prior 1960) drift velocity–field relationship for n- and p-types of germanium and the corresponding values of ϵ. In applying these results to the electrons and holes simultaneously present in a single specimen it is assumed that electron hole scattering is negligible; this is supported by the experimental and theoretical results on germanium of Paige and McLean (1960).

The motion of a carrier density distribution may be determined by considering the time rate of change of carrier density in a region where the density is varying with position. From the space charge neutrality assumption consideration of the density changes of one type of carrier only is necessary, holes being chosen. The net rate of entry of holes at x per unit length of crystal is

$$\left(\frac{\partial p}{\partial t}\right)_x = -\left(\frac{\partial}{\partial x}\right)_t \{pv(1+\epsilon)\}. \qquad \ldots\ldots(1)$$

Using

$$j = pv(1+\epsilon) + (p+N)bv \qquad \ldots\ldots(2)$$

to eliminate v, and differentiating, we may write (1)

$$\left(\frac{\partial p}{\partial t}\right)_x = -\frac{jNb(1+\epsilon)}{[p(1+b+\epsilon)+Nb]^2}\left\{1+\frac{p(N+p)}{N(1+\epsilon)}\frac{d\epsilon}{dp}\right\}\left(\frac{\partial p}{dx}\right)_t. \qquad \ldots\ldots(3)$$

The position of a given hole density p is thus seen from (3) and (2) to move along

the specimen with a density distribution velocity

$$V = -\frac{(\partial p\ \partial t)_x}{(\partial p\ \partial x)_t} = b\tau\,\frac{1+\epsilon}{(p\ N)(1+b+\epsilon)+b}\left\{1+\frac{1+(p\ N)}{1+\epsilon}\,\frac{d\epsilon}{dE}\,\frac{dE}{dp/p}\right\} \quad \ldots\ldots(4)$$

where

$$\left(\frac{dE}{dp\ p}\right) = -\{|v_p|+|v_n|\}\left\{\frac{d|v_p|}{dE}+\left(1+\frac{N}{p}\right)\frac{d|v_n|}{dE}\right\}^{-1} \quad \ldots\ldots(5)$$

v_n and v_p being the electron and hole drift velocities at electric field E.

Using the experimental data of figure 1, V has been calculated as a function of field for various values of $N\ p$, and the results are shown in figure 2, on which are indicated the conductivity σ corresponding to the values of N/p in terms of the intrinsic conductivity σ_i.

The most striking feature of these results is the reversal of the density distribution velocity from its normal direction over a range of values of field in n-type germanium, and the substantial velocity, except at low fields, in intrinsic germanium. For germanium $d\epsilon\ dp$ is always negative, and for n-type germanium N is positive, so that the right-hand term in the final bracket of (4) is negative. Reversal thus occurs when

$$\left|\frac{1+p/N}{1+\epsilon}\,\frac{d\epsilon}{dE}\,\frac{dE}{dp/p}\right| > 1.$$

For p-type material N is negative and the effect is simply to increase the velocity.

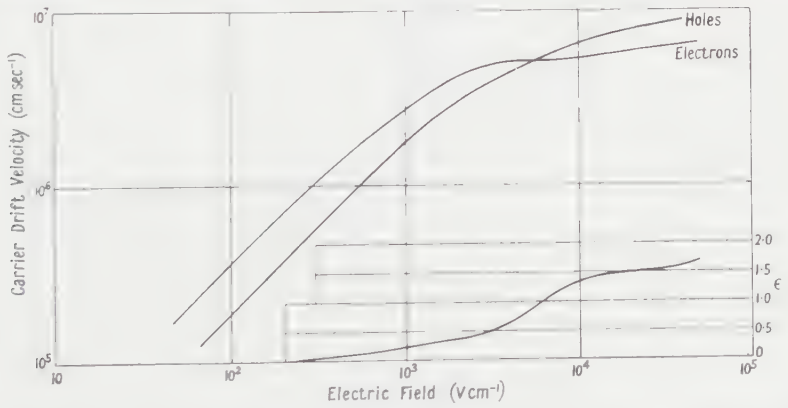

Figure 1. Drift velocities of electrons and holes, and the value of ϵ, as a function of electric field, in germanium at 300° K.

The general effect is not dependent on the detailed shape of the drift velocity–field relationship for holes or electrons separately, but principally on the variation of the drift velocity ratio with field. However, the close approach of the density distribution velocity to the electron drift velocity at a field of 6000 V cm^{-1}, over a range of impurity concentrations, is due to a particular feature of the electron drift velocity curve. For n-type germanium Gunn (1956) found that at around 6000 V cm^{-1} the drift velocity was, within the limits of experimental error, independent of the field. If this is taken as accurately true and (5) is substituted in (4) with $d|v_n|/dE = 0$, the result reduces to $V = -b\tau$, the electron drift velocity, independent of the number of impurities N.

The motion of an injected distribution is determined by the resultant changes in field necessary to maintain current continuity. If the electron drift velocity

cannot be varied the field changes must be determined entirely by the properties of the holes, and the material behaves differentially as though the electrons were replaced by fixed negative ions. The effect is therefore as though the material were perfectly p-type, from which the result just obtained from the equations is an obvious conclusion.

In figure 2 it will be noted that the peak reverse velocity does fall somewhat as N increases. This is because in the calculation the minimum value of the slope mobility $d|v_n|/dE$ at 6000 v cm^{-1} was not taken as exactly zero, but arbitrarily, for the purpose of illustration as $(1/40)(d|v_p|/dE)$, since this is within the range of experimental error of the drift velocity data for electrons. For sufficiently large values of N/p, the density distribution velocity is thus a very sensitive measure of the slope mobility in this region.

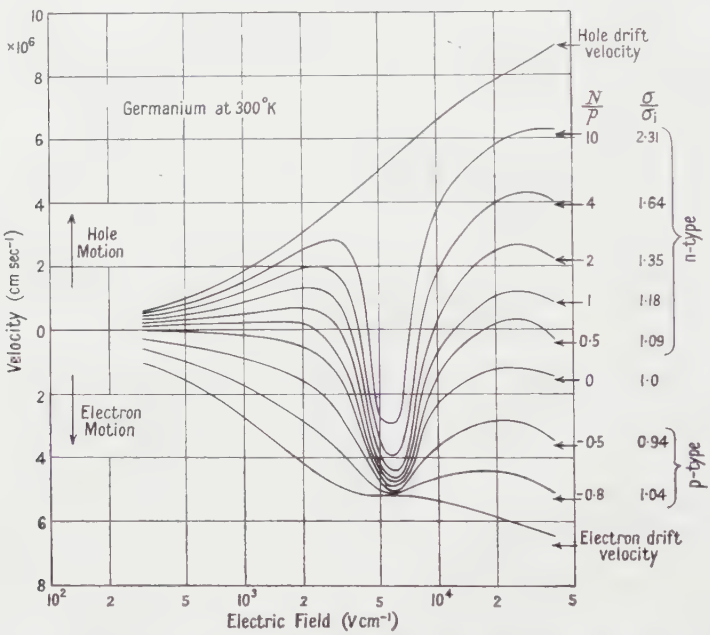

Figure 2. Velocity of carrier distribution for low level injection calculated from electron and hole drift velocities.

Some caution is necessary in interpreting these conclusions, particularly for the more strongly n-type material. The algebraic treatment uses the derivative $d\epsilon/(dp/p)$, and it is not valid to apply the results to finite values of δp unless $\delta p/p$ is small. The criterion for validity is roughly that the number of injected holes must not exceed 10–20% of the number present in the material before injection. For a large injected signal the condition for current continuity will cause the field to move outside the range in which the differential electron mobility is very small, and if the electron concentration sufficiently exceeds the hole concentration the behaviour will revert to that normal for n-type material, and the distribution will move in the direction of the holes. It is clear that, in the limiting condition of negligible hole concentration outside the injected region, the distribution must move with the hole velocity, since holes are present only in the injected region.

For large injected signals in germanium of any impurity concentration, both the field and the value of N/p will vary throughout the distribution, and analysis of the detailed behaviour to be expected under particular circumstances would in general be complex. However, some fairly general conclusions can be drawn. Consider a bar of near intrinsic n-type germanium with the central region strongly injected by illumination. If the current density is such that the field is everywhere below about 1000–2000 v cm^{-1} (depending on the impurity concentration) the behaviour will be approximately normal, with the distribution moving in the hole direction, the leading edge being somewhat spread out and the trailing edge steepened by the conductivity modulation mechanism discussed by Herring (1949).

If the current is increased such that the field approaches 6000 v cm^{-1} in the region which has not been injected, the whole distribution will move in the reverse direction; near the base of the distribution the field, and consequently the reverse velocity, will be high, while at the top the field will be lower and the velocity will either tend to be in the normal direction, or reversed but small. This will result in a spreading out of the new leading edge, and a marked steepening of the new trailing edge. For some intermediate current density the velocity of the latter edge will be zero though the edge will still be steepened, producing the effect of a stationary shock wave.

These considerations suggest that when a large field is applied the reverse travelling trailing edge is first steepened, but then retains its shape while subsequently travelling along the specimen. If no changes of shape occur the velocity of this shock wave can be found by a very simple treatment. If the specimen is imagined as divided into a low carrier density region (suffix 1), a transition region where all the concentration changes occur and a high density region (suffix 2), then equating the net flow of holes into the transition region to the change in numbers due to the velocity V of the density step, this is found to be, in obvious notation,

$$V = \frac{v_{p_1} - v_{p_2} p_2/p_1}{(p_2/p_1) - 1} \qquad \ldots\ldots (6)$$

where current continuity considerations give

$$\frac{p_2}{p_1} = \frac{v_{p_1} + v_{n_1} - (N/p_1)(v_{n_1} - v_{n_2})}{v_{p_2} + v_{n_2}} \qquad \ldots\ldots (7)$$

The approach represented by equations (6) and (7) is essentially independent of the differential approach of equations (1) (5). The latter can be applied directly only over regions where the relative changes in carrier density and field are small. For situations where large changes occur integration of these equations would be required, probably by numerical methods. Equations (6) and (7) are equivalent to an approximate integrated solution of (1) (5) throughout a transition region between two regions of different but uniform carrier concentrations. The experimental verification of the theory described later makes use of equations (6) and (7).

2.2. *Cross Section Variation*

The effect of variation of cross section can be seen by a simple extension of the above treatment. p and N are numbers per unit length, and cross section does

not enter explicitly into the calculation. Provided therefore that variations in cross section are sufficiently gradual that current density and carrier concentration can be taken as uniform over the cross section, such variations can be taken into account by making the appropriate variations in p and N. (Variations in N due to impurity volume concentration changes cannot be taken into account in this simple way, because the latter involve built-in electric fields.) For a specimen having initially uniform volume concentrations of carriers and impurities, p and N can be expressed as

$$p = p_0 f(x) \quad \text{and} \quad N = N_0 g(x)$$

where $g(x)$ expresses the variation of cross section, and $f(x)$ is initially equal to $g(x)$ before a high field is applied.

If these substitutions are made in (1) and (2) the expression for V is found to be

$$V = bv \frac{1+\epsilon}{(p/N)(1+\epsilon+b)+b} \left\{ 1 + \frac{1+p/N}{1+\epsilon} \frac{d\epsilon}{dE} \frac{dE}{dp} \frac{p}{} - \frac{f(x)g'(x)}{g(x)f'(x)} \right\} \qquad \ldots\ldots (8)$$

where for example $g'(x) = dg(x)/dx$.

For intrinsic material $N = 0$ and (8) reduces to

$$V = \frac{bv}{1+\epsilon+b} \frac{d\epsilon}{dE} \frac{dE}{dp/p}. \qquad \ldots\ldots (9)$$

This is identical with (4) when $N = 0$, and is the intrinsic curve plotted in figure 2. This is physically obvious since, with the neglect of recombination and in the absence of impurities and with only slow cross section changes, there is no essential physical difference between an injected carrier distribution, (4), and a thermally generated distribution, (9). Thus in intrinsic material, the distribution originally determined by the cross section moves freely along the specimen in the electron flow direction, though with considerable distortion for large variation in cross section.

In the presence of impurities the situation is more complicated, the impurities acting as an anchor tending to impede the free movement of the distribution. Initially $f(x) \equiv g(x)$ and (8) becomes

$$V = bv \frac{1+\epsilon}{(p/N)(1+\epsilon+b)+b} \frac{1+p/N}{1+\epsilon} \frac{d\epsilon}{dE} \frac{dE}{dp/p} \qquad \ldots\ldots (10)$$

corresponding to a rate of injection of carriers $-V(\partial p/\partial x)$. This injection will build up a distribution which will then travel along the specimen with velocity given by (4). Equation (8) can thus be interpreted as the combined effect of an injection or extraction at a region of varying cross section, together with the motion of the injected distribution. The net effect to be expected is an increase in the carrier density where the cross section is decreasing in the direction of electron flow, and a decrease where the cross section is increasing, together with a continuous movement of the modified part of the distribution. If the conditions are such that (4) gives normal or zero velocity, then the continuous movement will not occur but only, if the field is sufficient, changes in the carrier concentration where the cross section is varying.

An important practical implication of these theoretical results is that in general, at high fields, either injection or extraction will occur from the negative as well as from the positive terminal of a not too strongly n-type germanium specimen, and that the use of enlarged ends does not remove the difficulty. No

detailed theoretical study has yet been made of the properties of the various types of contacts that could be used for the negative end, but some experimental results obtained with different contacts are mentioned in a later section.

§ 3. Experimental

3.1. *Distribution Movement*

To test some of the main features of the theory large current pulses were passed through a bar of near intrinsic n-type germanium at room temperature (extrinsic electron concentration $\sim 1 \times 10^{13}$ cm $^{-3}$), and the movement of a carrier distribution produced by the strong illumination of a part of the specimen was examined. Specimens were typically about 1 cm long by 1 mm^2.

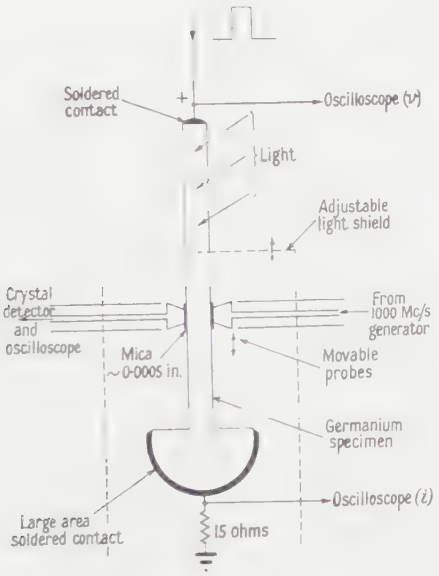

Figure 3. Experimental arrangement.

The arrangement is indicated in figure 3. The filament of a 24 watt bulb was focused to illuminate the top face of the specimen approximately uniformly, and a shield could be adjusted to blank off any length from the negative end. The specimen was gripped in between two wedge shaped spring loaded probes extending across the specimen and about 0·5 mm wide. The probes with mica insulation could be released and moved to any position along the specimen. Scales were fitted to indicate the positions of shield and probes. The 1000 Mc/s signal picked up through the probes was a measure of the conductance between them; for calibration, the conductivity was varied by illumination of the whole specimen, and the probe signal compared with the low field d.c. conductance along the specimen.

Contacts to both ends of the specimen were made by soldering. The first specimen used was a plain bar with equal area contacts at both ends, but this showed large injection effects from the negative end. The second specimen had an enlarged negative end so proportioned that, with the largest current used,

the field in the germanium at the soldered contact was less than 1000 v cm $^{-1}$, so that injection could not occur at the metal to germanium contact, and any injection from the negative end could only be due to a cross section effect. After preparation the specimens were etched in hydrogen peroxide.

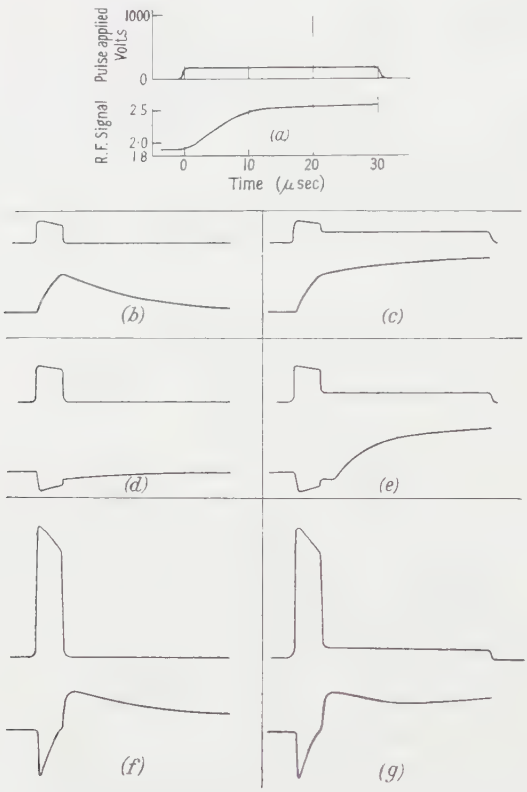

Figure 4. Typical pulse shapes with light shield covering probes and extending approximately 1·5 mm beyond probe centres. The upper curve in each set shows the pulse applied and the lower curve the corresponding r.f. signal. The scales shown on (*a*) apply to all diagrams.

In figure 4 are shown typical oscilloscope traces. The pulse generator was arranged to give either a 30 μsec 170 v constant amplitude pulse, or a larger variable amplitude 4 μsec pulse, or a combination of both. Figure 4 (*a*) shows the effect produced by the small pulse; the r.f. signal increases as the carriers from the highly injected region are swept in between the probes in the normal hole direction. (*b*) shows a similar result with a short pulse; the subsequent decay with a time constant of the order of 20 μsec is presumably due mainly to recombination. The expected result of the combination of both pulses is seen in (*c*). In (*d*) the pulse is large enough to cause reversal of the density distribution velocity, and the carrier density decreases in between the probes; the decrease in the probe signal is due both to the decrease in the number of carriers, and also to the decrease in conductivity beyond the linear region of the (drift velocity, field) curves. The step at the end of the pulse is due to the disappearance of the latter effect, leaving only the effect due to a reduction in carrier numbers. This interpretation is confirmed by (*e*) in which the subsequent small long pulse causes

the distribution, which has been moving away from the probes, to return after about 2 μsec. In (*f*) the situation is similar except that immediately after the light injected distribution has moved beyond the probes, the distribution injected from the cross section discontinuity at the negative end begins to move in, and by the end of the pulse has substantially raised the carrier density above its original value. In (*g*) the light injected and the end injected distributions have merged, and no abrupt changes are seen as the distribution is moved back by the small long pulse.

In (*b*), (*d*) and (*f*) changes after the pulse indicate a carrier lifetime of the order of 20 μsec. Other measurements indicate that the small signal life time to be expected from an etched specimen of the dimensions used would be about 200 μsec. The much smaller value of about 20 μsec observed is presumably due to the high injection level of about $4 \times 10^{14}\,\mathrm{cm}^{-3}$ used.

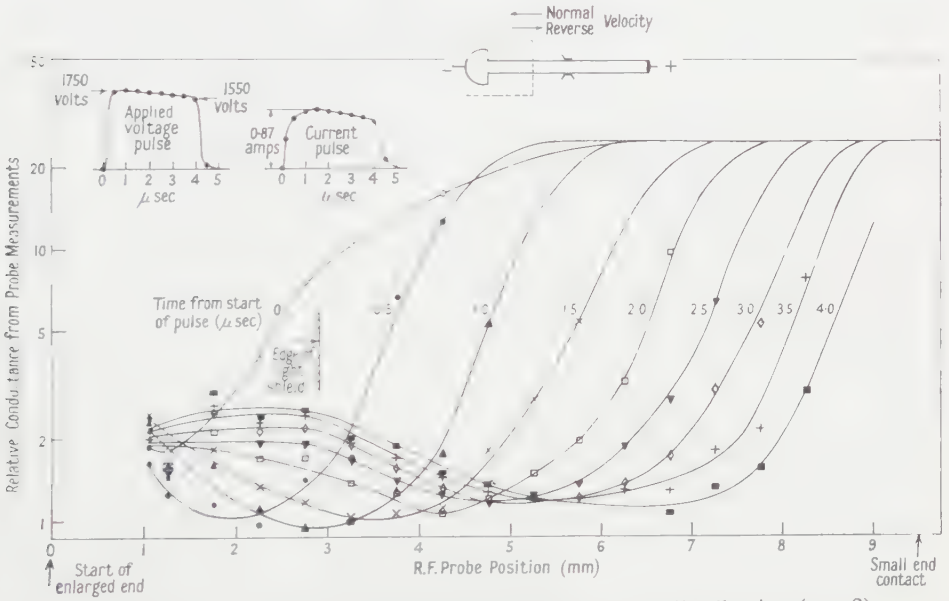

Figure 5. Reverse motion of injected carrier density distribution (run 2).

If the probes are moved towards the positive end, keeping the light shield in the same position, results similar to (*d*) and (*f*) are obtained, but the sharp drop in the probe trace occurs only some time after the beginning of the pulse. This is to be expected, as the drop occurs when the steep carrier density edge passes the probes. By observing the time interval between the start of the pulse and the sharp drop in the r.f. signal, as a function of probe position, a measure of the velocity of the edge can be obtained. To obtain further detail the signal amplitude at $\frac{1}{2}$ μsec intervals during the pulse was measured for various probe positions, and using the calibration of pulse amplitude against conductivity, an indication of the motion of the whole distribution was obtained. Results of measurements of this kind are shown in figure 5. The sensitivity of the r.f. probe measurements fell rapidly at the high conductance end of the range, so that in this figure the limiting high density value was assumed to be constant and equal to the value obtained from low field d.c. measurements with the specimen completely illuminated. These curves show the initial steepening of the front after

the pulse is first applied, and the subsequent motion without much change of shape. Since the resolution of the probes cannot be much better than 1 mm, the actual front may be substantially steeper than that indicated. If no injection were taking place from the negative end, the density should remain at a constant low level to the left of the front. That a rise occurs, moving in from the left, is a clear indication of injection from the enlarged negative end.

As a check on the theory, a comparison has been made, for two runs, between the observed velocities of the front as deduced directly from plots such as figure 5, and that deduced from the theory for the same observed density distributions. For the calculation, the data of figure 5 were plotted reciprocally to give relative resistance, and hence relative field, as a function of position. The absolute scale of field was found for each curve by comparing the area under the curve, with an allowance for end effects, with the voltage applied between the ends of the specimen. The simplified theory of equations (6) and (7) was applied, with the constant high density region defining one side, and the density minimum, field maximum point defining the other side. N was obtained from Hall coefficient measurements by Dr. E. H. Putley on an adjacent sample from the same crystal; this showed the material to have a net donor impurity density of $1{\cdot}16 \times 10^{13}$ cm^{-3}. This, together with the measurement of the current pulse through the specimen, enabled N/p_1 to be deduced. The field in the high density region was deduced from the current pulse, on the assumption that the density was the same as that obtained from the low field measurements with the whole length of the specimen illuminated.

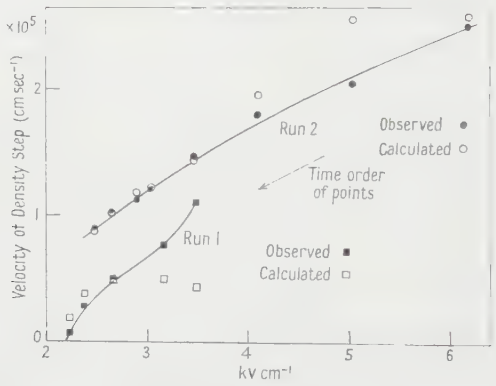

Figure 6. Reverse velocity of carrier density step as a function of the electric field in the extracted region.

The observed and calculated velocities are plotted in figure 6 (run 2). Also shown are the results of a slightly simplified calculation of another rather less detailed set of measurements of run 1, taken with a smaller pulse and a shorter length of specimen illuminated. The choice of field in the extracted region against which to plot the velocities is somewhat arbitrary, since the velocity depends on the densities and fields in both regions. The analysis indicates that, presumably due to injection from the enlarged end, the low density region was never completely extracted to the normal equilibrium level of the material. During run 1 the minimum density varied from 2–2½ times the normal value, while for run 2 it varied from 3–4 times the normal value. The lower level in run 1 is accounted for both by the lower field and the greater initial distance of the

injected region from the negative end. The difference in step velocity between run 1 and run 2 at the same maximum field is due mainly to this difference of level in the high field region. Run 1 demonstrates the stationary shock wave phenomenon, in that the final velocity of the step at the end of the pulse was almost zero. The distribution curves similar to figure 5 showed successively less change of either shape or position of the edge towards the end of the pulse. Because of the injection from the enlarged end, this condition would not be expected to persist indefinitely, but the pulse was not long enough to show the subsequent change.

In general, the agreement between the observed and calculated velocities is at least as good as could be expected from the nature of the measurements and the treatment used. This does not apply, however, to the two highest field points of run 1. The reason for the discrepancy here was apparent from an inspection of the experimental density distribution curves. The final stationary distribution was in approximately the same position relative to the initial distribution as that of the 1 μsec to the 0 μsec curves of figure 5, and the two earliest distributions corresponding to the two highest field points of figure 6 were changing in shape substantially; the assumptions of equations (6) and (7) are thus not valid. These equations will still give a crude estimate if suitably reduced carrier densities are taken for the high density region. Good agreement can be obtained with reasonable values for these densities. This argument might also apply to a smaller extent to the highest field point of run 2, and would put the theoretical above the experimental point. The difference between the observed and theoretical values for the three highest field points of run 2 may then be due to another partially invalid assumption of the experimental procedure. In determining the longitudinal d.c. field use was made of the transverse differential conductance between the r.f. probes; the transverse differential conductance is equal to the total longitudinal conductance (i I, not di dI) and is therefore the quantity required. However, due to the spreading of the current between the probes the quantity actually measured is not purely transverse, the spreading being less at the high than at the low d.c. fields. This effect would increase with field, and would tend to make the calculated maximum field, and hence the calculated velocity, too high.

3.2. *Current Voltage Characteristics*

In the experiment so far described the importance of injection from the enlarged negative end is emphasized by an examination of the shapes of the voltage and current pulses in figure 5. In the absence of injection, the current would steadily fall as the length of the extracted region increases, whereas initially the reverse happens, and the current maximum occurs later than the voltage maximum. The effect of the movement of the step during the first 1·5 μsec is more than compensated by the injection.

Some interesting current voltage characteristics have been obtained with other specimens having different end contacts. The first specimen tried had soldered end contacts and this showed strong injection from the negative end as indicated both by the shape of the current pulses and the r.f. probe observations. Another specimen however, also with soldered end contacts, behaved quite differently and showed that while the positive contact was injecting, the negative contact extracted above a certain critical pulse size; both processes could occur

simultaneously, with a density step appearing at a position in the specimen depending on the pulse size. Qualitatively the same result was obtained whether the specimen was illuminated or not, but tended to be most striking without illumination. Generally similar results were obtained with a specimen having p-type alloyed contacts at both ends. Pulse shapes, and the current–voltage characteristics are shown in figure 7.

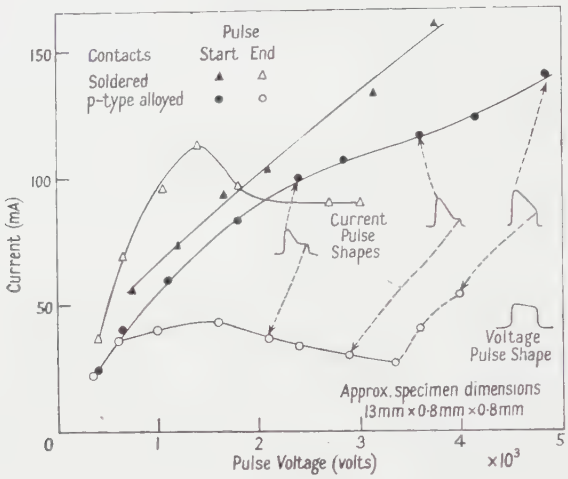

Figure 7. Current, voltage characteristics (no illumination).

If uniform extraction from the negative end is assumed the approximately constant current at the end of the pulse, independent of the size of the applied voltage pulse, is a straightforward consequence of the preceding theory of the motion of a density step. However, it seems reasonable to suppose that the efficiency of extraction will increase with field and further enhance the current limitation. These two factors, taken together with the tendency towards saturation of the hole and especially of the electron drift velocities, seems to offer a plausible explanation for the observed negative resistance characteristics shown in figure 7. On this argument, apart from any change in the length of the extracted region, an increase in the applied voltage would result in an increase in the field in the extracted region; this in turn would increase the extraction efficiency, and because of the relative insensitivity of the drift velocity to field changes the reduction in carrier density would more than compensate for the increase in field, and an actual reduction in current would occur. For the specimen with p-type contacts, rough calculation for the point at the bottom of the negative resistance slope indicates that the extraction here must be substantially complete; that is, the extrinsic electrons carry the greater part of the current.

3.3. *A Piezoresistance Effect*

For taking the r.f. measurements of the density distributions the specimens were gripped in between the spring loaded probes. It was noticed that removal of the probes sometimes produced changes both of shape and of amplitude, up to about 20%, in the d.c. current pulse, when this was large enough for velocity reversal to occur. For small pulses, for which the shapes of the current and voltage pulses were similar, the probes had no observable effect.

In addition to the thin mica insulation between the probes and the crystal, the probes were connected through high voltage blocking filters; no failures in this insulation were evident, and increasing the thickness of the mica insulation ten times did not alter the effect. The capacitance to the probes was several orders too small to have any significant effect on the d.c. current pulse. The probes had some thermal effect by helping to cool the specimen, but this could be clearly distinguished by its time constant from the main effect of pressing the probes into position. The effect therefore seems to be due directly to the pressure exerted by the probes; this could not be measured readily, but seems likely to have been of the order of kg mm^{-2}. From the measurement of Smith (1954), mechanical stress of this magnitude could, for a suitably oriented specimen, produce changes in mobility of both electrons and holes of the order of a few per cent. For a specimen oriented to give the maximum effect, transverse compression should increase the electron mobility and decrease the hole mobility. Paige (1958) has shown that the effect of stress decreases with field, and this is taken into account in figure 8 which shows qualitatively the way in which the electron mobility μ_n and hole mobility μ_p would be expected to vary in the region of the probes, when the specimen had been extracted to the position indicated. The reverse step velocity, as shown by the preceding high field theory, arises when the effect of the increase of μ_n/μ_p with increased density is sufficient to counteract the normal motion in the n-type material. As drawn on figure 8, to the right of the line YY the effect of the stress gradient is to oppose this tendency for μ_n/μ_p to increase with density. Since the balance between the opposing factors is fairly sensitive, a relatively small stress effect will be sufficient to prevent the reverse velocity. It seems probable therefore that the observed effect of the stress was due to the freezing of the distribution in the region indicated in figure 8.

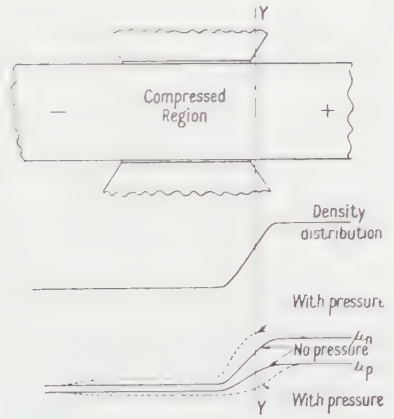

Figure 8. Qualitative variation of mobilities in a region of stress and carrier density gradients.

This suggestion agrees well with the detailed observations. With the probes about half way along the specimen their effect was to increase the current pulse towards the end, as would be expected if the extracted region were prevented from extending. Further, the r.f. signal showed some unusual features. During the pulse extraction was clearly indicated, but immediately after the end of the pulse the signal increased above its original value, corresponding to a carrier

density increase; this would be expected only if the density step were very close to the probes. The probes could be moved over a range of about 2 mm without much altering this signal, showing that the final position of the density step must have been moving with the probes. When the probe pressure was released sufficiently for the d.c. current to be changed substantially, but without much changing the amplitude of the r.f. signal, the latter still showed extraction during the pulse, but did not show the subsequent rise, indicating that the step was now no longer locked to the probes. With the specimen illuminated the effect of applying the probes was scarcely detectable. This also would be expected since with large injection the change in field at the step, and hence the gradient of the mobility ratio, is large, and the relatively small change due to the stress is insignificant.

Since the change of mobility ratio with stress is not confined to high fields, it is of interest to investigate whether any significant effects should result at low fields. The following much simplified treatment shows this to be so.

With the same notation as before, and neglecting both diffusion and recombination

$$j = pE\mu_p + (p+N)E\mu_n \qquad \ldots\ldots(11)$$

and

$$\left(\frac{\partial p}{\partial t}\right)_x = -\left(\frac{\partial}{\partial x}\right)_t pE\mu_p. \qquad \ldots\ldots(12)$$

Taking the mobilities as functions of stress, and hence of position in an inhomogeneously stressed material, but not of E, we find

$$\left(\frac{\partial p}{\partial t}\right)_x = -V_0\left\{\left(\frac{\partial p}{\partial x}\right)_t - \frac{p}{N}(p+N)\left(\frac{1}{\mu_n}\frac{d\mu_n}{dx} - \frac{1}{\mu_p}\frac{d\mu_p}{dx}\right)\right\} \qquad \ldots\ldots(13)$$

where

$$V_0 = E\mu_p\left[1+\frac{p}{N}\left(1+\frac{\mu_p}{\mu_n}\right)\right]^{-1}$$

is the normal density distribution velocity for constant mobilities.

Equation (13) can be simplified slightly to

$$\left(\frac{\partial p}{\partial t}\right)_x = -V_0\left\{\left(\frac{\partial p}{\partial x}\right)_t - \frac{p}{N}(p+N)\frac{\alpha}{\mu_n}\frac{d\mu_n}{dx}\right\} \qquad \ldots\ldots(14)$$

where α is a little less than 2, since the change in μ_p is of opposite sign and rather smaller than that in μ_n.

A steady state solution is obtained by equating the right-hand side to zero. This gives

$$\frac{p}{p_0} = \left(\frac{\mu_n}{\mu_{n_0}}\right)^{\alpha}\left[1+\frac{p_0}{N}\left\{1-\left(\frac{\mu_n}{\mu_{n_0}}\right)^{\alpha}\right\}\right]^{-1} \qquad \ldots\ldots(15)$$

where the subscripts zero refer to the unstrained region.

$(\mu_n/\mu_{n_0})^{\alpha}$ could approach 1·1 at the breaking strain in tension along the line of the current, and could probably be even greater for transverse compression. For this value

$$\frac{p}{p_0} = \frac{1\cdot1}{1-0\cdot1p_0/N}. \qquad \ldots\ldots(16)$$

According to this p will tend to infinity as p_0/N tends to 10. In fact diffusion and recombination will determine the final value, which will thus depend on the current. Apart from the neglect of diffusion and recombination, for very near

intrinsic material ($p_0 |N|$ large) this expression has little physical meaning since, in this region, distribution velocities tend to zero and are likely to be modified by the mobility ratio changes, so that the hypothetical stationary state would never be attained. Nevertheless quite substantial changes in concentration seem possible. The magnitude of the effect falls rapidly as the impurity concentration increases, but might, under some conditions, be significant in the interpretation of piezoresistance measurements on germanium above perhaps 10–20 ohm cm resistivity.

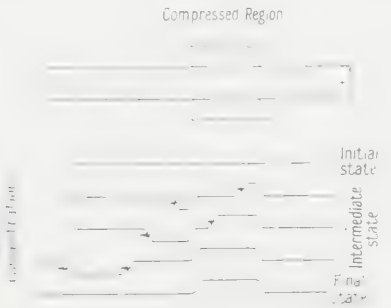

Figure 9. Expected result of current flow through inhomogeneously strained n-type germanium at low fields.

For small changes of p the approximate solution of (14) indicates the way in which the stationary state is approached. Consider an n-type germanium bar with a central region under transverse compression, and with uniform carrier concentrations everywhere before the current flows (energy band changes are neglected). Figure 9 shows the expected result. An extracted pulse moves out from the compressed region, leaving this with an increased concentration. The magnitude of the current effects only the rate of this process, and not the final concentration, except in so far as this is modified by diffusion and recombination.

§ 4. Discussion and Conclusion

In this paper it has been shown that the variation of the mobility ratio with electric field in germanium can cause the motion of a carrier density distribution, at high fields, to be completely different from the normal low field behaviour, and that an actual reversal of the direction of motion can occur. For this field dependent phenomenon the mobility ratio variation, being due to the field and hence the distribution carrying the current, is spatially tied to the distribution, but the effect of mechanical stress has shown that a variation fixed relative to the crystal can also be significant. In general, new effects of this kind may result from any phenomenon, such as for example magnetoresistance, which can influence electron and hole mobilities unequally.

The detailed high field behaviour is known for relatively few semiconductors. From measurements on silicon (Prior 1960) the difference between the drift velocity–field relationship for holes and electrons appears sufficient to cause a reverse carrier transport effect in near intrinsic material, if this were available, or in suitably injected material. For indium antimonide Prior (1958) found no variation of electron mobility with field up to 800 V cm^{-1} at 300° K, but Glicksman and Steele (1958, 1959) have shown that at 77° K the electron drift velocity is not

linear with field, and in the presence of a transverse magnetic field the velocity exhibits saturation. Data for holes are not available but seem likely to be quite different, so that with this material at 77°K the necessary conditions for the reverse transport effect appear to exist, particularly in the presence of a suitable magnetic field.

The main practical implication of the results obtained for germanium is that, where high fields are involved, particularly in near intrinsic material, anomalous velocities of a density distribution are likely, and the possibility of injection or extraction from the negative contacts of n-type specimens should be considered.

The apparent negative resistance shown in figure 7 appears to warrant further study. The experiment does not prove conclusively that a true negative resistance was in fact obtained since each point on the curve is associated with a different past history, and it is not necessarily possible to traverse directly from one point to another on the drawn curve. The associated time constant of the effect was a few microseconds, but if the same phenomenon occurred with a shorter specimen this would presumably be reduced, as would also the voltage scale. It is hoped to investigate these points more fully. Further work on the injection and extraction properties of different contacts and the effects of cross section variations is also proposed.

Acknowledgments

The author is indebted to Mr. I. G. Cressell of Marconi's Wireless Telegraph Company Ltd., for the supply of the high quality germanium crystal used in the investigation, and to his colleague Dr. D. P. Jenkins for discussion of equation (13). This paper is published by permission of the Controller, H.M. Stationery Office.

References

Glicksman, M., and Steele, M. C., 1958, *Phys. Rev.*, **110**, 1204.
—— 1959, *J. Phys. Chem. Solids*, **8**, 242.
Gunn, J. B., 1956, *J. Electron.*, **2**, 87.
Herring, C., 1949, *Bell Syst. Tech. J.*, **28**, 401.
Paige, E. G. S., 1958, *Proc. Phys. Soc.*, **72**, 921.
Paige, E. G. S., and McLean, T. P., 1960, *J. Phys. Chem. Solids.*, in the press.
Prior, A. C., 1958, *J. Electron.*, **4**, 165.
—— 1960, *J. Phys. Chem. Solids*, **12**, 175.
Ryder, E. J., 1953, *Phys. Rev.*, **90**, 766.
Smith, C. S., 1954, *Phys. Rev.*, **94**, 42.

A Phenomenological Theory of the Characteristic Energy Losses of Fast Electrons in Metals

By C. B. WILSON

Department of Theoretical Physics, University of Liverpool

Communicated by H. Fröhlich; MS. received 19th February 1960

Abstract. The characteristic energy loss levels are derived phenomenologically for a target metal having an optical absorption band of similar energy to the free electron plasma frequency. The various relative positions of the band and plasma frequency are considered and it is shown that the presence of an optical band introduces further particle absorption levels and may shift in either direction or completely screen out the plasma line. The theory agrees with the general experimental picture, and predicts certain results which had hitherto been unsatisfactorily accounted for, but the lack of information concerning optical absorption bands in the relevant energy region precludes any detailed comparison for a particular metal.

§ 1. Introduction

The work of Bohm, Pines *et al.*† on the collective behaviour of electrons in solids has awakened a renewed interest in the characteristic energy losses observed when a fast electron passes through a thin target. Although the losses in certain metals (e.g. Al) seem to be well explained in terms of plasma excitation, the loss spectra in many cases have not yet been accounted for in a satisfactory way.

Since in most metals optical absorption levels occur at similar energies to the plasma frequency, it seems likely that along with plasmon excitation there is the possibility that the fast electron may excite an optical transition. In a recent paper Fröhlich (1958a) has given in a general way a phenomenological dielectric approach whereby the particle energy losses may be related to the transition frequencies available in the target.

It is the purpose of the present paper to show on the basis of a simple model that the combination of losses to the excitation of plasmons and of optical transitions leads to a prediction of many of the features of the general experimental picture.

The model which we choose for the target is that of a solid containing two sets of oscillators. One set represents free electrons, the other represents bound electrons which can undergo transitions giving rise to an optical absorption band. We consider two cases: that of a very narrow band (§ 3) and that of a broad band (§ 4).

We find: (*a*) The presence of an optical band may shift the free electron plasma frequency upwards or downwards in energy depending upon the relative positions of the band and the plasma frequency. (*b*) Due to the band there appears a particle absorption line which corresponds to the set of bound electrons in a similar way to that in which the free electron plasma line corresponds to the

† For detailed references and a review of relevant material see Pines (1956).

free electrons. (*c*) In the case of a broad optical band there is present one or more (relatively) narrow particle absorption bands lying inside the optical band.

Since the paper by Fröhlich, referred to above, may not be readily available we give in the next paragraph a brief account of his assumptions and results relevant to the present work.

§ 2. The Probability of Energy Loss

Let $P(\omega)\,d\omega$ be the probability per second that the incoming electron loses an energy quantum $\hbar\omega$ in the range $d\omega$ to the target, then the rate of energy transfer is given by

$$\frac{dW}{dt} = \int_0^\infty P(\omega)\hbar\omega\, d\omega. \qquad \ldots\ldots (2.1)$$

If we assume that the incoming electron is non-relativistic, that the energy transfer is so small that its velocity may be considered constant, and that the magnetic susceptibility of the solid is zero so that magnetic interactions maybe ignored, an expression for dW/dt can be derived from electromagnetic field theory which, on comparison with (2.1), gives

$$P(\omega) = \frac{1}{\pi^2}\frac{e^2Z^2}{\hbar v}\sum_{\alpha,\,\beta=1}^{3}\int_0^{k_{n_0}} k_{n}\,dk_{n}\int_0^{2\pi} d\phi[\epsilon^{-1}(\mathbf{k},\omega)]_{2\alpha\beta}\frac{k_\alpha k_\beta}{[k_{n}^{\,2}+(\omega^2/v^2)]^2}\cdot \qquad (2.2)$$

The wave vector $\mathbf{k}$ has been expressed in cylindrical coordinates k_v, k_{n} and ϕ and we have introduced an upper limit k_{n_0} because there exists a maximum k_0 to the magnitude of the momentum transfer.

$\epsilon_{\alpha\beta}(\mathbf{k},\omega)$ is the tensorial complex dielectric constant and

$$(\epsilon^{-1})_{\alpha\beta} = (\epsilon^{-1})_{1\alpha\beta} + i(\epsilon^{-1})_{2\alpha\beta}. \qquad \ldots\ldots (2.3)$$

If we suppose the target to be isotropic so that the dielectric constant depends only on k (the magnitude of $\mathbf{k}$) and then assume that ϵ is independent of k for $k<k_0$, (2.2) reduces to

$$P(\omega) = \frac{2}{\pi}\frac{e^2Z^2}{\hbar v}\frac{\epsilon_2(\omega)}{\epsilon_1^{\,2}(\omega)+\epsilon_2^{\,2}(\omega)}\log\frac{k_0 v}{\omega}. \qquad \ldots\ldots (2.4)$$

Since the logarithmic term is slowly varying it is essentially the expression $\epsilon_2(\omega)/[\epsilon_1^{\,2}(\omega)+\epsilon_2^{\,2}(\omega)]$ which gives information about the particle absorption levels.

§ 3. A Narrow Optical Absorption Band

The complex dielectric constant of n electrons (in unit volume) all of which may undergo a transition of frequency ω_1 with oscillator strength f_1 and relaxation time τ_1 may be represented by (Kramers and Heisenberg 1925)

$$\epsilon(\omega\,;\omega_1) = 1 + \frac{\omega_p^{\,2}f_1}{\omega_1^{\,2}-\omega^2-i\omega/\tau_1} \qquad \ldots\ldots (3.1)$$

where, as usual

$$\omega_p^{\,2} = 4\pi ne^2/m.$$

Splitting this into real and imaginary parts

$$\epsilon_1(\omega\,;\omega_1) = 1 + \frac{\omega_p^{\,2}f_1(\omega_1^{\,2}-\omega^2)}{(\omega_1^{\,2}-\omega^2)^2+\omega^2/\tau_1^{\,2}} \qquad \ldots\ldots (3.2)$$

$$\epsilon_2(\omega\,;\omega_1) = \frac{(\omega/\tau_1)\omega_p^{\,2}f_1}{(\omega_1^{\,2}-\omega^2)^2+\omega^2/\tau_1^{\,2}}. \qquad \ldots\ldots (3.3)$$

The optical absorption is proportional to ϵ_2, which, as we see from (3.3), becomes a δ-function as the relaxation time becomes large such that

$$\omega_1\tau_1 \gg 1. \qquad \ldots\ldots(3.4)$$

If we suppose the optical absorption band in the target to be so narrow that it may be well approximated by a line, equations (3.2) and (3.3) represent that part of the dielectric constant due to the bound electrons. Adding to this the contribution from the free electrons

$$\epsilon_1(\omega\,;0,\omega_1) = 1 - \frac{\omega_1{}^2 f_0\omega^2}{\omega^4+\omega^2/\tau_0{}^2} + \frac{\omega_p{}^2 f_1(\omega_1{}^2-\omega^2)}{(\omega_1{}^2-\omega^2)^2+\omega^2/\tau_1{}^2} \qquad \ldots\ldots(3.5)$$

$$\epsilon_2(\omega\,;0,\omega_1) = \frac{(\omega/\tau_0)\omega_p{}^2 f_0}{\omega^4+\omega^2/\tau_0{}^2} + \frac{(\omega/\tau_1)\omega_p{}^2 f_1}{(\omega_1{}^2-\omega^2)^2+\omega^2/\tau_1{}^2} \qquad \ldots\ldots(3.6)$$

where the suffix 0 refers to the free electrons and 1 to the bound electrons.

For large τ_0 and τ_1, $\epsilon_2(\omega\,;0,\omega_1)$ approaches a sum of two δ-functions and the expression $\epsilon_2/(\epsilon_1{}^2+\epsilon_2{}^2)$ is zero except at the solutions of $\epsilon_1(\omega\,;0,\omega_1)=0$ where it is a δ-function; that is, at the solutions of

$$1 - \frac{\omega_p{}^2 f_0}{\omega^2} + \frac{\omega_p{}^2 f_1}{\omega_1{}^2-\omega^2} = 0. \qquad \ldots\ldots(3.7)$$

We find it most profitable to study the solutions of (3.7) graphically. In figure 1 we have drawn $1-\omega_p{}^2 f_0/\omega^2$ and $-\omega_p{}^2 f_1/(\omega_1{}^2-\omega^2)$ for $\sqrt{f_0}\omega_p$ below ω_1. The two particle absorption lines are indicated. It is easy to see how the positions of the lines vary with f_1 by altering the vertical scale of the $-\omega_p{}^2 f_1/(\omega_1{}^2-\omega^2)$ curve. In figure 2, $\sqrt{f_0}\omega_p$ is greater than ω_1.

The intensity of a line is given by

$$I = \int_R P(\omega)\hbar\omega\, d\omega \qquad \ldots\ldots(3.8)$$

where R is an energy region containing only the line in question ($P(\omega)$ is given by (2.4)).

The two lines are then specified by: lower line, position ω_{l_1}, intensity I_1; upper line, position ω_{l_2}, intensity I_2.

By considering the behaviour of the lines as $f_1 \to 0$ we can see which line corresponds to the plasma line. We see that in the first case the plasma line is shifted downwards in energy by the presence of an optical band, and in the other it is shifted upwards.

§ 4. A Broad Optical Absorption Band

If the optical absorption band is broad we may represent it by a continuous set of oscillators of frequency Ω in the range $\Omega_1 < \Omega < \Omega_2$. We may suppose that there is a total of nf_1 oscillators (electrons) comprising the band and define $nf(\Omega)\,d\Omega$ as the number oscillators with proper frequency Ω in the range $d\Omega$, where

$$\int_{\Omega_1}^{\Omega_2} f(\Omega)\,d\Omega = f_1. \qquad \ldots\ldots(4.1)$$

Then, if $f(\Omega)$ is zero for $\Omega<\Omega_1$, $\Omega>\Omega_2$ we may write, from (3.3)

$$\epsilon_2(\omega\,;b) = \int_0^\infty \epsilon_2(\omega\,;\Omega)\,d\Omega = \int_0^\infty d\Omega\, \frac{\omega_p{}^2 f(\Omega)\omega/\tau(\Omega)}{(\Omega^2-\omega^2)^2+\omega^2/\tau^2(\Omega)} \qquad \ldots\ldots(4.2)$$

where b implies the band $[\Omega_1, \Omega_2]$.

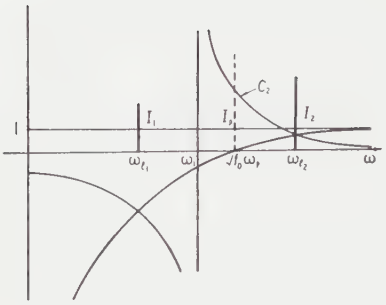

Figure 1. Unshifted plasma frequency below optical absorption line. As $f_1 \to 0$: $I_1 \to I_p$, $\omega_{l_1} \to \sqrt{f_0}\omega_p$; $I_2 \to 0$, $\omega_{l_2} \to \omega_1$.

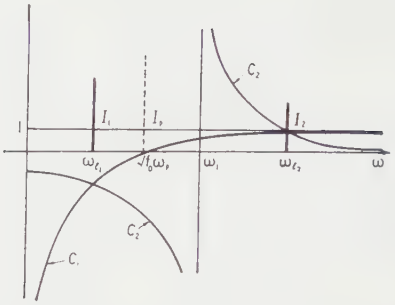

Figure 2. Unshifted plasma frequency above optical absorption line. As $f_1 \to 0$: $I_1 \to 0$, $\omega_{l_1} \to \omega_1$; $I_2 \to I_p$, $\omega_{l_2} \to \sqrt{f_0}\omega_p$.

Notes on the figures:
The following notes apply to all of the figures.

The unshifted plasma line is shown broken. It has position $\sqrt{f_0}\omega_p$ and intensity I_p.

Absorption bands are *indicated* by a rectangle; the width drawn has no significance.

The intensity (I) associated with each band is the total intensity of the band.

The heights of lines and bands are not drawn to scale. A band or line drawn higher than the rest is the one which remains when $f_1 \to 0$ or $f(\Omega) \to 0$.

$$C_1 \text{ is } 1-\omega_p^2 f_0/\omega^2,$$
$$C_2 \text{ is } -\omega_p^2 f_1/(\omega_1^2-\omega^2),$$
$$C_3 \text{ is } -\mathscr{P}\int_{\Omega_1}^{\Omega_2} d\Omega\, \frac{\omega_p^2 f(\Omega)}{\Omega^2-\omega^2}.$$

For large relaxation times $\epsilon_2(\omega;\Omega)$ becomes a δ-function, and we can perform the integration to give

$$\epsilon_2(\omega;b) = \tfrac{1}{2}\pi\omega_p^2 f(\omega)/\omega. \qquad \ldots\ldots (4.3)$$

By a similar generalization of (3·2) to a continuous band, we find

$$\epsilon_1(\omega;b) = 1+\frac{2}{\pi}\mathscr{P}\int_0^\infty d\Omega\, \frac{\omega_p^2 f(\Omega)}{\Omega^2-\omega^2}. \qquad \ldots\ldots (4.4)$$

The consistency of (4.3) and (4.4) is assured by showing that they satisfy the dispersion relation (Fröhlich 1958b)

$$\epsilon_1(\omega)-1 = \frac{2}{\pi}\mathscr{P}\int_0^\infty \epsilon_2(\mu)\,\frac{\mu}{\mu^2-\omega^2}\,d\mu.$$

Adding the contributions from the free electrons we have

$$\epsilon_2(\omega;0,b) = \begin{cases} \dfrac{(\omega/\tau_0)\omega_p^2 f_0}{\omega^4+\omega^2/\tau_0^2} + \dfrac{\pi}{2}\dfrac{\omega_p^2 f(\omega)}{\omega} & \\ \qquad \text{for} \quad \Omega_1 \leqslant \omega \leqslant \Omega_2 & \ldots\ldots (4.5) \\ \dfrac{(\omega/\tau_0)\omega_p^2 f_0}{\omega^4+\omega^2/\tau_0^2} & \\ \qquad \text{for} \quad \omega < \Omega_1,\ \omega > \Omega_2 & \end{cases}$$

$$\epsilon_1(\omega;0,b) = 1-\frac{\omega_p^2 f_0 \omega^2}{\omega^4+\omega^2/\tau_0^2}+\mathscr{P}\int_0^\infty d\Omega\,\frac{\omega_p^2 f(\Omega)}{\Omega^2-\omega^2}. \qquad \ldots\ldots (4.6)$$

Hence

$$\frac{\epsilon_2(\omega;0,b)}{\epsilon_1^2(\omega;0,b)+\epsilon_2^2(\omega;0,b)} = \begin{cases} \left[\dfrac{(\omega/\tau_0)\omega_p^2 f_0}{\omega^4+\omega^2/\tau_0^2}+\dfrac{\pi}{2}\dfrac{\omega_p^2 f(\omega)}{\omega}\right]A & \text{for } \Omega_1 \leqslant \omega \leqslant \Omega_2 \quad \ldots\ldots(4.7) \\ \left[\dfrac{(\omega/\tau_0)\omega_p^2 f_0}{\omega^4+\omega^2/\tau_0^2}\right]B & \text{for } \omega<\Omega_1, \omega>\Omega_2 \quad \ldots\ldots(4.8) \end{cases}$$

where

$$A^{-1}=\left\{1-\frac{\omega_p^2 f_0\omega^2}{\omega^4+\omega^2/\tau_0^2}+\mathscr{P}\int_{\Omega_1}^{\Omega_2}d\Omega\,\frac{\omega_p^2 f(\Omega)}{\Omega^2-\omega^2}\right\}^2+\left\{\frac{(\omega/\tau_0)\omega_p^2 f_0}{\omega^4+\omega^2/\tau_0^2}+\frac{\pi}{2}\frac{\omega_p^2 f(\omega)}{\omega}\right\}^2 \quad \ldots\ldots(4.9)$$

and

$$B^{-1}=\left\{1-\frac{\omega_p^2 f_0\omega^2}{\omega^4+\omega^2/\tau_0^2}+\int_{\Omega_1}^{\Omega_2}d\Omega\,\frac{\omega_p^2 f(\Omega)}{\Omega^2-\omega^2}\right\}^2+\left\{\frac{(\omega/\tau_0)\omega_p^2 f_0}{\omega^4+\omega^2/\tau_0^2}\right\}^2. \quad \ldots\ldots(4.10)$$

The expression (4.8) approaches a δ-function as $\tau_0\to\infty$ and gives two absorption lines at the two solutions of

$$1-\frac{f_0\omega_p^2}{\omega^2}+\int_{\Omega}^{\Omega_2}d\Omega\,\frac{\omega_p^2 f(\Omega)}{\Omega^2-\omega^2}=0 \quad (\omega<\Omega_1,\omega>\Omega_2). \quad \ldots\ldots(4.11)$$

These two lines occur one on either side of the optical absorption band and correspond to the two lines obtained in the previous section. However, (4.7) does not approach a δ-function for large relaxation times; it gives a particle absorption band situated inside the optical absorption band. We can see immediately that if $\epsilon_2(\omega;0,b)$, i.e. $\pi\omega_p^2 f(\omega)/2\omega$ does not vary considerably over the region where $\epsilon_1(\omega;0,b)$ is small, the maximum of the particle absorption probability occurs at ω_{l_3} and is given by

$$\frac{2\omega_{l_3}}{\pi\omega_p^2 f(\omega_{l_3})} \quad \ldots\ldots(4.12)$$

where ω_{l_3} is the solution of

$$1-\frac{\omega_p^2 f_0}{\omega^2}+\mathscr{P}\int_{\Omega_1}^{\Omega_2}d\Omega\,\frac{\omega_p^2 f(\Omega)}{\Omega^2-\omega^2} \quad (\Omega_1\leqslant\omega\leqslant\Omega_2). \quad \ldots\ldots(4.13)$$

Let us distinguish three cases:

(i) $\sqrt{f_0}\omega_p<\Omega_1$,

(ii) $\Omega_1\leqslant\sqrt{f_0}\omega_p\leqslant\Omega_2$,

(iii) $\sqrt{f_0}\omega_p>\Omega_2$,

and characterize the absorption levels by: lower line, position ω_{l_1}, intensity I_1; upper line, position ω_{l_2}, intensity I_2; band, maximum at ω_{l_3}, total intensity I_3, where

$$I_3=\int_{\Omega_1}^{\Omega_2}P(\Omega)\hbar\Omega\,d\Omega. \quad \ldots\ldots(4.14)$$

As in the last section, by considering $f(\Omega)\to 0$, we can see which of the absorption levels corresponds to the shifted plasma line. Figures 3, 4 (*a*), 4 (*b*), 5 (*a*), 5 (*b*) and 6 are based upon calculations which assume the optical absorption band to be flat.

It will be seen that cases (i) and (iii), figures 3 and 6, lead to a similar picture to that given by a narrow optical band, but with the addition of a particle absorption band inside the optical band. As $f(\Omega)\to 0$ this particle band approaches a

limiting position at one end of the optical band. From (3.12) the absorption probability increases in height, but in the limit $f(\Omega)=0$ there can be no particle absorption level in this position, so we conclude that its width must decrease rapidly with $f(\Omega)$ to make $I_3 \to 0$.

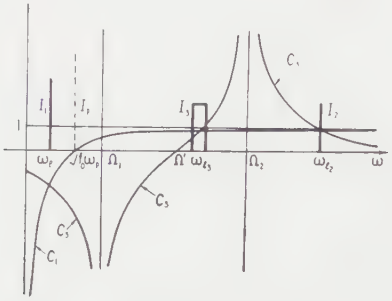

Figure 3. Unshifted plasma frequency below optical absorption band. As $f(\Omega)\to 0$: $I_1 \to I_p$, $\omega_{l_1} \to \sqrt{f_0}\omega_p$; $I_2 \to 0$, $\omega_{l_2} \to \Omega_2$; $I_3 \to 0$, $\omega_{l_3} \to \Omega_2$.

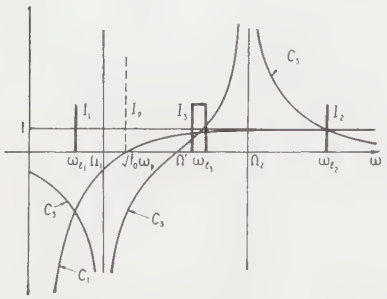

Figure 4(*a*). Unshifted plasma frequency towards bottom of strong optical absorption band. As $f(\Omega)\to 0$ the situation tends to that shown in figure 4(*b*).

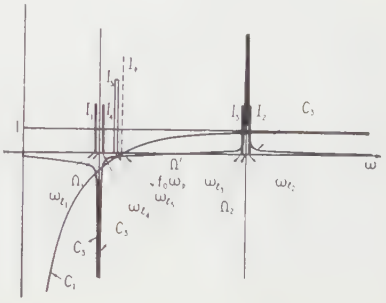

Figure 4(*b*). Unshifted plasma frequency towards bottom of weak optical absorption band. As $f(\Omega)\to 0$: $I_1 \to 0$, $\omega_{l_1} \to \Omega_1$; $I_2 \to 0$, $\omega_{l_2} \to \Omega_2$; $I_3 \to 0$, $\omega_{l_3} \to \Omega_2$; $I_4 \to 0$, $\omega_{l_4} \to \Omega_1$; $I_5 \to I_p$, $\omega_{l_5} \to \sqrt{f_0}\omega_p$.

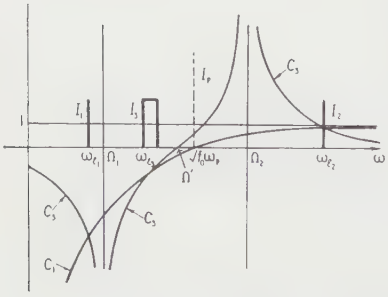

Figure 5(*a*). Unshifted plasma frequency towards top of strong optical absorption band. As $f(\Omega)\to 0$ the situation tends to that shown in figure 5(*b*).

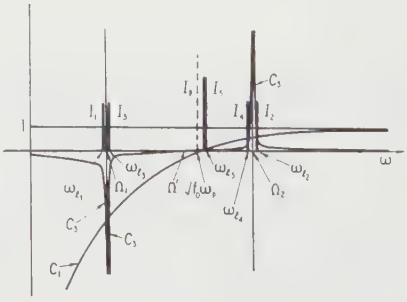

Figure 5(*b*). Unshifted plasma frequency towards top of weak optical absorption band. As $f(\Omega)\to 0$: $I_1 \to 0$, $\omega_{l_1} \to \Omega_1$; $I_2 \to 0$, $\omega_{l_2} \to \Omega_2$; $I_3 \to 0$, $\omega_{l_3} \to \Omega_1$; $I_4 \to 0$, $\omega_{l_4} \to \Omega_2$; $I_5 \to I_p$, $\omega_{l_5} \to \sqrt{f_0}\omega_p$.

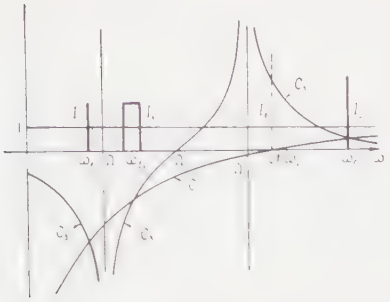

Figure 6. Unshifted plasma frequency above optical absorption band. As $f(\Omega)\rightarrow 0$: $I_1\rightarrow 0, \omega_{l_1}\rightarrow \Omega_1$; $I_2\rightarrow I_p, \omega_{l_2}\rightarrow \sqrt{f_0}\omega_p$; $I_3\rightarrow 0, \omega_{l_3}\rightarrow \Omega_1$.

The situation in case (ii) is more complicated. We must distinguish between (*a*) $\sqrt{f_0}\omega_p < \Omega'$ (figure 4 (*a*)) and (*b*) $\sqrt{f_0}\omega_p > \Omega'$ (figure 4 (*b*)), where Ω' is the solution of

$$\mathcal{P}\int_0^\infty d\Omega\,\frac{\omega_p^2 f(\Omega)}{\Omega^2-\omega^2} = 0$$

$$\text{for} \quad \Omega_1 \leqslant \omega \leqslant \Omega_2.$$

Consider case (*a*): as $f(\Omega)\rightarrow 0$ the particle absorption band moves towards the top of the optical absorption band, away from the natural plasma frequency. The two external lines also approach limiting positions at their respective ends of the optical band. Thus all three particle absorption levels shown in figure 4 (*a*) disappear with $f(\Omega)$. However, as $f(\Omega)$ becomes small, two more levels appear (figure 5 (*a*)) (giving a total of five particle absorption levels). One of these disappears with $f(\Omega)$ and the other becomes the plasma line. A similar situation prevails in case (*b*) (figure 5 (*b*)).

In the cases of figures 4 (*a*) and 4 (*b*) one can hardly say that the plasma line is shifted by the presence of the optical band; it is, in fact, completely screened out and another particle absorption level appears inside the optical band well removed from the plasma frequency.

§ 5. Conclusion

The presence of an optical absorption band in the target of similar energy to the plasma frequency will give rise to another particle absorption line lying outside the optical band. If the optical band is broad there will be a narrow particle absorption band inside the range of the optical band. The plasma line will be shifted downwards if it lies below the optical band and upwards if it lies above. If it lies inside the optical band, the situation is more complicated, the various possibilities being contained in figures 4 and 5. To distinguish between these cases requires more detailed information about $f(\Omega)$ in the relevant energy range (~ 3000 A to ~ 500 A) than is at present available. In fact, had we this information, we would be in a position to calculate the particle absorption levels. On the other hand, if we had reliable experimental results for the particle absorption levels, we should be able to say something about the expected optical absorption in this energy region. Unfortunately, the experimental results differ very much in detail from one experimenter to another.† We would, however, suggest that

† For a comprehensive review of the available experimental data see Marton, Leder and Mendlowitz (1955).

figure 4 (*a*) corresponds well (within our simple model) to the general experimental picture for several metals (e.g. Cu and Zn), in which the calculated plasma frequency is well below the most frequently observed absorption level, the level appearing as a band. In copper, for instance, the calculated plasma frequency is about 11 ev, whereas the only absorption level which most investigators agree upon is a band at around 20 ev. This suggests that there is, in copper, an optical absorption band stretching from below 11 ev to at least above 20 ev.

Acknowledgment

I should like to thank Professor Fröhlich for introducing me to this problem, and for much encouragement and advice.

References

Fröhlich, H., 1958 a, *Max Planck Festschrift* (Berlin: D.V.W.).

—— 1958 b, *Theory of Dielectrics* (Oxford: University Press) (2nd edn), Appendix A1(iii).

Kramers, H. A., and Heisenberg, W., 1925, *Z. Phys.*, **31,** 681.

Marton, L., Leder, L. B., and Mendlowitz, H., 1955, *Advances in Electronics and in Electron Physics*, **VII,** 183.

Pines, D., 1956, *Rev. Mod. Phys.*, **28,** 184.

On the Stripping of Two Nucleons

By H. C. NEWNS
Department of Theoretical Physics, University of Liverpool

MS. received 8th March 1960, in final form 14th April 1960

Abstract. Formulae are obtained for the differential cross sections of the (^{3}He, p), (t, p) and (d, α) reactions in which the structure of the projectile and captured nucleons is taken into account. The relationship of these formulae to the results of earlier theories in which the structure is neglected is considered. The application of the theory to the interpretation of experimental results is discussed.

§ 1. Introduction

Following the success of the (d, p) and (d, n) reactions, a considerable amount of experimental work has been directed to the study of more complicated reactions, many of which show features which suggest that they proceed, at least in part, by a direct process. In particular, considerable interest has centred recently on reactions which involve the transfer of two nucleons such as the (^{3}He, p), (t, p) and (d, α) reactions. If these are regarded as proceeding by a direct process, one can picture the reaction as being similar to a (d, p) reaction but with the difference that the stripping involves two nucleons.

The theoretical study of reactions which involve the stripping of more than one nucleon has been very limited. Soon after stripping was established, R. G. Thomas proposed a general type of stripping reaction in which several nucleons could be transferred from the projectile to the target nucleus. This work was never published but Tobocman (1956) and Butler (1957) have given very similar treatments. They all treat the stripped particles as having no structure. The projectile has a structure only in that it is treated as two 'lumps' of nuclear matter bound together, one of which is stripped off and captured by the target nucleus and the other emerges. These treatments yield an angular distribution of the form $g(\theta)[j_L(kr_0)]^2$, where L is the orbital angular momentum carried into the nucleus by the captured nucleons, k is the momentum transfer corresponding to scattering angle θ, and r_0 is a length of the order of magnitude of the nuclear radius†. The factor $g(\theta)$ comes from the internal wave function for the projectile representing the relative motion of its two constituents, and corresponds to the 'deuteron factor' of the ordinary stripping reaction.

It is of interest to investigate whether taking into account the structure of the projectile and stripped nucleons affects the cross section to any great extent. Indeed it is necessary to do this if one wishes to interpret the experiments with reference to the structure of the nuclei involved.

† One can use instead of the single spherical Bessel function the usual Butler Wronskian.

The only treatment which attempts to do this for the (^{3}He, p) and (d, α) reactions was given by el Nadi (1957). Unfortunately his results are invalidated by a serious error in summing and averaging over the magnetic quantum numbers of the initial and final states.†

In §§ 2 and 3 of this paper we obtain formulae for the differential cross sections of the (^{3}He, p), (t, p) and (d, α) reactions using a method which is similar to that used by el Nadi (1957). However, the results are presented in a form which affords easy comparison with the result of the simple theory and illustrates the difference produced in the cross section by taking into account the structure of the particles. Limiting cases of this result which produce a specially simple form for the angular distribution are discussed in § 4. Finally, in § 5 we discuss the applications of the theory and the interpretation of experimental results for the (^{3}He, p) reaction.

§ 2. Evaluation of the Matrix Element for the (^{3}He, p) and (t, p) Reactions

There are two approaches to stripping theory which in Born's approximation are equivalent. These differ in that one uses as perturbation the interaction in the initial channel, and the other the interaction in the final channel. The second method was originally used by Bhatia and Huang. For convenience we term the first the Butler approach since it yields the same result as his original method. The results obtained from these theories differ because of the extra approximations which are made in both theories in the evaluation of the matrix element. It has become customary to use the Butler approach in the treatment of these reactions. However, in the present case this leads to radial integrals which cannot be evaluated in simple terms and so in order to obtain an explicit expression for the differential cross section we use the Bhatia–Huang treatment.

We imagine a ^{3}He nucleus or triton which we label '3' incident upon an initial nucleus I. Two nucleons 1 and 2 are stripped from the projectile and captured by the initial nucleus to form the final nucleus F. A proton p emerges. Using the Bhatia–Huang approach we need to evaluate the matrix element

$$I = \langle J_F M_F, \mathrm{p} | V_{1I}(r_1) + V_{2I}(r_2) | J_I M_I, 3 \rangle. \qquad \ldots\ldots (1)$$

The V's should contain the coordinates of the nucleons in the initial nucleus. However, we shall treat the final nucleus from the point of view of the shell model and so it is not inconsistent to assume the V's to be functions of r_1 and r_2 only. This will yield the result that stripping will only lead to states of the final nucleus which contain the initial nucleus in its ground state—a result which arises in Butler's approach.

We now expand the final state into a sum of products of the states of the initial nucleus and of the two particles. We do this in stages. We decompose the final nucleus with spin J_F into states of the initial nucleus with spin J_I' and of the two particles having total angular momentum J. This latter we express in terms of the total orbital and spin angular momenta L and S. Finally we write L in terms of the individual orbital angular momenta of the two nucleons l_1 and l_2. We can then write

$$\langle J_F M_F | = \sum_{\substack{JLSJ_I' l_1 l_2 \\ M M_L M_S M_I' m_1 m_2}} A(JLSl_1l_2)\, C^{J_I' J}_{J_F M_F;\, M_I' M}\, C^{LS}_{JM;\, M_L M_S}\, C^{l_1 l_2}_{LM_L;\, m_1 m_2} \times \langle J_I' M_I' | \langle l_1 m_1 | \langle l_2 m_2 | \langle S M_S |. \qquad \ldots\ldots (2)$$

† This error has been carried over into the paper of el Nadi and el Khishin (1959).

The coefficient $A(JLSl_1l_2)$ takes into account such things as fractional parentage coefficients, configuration mixing etc. If we have two nucleons in a pure (LS) state outside a closed shell the coefficient A would be unity. If the two particles were in a mixture of (LS) configurations (and any wave function can be so expressed) then the A's would be relative amplitudes of these configurations.

We insert (2) into the matrix element (1). Integrating over the nuclear co-ordinates yields a factor $\delta_{J_\mathrm{I}, J_\mathrm{I}'}\,\delta_{M_\mathrm{I}, M_\mathrm{I}'}$ as pointed out previously. We also make the usual assumption of the Bhatia–Huang theory that the main contribution to the matrix element comes from $r_1 = r_2 = r_0$ where r_0 is a length of the order of magnitude of the nuclear radius. We shall retain the notation $\mathbf{r}_1$ and $\mathbf{r}_2$ for the position vectors of the two captured particles for convenience, but it is to be understood that eventually the magnitudes will be replaced by r_0. The expression for I is now

$$I = \sum_{\substack{JLSl_1l_2 \\ MM_LM_Sm_1m_2}} A(JLSl_1l_2)\, C^{J_\mathrm{I}J}_{J_\mathrm{F}M_\mathrm{F};\,M_\mathrm{I}M}\, C^{LS}_{JM;\,M_LM_S}\, C^{l_1l_2}_{LM_L;\,m_1m_2} \quad \ldots\ldots(3)$$

$$\times \langle \mathrm{p},\, l_1m_1,\, l_2m_2,\, SM_S|3\rangle,$$

where

$$\langle \mathrm{p},\, l_1m_1,\, l_2m_2,\, SM_S|3\rangle = \langle \mathrm{space}\rangle \langle \tfrac{1}{2}\mu_\mathrm{p},\, SM_S|\tfrac{1}{2}\mu_3\rangle, \quad \ldots\ldots(4)$$

μ_p and μ_3 being the spin components of the emerging proton and projectile respectively, and the space matrix element is given by

$$\langle \mathrm{space}\rangle = \int \exp(-i\mathbf{k}_\mathrm{p}\cdot\mathbf{r}_\mathrm{p}) f_{l_1}(r_1) f_{l_2}(r_2) \mathrm{Y}_{l_1}^{m_1*}(\theta_1, \phi_1) \mathrm{Y}_{l_2}^{m_2*}(\theta_2, \phi_2)$$

$$\times \chi_3 \exp(i\mathbf{k}_3\cdot\mathbf{r}_3)\, d\mathbf{r}_\mathrm{p} dw_1 dw_2, \quad \ldots\ldots(5)$$

where χ_3 is the internal wave function of the projectile.

The differential cross section is obtained from (cf. Huby 1953)

$$\sigma(\theta) = \frac{m_\mathrm{p}m_3}{4\pi^2\hbar^4}\frac{k_\mathrm{p}}{k_3}\frac{1}{2(2J_\mathrm{I}+1)} \sum_{M_\mathrm{I}, M_\mathrm{F}, \mu_\mathrm{p}, \mu_3} |I|^2. \quad \ldots\ldots(6)$$

The summations over a number of the magnetic quantum numbers can be carried out immediately to yield the result

$$\sigma(\theta) = \frac{m_\mathrm{p}m_3}{4\pi^2\hbar^4}\frac{k_\mathrm{p}}{k_3}\frac{(2J_\mathrm{p}+1)}{(2J_\mathrm{I}+1)} \sum_{JLSM_L} \frac{1}{(2S+1)(2L+1)}$$

$$\times \left| \sum_{\substack{l_1l_2 \\ m_1m_2}} A(J, L, S, l_1, l_2)\, C^{l_1l_2}_{LM_L;\,m_1m_2} \langle \mathrm{space}\rangle \right|^2. \quad \ldots\ldots(7)$$

It remains to evaluate the space matrix element. To do this we must introduce an explicit expression for χ_3. For ease of calculation we choose a Gaussian wave function

$$\chi_3 = (2\gamma^2/\pi^{1/2})^3 \exp\{-\gamma^2(|\mathbf{r}_1-\mathbf{r}_2|^2 + |\mathbf{r}_2-\mathbf{r}_\mathrm{p}|^2 + |\mathbf{r}_\mathrm{p}-\mathbf{r}_1|^2)\}.$$

The evaluation of the space matrix element now follows the method of el Nadi (1957) and we need only quote the result which is

$$\langle \mathrm{space}\rangle = F(\gamma, r_0) \exp(-K^2/8\gamma^2) \sum_{L_1, L_2, n, m} i^{L_1+L_2}(2l_1+1)^{1/2}(2l_2+1)^{1/2}(2n+1)$$

$$\times f_{l_1}(r_0) f_{l_2}(r_0) j_{L_1}(kr_0/2) j_{L_2}(kr_0/2) \mathrm{I}_{n-\frac{1}{2}}(3\gamma^2 r_0^2)(-)^m C^{l_1n}_{L_10;\,00} C^{l_1n}_{L_10;\,m_1-m}$$

$$\times C^{l_2n}_{L_20;\,00} C^{l_2n}_{L_20;\,m_2m}, \quad \ldots\ldots(8)$$

where $F(\gamma_1 r_0) = 64\sqrt{2}\pi^{5/2}\gamma^2 \exp(-3\gamma^2 r_0^2)/9r_0$, $\mathbf{k} = \mathbf{k}_3 - \mathbf{k}_p$, $\mathbf{K} = \frac{1}{3}\mathbf{k}_3 - \mathbf{k}_p$. The quantities L_1, L_2 and n correspond to the L, L' and n of el Nadi (1957). By inserting (8) in (7) we obtain a result for the differential cross section.

This form of the result is extremely inconvenient for calculation. The summations over the magnetic quantum numbers can be expressed as a Racah coefficient yielding for the differential cross section

$$\sigma(\theta) = \frac{m_p m_3}{4\pi^2\hbar^4}\frac{k_p}{k_3}\frac{(2J_F+1)}{(2J^1+1)} F^2(\gamma, r_0) \exp(-K^2/4\gamma^2) \sum_{JLS} \frac{1}{(2L+1)(2S+1)}$$
$$\times \Big| \sum_{l_1 l_2 L_1 L_2 n} A(JLSl_1l_2) i^{L_1+L_2} (2l_1+1)^{1/2}(2l_2+1)^{1/2}(2n+1)(2L_1+1)^{1/2}(2L_2+1)^{1/2}$$
$$\times (-)^{l_2-L_2} f_{l_1}(r_0) f_{l_2}(r_0) \mathrm{j}_{L_1}(kr_0/2)\mathrm{j}_{L_2}(kr_0/2)\mathrm{I}_{n+1/2}(3\gamma^2 r_0^2)$$
$$\times C^{l_1 n}_{L_1 0;\,00} C^{l_2 n}_{L_2 0;\,00} C^{L_1 L_2}_{L 0;\,00} W(L_1 L_2 l_1 l_2;\ Ln)\Big|^2. \quad \ldots\ldots (9)$$

A further rearrangement can be made which shows the relation to the simple theories more clearly. We write $\mathrm{I}_{n+1/2}(3\gamma^2 r_0^2) = \mathrm{I}_{1/2}(3\gamma^2 r_0^2) - (\mathrm{I}_{1/2}(3\gamma^2 r_0^2) - \mathrm{I}_{n+1/2}(3\gamma^2 r_c^2))$. The expression in the modulus then consists of two terms, one depending on $\mathrm{I}_{1/2}(3\gamma^2 r_0^2)$ and the other on $\mathrm{I}_{1/2}(3\gamma^2 r_0^2) - \mathrm{I}_{n+1/2}(3\gamma^2 r_0^2)$. The first of these is

$$\sum_{l_1 l_2 n L_1 L_2} A(JLSl_1l_2) i^{L_1+L_2} (2l_1+1)^{1/2}(2l_2+1)^{1/2}(2n+1)(2L_1+1)^{1/2}(2L_2+1)^{1/2}$$
$$(-)^{l_2-L_2} f_{l_1}(r_0) f_{l_2}(r_0) \mathrm{j}_{L_1}(kr_0/2)\mathrm{j}_{L_2}(kr_0/2)\mathrm{I}_{1/2}(3\gamma^2 r_0^2)\, C^{l_1 n}_{L_1 0;\,00} C^{l_2 n}_{L_2 0;\,00} C^{L_1 L_2}_{L 0;\,00}$$
$$\times W(L_1 L_2 l_1 l_2;\ Ln). \quad \ldots\ldots (10)$$

The summation over n can be carried out immediately using the properties of Racah coefficients. Further, the summations over L_1 and L_2 can be accomplished using the relation

$$\sum_{L_1 L_2} \frac{(2L_1+1)(2L_2+1)}{(2L+1)} i^{L_1+L_2-L} (C^{L_1 L_2}_{L 0;\,00})^2 \mathrm{j}_{L_1}(kr_0/2)\mathrm{j}_{L_2}(kr_0/2) = \mathrm{j}_L(kr_0).$$

Thus (10) becomes quite simply

$$\sum_{l_1 l_2} A(JLSl_1l_2) f_{l_1}(r_0) f_{l_2}(r_0) \mathrm{I}_{1/2}(3\gamma^2 r_0^2)(2l_1+1)^{1/2}(2l_2+1)^{1/2} i^L C^{l_1 l_2}_{L 0;\,00} \mathrm{j}_L(kr_0).$$
$$\ldots\ldots (11)$$

Using this result, the differential cross section becomes with a little further rearrangement

$$\sigma(\theta) = \frac{m_p m_3}{4\pi^2\hbar^4}\frac{k_p}{k_3}\frac{(2J_F+1)}{(2J_I+1)} F^2(\gamma, r_0) \exp(-K^2/4\gamma^2) \sum_{JLS} \frac{1}{(2S+1)} \Big| \sum_{l_1 l_2} A(JLSl_1l_2)$$
$$\times f_{l_1}(r_0) f_{l_2}(r_0) \mathrm{I}_{1/2}(3\gamma^2 r_0^2) \left[\frac{(2l_1+1)(2l_2+1)}{(2L+1)}\right]^{1/2} \Big\{ C^{l_1 l_2}_{L 0;\,00} j_L(kr_0) - \sum_{L_1 L_2 n} i^{L_1+L_2-L}$$
$$\times (2n+1)(2L_1+1)^{1/2}(2L_2+1)^{1/2}(-)^{l_2-L_2} \left(1 - \frac{\mathrm{I}_{n+1/2}(3\gamma^2 r_0^2)}{\mathrm{I}_{1/2}(3\gamma_2 r_0^2)}\right) \mathrm{j}_{L_1}(kr_0/2)\mathrm{j}_{L_2}(kr_0/2)$$
$$C^{l_1 n}_{L_1 0;\,00} C^{l_2 n}_{L_2 0;\,00} C^{L_1 L_2}_{L 0;\,00} W(L_1 L_2 l_1 l_2;\ Ln)\Big\}\Big|^2. \quad \ldots\ldots (12)$$

This is our final result for the differential cross section. In deriving this expression we have assumed, to avoid further complication, that the initial nucleus had infinite mass. To correct for this we simply alter the definition of

$\mathbf{k}$ to $\mathbf{k}=\mathbf{k}_3-(M_1/M_F)\mathbf{k}_p$ and use the appropriate reduced masses for the various particles.

Selection rules. These depend upon the particular reaction.

The (^{3}He, p) reaction. The selection rules are $\mathbf{J}_F=\mathbf{J}_I+\mathbf{J}$ where $\mathbf{J}=\mathbf{L}+\mathbf{S}$, $\mathbf{L}=\mathbf{l}_1+\mathbf{l}_2$ and $S=0$ or 1. There is a change or not in parity between the initial and final states according as L is odd or even.

The (t, p) reaction. The selection rules are the same as for the (^{3}He p) reaction except that $S=0$ only.

§ 3. The (d, α) Reaction

The treatment of the (d,α) reaction is very similar to that already given for the (^{3}He, p) and (t, p) reactions. There is a slight extra complication in that one has to introduce internal wave functions for both the deuteron and the α-particle. We again, for simplicity, choose a Gaussian wave function for the α-particle and it can then be shown that the shape of the angular distribution is independent of the form of the deuteron spatial wave function, provided only that it is an s-state. The matrix element separates into a product of two factors, one of which yields the analogous expression to that inside the square modulus in (12). The other contains the deuteron internal wave function and by a suitable change of variable the dependence on angle of scattering can be removed into a multiplying factor $\exp(-K^2/16\gamma^2)$ leaving the integral as a multiplier to the cross section.

The result is similar to (12) as far as the angular distribution is concerned, except that the factor $\exp(-K^2/4\gamma^2)$ should be replaced by $\exp(-K^2/8\gamma^2)$ and the argument $3\gamma^2r_0^2$ of the imaginary Bessel function replaced by $4\gamma^2r_0^2$. Also we have the revised definitions $\mathbf{k}=k_\alpha-(M_1/M_1)k_d$ and $\mathbf{K}=\frac{1}{2}\mathbf{k}_\alpha-\mathbf{k}_d$. The selection rules are exactly as for the (^{3}He, p) reaction except that $S=1$ only.

§ 4. Relation to the Simple Theory

The first term inside the modulus in (12) has just the form of angular distribution as is obtained from the simple theory. The infinite series (together with the term $\exp(-K^2/4\gamma^2)$) is the alteration produced by taking into account the structure of the particles. We discuss several limiting approximations.

(i) We may assume that the ^{3}He nucleus (or triton) is very small. This means we take the limit $\gamma\to\infty$. For large γ, $I_{n+1/2}(3\gamma^2r_0^2)/I_{1/2}(3\gamma^2r_0^2)\to 1$. Consequently $(1-I_{n+1/2}(3\gamma^2r_0^2)/I_{1/2}(3\gamma^2r_0^2))\to 0$ and the series vanishes. This yields an angular distribution proportional to

$$\left|\sum_{l_1l_2}A(JLSl_1l_2)\left[\frac{(2l_1+1)(2l_2+1)}{(2L+1)}\right]^{1/2}f_{l_1}(r_0)f_{l_2}(r_0)C^{l_1l_2}_{L0,00}j_L(kr_0)\right|^2. \quad \ldots\ldots(13)$$

This has the same form as the simple theory. However the structure of the captured particles still shows in that the coefficients involve l_1 and l_2.

(ii) A slightly less stringent approximation is to neglect the infinite series inside the square modulus in (12). This means that the result for the angular distribution is the same as (13) except that it is multiplied by the factor $\exp(-K^2/4\gamma^2)$. This approximation implies that the nucleons 1 and 2 are moving as a 'lump' in the projectile, i.e. they are always at the same place and moving together. They are of course allowed to move independently in the final nucleus.

(iii) The complementary approximation to this is to retain the structure of the projectile but assume the nucleons move as a lump in the final nucleus. In this case the angular distribution is proportional to

$$\exp(-K^2/4\gamma^2)|\bar{A}(JLS)\mathrm{j}_L(kr_0)|^2. \qquad \ldots\ldots(14)$$

(iv) The form of angular distribution often used by experimentalists is

$$|\bar{A}(JLS)\mathrm{j}_L(kr_0)|^2. \qquad \ldots\ldots(15)$$

This implies both that the projectile is small and that the captured nucleons are moving together in the nucleus.†

The approximations (iii) and (iv) are the ones usually used. Approximations (i) and (ii) are not generally quoted. (i) has the advantage of using a condition (γ large) which may be thought more justifiable than assuming the particles are captured as a 'lump', and is easier to assess physically. More important, both (i) and (ii) retain something of the structure of the captured particles and so permit a more detailed interpretation of results. An example is given in § 5.

Finally, it remains to be asked what effect the infinite series in (12) has on the angular distribution. A detailed investigation has not so far been attempted. However, calculations using (12) for the excitation of certain states in the ^{9}Be(^{3}He, p)^{11}B reaction have been carried out by Dr. S. Hinds (see figure 6 and the discussion above it in the paper of Hinds and Middleton 1959a). These show the angular distribution to be little affected. Although this is not evidence that the series always has a negligible effect, it seems a justifiable approximation to neglect it, especially when discussing results at low bombarding energies where the distortions by the coulomb and nuclear forces, and also possibly from compound nuclear processes, are large.

§ 5. Application of the Theory to (^{3}He, p) Reactions

Application of the selection rules for the reaction yields information about the spins and parities of nuclear levels in the usual way. We are particularly interested in attempting to correlate the results with the structure of the nuclear levels. The particular feature of the (^{3}He, p) reaction which, in principle at least, makes it very useful in this respect is that it is often possible to have transitions with two different values of L leading to the state under investigation. This can happen even when the initial nucleus has zero spin. Since the state formed is often simply due to recoupling of particles in a given shell (for example the 1p shell for the low lying states of nuclei below ^{16}O) the ratio of intensities of the two transitions depends only on the nuclear configurations and is independent of the amplitudes of the wave functions of the captured particles at the nuclear surface. It is therefore possible in principle to test the supposed configurations of such nuclei using this reaction. The difficulty is that the transitions for the higher values of L are naturally less intense than for the lower values. Consequently the method is sensitive only if the lower values of L are inhibited by the nuclear configurations. Since it is the *relative* intensities of the transitions which is significant one might hope that these are not as sensitive to the distortions produced

† When the nucleons are assumed captured as a 'lump' the matrix element can be evaluated by transforming away the nuclear interaction and one then obtains expressions for (14) and (15) in which the single Bessel function is replaced by the Butler Wronskian. However, it is difficult to see how to introduce the Wronskian into (13).

by the coulomb and nuclear forces as is the absolute cross section. However, so far this hope seems not to be borne out by the experiment. We will consider a particular reaction as an illustration both of the method of using the known nuclear configurations and of the difficulties introduced by the distortions.

The reaction we consider is the $^{16}O(^3He, p)^{18}F$ ground state reaction. The wave function of the ^{18}F ground state has been given in terms of (LS) configurations by Elliott and Flowers (1955). Due to mixing of the 2s and 1d shells in this region, the ground state is a mixture of the $(s^2)^3S$, $(d^2)^3S$, $(d^2)^3D$, $(d^2)^1P$ and $(sd)^3D$ configurations. The configuration $(d^2)^1P$ cannot be reached by the (^{3}He, p) reaction because of the parity selection rule. We take the amplitudes of these various configurations as given by Elliott and Flowers (1955) as the values of the A's in equation (13). We can then express the result in the form

$$(j_0(kr_0))^2+\alpha(j_2(kr_0))^2. \qquad \ldots\ldots(16)$$

However, there is a further complication in that we do not know the amplitudes of the wave functions for the s and d shells at the nuclear surface. We therefore use this ratio as an adjustable parameter and maximize the value of α. The result is $\alpha\sim 1/300$. In effect, this means a pure $L=0$ transition should be seen. The results of Hinds and Middleton (1959b) using a bombarding energy of 9·16 MeV bear this out. However, at the lower bombarding energy of 5·9 MeV a large secondary maximum is found. The angular distribution can be fitted by a formula of the type (16) with a value $\alpha\sim 3$. This secondary peak although it looks like a direct reaction peak corresponding to $L=2$ must then be completely spurious and due to the distortions. It is very disturbing that the effect of the distortions should act so selectively especially since the transitions to the excited states seem relatively unaffected by the change in bombarding energy.

Another example occurs in the ^{12}C (^{3}He, p)^{14}N ground state reaction. This is not as clear cut as the previous case since ^{14}N is not so well understood. However, if we accept Elliott's (1956) work on the subject the ground state of ^{14}N should be mainly a ^3D state. Assuming ^{12}C to be mainly a ^1S state the transition should be predominately $L=2$. The experimental results (Hinds and Middleton, 1960) carried out at a number of bombarding energies reveal a large peak in the forward direction which decreases with increasing bombarding energy and has disappeared at 10·14 MeV. This forward peak could well have been mistaken for an $L=0$ transition (and, as in the ^{16}O case, this would fit with the known spins and parities !) but again it would seem to be spurious. It is obvious that great care must be taken in the interpretation of results at such low energies since the fitting of a peak with a spherical Bessel function is no guarantee that it is genuine.†

In conclusion we might suggest that, while the results so far have been difficult to interpret, it is possible that for higher bombarding energies and selected states the (^{3}He, p) reaction could still be a useful tool in nuclear spectroscopy.

†I have received a preprint by Priest, Tendam and Bleuler who have investigated this reaction at 13·9 MeV. The transition to the ground state of ^{14}N is clearly an $L=2$ transition in agreement with the theoretical expectation.

Acknowledgments

The author is extremely grateful to Dr. R. Huby for his penetrating comments which have led to a number of improvements in this paper, and is indebted to Drs. S. Hinds and R. Middleton for communicating their results before publication.

References

Butler, S. T., 1957, *Phys. Rev.*, **106,** 272.
Elliott, J. P., 1956, *Phil. Mag.*, **1,** 503.
Elliott, J. P., and Flowers, B. H., 1955, *Proc. Roy. Soc.* A, **229,** 536.
Hinds, S., and Middleton, R., 1959 a, *Proc. Phys. Soc.*, **74,** 196.
—— 1959 b, *Ibid.*, **74,** 762.
—— 1960, *Ibid.*, **75,** 745.
Huby, R., 1953, *Progr. Nucl. Phys.*, **3,** 177.
el Nadi, M., 1957, *Proc. Phys. Soc.* A, **70,** 62.
el Nadi, M., and el Khishin, M., 1959, *Proc. Phys. Soc.*, **73,** 705.
Tobocman, W., 1956, *Tech. Rep. No.* 29, *Case Institute of Technology.*

A Note on the Theory of Space Charge Limited Currents

By C. RHYS-ROBERTS and R. H. TREDGOLD

Physics Department, University College of North Wales, Bangor

MS. received 31*st March* 1960, *in final form* 29*th April* 1960

Abstract. In order to explain the observed non-ohmic conductivity in barium titanate and cadmium sulphide, it is necessary to assume that the current is space charge limited. Previous work on space charge limited currents has failed to predict the correct thickness dependence. In this paper a model is proposed wherein there are thin layers of uncharged traps at the surface of the dielectric uniformly distributed in space and of one energy depth; the bulk of the material contains no traps. Using this model the observed experimental results can be explained.

§1. Introduction

Barium titanate and cadmium sulphide both show a striking non-ohmic apparent electrical conductivity. The former material has been studied by Branwood and Tredgold (1960) who find that for field strengths in the range 0 to 10 kv cm^{-1}, the current varies approximately as the square of the applied voltage over a wide range of temperature. Furthermore, the current is independent of the work function of the electrode material.

Results for cadmium sulphide have been reported by Smith and Rose (1955) and by Wright (1958) who find that the current increases as a power of the applied potential, varying between the second and the fourth depending on the particular specimen.

In the case of barium titanate a study was also made of the variation of current with thickness. It will be shown that these latter results are very pertinent to a theoretical explanation of the non-ohmic behaviour of the material.

Before proceeding to discuss what we believe to be the correct interpretation of the behaviour of barium titanate (and possibly of cadmium sulphide) we indicate why other possible interpretations are unsatisfactory.

If we assume that barium titanate is a conventional semiconductor, (the (temperature, conductivity) graph would support this view (Branwood and Tredgold 1960), then it would be necessary to assume a field-dependent mobility to explain the experimental results. This field-dependent mobility could result from either a field-dependent effective mass or a field-dependent mean free path. A simple order of magnitude calculation shows that the former supposition is untenable and the latter supposition is ruled out by the results of Barnes and Tredgold (to be published), who show that a field of greater than 10^5 volts cm^{-1} would be necessary to influence the mean free path, and even then the conductivity should *decrease* rather than increase with field.

Field emission and analogous surface effects can be shown to be unimportant until fields of the order 10^6 volts cm^{-1} are achieved.

§ 2. Space Charge Models

A discussion of space charge limited currents in solids was first given by Mott and Gurney (1940) who showed that under appropriate circumstances the electric current entering a dielectric at the cathode and passing through the material would vary as the square of the applied voltage. Suits (1957) has considered the same problem without neglecting the diffusion term, and with trapped electrons, but his results do not concern us here as the diffusion is only important for very small applied fields. In other respects he shows that trapping leads to results formally similar to those obtained by Mott and Gurney (1940), but with the dielectric constant effectively reduced by the influence of the trapping. He assumes throughout that there are many more traps than electrons.

Rose (1955) has discussed the case in which the traps are distributed in energy and the number of electrons is comparable with, though less than, the number of traps. He does not explicitly discuss the influence of thickness.

Lampert (1956) discussed the case of a single energy (in the forbidden zone) pertaining to all the traps and a number of electrons of the same order as the number of traps. In particular, he considered the breakdown effect resulting from the filling up of the traps.

Now all these treatments of the problem either fail to provide a result indicating the influence of the thickness of the specimen, or they show that, in the region in which the current varies as the square of the voltage, the current also varies as the inverse cube of the thickness. (This result will be obtained in a special case below.)

Now Branwood and Tredgold showed that the current passing through a single crystal of barium titanate is given approximately by

$$i = A\,V^2/L^2 \qquad \ldots\ldots(1)$$

where A is a function of temperature and is independent of electrode material. Results were obtained over a sufficient range of thickness to determine the power of L beyond reasonable doubt. In the following sections we discuss a model which leads to a result of this form.

§ 3. Trapping in One Layer

In this section we give a simple quantitative treatment of a model in which the traps all have the same energy and are uniformly distributed in space. In the following section we generalize this model to a case in which the spatial distribution is not uniform.

We suppose an excess density of electrons n at any point in the material such that there is an excess charge having a local density of $-n\boldsymbol{e}$. We further suppose that n_u of these electrons are in the conduction band and n_t in the traps. There are N_T traps per cm^3 having a depth $-E_T$. We measure energy from the bottom of the conduction band and write for the density of states

$$G(E) = 4\pi\left[\frac{2\boldsymbol{m}}{\boldsymbol{h}^2}\right]^{3/2} E^{1/2}. \qquad \ldots\ldots(2)$$

Then

$$n_u = \int_0^\infty \frac{G(E)dE}{\exp\{(E-\eta)/\boldsymbol{k}T\}+1} \qquad \ldots\ldots(3)$$

where η is the Fermi parameter

$$n_t = \frac{N_T}{\exp\{(-E_t - \eta)\, kT\} + 1} . \qquad \ldots\ldots (4)$$

If we assume that the Fermi surface is several kT below the bottom of the conduction band we can neglect the 1 in the denominator of (3) and obtain

$$\frac{n_u}{n_t}(N_T - n_t) = 2\left[\frac{2\pi mkT}{h^2}\right]^{3/2} \exp\frac{-E_T}{kT} = M \qquad \ldots\ldots (5)$$

where the parameter M is defined by (5).

Now
$$n = n_t + n_u \qquad \ldots\ldots (6)$$

and for the case in which we are interested $n \gg n_u$ so that

$$n_u = \frac{nM}{N_T - n} . \qquad \ldots\ldots (7)$$

For a large slab-like specimen, Poisson's equation yields

$$\frac{dF}{dx} = \frac{4\pi e n}{\kappa} \qquad \ldots\ldots (8)$$

where F is the electric field normal to the surface, x is the distance from the surface and κ is the dielectric constant of the material. If μ is the electron mobility and the diffusion constant is given by the Einstein relationship

$$D = \frac{kT\mu}{e} \qquad \ldots\ldots (9)$$

then the current normal to the surface per cm^2 is

$$j = n_u e \mu F - \frac{kT\mu}{e}\frac{dn_u}{dx} . \qquad \ldots\ldots (10)$$

Following Mott and Gurney (1940) we ignore the diffusion term, and using (7), (8) and (10), and the condition

$$\frac{dF}{dx} = \frac{4\pi N_0 e}{\kappa} \text{ at } x = 0 \qquad \ldots\ldots (11)$$

we obtain

$$V = \frac{-jL}{\mu e M} + \frac{\mu M \kappa}{12\pi N_T} j^{1/2}\left[\left(\frac{8\pi N_T L}{\mu M \kappa} + \frac{N_T^2 j}{N_0^2 \mu^2 e^2 M^2}\right)^{3/2} - \left(\frac{N_T^2 j}{N_0^2 \mu^2 e^2 M^2}\right)^{3/2}\right] . \quad \ldots (12)$$

Here L is the thickness of the specimen, N_0 is the density of electrons originating from the electrode material and having energy sufficient to enter the traps at the boundary between the metal and the dielectric. N_0 is given by

$$N_0 = 2\left[\frac{2\pi mkT}{h^2}\right]^{3/2} \exp\left(-\frac{\xi}{kT}\right) \qquad \ldots\ldots (13)$$

where ξ is the energy difference between the Fermi surface in the electrode and the traps.

If

$$N_0 \gg \frac{\kappa V}{16\pi e L^2} \qquad \ldots\ldots (14)$$

then

$$j \simeq \frac{9\mu M \kappa V^2}{32\pi N_T L^3} \qquad \ldots\ldots (15)$$

which in the case $\kappa = M = N_T = 1$ reduces to the result obtained by Mott and Gurney (1940).

If one assumes that equation (15) describes the experimental results, and if one puts realistic values of the parameters into (14) one obtains $N_0 > 10^{16}$, which means that ξ must be about 0·1 ev for j to be proportional to V^2. Now the different electrode materials employed (Ag, Au, Al, Cr, Zn), have work functions which differ by much more than 0·1 ev and thus one can only assume that the electrode material Fermi surface lies above the trap level in all cases, and that the traps in a small surface layer are all full. For a difference between electrode Fermi surface and trap level of the order 1 ev it is easy to show that this 'flooded' surface layer is only going to be a few atomic layers thick. In this case, as N_0 does not appear in (15), under the conditions discussed, the conduction current will be independent of the work function of the electrode material, as was found experimentally in the case of barium titanate.

§ 4. Model with Surface Trapping Layer

Evidence discussed below suggests that it is possible that there may be a surface layer in barium titanate which has different properties from the bulk material. We suggest that the surface layer is not stoichiometric and has a high trap density, and that the main body of the material has a low trap density.

A simple model based on this idea is now discussed. We suppose a surface layer of thickness l_1 having trap density N_T, a middle layer of thickness l_2 and free from traps and a further trapping layer of thickness l_1 on the other side. We also assume that the charge density in the middle layer is so small that $dF/dx = 0$ in this region to a good approximation. We 'join' the layers by ensuring that F is continuous across the boundaries. Then with the approximations already employed in the last section, we find

$$j = \frac{M\mu\kappa V^2}{8\pi N_T l_1 l_2^2} \simeq \left[\frac{(2\pi \boldsymbol{m}\boldsymbol{k}T)^{3/2}\mu\kappa}{4\pi \boldsymbol{h}^3 N_T l_1}\right] \exp\left(-\frac{E_T}{\boldsymbol{k}T}\right)\frac{V^2}{L^2} \qquad \ldots\ldots (16)$$

which is of the required form for barium titanate. (This material appears to have two activation energies associated with conduction but a modification of the theory to give this result is trivial.) It is worth noting that N_T and l_1 occur together and thus all one could measure would be the traps per cm in the surface layer. Also, the electrode work function does not appear, if we make assumptions as in the preceding section.

§ 5. External Evidence for Surface Layer

Several pieces of experimental evidence exist which lend support to the view that single crystals of barium titanate may have a surface layer of the order of 100 Å thick which differs in its properties from the bulk material.

Känzig (1955) using electron diffraction techniques has shown that there is a layer about 100 Å thick on the surface of the crystals which has a tetragonal symmetry even above the Curie temperature, though in this temperature region the bulk material has cubic symmetry.

Anderson, Brady, Herz and Remeika (1955) have shown that the shape of the hysteresis loop obtained with a single crystal of barium titanate is altered if

the crystal is placed in a vacuum of 10^{-6} mm Hg but is restored to its original form if the crystal is placed in oxygen. This experiment indicates that the surface layer is probably easily reduced by treatment in vacuum. Now the electrodes used in the experiments described by Branwood and Tredgold were all evaporated on in vacuum and thus they could possibly serve to seal in an oxygen-deficient layer.

It is also possible that water vapour or molecules of diffusion pump oil existing in the vacuum (of the order 10^{-4} mm Hg) could be swept up and trapped by the electrode material and could contribute to the formation of a surface layer.

It should be pointed out that a Frenkel (1947) ionic exhaustion layer would not lead to the correct result as the traps in such a layer would each have a charge of at least $\boldsymbol{e}$. Now since $N_T > n_t$ the field would be dominated by the presence of the charged traps. In these circumstances it can be shown that the apparent conductivity would be ohmic.

It would be inappropriate to speculate further on the nature of this postulated surface layer without the help of additional experimental evidence. However, the difficulty of proposing any other model which will explain the observed results is itself powerful evidence for the existence of such a layer.

References

Anderson, J. R., Brady, G. W., Merz, W. J., and Remeika, J. P., 1955, *J. Appl. Phys.*, **26,** 1387.

Branwood, A., and Tredgold, R. H., 1960, *Proc. Phys. Soc.*, **76,** 93.

Frenkel, J., 1947, *Kinetic Theory of Liquids* (New York: Dover Publications).

Känzig, W., 1955, *Phys. Rev.*, **98,** 551.

Lampert, M. A., 1956, *Phys. Rev.*, **103,** 1648.

Mott, N. F., and Gurney, R. W., 1940, *Electronic Processes in Ionic Crystals* (Oxford: University Press).

Rose, A., 1955, *Phys. Rev.*, **97,** 1540.

Smith, R. W., and Rose, A., 1955, *Phys. Rev.*, **97,** 1531.

Suits, G. H., 1957, *J. Appl. Phys.*, **28,** 454.

Wright, G. T., 1958, *Nature, Lond.*, **182,** 1296.

The Saturation Magnetostriction Constants of Nickel within the Temperature Range $-196°$ to $365°$C

By R. R. BIRSS† and E. W. LEE‡

† Imperial College, London
‡ Department of Physics, The University, Sheffield

MS. received 20*th April* 1960

Abstract. The spontaneous magnetostriction of cubic crystals can be expressed in the form

$$\lambda = C_0 + C_1(\alpha_1^2\beta_1^2 + \alpha_2^2\beta_2^2 + \alpha_3^2\beta_3^2) + C_2(\alpha_1\alpha_2\beta_1\beta_2 + \alpha_2\alpha_3\beta_2\beta_3 + \alpha_3\alpha_1\beta_3\beta_1)$$

where the α_i and β_i are, respectively, the direction cosines of the magnetization vector and the measuring direction, with respect to the crystal axes. The coefficients C_1 and C_2 have been determined for nickel within the temperature range $-196°$C to the Curie point ($365°$C) using calibrated strain gauges. At $-196°$C, $C_1 = -85{\cdot}0 \times 10^{-6}$ and $C_2 = -85{\cdot}4 \times 10^{-6}$. Both constants increase monotonically to zero at $365°$C. The room temperature ($20°$C) values are $C_1 = -77{\cdot}2 \times 10^{-6}$ and $C_2 = -70{\cdot}0 \times 10^{-6}$. For a polycrystal the spontaneous magnetostriction may be expressed in the form

$$\lambda = C + \tfrac{3}{2}\lambda_s \cos^2 x$$

where x is the angle between α and β. Measurements of λ_s have been made in the same way and they are in good agreement with the values calculated assuming uniform stress, namely $\lambda_s = \frac{4}{15}C_1 + \frac{1}{5}C_2$.

§ 1. Introduction

The experimental work of Bozorth and Hamming (1953) has shown that the spontaneous magnetostriction of nickel single crystals may be accurately represented by the expression

$$\lambda = C_0 + C_1(\alpha_1^2\beta_1^2 + \alpha_2^2\beta_2^2 + \alpha_3^2\beta_3^2) + C_2(\alpha_1\alpha_2\beta_1\beta_2 + \alpha_2\alpha_3\beta_2\beta_3 + \alpha_3\alpha_1\beta_3\beta_1) \quad \ldots\ldots (1)$$

where the α_i and β_i are the direction cosines of the spontaneous magnetization and the direction of measurement, with respect to the crystal axes. The present notation has been used instead of the more familiar expression in terms of λ_{100} and λ_{111} so as to avoid confusion with the saturation magnetostriction measured, from the ideal demagnetized state, in the [100] and [111] directions respectively. The magnetostriction constants C_1 and C_2 were evaluated at room temperature using a single crystal disc with its surface cut to a definite crystal plane and by measuring the strain in a given crystallographic direction as the direction of the saturation magnetization was varied in that crystal plane. In this way the β_i were kept constant and the coefficients C_1 and C_2 were determined by measuring λ as a function of α_i using the strain gauge technique (Goldman 1947).

The measurements of Bozorth and Hamming were carried out at room temperature only and subsequently two attempts have been made to supplement these with further measurements over a wider temperature range. Corner and Hunt (1955) and Corner and Hutchinson (1958) determined λ_{100} and λ_{111} (as defined above) on two separate prolate spheroids with their long axes coincident with the [100] and [111] directions respectively. They then made the assumption that the demagnetized state of their crystals was one in which the domain magnetization vectors were equally distributed between the eight easy directions. Under these conditions $\lambda_{100}=\frac{2}{3}C_1$ and $\lambda_{111}=\frac{1}{3}C_2$. Whilst this assumption may be true for the crystals used, it nevertheless remains an assumption. The lack of confidence which many workers have had in the correctness of this assumption is testified by the attempts which have been made to avoid it. Thus Takaki (1937) measured the magnetostriction of iron crystals between the remanent state and saturation, believing the remanent state to be less ambiguous than the demagnetized one. Tatsumoto and Okamoto (1959) passed a current down their crystals so that the accompanying magnetic field aligned the magnetic moment vectors perpendicular to the current, which was also the direction of measurement. It is quite clear that these methods, although alleviating the uncertainty of the initial state, do not eliminate it altogether. This can be done, however, by measuring the strain between two saturated states each making a definite angle with the crystal axes. This is the procedure now commonly employed and one to which the strain gauge method is specially suited.

The strain gauge technique has hitherto been confined almost exclusively to measurements at room temperature. This is because the gauge factor is usually known only at that temperature and because the problem of drift at any other temperature has always been regarded as so serious as to prevent the measurement of the small static magnetostrictive strains. Recently we have shown (Birss and Lee 1960) how these difficulties may be overcome so that it is now possible, using strain gauges, to make accurate measurements of magnetostriction constants over a wide range of temperatures in a manner which eliminates completely the uncertainties connected with the use of the demagnetized state. This paper reports some measurements on nickel carried out in this way.

§ 2. Apparatus and Materials

Full details of the apparatus together with the technique employed to obtain the constants C_1 and C_2 have been given elsewhere (Birss and Lee 1960).

Two thin disc shaped $(1\bar{1}0)$ crystals were employed. For one of these crystals the angles made by the [001] and [110] axes within the plane of the disc were 1° and 1½° respectively. This crystal was annealed for three hours at 1050 °C and was then furnace-cooled. In the other crystal, which was not annealed, the [001] direction made an angle less than 1° with the plane of the disc, whilst the [110] axis appeared to lie exactly in this plane. Above the point of technical saturation and within the temperature range −196° to 365 °C no significant difference was observed between the magnetostrictive behaviour of the annealed and unannealed crystals.

The constant C_1 was determined by measuring the difference in strain when the crystal was magnetized to saturation in the [001] direction and then in the perpendicular [110] direction. To the degree of approximation implicit in the

use of equation (1) this difference is C_1. The coefficient C_2 was evaluated by a similar procedure involving two directions in the plane of the disc, one parallel and the other perpendicular to the [111] axis, the strain measured in this case being $\frac{1}{2}C_2$. At room temperature these measurements were repeated for different values of the saturating applied magnetic field and an estimate was made of the forced magnetostriction. The values of C_1 and C_2 appropriate to zero applied field were deduced to be $C_1 = -77{\cdot}2 \times 10^{-6}$ and $C_2 = -70{\cdot}0 \times 10^{-6}$. At other temperatures the applied field was kept constant at 5000 Oe —a field that was found experimentally to be large enough to produce technical saturation at the lower temperatures. The correction for the forced magnetostriction was assumed to be the same as at room temperature. Figure 1 shows the observed

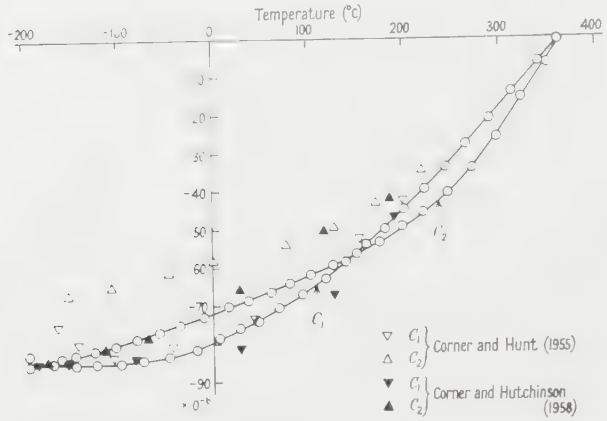

Figure 1. The magnetostriction constants of nickel. Additional points due to Corner and Hunt (1955) and Corner and Hutchinson (1958).

variation of C_1 and C_2 with temperature. For convenience in drawing, approximately four out of every five points have been omitted. Each point represents the mean of thirty-six measurements of the appropriate strain difference. For purposes of comparison some experimental points due to Corner and Hunt (1955) and Corner and Hutchinson (1958) have been added. It is estimated that the accuracy of the present determination is $\pm 3\%$, the limiting factor being the uncertainty in the constancy of the gauge factor and its temperature variation, from one gauge to another.

In addition to the single crystals, three polycrystalline discs were investigated in the same way. For a polycrystal the variation of magnetostriction with the angle x between the saturation magnetization and the direction of measurement may be expressed in the form (Birss 1959)

$$\lambda = C + \tfrac{3}{2}\lambda_s \cos^2 x$$

where λ_s is the polycrystalline magnetostriction constant. The most satisfactory method of evaluating λ_s is to measure the difference in strain when the specimen is magnetized first perpendicular, and then parallel, to the direction of measurement, this difference being $\frac{3}{2}\lambda_s$ for *any* initial domain orientation. This was the procedure adopted in the present investigation.

The specimens used were in the form of thin discs, one annealed as before, the other unannealed. Once again no significant differences in magnetostriction constants were detected. A third disc, cut from a sheet of cold-rolled nickel, was found to give values of λ_s approximately 5% smaller than those obtained with the other two. This was ascribed to preferential crystal orientation and the disc was rejected. A graph showing the results obtained with the annealed disc is shown in figure 2.

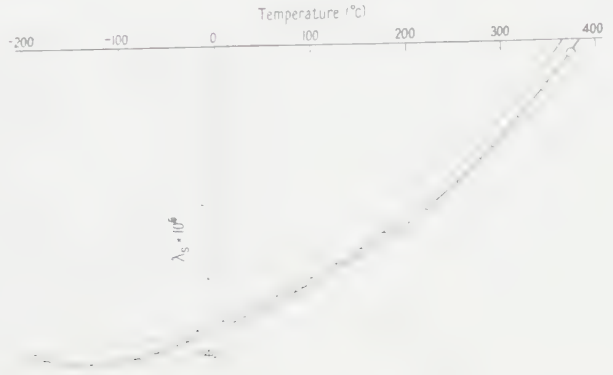

Figure 2. Polycrystalline magnetostriction constant λ_s of nickel. The broken line is the value of λ_s calculated from equation (2) and the data of figure 1.

§ 3. Discussion of Results

The single-crystal measurements reported here were undertaken primarily to check the results of Corner and Hunt, which were puzzling in two respects. First, the room temperature value of $|C_1|$ was considerably lower than that reported by Bozorth and Hamming, and secondly, $|C_2|$ apparently went through a maximum value at about 125 K. Since then Corner and Hutchinson have shown that the anomalous value of $|C_1|$ was a spurious one due to the effect of applied stress on the crystal. Their corrected results are now in good agreement with the present results. The same authors showed that the maximum observed at 125 K is also spurious, arising from the inability of Corner and Hunt to achieve saturation below that temperature. Bearing this in mind we are inclined to discount the apparent decrease in the magnitude of our own value of C_2 indicated by the liquid nitrogen temperature point on the graph. There is, however, no reason to believe that a minimum in either of the constants C_1 and C_2 is impossible or even unlikely. Magnetostriction is measured as a strain due to the orientation of the magnetization vector, and the magnetostriction constants can always be expressed as the sum of a number of terms each of which is a numerical factor times a product of the form BS, where B is the stress due to magnetization (the magnetoelastic coupling constant of Kittel 1949) and S is the appropriate elastic compliance modulus. Recent measurements by Alers, Neighbours and Sato (1958) show that all three elastic moduli of nickel decrease by about 6% in going from room temperature to liquid nitrogen temperature. If this decrease in the elastic moduli is accompanied only by a partially compensating change in the magnetoelastic coupling constants, then the magnitude of the magnetostriction constants will decrease. Since the fundamental interaction is given by the B's rather than by C_1 and C_2, it is clear

that simultaneous measurements of magnetostriction and elastic constants would be of considerable value.

The temperature variation of the polycrystalline magnetostriction constant λ_s has been investigated by a number of workers using mechanical methods and it has been pointed out elsewhere (Lee 1955) that there is considerable disagreement amongst the various sets of results. This may almost certainly be ascribed to the effect of preferred domain orientation, which, since the results cannot be brought into agreement by a single normalizing factor, must be presumed to be temperature dependent. The present results, being free from such uncertainties, are expected to be much more reliable. If it is assumed that a polycrystalline material is in a state of uniform stress, then λ_s may be related to the single crystal constants by averaging the equation (1) over all possible directions, the resulting expression being (Birss 1959)

$$\lambda_s = \tfrac{4}{15}C_1 + \tfrac{1}{5}C_2. \qquad \ldots\ldots (2)$$

The broken curve of figure 2 shows the temperature variation of $\frac{4}{15}C_1 + \frac{1}{5}C_2$ as derived from the present measurements on single crystals. It may be seen that this curve is in reasonable agreement with the values of λ_s obtained experimentally and it may be concluded that the assumption on which the derivation of equation (2) is based—that of uniform stress throughout the material—is a good one. The room temperature values are

$$\lambda_s = -35{\cdot}5 \times 10^{-6}, \quad \tfrac{4}{15}C_1 + \tfrac{1}{5}C_2 = -34{\cdot}6 \times 10^{-6}.$$

The difference between these two values is within the estimated error of $\pm 3\%$, and the value of λ_s agrees closely with that recently obtained by Stauss (1959), namely $-35{\cdot}1 \pm 1 \times 10^{-6}$.

Acknowledgment

This work was carried out whilst both authors were members of the Physics Department at Nottingham University and we should like to record our thanks to Professor L. F. Bates for allowing us the facilities of his laboratories and for his continued interest in this work.

References

Alers, G. A., Neighbours, J. R., and Sato, H., 1958, *J. Phys. Chem. Solids*, **9**, 21.
Birss, R. R., 1959, *Advanc. Phys.* (*Phil. Mag. Suppl.*), **8**, 252.
Birss, R. R., and Lee, E. W., 1960, *J. Sci. Instrum.*, **37**, 225.
Bozorth, R. M., and Hamming, R. W., 1953, *Phys. Rev.*, **89**, 856.
Corner, W. D., and Hunt, G. H., 1955, *Proc. Phys. Soc.* A, **68**, 133.
Corner, W. D., and Hutchinson, F., 1958, *Proc. Phys. Soc.*, **72**, 1049.
Goldman, J. E., 1947, *Phys. Rev.*, **72**, 529.
Kittel, C., 1949, *Rev. Mod. Phys.*, **21**, 541.
Lee, E. W., 1955, *Rep. Progr. Phys.*, **18**, 184 (London : Physical Society).
Stauss, H. E., 1959, *J. Appl. Phys.*, **30**, 1648.
Takaki, H., 1937, *Z. Phys.*, **105**, 92.
Tatsumoto, E., and Okamoto, T., 1959, *J. Phys. Soc. Japan*, **14**, 588.

On the Polymorphism of the Thallium Halides

By I. H. KHAN
Physics Department, Imperial College, London

Communicated by M. Blackman; MS. received 5th April 1960

Abstract. Experiments are described on the polymorphism of thallium halides formed as thin oriented layers by deposition *in vacuo* on to a variety of bases, in particular on to cleavage faces of crystals. The effect of varying the temperature of the base has been studied in some detail. Measurements have been made of the lattice constant of the abnormal rocksalt type form, using both the reflection and the transmission techniques. In the latter, which gives more accurate results, thallium halides were deposited on to a thin polycrystalline layer of alkali halide previously formed on an amorphous base.

§ 1. Introduction

It was first shown by Schulz in 1950, and confirmed in later work (Schulz 1951) that thin films of caesium and thallium halides possessed a rocksalt structure when deposited on to the cleavage faces of alkali halides, mica, and certain other crystals. A few exceptions to the general rule were found, e.g. thallium chloride had its normal form on rocksalt, and thallium bromide and iodide an unknown structure when deposited on mica. Pashley (1952) confirmed some of the earlier work and more recently Lüdemann (1957) carried out a series of experiments at room temperature and at higher temperatures, depositing thallium chloride and caesium chloride on a number of bases. In all cases the rocksalt form was found in the thinnest layers provided the rate of deposition was sufficiently low. In the work described below, which was started before Lüdemann's results were known, deposits of thallium halides were studied on a variety of bases at a series of temperatures between 20°c and 400°c.

§ 2. Experimental Procedure

The experiments were carried out *in situ* in an electron diffraction camera operating at 47 kv. The diffraction patterns were usually recorded on film which allowed a large number of photographs to be taken during a single experiment. Plates were used where some accuracy was desired in spacing measurements. Usually a single evaporator was employed, but in some cases two similar evaporators were used, their axes being nearly at right angles; this allowed deposition on to a layer previously formed in the camera without disturbing the existing conditions. The specimens to be heated were mounted on a small flat furnace, the maximum temperature obtainable being 450°c.

Four different types of substrate were employed; (*a*) cleavage faces of single crystals, (*b*) crystal surfaces prepared by grinding, polishing and subsequent etching, (*c*) monocrystalline films of silver and of gold formed on rocksalt and on mica and (*d*) thin polycrystalline films of alkali halides formed by deposition *in vacuo* on to amorphous bases.

§ 3. Experimental Results

3.1. *Thallium Chloride and Thallium Bromide*

TlCl and TlBr were observed to possess the abnormal, i.e. rocksalt, structure when deposited on to cleavage faces, of a series of crystals of the rocksalt structure (see table 1) at room temperature and at higher temperatures—the observations ranging up to 400 °c. Initially the diffraction pattern from the deposit consisted of streaks and these became more intense as the evaporation proceeded. The pattern (and the spacing) was consistent with the rocksalt form in a parallel orientation. Above a certain thickness a spot pattern due to the normal CsCl structure appeared. This thickness varied from substrate to substrate under similar conditions of evaporation. In the case of TlCl on LiF it was about twenty-five ångströms, whereas on KBr and on KI the critical thickness was several hundred ångströms. For TlBr on KCl a similar large value of the thickness was also found. The rate of deposition and the temperature of the base also influenced the thickness of the layer with the rocksalt structure. With a low rate of evaporation (~ 1 Å per minute) the abnormal layer was usually observed, with high rates (~ 30 Å per minute) both structures were usually obtained and in some cases only the normal structure. This is particularly the case where there is a large misfit between deposit and substrate. Increasing the temperature of the base, increased markedly the thickness of the layer with the rocksalt structure. While this was always found in an orientation strictly parallel to that of the base, the CsCl structure which appeared at greater thicknesses usually had the orientation, $(110)_{\text{deposit}} \parallel (100)_{\text{substrate}}$ and $[001]_d$ or $[1\bar{1}0]_d \parallel [01\bar{1}]_s$. Occasionally the (100), $[1\bar{1}1]$ orientation was present, but gave a weak diffraction pattern.

Experiments were also carried out using (110) etched surfaces of alkali halides (see table 1). At room temperature the deposit was normal in structure and, in the main, randomly orientated. As the specimen (base and deposit) was heated the deposit changed into an oriented layer having the rocksalt structure, with the (110) planes parallel. The temperatures at which this occurred ranged from about 150°c to 320°c. A particular example is shown in figure 1 (Plate).

The normal form was observed in other cases (see table 1) even with the slowest rates of evaporation and at elevated temperatures. Substrates of gold and silver come into this category, also mica and zinc blende.

In order to obtain more accurate values of the lattice constants of the rocksalt form than can be obtained from the reflection patterns, a number of polycrystalline films of the alkali halides (KI, KCl and NaCl) were used as bases. Here the transmission technique could be employed. Using two evaporators, the base was first deposited on formvar in the camera; the thallium halide was then evaporated with the base either at room temperature or at higher temperatures.

Table 1. Summary of the Main Results on Epitaxial Polymorphism of Thallium Halides

		Deposit TlCl				Deposit TlBr				Deposit TlI			
(1)	(2)	(3)	(4)	(5)	(6)	(3)	(4)	(5)	(6)	(3)	(4)	(5)	(6)
LiF	(100) cleavage	RT	A	P	+58	RT	A	P	+64				
NaF	(100) cleavage	RT	N	P	+37	RT	N	P	+43				
NaCl	(100) cleavage	RT	N	P	+13	RT	N	P	+17	20–170	B	O	5·2 10·5
	(110) etched	RT 150, 180	N N	Q Q	—	RT 145–180	N A	Q Q	—				
	(111) etched	20–170	N	E	—	20–170	N	E	—	20–180	B	E	—
PbS	(100) cleavage	RT, 100, 125	A	P	+12	RT	N	P	+17				
KCl	(100) cleavage	RT	N	P	+1	RT	N	P	+6	20–175 175–300	B A	O P	−5·2 +34 +11
	(110) etched	RT 180–210	N N	R Q		RT 185–200	N A	R Q	—	20–190 190	B A	Q Q	—
KBr	(100) cleavage	RT, 200–400	N	P	+4	RT	A	P	+6	175	B	O	
	(110) etched	RT RT–255	N N	R Q						175–210	A	P	+6
	(111) etched	·								180–195 >195	B A	F S	
RbBr	(100) cleavage	RT	A	P	−7	RT	N	P	+4				
KI	(100) cleavage	RT, 120, 200, 220	A	P	−10	RT	A	P	+6	RT–175 175–200	B A	O P	15·6 16·3 +6
	(110) etched)	RT 185–215	N N	R Q	—								
RbI	(100) cleavage	RT	N	P	−13	RT	A	P	+10				
MgO	(100) cleavage	20–190	N	R	—	RT	N	G		RT, 100, 120	E	R	
Ag	(100) oriented film	20–230	N	P	−6	20–230	N	P	+2·7				
	(111) oriented film	20–195	N	E	—	20–195	N	E					
Au	(100) oriented film	20–120	N	P	+6	20–120	N	P	+2·5				
	(111) oriented film	20–120	N	E	—	20–120	N	E					
ZnS	(110) cleavage	20–180	N	E	+8	20–180	N	E	3·5 +3·9				
CaF$_2$	(111) cleavage	RT, 100, 120	N	E	—	RT	N	E	—				
Mica	(001) cleavage	20–120	N	M, F	—	RT	N	E	—				

(1) Substrate; (2) type of substrate surface; (3) temperature (°C); (4) structure; (5) orientation; (6) % misfit.

RT—Room temperature
A—Abnormal structure (NaCl-type)
B—Abnormal structure (CsCl-type)
N—Normal structrue (CsCl-type)
F—(100) fibre orientation
G—(110) fibre orientation (partial)
R—Random orientation

P—Parallel orientation: $(100)_{dep} \parallel (100)_{sub}$ and $[01\bar{1}]_{dep} \parallel [01\bar{1}]_{sub}$
O—Orientation: $(110)_{dep} \parallel (100)_{sub}$ and $[001]$ and $[1\bar{1}0]_{dep} \parallel [01\bar{1}]_{sub}$
E—Orientation: $(110)_{dep} \parallel (110)_{sub}$ and $[001]_{dep} \parallel [1\bar{1}0]_{sub}$
M—Orientation: $(111)_{dep} \parallel (001)_{sub}$ and $[1\bar{1}0]$ and $[110]_{dep} \parallel [100]_{sub}$
Q—Orientation: (110) plane of deposit ∥ (110) plane in substrate
S—Orientation: (111) plane of deposit ∥ (111) plane in substrate

3.2. *Thallium Iodide*

Thallium iodide was always found to possess the CsCl structure when deposited on to cleavage faces of alkali halides (see table 1) though it is normally orthorhombic at room temperature (Helmholz 1936), transforming to the CsCl form above 175 °c. When the deposit was heated slowly the diffraction pattern changed to that of the rocksalt form at 175°c and above. The same result was obtained when the deposition was carried out above 175°c. The results differ from those reported by Schulz (1951) who found the rocksalt form at room temperature.

§ 4. Measurement of Lattice Constants

4.1. *Reflection Patterns*

The lattice constant of the rocksalt forms was measured at room temperature (i) by using the base as a standard when the deposit was thin and (ii) by comparison with the normal structure when the deposit was thick. The agreement (see table 2), using a variety of substrates, is well inside the experimental error except in one case—TlCl on PbS. Here the initial stages were unusual in that broad bands were found instead of the usual streaks—the streaks appeared at a later stage. The value given in table 2 is based on the streaks; it seems possible that some reaction takes place at the initial stage and that the streak pattern is not due to thallium chloride.

Table 2. Lattice Constants of the Abnormal Structures of Thallium Halides (from Reflection Patterns)

Substrate	Type of substrate surface	a_0 (Å) TlCl NaCl type	TlBr NaCl type	TlI CsCl type	TlI NaCl type
NaCl	(100) cleavage	6·35 ± 0·02	6·59 ± 0·05	4·20 ± 0·02	
	(110) etched	6·32 ± 0·02	6·60 ± 0·05		
	(111) etched			4·20 ± 0·02	
NaF	(100) cleavage	6·33 ± 0·05	6·59 ± 0·02		
LiF	(100) cleavage	6·33 ± 0 05	6·59 ± 0·05		
KCl	(100) cleavage	6·32 ± 0·05	6·63 ± 0·05	4·21 ± 0·05	6·97 ± 0·02
	(110) etched	6·32 ± 0·02	6·60 ± 0·05	4·21 ± 0·05	6·96 ± 0·02
KBr	(100) cleavage	6·32 ± 0·02	6·58 ± 0 02		6·98 ± 0·05
	(110) etched	6·33 ± 0·02			
	(111) etched			4·19 ± 0·05	6·98 ± 0·02
KI	(100) cleavage	6·35 ± 0·05	6·61 ± 0·05	4·20 ± 0 02	6·99 ± 0 02
	(110) etched	6·34 ± 0·02			
RbBr	(100) cleavage	6·37 ± 0·05	6·59 ± 0·05		
RbI	(100) cleavage	6·34 ± 0·02	6·60 ± 0·02		
PbS	(100) cleavage	6·62 ± 0·02†	6·59 ± 0·02		

† This unusually large value is discussed in § 4.

There is also a discrepancy between the results for TlCl on NaCl (table 2) and that given by Lüdemann (1957) which was 6·09 ± 0·06 Å or about 4% higher. A large number of experiments were carried out to check the value given in table 2 and in no case was a value found which differed from the value quoted by more than the experimental error.

4.2. *Transmission Patterns*

The polycrystalline alkali halide films referred to in § 3 were used as standards, and also the normal form of the thallium halide (see figure 2 (Plate)). This method was more accurate than that of § 4.1 in that sharp ring patterns were used. The results are given in table 3.

Table 3. Lattice Constants of Thallium Chloride (Rocksalt Type)

Experiment	a_0 (Å)	Standard
	$6{\cdot}360 \pm 0{\cdot}010$	KI
TlCl KI	$6{\cdot}246 \pm 0{\cdot}010$	TlCl (normal)
TlCl KCl	$6{\cdot}344 \pm 0{\cdot}010$	KCl (normal)
	$6{\cdot}337 \pm 0{\cdot}010$	TlCl (normal)
TlCl NaCl	$6{\cdot}355 \pm 0{\cdot}010$	NaCl
	$6{\cdot}339 \pm 0{\cdot}010$	TlCl (normal)

In the table the reference spacings used are $c_0 = 7{\cdot}066$ Å, 6·292 Å and 5·640 Å for KI, KCl and NaCl and 3·842 Å for TlCl in its normal form.

§ 5. General Comments

The results reported above confirm in the main those of previous investigators, and can be used to emphasize the remarkable influence of the cleavage face of the alkali halides in helping to produce structures which are unstable from the point of view of thermodynamics. The layers produced are in some cases remarkably thick—a hundred angstroms or more. The main aim of the present work was a more detailed investigation of the effect of the base temperature than had hitherto been available and it is by using heated substrates that it is possible to increase appreciably the thickness of layers with the abnormal structure.

In addition measurements were made of the lattice spacing of the rocksalt form. This is of interest in connection with any calculation of the free energy of the rocksalt form—though the relative free energy of the two forms will be very sensitive to the assumptions made in a calculation. If one uses, however, the simplest possible model of ionic forces and an nth power repulsion potential one can calculate the anion–cation distance for the two forms and obtain

$$(r_1/r_2)^{n-1} = \alpha_1 A_2^n / \alpha_2 A_1^n,$$

where r_1 and r_2 are these distances for the CsCl and NaCl forms respectively, α_1 and α_2 are the corresponding Madelung constants and A_1 and A_2 the lattice sums arising in the calculation of the repulsive part of the potential energy. From this one finds that $(r_1 - r_2)/r_1$ is 4·2% for $n = 8$, 4·7% for $n = 9$, and 5·3% for $n = 10$. This is very much what is found in experiment (cf. table 4, see also Schulz 1951).

Table 4. Interionic Distances r_1 and r_2

Substance	r_1 (Å)	r_2 (Å)	$r_1 - r_2$	$(r_1 - r_2)/r_1$
TlCl	3·32	3·17	0·15	0·047
TlBr	3·44	3·30	0·14	0·043
TlI	3·63	3·49	0·14	0·040

While it is true that the calculation of the internal energy and the free energy with this model gives the incorrect relative thermodynamic stability, the calculation of spacings is insensitive to the type of forces introduced and depends essentially on a repulsive potential changing very rapidly with distance.

Acknowledgments

The author would like to thank Professor H. Blackman and Dr. N. D. Lisgarten for their interest and guidance. He would also like to express his gratitude to the Commonwealth Relations Office (London) and the British Council for a Research Fellowship and a maintenance grant.

References

Helmholz, L., 1936, *Z. Krist.* A, **95,** 129.
Lüdemann, H., 1957, *Z. Naturf.*, **12a,** 226.
Pashley, D. W., 1952, *Proc. Phys. Soc.* A, **65,** 33.
Schulz, L. G., 1951, *Acta Cryst., Camb.*, **4,** 487.

Surface Re-orientation, Friction and Wear, in the Unidirectional Abrasion of Graphite

By P. V. K. PORGESS and H. WILMAN
Chemical Engineering Department, Imperial College, London

MS. received 13*th October* 1959, *in revised form* 1*st April* 1960

Abstract. Surface structure, friction and wear are investigated and correlated in the case of abrasion of graphite by emery papers of particle diameter $D = 5$ to 150 microns. For graphite and also for metals, the coefficient of friction μ of specimens approximately 1 cm long or more is low on the fine grades of emery, but rises rapidly with increasing D and then is practically constant at $D > 50$ microns. The ploughing component μ_p is concluded to be larger than the adhesion component μ_a when D is of the order of 30 microns or more. Earlier views that μ_p increases linearly with D and is always small are evidently incorrect.

Electron diffraction shows that the abrasion causes a re-orientation of the graphite at and near the surface by plastic flow by slip on (0001). A [001] 'fibre orientation' is developed (the usual compression texture) with its mean axis along the resultant of the normal load and the tangential frictional force, at $\tan^{-1}\mu$ (whatever the value of μ) to the specimen normal, towards the direction from which the abrasive particles came.

The wear per unit distance M also rises rapidly with D and then shows a much slower rate of increase at $D > 80$ microns. The plot of M against μ is a strongly curved locus at 200 g load, and is still curved even at 25 g load, for graphite; while for metals it is linear at least up to 2 kg load (Goddard, Harker and Wilman 1959). The difference in nature of the abrasion is also seen microscopically; cracking and some breakaway of graphite fragments occurs near the individual grooves, and is associated with a volume-wear rate about four times that of metals, at $D > 50$ microns.

A method of comparing the hardnesses of the work-hardened surface regions of abraded materials in terms of abrasion-groove widths is described. For the graphite specimen used this is of the order of one-fifth that of silver; the effective Vickers hardness is thus of the order of 20, and this agrees with estimates made using a diamond indenter.

§ 1. Introduction

Recent experiments (Barwell 1956, Piggott and Wilman 1957, Duckworth and Forrester 1957, Burwell 1958) have indicated that wear in metallic bearings or gears is often more of an abrasive character than had been realized previously. Serious abrasive wear can arise not only from adventitious grit, but as a result of oxides, carbides or other similar hard materials being present at the bearing surfaces either as part of the bearing material or as a surface layer which becomes fragmented under pressure. Abrasive processes such as grinding and honing are also much used in industry, but are not well understood

in detail. Studies of the abrasion process have therefore been made recently in this laboratory to elucidate the relation between the friction, wear and surface re-orientation occurring during uni-directional abrasion.

Although the surface structure of polished metallic and other solid surfaces has been studied extensively in this laboratory (see for example Finch 1937 a, b, 1950) and elsewhere, there have been very few studies of the surface structure of abraded surfaces. Courtel and Léger (1948) Courtel (1949, 1950 a, b) and Takahashi (1951) used electron diffraction to investigate the surface nature of various uni-directionally abraded metals, but their work led to no clear and valid conclusions as to the origin of the observed surface deformation textures, and indeed their interpretation of the rather complex electron diffraction patterns was evidently in some cases incorrect. Scott and Wilman (1958) showed, however, in the simpler case of the hexagonal metals beryllium and magnesium, that uni-directional abrasion (on emery papers) results characteristically in an oblique one degree orientation ('fibre orientation') whose axis [001] is inclined at an angle δ away from the normal to the specimen surface, towards the direction from which the abrasive particles came. The inclination δ was approximately equal to $\tan^{-1}\mu$, where μ was the observed coefficient of friction. They showed that this orientation corresponds to the usual [001] compression texture, arising from the obliquely directed compressive force which is the resultant of the normal load and the tangential force overcoming friction, exerted on the individual abrasive particles and thereby on the material in contact with them.

As part of a series of studies of the abrasion process in this laboratory, the following experiments were aimed particularly to show the relation between the surface re-orientation, the friction and the wear during abrasion of graphite, which is an important solid lubricant. Several new results of fundamental importance have been brought to light, in particular the general nature of the dependence of the coefficient of friction μ of solids on the mean emery-particle diameter D was shown for the first time. On 0000 emery paper, μ was 0·13, nearly equal to that (0·12) of graphite sliding on graphite (evidently due to clogging of the emery paper by the worn-off graphite); but with increasing emery particle diameter, μ rose to a practically constant value of 0·46 at D greater than about 50 microns.† Metals showed a similar variation of μ with D, but μ rose to much higher values of the order of 0·8 (cf. also Goddard, Harker and Wilman 1959). Previous results on metals had suggested only a very small linear rise of μ with D (Spurr and Newcomb 1957).

Secondly, our electron diffraction results showed that the [001] fibre orientation produced on the graphite surface by the abrasion varies correspondingly in its inclination, δ being of the order of 7° when μ was 0·13 (on 0000 emery), and for example of the order of 22° when μ was 0·42 (on grade 1 emery).† Previous electron diffraction work on polished graphite (for example Jenkins 1934, Finch, Quarrell and Wilman 1935) had only shown a surface orientation with the [001] axis normal to the specimen surface, due apparently to irregular polishing direction.

† These results were described in a lecture given by one of us (H. W.) at Tube Investments Ltd. Research Laboratories, Hinxton Hall, near Cambridge, in September 1958, and at a colloquium (by P. V. K. P.) at Imperial College, in January 1959.

Thirdly, our results on wear of the graphite specimens on various grades of emery paper show that at a constant load of 25 g or 200 g, the wear per unit distance M is related to the friction coefficient μ in a definite way, but this is not of the linear form $M = k(\mu - \mu_0)$ which other experiments in this laboratory have shown to be characteristic of the abrasive wear of most metals at loads up to a few kilogrammes (Goddard, Harker and Wilman 1959). The plot of M against μ for the graphite gives a curved locus, indicating a form of wear differing largely from that of metals.

§ 2. Experimental

Graphite specimens, upon which the experiments were performed, were cut from a large polycrystalline block of 2 in. square cross section, to a size 1·4 cm × 1·0 cm × 0·5 cm. This graphite, of density 1·77 g cm^{-2}, was kindly supplied to this Department by the Atomic Energy Research Establishment, Harwell. The grain diameter was estimated from micrographs to be of the order of 0·5 mm. As abrasives, emery papers from Messrs. Oakey and Sons Ltd. were mainly used. The grades used and the mean particle diameters for these were: 0000 (5 μ), 000 (10 μ), 00 (15 μ), 0 (35 μ), 1 (45 μ), 1F (40 μ), 1M (50 μ), 1G (70 μ), 2 (100 μ) and 3 (150 μ). Emery paper of mean particle diameter about 25–30 microns was not available from Messrs. Oakey but was obtained from Messrs. Hubert, (grade 00). Oakey's carborundum papers of meshes 600 (20 μ), 400 (36 μ), 280 (60 μ), 150 (99 μ) and 120 (166 μ) were also used. The effect of sliding the graphite under load on filter paper (Whatman No. 1) was also investigated.

For the electron diffraction investigations, the working surface (1·4 cm × 1·0 cm) was abraded uni-directionally in air, under the desired load (between 0·2 and 10 kg), on emery paper of a particular grade over a track length of at least 20 cm until the surface showed no further change in form. The surface structure of the specimen was then determined from electron diffraction photographs obtained from a Finch electron diffraction camera (Finch and Wilman 1937) with a camera length of approximately 47 cm and accelerating voltage in the region of 50–60 kv.

The surface layers were burned away in air, in 15 sec stages at red heat in a porcelain crucible, to expose sub-surface regions and allow their investigation by electron diffraction. This short heating at this temperature was insufficient to cause appreciable change in the structure by recrystallization, although the surface gradually became pitted and eventually crumbled. This process was repeated until the initial strongly [001]-orientated graphite at the abraded surface had been removed and the original texture of the specimen was observed, i.e. randomly oriented crystals. Assuming the graphite is removed evenly by burning, the weight loss (~2 mg per 15 sec) is an indication of the depth of graphite removed. This was estimated to be about 1·09 microns per milligramme for the specimen used.

The coefficient of friction was determined under a range of conditions similar to those used for the surface-deformation investigations. This was measured in terms of a horizontal force necessary to cause motion of the loaded specimen over the abrasive. The force was applied by means of a thread which was attached to the graphite and passed over a low-friction pulley to a scale pan. Measurements

of friction were made for graphite moving over graphite, No. 1 filter paper, emery paper of grades 3, 2, 1G, 1, 1F, 0, 00, 000 and 0000, and carborundum paper of abrasive sizes 600, 400, 380, 150 and 120 mesh.

To obtain information about the initial part of the sliding process, a continuous trace of the amount of the frictional force was recorded (figure 5 (Plate)). A suitable spring was attached at one end to the loaded specimen, and the other end was moved parallel to the sliding surface, at constant speed, by a geared electric motor. A needle, soldered to the specimen end of the spring, recorded the motion of this end on a smoked glass plate which was mounted on a base rigidly connected to the other end of the spring and was made to move on this base at a roughly constant speed perpendicular to the sliding direction of the specimen.

Wear measurements were made for graphite sliding on emery and carborundum papers. The graphite specimen was abraded at about 10 cm sec $^{-1}$ under loads between 25 and 500 g in a series of 20 cm strokes. The wear loss for each successive stroke was estimated on a semi-micro balance to 0·01 mg. With the fine emery grades, especially 0000 emery paper, producing low wear rates, the weight of the specimen was found to increase with time, e.g. $\sim$0·05 mg in 15 sec, due to adsorption of air on the fresh surface exposed by the abrasion. Reproducible results were only obtained if the specimens were weighed within 5 seconds after the abrasion. On the coarser grades, from 00 upwards, the weight increase with time was, however, very small in comparison with the wear. Since the friction and the wear on emery paper of any particular grade varied sightly from one sheet to another (i.e. the abrasive particle size, shape, etc. varied slightly), the friction and wear were normally both measured on the same sheet of emery. In this case the points in figure 7 varied slightly in position for different sheets of the emery paper, but they remained always close to the single locus shown.

A Vickers projection microscope was used to obtain optical photomicrographs of the specimen surface at suitable stages of the abrasion.

§ 3. Results

Electron diffraction photographs from the abraded graphite surfaces were recorded at various azimuths relative to the abrasion direction. The graphite abraded on various grades of emery paper showed oblique [001] orientation in all cases, the 00*l* arcs being centred on a radius which was tilted at an angle δ away from the normal of the specimen surface towards the direction from which the abrasive particles came, i.e. the reversed abrasion direction.

3.1. *Electron Diffraction Observations of the Surface Structure of Uni-directionally Abraded Graphite*

After abrasion, the immediate surface region was found to be the most strongly oriented layer. The degree of orientation of the graphite at the surface, however, decreased with increasing coarseness of the abrasive. For example, abrasion on 0000 emery paper (cf. figure 1(*b*) (Plate 1)) gave a higher degree of orientation than abrasion on grade 1 emery paper (cf. figure 1(*e*)).

The degree of orientation also appears to increase with increase in applied load and total length of the abrasion stroke. For example, starting with a relatively rough burnt-off surface, the degree of orientation was found to be higher for 500 g load and on No. 1 filter paper, than for 200 g load and the same abrasive and stroke length, and it was higher after a 600 cm stroke than after a 25 cm one. It seems possible, however, that these observations may be explained as largely due to disoriented graphite fragments worn off the projecting parts of the surface being deposited in the neighbouring depressions, so as to lead to rings in the diffraction pattern, until sufficient material is worn away to leave the surface smoothed off to its maximum extent.

The Coefficient of Friction μ and the Inclination δ of the Mean [001] 'Fibre Orientation' Axis, away from the Specimen Normal, for Graphite Abraded Uni-directionally on various Grades of Emery Papers

Grade of emery	0000	000	00	0	1	1G	2	3
μ	0·13	0·19	0·25	0·40	0·42	0·45	0·46	0·46
$\tan^{-1}\mu$ (deg)	7	11	14	22	23	24	24	24
δ observed (deg)	7	10	~14†	22	22	–	–	–

† The 002 arc appears to be strongest at about 7° from the vertical in figure 1 (*c*), but this arc extends with high intensity to about $\delta \sim 22°$.

The table shows the angles of inclination δ and the observed μ for the graphite sliding on a range of emery papers. It is seen that at the surface δ agrees closely with $\tan^{-1}\mu$. It is to be noted, however, that the patterns from the graphite abraded on 00 emery paper (cf. figures 1(*c*) and 1(*d*)) show 002 arcs which are strongest at about $\delta \simeq 7°$, though the arc extends with high intensity up to $\delta \sim 24°$. Figure 1(*d*) shows the clearer, more strongly arced pattern from graphite abraded on 00 emery paper followed by sliding (approximately 100 cm at about 0·5kg load) on filter paper to remove randomly disposed graphite fragments from the surface, and finally burning away the surface region sufficiently to remove the thin surface layer which had been re-oriented by the abrasive action of the filter paper. For graphite sliding on filter paper, cf. figure 1(*a*), δ was 7–8°, and μ was 0·13, thus $\tan^{-1}\mu = 8°$, again agreeing well with the observed δ.

Variation of load between 0·2 and 1 kg had no effect on either δ or μ for a given grade of abrasive, within the accuracy of the measurements.

It was of particular interest to determine whether or not higher loads cause development of some perpendicular [001] orientation similar to that which occurs together with the oblique [001] orientation in beryllium abraded uni-directionally at loads greater than about 1 kg (Scott and Wilman 1958). The specimen was therefore slid under loads of up to 10 kg on emery papers of grades 1 and 000 respectively. In neither case did the electron diffraction patterns from the abraded surface (cf. figure 2 (Plate II)) show clear presence of any perpendicular [001] orientation.

3.2. *The Variation of the Angle of Tilt δ with Depth for Abraded Graphite*

A graphite surface which had been burnt off until it showed random crystal orientation was slid under 500 g load on No. 1 filter paper, and after a single continuous 600 cm abrasion stroke the surface showed [001] fibre orientation with its axis inclined at 6°–7° from the specimen normal, this angle remaining constant and equal to $\tan^{-1}\mu$ at all depths at which the fibre orientation was detected, i.e. to 23 microns below the surface. For a 200 g load and a 20 cm stroke on No. 1 emery paper the depth was about 40 microns, and after burning off the graphite to this depth the surface exposed then yielded ring patterns with 00*l* arcs visible.

When the graphite had been abraded on coarser grades of emery and not, or insufficiently burnt-off, however, before abrasion on a finer grade, the variation of tilt δ with depth was found to depend on the previous abrasion history. For example, with successive abrasion on 3, 1, and 000 emery papers followed by a series of strokes on filter paper, the initial tilt was 8°, i.e. that typically due to the filter paper, and increased to 24°, which is the tilt obtained using the coarser grades of emery paper. The final abrasion on 000 emery paper had clearly not removed all the surface region of the graphite which had been re-oriented to greater depths by the prior abrasion on the coarser 3 and 1 emery paper.

The degree of orientation was found to decrease with depth. This was shown by the increasing length of the 00*l* and other arcs and the appearance of rings indicating much randomly oriented graphite.

3.3. *The Variation of the Coefficient of Friction μ of Graphite and Lead, with Diameter D of the Abrasive Particles*

Figure 4 shows the variation of μ for the graphite on emery papers and carborundum papers, at 0·2 to 1 kg load. For comparison, figure 4 also shows the variation of μ for lead, i.e. a similarly easily deformable metal, sliding on emery papers at 0·2 kg load and similar speed. The lead block was rectangular, the abraded face being 1·4 cm × 1·0 cm and the height 0·5 cm.

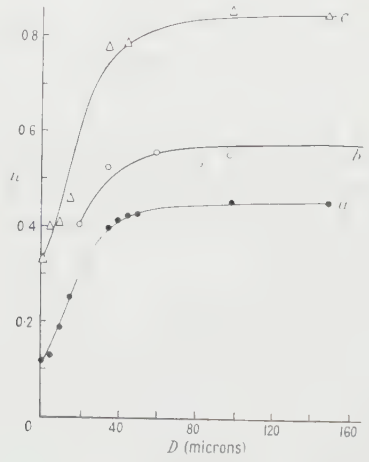

Figure 4. Variation of μ with the mean diameter D of the abrasive particles, at 200 g load, for (*a*) graphite on emery papers, (*b*) graphite on carborundum papers, (*c*) lead on emery papers.

The lead and the graphite show similar friction curves, and the curve for the graphite is similar in form for both emery and carborundum papers. The curves are characterized by a steep rise of μ with increasing D, up to a value which is practically constant at D more than about 45 to 50 microns. This variation of μ with D appears not to have been shown previously.

On 0000 emery paper, μ of both the graphite and the lead was nearly the same as that of graphite on graphite (0·12) and lead on lead (0·33) respectively. These observations indicate that when graphite or a metal slides on the finer grades of emery papers, the worn-off graphite or metal clogs the depressions between the emery particles so that a part of the load is borne on graphite–graphite or metal (+oxide?)–metal (+oxide?)† contacts and hence the friction is decreased.

3.4. *The Variation of μ of Graphite on Emery Papers at the Commencement of Sliding*

As a check on the relative values of μ during the initial acceleration at the commencement of sliding and during sliding at about 10 cm sec $^{-1}$, a record of μ was made as described in § 2, for graphite sliding on No. 1 emery paper at 1 kg load. This is shown in figure 5 (Plate III), where the vertical scale indicates the frictional force corresponding to the deflection of the pointer at the end of the spring. The horizontal axis corresponds to an approximate time scale. It is seen that the tangential force rose at practically constant rate until sliding motion occurred, after which any decrease in μ was evidently small and μ was constant to within about 6%. The slight initial rise above the mean μ level during sliding was probably due to the initial oscillation of the spring while the tension was being applied. There was thus little difference between the static and kinetic coefficients of friction.

3.5. *The Variation of μ and M of Graphite with Load W*

Although μ of graphite on emery paper of a given grade was constant, within the experimental error, at loads of 0·2 to 10 kg, some preliminary tests at 25 g load indicated a considerable increase in μ on 0000 emery, to 0·24 as compared with 0·13 at 0·2 kg or more load, this being apparently due to the lower wear causing less clogging of the emery and hence less load on graphite graphite contacts. On 00 and 1 emery paper, μ at 25 g load was 0·31 and 0·48 respectively as compared with 0·26 and 0·46 at 0·2 kg or more.

The variation of M with load W over the range 0 to 500 g was checked in the case of graphite sliding on No. 1 emery paper, over a distance of the order of 200 cm in each case. M was found to be closely proportional to W, for example $10^3 \times M$ was 0, 5·7, 11·2, 23·7 and 115 mg cm $^{-1}$ for W = 0, 22·8, 52·8, 102·8 and 502·8 g respectively.

3.6. *The Wear of Graphite on Emery and Carborundum Papers*

Figure 6 shows the wear per unit length of abrasion of the graphite M on emery and carborundum papers, as a function of the mean diameter D of the

† The low $\mu \sim 0{\cdot}3$ for metal sliding on metal in air, shows that the metal surfaces are covered with a thin layer of oxide (presumably) at least a few atoms thick; similarly the graphite is presumably covered with an adsorbed layer of oxygen and nitrogen and other gaseous molecules from the air.

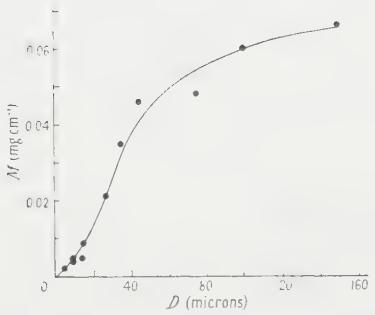

Figure 6. Variation of wear per unit distance M of graphite on emery papers, with mean emery particle diameter D.

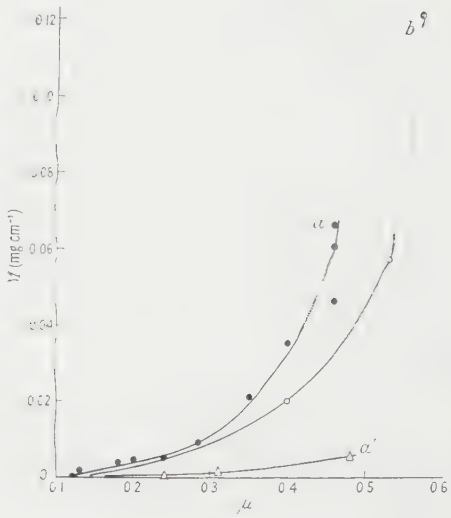

Figure 7. Variation of wear per unit distance M of graphite, with the coefficient of friction μ: a, a', 200 g and 25 g load with emery as abrasive ; b, 200 g load with carborundum as abrasive.

abrasive particles, at 200 g load. This variation is similar in form to that of μ, rising rapidly with increase in D, then flattening off more and more as D increased to the order of 150 microns, but still increasing with D even at this large value.

Figure 7 shows the relation between M and μ of the graphite specimen on the various grades of emery paper, for the 200 g and 25 g loads, and includes the point for graphite sliding on graphite, for which measurement showed that $M \simeq 0$ and $\mu = 0{\cdot}12$. The points in figure 7 lie on or near a curved locus which deviates considerably from the practically linear form of variation of M with μ found for most metals (Goddard, Harker and Wilman 1959).

For comparison the results are shown also in figure 7 for wear and friction of the graphite on several carborundum papers.

3.7. *Optical Examination of Graphite Surfaces Abraded on Emery Papers*

Figure 3 (Plate) illustrates typical micrographs from the graphite abraded about 3 mm path length (so as to show individual grooves clearly) under 200 g load on various grades of abrasive. Figure 3(a) shows the grooves produced by 0000 emery on graphite initially surfaced on 0000 emery paper followed by filter paper. In figure 3(b) the vertical fine grooves correspond to the initial surfacing on 0000 emery paper, and the horizontal wide groove was caused by one of the particles of the 0 emery paper. In both cases the grooves ploughed out by the emery particles show much irregularity of outline at their edges, apparently owing to break-away of pieces of graphite ; and there are many irregular cracks in the regions adjacent to the grooves, as can be seen in figure 3(b). The mean widths of the grooves caused at this load of 200 g varied from about 0·5 D on 0000 emery to about 0·25 D on grade 2 emery.

At least some of the graphite from the groove space is evidently displaced by plastic flow to become piled up at the sides of the groove, though again rather irregularly, as is seen in figure 3(*b*). Some of the graphite from the groove space is, however, worn away as loose particles, and in particular no coherent graphite strips in process of formation could be seen, such as have been observed still present at the front end of the grooves on metals, in this laboratory (Avient, Goddard and Wilman 1960).

Figure 3(*c*) shows a typical groove of more rounded form, caused by sliding the graphite under 200 g load on Scotchlite reflective sheeting, i.e. a two-dimensional array of glass spheres about 125 microns in mean diameter, stuck on to a thick backing layer. There is a slight pile-up at the sides of the grooves, but no clear evidence of any appreciable forward flow of material at the bottom region of the groove, such as is seen from the curving of the initial surfacing lines across the groove in figure 3(*d*), which was recorded by Dr. J. Goddard in this laboratory from a silver surface slid on Scotchlite at 1 kg load. It is noted that the groove widths in figures 3(*c*) and 3(*d*) are approximately equal ($\sim$30 microns, i.e. 0·25 *D*).

§ 4. Discussion

4.1. *The Variation of the Friction of Graphite and Lead with Particle Diameter D of the Emery*

Since, after sliding uni-directionally under load on the emery paper, the graphite or metal surfaces show parallel grooves which correspond at least in part to removal of material, i.e. wear, it is clear that the friction coefficient μ consists partly of a ploughing component μ_p (cf. Bowden and Tabor 1954). The results of Spurr and Newcomb (1957) had suggested that for metals sliding on emery papers μ rises gradually and linearly with increase in diameter *D* of the emery particles. They concluded that if this linear locus is extrapolated back to $D=0$, the value of μ then corresponded to the adhesion component μ_a, the excess slight linear rise being μ_p which was small, up to about 0·1 for Cu and 0·3 for Pb.

Our results in figure 4 show the variation of μ at both lower and higher *D* values than Spurr and Newcomb used, and allow recognition of the true non-linear form of variation of μ with *D*, in particular the virtually constant μ at *D* above about 50 microns and the rapid decrease in μ at *D* less than 50 microns (due to part of the load then being supported on the worn-off material which partially clogs the emery paper). Goddard, Harker and Wilman (1959) have now also found this for abrasion of many other metals, using specimens of the order of 1·5 to 2 cm long; and verified further in the case of Cu that use of specimens which are much shorter (< 2 mm) in the sliding direction, causes the locus of μ to show much less variation with *D*, rising from about 0·6 on 0000 emery but flattening off as before at about 0·8 on grades 1 to 3 emery. This indicates that Spurr and Newcomb's specimens, though of 3/16 in. diameter rods, must have had effective bearing lengths of only about 0·1 cm, and that their interpretation of their results as suggesting an inclined linear locus (as the mean over a narrower range of *D* than that used in the present work) is incorrect and corresponds only to a lowering of μ at low *D* due to clogging having been still appreciable on the finer grades of emery.

At the lowest D (5 microns) μ approximates closely to the value for graphite on graphite (0·12) or metal-oxide on metal-oxide respectively, and this with other observations such as the almost continuous layer of worn-off material on the emery paper, shows that when D is less than 50 microns, μ is reduced as a result of part of the load being carried on graphite–graphite or metal-oxide–metal-oxide contacts, due to partial clogging of the emery by the worn-off material.

Recent experimental and theoretical results of Avient, Goddard and Wilman (1960) have shown that the high and practically constant friction of most metals on the coarser emery papers ($D > 70$ microns) corresponds to absence of appreciable clogging of the emery during the single passage of the specimen over these rougher surfaces, and to the abrasive particles having angular form, this leading to μ_p being a large part of the total friction. μ_p and μ_a are functions of the properties of the graphite or the metal, and of the semi-apical angle θ of the pyramidal or conical shape of the indenting tips of the particles. Goddard, Harker and Wilman (1959) derived expressions for μ in terms of θ for pyramidal or conical particles. For example for cones

$$\mu = \mu_p + \mu_a = \frac{2}{\pi}\left\{\frac{p_m'}{p_m}\cot\theta + \frac{s}{p_m}\operatorname{cosec}\theta\right\}, \qquad \ldots\ldots (1)$$

where p_m is the flow pressure of the material, p_m' is the rather larger effective flow pressure owing to the pile-up of material ahead of the ploughing particle, and s is the shear force per unit area to shear the adhering surfaces which slide against each other. If the emery particles have substantially the same shape on emery papers of different grades, μ would thus indeed be expected to be constant at constant load, independent of the mean particle diameter.

The results for metals (Goddard, Harker and Wilman 1959, Avient, Goddard and Wilman 1960) show that the practically constant μ at D greater than 70 microns is lower (at constant load of 0·2 to 2 kg) the harder the metal, e.g. it is about 0·8 for Cu and Ag, but 0·53 for W. It was concluded that to account for the $\mu \sim 0{\cdot}80$ for Cu on emery ($D > 70$ microns), (Avient, Goddard and Wilman 1960) the effective θ was about 62°, if $p_m'/p_m \simeq 1{\cdot}5$, and in this case μ_p would be about 0·5 and μ_a about 0·3 and thus nearly the same as the μ ($= s/p_m$) of Cu (+oxide?) on Cu (+oxide?). For graphite on graphite μ ($= s/p_m$) is only 0·12, thus $(2/\pi)(s/p_m)\operatorname{cosec}\theta$ would be 0·09, hence μ_p would be the total μ of 0·46 minus 0·09, i.e. 0·37. If this is to equal $(2/\pi)(p_m'/p_m)\cot\theta$, then (p_m'/p_m) must be 1·1 for graphite. This lower value of (p_m'/p_m) as compared with that of 1·5 assumed for the Cu could be due to a much lower degree of pile-up of displaced material round the indenting particles, or a similar degree of pile-up but with some other contrary effect such as the cracking and weakening of this piled-up material (see § 3.7).

4.2. *The Relation between μ and the Inclination δ of the Orientation Axis for Graphite*

The above experimental results show that in the surface regions of the graphite an oblique [001] 'fibre' orientation is developed by the uni-directional abrasion. From its nature and axial direction it is clear that this orientation originates from the compression exerted by the abrasive particles on the graphite, and corresponds to the known [001] compression texture, this being developed as a result of plastic deformation by slip on the usual (0001) slip planes. This is

closely analogous to the oblique [001] 'fibre' orientation found on uni-directionally abraded Be and Mg (Scott and Wilman 1958). For the graphite, similarly, the outwardly directed orientation axis is inclined away from the specimen normal, back towards the direction from which the abrasive particles came, at an angle δ which approximates closely to $\tan^{-1}\mu$. The additional new results now show however (see table), that μ varies from 0·13 on 0000 emery paper to 0·46 on grade 3 emery, and that on any grade of emery paper in this range, the weighted mean δ observed is approximately equal to $\tan^{-1}\mu$.

The interpretation of these observations is thus quite clear in the two extreme cases when the load and shear during sliding are practically all on graphite–graphite contacts ($\mu = 0{\cdot}12$) as in abrasion on 0000 emery; or when they are practically entirely on emery–graphite contacts ($\mu \simeq 0{\cdot}46$) as on grade 1 emery paper and coarser grades.

On the intermediate grades of emery (000 to 0) the friction conditions are inhomogeneous in nature, the load W being partly (fW) supported on emery–graphite contacts having coefficient of friction μ_{eg} made up of ploughing and adhesion contributions, μ_p and μ_a respectively, and partly ($(1-f)W$) on graphite–graphite contacts of coefficient of friction μ_{gg} (adhesion). In such a case the total frictional force μW can be expressed as

$$\mu W = \mu_{gg}(1-f)W + \mu_{eg}fW. \qquad \ldots\ldots(2)$$

Therefore

$$\mu = (1-f)\mu_{gg} + f\mu_{eg} \qquad \ldots\ldots(3)$$

$$= (1-f)\mu_{gg} + f(\mu_p + \mu_a). \qquad \ldots\ldots(4)$$

On the horizontal graphite–graphite shear surface the resultant force must be inclined at $\tan^{-1}\mu_{gg}$ to the normal, because the vertical load is $(1-f)W$ and the horizontal frictional force is $\mu_{gg}(1-f)W$, and on the emery–graphite contact areas the resultant force will be at $\tan^{-1}\mu_{eg}$, the vertical load being fW and the horizontal frictional force $\mu_{eg}fW$. From the data in figure 4, $\mu_{gg} = 0{\cdot}12$ and $\mu_{eg} = 0{\cdot}46$ (μ when $f \simeq 1$, above $D \sim 50$ microns), hence for the graphite–graphite contact areas we should expect the orientation axis to be inclined at $\delta = \tan^{-1}(0{\cdot}12) = 7°$, and for the emery–graphite contact areas $\delta = \tan^{-1}(0{\cdot}46) = 24°$, in the absence of any further modification being caused by the act of sliding.

In comparison with these expectations our electron diffraction patterns from graphite abraded on 000, 00 or 0 emery from Messrs. Oakey & Son Ltd., and on 00 emery from Messrs. Hubert, do not show two separate groups of diffraction arcs, apparently because the arcs are long enough to overlap the positions of these two δ values. However, it is clearly seen (cf. figure 1(*c*) and 1(*d*)) that, for example, the 002 and 004 diffraction arcs (centred on a radius at about the 1 o'clock position, at distances of 0·75 cm and 1·5 cm from the central spot) are not symmetrical in intensity distribution along their length, relative to their centre. These arcs appear to correspond, at least approximately, to the coalescence of two arcs centred on radial directions at 7° and 24° from the vertical, having intensities roughly corresponding to the ratio $(1-f):f$, i.e. the relative areas of contact surface of the two types. In general the circumferential position of maximum intensity of the composite arc tends thus to be on a radius inclined at $\delta \simeq \tan^{-1}\mu$, even in this region.

4.3. *The Abrasive Wear of Graphite and its Relation to the Friction*

Figure 7 shows that the mass of wear M per unit length is not related to the friction coefficient μ by the linear expression $M = k(\mu - \mu_0)$ which was found (Goddard, Harker and Wilman 1959) to hold for the abrasion of metals on emery papers, μ_0 being often nearly the same as μ of the metal (oxide) on the metal (oxide). As stated above (§ 3.7), the mean groove width caused on the graphite at 200 g load on a given grade of emery paper (or on Scotchlite) was approximately the same as was observed on silver at 1 kg load on emery paper of the same grade (or on Scotchlite). We can thus compare the volume wear (M/ρ where ρ is the density) of the two materials at about the same degree of indentation, and we find that on the emery of grades 1 to 3, M/ρ is $3{\cdot}7 \times 10^{-5}\,\mathrm{cm}^2$ for the graphite (at $W = 200\,\mathrm{g}$), as compared with $0{\cdot}9 \times 10^{-5}\,\mathrm{cm}^2$ for silver according to the data published by Goddard, Harker and Wilman (1959). The volume per cm worn off the graphite (at 200 g load) is thus estimated to be about four times as much as that worn off the silver (at 1 kg load).

We would expect that the number of contacting emery particles (neglecting the small proportion that are only slightly indenting and thus not supporting much load) will be substantially constant for different materials when the mean groove width is the same. We have in fact checked that this is about the same number for graphite at 200 g as for silver at 1 kg load, being about 50. The fact that the volume wear of the graphite is four times that of silver thus shows that either the fraction of the groove volume removed as wear is four times that for the silver, or else some or all of the extra wear volume is removed from the regions at the sides of the grooves. Photomicrographs such as figure 3(*b*) confirm that a considerable amount of graphite is fragmented and removed from the regions at the sides of the grooves. Such a cracking and fragmentation must also occur in the region immediately ahead of the abrasive particle as it ploughs along, thus the proportion of groove volume removed as wear is also likely to be larger than in the abrasion of metals, for which this was estimated to be about 10% (Goddard, Harker and Wilman 1959).

M is still increasing at D values larger than that at which μ has become nearly constant. This may be associated with the fact that D then is approaching the same order of magnitude as the mean grain diameter of the graphite specimen, so that the wear may then involve loosening and removal of grains as a whole without much further increase in friction as D increases.

The relative importance of the lateral fragmentation compared with the wear volume removed from the grooves thus seems likely to be greater the coarser the abrasive, corresponding to the observed upward curve of the M/μ locus (cf. figure 7). The fact that the locus of M plotted against μ was still not linear even at a load as low as 25 g, for which the M/ρ was only about one-third that of silver at 1 kg load, emphasises still further the different nature of the wear compared with that of metals. The different wear properties of different graphite or graphitized carbon specimens may be due to the various degrees of prominence of this contribution to the wear, associated with different amounts and nature of the intercrystalline carbon, dependent on the nature of the formation of the material.

Our data above can be used to estimate the effective 'flow pressure' p_{m} or the Vickers diamond indentation hardness number H_{D}, of the work-hardened

surface regions of the graphite specimen. The load W on the graphite is balanced by the flow pressure p_m acting on the total horizontal projected area na_h, where a_h is the horizontal projected area of the indentation contact area of one emery particle and n is the number of indenting particles, assumed to share the load W approximately equally. We have thus

$$na_h = W/p_m. \qquad \ldots\ldots (5)$$

Similarly for a load W' on another material, e.g. silver, of which the flow pressure is p_m'

$$n'a_h' = W'/p_m'. \qquad \ldots\ldots (6)$$

From (5) and (6) we obtain

$$p_m/p_m' = (n'/n)(a_h'/a_h)(W/W'). \qquad \ldots\ldots (7)$$

If W and W' are chosen so that the groove widths are the same in the abrasion of the two materials on the same abrasive emery paper, then $a_h = a_h'$, and also it follows that $n = n'$ or practically so (we have checked this in the case of graphite and silver). Under these conditions,

$$p_m/p_m' = W/W'. \qquad \ldots\ldots (8)$$

On the graphite at 0·2 kg the grooves were about the same width as on silver at 1 kg load, using the same grade of emery paper, hence p_m for the work-hardened surface region of the abraded graphite used was evidently about one-fifth that of the abraded silver surface regions, which we had found corresponded to $H_D = 102$ when estimated at 100 g load. For the graphite, this gives $H_D \simeq 20$. We also obtained a value of the order of 20 when H_D was measured in the usual way by diamond indentation (at 100 g load), although the indentation was not well-defined, apparently due to surface fragmentation here also.

References

Avient, B. W. E., Goddard, J., and Wilman, H., 1960, *Proc. Roy. Soc.* A, **258,** 159.

Barwell, F. T., 1956, *Lubrication of Bearings* (London: Butterworths), p. 245.

Bowden, F. P., and Tabor, D., 1954, *The Friction and Lubrication of Solids,* 2nd edn. (Oxford: Clarendon Press).

Burwell, J. T., 1958, *Wear,* **1,** 119.

Courtel, R., 1949, *Rev. Métall.,* **46,** 24.

—— 1950 a, *Métaux et Corros.,* **25,** 117, 145, 188.

—— 1950 b, *Rev. Métall.,* **47,** 700.

Courtel, R., and Léger, R., 1948, *J. Rech.,* 161.

Duckworth, W. E., and Forrester, P. G., 1957, Paper No. 90, *Conference on Lubrication and Wear* (London: Inst. Mech. Engrs).

Finch, G. I., 1937 a, *Trans. Faraday Soc.,* **33,** 425.

—— 1937 b, *Science Progress,* **31,** 609.

—— 1950, *Proc. Phys. Soc.* B, **63,** 465.

Finch, G. I., Quarrell, A. G., and Willman, H., 1935, *Trans. Faraday Soc.,* **31,** 1050.

Finch, G. I., and Wilman, H., 1937, *Ergebn. exakt. Naturwiss,* **16,** 353.

Goddard, J., Harker, H. J., and Wilman, H., 1959, *Nature, Lond.,* **184,** 333.

Jenkins, R. O., 1934, *Phil. Mag.,* **17,** 457.

Mott, B. W., 1956, *Micro-Indentation Hardness Testing* (London: Butterworths).

Piggott, M. R., and Wilman, H., 1957, Paper 18, *Conference on Lubrication and Wear* (London: Inst. Mech. Engrs).

Scott, V. D., and Wilman, H., 1958, *Proc. Roy. Soc.* A, **247,** 353.

Spurr, R. T., and Newcomb, T. P., 1957, Paper 28, *Conference on Lubrication and Wear* (London: Inst. Mech. Engrs).

Takahashi, N., 1951, *Métaux et Corros.,* **26,** 189.

Nuclear Quadrupole Coupling with Conduction Electrons in Cubic Alloys

By C. P. FLYNN and E. F. W. SEYMOUR
Physics Department, University of Leeds

MS. received 4th February 1960, in final form 28th April 1960

Abstract. The coupling of the quadrupole moment of the solvent nuclei to the screening charge round an impurity is investigated by the partial wave treatment of conduction electron scattering. The magnitude of the interaction with the copper nuclei in the system CuZn is found to be an appreciable fraction of the experimental value obtained from nuclear resonance measurements.

§ 1. Introduction

In alloy systems forming solid solutions with cubic crystallographic symmetry, the magnetic resonance of solvent nuclei possessing appreciable quadrupole moments exhibits a rapid decrease in intensity with increasing solute concentration (Bloembergen and Rowland 1953, Rowland 1955, Chapman and Seymour 1958). This effect has been attributed to the disturbance from cubic symmetry of the surroundings of a solvent nucleus situated near an impurity atom, due partly to the distortion of the lattice by the size difference, and partly to electrostatic effects caused by the valency difference, between solute and solvent atoms. It is evident, however, that any excess charge must be screened by a local variation in electron density; using the Thomas–Fermi approximation, both the screening charge density and the potential round the impurity may be shown to take the form $r^{-1}\exp(-Kr)$ where, for copper, $K \sim 1{\cdot}8$ Å^{-1}. This is in rather poor agreement with the value $K \sim 3$ Å^{-1} necessary to explain the measured electrical resistivities of dilute copper alloys (Mott and Jones 1936). With this model, using either value of K, it is readily shown that the electric field gradients produced by the valence effect are insufficient to explain the quadrupolar interactions, which have therefore been interpreted as due predominantly to the size effect. This conclusion has been strengthened by the observation that silver produces as large a quadrupole effect in copper as does zinc.

More recently, the electrical resistivities of some dilute solid solutions have been recalculated by Friedel using a partial wave analysis in which the impurity centre was represented by a potential well of the above form with K adjusted to satisfy the Friedel sum rule (Friedel 1954). The improved agreement with experiment resulting from this treatment has been enhanced by Blatt (1957), who included in the specification of the potential well the modified ion density resulting from the distortion of the lattice by the size effect.

In this latter form, the partial wave method has been applied also to the theory of the Knight shift in alloys (Daniel 1959). It was found that there are oscillations of electron density up to quite large distances from an impurity atom. From consideration of the electron density at different nuclear sites around an impurity, it was possible to predict with some success the Knight

shifts and nuclear resonance line width variations of a series of silver alloys. It is therefore of interest to investigate the implications of the partial wave treatment in analogous alloy systems where the solvent nucleus possesses a quadrupole moment. The magnitude of the valence effect will be examined. The size effect will not be considered except in so far as it modifies the size of the potential well representing the impurity.

§ 2. General Expressions for the Field Gradients

We shall consider only small solute concentrations so that any solvent nucleus is appreciably affected by only one solute atom. Following both Blatt and Daniel, we represent the scattering centre in approximate fashion by an isotropic square potential well. The effect of this disturbing potential on a system of nearly free electrons may be expressed in terms of the wave functions of the various angular momentum states of the electrons near the well. Using approximate conduction electron wave functions $u_k(\mathbf{R}) = u(\mathbf{R}) \exp(i\mathbf{k}.\mathbf{R})$ where $u_k(\mathbf{R})$ is normalized in unit volume and $u(\mathbf{R})$ is assumed to be independent of the wave vector $\mathbf{k}$, the disturbance $\Delta\rho(\mathbf{R})$ of the electron density at a distance R from the centre of a square well of radius a may be written

$$\Delta\rho(\mathbf{R}) = eu^*(\mathbf{R})u(\mathbf{R})f(R^2), \quad R > a, \qquad \ldots\ldots(1)$$

where

$$f(R^2) = \sum_{l=0}^{\infty} (2l+1)\{[\mathrm{n}_l^2(kR) - \mathrm{j}_l^2(kR)]\sin^2\eta_l(ka) - \mathrm{n}_l(kR)\mathrm{j}_l(kR)\sin 2\eta_l(ka)\},$$

and

$$\Delta\rho(\mathbf{R}) = eu^*(\mathbf{R})u(\mathbf{R})g(R^2), \quad R < a,$$

where

$$g(R^2) = \sum_{l=0}^{\infty} (2l+1)A_l^2(ka)\mathrm{j}_l^2(k'R). \qquad \ldots\ldots(2)$$

In equations (1) and (2), $\mathrm{j}_l(kR)$ and $\mathrm{n}_l(kR)$ are spherical Bessel and Neumann functions of order l, $\eta_l(ka)$ is the phase shift introduced by the scattering centre into the lth partial wave, and the $A_l(ka)$ are functions chosen to satisfy the continuity conditions imposed on each partial wave at the well boundary. Explicit

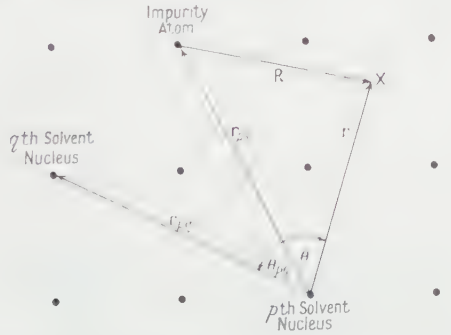

expressions for the $\eta_l(ka)$ are given by Daniel. The parameter k' is given by $k'^2 = k_0^2 + k^2$, where k_0 is a measure of the depth of the well.

It is convenient for our purpose to expand the function $f(R^2)$ corresponding to any point X in spherical harmonics about the nucleus p for which the

quadrupolar coupling is to be considered. The desired expansion is

$$f(R^2)=\sum_{\alpha=0}^{\infty}\phi_\alpha(r_{ps},r)r^\alpha \mathrm{P}_\alpha(\cos\theta),\quad \alpha=0,1,2,\ldots \qquad \ldots\ldots(3)$$

where $\mathbf{r}_{ps}$ is a vector from the pth nucleus to an impurity, $\mathbf{r}$ is a radius vector to the point X from the pth nucleus, and θ is the angle between $\mathbf{r}$ and $\mathbf{r}_{ps}$, as shown in the figure. It is known from the axial symmetry of $f(R^2)$ round $\mathbf{r}_{ps}$ that ϕ_α may be written

$$\phi_\alpha(r_{ps},r)=\sum_{\beta=0}^{\infty}\phi_{\alpha\beta}(r_{ps})r^{2\beta},\quad \beta=0,1,2\ldots \qquad \ldots\ldots(4)$$

The coefficients $\phi_{\alpha\beta}$ may be identified by comparison with the Taylor expansion of

$$f(R^2)=f(r_{ps}^2+r^2-2r_{ps}r\cos\theta)$$

round the point r_{ps}^2:

$$f(R^2)=\sum_{\gamma=0}^{\infty}\frac{(r^2-2r_{ps}r\cos\theta)^\gamma}{\gamma!}[f^\gamma(R^2)]_{R=r_{ps}} \qquad \ldots\ldots(5)$$

where the superscripts on $f(R^2)$ indicate repeated differentiation with respect to R^2.

If we assume that inside the pth atomic sphere the undisturbed wave functions possess spherical symmetry about the nucleus, then it is evident from equation (1) that $\Delta\rho(\mathbf{R})$ inside the cell has axial symmetry round $\mathbf{r}_{ps}$. The nuclear quadrupole interaction in an electric field of axial symmetry may be expressed in terms of the field gradient along the symmetry axis (Pound 1950)

$$\frac{\partial^2 V}{\partial r_{ps}^2}=eq=2\int\rho(r,\theta)r^{-3}\mathrm{P}_2(\cos\theta)\,dv \qquad \ldots\ldots(6)$$

where the integration extends over all charges ρ external to the nucleus. Since the cubic symmetry of the alloys considered precludes any contribution to the interaction from the undisturbed lattice, the contribution eq_{pp} from the pth cell to eq at the pth nucleus may be obtained by inserting the expansion (eqn (3)) of $f(R^2)$ round this nucleus into equation (6). On integrating over the atomic sphere the only non-zero term is that arising from the term in $\mathrm{P}_2(\cos\theta)$ in equation (3). After integrating over all values of k up to the Fermi limit k_F, we find

$$eq_{pp}=\frac{128}{45}er_{ps}^2\alpha^3\Big[U_1\int_0^{k_\mathrm{F}}k^2f^{\mathrm{II}}(r_{ps}^2)\,dk + U_3\int_0^{k_\mathrm{F}}k^2\Big\{f^{\mathrm{III}}(r_{ps}^2)-\frac{2r_{ps}^2}{7}f^{\mathrm{IV}}(r_{ps}^2)\Big\}dk+\ldots\Big] \qquad \ldots\ldots(7)$$

where α is the radius of the atomic sphere, and U_s is defined by

$$U_s=\int_0^{\alpha}u^*(r)u(r)r^s\{1-\gamma(r)\}\,dr.$$

A factor $4\pi\alpha^3/3$ enters on the right-hand side of equation (7) since $u(r)$ is now taken to be normalized within an atomic cell. The factor $1-\gamma(r)$ is included following Sternheimer (1950) in order to allow for the polarization of the solvent ion core by the disturbed conduction electron density.

In a similar manner the excess charge contained in the qth atomic sphere may be written in terms of the expansion of $f(R^2)$ around the qth nucleus, and the only non-vanishing term arises from that in $\mathrm{P}_0(\cos\theta)$ in equation (3). The contribution eq_{pq} to eq at the pth nucleus due to the excess charges located in all other cells containing solvent ions may then be found approximately from

equation (6) by taking the whole charge in the qth cell as located at the centre of the cell. It is not necessarily true that the field produced by these charges possesses axial symmetry about $\mathbf{r}_{ps}$, though it is for all nuclei p for which $\mathbf{r}_{ps}$ coincides with a three-fold or four-fold symmetry axis of the lattice. Since, however, it will be shown that eq_{pq} is small compared with eq_{pp}, deviations from axial symmetry in this term will be ignored. We obtain in this way

$$eq_{pq}=\frac{32}{3}e\alpha^3\sum_q \mathrm{P}_2(\cos\theta_{pq})r_{pq}^{-3}\{1-\gamma(r_{pq})\}\times\left[V_2\int_0^{k_\mathrm{F}}k^2f(r_{qs}^2)\,dk+V_4\int_0^{k_\mathrm{F}}k^2\left\{f^{\mathrm{I}}(r_{qs}^2)+\frac{2r_{qs}^2}{3}f^{\mathrm{II}}(r_{qs}^2)\right\}dk+\ldots\right] \quad \ldots\ldots(8)$$

where the summation extends over all cells containing solvent nuclei other than the pth, r_{pq} is the distance between nuclei p and q, θ_{pq} is the angle between $\mathbf{r}_{pq}$ and $\mathbf{r}_{ps}$, and V_s is defined by

$$V_s=\int_0^{\alpha}u^*(r)u(r)r^s\,dr.$$

The remaining contribution eq_{ps} to the interaction at p arises from the imperfect screening of the impurity within its own cell. Representing by σ the number of electrons the well must bind in order to be electrically neutral, we find from equations (2) and (6)

$$eq_{ps}=2e\{1-\gamma(r_{ps})\}r_{ps}^{-3}\left\{\sigma-\frac{4}{\pi}\int_0^{k_\mathrm{F}}k^2\int_0^{a}u^*(R)u(R)g(R^2)R^2\,dR\,dk\right\}. \quad \ldots\ldots(9)$$

§ 3. The Quadrupolar Coupling in CuZn

As an example of the application of equations (7), (8) and (9), we have considered the quadrupolar interaction with copper nuclei in the alloy CuZn for which experimental estimates of eq are available.

The values of σ, α and k_0 used in our calculations are those determined by Blatt. The anti-shielding factor $1-\gamma(\infty)$ was taken to be 16 (Sternheimer and Foley 1956), and its variation with r was estimated from the values of Foley, Sternheimer and Tycko (1954) in conjunction with the above value of $1-\gamma(\infty)$. It was found that the computed field gradients were relatively insensitive to the radial variation of $\gamma(r)$, since the important contributions to U_s occur at radii such that $\gamma(r)$ approaches $\gamma(\infty)$. We have also used the copper conduction electron wave functions $u(r)$ of Fuchs (1935). The integration over k extends to $k_\mathrm{F}\alpha=1{\cdot}929$.

With this data we find the contributions to eq at first and second neighbouring sites to a zinc impurity in copper, to be those listed in the table. The values of eq_{pp} include first- and second-order integrals, the latter contributing about 10% of the whole. The summation in eq_{pq} includes the twelve cells nearest the subject nucleus, the first-order integral only being included. The distorted impurity cell was found to have an unscreened positive charge of only $4\times10^{-2}|e|$; the proportions of s, p, d and f wave components in the screen were 51·5, 41, 7 and 0·5% respectively.

	1st Neighbour	2nd Neighbour
eq_{pp}(e.s.u.)	$+18\times10^{13}$	$+1{\cdot}8\times10^{13}$
eq_{pq}(e.s.u.)	$+0{\cdot}03\times10^{13}$	$+0{\cdot}5\times10^{13}$
eq_{ps}(e.s.u.)	$+3{\cdot}9\times10^{13}$	$+1{\cdot}3\times10^{13}$
Total eq (e.s.u.)	$+22\times10^{13}$	$+3{\cdot}6\times10^{13}$

It is interesting to note that the principal contribution to the field gradient at both first and second neighbouring sites arises from the disturbance in the immediate vicinity of the nucleus. Thus in spite of the high degree of screening of the impurity, the fluctuations in electron density caused by the scattered waves are sufficient to produce a considerable coupling of the nuclear quadrupole moments to the lattice. The total calculated eq should be compared with the experimental minimum value of 24×10^{13} e.s.u. at the nearest site to a zinc impurity (Bloembergen and Rowland 1953). Further, an estimate from these experimental results of eq at the second nearest neighbour position gives approximately 10×10^{13} e.s.u.

§ 4. Conclusion

Using a partial wave analysis of the scattering of conduction electrons by an impurity atom, expressions have been derived for the field gradient associated with the screening charge. These equations have been applied to the alloy system Cu Zn where we find:

(*a*) Although the impurity is almost totally screened, oscillations in the electron density in the immediate neighbourhood of a solvent nucleus close to an impurity centre, produce a considerable coupling with the nuclear quadrupole moment. This coupling is greatly enhanced by the Sternheimer anti-shielding effect.

(*b*) While the magnitude of the interaction is insufficient to explain fully the observed decrease in intensity of the solvent nuclear magnetic resonance in the alloy, the coupling remains an appreciable proportion of that observed experimentally, and is not negligible as has previously been supposed.

Computations of the field gradients have not been carried out for other alloy systems, but it may be noted that even in the case of silver dissolved in copper, where there is no valency difference, there will be a considerable field gradient produced by the mechanism we have considered. This is because the magnitude of the gradient due to the screening electrons is governed by the excess charge which, in the absence of the screen, would be associated with the solute ion: this excess includes a contribution from the size difference between the solute and solvent cells. Thus the excess charge computed by Blatt (1957) for silver in copper is $-0{\cdot}322$ times the electronic charge. This value is to be compared with the value $+0{\cdot}8858$ used above for zinc in copper. Further the contribution to the field gradient which is produced directly by the displacement of solvent ions near an impurity, and which is not included in the above discussion, may in some cases add to, and in other cases subtract from, that produced by the screening electrons. It is suggested, therefore, that the near equality of the gradients produced by silver and zinc in copper is not in itself evidence that the valence effect is negligible.

Acknowledgments

It is a pleasure to thank Mr. H. D. Ursell of the Mathematics Department, Leeds University, for his generous assistance and advice in connection with the expansions used in § 2. One of us (C. P. F.) wishes to thank the Department of Scientific and Industrial Research for a maintenance allowance.

References

Blatt, F. J., 1957, *Phys. Rev.*, **108,** 285.
Bloembergen, N., and Rowland, T. J., 1953, *Acta Metall.*, **1,** 731.
Chapman, A. C., and Seymour, E. F. W., 1958, *Proc. Phys. Soc.*, **72,** 797.
Daniel, E., 1959, *J. Phys. Rad.*, **20,** 769.
Foley, H. M., Sternheimer, R. M., and Tycko, D., 1954, *Phys. Rev.*, **93,** 734.
Friedel, J., 1954, *Advanc. Phys.*, **3,** 446.
Fuchs, K., 1935, *Proc. Roy. Soc.* A, **151,** 585.
Mott, N. F., and Jones, H., 1936, *Metals and Alloys* (Oxford: University Press).
Pound, R. V., 1950, *Phys. Rev.*, **79,** 685.
Rowland, T. J., 1955, *Acta Metall.*, **3,** 74.
Sternheimer, R. M., 1950, *Phys. Rev.*, **80,** 102.
Sternheimer, R. M., and Foley, H. M., 1956, *Phys. Rev.*, **102,** 731.

The Numerical Solution of the Exchange Equations for Slow Electron Collisions with Hydrogen Atoms

By T. L. JOHN

Department of Physics, University College, London

Communicated by M. J. Seaton; MS. received 11th April 1960

Abstract. Numerical methods are used to calculate phases in the exchange approximation for the s-, p- and d-wave scattering of electrons by hydrogen atoms, using small energy intervals. There is a discussion of experimental results.

§ 1. Introduction

The availability of high speed automatic digital computers makes it possible to get exact solutions of certain differential equations occurring in theoretical physics for many different values of the parameters. One such equation is the integro-differential equation arising from the quantal treatment of the elastic scattering of electrons by hydrogen atoms in the exchange approximation.

The wave functions obtained from this equation are of interest for another physical problem, the calculation of the bound–free and free–free transitions for the continuous absorption of the H^- ion. This is of importance in determining the opacity in stellar atmospheres.

§ 2. The Exchange Equation

Applying the Hartree–Fock method to the scattering of an electron by hydrogen atoms we obtain the exchange equation

$$L_l F_l^{\pm} = \pm K_l F_l^{\pm} \qquad \ldots\ldots (1)$$

(in atomic units $e = m = \hbar = 1$ and k^2 in units of 13·60 ev). A full account of this approximation is to be found in an earlier paper by Bransden *et al.* (1958). The differential operator L_l is defined by

$$L_l = \frac{d^2}{dr^2} - \frac{l(l+1)}{r^2} + 2\left[\frac{1}{r} - y_0(PP|r)\right] + k^2 \qquad \ldots\ldots (2)$$

and the exchange operator K_l by

$$K_l(r)F_l^{\pm}(r) = \left[-(1+k^2)\Delta(F_l^{\pm}P)\delta_{0,l} + \frac{2}{2l+1}\, y_l(F_l^{\pm}P|r)\right] P(r) \qquad \ldots\ldots (3)$$

where

$$\Delta(AB) = \int_0^{\infty} A(x)B(x)dx \qquad \ldots\ldots (4)$$

and

$$y_\lambda(AB|r) = r^{-\lambda-1}\int_0^r A(x)B(x)x^{\lambda}dx + r^{\lambda}\int_r^{\infty} A(x)B(x)x^{-\lambda-1}dx. \qquad \ldots\ldots (5)$$

$P(r)$ is the normalized ground state wave function of the hydrogen atom,

$$P(r) = 2r\exp(-r), \qquad \ldots\ldots (6)$$

thus

$$\frac{1}{r} - y_0(PP|r) = \left(1 + \frac{1}{r}\right)\exp(-2r). \qquad \ldots\ldots (7)$$

The function $F_l^{\pm}(r)$ has the asymptotic form

$$F_l^{\pm}(r)_{r\to\infty}\sim \mathrm{j}_l(kr)+(-1)^l\tan\eta_l^{\pm}\mathrm{n}_l(kr) \qquad \ldots\ldots(8)$$

$\mathrm{j}_l(kr)$ and $\mathrm{n}_l(kr)$ being the regular and irregular spherical Bessel functions, i.e.

$$\mathrm{j}_l(x)=(\tfrac{1}{2}\pi x)^{\frac{1}{2}}\mathrm{J}_{l+\frac{1}{2}}(x)$$

and

$$\mathrm{n}_l(x)=(\tfrac{1}{2}\pi x)^{\frac{1}{2}}\mathrm{J}_{-l-\frac{1}{2}}(x). \qquad \ldots\ldots(9)$$

The phase $\eta_l^{\pm}$ determines the scattering; the differential and total exchange cross sections $I(\theta)$ and Q being

$$I(\theta)=\tfrac{3}{4}|f^-(\theta)|^2+\tfrac{1}{4}|f^+(\theta)|^2, \qquad \ldots\ldots(10)$$

the amplitudes $f^{\pm}(\theta)$ being defined by

$$f^{\pm}(\theta)=\frac{1}{2ik}\sum_{l=0}^{\infty}(2l+1)\,[\exp(2i\eta_l^{\pm})-1]P_l(\cos\theta), \qquad \ldots\ldots(11)$$

and

$$Q=\sum_{l=0}^{\infty}Q_l \qquad \ldots\ldots(12)$$

where

$$Q_l=(\pi/k^2)(2l+1)[3\sin^2\eta_l^-+\sin^2\eta_l^+]. \qquad \ldots\ldots(13)$$

Numerical solutions of the central field equations, i.e. (1) with $K(r)\equiv 0$, have been calculated by McDougall (1932) for $l=0$ and more extensively by Chandrasekhar and Breen (1946) for $l=0$, 1 and $0\leqslant k^2\leqslant 1{\cdot}75$. Seaton (1957) has pointed out that incorrect equations were used in the $l=0$ exchange calculations of Morse and Allis (1933). Other numerical solutions of exchange equations (1) have been obtained by Seaton (1957) and Bransden *et al.* (1958) for the particular cases of $l=0$, $k=0$ and $l=1$, $k=0$ respectively.

§ 3. Solution of the Exchange Equations

A particularly successful method of solving (1) is the iterative method. It has been applied by Seaton (1953, 1957) and Bransden *et al.* (1958) in similar calculations. Using it we are able to solve the integro-differential equation (1) by the set of inhomogeneous differential equations

$$\begin{aligned} L_lG_l^{(0)}&=0 \qquad \ldots\ldots(14)\\ L_lG_l^{(n)}&=K_lG_l^{(n-1)}\end{aligned}$$

with the boundary conditions

$$G_l^{(n)}(0)=0, \quad (G_l^{(n)}(r)/r^{l+1})_{r=0}=a\delta_{0,n}, \qquad \ldots\ldots(15)$$

a being an arbitrary constant. Iterations are performed until the functions $G_l^{(n)}(r)$ are small, comparable with the error expected from the particular numerical integration method used for all values of r.

$G_l^{(0)}$ is the central field function and the exchange functions F_l^+ and F_l^- are given by

$$\begin{aligned} F_l^+&=G_l^{(0)}+G_l^{(1)}+\ldots+G_l^{(n)}\\ F_l^-&=G_l^{(0)}-G_l^{(1)}+\ldots+(-1)^nG_l^{(n)}. \qquad \ldots\ldots(16)\end{aligned}$$

This method is particularly convenient in hand computations because of the small magnitude of the functions $G_l^{(n)}$ for large n.

Burke, Burke, McCarroll and Percival (to be published) have prepared a programme to solve coupled integro-differential equations on the English Electric computer DEUCE by the iterative method just described. This programme has been adapted to solve the particular integro-differential equation (1).

It was found more convenient in machine computations to solve the equations

$$\left.\begin{aligned} L_l F_l^{(0)} &= 0 \\ L_l F_l^{\pm(n)} &= \pm K_l F_l^{\pm(n-1)} \end{aligned}\right\} \quad \ldots\ldots (17)$$

with the boundary conditions

$$F_l^{\pm(n)}(0) = 0, \quad (F_l^{\pm(n)}(r)/r^{l+1})_{r=0} = a \quad \ldots\ldots (18)$$

for all n, iterating until convergence has been attained, i.e. the difference between the functions of two consecutive iterations is smaller than the error expected from the numerical method.

Here

$$\left.\begin{aligned} F_l^{\pm} &= F_l^{\pm(n)} \\ G_l^{(0)} &= F_l^{(0)} \\ G_l^{(n)} &= F_l^{+(n)} - F_l^{+(n-1)} \end{aligned}\right\} \quad \ldots\ldots (19)$$

and

therefore

$$F_l^{-(n)} = 2F_l^{(0)} - 2F_l^{+(1)} + \ldots + 2(-1)^{n-1} F_l^{+(n-1)} + (-1)^n F_l^{+(n)}. \quad \ldots\ldots (20)$$

Obviously (20) saves a considerable amount of computation.

The programme uses the René de Vogelaere (1955) method to integrate the differential equations (17). To compute the inhomogeneous term $K_l F_l^{\pm(n-1)}$ the Δ term is evaluated by Simpson's rule and the y_l term by a method due to Hartree (1957) involving the solution of two first-order differential equations by the Fox–Goodwin method.

The wave functions $F_l^{\pm}(r)$ were integrated from $r = 0$ to $r = 12$ where they take on their asymptotic form (8). An interval of $\frac{1}{16}$ was used in the integration, but because the René de Vogelaere method involves a two-step integration formula similar to the Runge–Kutta method, the effective interval was $\frac{1}{8}$. The calculations are most probably reliable to four figures, although nine figures were used in the arithmetic performed.

§ 4. Computational Problems

The particular cases of the exchange equation covered were $l = 0$, 1 and 2 in the range $0 \leqslant k^2 \leqslant 1$ for symmetric and antisymmetric cases. As mentioned earlier, in the zeroth iteration central field functions were calculated. A large number of solutions for different energies at a small interval in k^2 were calculated because of their application in determining the continuous absorption of the H^- ion.

At first, the term $y_0(PP|r)$ in L_l was evaluated numerically by the general programme just described. This gave

$$\frac{1}{r_1} - y_0(PP|r)_{r\to\infty} \simeq \frac{\delta}{r}$$

with $\delta \neq 0$, i.e. a Coulomb term was introduced into the potential and so the phase as defined by (8) does not exist. This difficulty was eliminated by using the exact analytic expression (7).

The iteration procedure does not always converge. For the s-wave calculations, symmetric case at small energies, it was found that $F_0^{+(2n)}=f_1$ and $F_0^{+(2n+1)}=f_2$ for n large and these functions satisfied

$$L_0 f_1 = K_0 f_2, \quad L_0 f_2 = K_0 f_1. \qquad \ldots\ldots (21)$$

In this case the required solution is

$$F_0^{+} = \tfrac{1}{2}(f_1 + f_2).$$

The conditions

$$\begin{gathered} L_0 F_0^{+} = K_0 F_0^{+} \\ F_0^{+}(0) = 0, \quad (F_0^{+}(r)/r)_{r=0} = a \qquad \ldots\ldots (22) \\ F_0^{+}(r) \underset{r\to\infty}{\sim} \sin(kr + \eta_0^{+}) \end{gathered}$$

define F_0 uniquely. Similar conditions do not define F_0 uniquely, for if F_0^{-} is a solution of $L_0 F_0^{-} = -K_0 F_0^{-}$ then so is $F_0^{-}(r) + \alpha P(r)$, where α is an arbitrary number. It was found that at certain energies $\alpha P(r)$ dominated the function F_0^{-} and so for values $r > 6$, F_0^{-} tended to a small quantity. This quantity was less than the error in the numerical method and so the wave function was unreliable.

This difficulty was eliminated by a method used by Seaton (1953). He imposed the orthogonality condition

$$\Delta(PF_0^{-}) = 0$$

by solving the equations

$$L_0 F_0^{(a)} = 0, \quad L_0 u = \gamma P(r), \qquad \ldots\ldots (23)$$

γ an arbitrary number, and $L_0 F_0^{-(m)} = -K_0 W^{(m-1)}$ with the conditions

$$\begin{gathered} F_0^{-(m)}(0) = 0, \quad (F_0^{-(m)}(r)/r)_{r=0} = a \qquad \ldots\ldots (24) \\ u(0) = 0, \quad (u(r)/r)_{r=0} = 0. \end{gathered}$$

The function $W^{(m)}$ is defined by

$$W^{(m)} = F_0^{-(m)} + \mu_m u, \qquad \ldots\ldots (25)$$

where μ_m is chosen so that, at each stage of the iteration, $\Delta(W^{(m)}P) = 0$,

$$\text{i.e.} \quad \mu_m = -\Delta(F_0^{-(m)}P)/\Delta(uP). \qquad \ldots\ldots (26)$$

Again iterations are performed until convergence is reached and $\mu_m \to 0$. The appropriate programmes to calculate μ_m and $K_0 W^{(m)}$ were made and fitted into the main programme.

To get convergence for the s-waves, symmetric case, eight iterations were necessary at the lower energies and six at the higher. For the antisymmetric case five or six iterations were necessary (imposing the orthogonality condition).

For the p-waves, symmetric case, convergence was still quite slow varying from five to eight iterations, the largest number of iterations again being at the lower energies. Equation (20) was used to get the antisymmetric solutions.

For the d-waves calculations only three or four iterations were necessary and the functions were not too different from spherical Bessel functions due to the dominance of the term $l(l+1)\,r^2$ in L_l. Again antisymmetric cases were calculated from (20).

Tables 1 and 2 give the phases and these check quite well with central field calculations of Chandrasekhar and Breen (1946) and those of Seaton (1957) for $l=0$, $k=0$. Very recently similar calculations for certain values of the parameters have been obtained by Trefftz, quoted by Malik (1959), and Omidvar

(1959), and these again check quite well with present results. Comparison of tables 1 and 2 shows that exchange in general tends to increase the phase for $l \geqslant 1$.

Table 1. Central-field Phases (For $k=0$, $\lim_{k\to 0}(\eta_l/(2l+1)k^{2l-1})$ is tabulated.)

	$l=0$	$l=1$	$l=2$		$l=0$	$l=1$	$l=2$
k^2	η_0	η_1	η_2	k^2	η_0	η_1	η_2
1·0	0·9055	0·1115	0·0178	0·06	1·017	0·0037	—
0·8	0·9356	0·0924	—	0·05	0·9991	0·0029	—
0·5	0·9909	0·0584	0·0056	0·04	0·9726	0·0021	—
0·4	1·012	0·0457	—	0·03	0·9317	0·0014	—
0·3	1·034	0·0326	—	0·02	0·8626	0·0008	—
0·25	1·045	0·0260	0·0014	0·015	0·8070	0·0005	—
0·20	1·053	0·0196	—	0·010	0·7223	0·0003	+0·0000
0·15	1·058	0·0134	—	0·005	0·5727	0·0001	—
0·10	1·050	0·0077	0·0002	0	(9·45)	(0·2696)	—
0·08	1·039	0·0056	—				

Table 2. Exchange Phases (For $k=0$, $\lim_{k\to 0}(\eta_l^{\pm}/(2l+1)k^{2l+1})$ is tabulated.)

	$l=0$		$l=1$		$l=2$	
k^2	η_0^+	η_0^-	η_1^+	η_1^-	η_2^+	η_2^-
1·0	0·5429	1·391	−0·1058	0·3579	−0·0175	0·0555
0·8	0·5888	1·501	−0·1148	0·3433	—	—
0·5	0·7370	1·739	−0·1084	0·2866	−0·0108	0·0230
0·4	0·8248	1·849	−0·0978	0·2500	—	—
0·3	0·9488	1·987	−0·0811	0·2000	—	—
0·25	1·031	2·070	−0·0702	0·1692	−0·0039	0·0070
0·2	1·135	2·167	−0·0575	0·1348	—	—
0·15	1·270	2·282	−0·0430	0·0971	—	—
0·10	1·460	2·427	−0·0273	0·0586	−0·0006	0·0010
0·08	1·563	2·498	−0·0207	0·0436	—	—
0·05	1·693	2·580	−0·0144	0·0294	—	—
0·05	1·774	2·627	−0·0113	0·0228	—	—
0·04	1·871	2·679	−0·0084	0·0166	—	—
0·03	1·992	2·739	−0·0056	0·0110	—	—
0·02	2·153	2·812	−0·0032	0·0061	—	—
0·015	2·259	2·856	−0·0021	0·0040	—	—
0·010	2·396	2·908	−0·0012	0·0022	−0·0000	+0·0000
0·005	2·594	2·976	−0·0004	0·0008	—	—
0	(−8·095)	(−2·350)	(−1·2018)	(2·2015)	—	—

The results for $l=1$, $k=0$ do not agree exactly with a previous calculation of $A_1^+ = -1{\cdot}16$, $A_1^- = 2{\cdot}43$ ($A_1^{\pm} = \lim_{k\to 0}(\eta_1^{\pm}/3k^3)$). This is due to the fact that in the previous calculation it was assumed from the behaviour of the iterations that only three were necessary; however, to get the required accuracy eight iterations were needed, the rate of convergence being slow. The third iteration of the present calculations checked with previous results.

§ 5. Discussion

Table 3 gives the total exchange elastic scattering cross section, from which it can be seen that the main contribution comes from Q_0. The higher partial

waves are not expected to contribute significantly, as the contribution of Q_2 to Q is less than 1%.

Table 3. Total Exchange Cross Section (given in units of πa_0^2)

k^2	Q_0	Q_1	Q_2	Q
1·0	3·170	1·138	0·0476	4·356
0·8	4·118	1·324	—	5·442
0·5	6·736	1·509	0·0171	8·262
0·4	8·281	1·449	—	9·730
0·3	10·57	1·250	—	11·82
0·25	12·19	1·080	0·0032	13·27
0·2	14·38	0·8618	—	15·24
0·15	17·55	0·6008	—	18·15
0·1	22·76	0·3314	0·0002	23·09
0·08	26·02	0·2296	—	26·25
0·06	30·62	0·1400	—	30·76
0·05	33·74	0·1015	—	33·84
0·04	37·75	0·0674	—	37·82
0·03	43·08	0·0395	—	43·12
0·02	50·62	0·0182	—	50·64
0·015	55·70	0·0104	—	55·71
0·010	62·14	0·0047	0·0000	62·15
0·005	70·56	0·0012	—	70·56
0	82·10	0	—	82·10

In previous calculations by Bransden *et al.* (1958) variational methods were used to determine s- and p-phases. In the exchange approximation the phases are in very good agreement with the present results, indicating the reliability of the variational method. The present calculations, whilst they allow fully for the possibility of electron exchange, otherwise neglect the effect of the distortion of the atom by the scattered electron. In the variational s-wave calculations of Bransden *et al.* some allowance for distortion was made in the exchange-correlation approximation, and these phases are likely to give a truer physical picture than the present ones.

Recently atomic beam techniques have been used by Brackmann, Fite and Neynaber (1958) to measure the elastic scattering of electrons by hydrogen atoms. The cross section Q_A they measure, is that for scattering into a cone with a 90° apex angle. Brackmann *et al.* compared their measurements with a theoretical Q_A calculated from the variational phases mentioned above, and there was favourable agreement. Cross sections have also been measured by Bederson, Hammer and Malamud (1958), but their results are not in agreement with either the measurements of Brackmann *et al.* or theoretical calculations. In order to account for their cross section the contribution from the partial waves $l>0$ must be three or four times that for $l=0$.

Recent calculations on the bound–free transitions of the H^- ion by the author, an account of which will be given elsewhere (John 1960), and their favourable agreement with the measurements of Smith and Burch (1959), give an indication of the reliability of the exchange p-wave functions and so confirm that no large contribution from Q_1 is to be expected even when polarization is taken into account.

Acknowledgments

The author is grateful to Dr. M. J. Seaton for his supervision and continued encouragement in this work. He is also grateful to Dr. P. G. and Mrs. V. M. Burke, Dr. R. McCarroll and Dr. I. C. Percival for the use of their programme and their help in applying it, in particular he would like to thank Dr. Percival for many helpful discussions and suggestions. He would also like to thank Dr. W. L. Fite for interesting discussions. He wishes to extend his thanks to the English Electric Company for the use of the DEUCE computer at their London Computing Service, where the bulk of these computations were done, and in particular to Dr. V. E. Price and Mr. J. Wollgar. Part of these calculations was done when the author held a Department of Scientific and Industrial Research award. The completion of this work was supported by a contract with the Atomic Energy Research Establishment, Harwell, to whom thanks are due for permission to publish.

References

Bederson, B., Hammer, J. M., and Malamud, H., 1958, *Technical Report No.* 2. *Electron Scattering Project*, New York University.
Brackmann, R. T., Fite, W. L. and Neynaber, R. H., 1958, *Phys. Rev.*, **112,** 1157.
Bransden, B. H., Dalgarno, A., John, T. L., and Seaton, M. J., 1958, *Proc. Phys. Soc.*, **71,** 877.
Chandrasekhar, S., and Breen, F. H., 1946, *Astrophys. J.*, **103,** 41.
de Vogelaere, R., 1955, *J. Nat. Bur. Stand.*, **54,** 119.
Fox, L., and Goodwin, E. T., 1949, *Proc. Camb. Phil. Soc.*, **45,** 373.
Hartree, D. R., 1957, *The Calculation of Atomic Structures* (London: Chapman and Hall).
John, T. L., 1960, *Mon. Not. R. Astr. Soc.*, in the press.
MacDougall, J., 1932, *Proc. Roy. Soc.* A, **136,** 549.
Malik, F. B., 1959, *Z. Naturf.*, **14A,** 172.
Morse, P. M., and Allis, W. P., 1933, *Phys. Rev.*, **44,** 269.
Omidvar, K., 1959, *Research Report No.* CX-37, New York University.
Seaton, M. J., 1953, *Proc. Roy. Soc.* A, **218,** 400.
—— 1957, *Ibid.*, **241,** 522.
Smith, S. J., and Burch, D. S., 1959, *Phys. Rev.*, **116,** 1125.

The Spin–Orbit Potential in Proton–Proton Scattering

By D. W. L. SPRUNG† and J. B. WILLIS‡

† Department of Mathematical Physics, University of Birmingham
‡ Department of Computation, University of Southampton

Communicated by R. E. Peierls; MS. received 14*th April* 1960, *in final form* 5*th May* 1960

Abstract. An extension of the potential model for proton–proton scattering to relativistic energies is proposed. The treatment is based on a truncated two-particle Dirac equation, from which an approximate, semi-relativistic wave equation is derived by reduction to large components. Using a potential related to that of Gammel and Thaler, numerical calculations of p–p scattering at 635 and 1000 Mev have been carried out. Reasonable total and differential cross sections were obtained, but the polarization disagrees qualitatively with experiment. Agreement of the polarization can be obtained by reducing the spin–orbit splitting of the F phases. It appears possible to fit the experimental data up to 1000 Mev by choosing a spin-orbit potential which is attractive (in $J=L+1$ states) at short distances, but has a repulsive tail.

Phillips (1959) and Gammel and Thaler (1959) have recently reviewed work on the fitting of phenomenological nucleon–nucleon potentials. At large distances ($r>2$ fermis) the interaction can be chosen to consist of central and tensor potentials, in agreement with the one pion exchange potential. It has proved possible to fit the proton–proton scattering data up to 300 Mev by choosing the interaction at short distances to be a hard core, a strong spin–orbit potential, and a weak tensor potential (Gammel and Thaler 1957). In singlet states, where the spin dependent forces do not act, a hard core and attractive central potential is used.

We have been interested in extending this potential model of the proton–proton interaction to higher energies. Experiments at 635 and 1000 Mev provide data for comparison. At these higher energies more angular momentum states contribute to the scattering, so the calculations are much more sensitive to the details of the potential. As a first step we would like to see whether the potentials fitted at lower energies are consistent with the higher energy data, or whether new qualitative features must be used. At these energies it would not be sensible to use the non-relativistic wave equation, or kinematics. Following a suggestion by Brown (1959, private communication) we have begun with a truncated Dirac equation for two particles in the centre-of-mass system:

$$\{E+(\boldsymbol{\alpha}^{(1)}-\boldsymbol{\alpha}^{(2)})\,\mathbf{p}+(\beta^{(1)}+\beta^{(2)})\,m-\Lambda_1^{+}\Lambda_2^{+}V\}\psi^{2+}=0 \quad \ldots\ldots(1a)$$

where

$$\Lambda_1^{-}\psi^{2+}=\Lambda_2^{-}\psi^{2+}=0 \quad \ldots\ldots(1b)$$

and in our units $\hbar=c=1$. Here Λ_1^{-} is the positive energy projection operator for particle one, and ψ^{2+} is a wave function projected on to positive energy states for each particle. E is the total energy of the system in the centre-of-mass frame

of reference. Since we intend to discuss this equation more completely in a future paper, we will be brief.

A similar equation has been derived by Brown and Ravenhall (1951) in discussing the interaction of two electrons in helium. It would not be correct to write down a two-particle Dirac equation containing an ordinary potential V because in general this potential will couple positive and negative energy states of each particle. This difficulty does not arise in one-particle problems because the positive and negative energy states can be considered separately. In the two-particle case, one particle can fall to a negative energy state while the other particle takes up the energy. These transitions in fact dominate the process, and diverge, so such an equation has no solution. In equation (1 *a*) we have removed the elements of V, such as $\Lambda_1^+\Lambda_2^+ V \Lambda_1^-\Lambda_2^+$ which couple positive and negative energy states. We are then able to look at positive energy wave functions alone, which is condition (1 *b*).

One could also describe equation (1 *a*) as a one-time, truncated Bethe–Salpeter equation. It would be wrong to neglect completely the coupling to virtual pairs, however, and we propose that this be introduced phenomenologically. We regard the potential V as containing a strong repulsive core, which is as usual introduced as a phenomenological way to take account of the complicated nucleon–nucleon interaction at short distances, virtual processes of many meson production, virtual pair production, etc. That the nucleon–nucleon interaction can in fact be approximately described by some static potential is a major assumption of this work, which we do not attempt to justify. By using a relativistic equation we ensure that relativistic kinematics are included at all stages.

An approximate semi-relativistic equation can be derived from (1) by reduction to 'large' components and expansion in successive derivatives of the potential, plus one term in V^2. Including the first correction to V this gives

$$\mathbf{p}^2\phi = \left\{ p_0^2 - m_r \left(V + \frac{3}{2}\frac{1}{m_r(m+m_r)}\frac{1}{r}\frac{dV}{dr}\mathbf{S}\cdot\mathbf{L} + \ldots \right) \right\}\phi \qquad \ldots\ldots (2)$$

where

$$m_r = \sqrt{(p_0^2 + m^2)} = \tfrac{1}{2}E$$

is the relativistic mass of a proton in the centre-of-momentum system, p_0 being the incoming momentum. At low energies p_0^2 is negligible in comparison with m^2, and (2) is then the usual Pauli approximation. The inclusion of m_r in place of m may be regarded as a relativistic correction of order $(v/c)^2$ which at 635 Mev is about 0·3. The neglect of higher derivatives of V in (2) is not strictly valid in the region where V is very strong, but in such a region ϕ is already small which improves the approximation.

Compared with the Schrödinger equation, the static potential V will appear stronger as the energy is increased, while it will be accompanied by a spin–orbit force which is energy dependent, decreasing as $1/[m_r(m+m_r)]$. A strong, short range repulsive region in V would lead to a strong short-range spin–orbit force, attractive in $J = L + 1$ states, such as is found in the phenomenological potentials.

In the calculations reported here we have regarded the sum of the terms multiplying m_r in (2) as an effective potential U to be determined phenomenologically, but with the requirement that the spin–orbit part of this potential has the indicated energy dependence. We then solve the equation

$$\mathbf{p}^2\phi = (p_0^2 - m_r U)\phi. \qquad \ldots\ldots (3)$$

Initially we chose U so that at 310 Mev $(m_r^{(310)}/m)U$ was exactly the Gammel–Thaler potential. At higher energies the spin–orbit potential was reduced in magnitude as $1/[m_r(m+m_r)]$. This choice relates our calculation to the lower energy work, and in addition it has the qualitative features of fitting a potential V to equation (2).

To account for inelastic processes we have introduced a complex central potential. For convenience this was chosen to be a Gaussian, of the range found by Brown (1958). At 1000 Mev we adjusted the depth so as to reproduce the observed total inelastic cross section. At 635 Mev however, we know that pion production still goes mainly through the $^1D_2$ state. From an analysis of the partial inelastic cross sections Soroko (1958) has deduced the imaginary part of the $^1D_2$ phase shift. We have used this value, and adjusted the depth of the absorptive potential so as to obtain the remaining inelastic cross section from the other states. In fact, the results do not differ greatly if the same procedure is followed as at 1000 Mev.

Gammel and Thaler (1957) found that a Yukawa shape tensor potential gave too much scattering at higher energies and obtained a better fit with a potential going to zero at the core radius. We have not yet investigated the effects of taking different shapes for the tensor potential, but have carried out our calculations with the Gammel–Thaler (Yukawa shape) one, and again with no tensor potential. The scattering is dominated by the spin–orbit force, and inclusion of the tensor potential does not alter the cross section or polarization results qualitatively. This will remain true unless the tensor potential shows very singular behaviour right at the edge of the hard core.

Table 1

	1000 Mev			Exptl (970 Mev)	635 Mev			
	(1)	(2)	(3)	(3a)	(4)	(5)	(6)	(6a)
σ_{el} (mbn)	34·7	24·0	26·1	$25{\cdot}8 \pm 0{\cdot}9$	23·4	25·3	26·2	$26{\cdot}3 \pm 1{\cdot}8$
σ_{inel} (mbn)	23·7	24·2	26·7	$20{\cdot}9 \pm 1{\cdot}3$	14·0	11·9	14·6	$14{\cdot}4 \pm 1{\cdot}4$
σ_{tot} (mbn)	58·4	48·2	52·8	$46{\cdot}7 \pm 0{\cdot}5$	37·4	37·2	40·8	40·6
$d\sigma$ (90°) (mbn)		1·17		$1{\cdot}30 \pm 0{\cdot}2$	1·35	1·35		$2{\cdot}2 \pm 0{\cdot}2$

(1) Without velocity dependence in spin–orbit potential; (2), (3) including velocity dependence; singlet interaction as hard core, (3) as (2) with addition of attractive central potential in singlet states; tensor force is not included in these calculations; (3a) Batson *et al.* (1959); (4) absorptive potential same in all states; (5) D wave absorption handled correctly; (6) same as (4) but including tensor force; (6a) Batson and Riddiford (1956).

The energy dependent spin–orbit potential leads to reasonable values of the total elastic cross section, as can be seen at 1000 Mev by comparing columns (1), (2) and (3) of table 1. The Gammel–Thaler spin–orbit potential gave too high a value because of the large $^3F_3$ phase shift. Since the inelastic cross section is a parameter, the total cross section can of course be fitted although we have not always taken the trouble to make this adjustment. The angular distribution agrees well with experiment, in particular at 90° where previous fits (e.g. Brown 1958) were definitely low.

At 635 MeV the angular distribution agrees qualitatively with experiment, although here it is low at 90°. Columns (4) and (5) of table 1 show the effect of handling the D state absorption in a realistic manner, while column (6) illustrates the small effects of including tensor force.

The polarization at 635 MeV, however, is in strong disagreement with that measured by Meshcheryakov, Nureshev and Stoletov (1957), as shown in the figure. The dip at large angles occurs in our calculations from strong P and F wave interference.

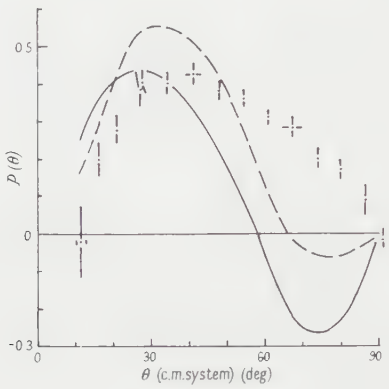

Polarization in proton–proton scattering at 653 MeV. The experimental points are from Meshcheryakov *et al.* (1957). The solid curve was calculated using a spin–orbit potential of Gammel–Thaler shape, the broken curve using a short range ($\hbar/mc$) spin–orbit potential.

We can see this by considering the expansion for the polarized cross section,

$$\sigma(\theta)P(\theta)=\frac{\sin\theta\cos\theta}{4p_0{}^2}\sum_{l=0}^{L}Q_{2l}P_{2l}(\cos\theta)$$

where $L+1\simeq l_{\max}$, the maximum angular momentum state important in the scattering. From their experimental results at 635 MeV Meshcheryakov *et al.* (1957) have deduced value of the coefficients Q_{2l} as in table 2, column (1). Also given in the table are values obtained in some of our calculations; we only include P and F wave contributions for convenience; but as indicated by the 'experimental' values, higher waves do not make large contributions. It is clear that our values of Q_0 are small, and it is the large (positive) ratio of Q_2/Q_0 which leads to negative polarization between 60° and 90°.

Table 2

	(1)	(2)	(3)	(4)
Q_0	9·79 ± 0·2	6·90	4·18	6·72
Q_2	9·58 ± 0·9	32·65	22·87	26·32
Q_4	3·67 ± 1·3	9·32	3·03	3·50
Q_6	−0·4 ± 1·5			

(1) Meshcheryakov *et al.* (1957) from analysis of experimental data (the units have been changed); (2) calculated spin–orbit potential of Gammel–Thaler shape; (3), (4) short range ($\hbar/mc$) spin–orbit potential; (4) as (3), but including tensor potential: (the calculated values include P and F contributions only).

The coefficients Q_l may, of course, be expressed in terms of the phase shifts, but the formulae become complicated when several partial waves are taken into account. To see the qualitative features of our calculation it should be sufficient to consider P and F waves, and neglect Coulomb effects which are only important at angles up to 10°. The main results of such a consideration are that, assuming the phase shifts are due to a potential of the type considered, Q_0 is practically independent of the F wave phase shifts, while Q_2 is extremely sensitive to the F wave spin-orbit splitting. In order to fit $Q_0 \simeq 10$, $Q_2 \simeq 10$ requires a slight increase in the spin–orbit effects in the P states, while the spin–orbit splitting in F states must be decreased by a factor of five. On arriving at these values we have allowed for the small effects of the Gammel–Thaler tensor force.

We have attempted to fit the polarization at 635 MeV using a shorter range spin-orbit force, with a range of one nucleon Compton wavelength. There was only a very slight improvement in the fit; the relevant coefficients are given in columns (2) and (3) of table 2. The F wave splitting is still too large by a factor of three. It would not be reasonable to attempt a fit with a shorter range spin-orbit potential, both because it would have to be extremely deep and because the nucleon cannot be pictured as being localized within a shorter distance. We believe, therefore, that the 635 MeV data cannot be fitted using a spin–orbit potential which is attractive (in $J = L + 1$) states at all radii.

It should be possible to fit the data, however, using a potential which is attractive at short distances, and repulsive at larger distances. We are now trying to do this. Such a potential has previously been suggested by Swart *et al.* (1957), but for $T = 0$ states only, because of difficulties in fitting the deuteron magnetic moment. With a potential of this type the F wave spin–orbit splitting can be made very small or even negative, without upsetting the need for a strong attractive spin–orbit force in P states. This is because the P waves are never well localized around their semi-classical impact parameter as the F waves are, but always penetrate well into the potential and so feel an average effect of the whole potential. At very low energies, the repulsive tail of the spin–orbit potential will tend to mask its effect in P states; this may be a reasonable picture in view of the success of Hamada *et al.* (1959) in fitting all the p–p data up to 150 MeV using only static central and tensor potentials.

It is also interesting to note that a recent measurement of the polarization in proton–proton scattering at 970 MeV (Homer *et al.* 1960) is in qualitative agreement with that at 635 MeV. This indicates that there is still no strong interference between P and F waves at large angles, and is consistent with our picture of a spin–orbit potential which changes sign.

Acknowledgments

We are grateful to Professor G. E. Brown for many helpful discussions throughout the course of this work, and to Professor R. E. Peierls for suggestions regarding the manuscript. One of us (D. S.) is supported by a scholarship from the National Research Council of Canada. We are also grateful to Dr. Hutchinson for communicating the results of his experiment.

References

Batson, A. P., Culwick, B. B., Hill, J. G., and Riddiford, L., 1959, *Proc. Roy. Soc.* A, **251**, 218.

Batson, A. P., and Riddiford, L., 1956, *Proc. Roy. Soc.* A, **237**, 175.

Brown, G. E., 1958, *Phys. Rev.*, **111,** 1178.
Brown, G. E., and Ravenhall, D. G., 1951, *Proc. Roy. Soc.* A, **208,** 552.
Gammel, J. L., and Thaler, R. M., 1957, *Phys. Rev.*, **107,** 291.
—— 1959, *Progress in Elementary Particle and Cosmic Ray Physics* (Amsterdam: North Holland).
Hamada, T., Iwadare, J., Otsuki, S., Tamagaki, R., and Watari, W., 1959, *Progr. Theor. Phys.*, **22,** 556.
Homer, R. J., Hutchinson. G. W., McFarlane, W. K., O'Dell, A. W., Rubinstein, R., and Sacharidis, E. J., 1960, *Nuovo Cim.*, **16,** 1132.
Meshcheryakov, M. G., Nurushev, S. B., and Stoletov, G. D., 1957, *Z. Eksper. Teor. Fiz.*, **33,** 37.
Phillips, R. J. N., 1959, *Rep. Progr. Phys.*, **22,** 562 (London : Physical Society).
Soroko, L. M., 1958, *Z. Eksper. Teor. Fiz.*, **35,** 276.
Swart, J. J., Marshak, R. E., Signell, P. S., 1957, *Nuovo Cim.*, **6,** 1189.

A Study of the $^{27}Al(^{3}He, d)^{28}Si$ Reaction

By S. HINDS and R. MIDDLETON
Atomic Weapons Research Establishment, Aldermaston, Berks.

Communicated by K. W. Allen; MS. received 10th *March* 1960,
in final form 28*th April* 1960

Abstract. The energy levels of ^{28}Si have been determined below an excitation energy of 10·37 MeV by magnetic analysis of the deuterons from the $^{27}Al(^{3}He, d)^{28}Si$ reaction. Angular distributions of several deuteron groups have been measured at incident energies of 5·7 and 9·16 MeV and from a comparison with stripping theory, certain l-value assignments have been made. Evidence is presented favouring the 9·314 and 9·379 MeV levels being respectively the first and second $T = 1$ states of ^{28}Si.

§ 1. Introduction

At the present time several laboratories are studying the $^{27}Al(p, \gamma)^{28}Si$ reaction. The analysis of the γ-ray spectra, however, has been complicated by a lack of precise information about the energy states of ^{28}Si. It was primarily with the intention of providing such information that a magnetic analysis study of the $^{27}Al(^{3}He, d)^{28}Si$ reaction was undertaken at Aldermaston.

Prior to this work, only the first and second excited states had been precisely determined by magnetic analysis, but several other states had been observed below an excitation energy of 10·3 MeV from studies of the $^{27}Al(d, n)^{28}Si$ reaction (see Endt and Braams 1957). Browne, Zimmerman and Buechner (1954) reported the first excited state to be at 1·777 ± 0·010 MeV from measurements made on inelastically scattered protons. More recently, Endt and Paris (1957) determined the first and second excited states to be respectively at 1·771 ± 0·008 and 4·617 ± 0·008 MeV from an investigation of the $^{31}P(p, \alpha)^{28}Si$ reaction.

§ 2. Experimental Procedure

Thin aluminium targets have been bombarded with 5·7 and 9·16 MeV ^{3}He particles from the Aldermaston Van de Graaff generator and the emitted deuterons analysed with the broad-range magnetic spectrograph. The lower energy results were obtained with the singly charged ^{3}He beam but to obtain 9·16 MeV, it was necessary to accelerate doubly charged particles using the method referred to in previous communications (Hinds and Middleton 1960). The targets were prepared by evaporating spectroscopically pure aluminium and consisted of self-supporting films ranging in thickness from 30 to 100 μg cm^{-2}. Adequate yields were obtained at the lower energy with the thin targets and exposures of about 2000 μC. At 9·16 MeV less intense beams were available and exposures were reduced to about 800 μC using the thicker targets.

In the broad-range magnetic spectrograph, particles differing in energy by a factor of 2·5 can simultaneously be recorded on the 30 in. long nuclear plate and because of this it was not possible to record the entire deuteron spectrum during a

single exposure. Since the first and second excited states had previously been precisely determined the spectrograph field was chosen, at the higher bombarding energy, to just include the second excited state and as many higher states as possible. At the lower bombarding energy even fewer states could be simultaneously recorded and a compromise was effected by choosing the field to record the fourth and as many higher excited states as possible. Two sets of overlapping exposures could have been made at both energies so as to include the ground and first excited states but this was not undertaken because of the extreme length of the exposure times.

§ 3. Results

3.1. *Energy Levels*

Deuteron energy spectra have been measured at six angles of observation at the lower bombarding energy and at seven angles at 9·16 Mev. In figures 1 and 2 respectively are shown typical energy spectra measured at each energy. The groups were identified by their characteristic variation of energy with angle and those assigned to states in ^{28}Si are labelled numerically. Impurity groups are labelled with the chemical symbol for the residual nucleus with a subscript referring to the appropriate excited state. It may be noted that many of the impurity groups arising from ^{12}C and ^{13}C appear as doublets. This is due to carbon depositions forming on both sides of the aluminium target film.

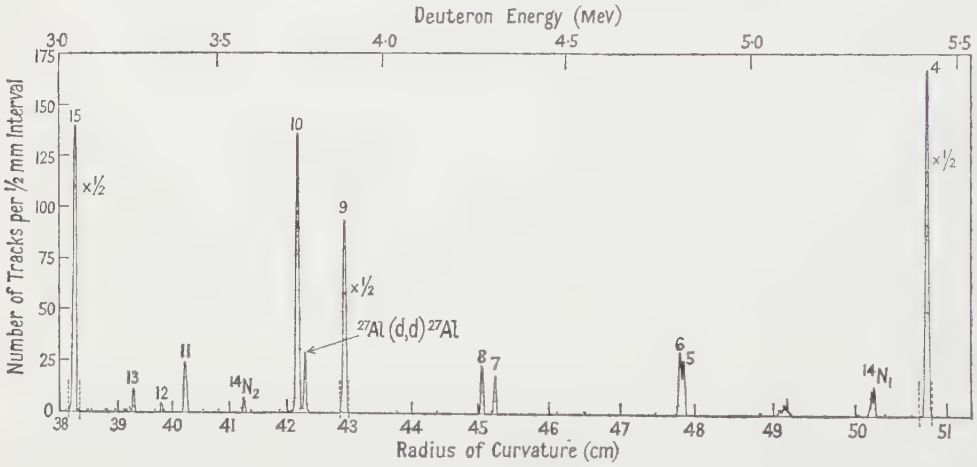

Figure 1. An energy spectrum of the deuterons from the ^{27}Al(^{3}He, d)^{28}Si reaction obtained at an incident energy of 5·7 Mev and an angle of observation of 15°.

At the lower bombarding energy resolution was better due to the use of thinner targets and a narrower beam defining slit. Thus, groups 5 and 6, which are separated by only 9 kev were clearly resolved while at 9·16 Mev they appeared as a single group. It is of interest to note that the group appearing at a radius of curvature of 42·3 cm in figure 1 arises from the elastic scattering of deuterons. These are accelerated in the form HD^{+} and are not completely resolved from the $^{3}He^{+}$ by the 90° analyser magnet.

At 9·16 Mev considerably more deuteron groups were observed and it was possible to make measurements, at seven angles of observation, on groups 2 to 29

inclusive. The weak group, occurring at a radius of curvature of about 49 cm in figure 2, was established as due to a target impurity but it was not possible to identify the impurity.

At both bombarding energies the energy of the incident beam was determined from measurements made on the elastically scattered ^{3}He particle. From these the Q-values of the various groups were calculated but since the ground and first excited states were not observed, it was possible to determine the energies of the excited states only with respect to that of the second excited state. However, the energy of the latter has been precisely determined to be $4{\cdot}617 \pm 0{\cdot}008$ MeV by Endt and Paris (1957) and the levels listed in the table have been normalized to this value. For the levels up to 8·6 MeV the values presented are the means of 13 determinations and the experimental error is ± 8 kev. The higher levels up to and including the 9·762 MeV state are in most cases the means of seven determinations and have an error of ± 10 kev except for the 9·41 MeV state for which ± 14 kev is

	$^{27}Al(^3He, d)^{28}Si$				$^{27}Al(d, n)^{28}Si$ (Calvert *et al.*)			
(1)	(2)	(3)	(4a)	(5)	(2)	(3)	(4b)	(5)
0	—				0	2	7·3	0·027
1	—				1·78	0	0·7	0·006
2	4·617‡	2	1·2	0·015	4·47	Weak		
3	4·975	–			4·91			
4	6·276	0	1·7	0·021	6·11			
5	6·880	2 or 3				0	2·0	0·021
6	6·889	or 2+3			6·65			
7	7·382	–			7·10	Weak		
8	7·415	–						
9	7·798	0	2·0	0·026	7·55	0	2·0	0·030
10	7·932	0	1·6	0·024				
11	8·260	(2 or 3)						
12	8·328	–						
13	8·411	(3)	(1·1)	(0·014)				
14	8·543	Weak						
15	8·587	0	11·1	0·14	8·18	0	5·0	0·075
16	8·902	–						
17	8·941	–						
18	9·167	Weak						
19	9·314	0	15·3	0·22				
20	9·379	0	6·4	0·091	9·16	0	14·0	0·27
21	9·41	–						
22	9·491	(2 or 3)						
23	9·700	(3)	(2·0)	(0·022)				
24	9·762	(2)	(1·1)	(0·013)				
25	9·932							
26	10·180							
27	10·273							
28	10·308							
29	10·375							

(1) Group number; (2) energy level (MeV); (3) l_p; (4) $(2J_f+1)\Omega$ (4a) in relative units, (4b) in 10^{-50} c.g.s. units; (5) $(2J_f+1)\theta^2$†.

† The reduced widths have been extracted without the use of the isotopic spin formalism (see Macfarlane and French 1959).

‡ Normalized to the value reported by Endt and Paris (1957) obtained from the $^{31}P(p, \alpha)^{28}Si$ reaction.

possible. An error of ±20 kev may be ascribed to the higher levels since in many cases they were not observed at all angles. The error of ±8 kev assigned by Endt and Paris to their determination of the second excited state has not been included in the above errors.

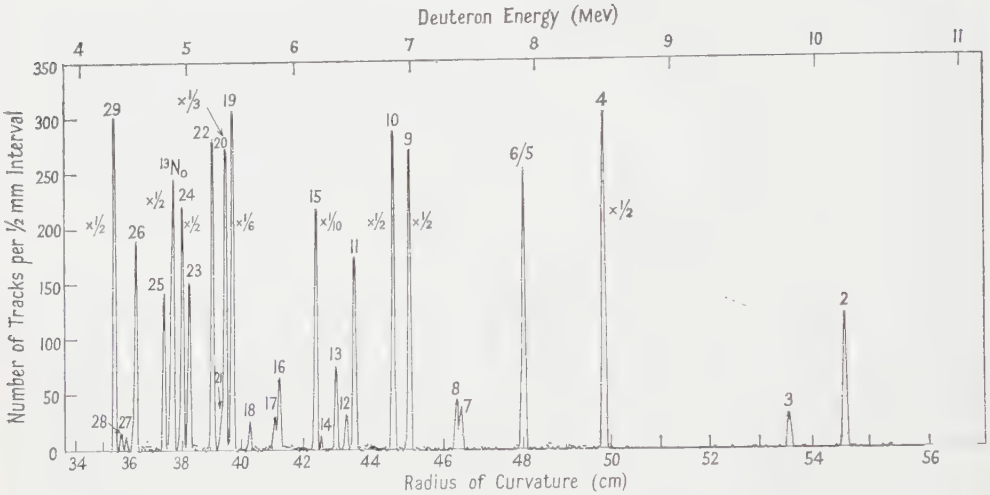

Figure 2. A deuteron energy spectrum obtained from the $^{27}Al(^3He, d)^{28}Si$ reaction at an incident energy of 9·16 Mev and at an angle of 15°.

It should be noted that it is considered possible that some weak groups may have escaped detection. This possibility arises because as in most stripping reactions the individual groups vary strongly in intensity and it is exceedingly difficult to detect with certainty a weak group neighbouring a very intense group.

3.2. *Angular Distributions*

The angular distributions of groups 2 to 24 inclusive, excepting groups 14 and 18 which were extremely weak, have been measured at 9·16 Mev and are shown in figure 3. Groups 25 to 29 were not measured since they were observed only over limited angular ranges. The thickness of the target used for the 9·16 Mev angular distributions was determined by weighing to be about 70μg cm^{-2}. From this value the arbitrary unit of cross section was calculated to be equivalent to 0·1 mbn sterad^{-1} with a possible error of ±30%. At the lower bombarding energy the angular distributions of groups 4 to 15 were measured, excepting group 14 which was again very weak. These are shown in figure 4 where the arbitrary unit of cross section is different from that used in figure 3. At both energies the angular distributions of groups 5 and 6 are combined.

The 9·16 Mev angular distributions shown in figure 3 have been fitted with Born approximation stripping curves calculated from the theory of Newns (1952) using in all cases a radius of interaction equal to the Gamow radius plus one fermi, i.e. 6·4 fermi. In several cases the agreement between the theoretical curves and the experimental points is good, particularly when it is considered that Coulomb effects are neglected in the theory, and it has been possible to make certain l-value assignments. These are listed in the third column of the table when the tentative assignments are in parenthesis. Also listed are the products of the relative proton capture probabilities Ω, and the spin factor $2J_f+1$.

It was not possible to fit all the distributions exhibiting characteristic $l=0$ stripping patterns with curves calculated from simple Butler theory using the Gamow radius. This was because the theory predicts pronounced secondary maxima for all $l=0$ groups above and including group 9. By applying a simple Coulomb correction, which has previously been used for (d, n) reactions (Butler 1957, Macfarlane and French 1959) better agreement was obtained. This was further improved by reducing the radii of interaction from 5·4 to 4·5 fermi for groups 19 and 20 and to 4·9 fermi for the remaining groups.

Absolute reduced level widths γ^2 were determined by fitting the Coulomb corrected Butler curves to the 9·16 MeV data which were measured in absolute units of cross section. For this purpose it was necessary to assume a value for the

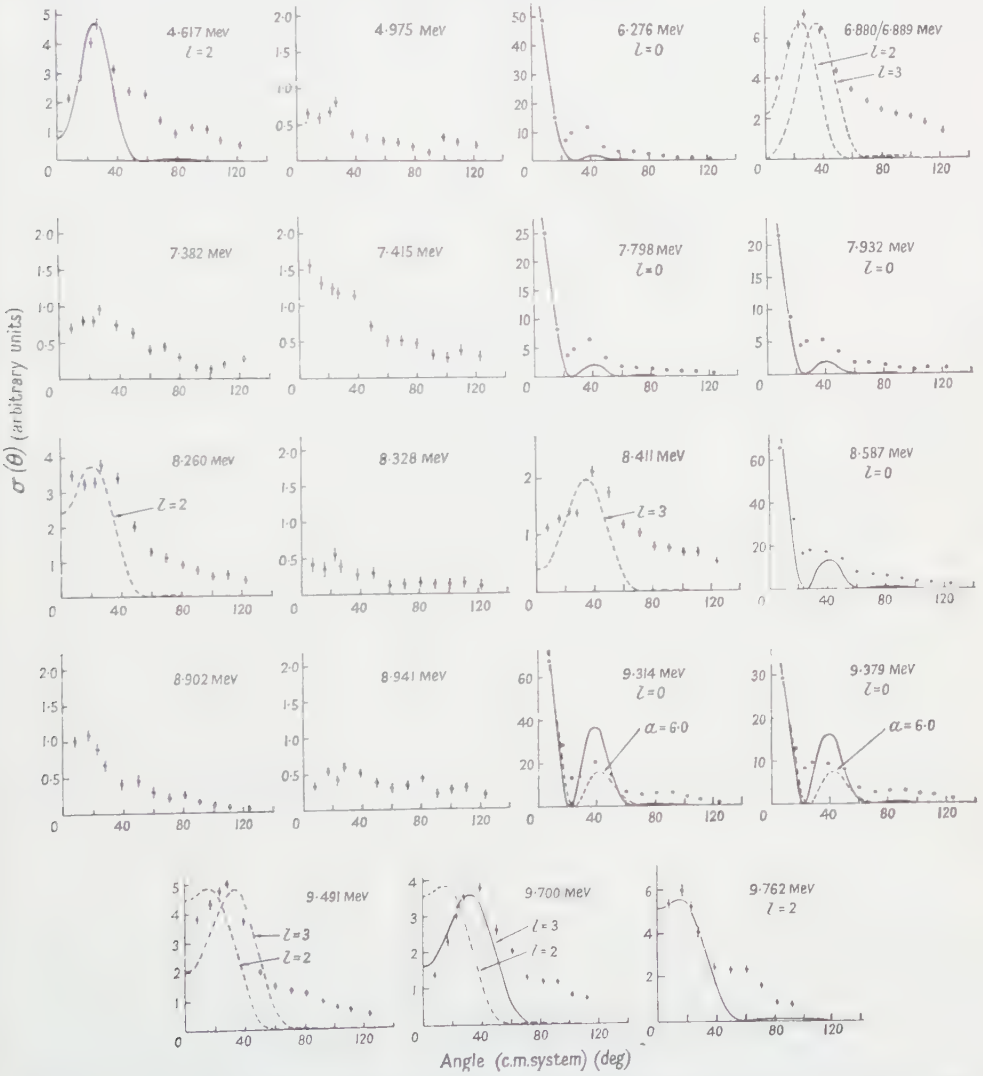

Figure 3. Angular distributions of nineteen deuteron groups from the $^{27}Al(^3He, d)^{28}Si$ reaction measured at an incident energy of 9·16 MeV. The curves shown were calculated from Born approximation stripping theory using in all cases a radius of interaction equal to 6·4 fermi.

constant Λ which occurs in the expression for the cross section of a (^{3}He, d) reaction. The value chosen was that quoted by Macfarlane and French which they determined from an analysis of several (d, ^{3}He) and (d, t) reactions. In the table are listed the values of $(2J_f+1)\theta^2$ where

$$\theta^2 = \gamma^2 \Big/ \frac{3}{2}\frac{h^2}{\mu r_0}.$$

The 5·7 MeV angular distributions do not exhibit such characteristic stripping patterns as those observed at 9·16 MeV. This is not surprising since the incident energy is almost 3 MeV less than the Coulomb barrier. However, Born approximation curves have been calculated using the same radius of interaction and l-values as were used at 9·16 MeV and these are shown in figure 4. It is noteworthy that the $l=0$ theoretical curves, which normally are least affected by Coulomb effects fit progressively worse for the higher excited state.

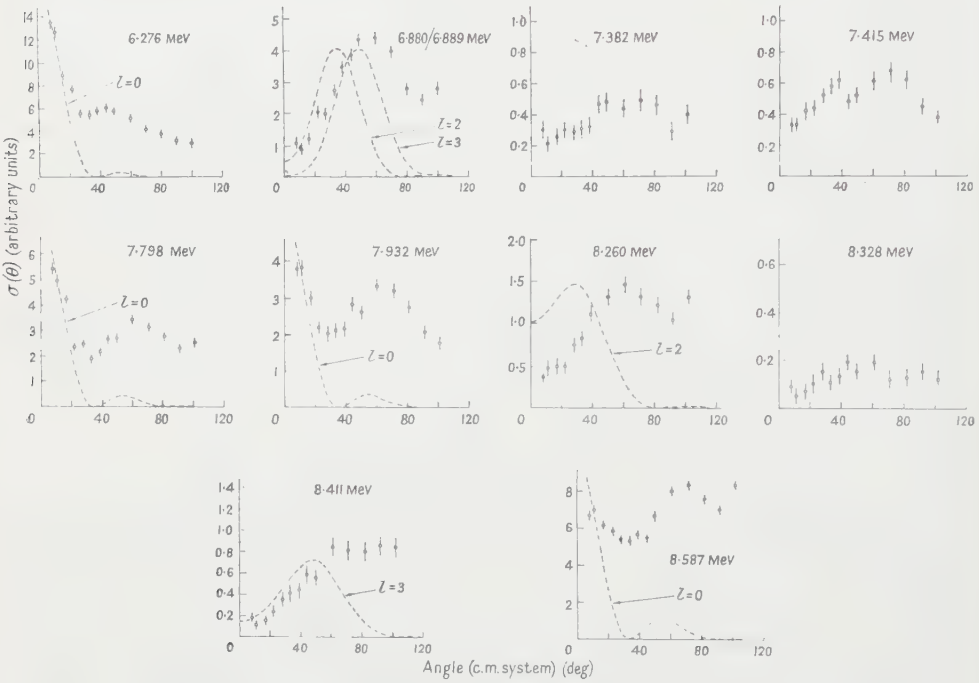

Figure 4. Angular distributions of ten deuteron groups from the ^{27}Al(^{3}He, d)^{28}Si reaction measured at an incident energy of 5·7 MeV. The curves shown were calculated from Born approximation stripping theory using the same radius and l-values as were required for the measurements made at 9·16 MeV.

§ 4. Discussion

The ^{27}Al(^{3}He, d)^{28}Si reaction is closely analogous to the ^{27}Al(d, n)^{28}Si reaction which has been studied by Calvert *et al.* (1955). These authors measured the angular distributions of several neutron groups at an incident energy of 9 MeV and their l-value assignments are listed in the table for comparison with those of the present investigation. Apart from resolving several of the (d, n) groups into multiplets, the present l-value assignments are consistent with those of the (d, n) study. The capture probabilities also agree within about a factor of two.

Values of $(2J_f+1)\theta^2$ have also been calculated for some states of ^{28}Si from the (d, n) data of Calvert *et al.* and these are shown in the table. They agree

surprisingly well with the present values particularly in view of the approximations occurring in the (d, n) and (^{3}He, d) stripping theories and the large experimental errors involved in the absolute cross section measurements.

Calvert *et al.* identified the level they observed at 9·16 Mev with the first $T=1$ state of ^{28}Si. This level, which occurs at about the expected excitation energy, has been resolved into two states at 9·314 and 9·379 Mev both of which are formed by strong $l=0$ transitions. The separation of 65 kev may be compared with the spacing of 31 kev separating the ground and first excited states of the $T_3=1$ analogue, ^{28}Al. Enge *et al.* (1956) has measured the angular distributions of the two proton groups from the ^{27}Al(d, p)^{28}Al reaction leading to the ground and first excited states and finds both to be intense and have $l=0$. He also reports the ratio of the reduced widths, multiplied by $2J_f+1$, to be 1·94 which compares favourably with the observed ratio of 2·4 for the 9·314 and 9·379 Mev states of ^{28}Si. In view of this evidence it is very likely that the 9·314 and the 9·379 Mev states are respectively the first and second $T=1$ states of ^{28}Si, and have spins of 3^+ and 2^+ respectively.

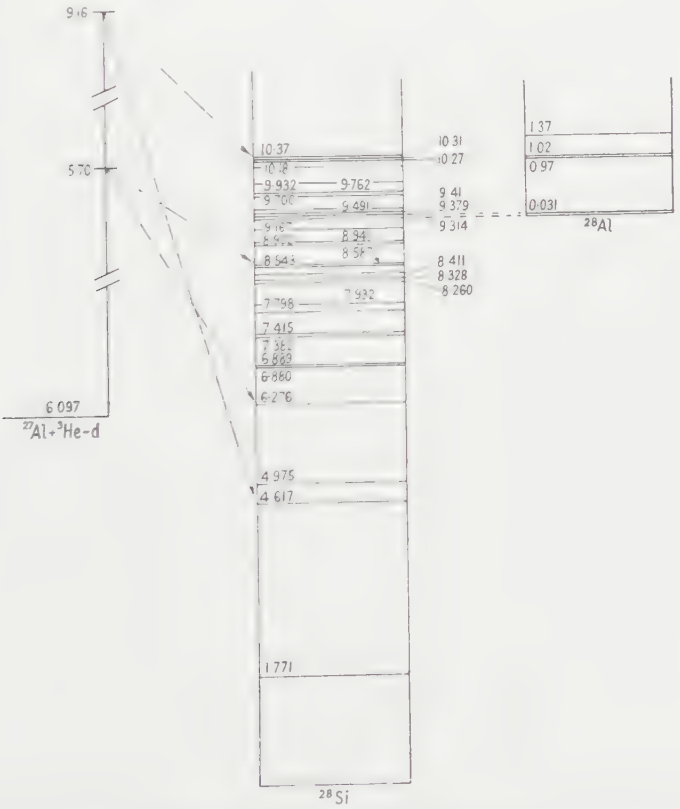

Figure 5. The energy levels of ^{28}Si.

The third and fourth $T=1$ states would be expected, from a comparison with the ^{28}Al level scheme, to occur respectively at about 0·97 and 1·02 Mev above the 9·314 Mev state, i.e. at 10·28 and 10·33 Mev. States were observed at 10·18, 10·27, 10·31 and 10·37 Mev but since angular distributions were not measured it was not possible to determine which have $T=1$.

An energy level diagram of ^{28}Si is shown in figure 5.

Acknowledgments

We would like to thank Dr. K. W. Allen for his continued interest in this work and for much helpful discussion and advice. We are grateful to Mr. D. A. Procter and Mr. H. Marchant for assisting in making the exposures, Mrs. N. E. Neville for scanning the nuclear plates and Mr. A. F. H. Muggleton for preparing the aluminium targets.

References

Browne, C. P., Zimmerman, S. F., and Buechner, W. W., 1954, *Phys. Rev.*, **96,** 725.
Butler, S. T., 1957, *Nuclear Stripping Reactions* (London: Pitman).
Calvert, J. H., Jaffe, A. A., Litherland, A. E., and Maslin, E. E., 1955, *Proc. Phys. Soc.* A, **68,** 1008.
Endt, P. M., and Braams, C. M., 1957, *Rev. Mod. Phys.*, **29,** 683.
Endt, P. M., and Paris, C. H., 1957, *M.I.T. Progress Report*, 47.
Enge, H. A., Angelman, C. C., and Jarrell, D. L., 1956, *M.I.T. Progress Report*, May 31.
Hinds, S., and Middleton, R., 1960, *Proc. Phys. Soc.*, **75,** 754.
Macfarlane, M. H., and French, J. B., 1959, *University of Rochester*, NYO-2846.
Newns, H. C., 1952, *Proc. Phys. Soc.* A, **65,** 916.

The Energy Levels of ^{24}Mg and ^{32}S

By S. HINDS and R. MIDDLETON
Atomic Weapons Research Establishment, Aldermaston, Berks.

Communicated by K. W. Allen; MS. received 10th March 1960, in final form 28th April 1960

Abstract. The energy levels of ^{24}Mg and ^{32}S have been determined from studies of the ^{23}Na(^{3}He, d)^{24}Mg and the ^{31}P(^{3}He, d)^{32}S reactions. In both cases ^{3}He particles of up to 10·2 MeV were used and the deuteron energy spectra were measured with a broad-range magnetic spectrograph. Thirty-nine states were observed in ^{24}Mg below an excitation energy of 11·861 MeV and twenty-four in ^{32}S below 8·496 MeV.

§ 1. Introduction

The (p, γ) reaction provides a powerful method of determining nuclear properties, such as spins and parities. Frequently, the analysis of the complicated γ-ray spectrum is impeded by a lack of knowledge of the excitation energies of the levels of the final nucleus. These can, in principle, be better determined from the (d, n) reaction proceeding from the same target nucleus but in practice it is extremely difficult to measure neutron energies with sufficient precision. A more satisfactory process is the (^{3}He, d) reaction, since the emitted charged particles can be studied by magnetic analysis. In the present communication the energy levels of ^{24}Mg and ^{32}S, measured respectively from the ^{23}Na(^{3}He, d)^{24}Mg and the ^{31}P(^{3}He, d)^{32}S reactions, are reported.

Prior to this work, only the first, second and third excited states of ^{24}Mg had been precisely determined although several higher states had been reported from studies of the ^{23}Na(d, n)^{24}Mg reaction and the inelastic scattering of high energy protons and deuterons (Endt and Braams 1957). Extremely accurate determinations have been made of the first and second excited states by Hedgran and Lind (1952) from precision measurements of the γ-rays accompanying the ^{24}Na β^--decay.

Endt *et al.* (1956) have precisely measured the states of ^{32}S below an excitation energy of about 4·7 MeV from a magnetic analysis study of the ^{35}Cl(p, α)^{32}S reaction. Several higher excited states have also been reported by Calvert *et al.* (1955) from an investigation of the ^{31}P(d, n)^{32}S reaction.

§ 2. Experimental Procedure

Doubly charged ^{3}He particles were accelerated in the Aldermaston Van de Graaff generators and used to bombard thin targets containing sodium and phosphorus. The sodium targets were prepared by evaporating either pure sodium metal or sodium bromide on to a thin carbon backing. These were then transferred directly into an evacuated gate-valve assembly and transported under vacuum to the target chamber. The metal targets were troublesome because of their low melting point. Exposures had to be carried out slowly with a beam

current not exceeding 0·05 μA and even then a target rarely lasted long enough to permit a second exposure to be made. An attempt was made to prepare phosphorus targets by directly evaporating red phosphorus but this was not successful. Targets were eventually prepared from zinc phosphide (Zn_3P_2) which was deposited by evaporation on to a thin carbon backing.

The energies of the emitted deuterons were measured with the broad-range magnetic spectrograph. Six exposures were made with sodium targets at an incident energy of 10·19 MeV and two at an energy of 8·47 MeV. The former were made at angles of 15°, 20°, 35° and 45° and also with a lower spectrograph field at 45° and 60°. At 8·47 MeV exposures were made at 15° and 45° only. With the phosphorus target, exposures were made at 15°, 20°, 30°, 45° and 60° at an incident energy of 10·19 MeV and a single exposure was made at 20° at an energy of 9·82 MeV.

§ 3. Results

3.1. $^{23}Na(^3He, d)^{24}Mg$ Reaction

A deuteron energy spectrum from the ^{23}Na(^{3}He, d)^{24}Mg reaction obtained at an incident energy of 10·19 MeV and an angle of 15° is shown in figure 1. This spectrum was measured from a sodium bromide target. Following our usual notation, groups ascribed to states in ^{24}Mg are labelled numerically and impurity groups by the chemical symbol for the residual nucleus with a subscript referring to the appropriate excited state. Identification was made from a detailed analysis of the relative positions of the groups in the spectra measured at different angles of observation. Strong impurity groups were observed arising from ^{12}C and ^{16}O, also a number of weaker impurity groups were identified as arising from ^{13}C which is normally present in natural carbon. It will be noticed from figure 1

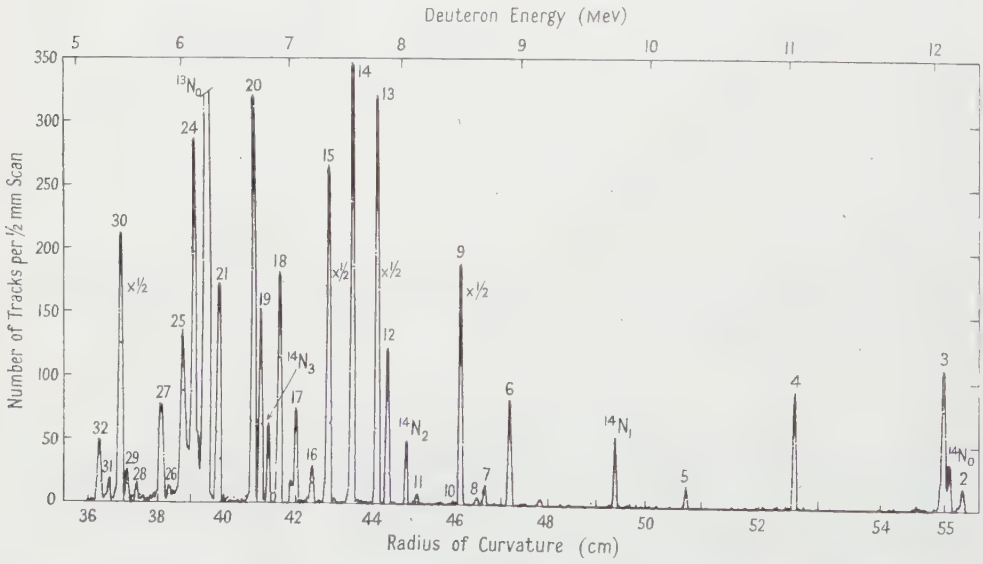

Figure 1. A deuteron energy spectrum from the ^{23}Na(^{3}He, d)^{24}Mg reaction obtained at an incident energy of 10·19 MeV, an angle of 15° and with a spectrograph field of 12 918 G. The target was a layer of sodium bromide supported on a thin carbon backing.

that the ground and first excited states were not observed. This was because the spectrograph magnetic field was set to record as many excited states as possible on one photographic plate. At the particular angle of observation shown in figure 1, the very intense impurity group from ^{12}C, corresponding to the formation of ^{13}N in its ground state, obscures groups 22 and 23.

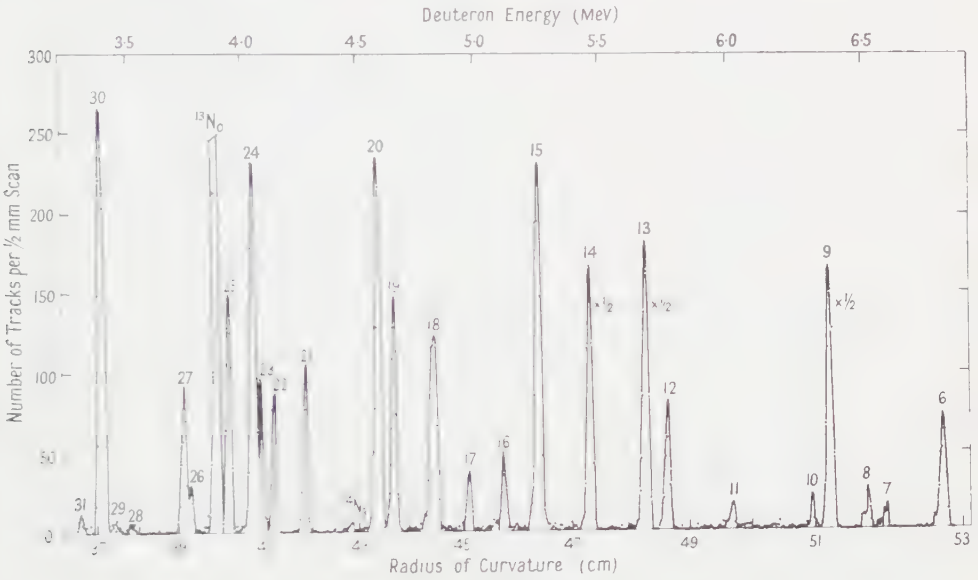

Figure 2. A deuteron energy spectrum from the $^{23}Na(^3He, d)^{24}Mg$ reaction obtained at an incident energy of 8·465 MeV, an angle of 45° and with a spectrograph field of 10 099 G. The target consisted of a layer of sodium metal supported on a thin carbon backing.

In figure 2 is shown a second spectrum obtained at an incident energy of 8·47 MeV and an angle of observation of 45 . The exposure was made with a sodium metal target and a substantially reduced spectrograph field. The latter, although preventing the observation of the ground and first five excited states resulted in improved energy resolution.

Since the ground and first excited states were not observed at any angles, it was possible only to calculate excitation energies with respect to that of the second excited state. The energy of this state however, has been very accurately determined to be 4·1215 ± 0·0014 MeV by Hedgran and Lind (1952) and our excitation energies listed in table 1 have been normalized to this value. Also included in the table are some of the lower resonance levels which overlap our highest excited states. These were obtained by resonance scattering of α-particles from ^{20}Ne by Goldberg *et al.* (1954). Agreement is exceptionally good except for the state reported by these authors at 11·726 MeV which we did not observe. It will be noticed that the 9·282 MeV state is indicated in table 1 as a possible doublet. This was thought possible because the corresponding group, 18, was consistently observed to be broader than neighbouring groups at all angles of observation. The assignment of group 26 to a state at 10·3 MeV in ^{24}Mg is possibly doubtful. The group was very weak at all angles of observation and generally ill-defined.

A summary of the energy levels of ^{24}Mg is presented in figure 3.

Table 1. Energy Levels of ^{24}Mg

Group number	Energy level (MeV)	Energy level (MeV)†	Group number	Energy level (MeV)	Energy level (MeV)‡
0	—	0·000	21	9·826 ± 0·012	
1	—	1·368	22	9·960 ± 0·015	
2	4·122 Datum	4·122	23	10·025 ± 0·015	
3	4·232 ± 0·008		24	10·055 ± 0·015	
4	5·224 ± 0·008		25	10·161 ± 0·015	
5	6·005 ± 0·008		26	(10·30 ± 0·050)	
6	7·350 ± 0·008		27	10·353 ± 0·020	
7	7·561 ± 0·010		28	10·577 ± 0·020	
8	7·620 ± 0·010		29	10·661 ± 0·020	
9	7·746 ± 0·010		30	10·723 ± 0·020	
10	7·808 ± 0·010		31	10·822 ± 0·020	
11	8·120 ± 0·010		32	10·916 ± 0·020	
12	8·357 ± 0·010		33	11·010 ± 0·020	
13	8·439 ± 0·010		34	11·188 ± 0·025	
14	8·654 ± 0·010		35	11·313 ± 0·025	
15	8·864 ± 0·010		36	11·380 ± 0·025	11·380
16	9·004 ± 0·012		37	11·446 ± 0·025	11·451
17	9·148 ± 0·012		38	11·511 ± 0·025	11·517
18	9·282 ± 0·012*			—	11·726
19	9·456 ± 0·012		39	11·861 ± 0·025	11·858
20	9·517 ± 0·012				

† Determined from precision measurements on the γ-rays accompanying the ^{24}Na β^--decay (Hedgran and Lind 1952). ‡ Determined from the resonance scattering of α-particles from ^{20}Ne (Goldberg *et al.* 1954).

* This level is possibly a doublet.

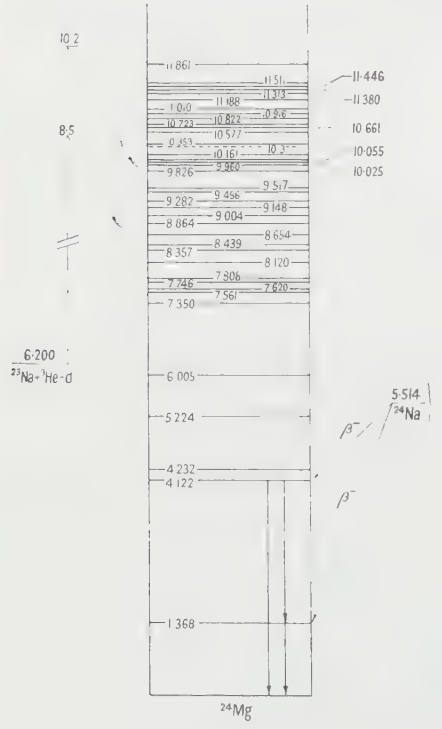

Figure 3. Energy level diagram of ^{24}Mg.

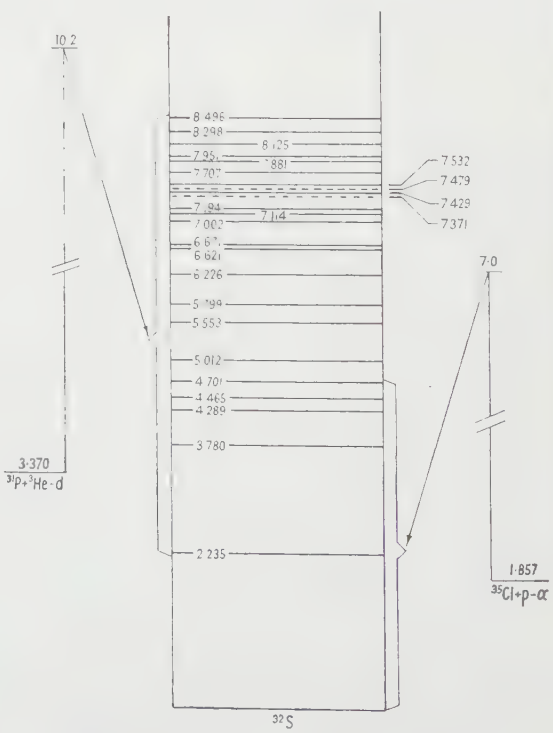

Figure 5. Energy level diagram of ^{32}S.

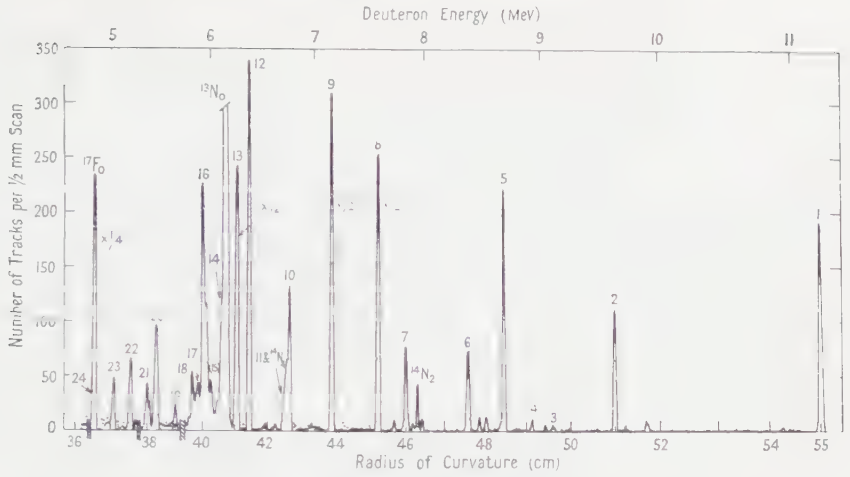

Figure 4. A deuteron energy spectrum from the $^{31}P(^3He, d)^{32}S$ reaction obtained at an incident energy of 10·19 MeV, an angle of 15° and with a spectrograph field of 12 448 G. The target was prepared from zinc phosphide.

3.2. $^{31}P(^3He, d)^{32}S$ Reaction

A typical deuteron energy spectrum obtained from the $^{31}P(^3He, d)^{32}S$ reaction at an angle of 15° and an incident energy of 10·19 MeV is shown in figure 4. The groups corresponding to states in ^{32}S were identified by their characteristic variation of energy with angle and are labelled numerically. The usual impurity groups due to ^{12}C, ^{13}C and ^{16}O were again observed and are labelled by the symbols of the residual nuclei. Several weak impurity groups were left unlabelled and examples of these can be seen at radii of curvature of 51·7, 51·3, 50·0, 49·4, 48·1 and 47·9 cm. These were established to be due to zinc but it was not possible to determine to which of the three principal zinc isotopes they corresponded.

As in the case of the sodium reaction the spectrograph field was set so that the ground state deuteron group was not observed and excitation energies were

Table 2. Energy Levels of ^{32}S

Group number	Energy level (MeV)	Energy level (MeV)*	Group number	Energy level (MeV)
0	0·000	0·000		
1	2·235†	2·237 ± 0·008	13	7·114 ± 0·008
2	3·780†	3·780 ± 0·008	14	7·194 ± 0·010
3	4·289†	4·287 ± 0·008	15	(7·371 ± 0·020)
4	4·465†	4·465 ± 0·010	16	7·429 ± 0·010
5	4·701†	4·698 ± 0·010	17	(7·479 ± 0·020)
6	5·012 ± 0·008		18	7·532 ± 0·012
7	5·553 ± 0·008		19	7·707 ± 0·012
8	5·799 ± 0·008		20	7·881 ± 0·012
9	6·226 ± 0·008		21	7·951 ± 0·012‡
10	6·621 ± 0·008		22	8·125 ± 0·015
11	6·671 ± 0·008		23	8·298 ± 0·015
12	7·002 ± 0·008		24	8·496 ± 0·015

* Determined from magnetic analysis of the $^{35}Cl(p, \alpha)^{32}S$ reaction (Endt *et al.* 1956).

† Mean datum.

‡ This level may possibly be a doublet.

calculated with respect to that of the first excited state. The excitation energies of the first five excited states however, have been precisely determined by Endt *et al.* (1956) from a magnetic analysis study of the $^{35}Cl(p, \alpha)^{32}S$ reaction. The excitation energies listed in table 2 were obtained by normalizing our values to those of Endt *et al.* such that the average deviation over the first five excited states was reduced to a minimum. The errors listed in table 2 are the estimated experimental errors and do not take into account the errors reported by Endt *et al.* Groups 15 and 17 were observed to be weak at most angles of observation and were frequently obscured by the strong impurity group arising from ^{12}C. Their assignment to states at 7·371 and 7·479 MeV respectively in ^{32}S must be regarded as doubtful. It may also be noted that group 21 was very broad at several angles and may be a doublet.

A summary of the energy levels of ^{32}S is shown in figure 5.

Acknowledgments

It is with pleasure that we thank Dr. K. W. Allen for his continued interest in this work and for useful discussion. We are also grateful to Mr. D. A. Proctor and Mr. H. Marchant for assisting in the exposures and to Mr. A. H. F. Muggleton for preparing the sodium and phosphorus targets.

References

Calvert, J. C., Jaffe, A. A., Litherland, A. E., and Maslin, E. E., 1955, *Proc. Phys. Soc.* A, **68,** 1008.

Endt, P. M., and Braams, C. M., 1957, *Rev. Mod. Phys.*, **29,** 683.

Endt, P. M., Paris, C. H., Sperduto, A., and Buechner, W. W., 1956, *Phys. Rev.*, **103,** 961.

Goldberg, E., Haeberli, W., Galonsky, A. I., and Douglas, R. A., 1954, *Phys. Rev.*, **93,** 799.

Hedgran, A., and Lind, D., 1952, *Arkiv. Fysik*, **5,** 177.

The Elastic and Inelastic Scattering of Electrons and Positrons from the s-states of Atomic Hydrogen†

By K. SMITH‡, W. F. MILLER‡ and A. J. P. MUMFORD§

‡ Argonne National Laboratory, Argonne, Illinois
§ Brookhaven National Laboratory, Upton, New York

MS. received 12*th February* 1960, *in revised form* 9*th May* 1960

Abstract. Total elastic and inelastic cross sections, for the scattering of electrons (without exchange) and positrons (neglecting the formation of positronium) from the 1s, 2s and 3s states of atomic hydrogen, have been calculated in three approximations using the method of partial waves. All significant partial wave contributions to the cross sections have been included. The results indicate that 's-state' distortion effects are negligible at incident energies greater than 30 ev.

§ 1. Introduction

The experiments of Bederson, Malamud and Hammer (1957) and of Brackman, Fite and Neynaber (1958) have given a new impetus to wave mechanical investigations on the scattering of electrons by hydrogen atoms. Furthermore, as noted by Massey and Moussa (1958), the advances in experimental techniques used to observe the collisions of positrons with gas atoms now justify a theoretical consideration of the simplest of such problems, the scattering of positrons by atomic hydrogen.

The purpose of the present paper is to examine the contributions to various cross sections from higher partial waves and the effect of s-state distortion.

The effect of exchange has been neglected in the electron scattering problem. However, calculations including exchange are being carried out and will be reported later. Notwithstanding the limitation of the approximations assumed in this report, excitation cross sections for 1s–2s are in much better agreement with the experiments of Lichten and Schultz (1959), than those calculations which neglect the $l>0$ contributions.

The effect of positronium formation has been neglected in the positron scattering problem presented here. However, the formalism for including real positronium formation has been developed, Cody and Smith (1960), and it is intended that the numerical calculations will be carried out as soon as the electron exchange problem is concluded.

A brief description of the theory employed is given in § 2. The electron scattering results are presented in § 3, where they are compared with other calculations and experiments, and the positron scattering results are given in § 4.

§ 2. Theory Employed

The usual procedure in wave mechanical scattering problems is to separate out the motion of the projectile and target by expanding the overall wave function

† Work performed under the auspices of the United States Atomic Energy Commission.

for the system in terms of the complete set of eigenfunctions of the target Hamiltonian. The number of terms taken in this expansion determines the approximation one is working in. The resulting systems of second-order differential equations for the expansion coefficients must be solved for the asymptotic parameters (phase-shifts and amplitudes) required to calculate the cross sections.

The differential equations appropriate to the electron–hydrogen-atom problem are well known, see Massey (1956). In addition, the connection between the asymptotic parameters and the cross sections is also well known, see, for example, Smith (1960) or Percival and Seaton (1957) for the general expressions when all states of the hydrogen atom are included in the eigenfunction expansion.

In the present report, the cross sections are calculated in three approximations corresponding to taking one, two, or three s-state terms in the eigenfunction expansion of the overall wave function of the projectile plus target system.

All cross sections presented herein are given in units of πa_0^2.

§ 3. Scattering of Electrons

The elastic scattering cross sections are presented in table 1.

Table 1. Elastic Scattering Cross sections for Electrons

k_0a_0		1s–1s		2s–2s		3s–3s	
1·0	a		2·6 (3); 2·6 (5)		57·4 (3); 58·3 (8)	208·7(3);	336·9(7)
	b	2·13(0);	2·3 (3)		55·0 (3)		
	c		2·6 (3)			204·0(3)	
	d				17·8 (3)	157·2(3)	
	e	2·13(0);	2·32(5)	2·18(0);	38·5 (3); 39·86(5)	149·4(3);	272·6(5)
	f	3·19(0)		1·56(0)			
1·2	a		1·76(3); 1·76(5)		32·3 (4); 33·3 (10)	50·6(3);	168·8(8)
	b	1·43(0);	1·61(3); 1·61(5)		31·3 (4); 32·1 (5)		
	c		1·7 (3)			50·4(3)	
	d				14·1 (4)	43·3(3);	80·4(4)
	e	1·41(0);	1·61(3); 1·61(6)	3·02(0);	27·3 (4); 28·4 (6)	47·9(3);	139·2(6)
	f	1·96(0)		3·03(0)			
1·5	a		1·09(5)		18·6 (5); 19·7 (10)	52·7(5);	89·0(9)
	b	0·83(0);	1·03(5)		18·1 (5); 18·7 (6)		
	c		1·07(5)			51·8(5)	
	d				8·7 (5)	49·3(5)	
	e	0·83(0);	1·03(5)	2·22(0);	16·75(5)	49·1(5)	
	f	1·06(0)		2·39(0)			
2·0	a		0·60(7)		8·6 (5); 10·6 (14)	20·6(5);	44·0(11)
	b	0·39(0);	0·58(7)		8·4 (5); 9·6 (7)		
	c		0·59(7)			19·1(5);	27·1(7)
	d				4·4 (5)	19·6(5)	
	e	0·39(0);	0·58(6)	1·12(0);	8·1 (5); 8·9 (6)	19·8(5);	24·8(6)
	f	0·47(0)		1·18(0)			

The number in parenthesis, in each case, is the number of partial waves taken into account. Row a corresponds to taking only one term in the eigenfunction expansion; rows b, c and d correspond to taking two terms; row e to three terms. In particular, b is for the results of 1s–2s coupling, c for 1s–3s coupling, and d for 2s–3s coupling. f: Marriott.

If the number of terms needed in the expansion of the total wave function can be considered to be a measure of the deformation caused by the incident electron, then table 1 shows that s-state distortion is negligible when calculating elastic scattering cross sections at energies greater than 13·6 ev. It would be interesting to extend the work of Khashaba and Massey (1958) and include P-states and (D-states, etc.) in order to examine quantitatively P-state distortion effects.

A second feature to emerge from table 1, is that contributions to Q_{1s-1s} from $l>0$ partial waves are quite small, whereas they are the dominant contributions to Q_{2s-2s} and Q_{3s-3s}.

The zero-order partial wave elastic scattering cross sections of the present calculations are compared with calculations in other approximations in table 2.

Table 2. $l=0$ Contributions to Q_{1s-1s}

k_0a_0	Bransden *et al.*	Marriott	Geltman	McEachran and Fraser	Present authors
0·9	7·5	4·11	4·0	4·02	2·66
1·0	6·0	3·19	3·2	3·14	2·13

The first notable feature of table 2 is the good agreement between the one-body exchange approximation of McEachran and Fraser (1960) and the strong coupling approximation of Marriott†, which supports the conclusion that s-state distortion is negligible when calculating elastic scattering cross sections above 11 ev. Comparison of Marriott's results with the corresponding no-exchange cross sections (present authors) shows the effect of including exchange.

The second feature brought out by table 2 is the good agreement between the s-state distortion calculation of Geltman (1960, to be published) and the results of Marriott and of McEachran and Fraser (1960). From the conclusions reached earlier, it would seem that Geltman's results are good as a consequence of including exchange rather than including the 2s and 3s states.

Finally, table 2 supports Martin, Seaton and Wallace (1958) in their assertion that the approximation of adiabatic distortion, as used by Bransden *et al.* (1958), is of questionable validity.

In table 3 we present the inelastic scattering cross sections as calculated in the three approximations.

In table 3, it is seen that including the $3s_i$-state only affects the 1s–2s excitation cross section by a few per cent—supporting the statements made earlier that s-state distortion is unimportant in electron–hydrogen-atom collisions.

Furthermore, exchange effects become increasingly important as the incident electron energy decreases, and the need for strong coupling exchange calculations for $l>0$ is apparent. If the pattern established by the agreement between the results of McEachran and Fraser (1960) and those of Marriott for Q_{1s-1s} is continued here, we would expect that Q_{1s-1s} would be affected only slightly by including the $3s_i$-state.

† We thank Dr. Marriott for sending to us his unpublished data on phase-shifts and amplitudes.

Table 3. Excitation Cross Sections for Electrons

k_0a_0		1s–2s		1s–3s	2s–3s	
	b	0·200(0);	0·517(3)			
	c			0·11 (3)		
	d				1·62(0);	15·58(3)
1·0	e	0·174(0);	0·435(5)	0·09 (3)	1·66(0);	22·07(5)
	f	0·074(0)				
	g	0·198(0)				
	b	0·102(0);	0·344(5)			
	c			0·07 (3)		
	d				0·334(0);	5·19 (4)
1·2	e	0·095(0);	0·320(6)	0·03 (3)	0·332(0);	8·03 (6)
	f	0·061(0)				
	g	0·127(0);	0·22			
	b	0·045(0);	0·215(6)			
	c			0·04 (5)		
	d				0·092(0);	2·02 (5)
1·5	e	0·043(0);	0·206(5)	0·01 (5)	0·091(0);	2·10 (5)
	f	0·034(0)				
	g	0·058(0);	0·165			
	b	0·015(0);	0·117(7)			
	c			0·02 (6)		
	d				0·024(0);	0·526(5)
2·0	e	0·015(0);	0·114(6)	0·002(6)	0·023(0);	0·725(6)
	f	0·012(0)				
	g	0·019(0);	0·104			

The values in row g are those of the ($l=0$) and the total Born approximations, Massey (1956, pp. 293 and 354). Rows b–f have the same meaning as in table 1.

Finally it is noted that, although the zero-order Born partial wave cross section is greater than the corresponding cross section being reported here, the total Born cross section is *less* than the total cross section as calculated here. (In this connection, we might point out that Swan's (1954) $Q_{2s\ 2s}$ are about 12% smaller than those presented in table 1.) It is interesting to compare the cross sections calculated here using three terms with the recent measurements of Lichten and Schultz (1959), see table 4.

Table 4. Q_{1s-2s}: Total Excitation Cross Section

	13·6 ev	19·6 ev	30·6 ev	40 ev
Present authors	0·435(5)	0·32(6)	0·206(5)	0·15(4)
Lichten and Schultz	0·31	0·21	0·17	0·135

Lichten and Schultz remarked that their results were larger than Marriott's results by a factor of seven. Table 4 suggests that this disagreement is probably due to the fact that Marriott only calculated the $l=0$ contribution. One would

therefore expect that if Marriott's calculations were extended to include $l>0$ contributions the close coupling exchange approximation would be in even closer agreement with experiment than the present calculation. Indeed, preliminary calculations indicate this to be the case.

§ 4. Scattering of Positrons

Since the positron and the atomic electron are distinguishable, then the problem of using correctly symmetrized wave functions does not arise. However, the possibility of the formation of positronium in these collisions does introduce into the problem an added complication somewhat like exchange effects in the electron scattering problem. That is, including real or virtual positronium formation transforms the problem from solving ordinary differential equations to solving integro-differential equations. The effect of positronium formation has been neglected in this work.

In table 5, we present the elastic scattering cross sections as calculated in the three approximations.

Table 5. Elastic Cross Sections for Positrons

k_0a_0		1s–1s	2s–2s		3s–3s	
	a	0·759(3, 4)	31·45(3);	31·94(6)	196·96(3);	232·81(7)
	b	0·689(3, 4)	31·42(3);	31·87(4)		
1·0	c	0·750(3)			196·87(3)	
	d		27·43(3)		194·08(3)	
	e	0·689(3)	27·12(3)		194·01(3)	
	a		21·72(4);	22·5 (10)	85·64(4);	139·16(8)
	b	0·586(4, 5)	21·65(4);	22·54(5)		
1·2	c	0·640(4)			85·78(4)	
	d		18·58(4)		81·80(4)	
	e	0·586(6)	18·48(4);	19·07(6)	82·04(4);	121·03(6)
	a		13·12(4);	15·13(12)	36·14(4);	78·53(9)
	b	0·475(5, 6)	13·06(4);	14·75(6)		
1·5	c	0·513(5)			36·05(4);	47·77(5)
	d		11·85(4)		34·71(4)	
	e	0·473(5)	11·77(4);	12·78(5)	34·75(4);	46·70(5)
	a		7·36(5);	8·96(13)	19·38(5);	40·39(11)
	b	0·349(7)	7·33(5);	8·45(7)	18·13(5);	26·0 (7)
2·0	c	0·366(7)				
	d		7·29(5)		19·15(5)	
	e	0·345(6)	6·94(5);	7·58(6)	18·99(5);	23·61(6)

Once again it is noted that including more s-states does not affect the cross sections, which supports the conclusions of Massey and Moussa (1958) that distortive effects are unimportant but conflicts sharply with Spruch and Rosenberg (1960) and Moussa (1959). Because of this disagreement, numerical solutions of the positron's integro-differential equations are needed.

Table 6. Excitation Cross Sections for Positrons

k_0a_0		1s–2s	1s–3s	2s–3s	
1·0	b	0·019 (4)			
	c		0·003(3)		
	d			0·97(3)	
	e	0·021 (3)	0·004(3)	0·98(3)	
1·2	b	0·049 (5)			
	c		0·003(4)		
	d			2·27(4)	
	e	0·048 (5)	0·002(4)	2·19(4);	2·86(6)
1·5	b	0·072 (6)			
	c		0·009(5)		
	d			1·07(4)	
	e	0·0703(5)	0·002(5)	1·05(4) ;	1·43(5)
2·0	b	0·067 (7)			
	c		0·01 (6)		
	d			0·49(5)	
	e	0·066 (6)	0·001(6)	0·47(5) ;	0·62(6)

In table 6 additional support is given to the assertion that s-state distortion is negligible. As in the electron case, the $l>0$ contributions to the excitation cross sections are very important. On comparing these results with the corresponding electron cross sections in table 3, it is seen that the positron cross sections are appreciably smaller at $k_0a_0=1$, but the cross sections are almost the same even at the quite modest energy of 54 ev.

References

Bederson, B., Malamud, H., and Hammer, J., 1957, *Bull. Amer. Phys. Soc.* [II], **2,** 172.
Brackman, R. T., Fite, W. L., and Neynaber, R. H., 1958, *Phys. Rev.*, **112,** 1157.
Bransden, B. H., Dalgarno, A., John, T. L., and Seaton, M. J., 1958, *Proc. Phys. Soc.*, **71,** 877.
Cody, W. J., and Smith, K., 1960, *Argonne National Laboratory Report,* ANL 6121.
Khashaba, S., and Massey, H. S. W., 1958, *Proc. Phys. Soc.*, **71,** 574.
Lichten, W., and Schultz, S., 1959, *Phys. Rev.*, **116,** 1132.
McEachran, R. P., and Fraser, P. A., 1960, *Canad. J. Phys.*, **38,** 317.
Marriott, R., 1958, *Proc. Phys. Soc.*, **72,** 121.
Martin, V. M., Seaton, M. J., and Wallace, J. B. G., 1958, *Proc. Phys. Soc.*, **72,** 701.
Massey, H. S. W., 1956, *Handb. d. Phys.*, Vol. 36 (Berlin: Springer), p. 295.
Massey, H. S. W., and Moussa, A. H. A., 1958, *Proc. Phys. Soc.*, **71,** 38.
Moussa, A. H. A., 1959, *Proc. Phys. Soc.*, **74,** 101.
Percival, I. C., and Seaton, M. J., 1957, *Proc. Camb. Phil. Soc.*, **53,** 654.
Smith, K., 1960, *Argonne National Laboratory Report,* ANL 6095.
Spruch, L., and Rosenberg, L., 1960, *Phys. Rev. Letters,* **4,** 44 (A).
Swan, P., 1954, *Proc. Phys. Soc.* A, **67,** 1086.

RESEARCH NOTES

Interband Photoconductivity in Germanium

By T. S. MOSS and T. D. H. HAWKINS
Royal Aircraft Establishment, Farnborough, Hants.

MS. received 29*th April* 1960, *in final form* 27*th May* 1960

It is known that in germanium there are three distinct valence bands, and absorption corresponding to transitions between these bands has been observed experimentally by Briggs and Fletcher (1952, see Moss 1959, figure 10.6, for later work). We have now succeeded in observing photoconductive effects which result from these transitions because of the different masses and mobilities in the various bands.

The effects are very weak, and the method finally adopted to confirm their existence was to record spectral sensitivity curves for specimens at two temperatures (room temperature and cooled with liquid nitrogen) with all other experimental conditions kept unchanged. At liquid air temperatures most of the transitions are from the V_1 heavy hole band to the split-off V_3 band, giving a relatively intense and narrow absorption band in the $3{\cdot}5\mu$ region. At room temperature this absorption band is weaker and much broader. Thus it would be expected that the low temperature photoconductive signal would exceed that at room temperature for wavelength between $3{\cdot}2\,\mu$ and $4{\cdot}1\,\mu$, with a flat maximum near $3{\cdot}8\,\mu$, while at wavelengths just outside this range the room temperature signal should be the larger.

Direct comparison of the spectral records obtained showed that the predicted behaviour occurred consistently, with the cold specimen giving a significantly higher signal in the $3{\cdot}8\,\mu$ region.

It was necessary to use high intensity radiation (with consequent poor resolution), high gain amplifiers, and long integration times to keep the noise to a minimum. Spectral purity was ensured by use of a double prism monochromator, and most of the short wavelength radiation was rendered ineffective by use of a Perspex chopper.

The specimen thickness was approximately the reciprocal of the peak absorption constant, and its length and width matched the smallest image of the spectrometer exit slit ($10\,\text{mm} \times 3\,\text{mm}$) which could be obtained. Best results were obtained with single crystal material of hole concentration $p = 4{\cdot}5 \times 10^{16}\,\text{cm}^{-3}$ and mobility $0{\cdot}12\text{m}^2\text{v}^{-1}\text{sec}^{-1}$, giving a specimen resistance $R = 6\,\Omega$. The polarizing current used was $i = 0{\cdot}2\,\text{A}$. The doping impurity was Ga, which has such a low activation energy (0·01 ev) that it would show no effect in this waveband and would be highly ionized at the relatively high temperatures used.

From the average of many spectral curves the peak excess signal from the cooled specimen compared with the warm specimen (when the curves were

adjusted to be as nearly equal as possible at long wavelengths, i.e. 4·5–5 μ region) was found to be 2×10^{-9} v r.m.s. across the specimen for an irradiation $Q = 9 \times 10^{15}$ quanta sec^{-1}. From known absorption data and specimen thickness, the ratio of this difference signal to the total signal if the material were fully absorbing should be $\eta \simeq 0{\cdot}25$, so that the corresponding total signal is $\Delta V = 8 \times 10^{-9}$ v r.m.s. An alternative estimate derived from the differences between signals at 3·8 μ and at short wavelengths (2·7μ), for which case $\eta \simeq 0{\cdot}33$, gave $\Delta V = 12 \times 10^{-9}$ v r.m.s. This latter figure was influenced somewhat by 'breakthrough' from the main band-to-band photoconductivity, so it can be taken only as an upper limit.

From simple photoconductivity theory

$$\Delta V = \frac{2^{1/2}}{\pi}\left(\frac{RiQ\tau}{P}\right)\left(\frac{\mu_3 - \mu_1}{\mu_1}\right) \text{ r.m.s.} \qquad \ldots\ldots (1)$$

where the numerical factor converts from a steady signal level to the root mean square of the fundamental when square wave chopping is used, P is the total number of holes in the specimen, μ_1 and μ_3 the mobilities in bands V_1 and V_3 and τ the time spent in V_3 before returning to V_1.

The main aim of the experiment is to obtain an estimate of τ.

Hence

$$\tau(\mu_3 - \mu_1)/\mu_1 = 5{\cdot}3 \times 10^{-11} \text{ sec.} \qquad \ldots\ldots (2)$$

To evaluate τ it is thus necessary to estimate the mobility in the V_3 band. The lattice scattering contribution can be found from deformation potential theory (see Brooks 1955, equation 6.11) which gives

$$(\mu_3)_L = 5{\cdot}2(e/E_3)^2(m/m_3)^{5/2} \text{ m.k.s. units at } 90^\circ\text{K} \qquad \ldots\ldots (3)$$

where $m_3/m = 0{\cdot}077$ and E_3, the shift in the V_3 band per unit dilation, should be similar to that for V_1, namely about 12 ev. Hence $\mu_3 = 20 \text{m}^2 \text{v}^{-1} \text{sec}^{-1}$.

The contribution of ionized impurity scattering may be estimated from the formula given by Brooks (1955, equation 6.40) giving

$$(\mu_3)_I = 1{\cdot}35 \text{m}^2 \text{v}^{-1} \text{sec}^{-1} \text{ at } 90^\circ\text{K}. \qquad \ldots\ldots (4)$$

The latter term is thus all important, the combination of (3) and (4) resulting in $\mu_3 = 1{\cdot}3 \text{m}^2 \text{v}^{-1} \text{sec}^{-1}$, and hence $\tau = 9 \times 10^{-12}$ sec.

Considering the inaccuracies in the measurements, the difficulties of interpretation and uncertainties in μ_3, the limits on τ are fairly wide but should not exceed the range

$$\tau = 4 \text{ to } 14 \times 10^{-12} \text{ sec.}$$

For comparison, the scattering time corresponding to the mobility μ_3 is $\tau_3 = 0{\cdot}55 \times 10^{-12}$ sec, so that a carrier excited to V_3 survives some 10 or 20 collisions before dropping back to V_1.

We wish to thank Dr. Rouse of the Associated Electrical Industries for kindly providing the germanium used in this work.

References

Briggs, H. B., and Fletcher, R. C., 1952, *Phys. Rev.*, **87**, 1130.

Brooks, H., 1955, *Advances in Electronics and Electron Physics* (New York: Academic Press), Vol. 7, pp. 146, 158.

Moss, T. S., 1959, *Optical Properties of Semiconductors* (London: Butterworths Scientific Publications; New York: Academic Press), pp. 50, 130, 138.

Measurements of Optimum Domain Widths in Silicon–Iron

By R. CAREY

Department of Physics, University of Nottingham

Communicated by L. F. Bates; MS. received 6th May 1960

§ 1. Introduction

The optimum domain size in a demagnetized crystal is that which leads to a minimum value for the sum of the free energies associated with the surface structures and with the walls separating the main domains (Kittel 1949). In a study of the domain structures in the surface layers of crystals of iron and silicon–iron having specific faces, Martin (1957) made calculations of the optimum domain size and showed it to depend on both the crystallographic orientation of the boundary face of the crystal and the crystal size. Crystals with main (100) surfaces and bounded at the ends by (111) faces (see figure 1 (*a*)) were considered, and the approximate relation between the length L of the crystal in the [100] direction and the domain width D was estimated to be

$$D = 1{\cdot}32\left(\frac{\gamma}{K}\right)^{1/4} L^{3/4},$$

where γ is the 180° wall energy per cm^2 and K is the first anisotropy constant. The length L is taken to be the mean length of the grain in the [100] direction and D is the average spacing between the 180° walls which separate the main domains in the grain.

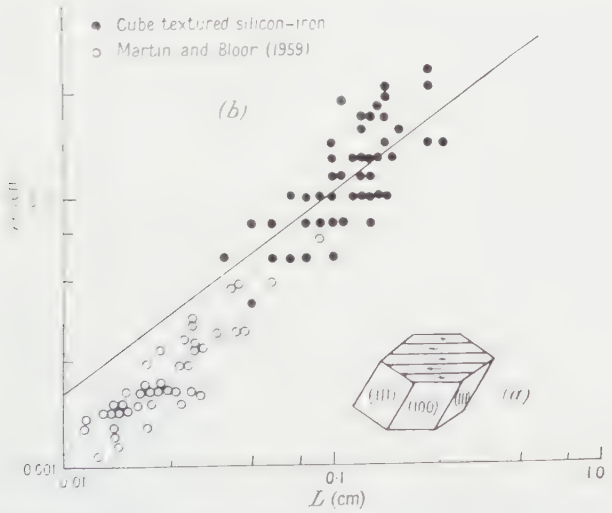

Figure 1 (*a*) Crystal bounded by four (100) faces and four (111) faces. (*b*) Variation of mean domain width D with mean grain length L in [100] direction. The line shows the theoretical relation for a crystal of the type shown in (*a*).

Measurements of the optimum domain width of crystals of this type referred only to: (*a*) single crystals with $L = 1{\cdot}0$ cm or greater (Martin 1957), and (*b*) crystals in a randomly oriented polycrystalline specimen of silicon–iron which were found to have the required orientation; in this case the crystallite length L

was 0·09 cm or less (Martin and Bloor 1959). Although the measurements made on the polycrystalline specimen agreed approximately with the calculated relation it was not possible, at the time, to make measurements in the intermediate range. Specimens, single crystal or otherwise, with a crystal length greater than 0·1 cm were not available.

Recent investigation of a new cube-textured polycrystalline silicon–iron sheet showed it to have an overall (100) [100] orientation (Bates and Carey 1960) with an average grain diameter of 0·1 cm. In the demagnetized strain-free state many grains showed a domain structure similar to that depicted in figure 1 (*a*) and were of approximately the required shape, thus making the following measurements of optimum domain widths possible.

§ 2. Experimental Results

The specimens used for these experiments were in the form of discs 2·4 cm in diameter and 0·3 cm thick. The average grain diameter was 0·1 cm. Most of the grain boundaries penetrated the sheet almost perpendicularly, and thus the grain shape from face to face was almost unchanged. A strain-free surface was obtained by electrolytic polishing, and the specimens were thermally demagnetized before domain width measurements were made.

The domains were observed by the usual colloid technique, and the measurements were made direct with a calibrated microscope eyepiece. The grains selected were as near as possible to the shape shown in figure 1 (*a*), and L varied from 0·04 cm to 0·3 cm.

The results are shown graphically in figure 1 (*b*) where the domain spacing D is plotted against the mean length L of the grain in the [100] direction. The measurements of Martin and Bloor for their randomly oriented material are also shown. The line shows the theoretical relation for a crystal of 3% silicon–iron of the type shown in figure 1 (*a*).

§ 3. Discussion

It is immediately obvious that the measured optimum domain widths agree satisfactorily in magnitude with the theoretical relation. In the polycrystalline specimens the grains were bounded by end faces of different orientations, whereas the theoretical relation applies strictly to crystals bounded by (111) faces. However, the measured domain widths would not be expected to differ greatly from the theoretical value as the surface energies at the crystal face would not be greatly different. It can be seen that some grains whose lengths varied over a small range had the same domain spacing, thus causing an apparent spread in the results. For example, nine grains with lengths varying in the range 0·06 cm to 0·16 cm had the same domain spacing, namely 0·01 cm. This effect is attributed to domain interaction between neighbouring grains. In the cube-textured material where the majority of the grains were of (100) [100] type orientation there is a marked tendency for a 180° wall to cross several grains without interruption. Thus, the optimum domain width in this material is not only dependent on the size and shape of the grain, but is affected also by the domain structure of the surrounding grains. The relation between the crystal size and the measured domain spacing can therefore be written as $D = AL$ where A is a constant.

Acknowledgments

I wish to thank Professor L. F. Bates for his kind interest in this work, Dr. Weston Morrill for the gift of specimens of cube-textured silicon–iron, and the Department of Scientific and Industrial Research for a maintenance grant.

References

Bates, L. F., and Carey, R., 1960, *Proc. Phys. Soc.*, in the press.
Kittel, C., 1949, *Rev. Mod. Phys.*, **21**, 541.
Martin, D. H., 1957, *Proc. Phys. Soc.* B, **70**, 77.
Martin, D. H., and Bloor, D., 1959, *Proc. Phys. Soc.*, **73**, 695.

The Hyperfine Structure of some Uranium and Americium lines in the 1·6–2·1 micron Region

By R. Beer† and L. Bovey‡

† The Physical Laboratories, The University, Manchester 13.
‡ Spectroscopy Group, Chemistry Division, Atomic Energy Research Establishment, Harwell, Didcot, Berks.

MS. received 6th April 1960

Abstract. A combination of intense microwave-excited sources, a grating spectrometer and a high pressure scanning Fabry-Perot interferometer has allowed a study (at a resolution of approximately 250 000) for about twelve lines. Isotope shifts for ^{235}U, ^{236}U, and ^{238}U, and magnetic hyperfine structures for ^{241}Am are reported together with some less definite results for plutonium.

---

§ 1. Introduction

In the visible region, the advantages of a Fabry–Perot interferometer as a scanning spectrometer were pointed out by Jacquinot (1954) who showed that it could have more than 200 times the luminosity of the equivalent grating instrument. When multilayer dielectric coatings have been used, both high resolution and luminosity have been obtained. Recent papers by Gerstenkorn (1960) and Diringer (1960) have shown the satisfactory application of the technique to the study of hyperfine structure in plutonium and uranium respectively. Similar work in the near infra-red such as that reported here has not been possible previously both because of lack of suitable coatings with pressure scanning systems, and weakness of the emission lines in this region. From several considerations, such as increased relative flatness of plates at longer wavelengths, work at 2 microns should give advantages in resolving power over that in the visible. However, this advantage may be at least partially offset by the fact that detectors in this region are less sensitive than those in the visible.

Relatively strong lines such as the mercury line 15295 Å (Blaise, Chabbal and Jacquinot 1954) and some emission lines of rare gases (Humphreys and Paul 1958) have been studied. Most high resolution work, however, in the

1–3 μ region has been carried out in absorption studies with a grating used in a multi-pass system and a figure of some 200 000 has been claimed for one such spectrometer (Rank, Wiggins and Shearer 1956). With a combination of a high resolution grating (used for the primary dispersion), microwave-excited sources and multilayer dielectric coatings, the 1·6–2·1 μ region of the spectrum has been examined for four elements (U, Np, Pu and Am) and the preliminary results given. It is hoped to give a more systematic study later and extend the range covered.

§ 2. Apparatus

2.1. *The Grating Spectrometer*

A 1 m, nominal F/7, Czerny–Turner type instrument, constructed at Harwell (Bovey and Steers 1959) gave the primary dispersion. The first-order blaze with maximum at 2 μ from a 300 lines/mm Bausch and Lomb grating (33.53.17.77) (masked to give a useful area of 3 in. high × $3\frac{3}{4}$ in. wide) was used. Curved Hilger slits of effective length 6 mm and width 2 mm were used. The detector was a Kodak PbS 'Ektron' detector cooled to dry ice temperatures and the 800 c/s modulated signal was amplified by a tuned amplifier and displayed on a Leeds Northrup recorder with a 1 sec response time. Ge and Si filters were used to eliminate second and higher order radiation.

2.2. *Sources*

The americium and neptunium tubes were supplied by Dr. Frank Tomkins of the Argonne Laboratories, U.S.A. The uranium and plutonium tubes were made by the method previously described (Bovey and Wise 1959). All tubes contained the iodide of the element together with neon at 2 mm pressure. When inserted in a tuned cavity and excited by microwave radiation (2425 Mc/s) from a nominal 200 w Deutsche Elektronik medical therapy set, atomic lines were strongly emitted. The microwave power (and hence the emission lines) was pulsed at 800 c/s to eliminate the thermal background radiation emitted by the tube and cavity walls.

2.3. *The Interferometer*

The fused silica optical flats were 3 in. in diameter but only the central area of about 1 in. diameter was used. This portion was flat to about $\lambda/20$ at 5461 Å giving a theoretical limiting interferometer finesse of about 37 at 2μ. This figure can be compared with the peak finesse of 35 obtained with a 50% transmission. The dielectric coatings were seven alternate $\lambda/4$ layers of zinc sulphide and cryolite with a peak reflectivity of 0·91 at 1·9 μ falling to 0·87 at 1·7 and 2·15 μ. 4 mm and 8 mm invar spacers were used. The etalon mount was brass and was mounted inside a steel pressure vessel containing calcium fluoride collimating and condensing lenses, and pressure windows. The pressure in the chamber could be controlled by a supersonic leak (Rank and Shearer 1956) to give a linear pressure rise of up to 40 atmospheres of nitrogen. The resulting maximum scan range was 1% of the wavelength. A detailed account of the design, construction and performance of the instrument is given elsewhere (Beer and Ring 1960).

The general procedure followed was to run first a grating spectrum which was identified from the existing wavelength lists (see individual references). With the Fabry–Perot interferometer in position, the grating was turned to an angle corresponding to lines thought sufficiently strong and isolated to be recorded. The grating was slightly rotated about this angle to a final fixed position to give maximum response during the pressure scan.

§ 3. Results

Uranium

Tubes containing mixtures of ^{235}U and ^{238}U, and mixtures of ^{235}U, ^{236}U and ^{238}U, in approximately equal proportions, were studied. The results are given in table 1. Other lines 5366·46(250), 5730·23(160), 5738·49(80), 5742·15(20), were examined but the isotope shift could not be unambiguously derived for them.

Table 1

Wave no. in air (cm^{-1})‡	Intensity‡	Width (cm^{-1})		Isotope shift (cm^{-1})†			
		$^{238,236}U$	^{235}U	$^{238}U-^{235}U$		$^{236}U-^{235}U$	
				Fabry–Perot	Grating‡	Fabry–Perot	Grating‡
5255·04	(130)	0·05	0·24§	1·040 ± 0·01	1·05 ± 0·06	0·44 ± 0·01	0·45 ± 0·06
5303·46	(160)	0·05	0·08	0·374 ± 0·008	0·39 ± 0·06	0·153 ± 0·008	0·15 ± 0·06
5566·47	(20)	0·05	—	none observed			
5570·76	(100)	0·05	0·05	0·213 ± 0·005	0·24 ± 0·06	0·085 ± 0·005	—
5641·18	(130)	0·05	0·14	0·348 ± 0·006	0·40 ± 0·12‖	0·144 ± 0·006	—

† Considered positive if wave number for heavier isotope greater than that of the lighter one.
‡ Data from Atherton and Bovey (1960).
§ Strongly asymmetrical. Height of maximum peak to minimum peak 1 : 0·33. This line is shown in figure 1.
‖ Overlap of order has increased experimental error.

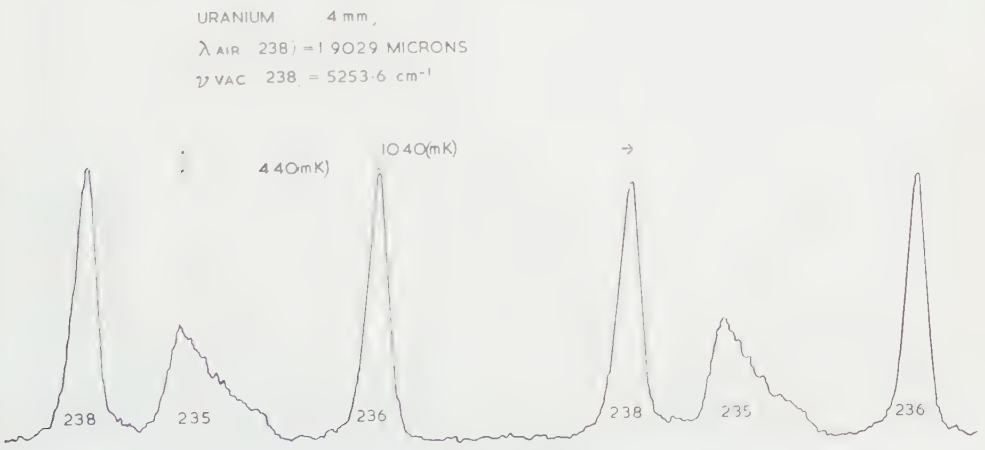

Figure 1. The 1·9μ line of three isotopes of uranium, taken with a 4 mm spacer in the Fabry–Perot interferometer. The large isotope shift and increased width of the ^{235}U line are clearly shown. (1000 mK = 1 cm^{-1}.)

Neptunium

No sufficiently strong Np line in this region was available.

Plutonium

A ^{239}Pu tube and another containing a small proportion ($\sim 10\%$) of ^{240}Pu were used.

The lines 4964·98 (80), 5025·12 (80), 5250·88 (70), 5918·10 (400), and 6085·2 (100) (data from Atherton, Bovey and Steers 1959) were examined but no magnetic hyperfine structure (expected from lines in the visible region to give two lines with about 0·10 cm^{-1} spacing) nor isotope shifts were observed. The average line width was about 0·06 cm^{-1}. The line 5976·93 (130) showed an unresolved satellite with a shift of about 0·1 cm^{-1} from the main line. Both lines had a width of approximately 0·1 cm^{-1}.

Americium

A tube containing ^{241}Am gave the following information (table 2); the first component had the highest frequency in each case, except where a negative sign appears.

Table 2

Wave no. in air† (cm^{-1})	Intensity grating†	Hyperfine structure (relative intensities in brackets)						
		1	2	3	4	5	6	7
4597·6	960	0‡	0·190	0·071	0·086	0·127	0·130	0·159
5790·0	60	0(1)	0·091(0·82)	0·082(0·65)	0·081(0·57)	0·072(0·50)	0·060(0·43)	—
6051·7	30	0*	−0·160	−0·167	−0·110	—	—	—
6105·4	60	§0(1)	0·091(0·63)	0·123(0·30)	0·124(0·26)	0·127(0·23)	—	—

* Intensities of components are not given because lines are not completely resolved, but components 1 and 3 are most intense.

† Data from Bovey, Steers and Tomkins (1959).

‡ Intensities of components are not given because lines are not completely resolved, but components 2, 4 and 5 are most intense.

§ Other components are probably lost in overlapping orders.

It is estimated that the error in measurement of the spacing is $\pm 0{\cdot}005$ cm^{-1} and that the relative intensities of resolved lines have an error of about 5%. The 5226·4, 5516·2, 5590·6 and 6219·6 lines were also studied and although structure was seen, it was not possible either for reasons of insufficient resolution or low signal–noise ratio to measure it.

§ 4. Discussion

The agreement between the interferometric and grating results for uranium is very satisfactory and it is clear that the addition of the interferometer has resulted in greatly increased accuracy of measurement. None of the lines has so far been assigned to transitions between levels; no comparisons can therefore be made with the expected isotope shifts in the levels. Indeed it is hoped that an extension of this study can help identify the spectral terms and their electronic configurations.

The first three lines of americium given in table 2 have not so far been assigned to transitions between known levels. It is likely that the Am line at 6105·4 cm^{-1} (6103·7 *in vacuo*) shown in figure 2, arises from a transition between the levels 21239·91 cm^{-1} and 15135·94 cm^{-1}. These are given as having widths of 0·432 and 1·062 cm^{-1} respectively (Fred and Tomkins 1957).

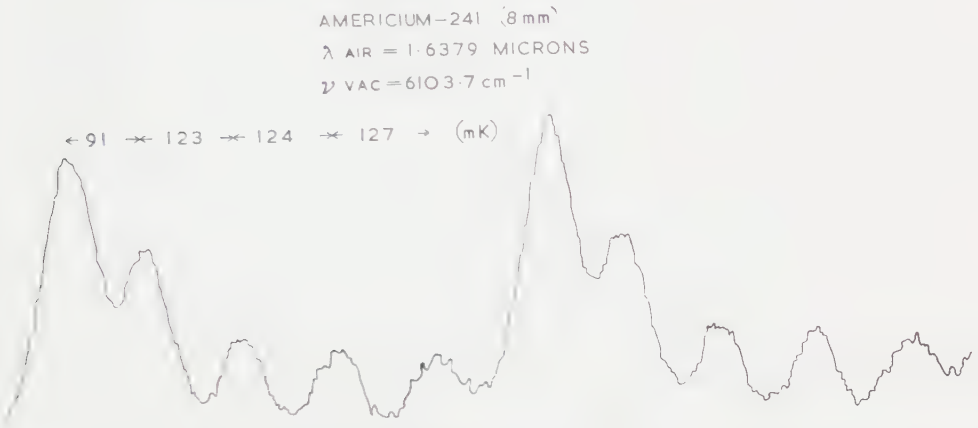

Figure 2. The 1·6μ line of amercium taken with an 8 mm spacer in the Fabry–Perot interferometer. Five components of ^{241}Am are clearly resolved. The spacings between the components are given in mK units (1000 mK = 1 cm^{-1}).

The line 21239·91 cm^{-1} from the transition 21239·91 cm^{-1} to 0·00 cm^{-1} (the ground state) has three components with relative spacing 0·00, −0·177 and −0·129 cm^{-1} (with the Fred and Tomkins sign convention that a pattern is considered positive if the weaker components have larger wave numbers). Since the ground state width is of the order 0·001 cm^{-1}, the components of the line must arise from the level 21239·91 cm^{-1}.

The structure of the level at 15135·94 cm^{-1} cannot be obtained by examination of a line arising from the ground state since of course it has the same parity. However several sets of lines relate it to the ground state as can be seen in the summary in table 3.

Table 3

Wave no. of line (cm^{-1})	Width (cm^{-1})	Hyperfine structure intervals (cm^{-1})						Classification
12873·84	1·062	0·000	0·279	0·247	0·227	0·173	0·136	28009·78–15135·94
28009·78	0·000	—						28009·78– 0·00
13344·92	1·157	0·000	0·279	0·255	0·241	0·200	0·182	28480·85–15135·94
28480·85	0·000	—						28480·85– 0·00

The level 15135·94 cm^{-1} would therefore seem to have six components with relative spacing similar to that given by the hyperfine structure intervals of the two lines at 12873·84 cm^{-1} and 13344·92 cm^{-1}. The experimental data for the line 6105·4 cm^{-1} seem in general agreement with the structure of its two associated

levels, but several more components of the 21239·91 cm^{-1} line with spacing of the order of 0·100 cm^{-1} would have been expected. Further discussion must await a more complete knowledge of the structure in both levels and lines but it can be seen that the extension of high resolution work to this wavelength region should help in generally elucidating the structure of levels.

Acknowledgments

The authors are indebted to Dr. J. Ring for many helpful discussions, Mr. N. Atherton for his willing assistance and Mr. H. Wise for preparation of the discharge tubes.

References

Atherton, N., and Bovey, L., 1960, *United Kingdom Atomic Energy Authority* (*Research Group*) *Report* R. 3226.

Atherton, N., Bovey, L., and Steers, E. B. M., 1959, *United Kingdom Atomic Energy Authority* (*Research Group*) *Report* R. 2977.

Beer, R., and Ring, J., 1960, *Infra-red Physics* (London: Pergamon Press) (in the press).

Blaise, J., Chabbal, R., and Jacquinot, P., 1954, *J. Phys. Radium*, **15**, 749.

Bovey, L., and Steers, E. B. M., 1959, *United Kingdom Atomic Energy Authority* (*Research Group*) *Report* C/R 2827.

Bovey, L., Steers, E. B. M., and Tomkins, F., 1959, *United Kingdom Atomic Energy Authority* (*Research Group*) *Report* R. 2978 (in preparation).

Bovey, L., and Wise, H. S., 1959, *United Kingdom Atomic Energy Authority* (*Research Group*) *Report* R. 2976.

Diringer, M., 1960, *C. R. Acad. Sci., Paris*, **250**, 828.

Fred, M., and Tomkins, F., 1957, *J. Opt. Soc. Amer.*, **47**, 1076.

Gerstenkorn, S., 1960, *C. R. Acad. Sci., Paris*, **250**, 825.

Humphreys, C. J., and Paul, E., 1958, *J. Phys. Radium*, **19**, 424.

Jacquinot, P., 1954, *J. Opt. Soc. Amer.*, **44**, 761.

Rank, D. H., and Shearer, J. N., 1956, *J. Opt. Soc. Amer.*, **46**, 463.

Rank, D. H., Wiggins, T. A., and Shearer, J. N., 1956, *J. Opt. Soc. Amer.*, **46**, 255.

Note on the Treatment of Impurity Scattering in Optical Absorption in Semiconductors

By B. Donovan

Department of Physics, Bedford College, London

MS. received 6th May 1960

Considerable attention has been given to the problem of infra-red absorption by free carriers in semiconductors, and in particular to the case of n-type germanium. Experimental and theoretical results have been given by Fan, Spitzer and Collins (1956, to be referred to as FSC), and certain improvements resulting from a Drude–Zener treatment were pointed out by Donovan and March (1957). More recently, two papers have appeared, by Rosenberg and Lax (1958, to be referred to as RL) and by Meyer (1958, to be referred to as M), which contain more elaborate calculations of the absorption cross section, i.e. ratio of absorption coefficient to carrier density. In both cases the detailed structure of the conduction band was taken into account, as well as the effect of induced photon emission, which was not the case in previous work.

The general picture which emerges is that, whereas the agreement between theory and experiment is satisfactory for lattice scattering, there remain discrepancies at low temperatures where scattering due to ionized impurities is important. Specifically, the total cross sections derived by RL are considerably smaller than the experimental results of FSC at 293 and 78 K. The treatment of impurity scattering used by RL is based on the Born approximation and the potential is of the screened Coulomb form, containing a factor $\exp(-qr)$. In the work of M, impurity scattering is not discussed in detail but an expression for the relevant cross section is given, and evaluated only for the two limiting cases $h\nu \ll 2kT$ and $h\nu \gg 2kT$. This expression is derived by a method which avoids the Born approximation but takes no account of screening; hence it might be expected that in this case (as in FSC) the cross section would in general be over-estimated (see RL, figure 3, also Wolfe 1954).

A more satisfactory approach to impurity scattering would clearly be a generalization of the Meyer calculation to include non-zero values of the screening parameter q; however, such a calculation would appear to be prohibitively complicated. The purpose of the present note is to evaluate the Meyer impurity cross section in the frequency range covered by the experimental data of FSC, and hence to assess the extent to which the discrepancy discussed by RL is due to the use of the Born approximation.

The impurity cross section σ_i is given in M, equation (6.1) (which does not, as stated, contain the induced emission factor, and also omits ν^3 from the denominator). The corrected form, in terms of the variable $x = h\nu/2kT$, and with the effective mass $m^* = 0{\cdot}096\ m$ (as in RL), is

$$\sigma_i(x) = 7{\cdot}098 \times 10^{-28} \frac{N_i}{\nu^3 (kT)^{3/2}} (1 - e^{-2x}) I(x),$$

where N_i is the concentration of ionized impurities and

$$I(x) = \int_0^\infty k' \exp\left(-\frac{k^2}{s}\right) \ln\left(\frac{k'+k}{k'-k}\right) dk.$$

Here k and k' are the magnitudes of the initial and final electron wave vectors respectively, and $s = 2m^* kT/\hbar^2$, so that $k'^2 - k^2 = 2xs$.

Introducing $y = ks^{-1/2}$ we obtain

$$I(x) = s \int_0^\infty (y^2 + 2x)^{1/2} \exp(-y^2) \ln\left[\frac{(y^2+2x)^{1/2} + y}{(y^2+2x)^{1/2} - y}\right] dy,$$

and for $x \gg 1$ the integrand, excluding the exponential factor, may be expanded in the form

$$2y + \frac{y^3}{3x} - \frac{y^5}{15x^2} + \frac{2}{105}\frac{y^7}{x^3} - \ldots .$$

Hence, on integrating term by term, we have

$$J(x) = \frac{I(x)}{s} = 1 + \frac{1}{6x} - \frac{1}{15x^2} + \frac{2}{35x^3} - O(x^{-4})$$

and for $x = 3$ this number of terms gives a result accurate to about 0·1%. For $x \leqslant 3$ the values of J have been found by direct numerical integration.

The total cross section may be evaluated by combining $\sigma_i(x)$ with the phonon contribution (RL, equations (3.5)–(3.8)) and the results are shown in figures 1 and 2. The experimental points are taken from FSC and reveal at the high

frequency end additional absorption, not covered by the present theories, due to transitions to [100] valleys. It will be seen that, whereas the RL curves lie considerably below the experimental points at both temperatures, the present treatment over-estimates the cross section at 293°K but leads to a distinct improvement, though still too low, at 78°K. It should be emphasized that the difference between the solid and broken curves in figures 1 and 2 is much greater than that due to neglecting screening. If q were taken as zero in the RL treatment, the low-frequency end of each curve would be raised slightly but the effect on the high-frequency end would be negligible. The quantitative significance of q may be

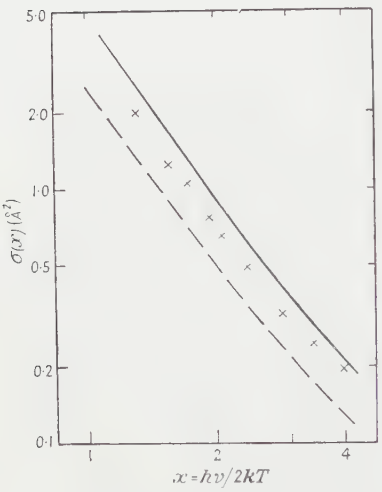

Figure 1. Absorption cross section for n-type germanium at 293°K.

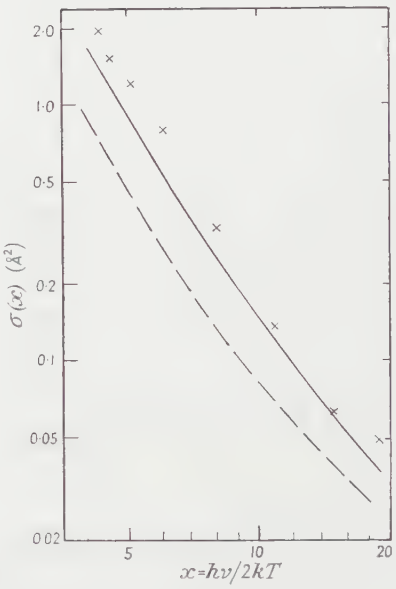

Figure 2. Absorption cross section for n-type germanium at 78°K.

Broken curve, Rosenberg and Lax; full curve, present treatment; crosses, experimental points.

judged from RL, figure 3 ($q \sim 1{\cdot}6 \times 10^6$ cm^{-1} for both RL curves considered here); with $q=0$ at $T=293$°K the RL impurity cross section at $x=1$ is still only about one-third of the value given by the present calculation. Conversely, if screening were included in the present treatment, the low-frequency end of each curve would probably be lowered slightly but the high-frequency end would remain unaffected; this would improve the agreement at 293°K but would make matters rather worse at 78°K. However, the conclusion which would appear from this note is that some improvement in the theory of impurity scattering may be obtained, even with an unscreened potential, if the Born approximation is avoided. The fact that a discrepancy is still evident at low temperatures suggests that a closer comparison with experimental data might well require a more detailed investigation of the approximations involved in the bremsstrahlung calculation from which the impurity cross section is derived.

The writer wishes to thank Dr. N. H. March for many helpful discussions on the subject of this note and for assistance with some of the numerical computations.

References

Donovan, B., and March, N. H., 1957, *Proc. Phys. Soc.* B, **70,** 833.
Fan, H. Y., Spitzer, W., and Collins, R. J., 1956, *Phys. Rev.*, **101,** 566.
Meyer, H. J. G., 1958, *Phys. Rev.*, **112,** 298.
Rosenberg, R., and Lax, M., 1958, *Phys. Rev.*, **112,** 843.
Wolfe, R., 1954, *Proc. Phys. Soc.* A, **67,** 74.

Total and Absorption Cross Section for High Energy Pions

By C. J. BATTY†

Physics Department, University of Birmingham

Communicated by R. E. Peierls; MS. received 21st April 1960

The optical model of the nucleus, extensively applied to a study of nucleon–nucleus scattering has also been used to a lesser extent to describe pion–nucleus interactions. This latter case is in some ways more interesting since complications due to spin-dependent forces are absent. Also since the optical model potentials can be related to the real and imaginary forward scattering amplitudes for the pion–nucleon interaction which can be calculated using dispersion relations, cross sections for pion–nucleus scattering can be calculated directly. Comparison of these values with experimental data then gives us a check of the relationship between the optical model potential and the pion–nucleon scattering amplitudes.

In this paper we wish to discuss the experimental data of Cronin, Cool and Abashian (1957) who have measured the diffraction and absorption cross sections of various nuclei for negative pions at energies between 0·6 and 1·4 Gev. Using pion–nucleon scattering amplitudes obtained by Cool, Piccioni and Clark (1956) they obtained reasonable agreement between experimental and theoretical values for the absorption cross section but for the diffraction cross section the experimental values were 20–30% too high. The calculation of the optical model potential has been reformulated by Bég (to be published) who has included effects of nucleon correlation due to the Pauli principle (see also Watson 1958) and the direct absorption of pions by pairs of nucleons and as a result obtains effective pion–nucleon cross section in nuclei rather larger than the free values. Using these effective values we have calculated the resulting diffraction and absorption cross sections for pion–nucleus scattering and obtain much better agreement with the experimental values of Cronin *et al.*

The optical model potential is written by Bég as

$$V(r) = \frac{kA}{2E}(\lambda + i)\bar{\sigma}\rho(r) = V_1(r) + iV_2(r)$$

where k and E are the wave number and energy of the incident pion, $\bar{\sigma}$ the average effective pion–nucleon total cross section, λ the ratio of real to imaginary part of the potential and $\rho(r)$ the nucleon density in the nucleus normalized to unit volume. Bég shows in his paper that $\bar{\sigma}$ should be taken to be different from the observed two-body cross section. In particular, the effect of the Pauli principle at these energies is to increase the effective cross section, rather than to decrease it as it

† Now at National Institute for Research in Nuclear Science, Rutherford High Energy Laboratory, Harwell.

does at lower energies. Using the semi-classical approximation the total (σ_t) and absorption (σ_a) cross sections are then given by

$$\sigma_t = 4\pi \int_0^\infty \{1 - \exp(-\chi_2)\cos\chi_1\} b\, db$$

$$\sigma_a = 2\pi \int_0^\infty \{1 - \exp(-2\chi_2)\} b\, db$$

where

$$\chi_2 = -\frac{E}{k}\int_{-\infty}^{\infty} V_2(r)\, dz = -A\bar{\sigma}\int_0^\infty \rho(r)\, dz$$

$$\chi_1 = \lambda\chi_2 \quad \text{and} \quad r^2 = z^2 + b^2.$$

For the nucleon density distribution the form

$$\rho(r) = \frac{1}{3a^3\pi^{3/2}}\left(1 + \frac{4}{3}\frac{r^2}{a^2}\right)\exp\left(-\frac{r^2}{a^2}\right)$$

was used. This has been found by Fregeau (1956) to give a best fit to the electron scattering data using $a = 1{\cdot}635$ fermi. In order to take into account the finite range of the pion–nucleon interaction Cronin *et al.* used a value for the radius 6% larger than the electron scattering value. In order to compare our calculations directly with theirs we used $a = 1{\cdot}732$ fermi, but we have also done calculations using other values for a and we shall later discuss these briefly.

For given values of $\bar{\sigma}$, λ and a the corresponding values of σ_a and $\sigma_d = \sigma_t - \sigma_a$ were calculated. The computations were performed using a Ferranti Pegasus Digital Computer and a modified programme originally developed for proton scattering calculations.

In table 1 we give the absorption cross sections for pions on carbon at various energies as calculated by Cronin, Cool and Abashian (1957) using 'free' scattering amplitudes and the present calculations using both 'free' and 'effective' amplitudes. In table 2 the corresponding data are given for the diffraction cross section.

Table 1. Absorption Cross Sections (in mbn) for Carbon

Energy (MeV)	Cronin *et al.*	Present Work		Experiment
		free	effective	
600	216	198	221	216 ± 10
800	240	228	253	238 ± 12
970	244	232	256	252 ± 13
1200	236	224	248	246 ± 14

It should be noted that the calculations of Cronin *et al.* were made using a tapered Fermi distribution for the nucleus. This is the reason for the apparent discrepancy between their computations and ours for the absorption cross section using 'free' amplitudes, the modified-Gaussian density distribution giving lower values for σ_a. The 'effective' amplitudes however give larger values for σ_a

Table 2. Diffraction Scattering Cross Sections (in mbn) for Carbon

Energy (MeV)	Cronin *et al.*	Present Work		Experiment
		free	effective	
600	45	47	60	70 ± 16
800	60	64	81	99 ± 19
970	61	67	84	78 ± 21
1200	59	62	79	105 ± 22

and these are in good agreement with the experimental data. Using effective amplitudes a marked improvement in the agreement between theoretical and experimental values for the diffraction cross section is obtained. Previously there was a marked discrepancy between the values calculated using the optical model and the experimental data. The difference is seen to be much reduced when the 'effective' pion–nucleon amplitudes are used in calculating the optical model potential although the theoretical values are still slightly low.

This remaining discrepancy may be due to systematic errors in the experimental data. Cronin *et al.* point out that almost all systematic errors are in a direction to make the measured diffraction scattering cross section appear larger than the true value. For example the value of σ_d may be too high by 10% due to loss of the beam by multiple Coulomb scattering. The remaining difference therefore between experimental and theoretical results is probably not significant.

As a further check we have calculated the absorption cross section for lead using a Fermi distribution for the nucleus. For 970 MeV pions the free cross sections give $\sigma_a = 1619$ mbn and for the effective cross sections $\sigma_a = 1666$ mbn. The measured $\sigma_a = 1690 \pm 100$ mbn, in good agreement with the 'effective' value. Unfortunately there are no measurements of the diffraction scattering cross section.

As would be expected from the above results the calculated values for σ_a and σ_d are both sensitive to small variations in $\bar{\sigma}$, the average effective pion–nucleon total cross section. However σ_a is completely independent of the value chosen for λ, the real part of the potential, whilst σ_d is relatively insensitive as the real part is small at these energies.

The radius parameter is important in determining the absorption cross section but not the diffraction scattering cross section. At 970 MeV, changing a from 1·635 fermi (the electron scattering value) to $a = 1{\cdot}8$ fermi increases σ_a from 239·2 mbn to 263·1 mbn whilst σ_d decreases from 84·3 mbn to 81·0 mbn. Hence changing the radius parameter within reasonable limits will not give diffraction cross sections in better agreement with experimental values. Also taking the effective values of $\bar{\sigma}$ given by Bég, the best agreement for σ_a is obtained in each case with values of a slightly larger than the electron scattering value indicating that the factor 1·06 used by Cronin *et al.* to obtain the potential radius and allow for the finite range of the pion–nucleon interaction is reasonable.

To summarize, we have shown that the optical model potential for high energy pions calculated using the pion nucleon scattering amplitudes and including effects due to the Pauli principle gives values for the absorption and diffraction scattering cross sections in good agreement with experimental values.

Acknowledgments

I am indebted to Dr. M. A. B. Bég for many discussions concerning his calculations and to the Department of Scientific and Industrial Research for a Research Fellowship during the period of this work.

References

Cool, R., Piccioni, O., and Clark, D., 1956, *Phys. Rev.*, **103,** 1083.
Cronin, J. W., Cool, R., and Abashian, A., 1957, *Phys. Rev.*, **107,** 1121.
Fregeau, J. H., 1956, *Phys. Rev.*, **104,** 225.
Watson, K. M., 1958, *Rev. Mod. Phys.*, **30,** 565.

LETTERS TO THE EDITOR

The Equilibrium Distribution of N Atoms on N Sites (or in N Cells)

Several papers (for detailed references see Prigogine 1957) have been published on the equilibrium properties of a system of N atoms distributed over N similar but distinct sites or cells with multiple occupation. This problem is greatly simplified by the use of the grand partition function as follows.

Notation:

- λ absolute activity
- ϕ partition function for internal degrees of freedom and translational kinetic energy multiplied by the volume per site (or cell)
- N number of atoms and number of sites (or cells)
- Ξ grand partition function of system
- η_i Boltzmann factor for i atoms on same site (or in same cell) averaged over all positions
- r maximum number of atoms on one site (or in one cell)
- F free energy of system
- F^{E} excess free energy relative to the state of one atom on each site (or in each cell).

The grand partition function Ξ is given by

$$\Xi = \left(\eta_0 + \eta_1\xi + \sum_{i=2}^{r} \frac{1}{i!}\eta_i\xi^i\right)^N \qquad \ldots\ldots (1)$$

and the free energy F by

$$-\frac{F}{N\boldsymbol{k}T} = \frac{1}{N}\ln\Xi - \ln\lambda$$

$$= \ln\phi + \ln\left(\frac{\eta_0}{\xi} + \eta_1 + \sum_{i=2}^{r}\frac{1}{i!}\eta_i\xi^{i-1}\right) \qquad \ldots\ldots (2)$$

and the excess free energy (of disorder) F^{E} relative to the state of one atom on each site (or in each cell)

$$-\frac{F^{\mathrm{E}}}{N\boldsymbol{k}T} = \ln\left(\frac{\eta_0}{\eta_1\xi} + 1 + \sum_{i=2}^{r}\frac{1}{i!}\frac{\eta_i}{\eta_1}\xi^{i-1}\right). \qquad \ldots\ldots (3)$$

The value of the parameter ξ is determined by the condition that the average degree of occupation of each site is unity, namely

$$\eta_0 = \sum_{i=2}^{r}\frac{i-1}{i!}\eta_i\xi^i. \qquad \ldots\ldots (4)$$

In the specially simple case of $r = 2$ formula (4) reduces to

$$\frac{\eta_0}{\xi} = \tfrac{1}{2}\eta_2\xi = \left(\frac{\eta_0\eta_2}{2}\right)^{1/2} \qquad \ldots\ldots (5)$$

and formula (3) reduces to

$$-\frac{F^{\mathrm{E}}}{N\boldsymbol{k}T}=\ln\left\{1+\left(\frac{\eta_0\eta_2}{2\eta_1{}^2}\right)^{1,2}\right\} \qquad \ldots\ldots(6)$$

in agreement with Janssens and Prigogine (1950). The quantity $\eta_0\eta_2/\eta_1{}^2$, unlike the individual η's, is clearly invariant with respect to the choice of energy zero.

Department of Chemistry, E. A. Guggenheim.
University of Reading.
25th May 1960.

Prigogine, I., 1957, *The Molecular Theory of Solutions* (Amsterdam: North Holland Publishing Company), p. 136.
Janssens, P., and Prigogine, I., 1950, *Physica*, **16**, 895.

REVIEWS OF BOOKS

Physik und Chemie der Grenzflächen, II: *Die Phänomene in Besonderen*, by K. L. Wolf. Pp. ii+360. (Berlin, Göttingen, Heidelberg : Springer, 1959.) DM. 58.

This volume is the second of a trilogy on The Physics and Chemistry of Interfaces. The first deals with general phenomena whilst the third will deal with practical and applied problems in this field. The second volume here under review deals with a number of individual phenomena in detail. These fall into four main groups: I, The geometry of liquid surfaces and soap films; II, surface films on water; III, adsorption at interfaces including solid–liquid and solid–vapour interfaces; IV, mechanical phenomena such as ponderomotive effects, friction, sedimentation.

Without having had the opportunity of studying the first volume it is not possible for the reviewer to assess how far there is duplication of material and how far omissions in this volume are covered in the first. However, regarding this volume in its own light there are certain conclusions and impressions. First the author is very conscious of the difficulty of preventing such a book from becoming merely a summary of individual items, and he has made a valiant effort to overcome this. If he has not entirely succeeded this is because the basic conception of the book makes such a task virtually impossible.

The treatment tends to be formal and geometric rather than molecular. For example a great deal of detail is given to the geometry of soap bubbles and films, very little to a discussion of the underlying molecular mechanism. To some extent the same applies to the sections on adsorption where the emphasis is rather on thermodynamics, equations of state and adsorption isotherms (incidentally equation (86) is wrong). It is not surprising that, for an English reader, these sections do not measure up to the elegance of Adam's classical book. What is surprising is that the work in these sections is hardly more up-to-date than that described by Adam twenty years ago. Excepting those fields in which the author has himself been involved there does indeed seem to be a fairly large gap in the literature between 1940 and the *Proceedings of the Second International Congress of Surface Activity* in 1957.

In spite of these criticisms it is clear that a great deal of effort has gone into this book. In addition it contains many themes of interest not usually dealt with in textbooks of surface science. These include the figures generated by soap films supported on wire frames, the surface tension-forces between floating bodies, and friction and lubrication. It is right that these should appear in a textbook dealing with surface phenomena, though the English reader interested in such subjects would probably turn to more specialized monographs. The author has indeed cast his net wide: this both adds to and detracts from its value as a textbook on the physics and chemistry of surfaces. D. T.

Advances in Electronics and Electron Physics, Volume 10, edited by L. Marton. Pp. x+320. (New York : Academic Press, 1958.) $10.00.

The tenth volume comprises six reviews, the relevant author and subject indexes and in addition rather exiguous cumulative indexes for the first ten volumes. The subjects and authors of the reviews are as follows, the numbers in

brackets indicating respectively the numbers of pages and of references to original literature: Non-uniform d.c. electron flow in magnetically focused cylindrical beams, by W. G. Dow (70,12); Defects in diamond type semiconductor crystals, by E. Billig and P. J. Holmes (36, 129); Microwave optics, by J. Brown (46, 82); Developments in computer logical organization, by W. L. Lawless, (32, 21); Some aspects of tube (= radio receiving valve) reliability, by E. G. Rowe (54, 88) and Recent developments in the cathode-ray oscilloscope, by J. E. Day (61, 70).

Of these the articles by Dow and by Brown appealed to the reviewer as models of what reviews of this sort should be: clearly presented, understandable to the uninitiated and yet with enough detail to form an excellent introduction to the subject. The topics of the logical organization of computers and the reliability of valves, especially the former, seem to the reviewer somewhat less appropriate to the *Advances* than do those of the other articles; and although neither article is without interest their quality falls short of the highest standard that has been reached in this series. The use of unexplained jargon is particularly prominent in Lawless' article and one hopes that the Editor will be firmer in this respect.

J. C. E. JENNINGS.

Advances in Electronics and Electron Physics, Volume 11, edited by L. MARTON. Pp. xi + 523. (New York: Academic Press, 1959.) $15.00.

This volume contains the following articles: 1. Recent advances in photoemission, by P. Görlich [Jena], reviewing recent work in the light of semiconductor physics; 2. Parity nonconservation in weak interactions, by R. M. Sternheimer [Brookhaven], reviewing the developments which have arisen out of Lee, Yang and Wu's discovery; 3. Quantum efficiency of detectors for visible and infrared radiation, by R. Clark Jones [Cambridge, Mass.], a discussion based on a subtle and important analysis of the concept of quantum efficiency; 4. Automatic data processing in the physical sciences, by G. E. Barlow [Washington, D.C.], J. A. Ovenstone [Victoria, Australia], and F. F. Thonemann [Salisbury, S. Australia]; 5. Operational amplifiers, by R. L. Konigsberg [Silver Spring, Md.]; 6. Radio telemetering, by Henry B. Riblet [Silver Spring, Md.]; 7. Electron diffraction structure analysis and the investigation of semiconducting materials, by Z. G. Pinsker [Moscow] (translated by Lewis B. Leder); 8. Secondary electron emission of solids, by O. Hachenberg and W. Braure [Berlin].

It is seen that the Editors have spread their net wide. Not only is the range of subjects such as would be acceptable in any general series of reports on progress in physics, but also the authors are truly representative of international collaboration. All authors have apparently a bias towards referring to work published in their own or related countries: this proves the value of such spreading of contributors.

The general tone of the essays is critical and analytical, they are certainly not mere collections of abstracts, and some of them appear to make original contributions. Hence a much wider range of scientists than are appealed to by the title of this series should acquaint themselves at least with the lists of contents of these volumes lest they miss an important contribution to their subject.

The Editors should perhaps in future years keep a stricter linguistic watch on the articles submitted in English from abroad in order to prevent unnecessary obscurities from spoiling the text.

W. EHRENBERG.

Project Sherwood: The U.S. Program in Controlled Fusion, by AMASA S. BISHOP. Pp. x+216. (Reading, Mass.: Addison-Wesley Publishing Company, 1958.) $5.75. 44*s*.

In spite of the widespread interest in controlled thermonuclear fusion there are not at the moment many books available for those wishing to become more familiar with the subject. This is in part due to the fact that it began by being ' classified ' and also due to its very rapid growth during the last few years.

This account by Dr. A. S. Bishop who was intimately concerned with the early work in the United States is written as an introduction for those who wish to take their knowledge beyond that contained in popular newspaper articles and to appreciate in detail what it is all about. He writes a very clear and readable book, requiring only that minimum of scientific background which most of us possess these days, and suitable either for the layman or for physicists or engineers in other fields. He begins his survey in 1951, when the Atomic Energy Commission first started to sponsor and co-ordinate activities, and finishes it in 1958 when the work had multiplied and extended enormously, and when the basic ideas were established.

The plan of the book is largely historical which is as good a way as any in this instance of organizing the material and adds to the interest of presentation. It starts with very clear, brief and well-written chapters on fundamental principles, and on the problems of containment of hot plasma. Following this are chapters on the three major experimental methods, the pinched discharge, the Stellarator, and the use of magnetic mirrors for containment. The initial work on the three methods is first described up to the time when the lack of stability of the plasma was apparent as a major difficulty. This is followed by a discussion on stability and by later chapters first outlining its effects on each method and then bringing the story up to date.

Most of the other lines of work, too numerous to mention here, which have been pursued significantly, find their place in the book. They illustrate the immense and varied activity in thermonuclear research in the United States. This was also very evident at the 1958 Geneva Conference.

The last chapter which summarizes the present position, and views the future with rather restrained optimism, is also a well-balanced account of progress and prospects in this field. It is true, as Dr. Bishop suggests, that the progress has been substantial, and it is pleasing that no one has proved in these seven years that controlled fusion is impossible. Thermonuclear temperatures, however, are similar to the absolute zero of temperature in that progress becomes more difficult the nearer one gets. Undue optimism is therefore out of place, but we are entitled to hope for an element of luck in future experiments.

A word should be said in conclusion about the extremely good coloured diagrams which are both helpful to the reader and a pleasure to look at.

R. LATHAM.

Handbuch der Physik, Vol. 111/2, *Principles of Thermodynamics and Statistics*, edited by S. FLÜGGE. Pp. vii+678. (Berlin, Göttingen, Heidelberg: Springer, 1959.) DM. 160.

Writers on statistical mechanics frequently concentrate on its applications and like to gloss over its fundamental principles. By studying the volume under review balance can be restored, at least partly.

In an article by A. Münster (in German) the laws of thermodynamics are deduced from the mechanics (or quantum mechanics) of molecules as coherently as the present state of knowledge permits. The article starts with a survey of the ergodic theory which is presented as a branch of physics rather than of mathematics. It is followed up by a review of the modern theory of the irreversible approach of equilibrium. Only then does the author start on statistical mechanics in its usual sense. Even in this familiar field there is plenty of innovation, partly by clarifying points that were habitually left obscure, partly by including the lesser known work of contemporary authors. The article could be criticized on various counts, but it has to be regarded as an outstanding and competent account of statistical physics.

In an article on stochastic processes by A. Ramakrishnan (in English) new ground is broken. The subject is of relatively recent origin and is here presented as a branch of physics. An article of this kind was due and the present attempt should be welcomed. However, its scope might have been better adjusted. On the one hand the generalized Fourier analysis of stochastic functions is omitted. On the other hand subjects are discussed of which adequate accounts are given in other articles.

The remaining parts of the volume are written on somewhat conventional lines. A lucid article by E. A. Guggenheim (in English) deals with macroscopic thermodynamics and with the statistical theory of equilibrium. An account on irreversible thermodynamics and the semi-macroscopic theory of fluctuations (by J. Meixner and H. G. Reik, in German) has the merit of including plenty of recent work.

It is unfortunate that the axiomatics of thermodynamics are presented by the way of an original paper (by G. Falk and H. Jung, in German) without any survey of the literature. A review article would have been preferable.

The present volume can be recommended as a work of reference and, in parts, as a treatise, superior to much of existing publications. The reviewer would not, however, regard it as a modern successor to Gibbs or Tolman. A work of that calibre has yet to be written. R. EISENSCHITZ.

Lectures on Nuclear Theory, by L. D. Landau and Ya Smorodinsky. Pp. vi + 108. (New York : Plenum Press; London : Chapman and Hall, 1958.) 45*s*.

This little book is based upon ten lectures delivered by Academician Landau in Moscow in 1954. In the foreword the authors explain " that the presentation makes no pretence at completeness and that the choice of subject matter is purely arbitrary ". There are, in fact, three lectures on nuclear forces, three on nuclear structure, two on nuclear reactions, and two on π-mesons and their interactions with nucleons. The treatment throughout emphasizes the qualitative aspects of the subjects treated. This being the case, a few more diagrams might have brought more life into the discussion. The treatment of stripping reactions, for example, seems singularly lifeless, which is a pity when their essential features can so readily be seen with the aid of a few diagrams. On the other hand, this is perhaps the only book of its kind which attempts to give proper place to the collective picture of nuclear structure. As an introduction to some topics of interest in nuclear physics in 1954 the book makes good reading; but it is now 1960 and much of the interest has changed. B. H. FLOWERS.

Mécanique Quantique, Vol. II, by A. MESSIAH. Pp. xvii + 541. (Paris: Dunod, 1960.) 4.800 *fr*.

I recall that my review of the first volume of Dr. Messiah's exposition of quantum mechanics showed a mixture of admiration and doubt: admiration that he should have found a new and essentially modern way of presenting the subject, doubt as to whether it was not asking rather too much of the student, or at least of the British student who has received a less adequate mathematical training than his French counterpart. Having now studied the second volume, the doubt remains; but the admiration is increased to the point at which I feel that there must be something wrong with our system of teaching if we cannot teach quantum mechanics in this way to those of our students who are specializing in theoretical physics.

The first volume dealt in the main with the formalism of quantum mechanics and rather little with applications except to the simplest of systems. It seemed rather a lot of formalism for the student to have to swallow before he had seen the need for much of it. The second volume is much more concerned with applications and to it, therefore, this criticism does not apply. It begins with some chapters on angular momentum, including one on the addition of angular momenta which gives a brief, but useful, introduction to the Racah coefficient and the properties of tensor operators as expressed by the Wigner–Eckart theorem. There follow some chapters on systems of identical particles and on the symmetry properties of the Hamiltonian treated from an elementary group theoretical standpoint. This includes a very useful discussion of time reversal. Afterwards come perturbation theory, the variational method, and scattering theory. It was no surprise to find that Green's function methods were used for much of this. The final part of the volume deals with relativistic quantum theory, the Dirac equation and a first introduction to field quantization. Many applications are worked out fully in the course of the work, and many further ones, some of them perhaps unnecessarily formal, are given at the end of each chapter as exercise for the reader.

There is no doubt that the contents of this great work ought to be mastered by every postgraduate research student in theoretical physics. I hope that it will very soon appear in English translation, for to my knowledge there is no other book like it.

B. H. FLOWERS.

Fluid Mechanics, by L. D. LANDAU and E. M. LIFSHITZ. Translated by J. B. SYKES and W. H. REID. Pp. xii + 536. (London, Oxford, New York, Paris, Los Angeles: Pergamon Press, 1959.) 105*s*.

The remarkable nine-volume *Course of Theoretical Physics* by Professors Landau and Lifshitz includes as its sixth volume this treatise on *Fluid Mechanics*. The clearness and accuracy of the authors' treatment of other parts of theoretical physics is well maintained in this account of the fluid-mechanical parts. To be sure, the book is strictly theoretical; there are no references at all to experimental techniques (for example, to wind tunnels or Pitot tubes), and rather few to experimental results; the authors expound the subject in a deductive manner, showing their very substantial knowledge of the experimental background principally by selecting for exposition those theories which correspond well with it! Again, the book is strictly physical, as opposed to technological; there is no account of fluid-flow machinery or of aeronautical applications of fluid mechanics.

However, to cover adequately what is left, the theory of the basic physical phenomena of fluid mechanics, in 530 pages, is a notable achievement. This has been helped by a tight organization into chapters as follows: Ideal fluids (46 pp.), Viscous fluids (55 pp.), Turbulence (43 pp.), Boundary layers (38 pp.), Heat transfer (36 pp.), Diffusion (11 pp.), Surface phenomena (15 pp.), Sound (65 pp.), Shock waves (37 pp.), One-dimensional gas flow (52 pp.), Intersection of surfaces of discontinuity (23 pp.), Two-dimensional gas flow (35 pp.), Flow past finite bodies (17 pp.), Fluid dynamics of combustion (25 pp.), Relativistic fluid dynamics (8 pp.), Dynamics of superfluids (16 pp.), Fluctuations in fluid dynamics (7 pp.). The treatment is similar to that in good Western textbooks of a not intensively specialized kind, except for the inclusion of the last three topics, giving the relativistic corrections to the equations of motion, the 'two-fluid' theory of liquid helium II, and the application of thermodynamic fluctuation theory to the problem of determining what fluctuation of macroscopic quantities in given macroscopic fluid motions results from the discreteness of molecules.

All the above topics are excellently treated, except possibly 'Surface phenomena', where some treatment of cavitation, and probably also of the stability of jets or sheets of liquid, would have been desirable, even in a physical text. It is perhaps a pity, too, that rotating fluids, secondary flows and the like, with their wide meteorological and hydrographical applications, were not mentioned. But these are very minor criticisms of an outstanding expository work, one of whose most useful functions will be to introduce theoretical physicists to modern fluid mechanics.

M. J. LIGHTHILL.

Semiconductors, by R. A. Smith. Pp. xvii+494. (Cambridge: University Press, 1959.) 65*s*.

This book starts with a brief historical survey and an outline of the elementary theory of semiconductors. The band theory of solids and the effective mass of charge carriers are then dealt with in a formal manner, followed by an account of crystal imperfections and excitons. The next chapter discusses the Fermi distribution and the theory of the charge-carrier concentration as a function of temperature. The theories of electrical conductivity, scattering mechanisms, Hall effect and magnetoresistance are then dealt with in terms of the band theory at a fairly advanced level. The discussions of thermal conductivity, thermoelectric power and thermomagnetic effects, optical absorption and magneto-optical effects are at a similar level.

The effects of inhomogeneities in carrier concentration are then discussed, leading to a consideration of carrier diffusion, injection and extraction, the properties of p n junctions, contacts and surfaces, and carrier recombination processes.

The theoretical sections outlined above comprise about three-fifths of the book. They are presented in a very clear and well integrated manner, and give a thorough and up-to-date account of all the important aspects of the fundamental physics of semiconductors.

The remainder of the book deals with methods for determining the main parameters of a semiconductor, the properties of the semiconducting elements, and in less detail, of some of the compound semiconductors. There is a final short chapter on the applications of semiconductors.

The book is well produced and indexed, and the important references to the literature are quoted. The book should prove of great value to undergraduates when solid state physics is included in a physics honours course, to postgraduate students taking a specialized course in this subject, and to research workers in all aspects of semiconductor and solid state physics. The electronic engineer who wishes to learn some of the fundamentals of semiconductors may however find the earlier part of the book rather heavy going. D. A. WRIGHT.

Quecksilber-Niederdruck-Gasentladungen, by M. J. SCHÖNHUBER. Pp. viii + 111. (München: HochschuleBuchhandlung Lachner, 1958.) DM. 18.

The greater part of this monograph is a dissertation on low pressure mercury arcs submitted by the author to the Technische Hochschule at Munich in 1956. Short accounts of the work have been published previously. The present volume contains a wealth of data obtained by use of Langmuir probes. A large number of semi-logarithm current-voltage plots are reproduced, which will enable the reader both to assess the validity of Dr Schönhuber's deductions, and to carry out alternative analyses of the data if he wishes. The most interesting results obtained are perhaps the conditions for establishment of double space-charge sheaths normal to the axis of a tube, between plasmas, and the related conditions for occurrence of a uniform column. In both instances, the results appear very similar to those obtained by Dr. R. L. F. Boyd and his collaborators by another, probably more accurate, method of probe analysis in somewhat different discharges. It is clear from both groups of researches that there are many low-pressure plasmas in which the energy distribution of the electrons is markedly different from the Maxwellian. The author has done a service to other workers in the field by making his results available in such detail. One wishes that it were possible to publish many other good dissertations in their entirety.

K. G. EMELEUS.

Éléments des Calculs d'Interpolation, by D. COT. Pp. 140. (Paris: Publications Scientifiques et Techniques du Ministere de l'Air, Bulletins des Services Techniques, No. 123, 1959.)

The book is an exposition of the more important ideas and uses of finite differences; most of it concerns interpolation in equal-interval tables but the general formulae of Newton and Lagrange are used as the basis from which to obtain the familiar formulae of Newton, Stirling, Gauss, Bessel and Everett for equal intervals. There are also a short chapter on numerical differentiation and two on integration, the formulae being obtained primarily from the interpolating polynomials, although some use is made of operator methods. Half the book is given to interpolation in double-entry tables, that is, functions of two variables; with a small amount on functions of three variables.

The pace is leisurely and the text very clear; there are many algebraic formulae (some so complicated as to be virtually unusable) but no great number of numerical examples, and the mathematical level is quite elementary; the use of automatic computers is not even mentioned. In all, a collection of derivations of known results with nothing new, either in content or comment.

J. HOWLETT.

The Electric Arc, by J. M. SOMERVILLE. Pp. ix + 150. (London : Methuen; New York : John Wiley, 1959.) 12*s.* 6*d.*

The electric arc was so called, in the early days of electrical science, because of the characteristic arched shape exhibited by the high current discharge between electrodes in the air, a shape brought about by the intense heat developed and the resulting thermal convection.

Today the term is extended to include all high current low voltage discharges between electrodes and the subject is of great technical importance. The arc is used in a wide variety of forms as a light source, for high intensity ' point ' sources, for low intensity diffuse sources, as a source of characteristic line spectra and as a quasi-black-body radiator at stellar temperatures. It is used too, in current rectification, in switching, welding and in chemical synthesis. It occurs as a nuisance in contact switches and in dielectric breakdown and it plays an important part in nuclear fusion research.

Of course the little monograph under review cannot even touch on all of these applications or discuss any of them in full. Instead it presents a very readable account of the processes occurring in the conducting column and at the electrodes of arcs, of the initiation and stages of growth from spark, glow or separating electrodes. It must be admitted that it sometimes reads more like natural history then physics (Poisson's equation does not once occur explicitly), but this is partly a symptom of the uncertainties still common in the subject, and the fault, if fault it be, is amply redeemed by the extensive bibliography.

The book is intended for the non-specialist. It will not be understood by those who are not at home with physics. On the other hand it may well make specialists of those who are, for it introduces the reader to many intriguing and challenging problems and gives a tantalizing glimpse of the extensive armoury of techniques, with which to attack them. R. L. F. BOYD.

Principles of Electricity and Magnetism, by Y. ROCARD. Pp. x + 779. (London: Sir Isaac Pitman, 1959.) 70*s.*

767 pages of principles for 70*s.* seems to be a good bargain, and in many respects this book is a remarkably good bargain. A tremendous lot of work must have gone into the writing of it and the translator has accomplished his immense task very well. And yet there is something very unsatisfactory about the whole work.

The title is misleading. Professor Rocard is not really interested in principles; he is interested in details and in apparatus. It is true that he writes on electrostatics for almost 100 pages, but the treatment is dull and heavy. Only one chapter compels attention and that is the one dealing with thunderstorms. Then follow 50 pages on magnetism. Once again the principles are stated in a rather pedestrian manner, and the professor seems to be more interested in the technical details of loudspeaker magnets and of high permeability alloys.

The discussion of current flow is not profound except for an interesting speculation on the transference of energy by electric charges. It is clear, however, that the professor is much more intrigued by methods of prospecting for oil by electrical means and he gives a gruesome discussion of the 'electric chair'. Faraday's law of electromagnetic induction is derived rather unsatisfactorily from virtual work considerations, but motional e.m.f.'s are treated in great detail.

Then follows a breathless treatment of electrical machines. First there are d.c. motors and generators including the amplidyne. There is a note on Ward–Leonard equipment and remote position control. Then follow transformers, synchronous machines, induction motors, hysteresis motors, repulsion motors and selsyns. Even in a book of this size there is no hope of explaining the operation of these devices. The treatment is terribly sketchy.

But more is to follow. Transmission lines, waveguides, radio aerials, electron optics, x-rays, travelling-wave tubes, magnetrons, transistors, plasma oscillations. Interspersed with all this there is a lot of mathematics and for good measure a chapter on systems of units. Surely this is no book of principles, but a one-volume encyclopaedia. The reader who buys it as such will get much pleasure from it. But if he wants a book on the principles of electricity and magnetism he would be well advised to look elsewhere. P. HAMMOND.

Studies in Crystal Physics, by M. A. JASWON. Pp. 46. (London: Butterworths Scientific Publications, 1959.) 10*s.* 6*d.*

This little book is a reprint of five articles from *Research*. The first four set out some of the consequences of the existence of crystal structure—the formal geometrical limitations and the physical principles controlling twinning and coherent phase changes, and the nature and diffraction properties of imperfections. The last is an elementary account of the thermodynamics of phase changes and transition rates. The book seems to the reviewer to fall between two stools—it is not a textbook or bibliography to any of the subjects, nor does it have a coherent thread of treatment which justifies binding them up as one book. The articles were far better suited to their original milieu, where they may well have caught the casual interest of some people unfamiliar with crystals. W. M. LOMER.

Himmelsmechanik, Vol. I, by K. STUMPFF. Pp. 508. (Berlin: Deutscher Verlag der Wissenschaften, 1959.) DM. 56.80.

The dramatic emergence of space rockets and artificial satellites around the earth in the past three years has once more focused attention on the celestial mechanics—a time-honoured branch of astronomy, which the cumulative efforts of theoretical astronomers in the past 250 years (from Newton, Euler, Lagrange, Gauss to Poincaré, to name only the greatest) have gradually developed to a degree of exactitude rendering it pre-eminent in the whole domain of exact sciences. It is true that, in our generation, celestial mechanics for a time rather ceased to be 'à la mode', and had to yield its traditional place in educational curricula of our universities to other branches of astronomical science, promising more immediate rewards. As a result, most standard texts and compendia on celestial mechanics (Tisserand, Charlier, Poincaré, Andoyer) were written and published more than fifty years ago; and although excellent and of lasting value, they are no longer readily accessible to readers without access to established professional libraries.

The book under review attempts to make good—and successfully so—the gap thus arising in the German scientific literature, and its timely appearance should be welcomed by all students of the subject who possess a reading knowledge of German. It constitutes the first volume of a more extended work, devoted to a thorough outline of the problem of two bodies, and of methods

for determination of planetary or cometary orbits based upon it. As such it encompasses fewer topics than the earlier and well-known treatises by Moulton or Smart; but it expounds them in more detail, and in a leisurely discursive style which should make the book particularly attractive to undergraduates. It can certainly hold its place side by side with Moulton's text (whose German translation, made from an earlier edition, is much more sketchy in the topics treated presently by Stumpff), and is likely to become popular with those users who are interested in the theory of the two-body problem mainly as a basis for applications. ZDENĚK KOPAL.

Introduction to Matrix Analysis, by RICHARD BELLMAN. Pp. xx+328. (New York, Toronto, London: McGraw-Hill, 1960.) 77*s.* 6*d.*

A thorough knowledge of matrix theory is now indispensible to research workers in many branches of applied mathematics, physics and engineering, but most relevant textbooks treat the subject from the stand-point of the algebraist. In this book the author has endeavoured to meet the requirements of those using matrix theory as a tool.

The book is divided into three main sections which are concerned with symmetric matrices and the related theory of quadratic forms, the theory of differential equations and a study of positive matrices. In addition to a treatment of the standard canonical forms there are excellent chapters on the Courant–Fischer min.–max. theorem, matrix inequalities and Perron's theorem on positive matrices. The proof of the Courant–Fischer theorem is unfortunately marred by several errors, the cumulative effect of which may be somewhat disconcerting. The canonical forms are introduced in a way which underlines their practical value; the Jordan form, for example, is related directly to the explicit solution of a system of ordinary differential equations with constant coefficients.

For information on such a wide field one would normally need to consult several books, and even then would be unlikely to find presentations which catered so well for the needs of the practical man. Each chapter includes an excellent collection of exercises, many of which cover results of considerable importance. There is an extensive bibliography which includes most of the relevant papers published in the last ten years. The author writes in a popular style which some may find a little irritating at times. For my part I found the book very stimulating and I am sure numerical analysts in particular will welcome this addition to the literature. J. H. WILKINSON.

Plasma Physics and the Problem of Controlled Thermonuclear Reactions, Vol. III, edited by M. A. LEONTOVICH. Pp. 422. (London, New York, Paris, Los Angeles: Pergamon Press, 1959.) £8.

This series of four volumes, of which Volumes II and III have now appeared, contains translations of papers on hitherto unpublished work done in the U.S.S.R. on the general problem of controlled thermonuclear fusion. They cover the period from 1951 to 1958 and therefore form part of the background to the material reported in 1958 as part of the Proceedings of the 3rd Geneva Conference.

It is not possible in a short review to make many useful comments on the papers themselves. There are twenty-six of them in this volume dealing with a wide range of topics on fusion research. Some of the papers are accounts of experimental work, but most have a strong theoretical basis.

As a brief though inadequate guide to the contents the following may be chosen for mention:

(*a*) *Theoretical*—work on the Boltzmann distribution function for low density plasma in a magnetic field, recombination radiation, heat transfer by radiation, cyclotron radiation, electromagnetic fields for heating and containing a plasma.

(*b*) *Theoretical but with practical bias*—basic work on magnetic mirrors relevant to machines, the problems of stability, the properties of various cusped fields for plasma containment, and detailed calculations on the linear pinched discharge (called rather strangely ' the theory of rapid processes ').

(*c*) *Experimental*—pressure measurements in discharges by the piezo effect, and a study of the behaviour of a ring current in a betatron-like magnetic field.

The papers are in general of a high level of sophistication being the equivalent of research reports. They were obviously written in the first place for the specialist in the thermonuclear and allied fields, though including many basic matters of interest to those working on plasmas in any context. The present reviewer found the papers mathematically rather difficult.

This volume contains no review or survey papers which might be used by the general reader for information on the state of the subject in the U.S.S.R.

No one engaged in the work, however, can fail to be impressed by the high standard of the papers and by the extent and scope of the Russian effort on the thermonuclear problem. The four volumes together will form a scientific account of this work which will be of the utmost value in plasma physics.

R. LATHAM.

The Unity of the Universe, by D. W. Sciama. Pp. 186. (London: Faber and Faber, 1959.) 21*s*.

After a concise account of the observed universe, Dr. Sciama presents an account of cosmological theory from the standpoint that the ' unity of the universe ' may require local phenomena as, for instance, the light of the night sky or the inertia of massive bodies to depend upon very large-scale features of the universe and, moreover, that features of the actual universe as, for instance, the masses of the galaxies or the abundances of the elements, should be uniquely predictable by the theory. He seeks, in fact, " a theory which describes all that actually happens, and nothing that does not, a theory in which everything that is not forbidden is compulsory ".

About this general aim, there is probably less difference of opinion than Dr. Sciama implies. About the means of achieving it, he is himself well known for the suggestions he has made, but here there is probably more difference of opinion than he implies. This difference is based partly on customary scientific grounds, particularly regarding the extent to which observers have discovered " at least the main outlines of the whole universe ". It is astonishing to read that " most astronomers believe . . . they have indeed done just this " (p. 19). When astronomers speak as though they do, it is because only by making some such hypothesis they can speak at all; it is naïve to suppose they are committing themselves to a *belief*. The difference depends also upon the fact that a ' theory ' such as that considered in the above quotation is conceptually farther removed from anything that has hitherto been achieved in science than is evident from Dr. Sciama's discussion.

Those who are prepared to ponder on the problems concerned will find in this book much to stimulate their thoughts.

W. H. McCrea.

Figure 1. Reflection pattern obtained from a thin deposit of TlCl (NaCl type) on a (110) etched surface of KBr at 220 c. The outer arced spots are due to the deposit, the inner spots to the KBr base. Parallel orientation [1$\bar{1}$0] azimuth.

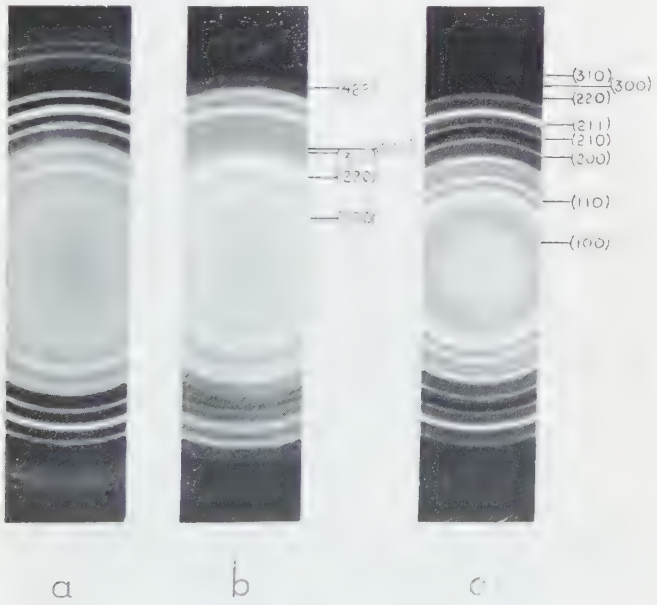

Figure 2. Transmission patterns obtained from TlCl deposited on to a polycrystalline film of KI at room temperature. (*a*) Ring pattern from the KI film. (*b*) Pattern from 120Å of TlCl (NaCl type) deposited on the base. The rings of TlCl are indexed. (*c*) Pattern from 200Å of TlCl deposited on the base; the rings of normal TlCl are indexed.

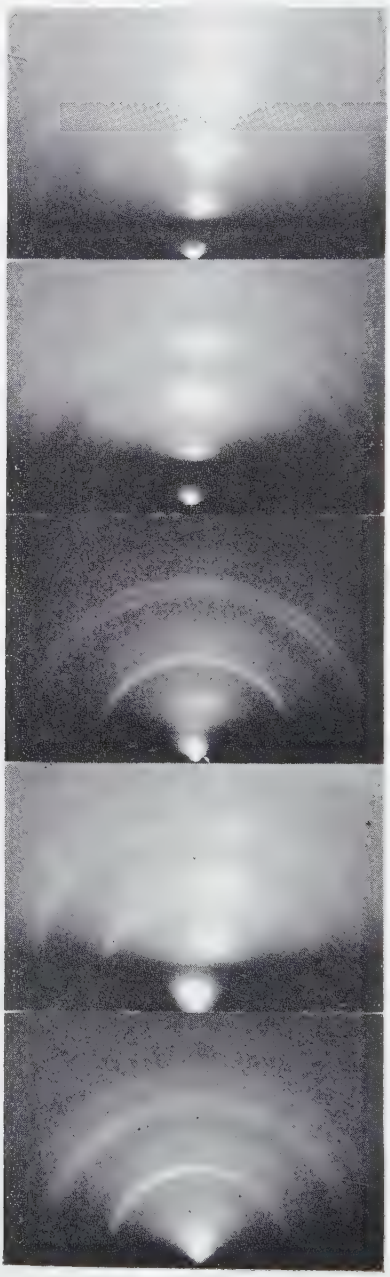

Figure 1. Graphite abraded (right to left) at 200 g load on: (*a*) filter paper, (*b*) 0000 emery, (*c*) 00 emery, (*d*) as (*c*) but sub-surface region, (*e*) 1 emery.

Plate I

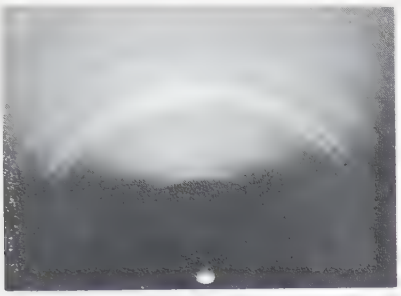

Figure 2. Graphite abraded (left to right) at 10 kg load on 000 emery

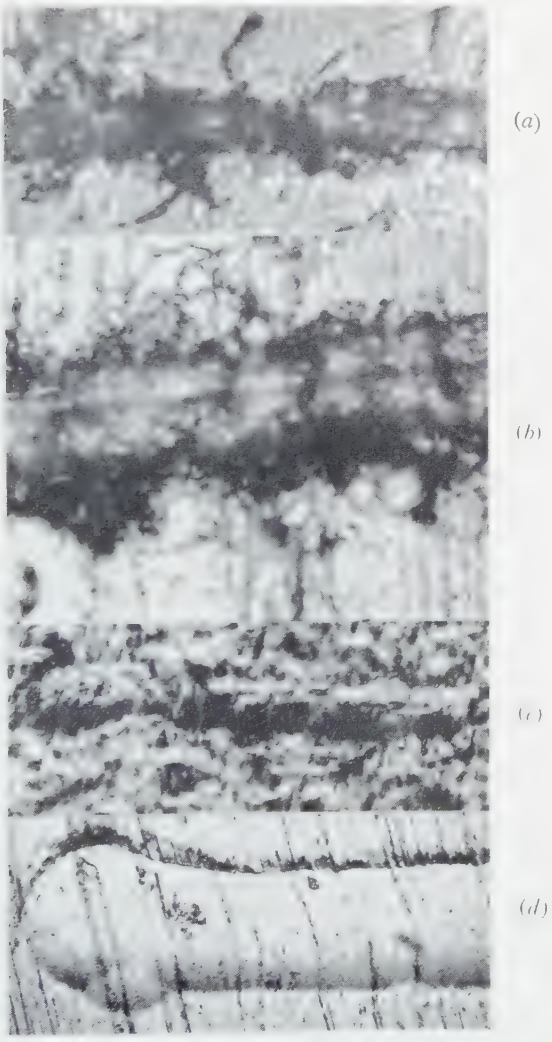

Figure 3. Micrographs of wear grooves produced by (*a*) 0000 emery on graphite (×940) (*b*) 0 emery on graphite (×940), (*c*) ' Scotchlite ' on graphite (×310), (*d*) ' Scotchlite ' on silver (×570).

Plate II

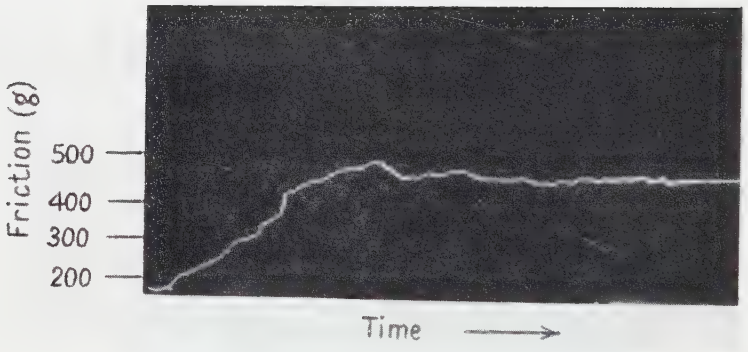

Figure 5. Friction trace for graphite sliding on 1 emery paper.

The Origin of the Characteristic Electron Energy Losses in Ten Elements

By C. J. POWELL†

Department of Physics, University of Western Australia,
Nedlands, Western Australia

Communicated by C. J. B. Clews; MS. received 12th January 1960, in revised form 27th April 1960

Abstract. Measurements have been made of the characteristic electron energy loss spectra of beryllium, antimony, bismuth, germanium, tin, cadmium, copper, platinum, lead and calcium using the reflection technique and with 750 ev and 1500 ev primary electrons. The spectra of each element were found to consist almost entirely of combinations of two fundamental energy losses which were identified as plasma and lowered plasma losses. A striking correlation between the lowered plasma losses and the corresponding calculated values of $\hbar\omega_p/\sqrt{2}$ was observed (ω_p is the plasma frequency), and it is suggested that the magnitude of the lowered plasma loss may be useful as an indication of the effective free electron density. If the specimen oxidized appreciably, the intensity of the lowered plasma loss decreased rapidly and a new modified lowered plasma loss appeared. It is considered that the present results are characteristic of clean metal surfaces and that many of the discrepancies in past work can be explained by the presence of surface contaminants.

§ 1. Introduction

An unsatisfactory feature of the many measurements of the characteristic electron energy losses in solids (Marton, Leder and Mendlowitz 1955) has been the wide disagreement in the results of different workers, and even of the same worker at different times. Possible reasons for such discrepancies have been discussed by Marton (1956) who has suggested that specimen impurities and certain instrumental effects may lead to erroneous or varying results. While all of the factors proposed by Marton are important, it would seem that the main reason for large differences in results has been the effect of (unknown) variations in specimen composition.

It has been found from previous work in this laboratory that the loss spectra of aluminium (Powell and Swan 1959a), magnesium (Powell and Swan 1959b) and aluminium-magnesium alloys (Powell 1960a) consisted entirely of combinations of two elementary energy losses, one of which was identified as the plasma loss (Pines and Bohm 1952, Pines 1956, Nozières and Pines 1958, 1959) and the other as a lowered plasma loss (Ritchie 1957). These results were obtained using a reflection technique; that is, by the energy analysis of electrons scattered from the surfaces of evaporated specimens. The effects of surface oxidation and contamination by the specimen support, practically unavoidable when the losses

† Now at the Department of Electrical Engineering, Imperial College of Science and Technology, London, S.W.7.

of electrons transmitted through thin films are being measured, could be eliminated by frequent evaporations of a sufficiently thick layer of specimen material. Further investigation (Powell and Swan 1960) has shown the considerable and significant effects of surface oxidation on the characteristic loss spectra of aluminium and magnesium. It was found that slight surface oxidation caused the rapid disappearance of the lowered plasma loss and the appearance of a new modified low-lying loss in each element. The latter loss eventually disappeared as oxidation proceeded, indicating that it was a metal loss which occurred only when a surface layer of oxide was present. It would seem likely that the presence of a substrate in transmission measurements of the energy losses would have a similar effect on the loss spectra.

In view of the frequent disagreements in the measurements of the loss spectra of many materials, it was considered desirable to make new determinations of the characteristic losses with the reflection technique and with specimens of high purity. Two groups of elements have been studied: those elements where the previously measured energy losses could be identified as arising from plasma excitation and those where the energy losses could only be qualitatively associated with plasma excitation (Nozières and Pines 1958, 1959).

§ 2. Origin of the Characteristic Losses

Pines and co-workers have suggested that the prominent energy loss in metals is due to the collective excitation of the conduction electrons in a conduction electron–ion core plasma. The fundamental energy loss is given in terms of $\hbar\omega_p$ where ω_p, the free electron plasma frequency, is equal to $(4\pi ne^2/m)^{1/2}$ and n is the free electron density. In a given solid, the observed energy loss may differ from $\hbar\omega_p$ on account of interband electronic transitions and the polarizability of the ion core. If the binding energies of the valence electrons are small and the binding energies of the core electrons are large compared with $\hbar\omega_p$, the observed energy loss should be close to $\hbar\omega_p$ (where n is calculated from the number of valence electrons per atom) and the half-width of the loss peak should be small compared with $\hbar\omega_p$. In other metals (such as the transition metals), there may be a considerable difference between the observed energy loss and $\hbar\omega_p$, and the half-width of the loss peak may be of the same order as $\hbar\omega_p$.

The close relationship between the characteristic losses in a solid and its optical properties has been pointed out by Marton, Leder and Mendlowitz (1955), Fröhlich and Pelzer (1955), Hubbard (1955) and Nozières and Pines (1959). These authors have found that the characteristic losses can be interpreted in terms of the frequency dependence of the complex dielectric constant $\epsilon(\omega)$ and that the electron energy absorption should be proportional to $\mathcal{I}\epsilon/|\epsilon|^2$. Mendlowitz (1960 a, b) has recently been able to correlate the measurements of the characteristic losses and of the optical transmittivity in several elements with this model; it can be shown that a material should become transparent, with increasing frequency, at ω_p. Nozières and Pines (1959) have further demonstrated that the characteristic loss spectrum can be compared with the optical absorption spectrum. Such a comparison should clearly indicate the origin of a particular energy loss, as a loss peak in the characteristic loss spectrum due to plasma excitation should not appear in the optical absorption spectrum at the corresponding absorption energy.

Rudberg and Slater (1936), Watanabe (1954), Leder, Mendlowitz and Marton (1956), Gornyi (1958) and Viatskin (1958) have proposed that the characteristic

losses are predominantly due to individual interband electronic transitions. In support of this hypothesis, Leder *et al.* have found some degree of correlation between the characteristic losses of a number of elements and the corresponding displacements of the absorption maxima from the K edge in the x-ray absorption spectra, while Gornyi and Viatskin have found a correlation between the estimated and observed values of the characteristic losses in some elements and compounds. It should be noted, however, that Ferrell (1956), Pines (1956) and Nozières and Pines (1959) have shown that an absorption peak at $\hbar\omega_p$ on the high-energy side of the x-ray absorption edge would be expected to be observed in the x-ray absorption spectra. Pines has also shown that energy loss by plasma excitation should predominate over energy loss due to interband transitions for small scattering angles.

Ritchie (1957) and Stern and Ferrell (1960) have shown that the effect of the specimen boundary would be expected to cause a decrease in intensity of the plasma loss and the appearance of an additional lowered plasma loss either at $\hbar\omega_p/\sqrt{2}$ or at $\hbar\omega_p/\sqrt{3}$, depending on whether the specimen is represented as a plane, parallel-sided film or as being made up of spherical grains. Ritchie has found that the ratio of the intensity of the plasma loss to that of the lowered plasma loss should decrease with decreasing values of the parameter $t = a\omega_p/v$, where a is the average distance travelled by the electrons in the specimen and v is the primary electron velocity. If a is assumed to vary with primary electron energy in the same manner as the electron range (Feldman 1960), the lowered plasma loss should become more prominent with respect to the plasma loss in a reflection-type experiment with decreasing primary energy. Stern and Ferrell (1960) have found that the lowered plasma loss should be extremely sensitive to the presence of surface films on the specimen (for example: oxide, carbonaceous contamination, or the specimen support). These authors have shown in particular that surface oxidation of an aluminium film should lead to the rapid disappearance of the $\hbar\omega_p/\sqrt{2}$ loss and to the appearance of a modified low-lying loss at about 6·5 ev. This prediction has been confirmed by experiment (Powell and Swan 1960). In general, the position of a low-lying loss would be expected to be modified by the presence of any surface contaminant. It can be concluded that identification of a lowered plasma loss by the experimental observation of its properties also indicates that the plasma-type loss does in fact arise from plasma excitation.

§ 3. Experimental Procedure

All specimens were prepared by rapid evaporation from tungsten or tantalum heaters, as indicated in table 1, onto a substrate at room temperature. The evaporation time was made short in order to reduce agglomeration; it was estimated that films of the order of 50 to 100 Å in thickness were deposited in a few seconds. With the more reactive metals it was necessary to 'getter' the chamber with a number of preliminary evaporations in order to obtain reproducible results. The pressure in the system was normally less than 5×10^{-6} mm Hg except during evaporations when it was less than 5×10^{-5} mm Hg.

A characteristic loss spectrum could be recorded in a few minutes by analysing with a 127° electrostatic electron spectrometer the energy distribution of electrons scattered by the target through 90°. The apparatus has been described in detail elsewhere (Powell, Robins and Swan 1958, Powell and Swan 1959a, Powell 1960b). Measurements were generally made with primary electron energies of

Table 1. Details of the Minimum Purity, the Supplier, and the Method of Evaporation of each Element

Element	Purity (%)	Supplier	Method of Evaporation
Be	99·97	JM	Ta boat, W basket
Sb	99·95	The Associated Lead Manufacturers Export Co. Ltd.	W basket
Bi	99·975	Mining and Chemical Products Ltd.	W basket
Ge	99·999	JM	W basket
Sn	99·998	JM	Ta boat, W basket
Cd	99·98	Imperial Smelting Corporation Ltd.	Ta boat, W basket
Cu	99·999	JM	W basket
Pt	Commercial	JM	W filament
Pb	99·998	JM	Ta boat, W basket
Ca	unknown	unknown	W basket
Li	98 (?)	unknown	W basket

JM, Johnson, Matthey and Co. Ltd.; Ta boat, evaporation from a tantalum boat; W basket, evaporation from a conical basket of tungsten wire; W filament, evaporation from a helical tungsten filament.

750 and 1500 ev in order to observe possible variations in the relative intensities of the energy losses. The probable error for each measured characteristic loss at each primary electron energy was obtained by adding an estimated probable error in the energy calibration procedure of 0·07 ev to $0{\cdot}6745\sigma/M^{1.2}$, where σ is the standard deviation of the single measurements about their mean and M is the number of measurements. The quoted errors in the final mean energy losses and in the quantum energy losses were calculated from the individual errors in the standard manner.

§ 4. Results

4.1. *Beryllium*

The normalized beryllium characteristic loss spectra are shown in figure 1 and the mean energy loss values are given in table 2 together with a summary of the measurements of other workers. It is seen that the loss spectra are comprised of a 11·9 ev low-lying loss and multiples of a prominent 19·9 ev loss. The 19·9 ev loss agrees well with other results (considering that the mean energy losses in a reflection experiment are higher than those measured in the forward direction on account of the dispersion of the energy losses with scattering angle (Watanabe 1956)), and is interpreted as arising from plasma excitation. The 11·9 ev low-lying loss disappeared with surface oxidation and was replaced by a modified low-lying loss of $7{\cdot}9 \pm 0{\cdot}1$ ev. Further oxidation resulted in the disappearance of both the 7·9 and 19·9 ev losses and the appearance of a single broad loss of $23{\cdot}8 \pm 0{\cdot}2$ ev. The 6·5 ev loss observed by Marton and Leder (1954) could probably be due to the presence of oxide as a similar loss in beryllium oxide has been observed by Watanabe (1956) and by Jull (1956).

4.2. *Antimony*

The normalized antimony loss spectra are shown in figure 2 and the loss values in table 3. The intensity scales for the spectra in figures 2 to 6, 8 and for the spectrum of lead in figure 9, have been adjusted so that the peak of elastically scattered electrons has an intensity of 50 units in each case. The spectra show a prominent energy loss of 15·9 ev, a low-lying loss of 11·3 ev, a combination of the

Table 2.† Characteristic Energy Losses of Beryllium (ev) found in the Present Work and by other Authors

Present Work		11·9 ± 0·2 (39)	19·9 ± 0·2 (56)		39·4 ± 0·3 (21)	58·4 ± 0·4 (3)		
Ruthemann (1948)			18·97		38·11	57·31		75·98
Marton and Leder (1954)	6·5		18·9					
Kleinn (1954)			17·3		36·7	54		
Watanabe (1954)			19		38	56		76 (?)
Jull (1956)			19·0		40·0	59·5		
Gauthé (1956)			19·1		39			
Gauthé (1958)			19	28	38·1			

Table 3. Characteristic Energy Losses of Antimony (ev) found in the Present Work and by other Workers

Present Work		11·3 ± 0·2 (26)	15·9 ± 0·2 (34)	26·5 ± 0·5 (7)	32·3 ± 0·3 (23)	47·9 ± 0·3 (16)
Mollenstedt (1949)			15	20	31	
Marton and Leder (1954)			14·2	24·3		
Leder and Marton (1954)	4·3		14·9		30·6	
Watanabe (1954)	6·5		18	24·5		46
Leder (1956)	5·3		15·6		30·2	
Gauthé (1959)			15·0		29·8	

Table 4. Characteristic Energy Losses of Bismuth (ev) found in the Present Work and by other Authors

Present Work	9·9 ± 0·2 (22)	14·7 ± 0·2 (26)	24·8 ± 0·2 (17)	29·0 ± 0·2 (14)		
Marton and Leder (1954)		13		25·2		
Fert and Pradal (1958)		15		30	45	60

† In tables 2 to 11, the quoted errors in the new measurements are the probable errors of the mean, and the figure in parentheses after each value is the number of observations associated with that mean.

two losses, and two multiples of the 15·9 ev loss. The 15·9 ev loss agrees with previous energy loss measurements, except for that of Watanabe (1954, 1956), and also with the onset of optical transmission at 15·0 ev measured by Rustgi, Walker and Weissler (1959). Surface oxidation led to the disappearance of the 11·3 ev loss and to the appearance of a new loss of $7{\cdot}0 \pm 0{\cdot}2$ ev. It is possible that this latter loss corresponds with the loss of 6·5 ev observed by Watanabe (1954, 1956), thus indicating that his 18 ev loss may also be due to oxide, and with the 6·8 ev loss observed by Leder (1956) in antimony trioxide.

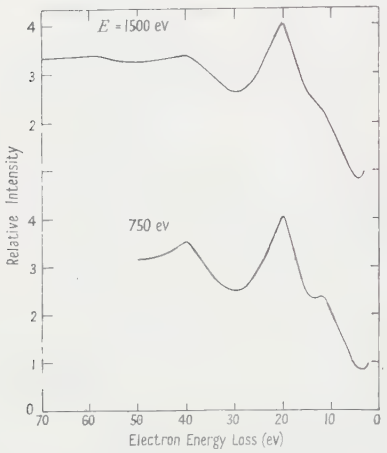

Figure 1. Characteristic loss spectra of beryllium for primary electron energies of 750 and 1500 ev. The spectra have been normalized for equal intensities of the 19·9 ev peak.

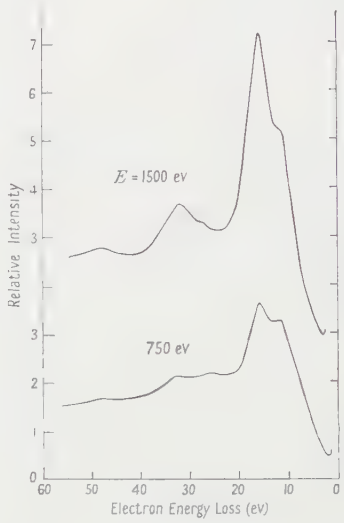

Figure 2. Characteristic loss spectra of antimony for primary electron energies of 750 and 1500 ev.

4.3. *Bismuth*

The bismuth spectra, shown in figure 3, consist of combinations and multiples of a plasma-type loss of 14·7 ev and a low-lying loss of 9·9 ev. The mean energy losses are shown in table 4 and agree reasonably with the results of other workers. The onset of transmission in bismuth films, as measured by Walker, Rustgi and Weissler (1959), was found to occur at 18·0 ev, though more recent measurements (Rustgi 1959, private communication) show the onset of transmission at 14·5 ev in much better agreement with the observed value of the plasma loss. Surface oxidation caused the appearance of a modified low-lying loss of $6{\cdot}0 \pm 0{\cdot}2$ ev and the disappearance of the 9·9 ev loss.

It was noticed that the intensity of the 24·8 ev loss seemed to be greater than would be expected if it were due solely to electrons which had lost 9·9 ev and 14·7 ev in separate events. It is therefore possible that the extra intensity might be due to the occurrence of an interband transition at the same energy. The existence of such a transition was in fact indicated by a large increase in optical absorption at 24 ev observed by Walker *et al.* (1959).

4.4. *Germanium*

The germanium loss spectra, shown in figure 4, are seen to consist of combinations of a low-lying loss of 11·1 ev and a plasma-type loss of 16·4 ev. The loss values are presented in table 5 and compared with the energy losses found by other workers. A surprising feature is that the observed value of the plasma loss in the present work is lower than most previous determinations. It is interesting to note that Sokolowski and Nordling (1959) have observed the characteristic loss in the photoelectron spectrum of germanium excited by Mo K_α-radiation.

Figure 3. Characteristic loss spectra of bismuth for primary electron energies of 750 and 1500 ev.

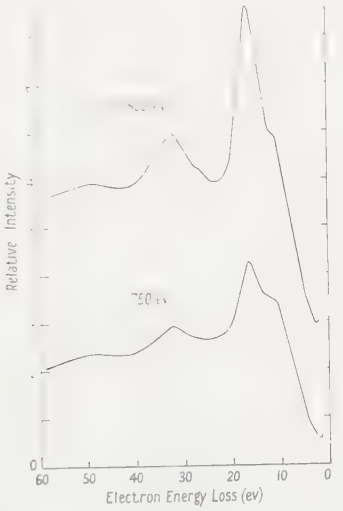

Figure 4. Characteristic loss spectra of germanium for primary electron energies of 750 and 1500 ev.

4.5. *Tin*

The tin loss spectra, shown in figure 5, exhibit two prominent energy losses of 10·4 and 14·1 ev, together with combinations and multiples of these losses. The 14·1 ev loss was identified as the plasma loss, and agreed fairly well with previous measurements (table 6) as well as with the onset of transmission at 13·6 ev measured by Walker *et al.* (1959).

The latter authors also found a large increase in optical absorption at 24·3 ev; an electron energy loss corresponding to such an interband transition would be obscured in the present work by the observed loss of 24·7 ev which is probably due mainly to electrons that have lost 10·4 and 14·1 ev in separate events. Surface oxidation caused the replacement of the 10·4 ev low-lying loss by a modified low-lying loss of $8{\cdot}3 \pm 0{\cdot}2$ ev.

4.6. *Cadmium*

A feature of the cadmium loss spectra, shown in figure 6, is the intense loss at 7·8 ev. Though a loss in this vicinity has been observed by several workers (table 7) it was not found to be as intense as the loss observed in the present work.

Table 5. Characteristic Energy Losses of Germanium (ev) found in the Present Work and by other Authors

Present Work	$11{\cdot}1 \pm 0{\cdot}2$ (27)	$16{\cdot}4 \pm 0{\cdot}1$ (36)	$27{\cdot}1 \pm 0{\cdot}1$ (4)	$32{\cdot}5 \pm 0{\cdot}2$ (27)		$48{\cdot}8 \pm 0{\cdot}2$ (19)
Marton and Leder (1954)		16·0		30·1		
Watanabe (1954)		17		34		
Gauthé (1956)		18		34		56
Watanabe (1956)		16·4		33·8		
Haberstroh (1956)		16·16		33·2		
Gauthé (1958)		18		34	44 (?)	56 (?)
Fert and Pradal (1959)		17·34				51
Sokolowski and Nordling (1959)		15				

Table 6. Characteristic Energy Losses in Tin (ev) found in the Present Work and by other Authors

Present Work		$10{\cdot}4 \pm 0{\cdot}1$ (26)	$14{\cdot}1 \pm 0{\cdot}1$ (35)	$24{\cdot}7 \pm 0{\cdot}2$ (20)	$27{\cdot}8 \pm 0{\cdot}2$ (21)	$38{\cdot}6 \pm 0{\cdot}2$ (4)	$41{\cdot}9 \pm 0{\cdot}2$ (18)	$56{\cdot}7 \pm 0{\cdot}3$ (7)
Marton and Leder (1954)	4·5		12·4	18·0	23·9			
Watanabe (1954)	6·3		13	19·5				

The broad loss of 15·2 ev does not agree at all well with previous measurements, though it should be noted that the latter do not agree particularly well with each other. Walker *et al.* (1959) attempted to measure the onset of transmission in cadmium films but could not observe a transmittivity greater than 0·3 %.

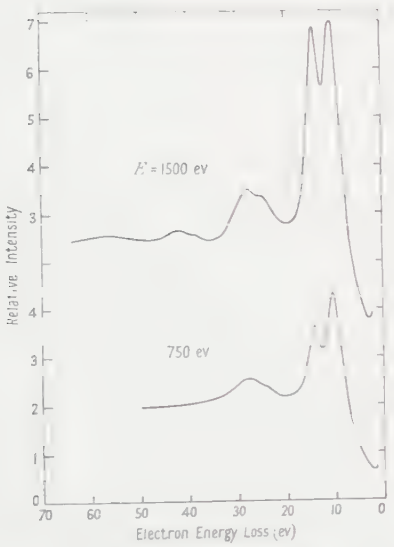

Figure 5. Characteristic loss spectra of tin for primary electron energies of 750 and 1500 ev.

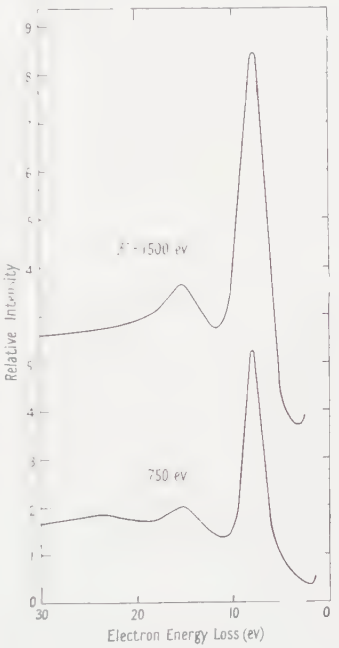

Figure 6. Characteristic loss spectra of cadmium for primary electron energies of 750 and 1500 ev.

Table 7. Characteristic Energy Losses in Cadmium (ev) found in the Present Work and by other Authors

Present Work		7·8 ± 0·1 (50)	15·2 ± 0·1 (36)	23·4 ± 0·2 (9)
Mollenstedt (1949)		9	21·5	
Marton and Leder (1954)			14·5	
Kleinn (1954)	3·9		20·7	
Marton *et al.* (1955)	4·4	8·1	19	
Leder *et al.* (1956)	4·4	8·1	18·7	
Gauthé (1959)			19·2	

4.7. *Copper*

Four energy losses were found in the copper loss spectra, shown in figure 7, and the loss values are compared with results of other workers in table 8. It is seen that there are considerable differences among the previous values as well as between some of these and the present results. A reason for such disagreements could be the dependence of the loss spectra on the degree of crystalline orientation of the target found by Pradal and Saporte (1958). Further, it was found in the present work that slight surface oxidation caused the disappearance of the 7·2 ev

loss and the appearance of a new modified low-lying loss of $3{\cdot}7 \pm 0{\cdot}4$ ev. The 4·4 ev loss is possibly due to an intraband transition, and the 27·1 ev loss peak could be due to electrons that have lost 7·2 ev and 19·9 ev in separate events.

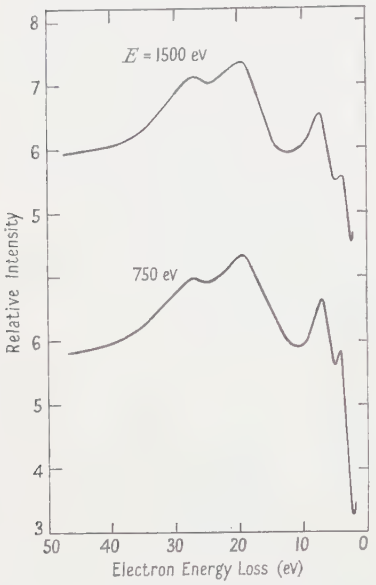

Figure 7. Characteristic loss spectra of copper for primary electron energies of 750 and 1500 ev. The spectra have been normalized for equal intensities of the 19·9 ev peak.

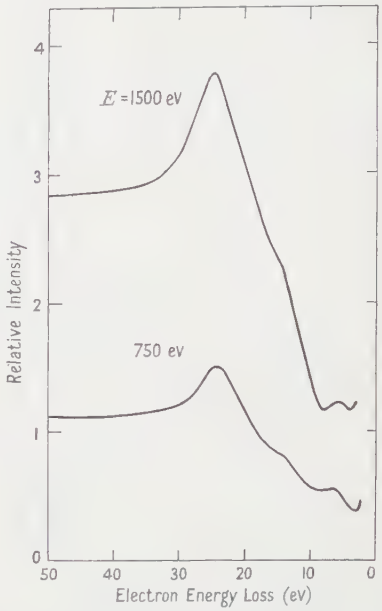

Figure 8. Characteristic loss spectra of platinum for primary electron energies of 750 and 1500 ev.

4.8. *Platinum*

The platinum loss spectra, drawn in figure 8, show a prominent broad loss peak at 24·4 ev and less intense peaks at 6·2 and 14·3 ev. The 24·4 ev loss agrees with most previous measurements (table 9) though only Mollenstedt (1949) has observed a low-lying loss near 14 ev. The 6·2 ev loss corresponds to the losses of 5·2 and 6·5 ev observed by Kleinn (1954) and Rudberg (1930) respectively, and is possibly due to an intraband transition. It might be noted that Albert (1956) has measured the isochromats at the short-wavelength limit of the continuous x-ray spectrum of platinum to be at 13, 21, 42, and 63 volts, in fair agreement with the characteristic loss measurements.

4.9. *Lead, Calcium and Lithium*

The loss spectra of these three elements were found to be very susceptible to surface oxidation and most measurements have been made only with a primary electron energy of 1500 ev.

The lead spectrum (figure 9) has two prominent losses at 10·6 and 13·9 ev together with combinations and multiples of these losses. The plasma loss of 13·9 ev agrees reasonably well with the previous measurements given in table 10.

Table 8. Characteristic Energy Losses in Copper (ev) found in the Present Work and by other Authors

Present Work		4·4 ± 0·2 (34)	7·2 ± 0·2 (66)		19·9 ± 0·2 (71)		27·1 ± 0·2 (61)				
Rudberg (1930)	3·4		6·9	12·3			25·5		34·5		
Rudberg (1936)		4·1	7·2								
Lang (1948)					19·1						
Reichertz and Farnsworth (1949)	3·0		6·0	12·3	20·0						
Mollenstedt (1949)					20·4						
Marton and Leder (1954)			6·9	11·3	19·6						
Kleinn (1954)	3·1	4·3 (?)	6·4		21						
Watanabe (1954)			7		19·5						
Blackstock *et al.* (1955)					22·6						
Simpson *et al.* (1956)					24						
Gauthé (1956)			7·3 (?)		17·4	22·7	27·8		40	49	60
Gauthé (1958)			7·3 (?)		18·7	23·7	28·4		41	49	
Fert and Pradal (1958)					25					49	
Pradal and Saporte (1958)		5			20						
Sokolowski *et al.* (1957)					16						

Table 9. Characteristic Energy Losses in Platinum (ev) found in the Present Work by and other Authors

Present Work	6·2 ± 0·2 (12)		14·3 ± 0·3 (13)	24·4 ± 0·2 (17)					
Rudberg (1930)	6·5	9·4		24·8	33·7				
Mollenstedt (1949)			14	22·4			46	61·4	
Kleinn (1954)	5·2			22·6					
Gauthé (1958)			18·5	23·9	30 (?)	37 (?)	47		

Table 10. Characteristic Energy Losses in Lead (ev) found in the Present Work and by other Authors

Present Work		10·6 ± 0·2 (9)	13·9 ± 0·2 (9)	20·1 ± 0·2 (4)	23·3 ± 0·2 (7)	27·5 ± 0·2 (9)	42·2 ± 0·4 (5)
Leder and Marton (1954)	5·1		12·1		21·8		
Kleinn (1954)	4·3		13·1		21·3		
Leder (1956)	6·7		13·8		21·4		

The observed loss at 23·3 ev appears to be broader and more intense than would be likely if it were solely due to electrons that had lost 10·6 and 13·9 ev. Leder (1956) has observed a loss of 21·4 ev in lead and has attributed it to the excitation of an interband transition; it is possible that such a loss may be superposed on the present loss spectrum. A few measurements were made of the loss spectrum of lead with a primary electron energy of 750 ev. These measurements showed the 10·6 ev loss more prominent than the 13·9 ev plasma loss, and also another loss of $7{\cdot}2 \pm 0{\cdot}2$ ev which could be a modified low-lying loss.

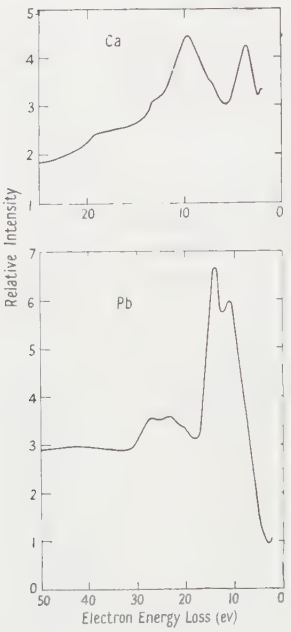

Figure 9. Characteristic loss spectra of lead and calcium for a primary energy of 1500 ev.

Table 11. Characteristic Energy Losses in Calcium (ev) found in the Present Work and by other Authors

Present Work	$3{\cdot}7 \pm 0{\cdot}2$ (13)	$9{\cdot}8 \pm 0{\cdot}2$ (13)	$13{\cdot}3 \pm 0{\cdot}3$ (3)	$19{\cdot}3 \pm 0{\cdot}3$ (3)		
Rudberg (1930)	4	8	12			
Leder (1956)	4·2	8·9	13·2	17·9	29·0	36·4

The calcium spectrum (figure 9) shows two prominent losses of 3·7 and 9·8 ev. Both losses were present during continuous metal evaporations but disappeared rapidly with surface oxidation. No other low-lying loss was detected. In some spectra, a weak loss of 7·5 ev was observed on the high-energy side of the 9·8 ev loss; this loss probably corresponds to the second multiple of the 3·7 ev loss. The present results are compared with previous measurements in table 11. The 3·7 ev loss is probably the same as the loss of 4·2 ev observed by Leder and the 4 ev loss observed by Rudberg. There was also some evidence of a fairly intense loss of about 37 ev, but this peak could not always be reproduced because of the rapid oxidation.

Due to the rapid surface oxidation, no reliable measurements of the lithium spectrum were obtained. There was, however, evidence for a plasma-type loss at 8·2 ev and for what is possibly a modified low-lying loss at 4·7 ev. The 8·2 ev loss is significantly lower than the value of 9·8 ev for the fundamental loss found by Marton, Leder and Mendlowitz (1955), but is in good agreement with the decrease to zero of the reflectivity at 8·0 ev found by Wood and Lukens (1938).

§ 5. Discussion

The new measurements of the characteristic energy losses of a number of elements have been compared with previous determinations in the preceding section. The present collation of the results of other authors in tables 2 to 11 shows clearly the wide variation in the measured energy losses referred to in the Introduction. The values in these tables have been arranged so as to compare losses of similar origin where this is possible. For example, the 25·2 ev loss found by Marton and Leder (1954) in bismuth would seem to be a second multiple of the loss of 13 ev found by the same authors and is therefore compared with the present loss of 29·0 ev rather than the loss of 24·8 ev which is numerically closer.

In the present series of measurements it was found that the observed loss spectra of a number of elements consisted almost entirely of combinations of two fundamental losses which could be identified as plasma and lowered plasma losses. In most cases, such a lowered plasma loss has not been previously observed; the detection of this loss in the present work is believed to be a result of the high purity of the specimens. The results are summarized in table 12 together with computed values of $\hbar\omega_p$ and $\hbar\omega_p/\sqrt{2}$, where the free electron density has been estimated from the valency. These values are compared with the measured quantum plasma loss ΔE_{pl}, the low-lying loss ΔE_{ll} and the modified low-lying loss $\Delta E_{mod.\,ll}$ which have been calculated as the mean of all appropriate observed losses.† The ratio $\Delta E_{pl}/\Delta E_{ll}$ is also tabulated to indicate the departures from the theoretical ratio of $\sqrt{2}$. Previous results for aluminium and magnesium are included in table 12 for comparison purposes.

It can be seen from the table that whereas the agreement between $\hbar\omega_p$ and ΔE_{pl} is generally quite good, the agreement between $\hbar\omega_p/\sqrt{2}$ and ΔE_{ll} is much better, especially in those cases where there are appreciable deviations of ΔE_{pl} from $\hbar\omega_p$. The displacement of ΔE_{pl} from $\hbar\omega_p$ for copper, platinum, and cadmium is in agreement with the estimates of Pines (1956) and Nozières and Pines (1958, 1959). Further, the half-width of the plasma loss peak in these elements is also greater than in those elements where there is better agreement between ΔE_{pl} and $\hbar\omega_p$. The half-width of the low-lying loss is generally observed to be small compared with $\hbar\omega_p$. There is also good agreement between the values of ΔE_{pl} and the onsets of transmission E_T in aluminium, bismuth, antimony and tin as measured by Walker *et al.* (1959), Rustgi *et al.* (1959) and Rustgi (1959, private communication), and between ΔE_{pl} and the disappearance of reflectivity in lithium found by Wood and Lukens (1938). It will be interesting to see how the results of similar future optical experiments compare with the present work.

From measurements of the magnitude of the ΔE_{ll} loss and a comparison with $\hbar\omega_p/\sqrt{2}$, the observed change in intensity of the loss relative to the plasma loss

† For example, if $n_1, n_2, n_3, \ldots$ measurements were made of the energy losses ΔE_1, ΔE_2, ΔE_3, ... which appear to be successive multiples of the ΔE_1 loss, then the mean quantum loss is calculated from $(n_1\Delta E_1+\frac{1}{2}n_2\Delta E_2+\frac{1}{3}n_3\Delta E_3+\ldots)/(n_1+n_2+n_3+\ldots)$.

Table 12. Summary of the Experimental Results

Element	V	$\hbar\omega_p$	$\hbar\omega_p/\sqrt{2}$	E_T	ΔE_{pl}	ΔE_{ll}	$\Delta E_{mod.\ ll}$	$\Delta E_{pl}/\Delta E_{ll}$	N
Be	2	18·4	13·0	—	19·8 ± 0·17	11·9 ± 0·17	7·9 ± 0·11	1·66 ± 0·04	1·67 ± 0·05
Sb	5	15·0	10·6	15·0	16·0 ± 0·13	11·2 ± 0·32	7·0 ± 0·16	1·43 ± 0·05	5·56 ± 0·32
Bi	5	13·9	9·8	14·5	14·6 ± 0·13	10·0 ± 0·26	6·0 ± 0·16	1·46 ± 0·05	5·15 ± 0·27
Ge	4	15·8	11·2	—	16·3 ± 0·11	11·0 ± 0·18	—	1·48 ± 0·04	3·88 ± 0·13
Sn	4	14·3	10·1	13·6	14·0 ± 0·14	10·5 ± 0·24	8·3 ± 0·13	1·33 ± 0·04	4·33 ± 0·19
Cd	2	11·3	8·0	—	15·2 ± 0·10	7·9 ± 0·16	—	1·92 ± 0·05	1·96 ± 0·08
Pt	2	13·5	9·5						
	4	19·1	13·5	—	24·4 ± 0·20	14·3 ± 0·24	—	1·71 ± 0·04	4·50 ± 0·15
Cu	1	10·8	7·6	—	19·9 ± 0·15	7·2 ± 0·26	3·7 ± 0·4	2·76 ± 0·12	0·89 ± 0·06
	2	15·3	10·8						
Pb	4	13·5	9·5	—	13·9 ± 0·15	10·1 ± 0·31	7·2 ± 0·11 (?)	1·38 ± 0·06	4·49 ± 0·28
Ca	2	8·0	5·7	—	9·7 ± 0·20	3·7 ± 0·23	—	2·62 ± 0·22	0·86 ± 0·11
Li	1	8·0	5·7	8·0	8·2 (?)	—	4·7 (?)	—	—
Al	3	15·9	11·2	14·6	15·3 ± 0·14	10·3 ± 0·20	7·1 ± 0·09	1·49 ± 0·04	2·56 ± 0·10
Mg	2	10·9	7·7	—	10·6 ± 0·06	7·1 ± 0·19	4·9 ± 0·09	1·49 ± 0·05	1·70 ± 0·09

The values of $\hbar\omega_p$ and $\hbar\omega_p/\sqrt{2}$, as calculated assuming the number of valence electrons V to be free, are compared with the observed quantum plasma loss ΔE_{pl}, the quantum low-lying loss ΔE_{ll}, and the observed modified low-lying loss $\Delta E_{mod.\ ll}$. All values are in ev. The effective number of free electrons per atom N, calculated from ΔE_{ll}, and the ratio $\Delta E_{pl}/\Delta E_{ll}$ are also shown for each element; E_T is the photon energy corresponding to the observed onset of optical transmission.

with different primary electron energies, and the sensitivity of the intensity of the loss to surface contamination of the specimens, it is considered that this loss is a lowered plasma loss. The observation of the modified low-lying loss in some elements confirms the identification of the lowered plasma loss and also the general predictions of Stern and Ferrell (1960). The identification of the lowered plasma loss in copper, platinum and cadmium was initially less certain than that for the other elements on account of the larger differences between ΔE_{pl} and $\hbar\omega_{\mathrm{p}}$. Apart from the other methods of identifying the lowered plasma loss, identification of the origin of the losses in copper was assisted and confirmed by measurements of the loss spectra of aluminium–copper alloys (Powell 1960 a).

It has been assumed in the preceding section that oxidation has caused the observed rapid decrease in intensity of the lowered plasma loss and the appearance of the modified low-lying loss. Though no independent analysis of the surface layers was made, it is considered that oxidation is the most likely surface contamination in the present work. It was observed that the rate at which the changes took place was affected greatly by 'gettering' evaporations of the target material. The presence of a liquid air trap surrounding the target ensured that the carbonaceous contamination rate was negligibly small and that formation of the hydroxide was unlikely. Except with beryllium, measurements were not made of any subsequent changes in the intensity of the modified low-lying loss as oxidation proceeded. It was found that the modified low-lying loss in beryllium (and also previously in aluminium and magnesium (Powell and Swan 1960)) eventually disappeared as oxidation continued. This observation shows that the modified low-lying loss in these elements is a metal loss that occurs only when a surface layer of oxide is present. It would be reasonable to presume that the modified low-lying losses in antimony, bismuth, tin, copper and lead have a similar origin.

The presence on the specimen of surface contaminants other than oxide would be expected to lead to the appearance of modified low-lying losses in different positions (Stern and Ferrell 1960). It is therefore suggested that the presence of contaminating surface films, such as the substrate in transmission experiments, layers of oxide or of carbonaceous contamination, could be the reason for the low-lying losses observed in varying positions by other workers. Several authors (Leder and Marton 1954, Leder 1956, Jull 1956, Gauthé 1959) have compared the characteristic loss spectra of a number of elements and their compounds. With some elements and compounds there appears to be some similarity in the loss spectra; with others there is not. While there is at present no reason to doubt the validity of these results in general, the present results emphasize the need for care in any future similar experiment. For example, it would be possible for the same modified lowered plasma loss to occur in a metal with a very thin surface layer of oxide and in the metal in an incompletely oxidized specimen.

The observation and identification of the lowered plasma loss is a strong indication that the other fundamental loss observed is due to plasma excitation in the manner considered by Pines *et al.* Further, the observation of the lowered plasma loss close to the position predicted by theory and the subsequent disappearance of the loss in some elements with oxidation indicate that the specimens are of high surface purity. It is therefore believed that many of the discrepancies between the results of different workers are due to specimen impurities, as well as possibly to some of the effects discussed by Marton (1956). It is significant that no unmodified lowered plasma loss has been generally observed by previous workers

(except perhaps in copper). Most previous measurements of the characteristic losses have been made by the energy analysis of electrons transmitted through thin specimen films and it has been shown that surface contamination of the foils in such work is generally unavoidable, particularly when the foils are prepared outside the analyser vacuum system.

The agreement between ΔE_{II} and $\hbar\omega_{\mathrm{p}}/\sqrt{2}$ is particularly striking. It is believed that the correlation is sufficient to warrant an estimation of N, the effective number of free electrons per atom, from the values of ΔE_{II}. Values of N have been calculated assuming the effective mass of the electrons to be equal to the rest mass, and are listed in table 12. The values of the energy losses and of N have not been corrected for the dispersion of the energy loss with scattering angle. As measurements of the dispersion coefficients and the distribution of loss intensity with scattering angle have been made for only a few elements, it was not considered desirable to make either an empirical or a theoretical correction. The energy losses in the present experiment will thus be of the order of 3% higher than those that would be measured in the forward direction, and the values of N will be approximately 6% larger than those obtained from losses corrected for dispersion. No account has also been taken in the present work of any departures from the simple theory caused by the form of the target. That is, though there is good agreement between ΔE_{II} and $\hbar\omega_{\mathrm{p}}/\sqrt{2}$, it is possible that the comparison should be made between ΔE_{II} and $\hbar\omega_{\mathrm{p}}/\sqrt{3}$ if the specimen was agglomerated to a large extent. It has been assumed that agglomeration is not appreciable with the present rapid rates of evaporation (Holland 1956).

It would be of some interest to compare the present values of N with other estimates such as those also obtained from measurements based on free electron considerations. For instance, it has been found that the optical properties of a number of metals can be interpreted in terms of the Drude free electron formulae over a wide wavelength range (Schulz 1957). Reliable measurements, consistent within themselves and with other workers, are unfortunately not available for many metals. Unpublished measurements of the optical constants of aluminium by Hass have indicated that there are 2·4 free electrons per atom in that element (Mendlowitz 1960a, Marton 1959, private communication) in good agreement with the value of N corrected for dispersion. Schulz (1957) has similarly found that there are effectively 0·69 free electrons per atom in copper, in fair agreement with the corrected value of N and with other determinations from electronic specific heat measurements. Free electron concentrations in tin have been estimated by Hodgson (1955) and by Chambers (1952) to be 1·33 and 1·1 electrons per atom, respectively; the measurements of these authors are much smaller than the present values of N for tin. It is to be hoped that measurements of the optical constant of the other metals can be performed in the near future.

§ 6. Conclusion

It has been found that the characteristic loss spectra of ten elements can be interpreted as arising almost entirely from combinations of two elementary energy losses, a plasma loss and a lowered plasma loss. There was evidence that one of the loss peaks in the spectra of bismuth, and possibly also of lead, might be partly due to individual interband electronic transitions while the peaks of lowest energy loss in the spectra of copper and platinum could be due to intraband transitions.

The identification of the plasma loss in antimony, bismuth and tin has been confirmed by measurements of optical transmittivity by Walker *et al.* (1959) and by Rustgi (1959, private communication). The lowered plasma loss has not been previously identified in any of the ten elements. The presence of such a loss indicates that the specimens were free of surface contaminants and that the loss spectra are characteristic of a clean surface. After a number of preliminary evaporations, the oxidation rate for most elements was sufficiently small to permit the reliable measurement of the entire loss spectrum. As oxidation proceeded, however, the lowered plasma loss was seen to decrease rapidly in intensity and to be replaced by a new modified lowered plasma loss; this observation again shows the necessity for uncontaminated specimen surfaces in the measurement of characteristic losses.

A feature of the results has been the close agreement between the observed lowered plasma losses and the values computed from $\hbar\omega_p/\sqrt{2}$ assuming the valence electrons to be completely free. This correlation indicates that the effective free electron concentrations calculated from the lowered plasma losses could be usefully compared with other measurements based on similar free electron considerations.

Acknowledgments

The author is indebted to Dr. J. B. Swan for his continuous interest and encouragement throughout this work. He would also like to thank Dr. Swan, Professor C. J. B. Clews, and Dr. L. Marton for their comments and suggestions for improving the manuscript, and Dr. Marton, Dr. E. A. Stern, Dr. H. Mendlowitz and Dr. O. P. Rustgi for communication of results prior to publication. The author wishes finally to acknowledge the financial support of the research by the Research Grants Committee of the University of Western Australia, and the tenure of a Commonwealth Scientific and Industrial Research Organization Senior Postgraduate Studentship.

References

Albert, L., 1956, *Z. Phys.*, **143,** 513.
Blackstock, A. W., Ritchie, R. H., and Birkhoff, R. D., 1955, *Phys. Rev.*, **100,** 1078.
Chambers, R. G., 1952, *Proc. Roy. Soc.* A, **215,** 481.
Feldman, C., 1960, *Phys. Rev.*, **117,** 455.
Ferrell, R. A., 1956, *Rev. Mod. Phys.*, **28,** 308.
Fert, C., and Pradal, F., 1958, *C. R. Acad. Sci., Paris,* **246,** 252.
—— 1959, *Ibid.*, **248,** 666.
Fröhlich, H., and Pelzer, H., 1955, *Proc. Phys. Soc.* A, **68,** 525.
Gauthé, B., 1956, *C. R. Acad. Sci., Paris,* **242,** 2634.
—— 1958, *Ann. Phys., Paris,* **3,** 915.
—— 1959, *Phys. Rev.*, **114,** 1265.
Gornyi, N. B., 1958, *Izvest. Akad. Nauk. S.S.S.R. Ser. Fiz.*, **22,** 475.
Haberstroh, G., 1956, *Z. Phys.*, **145,** 20.
Hodgson, J. N., 1955, *Proc. Phys. Soc.* B, **68,** 593.
Holland, L., 1956, *Vacuum Deposition of Thin Films* (London: Chapman and Hall).
Hubbard, J., 1955, *Proc. Phys. Soc.* A, **68,** 441.
Jull, G. W., 1956, *Proc. Phys. Soc.* B, **69,** 1237.
Kleinn, W., 1954, *Optik, Stuttgart,* **11,** 226.
Lang, W., 1948, *Optik, Stuttgart,* **3,** 233.
Leder, L. B., 1956, *Phys. Rev.*, **103,** 1721.
Leder, L. B., and Marton, L., 1954, *Phys. Rev.*, **95,** 1345.
Leder, L. B., Mendlowitz, H., and Marton, L., 1956, *Phys. Rev.*, **101,** 1460.

Marton, L., 1956, *Rev. Mod. Phys.*, **28,** 172.
Marton, L., and Leder, L. B., 1954, *Phys. Rev.*, **94,** 203.
Marton, L., Leder, L. B., and Mendlowitz, H., 1955, *Advances in Electronics and Electron Physics* (New York: Academic Press).
Mendlowitz, H., 1960 a, *Proc. Phys. Soc.*, **75,** 664.
—— 1960 b, *J. Opt. Soc. Amer.*, **50,** 739.
Mollenstedt, G., 1949, *Optik, Stuttgart*, **5,** 499.
Nozières, P., and Pines, D., 1958, *Phys. Rev.*, **109,** 1062.
—— 1959, *Ibid.*, **113,** 1254.
Pines, D., 1956, *Rev. Mod. Phys.*, **28,** 184.
Pines, D., and Bohm, D., 1952, *Phys. Rev.*, **85,** 338.
Powell, C. J., 1960 a, *Aust. J. Phys.*, **13**, 145.
—— 1960 b, *Plasma Physics*, in the press.
Powell, C. J., Robin, J. L., and Swan, J. B., 1958, *Phys. Rev.*, **110,** 657.
Powell, C. J., and Swan, J. B., 1959 a, *Phys. Rev.*, **115,** 869.
—— 1959 b, *Ibid*, **116,** 81.
—— 1960, *Ibid.*, **118,** 640.
Pradal, F., and Saporte, R., 1958, *C. R. Acad. Sci., Paris*, **246,** 2880.
Reichertz, P. P., and Farnsworth, H. E., 1949, *Phys. Rev.*, **75,** 1902.
Ritchie, R. H., 1957, *Phys. Rev.*, **106,** 874.
Rudberg, E., 1930, *Proc. Roy. Soc.* A, **127,** 111.
—— 1936, *Phys. Rev.*, **50,** 138.
Rudberg, E., and Slater, J. C., 1936, *Phys. Rev.*, **50,** 150.
Rustgi, O. P., Walker, W. C., and Weissler, G. L., 1959, *Bull. Amer. Phys. Soc. Ser. II*, **4,** 226.
Ruthemann, G., 1948, *Ann. Phys., Lpz.*, **6,** 113.
Schulz, L. G., 1957, *Adv. Phys.*, **6,** 102.
Simpson, J. A., McCraw, T. F., and Marton, L., 1956, *Phys. Rev.*, **104,** 64.
Sokolowski, E., and Nordling, C., 1959, *Arkiv. Fys.*, **14,** 557.
Sokolowski, E., Nordling, C., and Siegbahn, K., 1957, *Arkiv. Fys.*, **12,** 301.
Stern, E. A., and Ferrell, R. A., 1960, *Phys. Rev.*, in the press.
Viatskin, A. Ia., 1958, *Soviet Physics, Tech. Phys*, **3**, 2252.
Walker, W. C., Rustgi, O. P., and Weissler, G. L., 1959, *J. Opt. Soc. Amer.*, **49**, 471.
Watanabe, H., 1954, *J. Phys. Soc., Japan*, **9,** 920.
—— 1956, *J. Electronmicroscopy*, **4,** 24.
Wood, R. W., and Lukens, C., 1938, *Phys. Rev.*, **54,** 332.

Spin–Orbit Effects in the Inelastic Scattering of 12 MeV Neutrons in Carbon

By B. A. ROBSON† and D. ROBSON
Physics Department, University of Melbourne, Australia

Communicated by P. Swan; MS. received 8th December 1959,
in revised form 21st March 1960

Abstract. The angular distribution and polarization of elastic and inelastic scattering of 12 MeV neutrons in carbon are investigated using the distorted wave approximation, assuming direct interaction in inelastic collisions. The introduction of a spin–orbit potential enables the same optical parameters to describe the elastic and inelastic scattering. Calculations are performed for spin-independent potentials and the results compared with those of Levinson and Banerjee. It is found that the neglect of a spin-orbit potential leads to inconsistent optical model parameters and poor fits at intermediate angles. The inelastic polarization predicted is very similar to the elastic polarization in the outgoing channel, although it is slightly smaller. Even larger discrepancies are found in the two-body potential when a spin-orbit potential is included. Extension of the theory to include collective motion may be necessary.

§ 1. Introduction

The differential cross sections and polarizations for the elastic scattering of medium energy nucleons in carbon have been measured by several workers (e.g. Peelle 1957). In this energy range, the inelastic scattering of nucleons from the 2^- level at 4·43 MeV in carbon has also been measured (Peelle 1957, Conzett 1957). The present work is an investigation of the effects of a spin–orbit potential added to the complex potential recently used (Levinson and Banerjee 1958) in the distorted wave treatment of direct interaction inelastic scattering for neutrons of 12 MeV. In this method the states of the target nucleus are described by shell model wave functions, the projectile wave functions are taken to be the free particle wave functions distorted by an optical potential and the inelastic scattering is described by a two-body direct interaction between the free and bound nucleons.

Levinson and Banerjee (1958) studied in detail the case of a spin-independent optical potential and obtained fairly satisfactory agreement with the carbon data for incident proton energies of 14–185 MeV. However, their results show several 'anomalies': (*a*) the strength of the two-body interaction required to fit the experimental data is about twice as strong as that obtained from free nucleon–nucleon scattering; (*b*) the real part of the optical well needed to fit the inelastic data is considerably shallower than that generally used to fit the elastic results; (*c*) the calculated inelastic differential cross section curves are in poor agreement with experiment at backward angles for incident energies of about 14 MeV.

† Now at the Australian National University, Canberra.

It will be shown that (*b*) and (*c*) are substantially removed by the introduction of a spin–orbit potential required to fit the elastic polarization data. Moreover, it will be seen that the factor of two required for the two-body interaction found by Levinson and Banerjee is an underestimate.

The calculated inelastic polarization is large at backward angles reaching values comparable with the large elastic asymmetries (Levinson and Banerjee's theory gives no polarization), and is similar to the elastic polarization in the outgoing channel. Unfortunately no inelastic polarization data exist at present, with which to make a comparison. A theoretical derivation of the inelastic polarization of neutrons by a complex nucleus is given in § 2.

§ 2. Theory

The inelastic differential cross section is calculated in first-order perturbation theory, in which the two-body interaction is regarded as a perturbation on the nucleon–nucleus elastic interaction (Mott and Massey 1949), that is

$$\sigma(\theta)=\frac{k'}{k}(m/2\pi\hbar^2)^2\Sigma_{\rm av}|\mathfrak{M}|^2, \qquad \ldots\ldots(2.1)$$

where k' and k are the final and initial wave numbers respectively for the inelastically scattered particle of reduced mass m, and $\mathfrak{M}$ is the matrix element for the transition due to the direct interaction between an extra-core nucleon and the incident nucleon. $\Sigma_{\rm av}$ indicates an average over initial spin states and a sum over final spin states.

The projectile wave functions are taken to be the wave functions for a free particle moving in the field of a complex spin-dependent potential. This is the distorted wave treatment, where the free particle wave functions are distorted by the nucleus as a whole, and which attempts to take into account the effect of elastic scattering on the inelastic cross section.

The distorting potential is assumed to be the usual Woods–Saxon optical potential plus a Thomas–Fermi type spin–orbit potential,

$$V_{\rm D}(r)=-(V+iW)g(r)+V_{\rm S}\left(\frac{\hbar}{m\pi c}\right)^2 r^{-1}\frac{dg}{dr}\,\boldsymbol{\sigma}.\mathbf{L}, \qquad \ldots\ldots(2.2)$$

in which $\boldsymbol{\sigma}.\mathbf{L}=L$ for $J=L+\frac{1}{2}$ and $\boldsymbol{\sigma}.\mathbf{L}=-(L+1)$ for $J=L-\frac{1}{2}$. The potential parameters V and W are positive real functions so that the central force is attractive and absorptive, and $V_{\rm S}$ is a positive real quantity corresponding to the sign of the spin–orbit force in the shell model. $\mathbf{L}$ and $\boldsymbol{\sigma}$ represent the orbital and spin angular momenta of the nucleon and $\mathbf{J}$ is its total angular momentum. $\hbar/m\pi c$ is the Compton pion wavelength and $g(r)$ is the Woods–Saxon (1954) form factor

$$g(r)=\{1+\exp[(r-R)/a]\}^{-1}, \qquad \ldots\ldots(2.3)$$

where a is the diffuseness parameter. A similar potential has been used to study elastic cross sections and polarizations in the medium energy range 5–50 Mev (Fernbach and Bjorklund 1958, Nodvik and Saxon, private communication).

For a particle moving in such a potential the constants of motion are J^2, L^2, S^2, J_z (Lepore 1950) and hence the appropriate partial wave expansions are (Sawicki 1955, 1956)

$$|k\rangle=\sum_{LM_L}\sum_{JM_J}a(LM_L)c(L\tfrac{1}{2}J,\,M_L\mu_{\rm p}M_J)R_{JL}(r_1)|JLM_J\rangle_1, \qquad \ldots\ldots(2.4)$$

$$\langle k'|=\sum_{L'ML'J'M_{J'}}\sum a^*(L'M_{L'})c(L'\tfrac{1}{2}J',\,M_{L'}\mu_{\rm p'}M_{J'})R_{J'L'}(r_1)\langle J'L'M_{J'}|_1, \qquad \ldots\ldots(2.5)$$

in which $|JLM_J\rangle$ is a spin–angle function which may be expanded in terms of spherical harmonics,

$$|JLM_J\rangle = \sum_{\bar{M}_L \bar{\mu}_p} c(L\tfrac{1}{2}J, \bar{M}_L \bar{\mu}_p M_J) Y_L^{\bar{M}_L}(\theta_1, \phi_1) X_{\bar{\mu}_p}(\sigma_p), \quad \ldots\ldots (2.6)$$

where $Y_L^{\bar{M}_L}(\theta_1, \phi_1)$ is a spherical harmonic as defined by Condon and Shortley (1935) and θ_1, ϕ_1 are the polar angles made by $\mathbf{r}_1$ with the quantization axis. The Clebsch–Gordan coefficients are as defined by Rose (1957). The quantum numbers J, L and σ_p have their usual meaning and their respective projection quantum numbers are M_J, M_L and μ_p. A prime is used to denote the final state quantum numbers. The functions $R_{JL}(r)$ are radial solutions of the spin-dependent Schrödinger equation

$$\left\{\left(\frac{d^2}{dr^2}\right) - V_D(r) + k^2 - \frac{L(L+1)}{r^2}\right\} rR_{JL}(r) = 0, \quad \ldots\ldots (2.7)$$

such that asymptotically $|k\rangle$ represents an incoming plane wave and an outgoing spherically scattered wave. Note that the Green's function $\langle k'|$ is not quite the adjoint of $|k'\rangle$, since the radial function in equation (2.5) is not starred (Mott and Massey 1949). Thus the functions $a(LM_L)$ and $a^*(L'M_{L'})$ are given by

$$a(LM_L) = 4\pi i^L Y_L^{M_L *}(\theta_k, \phi_k), \quad \ldots\ldots (2.8)$$

and

$$a^*(L'M_{L'}) = 4\pi i^{-L'} Y_{L'}^{M_{L'}}(\theta_{k'}, \phi_{k'}). \quad \ldots\ldots (2.9)$$

The assumption of j j coupling is used here for the shell model wave functions. This is a reasonable approximation for carbon (Levinson and Banerjee 1957 b) and on account of an L–S expansion is equally applicable to intermediate coupling. Let the wave functions $|\psi(J_i L_i M_{J_i})\rangle$ and $\langle\psi(J_f L_f M_{J_f})|$ denote the initial and final states of the nucleus, where J_i and J_f are the total spins of the two states respectively. The method of fractional parentage is used to reduce the many-body shell model wave functions to single-particle wave functions.

The direct interaction two-body potential V_I may be expanded in spherical harmonics (Levinson and Banerjee 1957 a) specified by the transfer quantum numbers K and μ,

$$V_I = 4\pi N \sum_K (2K+1)^{-1} v_K(r_1, r_n) \sum_\mu Y_K^\mu(\theta_1, \phi_1) Y_K^{\mu *}(\theta_n, \phi_n), \quad \ldots\ldots (2.10)$$

where N is the number of extra-core particles. It is assumed that V_I is spin-independent and all forms of exchange are neglected. Calculations carried out by the present authors indicate that the effects of exchange are small. These effects were also considered by Glendenning (1959), who reached similar conclusions. The neglect of spin in the two-body interaction is a less certain approximation, since spin-dependent two-body forces can produce polarizations. This type of polarization has been discussed by several authors (Newns 1953, Huby, Refai and Satchler 1958, Okai 1959) and results seem to indicate small polarizations.

The matrix element $\mathfrak{M} = \langle \mathrm{f}|V_{\mathrm{I}}|\mathrm{i}\rangle$ may be evaluated from

$$|\mathrm{i}\rangle = \sum_{LJM_L M_J} a(LM_L)c(L\tfrac{1}{2}J,\ M_L\mu_{\mathrm{p}}M_J)R_{JL}(r_1)|JLM_J\rangle_1|\psi(J_{\mathrm{i}}L_{\mathrm{i}}M_{J_{\mathrm{i}}})\rangle_n, \qquad \ldots\ldots(2.11)$$

and

$$\langle \mathrm{f}| = \sum_{L'J'M_{L'}M_{J'}} a^*(L'M_{L'})c(L'\tfrac{1}{2}J',\ M_{L'}\mu_{\mathrm{p}'}M_{J'})R_{J'L'}(r_1)\langle J'L'M_{J'}|_1\langle\psi(J_{\mathrm{f}}L_{\mathrm{f}}M_{J_{\mathrm{f}}})|_n, \qquad \ldots\ldots(2.12)$$

so that

$$\mathfrak{M} = 4\pi N \sum_{LL'JJ'K}(2K+1)^{-1}R_{JJ'LL'K}\sum_{M_L M_{L'}M_J M_{J'}\mu}(-1)^{\mu}c(L\tfrac{1}{2}J,\ M_L\mu_{\mathrm{p}}M_J)c(L'\tfrac{1}{2}J',\ M_{L'}\mu_{\mathrm{p}'}M_{J'})$$
$$\times a(LM_L)a^*(L'M_{L'})\langle J'L'M_{J'}|Y_K^{\mu}|JLM_J\rangle_1\langle J_{\mathrm{f}}L_{\mathrm{f}}M_{J_{\mathrm{f}}}|Y_K^{-\mu}|J_{\mathrm{i}}L_{\mathrm{i}}M_{J_{\mathrm{i}}}\rangle_n, \qquad \ldots\ldots(2.13)$$

where (anticipating the use of fractional parentage)

$$R_{JJ'LL'K} = \int\int dr_1 dr_n r_1^2 r_n^2 R_{J'L'}(r_1)R_{j_{\mathrm{f}}l_{\mathrm{f}}}(r_n)\tau_K(r_1,r_n)R_{JL}(r_1)R_{j_{\mathrm{i}}l_{\mathrm{i}}}(r_n), \qquad \ldots\ldots(2.14)$$

and

$$|\psi(J_{\mathrm{i}}L_{\mathrm{i}}M_{J_{\mathrm{i}}})\rangle_n = R_{j_{\mathrm{i}}l_{\mathrm{i}}}(r_n)\Psi_0(\xi)|J_{\mathrm{i}}L_{\mathrm{i}}M_{J_{\mathrm{i}}}\rangle_n. \qquad \ldots\ldots(2.15)$$

$\Psi_0(\xi)$ is the common parent radial wave function and $R_{j_{\mathrm{i}}l_{\mathrm{i}}}(r_n)$ the appropriate single-particle shell model radial wave function. An analogous expansion to (2.15) is used for $\langle\psi(J_{\mathrm{f}}L_{\mathrm{f}}M_{J_{\mathrm{f}}})|_n$.

Since the operator $Y_K^{-\mu}(\theta_n, \phi_n)$ is only a function of the single-particle coordinates the use of fractional parentage is applicable. The nuclear wave functions are firstly expanded in terms of a complete set of L–S wave functions (including now the isotopic spin quantum numbers T and T_z explicitly),

$$|J_{\mathrm{i}}M_{J_{\mathrm{i}}}T_{\mathrm{i}}T_z\rangle = \sum_{L_{\mathrm{i}}S_{\mathrm{i}}[\lambda_{\mathrm{i}}]} a^{J_{\mathrm{i}}T_{\mathrm{i}}}_{L_{\mathrm{i}}S_{\mathrm{i}}[\lambda_{\mathrm{i}}]}|\psi(l^n[\lambda_{\mathrm{i}}]J_{\mathrm{i}}L_{\mathrm{i}}M_{L_{\mathrm{i}}}S_{\mathrm{i}}M_{S_{\mathrm{i}}}T_{\mathrm{i}}T_z)\rangle, \ldots\ldots(2.16)$$

in which $a^{J_{\mathrm{i}}T_{\mathrm{i}}}_{L_{\mathrm{i}}S_{\mathrm{i}}[\lambda_{\mathrm{i}}]}$ are the admixture parameters (Levinson and Banerjee 1957 b). It is implied that the nucleus consists of a core and an l^n configuration, $\mathbf{L}_{\mathrm{i}}$ is the total orbital angular momentum of the initial state, $\mathbf{S}_{\mathrm{i}}$ is the total spin and these couple vectorially to give $\mathbf{J}_{\mathrm{i}}$, the total angular momentum. $[\lambda_{\mathrm{i}}]$ denotes symmetry and other quantum numbers and $\mathbf{T}_{\mathrm{i}}$ is the total isotopic spin. A similar expansion is required for the final state nuclear wave function. The right-hand side of equation (2.16) may be expanded in terms of parent and single particle states by the use of the fractional parentage expansion (Racah 1943)

$$|l^n[\lambda_{\mathrm{i}}]L_{\mathrm{i}}M_{L_{\mathrm{i}}}S_{\mathrm{i}}M_{S_{\mathrm{i}}}T_{\mathrm{i}}T_z\rangle = \sum_{L_{\mathrm{P}}S_{\mathrm{P}}T_{\mathrm{P}}[\lambda_{\mathrm{P}}]}\langle l^{n-1}[\lambda_{\mathrm{P}}]L_{\mathrm{P}}S_{\mathrm{P}}T_{\mathrm{P}}|l^n[\lambda_{\mathrm{i}}]L_{\mathrm{i}}S_{\mathrm{i}}T_{\mathrm{i}}\rangle$$
$$\times|l^{n-1}[\lambda_{\mathrm{P}}]L_{\mathrm{P}}S_{\mathrm{P}}T_{\mathrm{P}},\ l;\ L_{\mathrm{i}}M_{L_{\mathrm{i}}}S_{\mathrm{i}}M_{S_{\mathrm{i}}}T_{\mathrm{i}}T_z\rangle. \qquad \ldots\ldots(2.17)$$

The functions $|l^{n-1}[\lambda_{\mathrm{P}}]L_{\mathrm{P}}S_{\mathrm{P}}T_{\mathrm{P}},\ l;\ L_{\mathrm{i}}M_{L_{\mathrm{i}}}S_{\mathrm{i}}M_{S_{\mathrm{i}}}T_{\mathrm{i}}T_z\rangle$ are formed by the vector coupling of the parent state and the single-particle state, and $\langle l^{n-1}[\lambda_{\mathrm{P}}]L_{\mathrm{P}}S_{\mathrm{P}}T_{\mathrm{P}}|l^n[\lambda_{\mathrm{i}}]L_{\mathrm{i}}S_{\mathrm{i}}T_{\mathrm{i}}\rangle$ are the fractional parentage coefficients. The suffix P denotes parent quantum numbers. L–S parentage coefficients are tabulated for core plus one to core plus twelve (Jahn and Van Wieringen 1951).

The Wigner–Eckart theorem (Rose 1957) gives a quick method of evaluating the matrix elements,

$$\langle J_f M_{J_f}|Y_K^{-\mu}|J_i M_{J_i}\rangle = c(J_i K J_f,\ M_{J_i}-\mu M_{J_f})\langle J_f L_f||Y_K||J_i L_i\rangle. \quad \ldots\ldots (2.18)$$

From (2.16), (2.17) and (2.18) the matrix element becomes

$$\begin{aligned}\langle J_f M_{J_f}|Y_K^{-\mu}|J_i M_{J_i}\rangle = c(J_i K J_f,\ M_{J_i}-\mu M_{J_f}) \Bigg\{ & \sum_{\substack{L_i S_i T_i[\lambda_i] \\ L_f S_f T_f[\lambda_f]}} a^{J_f T_f}_{L_f S_f[\lambda_f]}\, a^{J_i T_i}_{L_i S_i[\lambda_i]} \\ \times \sum_{L_P S_P T_P[\lambda_P]} & \langle l^{n-1}[\lambda_P] L_P S_P T_P|l^n[\lambda_f] L_f S_f T_f\rangle \langle l^{n-1}[\lambda_P] L_P S_P T_P|l^n[\lambda_i] L_i S_i T_i\rangle \\ \times u(S_i L_i J_f K;\ J_i L_f) & u(L_P l L_f K;\ L_i l)\delta_{S_i S_f}\delta_{T_i T_f}\left(\frac{2K+1}{4\pi}\right)^{\frac{1}{2}} \\ \times c(lKl,\ 000)\Bigg\}, & \quad \ldots\ldots (2.19)\end{aligned}$$

where Rose's (1957) definition for the reduced matrix elements has been used

$$\langle l||Y_K||l\rangle = \left(\frac{2K+1}{4\pi}\right)^{\frac{1}{2}} c(lKl,\ 000), \quad \ldots\ldots (2.20)$$

and

$$\langle j_1' j_2' j'||T_K(2)||j_1 j_2 j\rangle = u(j_1 j_2 j' K;\ j j_2')\langle j_2'||T_K(2)||j_2\rangle. \quad \ldots\ldots (2.21)$$

The orthogonal coefficients $u(j_1 j_2 j' K;\ j j_2')$ are related to the Racah coefficients by

$$u(j_1 j_2 j' K;\ j j_2') = (\hat{j}\hat{j}_2')^{\frac{1}{2}} W(j_1 j_2 j' K;\ j j_2'), \quad \ldots\ldots (2.22)$$

where $\hat{j} = 2j+1$.

For simplicity of notation the expression in curly brackets in (2.19) is replaced by $F(\alpha_P \alpha_n,\ Kl)$ where α_P and α_n represent the parent and shell model quantum numbers. Using the same techniques for the matrix elements

$$\langle J' L' M_{J'}|Y_K^{\mu}\ |J L M_J\rangle$$

the final expression for $\mathfrak{M}$ becomes

$$\begin{aligned}\mathfrak{M} = (4\pi)^{\frac{1}{2}} N \sum_K (-1)^K (1/\hat{K}) F(\alpha_P \alpha_n,\ Kl) & \sum_{LL'JJ'} (-1)^{\frac{1}{2}-J'} (\hat{J}')^{-\frac{1}{2}} Z(LJL'J';\tfrac{1}{2}K) \\ \times R_{JJ'LL'K} & \sum_{M_L M_{L'} M_J M_{J'} \mu} (-1)^{\mu} c(J_i K J_f,\ M_{J_i}-\mu M_{J_f}) c(JKJ',\ M_J \mu M_{J'}) \\ \times c(L\tfrac{1}{2}J,\ M_L \mu_p M_J) & c(L'\tfrac{1}{2}J',\ M_{L'} \mu_p M_{J'}) a(LM_L) a^*(L'M_{L'}), \quad \ldots\ldots (2.23)\end{aligned}$$

and the Z coefficient is defined by the relation

$$Z(LJL'J';\ SK) = (\hat{L}\hat{J}\hat{L}'\hat{J}')^{\frac{1}{2}} c(LL'K,\ 000) W(LJL'J';\ SK). \quad \ldots\ldots (2.24)$$

In the evaluation of $\Sigma_{av}|\mathfrak{M}|^2$ for the cross section, there appears the term

$$\sum_{M_{J_i} M_{J_f}} c(J_i K J_f,\ M_{J_i}-\mu M_{J_f}) c(J_i K' J_f,\ M_{J_i}-\mu' M_{J_f}) = (\hat{J}_f/\hat{K})\delta_{KK'}\delta_{\mu\mu'}, \quad \ldots\ldots (2.25)$$

on account of the orthonormality of the Clebsch–Gordan coefficients. For numerical calculation it is convenient to reduce the Z coefficient in (2.23) by a formula due to Ford and Levinson (1955)

$$\begin{aligned} Z(LJL'J';\ \tfrac{1}{2}K) &= (-1)^{J-\frac{1}{2}} (\hat{K}\hat{J})^{\frac{1}{2}} c(JKJ',\ \tfrac{1}{2}0\tfrac{1}{2}) \quad \text{for } L+K+L' \text{ even} \\ &= 0 \qquad\qquad\qquad\qquad\qquad\quad \text{for } L+K+L' \text{ odd.} \end{aligned} \quad \ldots\ldots (2.26)$$

The cross section is given by (2.1) and (2.23)

$$\sigma(\theta)=N^2\frac{k'}{k}\left(\frac{m}{2\pi\hbar^2}\right)^2\sum_K S_K \sum_{\mu\mu_p\mu_{p'}} |C^{K\mu\mu_p\mu_{p'}}|^2, \qquad \ldots\ldots (2.27)$$

where

$$S_K=4\pi^3(\hat{J}_f/2\hat{J}_i\hat{K}^2)F^2(\alpha_p\alpha_n, Kl), \qquad \ldots\ldots (2.28)$$

and

$$C^{K\mu\mu_p\mu_{p'}}=16\pi\sum_{LL'JJ'}(-1)^{J-J'}(\hat{J}/\hat{J}')i^{(L-L')}c(JKJ', \tfrac{1}{2}0\tfrac{1}{2})R_{JJ'LL'K}$$
$$\times\sum_{M_LM_{L'}M_JM_{J'}}(-1)^{\mu+M_L}Y^{-M_L}_{L}(\tfrac{1}{2}\pi, 0)Y^{M_{L'}}_{L'}(\tfrac{1}{2}\pi, \theta)c(L'\tfrac{1}{2}J', M_{L'}\mu_{p'}M_{J'})$$
$$\times c(L\tfrac{1}{2}J, M_L\mu_pM_J)c(JKJ', M_J\mu M_{J'}), \qquad \ldots\ldots (2.29)$$

in which the axis of quantization is chosen as the vector $\mathbf{n}$ parallel to $\mathbf{k}\times\mathbf{k}'$. (2.27) can be separated into two parts, i.e.

$$\sigma(\theta)=N^2\frac{k'}{k}\left(\frac{m}{2\pi\hbar^2}\right)^2\sum_{K\mu}S_K\{\sum_{\mu_p=\mu_{p'}}|C^{K\mu\mu_p\mu_p}|^2+\sum_{\mu_p=-\mu_{p'}}|C^{K\mu\mu_p-\mu_p}|^2\}, \qquad \ldots\ldots (2.30)$$

the second term in (2.30) being the 'spin-flip' cross section which tends to zero as the spin–orbit potential approaches zero, and adds incoherently to the 'non-spin-flip' cross section.

The polarization for this choice of axis is given (Sawicki 1956, Wolfenstein 1949) by

$$P(\theta)=P_z=\frac{\sum_{K\mu\mu_p}|\mathfrak{M}(\mu_{p'}=+\frac{1}{2})|^2-\sum_{K\mu\mu_p}|\mathfrak{M}(\mu_{p'}=-\frac{1}{2})|^2}{\sum_{K\mu\mu_p}|\mathfrak{M}(\mu_{p'}=+\frac{1}{2})|^2+\sum_{K\mu\mu_p}|\mathfrak{M}(\mu_{p'}=-\frac{1}{2})|^2}, \qquad \ldots\ldots (2.31)$$

and

$$\mathfrak{M}(\mu_{p'}=\pm\tfrac{1}{2})=NS_K{}^{\frac{1}{2}}C^{K\mu\mu_p\mu_{p'}=\pm\frac{1}{2}}. \qquad \ldots\ldots (2.32)$$

For K single-valued the fractional parentage functions vanish from the polarization formula, which becomes

$$P(\theta)=\frac{\sum_{\mu\mu_p}|C^{K\mu\mu_p\frac{1}{2}}|^2-\sum_{\mu\mu_p}|C^{K\mu\mu_p-\frac{1}{2}}|^2}{\sum_{\mu\mu_p}|C^{K\mu\mu_p\frac{1}{2}}|^2+\sum_{\mu\mu_p}|C^{K\mu\mu_p-\frac{1}{2}}|^2}. \qquad \ldots\ldots (2.33)$$

Such a case is the transition to the first excited state in ^{12}C in which exchange is neglected.

In the present work, a zero range force of the form $v_i\delta(r_1r_{ji})$ is taken in order to reduce the complexity of numerical calculations. A simple calculation using a Yukawa finite range force was carried out and the shape of the cross section was only slightly affected, nevertheless this feature is a shortcoming of the present calculation. One disadvantage is that absolute magnitudes cannot be calculated. However, relative magnitudes can be obtained, which may usefully be compared with the results of Levinson and Banerjee (1958). In this approximation $R_{JJ'LL'K}$ reduces to a single integral

$$R_{JJ'LL'}=v_1\int_0^\infty dr\, r^2R_{J'L'}(r)R_{j_fl}(r)R_{JL}(r)R_{j_il}(r), \qquad \ldots\ldots (2.34)$$

where the bound wave functions are normalized so that

$$\int_0^\infty dr\, r^2R^2_{jl}(r)=1. \qquad \ldots\ldots (2.35)$$

In order to compare the present results with those of Levinson and Banerjee, calculations were carried out neglecting the spin–orbit potential. In this case (2.27) becomes

$$\sigma(\theta)=N^2\,\frac{k'}{k}\left(\frac{m}{2\pi\hbar^2}\right)^2\sum_{K\mu}S_K|C^{K\mu}|^2, \qquad \ldots\ldots(2.36)$$

where

$$C^{K\mu}=16\pi(2)^{\frac{1}{2}}\sum_{LL'}R_{LL'}i^{(L-L')}(\hat{L}/\hat{L}')^{\frac{1}{2}}c(LKL',000)\sum_{M_LM_{L'}}(-1)^{\mu+M_L}$$
$$\times Y_L^{-M_L}(\tfrac{1}{2}\pi,0)Y_{L'}^{M_{L'}}(\tfrac{1}{2}\pi,\theta)c(LKL'M_L\mu M_{L'}), \qquad \ldots\ldots(2.37)$$

and

$$R_{LL'}=v_1\int dr\,r^2R_{L'}(r)R_{j_1l'}(r)R_L(r)R_{j_1l}(r). \qquad \ldots\ldots(2.38)$$

The surface model proposed by Glendenning (1959) consists in replacing the radial integrals (2.38) by point functions at an interaction radius R_1, i.e.

$$R_{LL'}=\mathcal{N}R_{L'}(R_1)R_L(R_1), \qquad \ldots\ldots(2.39)$$

where $\mathcal{N}$ is an integral over radial oscillator wave functions and a Gaussian potential function. However, this is only a reasonable approximation if the functions $R_L(r)$ and $R_{L'}(r)$ are slowly varying functions with r, and therefore the surface model may be useful only as a nucleon spectroscopy tool, since this condition is not always satisfied.

§ 3. Elastic Polarization of 7·57 MeV and 12·0 MeV Neutrons by ^{12}C

The differential cross section and the polarization for elastic scattering using the complex spin-dependent potential of equation (2.2) are given (Lepore 1950) by

$$\sigma(\theta)=|A(\theta)+B(\theta)\boldsymbol{\sigma}\,.\,\mathbf{n}|^2=A^*A+B^*B, \qquad \ldots\ldots(3.1)$$

and

$$\mathbf{P}(\theta)=P(\theta)n=\{[A^*B+B^*A]/[A^*A+B^*B]\}\mathbf{n}, \qquad \ldots\ldots(3.2)$$

where $A(\theta)$ and $B(\theta)$ are the amplitudes for spin-independent and spin-dependent scattering respectively. For neutrons, the scattering amplitudes are

$$A(\theta)=(2ik)^{-1}\sum_{L=0}^{\infty}\{(L+1)\exp(2i\delta_L^+)+L\exp(2i\delta_L^-)-(2L+1)\}P_L(\cos\theta), \qquad \ldots\ldots(3.3)$$

and

$$B(\theta)=(2ik)^{-1}\sum_{L=0}^{\infty}\{\exp(2i\delta_L^+)-\exp(2i\delta_L^-)\}iP_L^1(\cos\theta). \qquad \ldots\ldots(3.4)$$

The complex phase shifts $\delta_L^{\pm}$ were obtained by numerical integration of the complex Schrödinger equation using the digital computer CSIRAC.

The optical model parameters used were obtained by a consideration of recent exact phase shift analyses (Fernbach and Bjorklund 1958, Nodvik and Saxon, private communication) of medium energy nucleon polarization data. The values taken were $V=45$ MeV, $W=10$ MeV, $V_s=10$ MeV for neutrons of 12·0 MeV and $V=45$ MeV, $W=5$ MeV, $V_s=10$ MeV for neutrons of 7·57 MeV.

Figure 1 shows the polarizations obtained for a carbon radius of 2·75 fermi and a diffuseness parameter of 0·4 fermi. For comparison, the 11·5 MeV proton experimental data (Rosen 1959) are also shown.

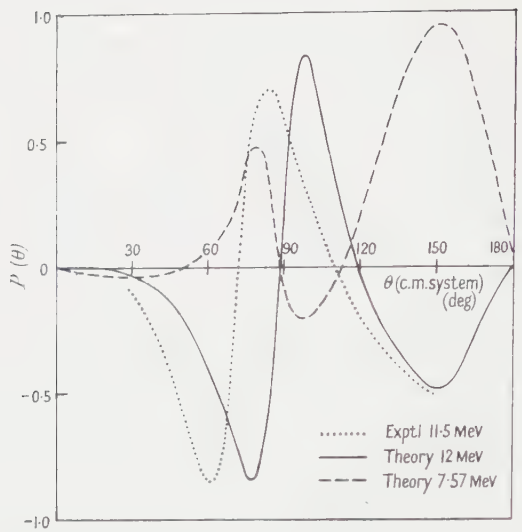

Figure 1. Polarization in the elastic scattering of 7·57 MeV and 12 MeV neutrons from ^{12}C. The optical model parameters used are $V=45$ MeV, $r_S=1{\cdot}2$ f, $W=10$ MeV (12 MeV scattering), $W=5$ MeV (7·57 MeV scattering), $V_S=10$ MeV and $a=0{\cdot}4$ f.

§ 4. Inelastic Scattering Results

The inelastic scattering to the first excited state at 4·43 MeV in ^{12}C is now discussed on the basis of § 2. Firstly it is necessary to investigate the selection rules for the transfer quantum number K. A detailed treatment of the selection rules in general has already been given by Levinson and Banerjee (1957 a) and therefore will not be repeated here.

The selection rules in the present case are contained in the factors

$$Z(LJL'J';\ \tfrac{1}{2}K)$$

for the free particle states and

$$u(S_iL_iJ_fK;\ J_iL_f)u(L_plL_fK;\ L_il)\ \ \delta_{S_iS_f}\delta_{T_iT_f}\,c(lkl,\,000)$$

for the nuclear states. For ^{12}C, according to the shell model with the transition taken as $(1s_{1/2})^4(1p_{3/2})^{\gamma}\rightarrow(1s_{1/2})^4(1p_{3/2})^{\gamma}(1p_{1/2})$, the ground state and the first excited state of ^{12}C have spins zero and two respectively. Also, the term $u(S_iL_iJ_fK;\ J_iL_f)$ for $J_i=0$ reduces to a term involving δ_{J_fK} so that K is single-valued: $K=J_f=2$, and equations (2.30) and (2.33) are appropriate for this transition.

For simplicity, the 1p wave functions are taken to be the square-well solutions of the Schrödinger equation and the same wave function is used for the excited state as for the ground state. Any errors introduced by this approximation should be relatively small, since the energy difference of 4·43 MeV is small in comparison with the well depth.

Figure 2 shows the result of taking a real square well as the distorting potential in equation (2.36) for 12 MeV neutrons. The depth of the well is 45 MeV and the radius parameter r_0 is 1·2 fermi. The bound nucleon wave functions are taken to occupy a square well of radius $R=2{\cdot}75$ fermi, and to have a binding energy $\epsilon_p=14$ MeV. There is a considerable disagreement with experiment around 90°, which could not be removed by any reasonable changes in the parameters.

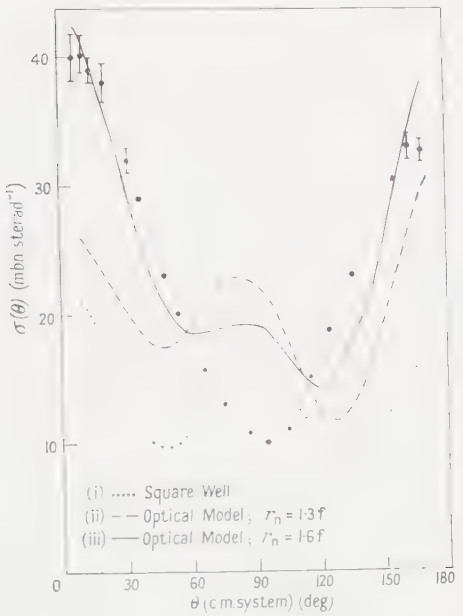

Figure 2. Angular distribution of 12 MeV nucleons, inelastically scattered from the 2^+ level at 4·43 MeV in ^{12}C. (i) shows the theoretical prediction of equation (2.36) for neutrons when a square-well distorting potential is used. (ii) and (iii) are the theoretical predictions when the square well is replaced by a spin-independent optical potential for $r_n = 1{\cdot}3$ f, $V_0 = 45$ MeV, $\epsilon_p = 14$ MeV and $r_n = 1{\cdot}6$ f, $V_0 = 27$ MeV, $\epsilon_p = 7$ MeV respectively. The points are the experimental results of Conzett for 12 MeV protons. The optical model parameters used are $V = 45$ MeV, $r_S = 1{\cdot}2$ f, $W = 10$ MeV (initial channel), $W = 5$ MeV (final channel), $V_S = 0$ and $a = 0{\cdot}4$ f. The theoretical curves are arbitrarily normalized.

The results for a spin-independent optical distorting potential are also shown in figure 2. The optical model parameters are taken to be the same as those used in the elastic calculations, except that no spin–orbit potential was included: $V = 45$ MeV, $W = 10$ MeV (for initial 12·0 MeV channel) and 5 MeV (for final 7·57 MeV channel), radius parameter of Saxon well $r_S = 1{\cdot}2$ fermi and diffuseness parameter $a = 0{\cdot}4$ fermi. The two sets of nuclear parameters used are, (*a*) radius parameter of square well for 1p bound nucleons $r_n = 1{\cdot}3$ fermi, depth of square well $V_0 = 45$ MeV and binding energy of 1p nucleons $\epsilon_p = 14$ MeV and (*b*) $r_n = 1{\cdot}6$ fermi, $V_0 = 27$ MeV, $\epsilon_p = 7$ MeV. Figure 2 indicates that the present results for a spin-independent optical potential are consistent with those of Levinson and Banerjee (1958). The cross section for $r_n = 1{\cdot}6$ fermi has more forward peaking than the cross section for $r_n = 1{\cdot}3$ fermi, and the anomalous 'hump' around 90° still persists. Furthermore the shape of the cross section is fairly insensitive to the inclusion of an imaginary potential, although the magnitude of the cross section is reduced when it is included.

Calculations for the angular distribution using a spin-orbit potential are given in figure 3 and the results show important changes. The same spin–orbit potential $V_S = 10$ MeV is used in both channels as in the elastic scattering. Set (*a*) for the nuclear parameters yields little resemblance either to experiment or to the

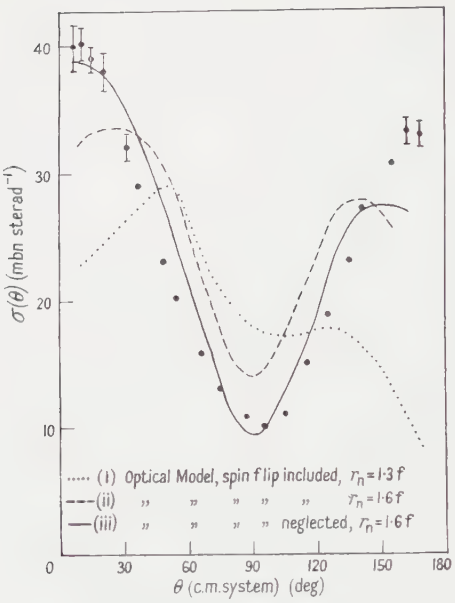

Figure 3. Angular distribution of 12 MeV nucleons inelastically scattered from the 2^+ level at 4·43 MeV in ^{12}C. (i) and (ii) illustrate the theoretical predictions of equation (2.30) for neutrons using (i) $r_n = 1{\cdot}3$ f, $V_0 = 45$ MeV, $\epsilon_p = 14$ MeV and (ii) $r_n = 1{\cdot}6$ f, $V_0 = 27$ MeV and $\epsilon_p = 7$ MeV. (iii) is the theoretical prediction for $r_n = 1{\cdot}6$ f, $V_0 = 27$ MeV, $\epsilon_p = 7$ MeV when spin-flip is neglected. The points are the experimental results of Conzett for 12 MeV protons. The optical model parameters used are $V = 45$ MeV, $r_S = 1{\cdot}2$ f, $W = 10$ MeV (initial channel), $W = 5$ MeV (final channel), $V_S = 10$ MeV and $a = 0{\cdot}4$ f. The theoretical curves are arbitrarily normalized

spin-independent case, but shows how rapidly the cross section may change with the inclusion of the spin–orbit potential. However for set (*b*) the results are encouraging as the anomalous 'hump' is now washed out, and the form of the cross section is correct although too flat. The contribution due to spin-flip is fairly important since it contributes mainly at the angles where the non-spin-flip cross section is smallest. The almost perfect fit for the non-spin-flip cross section probably indicates that the size of the spin–orbit potential has been overestimated, but the rapid variation of the cross section with optical parameters makes it difficult to speculate. The persistent disagreement of the Levinson and Banerjee calculations at backward angles at energies close to 14 MeV is no doubt due to the neglect of a spin–orbit potential. The inclusion of a spin–orbit potential yields a more consistent explanation of the experimental data due to the large D-phase splitting which leads to important interference effects between the two partial waves.

A sensitive method of testing the models is to investigate the polarization of the inelastically scattered particles. The results are shown in figure 4 and there is a strong resemblance to the 7·57 MeV elastic polarization in figure 1. Since Levinson and Banerjee's theory predicts zero polarization, the large polarizations obtained here indicate that the theory which neglects spin–orbit forces should not

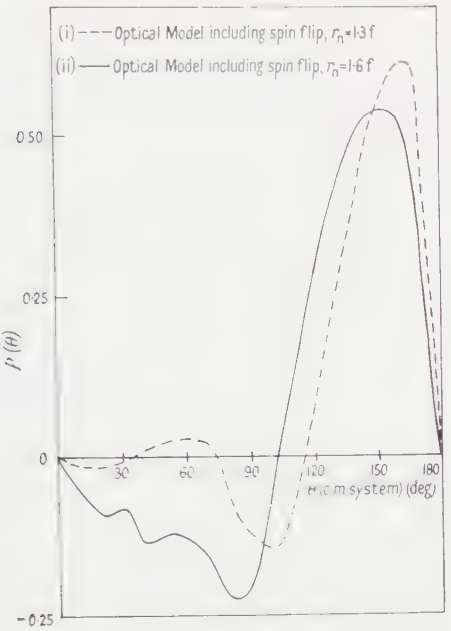

Figure 4. Polarization of 12 MeV neutrons inelastically scattered from the 2^+ level at 4·43 MeV in ^{12}C. (i) and (ii) illustrate the theoretical predictions of equation (2.41) for (i) $r_n = 1{\cdot}3$ f, $V_0 = 45$ MeV, $\epsilon_p = 14$ MeV and (ii) $r_n = 1{\cdot}6$ f, $V_0 = 27$ MeV and $\epsilon_p = 7$ MeV. The optical model parameters used are $V = 45$ MeV, $r_S = 1{\cdot}2$ f, $W = 10$ MeV (initial channel), $W = 5$ MeV (final channel), $V_S = 10$ MeV and $a = 0{\cdot}4$ f.

be taken too seriously. A measurement of the inelastic polarization would be very useful to determine how important the spin–orbit effect is in inelastic scattering at these energies.

Finally it is important to note that the relative cross section for a spin–orbit potential is about two times smaller than for no spin–orbit potential. This is due to the contribution from one spin state to the cross section being considerably reduced and indicates that the two-body force required to fit the data will be about two to four times that expected from nucleon–nucleon scattering.

§ 5. Concluding Remarks

The inelastic calculations indicate that two of the 'anomalies' found by Levinson and Banerjee are removed by the inclusion of a spin–orbit potential. It is interesting to note that recent calculations by Tobocman (1959) for stripping reactions show a similar consistency between the optical model parameters, although in this case spin–orbit effects were neglected.

The possibility of first fitting the elastic data and then using the same parameters to fit the inelastic data would be a very stringent test of both the optical model and the distorted wave approximation. The validity of the latter has been discussed by Austern (1958) and Mohr (1959). It is pointed out by Austern that the perturbation treatment should be invalid for ^{12}C, since the total cross section at 12 MeV for direct interaction to the 4·43 level is larger than the elastic cross section for neutrons. A Yoshida (1956, 1958) type calculation, in which

the strong coupling between elastic and inelastic channels is accounted for, would be more realistic but unfortunately far more complicated and lengthy. Nevertheless, the present results indicate that the distorted wave approximation is capable of predicting fairly accurately the shape of the cross section, if not its absolute magnitude.

It appears that the discrepancy in the magnitude of the cross section may only be removed by the use of a model which includes some form of collective motion. This view is supported by measurements of the lifetime of the first excited state in ^{12}C (Devons, Manning and Towle 1956), which indicate that the single particle estimate is in error by about a factor of 10.

Acknowledgments

The authors wish to thank Dr. F. Hirst and his computer staff for their willing assistance in the operation of CSIRAC, and Associate Professor C. B. O. Mohr for his encouragement and interest in this work. We are grateful to Dr. D. S. Saxon and Dr. J. S. Nodvik for communicating to us a preprint of their analysis of low energy elastic scattering. One of the authors (D. R.) wishes to acknowledge the award of a University of Melbourne Research Scholarship.

References

Austern, N., 1958, *Fast Neutron Physics* (to be published), Ch. 5. Private communication.
Condon, E. U., and Shortley, G. H., 1935, *Theory of Atomic Spectra* (Cambridge: University Press).
Conzett, H. E., 1957, *Phys. Rev.*, **105**, 1324.
Devons, S., Manning, G., and Towle, J. H., 1956, *Proc. Phys. Soc.* A, **69**, 173.
Fernbach, S., and Bjorklund, F., 1958, *Phys. Rev.*, **109**, 1298.
Ford, K. W., and Levinson, C., 1955, *Phys. Rev.*, **100**, 1.
Glendenning, N. K., 1959, *Phys. Rev.*, **114**, 1297.
Huby, R., Refai, M. Y., and Satchler, G. R., 1958, *Nucl. Phys.*, **9**, 94.
Jahn, H. A., and Van Wieringen, H., 1951, *Proc. Roy. Soc.* A, **209**, 502.
Lepore, J. V., 1950, *Phys. Rev.*, **79**, 137.
Levinson, C., and Banerjee, M., 1957 a, *Ann. Phys., New York*, **2**, 471.
—— 1957 b, *Ibid.*, **2**, 499.
—— 1958, *Ibid.*, **3**, 67.
Mohr, C. B. O., 1959, *Proc. Phys. Soc.*, **73**, 894.
Mott, N. F., and Massey, H. S. M., 1949, *The Theory of Atomic Collisions*, 2nd Edn. (Oxford: University Press), Ch. VIII.
Newns, H., 1953, *Proc. Phys. Soc.* A, **66**, 477.
Okai, S., 1959, *Progr. Theor. Phys.*, **22**, 89.
Peelle, R. W., 1957, *Phys. Rev.*, **105**, 1310.
Racah, G., 1943, *Phys. Rev.*, **63**, 367.
Rose, M. E., 1957, *Elementary Theory of Angular Momentum* (New York: John Wiley and Sons).
Rosen, L., 1959, *Proceedings of the International Conference on the Nuclear Optical Model, Florida State University, Tallahassee.*
Sawicki, J., 1955, *Nuovo Cim.*, **2**, 1322.
—— 1956, *Phys. Rev.*, **104**, 1441.
Saxon, D. S., and Woods, R. D., 1954, *Phys. Rev.*, **95**, 577.
Tobocman, W., 1959, *Phys. Rev.*, **115**, 98.
Wolfenstein, L., 1949, *Phys. Rev.*, **75**, 1664.
Yoshida, S., 1956, *Proc. Phys. Soc.* A, **69**, 668.
—— 1958, *Progr. Theor. Phys.*, **19**, 169.

The Relativistic Theory of K Ionization by Electrons

By H. S. PERLMAN
Physics Department, University of Melbourne

Communicated by P. Swan; MS. received 8th March 1960

Abstract. Relativistic cross sections for the K shell ionization of light to heavy atoms by fast electrons are developed using the Møller interaction. The effect of electron exchange and the validity of the Born approximation are discussed. Suitable kinds of wave function for the K electrons are considered.

Ionization cross sections are calculated for mercury using Dirac wave functions and for nickel using Darwin wave functions.

The cross sections for nickel agree well with experiment. Those for mercury await experimental confirmation.

§ 1. Introduction

There has hitherto been no adequate theoretical account of inner-shell ionization by electrons for any but the lightest atoms, where relativistic effects are unimportant except at high incident energies. Non-relativistic work in this field was pioneered by Bethe (1930) and Massey and Mohr (1933) for low energy electrons in hydrogen and helium. Subsequently Burhop (1940) calculated K and L shell ionization cross sections for a number of elements up to mercury. For the lighter elements, his K shell cross sections were in good agreement with experiment at incident energies near the K absorption edge, even though he used the Born approximation. But even for nickel ($Z=28$) and certainly for silver ($Z=47$), this agreement deteriorated markedly at higher incident energies ($\geqslant$ five times the K ionization energy, say). For mercury ($Z=80$) though there is as yet no experimental evidence, Burhop's results can be expected to be considerably in error. This failure at higher Z and higher incident velocities is undoubtedly due to neglect of relativity. For at $Z=80$, the velocity of the K electron is about half that of light; also the incident energies considered lie between $2I_K$ and $20I_K$ (I_K denotes the K ionization energy), and consequently the incident electrons have velocities $v\sim c$, i.e. $\gamma\gg 1$. Even for nickel ($I_K=8$ kev) the incident energies considered are of the order of 100 kev, at which $v/c\simeq 0{\cdot}5$. Thus relativistic effects enter through both the atomic K and incident electrons. Arthurs and Moiseiwitsch (1958) have employed the relativistic cross section derived by Møller (1932) for high incident energies but very low Z to calculate nickel K cross sections which agree with experiment.

But apart from any intrinsic interest, electron ionization theory is of some moment by virtue of its connection with the so-called Møller interaction (the first-order interaction Hamiltonian for relativistic electrons used here). To determine the adequacy of this interaction for the description of collision processes Williams and Terroux (1929), Williams (1930), Champion (1932) and others, for example, Groetzinger *et al.* (1950), measured the differential cross

section for free electron–electron collisions using cloud chambers. But the results were rather inconclusive, mainly because most of the scattering is through small angles and at these angles, for free electrons, the effect of the additional spin term is small, and relativity can be included classically to give nearly the same cross section as does the use of the Møller interaction (Møller 1932). Recent use of coincidence methods (Ashkin, Page and Woodward 1954) has yielded large-angle cross sections which do tend to verify the Møller interaction fairly well. Nevertheless, when atomic binding is not negligible, i.e. for large Z, the classical approach fails at all angles and therefore comparison between experimental and theoretical cross sections for heavy elements constitutes a definitive test of the adequacy of the Møller interaction for collision processes.

Yet another reason for interest in relativistic inner-shell ionization by electrons concerns the question of the range of validity of the Born approximation in inelastic atomic collision theory. For the incident electron energies considered here, theoretical justification is notoriously difficult and therefore any empirical test of its validity would be particularly welcome.

The difficulty is that for light elements the hydrogenic atomic wave functions usually employed to facilitate theoretical (Born) estimates introduce considerable errors, quite apart from any that might arise from the Born approximation itself, and consequently the situation remains obscure. But for the inner shells of heavy elements, particularly the K shell, hydrogenic wave functions are certainly adequate and theoretical calculations—if relativistic—allow an unambiguous verification.

§ 2. Derivation of Relativistic Cross Section

The potential energy of interaction of two relativistic electrons in the field of a heavy nucleus was first derived by Møller (1931, 1932) on the basis of semi-classical considerations. A field theoretical treatment was subsequently shown (e.g. Brown 1952) to yield the same interaction to the order of $Z\alpha^2$, namely

$$(\alpha/r_{12})(1-\boldsymbol{\alpha}_1\cdot\boldsymbol{\alpha}_2)\exp(i|E^0-E^1|r_{12}). \qquad \ldots\ldots(1)$$

Relativistic units are employed throughout.

If the interaction between the three electrons (the two K shell electrons and the incident electron) is considered a small perturbation, first-order time-dependent perturbation theory yields the following transition probability per unit time dP for a transition from an initial state i to a final state f such that the final momentum of the incident particle lies between $\mathbf{p}^1$ and $\mathbf{p}^1+d\mathbf{p}^1$;

$$dP=(2\pi)^{-2}|\langle \mathrm{f}|H_\mathrm{i}|\mathrm{i}\rangle|^2\,d\mathbf{p}^1. \qquad \ldots\ldots(2)$$

Inserting the total relativistic wave functions, properly antisymmetrized, one obtains

$$dP=(2\pi)^{-2}|F+2G|^2\,d\mathbf{p}^1 \qquad \ldots\ldots(3)$$

where

$$F=\int[\phi_{E^1}(1)\psi_W(2,3)]^*H_1\phi_{E^0}(1)\psi_{W^0}(2,3)\,d\tau$$

and

$$G=\int[\phi_{E^1}(2)\psi_W(3,1)]^*H_1\phi_{E^0}(1)\psi_{W^0}(2,3)\,d\tau.$$

Here ϕ_{E^0} and ϕ_{E^1} denote the relativistic wave functions of the incident electron

initially and finally and ψ_{W^0} and ψ_W the corresponding total relativistic wave functions of the two K electrons.

In the non-relativistic limit it is easy to show that $|F+2G|^2$ reduces to $|f-g|^2$, f and g being defined as in Massey and Mohr (1931, eqn (7)) except for the presence of the nuclear potential in their g.

We now neglect in H_i the interaction between the two K electrons and instead take account of it by putting $Z-0{\cdot}3$ in place of Z in the atomic wave functions ψ_{W^0} and ψ_W. Thus H_i becomes

$$H_i=\alpha \sum_{j=2}^{\infty} \{(1/r_{1j})(1-\boldsymbol{\alpha}_1 . \boldsymbol{\alpha}_j) \exp (i|E^0-E^1|r_{1j})\} \qquad \ldots\ldots (4)$$

where $\boldsymbol{\alpha}_i$ operates on particle i, $i=1$ denoting the incident electron.

We next replace the incident electron wave functions by Dirac plane waves (the first Born approximation), and put

$$\left.\begin{aligned} \phi_{E^0}(i) &= N^0 a_{E^0} \exp (i\mathbf{p}^0 . \mathbf{r}_i) \\ \phi_{E^1}(i) &= N^1 a_{E^1} \exp (i\mathbf{p}^1 . \mathbf{r}_i) \end{aligned}\right\} \qquad \ldots\ldots (5)$$

where the spinors $a_E = a_{p,s}$ for the two opposite spin states $s=\alpha$ and $s=\beta$ can be represented by the column matrices

$$a_{p,\alpha}=\begin{pmatrix} -p_x+ip_y \\ p_z \\ 0 \\ F \end{pmatrix}; \qquad a_{p,\beta}=\begin{pmatrix} -p_z \\ -p_x-ip_y \\ F \\ 0 \end{pmatrix}$$

and where, if we normalize to one electron per unit volume,

$$N=(2EF)^{-1/2} \quad \text{with} \quad F=1+E \quad \text{and} \quad E=(1+p^2)^{1/2}.$$

The validity of this approximation will be discussed presently. Adopting it for the moment one finds, on substituting (4) and (5) into (3) for F and G, that

$$F=\alpha N^1 N^0 \sum_{j=2}^{3} \int (r_{1j})^{-1} \exp [i(\mathbf{p}^0-\mathbf{p}^1) . \mathbf{r}_1 + i|E^0-E^1|r_{1j}] \psi_W{}^*(2,3) \times \{a_{E^1}{}^* a_{E^0} - a_{E^1}{}^* \boldsymbol{\alpha}_1 a_{E^0} . \boldsymbol{\alpha}_j\} \psi_{W^0}(2,3)\, d\tau$$

and

$$G=\alpha N^1 N^0 \sum_{j=2}^{3} (r_{1j})^{-1} \exp [-i\mathbf{p}^1 . \mathbf{r}_2 - i\mathbf{p}^0 . \mathbf{r}_1 + i|E^0-E^1|r_{1j}] \psi_W{}^*(3,1) \times \{a_{E^1}{}^* a_{E^0} - a_{E^1}{}^* \boldsymbol{\alpha}_1 a_{E^0} . \boldsymbol{\alpha}_j\} \psi_{W^0}(2,3)\, d\tau. \qquad \ldots\ldots (6)$$

The integration over $\mathbf{r}_1$ in F is standard (cf. Møller 1932). We obtain

$$F=4\pi\alpha N^1 N^0 [q^2-(E^0-E^1)^2]^{-1} \sum_{j=2}^{3} \int \exp (i\mathbf{q} . \mathbf{r}_j) \psi_W{}^*(2,3) \times \{(a_{E^1}{}^* a_{E^0}) - (a_{E^1}{}^* \boldsymbol{\alpha} a_{E^0}) . \boldsymbol{\alpha}_j\} \psi_{W^0}(2,3)\, d\tau_2\, d\tau_3 \qquad \ldots\ldots (7)$$

where $\mathbf{q}=\mathbf{p}^0-\mathbf{p}^1$.

The corresponding integration in G would occasion far more difficulty. Fortunately it is possible to argue plausibly that for medium to heavy elements and for incident energies of the order of 10 times the K absorption edge (i.e. the regions of interest here), G is negligible compared with F.

For in the non-relativistic limit $|F+2G|^2$ tends to $|f-g|^2$ where f and g (cf. Massey and Mohr 1931, 1933) are defined by (apart from a constant factor)

$$\left.\begin{aligned} f &= \int (r_{12}^{-1}+r_{13}^{-1}) \exp\,[i(\mathbf{p}^0-\mathbf{p}^1)\,.\,\mathbf{r}_1]\psi_W^*(2,3)\psi_{W^0}(2,3)\,d\tau, \\ g &= \int (r_{12}^{-1}+r_{13}^{-1}) \exp\,[-i\mathbf{p}^1\,.\,\mathbf{r}_2+i\mathbf{p}^0\,.\,\mathbf{r}_1]\psi_W^*(3,1)\psi_{W^0}(2,3)\,d\tau. \end{aligned}\right\} \quad \ldots\ldots(8)$$

Expressing the two-electron Schrödinger (spinless) wave functions ψ_W and ψ_{W^0} in terms of single-electron Schrödinger wave functions ϕ_W and ϕ_{W^0} yields

$$\begin{aligned} f &= \int r_{12}^{-1} \exp\,(i\mathbf{q}\,.\,\mathbf{r}_1)\phi_W^*(2)\phi_{W^0}(2)\,d\tau \quad \pm \text{same}, \\ g &= \pm \int r_{12}^{-1} \exp\,[i(\mathbf{p}^0\,.\,\mathbf{r}_1-\mathbf{p}^1\,.\,\mathbf{r}_2)]\phi_W^*(1)\phi_{W^0}(2)\,d\tau \\ &\quad + \int r_{13}^{-1} \exp\,[i(\mathbf{p}^0\,.\,\mathbf{r}_1-\mathbf{p}^1\,.\,\mathbf{r}_2)]\phi_W^*(3)\phi_{W^0}(3)\phi_{W^0}^*(1)\phi_{W^0}(2)\,d\tau \\ &\quad \pm \int r_{13}^{-1} \exp\,[i(\mathbf{p}^0\,.\,\mathbf{r}_1-\mathbf{p}^1\,.\,\mathbf{r}_2)]\phi_W^*(1)\phi_{W^0}(2)\phi_{W^0}^*(3)\phi_{W^0}(3)\,d\tau. \end{aligned} \quad \ldots\ldots(9)$$

We now approximate to g by means of the following substitutions. We put, in the first integral,

$$\phi_W^*(1) \rightarrow \exp\,(-i\mathbf{p}\,.\,\mathbf{r}_1)$$

and

$$\exp\,(-i\mathbf{p}^1\,.\,\mathbf{r}_2) \rightarrow \phi_{W^1}^*(2) \quad \ldots\ldots(10)$$

where $W^1=[1+(p^1)^2]^{1/2}$ and $p=(W^2-1)^{1/2}$.

Making similar substitutions in the second and third integrals, which consequently vanish by orthogonality, leaves

$$g = \pm \int r_{12}^{-1} \exp\,[i(\mathbf{p}^0-\mathbf{p})\,.\,\mathbf{r}_1]\phi_{W^1}^*(2)\phi_{W^0}(2)\,d\tau. \quad \ldots\ldots(11)$$

The approximations (10) are justified at the energies under consideration. The first of these has been employed in direct ionization cross section calculations with considerable success (Wetzel 1933) and the second seems at least as justifiable as the first. The two approximations would affect g in opposite directions and the net result would therefore probably not differ from the true value of g by more than about 30%.

Summing over final spin states we eventually obtain, in the notation of § 6,

$$\frac{|g|^2}{|f|^2} \simeq \frac{|\epsilon_{W^1W^0}(q^1)|^2}{|\epsilon_{WW^0}(q)|^2}, \quad \ldots\ldots(12)$$

$\mathbf{q}$ and $\mathbf{q}^1$ being defined by $\mathbf{q}=\mathbf{p}^0-\mathbf{p}^1$ and $\mathbf{q}^1=\mathbf{p}^0-\mathbf{p}$ respectively.

The ratio of these matrix elements, for which closed expressions are available (Bethe 1930, Massey and Mohr 1933), was computed for $Z=80$ and an incident energy equal to ten times the K ionization energy of Hg, for a pertinent range of values of W, q, W^1 and q^1.

In all cases it was found that $|g|^2/|f|^2<0{\cdot}001$ so that the contribution of the exchange term to the total cross section was less than 5%. Extrapolation to the

relativistic region consequently justifies the neglect of G, and hence

$$dP = (2\pi)^{-2}|F|^2\, d\mathbf{p}^1. \qquad \ldots\ldots(13)$$

Since the total K ionization cross section σ_K is just

$$\sigma_K = \sum \int \frac{dP}{v} \qquad \ldots\ldots(14)$$

where $v = p^0/E^0$ denotes the velocity of the incident electron, we finally obtain the differential cross section (cf. Bethe 1933), using Σ' to denote an average over initial values and a sum over final values,

$$\Phi(W^0, \mathbf{p}^0, \mathbf{p}^1)\, d\mathbf{p}^1 = 4\alpha^2 E^0\, d\mathbf{p}^1 \{p^0[q^2 - (E^0 - E^1)^2]^2\}^{-1} \sum'_{\substack{\text{atomic}\\ l,\,m}} \sum'_{\substack{\text{atomic}\\ \text{spins}}} \sum'_{\substack{\text{incident}\\ \text{spins}}} |AO - \mathfrak{A}\,.\,\mathbf{Q}|^2 \qquad \ldots\ldots(15)$$

where

$$\mathbf{Q} = \sum_{j=1}^{\bar{z}} \int \psi_W^*(\mathbf{r}_1, \mathbf{r}_2)\boldsymbol{\alpha}_j \psi_{W^0}(\mathbf{r}_1, \mathbf{r}_2) \exp(i\mathbf{q}\,.\,\mathbf{r}_j)\, d\tau$$

$$O = \sum_{j=1}^{\bar{z}} \int \psi_W^*(\mathbf{r}_1, \mathbf{r}_2)\psi_{W^0}(\mathbf{r}_1, \mathbf{r}_2) \exp(i\mathbf{q}\,.\,\mathbf{r}_j)\, d\tau$$

$$\mathfrak{A} = N^1 N^0 a^{1*} \boldsymbol{\alpha} a^0$$

$$A = N^1 N^0 a^{1*} a^0.$$

E^0/p^0 is the initial total incident energy/momentum, E^1/p^1 the final total incident energy momentum, W^0 denotes the energy of the initial atomic (K electron) state and W/p the energy/momentum of the final atomic state.

Returning to a consideration of the validity of the first Born approximation in the present context, one must perforce be content with the satisfaction of vague criteria, failing something like a second Born calculation, the labour of which is nearly as prohibitive as that involved in proceeding without recourse to Born approximation at all.

Of all the criteria suggested (and some have long been known to be too restrictive (cf. Henneberg 1933)) the sufficient requirement that $E \gg V$ appears most founded. Thus, in the evaluation of cross sections for the K ionization of medium to heavy atoms by electrons with energies ranging from 3 to 20 times the K ionization energy, it would appear that use of the first Born approximation is theoretically justified only in the upper energy range. Nevertheless, even in the lower energy range, some confidence is afforded by the good agreement between experiment and Burhop's (1940) Born approximation calculations for nickel and silver at incident energies close to the threshold (where relativistic effects are negligible) (cf. Massey 1956).

This confidence is strengthened by an examination of the regions of the configuration space of the incident electron, and hence those values of l, which contribute predominantly to the cross section. Accepting the Born approximation as at least qualitatively reliable, a typical integral over the configuration space of the incidence electron (cf. (7)) reduces, on angular integration, to a radial integral of the form

$$\int_0^\infty \sin qr^1 \exp(i|E^0 - E^1|r^1)\, dr^1 \qquad \ldots\ldots(16)$$

where $\mathbf{r}^1 = \mathbf{r} - \mathbf{R}$, $\mathbf{r}$ and $\mathbf{R}$ being the position vectors of the incident and K electron respectively. This integral is not convergent, but it can be calculated by inserting

an integrating factor $\exp(-\lambda r^1)$ into the integrand, integrating, and then taking the limit $\lambda \to 0$ (cf. Bethe 1930).

We may therefore replace (16) by the integral

$$\int_0^\infty \sin qr^1 \exp(-\lambda r^1 + i|E^0 - E^1|r^1)\, dr^1 \qquad \ldots\ldots (17)$$

where λ is very small compared with $|E^0 - E^1|$, q and unity. Now it is evident that most of the contribution to (17) arises from distance $r^1 \gg 1$. But for $Z = 80$, the K shell radius $a_K = 1/\alpha Z \sim 2$ and since $R \sim a_K$, one can conclude that the predominant contribution in the integration over the configuration space of the incident electron arises from distances, denoted by r_{eff}, such that $r_{\text{eff}} \gg a_K$. Hence the Born condition $E \gg V$ is less restrictive than the form $E \gg V(a_K)$ suggests. For we have found that the relaxed criterion that E be slightly greater than $V(a_K)$ entails the more realistic condition $E \gg V(r_{\text{eff}})$ which in turn justifies the use of the Born approximation here.

Introduction of the spinors a^1 and a^0 into (15) followed by a summation over incident electron spins, yields, after some tedious algebra

$$\begin{aligned}\Phi(W^0, \mathbf{p}^0, \mathbf{p}^1)\, d\mathbf{p}^1 = \alpha^2\, d\mathbf{p}^1 \{E^1 p^0 F^0 F^1 [q^2 - (E^0 - E^1)^2]^2\}^{-1} \\ \times \sum' \sum' \{[(F^0 F^1 + \mathbf{p}^1 \cdot \mathbf{p}^0)^2 + |\mathbf{p}^1 \times \mathbf{p}^0|^2]|O|^2 \\ + 2[\{(F^1)^2 + (p^1)^2\} F^0 \mathbf{p}^0 + \{(F^0)^2 + (p^0)^2\} F^1 \mathbf{p}^1] \cdot \mathscr{R}(O^* \mathbf{Q}) \\ + |F^1 \mathbf{p}^0 - F^0 \mathbf{p}^1|^2 |\mathbf{Q}|^2 \\ + 4F^1 F^0 \mathscr{R}[(\mathbf{p}^0 \cdot \mathbf{Q}^*)(\mathbf{p}^1 \cdot \mathbf{Q})]\}. \qquad \ldots\ldots (18)\end{aligned}$$

It is convenient to consider the cross section $\Phi\, d\mathbf{p}^1$ with respect to a coordinate system x, y, z such that z is along $\mathbf{p}^0$. Let p^1, θ, ϕ be the spherical polar coordinates of $\mathbf{p}^1$ referred to this system.

Then $d\mathbf{p}^1 = (p^1)^2\, dp^1 \sin\theta\, d\theta\, d\phi$ and since $q^2 = (\mathbf{p}^0)^2 + (\mathbf{p}^1)^2 - 2p^0 p^1 \cos\theta$, $p^1 = \{(E^1)^2 - 1\}^{1/2}$ and $dE^1 = dW$ (this latter by energy conservation), we have

$$d\mathbf{p}^1 = (E^1/p^0)\, dW q\, dq\, d\phi. \qquad \ldots\ldots (19)$$

Let q, α, β be the coordinates of $\mathbf{q}$ relative to the chosen coordinate system and hence

$$\cos\alpha = [(p^0)^2 - (p^1)^2 + q^2]/2p^0 q \quad \text{and} \quad \beta = \phi. \qquad \ldots\ldots (20)$$

If, for convenience, we now consider another coordinate system with polar axis along $\mathbf{q}$ and temporarily distinguish vectors referred to it by a prime, we can write

$$\left.\begin{aligned}\mathbf{p}^0 \cdot \mathbf{Q} = \mathbf{p}^{0\prime} \cdot \mathbf{Q}' = -p^0 \sin\alpha Q_y' + p^0 \cos\alpha Q_z', \\ \mathbf{p}^1 \cdot \mathbf{Q} = \mathbf{p}^{1\prime} \cdot \mathbf{Q}' = -p^0 \sin\alpha Q_y' + (p^0 \cos\alpha - q) Q_z'.\end{aligned}\right\} \qquad \ldots\ldots (21)$$

Substituting (19) and (21) into (18), dropping the primes on the O's and $\mathbf{Q}$'s, it being understood that henceforth $\mathbf{Q}$ is referred to a coordinate system with polar axis along $\mathbf{q}$, and integrating over ϕ, yields the total cross section

$$\sigma(W^0, p^0) = \int_{W_{\min}}^{W_{\max}} \int_{q_{\min}}^{q_{\max}} \Phi^1(W^0, p^0, W, q)\, dW\, dq \qquad \ldots\ldots (22)$$

where

$$\begin{aligned}\Phi^1\, dW\, dq = 2\pi\alpha^2 q\, dW\, dq \{(p^0)^2 F^0 F^1 [q^2 - (E^0 - E^1)^2]^2\}^{-1} \qquad \ldots\ldots (22a) \\ \times \sum_{\substack{\text{atomic} \\ \text{spin}}}' \sum_{l,m}' \{A|O|^2 + B_1 \mathscr{R}(O^* Q_y) + B_2 \mathscr{R}(O^* Q_z) \\ + C_1 |\mathbf{Q}|^2 + C_2 |Q_y|^2 + C_3 |Q_z|^2 + C_4 \mathscr{R}(Q_y^* Q_z)\},\end{aligned}$$

the coefficients A, B_1, B_2, C_1, C_2, C_3 and C_4 being defined by

$$A(p^0,p,q)=\{F^0F^1+[(p^0)^2+(p^1)^2-q^2]/2\}^2-(p^1p^0)^2-[(p^0)^2+(p^1)^2-q^2]^2/4$$
$$B_1(p^0,p,q)=-2p^0\sin\alpha\{F^0[(F^1)^2+(p^1)^2]+F^1[(F^0)^2+(p^0)^2]\}$$
$$B_2(p^0,p,q)=2p^0\{F^0[(F^1)^2+(p^1)^2]\cos\alpha+F^1[(F^0)^2+(p^0)^2](\cos\alpha-q/p^0)\}$$
$$C_1(p^0,p,q)=(F^1)^2(p^0)^2+(F^0)^2(p^1)^2-F^0F^1[(p^0)^2+(p^1)^2-q^2]$$
$$C_2(p^0,p,q)=4F^0F^1(p^0)^2\sin^2\alpha$$
$$C_3(p^0,p,q)=4F^0F^1p^0\cos\alpha(p^0\cos\alpha-q)$$
$$C_4(p^0,p,q)=4F^0F^1p^0\sin\alpha(q-2p^0\cos\alpha). \qquad \ldots\ldots(22b)$$

Energy conservation $E^0-E^1=W-W^0$ and equation (29) provide the limits in q and W, namely, $q_{\max}=p^0+p^1$, $q_{\min}=p^0-p^1$ where

$$(p^1)^2=(p^0)^2-2E^0[(p^2+1)^{1/2}+D-1]+[(p^2+1)^{1/2}+D-1]^2 \qquad \ldots\ldots(23)$$

and $W_{\max}=E^0-1+W^0$, $W_{\min}=1$.

It is of interest to compare the cross section (22), in the limit of low Z, with Møller's result (Møller 1932). To this end, it is more convenient to consider (18) with $d\mathbf{p}^1$ given by (19).

Using the fact that for $(Z\alpha)^2\ll 1$, $E^0-E^1=W-W^0$ and q are very small compared with p^0 and p^1 (for relativistic p^0), it is seen, after some manipulation, that

$$\sigma=\int\int\frac{8\pi\gamma^2\alpha^2q\,dq\,dW}{(\gamma^2-1)[q^2-(E^0-E^1)^2]^2}\sum_{\text{spin}}'\sum_{l,m}|O+[(\gamma^2-1)^{1/2}/\gamma]Q_z|^2. \qquad \ldots\ldots(24)$$

Møller employed Darwin wave functions, and this is quite justified if $(Z\alpha)^2\ll 1$ and if the collisions are distant. Anticipating the results and notation of § 6, these conditions yield

$$\sigma=\frac{8\pi e^4}{\hbar^2c^2}\int\int\frac{q\,dq\,dW}{[q^2-(E^0-E^1)^2]^2}\sum_{l,m}|\epsilon_{W^0W}+i\frac{\sqrt{(\gamma^2-1)}}{\gamma}\epsilon^1{}_{W^0W}|^2 \qquad \ldots\ldots(25)$$

which is the result obtained by Møller (1932, cf. also Arthurs and Moiseiwitsch 1958).

It will be appreciated that (25) is a satisfactory approximation only when $(Z\alpha)^2\ll 1$. For large Z it is seriously in error.

§ 3. The Relativistic Atomic (K) Wave Functions

Neglecting correlations between the electrons, we write the atomic wave functions in the form of an antisymmetrized product of the solutions of the Dirac equation for a single electron in an effective central potential $V(r)$.

The method for obtaining $V(r)$ adopted here (cf. Merzbacher and Lewis 1958) depends on the fact that the wave function for an electron with small principal quantum number n (and generally small $n-l$) is concentrated over a reasonably small range of radial distances near some value r_0, and therefore if one does not require too high an accuracy, it is possible to replace $V(r)$ by a simple analytic function which is a good approximation for r near r_0 (cf. Brenner and Brown 1953).

Thus for the effective potential $V(r)$ for a K electron, we may take

$$-eV(r)=-Z_{\text{eff}}\alpha r^{-1}+V \qquad \ldots\ldots(26)$$

where $Z_{\text{eff}}=Z-0{\cdot}3$ takes account of inner screening (Slater 1930) and the outer screening constant V represents the constant potential produced near r_0 by that part of the electron cloud charge which lies outside r_0.

The form (26) has the great advantage that the K electron wave function reduces to a hydrogenic wave function for charge Z_{eff}. The constant V only shifts the energy levels without affecting these wave functions.

Thus, by virtue of the Dirac fine structure formula, it is clear that if W^0 denotes the total energy of a K electron in its ground state, then

$$W^0-V=-D+1 \qquad \ldots\ldots(27)$$

where

$$D=1-[1+(\alpha Z_{\text{eff}})^2(1-\alpha^2 Z_{\text{eff}}{}^2)^{-1}]^{1/2}$$

since $j=\frac{1}{2}$, $n=1$. But $W^0=-I+1$, I being the experimental K ionization energy, and consequently

$$V=D-I. \qquad \ldots\ldots(28)$$

And for a continuum state characterized by a total energy W, we have

$$W-V=(p^2+1)^{1/2},$$

i.e.

$$(p^2+1)^{1/2}=W-D+I. \qquad \ldots\ldots(29)$$

Adequate provision for inner and outer screenings can thus be achieved merely by using, firstly, hydrogenic Dirac wave functions $\psi(\mathbf{r})$ with effective charge $Z_{\text{eff}}=Z-0{\cdot}3$, and secondly, the relation (29).

The total excited wave function $\psi_W(\mathbf{r}_1,\mathbf{r}_2)$ for the two K electrons is consequently just

$$\psi_W(\mathbf{r}_1,\mathbf{r}_2)=2^{-1/2}\{\psi_W(\mathbf{r}_1)\psi_{W^0}(\mathbf{r}_2)-\psi_W(\mathbf{r}_2)\psi_{W^0}(\mathbf{r}_1)\}. \qquad \ldots\ldots(30)$$

The continuum Coulomb Dirac wave functions $\psi_W(\mathbf{r})$ have been discussed in some detail previously (Perlman and Robson 1959, to be referred to as I). The notation of I will be adhered to here.

For the ground state K Dirac wave functions $\psi_{W^0}(\mathbf{r})$, $n'=0$, $l=0$, $j=\frac{1}{2}$ and $m=\pm\frac{1}{2}$. Hence $\kappa=-1$ and $\gamma=\sqrt{(1-\alpha^2Z^2)}\equiv\gamma'$.

Written explicitly, the two K wave functions corresponding to $m=\pm\frac{1}{2}$ are (cf. Bethe 1933, Bethe and Salpeter 1957)

$$\begin{array}{ll}
m=\frac{1}{2}: & m=-\frac{1}{2}: \\
\psi_1=i(4\pi)^{-1/2}\cos\theta f^0 & \psi_1=-i(4\pi)^{-1/2}\sin\theta e^{i\phi}f^0 \\
\psi_2=i(4\pi)^{-1/2}\sin\theta e^{i\phi}f^0 & \psi_2=i(4\pi)^{-1/2}\cos\theta f^0 \\
\psi_3=(4\pi)^{-1/2}g^0 & \psi_3=0 \\
\psi_4=0 & \psi_4=-(4\pi)^{-1/2}g^0
\end{array} \qquad \ldots\ldots(31)$$

where

$$\begin{Bmatrix} f^0 \\ g^0 \end{Bmatrix}=\begin{Bmatrix} N_{f^0} \\ N_{g^0} \end{Bmatrix} r^{\gamma'-1}\exp(-Z\alpha r)$$

and

$$\begin{Bmatrix} N_{f^0} \\ N_{g^0} \end{Bmatrix}=\mp(1\mp\gamma')^{1/2}[\Gamma(2\gamma'+1)]^{-1/2}2^{\gamma'}(Z\alpha)^{\gamma'+1/2}.$$

The complete K ground state wave function $\psi_{W^0}(\mathbf{r}_1, \mathbf{r}_2)$ is therefore

$$\psi_{W^0}(\mathbf{r}_1, \mathbf{r}_2) = 2^{-1/2}\{\psi_{W^0,\,\alpha,\,0,\,1/2}(\mathbf{r}_1)\psi_{W^0,\,\alpha,\,0,\,-1/2}(\mathbf{r}_2) - \psi_{W^0,\,\alpha,\,0,\,1/2}(\mathbf{r}_2)\psi_{W^0,\,\alpha,\,0,\,-1/2}(\mathbf{r}_1)\}. \quad \ldots\ldots (30')$$

For light atoms and low energy states, the so-called Darwin wave functions χ_α, χ_β may sometimes be used in place of Dirac functions. These may be written

$$\chi_\alpha = \tfrac{1}{2}\begin{vmatrix} i\dfrac{\partial}{\partial z} \\ i\dfrac{\partial}{\partial x} - \dfrac{\partial}{\partial y} \\ 1 \\ 0 \end{vmatrix}\psi, \qquad \chi_\beta = \tfrac{1}{2}\begin{vmatrix} i\dfrac{\partial}{\partial x} + \dfrac{\partial}{\partial y} \\ -i\dfrac{\partial}{\partial z} \\ 0 \\ 1 \end{vmatrix}\psi, \quad \ldots\ldots (32)$$

the ψ's being appropriate Schrödinger hydrogenic wave functions. In this approximation, the $\psi(\mathbf{r}_1, \mathbf{r}_2)$'s are just antisymmetrized products of χ's.

§ 4. Analytic Evaluation of Matrix Elements using Dirac Wave Functions

By virtue of the symmetry of the initial $m = \frac{1}{2}$ and $m = -\frac{1}{2}$ states, substitution of the wave functions (30) and (30′) into O and $\mathbf{Q}$ allows us to write (22*a*) in the form

$$\begin{aligned}\Phi^1\, dW\, dq = {} & 4\pi\alpha^2 q\, dW\, dq\{(p^0)^2 F^0 F^1[q^2 - (E^0 - E^1)^2]^2\}^{-1} \\ & \times \sum_l \sum_m \sum_s \{A|O|^2 + B_1\mathscr{R}(O^* Q_y) + B_2\mathscr{R}(O^* Q_z) + C_1|\mathbf{Q}|^2 \\ & + C_2|Q_y|^2 + C_3|Q_z|^2 + C_4\mathscr{R}(Q_y{}^* Q_z)\} \qquad \ldots\ldots (33)\end{aligned}$$

where O and $\mathbf{Q}$ now denote the single electron matrix elements

$$O^{s,l,m} = \int \psi_{W,\,s,\,l,\,m}{}^*(\mathbf{r})\psi_{W^0,\,\alpha,\,0,\,1/2}(\mathbf{r}) \exp(i\mathbf{q}\,.\,\mathbf{r})\, d\tau \qquad \ldots\ldots (33')$$

and

$$\mathbf{Q}^{s,l,m} = \int \psi_{W,\,s,\,l,\,m}{}^*(\mathbf{r})\boldsymbol{\alpha}\psi_{W^0,\,\alpha,\,0,\,1/2}(\mathbf{r}) \exp(i\mathbf{q}\,.\,\mathbf{r})\, d\tau.$$

The choice of coordinate system permits the expansion

$$\exp(i\mathbf{q}\,.\,\mathbf{r}) = \exp(iqr\cos\theta) = \sum_{l^1=0}^{\infty} i^{l^1}(2l^1+1)\mathrm{j}_{l^1}(qr)\mathrm{P}_{l^1}(\cos\theta). \qquad \ldots\ldots (34)$$

Substituting (34) together with the Dirac wave functions (I,1) and (31) into (33′) and employing the identities

$$\begin{aligned}\cos\theta\,\mathrm{P}_{l^1}{}^0 &= (4\pi)^{1/2}(2l^1+1)^{-1}[l^1(2l^1-1)^{-1/2}\mathrm{Y}_{l^1-1,\,0} + (l^1+1)(2l^1+3)^{-1/2}\mathrm{Y}_{l^1+1,0}] \\ \sin\theta e^{i\phi}\mathrm{P}_{l^1}{}^0 &= (4\pi)^{1/2}(2l^1+1)^{-1}\{[(l^1+2)(l^1+1)]^{1/2}(2l^1+3)^{-1/2}\mathrm{Y}l_{l^1+1,\,1} \\ &\quad - [l^1(l^1-1)]^{1/2}(2l^1-1)^{-1/2}\mathrm{Y}_{l^1+1,\,1}\} \\ \mathrm{P}_{l^1}{}^0 &= (4\pi)^{1/2}(2l^1+1)^{-1/2}\mathrm{Y}_{l^1,\,0}\end{aligned}$$

allows the angular integrations to be effected very simply by using the orthonormality of spherical harmonics. Only the values $m = \frac{1}{2}$, $-\frac{1}{2}$ and $\frac{3}{2}$ give non-vanishing contributions.

Using the abbreviation $D_{ln}=i^n(2l^1+1)j_n(qr)r^2$ we obtain

$m=\frac{1}{2}$:

$$O^{\alpha,l,1/2}=(l+1)^{1/2}(2l+1)^{-1}\int f_\kappa{}^*f^0D_l\,dr+(l+1)^{1/2}(2l+1)^{-1}\int g_\kappa{}^*g^0D_l\,dr$$

$$Q_z{}^{\alpha,l,1/2}=i2l(l+1)^{1/2}(2l+1)^{-1}(2l-1)^{-1}\int g_\kappa{}^*f^0D_{l-1}\,dr+i(l+1)^{1/2}(2l+1)^{-1}$$
$$\times(2l+3)^{-1}\int g_\kappa{}^*f^0D_{l+1}\,dr-i(l+1)^{1/2}(2l+3)^{-1}\int f_\kappa{}^*g^0D_{l+1}\,dr$$

$$O^{\beta,l,1/2}=l^{1/2}(2l+1)^{-1}\int f_\kappa{}^*f^0D_l\,dr+l^{1/2}(2l+1)^{-1}\int g_\kappa{}^*g^0D_l\,dr$$

$$Q_z{}^{\beta,l,1/2}=-il^{1/2}(2l+1)^{-1}(2l-1)^{-1}\int g_\kappa{}^*f^0D_{l-1}\,dr+i2l^{1/2}(l+1)(2l+1)^{-1}$$
$$\times(2l+3)^{-1}\int g_\kappa{}^*f^0D_{l+1}\,dr-il^{1/2}(2l-1)^{-1}\int f_\kappa{}^*g^0D_{l-1}\,dr$$

$$Q_x{}^{\alpha,l,1/2}=Q_y{}^{\alpha,l,1/2}=Q_x{}^{\beta,l,1/2}=Q_y{}^{\beta,l,1/2}=0.$$

$m=-\frac{1}{2}$:

$$Q_x{}^{\alpha,l,-1/2}=-il(l+1)^{1/2}(2l+1)^{-1}(2l-1)^{-1}\int g_\kappa{}^*f^0D_{l-1}\,dr-i(l+1)^{3/2}(2l+1)^{-1}$$
$$\times(2l+3)^{-1}\int g_\kappa{}^*f^0D_{l+1}\,dr-i(l+1)^{1/2}(2l+3)^{-1}\int f_\kappa{}^*g^0D_{l+1}\,dr$$

$$Q_y{}^{\alpha,l,-1/2}=iQ_x{}^{\alpha,l,-1/2}$$

$$Q_x{}^{\beta,l,-1/2}=il^{3/2}(2l+1)^{-1}(2l-1)^{-1}\int g_\kappa{}^*f^0D_{l-1}\,dr+il^{1/2}(l+1)(2l+1)^{-1}$$
$$\times(2l+3)^{-1}\int g_\kappa{}^*f^0D_{l+1}\,dr+il^{1/2}(2l-1)^{-1}\int f_\kappa{}^*g^0D_{l-1}\,dr$$

$$Q_y{}^{\beta,l,-1/2}=iQ_x{}^{\beta,l-1/2}$$

$$Q_z{}^{\alpha,l,-1/2}=O^{\alpha,l,-1/2}=Q_z{}^{\beta,l,-1/2}=O^{\beta,l,-1/2}=0.$$

$m=\frac{3}{2}$:

$$Q_x{}^{\alpha,l,3/2}=i[l(l+1)(l+2)]^{1/2}(2l+1)^{-1}(2l-1)^{-1}\int g_\kappa{}^*f^0D_{l-1}\,dr$$
$$-i[l(l+1)(l+2)]^{1/2}(2l+1)^{-1}(2l+3)^{-1}\int g_\kappa{}^*f^0D_{l-1}\,dr$$

$$Q_y{}^{\alpha,l,3/2}=-iQ_x{}^{\alpha,l,3/2}$$

$$Q_x{}^{\beta,l,3/2}=i[(l-1)l(l+1)]^{1/2}(2l+1)^{-1}(2l-1)^{-1}\int g_\kappa{}^*f^0D_{l-1}\,dr$$
$$-i[(l-1)l(l+1)]^{1/2}(2l+1)^{-1}(2l+3)^{-1}\int g_\kappa{}^*f^0D_{l-1}\,dr$$

$$Q_y{}^{\beta,l,3/2}=-iQ_x{}^{\beta,l,3/2}$$

$$Q_z{}^{\alpha,l,3/2}=O^{\alpha,l,3/2}=Q_z{}^{\beta,l,3/2}=O^{\beta,l,3/2}=0. \qquad \ldots\ldots(35)$$

Substituting the expressions (I, 8) and (31) for $f_\kappa{}^*$, $g_\kappa{}^*$ and f^0, g^0 respectively yields the two types of radial integral (putting $\rho=2pr$):

$$\left.\begin{aligned}\int f_\kappa{}^*\begin{Bmatrix}f^0\\g^0\end{Bmatrix}D_\lambda\,dr&=-2i^\lambda|N_-|\begin{Bmatrix}N_{f^0}\\N_{g^0}\end{Bmatrix}(2\lambda+1)(2p)^{-2-\gamma^1}(y\mathscr{I}_X+x\mathscr{I}_Y)\\ \int g_\kappa{}^*\begin{Bmatrix}f^0\\g^0\end{Bmatrix}D_\lambda\,dr&=2i^\lambda N_+\begin{Bmatrix}N_{f^0}\\N_{g^0}\end{Bmatrix}(2\lambda+1)(2p)^{-2-\gamma^1}(x\mathscr{I}_X-y\mathscr{I}_Y)\end{aligned}\right\}\quad\ldots\ldots(36)$$

where

$$\begin{Bmatrix} \mathscr{I}_X \\ \mathscr{I}_Y \end{Bmatrix} = \int_0^\infty \mathrm{j}_\lambda\left(\frac{q}{2p}\rho\right) \begin{Bmatrix} X(|\kappa|, p, \rho) \\ Y(|\kappa|, p, \rho) \end{Bmatrix} \rho^{\gamma_1 - 1/2} \exp\left(\frac{-Z\alpha}{2p}\rho\right) d\rho,$$

i.e. where

$$\mathscr{I} = \mathscr{I}_X + i\mathscr{I}_Y = \int \mathrm{j}_\lambda\left(\frac{q}{2p}\rho\right) \mathrm{M}(|\kappa|, p, \rho)\rho^{\gamma_1 - 1/2} \exp\left(\frac{-Z\alpha}{2p}\rho\right) dp,$$

λ taking the values l, $l \pm 1$.

The analytic evaluation of $\mathscr{I}$ is perhaps best pursued by expressing j and the Whittaker hypergeometric function M in terms of confluent hypergeometric functions. The resulting integral is of the general form

$$\mathscr{I}^1 = \int_0^\infty \rho^g \mathrm{e}^{-\sigma\rho}{}_1F_1(a\,;\, b\,;\, c\rho)\,{}_1F_1(x\,;\, y\,;\, z\rho)\, d\rho \qquad \ldots\ldots(37)$$

the parameters being complex, with $\mathscr{R}\sigma > 0$, $\mathscr{R}g > -1$. Putting

$$f(\rho) \equiv \mathrm{e}^{-\sigma_1\rho}{}_1F_1(x, y\,;\, z\rho)$$

$$F(\rho) \equiv \mathrm{e}^{-\sigma_2\rho}\rho^g{}_1F_1(a\,;\, b\,;\, c\rho) \quad \text{and} \quad \phi(\beta) \equiv \int_0^\infty \mathrm{e}^{-\beta\rho}F(\rho)\, d\rho$$

with $\sigma_1 + \sigma_2 = \sigma$, $\mathscr{R}\sigma_2 > 0$, $\mathscr{R}\beta > 0$, one can show that

$$f^j(0) = (-\sigma_1)^j{}_2F_1(-j, x\,;\, y\,;\, z/\sigma_1)$$

$$\phi^j(0) = \frac{\Gamma(g+1+j)}{\sigma_2{}^{g+1}}(-\sigma_2)^{-j}{}_2F_1(a, g+1+j\,;\, b\,;\, c/\sigma_2).$$

Application of the theorem due to Willis (1948) that under certain conditions which hold here

$$\int_0^\infty f(\rho)F(\rho)\, d\rho = \sum_{j=0}^{\infty} (-1)^j \frac{\phi^j(0)f^j(0)}{j!}$$

yields the formal expansion

$$\mathscr{I}^1 = \sigma_2{}^{-g-1} \sum_{j=0}^{\infty} \frac{\Gamma(g+1+j)}{j!}\left(\frac{-\sigma_1}{\sigma_2}\right)^j {}_2F_1(-j, x\,;\, y\,;\, z/\sigma_1)\,{}_2F_1(a, g+1+j\,;\, b\,;\, c/\sigma_2). \qquad \ldots\ldots(38)$$

If we make $\sigma_1 \to 0$ and employ the analytic continuation of the ${}_2F_1$, we eventually obtain

$$\mathscr{I}^1 = \Gamma(g+1)\sigma^{-g-1}F_2(g+1, a, x\,;\, b, y\,;\, c/\sigma, z/\sigma) \qquad \ldots\ldots(39)$$

which is just the result obtained by substituting integral representations for the confluent hypergeometrics in (37) (cf. Erdelyi 1936), F_2 being an Appell hypergeometric function in two variables.

No attention has been paid to convergence. It is sufficient to point out that this may be achieved by recourse to the analytic continuation of the Gauss and two-variable hypergeometric functions (cf. Erdelyi *et al.* 1953).

Because two of the parameters in (37) originate in a spherical Bessel function, the doubly infinite series which in general results from the integration can be reduced here to a finite sum of infinite series (cf. Hulme *et al.* 1935). Even so, the task of summing several slowly convergent complex infinite series for each required combination of λ, q and p is a formidable one. We therefore adopted the alternative procedure for mercury of computing the Dirac radial wave functions and then performing the radial integrations numerically. The method

of computing the Dirac radial wave functions, together with tables of the functions, appears in I.

§ 5. Computation, for Mercury, of Dirac Matrix Elements and thence K Ionization Cross Sections

Since $Z=80$ for mercury, use of Dirac wave functions is essential. The corresponding radial integrals (36) were computed by Simpson's rule, the functions (X, Y), (x, y) and j_λ being tabulated in I, tables 1 and 2 and National Bureau of Standards (1947) respectively. The interval in ρ employed was 0·2 in those integrals involving considerable cancellation and 0·4 in those in which cancellation was negligible. The maximum value of ρ considered varied for the different values of p. The criterion used for terminating the integration at a point $\rho=\rho_{\max}$ (at which the integrand has a zero) was that the next loop contributed less than 0·5% to the integral. The range of ρ for which X and Y are tabulated is sufficient to allow this in nearly all cases.

The integrations were performed for the following values of the parameters in the first instance: $p=0{\cdot}2$, 0·4, 0·6, 0·8; $|\kappa|=1$, 2, 3, 4; $\lambda=0$, 1, 2, 3 and 4 and a range of four values of q for each p (a different range, usually, for each p). These are the values which contribute predominantly to the ultimate total ionization cross section.

Supplementary radial integrals for additional values of the parameters p, q were obtained by interpolation where possible, and otherwise by computation of the $\mathcal{I}_X$'s and $\mathcal{I}_Y$'s at these points using interpolated values of the X's and Y's.

Table 1. Dirac Matrix Elements for Mercury

p	q	$\sum_{l,m,s} \lvert O\rvert^2$	$\sum_{l,m,s} \mathscr{R}(O^*Q_z)$	$\sum_{l,m,s} \lvert \mathbf{Q}\rvert^2$	$\sum_{l,m,s} \lvert Q_z\rvert^2$	$\sum_{l,m,s} \lvert Q_y\rvert^2$
0·2	0·2	0·328	−0·297	0·950	0·271	0·339
	0·4	1·27	−0·620	0·881	0·311	0·284
	0·6	1·77	−0·576	0·768	0·199	0·284
	0·8	1·36	−0·348	0·605	0·103	0·250
0·4	0·16	0·076	−0·124	0·566	0·203	0·182
	0·4	0·679	−0·446	0·720	0·293	0·214
	0·6	1·44	−0·629	0·793	0·276	0·259
	0·8	1·62	−0·529	0·760	0·173	0·294
0·6	0·24	0·0542	−0·0836	0·341	0·131	0·105
	0·42	0·318	−0·258	0·475	0·210	0·133
	0·6	0·822	−0·476	0·633	0·276	0·179
	0·8	1·33	−0·538	0·786	0·211	0·288
0·8	0·32	0·0390	−0·0529	0·188	0·0733	0·0574
	0·56	0·238	−0·198	0·345	0·165	0·0907
	0·8	0·784	−0·450	0·570	0·259	0·155
	1·2	1·04	−0·402	0·729	0·155	0·287

Substitution of the radial integrals into (35) yields the matrix elements Q_i and O (for the permitted $m=\frac{1}{2}, -\frac{1}{2}, \frac{3}{2}$ for each of $l=0$, 1, 2, 3, a total of 24 elements for each of the 50 odd values of (p, q)). These are then combined appropriately to yield the total 'squared' matrix elements appearing in (33). The matrix elements $\Sigma_{l,m,s}\,\mathscr{R}(O^*Q_y)$ and $\Sigma_{l,m,s}\,\mathscr{R}(Q_{\prime\prime}{}^*Q_z)$ vanish because of selection rules

for m (cf. (35)). The remaining five (summed over l, m and s) are shown in table 1 for the p, q values considered in the first instance.

The integrations over q and then over $W(p)=(p^2+1)^{1/2}+D-I$ (between the limits (23)) were carried out for each of six incident energies by evaluating Φ^1 (see (33), (22*b*)) for about 50 different combinations of q and $W(p)$ and estimating the areas under the curves by counting squares. This procedure yields total K ionization cross sections for mercury with a computational uncertainty of not more than 5% (see table 2).

Table 2. Cross Sections for K Ionization of Mercury by Electrons

(1)	(2)	(3)	(4)	(5)	(6)
3	0·25	6·38	5·32	—	1·20
6	0·50	7·81	4.4 (est.)	14·6	1·78
9	0·75	8·74	3·35 (est.)	—	2·61
12	1·00	9·33	2.8 (est.)	—	3·33
15	1·25	10·2	2·39	21·5	4·27
18	1·50	13·1	2·1 (est.)	—	6·23

(1), (2) Kinetic energy of incident electron: (1) in units of $I_K=83{\cdot}1$ kev, (2) in kev; (3), (4), (5) $\sigma_K\times10^{24}$ (cm^2): (3) relativistic (present work) comp. error $<5\%$, (4) non-relativistic (Burhop 1940), (5) semi-relativistic (present work) comp. error $<10\%$; (6) σ_K relativistic/σ_K non-relativistic.

§ 6. Calculation of K Cross Sections for Nickel using Darwin Wave Functions

For lighter elements, the use of Darwin wave functions reduces the matrix elements to Schrödinger type elements, which may be integrated analytically over configuration space.

Employing the wave functions (32) and making no approximation other than that implicit in the use of such wave functions† eventually yields the single electron matrix elements.

$$\sum_s |O|^2=|\epsilon_{W^0W}|^2$$

$$\sum_s |\mathbf{Q}|^2=\left|\int e^{i\mathbf{q}\cdot\mathbf{r}}\psi_W{}^*\nabla\psi_{W^0}\,d\tau\right|^2+\left|\int e^{i\mathbf{q}\cdot\mathbf{r}}\psi_{W^0}\nabla\psi_W{}^*\,d\tau\right|^2$$
$$+\mathscr{R}\left\{\int e^{i\mathbf{q}\cdot\mathbf{r}}\psi_W{}^*\nabla\psi_{W^0}\,d\tau\,.\int e^{-i\mathbf{q}\cdot\mathbf{r}}\psi_{W^0}{}^*\nabla\psi_W\,d\tau\right\}$$

$$\sum_s |Q_{x_i}|^2=\tfrac{1}{4}\left|\int e^{i\mathbf{q}\cdot\mathbf{r}}(\psi_W{}^*\nabla\psi_{W^0}+\psi_{W^0}\nabla\psi_W{}^*)\,d\tau\right|^2$$
$$-\mathscr{R}\left\{\int e^{i\mathbf{q}\cdot\mathbf{r}}\psi_W{}^*\frac{\partial}{\partial x_i}\psi_{W^0}\,d\tau\,.\int e^{-i\mathbf{q}\cdot\mathbf{r}}\psi_{W^0}{}^*\frac{\partial}{\partial x_i}\psi_W\,d\tau\right\}$$

and

$$\sum_s \mathscr{R}(O^*Q_z)=\tfrac{1}{2}\mathscr{R}\left\{i\epsilon_{W^0W}{}^*\left(\epsilon^1{}_{W^0W}-\int e^{i\mathbf{q}\cdot\mathbf{r}}\psi_{W^0}\frac{\partial}{\partial z}\psi_W{}^*d\tau\right)\right\}$$

where

$$\epsilon_{W^0W}=\int e^{i\mathbf{q}\cdot\mathbf{r}}\psi_W{}^*\psi_{W^0}\,d\tau \quad\text{and}\quad \epsilon^1{}_{W^0W}=\int e^{i\mathbf{q}\cdot\mathbf{r}}\psi_W{}^*\frac{\partial}{\partial z}\psi_{W^0}\,d\tau. \qquad \ldots\ldots(40)$$

† Previous use of Darwin wave functions (e.g. Møller 1931, 1932, Arthurs and Moiseiwitsch 1958) has involved the additional explicit condition $(Z\alpha)^2\ll1$.

As in the Dirac case, the matrix elements $\Sigma_s \mathscr{R}(O^* Q_y)$ and $\Sigma_s \mathscr{R}(Q_y^* Q_z)$ vanish.

Adopting a coordinate system with polar axis along $\mathbf{q}$, these matrix elements, which are now identified as those validating the differential cross section (33), can be simplified still further with the help of Schrödinger's equation.

We obtain ultimately

$$\sum_s |Q_z|^2 = (W - W^0)^2 q^{-2} |\epsilon_{W^0 W}|^2$$

$$\sum_s |Q_y|^2 = \tfrac{1}{2} q^2 |\epsilon_{W^0 W}|^2 + \left| \int e^{iqz} \psi_W^* \frac{\partial}{\partial y} \psi_{W^0} \, d\tau \right|^2$$

$$\sum_s \mathscr{R}(O^* Q_z) = [q^2 - 2(W - W^0)](2q)^{-1} |\epsilon_{W^0 W}|^2$$

$$\sum_s |\mathbf{Q}|^2 = \tfrac{1}{2}[(W - W^0)^2 q^{-2} + 3q^2/4] |\epsilon_{W^0 W}|^2 + \left| \int e^{iqz} \psi_W^* \frac{\partial}{\partial y} \psi_{W^0} \, d\tau \right|^2 . \quad \ldots\ldots (41)$$

For the case of Schrödinger K wave functions $\Sigma_{l,m} |\epsilon_{W^0 W}|^2$ is well known (Bethe 1930, Massey and Mohr 1933). Making allowance for present relativistic units and energy scale normalization, one has

$$\sum_{l,m} |\epsilon_{W^0 W}|^2 \, dW = \frac{2^5 (Z\alpha)^6 q^2 [3q^2 + p^2 + (Z\alpha)^2] \exp\left[-\frac{2Z\alpha}{p} \arctan \frac{2Z\alpha p}{q^2 - p^2 + Z^2\alpha^2} \right] dW}{3[(q-p)^2 + (Z\alpha)^2]^3 [(q+p)^2 + (Z\alpha)^2]^3 [1 - \exp(-2Z\alpha\pi/p)]} . \quad \ldots\ldots (42)$$

For the remaining matrix element we use the method of Massey and Mohr (1933) of transforming to parabolic coordinates and employing the Sommerfeld (1931) integral representation for Coulomb waves. This gives

$$\sum_{l,m} \left| \int e^{iqz} \psi_W^* \frac{\partial}{\partial y} \psi_{W^0} \, d\tau \right|^2 = \frac{[(Z\alpha)^2 + p^2][(Z\alpha)^2 + (q+p)^2][(Z\alpha)^2 + (q-p)^2]}{4q^2[(Z\alpha)^2 + 3q^2 + p^2]} \sum_{l,m} |\epsilon_{W^0 W}|^2 . \quad \ldots\ldots (43)$$

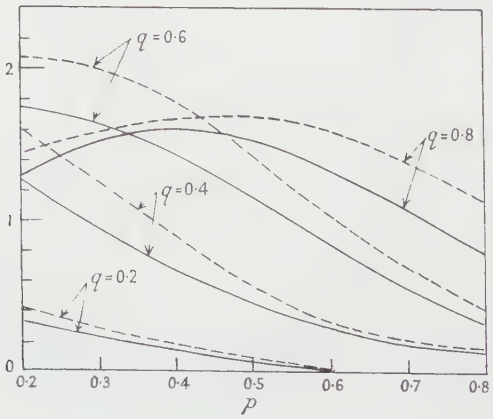

Figure 1. Comparison between $\Sigma |O_{W^0 W}|^2$ (Dirac), full line, and $\Sigma |\epsilon_{W^0 W}|^2$ (Schrödinger), broken line.

These results were used to evaluate K ionization cross sections for nickel (for which the Darwin approximation is reasonably good) and for mercury (for which it is inappropriate) for several different incident energies. The integrations over q and W were performed in the same manner as those described in § 5. The results are discussed in the next section. For interest, some of the Schrödinger matrix elements $\Sigma_{l,m,s}|\epsilon_{W^0W}|^2$ for mercury are compared with corresponding Dirac matrix elements in figure 1.

§ 7. Discussion of Results

Unfortunately no experimental information is as yet available concerning the K ionization of heavy elements by fast electrons. When such information becomes available, the results computed here should provide some check on the adequacy of the Møller interaction for inelastic collision processes, and also an indication of the accuracy of the Born approximation in this context.

But even in the absence of relevant experimental evidence, considerable understanding of the role of relativity in electron ionization theory is afforded by comparison of the relativistic cross sections computed here for mercury with those provided by both semi-relativistic (Darwin approximation) and non-relativistic theory.

Table 3. Cross Sections for K Ionization of Nickel by Electrons

(1)	(2)	(3)	(4)	(5)	(6)	(7)
3	0·25	4·4	4·20 (est.)	4·50	2·98	4·18
					4·28	4·11
6	0·50	4·0	4·1 (est.)	3·4 (est.)	5·54	3·90
					6·67	3·62
9	0·75	3·3	3.3 (est.)	2·7 (est.)	9·04	3·20
					11·41	2·96
12	1·00	2·9	2·85 (est.).	2.2 (est.)		
15	1·25	2·7	2·6 (est.)	1·9	14·94	2·62
					18·37	2·40
18	1·50	2·5	2·35 (est.)			
20	1·75		2·2		22·0	2·22

(1), (2) Kinetic energy of incident electron: (1) in units of $I_K = 8{\cdot}35$ kev, (2) in Mev; (3), (4), (5) $\sigma_K \times 10^{22}$ (cm^2): (3) semi-relativistic (present work) comp. error $< 5\%$, (4) semi-relativistic (Arthurs and Moiseiwitsch 1958), (5) non-relativistic (Burhop 1940); (6) incident energies in units of I_K; (7) $\sigma_K \times 10^{22}$ (cm^2) experimental (Smick and Kirkpatrick 1945, Pockman *et al.* 1947) exptl. error $< 6\%$.

Figure 2 shows that relativistic modifications are surprisingly large, $\sigma_{K\,rel}/\sigma_{K\,non\text{-}rel}$ being greater than 2 for incident energies greater than 0·5 Mev (6 times the K ionization energy), and greater than 6 at 1·5 Mev. For an explanation we refer to the structure of expression (33) and notice that the differential cross section involves the sum of a number of terms, each of which consists of a different type of atomic matrix element multiplied by a function of p and q arising from the incident electron wave functions and the Møller interaction.

It so happens that these terms do not all have the same sign and furthermore their absolute magnitudes are comparable. Thus relatively small changes in the

atomic wave functions could lead to large changes in ionization cross section. This explains the large difference between relativistic and semi-relativistic cross sections in spite of the fairly small differences between the Schrödinger and Dirac matrix elements (cf. figure 1). Again, we observe that the use of a Coulomb rather than a Møller interaction, even with relativistic wave functions, would give rise only to the first of the matrix elements in (33), i.e. to the $|O|^2$, with the denominator in the external factor having the value q^4 instead of $[q^2 - (E^0 - E^1)^2]^2$. The consequent impossibility of any cancellation of matrix elements, viewed in the light of figure 1, suggests that such a procedure would yield cross sections far closer to Burhop's (non-relativistic) than to the present completely relativistic results.

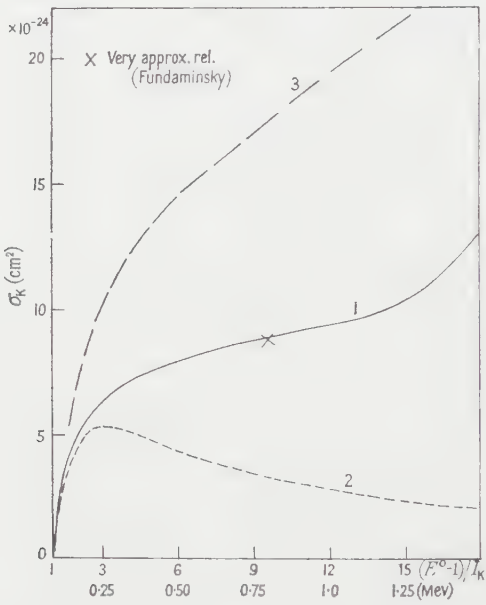

Figure 2. Cross sections for the K ionization of Hg by electrons. 1, exact relativistic (present); 2, non-relativistic (Burhop); 3, semi-relativistic (present).

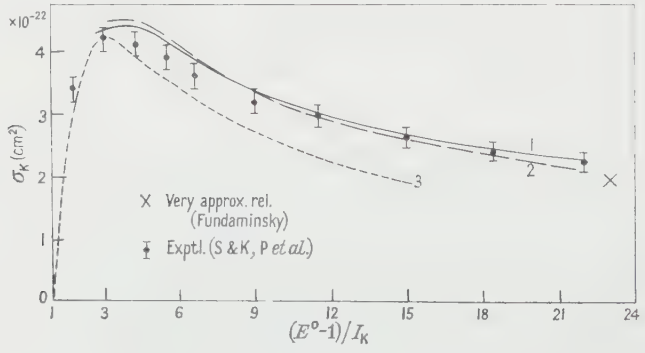

Figure 3. Cross sections for the K ionization of Ni by electrons. 1, Darwin relativistic (present); 2, Darwin semi-relativistic (Arthurs and Moiseiwitsch); 3, non-relativistic (Burhop). S & K, Smick & Kirkpatrick; P *et al.*, Pockman *et al.*

It is of interest that very approximate relativistic calculations for the K ionization of mercury by electrons by Fundaminsky (unpublished, but reported by Massey and Burhop 1952, p. 155), in which the relativistic energy–momentum relation is used in an otherwise completely non-relativistic treatment, give a cross section which at 0·8 MeV is approximately 2·7 times the non-relativistic cross section, and which is " practically constant or slightly increasing in the range 0·3 to 0·8 MeV ". This is, fortuitously of course, in excellent agreement with the present relativistic results.

With regard to the K ionization cross sections for electrons in light to medium elements, as typified here by nickel, comparison with experiment is possible (cf. figure 3).

It is seen that the present results for nickel agree with observation to within computational and experimental error, but differ significantly from Burhop's non-relativistic cross sections at the higher energies. This tends to vindicate further (cf. § 2) the use of the Born approximation in these calculations. There is no significant difference between the present results and those of Arthurs and Moiseiwitsch for nickel, though for higher Z considerable difference can be expected because of the additional approximation explicit in their analysis. However, this is only of academic interest, since at higher Z, both semi-relativistic treatments fail by virtue of the inadequacy of Darwin wave functions for such Z.

The very approximate relativistic cross section for nickel computed by Fundaminsky (Massey and Burhop 1952, p. 155) again agrees surprisingly well with present results.

Acknowledgment

The author wishes to express his gratitude to Associate Professor C. B. O. Mohr for his continued encouragement and assistance.

References

Arthurs, A. M., and Moiseiwitsch, B. L., 1958, *Proc. Roy. Soc.* A, **247,** 550.
Ashkin, A., Page, A. L., and Woodward, W. M., 1954, *Phys. Rev*, **94,** 357.
Bethe, H., 1930, *Ann. Phys., Lpz.*, **5,** 325.
—— 1933, *Handb. d. Phys.* (Berlin: Springer), **24,** 273.
Bethe, H., and Salpeter, E., 1957, *Handb. d. Phys.* (Berlin: Springer), **35,** 88.
Brenner, S., and Brown, G. E., 1953, *Proc. Roy. Soc.* A, **218,** 422.
Brown, G. E., 1952, *Phil. Mag.*, **43,** 467.
Burhop, E. H. S., 1940, *Proc. Camb. Phil. Soc.*, **36,** 43.
Champion, F., 1932, *Proc. Roy. Soc.* A, **137,** 688.
Erdelyi, A., 1936, *Math. Z.*, **40,** 693.
Erdelyi, A., Magnus, W., Oberhettinger, F., and Tricomi, F. G., 1953, *Higher Transcendental Functions*, Vol. I, Bateman Manuscript Project (New York: McGraw-Hill).
Groetzinger, G., Leder, L. B., Ribe, F. L., and Berger, M. J., 1950, *Phys. Rev.*, **79,** 454.
Henneberg, W., 1933, *Z. Phys.*, **84,** 592.
Hulme, H. R., McDougall, J., Buckingham, R. A., and Fowler, R. H., 1935, *Proc. Roy. Soc.* A., **149,** 131.
Massey, H. S. W., 1956, *Handb. d. Phys.* (Berlin: Springer), **36,** 307.
Massey, H. S. W., and Burhop, E. H. S., 1952, *Electronic and Ionic Impact Phenomena* (Oxford: University Press).
Massey, H. S. W., and Mohr., C. B. O., 1931, *Proc. Roy. Soc.* A, **132,** 605.
—— 1933, *Ibid.*, **140,** 613.
Merzbacher, E., and Lewis, H. W., 1958, *Handb. d. Phys.* (Berlin: Springer), **34,** 166.

Møller, C., 1931, *Z. Phys.*, **70,** 780.
—— 1932, *Ann. Phys., Lpz.*, **14,** 531.
National Bureau of Standards, 1947, *Tables of Spherical Bessel Functions*, Math. Tables Project (New York: Columbia).
Perlman, H. S., and Robson, B. A., 1959, *Aust. J. Phys.*, **12,** 30.
Pockman, L., Webster, D., Kirkpatrick, P., and Harworth, K., 1947, *Phys. Rev.*, **71,** 330.
Slater, J. C., 1930, *Phys. Rev.*, **36**, 57.
Smick, A., and Kirkpatrick, P., 1945, *Phys. Rev.*, **67,** 153.
Sommerfeld, A., 1931, *Ann. Phys., Lpz.*, **11,** 257.
Wetzel, W., 1933, *Phys. Rev.*, **44,** 25.
Williams, E. J., 1930, *Proc. Roy. Soc.* A, **130,** 328.
Williams, E. J., and Terroux, F., 1929, *Proc. Roy. Soc.* A, **126,** 289.
Willis, H. F., 1948, *Phil. Mag.*, **39,** 455.

Relativistic K Electron Wave Functions by the Variational Principle

By W. N. ASAAD†
Physics Department, University College, London

Communicated by E. H. S. Burhop; MS. received 28th January 1960, in revised form 9th May 1960

Abstract. The variational principle is applied to obtain the Dirac wave functions of the K electrons of heavy atoms, using the method of variable parameters. In formulation, three parameters are used. The Coulomb and spin–spin interactions of the two K electrons are taken into consideration as well as the effect of the rest of the atom. A numerical example for mercury, $Z=80$, is given. Its K absorption edge is calculated and relativistic wave functions obtained, using one variable parameter. The results justify the use of screened hydrogenic wave functions although the screening constant ($\sim 0{\cdot}5$) is somewhat higher than that given by Slater's rules. Calculations using two variable parameters are also given and the total energy is found to have a saddle point and not a true minimum. This is briefly discussed in the light of the hydrogen atom.

§ 1. Introduction

The variational principle has been widely applied to the calculation of non-relativistic wave functions. Successful use has been made of the method of variable parameters as well as the method of arbitrary functions, the latter giving rise to the well-known self-consistent field. On the other hand, although a relativistic self-consistent field theory was formulated by Swirles (1935), it seems that the tedious and long calculations involved considerably limited its application. Burhop (1937) applied the method of variable parameters to the calculation of the Dirac wave functions for the K electrons of the heavy elements, taking into account the Coulomb attraction of the nucleus and the Coulomb and spin–spin interactions of the two K electrons, but neglecting the effect of electrons in outer shells.

An attempt to include, approximately, the effect of outer electrons is described in this paper; refined formulation of the problem using three parameters throughout is given, use being made of the relevant ideas given by Brenner and Brown (1953) in their paper on the calculation of the K absorption edges in some heavy atoms. An account of calculations carried out for mercury, using only one parameter, is described, and the quite satisfactory value for the K absorption edge obtained justifies the use of screened hydrogenic wave functions for the K electrons of heavy elements. The results of calculations done using two parameters are also given. These reveal a rather interesting point; the energy as function of the two used parameters has a saddle point and not a true minimum. This is discussed in the light of a study made on the hydrogen atom.

† Now at Faculty of Engineering, Cairo University, Egypt.

§ 2. Mathematical Formulation of the Problem

For a two-electron system moving in a spherically symmetric electrostatic potential $V(r)$, the Hamiltonian, in atomic units, can be written as the matrix

$$H=\sum_{s\neq t=1}^{2}[VI^{(s)}+ic\boldsymbol{\alpha}^{(s)}.\nabla^{(s)}-c^2\beta^{(s)}]I^{(t)}+\frac{1}{r_{12}}I^{(1)}I^{(2)}-\frac{\boldsymbol{\alpha}^{(1)}.\boldsymbol{\alpha}^{(2)}}{r_{12}}, \quad \ldots\ldots(1)$$

where the superscripts (1) and (2) denote the electron on whose coordinates the operations are to be performed. $I^{(s)}(s=1, 2)$ are 4×4 unit matrices and $\boldsymbol{\alpha}$ and β are the 4×4 Dirac matrices which can be represented by

$$\boldsymbol{\alpha}=\begin{pmatrix}0 & \boldsymbol{\sigma}\\ \boldsymbol{\sigma} & 0\end{pmatrix}, \qquad \beta=\begin{pmatrix}I & 0\\ 0 & -I\end{pmatrix}. \quad \ldots\ldots(2)$$

In (2), each element is a 2×2 matrix, $\boldsymbol{\sigma}=(\sigma_1, \sigma_2, \sigma_3)$ being the Pauli spin matrices. The last two terms in the Hamiltonian (1) represent, respectively, the Coulomb and spin–spin interaction energies of the two electrons, while their spin–orbit interaction energies are taken account of by the terms in the summation (see Schiff 1955). The total wave function Ψ of the two K electron system can be formally written as

$$\Psi=\frac{1}{\sqrt{2}}[\psi_{-1,1/2}{}^{(1)}\psi_{-1,-1/2}{}^{(2)}-\psi_{-1,-1/2}{}^{(1)}\psi_{-1,1/2}{}^{(2)}], \quad \ldots\ldots(3)$$

where $\psi_{\kappa,\mu}$ denotes the single electron 4-component wave function defined in an earlier paper† (Asaad 1959). This total wave function will be normalized to unity if we impose the condition

$$\int_0^\infty[f^2(r)+g^2(r)]dr=1 \quad \ldots\ldots(4)$$

on the radial wave functions $f(r)$ and $g(r)$ of the single electron wave functions. If we now choose appropriate forms, depending on some variable parameters, for the radial wave functions, then, by the variational principle (Swirles 1935, Burhop 1937), the wave function of the form chosen, which approximates most closely to the actual wave function, will be given by choosing the parameters to make the expression

$$\int\int\Psi^\dagger H\Psi d\tau_1 d\tau_2 \quad \ldots\ldots(5)$$

stationary, provided $f(r)/r$ and $g(r)/r$ are chosen so as to vanish more rapidly than $1/r$ as r tends to infinity.

The expression (5) for the total energy of the two K electron system could be reduced, after a direct, but rather long and tedious calculation, to the following

$$\begin{aligned}&2\int_0^\infty V(r)[f^2(r)+g^2(r)]dr-2c\int_0^\infty[f(r)\frac{dg(r)}{dr}-g(r)\frac{df(r)}{dr}-\frac{2}{r}f(r)g(r)]dr\\&-2c^2\int_0^\infty[f^2(r)-g^2(r)]dr+\int_{r_1=0}^\infty dr_1[f^2(r_1)+g^2(r_1)]\left\{\frac{1}{r_1}\int_{r_2=0}^{r_1}[f^2(r_2)+g^2(r_2)]dr_2\right.\\&\left.+\int_{r_2=r_1}^\infty\frac{1}{r_2}[f^2(r_2)+g^2(r_2)]dr_2\right\}+\frac{8}{3}\int_{r_1=0}^\infty dr_1 f(r_1)g(r_1)\left\{\frac{1}{r_1{}^2}\int_{r_2=0}^{r_1}r_2 f(r_2)g(r_2)dr_2\right.\\&\left.+r_1\int_{r_2=r_1}^\infty\frac{1}{r_2{}^2}f(r_2)g(r_2)dr_2\right\}. \quad \ldots\ldots(6)\end{aligned}$$

† The radial wave functions will be denoted by f and g for the K shell (the suffix 0 will be dropped throughout).

For heavy atoms, the K electrons move in a Coulomb field, approximately; in atomic units, the potential $V(r)$ of a K electron can be written in the form

$$V(r) \simeq -\frac{Z}{r} + a + b(r); \quad b(0) = 0. \qquad \ldots\ldots (7)$$

The first term is due to the nuclear charge Z and the latter two due to the outer electrons, b being a correction to a, small ($\sim 2^{0}_{0}$) in the region of the K shell (Brenner and Brown 1953).

This suggests that the wave functions of such electrons will not differ much from hydrogen-like wave functions, and that we may take our trial radial functions to be

$$f(r) = \lambda g(r), \quad g(r) = N_{\mathrm{K}} r^{\alpha-1} \exp(-\beta r), \qquad \ldots\ldots (8)$$

where α, β and λ are three variable parameters†, and N_{K} is the normalizing factor given by

$$N_{\mathrm{K}}^{2} = \frac{(2\beta)^{2\alpha+3}}{(\lambda^{2}+1)\Gamma(2\alpha+3)}. \qquad \ldots\ldots (9)$$

With these trial wave functions, the expression (6) for the total energy reduces to the sum of the following five terms‡

$$\text{(i)} \quad 2\frac{(2\beta)^{2\alpha+3}}{\Gamma(2\alpha+3)} \int_{0}^{\infty} V(r) r^{2\alpha-2} \exp(-2\beta r)\, dr,$$

$$\text{(ii)} \quad \frac{4c\lambda\beta}{(\lambda^{2}-1)(\alpha-1)},$$

$$\text{(iii)} \quad -2c^{2}\frac{\lambda^{2}-1}{\lambda^{2}+1},$$

$$\text{(iv)} \quad 2\frac{(2\beta)^{4\alpha+6}}{[\Gamma(2\alpha+3)]^{2}} \int_{r_1=0}^{\infty} dr_1 \cdot r_1^{2\alpha+1} \exp(-2\beta r_1) \int_{r_2=0}^{r_1} r_2^{2\alpha+2} \exp(-2\beta r_2)\, dr_2,$$

$$\text{(v)} \quad \frac{16}{3}\frac{\lambda^{2}(2\beta)^{4\alpha+6}}{(\lambda^{2}-1)^{2}[\Gamma(2\alpha+3)]^{2}} \int_{r_1=0}^{\infty} dr_1 r_1^{2\alpha} \exp(-2\beta r_1) \times \int_{r_2=0}^{r_1} r_2^{2\alpha+3} \exp(-2\beta r_2)\, dr_2. \qquad \ldots\ldots (10)$$

Following Brenner and Brown, we can use the successive transformations

$$2\beta r_1 = r\cos\theta, \qquad 2\beta r_2 = r\sin\theta,$$
$$\cos\theta/(\cos\theta+\sin\theta) = q$$

to put the last two terms (iv) and (v) in (10), which give, respectively, the electrostatic and spin–spin interactions of the two electrons, in the closed analytical forms

$$\text{(iv)}' \quad \frac{\beta}{\alpha+1}\left[1 - \frac{\Gamma(2\alpha+5/2)}{\Gamma(\tfrac{1}{2})\Gamma(2\alpha+3)}\right],$$

$$\text{(v)}' \quad \frac{8\lambda^{2}\beta}{3(\lambda^{2}+1)^{2}(\alpha+1)(2\alpha+1)}\left[2\alpha+3 - \frac{(6\alpha+7)\Gamma(2\alpha+5/2)}{\Gamma(\tfrac{1}{2})\Gamma(2\alpha+3)}\right]. \qquad \ldots\ldots (10)$$

† The parameters α and β are introduced at the slight risk of confusion with the Dirac matrices α and β.

‡ All expressions can be made to agree with those given by Burhop (1937) except term (v), which gives the spin–spin interaction.

§ 3. The Electrostatic Potential Energy

To evaluate the electrostatic potential energy (expression (10)(i)) for the two K electrons of a heavy element we use the self-consistent field calculated non-relativistically and make the necessary modifications. In such a Hartree field, both the effective potential charge Z_p for the neutral atom and the contributions to the field charge Z_f from each subshell (calculated together with an equal positive charge placed at the nucleus) are tabulated as functions of r or of some other independent variable (such as $\rho = \log(1000\, r)$ in the field calculated for mercury by Hartree and Hartree (1935)). The scalar potential due to the two K electrons under consideration, calculated from their field charge $Z_f(1s^2)$, is subtracted from the potential Z_p/r to yield the scalar potential V_s in which the K electrons are supposed to move.

Two more modifications are still to be made to compensate, more or less, for the neglect, in the calculation of the Hartree field used, of both relativity and exchange effects.

To take account of the relativistic effect, following Brenner and Brown (1953), we consider only the relativistic correction in a given in (7). In atomic units,

$$\Delta a = \sum_s \Delta a_s = \sum_s \left\{ \left\langle \frac{1}{r_s} \right\rangle_{\text{rel.}} - \left\langle \frac{1}{r_s} \right\rangle_{\text{non-rel.}} \right\}, \qquad \ldots\ldots (11)$$

where the summation is over all electrons in the outer shells, and the expectation values of $1/r_s$ are calculated between relativistic and non-relativistic wave functions, respectively. Hydrogen-like wave functions with suitable screening constants were used by Brenner and Brown for evaluating this correction and the value given, for mercury, is

$$\Delta a = 32 \text{ atomic units.} \qquad \ldots\ldots (12)$$

It is to be noted that this relativistic correction does not interfere with the variational method to be applied, as it merely shifts the levels up or down.

Turning now to the correction for exchange, we note that the change of energy for a K electron with projection quantum number ν resulting from the exchange terms in its interaction with an electron in the state κ, μ is given, in atomic units, by (see Brenner and Brown 1953)

$$\Delta E = -\int\int \psi_{-1,\nu}^{\dagger}(1)\psi_{\kappa,\mu}^{\dagger}(2)\frac{1}{r_{12}}\psi_{-1,\nu}(2)\psi_{\kappa,\mu}(1)\, d\tau_1 d\tau_2 \qquad \ldots\ldots (13)$$

provided the wave functions ψ are normalized to unity. Only contributions of the L electrons to the exchange energy correction of the K electron were considered, as even these, when evaluated are found to be small. Screened hydrogen-like wave functions were used for $\psi_{\kappa,\mu}$ in (13) for the L electrons while the trial wave functions (see §2) were used for the K electrons. Closed expressions were obtained, but these are too lengthy to be inserted in this paper (see, however, Asaad 1958).

§ 4. Results and Discussion

Summing up, the expression to be minimized, for the two K electron system, consists of the following terms:

(i) the electrostatic potential energy given in (10)(i) with $V(r) = -V_s$; to this is added the correction $2(\Delta E_{2s} + \Delta E_{2\bar{p}} + \Delta E_{2p})$ for the exchange energy (see §3). The relativistic correction Δa (11) does not affect the minimization,

(ii) the kinetic energy† given in (10)(ii),

(iii) the mass energy† given in (10)(iii),

(iv) the electrostatic interaction energy given in (10)(iv)′,

(v) the spin–spin interaction energy given in (10)(v)′.

We have formulated the problem working throughout with the three parameters α, β and λ. It is at once evident that the calculations involved are extremely lengthy, unless we are content, at least as a first approximation, with reducing the parameters to only one, say α, by means of the relations valid for the Coulomb field:

$$\beta=\gamma c, \quad \lambda=\gamma/(2+\alpha), \quad \text{where } \gamma=\sqrt{[-\alpha(\alpha+2)]}. \qquad \ldots\ldots(14)$$

Table 1 gives, in atomic units, the values of the above five terms, as well as the total energy, for the two K electrons of mercury, as functions of the parameter α.

By the method of finite differences, we find that the total energy is a minimum when $\alpha=-0{\cdot}185458$ which gives an effective nuclear charge for the K shell of $\beta=\gamma c=79{\cdot}47$. Thus the screening constant $\sigma=0{\cdot}53$. (The value given by Burhop (1937) is 0·5.) The minimum total energy $W(1s^2)$ for the system is

$$W(1s^2)=31\,278{\cdot}955 \text{ atomic units.} \qquad \ldots\ldots(15)$$

Table 1. Energy of the Two K Electrons of Mercury as Function of the Parameter α

(1)	(2)	(3)	(4)	(5)	(6)	(7)	(8)
−0·1925	−15259·480	−11·863	16174·752	30311·935	58·910	7·951	31282·205
−0·19	−15117·283	−11·880	15937·430	30405·780	58·439	7·800	31280·286
−0·1875	−14975·117	−11·899	15700·990	30499·625	57·968	7·649	31279·216
−0·185	−14833·003	−11·920	15465·426	30593·470	57·496	7·499	31278·968
−0·1825	−14690·923	−11·943	15230·728	30687·315	57·022	7·350	31279·549
−0·18	−14548·641	−11·969	14996·889	30781·160	56·547	7·202	31281·188

(1) α; (2) electrostatic potential energy without exchange; (3) electrostatic potential energy exchange correction; (4) kinetic energy; (5) mass energy; (6) electrostatic interaction energy; (7) spin–spin interaction energy; (8) total energy.

If we subtract the sum of the electrostatic and spin-spin interaction energies from the total energy, as given in table 1, and divide the result by 2, we can readily find the total energy, as function of the parameter α, for the case of a single electron in the K shell moving in the same electrostatic field. The corresponding results for a stationary value of the total energy are $\alpha=-0{\cdot}187392$, $\beta=79{\cdot}84$, $\sigma=0{\cdot}16$ and

$$W(1s)=15\,606{\cdot}800 \text{ atomic units.} \qquad \ldots\ldots(16)$$

The latter screening constant is entirely due to the electrons in outer shells, whose contributions are totally ignored by Slater (1930) in his empirical rules. A measure of the screening due to the presence of a second electron in the K shell can be obtained by subtraction: $0{\cdot}53-0{\cdot}16=0{\cdot}37$. This is the value to be compared with the value 0·30 given by Slater's rules.

† This nomenclature should not be taken too literally.

It is quite straightforward now to calculate the ionization energy of mercury, required to remove one K electron out of the atom. In atomic units, this is given by

$$I(1s) = [W(1s) + \Delta a - c^2] - [W(1s^2) + 2\Delta a - 2c^2]$$
$$= W(1s) - W(1s^2) + c^2 - \Delta a; \quad c = 137, \qquad \ldots\ldots (17)$$

where Δa is the relativistic correction given in (12). Thus

$$I(1s) = 3064{\cdot}8 \text{ atomic units}, \qquad \ldots\ldots (18)$$

in good agreement with the values 3064·5 given by Brenner and Brown in their theoretical treatment and $3059{\cdot}5 \pm 4$ obtained experimentally by Mack and Cork (1927).

As a second approximation, we maintain two parameters, say α and λ. β is then expressed in terms of α as in the case of a Coulomb field:

$$\beta = c\sqrt{[-\alpha(\alpha+2)]}. \qquad \ldots\ldots (19)$$

To facilitate calculations, we ignore the exchange correction and get the total energy as a function of α and λ. The result is given in table 2.

Table 2. Total Energy W, in A.U., of the Two K Electrons of Mercury as Function of the Two Parameters α and λ (exchange correction neglected)

$\alpha \backslash \lambda$	0·3125	0·3150	0·3175	0·3200	0·3225	0·3250	0·3275
−0·1925	31278·783	31283·714	31287·677	31290·676	31292·716	31293·802	31293·935
−0·19	31281·555	31285·574	31288·629	31290·725	31291·865	31292·055	31291·297
−0·1875	31284·333	31287·440	31289·588	31290·780	31291·021	31290·316	31288·668
−0·185	31287·084	31289·278	31290·519	31290·808	31290·151	31288·550	31286·011
−0·1825	31289·808	31291·092	31291·425	31290·811	31289·254	31286·758	31283·329
−0·18	31292·727	31293·099	31292·524	31291·006	31288·551	31285·161	31290·841

From table 2, it is at once seen that the surface $W = f(\alpha, \lambda)$ has a saddle shape with one section having a minimum and another having a maximum, these two sections being roughly in the directions given by the two diagonals of the table. The one giving the minimum corresponds to that obtained when λ is related to α as for a Coulomb field. The neglect of exchange as well as the closeness of the figures given in the table might lead one to question the accuracy of the numerical calculations and to think that the peculiar saddle-shaped surface is not an essential feature resulting from the parameters chosen.

To clear up this point, we study the hydrogen atom which lends itself easily to exact analytical investigation. In this case the electron moves in a true Coloumb field, and one expects the ground state to be a true minimum. In terms of the three parameters α, β and λ, the total energy of the electron in the 1s state is given by

$$W_H = \int \psi^\dagger H_H \psi d\tau = -\frac{\beta}{\alpha+1} + \frac{2c\lambda\beta}{(\alpha+1)(1+\lambda^2)} + c^2 \frac{1-\lambda^2}{1+\lambda^2}, \qquad \ldots\ldots (20)$$

which reduces to the two-parameter expression

$$W_H = f(\lambda, \mu) \equiv -\frac{1}{\mu} + \frac{2c\lambda}{\mu(1+\lambda^2)} + c^2 \frac{1-\lambda^2}{1+\lambda^2}, \qquad \ldots\ldots (21)$$

if we put

$$(\alpha+1)/\beta = \mu; \qquad \ldots\ldots (22)$$

and reduces to the one-parameter expression

$$W_H = F(\alpha) \equiv \frac{c}{\alpha+1}\{c - \sqrt{[-\alpha(\alpha+2)]}\}, \qquad \ldots\ldots (23)$$

if β and λ in (20) are expressed in terms of α by means of the relations (14) valid for the Coulomb field.

We begin first by discussing the case when one parameter only is used. The total energy W_H, as a function of the parameter α, has stationary points when $dF(\alpha)/d\alpha = 0$; i.e. when α is a root of the quadratic equation $\alpha^2 + 2\alpha + (1/c^2) = 0$. This gives two values of α:

$\alpha_1 = -1 + \sqrt{[1-(1/c^2)]} \simeq -1/2c^2$ and $\alpha_2 = -1 - \sqrt{[1-(1/c^2)]} \simeq -2 + (1/2c^2)$

both giving rise to a value of the effective nuclear charge β equal to one, the charge of the proton, as it should be. As $d^2F(\alpha)/d\alpha^2 = c^4/(\alpha+1)$, α_1 yields a minimum value for the total energy

$$W_{H_{min}} = F(\alpha_1) = c^2\sqrt{[1-(1/'137')^2]} \text{ atomic units},$$

the well-known total energy of the hydrogen atom in its ground state. At α_2 there is a maximum

$$W_{H_{max}} = F(\alpha_2) = -W_{H_{min}}$$

giving the corresponding negative energy state. The values of the parameter λ at these two extremes are approximately $1/2c$ and $2c$, respectively. We see that these mathematical results are plausible, once we note that λ is merely the ratio of the 'smaller' to the 'larger' components of the radial wave functions for the positive energy state, and that, when the roles played by these components are interchanged, the corresponding negative energy state results.

The essential features, discussed above, of the total energy of the hydrogen atom as a function of the one parameter α will be maintained for the K electrons of any heavy atom, as the field in which these electrons move is nearly Coulombic. Table 1 was a study of the total energy of the two K electrons of mercury, $Z = 80$, near its true minimum.

We now return to the case when the two independent parameters λ and μ are used in the expression (21) for the total energy W_H of the hydrogen atom. For the stationary points on the surface $W_H = f(\lambda, \mu)$, we should have

$$\frac{\partial W_H}{\partial \lambda} \equiv \frac{2c}{\mu(1+\lambda^2)^2}(1 - 2c\mu\lambda - \lambda^2) = 0$$

and

$$\frac{\partial W_H}{\partial \mu} \equiv \frac{1}{\mu^2(1+\lambda^2)}(1 - 2c\lambda + \lambda^2) = 0,$$

which means that there will be stationary points at $\mu = (1-\lambda^2)/2c\lambda$ where λ is a root of the quadratic equation $\lambda^2 - 2c\lambda + 1 = 0$. It can easily be shown that the values of the parameters α, β and λ at the two stationary points check exactly with their values at the two extremes of the total energy when treated as a function of only one parameter. However, at the two stationary points of the surface $W_H = f(\lambda, \mu)$,

$$\frac{\partial^2 W_H}{\partial \lambda^2} = -1/\mu\lambda^2 \simeq -4c^2 \text{ and } 1/4c^2,$$

$$\frac{\partial^2 W_H}{\partial \lambda \partial \mu} = (\lambda - c)/c\mu^2\lambda \simeq -2c \text{ and } 1/2c,$$

while

$$\frac{\partial^2 W_H}{\partial \mu^2} = 0.$$

Hence, at these points $(\partial^2 W_H/\partial\lambda^2)(\partial^2 W_H/\partial\mu^2) = 0 < (\partial^2 W_H/\partial\lambda\partial\mu)^2$, which means that these stationary points are no longer points of maxima and minima, but are actually saddle-points. To investigate the matter further, we study the shape of the surface at the first stationary point, which corresponds to the true minimum in the one-parameter case. We have, in the neighbourhood of this point, by Taylor's expansion,

$$W_H = \mu_1 c^2 - \tfrac{1}{2}\left[\frac{(\delta\lambda)^2}{\mu_1\lambda_1^2} + \frac{2(c-\lambda_1)}{c\mu_1^2\lambda_1}\delta\lambda\delta\mu\right] \simeq c^2 - 2c\delta\lambda(\delta\mu + c\delta\lambda), \quad \ldots\ldots (24)$$

where we have neglected infinitesimals of the third and higher orders, and used the suffix 1 to denote the values of the parameters at the stationary point under consideration. If we take this point as origin, it is at once evident that the curve of intersection of the surface with any vertical plane through the origin has a true minimum there as long as the plane lies in the acute dihedral angle between the plane $\mu + c\lambda = 0$ and the reference plane $\lambda = 0$. It can be easily shown that the relations (14), valid for the Coulomb field, give rise to such a plane, the infinitesimals $\delta\mu$ and $\delta\lambda$ being approximately connected by the relation $\delta\mu + 2c\delta\lambda = 0$.

Again, these main results will be maintained for the innermost electrons of any heavy atom, and our calculated values for mercury, $Z = 80$, listed in table 2, are in good agreement with the results we have obtained in the above analysis.

This analysis shows that, in the use of variable parameters in the application of the variational principle to obtain relativistic wave functions, we should not expect the total energy, even in the ground state, to be a true minimum. The parameters are to be chosen so as to render expression (5) stationary, and our requirements at the stationary points should be sufficiently relaxed so as to include such reasonable saddle-points as may arise. In contrast with the non-relativistic case, there are now negative energy states, and as these may interfere with the positive energy states through some of the parameters chosen (e.g. the parameter λ used above), the stationary points may no longer be extreme points. This conclusion, however, does not, by any means, violate the physical requirement of a true minimum for a stable ground state, as our parameters for such a state will be found to be physically restricted in their variations to regions giving rise to a true minimum for the total energy.

§ 5. Conclusion

It appears that the method of variable parameters justifies the use of hydrogen-like relativistic wave functions, with appropriate screening constants, for the K electrons of heavy atoms. The screening constants are greater than those given by Slater, being about 0·53 when both electrons are present in the K shell and about 0·16 when one of them is missing. It is rather difficult, however, to see how it would be possible to extend the application of this variational method to the case of outer electrons, as the field in their regions differs from the Coulomb field, and as the calculations with the more formidable forms of wave functions become prohibitive.

Acknowledgments

Thanks are due to Professor Sir Harrie Massey and to Dr. E. H. S. Burhop for suggesting the problem and for their interest and valuable discussions throughout the work.

References

Asaad, W. N., 1958, *Ph.D. Thesis*, University of London.
—— 1959, *Proc. Roy. Soc.* A, **249,** 555.
Brenner, S., and Brown, G. E., 1953, *Proc. Roy. Soc.* A, **218,** 422.
Burhop, E. H. S., 1937, *Ph. D. Thesis*, University of Cambridge.
Hartree, D. R., and Hartree, W., 1935, *Proc. Roy. Soc.* A, **149,** 210.
Mack, J. E., and Cork, J. M., 1927, *Phys. Rev.*, **30,** 741.
Schiff, L. I., 1955, *Quantum Mechanics* (New York : McGraw-Hill).
Slater, J. C., 1930, *Phys. Rev.*, **36,** 57.
Swirles, B., 1935, *Proc. Roy. Soc.* A, **152,** 625.

The Stochastic Problem of Electron-Photon Cascades including Polarization

By N. R. RANGANATHAN and R. VASUDEVAN†
Department of Theoretical Physics, Madras University, Madras

Communicated by A. Ramakrishnan; MS. received 22nd September 1959, in revised form 5th May 1960

Abstract. The theory of electron–photon cascades is studied by the product density functions well known in stochastic theory so as to include a description of the state of polarization of the multiplying particles. Defining a suitable longitudinal polarization product density function of degree one, an expression for the mean number of longitudinally polarized particles produced in the medium from 0 to t has been obtained. Equations for product densities of degree two have been briefly dealt with.

§ 1. Introduction

Since the first formulation of the cascade theory, it has been realized that cascade multiplication of particles is essentially statistical in nature and the stochastic aspect of the cascade theory has claimed the attention of both physicists and mathematicians. Once the quantum mechanical cross sections of the fundamental processes responsible for the development of the cascade are assumed, the problem can be formulated according to classical theory of stochastic process. A limited objective in such treatments is to calculate the mean number of particles above a certain energy at a given depth and the fluctuation in them. The parameters entering the process when we are interested only in the longitudinal development of the cascade were mainly the thickness of matter traversed, and the energies of the different types of particles comprising the cascade. The question arises whether it is possible to include the state of polarization of the particles in the description of the cascade.

As has been first pointed out by Dyson (1958, unpublished) this problem is of interest now as it is possible to study cascades initiated by polarized electrons (e.g. available from the μ-meson decay etc.). Dyson has formulated the equations for this problem and has dealt with mean numbers. The object of the present paper is two-fold, (i) to take over Dyson's formulation to the new approach to cascade theory developed recently by Ramakrishnan and Srinivasan (1956), (ii) to deal with the fluctuation problem briefly.

The inclusion of polarization brings in its wake a new feature hitherto not present in cascade theory. An electron can exist in a 'forward' (F) or 'backward' (B) polarization pure state with respect to its direction of motion or in any other state of polarization which can be expressed as a linear combination of the F and B states. This feature has to be included in the standard product

† Now at the Scripps Institute of Oceanography, La Jolla, California, U.S.A.

density functions (Ramakrishnan 1950) which are defined only in terms of energy. As has been done by Dyson, the description of 'mixture states' is achieved by means of the density matrix method (Fano 1957) well known in quantum mechanics. Though the inclusion of this quantum mechanical feature complicates the cascade equations, great simplification results if we neglect the angular distribution of particles by integrating over the angles. It is possible to write down the cascade equations for a suitable choice of function as has been done by Dyson.

§ 2. Product Density of Degree One

In this section, we briefly summarize some results of Dyson's work which are necessary. The state of polarization of the electron and photons can be described by the $2 \cdot 2$ density matrices $\pi_{ij}(E,t)$, $\gamma_{ij}(E,t)$ where the labels i and j are F and B denoting the forward and backward polarizations of the particles with respect to their direction of motion. As in the standard theory $\pi_{ij}(E,t)$ and $\gamma_{ij}(E,t)$ are the mean number of electrons and photons with energies lying between E and $E-dE$ at the depth t with their states of polarization represented by the labels i and j and hence they are the usual product density functions of degree one (Ramakrishnan 1950). We note that the above functions are product densities only in the E space and the various values of the suffixes i and j yield the four types of product densities π_{FF}, π_{FB}, π_{BF} and π_{BB} for the electron and similarly for the photons.

The usual cascade diffusion equations involve the bremsstrahlung and pair production total cross sections. When polarization is included in the cascade theory, we note that the progeny of a particle in the cascade depends very much on the state of the polarization of the 'parent' which will be determined by the relative phases of the production matrix elements for the parent. We now define the production matrix elements for the bremsstrahlung $M_{ikl}(E|E_0)$ where i, k and l take the values F and B representing respectively the spin states of the incident electron, the photon and the outgoing electron and E and E_0 denote the energies of the photon and the incident electron. Similarly $N_{ikl}(E|E_0)$ is the pair production matrix element where i, k and l refer as before to the spin states of incident photon, the positron and the electron, and E_0 and E are the energies of the photons and the positrons.

Considering a bremsstrahlung process by an incident electron described by a density matrix π_{ij}, the outgoing two particles can be described by the 4×4 joint density matrix

$$J_{klmn} = \sum_{ij} \pi_{ij} M_{ikl} M_{jmn}^{*}. \qquad \ldots\ldots (1)$$

Since we are interested only in the polarization of one of the outgoing particles, we sum incoherently over the spin indices of the other particle and thereby obtain the contracted (2×2) density matrix π'_{ln} given by

$$\pi'_{ln} = \sum_{k} J_{klkn} = \sum_{ijk} \pi_{ij} M_{ikl} M_{jkn}^{*}. \qquad \ldots\ldots (2)$$

For the outgoing photon, we have

$$\gamma'_{ln} = \sum_{l} J_{klml} = \sum \pi_{ij} M_{ikl} M_{jml}^{*}. \qquad \ldots\ldots (3)$$

In a similar way, we can obtain the 'contracted' density matrices for particles

resulting from pair-production. The values of the different production matrix elements in their relativistic limits are given below:

$$\left.\begin{aligned} &M_{\mathrm{FFF}}=E_0A^*,\ M_{\mathrm{FFB}}=mkB,\ M_{\mathrm{FBF}}=EA,\ M_{\mathrm{FBB}}=0\\ &M_{\mathrm{BBB}}=E_0A,\ M_{\mathrm{BBF}}=-mkB,\ M_{\mathrm{BFB}}=EA^*,\ M_{\mathrm{BFF}}=0\\ &N_{\mathrm{FFF}}=-mkB,\ N_{\mathrm{FFB}}=E_+A,\ N_{\mathrm{FBF}}=-E_-A,\ N_{\mathrm{FBB}}=0\\ &N_{\mathrm{BBB}}=mkB,\ N_{\mathrm{BBF}}=E_+A^*,\ N_{\mathrm{BFB}}=-E_-A^*,\ N_{\mathrm{BFF}}=0 \end{aligned}\right\} \quad \ldots\ldots(4)$$

where m, E_0, E, E_+ and E_- stand for the mass, initial energy, final energy and the electron energies of the positron and electron respectively. k stands for the photon energy. A and B have the same meaning and expressions as in McVoy and Dyson (1957). Because of the peculiar angular dependence of these matrix elements, we note that on integrating over angles the sum $\Sigma_k M_{lki}M_{nkj}{}^*$ will always vanish except when $l=n$, $i=j$ or $l=i$, $n=j$. Similarly the two sums $\Sigma_k M_{lik}M_{njk}{}^*$ and $\Sigma N_{lki}N_{nkj}{}^*$ are non-vanishing only in the case $l=n$, $i=j$; $\sigma_{ikl}(E|E_0)\,dE$ represents the cross section integrated over angles for an electron of energy E_0 to radiate photons in the energy range $(E+dE, E)$ and $\tau_{ikl}(E|E_0)\,dE$ is the cross section for pair production. They are

$$\begin{aligned} \sigma_{ikl}(E|E_0)&=\int d\Omega|M_{ikl}(E|E_0)|^2\\ \tau_{ikl}(E|E_0)&=\int d\Omega|N_{ikl}(E|E_0)|^2. \end{aligned} \quad \ldots\ldots(5)$$

The diffusion equation for the product densities of degree one $\pi_{ij}(E|E_0,t)$ and $\gamma_{ij}(E|E_0,t)$ are given below.

$$\begin{aligned} \frac{\partial}{\partial t}\pi_{ij}(E|E_0,t)=&\int_E^\infty dE'\int d\Omega\sum_{lnk}\pi_{ln}(E'|E_0,t)M_{lki}M_{nkj}{}^*\\ &-\tfrac{1}{2}\int_0^E dE'\int d\Omega\sum_{kl}\pi_{ij}(E|E_0,t)[|M_{ikl}|^2+|M_{jkl}|^2]\\ &+2\int_E^\infty dE'\int d\Omega\sum_{lnk}\gamma_{ln}(E'|E_0,t)N_{lki}N_{nkj}{}^*. \end{aligned} \quad \ldots\ldots(6)$$

$$\begin{aligned} \frac{\partial}{\partial t}\gamma_{ij}(E|E_0,t)=&\int_E^\infty dE'\int d\Omega\sum_{lnk}\pi_{ln}(E'|E_0,t)M_{lik}M_{njk}{}^*\\ &-\tfrac{1}{2}\int_0^E dE'\int d\Omega\sum_{kl}\gamma_{ij}(E|E_0,t)[|N_{ikl}|^2+|N_{jkl}|^2]. \end{aligned} \quad \ldots\ldots(7)$$

Using the properties of matrix elements under angular integration, the above equations separate into four uncoupled equations for the transverse polarization $(i\neq j)$ and two coupled equations for longitudinal polarization and two coupled equations for the total populations where the total population functions are

$$\begin{aligned} \pi(E|E_0,t)&=\pi_{\mathrm{FF}}(E|E_0,t)+\pi_{\mathrm{BB}}(E|E_0,t)\\ \gamma(E|E_0,t)&=\gamma_{\mathrm{FF}}(E|E_0,t)+\gamma_{\mathrm{BB}}(E/E_0,t) \end{aligned} \quad \ldots\ldots(8)$$

and the longitudinal polarization functions are

$$\begin{aligned} \pi_{\mathrm{L}}(E|E_0,t)&=\pi_{\mathrm{FF}}(E|E_0,t)-\pi_{\mathrm{BB}}(E|E_0,t)\\ \gamma_{\mathrm{L}}(E|E_0,t)&=\gamma_{\mathrm{FF}}(E|E_0,t)-\gamma_{\mathrm{BB}}(E|E_0,t). \end{aligned} \quad \ldots\ldots(9)$$

The degree of longitudinal polarization for electrons of energy E at depth t is given by $\pi_{\mathrm{L}}(E|E_0,t)/\pi(E|E_0,t)$.

§ 3. New Approach to Cascade Theory with Inclusion of Polarization

In the new approach to cascade theory developed by Ramakrishnan and Srinivasan (1956) instead of considering the average number of particles above a certain energy E_c at a depth t, they consider the probability $\pi(n_j, t)$ that there are n_j particles of type j each with energy greater than E_c at the time of production in the medium between 0 and t. They have defined the product densities of degree k

$$F_k(E_1, E_2, \ldots E_k;\ t_1, t_2, \ldots t_k)\, dE_1\, dE_2 \ldots dE_k\, dt_1\, dt_2 \ldots dt_k$$

as the joint probability that an electron of energy $(E_1 + dE_1, E_1)$ is produced between t_1 and $t_1 + dt_1$, an electron $(E_2 + dE_2, E_2)$ between t_2 and $t_2 + dt_2$ etc. From this function we can find the mean number and higher moments of the number of all the electrons produced between 0 and t with their energies at the time of production more than E_c.

Let $F(E|E_0, t)\, dE\, dt$ and $G(E|E_0, t)\, dE\, dt$ be the product densities of degree one for electrons and photons produced between t and $t + dt$, with their energies at the time of production lying between E and $E + dE$. The unpolarized cross section for bremsstrahlung and pair production $R(E'|E)\, dE'$ and $\rho(E'|E)\, dE'$ are related to $\sigma_{ikl}(E'|E)\, dE'$ and $\tau_{ikl}(E'|E)\, dE'$ as follows:

$$\sum_{kl} \sigma_{ikl}(E'|E) = R(E'|E) = \frac{1}{E}\phi_0\left(\frac{E'}{E}\right) = \frac{1}{E}\phi_0(u)$$

$$\sum_{kl} \tau_{ikl}(E'|E) = \rho(E'|E) = \frac{1}{E}\psi_0\left(\frac{E'}{E}\right) = \frac{1}{E}\psi_0(u) \qquad \ldots\ldots (10)$$

Hence

$$\begin{aligned} F(E|E_0, t) &= 2\int_E^\infty dE'\gamma(E'|E_0, t) \sum_{kl} \tau_{ikl}(E|E') \\ &= 2\int_0^1 \frac{du}{u}\psi_0(1-u)\gamma\left(\frac{E}{u}|E_0, t\right) \\ G(E|E_0, t) &= \int_E^\infty \pi(E'|E_0, t) \sum_{kl} \sigma_{ikl}(E|E')\, dE' \\ &= \int_0^1 \frac{du}{u}\phi_0(u)\pi\left(\frac{E}{u}|E_0, t\right). \qquad \ldots\ldots (11) \end{aligned}$$

If $p(s, t)$ and $q(s, t)$ are the Mellin transforms of F and G they are related to the π and γ function old cascade theory as

$$p(s, t) = B_s\gamma(s, t), \quad q(s, t) = C_s\pi(s, t) \qquad \ldots\ldots (12)$$

where B_s and C_s are the usual expressions.

If we denote by $\epsilon\{N(E_c|E_0, t)$ the mean number of electrons produced between 0 and t with energies greater than E_c at the time of production, it is shown that

$$\epsilon\{N(E_c|E_0, t)\} = \frac{1}{2\pi i}\int_{\sigma - i\infty}^{\sigma + i\infty} \frac{B_s C_s}{\mu_s - \lambda_s}\left(\frac{E_0}{E}\right)^{s-1} \frac{1}{s-1}\left\{\frac{1 - \exp(-\lambda_s t)}{\lambda_s} - \frac{1 - \exp(-\mu_s t)}{\mu_s}\right\} ds \qquad \ldots\ldots (13)$$

where the symbols used are well known in standard shower theory and the mean number from this expression has been evaluated (Srinivasan and Ramakrishnan 1957).

Taking into account the state of polarization of the particles, we now define as before the function $F_{ij}(E|E_0,t)$ and $G_{ij}(E|E_0,t)$ as the product density of electron and photon to be produced between $t+dt$ and t with energies lying between $E+dE$ and E, the state of polarization being defined by the suffixes i and j. Since we are interested only in the longitudinal polarization functions, i.e. F_{L} and G_{L}, we find for the diagonal terms

$$F_{\mathrm{FF}}(E|E_0,t)=2\int_E^\infty dE'\sum_{nk}\gamma_{nn}(E'|E_0,t)\tau_{nk\mathrm{F}}(E'-E|E')$$
$$F_{\mathrm{BB}}(E|E_0,t)=2\int_E^\infty dE'\sum_{nk}\gamma_{nn}(E'|E_0,t)\tau_{nk\mathrm{B}}(E'-E|E'). \quad \ldots\ldots(14)$$

Hence

$$F_{\mathrm{L}}(E|E_0,t)=2\int_0^1\gamma_{\mathrm{L}}\left(\frac{E}{u}|E_0,t\right)\psi_1(1-u)\frac{du}{u} \quad \ldots\ldots(15)$$

where

$$\sum_{nk}(-1)^{n-i}\tau_{nki}(E|E')=\frac{1}{E'}\psi_1\left(\frac{E}{E'}\right)=\frac{1}{E'}\psi_1(u). \quad \ldots\ldots(16)$$

Similarly for the photons

$$G_{\mathrm{L}}(E|E_0,t)=\int_0^1\pi_{\mathrm{L}}\left(\frac{E}{u}|E_0,t\right)\phi_2(u)\frac{du}{u} \quad \ldots\ldots(17)$$

where

$$\sum_{nk}(-1)^{n-i}\sigma_{nik}(E|E')=\frac{1}{E'}\phi_2\left(\frac{E}{E'}\right)=\frac{1}{E'}\phi_2(u). \quad \ldots\ldots(18)$$

$F_{\mathrm{L}}(E|E_0,t)$ and $G_{\mathrm{L}}(E|E_0,t)$ denote the mean excess of particles with polarization in the forward direction over the particles with polarization in the backward direction which are produced between t and $t+dt$ and with their energies at their time of production lying in $(E,E+dE)$.

As in the case of total population function, the Mellin transforms of F_{L} and G_{L} are related to the Mellin transforms of γ_{L} and π_{L} as†

$$p_{\mathrm{L}}(s,t)=B_{\mathrm{L}}(s)\gamma_{\mathrm{L}}(s,t)$$
$$q_{\mathrm{L}}(s,t)=C_{\mathrm{L}}(s)\Pi_{\mathrm{L}}(s,t) \quad \ldots\ldots(19)$$

where

$$B_{\mathrm{L}}(s)=\frac{2}{s+1}-(\tfrac{4}{3}+2b)\frac{2}{(s+1)(s+2)}$$
$$C_{\mathrm{L}}(s)=\frac{1}{s+2}+(\tfrac{1}{3}+2b)\frac{1}{(s+1)(s+2)}$$
$$A_{\mathrm{L}}(s)=A(s)+(\tfrac{2}{3}-2b)\frac{1}{(s+1)(s+2)}$$
$$b=0{\cdot}0135$$

and

$$D=\tfrac{7}{9}-\tfrac{1}{3}b. \quad \ldots\ldots(20)$$

† The Mellin transform for this part is defined as

$$p_{\mathrm{L}}(s,t)=\int_0^1 F_{\mathrm{L}}(E,t)E^s\,dE$$

and

$$\pi_{\mathrm{L}}(s,t)=\int_0^1\pi_{\mathrm{L}}(E,t)E^s\,dE.$$

This is different from the Mellin transform definition in Bhabha and Ramakrishnan (1950) where $(s-1)$ is used for s. This is necessitated since Dyson's tables $A_{\mathrm{L}}(s)$ etc. have been computed on the above definitions.

Proceeding in exactly the same fashion as for the total population we find that

$$\epsilon\{N_{\mathrm{L}}(y,t)\} = \frac{\exp\{\phi_{\mathrm{L}}^{(1)}(s_1)\}}{[2\pi\phi_{\mathrm{L}}^{(1)\prime\prime}(s_1)]^{1/2}} - \frac{\exp\{\phi_{\mathrm{L}}^{(2)}(s_2)\}}{[2\pi\phi_{\mathrm{L}}^{(2)\prime\prime}(s_2)]^{1/2}}. \quad \ldots\ldots(21)$$

s_1 and s_2 are the saddle points of the functions $\phi_{\mathrm{L}}^{(1)}(s)$ and $\phi_{\mathrm{L}}^{(2)}(s)$ for a given $y = \log(E_0/E_{\mathrm{c}})$,

$$\phi_{\mathrm{L}}^{(1)}(s) = \log\frac{B_{\mathrm{L}}(s)C_{\mathrm{L}}(s)}{\mu_{\mathrm{L}}(s)\lambda_{\mathrm{L}}(s)} - \log s + ys$$

$$\phi_{\mathrm{L}}^{(2)}(s) = \log\frac{B_{\mathrm{L}}(s)C_{\mathrm{L}}(s)}{[\mu_{\mathrm{L}}(s)-\lambda_{\mathrm{L}}(s)]\lambda_{\mathrm{L}}(s)} - \log s + ys - \lambda_{\mathrm{L}}t. \quad \ldots\ldots(22)$$

§ 4. Product Density of Degree Two

To solve the fluctuation problem of the cascade theory with the inclusion of the state of polarization of the multiplying particles, it is obvious that we should define (4×4) density matrices $\pi_{ij,\,kl}(E_1, E_2, t)\,dE_1\,dE_2$ where (ij) and (kl) describe the states of polarization of the particles 1 and 2 with energies lying between $(E_1 + dE_1, E_1)$ and $(E_2 + dE_2, E_2)$ respectively. Similar functions for photons $\gamma_{ij,\,kl}(E_1, E_2, t)\,dE_1\,dE_2$ and mixed functions $\pi_{ij}\gamma_{kl}(E_1, E_2, t)\,dE_1\,dE_2$ can be defined. The diffusion equations for these functions can easily be written down using essentially the same arguments necessary for the equations of product densities of degree one. It is easy to verify that when we add the equations for the diagonal terms $\pi_{\mathrm{FF,\,FF}}$, $\pi_{\mathrm{FF,\,BB}}$, $\pi_{\mathrm{BB,\,FF}}$ and $\pi_{\mathrm{BB,\,BB}}$ of the electrons, we obtain the usual diffusion equation for $\pi(E_1, E_2, t)$, the total population function involving only the total cross section for bremsstrahlung and pair production (Bhabha and Ramakrishnan 1950).

To solve the fluctuation in longitudinal polarization in particular, we have to define four functions of the second degree for the electrons given by

$$\begin{aligned}
\pi_{\mathrm{L_1L_1}}(E_1, E_2, t) &= \pi_{\mathrm{FF,\,FF}}(E_1, E_2, t) - \pi_{\mathrm{BB,\,BB}}(E_1, E_2, t)\\
\pi_{\mathrm{L_1L_2}}(E_1, E_2, t) &= \pi_{\mathrm{FF,\,BB}}(E_1, E_2, t) - \pi_{\mathrm{BB,\,FF}}(E_1, E_2, t)\\
\pi_{\mathrm{L_2L_1}}(E_1, E_2, t) &= \pi_{\mathrm{BB,\,FF}}(E_1, E_2, t) - \pi_{\mathrm{FF,\,BB}}(E_1, E_2, t)\\
\pi_{\mathrm{L_2L_2}}(E_1, E_2, t) &= \pi_{\mathrm{BB,\,BB}}(E_1, E_2, t) - \pi_{\mathrm{FF,\,FF}}(E_1, E_2, t)\\
&= -\pi_{\mathrm{L_1L_1}}(E_1, E_2, t) \qquad \ldots\ldots(23)
\end{aligned}$$

where L_1 and L_2 refer to the cases where an excess of electrons are polarized in the ' forward ' or ' backward ' direction respectively. Similarly the longitudinal polarization functions for other product densities of degree two can be defined. The diffusion equations for these functions are related and can conveniently be cast in a vector-matrix form with some approximation (Vasudevan and Ranganathan 1959). A formal transform solution for the vector can be obtained and inverting this, we can recover the functions like $\pi_{\mathrm{L_1L_1}}(E_1, E_2, t)$. From the theory of product densities (Ramakrishnan 1950), the mean square number of longitudinally polarized electrons with energy above E_{c} is given by

$$\begin{aligned}
&\epsilon\{N_{\mathrm{L_1}}{}^2(E > E_{\mathrm{c}}, t)\}\\
&\quad = \int_{E_{\mathrm{c}}}^{E_0} \pi_{\mathrm{L_1}}(E|E_0, t)\,dE + \int_{E_{\mathrm{c}}}^{E_0}\int_{E_{\mathrm{c}}}^{E_0} \pi_{\mathrm{L_1L_1}}(E_1, E_2, t)\,dE_1 dE_2. \quad \ldots\ldots(24)
\end{aligned}$$

Knowing $\pi_{\mathrm{L_1}}(E, t)$ and $\pi_{\mathrm{L_1L_1}}(E_1, E_2, t)$ from their transforms, we can in principle evaluate the mean square number. However it is too much to hope that it will

be of interest to experimenters at the present stage of measuring polarization of particles in the cascade showers.

Acknowledgments

We are very grateful to Professor Alladi Ramakrishnan for providing us with the pre-print of Dyson's paper and for the constant encouragement and helpful suggestions in the preparation of the work. We wish to acknowledge many fruitful discussions with Dr. S. K. Srinivasan. One of us (R. V.) thanks the University of Madras for the award of Government of India Fellowship and the other (N. R. R.) thanks the Atomic Energy Commission for the award of Junior Research Fellowship.

References

Bhabha, H. J., and Ramakrishnan, A., 1950, *Proc. Ind. Acad. Sci.*, **32**, 141.
Fano, U., 1957, *Rev. Mod. Phys.*, **26**, 70.
McVoy, K. W., and Dyson, F. J., 1957, *Phys. Rev.*, **106**, 1360.
Ramakrishnan, A., 1950, *Proc. Camb. Phil. Soc.*, **46**, 595.
Ramakrishnan, A., and Srinivasan, S. K., 1956, *Proc. Ind. Acad. Sci.*, **44**, 263.
Srinivasan, S. K., and Ranganathan, N. R., 1957, *Proc. Ind. Acad. Sci.*, **45**, 69.
Vasudevan, R., and Ranganathan, N. R., 1959, *Proceedings of the Summer School of Theoretical Physics* (*Mussorie*), Ministry of Scientific Research and Cultural Affairs, Government of India, New Delhi. Part II, p. 261.

Electrodynamics of a Charged Particle moving through a Plasma without Magnetic Field

By S. K. MAJUMDAR
Saha Institute of Nuclear Physics, Calcutta, India

MS. received 14*th January* 1960, *in revised form* 22*nd March* 1960

Abstract. The motion of a charged particle through a low density electron plasma has been investigated using equation of momentum transfer in a plasma and Maxwell's equations for electromagnetic field. It is shown that for a particle velocity greater than the average thermal velocity of the plasma electrons, a Čerenkov-like effect is set up in the plasma, only in the case of longitudinal wave motion. The existence of Mach cone is derived and the nature of the energy loss investigated.

§ 1. Introduction

The problem of the interaction of a charged particle moving in an electron plasma has already been investigated by Vlasov (1945), Bohm and Pines (1952), Akhiezer and Sitenko (1952) and others. All these investigations are mainly concerned with the process of energy exchange between the particle and the medium, except in the paper of Bohm and Pines where the mechanism of excitation of collective oscillation is considered in greater detail. Recently, Kraus and Watson (1958) have considered the case of the interaction of a charged body moving through the ionosphere from hydrodynamic standpoint.

When a charged particle moves through an electron plasma which is neutralized by a background of positive ions, we know that its interaction with the surrounding medium consists of both short and long range interactions. Except in the case of high density plasma this short range interaction is of no great significance and can be looked upon as ordinary two-body interaction within a range of the order of Debye length. On the other hand, the long range interaction between the plasma particles can be looked upon as simultaneous many body interaction of each particle with every other particle, each interaction producing a small perturbation in velocity and its contribution to density distribution of the individual particles. All these small perturbations may act coherently under favourable conditions giving rise to the phenomenon of plasma oscillation (Bohm and Gross 1949), and can be conveniently described by defining parameters which give description of the system of plasma particles taken collectively, and thus may be called collective oscillations (Bohm and Pines 1952).

These plasma oscillations actually move through the body of the plasma, giving rise to what is known as 'plasma waves'. Along with these there are also associated transverse electromagnetic waves which are in general coupled with the longitudinal plasma waves. A charged particle moving through a plasma will excite both these types of waves. Now, from the earlier work reported by various authors it is known that in a plasma without magnetic field Čerenkov

effect does not take place (Kolomenskii 1956). This follows from the fact that a plasma without magnetic field has a dielectric constant equal to $(1-\omega_p^2)/\omega^2$, for a circular frequency ω, where $\omega_p^2 = 4\pi n_0 e^2/m$ is the characteristic plasma frequency. All these works previously done were mainly concerned with the energy exchange between a moving charged particle and the disturbances excited by it, and no calculation was made for the electric and magnetic field distributions in a plasma arising as a result of its interaction with a moving charged particle. It is the purpose of our paper to clarify the question of Čerenkov effect in a plasma, by calculating the field distributions produced by a moving charged particle, as was done by Sommerfield (1954) for an ordinary dielectric medium. It is found that it is actually the longitudinal electric field and not the transverse electromagnetic field which behaves in a plasma without magnetic field in a manner similar to that of an electromagnetic wave in an ordinary dielectric medium having no electromagnetic periodicity of its own.

This particular behaviour of the longitudinal disturbance in a plasma was studied by Bohm and Pines (1952) from another stand-point. The fluctuation in density produced by moving electrons in a plasma was separated into two parts: one part was associated with the random motion of the electrons and the other part was found to be responsible for the organized collective behaviour of the medium. This latter part was shown to possess a Čerenkov-like effect. In their work Bohm and Pines were mainly interested in the behaviour of an electron gas, so far as the above-mentioned separation in the density fluctuations is concerned; no attempt was made to study the behaviour of the various electrical disturbances excited by a moving charged particle. In the present paper we shall treat this particular aspect from a phenomenological stand-point, starting from Maxwell's equations for the electromagnetic field and the equation of momentum transfer. By calculating the various field distributions for different particle velocities we shall find out, that the 'collective oscillations' of Bohm and Pines are in fact hyberbolic longitudinal electrostatic waves, which are always confined within a Mach cone behind the moving particle.

§ 2. Electrodynamic Potentials

Let us consider a particle of charge q in e.s.u., mass M, moving with a velocity $\mathbf{u}$ through a plasma without any external magnetic field, and let n_0 be the average density and V, the average thermal velocity of the plasma electrons. Due to their heavy mass, we neglect the motion of the ions as compared with that of the electrons. We shall also assume that the plasma is of sufficiently low density so that there is no 'collision' between the particles. This is equivalent to neglecting the short range interaction. The equation of motion of such a plasma is given by

$$m\frac{\partial \mathbf{v}}{\partial t} = -e\mathbf{E} - \frac{1}{n_0}\nabla p. \qquad \ldots\ldots(1)$$

Because the plasma is of low density, the particle velocities are not randomized, and the relation between the density and pressure perturbation is

$$p = \frac{\gamma p_0 n}{n_0} = mV^2 n, \qquad \ldots\ldots(2)$$

where γ = ratio of the two specific heats, is 3 and not 5/3 (Spitzer 1956), and p and n are the perturbations in pressure and density.

The quantity **E** is the electric field set up within the plasma due to the interaction of the moving particle considered.

This again is given by the Maxwell's equations:

$$\nabla \times \mathbf{E} = -\frac{1}{c}\frac{\partial \mathbf{H}}{\partial t}, \qquad \ldots\ldots(3)$$

$$\nabla \cdot \mathbf{H} = \frac{1}{c}\frac{\partial \mathbf{E}}{\partial t} + \frac{4\pi}{c} n_0 e \mathbf{v} = \frac{4\pi}{c} q\mathbf{u}\delta(\mathbf{r} - \mathbf{u}t), \qquad \ldots\ldots(4)$$

$$\nabla \cdot \mathbf{E} = -4\pi e n + 4\pi q \delta(\mathbf{r} - \mathbf{u}t), \qquad \ldots\ldots(5)$$

$$\nabla \cdot \mathbf{H} = 0, \qquad \ldots\ldots(6)$$

where the Gaussian system of units is used, and $\delta(\mathbf{r} - \mathbf{u}t)$ exactly locates the specified particle 'q' at the point $\mathbf{r} = \mathbf{u}t$.

Equations (1) to (6) are a set of self-consistent equations, from which eliminating the quantities **H**, **v** and n we get,

$$-\nabla \times \nabla \times \mathbf{E} = \frac{1}{c^2}\left(\frac{\partial^2}{\partial t^2} + \omega_p^2\right)\mathbf{E} + \frac{1}{c^2}\left[\frac{q}{e}\nabla\delta(\mathbf{r} - \mathbf{u}t) - \frac{\nabla(\nabla \cdot \mathbf{E})}{4\pi e}\right]4\pi e + \frac{4\pi}{c^2} q\mathbf{u}\frac{\partial}{\partial t}\delta(\mathbf{r} - \mathbf{u}t). \qquad \ldots\ldots(7)$$

We solve (7) for **E** by performing a Fourier transformation in unbounded configuration space:

$$\left.\begin{aligned} \mathbf{E}(\mathbf{r}, t) &= \int \mathbf{E}_K \exp\left[i\mathbf{K} \cdot (\mathbf{r} - \mathbf{u}t)\right] d\mathbf{K} \\ \delta(\mathbf{r} - \mathbf{u}t) &= \frac{1}{8\pi^3}\int \exp\left[i\mathbf{K} \cdot (\mathbf{r} - \mathbf{u}t)\right] d\mathbf{K}. \end{aligned}\right\} \qquad \ldots\ldots(8)$$

We substitute equations (8) in equation (7) and then break up the Kth Fourier component $\mathbf{E}_K$ for the electric field into its transverse and longitudinal parts by means of the relations:

$$\mathbf{E}_K = \mathbf{E}_K^{\parallel} + \mathbf{E}_K^{\perp}$$

such that

$$\mathbf{E}_K^{\parallel} \times \mathbf{K} = 0 \qquad \ldots\ldots(9)$$

and

$$\mathbf{E}_K^{\perp} \cdot \mathbf{K} = 0,$$

where $\mathbf{E}^{\parallel}$ and $\mathbf{E}^{\perp}$ denote respectively the longitudinal and transverse electric field. Using relations (9) we get from (7), by straightforward calculations:

$$\mathbf{E}_K^{\parallel} = i\frac{q}{2\pi^2}\frac{\mathbf{K}}{K^2}\frac{(\mathbf{K} \cdot \mathbf{u})^2 - (KV)^2}{\omega_p^2 + (KV)^2 - (\mathbf{K} \cdot \mathbf{u})^2}, \qquad \ldots\ldots(10)$$

and

$$\mathbf{E}_K^{\perp} = i\frac{q}{2\pi^2}\frac{1}{K^2}\frac{K^2(\mathbf{K} \cdot \mathbf{u})\mathbf{u} - \mathbf{K}(\mathbf{K} \cdot \mathbf{u})^2}{\omega_p^2 + (Kc)^2 - (\mathbf{K} \cdot \mathbf{u})^2}. \qquad \ldots\ldots(11)$$

Use of the first equation of (8) will then at once yield the following expressions for the field quantities:

$$\left.\begin{aligned} \mathbf{E}^{\parallel}(\mathbf{r}, t) &= -\nabla\phi(\mathbf{r}, t), \\ \mathbf{E}^{\perp}(\mathbf{r}, t) &= -\nabla\psi(\mathbf{r}, t) - \frac{1}{c}\frac{\partial}{\partial t}\mathbf{A}(\mathbf{r}, t), \\ \mathbf{H}(\mathbf{r}, t) &= \nabla \times \mathbf{A}(\mathbf{r}, t). \end{aligned}\right\} \qquad \ldots\ldots(12)$$

and

where
$$\phi(\mathbf{r}, t) = \frac{q}{|\mathbf{r}-\mathbf{u}t|} - \frac{q\omega_p^2}{2\pi^2}\int \frac{\exp[i\mathbf{K}.(\mathbf{r}-\mathbf{u}t)]}{K^2[\omega_p^2+(KV)^2-(\mathbf{K}.\mathbf{u})^2]}\,d\mathbf{K}, \quad \ldots\ldots(13)$$

$$\psi(\mathbf{r}, t) = \frac{q}{2\pi^2}\int \frac{(\mathbf{K}.\mathbf{u})^2\exp[i\mathbf{K}.(\mathbf{r}-\mathbf{u}t)]}{K^2[\omega_p^2+(Kc)^2-(\mathbf{K}.\mathbf{u})^2]}\,d\mathbf{K}, \quad \ldots\ldots(14)$$

and
$$\mathbf{A}(\mathbf{r}, t) = \frac{cq\mathbf{u}}{2\pi^2}\int \frac{\exp[i\mathbf{K}.(\mathbf{r}-\mathbf{u}t)}{\omega_p^2+(Kc)^2-(\mathbf{K}.\mathbf{u})^2}\,d\mathbf{K}. \quad \ldots\ldots(15)$$

Equations (12) to (15) completely define the electromagnetic field due to a charged particle moving through a plasma without external magnetic field. We notice that the scalar part of the potentials are different in the two cases of longitudinal and transverse waves. We shall now investigate the nature of these potentials separately.

§ 3. Longitudinal Electric Field

Equation (13) shows that besides the ordinary electrostatic potential due to a charge at rest, ϕ contains another part involving the integral

$$I = \int \frac{\exp[i\mathbf{K}.(\mathbf{r}-\mathbf{u}t)]}{K^2[\omega_p^2+K(V)^2-(\mathbf{K}.\mathbf{u})^2]}\,d\mathbf{K}. \quad \ldots\ldots(16)$$

To evaluate this integral we shall consider two different cases: $u < V$ and $u > V$. We take the velocity $\mathbf{u}$ to be along the x-axis and decompose $\mathbf{r}$ and $\mathbf{K}$ along and at right angles to $\mathbf{u}$ in the following way:

$$\left.\begin{aligned} &\mathbf{K} = \mathbf{K}_x + \mathbf{K}_\rho; \quad \mathbf{K}_x \| \mathbf{u},\ \mathbf{K}_{\rho\perp}\mathbf{u}, \\ &\mathbf{r}' = \mathbf{r}-\mathbf{u}t = \mathbf{r}_x' + \mathbf{r}_\rho'; \quad \mathbf{r}_x' \| \mathbf{u},\ \mathbf{r}_\rho'{}_\perp \mathbf{u}, \\ &|\mathbf{r}_x'| = |x-ut|,\ r_\rho'^2 = y^2+z^2. \end{aligned}\right\} \quad \ldots\ldots(17)$$

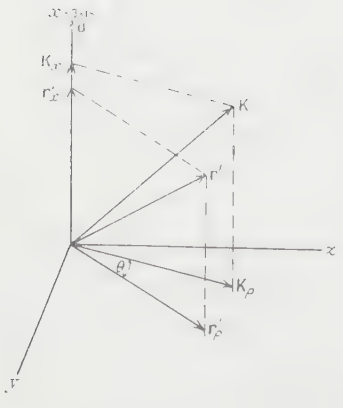

Figure 1. Resolution of $\mathbf{k}$ and $\mathbf{r}' = \mathbf{r}-\mathbf{u}t$ along and at right angles to $\mathbf{u}$. θ is the angle between $\mathbf{r}_\rho'$ and $\mathbf{k}_\rho$ in yz plane.

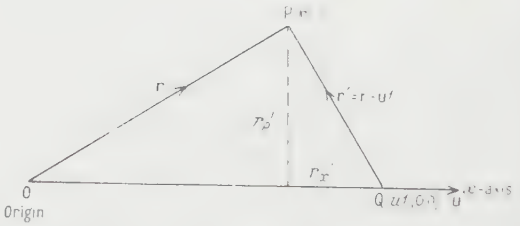

Figure 2. Diagram showing different vectors with reference to origin O. P is the point of observation and Q is the instantaneous position of the moving charge.

With reference to figure 1, if θ be the angle between the component vectors $\mathbf{K}_\rho$ and $\mathbf{r}_\rho'$, then (16) gives after integration over θ:

$$I = 2\pi\int_0^\infty K_\rho J_0(K_\rho r_\rho')dK_\rho \int_{-\infty}^{+\infty} \frac{\exp(iK_x r_x')}{(K_x^2+K_\rho^2)[\omega_p^2+K_\rho^2V^2+K_x^2(V^2-u^2)]}\,dK_x, \quad \ldots\ldots(18)$$

where $J_0(x)$ is the zero order Bessel function of first kind.

Case I: $u < V$.

In this case the integral over K_x in (18) is easily evaluated by integrating in complex K_x-plane, giving

$$I = I_1 = 2\pi^2 \int_0^\infty \frac{J_0(K_\rho r_\rho') \exp(-K_\rho r_x')}{(\omega_p^2 + K_\rho^2 u^2)} dK_\rho - 2\pi^2 (V^2 - u^2)^{1/2}$$

$$\times \int_0^\infty \frac{K_\rho J_0(K_\rho r_\rho') \exp\left[-r_x' \left(\frac{\omega_p^2 + K_\rho^2 V^2}{V^2 - u^2}\right)^{1/2}\right]}{(\omega_p^2 - K_\rho^2 u^2)(\omega_p^2 - K_\rho^2 V^2)^{1/2}} dK_\rho. \quad \ldots\ldots (19)$$

To evaluate the integrals over K_ρ we now make some simplifications. The range of integration in the above integrals can be divided as follows:

$$\int_0^\infty = \int_0^{\omega_p/u} + \int_{\omega_p/u}^\infty .$$

In the first integral on the right-hand side we expand the factor $(\omega_p^2 + K_\rho^2 u^2)$ in a series of powers of $(K_\rho^2 u^2)\,\omega_p^2$ and neglect all other terms except the first. In the second integral we make the expansion in powers of $\omega_p^2 / K_\rho^2 u^2$ and keep only the first term. We thus obtain:

$$I_1 = \frac{2\pi^2}{\omega_p^2} \int_0^\infty J_0(K_\rho r_\rho') \exp(-K_\rho r_x') dK_\rho - \frac{2\pi^2}{\omega_p^2} (V^2 - u^2)^{1/2}$$

$$\times \int_0^\infty \frac{K_\rho J_0(K_\rho r_\rho') \exp\left[-r_x' \left(\frac{\omega_p^2 + K_\rho^2 V^2}{V^2 - u^2}\right)^{1/2}\right]}{(\omega_p^2 + K_\rho^2 V^2)^{1/2}} dK_\rho$$

$$- 2\pi^2 \int_{\omega_p/u}^\infty J_0(K_\rho r_\rho') \exp(-K_\rho r_x') \left(\frac{1}{\omega_p^2} - \frac{1}{K_\rho^2 u^2}\right) dK_\rho$$

$$+ 2\pi^2 (V^2 - u^2)^{1/2} \int_{\omega_p/u}^\infty \frac{K_\rho J_0(K_\rho r_\rho') \exp\left[-r_x' \left(\frac{\omega_p^2 + K_\rho^2 V^2}{(V^2 - u^2)}\right)^{1/2}\right]}{(\omega_p^2 + K_\rho^2 V^2)^{1/2}}$$

$$\times \left(\frac{1}{\omega_p^2} - \frac{1}{K_\rho^2 u^2}\right) dK_\rho. \quad \ldots\ldots (20)$$

For $u < V$ we can write

$$\frac{\omega_p}{u} > \frac{\omega_p}{V} \simeq K_D,$$

where K_D is the wave number corresponding to Debye length. Hence, so far as the long range part of the interaction is concerned, which occurs only for length greater than Debye length, we can neglect the last two integrals in equation (20), giving

$$I_1 = \frac{2\pi^2}{\omega_p^2} \int_0^\infty J_0(K_\rho r_\rho') \exp(-K_\rho r_x') dK_\rho - \frac{2\pi^2}{\omega_p^2} (V^2 - u^2)^{1/2}$$

$$\times \int_0^\infty \frac{K_\rho J_0(K_\rho r_\rho') \exp\left[-r_x' \left(\frac{\omega_p^2 + K_\rho^2 V^2}{V^2 - u^2}\right)^{1/2}\right]}{(\omega_p^2 + K_\rho^2 V^2)^{1/2}} dK_\rho \quad \ldots\ldots (21)$$

As we are interested in studying the nature of the field distribution in plasma due to the moving charged particle, rather than evaluating them quite rigorously, we

can use equation (21) in place of equation (19), and this along with the use of equations (13), (16) and (17) gives (see Appendix A):

$$\phi^{u<V} = \frac{q \exp\left[-\frac{\omega_p}{V}\{(x-ut)^2\alpha^2 + y^2 + z^2\}^{1/2} \right]}{\alpha[(x-ut)^2\alpha^2 + y^2 + z^2]^{1/2}}, \qquad \ldots\ldots (22)$$

where $$\alpha = \frac{V}{(V^2-u^2)^{1/2}},$$

and $$(x-ut)^2 + y^2 + z^2 = r'^2.$$

We thus see that the equipotential surfaces are ellipsoids surrounding the moving charged particle, its shape being compressed in the direction of particle motion in the ratio of $1/\alpha$. These equipotential surfaces actually correspond to 'Heaviside ellipsoids' in vacuum electrodynamics. In plasma, we say that the potential due to the moving particle is 'screened' within a distance of the order of ω_p/V, i.e. Debye length, and falls off as $\exp(-Kr)\, r$ with distance, the rate of fall being maximum in the direction of particle motion.

Case II: $u > V$.

In this case we perform the integration over K_x in equation (18) again in the complex K_x-plane. For $u > V$, the two singularities on the real axis can be indented either in the upper or lower half-plane, and so the residue theorem gives

$$I = I_2 = 2\pi^2 \int_0^\infty \frac{J_0(K_\rho r_\rho')\exp(-K_x r_x')}{(\omega_p^2 + K_\rho^2 u^2)}\, dK_\rho$$

$$+ 2\pi^2 (u^2 - V^2)^{1/2} \int_0^\infty \frac{K_\rho J_0(K_\rho r_\rho') \sin\left\{ r_x' \left(\frac{\omega_p^2 + K_\rho^2 V^2}{u^2 - V^2} \right)^{1/2} \right\}}{(\omega_p^2 + K_\rho^2 u^2)(\omega_p^2 + K_\rho^2 V^2)^{1/2}}\, dK_\rho. \qquad \ldots\ldots (23)$$

Here we make the same simplifications as used in Case I. But in this case because $\omega_p/u < K_D$, the integrals corresponding to the last two integrals of equation (20) cannot be neglected without some error. However, by dividing that range of integration from ω_p/u to ∞ as

$$\int_{\omega_p/u}^{\infty} = \int_{\omega_p/u}^{\omega_p/V} + \int_{\omega_p/V}^{\infty},$$

we can easily neglect the second integral with limits from ω_p/V to ∞ on the right-hand side for long range interaction, and if u is not very much greater than V the first integral on the right-hand side with limits from ω_p/u to ω_p/V can also be neglected in comparison with those with limits from 0 to ∞.

With these considerations in mind, equation (23) can be replaced by

$$I_2 = \frac{2\pi^2}{\omega_p^2} \int_0^\infty J_0(K_\rho r_\rho') \exp(-K_\rho r_x')\, dK_\rho$$

$$+ \frac{2\pi^2}{\omega_p^2} (u^2 - V^2)^{1/2} \int_0^\infty \frac{K_\rho J_0(K_\rho r_\rho') \sin\left\{ r_x' \left(\frac{\omega_p^2 + K_\rho^2 V^2}{u^2 - V^2} \right)^{1/2} \right\}}{(\omega_p^2 + K_\rho^2 V^2)^{1/2}}\, dK_\rho,$$

and this last equation along with equations (13), (16) and (17) gives (see Appendix B)

$$\phi^{u>V}=0, \quad \text{for} \quad \left(\frac{r_\rho'}{r_x'}\right)^2\left(\frac{u^2-V^2}{V^2}\right)>1,$$

$$=-\frac{q\cos\left\{\frac{\omega_p}{V}[(x-ut)^2\beta^2-y^2-z^2]^{1/2}\right\}}{\beta[(x-ut)^2\beta^2-y^2-z^2]^{1/2}}, \quad \text{for} \quad \left(\frac{r_\rho'}{r_x'}\right)^2\left(\frac{u^2-V^2}{V^2}\right)<1, \qquad \ldots\ldots(24)$$

with $$\beta=\frac{V}{(u^2-V^2)^{1/2}}$$

and $$(x-ut)^2+y^2+z^2=r'^2.$$

Now, with reference to figure 2, we note that the relation

$$\left(\frac{r_\rho'}{r_x'}\right)^2\left(\frac{u^2-V^2}{V^2}\right)=1$$

defines a cone with semi-vertical angle μ, given by $\sin\mu=V/u$, with the moving particle as its vertex. Hence, for a particle moving with a velocity greater than the average thermal velocity of the plasma electrons, the longitudinal field is everywhere zero except within a Mach cone, as given by the angle μ. It is to be noted that the Mach cone can exist on both sides of the particle, but the proper choice of the cone can be made as follows. During a time interval t the particle moves from O to Q, the length of which is ut. But from the dispersion relation of the longitudinal waves in plasma, namely

$$\omega^2=\omega_p^2+K^2V^2, \qquad \ldots\ldots(25)$$

we find the group velocity to be

$$\frac{\partial\omega}{\partial K}=\frac{V^2}{\left(\frac{\omega_p^2}{K^2}+V^2\right)^{1/2}}.$$

The maximum group velocity is obtained by putting

$$K=K_D=\frac{2\pi}{\lambda_D},$$

where $\lambda_D=(T/4\pi n_0e^2)^{1/2}$ is the Debye length. Thus, using $\frac{1}{2}mV^2=\frac{3}{2}T$, where T is the electron temperature of the plasma (in ergs), we get

$$\left(\frac{\partial\omega}{\partial K}\right)_{\max.}=\left(\frac{12\pi^2}{12\pi^2+1}\right)^{1/2}V. \qquad \ldots\ldots(26)$$

Hence, in this case the disturbance cannot exist ahead of the particle which is now moving with a velocity $u>V$. Thus the potential is confined only in the cone behind the particle. The forward cone corresponds to the 'advanced potential' in vacuum electrodynamics.

Let us now discuss the nature of this longitudinal field. From (24) we observe that the equipotential surfaces are hyperboloids of revolution with the direction of **u** as the axis and the Mach cone as the asymptotic surface. Now, the longitudinal electric field being given by

$$\mathbf{E}^{\parallel}=-\nabla\phi,$$

we have for $u > V$

$$E_x^{\parallel} = -q\beta(x-ut)[D]$$

$$E_y^{\parallel} = \frac{q}{\beta} y[D]$$

$$E_z^{\parallel} = \frac{q}{\beta} z[D]$$

where

$$[D] = \left[\frac{\frac{\omega_p}{V} \sin\left\{\frac{\omega_p}{V}[(x-ut)^2\beta^2 - y^2 - z^2]^{1/2}\right\}}{(x-ut)^2\beta^2 - y^2 - z^2} + \frac{\cos\left\{\frac{\omega_p}{V}[(x-ut)^2\beta^2 - y^2 - z^2]^{1/2}\right\}}{[(x-ut)^2\beta^2 - y^2 - z^2]^{3/2}} \right].$$

Therefore, the electric field has the direction of the vector $-(x-ut)\beta^2, y, z$, which is the same as that of the inward drawn normal to the hyperboloid

$$(x-ut)^2\beta^2 - y^2 - z^2 = \text{const.} \qquad \ldots\ldots (27)$$

Thus, for $u > V$, the disturbances set up by the moving particle in the plasma will travel in the form of hyperbolic waves (due to the cosine dependence on x, y, z and t) in directions normal to the Mach cone.

Again, taking the instantaneous position of the particle as the origin, the equation to the system of hyperboloids is $X^2\beta^2 - Y^2 - Z^2 = A^2$, a constant. $\phi^{u>V}$ will be zero for values of A given by

$$A = \frac{V}{\omega_p}(2n+1)\frac{\pi}{2} = \frac{\sqrt{3}}{2}\lambda_D \pi(2n+1), \quad n = 0, 1, 2, \ldots\ldots$$

Considering the propagation only along X-axis, i.e. with $Y = Z = 0$, this gives the wave length for this wave as

$$\lambda = \frac{\sqrt{3}}{\beta} 2\pi\lambda_D = 2\sqrt{3}\pi\lambda_D \left(\frac{u^2}{V^2} - 1\right)^{1/2}.$$

Setting $\lambda = \lambda_D$ we get

$$u = \left(\frac{12\pi^2 + 1}{12\pi^2}\right)^{1/2} V. \qquad \ldots\ldots (28)$$

So, for velocities $u \geqslant (1 + 1/12\pi^2)^{1/2} V$ the disturbances proceed with wavelengths $\lambda \geqslant \lambda_D$. These waves can, therefore, be looked upon as due to coherent plasma oscillations, or collective oscillations, which as is already known, can exist only with a wave length greater than λ_D. The discrepancy between the two limiting velocities given by equations (26) and (28) is due to the use of the dispersion relation (25) which is not permissible near the Debye length, as has been pointed out by Bohm and Pines (1952).

It may be noted in passing that the value of the potential on the Mach cone itself is infinite. This is due to the point nature of the moving particle considered and this difficulty arises in other problems like the one we have treated here.

§ 4. Transverse Electric Field: ψ and **A**

The scalar and vector potentials ψ and **A** associated with the transverse disturbances and given by equations (14) and (15) are free of plasma temperature. This is because our starting equation on plasma motion does not take into account the velocity distribution of the plasma particles. Even if it is taken into account this average velocity V enters into the relations narrating the properties of the

transverse field within the plasma, such as the dispersion relation for transverse waves, only as a second order effect.

We first evaluate the vector potential by following the method of Bohm and Pines (1952). We take **u** in the direction of x-axis and make the following changes of variable:

$$c^2K_x'^2=(c^2-u^2)K_x^2,$$
$$K_y'^2=K_y^2, \quad K_z'^2=K_z^2,$$

and

$$(c^2-u^2)x'^2=c^2X^2; \quad (X=x-ut),$$
$$y'^2=y^2, \quad z'^2=z^2.$$

With these substitutions, straightforward integration of equation (15) will result in

$$\mathbf{A}=\mathbf{J}\gamma\frac{\exp\left\{-\frac{\omega_p}{c}[(x-ut)^2\gamma^2+y^2+z^2]^{1/2}\right\}}{[(x-ut)^2\gamma^2+y^2+z^2]^{1/2}}, \qquad \ldots\ldots(29)$$

where $\mathbf{J}=(q/c)\mathbf{u}$ is the current in e.m.u., due to the moving charge, and $\gamma=c\,(c^2-u^2)^{1/2}$.

The scalar potential ψ can be divided into two parts $\psi=\psi_1+\psi_2$ where

$$\psi_1=\frac{q}{2\pi^2}\int\frac{(\mathbf{K}\,.\,\mathbf{u})^2-K^2c^2}{K^2[\omega_p^2-K^2c^2-(\mathbf{K}\,.\,\mathbf{u})^2]}\exp\left[i\mathbf{K}\,.\,(\mathbf{r}-\mathbf{u}t)\right]d\mathbf{K}$$

and

$$\psi_2=c^2\frac{q}{2\pi^2}\int\frac{\exp\left[i\mathbf{K}\,.\,(\mathbf{r}-\mathbf{u}t)\right]}{\omega_p^2+K^2c^2-(\mathbf{K}\,.\,\mathbf{u})^2}d\mathbf{K}.$$

ψ_1 is exactly of the same form as the longitudinal scalar ϕ with c in place of V, and u being always less than c we shall get no Mach cone in this case. Thus

$$\psi_1=\frac{q\exp\left\{-\frac{\omega_p}{c}[(x-ut)^2\gamma^2+y^2+z^2]^{1/2}\right\}}{\gamma[(x-ut)^2\gamma^2+y^2+z^2]^{1/2}}, \qquad \ldots\ldots(30)$$

and following the same method of evaluating **A** we have

$$\psi_2=q\gamma\frac{\exp\left\{-\frac{\omega_p}{c}[(x-ut)^2\gamma^2+y^2+z^2]^{1/2}\right\}}{[(x-ut)^2\gamma^2+y^2+z^2]^{1/2}}. \qquad \ldots\ldots(31)$$

From these equations for transverse field it can be seen that the equipotential surfaces are all of ellipsoidal shape surrounding the moving particle. Also, these fields are exponentially decaying with distances and any electromagnetic energy flux associated with them will very rapidly die out as we move away from the particle. In fact, the Poynting flux is confined within a region less than Debye sphere and there will be no Čerenkov effect.

§ 5. Calculation of Energy Loss

In order to calculate the energy loss due to the long range part of the interaction we divided the range of variation in the integral over K_ρ in equation (18) into two parts: one, from 0 to K_m, and the other from K_m to ∞, where K_m corresponds to some minimum value of the impact parameter of the moving

particle in the plasma, so that 'collision' can be neglected. The first part from 0 to K_m takes account of the long range part of the Coulomb force, and the second part from K_m to ∞ gives the potential energy of short-range interaction between the particles. For low density plasma, the latter part is very small, and so far as the interaction energy due to long range forces are concerned we have to take the limits of K_ρ as 0 and K_m. This interaction energy comes from the moving particle and is used to set up collective oscillations in the plasma in the form of hyperbolic waves, as we have already seen. The direction of the energy flow will be along the normals to the system of hyperboloids representing the equipotentials. Therefore, for a particle moving along the x-axis these flow lines (of energy) are a system of rectangular hyperboloids which are conjugate to the family of curves (27).

To calculate the interaction energy due to long-range forces in the case of $u > V$, we set after equations (13), (16) and (23)

$$\mathbf{E}^{\parallel} = -\nabla\left[-q\omega_p^2(u^2-V^2)^{1/2}\int_0^{K_m}\frac{K_\rho J_0(K_\rho r_\rho')\sin\left\{r_x'\left(\frac{\omega_p^2+K_\rho^2V^2}{u^2-V^2}\right)^{1/2}\right\}}{(\omega_p^2+K_\rho^2u^2)(\omega_p^2+K_\rho^2V^2)^{1/2}}dK_\rho\right]. \quad \ldots\ldots(32)$$

The loss of energy by the moving particle per unit length of its path is given by

$$\epsilon = \frac{q}{u}(\mathbf{E}^{\parallel}.\mathbf{u}) \text{ at } \mathbf{r} = \mathbf{u}t.$$

For $\mathbf{u}$ along the x-axis this gives from equation (32)

$$\epsilon = \frac{q^2\omega_p^2}{2u^2}\ln\left(1+\frac{K_m^2u^2}{\omega_p^2}\right)$$

$$= \frac{M}{m}\frac{q^2e^2n_0\pi}{E_0}\ln\left(1+\frac{2u^2}{V^2}\right), \quad \ldots\ldots(33)$$

after setting $K_m^2 \simeq \dfrac{2\omega_p^2}{V^2}$ and $E_0 = \frac{1}{2}Mu^2$, the energy of the incident particle.

§ 6. Discussion

The expression for energy loss represented by equation (33) has already been obtained by Bohm and Pines (1952), and Akhiezer and Sitenko (1952). We have already pointed out that this energy is confined within the Mach cone behind the particle which therefore is the region for 'collective oscillations' or plasma oscillations excited by the moving particle. In this connection we may mention that if instead of a single particle we have a beam of particles moving through the plasma, some sort of coherence phenomenon may take place modifying the field distribution and the interaction process may result in much more energy transference to the plasma than is given by equation (33).

In conclusion, we may note one point in the derivation of our results. We have used equation (2) in our calculations which gives only a local distribution of pressure, which is rather an inadequate assumption for a collisionless gas. A rigorous method would be the use of Boltzmann's equation instead of equation (1), which takes account of the velocity distribution of the plasma particles. We have limited ourselves to the simpler equation, because the use of Boltzmann equation would make the mathematical treatment extremely complicated, whereas the essential results obtained here would not have changed much. Qualitatively, we can say that if we take account of the velocity distribution instead of

the average velocity V of the plasma electrons, the Mach cone will become somewhat diffused instead of having a sharp boundary as obtained by us. This usually happens when Čerenkov effect takes place in a dispersive medium, so that the use of Boltzmann's equation will automatically take account of the dispersive property of a plasma. Apart from this, the use of Boltzmann's equation will give rise to the phenomenon of Landau damping. This Landau damping will therefore be present in the 'collective oscillations' within the Mach cone so that they will experience a damping decrement with time, in addition to 'collision damping' which we have not taken into account in this paper. However, the use of the full Boltzmann equation will be carried out in a future work.

Acknowledgments

The author wishes to express his sincere gratitude to the Director, Professor B. D. Nag for his kind interest in this work and the constant encouragement given by him to the author. He also wishes to thank Dr. S. Mukherjee for many valuable discussions.

Appendix A

We have to evaluate the integrals

$$A=\int_0^\infty J_0(K_\rho r_\rho')\exp(-K_\rho r_x')\,dK_\rho, \qquad \ldots\ldots(34)$$

$$B=\int_0^\infty K_\rho J_0(K_\rho r_\rho')\,\frac{\exp\left[-r_x'\left(\frac{\omega_p^2+K_\rho^2V^2}{V^2-u^2}\right)^{1/2}\right]}{(\omega_p^2+K_\rho^2V^2)^{1/2}}\,dK_\rho. \qquad \ldots\ldots(35)$$

We first evaluate B. Using the relations

$$e^{-z}=\cosh z-\sinh z,$$

$$J_{1/2}(zi)=(1-i)\left(\frac{1}{\pi z}\right)^{1/2}\sinh z,$$

$$-Y_{1/2}(zi)=J_{-1/2}(zi)=(1-i)\left(\frac{1}{\pi z}\right)^{1/2}\cosh z,$$

where J and Y are the Bessel functions of first and second kind respectively, we can write

$$e^{-z}=\frac{(\pi z)^{1/2}}{2}(i-1)H_{1/2}^{(1)}(zi), \qquad \ldots\ldots(36)$$

where $H_\nu^{(1)}$ is the Hankel function of the first kind. Writing the integral form of $H_\nu^{(1)}(z)$, (Watson 1952, p. 178)

$$H_\nu^{(1)}(z)=\frac{1}{\pi i}(\tfrac{1}{2}z)^\nu(-1)^{-\nu}\int_0^\infty \exp\left(-x+\frac{z^2}{4x}\right)\frac{dx}{x^{\nu+1}}$$

and putting

$$z=r_x'\left(\frac{\omega_p^2+K_\rho^2V^2}{V^2-u^2}\right)^{1/2}$$

we get from (36)

$$\frac{\exp\left[-r_x'\left(\frac{\omega_p^2+K_\rho^2V^2}{V^2-u^2}\right)^{1/2}\right]}{(\omega_p^2+K_\rho^2V^2)^{1/2}}=\frac{a}{2\pi^{1/2}}\int_0^\infty \exp\left[-t-\frac{a^2(\omega_p^2+K_\rho^2V^2)}{4t}\right]\frac{dt}{t^{3/2}}, \qquad \ldots\ldots(37)$$

where $a = r_x'/(V^2-u^2)^{1/2}$. Using equation (37) in (35) and interchanging the order of integration of t and K_ρ, we get

$$B = \frac{a}{2\pi^{1.2}}\int_0^\infty \frac{dt}{t^{3.2}} \exp\left[-t - \frac{a^2\omega_p^2}{4t}\right]\int_0^\infty K_\rho J_0(K_\rho r_\rho') \exp\left(-\frac{a^2V^2}{4t}K_\rho^2\right)dK_\rho. \quad \ldots\ldots(38)$$

The integral over K_ρ in (38) can be evaluated according to Watson (1952, p. 393), giving

$$B = \frac{1}{aV^2\pi^{1/2}}\left(1+\frac{r_\rho'^2}{a^2V^2}\right)^{-1/2}\int_0^\infty \frac{dz}{z^{1/2}}\exp\left[-z - \frac{a^2\omega_p^2}{4z}\left(1+\frac{r_\rho'^2}{a^2V^2}\right)\right]$$

$$= \left(\frac{2\omega_p}{\pi V^3}\right)^{1/2}\frac{1}{(r_x'^2\alpha^2+r_\rho'^2)^{1/4}}K_{-1/2}\left[\frac{\omega_p}{V}(r_x'^2\alpha^2+r_\rho'^2)^{1/2}\right], \quad \ldots\ldots(39)$$

where $K_\nu(z)$ is the modified Bessel function of the second kind (Watson 1952, p. 183), and $\alpha = V/(V^2-u^2)^{1/2}$.

The integral A is easily evaluated according to Watson (1952, p. 384, equation (1)). The result is

$$A = \frac{1}{(r_x'^2+r_\rho'^2)^{1/2}}. \quad \ldots\ldots(40)$$

Using the results

$$K_{1/2}(z) = K_{-1/2}(z) = \left(\frac{\pi}{2z}\right)^{1/2}e^{-z}$$

and the relations (17), equation (22) will at once follow from equations (13), (18), (39) and (40).

APPENDIX B

We have to evaluate the integral

$$C = \int_0^\infty K_\rho J_0(K_\rho r_\rho') \frac{\sin\left[r_x'\left(\frac{\omega_p^2+K_\rho^2V^2}{u^2-V^2}\right)^{1/2}\right]}{(\omega_p^2+K_\rho^2V^2)^{1/2}}dK_\rho \quad \ldots\ldots(41)$$

The relation

$$J_{1/2}(z) = \left(\frac{2}{\pi z}\right)^{1/2}\sin z$$

when used in (41) gives

$$C = \left(\frac{\pi b}{2}\right)^{1/2}\int_0^\infty \frac{K_\rho J_0(K_\rho r_\rho')J_{1/2}[b(\omega_p^2+K_\rho^2V^2)^{1/2}]}{(\omega_p^2+K_\rho^2V^2)^{1.4}}dK_\rho, \quad \ldots\ldots(42)$$

where $b = r_x'/(u^2-V^2)^{1/2}$. Using the relation (Watson 1952, p. 177).

$$J_\nu(z) = \frac{(\frac{1}{2}z)^\nu}{2\pi i}\int_{\sigma-i\infty}^{\sigma+i\infty}\frac{dt}{t^{+1}}\exp\left(t-\frac{z^2}{4t}\right), \quad \ldots\ldots(43)$$

(where σ has any positive value), with $\nu = \frac{1}{2}$ and $z = b(\omega_p^2+K\rho^2V^2)^{1/2}$ in equation (42), we get after changing the order of integrations

$$C = \left(\frac{\pi b^2}{4}\right)^{1.2}\frac{1}{2\pi i}\int_{\sigma-i\infty}^{\sigma+i\infty}\frac{dt}{t^{3.2}}\exp\left(t-\frac{b^2\omega_p^2}{4t}\right)\int_0^\infty K_\rho J_0(K_\rho r_\rho')\exp\left(-\frac{b^2V^2}{4t}K_\rho^2\right)dK_\rho. \quad \ldots\ldots(44)$$

The integral over K_ρ in equation (44) can again be evaluated according to Watson (1952, p. 393), giving

$$C = \frac{1}{2\pi i}\frac{\pi^{1/2}}{bV^2}\int_{\sigma-i\infty}^{\sigma+i\infty}\frac{dt}{t^{1/2}}\exp\left[t\left(1-\frac{r_\rho'^2}{b^2V^2}\right)-\frac{b^2\omega_p^2}{4t}\right].$$

When $r_\rho'^2/b^2V^2 > 1$, the contour in the above integral can be closed only through the right half of the t-plane and thus the contour will include no singularity, because all the singularities of the integral in equation (43) lie on the negative real axis of t. Hence this gives $C=0$. For $r_\rho'^2/b^2V^2 < 1$, the contour can be closed by a semicircle through the left half plane of t. This integral along the semicircle is zero as its radius tends to infinity by Jordan's lemma, and we can apply relation (43) again to get

$$C = \frac{\pi^{1/2}}{bV^2}\frac{(\frac{1}{2}b\omega_p)^{1/2}}{\{1-r_\rho'^2/b^2V^2\}^{1/4}}\,J_{-1/2}\left(b\omega_p\left\{1-\frac{r_\rho'^2}{b^2V^2}\right\}^{1/2}\right). \qquad \ldots\ldots (45)$$

Using

$$J_{-1/2}(z) = \left(\frac{2}{\pi z}\right)^{1/2}\cos z$$

in equation (45), we at once get equation (24).

References

Akhiezer, A. I., and Sitenko, A. G., 1952, *J. Exp. Theor. Phys., U.S.S.R.*, **23**, 161.

Bohm, D., and Gross, E. P., 1949, *Phys. Rev.*, **75**, 1851.

Bohm, D., and Pines, D., 1952, *Phys. Rev.*, **85**, 338.

Kraus, L., and Watson, K. M., 1958, *Phys. Fluids*, **1**, 480.

Kolomenskii, A. A., 1956, *Dokl. Akad. Nauk SSSR*, **106**, 982.

Sommerfeld, A., 1954, *Optics* (New York : Academic Press).

Spitzer, L., 1956, *Physics of Fully Ionised Gases* (New York : Interscience Publishers), p. 13.

Vlasov, A. A., 1945, *Theory of Vibrational Properties of an Electron Gas*, GTTI, Moscow, Part 2, Section 1.

Watson, G. N., 1952, *Theory of Bessel Functions*, 2nd Edition (Cambridge: University Press).

Particle Excited Luminescence in Diamond

By P. J. DEAN, P. J. KENNEDY† and J. E. RALPH‡
Wheatstone Physics Laboratory, King's College, London

MS. received 2nd November 1959, in revised form 18th March 1960

Abstract. The luminescent effects, excited in the diamond crystals under bombardment by monoenergetic α- and β-particles and by 50 kev monoenergetic electrons, have been investigated for some 50 natural diamonds and for several specimens which had suffered previous radiation damage. The wavelength spectrum in the luminescent emission has been measured and also the effect of crystal temperature on this spectrum. Emphasis has been placed on the differences between the wavelength spectra of the luminescence arising from the different types of excitation and, also, the relative dependence of the wavelength spectra on the condition of the crystal. A comparison has been made of the luminescent and conduction counting efficiencies of the crystals. The results indicate the importance, in diamond, of defects which trap the carriers but do not give rise to the emission of visible or near infra-red radiation.

§ 1. Introduction

It has been shown by many workers (Klick and Shulman 1957, Lax 1956, Williams 1949) that the detailed study of luminescent spectra in solids is capable of yielding valuable information on the electronic properties of the material. For diamond, ultra-violet excited fluorescence has been studied by Martin (1957) and by Dyer and Matthews (1957) and that excited by x-rays by Matthews (1958). Such work suggested that a similar investigation of particle excited luminescence might prove to be equally informative. A survey of the scintillation properties of diamonds subjected to α-particle bombardment has been given recently by Ralph (1959). The present paper is concerned primarily with further experimental results on the luminescence stimulated in diamond by α-particle, monoenergetic β-particle and monoenergetic electron bombardment. § 2 gives a brief outline of the results obtained in the preliminary experiments on the prompt scintillation produced in diamond by both α- and β-particles and §§ 3 and 4 give a more detailed treatment of certain aspects of this and other luminescent behaviour.

§ 2. Preliminary Experiments

The apparatus illustrated in figure 1 was used for the work described in this section.

To facilitate the comparison of the scintillation properties of diamond specimens it was thought useful to compare their efficiency with other well-known scintillators. β-particles of 1 Mev energy and α-particles of 5·3 Mev energy were used to produce scintillations in anthracene, in the commercial phosphor Pamelon and in a number of gem quality colourless diamonds. The maximum scintillation

† Now at the Department of Natural Philosophy, University of Edinburgh.
‡ Now at the Mellon Institute, Pittsburgh, U.S.A.

Figure 1. Schematic representation of scintillation detection apparatus. P, photomultiplier; I.F., interference filter; V, vacuum seal; L, light pipe; W.F., Wratten filter; S, specimen; E, electrode system; B, variable temperature block.

pulse height was measured in each case and the relative efficiency per unit energy was calculated with the efficiency of anthracene for 1 Mev β-particles taken as 100%. The results are given in table 1 where the efficiency of the large specimen S 5 is taken as typical of that for diamond. It is seen that diamond differs from the other scintillators in that the ratio E_β/E_α is less than unity.

Table 1

	Anthracene	Pamelon	Diamond S5
β-efficiency E_β (%)	100	42	2
α-efficiency E_α (%)	12·6	4·7	10·8
Ratio E_β/E_α (%)	8	9	0·2

The luminescent efficiency of anthracene for absorption of 1 Mev β-particles has been taken as 100%. Efficiencies are calculated for unit energy of the primary particle.

This fact, together with the difficulty of achieving large β-ray energy dissipation in the small diamonds normally available (Kennedy 1959) suggested that a detailed study of electron induced luminescence could best be made under conditions of high particle flux as, for example, in those experiments described in § 3.

It is now well known that, when certain diamonds are subjected to bombardment with ionizing particles and an electric field is established across them, the phenomenon of 'conduction counting' is observed. Since it may be assumed that the same ionizing processes are involved in the production of both conduction and scintillation pulses, it was thought possible that some relationship existed between the two pulse systems. To investigate this the apparatus in figure 1 was arranged so that the α-particle induced conduction and scintillation pulse spectra could be taken at the same time. The spectra were obtained under conditions where the polarization fields in the crystal were small when compared

with the applied field (McKay 1948, Chynoweth 1950). When a field was applied to the diamond crystals it was generally found that a marked reduction occurred in the scintillation pulse magnitude. Figure 2 shows the effect on the scintillation pulse spectrum for the good conduction counting specimen K 80. Figure 3 shows the effect of increasing field strength on both the maximum conduction pulse and the maximum scintillation pulse. A series of such experimental curves shows an intimate connection between the scintillation pulse and

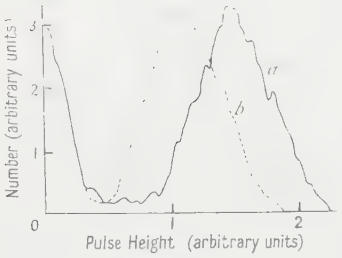

Figure 2. Scintillation pulse spectra; *a*, for no applied field; *b*, applied field $3{\cdot}5 \times 10^4$ v cm^{-1}.

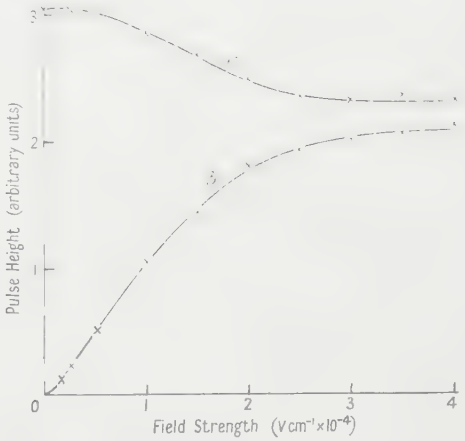

Figure 3. The effect of an applied field on *a*, the maximum scintillation pulse; *b*, the maximum conduction pulse.

conduction pulse response to increasing field strength. For a specimen where the conduction pulse height shows only a small increase with increasing field, the scintillation pulse decreases only slowly and vice versa. In those diamonds normally classified as 'poor' conduction counters the application of an electric field produced a reduction in scintillation pulse height comparable in magnitude with that found in good counters. 'Non'-counters showed a smaller reduction and in some cases no diminution was observed.

From these experiments it semed probable that the presence of polarization fields, produced during irradiation, would be reflected in the behaviour of the scintillation spectra. A series of experiments were carried out in which polarization fields were allowed to build up over periods of minutes. It may be seen from typical results, illustrated in figure 4, that, as the polarization field inhibits the conduction pulse height so the scintillation pulse increases towards its original value.

When the scintillation pulse and conduction pulse produced by an individual incident particle were examined, it was found that, although a large scintillation was more frequently associated with a small conduction pulse and vice versa, there appeared to be no consistent relationship between the magnitude of the two pulses. The conduction pulse was always associated in time with the prompt scintillation pulse and never with the phosphorescent pulses which follow the prompt emission.

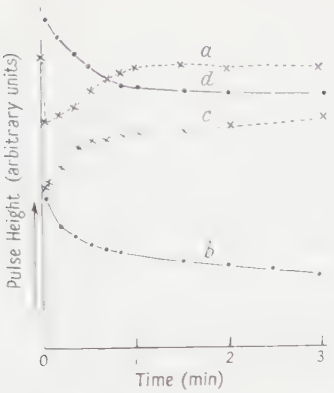

Figure 4. The change inpulse height with increasing polarization; *a*, scintillation pulse at 10 kv cm^{-1}; *b*, conduction pulse at 10 kv cm^{-1}; *c*, scintillation pulse at 40 kv cm^{-1}; *d*, conduction pulse at 40 kv cm^{-1}.

The rough limits to the wavelength distribution of the α-particle induced prompt scintillation were obtained using optical filters in the position indicated in figure 1. Pulse spectra were obtained under conditions in which the contribution from wavelengths below a known limit were cut out. For the specimens investigated the wavelengths contributing lay predominantly within the range 3000 Å to 4800 Å and the application of an electric field appeared to reduce all wavelength contributions proportionately.

The prompt scintillation was found to be markedly temperature dependent. Pulse height spectra taken at different crystal temperatures showed little change with increasing temperature in the range −160°c to −50°c, but thereafter, decreased steadily in magnitude until the prompt scintillation virtually disappeared at about 100°c.

§ 3. Experiments on Cathodoluminescence

The experience gained in the experiments described in § 2 indicated that, to obtain more detailed knowledge of the wavelength dependence of particle induced luminescence would require a substantial increase in the intensity of the emitted radiation. To obtain such high intensity is difficult with radioactive sources, particularly for β-particle excitation (table 1) and for the experiments described below it was therefore decided to use an electron beam to stimulate the emission.

The crystal specimen was introduced on a probe into the electron beam of a modified Siemens electron microscope operating in the energy range 40–90 kev. The beam was focused by the condenser lens only and beam currents of up to 40 microamperes were used. The temperature of the probe could be varied at will within the range −180°c to 100°c. Under these conditions strong cathodoluminescence was observed in all the specimens. The emission was analysed by a Hilger constant deviation spectrometer and recorded on Kodak P1200 and Ilford long range photographic plates. Intensity measurements of the wavelength spectra were obtained from the plates using a microdensitometer and the resulting wavelength scale was accurate to ± 5 Å.

In those experiments in which the variation with temperature of the intensity of a given wavelength band was measured, an EMI 6094 photomultiplier replaced the camera at the output end of the spectrometer.

3.1. *Spectral Characteristics at* $-180°$C

About fifty natural diamonds have been examined and all showed strong cathodoluminescence. The crystals normally appeared uniformly blue during excitation but many specimens, when viewed through an optical microscope, showed various combinations of green, yellow and blue regions. Some of these were sharply defined and others diffuse and overlapping.

The spectrographic analysis of the spectral distribution showed a wide variation in detail but certain features were common to almost all specimens. The emission was in general limited to the visible spectrum, seldom extending below 3900 A and only in two cases down to 3500 A. It may be roughly divided into two bands, with wavelengths greater and less than 5000 Å. The relative intensities of these were markedly specimen dependent.

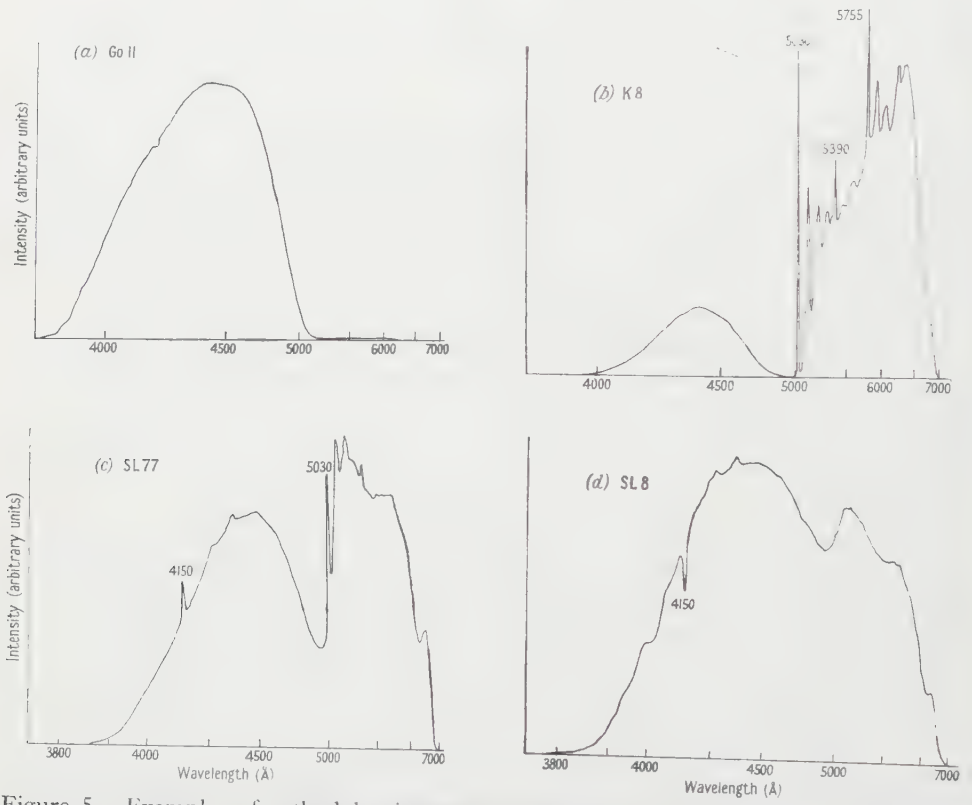

Figure 5. Examples of cathodoluminescence spectra for natural diamonds; (*a*) showing 4400 Å ' blue ' band; (*b*) showing typical long wavelength structure; (*c*) and (*d*) showing 4150 Å system with principal line in emission and in absorption.

Figures 5 (*a*) and (*b*) illustrate wavelength spectra for extreme cases found in naturally occurring crystals. Figure 5 (*a*) is for the specimen Go11, which gives an emission confined almost entirely to a broad band extending from 3900 Å to 5100 Å and centred about 4400 Å. Figure 5 (*b*) for the specimen K8 shows a spectrum with a very strong long wavelength contribution. The other specimens examined showed a behaviour intermediate between these cases, i.e. both bands were present but in widely varying relative intensity.

Figure 5 (*a*) indicates that the short wavelength or 'blue' band is generally featureless. It appeared in the spectrum of all natural specimens but only in a few cases did it show any detail. An emission-absorption system centred around 4150 Å has frequently been reported for ultra-violet excitation of diamonds (Dyer and Matthews 1958). Figures 5 (*c*) and (*d*) give spectra which show the only two cases where this system was detected in appreciable intensity under particle excitation. In figure 5 (*c*) the principal line appears in emission and in 5 (*d*) it appears as an absorption line. In both cases the subsidiary lines are in emission and are spaced at approximately 0·08 ev, as reported by Dyer and Matthews. The two crystals concerned had been found to be strongly fluorescent under ultra-violet excitation when most of the emission was associated with the 4150 Å system. Much weaker absorption lines at 4150 Å were found in several non-fluorescent crystals but no associated band had been observed in these cases.

Figure 5 (*b*) shows that the longer wavelength emission has considerable structure and may be roughly divided into three constituent overlapping bands centred about 5200 Å, 5900 Å and 6300 Å. The first or 'green' band is the most common and usually contains a line system of which the sharp line at 5030 Å is the principal, with other lines appearing at approximately 0·04 ev spacing on the long wavelength side. A similar system has been reported by Dyer and Matthews for ultra-violet excitation. The second or 'yellow' band, often less well defined than the green band, sometimes contains a system which has a principal line at 5755 Å and rather irregularly spaced subsidiary lines separated by approximately 0·05 ev. A line at 5390 Å (as in figure 5 (*b*)) is always present with the 5030 Å system, except when the 5755 Å system occurs alone. The remainder of the spectrum or 'red' band consists of broad red lines at 6240 Å, 6350 Å and 6770 Å. It should be emphasized that the specimen spectrum illustrated in figure 5 (*b*) is exceptional in showing such high intensity emission in the longer wavelengths. The red emission is not commonly as strong as the yellow and green. Broad lines have been detected in other crystals at 7250 Å and 8000 Å.

Several other sharp lines, which are normally present with the 5755 Å system, are shown at 4845 Å and 4910 Å on the long wavelength side of the 4400 Å band and at 3940 Å on the short wavelength side. In certain crystals which had suffered high energy electron radiation damage a system of blue lines was induced which was somewhat similar to the 4150 Å system but with its principal line at 3940 Å. This system has been found to be identical with the 4150 Å luminescence system if the first and second bands of the latter are neglected. Pringsheim (1953) has shown that the strength of the corresponding short wavelength components of the 4150 Å absorption system can alter independently of the strength of the lines at 4150 Å and 4030 Å. The effects of radiation damage are discussed more fully by Ralph (1960).

No correlation has been found between the type I and type II classification (which is based on ultra-violet absorption spectra) and the detailed cathodoluminescence spectra. A similar lack of correlation has been found between this classification and the scintillation response in diamond (Ralph 1959) and with the ultra-violet and x-ray excited luminescent spectra (Dyer and Matthews 1958). Between the ultra-violet excited and electron excited luminescence spectra the only consistent correspondence is found in the appearance of the 5030 Å system.

3.2. *The Effect of Temperature on Cathodoluminescent Spectra*

3.2.1. *Total spectrum.*

The crystal temperature was increased steadily from $-180°$C to $+140°$C and spectra were taken at various intermediate temperatures. The temperature was held constant at about $\pm 3°$C during exposures of 3 minutes to 20 minutes. The results illustrated have not been corrected for the spectral sensitivity of the P1200 plate used. Visual inspection showed that a crystal, which under bombardment appeared blue at $-180°$C, tended to become yellow in colour as the temperature increased. Regions of intense blue colour at $-180°$C were the last to disappear but at $+140°$C only yellow regions remained visible.

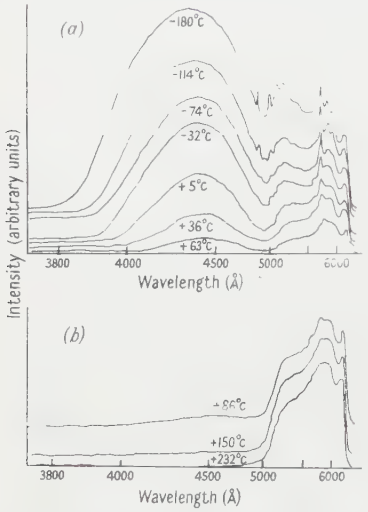

Figure 6. Variation of cathodoluminescence spectrum with temperature for diamond C″116. Ordinate scale of (*b*) different from that of (*a*).

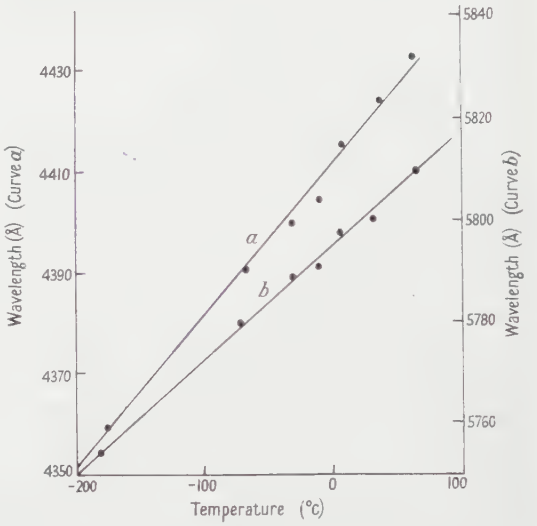

Figure 7. Temperature shifts of the four broad cathodoluminescence bands and 5755 Å line for diamond C″116; slopes: curve *a*, 0·30 Å deg^{-1}; curve *b*, 0·23 Å deg^{-1}.

The detailed behaviour is illustrated in figure 6 for the crystal C″116 which, at $-180°$C, has approximately equal intensity distribution between the blue band and the longer wavelength emission and also shows sharp line structure in the latter at that temperature. These curves show that the ratio of the intensity of the three broad bands constituting the long wavelength emission to that of the blue 4400 Å band increases with increasing temperature. The positions of the peaks in the blue, green and yellow bands shift towards the longer wavelengths with increasing temperature. Figure 7 shows that this is a linear shift at about 0·30 Å deg^{-1} in the case of the 4400 Å band (and the other broad bands) and that the line at 5755 Å shifts linearly at about 0·23 Å deg^{-1}. The sharp lines of the longer wavelength emission broaden and decrease in intensity with increasing temperature.

3.2.2. *The* 4400 Å *system.*

The wide variation in intensity with temperature of this band makes the photographic method of recording inconvenient and a photoelectric technique was therefore adopted. The emission from a wavelength interval of 100 Å

centred about 4400 Å was allowed to fall on to a photomultiplier and the intensity variation in the temperature range −180°C to +140°C was recorded directly by a pen recorder. The results obtained for the specimens C″116 and SL26 are illustrated in figure 8 and are typical of the behaviour shown in these experiments.

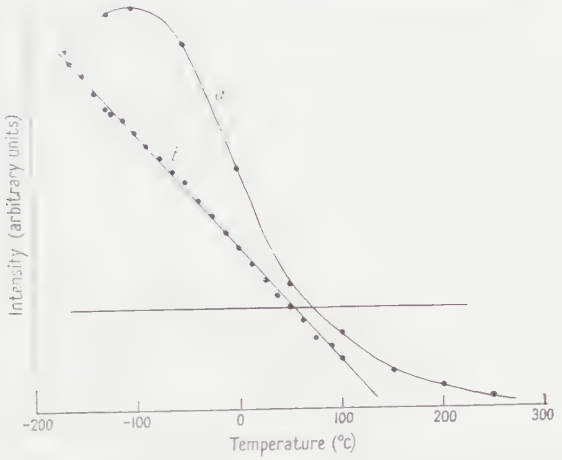

Figure 8. Temperature variation of selected wavelength regions of cathodoluminescence spectrum. Curve *a*, 4400 Å band for diamond C″116; curve *b*, 4400 Å band for diamond SL26; curve *c*, 5900 Å band for diamond C″116.

Those crystals which show a sharp line structure in the long wave region appear generally to follow the curve exemplified by C″116, whereas those have a response similar to SL26 generally exhibit either no line structure or very weak structure in this region. Diamond SL26 was completely free of line structure and appears to represent an extreme case.

3.2.3. *Long wavelength region.*

The photoelectric technique was again used in this investigation. In those crystals which gave an intensity sufficient for reliable measurements, the emission appeared to be practically independent of temperature (figure 8, curve *c*). It is probable that the 4400 Å band may be assumed to be symmetrical and that its long wavelength tail extends into the green band. In those crystals in which a variation of intensity with temperature was observed for the green band the ratio of its intensity to that of the blue band was small and it is probable that the variation is due to the change in intensity of the 4400 Å band tail.

Unfortunately reliable measurements in the yellow and red bands, well away from this blue band tail, were limited by the low sensitivity of the multiplier in these regions.

§ 4. Experiments on the α- and β-particle induced Luminescence

The work described in § 2 is almost exclusively concerned with the properties of the prompt α-particle induced scintillation pulses. The cathodoluminescence experiments described in § 3 were designed to provide well-resolved wavelength spectra of the emission stimulated by the absorption of low energy electrons. Efforts have also been made to obtain, using the same set of crystals, well-resolved wavelength spectra for the scintillation effects produced by α-particles in diamond

to enable a comparison to be made. Since these methods usually involved direct intensity measurements of the luminescent output, the effects of the main (prompt) and after (delayed) scintillation pulses (the phosphorescence) were recorded simultaneously. The spectra obtained in the experiments described in this section exhibit considerable similarity to the cathodoluminescence spectra but also a number of important differences.

4.1. *Quantum Efficiency of Scintillation Processes*

A fairly reliable estimate can be made of the efficiency of the scintillation process for diamonds which possess good geometrical properties since the self-absorption of the luminescence is known to be negligible for most diamonds. For crystals of less regular external habit or with significant absorption at the surfaces or in the interior regions, the measured efficiencies will be lower even if the same amount of light is actually liberated following the absorption of the energetic primary particle. This reduction was usually observed for crystals which had been heavily annealed, because of the slight graphitization of the surfaces which this treatment often produced.

The scintillation pulses were detected with an EMI type 6097 photomultiplier and the resulting voltage pulses measured with a Tektronix type 545 oscilloscope. The rise-time of the pulses was limited to 20 nsec by the upper bandwidth limit of the oscilloscope amplifiers and the differentiating time was adjusted to provide an acceptable resolution of the phosphorescence pulse structure consistent with minimum reduction in the voltage gain of the system. The arrangement of the apparatus was again similar to that shown in figure 1. To minimize the effect of the competition from a radiationless energy loss process (§ 2) the results leading to table 2 were obtained at 90 K. The magnitude of the maximum height of the main pulses was estimated from a suitable number of oscilloscope photographs of individual scintillation events. These results so obtained were checked for many crystals using a photographic method of pulse height analysis (Kennedy and Dean 1959). The energy contained in the phosphorescence system was also estimated from the photographs by the integration of the heights of all the pulses contained in this system. In this way a 'total equivalent voltage pulse' was estimated for the after pulse radiation of each scintillation event and an average value was obtained for each experimental arrangement. The photographic method of analysis was not suitable for the investigation of the magnitude of the energy of the phosphorescence.

Table 2 gives an indication of the α- and β-scintillation efficiencies for a number of specimens of diamond of various sizes, external shapes and previous treatment. In agreement with Ralph (1959) no significant correlation was found between these properties and the type I, type II classification. This classification has therefore not been employed in table 2. The efficiency E is presented as the ratio of the number of electrons which must undergo transitions in energy in order to produce the observed intensity of the emitted radiation to the number of electron–hole pairs which are known (Kennedy 1959) to be created by the absorption of the primary particles. The absolute values of these ratios are not very accurate since only an approximate estimate can be made of some of the factors which enter into the calculation. Such factors are the solid angle of collection of the

Table 2

(1)	(2)	(3)	(4)	(5)	(6)	(7)	(8)
SL8	AB2 strong ultra-violet fluorescence	0·042	0·33	0·36	0·012	0·28	0·033
C″116	AC2	0·81	0·33	0·42	0·018	0·22	0·043
K80	AC2	0·087	0·27	0·36	0·009	0·10	0·025
Go11	AC3	0·027	0·27	0·30	0·003	0·11	0·010
BB96	AC1 U	0·057	0·33	0·39	0·021	0·37	0·005
BB96	EC1 V	0·108	0·21	0·33	0·027	0·25	0·008
K88	AC2 U	0·027	0·24	0·27			
K88	EC2 V	0·021	0·06	0·09	0·003	0·14	0·033
Co7	DC2 V	0·104	0·24	0·36	0·030	0·26	0·083
S5	AC3	0·108	0·36	0·45	0·024	0·22	0·053
' Octahedron '	AC3	0·024	0·27	0·30	0·015	0·62	0·050
K124	AC2	0·015	0·21	0·24	0·0024	0·16	0·010
B32	AC2 U	0·036	0·33	0·36			
B32	EC2 V	0·084	0·30	0·38	0·021	0·25	0·054

(1) crystal; (2) state; (3)–(5) α-scintillation: (3) main E_{α_1}, (4) after pulse E_{α}, (5) total E_{α_2}; (6) E_{β} scintillation; (7) E_{β}/E_{α_1}; (8) E_{β}/E_{α_2}.
U, before electron irradiation and annealing. V, after electron irradiation and annealing.
Key to size: 1 : 1 mm × ¾ mm × ¾ mm
2 : 2 mm × 1½ mm × 1 mm
3 : larger.
Faces and transparency: Clear, A; irregular, B; smooth, C; frosty, D; dark, E.

emitted radiation by the light pipe, the average quantum efficiency of the photocathode of the photomultiplier and the size of the voltage pulse present in the oscilloscope display which should be taken to be caused by the liberation of one electron from the multiplier cathode. For comparative purposes, however, an estimation of the ratios to two significant figures in table 2 is justified.

Table 2 shows that the efficiency is much higher for α-particles than for β-particles, especially if the phosphorescence energy, typically about ten times that of the main pulses, is included in the calculation. If a similar phosphorescent effect exists for the β-scintillations, then its importance relative to the main β-scintillation pulse is considerably less than for α-particle excitation since no evidence of a phosphorescent component for β-scintillations was found in the present experiments. The energy contained in the phosphorescence appears to be much less specimen dependent than that comprising the main α- or the β-induced emission, especially if an allowance is made for the optical properties of the crystals. The variation in the magnitude of the main α- and the β-pulses

for different surface regions of a given specimen was also much wider than the corresponding variation for the phosphorescence between the same regions. This was particularly noticeable for crystals containing obvious surface flaws and for those which had been damaged by irradiations with high energy particles. A comparison of the efficiencies of cathodoluminescence and of the main α-scintillations showed qualitatively similar variations for the two processes from point to point over the surface of these inhomogeneous crystals, although the intensity of the phosphorescent emission was effectively constant. The 50 kev electrons which were used in the cathodoluminescence experiments had roughly the same range in diamond as 5·3 MeV α-particles.

4.2. *Wavelength Dependence of the Scintillation Intensity*

The difficulties involved in the accurate experimental determination of the scintillation wavelength spectra when radioactive sources are used as the stimulating radiation have already been mentioned in § 3. Measurements were found to be possible only for the α-stimulated emission when the more accurate method of analysis was used, since the intensity of the β-scintillations was generally less than 2% of that produced by α-particles for a given specimen. The principal consideration in the design of the apparatus, shown in figure 9, was the need

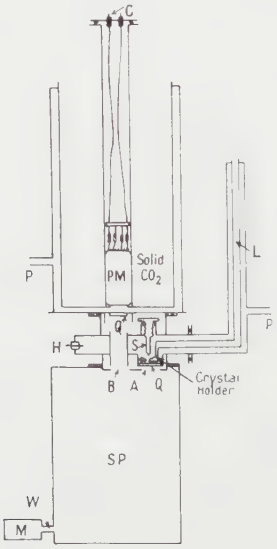

Figure 9. Apparatus used for photoelectric recording of scintillation wavelength spectrum. C, photomultiplier, h.t. and signal connectors; PM, photomultiplier; P, vacuum pump connections; L, liquid air Dewar flask; Q, quartz windows; S, ^{210}Po α-particle source; A, entrance slit of spectrometer; B, exit slit of spectrometer; SP, Littrow flint spectrometer; W, wavelength scan; M, motor.

for the attainment of the maximum possible signal-to-noise ratio so as to permit an adequate spectral solution. Cooling the photomultiplier to -80°C resulted in an improvement in the signal-to-noise ratio of about 15 : 1 over the room temperature value. This increase in sensitivity was especially necessary for the low temperature measurements, where an unavoidable decrease in the efficiency of collection of the luminescence by the monochromator was incurred due to the inferior geometry imposed by the need to evacuate the specimen chamber.

The wavelength distributions of the α-scintillation emission were derived from pen recorder charts of the photomultiplier current. A correction was made for the non-linear wavelength response of the monochromator and photomultiplier by means of calibration traces obtained with the use of a tungsten strip filament source. Room temperature spectra were also obtained for three crystals using a photographic plate (Kodak P1200) to record the emission. The cathodoluminescence spectra for these crystals, which had been obtained for the same surface regions of the crystals as were used in these α-particle experiments, were easily distinguishable from one another (compare figures 5 (*a*) and 5 (*b*)). On the contrary, the spectra resulting from the α-excitation of the luminescence were virtually indentical and were similar to those obtained when the experiment was repeated with the photomultiplier detector (figure 10). The photographic method of analysis was not very convenient because exposures of at least ten days were required to allow the accurate use of the densitometer and it was therefore impracticable to record the spectra under varying crystal conditions. The degree of linearity of the wavelength response was however much greater than for the photoelectric method. In the latter case it was not possible to derive the precise shapes of the component parts of the spectrum.

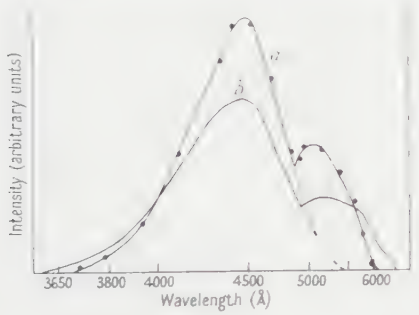

Figure 10. α-scintillation spectra for diamond B31. Curve *a*, obtained from photoelectric recording +20°c; curve *b*, from photographic recording +20°c (not corrected for spectral sensitivity of P1200 plates).

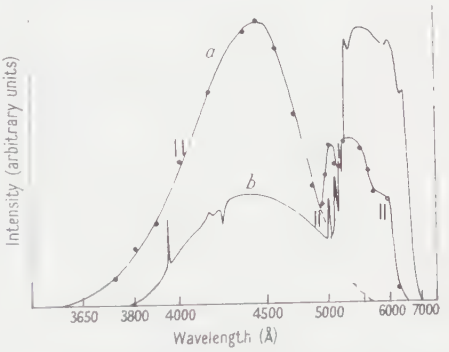

Figure 11. Variation of luminescence with wavelength for diamond B32, temperature −190°c Curve *a*, α-excitation (apparatus as figure 10); curve *b*, 50 kev electron excitation.

In figure 11 is given the scintillation spectrum containing the best resolution which was achieved. The detail in the radiation contained in the long wavelength region of the spectrum may be compared with the same section of the cathodoluminescence spectrum for the same crystal at the same temperature. The general features in this long wavelength radiation appear to be similar for both modes of excitation.

The blue bands, however, exhibit certain differences in their properties. Some of these differences are emphasized in table 3 in which are listed the values of the ratios of the total energy contained in the broad blue band to that in the rest of the spectrum, (*a*) for the total α-scintillation output (ratio R_a), (*b*) for the cathodoluminescence (ratio R_b), (*c*) for the main α-scintillation (ratio R_c) and (*d*) for the total α-scintillation output as determined by pulse measurements.

Table 3

(1)	(2)	(3)	(4)	(5)	(6)	(7)	(8)
SL8 + 20	Natural	4·0 : 1	2·1 : 1	5·4 : 1	1·5 : 1	4490	4540
SL8 −180	Natural	5·4 : 1	3·5 : 1	7·2 : 1	3·4 : 1	4400	4450
C″116 + 20	Natural	5·4 : 1	4·0 : 1	6·0 : 1	4·2 : 1	4480	4420
K35 + 20	Electron irrn. and 10 min at 480°C	4·8 : 1	3·1 : 1	6·2 : 1	2·6 : 1	4460	4410
B31 −180	Natural	5·3 : 1	4·0 : 1	5·3 : 1	2·7 : 1	4410	4380
B4 + 20	Neutron irrn. and 45 min at 800°C	2·3 : 1	0·7 : 1	3·3 : 1	0·29 : 1	4470	4330 & 4440
Co7 + 20	Electron irrn. and 30 min at 800°C	2·7 : 1	0·15 : 1	5·0 : 1	0·10 : 1	4490	4410
S5 + 20	Natural	4·4 : 1	2·5 : 1	8·0 : 1	7·6 : 1	4490	4450
Go11 + 20	Natural	4·8 : 1	12·0 : 1	5·6 : 1	very large†	4460	4440
Go11 −180	Natural	6·3 : 1	16 : 1	7·9 : 1	very large†	4380	4360
BB96 + 20	Natural	4·4 : 1	5·7 : 1	5·6 : 1	3·2 : 1	4460	4420
BB96 + 20	Electron irrn. and annealed (in accelerator)	2·5 : 1	0·45 : 1	4·7 : 1	0·42 : 1	4490	4360
K88 + 20	Electron irrn. and 10 min at 540°C	4 0 : 1	0·35 : 1	5·6 : 1	1·8 : 1	4500	4400
K80 + 20	Natural	5·6 : 1	2·4 : 1	10 : 1	very large†	4480	4430
K80 −180	Natural	8·1 : 1	3·8 : 1	8·0 : 1	very large†	4410	4370
B32 + 20	Natural	4·8 : 1	3·2 : 1	5·4 : 1	2·4 : 1	4500	4290
B32 + 20	Electron irrn. and 10 min at 800°C	2·6 : 1	0·34 : 1	4·0 : 1	0·35 : 1	4520	4360
B32 −180	Electron irrn. and 10 min at 800°C	3·5 : 1	0·56 : 1	5·0 : 1	0·73 : 1	4390	4350
K8 + 20	Electron irrn. and 10 min at 500°C	3·9 : 1	3·0 : 1	4·9 : 1	2·3 : 1	4500	

(1) Crystal and temperature (°C); (2) state; (3), (4) α-scintillation (pulse): (3) ' blue '/(green + red) total output R_d, (4) ' blue '/(green + red) main pulse R_c; (5) total α-scintillation output ' blue ' band/rest R_a; (6) cathodoluminescence output ' blue ' band/rest R_b; (7) position of blue peak—x-spectrum (Å); (8) position of blue peak—cathodoluminescence spectrum (Å).

† See figure 7 (*a*).

The results have been obtained for a range of crystal conditions as indicated by column (2). The lack of exact agreement between the ratios R_a and R_a of columns (3) and (5) is probably due to the use of a Wratten 12 filter, which divides the spectrum at 5000 Å, in the scintillation pulse experiments. Figure 12 shows that this does not allow a complete resolution of the blue band radiation from the rest of the spectrum.

Table 3 shows that, except for the specimen K80, R_a and R_d only vary between the different specimens in the ranges 8 : 1 to 5 : 1 and 6·5 : 1 to 2·5 : 1 respectively. Subsequent ultra-violet and infra-red measurements have indicated that K80 contains an abnormally low percentage of impurities and crystal defects. Ratios R_a and R_d show a good correlation in their fluctuations from specimen to specimen and the table shows that the relatively perfect crystals have high values of R_a and R_d, while the lowest ratios are to be found for those crystals which have been subjected to bombardment damage and subsequent annealing treatments. This last statement is also true for the ratios R_b, but the range of variation of R_b, is much larger than either R_a or R_d. For example crystals Go11 and K80 exhibited no detectable long wavelength cathodoluminescence at all, whereas for Co7 the radiation was almost entirely confined to the components in this wavelength region.

The ratios R_c in column (4) for the main α-scintillation pulse radiation vary in step with R_b and over a wider range than R_a or R_d. The values are systematically greater than R_b and this is probably due to the presence in the main α-pulses of a significant component of radiation which, like the phosphorescence radiation, is relatively specimen independent.

Columns (7) and (8) of table 3 contain the wavelengths of the maxima of the blue bands (total emission) produced by α-particle and low energy electron excitation. These results combined with others, not given in the table, suggest that the position (as well as the shape) of the blue band produced by either method of excitation is unaffected by the state of the crystal provided that the temperature is held constant. The presence of the 3940 Å system in the cathodoluminescence spectra of some crystals after irradiation, mentioned in § 3, does not alter the mean position of the band and the system appears to be superimposed on the normal blue band. The blue band maxima are temperature dependent, however, and the mean values of the temperature coefficient have been obtained from the data of table 3. For α-scintillations these values are 4485 Å at +20°C and 4398 Å at −180°C giving $d\lambda/dT = +0{\cdot}42$ Å deg^{-1} or $dE/dT = -3{\cdot}0 \times 10^{-4}$ ev deg^{-1}. The corresponding cathodoluminescence values are 4417 Å; 4356 Å; +0·30 Å deg^{-1} and $-2{\cdot}1 \times 10^{-4}$ ev deg^{-1}. The mean value and the temperature coefficient of the mean value of the cathodoluminescence blue band are therefore different from the α-scintillation blue band values. Crystals B32 and B4 produced α-excited spectra which contained an exceptionally high proportion of long wavelength radiation which enabled a measurement of the temperature coefficient to be made on the uncorrected recorder spectra for a peak close to 5750 Å. Values of 0·25 Å deg^{-1} and $-1{\cdot}5 \times 10^{-4}$ ev deg^{-1} were obtained for $d\lambda/dT$ and dE/dT. This result is close to that found by Ralph (1960) for the coresponding line of the cathodoluminescence spectrum (figure 7). Specimen results of the variation of these α-scintillation peak positions with temperature are included in figure 12 and it can be seen that the assignment of a linear temperature coefficient for the whole of the measured range of temperatures is justified.

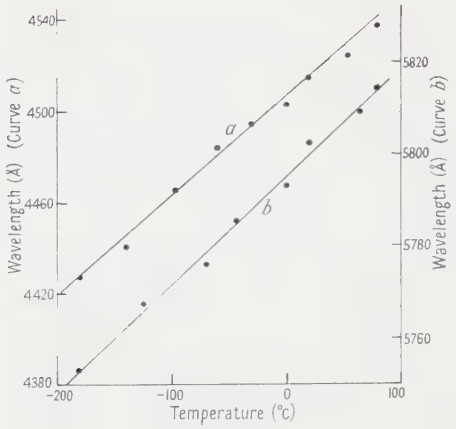

Figure 12. Temperature shifts of α-scintillation ' blue ' band peak and peak at 5750 Å for diamond B32. Slopes: curve *a*, 0·42 Å deg^{-1}; curve *b*, 0·25 Å deg^{-1}.

The results given in table 3 were checked by a second experimental method. Information on the wavelength distribution for the main α-scintillation pulse radiation alone was obtained with the use of a monochromator in which the wavelength selection was achieved by means of the positional adjustment of a first-order graded interference filter. The instrument was used with a specially designed light pipe (shown only schematically in figure 1) which produced a high effective 'F number' (about F0·8:1 according to calculations which include the effects of reflection losses at the filter) but the measured spectral resolution was only 340 Å (Rayleigh criterion). The scintillations were detected using standard pulse counting techniques and the intensity axis of the wavelength spectra presented in terms of the counting rate above a given variable discriminator level. Suitable adjustment of this level enabled the effects of the phosphorescence to be excluded from the measurements. Figure 13 shows the

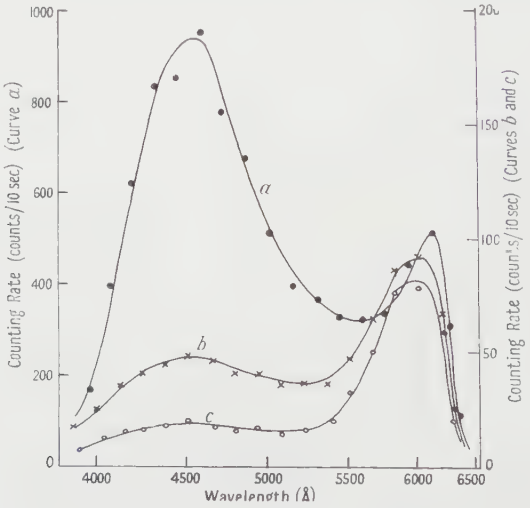

Figure 13. Variation of scintillation output with wavelength for diamond Co7 using graded filter spectrometer; curve *a*, using α-particle excitation with high discriminator bias; curve *b*, using α-particle excitation with high discriminator bias; curve *c*, using β-particle excitation with low discriminator bias.

changes produced in the spectral distribution as the result of such an adjustment (curves *a* and *b*) for a crystal which had been electron irradiated and annealed.

Figure 13 (curve *c*) shows the spectrum obtained for β-particle scintillations in the same crystal. In agreement with the results of table 3, curve *c* is similar to curve *b* rather than to curve *a*. These curves have been corrected for the non-linear spectral response of the photomultiplier, but once again the shapes are not entirely reliable because of the poor wavelength resolution and the fact that the ordinate scale is not simply proportional to the scintillation energy. Results were also obtained for α-particle stimulation, using this technique, which confirmed the sensitivity of the ratio R_c (table 3) to the condition of the region of the crystal which was undergoing stimulation, while R_d was again found to be approximately constant.

4.3. *General Conclusions*

The main conclusions which may be drawn from the results presented in § 4 are:

(i) The properties of the blue band of wavelengths in the scintillation spectrum are different for α- and β-particle stimulation. The existence of strong phosphorescence for α-excitation seems to be the main visual distinction between the two scintillation processes. The results indicate that the phosphorescence is predominantly blue band and probably of a different origin from part of the blue band radiation in the main α-scintillations and in the cathodoluminescence spectra.

(ii) The agreement of curve *c* in figure 13 with curve *b* rather than curve *a*, which was found to be general where curves *b* and *a* were significantly different, indicates that except for the absolute magnitude the scintillation effects produced by electrons in diamond are not strongly dependent on the electron energy. This conclusion is justified by virtue of the fact that ratios obtained from curve *c* exhibit similar specimen dependent values to ratios R_b of table 3 which were calculated from the cathodoluminescence spectra. The energy of the electrons used in the latter experiments was about 50 kev whereas β-particle energies of up to 1 Mev were used to obtain the results shown in figure 13, curve *c*.

(iii) The intensity of the blue band emission relative to the long wavelength emission is much less specimen dependent for α-particles than for β-particles unless the radiation in the main α-scintillation pulse is considered alone. This suggests that the centres responsible for the α blue-band radiation are somehow privileged in the competition for secondary electrons and are therefore less affected by the presence of defect and impurity sites. Certain of the latter appear to have a dominant effect on the β-particle and cathodoluminescence radiation.

(iv) The efficiency of the α-scintillation process in diamond is also comparatively specimen independent, in contrast to the β-particle induced process.

§ 5. Discussion

Measurements of the α- and β-conduction counting efficiencies have been made on the 44 crystals used in the experiments already described. The efficiencies cover the full range of possible values for both types of primary particle (Kennedy 1959). In view of conclusions (iii) and (iv) above, it is apparent that the centres, or defects, responsible for the scintillation effects are not

primarily responsible for the existence of non-counting diamonds. Crystal treatments, such as 0·5 MeV electron irradiation with a total incident flux of 10^{17} electrons, which produce disorder in the lattice sufficient to reduce the conduction counting efficiency of the crystal practically to zero do not produce any significant increase in the scintillation efficiency. For the majority of crystals, such treatment does not even affect the detailed structure of the luminescence spectrum. The important conclusion seems inevitable that close vacancy–interstitial pairs, while acting as charge traps during the passage of the conduction pulse through the crystal, are inoperative either as luminescent or quenching centres for the scintillation effects produced by ionizing particle excitation. Subsequent annealing treatments have been shown to produce a marked increase in the total scintillation output under electron stimulation and also a change in the spectrum of the emitted radiation. The treatments are known to be capable of producing a considerable recovery of the β-conduction counting efficiency, usually to about 50% of the efficiency before the irradiation treatment (Stratton 1957, Champion and Wright 1959). Such behaviour is therefore consistent with an annealing process which is at least two-fold. The first component is the restoration of the original lattice due to the recombination of some of the vacancy interstitial pairs, which partially restores the conduction behaviour, the scintillation behaviour remaining unaffected by this process. The second component consists, at least partly, of the migration of residual vacancies and interstitials either to form aggregate defects or to become anchored at defects which were present in the lattice before the irradiation treatment. The first component is expected to become important at lower temperatures than those required for the second (Billig and Holmes 1958). This theoretical prediction is supported in diamond, since significant annealing of the scintillation properties has not been observed below 580°C (Ralph 1959) whereas appreciable annealing of conduction counting was found between 300°C and 500°C (Wright 1957). It appears to be necessary to consider the presence of these additional defects (the charge traps), at which radiative transitions with wavelengths shorter than about 8500 Å do not occur, in attempts to evaluate the behaviour of diamond after the absorption of ionizing radiations.

Additional evidence for the existence of non-radiating defects is provided by the breadth of the experimental β-conduction counting pulse height spectra (Kennedy 1959). The α-conduction counting spectra are still more diffuse than the β-spectra and even the most perfect crystals exhibit about 25% lower conduction counting efficiencies for α-particles than for electrons. The values of E_α and E_β in table 2 suggested that this relative reduction would be expected if the majority of the scintillation energy in a given event originates close to the region of the crystal in which the α-particle was absorbed. Moreover, such a confined region of emission would be consistent with the small response of the total α-scintillation emission to the presence of widely distributed and annealed radiation damage.

Acknowledgments

During the course of this work one of us (P. J. D.) was in receipt of a grant from the Layton Research Studentship and another (J. E. R.) of a grant from the Department of Scientific and Industrial Research who, in addition, made an

award for the purchase of apparatus. We wish to express our gratitude to Professor F. C. Champion who suggested the problem and who, by advice, discussion and criticism, helped us throughout the work.

References

Billig, E., and Holmes, P. J., 1958, *Advances in Electronics* (New York: Academic Press), **10,** 71.
Champion, F. C., and Wright, S. B,, 1959, *Proc. Phys. Soc.*, **73,** 385.
Chynoweth, A. G., 1950, *Ph.D. Thesis*, University of London.
Dyer, H. B., and Matthews, I. G., 1958, *Proc. Roy. Soc.* A, **243,** 320.
Kennedy, P. J., 1958, *Ph.D. Thesis*, University of London.
—— 1959, *Proc. Roy. Soc.* A, **253,** 37.
Kennedy, P. J., and Dean, P. J., 1959, *J. Sci. Instrum.*, **36,** 126.
Klick, C. C., and Schulman, J. H., 1957, *Solid State Physics*, **5,** 97.
Lax, M., 1956, *Photoconductivity Conference* (New York: John Wiley), p. **111.**
Martin, R. W., 1957, *M.Sc. Thesis*, University of London.
Matthews, I. G., 1958, *Proc. Phys. Soc.*, **72,** 1074.
McKay, K. G., 1948, *Phys. Rev.*, **74,** 1606.
Pringsheim, P., 1953, *Phys. Rev.*, **91,** 551.
Ralph, J. E., 1959, *Proc. Phys. Soc.*, **73,** 233.
—— 1960, *Proc. Phys. Soc.*, **76,** 688.
Stratton, K., 1957, *Ph.D. Thesis*, University of London.
Williams, F. E., 1949, *J. Opt. Soc. Amer.*, **39,** 648.
Wright, S. B., 1957, *Ph.D. Thesis*, University of London.

Radiation Induced Changes in the Cathodoluminescence Spectra of Natural Diamonds

By J. E. RALPH†
Wheatstone Physics Laboratory, King's College, London

MS. received 2nd November 1959

Abstract. The effect of 500 kev electron and neutron irradiation on the cathodoluminescence spectra of a number of natural diamonds excited by 70 kev electrons has been studied. In certain crystals a line system has been induced at 3940 Å by 500 kev electron irradiation without annealing. Further systems at 5030 Å and 5755 Å appeared in all the crystals examined when electron or neutron irradiation was followed by vacuum annealing at temperatures between 600°C and 800°C. The effect of different annealing temperatures was also studied.

§ 1. Introduction

The luminescence spectra of diamonds have been studied during excitation with ultra-violet radiation of various wavelengths by Bull and Garlick (1950), Martin (1957) and Dyer and Matthews (1958), and with x-rays by Matthews (1958). The wavelength distribution of the scintillation pulses emitted under α-particle bombardment has been examined by Kennedy (1958), by Ralph (1959) and by Dean (1959, private communication). A comparison of these results indicates that the emission spectra are strongly dependent upon the type of radiation employed.

The general description of the emission spectra obtained under excitation with electrons of energy in the range 30–90 kev is given elsewhere (Dean, Kennedy and Ralph 1960) and the work described below is limited to the spectral changes produced by radiation damage and subsequent annealing. A considerable amount of work has been carried out on the effects of radiation damage on various characteristics of diamond. Changes have been observed in their conduction counting properties by Benny and Champion (1956), by Champion and Wright (1959) and by Stratton and Champion (1956). Ditchburn *et al.* (1954) and Clark, Ditchburn and Dyer (1956) measured corresponding changes in the ultra-violet absorption, and Dyer and Matthews (1958) studied the effect on ultra-violet stimulated fluorescence. The changes which have been observed in the cathodoluminescence spectra show some similarities to those for ultra-violet excitation, but there are also some distinct differences which must arise from the different methods of excitation.

The defects produced by 500 kev electrons are largely single vacant sites and neighbouring interstitial carbon atoms with relatively few more complex defects.

† Now at the Mellon Institute, Pittsburgh, U.S.A.

When neutron bombardment is used, more extensive damage may be expected (Seitz and Koehler 1956). It has been established by Dyer and Matthews that no changes in the ultra-violet excited fluorescence emission spectrum are produced by 500 kev electron irradiation alone. This shows that none of the natural features of these spectra are due to single vacant sites or interstitials or to close vacancy–interstitial pairs. Annealing of this damage in type I specimens induces sharp line emission systems and is attributed to movement of the induced defects and the anchoring of these at permanent crystal imperfections.

The results discussed below show that new centres are produced in certain diamonds by irradiation alone, but that in others subsequent annealing is necessary to alter the emission spectrum.

§ 2. Experimental

The apparatus used for this work was basically a modified Siemen's electron microscope. This provided a beam of electrons at a current of up to 40 μA and of energy between 30 and 90 kev. The beam could be focused down to a diameter of about 0·2 mm at the crystal or defocused to cover a circle of about 0·5 cm diameter. This allowed the excitation of either a part or the whole of a given crystal surface.

The emitted light was focused on to the input slit of a constant deviation spectrometer which was normally arranged to have a resolution of about 10 Å. The spectra were recorded photographically using Ilford long range spectrum or Kodak P1200 plates. The photographs obtained were analysed by means of a photodensitometer to give the type of trace shown below. These spectra have not been corrected for the spectral sensitivity variations of the photographic plates but the sensitivity curves provided by the manufacturers indicate that the correction would be small at the relevant wavelengths. The crystals were mounted on a copper block on the end of a stainless steel Dewar. A small electric heater was attached to the copper block. With liquid oxygen in the Dewar, temperatures down to -180 c were available and the heater permitted the temperature to be raised to about $+200$ °c. The Dewar, heater and crystal holder were demountable as one unit and a vacuum tight joint allowed this unit to be inserted into the side of the electron microscope so that the crystal was in the electron beam. Most of the spectra were obtained at -180 °c since at this temperature the line features are sharp.

For irradiation of the crystals with 500 kev electrons a Van de Graaff machine was used at a current density of up to 20 μA mm^{-2}. The crystals were mounted in water cooled Wood's metal, it being estimated that their temperature would not rise above about 50 c during the irradiation. The experiments consisted of the measurement of the emission spectra at -180 c of various types of diamond before and after electron doses ranging from 5 to 20 minutes at 20 μA. The natural spectra were classified into those which showed line emission at -180 c and those which did not.

Neutron irradiations were carried out on a number of crystals and the results for three of these are discussed below. These were each given 8 hours in BEPO at Harwell at a position where the thermal flux and the fast neutron flux were each $9{\cdot}8 \times 10^{11}$ neutrons cm^{-2} sec^{-1}.

§ 3. Results

3.1. *General Features of Spectra before Radiation Damage*

The spectra of several natural diamonds obtained by this method have been presented in a separate paper by Dean, Kennedy and Ralph (1960) and only a brief summary of these will be given here. The main features were: (i) a broad blue emission band centred at about 4400 A and extending from 3800 Å to 5200 A; (ii) three overlapping broad bands at about 5150 Å, 5750 Å and 6300 Å; (iii) sharp line emission systems with principal lines at 5030 A and 5755 A and less frequently at 4150 Å. The latter usually appeared as an absorption line; (iv) a number of other sharp lines including those at 3940 Å, 4845 A and 4910 A which were normally only present with the 5755 Å system, and at 5390 Å only when the 5030 Å system was present. The 4400 A band was always present to some extent in natural diamonds although the long wavelength bands were sometimes very weak or absent. The 4400 Å band was found to be strongly temperature dependent between -180°C and $+100$°C whereas the other three broad bands were not. This aspect is discussed more fully in the paper referred to above.

The line systems appeared in a wide range of intensities relative to one another and relative to the broad band systems. However, the relative intensities of the component lines and their energy separations within a given system were fairly constant. This is in agreement with the results of Dyer and Matthews (1958).

3.2. *Radiation Damage by Electrons*

3.2.1. *Crystals with no natural line emission.*

It was found that the spectra of crystals in this class were not affected by irradiation alone although the usual change of colour of the crystal from water-white to pale blue occurred. Annealing of this damage at temperatures between 600°C and 800°C *in vacuo* caused sharp line features to appear in the emission spectra of all of the twelve specimens examined. Figure 1 shows the spectra before and after irradiation and complete annealing (i.e. 20 minutes at 800 C).

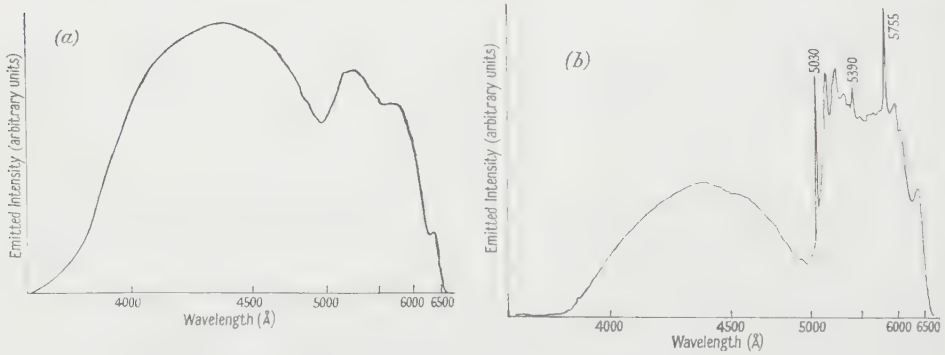

Figure 1. Cathodoluminescence spectrum of diamond (*a*) before irradiation, (*b*) after annealed radiation damage.

The normal four broad bands are shown in (*a*) and in (*b*) are shown the line systems at 5030 Å and 5755 Å superimposed on these broad bands after treatment. The electron dose in this case was 10 minutes at 20 μA. The induced line wavelengths and energy positions are presented in table 1 together with the component

energy separations for each system. The three long wavelength band intensities are also shown to have increased following this treatment, changing the colour of the emission from whitish-blue to green.

Table 1

5755 Å system

Wavelength (Å)	5755	5870	5980	6170
E(ev)	2·14	2·09	2·06	2·00
Energy spacing (ev)		0·05	0·03	0·06

5030 Å system

Wavelength (Å)	5030	5125	5210	5300	5360	5470	6500
E(ev)	2·45	2·41	2·37	2·33	2·30	2·25	2·20
Energy spacing (ev)		0·04	0·04	0·04	0·03	0·05	0·05

The spectra from the non-irradiated face before and after irradiation and annealing were practically unchanged and were both very similar to that shown in figure 1 (*a*).

To determine at what temperature the annealing actually takes place the crystal discussed above was annealed for periods of ten minutes at different temperatures starting well below the expected critical temperature of about 500°c (Dyer and Matthews 1958). The spectrum was determined after each annealing and the relative intensities of the induced lines and the broad bands

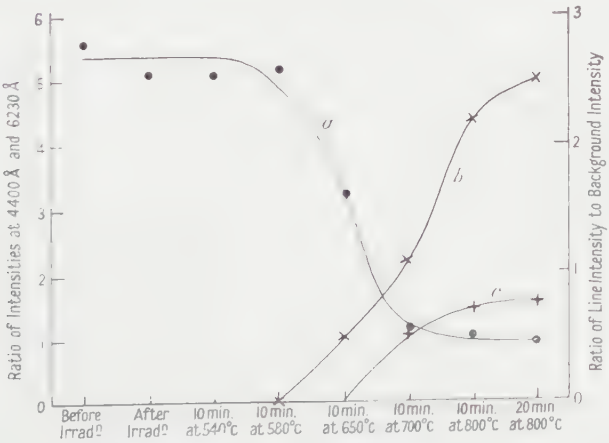

Figure 2. Variation of intensity ratio with annealing temperature; *a*, general background at 4400 Å and 6230 Å, left-hand scale; *b*, 5030 Å line to background, right-hand scale; *c*, 5755 Å line to background, right-hand scale.

were measured. Some of these are shown in figure 2, where the curves show clearly that the annealing for these phenomena begins to occur at about 580 c. However, much longer annealing times at lower temperatures have been reported to have an effect on some aspects of radiation damage. By about 800 c all of the changes whose variation was followed appeared to have saturated. These curves are typical of the results of several similar experiments.

3.2.2. *Crystals with natural* 5030 Å *emission system alone.*

This type of crystal was found to be less common than those showing both the 5030 Å and the 5755 Å systems and only two were examined. The results were similar to those of the previous section.

3.2.3. *Crystals with natural* 5755 Å *emission system.*

It was found that all crystals which showed the 5755 Å line system in their emission spectra before treatment showed changes in these spectra after periods of 500 kev electron irradiation alone. No significant difference was observed between the behaviour of crystals showing the 5755 Å system alone and those in which the 5030 Å system was also present.

Typical examples of these induced changes are shown in figure 3. The first two traces are of a crystal with a strong 5755 Å system, before and after a ten minute irradiation with 500 kev electrons at 20 μA. A fairly strong line at 3940 Å and weaker lines at 4845 Å and 4910 Å were, as usual, associated with the 5755 Å

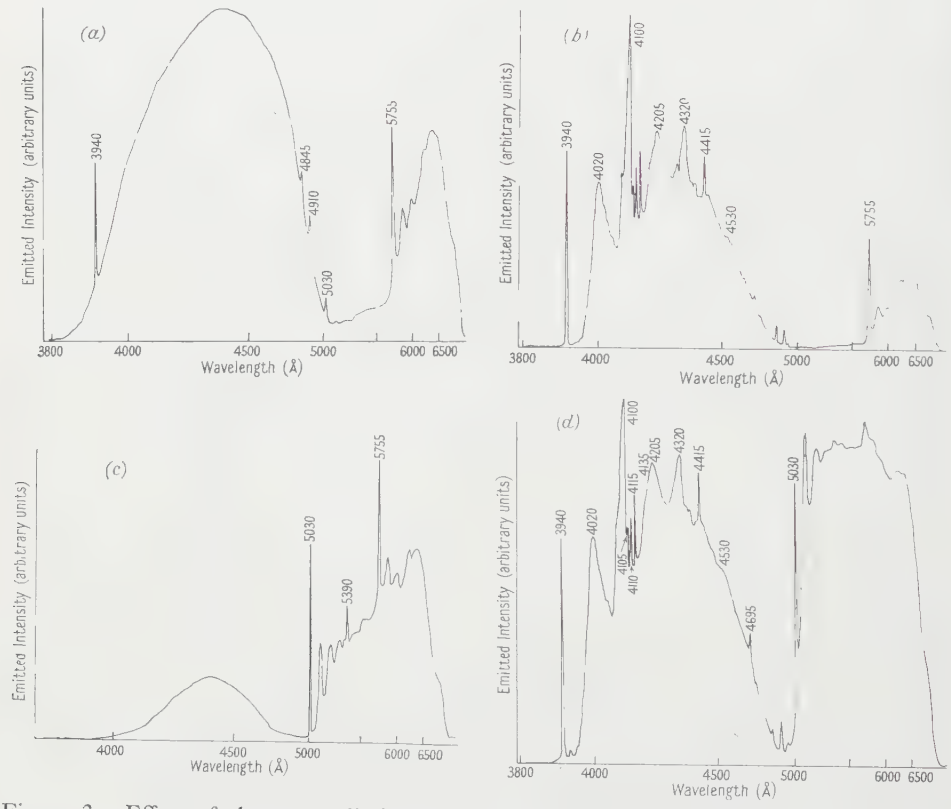

Figure 3. Effect of electron radiation damage on two specimens of diamond; (*a*) before irradiation, (*b*) after annealed radiation damage, (*c*) before irradiation with strong 5030 Å line, (*d*) after annealed radiation damage.

system (Dean, Kennedy and Ralph 1960), and a very weak 5030 Å line was also present before treatment. After the irradiation the 3940 Å line is shown to have increased greatly in intensity while a system of broad and sharp lines has appeared on the long wavelength side of it. The main induced system consisted of the

3940 Å principal line together with the broader lines at 4020 Å, 4100 Å, 4205 Å, 4320 Å, 4415 Å and 4530 Å. The weaker sharp lines were situated at 4105 Å, 4110 Å, 4115 Å, 4415 Å and 4695 Å. The energy positions and separations of the components of this system are presented in table 2. Also included in this table are the corresponding details of the normal 4150 Å system (Dyer and Matthews 1958) and these systems are compared later.

Table 2

3940 Å system			4150 Å system			
(1)	(2)	(3)	(1)	(2)	(3)	(4)
3940	3·150		4150	2·987		0·16
		0·06			0·09	
4020	3·090		4277	2·899		0·19
		0·07			0·07	
4100	3·025		4386	2·827		0·20
		0·07			0·09	
4205	2·950		4528	2·739		0·21
		0·08			0·07	
4320	2·875		4645	2·670		0·21
		0·07			0·07	
4415	2·805		4770	2·599		0·21
		0·07				
4530	2·730					

Other sharp lines in 3940 Å system

Wavelength (Å)	4105	4110	4115	4135	4415	4695	4710	4740	4750
E(ev)	3·020	3·015	3·010	3·000	2·800	2·645	2·630	2·615	2·610

(1) Wavelength (Å); (2) E(ev); (3) energy spacing (ev); (4) energy drift of corresponding components (ev).

The remaining two spectra of figure 3 show the effect of a similar radiation dose on a diamond whose spectrum contained both the 5755 Å and 5030 Å systems before treatment. In this case the 3940 Å line was not present naturally but after the irradiation the complete 3940 Å system appeared and was identical with that described above. The long wavelength end of the spectrum after treatment was allowed to over-expose the photographic plate in order to show the 3940 Å system more clearly.

Crystals of each of the types described in this section were annealed *in vacuo* at about 800°C for ten minutes and the spectra again recorded. No change was observed in the 3940 Å systems of any of these. However, the 5755 Å system was increased in intensity and the 5030 Å system was induced, where it was not already present, by this annealing. The colour of the fluorescence again changed from whitish-blue to green.

3.2.4. *Electron irradiation at a high temperature.*

Two crystals were examined in this experiment. One had a very strong 5755 Å system, but no 5030 Å system and the other had no natural line emission. Each of these was given a dose of 500 kev electron irradiation at an electron density of 20 μA mm^{-2} for ten minutes under conditions in which the specimens were very inefficiently cooled. The high temperature of the crystals was indicated by the yellow-green fluorescence emitted during the irradiation. With efficient cooling this colour was normally whitish-blue. This temperature dependence is discussed by Dean, Kennedy and Ralph (1960).

The spectra obtained after irradiation were both similar to those obtained by separate irradiation and annealing at about 800 °C and are described in an earlier section. This indicates that the crystal temperature during irradiation

was well above 600°c. The most striking feature of this experiment was that no 3940 Å system was induced in the crystal with the natural 5755 Å system when the electron irradiation was carried out at this high temperature instead of at less than 50°c. This shows that the 3940 A system is not produced by partial annealing during the irradiation.

3.2.5. *Electron irradiation of crystals with an artificially produced* 5755 Å *system.*

After it was firmly established that the 3940 A system could only be induced in natural crystals which already showed the 5755 A system, an examination was carried out on crystals in which the latter had been artificially produced. This was done by electron and neutron irradiation and subsequent annealing and also by annealing alone in certain crystals. In the latter case the induced 5755 Å system was usually very weak.

Electron irradiation of several crystals of each of these types with doses up to twenty minutes at 20 μA failed to produce any indication of an induced 3940 Å system.

3.3. *Radiation Damage by Neutrons*

Two of the diamonds subjected to neutron bombardment had no natural line emission and no change in the emission spectra was observed after treatment, although the crystals showed the usual deep green coloration. Annealing of this

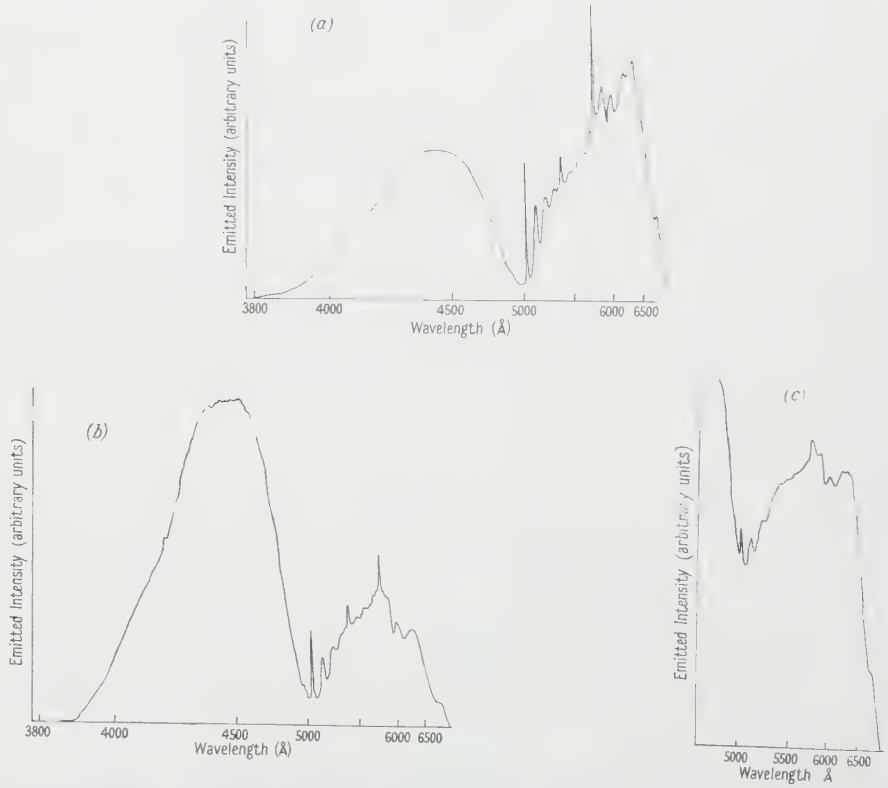

Figure 4. Effect of neutron damage on diamonds; (*a*) rough surfaces, (*b*) irregular but flat faces, (*c*) highly perfect.

damage at 800 c for ten minutes produced a similar change to that described above for electron irradiation and annealing. The 5030 A and 5755 A systems were induced and the long wavelength bands increased in intensity relative to the 4400 A band. The strengths of the induced line systems was strongly dependent on the surface condition of the crystals and figure 4 shows the spectra after treatment for each specimen. Spectrum (*a*) was for a crystal with very rough surfaces and of irregular shape; (*b*) was for a badly-shaped crystal with several flat faces and (*c*) was for a perfectly shaped diamond. In each case the whole of one elevation was excited. The last trace of figure 4 has been limited to the long wavelength region since the 4400 Å band was very strong.

The specimen whose spectrum is shown in figure 4(*a*) showed a fairly strong 5755 Å system before irradiation, but in this case no 3940 A was induced by the irradiation alone.

§ 4. Discussion

The main result of the work described above was to establish that the 4150 Å, 5030 Å and the 5755 Å systems were not induced by either 500 kev electron or neutron irradiation alone. This is in agreement with the results of Dyer and Matthews and indicates that none of these systems is due to the presence of simple defects such as single vacant sites and interstitial carbon atoms formed by 500 kev electrons or to the more complex defects produced by neutrons.

Annealing of the damage induced by either of these two types of irradiation at temperatures between 600°c and 800°c produces centres giving emission systems at 5030 Å and 5755 Å but not at 4150 Å. Some recombination of single vacant sites and interstitials would be expected to take place on annealing, and this may partly explain the absence of any simple relationship between the induced line intensity and the radiation dose received. The new centres are presumably formed by the anchoring at some type of large natural defect of the vacancies and interstitials made mobile at the higher temperature. The neutron irradiation experiments suggest that these exist chiefly near the surfaces.

Some evidence for a relationship between the centres responsible for the different induced sharp line emission systems is provided by the approximately equal energy separations of the 5030 Å (2·45 ev), the 5390 Å (2·29 ev) and 5755 Å (2·135 ev) lines. These separations are, respectively, 0·16 ev and 0·155 ev. It is interesting to note that the induced red line observed by Dyer and Matthews at 6195 Å is separated from the 5755 Å line by 0·15 ev.

Although the 4150 A system cannot itself be induced artificially, a system at 3940 A with components of similar energy separations and relative intensities has been produced by irradiation with 500 kev electrons of diamonds showing a natural 5755 A emission system. Since the temperature at which this system is formed is too low for movement of the induced defects, the centres responsible are probably formed by the production of damage in or near those centres giving the 5755 A system. The absence of the 3940 A system after irradiation at a high temperature supports the suggestion that its appearance is not due to annealing.

Neither the 5755 Å nor the 3940 Å system has been reported where ultra-violet or x-ray excitation was employed. Conversely, the 4150 Å system can normally only be excited by ultra-violet radiation. In table 2 are shown the wavelength and energy positions of the components of the 4150 Å and 3940 Å

systems together with the corresponding energy spacings. Also shown in this table are the energy separations of corresponding components of the two systems. Clearly, these two systems are internally very similar to one another but the corresponding components are shifted by approximately equal energies. This result suggests that the 3940 A system may be formed by some modification of the 4150 Å centres by the irradiation with 500 kev electrons.

§ 5. Conclusions

The results presented above do not permit any detailed deductions about the nature of the centres responsible for the various luminescence spectral features. However, it has been confirmed that the simplest types of lattice defects are not alone responsible. It is also clear that the features observed are strongly dependent upon the nature of the exciting radiation.

Acknowledgments

Thanks are due to the Department of Scientific and Industrial Research for a maintenance grant and for a grant towards some of the apparatus; also to Professor F. C. Champion for suggesting the problem and for critical discussion.

References

Benny, A. H. B., and Champion, F. C., 1956, *Proc. Roy. Soc.* A, **234,** 432.
Bull, C., and Garlick, G. F., 1950, *Proc. Phys. Soc.* B, **65,** 415.
Champion, F. C., and Wright, S. B., 1959, *Proc. Phys. Soc.*, **73,** 385.
Clark, C. D., Ditchburn, R. W., and Dyer, H. B., 1956, *Proc. Roy. Soc.* A, **237,** 75.
Dean, P. J., Kennedy, P. J., and Ralph, J. E., 1960, *Proc. Phys. Soc.*, **76,** 670.
Ditchburn, R. W., Mitchell, E. W. J., Paige, E. G. S., Custers, J. F., Dyer, H. B., and Clark, C. D., 1954, *Optical Effects of Radiation Damage in Diamond and Quartz, Conference on Defects in Crystalline Solids* (London: Physical Society), p. 92.
Dyer, H. B., and Matthews, I. G., 1958, *Proc. Roy. Soc.* A, **243,** 320.
Kennedy, P. J., 1958, *Ph.D. Thesis*, University of London.
Martin, R. W., 1957, *M.Sc. Thesis*, University of London.
Matthews, I. G., 1958, *Proc. Phys. Soc.*, **72,** 1024.
Ralph, J. E., 1959, *Proc. Phys. Soc.*, **73,** 233.
Seitz, F., and Koehler, J. S., 1956, *Solid State Physics*, **2,** 305 (New York, London: Academic Press).
Stratton, K., and Champion, F. C., 1956, *Proc. Phys. Soc.* B, **65,** 473.

Spin–Lattice Relaxation Times in Ruby at 34·6 Gc/s

By J. H. PACE, D. F. SAMPSON and J. S. THORP

Royal Radar Establishment, Malvern, Worcs.

MS. received 1st April 1960, in revised form 20th May 1960

Abstract. Measurements of spin–lattice relaxation time in ruby have been made at 34·6 Gc/s by a pulse saturation method at temperatures from 1·4° to 90°K. With weak concentrations the values for the first-order transitions (e.g. 22 msec at 4·2°K) are of the same order of magnitude as those reported at lower frequencies, and the variation of relaxation time with temperature is in fair agreement with theory. A successive increase in relaxation time with the order of the transition, pronounced at 1·4°K, decreases with increasing temperature, and at about 77 °K a common value of about 44 μsec is obtained for all transitions. The main effects of increasing concentration are to reduce the relaxation time and alter its temperature dependence.

§ 1. Introduction

The importance of measurements of spin–lattice relaxation times T_1 in paramagnetic materials has grown recently because of the rapid developments in the maser field. Although several theories have been proposed (e.g. Van Vleck 1940, Al'tshuler 1956, Gill 1959, unpublished) the physical basis of the relaxation process is not clearly understood, and the formulation of a general theory applicable to a range of materials awaits the accumulation of more experimental data. Specific problems occur, however, which demand knowledge of relaxation times and their dependence on certain parameters. Two examples are the extension of maser techniques for amplification or oscillation to the short millimetre wavelength region (Foner, Momo and Mayer 1959), and the operation of lower frequency masers at elevated temperatures (Ditchfield and Forrester 1958) with increased bandwidth and power handling capacity. In the former case the magnitude and frequency dependence of the relaxation time are important, and in the latter the effects of temperature and concentration. This paper describes measurements of the spin–lattice relaxation time in synthetic ruby made at 34·6 Gc/s with the object of investigating these effects. The temperature and concentration ranges covered were 1·4° to 90 °K and 0·03% Cr to 0·78% Cr respectively, using the fixed polar angle $\theta = 90°$. The concentration is defined as the ratio of weights of chromium and aluminium oxide. Ruby was selected because it is known to be a suitable material for many maser applications and the frequency was chosen, bearing in mind the current interest in millimetre wavelength masers, as being the highest at which sufficient microwave power and components were easily obtainable. Preliminary results have already been reported by the authors Pace, Sampson and Thorp (1960).

§ 2. Apparatus and Technique

2.1. *General Features*

A pulse saturation method was used in which the transition studied was saturated by a short pulse, recovery to thermal equilibrium being observed by measuring the absorption of a low power, c.w. monitoring signal of the same frequency (cf. Davis, Strandberg and Kyhl 1958).

The general arrangement of the equipment followed conventional lines. The low temperature assembly however was a straight silver-plated cupro-nickel waveguide (inside dimensions 0·280 in. × 0·140 in., wall thickness 0·005 in.) terminated by a removable plane plunger on which the specimen was mounted. Use of this system removed difficulties of cavity tuning on cooling, permitted large samples to be used, and enabled the whole structure to be made easily removable for sample changing at helium temperatures. It also led to a small structure, a particularly valuable feature at high magnetic fields where space in the gap is restricted. Magnetic fields of up to 16 000 gauss over a 4·5 cm gap were provided by a Newport Instruments Type D electromagnet. These were uniform to at least 1 in 10^4 over a volume of about 2 cm cube, and field stabilities of the same order were readily obtained using a bank of batteries to drive the electromagnet. Additional coils enabled low frequency field modulation to be supplied when required.

2.2. *Microwave System*

The microwave arrangement, shown in figure 1, consisted of a waveguide bridge, a low power monitor source, a high power pulsed source, and a superheterodyne receiver.

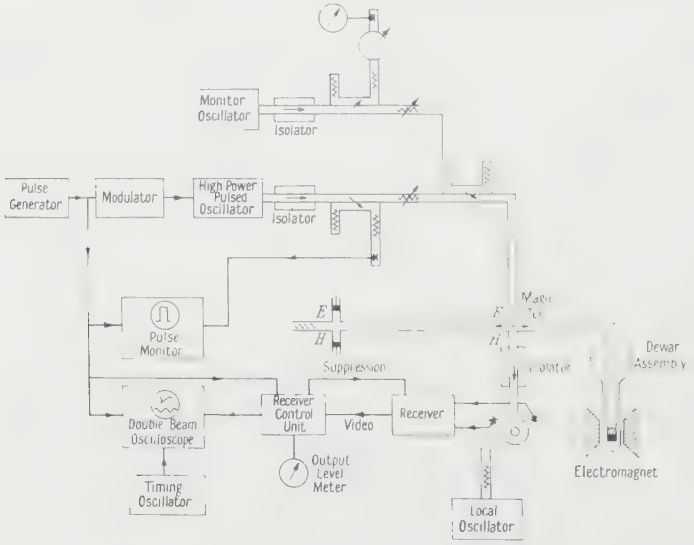

Figure 1. Microwave arrangement for relaxation time measurement.

One arm of the bridge was the low temperature assembly described above. Balance was obtained when off magnetic resonance by adjusting the *E–H* tuner in the other arm for cancellation of reflected power into the balanced mixer.

When absorption occurred in the sample, i.e. on magnetic resonance, the bridge became unbalanced and a signal proportional to the degree of absorption was fed into the receiver.

The bridge input consisted of two signals mixed in a 6 dB directive feed, viz: (i) a low power, c.w. monitoring signal, variable between 1 μW and 10 μW to allow for sensitivity changes, supplied from a VX.5023 reflex klystron and (ii) a high power pulse, generated by an Elliott Type B.579 floating drift tube klystron. The latter valve was pulsed by a hard valve modulator driven by a pulse generator, and produced pulses variable in length from 50 μsec to 500 μsec at pulse repetition frequencies up to 25 c/s. The maximum pulse power available was 6 watts peak. With a pulse duration of 200 μsec the minimum power required for saturation was 60 mW at 1·4°K.

The frequency of measurement was determined by the fixed frequency of the drift tube klystron, 34·6 kMc/s, to which the monitor oscillator was tuned. It was unnecessary to stabilize the monitor oscillator because with the samples used, whose line widths were not less than about 30 gauss, saturation occurred if the pulse frequency was within $\pm$ 50 Mc/s of the absorption frequency.

The receiver was of conventional design, employing a second VX.5023 as the local oscillator. An intermediate frequency bandwidth of 10 Mc/s allowed operation without frequency stabilization or automatic frequency control. The overall gain to the second detector was 110 dB at 45 Mc/s and the total noise factor, including the mixer, was 15 dB. The recovery time to maximum sensitivity, after suppression during the saturating pulse, was 5 μsec.

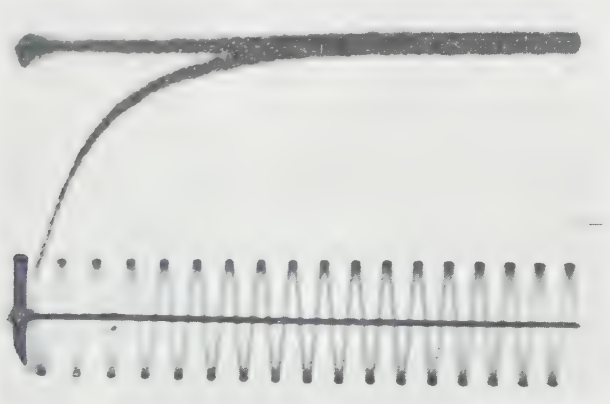

Figure 2. Presentation of recovery curve.

The second detector output was coupled via a cathode follower to one trace of a Cossor double beam oscilloscope type 1049, the other trace displaying a sinusoidal timing waveform. Use of d.c. amplification in the oscilloscope sinabled the maximum and minimum levels of absorption to be displayed independent of the form and duration of the recovery curve. A facility for emultaneous interruption of the timing waveform and the drive pulse to the modulator enabled the maximum absorption level to be displayed independently. In this way a composite photographic record was taken showing (*a*) the recovery

curve, (*b*) the maximum absorption level in the absence of the saturating pulse superimposed on this, and (*c*) the timing waveform (figure 2); the value of relaxation time could be derived from this. The overall accuracy of the measurements was estimated to be within about $\pm 10\%$, and the minimum measurable relaxation time, set by the receiver recovery, was about $10\,\mu$sec.

§ 3. Relaxation Times for Low Chromium Concentration

The primary factor governing the orientation chosen was the need to assess ruby as a material for pulsed field maser experiments. In these use of the maximum available relaxation time would reduce the complexity of the circuitry required. Since it was known from the work of Bloembergen *et al.* (1959) that cross relaxation processes can be very important and that they reduce relaxation times a position was selected at which these would be negligible. This orientation was with the *c* axis of the crystal perpendicular to the d.c. magnetic field, $\theta = 90°$ (cf. Mims 1959). The first measurements were made on a sample of nominal concentration 0·1% Cr as it was known that crystals of this concentration had been successfully used in three level masers. (Analysis subsequently showed that this crystal contained 0·03% Cr). Figure 3 shows the energy level diagram at $\theta = 90°$ together with possible transitions at 34·6 Gc s. The measured relaxation times are given in the table.

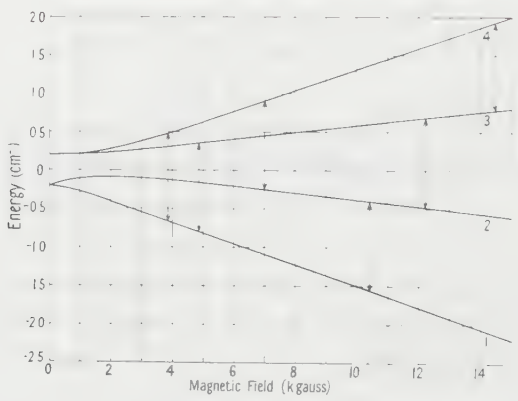

Figure 3. Energy level diagram for ruby at $\theta = 90°$ showing 34·6 Gc/s transitions.

Relaxation Times (msec) in Nominal 0·1% Cr Ruby
34·6 Gc/s, $\theta = 90°$

Transition	1·4°K	4·2°K	10·1°K	20·3°K	56°K	77°K	90°K
3–4	60	21	16	4	0·086	—	0·016
2–3	64	16	10	8	0·083	0·045	0·015
1–2	59	22	10	6	0·10	0·044	0·017
2–4	147	54	12	10	0·16	0·049	—
1–3	100	56	—	12	0·13	—	—
1–4	296	—	—	—	0·12	—	—

The conclusions which may be drawn from these results will now be discussed.

3.1. *Variation of Relaxation Time with Frequency*

The measured value of T_1 at 4°K for the 1–2 transition is 22 msec. As far as comparison with previous measurements can be made this is of the same order as those reported at 7·2 Gc/s (Mims†) and 9·3 Gc/s (Gill and Harvey 1958, unpublished) and 24 Gc/s (Kikuchi *et al.* 1959). It therefore appears that over this range the spin-lattice relaxation time does not vary appreciably with frequency. No general theoretical rule for the frequency dependence can be made, since this is determined by the material and the coupling mechanism. It may be noted however that a variation as (frequency)$^{-2}$ or (frequency)$^{-4}$, predicted by Van Vleck for chromium alum, is not found.

3.2. *Variation of Relaxation Time with Temperature*

The effect of temperature on the relaxation time of the 1–2 transition is shown in figure 4. In the range of temperature from 1·4° to 20°K the relaxation time is approximately inversely proportional to temperature. This behaviour is similar to that reported in ruby at 9·3 Gc/s (Harvey 1958, unpublished)

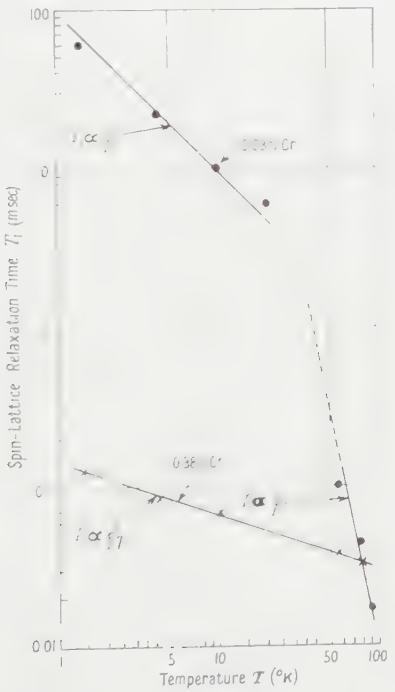

Figure 4. Variation of relaxation time with temperature (1–2 transition, $\theta = 90°$).

and in potassium chromicyanide in the helium range when cross relaxation effects are negligible (Shapiro and Bloembergen 1959): it would be expected if relaxation were due to a direct exchange of energy between the spin system and lattice phonons. Between 20 and 56 K this relation breaks down, and above 56 K the rapid decrease in relaxation time with increasing temperature is consistent with the predominance of Raman effects; preliminary observations

† Paper given at Radio-frequency Spectroscopy Conference, Oxford, 1959.

suggest that the variation is as (temperature)$^{-5}$. This is not quite so rapid as the (temperature)$^{-7}$ suggested by the Van Vleck model. For the other transitions a broadly similar temperature dependence was found.

3.3. *Relaxation Times for Transitions of Different Order*

At 1·4°K the relaxation times associated with the different transitions are not equal, and the second- and third-order transitions have significantly longer relaxation times than the first-order transitions although the recovery curves remain substantially single exponentials. This is contrary to predictions based on the Van Vleck model, but a recent development of Al'tschuler's theory (Gill 1959, unpublished) has shown that different relaxation times for the various transitions are to be expected if the relaxation process is governed by near-neighbour interaction and gives close agreement with experiment. As the temperature is increased the difference between the relaxation times for the various transitions decreases, and a common value is reached at about 77°K. The occurrence of this common value has previously been observed in ruby at 77°K at 9·3 Gc/s (Gill 1959, unpublished) and is presumably a consequence of the different relaxation process occurring at higher temperatures.

§ 4. Effects due to Increased Concentration

It is found that the relaxation time for a given transition is a function of the concentration of paramagnetic centres and the temperature. Ruby samples of known concentration were available only in small sizes, and measurements were therefore confined to the strong first-order transitions. The concentration range covered was from 0·02% Cr to 0·38% Cr.

4.1. *Behaviour at Fixed Temperatures*

At helium temperatures the relaxation time decreases with increasing concentration N. The results at 1·4°K are shown in figure 5 (lower curve) and can be expressed approximately by $T_1 \propto N^{-2}$. A similar concentration dependence has also been observed at 4·2°K and 9·3 Gc/s (de Grasse *et al.* 1959). It may be noted that a concentration dependence is not predicted by theories based on the Van Vleck model, but is a consequence of theories based on near neighbour interaction.

At 77°K the effect of concentration is much smaller (figure 5, upper curve) and is approximately given by $T_1 \propto N^{-0\cdot1}$. This result is of importance in connection with the operation of three level masers at nitrogen temperatures, because it implies that a higher concentration can be used—thereby increasing both the inherent bandwidth and the power handling capacity of the maser—without undue increase in the pump power requirement.

4.2. *Relaxation Time–Temperature Dependence*

The dependence of relaxation time on temperature has already been discussed for a low concentration sample (figure 4, upper curve). The curve is characterized by two regions over which $T_1 \propto T^{-1}$ and $T_1 \propto T^{-5}$ respectively. As the concentration is increased this behaviour changes and at concentrations above about 0·3% Cr, a smooth variation from 1·4° to 90°K is found (figure 4, lower curve). It is found that, approximately, $T_1 \propto T^{-1\cdot3}$ and it is thus clear

that a different relaxation process occurs. This slow variation suggests that, with the correct material, maser action should be possible at relatively high temperatures.

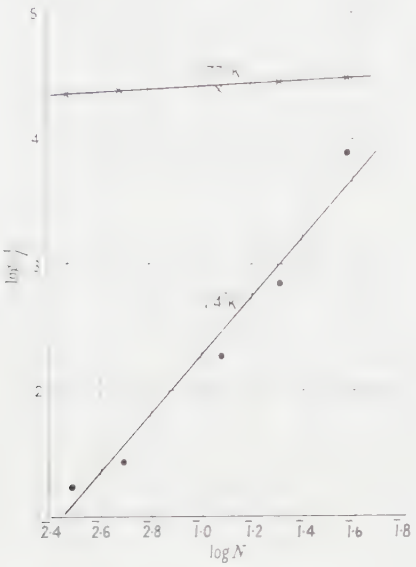

Figure 5. Variation of relaxation time with concentration (1–2 transition, $\theta = 90°$).

It is interesting to note that somewhat similar concentration effects have been observed in other materials. In nickel fluosilicate Bowers and Mims (1959) found that in the helium range there was a general tendency for the relaxation times to be less temperature dependent at high concentrations while in potassium chromicyanide Shapiro and Bloembergen (1959) have shown that the smaller relaxation times observed at high concentrations can be explained by the growing importance of cross relaxation.

§ 5. Very High Concentration

One sample was available with a chromium concentration of 0·78% Cr. In preliminary observations on this sample it was found that at 77 K a simple exponential recovery curve was obtained. This gave a relaxation time of about 30 μsec, as would be expected from the foregoing results. At helium temperatures, however, the recovery curve had a fast initial rise (corresponding to a relaxation time of about 15 μsec) followed by a much slower rise (corresponding to a 20 msec relaxation time). A similar effect at 9 Gc s has been reported (de Grasse *et al.* 1959) and the results suggest that the fast recovery is due to effects within the spin system while the slow recovery is at a rate comparable with the relaxation time for a dilute sample.

§ 6. Conclusions

Using a given polar angle, $\theta = 90°$, the spin-lattice relaxation time in ruby at 34·6 Gc s has been shown to depend on the temperature, the transition, and the chromium concentration. Comparison with results obtained at lower frequencies suggest that the relaxation time is substantially independent of

frequency. At low concentrations the temperature variation found agrees broadly with predictions based on the Van Vleck model; the remaining observations can best be explained by assuming that the dominant mechanism in the relaxation process is near neighbour interaction.

Because of the long relaxation times obtainable ruby appears to be a promising material for pulsed field masers intended to amplify or oscillate at millimetre wavelengths. At lower microwave frequencies it appears that improvements are to be gained in the operation of masers at elevated temperatures by using ruby with high chromium concentration.

Acknowledgments

We wish to record our thanks to Dr. D. J. Howarth, Royal Radar Establishment, Malvern, for supplying the data given in figure 3, to the Chemical Inspectorate, Woolwich, for the analysis of the samples, and to colleagues in the Laboratory for helpful discussions.

This paper is published by permission of the Controller, Her Majesty's Stationery Office.

References

Al'tshuler, S. A., 1956, *Bull. Acad. Sci. U.S.S.R.* (*Phys. Ser.*), **20**, (11), 1207.

Bloembergen, N., Shapiro, S., Pershan, P. S., and Artman, J. D., 1959, *Phys. Rev.*, **114**, 445.

Bowers, K. D., and Mims, W. B., 1959, *Phys. Rev.*, **115**, 285.

Davis, C. F., Strandberg, M. W. P., and Kyhl, R. L., 1958, *Phys. Rev.*, **111**, 1268.

de Grasse, R. W., Geusic, J. E., Shulz-Dubois, E. O., and Scovil, H. E. D., 1959, 9th *Interim Report on Microwave Solid State Devices*, Bell Telephone Laboratories.

Ditchfield, C. R., and Forrester, P. A., 1958, *Phys. Rev. Lett.*, **1**, 448.

Foner, S., Momo, L. R., and Mayer, A., 1959, *Phys. Rev. Lett.*, **3**, 36.

Kikuchi, C., Lambe, J., Makhow, G., and Terhune, R. W., 1959, *J. Appl. Phys.*, **30**, 1061.

Pace, J. H., Sampson, D. F., and Thorp, J. S., 1960, *Phys. Rev. Lett.*, **4**, 18.

Shapiro, S., and Bloembergen, N., 1959, *Phys. Rev.*, **116**, 1453.

Van Vleck, J. H., 1940, *Phys. Rev.*, **57**, 426.

Transmission of Slow Electrons through Thin Films†

By O. KLEMPERER and A. THETFORD
Physics Department, Imperial College, London

with a note by F. LENZ‡
Technische Hochschule, Aachen, Germany

MS. received 29*th January* 1960, *in revised form* 5*th April* 1960

Abstract. The transmission of electrons with energies of 600–6000 ev through films of aluminium and of aluminium oxide of 180–1100 Å thickness has been investigated. The transmittance was measured for angles of acceptance between 18° and 36° and the results were compared with Bothe's formula. The range of the electrons as a function of their initial energy was found by extrapolation. Energy distributions for electrons transmitted through the films have been measured and values for the transmitted energies as a function of the primary energy and of the film thickness were compared with the available theoretical results.

Some modifications of Bothe's theory of multiple scattering in the region of low electron energies have been suggested and numerical values for the relevant correction factors have been calculated. The results show that the discrepancies between the theory and the experimental results presented in the paper are considerably reduced.

§ 1. Introduction

Little information has been available so far on the transmission of electrons of relatively low energy through thin films. The theory of Bothe (1933) deals quite generally with the multiple elastic scattering of electrons through very small angles, and it has been developed—only for somewhat faster electrons—by Williams (1939), Molière (1948) and Lenz (1954). In a theoretical part by Lenz at the end of this paper, Molière's theory is, in a simplified form, applied to the present problems and the laws of multiple scattering are extended to the region of low initial electron energies.

Experiments on the transmission of electrons below 6 kev through solids have been carried out by Becker (1927), Lane and Zaffarano (1954), Hoffman (1955), Young (1956 a, b, 1957), Vyatskin and Makhov (1958) and Holliday and Sternglass (1959). However, the information available for this relatively low energy range is still very incomplete.

We shall discuss here some significant results on the transmission of electrons in this low energy range through thin films.

§ 2. The Experimental Arrangement

An electron gun containing a hairpin filament, a flat grid electrode, a tubular anode and three tubular focusing electrodes was used for projecting an electron beam of 2° semi-convergence. A focus of about 0·3 mm diameter was obtained

† This paper contains material from a thesis by A. Thetford approved by the University of London for the degree of Ph.D.

‡ Now at the Institut für angewandte Physik, Universität, Tübingen, Germany.

on the specimen film. In figure 1 there is shown the final focusing electrode T of the gun and a movable flap H holding several specimen films which were mounted over apertures 0·5 mm in diameter. P is an apertured diaphragm which prevented stray electrons from reaching the specimen. C is a wheel containing a series of aperture stops each of which could be aligned with the beam axis in order to define the angle of acceptance for the electrons collected in the Faraday cage F. The funnel shaped electrode A, which was always kept at the potential of the specimen, was introduced for attenuating the retarding field in front of the Faraday cage so that the electrons emerging from the specimen film were spread into a substantially field free space. The apertured shields J and S were kept at a negative potential with respect to the Faraday cage F in order to prevent loss of current from F. The electrodes T, P, H, C and A were kept at a common

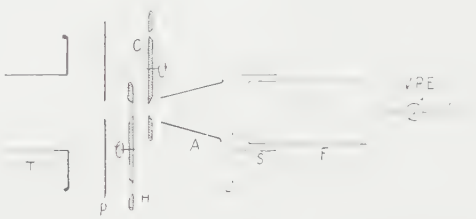

Figure 1. Scheme of apparatus for investigation of electron transmission through thin films.

variable positive potential with respect to the Faraday cage F which was earthed via the vibrating reed electrometer VRE. In this way, the energy distribution of the collected electrons could be measured by the retarding field method. The energy of the primary electrons striking the specimen was given by the potential difference between the specimen H and the filament of the gun which was at a high negative voltage. The beam current striking the specimen was of the order of 10^{-8} amp while in the present measurements currents down to 10^{-12} amp were registered in the Faraday cage.

§ 3. Transmittance of Scattered Electrons

For the investigation of the angular distribution of scattered electrons, the potential difference between the specimen film and the Faraday cage was kept at 32 v. This voltage prevented secondary electrons released at the film from entering the Faraday cage. The number of incident electrons n_0 was compared with the number $n(\theta)$ of electrons scattered into a cone with semi-angle θ of acceptance. θ was changed in steps between 9° and 18° and a large number of aluminium films and aluminium oxide films was tested with incident electron energies between 600 and 6000 ev.

Free Al films were made by evaporation on substrates of evaporated rock salt or of Bedacryl (see Bradley 1954) the substrate subsequently being dissolved off. A general relationship between the thickness of an aluminium film and its light transmittance was determined first, so that in the subsequent investigations of electron scattering the thickness of each film could simply be obtained from its light transmittance value.

In order to determine the above relationship, the actual film thickness was measured with the help of an interferometric method due to Tolansky (1948).

If Bedacryl was used as substrate for the aluminium, the light transmittance against film thickness relation was found to be in good agreement with values given by Bond (1954). On the other hand, if rock salt was used as a substrate, film thicknesses greater than those given by Bond had to be attributed to the measured light transmittance values. The greater thickness was found to be due to a coarser grain structure of the films evaporated on rock salt. The electron scattering properties of both kinds of film, however, were the same if they were referred to interferometrically measured thickness.

Light transmittance measurements before and after exposing the Al films to air showed that oxidation of the film surfaces resulted in an increase in mass thickness equivalent to an additional layer of 20 Å of aluminium at each side of the film.

The values x for film thickness in subsequent tables contain this correction factor for oxidation. A justification for the assumption that the scattering properties of a film for slow electrons depends on its mass thickness only, will be given below.

The scattering properties of the Al films agree well with those of Al_2O_3 films of equivalent mass thickness if interferometric thickness measurements of the Al films are assumed to yield the average thickness of their granular structure.

Aluminium oxide films were prepared using an anodizing process similar to that described by Hass (1949) and by Harris (1955), the thickness of the films being given by the anodizing voltage, namely 13 Å per anodizing volt. Electron micrographs showed these films to be grainless.

A selection of significant values for the transmittance of the films for electrons as a function of film thickness x, electron energy eV and scattering angle θ are presented in table 1. There, the experimental values are compared with a formula derived by Bothe (1927) namely

$$n(\theta) = n_0[1 - \exp(-\theta^2/2\lambda^2)] \qquad \ldots\ldots(1)$$

where λ (radians), the most probable angle in the process of multiple elastic scattering is, in the present relatively low voltage range, given by

$$\lambda^2 = (8Z\rho x/V^2) \times 10^9. \qquad \ldots\ldots(2)$$

In equation (2) Z is the atomic number of the scattering substance, ρ (kg m^{-3}) the density, x (m) the film thickness, and V (ev) the energy of the incident electrons.

Taking $Z = (2 \times 13 + 3 \times 8)/5$ and $\rho = 3{\cdot}4 \times 10^3$ for Al_2O_3 and $Z = 13$, $\rho = 2{\cdot}7 \times 10^3$ for Al; $Z\rho = 3{\cdot}5 \times 10^4$ (kg m^{-3}) may be used for both substances and equation (1) can be written

$$-\log\left(1 - \frac{n(\theta)}{n_0}\right) = \frac{(\theta V)^2}{3{\cdot}7 \times 10^{10} Z\rho x} = \frac{(\theta V)^2}{1{\cdot}30 \times 10^{15} x}. \qquad \ldots\ldots(3)$$

It may be expected that equation (3) should agree with the experimental transmittance values as long as the conditions for multiple scattering are fulfilled, provided equation (2) is applicable. It can be seen from table 1 that there are substantial discrepancies between our experimental results and the values given by equation (3). Now, if the conditions for multiple scattering are fulfilled while equation (2) is wrong, $-\log[1 - n(\theta)/n_0]$ should still be proportional to θ^2, since this proportionality follows from equation (1) irrespective of the assumptions made about λ. If, on the other hand, $-\log[1 - n(\theta)/n_0]$ is not proportional to θ^2, it can be concluded that the conditions for multiple scattering are not fulfilled, and that equation (1) must be replaced by a more complicated function of $n(\theta)$ describing plural scattering.

Table 1. Transmittance of Electrons of Various Energies eV through Various Thicknesses x of Al and Al_2O_3 for the Semi-angles of Acceptance 9° and 17° 50′

Al								
eV		610	810	1000	1500	2000	4000	6000
				$x = 178$ Å				
Exptl	9°	0·4	2·8	7	16	40	180	300
	17° 50′	1·6	9·5	25	66	120	380	600
Bothe	9°	0·4	0·7	1·1	2·4	4·3	17	38
	17° 50′	1·6	2·7	4·2	9·4	17	67	151
				$x = 307$ Å				
Exptl	9°		0·7	0·9	6	15	60	150
	17° 50′		2·5	3·1	23	55	190	370
Bothe	9°		0·4	0·6	1·4	2·5	10	22
	17° 50′		1·6	2·4	5·5	9·7	39	88

Al_2O_3							
eV		810	1000	1500	2000	3000	6000
			$x = 208$ Å				
Exptl	9°	0·3	1·6	7	20	40	200
	17° 50′	1	5·4	31	66	130	430
Bothe	9°	0·6	0·9	2·1	3·6	8·2	33
	17° 50′	2·4	3·6	8·1	14·4	32	130
			$x = 340$ Å				
eV		1500	2000	3000	4000	5000	6000
Exptl	9°	3	7	20	42	58	94
	17° 50′	9	29	74	130	170	250
Bothe	9°	1·3	2·2	5	9	14	20
	17° 50′	5	9	19	35	55	79
			$x = 610$ Å				
Exptl	9°	—	1	8	18	24	40
	17° 50′	—	3	30	60	85	120
Bothe	9°	0·7	1·2	2·8	5	8	11
	17° 50′	2·7	4·9	11	20	31	44
			$x = 1080$ Å				
Exptl	9°		—	1·5	6	12	20
	17° 50′		—	5	26	47	70
Bothe	9°		0·7	1·6	2·8	4·5	6·4
	17° 50′		2·7	6·2	11	17	25

Experimental values of $-\log [1-n(\theta)/n_0]$ in units of 10^{-3} are compared with Bothe's formula, equation (3).

For this reason $\log [1-n(\theta)/n_0]$ has been plotted here as a function of θ^2. In figures 2 (*a*)–(*d*) there are shown such plots for different electron energies between 810 and 6000 ev. Deviations from proportionality are not noticeable below 3000 ev, which suggests that multiple scattering still predominates there at all angles investigated, i.e. for $9° < \theta < 18°$. Since substantial discrepancies between our experimental results and equation (3) exist even for much smaller electron energies than 3000 ev, the validity of equation (2) must be doubted.

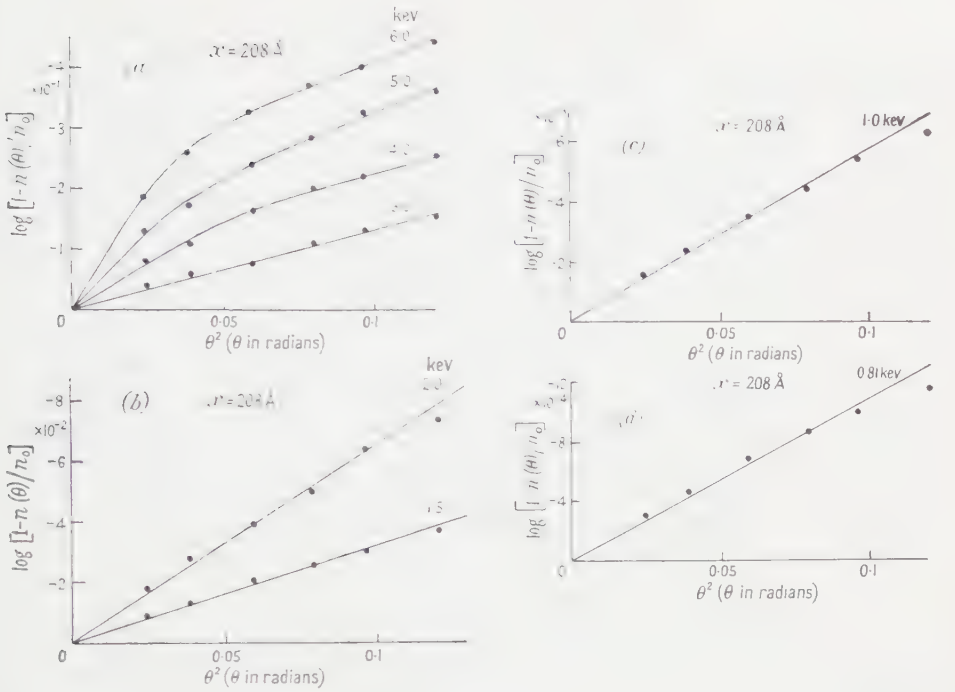

Figure 2. Transmission of 0·81 – 6 kev electrons through 208 Å of Al_2O_3 into cones of various semi-apertures θ.

The above results seem to indicate that Bothe's theory ceases to be applicable at relatively low energy electron scattering which has been investigated here, and there are other experimental results which support this conclusion. First, it was found throughout the present investigations that the scattering properties of Al and Al_2O_3 are identical for films of the same mass-thickness ρx but not of the same thickness x. This is in contradiction to equation (3) according to which multiple scattering depends upon $Z\rho x$ or, as shown above for a comparison of Al and Al_2O_3, only on the thickness x. Moreover, Holiday and Sternglass (1959) found that the back scattering of films of equal mass-thickness in the low energy region is nearly the same for materials with atomic numbers Z as different as those of gold and aluminium. On the other hand, it has been known for a long time (Lenard 1925) that in the region of higher energies multiple scattering depends substantially on Z.

An agreement between Bothe's theory and experimental results is expected as long as Born's approximation can be assumed to be valid and as far as inelastic scattering is negligible. Both these assumptions are probably not valid for slow electrons, and therefore one does not get agreement between theory and experiment in this region. In § 7 of this paper it will be shown that an adaptation of the theory of Molière (1948) together with a correction which accounts for inelastic scattering leads to a reasonably close agreement between theory and experiment.

§ 4. The Absorption Coefficient

The attenuation of electron rays through solids (and through gases) is frequently represented by an exponential law of the form

$$n(x,\theta)=n_0\exp\left[-\mu(\theta)x\right] \qquad \ldots\ldots(4)$$

where n is the total number of electrons transmitted through a film of thickness x and n_0 is the number of incident electrons which are supposed to be completely diffused, i.e. of random direction. Lenard (1925) has presented numerical values for μ/ρ, the mass attenuation coefficient, and Bothe (1929) has derived a theoretical expression for μ/ρ which for small electron energies can be written

$$\mu/\rho=CZ/V^2 \qquad \ldots\ldots(5)$$

where $C=1{\cdot}1\times10^{10}$ ($\mathrm{m^2\,kg^{-1}\,v^2}$). Experimental values for μ are obtained after passing an electron beam through a preliminary film in order to make it completely diffuse. Combining the results in table 1 which lead to values of electron transmittance n_1/n_0 and n_2/n_0 respectively for two different thicknesses x_1 and x_2, the coefficient μ for the thickness $x=x_2-x_1$ is calculated from

$$\mu=\frac{1}{x_2-x_1}\times\ln\frac{(n_1/n_0)}{(n_2/n_0)} \qquad \ldots\ldots 6)$$

provided that both n_1/n_0 and n_2/n_0 are collected over the same angle θ and that $n_1(\theta)/n_1(90^\circ)=n_2(\theta)/n_2(90^\circ)$ which certainly will hold when complete diffusion is obtained; $n(90^\circ)$ is the total number of transmitted electrons. Table 2 shows

Table 2. 'Absorption' Coefficients μ in Al_2O_3

x_1	x_2	eV	μ (exptl)	μ (Bothe)	μ (Lenard)
$2{\cdot}08\times10^{-8}$	$3{\cdot}4\times10^{-8}$	1500	1×10^{8}	2×10^{8}	5×10^{8}
$2{\cdot}08\times10^{-8}$	$6{\cdot}1\times10^{-8}$	2000	$0{\cdot}8\times10^{8}$	1×10^{8}	4×10^{8}
$6{\cdot}1\times10^{-8}$	$10{\cdot}8\times10^{-8}$	3000	$0{\cdot}4\times10^{8}$	$0{\cdot}6\times10^{8}$	2×10^{8}
$6{\cdot}1\times10^{-8}$	$10{\cdot}8\times10^{-8}$	4000	$0{\cdot}2\times10^{8}$	$0{\cdot}3\times10^{8}$	1×10^{8}

the values of μ (exptl) which have been calculated from the experimental data of table 1 for the scattering angle $\theta=18^\circ$ and for the available film thicknesses x_1 and x_2 noted here. For comparison, absorption coefficients μ (Bothe) have been calculated from equation (5), and the values for μ extrapolated by Lenard (1925) are given in the last column of table 2. Young (1957) maintains that no relationship similar to equation (4) applies to the scattering absorption of slow electrons, but that the number of electrons decreases almost linearly with increasing thickness. His measurements, however, apply to approximately parallel rays and follow the decay of intensity down to $n/n_0\gtrsim1/10$ only. The results obtained here favour an exponential law as given by equation (4) if the film thickness is sufficiently great to provide multiple scattering. Admittedly, the range of thicknesses over which exponential decrease in intensity has been tested here is small, also the value of μ obtained here is likely to be somewhat reduced by the fact that the beams absorbed in the present experiments were not completely diffuse as is asssumed in the derivation of Bothe's formula, equation (5). In the present circumstances, however, it seems satisfactory that an experimental value for μ is obtained fairly near to the theoretical expectation.

§ 5. The Practical Range

Hoffman (1955) and Young (1956a, b) have determined a 'practical range' of slow electrons in Al_2O_3. For a given film of mass-thickness ρx, they plotted the total number of electrons transmitted as a function of the incident electron energy. The linear portion of the curve obtained was produced back to determine the voltage V_p below which no electrons were transmitted. The thickness x of the given film can then be defined as the practical range R_p of electrons which have been accelerated by a voltage V_p. The corresponding mass thickness ρx, where ρ is the density of the film, is defined as the 'mass range' ρR_p of the electrons.

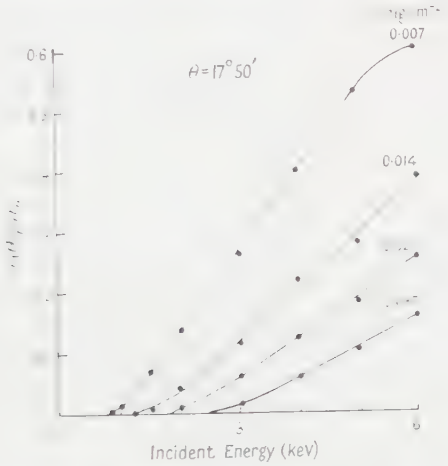

Figure 3. Electron transmittance through Al_2O_3 films of various mass-thicknesses as a function of the incident electron energy.

From plots of experimental data of electron transmittance against electron energy, as shown in figure 3, practical range determinations have been made here for a perpendicular incidence of rays. The results are shown in table 3 for angles of acceptance $\theta = 9°$ and $\theta = 17° 50'$. Also included are the values obtained by Young (1956a) which agree well with measurements by Hoffman (1955) which were carried out at $\theta = 42°$. The maximum scattering angle in Young's experiments is estimated from the published diagram of his apparatus to be 70°–80°.

Table 3. Practical Range in Al_2O_3

Range (ρR_p)	Energy V_p (ev)			
	$\theta = 9°$	$\theta = 17° 50'$	Young	$V(x_L)$
$0{\cdot}7 \times 10^{-4}$	1900	1000	700	800
$1{\cdot}4 \times 10^{-4}$	2100	1700	1200	1400
$2{\cdot}1 \times 10^{-4}$	2700	2200	1600	1800
$3{\cdot}7 \times 10^{-4}$	2800	2900	2400	2700

Table 3 shows that the practical range as defined above, depends on the maximum scattering angle of the electron collected. The unexpected great increase of R_p with increasing θ is possibly due to the way in which V_p is extrapolated. With increasing incident electron energy, the proportion of plural to multiple scattering will increase, but it will also increase with larger angles. Therefore R_p will depend on θ.

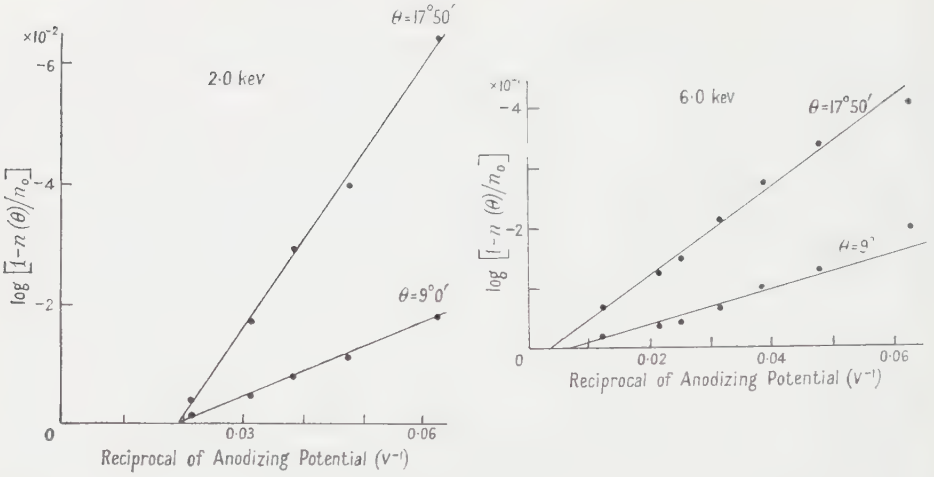

Figures 4 and 5. Electron transmission and anodizing potential used for the preparation of Al_2O_3 films.

An alternative way of extrapolating a practical range is obtained from plots of $\log [1 - n(\theta)\ n_0]$ against the reciprocal film thickness. If equation (3) applies, such a plot should pass through the origin. Now, it has been shown in § 3 that this equation does not represent the experimental results. Moreover, for the largest film thicknesses taken into account for the extrapolation of ranges, back-scattering is possibly no longer negligible. n_0 in equations (1) and (3) can, however, only be taken as the number of incident electrons for sufficiently thin films for which this number is not noticeably different from the total number of electrons transmitted. Hence $-\log [1 - n(\theta)/n_0]$ should be expected to converge towards zero more quickly than in proportion to $1/x$. The latter conclusion is confirmed by the experimental results, they also show clearly that $-\log [1 - n(\theta)/n_0]$ decreases not in proportion to, but linearly with $1/x$. For example, figures (4) and (5) show plots of $\log [1 - n(\theta)/n_0]$ against the reciprocal anodizing potential $1/P$ which was used in the production of Al_2O_3 films. The thickness of the film is given by $x = 13 \times 10^{-10} P(\mathrm{m})$. The curves are perfectly linear, hence, their intercepts with the abscissa can be extrapolated accurately. Though in these curves the ratio of plural to multiple scattering varies with θ, the intercepts are found to be independent of the scattering angle up to nearly 4000 ev incident electron energy. For greater incident electron energies, the extrapolated intercepts would correspond to slightly larger film thickness x_L for the larger θ. This would again correspond to a decreasing V_p with increasing θ. However, the dependence of the intercept of the straight lines upon θ is small and may be inside the limits of experimental errors.

The following limiting mass-thicknesses x_L have been extrapolated from plots such as shown in figures 4 and 5, taken at different electron energies:

Energy (10^3 ev)	1·5	2·0	3·0	4·0	5·0	6·0
ρx_L (10^{-4} kg m^{-2})	1·6	2·2	4·1	4·7	$7{\cdot}5 \pm 0{\cdot}6$	10 ± 2

From these x_L values, voltages $V(x_L)$ have been interpolated which correspond to the mass ranges ρR_p listed in table 3. These $V(x_L)$ values have been added as a last column of the table; they seem to be in fair agreement with the ρR_p values obtained for largest θ.

Abnormally large ranges of very slow electrons leading to selective transmission of rays, below 100 ev, which have been reported by various earlier authors (Becker 1927, 1929, Katz 1938) could not be observed here. On the other hand, the absence of pinholes is demonstrated by the complete attenuation of slow electrons by the films used in these investigations.

§ 6. Energy Losses

The theory of energy losses of electrons in solids, developed by Bohr and adapted to quantum mechanics by Bethe (see Bethe 1933, or Mott and Massey 1933) leads to the following formula

$$-\frac{dW}{dx}=\frac{e^4 n_{at} Z}{4\pi\epsilon_0{}^2 mu^2}\ln\frac{mu^2}{W_m} \qquad \ldots\ldots(7)$$

where dW (joule) is the change in energy of the electron along a path dx (m), e (coul) is the electronic charge, n_{at} (m^{-3}) the density of atoms in the solid, and Z the atomic number; ϵ_0 is the dielectric constant *in vacuo*, m and u are mass and velocity of the electron, and W_m is a mean energy of excitation of the atomic electrons (see Mott and Massey 1933). n_{at} can be calculated from the atomic weight and density of the film together with Avogadro's number. By introducing $eV=mu^2/2=W$ and by using numerical values for e, ϵ_0 etc., one obtains from equation (7):

$$-\frac{dV}{dx}=0{\cdot}9\times10^{10}\frac{\rho}{V}(\log 2V-\log V_m) \qquad \ldots\ldots(8)$$

where ρ is the density of the solid and V is the electron energy (ev). $V_m=W_m/e$ is given (see Mott and Massey) by $\ln(2V/V_m)\simeq 5{\cdot}5$ for $V_m\ll V$. With decreasing primary energy V, the term in brackets in equation (8) should decrease slowly.

Experimental investigations of energy losses of relatively fast electrons have tended to confirm the validity of the Thomson–Whiddington law, namely

$$V_0{}^2-V^2=bx \qquad \ldots\ldots(9)$$

where V_0 is the incident electron energy (ev), V is the most frequent energy in the energy distribution of the electrons transmitted through a thin film of thickness x(m) and where b was found to be a constant of the film material. One of the best determinations for Al (Terrill 1923) yielded the result $b=1{\cdot}1\times10^{11}$ ($v^2 m^{-1}$) for $25\,000<V<50\,000$ ev.

Differentiation of equation (9) leads to

$$-\frac{dV}{dx}=\frac{b}{2V}. \qquad \ldots\ldots(10)$$

Comparison with equation (8) shows that b cannot be expected to be constant over large intervals of V. In particular, for low electron energies, b is likely to decrease noticeably with decreasing V. According to observations by Terrill (1923), b is approximately constant between 25 000 and 50 000 ev. Hence, we can assume that the above value 5·5 for $\ln(2V/V_m)$ is valid at these relatively high electron energies, and therefore $\log V_m\simeq 2{\cdot}3$. Using equation (8) with this value

for $\log I_m$ and combining it with equation (10), the values of b in table 4 marked 'b (theor)' have been calculated. The experimental values of b tabulated in the third column have been taken or calculated respectively from the results of authors noted in the fourth column.

Table 4. The Factor b in Thomson–Whiddington's Law Equation (10) per Unit Film Density ρ

V	b/ρ (theor) (eqns (8) and (10))	b/ρ (exptl)	Observed by:
25000	$4{\cdot}3\times10^{10}$	$4{\cdot}2\times10^{10}$	Terrill (1923)
16000	$4{\cdot}0\times10^{10}$	$2{\cdot}2\times10^{10}$	Whiddington (1912)
10000	$3{\cdot}6\times10^{10}$	$2{\cdot}0\times10^{10}$	Klemperer (1925)
6000	$3{\cdot}2\times10^{10}$	$1{\cdot}8\times10^{10}$	Klemperer (1925)
6000	$3{\cdot}2\times10^{10}$	$5{\cdot}5\times10^{10}$	Young (1957)
2000	$2{\cdot}3\times10^{10}$	$2{\cdot}7\times10^{10}$	Young (1957)
2000	$2{\cdot}3\times10^{10}$	$1{\cdot}5\times10^{10}$	Thetford (1958)
1000	$1{\cdot}3\times10^{10}$	$1{\cdot}7\times10^{10}$	Young (1957)
1000	$1{\cdot}3\times10^{10}$	$0{\cdot}9\times10^{10}$	Thetford (1958)

Whiddington's b value is the average measured between 8 and 20 kev. The fact that Whiddington's result amounts to hardly half the theoretical value cannot be explained by inaccuracies of these very careful measurements, and Bothe (1933) remarks in his detailed discussion that no obvious reason can be given for this discrepancy. It may be suggested here that an inhomogeneity of the film thickness might reduce the experimental value of b. Whiddington was working with beaten films which are liable to very great fluctuations in thickness. For the same reason the b values at 10 kev and at 6 kev obtained by Klemperer (1925) might not come up to the theoretical value.

Quite generally, the experimental b values should be expected to be even larger than those derived from equation (8) since, owing to the multiple scattering, the electron path in the solid is much larger than the thickness x of the film. The 'diversion factor' (see Lenard 1925) which gives the ratio of the path length to the film thickness is particularly large for the relatively low electron energies studied here where it will be of the order of two.

The results obtained by the present authors (Thetford 1958) were measured with the retarding field method described in § 2, they are much below the theoretical values. On the other hand, b values calculated from an empirical formula given by Young (1957) come much nearer to the theoretical expectation.

§ 7. On the Laws of Multiple Scattering in the Region of Low Electron Energies

By F. Lenz

When fast electrons are scattered by atoms, the angular distribution of the scattered electrons can be characterized by the 'differential scattering cross section' $d\sigma/d\Omega$ which is a function of the scattering angle θ, the electron energy eV, and the atomic number Z of the scattering atoms. For sufficiently fast electrons the overwhelming majority of electrons is scattered into small angles θ so that in integrals containing $d\sigma/d\Omega$ as a factor in the integrand, $\sin\theta$ may be

replaced by θ, and the upper limit π by ∞. When an electron passes through a thin foil of thickness x, the average number k of scattering act is given by

$$k = \frac{\sigma \rho x}{A M_0}, \qquad \ldots\ldots (11)$$

where σ is the density of the scattering medium, A the atomic weight of the scattering atoms, $M_0 = 1{\cdot}66 \times 10^{-24}$ g the atomic mass unit, and where

$$\sigma = 2\pi \int_0^{\pi} \frac{d\sigma}{d\Omega} \sin\theta \, d\theta \simeq 2\pi \int_0^{\infty} \frac{d\sigma}{d\Omega} \theta \, d\theta \qquad \ldots\ldots (12)$$

is the 'total scattering cross section'. The mean free path between two scattering acts is

$$l = \frac{A M_0}{\rho \sigma}. \qquad \ldots\ldots (13)$$

If an electron is scattered k times, it follows from the general law of error propagation (Bothe 1921) that the mean square scattering angle after k scattering acts is given by

$$\overline{\theta^2} = k\theta_m{}^2 = k \int_0^{\infty} \frac{d\sigma}{d\Omega} \theta^3 \, d\theta \Big/ \int_0^{\infty} \frac{d\sigma}{d\Omega} \theta \, d\theta = \frac{2\pi k}{\sigma} \int_0^{\infty} \frac{d\sigma}{d\Omega} \theta^3 \, d\theta \qquad \ldots\ldots (14)$$

where $\theta_m{}^2$ is the mean square scattering angle in *one* scattering act. Since the mean number k of scattering acts in a foil of thickness x is given by (11), the mean square scattering angle is

$$\overline{\theta^2} = \frac{2\pi \rho x}{A M_0} \int_0^{\infty} \frac{d\sigma}{d\Omega} \theta \, d\theta. \qquad \ldots\ldots (15)$$

From the theory of electron scattering in the Born approximation and with some simplifying assumptions concerning the charge density distribution in the atomic electron cloud it follows for non-relativistic electrons ($eV \ll m_0 c^2$) that

$$\overline{\theta^2} = \text{const.} \frac{\rho x Z^2}{A V^2}. \qquad \ldots\ldots (16)$$

The value of the constant in (16) can in principle be calculated if the charge density distribution in the atomic electron cloud is known. Bothe has, however, estimated the constant in (16) from empirical data, and he found

$$\overline{\theta^2} = 3{\cdot}2 \times 10^{10} \frac{\rho x Z^2}{A V^2} \ \text{m}^2 \text{kg}^{-1} \text{v}^2. \qquad \ldots\ldots (17)$$

Equation (17) is in agreement with equation (2) of § 3 considering that $\overline{\theta^2}$ is twice the square of the 'most probable' scattering angle λ, and that for light elements, $Z \simeq 0{\cdot}5A$. In the case of multiple scattering ($k \gtrsim 1$), the general law of error propagation again applies and the angular distribution of the scattered electrons is given by

$$\frac{1}{n_0} \frac{dn(\theta)}{d\theta} = \frac{2\theta}{\overline{\theta^2}} \exp\left(-\frac{\theta^2}{\overline{\theta^2}}\right) \qquad \ldots\ldots (18)$$

where $n(\theta) = \int dn(\theta)$ from 0 to θ is the number of electrons scattered into angles smaller than θ, and where $n_0 = \int dn(\theta)$ from 0 to ∞ is the total number of scattered electrons. Integration of (18) results in

$$n(\theta) = \frac{2n_0}{\overline{\theta^2}} \int_0^{\theta} \exp\left(-\frac{\theta^2}{\overline{\theta^2}}\right) \theta \, d\theta = n_0 \left(1 - \exp\left(-\frac{\theta^2}{\overline{\theta^2}}\right)\right). \qquad \ldots\ldots (19)$$

We shall now discuss the range of validity of (17) and (19).

7.1. *A Comparison of Bothe's and Molière's Theories*

A more recent theory of multiple scattering (Molière 1947, 1948) leads to a correction of (17). In the case of multiple scattering, a comparison of Molière's and Bothe's mean square scattering angles yields

$$\frac{\overline{\theta^2}_{\text{Molière}}}{\overline{\theta^2}_{\text{Bothe}}} = 0{\cdot}122B \qquad \ldots\ldots(20)$$

where B is a function of the electron energy eV, of the foil thickness x, and of the foil material which has been defined in Molière's paper. A numerical evaluation of Molière's formula for aluminium and for various values of x and V yields

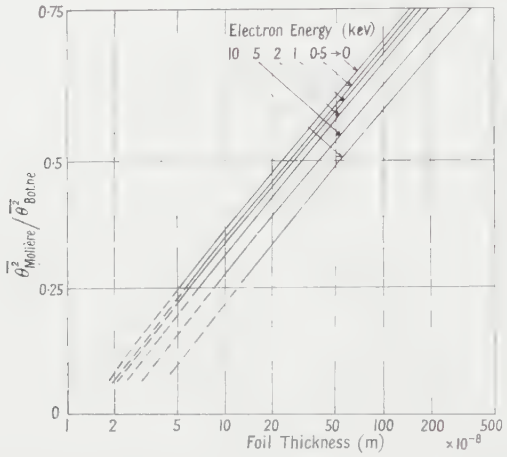

Figure 6. Comparison of theoretical mean square scattering angles.

for non-relativistic electrons the results shown in figure 6. The lines are dotted in the plural scattering region where the multiple scattering theory is not applicable. One of the reasons for the discrepancies between the results of Molière's and Bothe's theories is that Bothe's theory is based on the first Born approximation while Molière's formula contains a factor accounting for deviations from the Born approximation for values of $Zc/137u$ (u/c = electron velocity in terms of light velocity) which are not small compared with unity (for Al this is the case if V is small compared with 24 kv).

Figure 6 shows that for foil thicknesses below $5\,\mu$ (i.e. for all foils that are penetrable for electrons of less than some 10^4 ev and for all electron energies according to Molière's theory) the angular distributions of the scattered electrons are narrower than according to Bothe's formula.

7.2. *Correction for Energy Losses in the Foil*

In Molière's as well as in Bothe's theories energy losses in the scattering foils are neglected. This is admissible only if the energy loss of the electrons in the foil is small compared with their initial energy, i.e. for fast electrons and thin foils. When energy losses cannot be neglected, V depends on x, and in

$$\overline{\theta^2} = \frac{\rho}{AM_0}\int_0^x \sigma(V)\theta_{\text{m}}^2(V)\,dx \qquad \ldots\ldots(21)$$

we can no longer consider $\sigma(V)$ and $\theta_m^2(V)$ to be independent of x. But since in the Born approximation $\sigma\theta_m^2$ is proportional to V^{-2} we find from (21)

$$\overline{\theta^2} = \frac{\rho}{AM_0}\sigma(V_0)\theta_m^2(V_0)\int_0^x \frac{V_0^2}{V^2}\,dx\,. \qquad \ldots\ldots(22)$$

Hence for slow electrons and thick foils the right-hand side of Bothe's formula (17) or any other multiple scattering law of the form of (16) has to be multiplied by a correction factor

$$L = \frac{1}{x}\int_0^x \frac{V_0^2}{V^2}\,dx. \qquad \ldots\ldots(23)$$

The value of this correction depends on the deceleration law $V(x)$. For the special case of the Thomson–Whiddington law

$$V_0^2 - V^2 = bx \qquad \ldots\ldots(24)$$

which is a good approximation for fast electrons we obtain for the correction factor

$$L = -\frac{V_0^2}{bx}\ln\left(1-\frac{bx}{V_0^2}\right). \qquad \ldots\ldots(25)$$

In figure 7 the correction factor (25) is represented graphically as a function of the relative foil thickness $bx/V_0^2 = x/R$ with $R = V_0^2/b$. According to recent

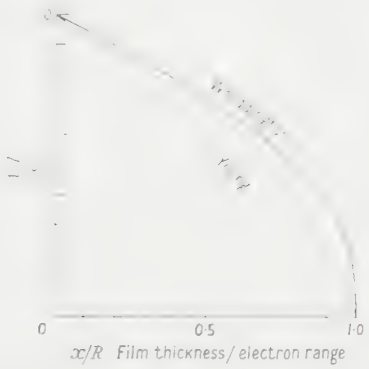

Figure 7. Correction factor for energy losses in the foil.

experimental investigations by Young (1957), and by Vyatskin and Makhov (1958) the energy of electrons below 20 kev decreases according to the empirical law

$$\frac{dV}{dx} = \frac{C}{V^\alpha}. \qquad \ldots\ldots(26)$$

For Al_2O_3 Young found $\alpha = 0{\cdot}35$ and $C = 0{\cdot}87\times10^5\,\mathrm{cm^2\,g^{-1}\,kv^{1{\cdot}35}}$ for primary energies between 2·5 and 10 kev. Vyatskin and Makhov found $\alpha = 0{\cdot}4$ and values between $C = 0{\cdot}44$ and $0{\cdot}70\times10^5\,\mathrm{cm^2\,g^{-1}\,kv^{1{\cdot}4}}$ for Ge, Cu, Si and Bi with primary energies between 2 and 18 kev. With (26) it follows from (23) that

$$L = \frac{V_0^{\alpha+1}}{C\rho x(\alpha-1)}\left[1-\left(1-\frac{C\rho x(\alpha+1)}{V_0^{\alpha+1}}\right)^{(\alpha-1)/(\alpha+1)}\right]. \qquad \ldots\ldots(27)$$

In figure 7 the reciprocal of this correction factor L is plotted for $\alpha = 0{\cdot}35$ as a function of the relative foil thickness x/R, where $C\rho x(\alpha+1)V_0^{-\alpha-1} = x/R$ with $R = V_0^{\alpha+1}/C\rho(\alpha+1)$. Corresponding ranges of electrons calculated from Whiddington's and from Young's law respectively are shown in figure 8. Experimental values obtained by Klemperer and Thetford are also plotted in this

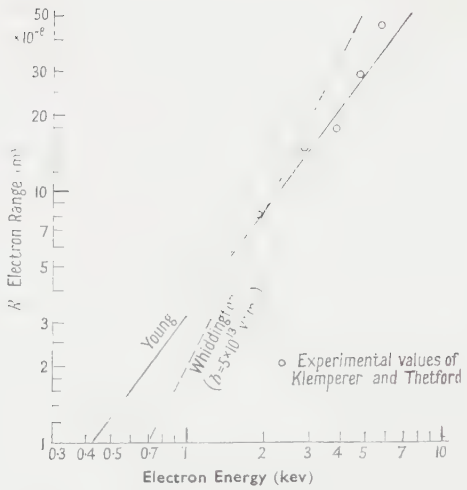

Figure 8. Range of electrons in aluminium.

figure. Klemperer and Thetford have given values of $-\log\{1-n(\theta)/n_0\}$, which are, according to equation (19), proportional to $\theta^2/\overline{\theta^2}$, namely

$$-\log\left(1-\frac{n(\theta)}{n_0}\right)=0{\cdot}434\frac{\theta^2}{\overline{\theta^2}}. \qquad \ldots\ldots(28)$$

If we take into account the above corrections to the Bothe formula, we have

$$\overline{\theta^2}=\overline{\theta^2}_{\text{Bothe}}\frac{\overline{\theta^2}_{\text{Molière}}}{\overline{\theta^2}_{\text{Bothe}}}L. \qquad \ldots\ldots(29)$$

In table 5, the experimental values of Klemperer and Thetford† for $x=1080$ Å and $\theta=17^\circ 50'$ are compared with the uncorrected values of Bothe, and with the corrections proposed in this paper. For C and α Young's values have been taken.

Table 5. Comparison of Experimental and Theoretical Values of $-\log[1-n(\theta)/n_0]$ for $x=1080$ Å and $\theta=17^\circ 50'$

V_0 (ev)	K & T	Bothe	$\frac{\overline{\theta^2}_{\text{M}}}{\overline{\theta^2}_{\text{B}}}$	$\frac{1}{L}$	Corrected value
3000	0·005	0·006	0·32	0·36	0·007
4000	0·026	0·011	0·30	0·72	0·027
5000	0·047	0·017	0·28	0·79	0·050
6000	0·070	0·025	0·26	0·84	0·082

In figure 9 these results are presented graphically. The dotted line shows the average number of scattering acts, estimated from (11) with (Lenz 1954)

$$\frac{AM_0}{\sigma}=2\times10^{-10}V_0 \quad \text{g cm}^{-2}\,\text{v}^{-1}. \qquad \ldots\ldots(30)$$

† These experimental values actually refer to Al_2O_3. The corresponding transmittance values for Al would be larger in the ratio of the densities, i.e. 3·4/2·7.

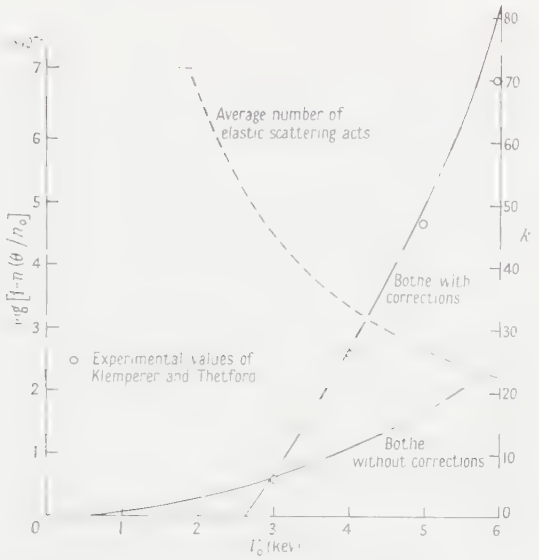

Figure 9. Comparison of experimental and theoretical values characteristic for multiple scattering in a 1080 Å thick Al foil.

The real number of scattering acts is even larger because the electrons are slowed down in the foil so that the average scattering cross section σ is larger than that given by (30). Thus, the number of scattering acts is more than 20 even for 6 kev electrons. For this reason, the application of the theory of multiple scattering is probably justified to a foil of 1080 Å thickness, while for substantially thinner foils noticeable deviations from the multiple scattering laws should be expected.

§ 8. Conclusions

(i) Experimental results have been obtained for the transmittance of relatively slow electrons through thin films of Al and of Al_2O_3 into cones of various semi-apertures. These results have been compared in detail with expectations of Bothe's theory of multiple scattering and definite deviations between experimental and theoretical results have been noted.

(ii) An exponential law for the scattering absorption as valid for faster electrons, was found to apply to some approximation also for relatively slow electrons. The scattering absorption coefficient calculated by Bothe agrees, within the order of magnitude, with the experimental values.

(iii) The conventional way of determining 'practical ranges' of electrons from plots of electron energy against transmitted number was found to be unsuitable for relatively slow electrons because the result appears to depend strongly upon the angle over which the electrons are collected. An alternative method for range determinations from plots of reciprocal film thickness against a logarithmic function of the number of transmitted electrons was found to be more suitable for the slow electrons.

(iv) The energy distribution of initially homogeneous, relatively slow electrons transmitted through thin films has been measured. The most frequent energy losses were determined as a function of the initial energies. It was found that

these losses can be represented by the Thomson Whiddington law only, if the parameter connecting electron energies and film thickness strongly decreases with decreasing electron energies.

(v) Shortcomings of Bothe's theory of multiple scattering in the region of low electron energies are discussed and some modifications are suggested so that this theory becomes applicable to the low energy region. Two correction factors for the mean square scattering angle are proposed, one of which is taken from Molière's paper and accounts for deviations from Born's approximation while the other accounts for energy losses in the scattering foil. Numerical values for both correction factors have been calculated and applied to Bothe's formula. The results show that discrepancies between the theory and the experimental results presented in this paper are considerably reduced.

Acknowledgments

The experimental work described in this paper was carried out in the Physics Department of Imperial College, University of London. One of the authors (A. T.) was in receipt of a maintenance grant from the Department of Scientific and Industrial Research. We are much obliged to Mr. B. Weekly for preparing the aluminium oxide films.

References

Becker, A., 1927, *Ann. Phys., Lpz.*, **84,** 779.
—— 1929, *Ibid.*, **2,** 249.
Bethe, H., 1933, *Handb. d. Phys.*, **24,** 519.
Bond, W. L., 1954, *J. Opt. Soc. Amer.*, **44,** 429.
Bothe, W., 1921, *Z. Phys.*, **5,** 63.
—— 1927, *Handb. d. Phys.*, **24** (see also 1933, *Ibid.*, **22/2.**)
—— 1929, *Z. Phys.*, **54,** 161.
Bradley, D. E., 1954, *Brit. J. Appl. Phys.*, **5,** 65.
Harris, L., 1955, *J. Opt. Soc. Amer.*, **45,** 27.
Hass, G., 1949, *J. Opt. Soc. Amer.*, **39,** 532.
Hoffmann, C., 1955, *Z. Phys.*, **143,** 147.
Holiday, J. E., and Sternglass, E. J., 1959, *J. Appl. Phys.*, **30,** 1428.
Katz, H., 1938, *Ann. Phys., Lpz.*, **33,** 160.
Klemperer, O., 1925, *Z. Phys.*, **34,** 532.
Lane, R. O., and Zaffarano, D. J., 1954, *Phys. Rev.*, **94,** 960.
Lenard, P., 1925, *Quantitatives über Kathodenstrahlen* (see also 1927, *Handb. d. Expt. Phys.*, **14**).
Lenz, F., 1954, *Z. Naturf.*, **9a,** 185.
Molière, G., 1947, *Z. Naturf.*, **2a,** 133.
—— 1948, *Z. Naturf.*, **3a,** 78.
Mott, N. F., and Massey, H. S. W., 1933, *Theory of Atomic Collisions* (Oxford: Clarendon Press), p. 188.
Terrill, H. M., 1923, *Phys. Rev.*, **22,** 101.
Thetford, A., 1958, *Ph.D. Thesis*, University of London.
Tolansky, S., 1948, *Multiple Beam Interferometry of Surfaces and Films* (Oxford: University Press).
Vyatskin A. Ya., and Makhov, A. F., 1958, *Zh. Tekh. Fiz.*, **28,** 740 (transl. *Soviet Physics, Tech. Phys.*, **3,** 690).
Whiddington, R., 1912, *Proc. Roy. Soc.*, **86,** 360.
Williams, E. J., 1939, *Proc. Roy. Soc.* A, **169,** 531.
Young, J. R., 1956 a, *Phys. Rev.*, **103,** 292,
—— 1956 b, *J. Appl. Phys.*, **27,** 1.
—— 1957, *Ibid.*, **28,** 524.

Further Electrical Effects of the Adsorption of Water Vapour by Anodized Aluminium

By C. J. L. BOOKER† and J. L. WOOD‡
Sir John Cass College, London

MS. received 13*th November* 1959, *in revised form* 11*th April* 1960

Abstract. Measurements have been made of the equivalent parallel capacitance and resistance of porous anodized aluminium oxide layers. The measurements, made in air at relative humidities from 0·0 to 0·85 and at frequencies from 50 c/s to 1 Mc/s, extended up to 433 days after formation of the anodic layer. The influence of the humidity and of the frequency of measurement on the dielectric properties of these layers may be explained satisfactorily on the basis of an equivalent circuit. The variation in properties found among layers anodized in the same conditions is due to differences in conductivity arising from varying amounts of stray ions incorporated in the layers. Ageing is primarily due to a decrease in conductivity, and not to structural changes of the oxide layer. The ageing may be reversed by brief immersion of the layers in electrolytes. The results indicate that, in addition to the dielectric losses arising from the main porous structure, losses also occur within the amorphous alumina, showing that this is permeable to water. This can account for measurements of the surface area of porous anodic layers, and of the humidity dependence of the losses in 'non-porous' anodic layers.

§ 1. Introduction

The electrical properties of an anodized aluminium surface are very markedly influenced by the amount of water adsorbed on the oxide. An equivalent circuit based on the structure of the oxide layer has been proposed by Jason and Wood (1955) to account for these effects. The present paper presents the results of an extended investigation of the electrical characteristics of these layers.

§ 2. Experimental

2.1. *Preparation of Samples*

Rods of 99·99% pure aluminium (from the Aluminium Wire and Cable Co.) were degreased with trichloroethylene followed by dilute sodium hydroxide, and washed with dilute nitric acid and distilled water. The dry rods were coated with Araldite to within 5 cm of one end, which was left exposed. The rods, eight at a time, were anodized at constant current density in 17·5% v/v sulphuric acid kept at 20°c. The anodizing conditions were as shown in the table.

After anodizing the rods were washed, dried, and the anodized surface stopped down to a central 4 cm length with polystyrene. Aluminium was evaporated

† Now at Department of Metallurgy, University of Cambridge.
‡ Now at Department of Physical Chemistry, Imperial College, London, S.W.7.

in vacuo on to the oxide outer surface to form a permeable conductor, and a connecting lead was secured to this, the rod itself providing the other contact. Earlier work (Jason and Wood 1955) has shown that with this form of connection the characteristics measured are those of the oxide itself, and not of the outer conductor or contacts.

Anodizing Conditions

Batch number	I	II	III	IV	V	VI	VII	VIII	IX
Current density I_f (mA cm^{-2})	10·7	10·7	21·5	21·5	2·15	21·5	32·2	43·0	43·0
Anodizing time t (min)	30	90	15	30	45	60	30	22·5	30
Product $I_f \times t$	321	963	322	645	967	1290	966	969	1290
Final anodizing voltage V_f	10·8	11·1	14·6	15·0	15·2	15·3	17·3	18·5	18·5

2.2. *Electrical Measurements*

A.C. bridge methods were used to measure the parallel capacitance C_p, and resistance R_p of the elements. The relative humidity was varied from 0·0 to 0·85 by means of a series of saturated salt solutions maintained at 25°c. For a typical batch, measurements were made (over this humidity range) at 1, 10, 23, 60 and 400 days after anodizing. Only in the final calibration was the frequency varied, while in the remainder all measurements were made at a frequency of 1 kc/s.

§ 3. Discussion and Results

3.1. *The Equivalent Circuit*

The structure of porous anodized oxide layers, described elsewhere (Booker, Wood and Walsh 1957, Booker 1958) is shown in figure 1 (*a*). Pores of less than 200 Å diameter penetrate through the outer part of the amorphous alumina, stopping some hundreds of ångstroms short of the metal. The dielectric properties of the anodized layer can be represented quite generally by the equivalent circuit in figure 1 (*b*) where C_1 and R_1 refer to the porous outer layer of oxide, and C_2 and R_2 to the non-porous inner layer. Although these electrical parameters are not constant, R_1 is greater than R_2 and C_2 is greater than C_1, except at very high humidities, and it is then possible to replace this circuit by that shown in figure 1 (*c*), which has previously been used to represent the oxide layer. As before, C_2 and R_2 refer to the inner non-porous layer, while R_1 refers to the resistance between this layer and the outer conductor, and C_0 to the capacitance of the entire oxide layer when R_1 is large. It has been found more convenient to use this circuit as a basis for discussion, with the added advantage that the theory already developed (Jason and Wood 1955) may be extended.

3.2. *The Magnitude of C_0*

At low relative humidities R_1 is very large, so that C_0 can be taken as equal to the measured parallel capacitance C_p of the anodic layer. The earlier observations that C_0 is inversely proportional to the thickness of the oxide layer and proportional to the amount of water added to the layer are confirmed. However, adsorption isotherms for the addition of water to porous anodized layers (Jason, private

communication) show that the increase in C_0 is about three times as great as that to be expected from a simple additive relationship. The fact that C_0 follows changes in the humidity fairly rapidly suggests that the amorphous alumina contains micropores into which the water penetrates, leading to Wagner type losses which give rise to the high values of C_0. Additional evidence of the presence of micropores is provided by a surface area determination (Reay, private communication) showing a surface available to nitrogen adsorption two-fold greater than that anticipated from the *macro*porous structure. When water is added to powdered alumina the dielectric properties also appear to be due to Wagner type losses (Wood 1959) arising from the absorption of water by the porous oxide particles. Further evidence of the absorption of water into the amorphous alumina will be provided in §§ 3.3 and 3.4.

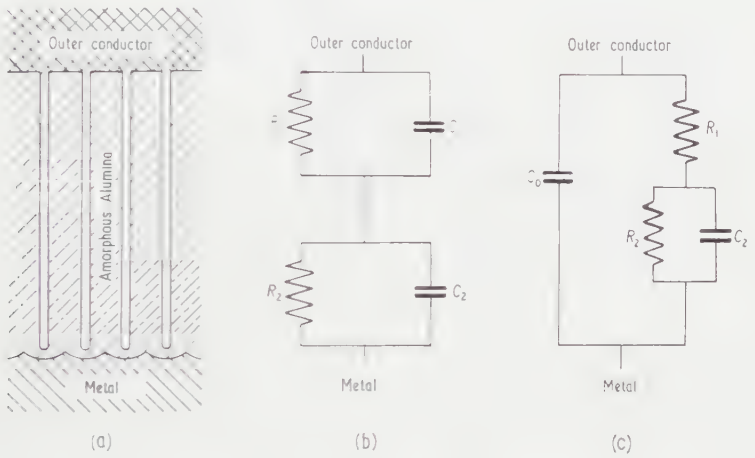

Figure 1. Diagram of porous oxide layer structure and two equivalent circuits.

At higher relative humidities C_p becomes increasingly greater than C_0, which is calculated by assuming that the proportionality found at lower humidities to the quantity of water added continues to hold good. At high humidity (relative humidity $\rho > 0{\cdot}65$), C_0 is very much less than C_p.

3.3. *Variation of Electrical Characteristics within a Batch*

One object of these experiments was to determine the cause of the variability of the capacitance and resistance among oxide layers which had been anodized together under the same conditions. To discuss the results, we shall introduce expressions for the parallel capacitance and resistance of the circuit in figure 1 (*c*).

$$C_p - C_0 = \frac{R_2\tau_2}{(R_1+R_2)^2+\omega^2\tau_2^2R_1^2} \qquad \ldots\ldots(1)$$

$$\frac{1}{R_p} = \frac{R_1+R_2+\omega^2\tau_2^2R_1}{(R_1+R_2)^2+\omega^2\tau_2^2R_1^2} \qquad \ldots\ldots(2)$$

where $\tau_2 = C_2R_2$ is the time constant of the pore base layer.

Although all the parameters determining C_p and R_p appear to vary as the humidity changes, it seemed probable that the pore conductivity R_1 would show

the greatest humidity dependence. When R_1 is eliminated between equations (1) and (2) one obtains

$$C_p - C_0 = \frac{A}{2\omega^2} - \frac{1}{2}\left[\left(\frac{A}{\omega^2}\right)^2 - \frac{4}{\omega^2 R_p{}^2}\right]^{1/2}. \qquad \ldots\ldots(3)$$

where

$$A = C_2(\omega^2 + 1/\tau_2{}^2).$$

When $\omega R_p(C_p - C_0) \ll 1$, as is the case at 1 kc/s at all but the highest humidities, it may be shown (see Appendix I) that (3) simplifies to

$$C_p - C_0 = 1/AR_p{}^2. \qquad \ldots\ldots(4)$$

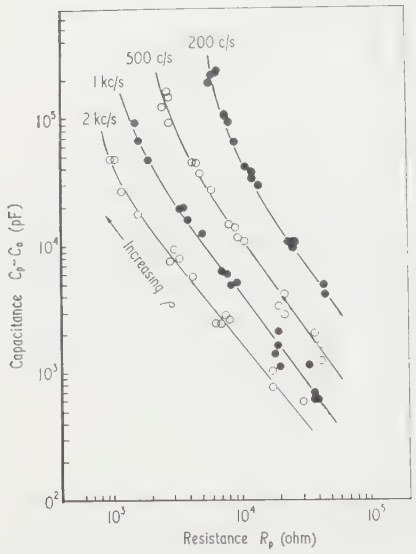

Figure 2. The observed relationship between C_p–C_0 and R_p at various frequencies: 'characteristic curves'. Four elements from batch VII used for illustration.

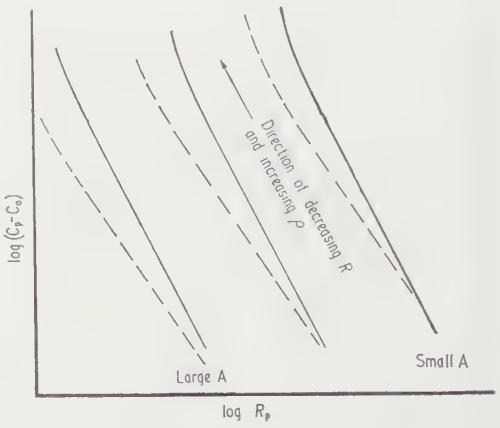

Figure 3. The relationship between $\log(C_p - C_0)$ and $\log R_p$ implicit in equations (1) and (2). The different curves correspond to various values of frequency. For the full line the slope $= -2$ and A is constant along the curve. For the broken line the slope $= -3/2$ and A increases slightly up the curve, but A^2R_1 is constant along the curve. Deviation from linearity occurs at high ρ when $\omega R_p(C_p - C_0) \not\ll 1$.

If A were independent of relative humidity a $(\log(C_p - C_0), \log R_p)$ plot would, according to equation (4), be linear and of slope -2. Although the experimental values of $\log(C_p - C_0)$ and $\log R_p$ give a linear plot over most of the humidity range, the slope differs from -2, showing a variation for different specimens from about $-1{\cdot}4$ to $-1{\cdot}6$. (Figure 2 shows data for a single batch at various frequencies.) This implies that A is not a constant at a fixed frequency, but rises slightly with increasing humidity (shown in figure 3). Such a variation of A is to be expected from the microporosity of the amorphous oxide, for Wagner losses due to water absorbed in the amorphous alumina would lead to an increase in C_2 and a fall in τ_2 as the humidity rises. Both effects would increase A. It

should be mentioned here that the data of Jason and Wood (1955), when re-examined in this manner, were found to give ($\log(C_p - C_o)$, $\log R_p$) plots of slope very near to -2. This would imply that the amorphous alumina of their oxide layers was much less permeable than is the case here.

At high humidities, when $\omega R_p(C_p - C_o)$ is no longer much less than 1, equation (3) predicts that the ($\log(C_p - C_o)$, $\log R_p$) plot will deviate from linearity towards the right (also shown on figure 3). A detailed consideration of equations (1) and (2) shows that even when the slope of the ($\log(C_p - C_o)$, $\log R_p$) curve is no longer -2, this deviation to the right will still arise when $\omega R_p(C_p - C_o)$ is no longer small compared with 1. This departure from linearity was observed in all the layers investigated, and was also shown by the data of Jason and Wood (1955).

Although C_p and R_p, measured at the same frequency, relative humidity and interval after anodizing may vary by several-fold among oxide layers anodized in the same batch, all the values lie quite closely on the same ($(C_p - C_o)$, R_p) curve (figure 2) which may be termed the 'characteristic' curve of the batch. As mentioned above R_1 varies greatly and A slightly along the curves so that it would appear that differences in the amount of stray ions left on the sides of the macropores, and also in the amorphous oxide, are responsible for the individual variation among otherwise similar oxide layers. The observation that the points remain on the same curve implies that the same relationship is maintained between R_1 and A whether these quantities are caused to vary by change in the relative humidity or by variations in the load of stray ions.

At low humidities, when R_1 is much larger than R_2, equation (2) shows that $R_p \simeq R_1$. If the dependence of R_p on the humidity is then taken as a measure of the variation of R_1 with the quantity of added water q_w, the logarithmic relation

$$-\log R_1 = kq_w + \text{constant}$$

is found. A similar result has been obtained by Wood (1959) for the conductivity of powdered alumina in the presence of water, and by Kawasaki (1955) for the conductivity of water films on various solids, including glass.

3.4. *Effect of Ageing*

In the intervals between calibrations, which were made up to 433 days after anodizing, the specimens were stored in a closed cabinet at fixed relative humidity (0·53) and at room temperature. At fixed frequency and humidity the observed parallel resistance of the anodized layer increased continually with age, while C_p fell, but (C_p, R_p) remained on the characteristic curve of the batch (figure 4). (Actually there is a much smaller shift of the curve to the right with age.) This behaviour on ageing may be interpreted as due to a progressive fall in the conductivity both along the pores and through the amorphous alumina, while maintaining the relationship between R_1 and A which holds on a characteristic curve.

It seems probable that the conductivity is associated with the presence of stray ions from the anodizing bath which were not removed by the washing process. In confirmation of this interpretation it is observed that if the surface is dipped in an electrolyte solution, such as aqueous sodium chloride, there is a rapid increase in C_p and $1/R_p$, followed by a slow decline; the values of C_p and R_p remaining throughout on the characteristic curve. When the surface is

dipped in a solution of sodium tungstate (Jason, private communication) the rate of decline of C_p and $1/R_p$ is much reduced, suggesting that the tungstate ions are less easily incorporated in the body of the amorphous alumina, and remain effective in promoting conduction for a much greater period.

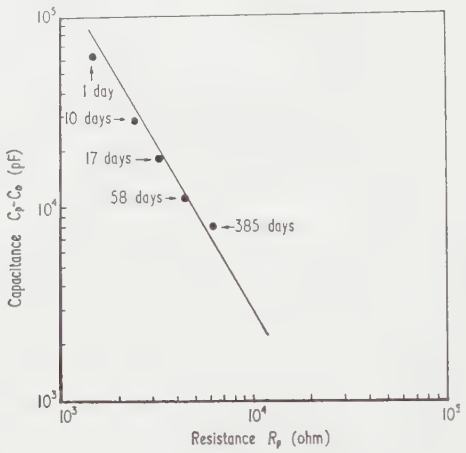

Figure 4. The effect of ageing compared with humidity dependence. The full line is the 'characteristic curve' from the *humidity dependence* at 58 days. Points refer to $\rho = 0{\cdot}75$; all measurements at 1 kc/s. An element from batch IX used for illustration.

It should be understood that this discussion does not imply that the pore side conduction takes place by a similar process to conduction in a bulk electrolyte. The adsorption isotherm combined with the surface area data indicate that at 0·50 relative humidity there is less than a monolayer of water on the alumina surface, so that, although the conductivity is very sensitive to the amount of water or ions on the surface, the conduction mechanism can hardly be similar to that in the bulk liquid.

3.5. *Variation of Electrical Properties between Batches*

The position of the characteristic curve (the $(\log(C_p - C_o), \log R_p)$ plot) is found to depend on the anodizing conditions used in preparing the surfaces. In §§ 3.3 and 3.4 it has been seen that on a characteristic curve there is a relationship between A and R_1 which is maintained throughout changes of the humidity and electrolyte content. However, when the structure of the oxide layer is changed by varying the anodizing conditions, this relationship is altered, with a consequent shift in the position of the curve.

These observations may be examined quantitatively. If the slope of the linear portion of a characteristic curve is taken as $-1{\cdot}5$, this means that $(C_p - C_o)R_p^{3/2}$ is a constant X. This constant is independent of the humidity, but is dependent on the structure of the oxide layer, as determined by the anodizing conditions. It is shown in Appendix II that the value of this constant, which fixes the position of the characteristic curve, is approximately $1/AR_1^{1/2}$. To investigate the dependence of X on the anodizing conditions, the value of X for each batch was determined. Rather than rely on the value of the constant obtained from the characteristic curve of each batch at the single frequency of

1 kc/s, the data for the batch at all frequencies were used in the following way. Recalling that $A = C_2\omega^2(1 + 1/\omega^2\tau_2^2)$, then

$$X \simeq [R_1^{1/2}C_2\omega^2(1 + 1/\omega^2\tau_2^2)]^{-1} \qquad \ldots\ldots(5)$$

so that when $\omega\tau_2 \gg 1$, $X \simeq 1/R_1^{1/2}C_2\omega^2$ and so X may be expected to be approximately proportional to ω^{-2}. This was borne out, and therefore for each batch X was measured from the position of the characteristic curve at each frequency, and the result multiplied by ω^2 to give a product approximately equal to $1/R_1^{1/2}C_2$.

This product, independent of the humidity, may be expected to be proportional to the (total thickness of the oxide layer)$^{-1/2}$. The total thickness of the oxide layer was found to be proportional to the product of the anodizing current density I_f and the anodizing time t. A good correlation between ω^2X and $(I_f t)^{-1/2}$ for different batches is found (figure 5).

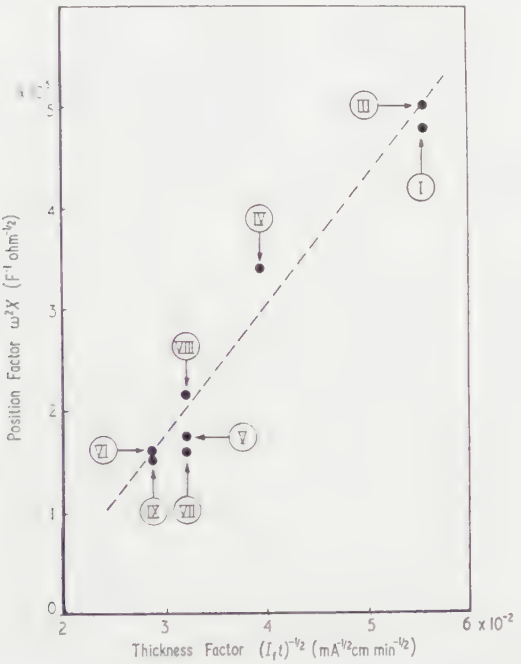

Figure 5. The dependence of the position of the ' characteristic curves ' on the thickness of the oxide layer. Batch number inside circle.

The other structural parameter determining the value of the product ω^2X is the thickness of the non-porous layer, which determines C_2. Keller, Hunter and Robinson (1953) have shown that the thickness of the non-porous layer is linearly dependent on V_f, the final anodizing voltage, but no clear influence of V_f on the value of ω^2X can be distinguished in the present results. An explanation may be that, firstly, the range of variation of V_f (see table) was too small for its influence to be clear, and secondly, that the effective voltage at the pore base, determining the pore base thickness, did not vary as greatly as did V_f.

3.6. *Effect of Frequency of Measurement*

This may be represented as a shift of the characteristic curve parallel to itself, corresponding with the dependence of X on the frequency (figure 2).

Alternatively, the results may be represented as loss curves at constant relative humidity. The form of these loss curves may be derived as follows. When $\omega^2\tau_2^2 \gg (R_1+R_2)/R_1$, equations (1) and (2) become

$$\left.\begin{aligned} C_p - C_0 &\simeq C_2E^2/(1+\omega^2R_1^2C_2^2E^2) \\ \text{and} \quad 1/\omega R_p &\simeq \omega R_1C_2^2E^2/(1+\omega^2R_1^2C_2^2E^2) \end{aligned}\right\} \quad \ldots\ldots (6)$$

where $E = R_2/(R_1+R_2)$.

By comparison with the Debye equations (Fröhlich 1949) for dipole relaxation, it may be seen that (6) is the parametric equation of an ellipse of eccentricity E which passes through the origin and has its centre on the $1/\omega R_p = 0$ axis. The maximum value of $1/\omega R_p$ occurs when $\omega^2R_1^2C_2^2E^2 = 1$, i.e. when $\omega\tau_2 = (R_1+R_2)/R_1$ at which frequency the loss arising from the pore conductivity $1/\omega R_p(C_p - C_0)$ is equal to $1/E$. At higher frequencies $\omega\tau_2 > (R_1+R_2)/R_1$ and $\omega R_p(C_p - C_0) < E$. When $(R_1+R_2)/R_1$ is no longer negligible compared with $\omega\tau_2$ the values of $1/\omega R_p$ become greater than those given by equation (6), and deviation from the ellipse will occur. These loss curves, implied by the use of the equivalent circuit (figure 1 (*c*)), are shown in figure 6. With increasing humidity, E approaches unity, and the loss curves tend to the familiar semicircular shape.

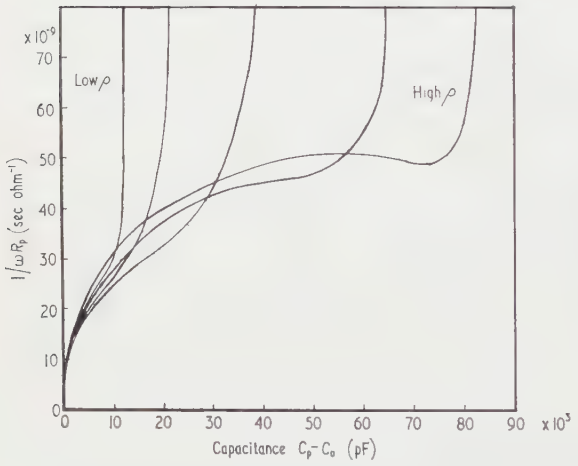

Figure 6. Calculated loss curves at various humidities using equations (1) and (2).

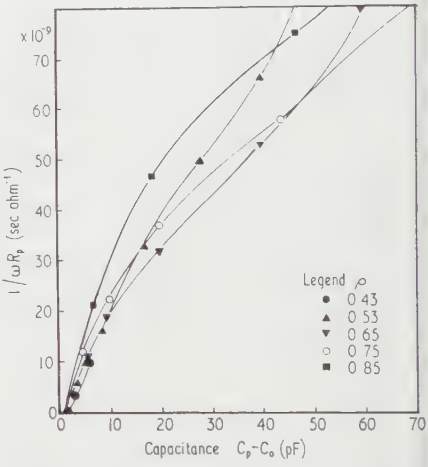

Figure 7. Experimental loss curves at v ous humidities. An element fr batch VI used for illustration.

The experimental loss curves were found to show these characteristics although the data for any single element, e.g. figure 7, are not sufficiently extensive to provide a very satisfactory illustration. A quantitative comparison is made in the following manner. From equation (6)

$$(C_p - C_0)(\omega R_p)^2 = \frac{C_2E^2(1+\omega^2R_1^2C_2^2E^2)}{(\omega R_1C_2^2E^2)^2}.$$

When $\omega^2R_1^2C_2^2E^2$ is much larger than unity, this reduces to

$$(C_p - C_0)(\omega R_p)^2 \simeq 1/C_2. \quad \ldots\ldots (7)$$

For sufficiently large values of ω, the experimental values of $C_p - C_0$ plotted against $(1/\omega R_p)^2$ give good straight lines, from which values of C_2 are obtained (figure 8). The values of C_2 thus obtained increase with humidity confirming the deduction

made from the slope of the characteristic curve. These values of C_2 again show no consistent dependence on the final formation voltage V_f.

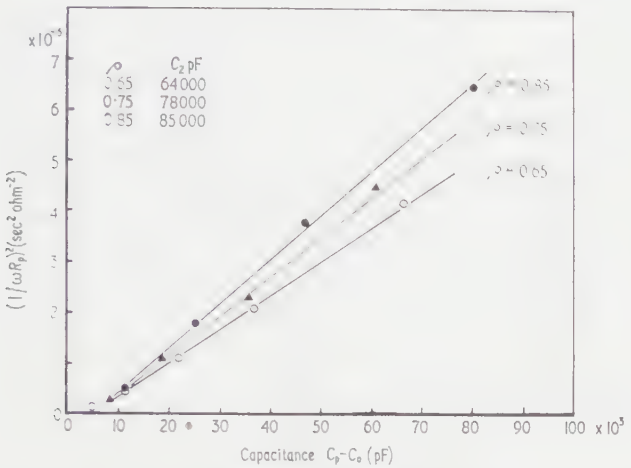

Figure 8. The relationship $(C_p - C_0)(\omega R_p)^2 = 1/C_2$ and the dependence of C_2 on relative humidity. An element from batch IV used for illustration.

Two further observations support the suggestion that water penetrates into the amorphous alumina. Firstly, the capacitance of porous layers measured in the anodizing bath are considerably larger than the values of the pore base capacitance C_2 obtained from measurements in humid air (Jason and Wood 1955). It seems likely that the electrolyte penetrates into the pore base layer, when this is measured in the bath, the consequent Wagner losses giving rise to large values of the capacitance. One consequence is that deductions of the pore base dimensions based on measurements of the capacitance of the anodized surface in the electrolyte, combined with the bulk value of the dielectric constant of alumina, are unreliable. A second observation is that the measured capacitances of 'non-porous' layers (e.g. as formed in ammonium borate) also increase, though less markedly, with humidity, but quite markedly when the measurements are made by placing the surface in an electrolyte (Jason and Wood 1955) indicating that these layers, too, are permeable. It is possible that the permeability of the amorphous alumina explains the observation that when porous layers are sealed by boiling in aqueous solutions a volume expansion of at least 10% is needed to fill the large pores, yet the amorphous alumina accommodates the strains involved and remains firmly attached to the underlying metal.

§ 4. Conclusion

The present work can be regarded as a study of the effects of the superimposition of Wagner type losses. At high humidities conduction in the macropores accounts for nearly all the dielectric loss. The time constant of this loss is large, and increases at low humidities. Consequently, at sufficiently high frequencies or low humidities, the losses arising from this effect are negligible, and it is then possible to observe the dielectric behaviour of the amorphous alumina alone. This shows that the capacitance of the alumina itself increases with humidity, indicating that the alumina is permeable to water. The magnitude of the increase

indicates that Wagner losses occur *within* the alumina, and evidence confirming this suggestion is found in the nitrogen adsorption isotherms for these layers, and also in the electrical properties of 'non-porous' anodized layers.

The electrical characteristics of porous anodized oxide layers resulting from both the losses due to conduction in the pores and in the alumina itself are represented quite satisfactorily by the equivalent circuit of figure 1(*c*). Comparison with the observations indicates that all the parameters shown in this circuit are dependent, but to varying extents, on the humidity and the stray ionic content of the oxide layer. On the basis of this circuit ageing may be interpreted as resulting from a slow decrease in conductivity associated with the migrating of ions to more fixed positions. In accordance with this the electron microscope examination of the layer (Booker 1958) shows that little change in the physical structure appears to take place on ageing. Work is in progress at the Torry Research Station, Aberdeen, to determine the best manner of preventing this slow decrease of conductivity.

Although generally successful, the quantitative treatment of the dielectric losses in these anodized layers is not complete owing to the complexity of their dielectric properties. The equivalent circuit chosen represents a compromise which simplifies the discussion of their behaviour sufficiently to enable a reasonable understanding to be reached of the physical mechanism underlying the dielectric losses in these layers.

Acknowledgments

This work forms part of a research programme on the behaviour of a capacitance–resistance hygrometer undertaken by the Food Investigation Organisation of the Department of Scientific and Industrial Research, to whom one of us (C. J. L. B.) is indebted for a grant. The authors are particularly grateful to Dr. A. C. Jason for his encouragement and many stimulating discussions.

References

Booker, C. J. L., 1958, *Ph.D. Thesis*, University of London.
Booker, C. J. L., Wood, J. L., and Walsh, A., 1957, *Brit. J. Appl. Phys.*, **8**, 347.
Fröhlich, H., 1949, *Theory of Dielectrics* (Oxford: Clarendon Press), p. 70.
Jason, A. C., and Wood, J. L., 1955, *Proc. Phys. Soc.* B, **68**, 1105.
Kawasaki, K., 1955, *Bull. Electrotech. Lab., Tokyo*, **19**, 825.
Keller, F., Hunter, M. S., and Robinson, D. L., 1953, *J. Electrochem. Soc.*, **100**, 411.
Wood, J. L., 1959, *Brit. J. Appl. Phys.*, **10**, 404.

APPENDIX I

Equation (3) can be greatly simplified when $\omega\tau_2$ is large. For then

$$(\omega\tau_2 - 1)^2 \gg 0, \quad \text{i.e. } \omega^2\tau_2^2 + 1 \gg 2\omega\tau_2.$$

For the oxide layers used $R_p > R_2$, so that

$$\omega\tau_2 \frac{R_p}{R_2}(\omega^2\tau_2^2 + 1) \gg 2\omega^2\tau_2^2,$$

i.e.
$$\omega R_p C_2(\omega^2\tau_2^2 + 1) \gg 2\omega^2\tau_2^2,$$

i.e.
$$A \gg 2\omega/R_p, \quad \text{i.e. } A/\omega^2 \gg 2/\omega R_p.$$

The term inside the square brackets on the right-hand side of (3) may then be completed by the addition of the small quantity $[(2/\omega R_p)^2/(2A/\omega^2)]^2$ to give equation (4). The condition that $\omega\tau_2$ is large, i.e. that $\omega\tau_2 \gg (R_1+R_2)/R_1 > 1$ is equivalent to $\omega R_p(C_p - C_o) \ll R_2/(R_1+R_2) < 1$.

For if $1/\omega\tau_2 < R_1/(R_1+R_2)$ then

$$\frac{(R_2\ R_1)\omega\tau_2}{\omega^2\tau_2{}^2} < \frac{R_2}{R_1+R_2}$$

and

$$\frac{(R_2/R_1)\omega\tau_2}{(R_1-R_2)\ R_1-\omega^2\tau_2{}^2} < \frac{R_2}{R_1-R_2},$$

i.e. $\omega R_p(C_p - C_o) < R_2/(R_1+R_2) < 1$, using equations (1) and (2) combined.

APPENDIX II

Equation (3) shows that $(C_p - C_o)R_p{}^2 = 1/A$. When $(C_p - C_o)R_p{}^{3/2}$ is found to be a constant X independent of the humidity, this constant will be equal to $1/AR_p{}^{1/2}$.

On the linear part of a characteristic curve, $\omega R_p(C_p - C_o) \ll 1$, i.e. $\omega\tau_2 \gg 1$, and then R_p is approximately equal to R_1, and the constant X can be taken as $1/AR_1{}^{1/2}$ to a good approximation.

The Specific Heats of Solid Argon and an Equimolar Argon–Krypton Mixture

By B. F. FIGGINS†

Department of Physics, Queen Mary College, London

Communicated by G. O. Jones; MS. received 7th April 1960

Abstract. The specific heat of argon has been measured over the temperature range 16° to 35°K. The results are used to calculate a value for the Debye θ, which is in excellent agreement with lattice dynamics. The specific heat of an equimolar argon–krypton mixture has been measured from 12°K to the melting point. No evidence of any phase separation can be found from the results.

§ 1. Introduction

It is well known that the thermodynamic properties of the soldified inert gases serve as a useful experimental basis for theoretical investigations of the solid state (Dobbs and Jones 1957). An accurate experimental value of the specific heat of argon is then of great importance. However, the existing data (Eucken 1916, Clusius 1936) are not in good agreement and differ from the more recent unpublished results of Hill‡ where they overlap.

Measurements on condensed mixtures of these elements are also of value as an approach to the study of the theory of solutions, and for the information which they might provide about the state of solution in a particular case. Argon and krypton are very suitable since they are known to form solid solutions over the whole range of composition at temperatures somewhat below their melting points and are not complicated by quantum effects as in the case of helium (Jones 1955).

§ 2. Experimental

The method employed to determine the specific heat was that of discrete heating. The specimen was condensed as a solid in a copper calorimeter which could be cooled to about 10°K by liquid hydrogen in a miniature hydrogen liquefier cryostat. The formation of solid in the tube through which the gaseous specimen entered the calorimeter was prevented by employing a device similar to that used by Pryde and Jones (1952), by means of which a large temperature gradient could be maintained between the calorimeter and inlet tube during condensation. The mass of the specimen was determined from the pressure changes in a gas reservoir of known volume.

The temperature of the calorimeter was measured with a platinum resistance thermometer calibrated directly against the vapour pressures of hydrogen and neon between 9° and 28°K (Linder 1950). Above 30°K the oxygen boiling point was used in conjunction with published data (Hoge and Brickwedde 1939) to complete the calibration.

† Now at British Oxygen Research and Development Ltd., Morden, Surrey.
‡ Thesis, University of Oxford, 1952.

The stray heat exchange between the calorimeter and surroundings was reduced to a minimum by taking the usual precautions and in addition by making use of a heat switch (Jones 1951). This was situated between the radiation shield and the gas inlet tube to the calorimeter, at the point where the tube entered the constant temperature enclosure. The inlet tube could then be anchored to the radiation shield during measurements and at other times isolated thermally so that its temperature could be raised to prevent blockages. The apparatus also incorporated a semi-automatic device operated by a chronometer to switch the calorimeter heater on and off (Martin 1955).

The argon was stated by the British Oxygen Co. to be 99·999% pure. The krypton had up to 0·5% xenon as an impurity but otherwise was of the same degree of purity as the argon. At the end of the measurements a sample of the gas used was checked spectroscopically to confirm that no contamination had occurred.

§ 3. Results and Discussions

Argon

The results obtained here for pure argon are shown in figure 1, compared with the results of Clusius and of Hill, and in table 1. It will be seen that the present work is in good agreement with the values obtained by Hill within the estimated accuracy of $\pm \frac{1}{2}$%. There is, however, a large discrepancy between these results and those of Clusius which reaches a maximum value of 5% at about 20°K.

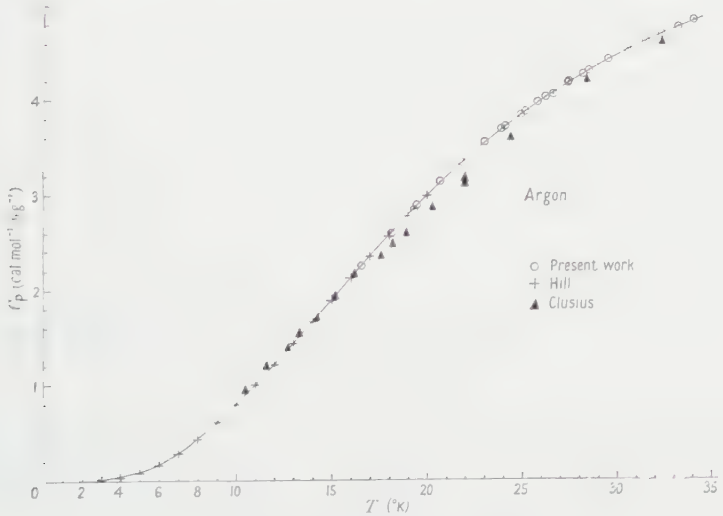

Figure 1. Specific heat of solid argon.

Following Blackman the comparison between experimental and theoretical results is made in terms of the equivalent Debye temperature θ_D. Values were obtained for each temperature by finding C_V, using the most recent data for the compressibility (Barker and Dobbs 1955), and thermal expansion (Dobbs *et al.* 1956) and hence θ_D/T by comparison with published tables for the Debye model (Landolt and Börnstein 1927). The values of θ_D were found to have a nearly constant value of 81 ± 1°K. They lie on a smooth curve within $\frac{1}{4}$ K, having a minimum of 80°K at about 25°K.

Table 1. Specific Heat of Argon (cal mol^{-1} deg^{-1})

T(°K)	16·53	18·10	19·33	19·45	20·67	20·69	21·84	21·86	23·02	23·95	24·13	24·94	25·14
C_p	2·26	2·60	2·85	2·90	3·15	3·15	3·35	3·35	3·57	3·71	3·73	3·86	3·89
T(°K)	25·82	26·25	26·66	27·44	27·49	28·26	28·54	29·57	30·56	31·51	32·40	33·26	34·07
C_p	3·99	4·04	4·07	4·20	4·21	4·29	4·33	4·45	4·56	4·64	4·72	4·80	4·88

Our values agree with the Debye approximation (Kane 1939) but this theory does not explain the rise in θ_D observed by Hill below about 10°K. A more adequate explanation is provided by lattice dynamics. This has been used by Leighton (1948) for harmonic vibrations of a face-centred cubic lattice. In the temperature range of the present work and for central force interactions this leads to a value of $\theta_D = 81$°K. Montroll (1943) made similar calculations using a different analytic method, but did not consider a face-centred cubic lattice. His work had been applied to this case by Domb and Salter (1952). They investigated the effect of distant neighbour interactions and concluded that it is small in the face-centred cubic lattice ($\simeq 3\%$). When all neighbour interactions are taken into account it is found that $\theta_D = 80$°K (Domb and Zucker 1956). The present experimental work is therefore seen to be in excellent agreement with deductions from lattice dynamics.

Argon–krypton mixture

An accurate specific heat curve of an equilibrium solid mixture would show the existence of any phase separation. The critical temperature at which this occurred would then provide data concerning the intermolecular forces. For instance, if the mixture may be considered as a 'regular solution' as defined by Guggenheim, then the energy ω gained on mixing a pair of atoms, one of each constituent, follows at once for a mixture of the composition used here (Guggenheim 1952) from the formula

$$T_c = \frac{\omega}{2K}$$

where $\omega = z\{\frac{1}{2}(\omega_{AA} + \omega_{BB}) - \omega_{AB}\}$, z being the coordination number, and ω_{AA} the energy of an AA pair. A value of ω_{AB} may be found theoretically from

$$\omega_{AB} = \lambda\ (\omega_{AA}\omega_{BB}).$$

This formula may be derived from the work of London (1937) assuming dispersive forces only and ignoring differences in size. If the known heats of sublimation of the pure substances are used to make an estimate of ω_{AB} we find from the above formula that the critical temperature might be expected between 10° and 40°K. We find also from the theory of regular solutions that the energy of mixing might be about 20 cal mol^{-1} so that we should expect very obvious evidence of phase separation. We conclude that $\omega_{AB} > 0$ and therefore that an order–disorder transition is not to be expected as an alternative to phase separation. Experimentally, the sign of ω_{AB} may be deduced from vapour pressure measurements (Heastie 1957) by noting the deviations from Raoult's law.

Previous work on the specific heat of a solidified mixture of argon and krypton is that of Eucken and Veith (1936) who chose a ratio of 40·5% argon : 59·5% krypton. They were unable to find any sign of a phase separation. However,

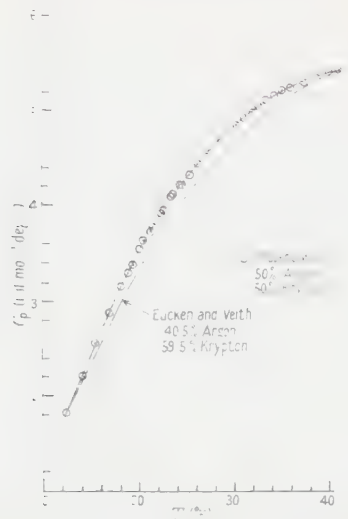

Figure 2. Specific heat of a solid equimolar argon–krypton mixture.

Table 2. Specific Heat of Equimolar Argon–Krypton Mixture
(cal mol^{-1} deg^{-1})

T(°K)	12·44	14·09	15·39	16·87	18·21	18·90	19·40	20·14	20·48	21·25	21·46	22·33
C_p	1·82	2·21	2·56	2·88	3·16	3·30	3·39	3·55	3·64	3·74	3·79	3·93
T(°K)	22·50	23·42	23·56	24·43	24·51	25·38	26·26	27·29	28·35	29·30	30·27	31·12
C_p	3·96	4·11	4·13	4·23	4·23	4·34	4·45	4·59	4·68	4·78	4·85	4·94
T(°K)	31·97	32·69	33·54	34·34	35·09	35·95	37·53	38·77	39·97	41·12		
C_p	5·00	5·06	5·13	5·17	5·23	5·26	5·32	5·37	5·42	5·45		

for a regular solution the maximum critical temperature would be expected for a 50 : 50 mixture, possibly above the lowest temperature (12 K) used by Eucken and Veith. The results obtained here for the specific heat of the 50 : 50 mixture of argon and krypton between 12 and 40 K are shown in figure 2, compared with the results of Eucken and Veith, and in table 2. Between 40 K and the melting point the present results fall on a smooth curve to within $\pm \frac{1}{2}\%$ but they will not be quoted since no correction for vaporization can be applied using present data. There is no evidence from these curves to suggest any phase separation. Above 60 K this is confirmed by the work of Heastie. It thus appears that the expected phase separation must occur below 12 K and we do not confirm the prediction of Halsey and Freeman (1956) of a critical temperature of 62 K. We were not able to detect any indication of the system being out of thermal equilibrium. For instance, measurements repeated at any one temperature after waiting periods of up to 10 hours gave the same value of the specific heat within the experimental accuracy. It is obviously necessary to determine by some independent method what is the state of solution of the solid and attempts are being made to examine this by means of x-ray measurements.

Acknowledgments

I am indebted to Professor G. O. Jones for suggesting the problem and for his constant interest and advice. I am grateful to Dr. R. O. Davies, Dr. R. W. Heastie and Dr. D. L. Martin for many helpful discussions and acknowledge with thanks the careful workmanship of Mr. W. A. G. Baldock and the assistance of Mr. W. Eagers. I am also indebted to the British Oxygen Co. for a Research Fellowship. The work has been assisted by the loan of apparatus from the Central Research Fund of the University of London.

References

Barker, J. R., and Dobbs, E. R., 1955, *Phil. Mag.*, **46,** 1069.
Clusius, K., 1936, *Z. Phys. Chem.* B, **31,** 459.
Dobbs, E. R., Figgins, B. F., Jones, G. O., Piercey, D. C., and Riley, D. P., 1956, *Nature, Lond.*, **178,** 483.
Dobbs, E. R., and Jones, G. O., 1957, *Rep. Prog. Phys.*, **20,** 516 (London : Physical Society).
Domb, G., and Salter, L., 1952, *Phil. Mag.*, **43,** 1083.
Domb, G., and Zucker, I. J., 1956, *Nature, Lond.*, **178,** 484.
Eucken, A., 1916, *Deutsch. Phys. Ges., Verh.* 18.1, 4.
Eucken, A., and Veith, H., 1936, *Z. Phys. Chem.*, **13,** 34, 275.
Guggenheim, E. A., 1952, *Mixtures* (Oxford: University Press).
Halsey, G. D., and Freeman, M. P., 1956, *Nature, Lond.*, **178,** 431.
Heastie, R. W., 1957, *Thesis*, University of London.
Hoge, H. J., and Brickwedde, F. G., 1939, *J. Res. Nat. Bur. Stds.*, **22,** 351.
Jones, G. O., 1951, *J. Sci. Instrum.*, **28,** 181.
—— 1955, *see* Domb, C., 1955, *Nature, Lond.*, **175,** 661.
Kane, G., 1939, *J. Chem. Phys.*, **7,** 603.
Landolt–Börnstein, 1927, *Physikalish-Chemische Tabellen* (Berlin: Springer).
Leighton, R. B., 1948, *Rev. Mod. Phys.*, **20,** 165.
Linder, C. T., 1950, Research Report R-94433-2-A, Westinghouse Research Laboratories, Pittsburgh.
London, F., 1937, *Trans. Faraday Soc.*, **33,** 19.
Martin, D. L., 1955, *Phil. Mag.*, **46,** 751.
Montroll, E. W., 1943, *J. Chem. Phys.*, **11,** 481.
Pryde, J. A., and Jones, G. O., 1952, *Nature, Lond.*, **170,** 685.

Radiative Transitions in ^{8}Be

By I. S. GRANT
Department of Physics, University of Manchester

Communicated by B. H. Flowers; MS. received 14th March 1960

Abstract. A measurement has been made of the angular correlation between the 14·7 MeV γ-radiation from the reaction ^{7}Li(p,γ) and the α-particles from the break-up of the 2·9 MeV excited state of ^{8}Be. The electric quadrupole to magnetic dipole amplitude ratio δ can be derived from the angular correlation. Under the assumption that the resonant component of the γ-radiation has an isotropic angular distribution, δ is found to be $0{\cdot}21 \pm 0{\cdot}07$. The predictions of the independent particle model, using a central force fitted to the properties of neighbouring nuclei, are in good agreement with the observed ratio δ and with the widths of both the 17·6 MeV and the 14·7 MeV transitions when the intermediate coupling parameter a/K is about 2.

§ 1. Introduction

The spins and parities of the broad 2·9 MeV level of ^{8}Be and the 17·6 MeV level formed at the 440 keV resonance in the reaction ^{7}Li(p,γ) are well established to be 2^- and 1^- respectively (Ajzenberg-Selove and Lauritsen 1959, Boyle 1956). Both electric quadrupole (E2) and magnetic dipole (M1) transitions may occur between the two levels, and the angular correlation between the resonant radiation and the α-particles from the break-up of the 2·9 MeV level depends on the ratio of the reduced E2 and M1 transition amplitudes. The angular distribution of the 14·7 MeV radiation has not been accurately measured independently of the more intense 17·6 MeV radiation from the ground state transition, but the deviation from isotropy of the combined resonant radiation is only a few per cent. The resonant state is formed by incoming p-wave protons, and the angular distribution of the radiation is of the form $1 + c\,P_2(\cos\theta)$. The coefficient c is always ten times as great for the 17·6 MeV transition as for the 14·7 MeV transition, whatever the channel spin mixture, and the 14·7 MeV radiation must therefore be very nearly isotropic. The γ–α correlation is thus completely determined by δ and the correlation angle θ, and is found to be

$$I(\theta) = (1+\delta^2) - P_2(\cos\theta)\left\{\frac{1}{2} - \frac{5}{14}\delta^2 - \sqrt{5}\delta\right\} + \frac{8}{7}\delta^2 P_4(\cos\theta) \qquad \ldots\ldots(1)$$

in centre-of-mass coordinates.

§ 2. Experimental Measurements

The 2·9 MeV level of ^{8}Be is extremely broad, having an apparent half-width in this reaction of about 2 MeV, and the energy of the α-particle following its break-up is therefore ill-defined. Measurement of the direction of the α-particle in the laboratory is not sufficient to determine its direction in the centre-of-mass space, and it is impossible to derive the centre-of-mass correlation explicitly from the laboratory correlation if all α-particles from the broad level are accepted. In the experimental measurement of the γ–α correlation, the α-particles were

accordingly analysed in a magnetic spectrometer with resolution 2% in momentum. High resolution had the incidental advantage of greatly reducing the intense background of α-particles and the ^{3}He ions from the ^{7}Li(p, α) reaction, and enabling natural lithium targets to be used. After passing through the spectrometer, α-particles were detected in a thin plastic scintillator, with good discrimination against the γ-radiation background. The α-particles were always observed horizontally, and perpendicularly to the proton beam, with the spectrometer adjusted at each correlation angle to accept α-particles of centre-of-mass energy 1·45 MeV.

As well as the resonant radiation in the ^{7}Li (p, γ) reaction, there is a background radiation with an intensity which rises slowly with increasing bombarding energy, and which is about 1% of the resonant intensity at 440 kev. This background is due to a direct electric dipole transition which may show interference with the resonant transition of opposite parity. The interference term must be zero at right angles to the proton beam, since all the odd Legendre polynomials are zero at $\theta = 90°$. The γ-radiation was therefore observed perpendicularly to the beam, where no interference terms could perturb the correlation (1). The γ-detector was a 2 in. diameter × 4 in. long cylindrical NaI(Tl) crystal, which could be rotated about the proton beam to vary the γ–α correlation angle from 45 to 180°.

The α- and γ-detectors operated two similar biased diode coincidence circuits, which gated the proportional output of the γ-counter. After gating, the γ-counts were biased off at 6 MeV. A third proportional γ-counter output, which also had discrimination at 6 MeV, served as a monitor. Figure 1 shows a delayed coincidence curve measured at a correlation angle of 90°. The ordinate is the difference of the two gated proportional counts, and the abscissa the delay inserted in the 'genuine' coincidence circuit to compensate for the time-of-flight of the α-particles in the spectrometer. The coincidence rate was similarly measured at several other angles at equal intervals in $\cos^2\theta$, where θ is the correlation angle in centre-of-mass coordinates. The results are summarized in the table.

Laboratory angle (deg)	$\cos^2\theta$	Laboratory counting rate in counts per 10^6 monitor counts	Solid angle factor	Centre-of-mass counting rate
180	0·98	5·13 ± 0·66	0·821	4·22 ± 0·54
152½	0·75	5·88 ± 0·51	0·854	5·01 ± 0·44
138½	0·50	5·76 ± 0·48	0·883	5·08 ± 0·42
123¾	0·25	5·08 ± 0·47	0·916	4·66 ± 0·43
90½	0	4·57 ± 0·37	1·032	4·71 ± 0·38
63¼	0·25	3·90 ± 0·35	1·152	4·50 ± 0·40
47½	0·50	3·28 ± 0·60	1·205	4·00 ± 0·72

The column headed 'solid angle factor' contains the product of the velocity ratio v_c/v_1 with the Jacobian $\partial[v_1, (\cos\theta)_1, \phi_1]/\partial[v_c, (\cos\theta)_c, \phi_c]$ of the transformation from laboratory to centre-of-mass coordinates. The factor v_c/v_1 is required because the magnet accepts a range of momenta proportional to the momentum in laboratory coordinates. Note that after multiplication by the solid angle factor, there is no significant difference between two measurements corresponding to the same value of $\cos^2\theta$.

Before the theoretical correlation (1) can be compared with the measurements, one last geometrical correction must be made to allow for the finite geometry of the γ-counter. After averaging over solid angle, (1) becomes

$$I_{\mathrm{corr}}(\theta) = (1+\delta^2) - 0{\cdot}910\mathrm{P}_2(\cos\theta)\left(\frac{1}{2} - \frac{5}{14}\delta^2 + \sqrt{5}\delta\right) + 0{\cdot}714\mathrm{P}_4(\cos\theta)\left(\frac{8}{7}\delta^2\right). \quad \ldots\ldots(2)$$

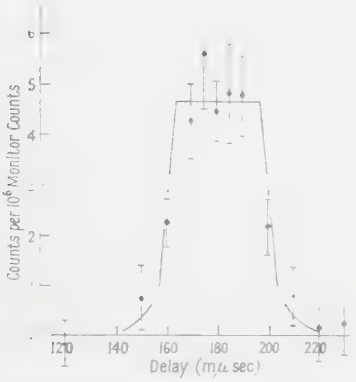

Figure 1. Delayed coincidence curve at a correlation angle of 90°.

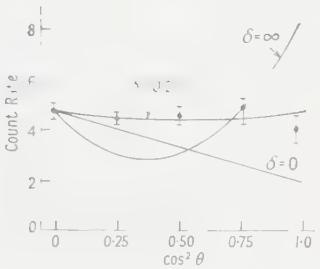

Figure 2. The angular correlation in centre-of-mass coordinates.

The best value of δ in (2) is found from a least squares fit of the measurements in the table to be $\delta = 0{\cdot}21 \pm 0{\cdot}07$. The minimum χ^2 is not significantly different from its expectation value, and the quoted errors are taken at the 5% significance value of χ^2. In figure 2 the observed centre-of-mass correlation is plotted, and compared with the theoretical distribution for $\delta = 0{\cdot}21$, and with the pure M1 ($\delta = 0$) and E2 ($\delta = \infty$) transitions.

§ 3. Theoretical Transition Probabilities

It is interesting to compare the measured value of the ratio δ, and the other characteristics of the radiation from the ^{7}Li (p, γ) reaction, with the predictions of the independent particle model. In two respects this reaction is at the extreme range of nuclear reactions and may be expected to impose a great strain on the assumptions of the theory. Firstly, the transitions are of great energy: the energy of the 14·7 Mev transition is greater than that of any other quadrupole radiation whose strength is known with the exception of the ground state transition in the 167 kev resonance of the reaction ^{11}B (p, γ). Secondly, the width of the first excited state of ^{8}Be is so great that its lifetime is of the order of the time taken by a nucleon to cross the nucleus, and it is not clear that quasi-stationary wave-functions will be at all adequate to describe this state. The width of the 17·6 Mev state itself is many kilovolts, and it has a sufficiently short lifetime for it to be possible that the mode of formation of the resonant state affects the subsequent radiative decay.

Intermediate coupling wave functions have been set up in an L–S coupling representation for the states of ^{8}Be at 17·6 Mev and 2·9 Mev, and for the ground state, assuming that the 17·6 Mev state is the one which goes over to a ^{33}P[31] state in L–S coupling. An independent particle spin-orbit force of the form

$a\Sigma_i l_i . s_i$ was used, and four different exchange mixtures were chosen for the central part of the interaction.

(i) *The Rosenfeld force.*

$$V_R = (-0{\cdot}13 + 0{\cdot}93P_M + 0{\cdot}46P_B - 0{\cdot}26P_H)V(r)$$

where P_M, P_B, P_H are the Majorana, Bartlett and Heisenberg exchange operators. The many-particle interaction for a general central force has been given in terms of the single particle direct and exchange integrals L and K (Elliott, Hope and Jahn 1954), and the ratio L/K has here been chosen to be 6, a value which has been found to give reasonable agreement with the level spectra of many light nuclei (Inglis 1953).

(ii) *The Serber force.*

$$V(\text{Serber}) = \tfrac{1}{2}(1 + P_M)V(r) \text{ again with } L/K = 6.$$

(iii) *The Soper force* (*a*).

Soper has derived a central force exchange mixture which gives a good fit to the level spacings in ^{6}Li (Soper 1957).

$$V(a) = (0{\cdot}4 + 0{\cdot}3P_M + 0{\cdot}2P_B + 0{\cdot}1P_H)V(r).$$

The interaction strengths found by Soper are

$$L = 5{\cdot}45 \text{ MeV}, \quad K = 1{\cdot}18 \text{ MeV}, \quad a = 1{\cdot}554 \text{ MeV}.$$

The same value $L/K = 4{\cdot}6$ has been retained, while a/K is left as a floating parameter.

(iv) *The Soper force* (*b*).

Recently Soper has analysed data on ^{6}Li, ^{7}Li, and ^{8}Li to derive a slightly different exchange mixture (Soper, to be published).

$$V(b) = (0{\cdot}3 + 0{\cdot}43P_M + 0{\cdot}27P_B)V(r).$$

For ^{6}Li and ^{7}Li, $L/K = 4{\cdot}6$, but a slightly larger value gives the best results for ^{8}Li. $L/K = 4{\cdot}6$ has been used here.

The relative strength of the spin–orbit force has been allowed to vary, and wave functions have been computed for each of the central interactions (i) to (iv), with the intermediate coupling parameter $a/K = 1$, 2, 4 and 6.

Fractional parentage coefficients have been tabulated for L–S coupling in the p-shell (Jahn and van Wieringen 1951), and once the intermediate coupling wave functions are known as a sum of the L–S coupling base vectors, the M1 and E2 transition widths can be expressed in terms of single particle widths. The M1 single particle widths are known exactly, but the E2 width depends on the mean square radius of the nucleon distribution. Lane and Radicati (1954) have calculated the matrix element $\langle 1p||E2||1p\rangle$ for an electric quadrupole transition in the p-shell with wave functions in a square potential well whose depth and radius have been chosen to fit the properties of the first excited state of ^{13}N. They find

$$\langle 1p||E2||1p\rangle = -1{\cdot}15 \times 10^{-25} \text{ cm}^2. \qquad \ldots\ldots (3)$$

The value of this matrix element is not likely to change very rapidly from one nucleus to another in the p-shell, and (3) has been assumed to be a reasonable approximation for ^{8}Be. The calculated width of the 17·6 MeV transition, and

the M1 and E2 amplitudes of the 14·8 MeV transition, are compared in figures 3, 4 and 5 with the measured values derived from the total radiative width of 30 eV of the 17·6 MeV state (Bonner and Evans 1948), the intensity ratio of the two γ-rays, and the coefficient δ. The electric quadrupole transition has arbitrarily been given a positive amplitude.

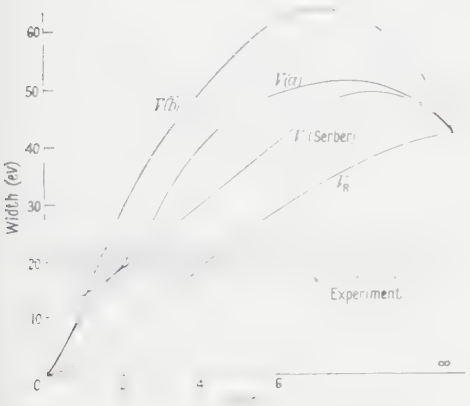

Figure 3. The width of the 17·6 MeV transition.

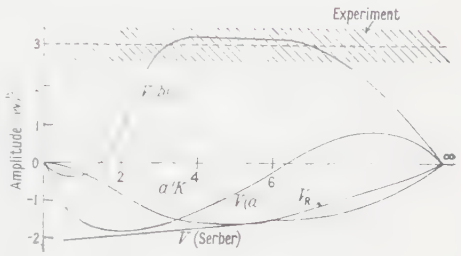

Figure 4. The M1 amplitude of the 14·8 MeV transition.

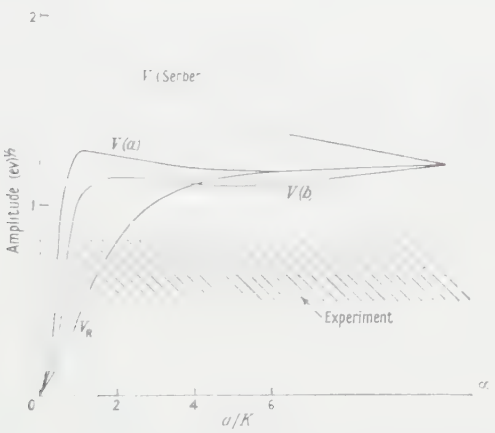

Figure 5. The E2 amplitude of the 14·8 MeV transition.

The four central forces predict quite different amplitudes for the M1 component of the mixed transition (figure 4). This is because the transition is completely forbidden in both L–S and j–j coupling extremes, and as a/K increases, the total transition amplitude in the L–S representation is very much less than the contribution from each L–S component. The other two transitions are also unfavoured since their experimental widths are in each case less than 1/15 of the single particle widths. In these circumstances it is astonishing that the Soper (b) force gives good agreement with each experimental quantity when a/K is near 2. Soper required $a/K = 1{\cdot}3$ to fit the properties of ^6Li; it is reasonable to find a greater value for ^8Be since the spin–orbit strength a is expected to increase throughout the p-shell (Lane and Elliott 1954).

Kurath (1957) has calculated the widths of the two transitions using a simplified central force similar to the Rosenfeld force, and obtained results in essential agreement with those given here. He found the calculated widths of the 14·7 MeV transition to be too small, and suggested that this was because the E2 component was enhanced by collective motion: inspection of figures 4 and 5 shows that this is not so. The Rosenfeld force underestimates the strength of the M1 component, and all the intermediate coupling calculations slightly overestimate the E2 amplitude at $a/K=2$. No doubt this is because the mean square radius needed for the matrix element (3) should be smaller in ^{8}Be than in ^{13}N. The majority of E2 transitions even in light nuclei are in fact enhanced by collective motion of the nucleus, and usually occur more readily than a single particle transition (Wilkinson 1958). But collective motion is not likely to increase the quadrupole strength of the 14·7 MeV transition, whose initial state has $T=1$, and cannot include components which may be regarded as rotational or vibrational modes of the lower $T=0$ state. There are two similar transitions whose quadrupole widths are known, and both are weaker than a single particle transition: (i) The ground state radiation from the 160 keV resonance in ^{11}B (p,γ) has a width of 0·8 single particle units (Beckman, Huus and Zupančič 1953). (ii) In ^{19}F (p,γ), the quadrupole transition from the 13·5 MeV state of ^{20}Ne to the 1·63 MeV state is very unfavoured, and has a width less than 0·015 single particle units (Clegg, Jones and Wilkinson 1955). This suggests that the higher state may have $T=1$.

The intermediate coupling description of the transition strengths in the reaction ^{7}Li (p,γ) is thus entirely satisfactory. The only remaining property to be discussed is the angular distribution of the radiation at resonance. The amplitude for formation of the L–S compound state $|J(LS)T[f]\rangle$ from the state $\langle J_t(L_tS_t)T_t[f_t]|\langle l\sigma\tau|$ representing a target state t and a bombarding l-wave particle, is proportional to some matrix element

$$\langle J_t(L_tS_t)T_t[f_t]|\langle l\sigma\tau|H|J(LS)T[f]\rangle.$$

Expanding the compound state in terms of its parent states, the matrix element can be re-written as

$$\sum_{f,p} C_{T_p\tau}{}^{T}C_{J_p\sigma}{}^{f}C_{Lf}{}^{J}(-)^{l+L_p}\,{}^{L}\!\{(2L+1)(2S+1)(2J_p+1)(2f+1)\}^{1/2}W(L_pJ_pS\sigma,S_pf)$$
$$\times W(lL_pJS,Lf)\langle\alpha|\}\alpha_p\rangle\langle J_t(L_tS_t)T_t[f_t]|\langle l\sigma\tau|H|l\sigma\tau\rangle|J_p(L_pS_p)T_p[f_p]\rangle$$

where the symbols all have their usual meaning. The amplitude of the initial state associated with channel spin f is $C_{T_p\tau}{}^{T}C_{J_p\sigma}{}^{f}C_{Lf}{}^{J}$ and the amplitude for formation of the compound state with channel spin f is proportional to

$$\sum_{p}(-)^{l+L_p}\,{}^{L}\!\{(2L+1)(2S+1)(2J_p+1)(2f+1)\}^{1/2}W(L_pJ_pS\sigma,S_pf)W(lL_pJS,Lf)$$
$$\times\langle\alpha|\}\alpha_p\rangle\langle J_t(L_tS_t)T_t[f_t]|\langle l\sigma\tau|H|l\sigma\tau\rangle|J_p(L_pS_p)T_p[f_p]\rangle. \quad \ldots\ldots(4)$$

Now assume that formation of the compound nucleus depends only on some simple sticking probability: the only term in the sum (4) is then $p=t$, and the matrix element H is independent of the quantum numbers L_t, S_t and f_t. The argument now immediately extends to the intermediate coupling situation, where the amplitudes of the L–S components in the compound state are $\langle J|L_cS_c[f_c]\rangle$ and in the target state $\langle J_t|L_tS_t[f_t]\rangle$. The intensity associated with

channel spin f becomes

$$\left\{\sum_{L,c}(-)^{l+L}p^{-L}\{(2L+1)(2S+1)(2J_p+1)(2f+1)\}^{1/2}W(L_pJ_pS\sigma,S_pf)\right.$$
$$\left.\times W(lL_pJS,Lf)\langle\alpha|\}\alpha_p\rangle\langle J|L_cS_c[f_c]\rangle\langle J_t|L_tS_t[f_t]\rangle\right\}^2. \qquad \ldots\ldots(5)$$

Channel spin intensity ratios have been computed from (5) for all four central force mixtures. The coefficients of the Legendre polynomial $P_2(\cos\theta)$ in the resulting angular distributions for the 17·6 MeV radiation are plotted in figure 6.

Figure 6. The angular distribution of the 17·6 MeV radiation.

The measured value of the coefficient for the 17·6 MeV radiation is 0·018 (Neuert and Retz-Schmidt 1958). None of the central force mixtures can produce this near isotropy at $a/K=2$, but the discrepancy is not really very serious, because the channel spin mixture in j–j coupling is $(f=1):(f=2)=5:1$, whereas the ratio required for isotropy is 1 : 5. The angular distribution is thus fortuitously sensitive to variations in the small intensity of the channel spin one component. Its intensity is indeed small except for the Serber force, and it would certainly be possible to achieve isotropy at small a/K by making a minor adjustment to the Soper force.

The independent particle model is thus able to account remarkably well for all the properties of the radiation from the 440 keV resonance of ^{7}Li (p, γ), in spite of the high excitation of the initial state and the enormous width of the 3 MeV state. These properties all depend rather critically on the nature of the central force, and small admixtures of far-away L–S coupling states (even in the two low-lying levels) make an important contribution to the transition amplitudes. The central force derived from the neighbouring Li nuclei is markedly the most successful, and one must conclude that some allowance for the inadequacies of the theoretical model has been built into this force.

Acknowledgment

I would like to thank Mr. E. B. Fossey and Mr. P. D. Preston for diagonalizing the energy matrices on the Atomic Energy Research Establishment MERCURY computer, and Dr. J. M. Soper for his kindness in showing me his results before publication.

References

Ajzenberg-Selove, F., and Lauritsen, T., 1959, *Nucl. Phys.*, **11,** 1.
Beckman, O., Huus, T., and Zupančič, Č., 1953, *Phys. Rev.*, **91,** 606.
Bonner, T. W., and Evans, J. E., 1948, *Phys. Rev.*, **73,** 666.
Boyle, A. J. F., 1956, *Nucl. Phys.*, **1,** 1.
Clegg, A. B., Jones, G. A., and Wilkinson, D. H., 1955, *Proc. Phys. Soc.* A, **68,** 538.
Elliott, J. P., Hope, J., and Jahn, H. A., 1954, *Phil. Trans. Roy. Soc.* A, **246,** 241.
Inglis, D. R., 1953, *Rev. Mod. Phys.*, **25,** 390.
Jahn, H. A., and van Wieringen, H., 1951, *Proc. Roy. Soc.* A, **209,** 502.
Kurath, D., 1957, *Phys. Rev.*, **106,** 975.
Lane, A. M., and Elliott, J. P., 1954, *Phys. Rev.*, **96,** 1160.
Lane, A. M., and Radicati, L. A., 1954, *Proc. Phys. Soc.* A, **67,** 167.
Neuert, H., and Retz-Schmidt, T. R., 1958, *Z. Naturf.* A, **13,** 829.
Soper, J. M., 1957, *Phil. Mag.*, **2,** 1219.
Wilkinson, D. H., 1958, *The Proceedings of the Rehovoth Conference on Nuclear Structure* (New York: Interscience Publishers), p. 175.

Performance of Large Area Scintillation Counters

By C. F. BARNABY† and J. C. BARTON‡

† Department of Clinical Research, Medical Research Council, University College Hospital Medical School, London

‡ Northern Polytechnic, London

MS. received 21*st December* 1959, *in revised form* 11*th March* 1960

Abstract. The light collection in large plastic and liquid scintillation counters is analysed and it is shown that it is more efficient for the photomultiplier to be in optical contact with one side of the phosphor than to be viewed from above. Experimental results obtained with a large plastic scintillation counter support this conclusion, as does a survey of other published results. The uniformity of response is about equally good for the two types of counter.

§ 1. Introduction

This paper is concerned with scintillation counters which are 'large' in the sense that the area of the counters is much greater than the area of the cathodes of the photomultipliers used with them. Such counters are used both for cosmic ray work and for certain types of radioactivity measurement, particularly the study of 'whole-body' radiation. The need to minimize the area and number of photomultipliers is largely an economic one, but with increasing cathode area the problem of noise pulses being superimposed during the resolving time of the electronic equipment also becomes important. It is therefore important to design the counter so that the efficiency of light collection is as high as possible.

In the first part of this paper various possible arrangements are considered and assessed for their optical efficiency and uniformity of response. The performance of a counter, designed on the basis of the analysis, is then described. Finally a comparison is made between this counter and others on which data have been published.

§ 2. Methods of Light Collection

Despite the great body of theoretical methods which is available for solving problems in geometrical optics much less attention has been paid to systems which lack axial symmetry or in which the rays are widely divergent. For scintillation counter systems the application of the conventional ideas of lens optics is of very little help, and can even be misleading. Instead it is necessary to make use of rather different concepts. The most important of these is the *escape cone* which limits the directions in which light can escape from a luminous source in a medium with a plane surface. For material with a refractive index 1·5, which applies to most liquid scintillators, the critical angle is 42 and the escape cone 12½% of the total solid angle. For plastic phosphors the refractive

index is rather larger ($\sim 1{\cdot}58$) and hence the escape cones are smaller, but it will be a sufficient approximation to consider only the one value. In a rectangular solid there are six cones, so that only 75% of the light can escape; the remainder of the light will be referred to as *trapped light*.

There are two classes of experimental arrangements which have been used. In the first class the photomultiplier views the scintillating material from a distance whereas in the second the two are in optical contact. It is necessary to analyse the two classes separately.

2.1. *Class* 1: *Photomultiplier not in contact with Scintillator*

The simplest case in this class is shown in figure 1 (*a*) where the scintillating material is in the form of a cylindrical disc. Other shapes of material and case have been used and the whole system may be folded up, as in figure 1 (*b*), but the theory is not essentially different.

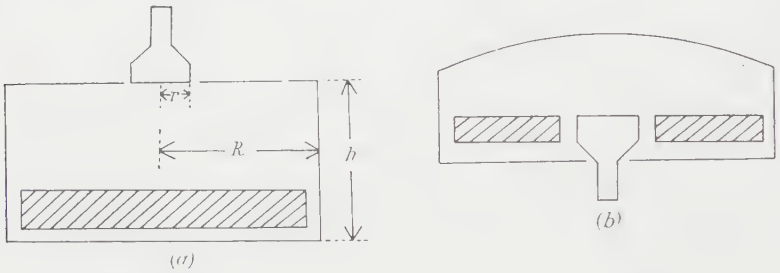

Figure 1. First class of counter; photomultiplier viewing phosphor from a distance.

It is obviously wise to make the bottom surface of the container reflecting so that the light escaping from the top surface is that in the upper and lower escape cones, i.e a fraction of about 0·25. It is not easy to calculate the proportion of the light escaping through the periphery, as the geometry of the escape cones is much more complicated and depends on the source position. Possibly for the latter reason, most existing counters in class 1 have not attempted to collect much of this light.

If the response is to be reasonably uniform the photomultiplier must be at a distance from the phosphor comparable with the maximum dimension of the latter. The proportion of light received directly by the photomultiplier is then, very approximately, equal to its area divided by the total surface area of the upper part of the container. So the proportion of light which reaches the photocathode is

$$\Omega = 0{\cdot}25 \times \frac{\pi r^2}{\pi R^2 + 2\pi Rh}.$$

If we put $\pi r^2 = S$, $\pi R^2 = A$ and take $h = R$ for a typical counter, then $\Omega = 0{\cdot}08 S/A$.

This is very poor and it is therefore customary to attempt to collect more of the light by coating the inside of the container with reflecting material. The cases of diffuse and specular reflectors must be considered separately.

The effect of a diffusing reflector has been estimated by Koechlin (1955) and others. If the reflecting power is p then the improvement is by a factor $1/(1-p)$.

This result is only exact for a spherical container but other geometries will not change it greatly. At the same time the diffuse reflector will improve the uniformity of response. Different authors have given various estimates for p but it seems unlikely that it ever exceeds 0·85 in the wavelength region of importance; it may well be that even this value is only possible for freshly prepared surfaces. Hence we can estimate the geometric factor in this case as

$$\Omega \simeq 0{\cdot}55 S/A.$$

The use of a specular reflector can be attempted with systems of the type shown in figure 1 (*b*). It does not seem easy to analyse this system in detail but one can estimate an upper limit to the geometric factor by considering an ideal optical system, i.e. one that images the phosphor disc on the photomultiplier cathode. Then we can apply the sine relation (see e.g. Conrady 1957) for the divergence of the light at the object and image,

$$n_1 y_1 \sin\theta_1 = n_2 y_2 \sin\theta_2.$$

Hence the semi-angle of the cone of light leaving the object is given by

$$\sin\theta_1 = \frac{n_2 y_2 \sin\theta_2}{n_1 y_1} \leqslant \frac{r}{nR}$$

so that at best the proportion of light going into this cone and the vertically opposite one is

$$\Omega = 1 - \left(1 - \frac{r^2}{n^2 R^2}\right)^{1/2} \simeq \frac{r^2}{2n^2 R^2} = 0{\cdot}22 \frac{S}{A}.$$

It is not easy to see whether a reflector can be designed which is even as efficient as this, so it is not surprising that most workers have preferred to use diffuse reflectors.

2.2. *Class* 2: *Photomultiplier in optical contact with Scintillator*

Brini *et al.* (1955) have given a very careful analysis of the case, figure 2 (*a*), in which the entire area of one side is covered with photocathodes. They show that the conditions under which the uniformity is best, and limited only by the absorption in the phosphor, are: (i) the phosphor must be rectangular; (ii) a short uniform cross-section light guide must be included; (iii) the faces of the phosphor, or transparent container, should be polished; a mirror should be placed behind the face opposite to the photomultipliers but *not* on the other faces.

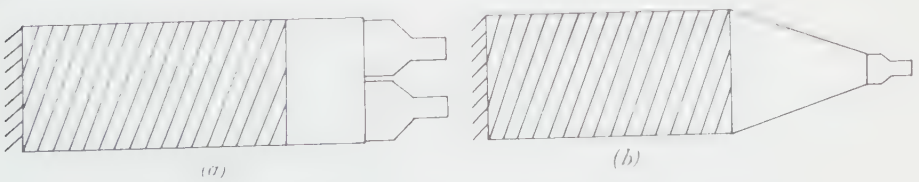

Figure 2. Second class of counter; photomultiplier in optical contact with phosphor.

If these conditions are satisfied the light in four of the escape cones is lost and the remainder, ~0·5, except for the fraction absorbed, reaches the cathodes.

The high value is a result of using total internal reflection, which is far more efficient than any other type of reflection. It is not profitable to add further reflectors, either specular or diffuse, as any light reflected back into the phosphor will be travelling in directions such that it will not readily reach the photocathodes.

A modification of this counter, shown in figure 2 (*b*), uses a tapered light guide and a single photomultiplier. For a sufficiently long guide one can apply the theory of adiabatic guides (Garwin 1952) and deduce that $\Omega = 0{\cdot}5S/A'$, where A' is the area of the side of the counter to which the light guide is attached.

These estimates must be corrected for absorption and scattering, and some idea of the magnitude of these effects is reported below. If the uniformity of response is to be reasonably good the absorption must be small, so that these estimates are applicable if the counter is otherwise feasible.

Comparing the two classes of counters the advantages of the second are obvious. The thickness of scintillating material is usually only a fraction of the other dimensions so that $A \gg A'$ and the light collection efficiency should be at least an order of magnitude better. The only uncertainty is whether light absorption in the scintillating material will lead to a seriously non-uniform response. Unfortunately data on the absorption are very sparse, particularly for plastic phosphors; the counter described here was built to see how serious its effect would be in practice.

The above considerations do not apply to Čerenkov counters as the radiation is mostly emitted within the downward escape cone. It therefore becomes necessary to use specular or diffuse reflectors instead of relying on total internal reflection. Non-focusing Čerenkov counters of these types have been analysed in detail by Mandò (1954), who shows that it is possible to obtain good uniformity only if the depth of the counter is comparable with the other dimensions. Thus his analysis may be of use in designing scintillation counters of large *volume* but is not helpful in respect of large *area* counters.

§ 3. Design of Counter

The counter was designed to discover whether the economies inherent in counters of the type shown in figure 2 (*b*) could be realized in practice, and the size chosen, 55 cm × 17·5 cm, was considered sufficient for this purpose. The plastic phosphor used was a polished block, 3·8 cm thick, of NE 102 by Nuclear Enterprises Ltd.

The shape of the light guide was determined by means of model experiments. An open tank of thin Perspex was filled with pure glycerine ($n = 1{\cdot}47$) and the light emitted from an immersed point source measured by a barrier-layer photocell. Preliminary experiments without a light guide established the validity of the method, although it was found that light which made long paths in the model before reaching the photocell was considerably attenuated.

Experiments with various shapes and sizes of light guides confirmed the application of the 'adiabatic' theory but the uniformity deteriorated with shorter guides. It was found that two small stops, seen in figure 3, helped to reduce high spots near the corners of the counter. The light collected was about 0·06 of the total and the maximum non-uniformity was $\pm 15\%$. Theoretically the geometric factor should have been nearly double this, which again shows that light making the less direct paths in the model was largely lost.

The phosphor, Perspex light-guide and photomultiplier (type EMI 9514B) were mounted in optical contact using silicone oil type MS 200 1 000 000 cs and enclosed in a case made of brass sheet. The phosphor was supported by an array of small rubber studs in order to minimize frustration of the total internal reflection.

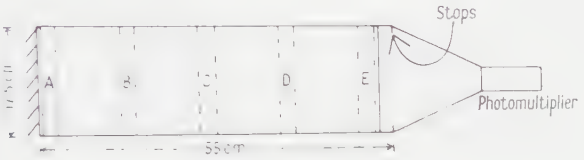

Figure 3. Diagram of experimental counter. The thickness of the counter is 3·8 cm.

Some difficulty was experienced in trying to analyse the heights of pulses from this counter. The pulse length is determined by the photomultiplier and is only of the order of 20 ns (mμsec) with a rise-time which is not sufficient for reliable operation with commercially available discriminators. Higher speed discriminators were built and tested but these were insufficiently stable for operation over long periods. Finally it was decided to lengthen the pulses to about 150 ns so that more conventional electronic circuits could be used. With only a small area photomultiplier the problem of build-up of noise pulses was still unimportant but with larger counters it will become essential to use faster discriminators.

§ 4. Performance

In reporting the performance of scintillation counters used for γ-ray spectroscopy it has become the custom to quote the *resolution* for a particular γ-ray peak. This is defined as the width of the peak in the differential pulse height distribution at half maximum height, expressed as a percentage of the position of the peak. For large area counters a similar measure can be derived for the peak in the pulse height distribution due to cosmic rays. The width of this peak is due to a number of different factors: (*a*) variations in the proportion of light collected from different regions of the phosphor, (*b*) variations in the path length of cosmic rays inclined to the vertical, (*c*) the composite nature of the cosmic ray beam, (*d*) the 'Landau' (1944) distribution of the energy loss of fast charged particles, and (*e*) the statistics of the emission of electrons from the photocathode.

The counter was first operated in coincidence with a Geiger counter telescope containing 15 cm lead absorber in order to minimize the effects of the first three factors. Using only a small region of the phosphor the resolution was found to be $22 \pm 2\%$. The width of the Landau distribution for relativistic particles in an absorber of this thickness is about 17%. The distribution due to the photomultiplier can be assumed Gaussian with a root mean square deviation equal to $[Nm/(m-1)]^{1/2}$ (Morton 1949) where N is the number of photo-electrons and m is the gain of the first stage, $\sim 4{\cdot}5$. Hence its contribution to the half-width is $2[(2\ln 2)(4{\cdot}5N/3{\cdot}5)]^{1/2} = 2{\cdot}68N^{1/2}$. The two effects act independently and hence can be added quadratically. In this way we find that the resolution due

to the photomultiplier alone would be 14% and hence the number of photoelectrons $N=(2{\cdot}68/0{\cdot}14)^2\sim 350$. The uncertainty in this figure is considerable because of the statistical errors and the remaining inhomogeneity of the cosmic ray beam.

Assuming that the phosphor efficiency is about 1 photon per 140 ev energy liberated† and that the photocathode efficiency is 10% we can estimate N, using the results of the model experiment, as

$$\frac{7{\cdot}5\ \text{MeV}}{140\ \text{ev}}\times 0{\cdot}06\times 0{\cdot}10=300.$$

Neither estimate of N is reliable to better than ± 50 but it is clear that the true value is about 300.

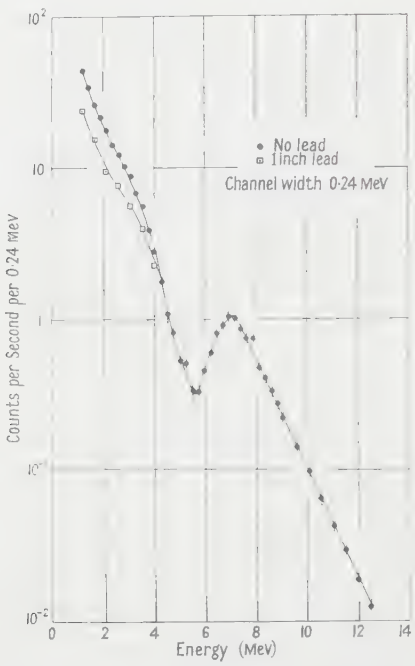

Figure 4. Differential pulse height distribution from experimental counter.

The uniformity of the counter was tested by selecting different regions of the phosphor with the counter telescope. The relative heights of the cosmic-ray peak at the positions marked in figure 3 were

A	B	C	D	E
0·83	0·99	1·00	1·00	1·15

so the maximum non-uniformity is $\pm 16\%$ compared with the value $\pm 15\%$ obtained in the model experiment. (The model experiments had shown that the variation across the width of the counter was relatively small.) The agreement here and between the estimates of N shows that the model experiments can be relied upon as an aid to the design of scintillation counters.

† We have adopted this figure as the most reasonable estimate which we can make at the present time. Absolute measurements of scintillation efficiency are known to be unreliable (Swank 1954) so that the uncertainty is at least $\pm 20\%$.

Figure 4 shows the differential pulse height distribution for all pulses from the counter. The resolution of the cosmic-ray peak, $32 \pm 3\%$, is now wider than before, partly because of the non-uniformity of phosphor response and partly because cosmic rays now traverse the phosphors at all angles to the vertical. Estimates of these two effects are found to be sufficient to account for the difference quantitatively.

Figure 4 also shows the effect of 2·5 cm of lead around the counter. The reduction of the number of small pulses indicates that a proportion of these are due to γ-rays from the laboratory; the apparent presence of γ-rays with energies up to 4 Mev is due to the statistical and geometric variations. Even with the lead screening the background in the counter is larger than expected. The lower energy events may well be due to radioactive impurities in the materials of the counter but it is less easy to explain the events in the energy region 4–6 Mev. It is possible that they are due to low energy neutrons in the cosmic radiation, though the neutron intensity necessary is several times greater than expected.

§ 5. Comparison of large Counters

Modern liquid and plastic phosphors all have fairly similar efficiencies; the choice between them is usually determined by the relative importance of cost, convenience, fire hazard and long-term stability. Assuming again that the phosphor efficiency is such that a particle expends about 140 ev per photon produced, that this figure is relevant for antimony-caesium photocathodes, and that these have a conversion efficiency of 10%, the number of photo-electrons produced by a minimum ionizing particle will be $N = 1500 l\Omega$ where l is the track length in cm and Ω is the geometric factor. The optical merit of any particular counter is then expressed by $\Omega A/S = NA/1500 lS$. The other important parameter is the maximum non-uniformity; it might be more valuable to know the standard deviation of the response, but more detailed information than is usually available would be necessary to calculate this.

Unfortunately many authors who have described large counters have not provided data on all the necessary quantities, nor have they published the differential pulse height distribution. The collected results of the table have therefore been supplemented by theoretical estimates where possible; these have been placed in parentheses when the uncertainty in the validity of the estimate is large. Green (1958) does show that in his very large counter the cosmic-ray peak was just distinguishable, but it is not possible to make any estimate of N because the non-uniformity was very bad.

A variety of very large counters has been built by the Los Alamos group (Reines *et al.* 1954) but the majority of these are essentially large *volume* counters and not strictly comparable with those discussed in this paper. The information on their 'whole-body' counter (Anderson *et al.* 1956) which could be classed as a large area counter, is insufficient to provide any useful comparison. The counter of Bird and Burch (1958) has been included although its classification is rather uncertain.

From the table it is seen that the performance of counters in the first class agrees reasonably well with the theoretical predictions, so that there is not much room for further improvement. Counters of the second class always use the available light much more efficiently.

(1)	(2)	(3)	(4) A	(5)	(6) S	(7) l	(8)	(9)	(10)	(11)
Tennent *et al.*†	1(*b*) (diffuse)	plastic	700	1	15	0·85	12	0·44	± 7	Hemispherical diffuse reflector.
Brennan	1(*a*) (diffuse)	liquid	2500	1	95	10	100	0·18	± 10	
Clark *et al.*	1(*b*) (diffuse)	plastic	1250	1	15	6·3	(50)	(0·37)	± 25	
Clark *et al.*	1(*b*) (diffuse)	plastic	8450	1	95	7·6	50	0·37	± 15	
Oda *et al.*† (Tokyo)	1(*a*) (diffuse)	plastic	10000	1	95	4·5	30	0·47	± 3	Phosphor thickness increases towards edge.
Green	1(*a*) (diffuse)	liquid	70000	1	1000	15	—	—	± 35	
Brini *et al.*	2(*a*)	liquid	324	3	40	2	(1200)	(2·7)	± 11	
Millar *et al.*	2(*a*)	liquid	5700	8	110	5	(400)	(2·5)	(± 10)	Tank surrounded by diffuse reflector.
Bird & Burch	2(*a*)	plastic	1100	2	190	15	(4000)	(1·0)	—	Special shape; diffuse reflector used.
Barnaby & Barton	2(*b*)	plastic	960	1	15	3·8	300	3·4	± 16	

(1) Authors; (2) class of counter; (3) phosphor; (4) area (cm²); (5) number of photomultipliers; (6) total area of cathodes S (cm²); (7) track length l (cm); (8) photoelectrons per particle N; (9) 'optical merit' $NA/1500lS$; (10) maximum non-uniformity (%); (11) remarks.

† Private communication.

The uniformity of the Tokyo counter is exceptionally good (Oda *et al.* 1959, private communication); the idea of increasing the thickness of the phosphor towards its edges could be applied to most of the other counters, although of course the method is useless if the counter is required for γ-ray spectroscopy. For most applications there seems little advantage in having the non-uniformity much less than the resolution of the counter, as limited by the Landau and photomultiplier effects.

From this comparison it appears that counters of the second type can give better performance than the others, in addition to being often mechanically more convenient. Unfortunately it is not clear how much larger they can be made. The limit will depend on the light absorption in the phosphor and this is still uncertain for both liquid and plastic phosphors. However the results already available show that, by putting one photomultiplier at each end of a plastic phosphor, counters over a metre long are certainly feasible and that longer ones are worth investigating.

Acknowledgment

We are indebted to H. A. P. Knight for useful discussions of this work.

References

Anderson, E. C., Schuch, R. L., Perrings, J. D., and Langham, W. H., 1956, *Nucleonics*, **14**, 1, 26.
Bird, P. M., and Burch, P. R. J., 1958, *Phys. Med. Biol.*, **2**, 217.
Brennan, M. H., 1957, *Nuovo Cim.*, **6**, 216.
Brini, D., Peli, L., Rimondi, O., and Veronesi, P., 1955, *Nuovo Cim., Suppl.*, **2**, 1048.
Clark, G. W., Scherb, F., and Smith, W. B., 1957, *Rev. Sci. Instrum.*, **28**, 433.
Conrady, A. E., 1957, *Applied Optics and Optical Design* (New York: Dover), p. 367.
Garwin, R. L., 1952, *Rev. Sci. Instrum.*, **23**, 755.
Green, J. R., 1958, *Rev. Sci. Instrum.*, **29**, 10.
Koechlin, Y., 1955, *J. Phys. Radium*, **16**, 849.
Landau, L., 1944, *Zh. Fiz., S.S.S.R.*, **8** (4), 201.
Mandò, M., 1954, *Nuovo Cim.*, **12**, 5.
Millar, C. H., Hincks, E. P., and Hanna, G. C., 1958, *Canad. J. Phys.*, **36**, 54.
Morton, G. A., 1949, *R.C.A. Rev.*, **10**, 525.
Reines, F., Cowan, C. L., Harrison, F. B., and Carter, D. S., 1954, *Rev. Sci. Instrum.*, **25**, 1061.
Swank, R. K., 1954, *Ann. Rev. Nuclear Sci.*, **4**, 111.

Domain Patterns on ' Cube-textured ' Silicon–Iron Sheet

By L. F. BATES and R. CAREY
Department of Physics, University of Nottingham

MS. received 4th April 1960

Abstract. The surface domain structure of a cube-textured 3% silicon–iron sheet was examined by the colloid technique. The patterns observed on most grains were typical of those previously reported on (100) surfaces in the single crystals, i.e. most grains contained two easy axes of magnetization in the surface, and usually one of these was parallel to the rolling direction of the sheet.

A new band-structure pattern was found, and by comparison with similar patterns on a single crystal was thought to be associated with bulk strain in the material.

§ 1. Introduction

A new 3% silicon–iron magnetic sheet material has recently been produced in an attempt to obtain equal magnetic properties in two directions in the sheet, respectively parallel and perpendicular to the rolling direction. The more well-known, and widely used, ' grain-oriented ' silicon-iron sheet has magnetic properties which closely resemble those of a specifically oriented single crystal. Most of the crystals in a sheet of the material have surfaces which approximate to the (110) plane of the cubic structure, and therefore contain one axis of easy magnetization. In a sheet the easy directions of the separate crystals are aligned approximately parallel to the rolling direction. Consequently, grain-oriented sheet has the advantages over non-oriented material of high permeability in the rolling direction and lower hysteresis loss. However, as the [111] and [110] directions are harder directions of magnetization than the [001] direction, small permeability and greater losses result when the flux has to travel at an angle to the rolling direction; this means that the use of the grain-oriented sheet is for the most part limited to components in which the flux is required to travel in one direction only.

The new material represents an attempt to reduce the losses in the cross direction by the provision of a second easy direction of magnetization perpendicular to the rolling direction. In this material, the crystal surfaces approximate to (100) planes with two mutually perpendicular easy directions in the surface, one being parallel to the rolling direction. Its magnetic properties have been recorded by Walter *et al.*(1958), who showed that it has in fact equal magnetic properties in two directions in the surface and that the desired cubic texture, as determined by torque magnetometer tests, is of the order of 90% or greater compared with a single crystal with a (100), [001] orientation.

In order to ascertain the exact nature of the surface orientation of the separate grains, specimens of the new material were obtained from the General Electric Company (U.S.A.) and their surface domain structure were investigated.

§ 2. Experimental Technique

Three specimens of the cube-textured sheet, with almost identical magnetic properties, were received. They were in the form of pressed discs, 2·4 cm in diameter and 0·03 cm thick. The peak values of torque when compared with those of a similar single crystal were 0·91, 0·93 and 0·94, respectively, and consequently, as far as surface domain pattern investigations were concerned, the specimens could be considered identical. The grain size was large relative to the sheet thickness, so that most of the grain boundaries penetrated the sheet almost perpendicularly and thus preserved the grain shape from face to face almost unchanged. The average grain diameter was of the order of 0·1 cm.

The discs were mechanically polished through 000 metallographic paper followed by fine polishing on 6μ, 1μ and $\frac{1}{4}\mu$, commercial diamond compound. The strained surface layer was removed by electropolishing in a mixture of chromic and acetic acids when the grain boundaries were sufficiently etched for them to be seen clearly. The specimens were mounted horizontally and their domain structure investigated by the colloid technique, using colloid prepared from the Bozorth recipe. Small normal fields could be applied by a small electromagnet mounted below the usual metallurgical microscope stage.

§ 3. Experimental Observations

Examination of the surface domain structures of a large number of grains in a specimen in the demagnetized state immediately showed that the material possessed a high degree of (100) orientation. The Bitter patterns observed were in most cases identical with those previously reported on (100) surfaces in the single crystal (Williams, Bozorth and Shockley 1949). In most grains two of the three easy axes of magnetization lay almost exactly in the surface, with one axis parallel to the rolling direction.

In the grains which were perfectly oriented with respect to the (100) plane of the crystal structure and the rolling direction the domain structure consisted of 'slab' domains or main 180° domains alternately magnetized along the [100] and [$\bar{1}$00] directions, the [100] direction being taken as collinear with the rolling direction. A typical example of such a grain is shown in figure 1†. One wall bisects a group of inclusions and closure domains have formed, while another is tied to a large inclusion by a 'tube'. Figure 2 shows a similar grain, but the main domains are now magnetized along the [010] and [0$\bar{1}$0] directions. Prismatic closure is seen at surface imperfections, but not at the grain boundaries.

Adjacent grains have a similar domain structure and there is a tendency for 180° domain walls to cross the grain boundaries, in spite of any slight change in surface orientation. In figure 3 it is clear that the surface of the upper grain is at a small angle to the (100) plane, and there is a transition in the domain structure, the main domains appearing alternately light and dark (Mee 1950), and 'fir-trees' have formed. The branches of the fir-tree structure extend into the main domains to a distance approximately equal to half the domain spacing. Williams, Bozorth and Shockley calculated that this transition occurs when the surface is about 0·5° off the (100) orientation in one direction. When such misorientation increases to about 1·3°, the 180° wall forming the trunk of the tree structure is eliminated, and this kind of transition is approached by the surface shown in figure 5 and reached in figure 6.

† All the figures are printed as Plates.

If a grain surface is slightly misoriented with respect to more than one of the cubic axes, further closure domains are formed within the branches of the fir-trees. This type of closure is just beginning to form in the branches of the fir-trees of figure 6. When the degree of misorientation at right angles to the direction of the fir-trees is increased, these new closure domains become more pronounced in one branch of the fir-tree. The other branch shrinks and eventually disappears. In figure 7 the surface makes a small angle with the [100] direction (rolling direction) and is also considerably rotated about the latter direction, the branch which displays the new closure domains being on the 'downhill' side, the (100) plane being regarded as horizontal. In figure 8 the degree of rotation of the surface about the [100] direction is even more pronounced. No 180° walls are apparent and the domain patterns appear as long thin 'combs'. These appear where 'spikes' or branches of fir-trees cut the surface. In this grain they are probably due to spike formations from the grain boundary. Similar patterns have been reported and fully explained by Yamamoto and Iwata (1953) in the case of nickel single crystal surfaces of varied orientations.

The patterns described above are representative of the domain structures observed on more than half the total number of grains examined. For the rest one particular pattern was predominant; this pattern is shown with low magnification on several grains in figure 9. The new structure, called 'band structure' for the purpose of this report, was common to all three specimens and is described in detail below.

A few grains were of some random orientation whose domain structure was not interpretable in terms of any previously reported. The surfaces contained no easy directions of magnetization, and on them were seen complicated free pole 'closure' structures typical of such surfaces.

Two grains, one of which is shown in figure 4 (Plate I), showed a series of 180° 'slab' domains and spikes of reverse magnetization (Davis 1958), a structure appropriate to the (110) surface of a single crystal. It is interesting that the one easy direction in these surfaces was parallel to the rolling direction although the surfaces were 45° off the required (100) orientation.

§ 4. The Band Structure

The band structure domain pattern was so predominant in the cube textured specimens as to warrant special investigation. Figure 9 shows its general appearance within several grains, and figure 10 is a photograph of greater magnification. It is seen as a series of light and dark bands, with boundaries between the bands in the form of zigzag 'walls'. The direction of magnetization in each band, deduced from the colloid striations in the dark bands, is perpendicular to the long direction of the bands. At a zigzag 'wall' the directions of magnetization of the surfaces on either side of the wall are 180° out of phase, and they meet head-on at the wall. The middle of each band shows a regular series of closure domains similar in appearance to the well-known Néel spikes which form at non-magnetic holes or inclusions on a (100) surface. However, the regularity of these closure domains suggests that they do not need surface inclusions for their formation, although they do appear wherever possible to nucleate from such inclusions.

The patterns shown in figures 9 and 10 were photographed with a small magnetic field normal to the surface of the specimen. When the field direction was reversed the domain pattern remained the same in outline but the light bands appeared dark and vice versa.

Zigzag walls of this type, without the intermediate closure domains, have previously been observed in this laboratory (Martin 1954) on (100) surfaces of single crystals of silicon–iron, their formation being attributed to some kind of internal strain mechanism. For this reason, it was decided to investigate this pattern further on a single crystal specimen.

Figure 11 shows the domain structure on a (100) surface of a single crystal of silicon–iron. The specimen is in a strained state and two types of strain are immediately apparent. The maze domain, usually associated with a strained surface layer produced during the process of mechanical polishing (Chikazumi and Suzuki 1955) has been partly removed by electropolishing to reveal the zigzag walls due to the strain in the bulk of the specimen. Figure 12 shows the surface of the specimen after the strained surface layer has been completely removed.

At one edge of the single crystal specimen, which had become slightly concave due to the electropolishing, the zigzag wall of the strain pattern developed into a band structure exactly the same as that seen on the polycrystalline material, figure 13. This band structure is shown with a greater magnification in figure 14. It will be noted that the closure domains, in the bands, point in the down-hill direction both in the light and the dark bands. In this region in an un-strained specimen we would expect the well-known fir-tree structure, the branches of the trees pointing to the edge of the specimen.

One of the specimens of the cube-textured material was annealed for 72 hours at 650° c in dry hydrogen. After a light mechanical polishing followed by electropolishing, the domain structure was examined. Most of the band structure had disappeared, the strain had been relieved and the material had retained its cubic texture. In one grain, the strain was only partly relieved and the band structure was still apparent, figure 15, but in the middle of the grain the fir-tree structure was in evidence. Part of this surface is shown in a greater magnification, figure 16, where the effect can be seen more clearly.

§ 5. Summary

The examination of the domain structure of the cube-textured material by the colloid technique has shown it to have a high degree of (100), [100] type texture, with most of the [100] directions in the grain surfaces aligned with the rolling direction of the sheet. Most of the grain surfaces showed domain patterns identical with those previously reported on surfaces oriented to within approximately 3° of the (100) plane in a single crystal of silicon iron. In the rest, a pattern peculiar to some form of bulk strain in the material was predominant. It was found, however, that this pattern appeared only on surfaces which were a few degrees off the (100) surface orientation and in these surfaces also a [100] type direction was close to the rolling direction.

Such internal strain was, to a large extent, removed from one specimen by annealing it at 650° c, the domain structures observed after the anneal conforming to those normally expected on surfaces oriented in this way.

Since, in the grains which showed a surface domain ' band ' structure, the easy axes of magnetization were nevertheless well oriented with respect to the rolling direction of the sheet, the magnetic properties of the sheet were not seriously affected, a fact which is borne out by the torque-curve measurements of Walter *et al.*

Acknowledgments

We are indebted to Dr. Weston Morrill of the G.E.C. Laboratories, Pittsfield, Mass., U.S.A. for the kind gift of the specimens of cube-textured material. One of us (R.C.) thanks the Department of Scientific and Industrial Research for a maintenance grant.

References

Chikazumi, S., and Suzuki, K., 1955, *J. Phys. Soc. Japan*, **10**, 523.
Davis, P. F., 1958, *Ph.D. Thesis*, University of Nottingham.
Martin, D. H., 1954, *Ph.D. Thesis*, University of Nottingham.
Mee, C. D., 1950, *Proc. Phys. Soc.* A, **63**, 922.
Walter, J. L., Hibbard, W. R., Fiedler, H. C., Grenoble, H. E., Pry, R. H., and Frischmann, P. G., 1958, *J. Appl. Phys.*, **29**, 363.
Williams, H. J., Bozorth, R. M., and Shockley, V., 1949, *Phys. Rev.*, **75**, 178.
Yamamoto, M., and Iwata, T., 1953, *Sci. Rep. Res. Insts Tôhoku Univ.*, A, **5**, no. 5.

Multipolarity and Character of 961 kev Resonance and 840 kev Fluorescence Radiation in ^{152}Sm

By B. S. SOOD

Department of Physics, University of Birmingham

Communicated by P. B. Moon; MS. received 14th March 1960

Abstract. The ratio of the intensities of the 961 kev resonance and 840 kev fluorescence radiation in ^{152}Sm has been measured at angles ranging from 55° to 155° and compared with theoretical values. The results are in agreement with the spin and parity assignments of 0^+, 2^+ and 1^- to the ground, 122 kev and 961 kev states respectively.

§ 1. Introduction

The directional correlation and the directional polarization correlation of the 840 kev–122 kev γ–γ cascade in ^{152}Sm have been studied (Grodzins and Kendall 1956, Wood and Nathan 1959, Wood 1959) in order to find the multipole orders and the characters of the transitions and hence show the existence of the theoretically predicted 1 octupole vibrational state (Alder *et al.* 1956). In this paper we report experiments that are relatively simple to perform and easy to analyse but yield similar information.

The multipolarities of the transitions in question can be determined from the measurement of the angular distributions of the 961 kev resonance and 840 kev fluorescence radiation that result when the 961 kev resonantly excited level decays to the ground and the first excited states respectively (for details, see Metzger 1959). Information about the characters of the transitions is derived from considerations of their lifetimes. The experiment is even further simplified if instead of measuring the absolute intensitites of the resonance and fluorescence radiations individually at various angles, their ratio is determined and compared with the theoretical predictions; this method has the advantage of avoiding many large corrections to the experimental data which would otherwise be essential.

§ 2. Experimental Procedure

The experimental arrangement used to measure the ratio of the intensities of the resonance and fluorescence radiations at angles ranging from 55 to 155 is shown in figure 1. The gamma rays from the $^{152m}Eu_2O_3$ source were scattered from interchangeable ring scatterers of Sm_2O_3 and Gd_2O_3 or TaC. The elastically scattered radiation was detected with a $1\frac{1}{2}$ in. diameter × 2 in. NaI(Tl) crystal mounted on 6260 EMI photomultiplier, the pulses from which were amplified and analysed with a 100-channel pulse height analyser. The pile-up from inelastic scattering was reduced by surrounding the crystal with 5 mm of lead. The detector was shielded against the direct radiation from the radioactive source with a cone of heavy alloy which attenuated them by a factor of about 10^6. The source holder, shielding cone, scatterer and detector had a common axis.

The scattering angle was changed by moving the scatterer relative to source and detector. The scatterers were interchanged every five minutes. The incident radiation being a mixture of 961 kev and 840 kev gamma rays, the elastic scattering

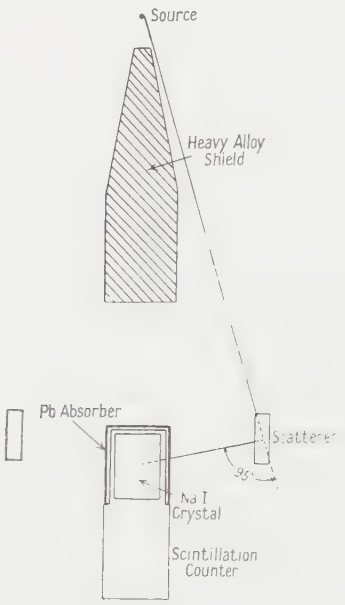

Figure 1. Experimental arrangement. The relative position of the source, scatterer and detector shown corresponds to a mean scattering angle of 95°.

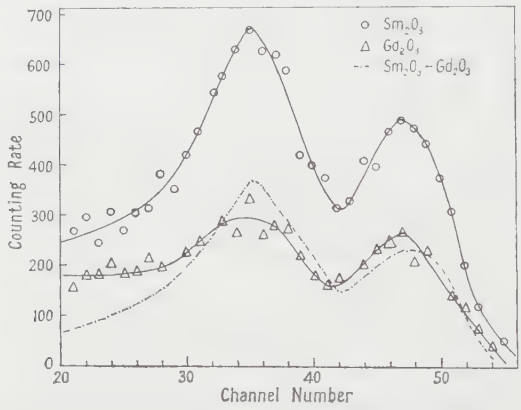

Figure 2. Energy spectra of the radiation scattered through 95° from the resonant (Sm_2O_3) and comparison (Gd_2O_3) scatterers as recorded by multichannel pulse height analyser. The difference spectrum gives the contributions of the resonance and fluorescence intensities.

from Sm_2O_3 contained 961 kev resonance, 840 kev fluorescence and Rayleigh–Thomson scattering of both, whereas the comparison scatterers of TaC or Gd_2O_3 gave rise only to Rayleigh–Thomson components. The difference between the scattering from Sm_2O_3 and TaC or Gd_2O_3 scatterers gave the contribution of

resonance and fluorescence intensity; the scatterers being matched for equal non-resonant scattering. Typical spectra of the radiation scattered at 95° from Sm_2O_3 and Gd_2O_3 are shown in figure 2. Two independent experiments were performed; in the first TaC, and in the second Gd_2O_3, was used as the comparison scatterer. In all, six sources were used and measurements were made at angles of 57°, 70°, 95°, 130° and 152°. The sequence of observations was so arranged that the source decay corrections were eliminated.

§ 3. Results and Discussion

^{152}Sm is an even–even nucleus; the systematics of this type of nucleus shows that the ground state is 0^+ in all cases and the first excited state is 2^+ in almost all cases (there being five exceptions: ^{16}O, ^{40}Ca, ^{72}Ge, ^{90}Zr and ^{208}Pb). Coulomb excitation of the 122 kev level in ^{152}Sm is in agreement with the systematics of even–even nuclei. The spin and parity assignments of 0^+ to the ground state, 2^+ to the first excited 122 kev state, and the lifetimes of the order of 10^{-13} sec of the resonance and fluorescence transitions (Shute and Sood 1960) with low conversion coefficient approximately 10^{-3} (Nathan and Waggoner 1957) make it very unlikely that the 961 kev state will have spin and parity other than 1^-. The ratio of the intensities of the resonance and fluorescence radiation, on this assumption, is proportional to

$$\frac{[1+0{\cdot}5P_2(\cos\theta)]}{[1+0{\cdot}05P_2(\cos\theta)]} \quad \text{where } [1+0{\cdot}5P_2(\cos\theta)] \text{ and } [1+0{\cdot}05P_2(\cos\theta)]$$

represent the angular correlation in its standard form for 0(1)1(1)0 (resonance) and 0(1)1(1)2 (fluorescence) cascades respectively. The experimental data are compared with the theoretical curve in figure 3. A good agreement of experiment with theory supports this assignment. In order to ensure that the only

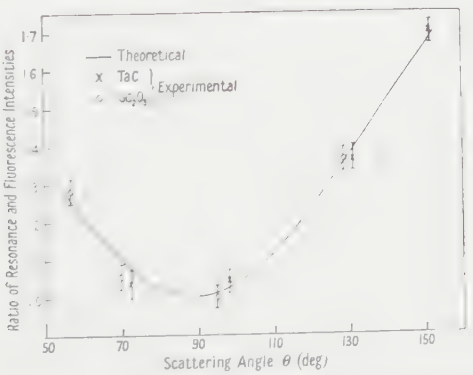

Figure 3. The ratio of the intensities of the 961 kev resonance and 840 kev fluorescence radiation at various angles. The experimental points were obtained with TaC and Gd_2O_3 as comparison scatterers.

cascades that agree with the experimental data are the ones given above, calculations were made for other possible dipole and quadrupole cascades (higher multipoles were not considered because of the short lifetimes involved) representing resonance and fluorescence transitions, on the assumption that the 961 kev could have spins 1 or 2; the experimental data did not fit any spin sequence

other than 0(1)1(1)0 and 0(1)1(1)2. The assignment of even parity to the 961 kev state is contradicted by the short lifetimes, of the order of 10^{-13} sec, and low conversion coefficients approximately $1{\cdot}4 \times 10^{-3}$, for both the resonance and fluorescence transitions. It is, therefore, concluded that both the resonance (0^+–1^-–0^+) and the fluorescence (0^+–1^-–2^+) radiation in ^{152}Sm are electric dipoles.

Acknowledgments

It is a great pleasure to thank Professor P. B. Moon for his help and advice. A research fellowship from the University of Birmingham is gratefully acknowledged.

References

Alder, K., Bohr, A., Huus, T., Mottleson, B., and Winther, A., 1956, *Rev. Mod. Phys.*, **28**, 432.

Grodzins, L., and Kendal, H., 1956, *Bull. Amer. Phys. Soc.*, **1**, 163.

Metzger, F. R., 1959, *Progr. Nucl. Phys.*, **7**, 53.

Nathan, O., and Waggoner, M. A., 1957, *Nucl. Phys.*, **2**, 548.

Shute, G. G., and Sood, B. S., 1960, *Proc. Roy. Soc.* A, **257**, 52.

Wood, G. T., 1959, *Phys. Rev.*, **116**, 1499.

Wood, G. T., and Nathan, O., 1959, *Proc. of the International Conference on Nucl. Phys.* (London: Crosby Lockwood), p. 861.

An Investigation of the Cubic–Hexagonal Transition in Barium Titanate

By R. M. GLAISTER† and H. F. KAY
H. H. Wills Physical Laboratory, University of Bristol

MS. received 25th February 1959, in revised form 23rd May 1960

Abstract. Normal perovskite-type barium titanate may be converted to the hexagonal polymorph by firing in a hydrogen atmosphere at 1330 °c, 130 ° lower than that previously reported for firing in air. With suitable additives such as $MnCO_3$ the conversion begins at temperatures as low as 1100 °c. Conversion is inhibited by a number of impurities, especially Si, Fe and Sr, such as are present in barium titanate of commercial quality.

The effect of atmospheres of hydrogen and oxygen on the rate of reconversion to the cubic polymorph has also been studied. In hydrogen this reaches a peak rate at about 1200 °c, while in oxygen it rises continuously.

All the phenomena associated with the transition appear to be compatible with a proposed hypothesis about the dependence of free energy on vacancy concentration.

The hexagonal polymorph has a permittivity of about 440 and a temperature coefficient of $+0{\cdot}0028\,(\text{deg c})^{-1}$.

§ 1. Introduction

Barium titanate is polymorphic. The perovskite-type form is normally employed in dielectric applications, but for barrier-layer dielectrics‡ the hexagonal form has been found preferable. The nature of the relationship between these two forms may be better understood by a study of the transition between them. It seemed possible, from some preliminary observations, that departures from stoichiometric compositions, in particular the effect of oxygen vacancies, might influence this. To study this, experiments were carried out to determine the course of the conversion of nearly pure material in atmospheres of oxygen and hydrogen, and to compare these with materials containing small additions of selected impurities. From the results it is possible to draw conclusions about the role of oxygen vacancies, which can be described in terms of free energy curves for the material.

It should be noted that the perovskite-type form itself undergoes a transition, being cubic above 120 °c and tetragonal below. This change is reversible, and the cubic form cannot be retained by quenching; hence the existence of the cubic form at the firing temperature is deduced from the experimental observation of the tetragonal form at room temperature.

The opportunity has been taken to describe the dielectric properties of hexagonal barium titanate.

† Now with G. V. Planer Ltd., Sunbury-on-Thames, Middlesex.

‡ Barrier-layer dielectrics are those exhibiting an anomalously high dielectric constant as a result of continuous thin layers of low-loss dielectric enclosing regions of high conductivity. With the present materials the dielectric consists of sintered grains with a stoichiometric surface enclosing a semiconducting reduced core (Glaister 1957).

§ 2. Literature Survey

A hexagonal polymorph of $BaTiO_3$ was first reported by Bourgeois (1883), and subsequently by Megaw (1946) and Blattner, Matthias and Merz (1947). Burbank and Evans (1948a) reported it as having the hexagonal space group $C6_3/mmc$ and subsequently described the detailed structure (1948b). In a detailed phase diagram for the system BaO–TiO_2 Rase and Roy (1952a) suggest that for stoichiometric $BaTiO_3$ in air the hexagonal polymorph is stable relative to the cubic form above 1460°c, but that this temperature rises steeply to 1600°c for a 2% molar excess of TiO_2, while it is unaffected by up to 16% molar excess of BaO. Since most preparations involving equimolar starting materials ($BaCO_3$: TiO_2) result in a slight excess ($\frac{1}{2}$–1%) of TiO_2, these are likely to have a transition temperature in excess of 1460°c. By quenching from above this temperature it is possible to preserve the hexagonal phase which has subsequently to be fired above about 1050°c (Burbank and Evans 1948b) for a considerable period for reconversion to the cubic polymorph. Thus $BaTiO_3$ crystals grown from a pure melt (melting point 1618°c) by the Stockbarger process are hexagonal. According to de Bretteville (1953) this can be prevented by the addition of a few per cent of $SrTiO_3$. De Vries and Roy (1955) have also shown that a small replacement of Ba by Ca results in a sharp increase in transition temperature.

§ 3. Experimental Procedure

3.1. *Preparation of Pure Specimens*

Experiments were conducted on the materials shown in table 1 which had the spectroscopic analyses shown in table 2.

Ceramic plates were made by pressing 2–3 g of $BaTiO_3$ mixed to a stiff paste with Analar acetone in a 5 cm × 1 cm stainless steel die under a load of 4 tons, the pressure being released slowly. Specimens to be fired in hydrogen were placed in molybdenum boats with lids, and those in oxygen on 5 cm × 1 cm refractory thoria plates. Specimens were fired at various temperatures in hydrogen or

Table 1. Physical Properties of Barium Titanate Materials used in this Work

Material number	Supplier	Batch	Date received	BaO/TiO_2 ratio	Particle size (μ)	x-ray analysis
T2†	B.T.P.	Ticon (B)2	1953	—	1	Tetragonal
T3	B.D.R.	90	1953	—	2	Fuzzy cubic
T6	P.	C65A	1956	1·01	6	Fuzzy cubic
T8	B.D.R.	1/127	1956	—	1	Fuzzy cubic
T9	P.	C70	1957	0·995	6	Fuzzy cubic

B.T.P.: British Titan Products Co. Ltd.; B.D.R.: British Dielectric Research Ltd.; P.: Plessey.

† Material T2 exhibited solarization (Weyl and Förland 1950), becoming pink on exposure to a few hours of daylight.

Table 2. Spectroscopic Analyses of Barium Titanate Materials

Material number	Al(%)	Ca(%)	Cr(%)	Cu(%)	Fe(%)	Mg(%)	Na(%)	Si(%)	Sn(%)	V(%)
T2	0·10	0·10	<0·01	0·01	0·02	0·01	0·10	0·20	0·002	<0·01
T3	0·01	0·08	<0·01	0·01	0·01	0·05	<0·01	0·003	0·006	0·01
T6	<0·01	0·01	<0·01	<0·01	<0·01	<0·01	<0·01	<0·01	<0·01	<0·01
T8	0·01	0·03	<0·01	<0·01	0·01	0·01	<0·01	<0·01	0·01	0·02

Material T9 made to same specification as T6.

oxygen in a platinum-wound tube furnace normally for 5-hour periods, an automatic programme controller being used. On cooling, the density (from dimensions and mass) and linear shrinkage (in the 5 cm direction) were measured.

3.2. *Preparation of Specimens with Controlled Impurity*

Additions of Al_2O_3, Na_2CO_3, SiO_2, Fe_2O_3, FeO, NiO and $MnCO_3$ were made to pure $BaTiO_3$ from batches T8 and T9. The additions were mixed thoroughly in a glass mortar, the use of a ball-mill being avoided to prevent the contamination it is known to introduce. Ceramic plates were then made as for the pure material.

When only the crystallographic form of a fired mixture was required samples of powder were fired in small platinum boats.

3.3. *Temperature Control and Measurement*

The furnace temperature was controlled by a Pt–(Pt 87% Rh 13%) thermocouple placed directly over the specimen and connected to an Elliott recording potentiometer fitted with a semi-proportional programme controller, the cold junction being kept in melting ice.

The main error was introduced by the temperature ripple resulting from the action of the controller. This had an amplitude of about 4°. The recorder was calibrated against a National Physical Laboratory standard cell and was correct to within $\pm 1°$. Further errors arose from the temperature gradient caused by the gas flow and the absolute accuracy of the thermocouple. The errors are estimated to total about $\pm 5°$.

3.4. *X-ray Identification Technique*

The relative proportions of crystal phases were obtained non-destructively by placing ceramic specimens on a Geiger counter diffractometer employing Cu K_α radiation. In some cases relatively large hexagonal crystals were found to be embedded in a fine-grain ceramic matrix of tetragonal material. These gave rise to a spurious distribution of intensities in relation to intensities expected from a uniform distribution of the two phases, making assessment of the hexagonal-to-tetragonal ratio difficult. In such cases samples were powdered and assessed by means of a Guinier quadruple-exposure monochromator camera. A series of standards were made from mixtures of the hexagonal and tetragonal polymorphs.

§ 4. Cubic to Hexagonal Transition

Pure $BaTiO_3$ (T6) fired for 5 hours in hydrogen at temperatures below 1330 c was tetragonal at room temperature, and hence must have been cubic at the firing temperature, although the ceramic was slightly reduced and grey in colour. Samples fired at temperatures above 1330 c consisted of the hexagonal polymorph, while one sample fired at 1330 c showed tetragonal and hexagonal phases in coexistence.

A series of samples (T9) fired at 1347°c for different periods showed an increasing proportion of the hexagonal phase, no tetragonal phase being detected after 1 hour, as shown in figure 1. A conversion of 50% was obtained in only 6 minutes, so the transition temperature obtained from 5-hour firing periods should be quite accurate. Thus the transition temperature in hydrogen was established as 1330 ± 5°c.

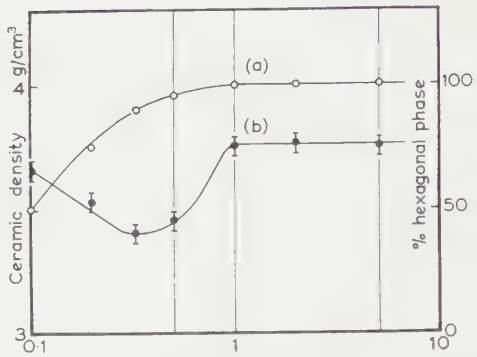

Figure 1. Influence of firing duration (in hours) in hydrogen atmosphere at a constant temperature (1347°c) on cubic barium titanate ceramic. Curve (*a*) shows the percentage conversion to the hexagonal polymorph, and curve (*b*) the ceramic density. The vertical strokes show the estimated limits of error in the density measurements.

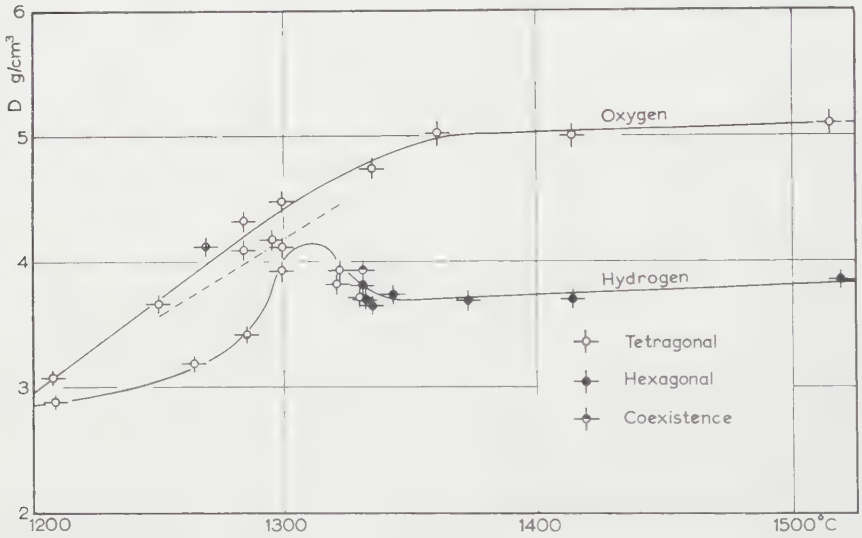

Figure 2. Effect of firing temperature on density *D* of barium titanate ceramic prepared by sintering powder compresses for 5-hour periods in hydrogen or oxygen atmospheres. The chain line separates results obtained in hydrogen and oxygen.

The transition was found to be accompanied by a fall in the density of the ceramic, as illustrated by the graphs of density against time and against temperature in figures 1 and 2 respectively. It was also found that samples fired in hydrogen had a lower density than samples fired in oxygen at the same temperature. Three factors may contribute towards this; these are oxygen loss, a difference in density between the polymorphs, and crystal growth.

Measurements of weight loss during firing in hydrogen showed that the oxygen loss was normally less than 0·5 mol%, so would make a negligible contribution to density change. The single-crystal densities of the two polymorphs calculated from their published lattice parameters (Megaw 1947, Burbank and Evans 1948 b) are 6·10 and 5·80 g/cm³ for the tetragonal and hexagonal modifications respectively. This difference is sufficient to account for most of the observed difference, the balance probably being accounted for by crystal growth.

The same transition temperatures for various conditions were found with materials T8 and T9, although these were not obtained so accurately.

§ 5. Transition Catalysers

When certain impurities enter into solid solution with a host oxide, oxygen is displaced in order to maintain electroneutrality; the effect is thus analogous to firing in hydrogen and might therefore be expected to encourage transition to the hexagonal polymorph. The effect of additions of FeO, MnO (as $MnCO_3$) and NiO to sample T8 was investigated with the results recorded in table 3.

Table 3. Transition Catalysers: The Percentage of Hexagonal Polymorph resulting on firing Mixes for 5 hours in Oxygen at the Temperature stated

Temperature (°c)	1000	1100	1150	1200	1250	1300	1350	1400
Addition:								
2 Mol% FeO	—	—	—	—	—	0	0	0
10 Mol% FeO	—	—	—	—	—	0	0	50
2 Mol% NiO	—	—	—	—	—	0	0	0
10 Mol% NiO	—	—	—	—	—	0	0	50
2 Mol% $MnCO_3$	0	2	5	10	25	50	75	75
10 Mol% $MnCO_3$	0	5	25	50	90	100	100	100

From this it is apparent that while Fe, Mn and Ni all catalyse the transition, Mn is by far the most efficient. Mn has valencies of 2, 3, 4, 6 and 7 with ionic radii (Pauling) of 0·80, ~0·64, 0·50, ~0·48, 0·46 Å respectively, compared with 0·64 Å for Ti^{4+}. Possibly Mn^{3+} replaces Ti^{4+}, but in this case Fe^{3+} (0·67 Å) should be just as effective. Probably the decomposition of $MnCO_3$ leaves the oxide in a more reactive form.

The colour of the resulting material darkened as the firing temperature was increased and all additions produced a similar range of colours. These are probably indicative of a gradually increasing oxygen-vacancy concentration.

The most interesting feature is, however, that the transition may take place at temperatures as low as 1100 °c. This suggests that it may be the concentration of oxygen vacancies that determines the stable polymorphic form.

§ 6. Transition Inhibitors

Samples of T2 and T3, fired simultaneously for 5 hours at 1400 °c in hydrogen, were found to be tetragonal and hexagonal respectively. The former material had a considerably higher impurity concentration of Al, Na and Si and a slightly higher concentration of Fe, than the latter, cf. table 2.

The effect of small additions of Al, Na, Si and Fe, added as the oxide or carbonate, was examined with materials T9 and T8. These experiments are summarized in table 4. From this it may be seen that while Si and Fe had a considerable inhibiting action on material T8, only the former had any effect on material T9. The larger particle size of material T9, which did not allow a sufficiently homogeneous solid solution to be formed within the firing time, is probably responsible for this difference.

It seems highly probable that the SiO_2 content was responsible for inhibiting the transition in material T2.

A strontium content of less than 1% has also been found sufficient to inhibit the transition, even when fired at 1500°c in hydrogen.

Table 4. Transition Inhibitors

				Result		
(1)	(2)	(3)	(4)	(5)	(6)	(7)
T9	1347	0	None	3·74	6·0	100 : 0
	1347	1	SiO_2	4·68	13·6	100 : 0
	1347	3	SiO_2	4·93	15·0	60 : 40
	1347	1	Al_2O_3	4·49	10·2	100 : 0
	1347	1	Na_2CO_3	4·58	10·8	100 : 0
	1347	2	FeO	4·65	11·0	100 : 0
T8	1353	0	None	5·12	17·6	100 : 0
	1347	2	FeO	5·64	20·2	0 : 100
	1347	3	SiO_2	5·32	18·0	5 : 95
	1414	2	FeO	†	—	100 : 0
	1414	3	SiO_2	†	—	100 : 0

Samples fired for 5 hours in hydrogen.

† Fired as powder. (1) $BaTiO_3$ sample number; (2) firing temperature (°c); (3) mol%; (4) additive; (5) density (g cm^{-3}); (6) shrinkage (%); (7) crystalline form, ratio of hexagonal to tetragonal phase present.

§ 7. Reconversion of the Hexagonal Polymorph to Cubic

A number of second firing treatments were given to hexagonal T9 ceramic to establish the reconversion conditions. These are summarized in table 5.

Table 5. Reconversion of the Hexagonal Ceramic to Cubic

(1)	(2)	(3)	(4)	(5)
1015	20	0	0	—
1090	20	0	10	—
1145	20	25	25	—
1200	5	50	100	50
1250	5	—	—	0
1300	5	0	100	0
1400	2[a]	—	100	—

(1) Temperature (°c); (2) time (hrs); (3), (4), (5) percentage reconversion: (3) cylinder hydrogen[a]; (4) cylinder oxygen; (5) purified hydrogen prepared by passing cylinder hydrogen through Baker ' Deoxo ' catalytic purifier and drying tower to remove oxygen and water vapour, (a) brought up to 1400°c in hydrogen so that structure remained hexagonal. Atmosphere successively changed through nitrogen to oxygen. After 2 hours quenched into water at 15°c within 2 seconds.

From this it may be seen that conversion in oxygen commences at about 1090°c and becomes rapid at 1200°c. Conversion in hydrogen reaches a maximum rate at 1200°c before falling off to zero as the 1300°c transition temperature is approached.

It was at first thought possible that the oxygen content of the cylinder hydrogen might be responsible for the reconversion in this atmosphere. However, the experiments with purified hydrogen show this not to be the case.

The result of the quenching experiment (table 5, note (a)) shows that hexagonal $BaTiO_3$ is stable above 1330°c only in the presence of a hydrogen atmosphere.

An experiment was carried out to see if reconversion could be effected in a manner analogous to that observed in ZnS. The normal form of ZnS, sphalerite, is cubic and undergoes transition at 1020°c to a hexagonal form wurtzite, which may be reconverted by grinding (Schleede and Gantzckow 1923, Fuller 1929, Frey 1948, Short and Steward 1955) or by the application of high pressure (Bridgman 1939).

Two hexagonal $BaTiO_3$ powder samples, one of which had been re-oxidized at 800°c and was a light green in colour, were each powdered energetically for 15 minutes with an agate mortar and pestle. In neither case did x-ray powder photographs show any detectable change. Such treatment has been found (Short 1957, private communication) to produce the onset of conversion in ZnS. Similar negative results were also obtained after ball-milling for 48 hours.

§ 8. Dielectric Properties of the Hexagonal Polymorph

Some observations on dielectric properties may conveniently be recorded here, though they are not used in the subsequent argument.

Barrier-layer dielectrics based on the hexagonal polymorph show no dielectric anomalies within the temperature range −183°c to 100°c, and the intrinsic loss is evidently much lower than that of the ferroelectric polymorph. A further advantage of the hexagonal form is the elimination of complex behaviour of resistivity against temperature associated with the Curie temperature of the ferroelectric form.

Measurements of the intrinsic dielectric properties of stoichiometric hexagonal barium titanate are made difficult by the fact that re-oxidation even at temperatures near the reconversion temperature is excessively slow.

A disc of To ceramic obtained by firing in hydrogen for two hours at 1400°c, was re-oxidized for 60 hours at 1000°c. The ceramic was red-brown in colour and still had a loss tangent of 0·1. The dielectric properties for this sample are shown in figure 3. The ceramic had a density defect porosity of 38%. Applying the correction due to Van Santen (1946) this gives a true permittivity 2·32 times as great as the apparent value. Thus the true permittivity at 20°c is approximately 440. The dielectric has a positive temperature coefficient $(1/K)dK/dt$ of 0·0028 deg^{-1}.

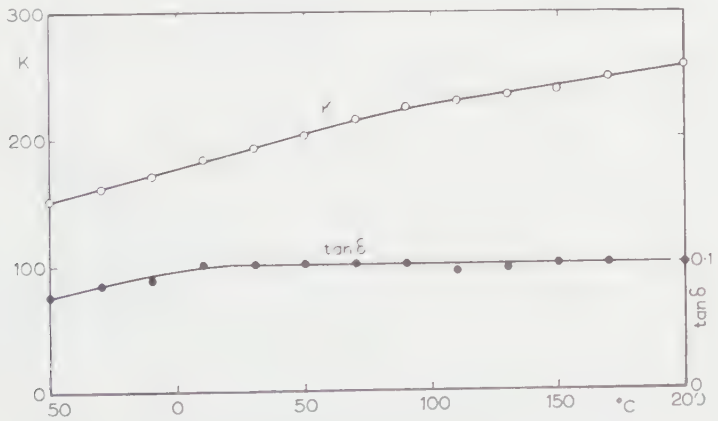

Figure 3. Variation of permittivity K and loss tangent tan δ with temperature for slightly non-stoichiometric barium titanate of the hexagonal polymorph.

§ 9. Summary of Experimental Conclusions

(i) The cubic–hexagonal transition occurs at 1330 ± 5°c in hydrogen, a much lower temperature than in oxygen (1460°c).

(ii) The transition in hydrogen is rapid; at 1347°c it is complete in 1 hour.

(iii) The transition is accompanied by a fall in the density of the ceramic, largely due to the density difference between the polymorphs.

(iv) The impurities commonly found in commercial 'pure' materials may inhibit this transition, or raise it towards the oxygen transition temperature.

(v) The transition may also be catalysed at temperatures as low as 1100°c with suitable additions, Mn being particularly efficacious. These are additions causing deficiency of oxygen.

(vi) Reconversion to the cubic polymorph commences at about 1090°c in oxygen and becomes rapid at 1200°c. Reconversion in hydrogen commences at a similar temperature and reaches a peak rate at 1200°c before falling to zero as the 1330°c transition temperature is approached.

(vii) The hexagonal polymorph is stable in oxygen or air above 1460°c, and in hydrogen above 1330°c. It is metastable in all these atmospheres below about 1000°c.

(viii) Powdering the hexagonal material does not cause reconversion.

§ 10. Discussion

The above conclusions all appear to be compatible with the simple hypothesis illustrated by figure 4. The free energy G of the hexagonal polymorph aa′ in figure 4 is reduced by the presence of oxygen vacancies to bb′ and cc′ as the number of vacancies increases. Thus the point of intersection of free energy curves for hexagonal and cubic polymorphs is depressed to lower temperatures.

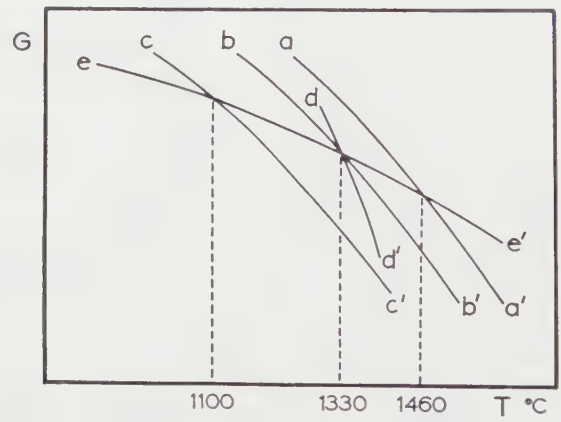

Figure 4. Postulated curves of free energy G for barium titanate showing effect of vacancy concentration. Curve ee′ shows the free energy of the cubic polymorph. Curves aa′, bb′ and cc′ show the free energy of the hexagonal polymorph with increasing oxygen vacancy concentration. Curve dd′ shows the free energy of the hexagonal polymorph in equilibrium with an atmosphere of hydrogen.

In a hydrogen atmosphere the equilibrium vacancy concentration increases with increasing temperature in such a way that at 1330°c sufficient vacancies are available to cause the conversion, that is the hexagonal phase lies along bb′.

This variation of vacancy concentration with temperature will cause the free energy curve to depart from the curve bb′ corresponding to a fixed vacancy level, the steeper curve dd′ representing the free energy of hexagonal barium titanate in equilibrium with a hydrogen atmosphere.

When a vacancy concentration is induced by suitable additives the transition temperature may be made as low as 1100°c, curve cc′ figure 4.

The hexagonal phase may be preserved at room temperature by quenching from above 1330°c in hydrogen or 1460°c in oxygen. Reconversion takes place slowly at low temperatures well below 1330 c, for a latent heat is required for this first-order transition. Reconversion at temperatures well below 1330°c takes place at similar rates in oxygen and hydrogen because the hydrogen equilibrium concentration of vacancies is so small as not to influence the rate of reconversion. Reconversion of hexagonal material between 1330 and 1460 c will proceed more rapidly in oxygen while ceasing altogether in hydrogen, because in hydrogen the hexagonal material is the stable phase.

The mechanism of transition-inhibiting impurities may be two-fold. They may reduce the equilibrium oxygen vacancy concentration at a given temperature, thus increasing the free energy of the hexagonal phase and the transition temperature. Alternatively they may raise the intrinsic free energy of the hexagonal polymorph. Rase and Roy (1955 b) in a phase diagram for the system $BaTiO_3$–SiO_2 show that the normal transition temperature rises linearly with SiO_2 content up to 1575 c at 4 mol %, while de Vries and Roy (1955) find a similar effect in the system $BaTiO_3$–$CaTiO_3$.

Thus the mechanism of a vacancy-sensitive free energy for the hexagonal polymorph appears to explain the observed phenomena.

References

Blattner, H., Matthias, B., and Merz, W., 1947, *Helv. Phys. Acta*, **20,** 225.
Bourgeois, L., 1883, *Z. Krist.*, **14,** 280.
de Bretteville, A. P., 1953, *Ceramic Age*, **62,** 4, 18.
Bridgman, P. W., 1939, *Amer, J. Sci.*, **237,** 7.
Burbank, R. D., and Evans, H. T., 1948 a, *J. Chem. Phys.*, **16,** 634.
—— 1948 b, *Acta Cryst.*, **1,** 330.
Frey, F., 1948, *Ann. Phys., Lpz.*, **2,** 147.
Fuller, M. L., 1929, *Phil. Mag.*, (7), **8,** 658.
Glaister, R. M., 1957, *Ph.D. Thesis*, University of Bristol.
Megaw, H. D., 1946, *Proc. Phys. Soc.*, **58,** 133.
—— 1947, *Proc. Roy. Soc.* A, **189,** 261.
Rase, D. E. and Roy R., 1955 a, *J. Amer. Ceram. Soc.*, **38,** 102.
—— 1955 b, *Ibid.*, **38,** 389.
Schleede, A., and Gantzckow, H., 1923, *Z. Phys. Chem*, **106,** 37.
Short, M. A., and Steward, E. G., 1955, *Acta Cryst.*, **8,** 733.
Van Santen, J. H., 1946, *Trans. Faraday Soc.*, **42A,** 249.
de Vries, R. C., and Roy, R., 1955, *J. Amer. Ceram. Soc.*, **38,** 142.
Weyl, W. A., and Förland, T., 1950, *Indust. Engng. Chem.*, **42,** 257.

RESEARCH NOTES

The Effect of Attenuation on the Acoustic Resonant Frequencies of Gases in Tubes

By H. J. WINTLE†

Department of Physics and Telecommunications, Woolwich Polytechnic, London

MS. received 16*th June* 1960

Abstract. The change in the resonant frequencies of a sound tube due to the dependence of attenuation on frequency is worked out for two cases of practical interest. The effect on measured values of the velocity of sound is shown to be significant in accurate work.

RECENTLY some accurate values for the velocity of sound in gases have been reported (Harlow 1954, Wintle 1959 a, b, Smith and Wintle 1960, Smith and Harlow, to be published). The method used was to excite plane waves at constant amplitude from a loudspeaker at one end of a sound tube which had a reflector at the other end, and to measure the current required to maintain this amplitude as the frequency was changed by steps in the neighbourhood of a resonance of the gas column. The specific acoustic impedance at the flat face of the loudspeaker has the value (Zwikker and Kosten 1949)

$$\frac{p}{v} = \frac{i\omega\rho}{q}\coth ql$$

where p is the pressure amplitude, v the particle velocity, $q = \alpha + i\beta$ is the propagation constant, α the amplitude attenuation per unit length, $\beta = \omega/c$ is the wavelength coefficient, c the speed of sound in the tube, l the length of the tube, ω the angular frequency and ρ the average density of the gas.

The amplitude is maintained at a constant value a_0 by the method described by Smith (1945), so that

$$\frac{p}{i\omega a_0} = \frac{i\omega\rho}{q}\coth ql$$

or

$$\frac{p}{i\omega a_0} = \frac{c\rho}{1+\alpha c/i\omega}\coth ql.$$

The force exerted on the loudspeaker by the current I is proportional to the current, so that in steady oscillation $p \propto I$ and therefore

$$E = \frac{I}{f} \propto \frac{\coth ql}{1+\alpha c/i\omega} \qquad \ldots\ldots(1)$$

where f is the frequency of oscillation.

† Now at Physics Branch, Royal Military College of Science, Shrivenham, Swindon, Wilts.

The function coth ql executes a circle in the complex plane, shown in figure 1, when the variations of c and α with frequency are neglected. The maximum value corresponding to point A occurs when $\cos 2\beta l = -1$, that is when

$$\frac{4\pi f l}{c} = 2n\pi \quad (n \text{ integral}). \qquad \ldots\ldots(2)$$

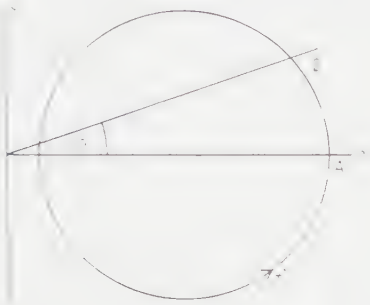

Figure 1. The function coth ql.

The experimental values of I/f contain a contribution from the transfer impedance of the loudspeaker, but by drawing the circle from a suitably placed origin this can be cast out.

The relation between position and frequency of any point D is given by

$$\tan\phi = \frac{\mathcal{I}(\coth ql)}{\mathcal{R}(\coth ql)} = \frac{\sin 2\beta l}{\sinh 2\alpha l}.$$

Since at the maximum value of coth ql the function $\sin 2\beta l$ vanishes, this expression can be expanded for nearby frequencies when $\alpha l \ll 1$, giving

$$\tan\phi = \frac{2\pi}{c\alpha}(f - f_n). \qquad \ldots\ldots(3)$$

Thus a plot of $\tan\phi$ against f gives both the value of c from the intercept by using equation (2) and the value of α from the slope using equation (3). This is the relation used by Harlow (1954).

The effect of the change in attenuation with frequency is to turn the circle into a low pitched spiral. The frequency f_n found by using equation (3) is that at which the expression (1) has an absolute maximum and this will now be found theoretically and used to apply a correction to equation (2).

The frequency required is given most simply by setting

$$\frac{\partial |E|^2}{\partial \omega} = 0.$$

The value of c which should be used is the tube velocity which is itself frequency dependent. However, since the fractional changes with frequency

$$\frac{1}{\alpha}\frac{\partial \alpha}{\partial f} \quad \text{and} \quad \frac{1}{c}\frac{\partial c}{\partial f}$$

stand in the ratio of 100 : 1 in the work under consideration, the latter can be ignored.

Since
$$E = \frac{\omega}{\alpha + i\omega/c}\frac{(\operatorname{sh} 2\alpha l + i\sin 2\beta l)}{(\operatorname{ch} 2\alpha l - \cos 2\beta l)}$$

then
$$E^2 = \frac{1}{1 + (\alpha c/\omega)^2}\frac{(\operatorname{sh}^2 2\alpha l + \sin^2 2\beta l)}{(\operatorname{ch} 2\alpha l - \cos 2\beta l)}.$$

By carrying out the differentiation indicated above, approximating the hyperbolic functions by $\mathrm{sh}\,2\alpha l \simeq 2\alpha l$, $\mathrm{ch}\,2\alpha l \simeq 1+(\alpha l)^2/2$, and making the substitution $2\beta l \simeq 2n\pi+\theta$ so that $\sin 2\beta l \simeq \theta$, $\cos 2\beta l \simeq 1-\theta^2/2$, we obtain

$$2\left(1+\left(\frac{\alpha c}{\omega}\right)^2\right)\left(2\alpha l c\frac{\partial\alpha}{\partial\omega}+\theta\right)=\left(\frac{\alpha c}{\omega}-c\frac{\partial\alpha}{\partial\omega}\right)(4\alpha^2l^2+\theta^2)\,\frac{c^2\alpha}{\omega^2 l}.$$

Now $(\alpha c/\omega)^2 \leqslant 10^{-4}$ and can be ignored, so

$$\theta \simeq -2\alpha l c\frac{\partial\alpha}{\partial\omega}+\tfrac{1}{2}\frac{\alpha c^2}{l\omega^2}\left(\frac{\alpha c}{\omega}-c\frac{\partial\alpha}{\partial\omega}\right)(4\alpha^2l^2+\theta^2).$$

The first and second terms have magnitudes of about 10^{-5} and 10^{-11}, so only the first need be retained. The result may be stated thus

$$4\pi f l/c = 2n\pi+\theta,$$

where

$$\theta = -\frac{\alpha c l}{\pi}\frac{\partial\alpha}{\partial f}.$$

The simple theory gives the value

$$4\pi f l/c' = 2n\pi,$$

so that

$$c = c'(1+\theta/2n\pi)^{-1}.$$

The correction to the velocity arising from the frequency dependence of the attenuation is therefore

$$-\frac{c'\theta}{2n\pi}=\frac{\alpha cc' l}{2\pi^2 n}\frac{\partial\alpha}{\partial f}\simeq\frac{\alpha c^2 l}{2\pi^2 n}\frac{\partial\alpha}{\partial f}.$$

This leads directly to the formula quoted by Smith and Wintle (1960). In the experiments under consideration there are two main contributions to the attenuation due to the Helmholtz–Kirchhoff and relaxation effects. It has been shown that they add linearly at low frequencies (Wintle 1959 a, b, Smith and Wintle 1960). In the notation given in these references

$$\alpha_{\mathrm{HK}} = gf^{1/2},$$
$$\alpha_{\mathrm{r}} = H\tau f^2,$$

whence the corrections to the velocity found from equation (2) are

$g^2c^2l/4\pi^2n$ (Helmholtz–Kirchhoff)
and $c^5n^2H^2\tau^2/8\pi^2l^2$ (relaxation).

The cross product term can be neglected.

The quantities g and $H\tau$ are experimentally determined at the same time as the velocity measurements are taken. In the work referred to, the numerical values of the corrections are about $1/n$ cm sec^{-1} and $4n^2\times10^{-4}$ cm sec^{-1}, which means that the velocity results quoted by Harlow at the lowest frequency he used should be increased by about 1 cm sec^{-1}. This is of the same order as his experimental error at this frequency, and will have no effect on the final velocities he quoted. The sum of the terms is rather less than the experimental error quoted by Wintle for relaxing gases.

A similar calculation for the method used by Lee (1957), in which the particle velocity in the middle of a resonance tube is found, does have more significance. The formula which he employs runs

$$\xi_{(1/2)}/\xi_{(0)} = 2\,\mathrm{sech}\,\tfrac{1}{2}ql,$$

where $\xi_{(l\,2)}$ and $\xi_{(0)}$ are the particle velocity amplitudes at the mid-point of the tube and at the loudspeaker face respectively. On varying the frequency, the function sech $\frac{1}{2}ql$ goes through a dumb-bell figure in the complex plane which can be closely approximated by two adjacent circles as shown in figure 2. The maxima at points A and B occur near frequencies such that $c = \frac{1}{2}(2n-1)fl$ (n integral), and this relation was used by Lee. Detailed calculation allowing for the variation of attenuation with frequency yields the relation between the actual tube velocity and that calculated from the simplified relation above

$$c = c'\left(1 - \frac{c\alpha l}{2\pi^2(2n-1)}\frac{\partial\alpha}{\partial f}\right).$$

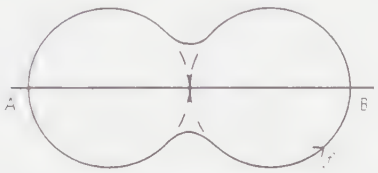

Figure 2. The function sech $\frac{1}{2}ql$.

Using Lee's smoothed value for the attenuation coefficient, $\alpha = 1{\cdot}88 \times 10^{-5} f^{1/2}$ c.g.s. units, the numerical value of the correction is $-1{\cdot}7/(2n-1)$ cm sec^{-1}. The mean values of the velocity of sound which he quotes for each experimental frequency (his table 6) are shown with the corrected values in the table. It is clear that the discrepancy which he noted between the results at the lowest frequency and the remainder is practically removed when this correction is taken into account.

Velocity of Sound in Dry Air free from Carbon Dioxide

Temperature 30°c, pressure 1 atmosphere.

Frequency (c/s)	n	Lee (m sec^{-1})	Corrected (m sec^{-1})
110	1	349·25	349·23
332	2	349·21	349·20
554	3	349·217	349·214
776	4	349·22	349·22
998	5	349·21	349·21
		Final average	349·21

Acknowledgments

The author wishes to thank the Governing Body of the Woolwich Polytechnic for providing facilities for the research, the London County Council for awarding an Assistantship and Dr. D. H. Smith for his constant encouragement.

References

Harlow, R. G., 1954, *Ph.D. Thesis*, London University.
Lee, T. A., 1957, *Ph.D. Thesis*, London University.
Smith, D. H., 1945, *Proc. Phys. Soc.*, **57**, 534.
Smith, D. H., and Wintle, H. J., 1960, *J. Fluid Mech.*, **9**, 29.
Wintle, H. J., 1959 a, *M.Sc. Thesis* London University.
—— 1959 b, *Nature, Lond.*, **184**, 2007.
Zwikker, C., and Kosten, C. W., 1949, *Sound Absorbing Materials* (Amsterdam: Elsevier).

Nuclear Resonance Absorption of Ultrasound in KI and KBr

By G. S. VERMA and S. K. JOSHI
Physics Department, Allahabad University, India

MS. received 23rd May 1960

Recently Kessel (1959) has given a theory of resonance absorption of ultrasound in paramagnetic nuclei in a cubic lattice assuming that the spin–lattice interaction is due to nuclear quadrupole forces. It is interesting to compare his theoretical computations with the recent experimental results of Bolef and Menes (1959) in KI and KBr. Kessel has computed $(\sigma T/\nu)\times 10^{17}$ for various orientations between the direction of propagation of acoustic waves and the magnetic field, here σ is the resonance absorption of ultrasound, T is the temperature and ν is the frequency of ultrasound. Taking average over all directions, $\{(\sigma T/\nu)\times 10^{17}\}_{\text{av}} = 10{\cdot}46$ for KI and 0·16 for KBr, provided we use Kessel's values of γ, where γ is the amplification factor by which quadrupole coupling exceeds that predicted on the basis of a simple ionic point charge model. It may be seen from the table that the agreement between the theory and the experiment is very poor. If we use the values of γ obtained by Bolef and Menes, agreement is much better.

Temperature 300°K

Crystal	Frequency (Mc/s)	σ (theoretical) (cm^{-1})		σ (experimental) (cm^{-1})
^{127}KI	7·91	$2{\cdot}18\times10^{-5}$ ($\gamma=500$, Kessel)	$12{\cdot}6\times10^{-8}$ ($\gamma=38$, Bolef and Menes)	$1{\cdot}4\times10^{-8}$
^{79}KBr	9·75	$5{\cdot}07\times10^{-7}$ ($\gamma=184$, Kessel)	$10{\cdot}1\times10^{-9}$ ($\gamma=26$, Bolef and Menes)	$0{\cdot}6\times10^{-9}$

If, however, we assume that Kessel's theory, which is based on Raman two-phonon process, is correct we can find out the value of γ from the experimentally observed values of σ. Using this procedure, we obtain $\gamma=12{\cdot}67$ for KI and $\gamma=6{\cdot}34$ for KBr. It has been shown by Mieher (1960) that the four-phonon process as proposed by Khutsishvili (1956) does not agree with the observed temperature dependence of the nuclear spin–lattice relaxation time.

References

Bolef, D. I., and Menes, M., 1959, *Phys. Rev.*, **114**, 1441.
Kessel, A. R., 1959, *J. Exp. Theor. Phys., U.S.S.R.*, **36**, 1451 (translation, 1959, *Soviet Phys. J.E.T.P.*, **5**, 1031).
Khutsishvili, G. R., 1956, *J. Exp. Theor. Phys., U.S.S.R.*, **31**, 424 (translation, 1957, *Soviet Phys. J.E.T.P.*, **4**, 382).
Mieher, R. L., 1960, *Phys. Rev. Lett.*, **4**, 57.

Correct Enumeration of Vibration Frequencies in the Brillouin Zone

By B. DAYAL and S. P. SINGH
Department of Physics, Banaras Hindu University, India

MS. received 30*th May* 1960

Abstract. In order to calculate the vibration frequencies by Born's method the Brillouin zone is sub-divided into a number of points. The actual number of frequencies used by the workers for the calculation of C_v is, however, different from the number of points of the zone, resulting in a non-uniform distribution of points. It has been shown that this results in an incorrect value of the specific heat. As an example Hsieh's theoretical results have been used to recalculate the specific heat of silicon with a proper number of frequencies. The difference between these revised results and Hsieh's original calculations is found to be large.

A number of workers who have used Born's theory to calculate the vibration frequencies and specific heat of crystals have found it convenient to use the first Brillouin zone as an alternative to the original formulation of the periodic lattice condition (Kellermann 1940, 1941, Smith 1948, Hsieh 1954). The zone is divided into smaller regions of the same shape as the unit cell of the reciprocal lattice. The points of the new sub-divided lattice define the wave vectors of the vibrations permitted by the Born theory. In view of the fact that crystals so far studied possess high symmetry it is usual to find the vibration frequencies of a much smaller number of points and get the numerical values of other points by symmetry. Obviously, the symmetry conditions must yield the correct number of frequencies corresponding to the sub-division of the Brillouin zone. If this is not so, the resulting frequency spectrum will not be the correct one as envisaged in Born's theory. This point does not seem to have been clearly appreciated by workers generally.

In his first paper on vibration frequencies of rock salt Kellermann (1940) calculated the values of 47 frequencies within the positive octant of the Brillouin zone and assigned the same statistical weight to each of them. Actually, the statistical weight of each frequency is different because some frequencies correspond by symmetry to 48 points, some to 24 points, some to 12 points and so on. In his later paper he seems to have realized his error and has stated that he has taken the statistical weight of each frequency into account. He has not actually stated the statistical weight of each frequency but it is clear that some error has crept in his enumeration of frequencies. He has divided the basic cell vectors of the reciprocal lattice into ten parts so that there should be $10^3 = 1000$ points in the reciprocal space corresponding to 6000 frequencies. The number of frequencies as stated by him, is however, 6700 which is about 11% more than the actual number.

Though Kellermann has not stated the method by which he obtained 6700 frequencies, it is quite probable that the difference has arisen because of the error in the enumeration of the points on the boundary of the zone. To get the correct number of points on the boundary one has to fill the whole space by zone-like polyhedra. The observed number of points on the surface, the edges and the

corners of the zone must be divided by the number of polyhedra which share these points. In this way it is possible to get exactly 1000 points and 6000 frequencies.

If this is the cause of the error it will not greatly effect the value of his calculated specific heat at high temperatures but at low temperatures where zone boundaries do not contribute to specific heat, Kellermann's calculated values will be about 11% lower than those obtainable from a more correct enumeration.

Smith (1948) has not stated the actual number of frequencies used by her though she has stated that she has taken the statistical weight of frequencies into account. On account of sub-division of basic cell vectors of the reciprocal lattice into eight parts she should have got 512 points and 512×6 frequencies including the frequency for the origin. She has not stated the total number of frequencies taken by her so it is not possible to judge whether she considered all the 512 points.

Hsieh (1954) has used Smith's method for the calculation of the vibration frequencies and the specific heat of silicon and germanium, but unlike Smith, has given the same statistical weight to all the frequencies. This method is, obviously, incorrect because it means that his points are not uniformly scattered in the Brillouin zone as they should be on Born's theory. For example, there are some frequencies which correspond to six points and others to forty-eight points of the zone. By giving equal weight to both sets, the density of the first set of points is artificially raised to a very high value. In order to illustrate the error that might arise from an incorrect enumeration we have revised Hsieh's calculations of the specific heat of silicon (next nearest neighbours approximation). In our enumeration the number of points come out to be exactly 8^3, i.e., 512 including the point 0, 0, 0. The specific heats have been calculated by numerical computation. The frequencies have been divided into twenty steps of $\Delta\omega = 0{\cdot}8 \times 10^{13}\,\mathrm{sec}^{-1}$. An Einstein function corresponding to the mid-point of each step multiplied by its statistical weight, gives the contribution of each step to the specific heat. The statistical weight is obtained from the number of points lying in that step. The results of calculation are shown in the table together with those calculated by Hsieh by the equal weight method. It is seen that the difference in the two sets of calculations is very large. The results show an imperative necessity of taking the correct statistical weight of frequency into account while calculating specific heat. We have also given the experimental values of specific heat for comparison. The agreement between calculated and experimental values is extremely poor.

Specific Heats of Silicon

T (deg K)	C_V revised	C_V (equal statistical weight) (Hsieh)	Experimental data†
20	0·0106	0·042	0·024
40	0·141	0·25	0·310
60	0·470	0·627	0·831
80	0·838	1·055	1·36
100	1·190	1·47	1·69

† Pearlman and Keesom (1952).

References

Hsieh, Y. C., 1954, *J. Chem. Phys.*, **22**, 306.
Kellermann, E. W., 1940, *Phil. Trans. Roy. Soc.* A., **238**, 513.
—— 1941, *Proc. Roy. Soc.* A., **178**, 17.
Pearlman, N., and Keesom, P. H., 1952, *Phys. Rev.*, **88**, 398.
Smith, H. M. J., 1948, *Trans. Roy. Soc.* A, **241**, 105.

Calculated Electron Mobility in Hydrogen

By A. E. D. HEYLEN
Electrical Engineering Department, Queen Mary College, London

MS. received 15*th March* 1960, *in revised form* 10*th June* 1960

The application of Boltzmann's equation to the transport of ions in gases has recently been concisely summarized by Allis (1956). By considering the drift velocity to result from a small asymmetry caused by the field in an otherwise spherically symmetrical distribution in velocity space, the electron mobility can be derived as

$$\mu = -\tfrac{1}{3}\int_0^\infty \frac{\epsilon}{N\theta(\epsilon)}\frac{d}{d\epsilon}\left(\frac{F(\epsilon)}{\epsilon^{1/2}}\right)d\epsilon \qquad \ldots\ldots(1)$$

in which μ is the mobility in $(\mathrm{eV})^{1/2}\,\mathrm{cm\,mm\,Hg\,V^{-1}}$, ϵ is the electron energy in ev, $F(\epsilon)\,d\epsilon$ is the electron energy distribution and $N\theta(\epsilon)$ is the elastic collision cross section in $\mathrm{cm^{-1}}$ at 1 mm Hg and is a function of the electron energy. The drift velocity $\epsilon_D{}^{1/2}$ in $(\mathrm{eV})^{1/2}$ is equal to $\mu E/p$ where E is the electric field in $\mathrm{V\,cm^{-1}}$ and p is the gas pressure in mm Hg. Strictly the momentum cross section should be used, but this is usually not very different from the elastic or total cross section. To evaluate equation (1), $N\theta(\epsilon)$ has to be specified and $F(\epsilon)d\epsilon$ has to be known.

Calculation of $F(\epsilon)d\epsilon$ in hydrogen by Lewis (1958) showed that a sharp break occurs at the excitation energy and $F(\epsilon)d\epsilon$ was found to be non-Maxwellian. A preliminary study has since been made in which the rotational and vibrational collisions have been included (Heylen and Lewis 1960). An equally good, and in the low E/p range better, agreement was reached with experimental Townsend alpha values and this is a sensitive test for $F(\epsilon)d\epsilon$. The general form of $F(\epsilon)d\epsilon$ was shown to be more nearly Maxwellian. Insertion of the Maxwellian energy distribution function $F_M(\epsilon)\,d\epsilon$ into equation (1) yields

$$\mu = \frac{1}{2\bar{\epsilon}}\int_0^\infty \frac{\epsilon^{1/2}}{N\theta(\epsilon)}F_M(\epsilon)\,d\epsilon \qquad \ldots\ldots(2)$$

in which $\bar{\epsilon}$ is the mean energy of the electron swarm.

A suitable function for $N\theta(\epsilon)$ is

$$N\theta(\epsilon) = N\theta_0\,\epsilon^n\,\mathrm{e}^{-k\epsilon} \qquad \ldots\ldots(3)$$

in which $N\theta_0$, n and k are adjustable constants. Substitution of equation (3) into (2) yields at once

$$\mu = \frac{\Gamma_{(2-n)}\,(3/2)^{n-1/2}\,(\bar{\epsilon})^{-(n+1/2)}}{\pi^{1/2}N\theta_0}\,(1-\tfrac{2}{3}k\bar{\epsilon})^{n-2}. \qquad \ldots\ldots(4)$$

The mobility corresponding to a constant mean free time or a constant mean free path (Druyvesteyn hard sphere) model can be obtained immediately from equation (4) by substituting for both cases $k=0$ and for each $n=-\frac{1}{2}$ and $n=0$ respectively. In addition the Ramsauer effect in gases can be taken account of by using $n \simeq 1$. Equation (2) need not be restricted to the use of a single cross section model to cover the entire energy range. It is generally found more accurate to use multiple cross section representations, each valid over a limited energy range. The corresponding mobility equation is obtained by integrating equation (2) by parts and making use of the tabulated incomplete Γ-functions (Pearson 1957). This allows the influence of the cross section variation on the mobility to be shown clearly.

Experimentally determined total collision cross section data by Normand (1930) and by Ramsauer and Kollath (1930) are shown in figure 1. The values obtained by Crompton and Sutton (1952) using the Townsend swarm technique, are shown on the same figure with the abscissa representing the mean energy of the swarm. Using microwave techniques Bekefi and Brown (1958) obtained $N\theta(\epsilon)=N\theta_0\epsilon^{0.28}$ where $N\theta_0=78\ \mathrm{cm}^{-1}$ and this is also shown. Cross section values have been calculated by Massey and Ridley (1956) and by Carter, March and Vincent (1958). Agreement between these two theoretical approaches is reported as satisfactory. Curve *e* (Massey and Ridley), shown in figure 1, includes full allowance for electron exchange and has been multiplied by 1·65 along the ordinate to agree with experiment.

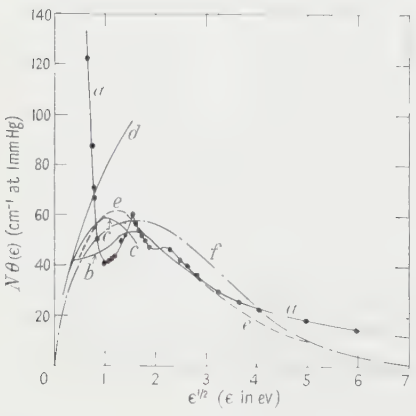

Figure 1. Total collision cross section in hydrogen. Solid lines are experimental: curve *a*, Normand (1930); *b*, Ramsauer and Kollath (1930); *c*, Crompton and Sutton (1952); *d*, Bekefi and Brown (1958), $N\theta(\epsilon)=78\epsilon^{0.28}$ cm^{-1}. Calculated curve *e*, Massey and Ridley (1956). Function used to represent experimental data, $N\theta(\epsilon)=60\epsilon^{0.25}e^{-0.1}{}_{\epsilon}$ cm^{-1}, curve *f*.

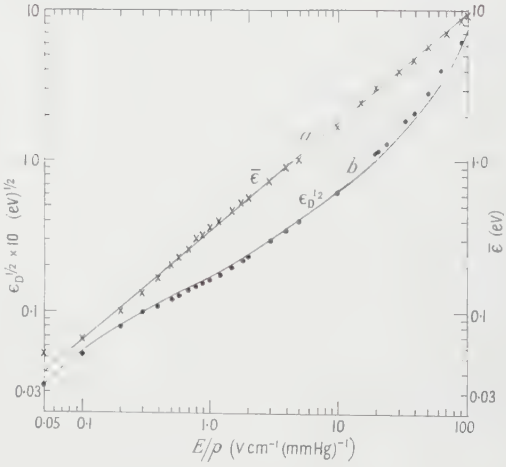

Figure 2. Electron mean energy: crosses, Crompton and Sutton (1952); curve *a*, according to equation (5). Electron drift velocity: points, Bradbury and Nielsen (1936) and Gill and von Engel (1949); curve *b* corresponds to equation (6).

Reputedly accurate data for ϵ_D[1,2] as a function of E/p, obtained by Bradbury as Nielsen (1936), are shown in figure 2. For $E/p > 20$, values by Gill and von Engel (1949) are represented with the absolute values adjusted to fit the Bradbury and Nielsen results at $E/p = 20$.

In contrast to the classical evaluation of μ by Compton (1923), we adopt the experimental values of $\bar{\epsilon}$ as a function of E/p by Crompton and Sutton (1952), and shown in figure 2. For $E/p > 20$, data by Emeleus, Lunt and Meek (1936) are used. Although Crompton and Sutton (1952) assumed a constant cross section, the mean energy obtained from the Einstein relation $D/\mu = \frac{2}{3}\bar{\epsilon}$ is independent of the collision model provided $F(\epsilon)\,d\epsilon$ is Maxwellian. An expression for the mean energy is

$$\bar{\epsilon} = 0{\cdot}357\left(\frac{E}{p}\right)^{0{\cdot}71} \text{ ev}, \qquad \ldots\ldots (5)$$

and this is shown in figure 2, curve *a*.

The cross section data of Normand (1930) can be approximated by two constant mean free time values separated by a small energy region in which a Ramsauer effect takes place. Integrating equation (2) by parts and using these cross sections together with incomplete Γ-functions enables good agreement with experiment over the range $2 < E/p < 50$ to be obtained but at low and high E/p the calculated velocity is smaller than the experimental values. This suggests that the data of Normand (1930), particularly in the region $E/p < 2$ are too large for $\epsilon < 1$ ev. The Ramsauer and Kollath (1930) data can be represented by a constant mean free path followed by a constant mean free time cross section. Although there is a marked improvement for $E/p < 2$, the calculated drift velocity remains increasingly too low with decrease in E/p.

In the low field region exact agreement is reached if the relation for $N\theta(\epsilon)$ put forward by Bekefi and Brown (1958) for low electron energies is used with $N\theta_0 = 63\ \text{cm}^{-1}$. This model can be combined with an exponential dependence at high energies, by suitable choice of constants in equation (3). An optimum relation is shown in figure 1, curve *f* for which $N\theta_0 = 60$, $n = 0{\cdot}25$ and $k = 0{\cdot}1$. Substitution of these values into equation (4) and making use of equation (5) yields a reliable formula for electron mobility in hydrogen as a function of E/p according to

$$\mu = 1{\cdot}72 \times 10^{-2}\left[1 - 2{\cdot}4 \times 10^{-2}\left(\frac{E}{p}\right)^{-0{\cdot}71}\right]^{-1{\cdot}75}\left(\frac{E}{p}\right)^{-0{\cdot}53} \qquad \ldots\ldots (6)$$

which agrees within 16% with experiment for $0{\cdot}1 < E/p < 100$, as shown in figure 2, curve *b*.

Although present agreement shows that for the particular case of hydrogen the use of an *a priori* Maxwellian electron energy distribution enables results of good precision to be obtained, in a complete solution of Boltzmann's transport equation the choice of $N\theta(\epsilon)$ influences the particular distribution obtained. It is well known that only for a constant mean free-time model will the distribution be accurately Maxwellian. In the case of hydrogen such a model represents the measured cross section reasonably well over the greater part of the energy range and the use of $F_M(\epsilon)\,d\epsilon$ is further justified. Only at lower electron energies does a positive power variation of $N\theta(\epsilon)$ become marked, but in this near thermal region $F(\epsilon)\,d\epsilon$ can be expected to remain Maxwellian and there is little influence of the small Ramsauer effect.

Equation (4) with n and $k=0$ has often been applied (Crompton and Sutton 1952, Frommhold 1959) to find the cross section when both μ and $\bar{\epsilon}$ are known. If the results so obtained show a strong variation in $N\theta(\epsilon)$ then interpretation is difficult as $N\theta(\epsilon)$ was inherently assumed constant. It is also clear that with a supposedly constant $N\theta(\epsilon)$ and a knowledge of μ, it is difficult to determine $\bar{\epsilon}$ for hydrogen as has been attempted (Raether 1949).

Acknowledgment

The award of an I.C.I. Fellowship by the University of London is gratefully acknowledged.

References

Allis, W. P., 1956, *Handb. d. Phys.*, Vol. 21 (Berlin: Springer).
Bekefi, G., and Brown, S. C., 1958, *Phys. Rev.*, **112**, 159.
Bradbury, N. E., and Nielsen, R. A., 1936, *Phys. Rev.*, **49**, 388.
Carter, C., March, N. H., and Vincent, D., 1958, *Proc. Phys. Soc.*, **71**, 2.
Compton, K. T., 1923, *Phys. Rev.*, **22**, 333.
Crompton, R. W., and Sutton, D. J., 1952, *Proc. Roy. Soc.* A, **215**, 467.
Emeleus, K. G., Lunt, R. W., and Meek, C. A., 1936, *Proc. Roy. Soc.* A, **156**, 394.
Frommhold, L., 1959, *Z. Phys.*, **156**, 144.
Gill, E. W. B., and von Engel, A., 1949, *Proc. Roy. Soc.* A, **197**, 107.
Heylen, A. E. D., and Lewis, T. J., 1960, *Proc. Fourth International Conference on Ionization in Gases, Uppsala*, Vol. 1, p. 156 (Amsterdam: North-Holland).
Lewis, T. J., 1958, *Proc. Roy. Soc.* A, **244**, 166.
Massey, H. S. W., and Ridley, R. O., 1956, *Proc. Phys. Soc.* A, **69**, 659.
Normand, C. E., 1930, *Phys. Rev.*, **35**, 1217.
Pearson, K., 1957, *Tables of the Incomplete Γ-Function* (Cambridge: University Press).
Raether, H., 1949, *Ergebn. Exakt. Naturw.*, **22**, 73.
Ramsauer, C., and Kollath, R., 1930, *Ann. Phys., Lpz.*, **4**, 91.

A Note on Electroluminescence due to Carrier Accumulation

By H. K. Henisch and B. R. Marathe†
Department of Physics, University of Reading

MS. received 20th May 1960, in revised form 8th July 1960

Electroluminescent materials are known to behave in complicated ways, and in zinc sulphide, for instance, the origin of the emission is not easy to identify. Most workers have assumed that impact ionization is responsible, but certain results cannot be explained in this way and have thus been ascribed to injection (Thornton 1959). These views are not contested here. The purpose of the present note is to draw attention to a third possible mechanism.

Low (1955) has shown theoretically that it should be possible to produce a localized excess of minority carriers in a semiconductor by a process which he termed 'carrier accumulation'. The phenomenon should occur whenever minority carriers drift under the influence of a field towards a region which otherwise contains them in smaller concentration. Thus, considering current flow from an n-type region (lightly doped) to an n^+ region (heavily doped), we would expect injection to manifest itself in the region n^+ and accumulation

† On leave of absence from the National Physical Laboratory, New Delhi, India.

in the n region immediately adjoining. The additional carrier concentration would be held in a steady state by recombination, by the field and by back diffusion. The last two factors operate in opposition.

The recombination of accumulated carriers should give rise to the emission of radiation in the usual way. This form of electroluminescence differs from that due to injection in two principal ways. It should occur near the cathode (on n-type material) whereas injection occurs at the anode. Moreover, accumulation should occur in a region which tends to equal one diffusion length when the applied field is very small and which must necessarily diminish when it is large. In contrast, injected carriers spread out within the material at higher fields. However, the interpretation of actual results is not simple, since any barrier which may exist at a cathode could give rise to electroluminescence (by impact ionization) on its own account. Low's calculations give the total excess of minority carriers P produced by any current. The rate of emission should then be $\beta P/\tau_f$ where τ_f is the filament lifetime and β the fractional radiative efficiency of the recombination process. At lowest field strengths, P is proportional to the current and to τ_f, as one would expect. The emission itself should then be insensitive to the lifetime, other things being equal. At higher fields, the emission must depend on current less than linearly. At very high fields, the situation is difficult to analyse, since the simplifying assumptions made by Low would no longer be true. Moreover, τ_f need not remain constant when the local concentration of additional minority carriers becomes very large.

We are not now aware of observations which provide compelling evidence for accumulation electroluminescence. However, some results which are now interpreted as the outcome of injection could alternatively be ascribed to accumulation. The phenomenon can certainly take place in simpler materials. By analogy with injection it thus provides a new interpretational model which could find application in connection with the familiar electroluminescent substances.

References

Low, G. G. E., 1955, *Proc. Phys. Soc.* B, **68**, 310.
Thornton, W. A., 1959, *Phys. Rev.*, **116**, 893.

Hall Coefficient and Electrical Conductivity Measurements on Lead Selenide Single Crystals Grown from the Vapour

By R. H. Jones

Royal Radar Establishment, Malvern, Worcs.

MS. received 28th March 1960, in revised form 9th June 1960

The development by Prior (1960) of a method of growing PbSe crystals from the vapour in a controlled Se atmosphere has led to the production of crystals having an excess carrier concentration about an order of magnitude less than that of crystals examined previously (Putley 1955). This reduction

in excess carrier concentration has made it possible to determine values of the intrinsic carrier concentration n_i from Hall constant and conductivity measurements alone at temperatures (300–600 K) lower than in the earlier work. The results were analysed by solving the equations for the Hall constant R and conductivity σ with the assumptions (i) that the excess carrier concentration was the same at all temperatures for each specimen and equal, therefore, to that given by the value of R in the exhaustion range, namely $1/Re$ (Allgaier and Scanlon 1958), and (ii) that the law for the majority carrier mobility μ obtained at low temperatures extended throughout the temperature range studied. This procedure required Hall and conductivity data in a temperature range extending upwards from about liquid nitrogen temperature. With the view to studying further the conduction properties of this material, measurements were extended to liquid helium temperature. The cryostat employed was similar to that described by Mitchell and Putley (1959), and measurements below room temperature were made using standard potentiometric techniques. Measurements above room temperature were made using a simple furnace through which a stream of argon was passed to prevent oxidation of the specimens (Putley 1955) and were recorded automatically (Carter, Howarth and Putley 1958).

Previous measurements on PbS, PbSe and PbTe between room temperature and 4°K have been reported by Allgaier and Scanlon (1958) for specimens having excess carrier concentrations about two orders of magnitude greater than those studied in the present work.

Our results below room temperature are shown in figures 1 and 2, which refer to four n-type and one p-type specimen varying in excess carrier concentration from $3{\cdot}0 \times 10^{16}$ cm^{-3} to $1{\cdot}58 \times 10^{17}$ cm^{-3}. It will be seen that R in each case was practically constant at temperatures below about 100 K. At the upper end of the temperature range the mobility variation for four of the specimens clearly followed a power law. The results for specimens C 32, C 35 and C 34 followed closely the $T^{-2\cdot5}$ law found by Putley (1952), whilst the value of the index obtained for C 11 was somewhat lower, being 2·25. It was not possible to obtain the form of the mobility variation for C 12 because, although the conductivity appeared to follow a power law, the value of R at these temperatures was falling appreciably. At the lower end of the temperature range the mobility for each specimen tended to become independent of temperature, the constant value of the mobility being as high as 400 000 cm^2 v^{-1} sec^{-1} in the case of C 34.

The behaviour observed over the whole temperature range was very similar to that described by Allgaier and Scanlon (1958) for the three lead salts PbS, PbSe and PbTe, and by Finlayson and Greig (1956) for natural galena. Furthermore, it was found, in accordance with the results of Allgaier and Scanlon, that unusually high values of the static dielectric constant (~ 100) were required to account for the behaviour of the mobility at the lower temperatures on the basis of degenerate impurity scattering (Mansfield 1956). It is interesting to note in particular that in spite of the appreciably lower excess carrier concentrations of the specimens examined, the present Hall measurements conform with those of the earlier authors in indicating a small, if not actually zero, activation energy for the impurities.

However, in the present case, non-uniformity along the length of the specimens was found in the three n-type specimens with the lower excess carrier concentrations. The effect was observed by measuring for the same specimen current

the potential differences appearing between the five different combinations of conductivity and Hall leads. The effect was small at room temperature but became progressively greater as the temperature was lowered. On the other hand, there was no evidence of rectifying barriers in any of the specimens. At the higher temperatures the form of the mobility variation and a comparison of mobility

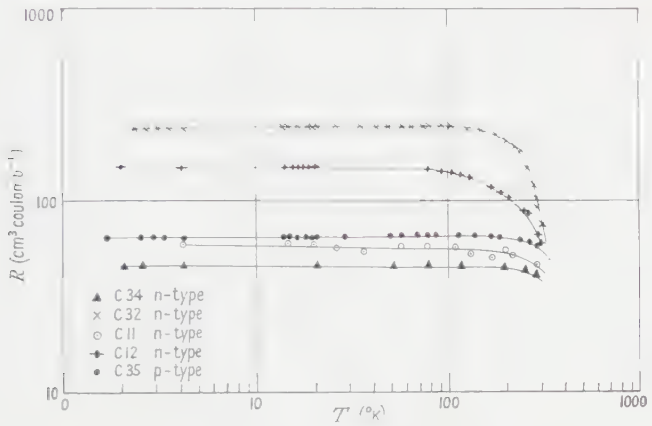

Figure 1. Variation of the Hall coefficient with temperature.

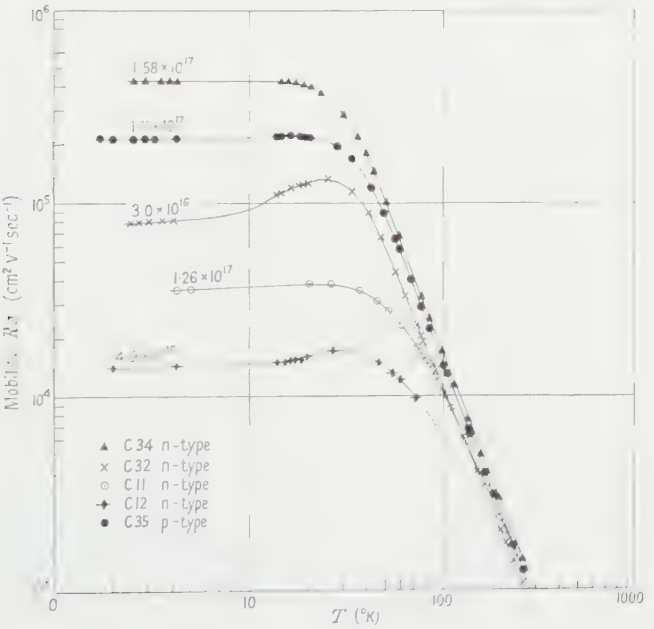

Figure 2. Variation of the majority carrier mobility with temperature. Numbers attached to the curves give the values of the excess carrier concentrations (cm^{-3}).

values with those obtained by Allgaier and Scanlon indicate that the present results are typical of those usually obtained. Allgaier and Scanlon report having examined the uniformity of the specimens they employed, but it is not clear that this was carried out for the specimens when cooled.

The method of analysis of measurements obtained above room temperature required that any permanent changes in excess carrier concentration due to heating of the samples (Scanlon 1953) should have only a small effect on the measured values of R and σ. This was verified by noting that no marked irreversibility in R and σ was obtained during cycles of heating and cooling. Appropriate values of μ $(=8R\sigma/3\pi)$ for specimens C 34, C 35 and C 32 were extrapolated according to the $T^{-2\cdot5}$ law, as indicated by the low temperature measurements. The low temperature variation of μ obtained with specimen C 11 indicated a $T^{-2\cdot25}$ rather than a $T^{-2\cdot5}$ law for the mobility, and values of n_i were calculated for both mobility variations, appreciably better agreement with the results for the other specimens being obtained using the $T^{-2\cdot25}$ law. Because no clear indication of the mobility law was obtained with specimen C 12 a value of μ was calculated at the highest temperature reached, using the mean value of n_i calculated for the other specimens together with the values of R and σ measured at that temperature; values of μ at lower temperatures were then calculated according to the $T^{-2\cdot5}$ law. On this basis the value 11 000 $cm^2 v^{-1} sec^{-1}$ was obtained for μ at 100°K. Inspection of the data in figure 2 indicates that this was not an unreasonable value.

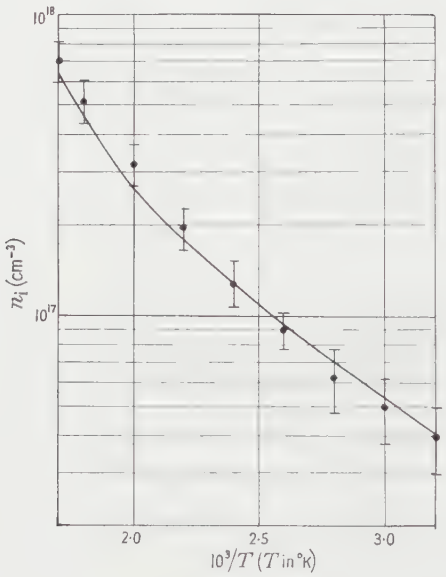

Figure 3. Variation of the intrinsic carrier concentration with temperature. Points give the results of the present measurements and the continuous curve the results obtained by Macfarlane and Pincherle (unpublished).

Figure 3 shows the results. The points denote the mean values of n_i, the length of the vertical lines representing the standard deviation as an indication of the scatter obtained. These values of n_i correspond fairly well with the results of unpublished calculations by Macfarlane and Pincherle shown by the continuous curve. The values of n_i calculated by these authors for this range of temperatures were based partly on optical data, assuming that the thermal energy gap was given by the energy E_0 of the optical absorption edge, and the

value of effective mass ratio required was calculated in the neighbourhood of 600°K where values of both E_0 and the intrinsic Hall coefficients (Putley 1955) were available. The results obtained were consistent with an energy gap given by $0{\cdot}153 + 3{\cdot}88 \times 10^{-4}\ T$ ev in the temperature range up to about 450°K and having a maximum value of 0·35 ev at 550°K; the value of the mass ratio was 0·38. Values of the electron to hole mobility ratio obtained in the present analysis were about 1·5.

Acknowledgments

The author is indebted to Drs G. G. Macfarlane and L. Pincherle for permission to quote the results of their unpublished calculations, and to colleagues in this laboratory, in particular Dr E. H. Putley, for help and useful discussion during the course of this work. Acknowledgment is made to The Controller, H.M. Stationery Office, for permission to publish this note.

References

Allgaier, R. S., and Scanlon, W. W., 1958, *Phys. Rev.*, **111**, 1029.
Carter, R. H. A., Howarth, D. J., and Putley, E. H., 1958, *J. Sci. Instrum.*, **35**, 115.
Finlayson, D. M., and Greig, D., 1956, *Proc. Phys. Soc.* B, **69**, 796.
Mansfield, R., 1956, *Proc. Phys. Soc.* B, **69**, 76.
Mitchell, W. H., and Putley, E. H., 1959, *J. Sci. Instrum.*, **36**, 134.
Prior, A. C., 1960, *Trans. Electrochem. Soc.*, in the press.
Putley, E. H., 1952, *Proc. Phys. Soc.* B, **65**, 388.
—— 1955, *Ibid.*, **68**, 22.
Scanlon, W. W., 1953, *Phys. Rev.*, **92**, 1573.

Speculation on the Centres formed by Nitrogen in Diamond

By R. J. Elliott
Clarendon Laboratory, Oxford

MS. received 15*th June* 1960

§ 1

Diamonds are broadly divided into two classes—type I which have defects present in appreciable numbers in solid solution and type II which appear essentially perfect in structure. It appears that there are several different kinds of defect in type I diamonds so that all definitions of the classification are not exactly equivalent. Although a great deal is known about the structural, optical, electrical and other properties of the defects their origin has remained a comparative mystery largely because it is not possible to control their introduction. Recently however Kaiser and Bond (1959) have demonstrated that nitrogen is a common impurity in type I diamonds and often present in concentrations of several tenths of one per cent. They further showed that the concentration was strongly correlated with the intensity of optical absorption called type A by Robertson *et al.* (1934, 1936) and Clark *et al.* (1956). The main features of this absorption are a shift in the continuous absorption edge from 2200 Å to 3300 Å with some line structure superimposed.

There is further absorption in the infra-red associated with the creation of single phonons. This absorption is forbidden in the perfect crystal but becomes allowed because of the imperfections which destroy the selection rule that wave vector $\mathbf{k}=0$ and create dipoles in the lattice. The salient feature of this absorption is the maximum at $7{\cdot}8\,\mu$ which provides a convenient measure of nitrogen content in a given diamond. The absorption coefficient at the maximum is $3\times10^{4}c\ \mathrm{cm}^{-1}$ where c is the concentration of nitrogen. The number n of such atoms per cm^3 is $1{\cdot}7\times10^{23}c$.

It is the purpose of this note to review other properties of type I diamonds in the light of this information and to speculate on the form of the defect produced by the nitrogen.

§ 2. Evidence on Nature of Defect

2.1. *Paramagnetic Resonance*

Independent evidence for the presence of nitrogen was found by Smith, Sorokin, Gelles and Lasher (1959) who found resonance from a single unpaired electron in a centre which consisted of a single nitrogen atom. The extra electron associated with this centre was largely on the nitrogen and on one of the neighbouring carbons. The extra electron causes this particular bond to be elongated by an amount which these authors estimate from the observed hyperfine structure to be about 10%.

Recently Thornley in this laboratory has examined a number of stones of good optical properties which had been measured at Reading University. They failed to find any trace of the nitrogen resonance so that only a small fraction of that present could have been in the form of this single nitrogen centre. A stone kindly lent by the American group which did show a strong resonance was clearly much more imperfect than the Reading ones.

It can be concluded that the A defect observed in optical absorption is not the single nitrogen centre observed in resonance. The A centre shows no resonance and cannot have an odd number of electrons. It is therefore probably a more complex centre than the simple donor. It is unlikely that simple ionization of these donors by acceptors can be responsible. For one thing no acceptors are ever observed in type I diamonds as they are in IIa's, and complete compensation could not occur in every stone. It is possible on the other hand that acceptors are always compensated in type I diamonds by electrons from the nitrogen whatever its form.

2.2. *Optical Absorption*

Regarding the $7{\cdot}8\,\mu$ vibrational absorption of the A centres as a line one can compute an f-value for oscillations of carbon atoms of approximately 0·2. This indicates that there must be considerable charge transfer in the defect, so that it is either charged or a dipole. The $7{\cdot}8\,\mu$ band is in the region of the optical modes in which the two sub-lattices of the diamond structure oscillate out of phase and the nearest neighbour bond lengths are strongly modulated. The centre of Smith *et al.* (1959) is essentially a dipole along one bond because the extra electron from the nitrogen spends part of its time on a neighbouring carbon. The simplest model where the electron spends half of its time on each would lead to an f-value of 1/4, but this configuration has been ruled out as

an A centre. The requirement of charge transfer rules out the possibility of pairs of atoms in the form of N_2 molecules. In this configuration the only effective dipoles could come from electron overlap on to the neighbouring carbons which must be small.

2.3. *X-ray Diffraction*

Another anomalous property of type I diamonds is the x-ray diffraction patterns, where spikes of diffuse intensity are observed around the Bragg reflections (Raman and Nilakantan 1940). These are not temperature dependent in the form of scattering by lattice vibrations but represent a lattice defect. Moreover their peculiar geometry was shown by Hoerni and Wooster (1955) to indicate that there were large planar defects in (100) planes, and Frank (1956) suggested silicon might be a likely impurity. Subsequently Cochran and Caticha-Ellis (1958) showed that this was not the case. Unfortunately to date no detailed work has been done to correlate this property with the optical or electrical properties of type I diamonds. The existence or otherwise of such correlations would be extremely interesting. Since we now know that nitrogen is a common impurity and that it exists in the crystal in some form of aggregate it is tempting to speculate that the nitrogen atoms form these planar defects.

Frank's analysis of the experimental data determines two other important properties of the defect besides its (100) planar character. From the fact that diffuse scattering is absent from the (300) reflection it follows that the defect must increase the separation between the perfect parts of the crystal by a third of a planar spacing in this direction (i.e. one-twelfth of the side of a cubic cell). Also because there is no scattering about (000) the total charge on the defect must be $6(n-1-2\delta)$, where 6 is the charge per carbon atom, δ the relative increase in spacing ($=1/3$) and n is a whole number. For $n=2$ the extra charge is 2 units (Frank chose $n=3$ and an extra charge of 8 since he thought Si a likely impurity). We see from this that two layers of nitrogen atoms would also be an acceptable defect. The sensitivity of the (000) reflection to the actual charge is not very great and measurements there are quite difficult so that the possibility of a single layer cannot be entirely ruled out.

2.4. *Lattice Dilation*

There is one further piece of experimental evidence which supports the view that the nitrogen atoms are segregated into double planes. Kaiser and Bond made observations of the dilation of the lattice with increasing nitrogen content. They found an increase of 15×10^{-5} Å in the cell size of 3·6 Å with 0·1%N. If these nitrogens are in double planes there is one defect every 6000 planes and with the displacement of 0·3 Å per defect found in the x-ray work this leads to a dilation of 20×10^{-5} Å per cell in reasonable agreement with the observation.

§ 3. Conclusion

It therefore appears that the conjecture that nitrogen in type I diamonds causing the A defect is segregated into planes is in agreement with the observed facts, and is sufficiently plausible to warrant further experimental test. The

most important experiment would be a test of the correlation between the optical absorption and the anomalous diffraction. On the other hand investigation of the optical and electrical properties of the single nitrogen donor centre would be very interesting.

It is difficult to reach any very definite conclusion about the actual structure of the proposed centre. The following suggestions are highly speculative.

In the single nitrogen centre one bond is elongated by about 10%. If the same effect occurs in the planar defect half the bonds to a neighbouring plane will be elongated and this would increase the planar spacing by about 15%. If the extra electron resonates between bonds connecting these two planes so that all are elongated it is possible to increase the interplanar spacing further, but it seems unlikely that the single plane could on this picture produce the increase of 33% required by the x-ray diffraction results.

A double layer of nitrogen atoms could readily give the extra spacing. However, two adjacent layers sharing their extra electrons so that there is one for each bond connecting the two planes will not produce the dipoles required to give the infra-red absorption. The most plausible arrangement is probably an N–C–N layer (figure 1 (*b*)), where the intervening carbon atoms are surrounded by a

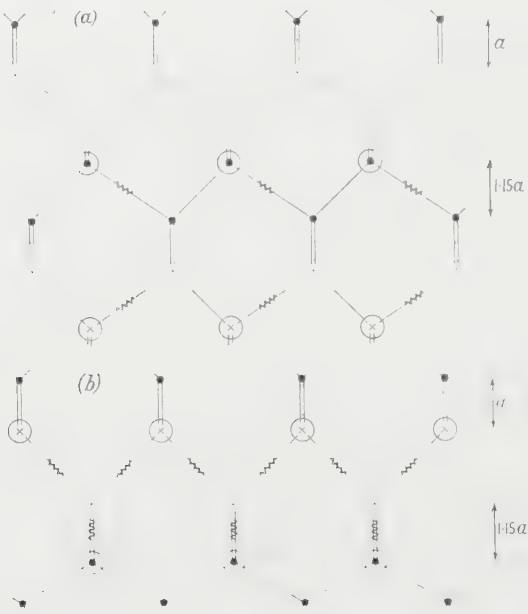

Possible arrangements of nitrogen atoms in a double layer parallel to (100) as seen in an (011) projection. Dots show atoms in the plane of the figure, crosses atoms $\sqrt{2}a$ above and below the plane (a = interplanar spacing = 1/4 cubic cell edge). The nitrogen atoms are circled. The bonds containing extra electrons are marked. (*a*) Electrons confined to particular bonds which are stretched by 10%; (*b*) N–C–N layer arrangement with extra electrons shared.

tetrahedron of nitrogen atoms with two extra electrons shared between the four bonds, causing them to be elongated. An alternative arrangement with two intervening carbon planes is shown in figure 1 (*a*), where the extra electrons are

confined to particular bonds. Many changes can clearly be rung on these arrangements but without more experimental evidence it does not seem profitable to speculate further. The most unsatisfactory feature of models of this type is the lack of any obvious energy gain from the creation of defect—except for packing considerations.

Acknowledgments

The author is indebted to Mr. J. Thornley for communicating his results, to Dr. E. W. J. Mitchell and his colleagues at Reading for many discussions, and to the participants at the 1960 Diamond Conference for their stimulating interest.

References

Clark, C. D., Ditchburn, R. W., and Dyer, H. B., 1956, *Proc. Roy. Soc.* A, **234,** 363.
Cochran, W., and Caticha-Ellis, S., 1958, *Acta Cryst. Camb.*, **11,** 245.
Frank, F. C., 1956, *Proc. Roy. Soc.* A, **237,** 170.
Hoerni, J. A., and Wooster, W. A., 1955, *Acta Cryst. Camb.*, **8,** 187.
Kaiser, W., and Bond, W. L., 1959, *Phys. Rev.*, **115,** 857.
Raman, C. V., and Nilakantan, P., 1940, *Proc. Ind. Acad. Sci.* A, **11,** 389.
Robertson, R., Fox, J. J., and Martin, A. E., 1934, *Phil. Trans. Roy. Soc.* A, **232,** 463.
—— 1936, *Proc. Roy. Soc.* A, **157,** 579.
Smith, W. V., Sorokin, P. P., Gelles, I. L., and Lasher, G. J., 1959, *Phys. Rev.*, **115,** 1546.

Soft X-ray Emission Spectra of Some Transition and Noble Metals

By C. Curry and D. J. McNeill†
Department of Physics, The University of Leeds

MS. received 3rd *May* 1960, *in final form* 4th *July* 1960

§ 1. General Introduction

Experiments are in progress on x-ray spectra of transition metals and alloys. $N_{II,III}$ emission spectra of rhodium, palladium and silver, which do not seem to have been reported previously, have been recorded, and some information about them is given here. On account of the low intensity of these spectra the accuracy of this information is rather limited, and extension of the work to alloys of these metals using the present methods seems unlikely to be fruitful. With the metals of the first transition group the $M_{II,III}$ spectra are considerably more intense, and more detailed information regarding these spectra can be obtained. The results of our experiments for nickel and copper are presented here. It is the intention to extend the experiments over the whole nickel–copper alloy range.

§ 2. Experimental Details

The instrument in use is a one-metre concave grating grazing-incidence vacuum spectrograph. The grating is ruled on glass with 1152 lines per millimetre; the angle of incidence is 84° 15′. Ilford Q1 emulsions on thin glass

† Now at the Plessey Company Limited, Towcester, Northants.

plates are used for photographing the spectra, and the shortest wavelength detectable by the instrument is about 40 Å. In the 150–250 Å region, where the spectra here reported occur, the dispersion ranges from about 1 to 2 mm ev^{-1}, and resolution of a few tenths of an electron volt is achieved. This resolution agrees reasonably with the theoretical limit of resolution (Mack, Stehn and Edlén 1932) for the slit breadth of 10^{-2} cm used in these experiments. Adjustment of focus and tests for resolution were performed using a finer slit and obtaining the optimum sharpness and distinctness of separation of the aluminium L_{II} and L_{III} edges at about 170 Å.

Separate silicone oil diffusion pumps with a common backing pump are used for evacuation of the x-ray tube and spectrograph; liquid nitrogen traps are used in the pumping lines. The x-ray tube pressure under operating conditions is less than 5×10^{-6} mm of mercury. Scraping techniques are used for exposing clean metal surfaces for the actual spectral exposures. Tests for possible contamination of target surfaces during the running of the tube were made as follows. With an aluminium target surface, exposures made using a fresh surface were compared with similar exposures using a surface which had been bombarded in the tube for up to 6 hours under the operating conditions of 40 mA tube current and 4000 v a.c. tube voltage. The spectra obtained showed no detectable differences, even in the sharpness of the high-energy emission edges; indicating that, with the vacuum arrangements used, conditions of surface purity are maintained for long periods. Nevertheless, when long exposures were made surfaces were periodically renewed during the exposures.

Spectroscopically pure target materials were used, and exposure times with 40 mA tube current were about 10 minutes for aluminium, 2 hours for nickel and copper, 6 hours for rhodium, palladium and silver. Except for aluminium the continuous background was by no means negligible. With copper and nickel the form of the background was determined by using also the adjacent metals cobalt and zinc, as described by Skinner, Bullen and Johnston (1954). Our spectra for copper and nickel seem, however, to be a good deal more prominent relative to the background than those of Skinner *et al.*

Density records from the spectrograms were taken using a Joyce-Loebl recording microdensitometer. A density/intensity conversion was made with the copper and nickel spectra, using a range of exposures for each metal. The rhodium, palladium and silver spectra are of small intensity relative to the background and the exposure latitude is very limited; emulsion calibration has therefore not been attempted.

§ 3. Results

3.1. *Rhodium, Palladium and Silver*

In figure 1 sample microdensitometer records are shown for the three metals. For rhodium and palladium the $N_{II,III}$ emission band is the central peak of the three appearing on the records. The outer peaks are high orders of the M_ζ line, which has peak wavelength about 47·5 Å for rhodium and 43·5 Å for palladium (see, for example, Siegbahn and Magnusson 1934). The corresponding silver line, at rather less than 40 Å, is not reflected by the grating and does not appear on the record.

Since the $N_{II,III}$ levels are p levels, the emission band represents the occupied 4d + 5s states. The peaks of the emission bands, and their estimated breadths, averaged for each metal over four or five exposures showing no effects of contamination, are:

	Energy at max. int. (ev)	Width of band (ev)
Rhodium	$47{\cdot}5 \pm 0{\cdot}4$	$1{\cdot}3 \pm 0{\cdot}3$
Palladium	$49{\cdot}6 \pm 0{\cdot}4$	$1{\cdot}3 \pm 0{\cdot}3$
Silver	$50{\cdot}6 \pm 0{\cdot}4$	$2{\cdot}1 \pm 0{\cdot}3$

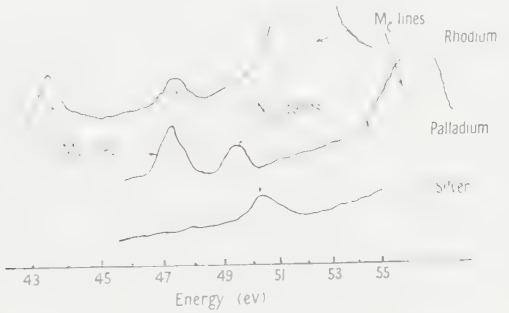

Figure 1. Rhodium, palladium and silver microdensitometer traces.

The emission bands occur at energies which are in reasonable agreement with those calculated from other experimental data (see, for example, Cauchois 1955).

Sauvenier (1939) reported bands for palladium and silver in the 150 A region. No trace of these was found in the present experiments. Bands in this vicinity would correspond to transitions to N_I levels. Since transitions to inner s levels have not generally been observed even in the more intense spectra from lighter elements, it seems doubtful whether Sauvenier's bands have been correctly identified.

3.2. *Copper and Nickel*

Figure 2 shows intensity energy curves for $M_{II,III}$ spectra of copper and nickel. The curves are closely reproducible and are obtained in each case from several exposures. All the main features of these curves are significant, and there is

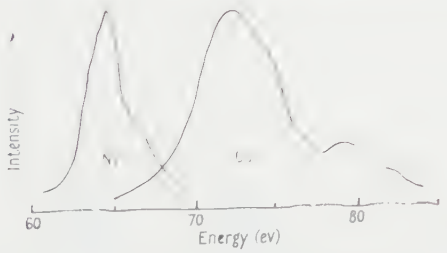

Figure 2. Intensity/energy curves for $M_{II,III}$ emission from copper and nickel.

agreement with the curves of other workers (for a summary, see Parratt 1959). In a general way the curves support the overlapping d- and s-band picture for these metals, the Fermi limit being below the top of the d-band in nickel but above it in copper. Interpretation of the spectra must be made with the following facts in

mind: (i) the probability of transition of an electron in a filled level in the valence band to a vacancy in the inner shell depends on the initial energy of the electron in a way which is not known in detail, (ii) the recorded emission consists of overlapping M_{II} and M_{III} spectra, and while there is a high probability that the M_{III} is much more intense than the M_{II} spectrum (Skinner 1940, Skinner *et al.* 1954), the actual ratio of intensities is unknown, (iii) satellite emission, corresponding to doubly ionized initial states, is likely to be present on the high energy side of the spectra and (iv) the rigid band model, on which the band form is unaltered, but the extent to which it is filled changes as elements of consecutive atomic numbers are considered, is likely to be only approximate at best.

It is hoped that experiments on Ni–Cu alloys should show how the Ni spectrum transforms into the Cu spectrum as the constitution is changed, and may throw light on some of the problems of interpretation.

Acknowledgments

We wish to thank Professor E. C. Stoner for the provision of facilities and for his interest in the work. One of us (D.J.McN.) wishes to express his thanks to the University of Leeds for a maintenance grant.

References

Cauchois, Y., 1955, *J. Phys. et Radium*, **16**, 253.
Mack, J. E., Stehn, J. R., and Edlén, B., 1932, *J. Opt. Soc. Amer.*, **22**, 245.
Parratt, L. G., 1959, *Rev. Mod. Phys.*, **31**, 616.
Sauvenier, H., 1939, *C.R. Acad. Sci., Paris*, **208**, 1724.
Siegbahn, M., and Magnusson, T., 1934, *Zeit. Phys.*, **88**, 559.
Skinner, H. W. B., 1940, *Phil. Trans. Roy. Soc.* A, **239**, 95.
Skinner, H. W. B., Bullen, T. G., and Johnston, J. E., 1954, *Phil. Mag.*, **45**, 1070.

On Pauling's Theory of Alkali Halide Molecules

By Y. P. Varshni and R. C. Shukla
Physics Department, Allahabad University,
Allahabad, India

MS. received 19*th May* 1960

In the study of alkali halide molecules ionic approach is quite successful and the potential energy consists of two parts: (*a*) attractive terms, consisting of a purely ionic term and polarization term etc., (*b*) short range repulsive term.

Two types of repulsive term have been tried in different studies, a simple inverse power term or an exponential term. Thus if U is the potential energy, it can be written as

$$U=\phi+\frac{A}{r^n} \text{ or } Be^{-r/\rho} \qquad \ldots\ldots(1)$$

where

$$\phi=-\frac{e^2}{r}-\frac{e^2(\alpha_1+\alpha_2)}{2r^4}-\frac{2e^2\alpha_1\alpha_2}{r^7}-\frac{c}{r^6}. \qquad \ldots\ldots(2)$$

Such a potential has been successfully applied by Rittner (1951) in the study of alkali halide molecules. He has taken the exponential type of repulsion term.

Varshni (1957 a) has applied this potential by taking both types of repulsion terms for the evaluation of α_e and $\omega_e x_e$ and concluded that exponential type of repulsion term is better than the inverse power one. Similar results were found by Rice and Klemperer (1957).

Recently Pauling (1956) has given a simple treatment which leads to values of r_e, ω_e of alkali halide molecules in reasonably good agreement with experimental values.

Since in alkali halide molecules the sum of the ionic radii is not equal to their r_e, he has included this sum in the potential energy function U in the following form:

$$U = \frac{Z_A Z_B e^2}{r_{AB}} + \beta_{AB} B_0 e^2 \frac{(r_A + r_B)^{n-1}}{r_{AB}{}^n} \qquad \ldots\ldots (3)$$

where U is the potential energy of ion pair compared with the completely separated ions, r_{AB} is the distance of separation of the two ions, $Z_A e$, $Z_B e$ are the charges on the ions, β_{AB} is a constant, unity for univalent cation anion interaction, 1·25 for cation–cation, and 0·75 for anion–anion interaction, B_0 is a constant such that $nB_0 = 0{\cdot}291$, r_A, r_B are constants, characteristic of the ions and equal to their crystal radii, and n is a constant, exponent of the inverse repulsive term.

Such a potential function has been applied for the calculation of the energies of gaseous alkali halide dimer molecules by Milne and Cubicciotti (1958).

It is of some interest to examine whether this potential will lead to satisfactory values of the rotational constant α_e and anharmonicity constant $\omega_e x_e$ also. This point has been treated in the present note.

The method for evaluating α_e and $\omega_e x_e$ from a potential function has been explained by Varshni (1957 b). By this method we get the following expressions of α_e and $\omega_e x_e$ from the potential function (3).

$$\alpha_e = \frac{n+1}{3} \frac{6B_e^2}{\omega_e} \qquad \ldots\ldots (4)$$

$$\omega_e x_e = \frac{2n^2 + 19n + 26}{3} \frac{W}{\mu_A r_e^2} \qquad \ldots\ldots (5)$$

where $W = 2{\cdot}1078 \times 10^{-16}$ and μ_A is reduced mass in atomic weight units.

The experimental data have been summarized in table 1.

Table 1

Diatom	ω_e (cm^{-1})	r_e (Å)	B_e(cm^{-1})	n
LiI	450 e	2·392 b	0·4429 b	9·5
NaCl	380 e	2·361 b	0·2179 b	8·6
NaBr	315 e	2·502 b	0·1511 b	8·9
NaI	286 e	2·711 b	0·1177 b	9·9
KF	400 a	2·171 d	0·2799 d	6·4 f
KCl	305 a	2·667 b	0·1285 b	8·6
KBr	230 a	2·821 b	0·0811 b	8·9
KI	200 a	3·048 b	0·0608 b	9·9
RbF	390 a	2·265 c	0·2107 c	6·3 f
RbCl	270 a	2·787 b	0·0876 b	8·5
RbBr	180 a	2·945 b	0·0475 b	8·8
RbI	145 a	3·177 b	0·0328 b	9·8
CsF	385 a	2·345 b	0·184 b	6·1 f
CsCl	240 a	2·906 b	0·072 b	8·3
CsBr	168 a	3·072 b	0·036 b	8·6
CsI	120 a	3·515 b	0·0236 b	9·6

a, Barrow and Caunt (1953); b, Honig, Mandel, Stitch and Townes (1954); c, Lew; Morris, Geiger and Eisinger (1958); d, Green and Lew (1960); e, Herzberg (1950), f, Milne and Cubicciotti (1958).

Table 2

Diatom	$10^4\alpha_e$ obs. (cm^{-1})	$10^4\ \alpha_e$ calc. (cm^{-1}) inverse power, Varshni	present note
LiI	40·9 b	55·2	91·5
NaCl	16·1 b	20·0	24·0
NaBr	9·4 b	11·8	14·4
NaI	6·5 b	8·47	10·56
KF	23·35 d	27·55 g	28·99
KCl	7·9 b	10·2	10·4
KBr	4·05 b	5·08	5·66
KI	2·7 b	3·44	4·03
RbF	15·18 c	18·67 g	16·62
RbCl	4·5 b	6·23	5·4
RbBr	1·86 b	2·37	2·46
RbI	1·10 b	1·40	1·60
CsF	11·0 b	15·9	12·5
CsCl	3·3 b	4·46	4·02
CsBr	1·2 b	1·63	1·48
CsI	0·68 b	0·814	0·984

g, recalculated values, utilizing new r_e data. Revised values of n in equation (1) are $n(KF) = 5{\cdot}82$, $n(RbF) = 6{\cdot}71$.

Table 3

Diatom	$\omega_e x_e$ obs.	$\omega_e x_e$ calc. inverse power, Varshni	present note
LiI	1·5 e	3·47	7·22
NaCl	(1·0) e	2·37	3·05
NaBr	1·15 e	1·71	2·22
NaI	0·75 e	1·48	2·01
KF	1·45 a	2·55 g	2·68
KCl	0·9 a	1·74	1·79
KBr	0·6 a	1·03	1·19
KI	0·5 a	0·837	1·04
RbF	1·3 a	2·39 g	1·98
RbCl	0·7 a	1·62	1·20
RbBr	0·35 a	0·664	0·683
RbI	0·25 a	0·462	0·551
CsF	1·23 a	2·40	1·66
CsCl	0·6 a	1·16	0·955
CsBr	0·3 a	0·602	0·503
CsI	0·2 a	0·258	0·344

Calculated values of α_e and $\omega_e x_e$ by (4) and (5) are given in tables 2 and 3 respectively. For comparison the values calculated by Varshni (1957 a) from the detailed potential energy function equation (1) with inverse power term, have also been reproduced.

It will be observed that the calculated values of α_e and $\omega_e x_e$ from potential function (3) are higher than the experimental values. In the case of α_e, except for five molecules viz. RbF, RbCl, CsF, CsCl and CsBr the calculated values by potential function (1) (with inverse power term) are in better agreement with experimental results than those calculated from equation (4). Similar results are obtained in the case of $\omega_e x_e$. Calculated values for the same five molecules from equation (5) are better than those calculated from potential function (1).

The experimental values of α_e are known to a high degree of accuracy from microwave spectroscopy. But the values of $\omega_e x_e$ are rather uncertain. Barrow and Caunt's (1953) values of $\omega_e x_e$, given in table 3, were obtained from the empirical relation $x_e \mu_A^{1\cdot2} = 0{\cdot}013$, but they have pointed out that the constant in this equation may be as high as 0·018. It means that the experimental values of $\omega_e x_e$ may be greater by about 40%. Results presented here are in favour of the higher value of the constant.

In view of the large uncertainties in the values of $\omega_e x_e$ we would like to emphasize that the comparison given in table 3 is much less significant than that given in table 2.

In general terms we may say that these results indicate that the Pauling model is not fully satisfactory. Polarization terms contribute appreciably and should be taken into account.

Recently Klemperer and Rice (1957, and Rice and Klemperer 1957) have given more accurate values for ω_e for a number of alkali halide molecules which differ from the values of Barrow and Caunt (1953). But as Pauling's data are based on older values, we have also used the same.

Acknowledgments

The authors are grateful to Professor D. S. Kothari (Delhi University) for his kind interest in the work and thank the Council of Scientific and Industrial Research for the financial assistance.

References

Barrow, R. F., and Caunt, A. D., 1953, *Proc. Roy. Soc.* A, **219**, 120.
Green, G. W., and Lew, H., 1960, *Canad. J. Phys.*, **38**, 482.
Herzberg, G., 1950, *Spectra of Diatomic Molecules* (New York: Van Nostrand).
Honig, A., Mandel, M., Stitch, M. L., and Townes, C. H., 1954, *Phys. Rev.*, **96**, 629.
Klemperer, W., and Rice, S. A., 1957, *J. Chem. Phys.*, **26**, 618.
Lew, H., Morris, D., Geiger, F. E., and Eisinger, J. T., 1958, *Canad. J. Phys.*, **36**, 171.
Milne, A., and Cubicciotti, D., 1958, *J. Chem. Phys.*, **29**, 846.
Pauling, L., 1956, *Proc. Nat. Acad. Sci. India*, **25**, Sec. A, Part I.
Rice, S. A., and Klemperer, W., 1957, *J. Chem. Phys.*, **27**, 573.
Rittner, E. S., 1951, *J. Chem. Phys.*, **19**, 1030.
Varshni, Y. P., 1957 a, *Trans. Faraday Soc.*, **53**, 132.
——1957 b, *Rev. Mod. Phys.*, **29**, 664.

Switching Properties of Tetramethylammonium-trichloro-mercurate

By E. Fatuzzo

Laboratories RCA Limited, Zurich, Switzerland

MS. received 12*th May* 1960

§ 1. Introduction

Tetramethylammonium-trichloro-mercurate (TTM) is a new ferroelectric material (Fatuzzo and Nitsche 1960) with a rather high spontaneous polarization ($1{\cdot}3\,\mu$C cm^{-2}). Since the coercive force in this material is quite high (3 kv cm^{-1}) the switching speed is expected to be rather low. The reversal of the polarization has been studied in most known room

temperature ferroelectrics: $BaTiO_3$ by Merz (1954, 1956), Little (1955), Wieder (1955), Landauer, Young and Drougard (1956), Landauer (1957), Chynoweth (1958), Miller (1958) and Burfoot (1959); Rochelle salt by Wieder (1958); GASH by Prutton (1957) and Wieder (1957); triglycine sulphate by Pulvari and Kuebler (1958) and Fatuzzo and Merz (1959).

§ 2. Measurements

The switching time t_s in TTM was measured as a function of applied field E and temperature T. The results are shown in figure 1. It can be seen that for all temperatures the switching time depends on field as

$$t_s = kE^{-n} \qquad \ldots\ldots(1)$$

where k is a constant and n is a large number which depends on temperature. The dependence of n on T is shown in figure 2; the exponent n decreases with temperature.

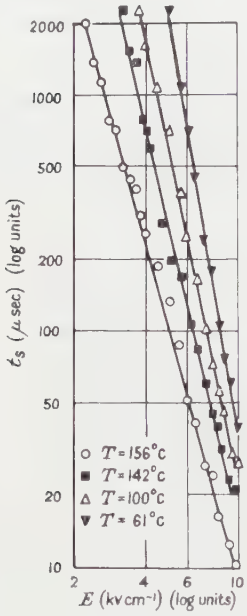

Figure 1. Log t_s plotted against log E for different values of the temperature T.

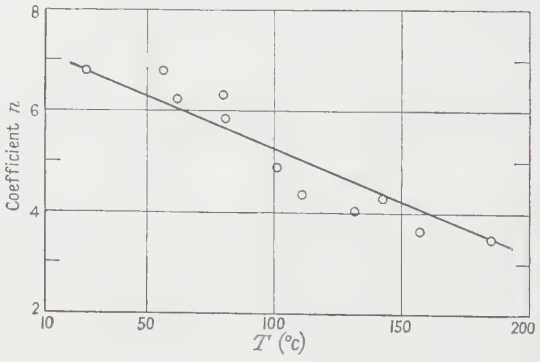

Figure 2. Exponent n of equation (1) plotted against temperature T.

§ 3. Discussion

A power law dependence of t_s on E has been found before in thiourea (Goldsmith and White 1959), in $BaTiO_3$ at very high fields (Stadler 1958) and in $LiH_3(SeO_3)_2$ (Fatuzzo 1960). However, in all these cases the exponent n is a small number (3/2 or 5/2) and hence the power law could be explained by invoking a certain amount of sideways wall motion (Burfoot 1960, Fatuzzo, to be published). It is not clear yet how the very high power dependence of t_s on E found in TTM can be explained, unless one assumes a very strong field-dependence of the forward wall mobility (Fatuzzo, to be published). More experiments have to be done using some different technique to understand this very unusual behaviour.

Acknowledgments

We wish to thank Dr. W. J. Merz for many helpful discussions, Dr. R. Nitsche and Miss S. Zingg for growing the TTM single crystals and Mr. H. Roetschi for his technical assistance.

References

Burfoot, J. C., 1959, *Proc. Phys. Soc.*, **73,** 641.
—— 1960, *Ibid.*, **75,** 312.
Chynoweth, A. G., 1958, *Phys. Rev.*, **110,** 1316.
Fatuzzo, E., 1960, *Helv. Phys. Acta*, **33,** 21.
Fatuzzo, E., and Merz, W. J., 1959, *Phys. Rev.*, **116,** 61.
Fatuzzo, E., and Nitsche, R., 1960, *Phys. Rev.*, **117,** 936.
Goldsmith, G. J., and White, J. G., 1959, *J. Chem. Phys.*, **31,** 1175.
Landauer, R., 1957, *J. Appl. Phys.*, **28,** 227.
Landauer, R., Young, D., and Drougard, M., 1956, *J. Appl. Phys.*, **27,** 752.
Little, E. A., 1955, *Phys. Rev.*, **98,** 978.
Merz, W. J., 1954, *Phys. Rev.*, **95,** 690.
—— 1956, *J. Appl. Phys.*, **27,** 938.
Miller, R. C., 1958, *Phys. Rev.*, **111,** 736.
Prutton, M., 1957, *Proc. Phys. Soc.* B, **70,** 1064.
Pulvari, C. F., and Kuebler, W., 1958, *J. Appl. Phys.*, **29,** 1742.
Stadler, H. L., 1958, *J. Appl. Phys.*, **29,** 1485.
Wieder, H. H., 1955, *Phys. Rev.*, **99,** 1161.
—— 1957, *Proc. Inst. Radio Engrs, N.Y.*, **45,** 1049.
—— 1958, *Phys. Rev.*, **110,** 29.

LETTERS TO THE EDITOR

The Stability of an Infinite Gravitating Cylinder of Paramagnetic Material in the Presence of Magnetic Field

The problem of the effect of longitudinal electric field on the stability of dielectric liquid cylinder has recently been studied by Nayyar and Murty (1960). Because of the equivalence of electrostatic and magnetostatic problems, this can be extended to the case of a paramagnetic liquid cylinder in the presence of a longitudinal magnetic field. One notes that the results of Chandrasekhar and Fermi (1953), Auluck and Kothari (1957) and Simon (1958), who studied the influence of magnetic field on the stability of a liquid cylinder of infinite electrical conductivity, follow as limiting cases of our problem by assigning different values to the permeability parameter.

Let us consider an infinite gravitating cylinder of paramagnetic material with permeability μ_1 embedded in a medium whose permeability is μ_2 and in which there is a prevalent uniform magnetic field **H** directed along the z axis. In order to study the stability, we suppose that the cylinder is subject to a perturbation, the result of which is to deform the boundary into

$$r = R + a\cos kz, \qquad \ldots\ldots (1)$$

where $a/R \ll 1$ and $k = 2\pi/\lambda$, is the wave number of the disturbance in the z direction. If we assume the liquid to be incompressible, then

$$R_0^2 = R^2 + \tfrac{1}{2}a^2, \qquad \ldots\ldots (2)$$

where R_0 is the radius of the undeformed cylinder. It can be shown (Nayyar and Murty 1960) that the change in magnetic energy ΔM per unit length of the cylinder, due to the deformation defined by equation (1), is given by

$$\Delta M = \frac{a^2 x(\mu_2 - \mu_1)^2 H^2 \mathrm{I}_0(x)\mathrm{K}_0(x)}{8[\mu_1 \mathrm{I}_1(x)\mathrm{K}_0(x) + \mu_2 \mathrm{I}_0(x)\mathrm{K}_1(x)]}, \qquad \ldots\ldots (3)$$

where $x = kR$ and I_n and K_n are the Bessel functions of order n for a purely imaginary argument, which have no singularity at the origin and at infinity, respectively. Also it has been shown by Chandrasekhar and Fermi (1953), that the corresponding change in the gravitational energy per unit length of the magnetic cylinder is

$$\Delta\Omega = 2\pi^2 G\rho^2 R_0^2 a^2 (\tfrac{1}{2} - \mathrm{I}_0(x)\mathrm{K}_0(x)). \qquad \ldots\ldots (4)$$

Thus the total change in energy per unit length of the cylinder is

$$\Delta W = 2\pi^2 G\rho^2 R_0^2 a^2 (\tfrac{1}{2} - \mathrm{I}_0(x)\mathrm{K}_0(x)) + \frac{a^2 x(\mu_2 - \mu_1)^2 H^2 \mathrm{I}_0(x)\mathrm{K}_0(x)}{8[\mu_1 \mathrm{I}_1(x)\mathrm{K}_0(x) + \mu_2 \mathrm{I}_0(x)\mathrm{K}_1(x)]}, \qquad \ldots\ldots (5)$$

If $\Delta W = 0$ for $x = x^*$

$$\Delta W < 0 \text{ for } x < x^*$$

and

$$> 0 \text{ for } x > x^*. \qquad \ldots\ldots (6)$$

The cylinder is stable for a given value of the magnetic field, for all transverse deformations with $k > x^* R_0$. The critical wave number (in units of $1/R$) x^* is given by the root of the equation

$$2\pi^2 G\rho^2 R_0^2 a^2 (\tfrac{1}{2} - \mathrm{I}_0(x)\mathrm{K}_0(x)) + \frac{a^2 x(\mu_2 - \mu_1)^2 H^2 \mathrm{I}_0(x)\mathrm{K}_0(x)}{8[\mu_1 \mathrm{I}_1(x)\mathrm{K}_0(x) + \mu_2 \mathrm{I}_0(x)\mathrm{K}_1(x)]} = 0. \quad \ldots\ldots (7)$$

We shall not solve the above equation for any specific numerical values of the parameters, but we shall show how the change in energy ΔW given by equation (5) can be used to deduce the changes in energy when the material of the cylinder is infinitely conducting.

First we consider the case when $\mu_1 = 1$ and $\mu_2 = 0$, i.e. the medium outside the cylinder acts as a 'superconductor'. Let us denote by $\Delta M(\alpha, \beta)$ the change in magnetic energy per unit length of the magnetic cylinder due to deformation when the permeability of the medium of the fluid cylinder is α and that of the medium outside the cylinder is β. Therefore in the present case we have to calculate $\Delta M(1, 0)$, which from equation (3) is given by

$$\Delta M(1, 0) = \frac{a^2 x \mathrm{I}_0(x)}{8\mathrm{I}_1(x)} H^2. \quad \ldots\ldots (8)$$

This is just the expression obtained by Chandrasekhar and Fermi (1953) for the change in magnetic energy due to deformation given by equation (1) when a uniform magnetic field **H** is frozen into an infinitely conducting cylinder and outside the field vanishes. This is due to the fact that the medium outside the cylinder acts as a 'superconductor' ($\mu_2 = 0$), and consequently the magnetic field outside the cylinder remains always zero. Thus the field inside the cylinder under all deformations has to follow the deformed boundary—a situation which is the same as though the magnetic field inside is frozen in the medium of the cylinder.

Next we consider the case when $\mu_2 = 1$ and $\mu_1 = 0$, the fluid cylinder behaves as a 'superconductor', while the medium outside the the cylinder has a magnetic field **H**. So in the present case, we have from equation (3)

$$\Delta M(0, 1) = \frac{a^2 x H^2 \mathrm{K}_0(x)}{8\mathrm{K}_1(x)}, \quad \ldots\ldots (9)$$

which is just the expression obtained by Auluck and Kothari (1957) for the change in magnetic energy, when the magnetic field inside the cylinder is zero and has a value **H** outside the cylinder. In the problem studied by Auluck and Kothari (1957), the fact that the fluid of the cylinder is assumed to be infinitely conducting prevents the field outside the cylinder from 'leaking' into the cylinder. In our point of view, we can treat this case as though the fluid of the cylinder is a 'superconductor', for in that case also the fluid cannot 'leak' into the fluid from outside.

Lastly, we consider Simon's (1958) problem when a uniform magnetic field **H** is present throughout the space and parallel to the z axis. The change in magnetic energy in this case can be obtained as the sum of the changes in the magnetic energy when (i) the field inside the cylinder is **H** and vanishes outside and (ii) the field inside is zero and has a value **H** outside the cylinder. The values of the changes in magnetic energy in (i) and (ii) are just those given

by equations (8) and (9) respectively. Thus the change in magnetic energy of the cylinder due to deformation in Simon's problem, which we denote by ΔM_S, is given by

$$\Delta M_S = \Delta M(1,0) + \Delta M(0,1) = \frac{a^2 x H^2}{8}\left[\frac{I_0(x)}{I_1(x)} + \frac{K_0(x)}{K_1(x)}\right], \quad \ldots\ldots (10)$$

which is just the expression one obtains in the problem discussed by Auluck and Kothari (1957), if one put $H_1 = H_2$ in their notation.

We are indebted to Professor D. S. Kothari and Professor F. C. Auluck for valuable discussions and comments.

Department of Physics,
University of Delhi,
India.

N. K. Nayyar.
G. S. Murty.†

25th April 1960, in revised form 14th June 1960.

† Now at The Royal Institute of Technology, Stockholm, Sweden.

Auluck, F. C., and Kothari, D. S., 1957, *Z. Astrophys.*, **42**, 101.
Chandrasekhar, S., and Fermi, E., 1953, *Astrophys. J.*, **118**, 116.
Nayyar, N. K., and Murty, G. S., 1960, *Proc. Phys. Soc.*, **75**, 369.
Simon, R., 1958, *Astrophys. J.*, **128**, 375.

Impurity Photoconductivity in n-type InSb

It has been estimated that if the dominant impurities in n-type InSb behave like hydrogenic impurity centres then they should have an ionization energy of about 7×10^{-4} ev but in the presence of a magnetic field of about 2000 gauss this energy should be doubled (Yafet, Keyes and Adams 1956). However, unless the concentration of impurities is less than about $10^{13}\,cm^{-3}$ neighbouring centres will interact, reducing the ionization energy. With concentrations of about $10^{14}\,cm^{-3}$ the interaction is so large that no ionization energy is observed. Sladek and others (Keyes and Sladek 1956, Frederikse and Hosler 1957, Sladek 1958, 1959) have observed that when material with about 10^{15} impurities per cm^3 is placed in a magnetic field of 10000 gauss or greater the interaction between adjacent impurities is reduced sufficiently for an ionization energy to be observed by Hall effect measurements below 4°K. More recently somewhat purer material has been prepared by J. B. Mullin of this laboratory, which, although not sufficiently pure to remove completely interactions between impurities, does show an ionization energy with fields as low as 4000 gauss.

Figure (1) shows Hall effect data for one of these samples. The results obtained at the lowest fields do not show an ionization energy but for fields between 4000 and 8000 gauss the carrier concentration falls as the temperature is lowered down to 1·8°K. Below 1·8°K the Hall effect tends to a constant value or passes through a maximum. This could indicate either that there is still some interaction between impurities, giving impurity band conduction, or that surface conduction is present. The electron concentrations above 1·8°K were sufficiently small so that classical statistics were valid and, as a first approximation in analysing the results, the behavour below 1·8°K was ignored. In the presence

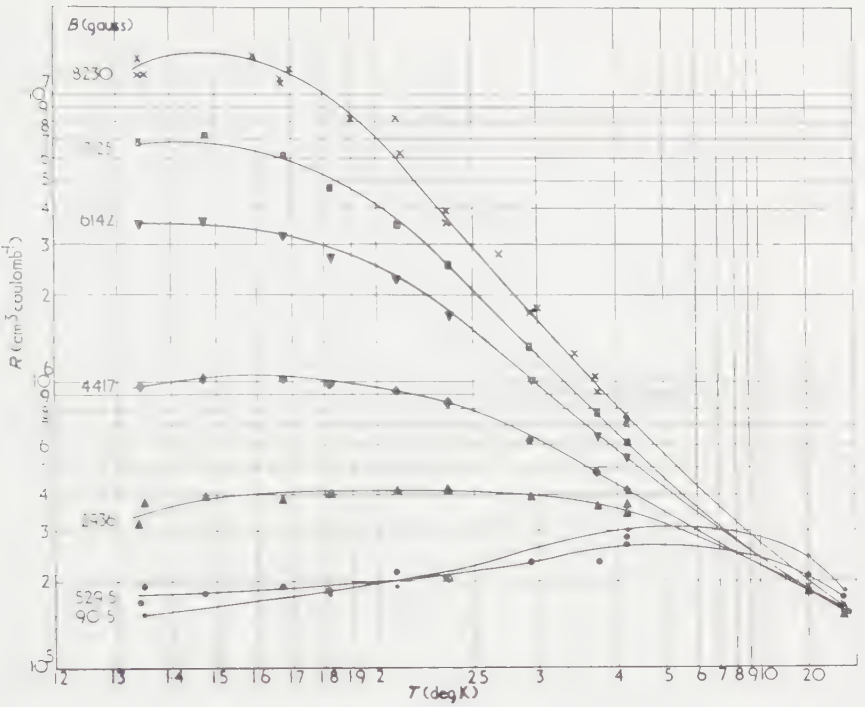

Figure 1. Hall coefficient of an n-type sample of InSb. Sample C158/84.

of a sufficiently large magnetic induction B the conduction band will be split into a series of degenerate Landau levels (for a recent discussion of this behaviour see Kahn and Frederikse 1959). If the temperature is so low that the separation between these levels is large compared with kT and the sample is sufficiently pure that all the conduction electrons can be accommodated in the lowest level; then the relation between the carrier concentration n, the concentration of acceptors N_A and the concentration N_D and ionization energy ϵ of donors becomes

$$\frac{(N_A+n)n}{N_D-N_A+n} = (2\pi m^* kT)^{1/2}\frac{eB}{h^2}\exp(-\epsilon/kT).$$

This expression also assumes that the free electron concentration is sufficiently small that classical statistics may be used. These conditions are easily satisfied by n-type InSb with a total impurity concentration of about 10^{14} cm^{-3} at a temperature of 4°K and in a magnetic induction of 3000 gauss or greater.

Application of this expression to results similar to those shown in figure (1) shows that in this type of material N_D is about 3×10^{14} cm^{-3}, N_D-N_A about 4×10^{13} cm^{-3} and ϵ varies from about 7×10^{-4} ev at 8000 gauss to 3×10^{-4} ev at 4500 gauss.

The values obtained for the ionization energies indicate that impurity photoconductivity ought to be observed if this material were illuminated with radiation of up to a few millimetres wavelength. Moreover, the values of the magnetic fields required would not be so high as to make the application of this effect impracticable.

Photoconductivity has been observed using a cryostat fitted with a light-pipe so that a specimen could be illuminated with radiation of wavelength between

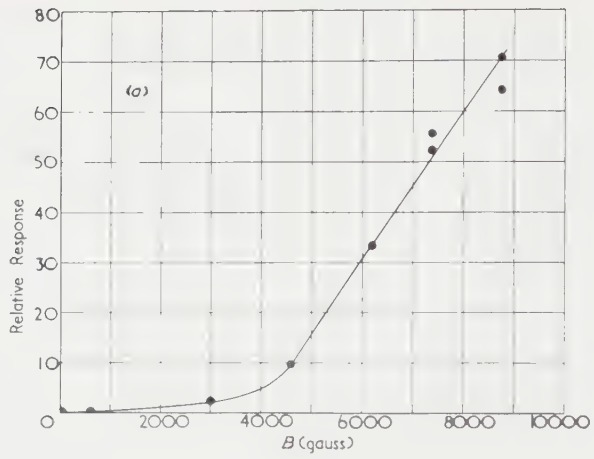

(*a*)

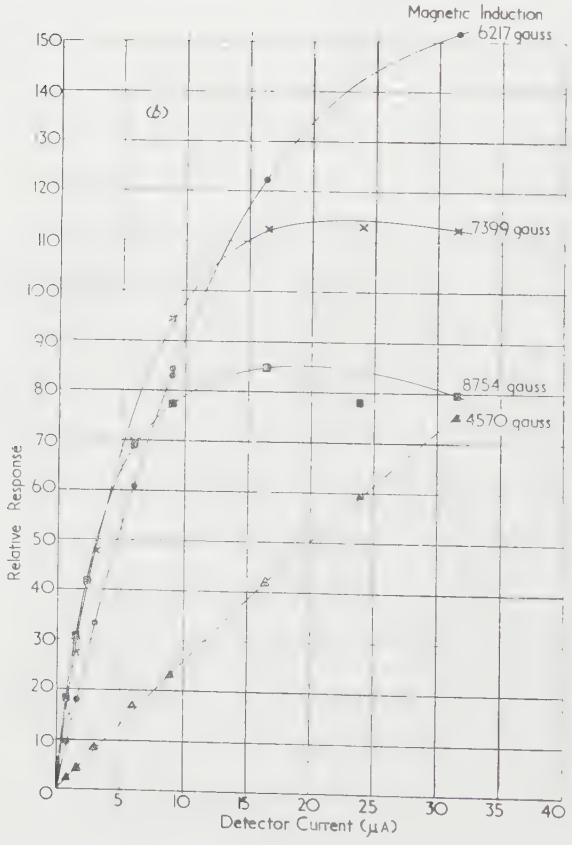

(*b*)

Figure 2. Relative response of detector at 4·208 mm wavelength (*a*) dependence upon magnetic conduction with detector current 0·75 μA, (*b*) dependence upon current and magnetic induction.

0·1 and 4·0 mm. The sources of radiation were a mercury lamp and grating spectrometer covering the range 0·1 to 1·4 mm and a Philips DX151 klystron and harmonic generator operating at 2 mm and 4 mm. The light-pipe was fitted with a black paper filter at room temperature and a black polythene filter in the helium to remove short-wave radiation.

The sample dimensions were 0·5 cm × 0·5 cm × 1·0 cm and indium electrodes were applied to opposite 0·5 cm × 1·0 cm faces. The magnetic field was applied at right angles to the direction of current flow and of the incident radiation. The radiation was directed along the long direction of the sample. For the majority of these experiments the radiation was modulated at 800 c s and detected using a tuned amplifier and phase sensitive detector.

When the temperature was reduced to below 1·5 °K and a magnetic induction of 6–8000 gauss applied, the sample resistance was about 10–30 kΩ. The sample was able to detect the applied radiation, the minimum detectable energy per unit bandwidth being approximately 5×10^{-10} w at 0·5 mm, 5×10^{-11} w at 2 mm and 10^{-10} w at 4 mm.

Figure 2 illustrates the dependence of the effect upon magnetic induction and specimen current. Figure 2(*a*) shows that the effect is negligible for inductions less than 3000 gauss but it rises rapidly as the induction is increased above 4000 gauss. Figure 2(*b*) shows that with the higher values of magnetic induction the effect at first increases linearly as the specimen current is increased, but at higher currents the effect passes through a maximum and it also appears that there is an optimum value for the magnetic induction of about 6000 gauss. The behaviour shown in figure 2 (*b*) is thought to be associated with non-ohmic effects in high electric and magnetic fields which have been observed in specimens similar to the one used here.

The modulation frequency of the radiation was varied between 16 and 1000 c/s and the performance was independent of frequency. This, together with the size of the sample and the fact that it was directly immersed in liquid helium, suggests that these results are unlikely to be due to bolometric effects.

These results probably do not represent the ultimate performance obtainable since in the first place the sensitivity was limited by amplifier noise and secondly no attempt has been made to optimize the purity and size of the sample.

It is a pleasure to acknowledge the valuable discussions I have had with Dr. G. G. MacFarlane and with Mr. V. Roberts. I also wish to thank Mr. W. E. Wilgoss, Mr. W. H. Mitchell and Mr. M. F. Kimmitt for their help in this work. This note is published by permission of the Controller, H.M. Stationery Office.

E. H. Putley.

Royal Radar Establishment,
Great Malvern, Worcs.
24th August 1960.

Frederikse, H. P. R., and Hosler, W. R., 1957., *Phys. Rev.*, **108**, 1136.
Kahn, A. H., and Frederikse, H. P. R., 1959, *Solid State Physics*, **9**, 257 (New York, London : Academic Press).
Keyes, R. W., and Sladek, R. J., 1956, *J. Phys. Chem. Solids*, **1**, 143.
Sladek, R. J., 1958, *J. Phys. Chem. Solids*, **5**, 157.
—— 1959, *Ibid.* **8**, 515.
Yafet, Y., Keyes, R. W., and Adams, E. N., 1956, *J. Phys. Chem. Solids*, **1**, 137.

Catalytic Magnetization of Atomic Hydrogen ?

A source of magnetized (spin-oriented) protons to be fed into an accelerator would be a powerful tool for investigating nuclear forces, but devices so far envisaged for this purpose use atomic beam methods with their attendant limitations of very low particle concentrations. In this note the following question is considered: is it possible to harness the high spin entropy of the ferromagnetic state to the magnetization of protons? Our starting point is the fact that hydrogen is observed to stick tightly to many transition metals and tends to reduce their paramagnetic, or, as has been observed in the case of catalytic nickel, ferromagnetic moment in the process (Selwood 1956); it seems likely that the electrons of these adsorbed atoms are pairing off the para- or ferromagnetic electrons in the metal. Suppose now that an adsorbed hydrogen atom gains enough energy to escape from a ferromagnetic surface: the atom is faced with two possibilities—either it carries off an electron with spin aligned against the ferromagnetic field direction leaving behind an oriented metal electron, or else it comes off with spin aligned in the field direction leaving behind an anti-oriented metal electron. But the latter possibility would cost extra energy of order kT_c where T_c is the Curie temperature, so that if the desorption could occur thermally at temperatures of order T_c one would have a mechanism for magnetizing atomic hydrogen gas. In external magnetic fields of strength less than 100 oersted this electron magnetization would speedily be shared with the protons through the hyperfine coupling.

The snag to this scheme lies in the large heats of binding observed for hydrogen on pure transition metals, of order 90 kcal (mole-H)$^{-1}$ ($\sim$4 ev per atom) assuming the hydrogen stuck on as atoms. At feasible temperatures only molecules will come off such a surface. This note is built round the speculation that it may be possible to find or prepare a ferromagnetic surface which, while interacting electronically with adsorbed hydrogen so as to generate exchange energy of order at least kT_c, would nevertheless bind it weakly enough for there to be a good chance of it coming off as atoms.†

We proceed to estimate the temperature and pressure dependence of the hydrogen recombination rate on a surface under conditions that would allow surface-bound, and by hypothesis magnetized, hydrogen atoms to escape in practical amounts.

For this purpose we consider a ferromagnetic surface on which there are a number of sites, of concentration σ_A cm^{-2}, which bind atomic hydrogen rather weakly with binding energy E_A. On excitation with energy q, the bound atoms are assumed to enter a mobile layer on the surface, becoming magnetized in the process, in which they are free to move around as a two-dimensional gas. If this surface is exposed to a gas of hydrogen atoms (from, e.g. a radio-frequency plasma) of concentration n_0 atoms cm^{-3} they will stick on the surface with sticking coefficient (probability of sticking per surface collision) α. Atoms in the mobile layer will collide with atoms in bound sites and may recombine with them to form molecules, this process being assumed to take place over a mean reaction

† One possibility might lie in ferromagnetic oxide surfaces, since it is known (Ehrlich 1959) that although atomic hydrogen forms a tightly bound layer on varius oxide surfaces it does not seem to recombine on these surfaces so fast as in the presence of metals. There may therefore be some chance of adsorbing residual atoms fairly weakly on such a surface without losing them too quickly.

radius a_R so that the probability per unit time for a bound atom to be absorbed by a mobile atom is of order $\bar{v}a_R\sigma_M$ where $\bar{v}$ is the thermal velocity and σ_M the occupation concentration for the mobile layer. (There will also be recombination directly with gas atoms, but this can be neglected for finite binding energy of the mobile atoms.) We show that, provided E_A is not too large, the chance per unit time for a bound atom to escape from the surface ν_E may be made greater than the chance for it to be swallowed up in a recombination process ν_R by suitable adjustment of temperature and pressure: under such conditions the adsorbed atoms form a quasi-equilibrium state so that their occupation concentration can be calculated from equilibrium theory, and ν_E follows from detailed balancing. At the low binding energies involved there is no risk of saturating the surface sites so that Boltzmann statistics apply. One then finds

$$\frac{\nu_R}{\nu_E} = \frac{1}{\alpha}\frac{a_R}{a(T)}\frac{n_0}{n(T)}\exp\{(2E_A - q)/kT\} \qquad \ldots\ldots(1)$$

where

$$a(T) = (\hbar^2/2MkT)^{1/2} \ (M = \text{mass of H atom}), \quad n(T) = \{\sqrt{(2\pi)}/a(T)\}^3.$$

Assuming a_R is of order 10^{-8} cm, and relative to gas concentration $10^{16}\,\text{cm}^{-3}$, temperature 500 °K, then

$$\frac{\nu_R}{\nu_E} \simeq \frac{1}{\alpha}\left(\frac{500}{T}\right)\left(\frac{n_0}{10^{16}}\right)\exp\{(2E_A - q)\,500/T\} \times 5 \times 10^{-10} \qquad \ldots\ldots(2)$$

where the energy is measured in kcal mole^{-1}. So for $\alpha \simeq 1$, and provided the surface binding energy satisfies

$$E_A - \tfrac{1}{2}q \lesssim 10\,\text{kcal mole}^{-1} \qquad \ldots\ldots(3)$$

the chance for a bound atom to evaporate before it recombines can be improved, as measured by (2), by reducing the gas pressure or increasing the temperature.

For our surface to act as a fairly efficient magnetizing catalyst, atoms in the mobile layer should have a fair chance of being trapped at magnetizing sites before being demagnetized by thermal spin lattice coupling, etc. Assuming a capture radius a_c of order 10^{-7} cm and a site density of $10^{14}\,\text{cm}^{-2}$, the average lifetime of a mobile atom before capture (this turns out to be shorter than its lifetime before evaporation for quite small binding energy in the mobile layer—of order 1 kcal mole^{-1}) is of order $(1/\bar{v}a_c\sigma_A^0) \simeq 10^{-10}$ sec. This seems to be fairly fast compared with observed spin lattice relaxation times (Bleaney and Stevens 1953), and since demagnetization due to gas collisions is extremely slow (of order of fractions of a second at 1 mm pressure) owing to the weak action of magnetic spin–orbit forces during collisions, the main demagnetizing process is likely to be that due to recombination, which on the catalyst surface can be controlled as discussed above.

Thus, if it is possible to find a catalyst for which our assumptions can hold, one may be able, by using it in a suitable apparatus, to construct a device by which atomic hydrogen gas at relatively high pressures can be continuously magnetized.

The author is grateful to Dr. D. Brennan for a very useful discussion and helpful comments.

S. Doniach†

Department of Theoretical Physics,
University of Liverpool.

7th June 1960.

† Now at Physics Department, Queen Mary College, London University.

Bleaney, B., and Stevens, K. W. H., 1953, *Rep Progr. Phys.*, **16,** 108.
Ehrlich, G., 1959, *J. Chem. Phys.*, **31,** 1111.
Selwood, P. W., 1956, *Magnetochemistry* 2nd Edn (New York: Interscience), p. 397.

CORRIGENDUM

Compression Waves in a Plasma in a Magnetic Field, by N. Anderson (*Proc. Phys. Soc.*, 1960, **75,** 905).

Equation (15) *should be* divided by k, the wave number.

Equation (16) *should be* divided by z.

The last line on page 911 *should read* $\dfrac{z^{1/2} f_0(z) e E_y}{\pi^{1/2} k \boldsymbol{k} T}$.

REVIEWS OF BOOKS

Electrolytic Solutions, by R. A. Robinson and R. H. Stokes. Pp. xv+559. (London : Butterworths Scientific Publications; New York : Academic Press, 1959.) 63*s*.

Since its first appearance in 1958, this book has rapidly established itself as the standard work on the physical chemistry of electrolytes. The style is easy to read, and leads one comfortably and enjoyably into the study of aqueous ionic solutions. The present edition has been considerably extended, in particular the chapter on " the theory of diffusion of electrolytes, and of conductance and diffusion in relation to viscosity in concentrated solutions ". Much more also appears in this edition on the topic of non-aqueous electrolytes. The book gives adequate accounts of work performed since the publication of the first edition, and a wealth of useful references is provided throughout the text. This edition is quite outstanding in its scope and coverage, and may be strongly recommended to physicists wishing to acquire a sound knowledge of the theory and practice of research into the properties of electrolytes. V. LITTLE.

The Structure of Electrolytic Solutions, edited by W. J. Hamer. Pp. xii+411. (New York : John Wiley; London : Chapman and Hall, 1959.) 148*s*.

This is a report on a symposium on electrolytic solutions held in Washington D.C. in May 1957. The coverage of the 27 papers contained in this volume is very wide, ranging from dilute solutions through all stages of concentration to the pure ionic state. In many ways this constitutes an ideal companion volume to *Electrolyte Solution* by Robinson and Stokes, in that it extends in great detail many of the general topics mentioned therein. The introduction by Walter J. Hamer gives an interesting account of the historical background to the subject, and paves the way for the highly specialized papers by many distinguished authors which follow. The value of this book lies in its wealth of ideas—which after all is what one should expect from the précis of a symposium. V. LITTLE.

Wellen. Ein Lehrbuch der theoretischen Physik, by W. Macke. Pp. xii+465. (Leipzig: Akademische Verlagsgesellschaft Geest and Portig K.-G., 1958.) DM. 29.50.

This textbook deals with the theoretical aspects of a wide range of wave phenomena encountered in many different branches of physics. It is divided into nine chapters, with the following headings : 1. oscillations; 2. systems of oscillators; 3. waves on strings; 4. scalar waves (acoustics); 5. rays (short waves); 6. transverse (electromagnetic) waves; 7. light propagation in matter; 8. theory of relativity; 9. systematic wave theory.

Auxiliary mathematical techniques, such as Fourier series, Fourier transforms and four-dimensional vectors are also discussed, with a sufficient rigour not to offend the pure mathematician, yet not too pedantic for the purposes of the physicist. There are numerous examples, and the solutions are provided in the final section. The printing is excellent and the main formulae are clearly displayed.

Wave motion is so basic a concept that a good textbook such as this, devoted entirely to the analysis of its many aspects is a welcome contribution to the physics literature. The book is clearly written and may be warmly recommended to University teachers and students, especially to those who specialize in theoretical physics. E. W.

Radiation Biology (Proceedings of the Second Australasian Conference on Radiation Biology held at the University, Melbourne, 15th–18th December 1958), edited by J. H. MARTIN. Pp. xi+304. (London: Butterworths Scientific Publications, 1959.) 63*s*.

Australia in terms of total population is still a small country. However, not only its standards of living but its scientific achievements are qualitatively very high, as illustrated by the letters after the name of Sir MacFarlane Burnet, O.M., F.R.S., who opened the Conference, of which this book is the printed proceedings.

Australian scientists have only recently been able to turn their attention to radiobiology. Thus invited contributors from the United Kingdom (Dr. L. H. Gray and the reviewer) and from the United States of America (Dr. H. H. Vogel, Dr. I. I. Oster) provided a substantial proportion of the papers. What is important for review, however, is the work of the Australian Laboratories much of which might normally escape the notice it deserves when published only in Australian journals.

Particularly meritorious are the reports by van den Brenk on radio-protective action of 5-hydroxytryptamine, and with Ruth Moore on the effects of respired oxygen on radio-protective action of certain amines; by Nossal (a name to follow as some horse-players follow jockeys) and Lois Larkin on immunological studies in lethally and sub-lethally irradiated animals; by Fraser and Hall on effect of x-irradiation on the mouse foetus; and by Jackson on the life span of mutagens produced in cells by irradiation. Metcalf (already with an international reputation) has a note on the effect of whole-body irradiation on thymus function and lymphocyte homeostasis and other short papers on the effect of irradiation on the problems of tissue grafting are given by Ilbery, Kent and Garvan *et al.*

In the more clinical aspects the work of Shiels (some effects on lymphoid cells in occupational and accidental exposure to ionizing radiations) should be much more widely known than it appears to be: some of the work of Thomas, Oddie and Rundle on radioactive iodine, noted here, is already acknowledged elsewhere.

Other work of general interest and importance to the radiobiologist in physical chemistry, radiochemistry, chemical synthesis on the one hand and on radioactive fall-out was also covered at the Conference.

The organizer and editor, J. H. Martin, contributes with Müller a paper on dosimetry (radiation quality and bone marrow dose in radiology). No one has given more thought and effort to this subject of extreme importance than Martin himself.

Dr. Martin is to be congratulated not only on his personal effort, but, libraries should note, in making available to readers of English the output of a small but increasingly important focus of radiobiological research.

JOHN F. LOUTIT.

Laboratory Instruments, 2nd edn, by A. Elliot and J. Home Dickson. Pp. xvi+514. (London: Chapman and Hall, 1959.) 55*s*.

This is the second edition of a book first published in 1951: considerable revisions and additions have been made but the general outline has been kept constant. This is more restricted that the title suggests: it is almost entirely concerned with mechanical design and with optical instruments. The mechanical part is an admirable introduction to drawing office and workshop practices and to the properties of most of the important materials used in instrument construction, including some materials of quite recent introduction. There are sections on kinematic and other constraints, and chapters which amount to short monographs on antivibration mountings and on the magnification of small displacements. The optical part contains very valuable collected information about optical materials, a fairly detailed account of optical workshop methods, and descriptions of a number of optical systems for special purposes. Some of these, and the interesting section on corrosion and protection of instruments, show the hand of designers of instruments for the Fighting Services. Very reasonably, optical design has not been treated in any general way, though a few special topics are discussed. In a future revision, the authors should take an opportunity to discuss in detail the setting up and squaring on of a train of optical components. This task falls on many workers who have never had to grind a lens, and I know of no full and easily available description.

I think the decision to exclude electrical topics has been made much too rigid: in certain fields optical and electrical techniques are intermixed and there are sections of the book where fairly detailed optical descriptions give place suddenly to very sketchy accounts of closely connected electrical elements.

The book will certainly be useful in institutions where instruments are occasionally designed for research applications and should be read by many recruits to the instrument making industries. H. J. J. Braddick.

Physics and Electronics in Physical Medicine, by A. Nightingale. Pp. x+292. (London: G. Bell and Sons, 1959.) 30*s*.

This textbook is written primarily for postgraduate medical students reading for a diploma in Physical Medicine, and for student physiotherapists.

Part I, Fundamentals, includes chapters on the structure of matter, mechanics and hydrostatics, heat, radiations (visible, ultra-violet and infra-red), and electricity to the stage of simple valve circuits. Part II deals with the principles of the therapeutic uses of electric currents (d.c., low-frequency and high-frequency or diathermy), ultra-violet and infra-red radiations, and with the apparatus used. Part III contains eight appendices; one contains a revision of elementary mathematics, others more advanced theory and apparatus, and there is a summary of the electronic aids to diagnosis, electromyography and pulse stimulators.

Previous books have been inadequate or inaccurate in their treatment of physical aspects of this subject, and Dr. Nightingale's book will undoubtedly become a standard textbook. It will be welcomed by all physicists who teach undergraduate or postgraduate medical students, or medical auxiliaries. It is a valuable contribution to the better understanding and use of physical science in clinical medicine.

The attempt to cover so much ground in a manner suitable for students of varying aptitude and knowledge has led to uneven treatment in Part I, and

students may find difficulty with some sections. Electron current has been used throughout, instead of conventional current, but it is questionable whether the small gain for the beginner balances the confusion of those who know the conventional rules: the author himself has mixed his conventions in diagrams of the electric motor and of experiments illustrating electromagnetic induction.

The second part and most of the appendices are of a high standard. The text is well illustrated by line diagrams. J. MCKIE.

The Many Body Problem, Report of the Summer School of Theoretical Physics, Les Houches, 1958, edited by CÉCILE DEWITT. Pp. xv+674. (London: Methuen; New York: John Wiley; Paris: Dunod, 1960.) £5.

Every year a course for research students and workers in theoretical physics is held in the French Alps at Les Houches. This book represents the notes on the lectures which were given in the Summer School of 1958 when the topic of the course was the many body problem. It is perhaps no exaggeration to say that this is, in fact, the only problem in physics since matter in all its forms, be it nuclei or solids or liquids, consists of a number of elementary particles interacting together. The techniques for dealing with these interactions when the system has a very large number of particles have had an explosive development over the last five years and a number of the theoretical physicists who have been prominent in this development have contributed in this volume. The form of the contributions varies from extensive review articles, through résumés of published work to original papers—with one exception all are written in English. It can be argued with some reason that there are adequate journals in existence to deal with reviews and papers without the necessity of publishing special and expensive books in this form. There is an undoubted advantage in having the whole collection of papers in one book, but whether this and an elegant binding are worth an expenditure of five pounds will cause some heart searching. On the whole this is probably a book for libraries and serious workers in the field.

The largest single contribution is appropriately that of K. A. Brueckner who reviews the perturbation theory methods he has largely developed for problems with a large number of particles, and discusses their application to nuclear matter, the electron gas, liquid ^{4}He and ^{3}He. N. M. Hugenholtz contributes a long article on the approach to this perturbation theory associated with his name and van Hove's. There are shorter articles by D. J. Thouless, B. R. Mottelson, V. F. Weisskopf and V. Strontinski on various aspects of nuclear matter. The problem of superconductivity is discussed by J. R. Schrieffer who gives a restatement of the now famous B.C.S. theory and by S. T. Beliaev who reviews Bogolyubov's somewhat different approach. E. A. Lynton contributes brief reviews of the experimental position in superconductivity and superfluidity. One further aspect of many body theory which receives full attention is the existence of collective motions and the attendant theoretical difficulties. D. Bohm appropriately provides an extensive review and D. Pines provides an up-to-date report on ' Electrons, plasmons and phonons.'

The other major topic of this volume concerns the thermal properties of such many-body systems and attempts to evaluate partition functions by techniques related to those discussed above. K. Huang provides an extensive discussion of his work with Yang and Lee on the hard sphere gas. Bloch and

de Dominicis contribute a paper on the Fermi gas in this context (in French and totally without references). The evaluation of partition functions has been developed even more over the last two years and it is interesting to note that the school of 1959 was devoted to this problem, and that we can look forward to another volume before long. R. J. ELLIOTT.

Annual Review of Nuclear Science, Vol. 9, edited by E. SEGRÈ and L. I. SCHIFF. Pp. vii + 625. (California : Annual Reviews, 1959.) $7.00 (U.S.A.), $7.50 (foreign).

Scientific reviews may bring before the reader either a stop-press survey of a new and rapidly developing subject, or a more reflective account of a well-established branch of knowledge. The present volume of this excellent series contains articles of each type. A new area of physics, at least as far as the general scientific public is concerned, is reviewed by R. F. Post, who has been enabled by de-classification to write fully on 'High Temperature Plasma Research and Controlled Fusion'. This is a well-balanced and valuable article. Another new subject, also recently released in part from control, is ' Technetium and Astatine Chemistry ', described in full detail by E. Anders. It is unlikely that official control will ever have to be applied to strong coupling, and the article ' The Pion–Nucleon Interaction and Dispersion Relations ', by G. F. Chew, is an account of recent important advances (sometimes referred to modestly as ' conjectures ') in this subject. This is probably the first review of the recent work of Mandelstam, and although the article will be found difficult by many, it will convey at least the notion of the existence of poles in scattering amplitudes.

There are several articles on more familiar subjects, in which a coverage of progress during the last five or six years is offered. D. H. Wilkinson, in an article which might be taken as a model for this sort of volume, shows how the independent particle model and the collective model contribute to our understanding of nuclear photo-disintegration. Progress in calculation of the deuteron photo-effect is also reported. The *Annual Review* welcomes a Russian author in L. Okun, who discusses the leptonic decays of elementary particles (' Strange Particles ; Decays '). Beta decay is a subject of long standing, and the reviews by E. J. Konopinski have contributed much to general knowledge of the phenomenon ; his latest article (' The Experimental Clarification of the Laws of β-radioactivity ') brings the subject up to date by inclusion of parity non-conservation and helicity experiments.

The article ' High-energy Nuclear Reactions ' (J. M. Miller and J. Hudis) shows how the intense beams from high energy nuclear accelerators have permitted detailed studies of the phenomena giving rise to the cascade and evaporation particles of nuclear stars. It is perhaps surprising that anything remains to be said on the subject of ' Nuclear Fission ', but I. Halpern, in an expert and comprehensive article, shows how knowledge of the ratio of particle to fission widths has grown. Among the radio-chemical techniques used in high-energy fission and spallation work, solvent extraction is one of the simplest, most efficient and most versatile, and H. Freiser and G. H. Morrison contribute an interesting account of this subject. ' Advances in Electronics associated with Nuclear Research ' (H. W. Kendall) is another technical article, showing in particular how the transistor is improving the efficiency of counting and recording instruments.

Two articles (' Fast Reactors ', by L. J. Koch and H. C. Paxton and ' Economics of Nuclear Power' , by J. A. Lane) are incursions into the vast territory of applied fission. They are written primarily from an American point of view ; little mention is made of experience in the United Kingdom on generation of electricity from nuclear fuel. The volume concludes with three biological articles (' Vertebrate Radiobiology ', by R. Rugh, ' Biochemical Effects of Ionizing Radiation ', by Margery G. Ord and L. A. Stocken and ' Cellular Radiobiology ', by K. C. Atwood). Of these articles, the first, on embryology, shows how a biological subject can be made readable and interesting even to a physicist ; the other two demand expert knowledge for full appreciation.

The reader may well put down this volume with the feeling that all branches of nuclear science are either enormously extensive or excessively obscure. In this he is probably correct, but such a conclusion should not lessen his debt of gratitude to the editors of this series and to the authors of this volume for their endeavours to ease his task of self-education. W. E. BURCHAM.

Handbuch der Physik, Vol. VIII/1 *Fluid Dynamics*, edited by S. FLÜGGE and C. TRUESDELL. Pp. vi+471. (Berlin, Göttingen, Heidelberg: Springer, 1959.) DM. 132.

This volume contains four articles: (i) Physical principles of fluid mechanics, by K. Oswatitsch (in German); (ii) Mathematical principles of classical fluid mechanics, by J. Serrin (in English); (iii) Laminar boundary layers, by L. Howarth (in English); and (iv) Transition to turbulence, by H. Schlichting (in German).

The first article is a rapid survey of the whole subject. The treatment is macroscopic, compressibility is included, and the fluid is assumed to have a thermodynamic equation of state. Electromagnetic and diffusion phenomena are not included. The mathematical theory is developed with a gratifying degree of rigour and clarity as far as is necessary for an understanding of the physical phenomena which are illustrated by photographs and diagrams. This article gives a very good idea of the spirit of viscous-fluid mechanics.

The second article treats the rigorous derivation of equations of motion from clearly stated principles, and the mathematical properties of their solutions. This is valuable because at present we believe that the Navier–Stokes equations (based on Newtonian viscosity) describe many phenomena adequately, though more evidence would be desirable. Much of the material was new to the reviewer.

The third article is a review article. As is well known, fluids of small viscosity are nearly free from vorticity except in certain narrow boundary layers (e.g. near solid walls) where the effect of viscosity may be important. Approximate equations for the flow in boundary layers can be obtained, and there is an extensive theory of their solutions. The theory of the laminar boundary layer for incompressible two- and three-dimensional flow is reviewed. The effects of compressibility, various aspects of shock-wave boundary-layer interaction, and the limitations of the boundary-layer approximation are discussed.

The last article is a general survey of hydrodynamic stability in both its theoretical and experimental aspects. The emphasis is on stability to infinitesimal

disturbances. (Little is known about finite disturbances.) Many results of recent work are presented clearly and attractively.

This volume is a worthy contribution to the new *Handbook of Physics*.

F. URSELL.

Physico-Chemical Measurements at High Temperatures, edited by J. O'M BOCKRIS, J. L. WHITE and J. D. MACKENZIE. Pp. viii+394. (London: Butterworths Scientific Publications; New York: Academic Press, 1959.) 75*s*. $13.50.

This book is a compilation by some twenty contributors who have been engaged in the measurement of certain properties of matter in the temperature range of 500 c to 2500°c. The first part discusses the ways of attaining, measuring and controlling these temperatures as well as a description of the relative stability of a large number of refractory materials. The remainder of the book gives a survey of methods for measuring a number of quantities at these experimentally difficult temperatures, for instance, phase and chemical equilibria, surface tension, ultrasonic velocity, diffusivity in liquid systems and viscosity. The contributors do not attempt to describe the methods in detail but refer freely to the original papers. What they have done is to assess critically the relative merits of the methods and to indicate the special difficulties which are met in measuring quantities at these high temperatures. Most of the chapters emphasize the importance of the art of compromise in the design of such experiments in which many conflicting factors have to be considered which do not worry experimenters who are concerned with measurements at lower temperatures. The book serves the useful purpose of bringing together for the first time the widespread literature upon this increasingly important subject.

The reviewer believes that this book would be extremely valuable for people interested in measurements at high temperature, especially those who are involved in the design and execution of such experiments.

T. EVANS.

Wilhelm Conrad Röntgen und die Geschichte der Röntgenstrahlen, 2nd Edn, by O. GLASSER. Pp. xii+381. (Berlin, Göttingen, Heidelberg: Springer, 1959.) DM. 58.

Die Fernrohre und Entfernungsmesser, by A. KÖNIG and H. KÖHLER. Pp. viii+475. (Berlin, Göttingen, Heidelberg: Springer, 1959.) DM. 88.

Physique et Technique des Tubes Electroniques, by R. CHAMPEIX. Pp. xvi+427. (Paris: Dunod, 1960.) 58 n fr.

Studies in Theoretical Physics, Proceedings of the Summer School of Theoretical Physics held at Mussoorie, May 1959. Parts 1 and 2. (New Delhi: Government of India, Ministry of Scientific Research and Cultural Affairs, 1960.)

Nukleonik, Vol. 1, Part 3, August 1958. Pp. iv+36. DM. 5.40. Vol. 1, Part 9, December 1959. Pp. iv+48. DM. 9.90 (Berlin, Göttingen, Heidelberg: Springer.)

Begründung der Funktionentheorie auf alten und neuen Wegen, by L. HEFFTER. Pp. viii+64. (Berlin, Göttingen, Heidelberg: Springer, 1960.) DM. 19.80.

X-ray Attenuation Coefficients from 10 kev *to* 100 mev, by Rosemary T. McGinnies. Supplement to N.B.S. Circular 583. Pp. 12. (Washington: U.S. Government Printing Office, 1959.) 15 cents.

Optics and Spectroscopy, translation of *Optika i Spektroscopiya*, Vol. 6, No. 1, January 1959. Editor S. E. Frish. Pp. iv + 84. (Mass.: Optical Society of America.) $3.00 per copy, $25.00 per year.

Quantum Particle Dynamics, 2nd revised Edn, by James McConnell. Pp. xi + 266. (Amsterdam: North Holland, 1960.) 40*s*.

The Theory of Homogeneous Turbulence, by G. K. Batchelor. Pp. xi + 197. (London: Cambridge University Press, 1959.) 18*s*. 6*d*.

A Simple Approach to Electronic Computers, by E. H. W. Hersee. Pp. viii + 104. (London, Glasgow: Blackie and Son, 1959.) 12*s*. 6*d*.

Progress in Semiconductors, Vol. 4, by A. F. Gibson, F. A. Kröger and R. E. Burgess. Pp. viii + 292. (London: Heywood, 1960.) 63*s*.

Foundations of Aerodynamics, 2nd Edn, by A. M. Kuethe and J. D. Schetzer. Pp. xiv + 446. (New York: John Wiley and Sons; London: Chapman and Hall, 1959.) 94*s*.

Journal of Nuclear Energy: Part C, Plasma Physics, Accelerators and Thermonuclear Research. Vol. 1, Nos. 1/2, October 1959. Editor-in-Chief, J. V. Dunworth. Pp. iv + 104. (New York, London, Paris, Los Angeles: Pergamon Press.) £7 per volume.

Lectures on Fourier Integrals, by Salomon Bochner. Translated by M. Tenenbaum and H. Pollard. Pp. x + 331. (Princeton: University Press; London: Oxford University Press, 1960.) 40*s*.

Modern Physics, 4th Edn, by H. A. Wilson. Pp. xv + 473. (London, Glasgow: Blackie and Son, 1959.) 40*s*.

Paris Symposium on Radio Astronomy, edited by Ronald N. Bracewell. Pp. xii + 612. (Stanford: University Press; London: Oxford University Press, 1959.) £6.

Paris: Publications Scientifiques et Techniques du Ministère de l'Air:

Méthodes Topologiques Appliquées a l'Electronique, par L. Sideriades. Pp. 136. No. N.T. 84, 1959. 3190 fr.

Nébulogranulomètre pour l'Etude des Brouillards Naturels et Artificiels, par A. Arnulf, J. Bricard, C. Véret et R. Burtin. Pp. 25. No. N.T. 86, 1959. 600 fr.

Mécanisme de la Déviation des Jets Propulsifs, par M. Kadosch. Pp. 156. No. B.S.T. 124, 1959. 4300 fr.

Explorations de la Couche Limite, en Turbulence Naturelle et en Turbulence Provoquée dans le Cas d'un Ecoulement Supersonique le Long d'une Plaque Plane, par J.-F. Dorand. Pp. 106. No. 355, 1959. 2830 fr.

Doublet d'Hélices Coaxiales Hélice Unique, par J. Cristescu. Pp. 276. No. 356, 1959. 8000 fr.

Fig. 1

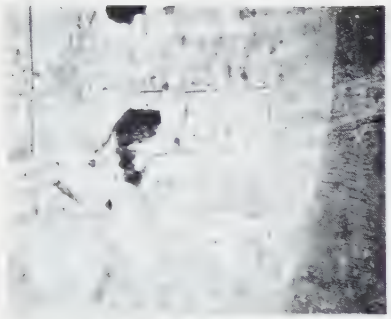

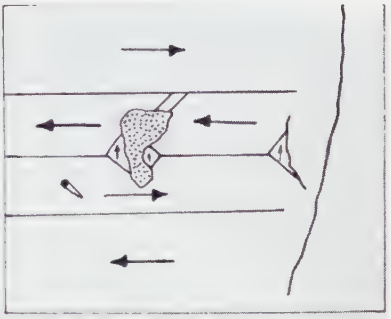

Fig. 1a

Fig. 2

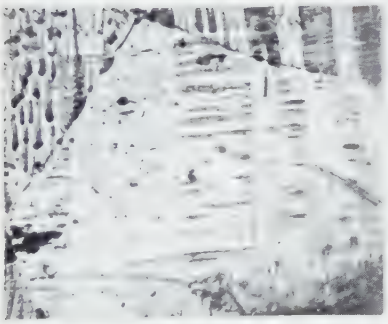

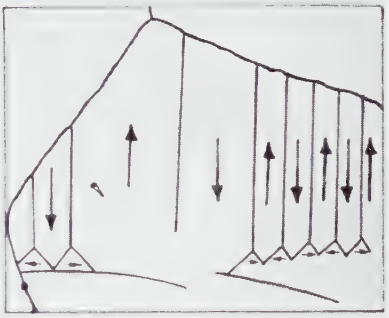

Fig. 2a

Fig. 3

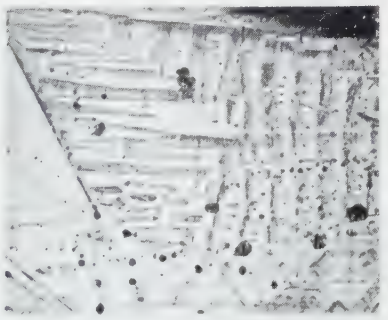

Fig. 4

Figure 1. Slab domains parallel to the rolling direction in a grain which has a perfectly oriented (100) surface.

Figure 2. Grain with main domains magnetized along the [010] and [0$\bar{1}$0] directions.

Figure 3. Grain boundary between two (100) surfaces. The formation of fir-trees in the upper grain shows it to be oriented at a small angle to a (100) surface.

Figure 4. Slab domains and spikes of reverse magnetization in a grain with (110) surface orientation.

Long arrow indicates rolling direction in all figures.

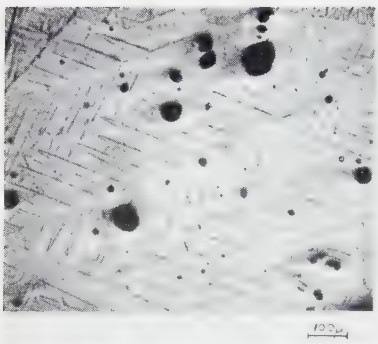

Fig. 5

Fig. 6

Fig. 7

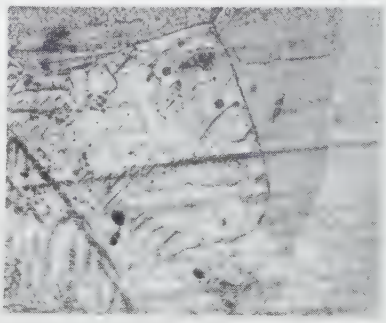

Fig. 8

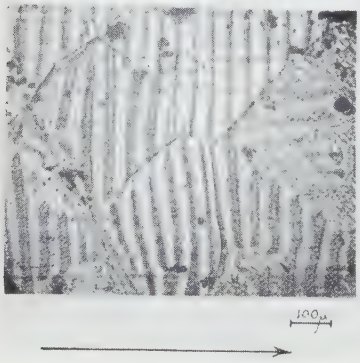

Fig. 9

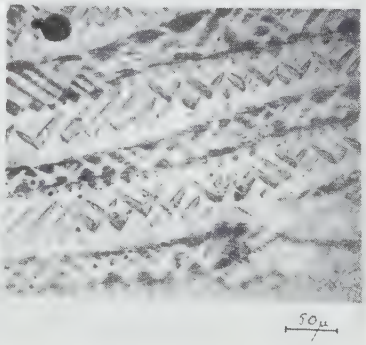

Fig. 10

Figures 5 and 6. Domain patterns showing the development of the fir-tree structure on surfaces which are misoriented with respect to a (100) surface.

Figures 7 and 8. Development of the ' comb ' pattern on surfaces which are inclined to a (100) surface by rotation about the rolling direction, ⟶.

Figure 9. Band structure across several grains.

Figure 10. Enlarged portion of the band structure.

Fig. 11

Fig. 12

Fig. 13

Fig. 14

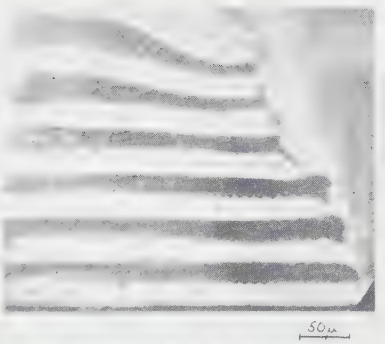

Fig. 15

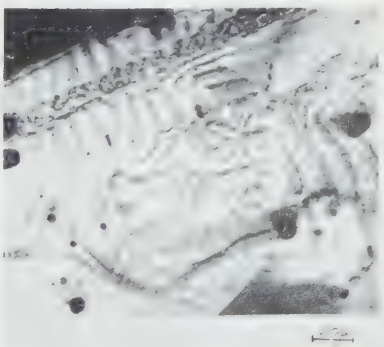

Fig. 16

Figure 11. Maze patterns on strained surface of the single crystal.
Figure 12. Zigzag walls on the (100) surface of the single crystal.
Figures 13 and 14. Band structure at the edge of the strained single crystal.
Figures 15 and 16. Patterns on the annealed cube-textured specimen.

The Influence of Ionic Conductivity on the Electric Strength of KCl and NaCl

By R. COOPER, R. M. HIGGIN and W. A. SMITH
Electrical Engineering Laboratories, University of Manchester

MS. received 10*th February* 1960, *in final form* 6*th June* 1960

Abstract. At high temperatures, the electric strengths of the alkali halides appear to decrease rapidly with rise in temperature. This behaviour is qualitatively similar to that predicted by Fröhlich's high temperature theory of breakdown. It can also be explained in terms of space charge and thermal effects due to the transport of ions and therefore speculation exists about the operative mechanism. The ionic conductivity of alkali halide crystals depends upon the amount of bivalent impurity they contain. This fact has been used to determine the influence of ionic conductivity upon the electric breakdown of KCl and NaCl. No evidence is provided to support Fröhlich's high temperature theory, the observed negative temperature coefficient of KCl being attributed to ionic phenomena. Changes of up to sixtyfold in the ionic conductivity of NaCl did not influence the impulse electric strength of this material except at temperatures below about −50 c, when the effect of increased conductivity was to *increase* the electric strength.

§ 1. Introduction

There is some evidence (Whitehead 1951) of a relationship between temperature and electric strength for the alkali halides that consists of two parts. With rise in temperature the electric strength increases slowly until a value T_c is reached, between about 100°c and 200°c, but with further rise in temperature the opposite effect appears to take place and the electric strength decreases relatively rapidly. This behaviour is in qualitative agreement with that predicted by the theories of breakdown due to Fröhlich (1939, 1947) but the decrease in electric strength at high temperatures can also be explained in terms of space charge formation and thermal effects arising from the ionic conductivity. Speculation therefore exists about the operative mechanism.

In the past, evidence of the above ionic effects has been sought by comparing values of electric strength obtained by using impulse voltages of widely differing durations. According to Fröhlich's high temperature theory the time lag in breakdown is entirely of a formative kind and is not likely to exceed about 10^{-6} sec (Fröhlich and O'Dwyer 1950). The duration of the impulse should not influence the measured value of electric strength provided it exceeds this value. On the other hand, if conditions permit the formation of ionic space charges, or if thermal breakdown can occur, the measured values of electric strength will decrease as the time of application of voltage, or the ionic conductivity, is increased.

The results of experiments carried out in relatively recent years using various alkali halides at temperatures above T_c are conflicting. Alger and von Hippel (1949) obtained an impulse effect using KBr, while Inuishi and Suita (1953) have observed an effect with KCl, but this was not confirmed by Calderwood and

Cooper (1953). Whether or not this difference arose from differences in the ionic conductivity of the crystals cannot be said because information has seldom been given about this property of the specimens.

§ 2. Method

The temperature range in which measurements of electric strength are generally made lies in the 'structure sensitive' region of ionic conductivity. In this region the ionic conductivity of the alkali halides can be increased by an order of magnitude or more by the addition of suitable bivalent impurities in quantities amounting to not more than one per cent (Seitz 1954). In the present investigation use is made of this fact and we have determined the effect upon electric strength at temperatures between -195 °c and $+220$ °c of adding cadmium to sodium chloride and lead to potassium chloride.

Each crystal was grown from the melt by withdrawing a seed crystal at the rate of approximately 2 cm per hour, the parent salt being of analar quality and the added cadmium chloride or lead chloride being of the purest quality available. Chemical analyses of a number of crystals showed that the impurity concentration was constant to well within 5 % throughout the length of the crystal, provided not more than about two thirds of the melt was used. Consequently groups of specimens could be prepared for electric strength investigation with practically the same impurity content and it was not necessary to analyse each specimen.

The present investigation is one of a series concerned with the electric breakdown of alkali halide crystals and experimental techniques have been standardized as far as possible with those described by Calderwood, Cooper and Wallace (1953) and Cooper, Grossart and Wallace (1957). The recessed specimens were all annealed and colloidal graphite electrodes were applied to the polished surfaces. Unless otherwise stated the voltage wave was a 1 : 8000 μsec impulse and a series of waves of increasing amplitude was applied to each specimen until it broke down. The voltage increment was 4 %. Each wave was recorded oscillographically and the time lag to breakdown (Cooper and Grossart 1956) was measured from the peak of the wave. The voltages at successive instants of time from the peak of a 1 : 8000 μsec wave are constant to within 1 % for about 50 μsec and as the majority of time lags recorded were less than this, the waves can be regarded as 'flat topped' ones.

To determine how the ionic conductivity was influenced by the impurity in the temperature range 100 to 250 °c planar specimens were used which were annealed and polished. Electrodes of either evaporated gold or colloidal graphite were applied to the polished surfaces. During the measurement the specimens were immersed in a bath of silicone oil and the temperature was constant to within $\pm 0{\cdot}3$ °c at all temperatures in the range of the measurements. The maximum field strength applied to the specimens was 15 kv cm $^{-1}$. When higher fields were used there occurred self heating with NaCl and polarization with KCl.

§ 3. Results

3.1. *Electric Strength of Potassium Chloride*

Previous experiments (Cooper, Grossart and Wallace 1957) using 1 : 50 μsec and 1 : 5000 μsec impulses have shown that the rate of decrease of electric strength with rise in temperature beyond T_c is greatest for specimens in which the field is applied in the (111) direction. Therefore only specimens of this kind were used

in the present investigation. Initially experiments were carried out to determine whether the value of T_c obtained for pure specimens was affected by changing the impulse wave form from those quoted above to a 1 : 8000 μsec wave. The results obtained by testing groups of between 15 and 20 specimens at temperatures up to 150 °C confirmed those of the previous investigation and the combined results are plotted in curve *a* of figure 1. At each temperature the spread in values of electric

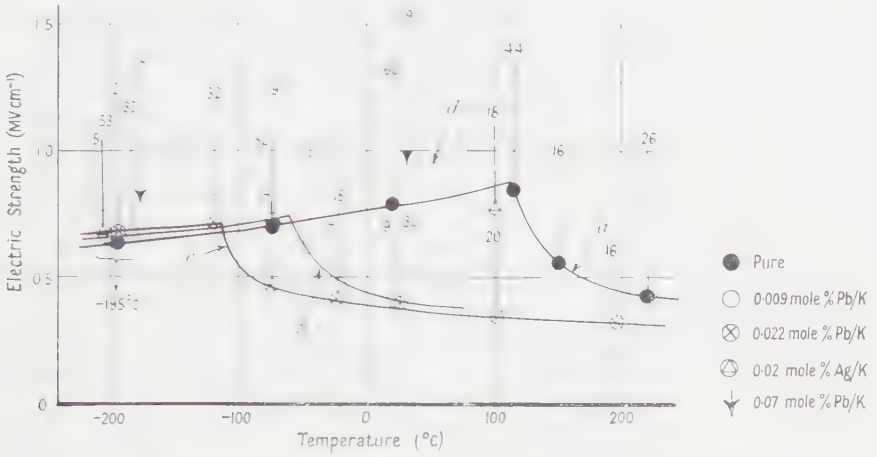

Figure 1. The electric strength of KCl–$PbCl_2$ mixed crystals.

strength is indicated and also the number of specimens tested at that temperature. Reasons certainly valid below T_c have been given previously (Cooper, Grossart and Wallace 1957) for attaching most significance to the low values in a group, and consequently the curve connecting electric strength with temperature has been drawn through the minimum values. Similar results obtained by testing specimens with concentrations of 0·009 mole % and 0·022 mole % of lead are plotted respectively in curve *b* and curve *c* of figure 1. A comparison of the three curves demonstrates the appreciable influence of lead impurity on the value of T_c. This was depressed from about 110 °C to about −60 °C by the addition of 0·009 % of lead, and to about −120 °C by the addition of 0·022 % of lead. Measurements made at −195 °C and +100 °C with specimens containing 0·02 % of silver showed that T_c is not greatly affected by small quantities of univalent impurity. The results are also illustrated in figure 1. At 100 °C the minimum value of electric strength was about 10 % lower than the value expected for pure crystals. This could have arisen from a reduction in T_c of about 10 °C, due to the addition of silver. This change is insignificant when compared with that of more than 200 °C caused by the addition of an approximately equal amount of lead. Finally in figure 1, curve *d*, are plotted the results of measurements made using 0·5 : 5 μsec impulses to breakdown specimens containing 0·07 % of lead. These measurements were made during an investigation of factors influencing the discharge track direction. The specimens were of the (110) type but the available evidence (Cooper, Grossart and Wallace 1957) shows that T_c does not depend on the direction of the applied field. The use of short duration impulses suppressed the mechanism responsible for the fall in electric strength with rise in temperature beyond T_c.

In the present investigation four sets of comparable values of electric strength were obtained at liquid nitrogen temperature, namely those for pure specimens,

and for impure specimens containing respectively 0·009% of lead, 0·022% of lead and 0·02% of silver. They show that such small amounts of impurity have little influence on the electric strength at this temperature. It follows that their presence did not significantly increase the probability of electron scattering at low temperatures and the theoretical investigation of Fröhlich (1941) provides no reason for expecting a different effect at higher temperatures.

3.2. *Electric Strength of Sodium Chloride*

The results obtained with sodium chloride are plotted in figure 2. On this diagram curve *a* refers to nominally pure specimens and it is based on the combined

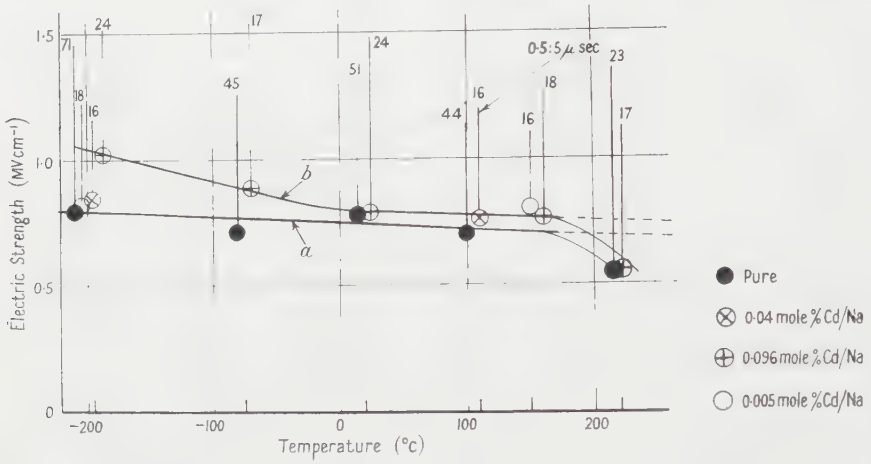

Figure 2. The electric strength of $NaCl–CdCl_2$ mixed crystals.

results of the present investigation and the preceding one in which 1 : 5000 μsec waves were used (Cooper, Grossart and Wallace 1957). In contrast with the nominally pure specimens of KCl there is little evidence of a transition in the slope of the curve at temperatures between −200°c and +200°c. The effect of 0·096% of cadmium impurity is illustrated by comparing curve *a* with curve *b*. In figure 2, at −195°c and at +150°c are also plotted values of electric strength corresponding to specimens containing 0·005% of cadmium, and values are given for specimens containing 0·04% of cadmium at −195°c and at +100°c. The duration of the impulse appears to have little influence. Specimens containing 0·096% cadmium and broken down with 0·5 : 5 μsec waves yielded similar values of electric strength to those obtained at the same temperature of 150°c using specimens containing 0·005% of cadmium and tested with 1 : 8000 μsec waves.

The addition of cadmium to sodium chloride produced no effect on the electric strength at high temperatures but at low temperatures it caused an increase in this quantity. This result is in strong contrast with the effect of lead on the electric strength of KCl.

3.3. *Time Lags*

At each temperature below T_c the distribution of time lags for potassium chloride was represented approximately by the formula $N_t = N_0 \exp(-t/\tau)$, where N_0 is the total number of time lags observed, N_t the number exceeding t μsec and τ is a constant, about 4 μsec in magnitude for pure specimens and about

7 μsec for specimens containing 0·022 mole% of lead. At temperatures beyond T_c but on the knee of the curve relating electric strength to temperature, the average time lag increased with rise in temperature and the distribution of time lags differed appreciably from that stated above. The effect is illustrated in figure

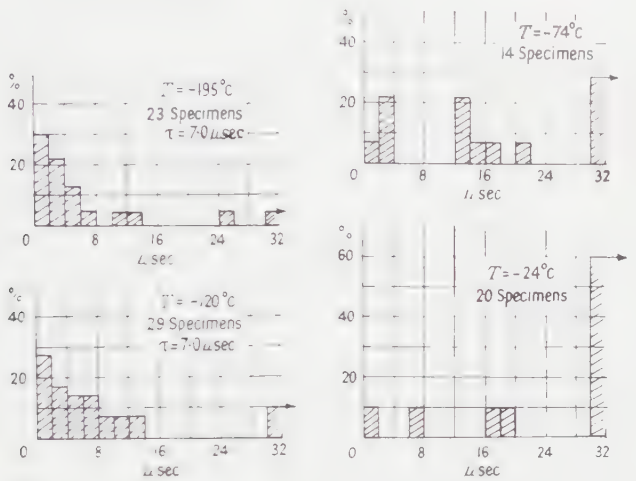

Figure 3. Time lag distributions for crystals of KCl–0·022 mole% Pb/K.

3 which refers to specimens containing 0·022% of lead and for which T_c is about -120°C.

The distribution of time lags observed with NaCl did not change appreciably with rise in temperature and in all cases was approximately of the form $N_t = N_0 \exp(-t/\tau)$. At 220°C, the highest temperature used, the voltage across many of the specimens did not collapse instantaneously at breakdown. Evidence was provided of the flow of appreciable current that increased with time during the period of about 3 μsec preceding breakdown. This effect was exhibited by about 80% of the pure specimens and a slightly smaller proportion of the impure ones. No specimens of KCl exhibited this effect at temperatures below the appropriate value of T_c. At temperatures just above T_c it was present in the breakdown of an occasional specimen but with increase in temperature the phenomenon became more frequent and at 220°C it occurred with 70% of the pure specimens. The time to breakdown for specimens exhibiting pre-breakdown current did not depend appreciably on temperature, time lags of a few microseconds duration being observed both at -74°C and $+220$°C.

3.4. *Ionic Conductivity*

The connection between impurity concentration and the ionic conductivity of the crystals remains to be stated. The law relating specific conductivity σ with temperature T in the range of 100°C to 250°C was determined by obtaining groups of between 6 and 12 specimens from three or four separate parent crystals each of the same impurity concentration. The law for both pure and impure specimens of KCl was $\sigma = a \exp(-b/T)$ mho cm^{-1} where a and b are constants and T is the temperature in degrees K. The constant b did not vary appreciably from specimen to specimen in a group nor did it depend on the impurity concentration. The value was $11\,100 \pm 7\%$. On the other hand, the constant a varied appreciably

specimen by specimen and the average value increased with the concentration of lead. The values of a obtained from ten nominally pure specimens ranged from 3·3 to 81·2 and the average value was 39·6. Corresponding values obtained from a group of six specimens containing 0·022% of lead ranged from 93·5 to 955 and the average value was 347. Considerable error may exist in the determination of the constant a because of the limited range of temperature in which measurements were made but the values of a and b quoted above give an adequate indication of the specific conductivity of the specimens when they are inserted in the above equation. Measurements made at 150° c indicated that the average conductivity of groups of specimens containing 0·009%, 0·022%, 0·037%, 0·071% and 0·125% of lead were respectively 4, 9, 13, 22 and 32 times the average conductivity of a similar group of pure specimens.

The behaviour of sodium chloride was qualitatively the same as that of potassium chloride but certain differences in detail were observed. First, with many specimens the slope of the straight line relating $\log \sigma$ with $1/T$ was appreciably smaller at temperatures below about 190° c for pure specimens, and below about 130° c for impure ones, than it was above these temperatures, average values for the constant b being respectively 8800 and 12 900. In contrast with KCl the constant b varied appreciably from specimen to specimen, the effect being greatest with the pure specimens, and with these it ranged from 10 400 to 17 000 at temperatures greater than 190°C. The range of values for the constant a was from 46·0 to 100 000.

The average conductivity at 220°C of groups of specimens containing 0·005%, 0·038% and 0·096% of cadmium were respectively 4, 20 and 60 times the average conductivity of a similar group of pure specimens. Although considerable spread existed in the conductivity of members of each group, the above figures, together with similar ones quoted previously for KCl give an adequate indication of the probable connection existing between impurity concentration and ionic conductivity for the kinds of specimens used in the electric strength investigations.

§ 4. Discussion

The transition occurring at T_c in the behaviour of the electric strength of KCl with respect to increase in temperature cannot be explained in terms of Fröhlich's high temperature mechanism of breakdown. This follows from the manner in which the electric strength and the time lag in breakdown vary with increase in temperature. According to Fröhlich's theory the electric strength E is related to the temperature T by

$$\log E = \text{constant} + \Delta V/2\boldsymbol{k}T$$

where ΔV is the spread of impurity levels just below the conduction band, $\boldsymbol{k}$ is Boltzmann's constant, and T is the temperature in deg K. When the values of electric strength shown in figure 1 at temperatures above T_c are plotted according to the above equation the linear relation is not obeyed. A casual inspection of figure 1, curve c, is sufficient to show that the electric strength does not decrease rapidly enough at the higher temperatures to obey an exponential law. Nevertheless when the best straight lines are drawn, values for ΔV of 0·24 ev, 0·08 ev, 0·03 ev are obtained from curves a, b and c respectively. These values are impossibly low for a material that is an insulator at room temperature. On the basis of Fröhlich's theory it is possible to account for the existence of time lags in

breakdown of about a microsecond by assuming the existence of deep traps (Simpson 1949) but time lags due to this mechanism decrease with rise in temperature. The opposite effect was observed.

The effects observed with KCl are clearly associated with the bivalent impurity because no significant change in electric strength or in the value of T_c or in the law governing the distribution of time lags was caused by the addition of univalent silver. In the alkali halides at temperatures below about 500°c the ionic conductivity is due to the transport only of positive ions. Ionic space charge may accumulate when the rate at which ions are transported through the crystal exceeds the rate of their discharge at the electrodes. When this occurs the initially uniform electric field is distorted until either equilibrium is re-established or disruption occurs. We assume here that breakdown will occur when the electric field throughout a small volume of the specimen becomes equal to or exceeds the intrinsic electric strength. When breakdown is conditioned by the formation of ionic space charge a time lag must exist between the application of a constant voltage and disruption of the specimen in order to permit the build up of space charge. This time lag must be added to any other lag involved in the more fundamental processes leading to intrinsic breakdown and its duration must decrease as the voltage is increased, and also as the ionic conductivity is increased, if all other factors are constant. When the impulse duration is long and sufficient to permit the formation of space charge, we expect the measured values of electric strength to decrease with increase in the ionic conductivity, i.e. with rise in temperature or with increase in the concentration of impurity at a fixed temperature. The behaviour of KCl at temperatures above T_c exhibits these characteristics and the changes that occurred in the behaviour of the material as the temperature increased above the appropriate value of T_c are attributed to the onset of space charge conditioned breakdown. The temperature T_c is the highest temperature at which the rate of discharge of ions at the cathode exceeds their rate of transport through the crystal. The random distribution of time lags at higher temperatures is probably explained by the fact that appreciable differences exist in the ionic conductivity of apparently similar specimens and therefore in the time taken for the build up of space charge.

In the case of sodium chloride the effect of increasing the ionic conductivity was opposite to that observed with KCl. At high temperatures a sixtyfold increase in the ionic conductivity did not influence the electric strength but at -195°c the minimum value was increased by about 30%. This effect is similar to that obtained when dipolar groups are added to non-polar polythene (Whitehead 1951) the rise in electric strength at low temperatures being attributed to the presence of the dipolar components. A similar explanation may apply in the case of the impure NaCl crystals in which structural components of a dipolar character are believed to exist. These consist of a Cd^{2+} ion in association with a lattice defect consisting of a missing positive ion (Seitz 1954). There is some evidence of a similar effect with KCl, for when the results of figure 1, curve *d*, which were obtained using (110) specimens containing 0·02 mole % of lead, are compared with the results obtained by Cooper, Grossart and Wallace (1957) using pure (110) specimens there is seen to be proportionately a greater increase in electric strength at -195°c than at $+20$°c. This cannot be explained in terms of voltage overshoot since the average time lag does not depend very much on temperature below T_c and the fact that the slope of curve *d* is similar to that of curve *a*, which refers to pure

specimens, indicates that the 0·5 : 5 μsec impulses were short enough to suppress ionic phenomena.

The cause of the pre-breakdown current observed with specimens of KCl at temperatures above T_c and with many of the specimens of NaCl at 220 °C is not known. It does not appear to be a simple case of thermal instability. This follows from calculations of the time t_m taken to reach melting point T_m, assuming a uniform field E of 10^6 v cm^{-1} is applied to specimens possessing conductivity constants equal to those determined by the measurements described in § 3.4. When pre-breakdown current was observed the specimen usually disrupted within a few microseconds after application of voltage. The heat lost by conduction in this time is very small and if it is ignored the time to reach melting point is

$$t_m = \frac{S\delta}{E^2 a} \int_{T_0}^{T_m} \exp\left(\frac{b}{T}\right) dT.$$

In this equation, S is the specific heat, δ is the density, a and b are the constants in the law relating conductivity with temperature (deg K). The changes occurring in these constants at temperatures above about 500 °C, due to the conductivity ceasing to be 'structure sensitive', can be ignored because the calculation shows that 90% of t_m is the time spent in raising the temperature through the first 100 K from T_0. The definite integral can be evaluated by use of

$$\int \frac{\exp(x)}{x^n} dx = \frac{\exp(x)}{x^n} + n \int \frac{\exp(x)}{x^{n+1}} dx.$$

When $x(=b/T) \gg 1$, a very good approximation is provided by:

$$t_m = \frac{S\delta}{E^2 a} \frac{T_0^2}{b} \left(1 + \frac{2T_0}{b}\right) \exp\left(\frac{b}{T_0}\right).$$

The calculated values of t_m for the pure specimens referred to in § 3.4 ranged from about 1 msec to about 20 msec, assuming the initial temperature to be 220 °C. At this temperature the measured time to breakdown was a few microseconds and the calculations are in error by factors of between 10^2 and 10^3. For impure specimens, calculated values of t_m are smaller than the above values but not significantly so. In this calculation we have used conductivity constants obtained by assuming uniform distribution of current through the specimens and also we have assumed that the constants do not depend on the electric field. Both assumptions may have led to an over-estimation of t_m. It is possible that paths of high conductivity exist through the crystal, provided perhaps by mosaic boundaries for which the values of a are relatively high and the values of b are relatively low. However, the measured values of t_m were not very sensitive to temperature. Occasional specimens of impure KCl exhibited pre-breakdown current at -74 °C and for those specimens the time to breakdown was only a few microseconds. The calculated values of t_m are insensitive to temperature when the value of b is about 1000 or less and using this value for b, the constant a must be about 10^{-3} in order to yield values of a few microseconds for t_m. This low value of a does not seem likely. At -74 °C about a week would be required to melt a specimen, subject to the assumption made above.

The ionic conductivity has throughout been assumed independent of electric field. According to the current theory of ionic conductivity (Mott and Gurney 1948) the mobile ions migrate from one position in the lattice to another by jumping

over a potential barrier and Ohm's law is obeyed if $eEa \ll kT$, where e is the electron charge, E the applied electric field, a the distance between adjacent lattice points, and k is Boltzmann's constant. This condition does not hold when fields of about 10^6 v cm^{-1} are applied to alkali halide crystals but the error involved in extrapolation amounts to only about 5%. We have made measurements using rectangular impulses of 1·24 sec in duration and Ohm's law was obeyed in fields up to about 0·3 mv cm^{-1}. With stronger fields it is difficult to avoid thermal effects. We know of no convincing evidence in support of the view that the conductivity of alkali halide crystals depends on the field applied.

This investigation has provided a way of reconciling the differing results obtained above 100 °c by various investigators using apparently the same material. There is no information about the conductivity of the specimens used in most previous investigations but this could have varied appreciably because of the sensitivity to bivalent impurity. Most work prior to about 1950 was carried out using steady or power frequency voltages and it is almost certain that either thermal or space charge effects influenced the measurements above 100°c. On the other hand because of the statistical time lags, measurements made using linearly rising voltage waves about 10^{-6} sec or less in duration are likely to have yielded high values of electric strength because of voltage overshoot.

No evidence is provided to modify, on account of space charge effects, the view previously expressed that below T_c the wide spread in values of electric strength, obtained from apparently similar specimens (Cooper, Grossart and Wallace 1957) is due to structural variations caused by mechanical treatment. The significant values of electric strength are the low ones provided the experiments are performed competently.

Acknowledgments

The work described is based on report L T 395 of the British Electrical and Allied Industries Research Association. The authors wish to thank the Association for a maintenance grant and also for permission to publish. Their thanks are also due to Mr. R. A. Shelton, who assisted with the chemical analyses of specimens.

References

Alger, R. S., and von Hippel, A., 1949, *Phys. Rev.*, **76**, 127.
Calderwood, J. H., and Cooper, R., 1953, *Proc. Phys. Soc.* B, **66**, 74.
Calderwood, J. H., Cooper, R., and Wallace, A. A., 1953, *Proc. Instn Elect. Engrs*, IIA, **100**, 105.
Cooper, R., and Grossart, D. T., 1956, *Proc. Phys. Soc.* B, **69**, 1351.
Cooper, R., Grossart, D. T., and Wallace, A. A., 1957, *Proc. Phys. Soc.* B, **70**, 169.
Fröhlich, H., 1939, *Rep. Progr. Phys.*, **6**, 411 (London: Physical Society).
—— 1941, *Proc. Roy. Soc.*, **178**, 493.
—— 1947, *Ibid.*, **188**, 521.
Fröhlich, H., and O'Dwyer, J., 1950, *Proc. Phys. Soc.* A, **63**, 81.
Inuishi, Y., and Suita, T., 1953 *Tech. Reports of Osaka University*, **3**, No. 80, 269.
Mott, N. F., and Gurney, R. W., 1948, *Electronic Processes in Ionic Crystals* (Oxford: Clarendon Press), p. 43.
Seitz, F., 1954, *Rev. Mod. Phys.*, **26**, 7.
Simpson, J. H., 1949, *Proc. Roy. Soc.* A, **197**, 269.
Whitehead, S., 1951, *Dielectric Breakdown of Solids* (Oxford: Clarendon Press), p. 76.

The Hole Mobility in Selenium

By W. E. SPEAR
Physics Department, University of Leicester

MS. received 10*th May* 1960, *in final form* 2*nd June* 1960

Abstract. A pulse method, developed for the study of effective mobility in insulating solids, is applied to evaporated specimens of vitreous Se. Charge carriers are generated near the top electrode by a 13 mμsec electron pulse and drift across the specimen in a pulsed applied field. The transit time of holes is measured with improved electronic apparatus having a bandwidth of 27 Mc/s. At 20°c the effective hole mobility μ lies between 0·13 and 0·14 $cm^2 sec^{-1} v^{-1}$. The temperature dependence of μ shows that it is controlled by a level of acceptor states lying $\epsilon = 0{\cdot}14$ ev above the valence band. The values of μ and ϵ are in close agreement with those found for single crystals of hexagonal Se which suggests that the centres controlling μ are common to both forms of Se. It is concluded that the hole conduction is determined by the short range order within the Se chain itself or in close proximity to it. The carrier density, however, depends on the arrangement of the chains in the solid. From x-ray data the density of acceptor states is estimated as $10^{20} cm^{-3}$, giving a value of about 60 $cm^2 sec^{-1} v^{-1}$ for the microscopic mobility.

§ 1. Introduction

Selenium possesses a number of unusual electric and optical properties which do not seem to fit into the framework of normal semiconductor theory and for which a satisfactory explanation has not yet been found. In particular, it has been shown that in both single crystals and microcrystalline specimens of hexagonal Se the hole mobility increases with temperature and is controlled by an activation energy; the carrier concentration, on the other hand, is almost independent of temperature.

Little is known about the insulating amorphous (or vitreous) modification. In this paper an investigation of the hole mobility and its temperature dependence in this form of Se is described. The experimental method, now being developed for the study of effective mobility in a wider range of insulating solids, is in principle the same as that used previously for the measurement of electron mobility (Spear 1957). However, the transit times of the generated holes are far shorter than those of electrons, and considerable improvements in the apparatus, described in § 2, were necessary before reliable measurements could be made.

The results are in surprisingly close agreement with those for single crystals of the hexagonal modification. This suggests a conduction mechanism common to both forms which is discussed in § 4 in the light of recent x-ray studies.

§ 2. Experimental Method

As the experiment was based on the assumption that the excitation pulse is of much shorter duration than the transit time, it was found essential to improve the

method of pulse formation. The thyratron used previously was replaced by the high speed relay M† (figure 1), which discharged the open ended delay line DL with a rise time of about 1 mμsec. A connecting line CL fed the pulse into its characteristic impedance connected inside the electron gun between grid G and filament F. The gun was normally biased off by the battery B. In most experiments a delay line of 1·5m length was used, giving a pulse length of 13 mμsec. The relay M was energized by the mains through a high tension coupling condenser connected to the amplifying and squaring unit A. The amplitude of the excitation pulse was controlled by the potentiometer P. A steady or pulsed potential V could be applied to the top electrode of the specimen S. The bottom electrode was connected through a pre-amplifier to the distributed amplifier of a Tektronix oscilloscope. With an input time constant of about 20 μsec, much

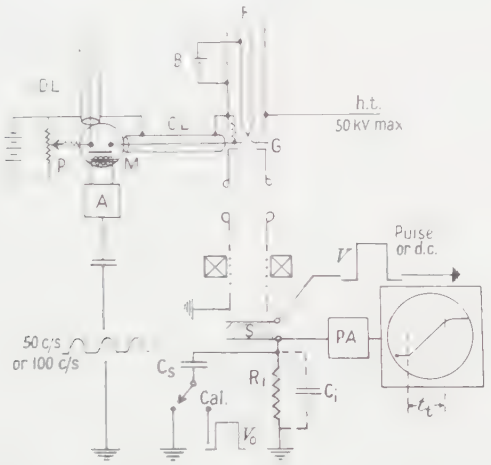

Figure 1. Experimental arrangement. F, filament, b, bias battery, G, control grid, DL, delay line, CL, connecting line, M, mercury wetted contact relay, A, amplifying and squaring unit, S, specimen, PA, pre-amplifier.

longer than the hole transit time t_t, the trace represented the charge displacement caused by the drift of the generated carriers between $t = 0$ and $t = t_t$. At maximum sensitivity and a band width of 27 Mc/s, 1 cm on the screen corresponded to the transit of about 5×10^2 charge carriers. To calibrate the system, a pulse of known amplitude also from a mercury relay, was applied to the input through a standard condenser C_s. The small number of electrons in the incident pulse was measured as follows: a potential divider connected across the delay line (not shown) provided a potential equal to the pulse amplitude. This was reversed and switched in series with the bias battery B so that the steady beam current then flowing was equal to that during the pulse. In this way 10^3 electrons per pulse could easily be measured with a galvanometer.

§ 3. Experimental Results

Nine specimens, ranging in thickness from 4 to 14 μ were investigated. Their preparation has been described previously (Spear 1956). In most experiments the amplitude of the bombarding pulse was adjusted to give about 2×10^4 incident electrons per pulse. Their energy was kept below 12 kev so that the generation

†Elliott Type 275 mercury wetted contact relay.

of free carriers was confined to a thin layer near the top electrode. The effective hole mobility is obtained from $1/t_t = \mu V/d^2$, where d is the specimen thickness and it is assumed that the applied field $E = V/d$. Figure 2 shows a typical graph of $1/t_t$ against V/d^2 for two specimens (8·3 and 12 μ thick) at 20°C and at lower temperatures. The results may be summarized as follows:

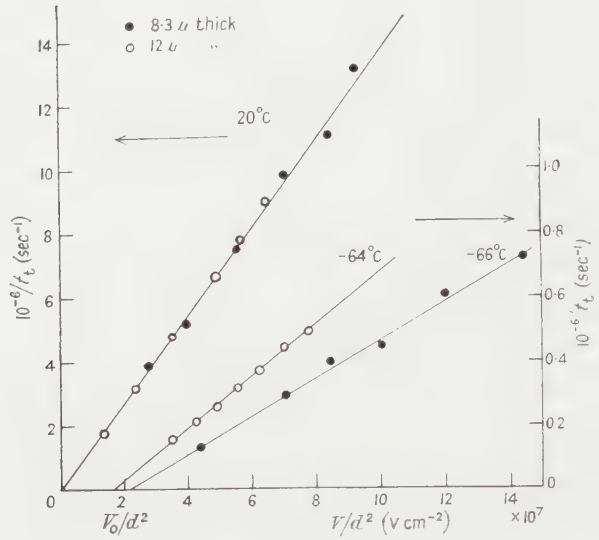

Figure 2. Experimental results for two specimens, 8·3μ and 12μ thick, at 20°C and at −64°C and −66°C.

(i) The hole pulses are similar in appearance to those observed for electrons. They show a linear rising edge, indicating that the hole cloud moves with a constant average drift mobility. Consistent values of t_t are obtained by direct measurement on the oscilloscope screen.

(ii) At low applied fields ($E \lesssim 2 \times 10^4$ v cm^{-1}), the height of the trace decreases to a fraction of its initial height with a time constant of about one second after switching on the field. This effect was eliminated by the use of a slowly pulsed field.

(iii) At room temperature and above, all graphs of $1/t_t$ against V/d^2 pass through the origin. At the lower temperatures, as shown in figure 2, the linear relation still holds but the applied potential appears to be reduced by a constant amount to $V - V_0$.

(iv) For the thinner specimens an apparent decrease in μ with decreasing thickness is observed (figure 3). But the group of thicker specimens (8 to 14μ)

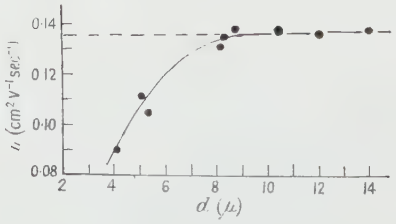

Figure 3. Graph of mobility against specimen thickness at 20°C.

leads to consistent mobility values at all temperatures. At 20 °C, μ lies between 0·13 and 0·14 $cm^2 sec^{-1} v^{-1}$.

The temperature dependence of μ has been investigated between 50 °C and −70 °C. Figure 4 shows that in this temperature range μ has an activation energy of $\epsilon = 0{\cdot}14 \pm 0{\cdot}01$ ev. The results have been interpreted here in terms of an effective mobility which is controlled by a discrete level of states of density N_t lying ϵ ev above the valence band and in thermal equilibrium with it. According to Rose (1951) μ is related to the microscopic mobility μ_0 by

$$\mu = \frac{N_v}{N_t} \exp\left(\frac{-\epsilon}{kT}\right) \mu_0 \qquad \ldots\ldots (1)$$

N_v, the effective density of states at the top of the valence band, is taken as $2{\cdot}5 \times 10^{19} (T/300)^{3/2} (m^*/m)^{3/2}$.

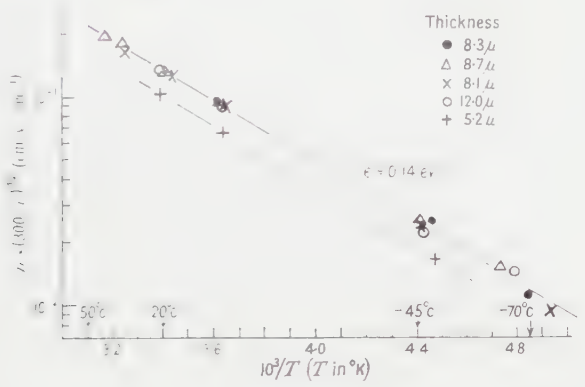

Figure 4. Temperature dependence of hole mobility.

§ 4. Discussion

First, the observed effects summarized above will be briefly discussed. The decrease in amplitude at low steady fields is almost certainly connected with the space charge set up by the filling of deeper traps in the specimen volume. The discharge effects described previously have been attributed to the same cause. Further confirmation is obtained from experiments with large bombarding pulses ($> 3 \times 10^5$ electrons per pulse). The observed hole pulse now loses its linear rising edge and shows a marked concave shape throughout the transit of holes across the first half of the specimen. This is consistent with the build-up of a positive volume charge. In fact, the pulse might be used as a probe for the study of the space charge distribution.

The observed reduction in the applied field at lower temperatures appears to result from a surface rather than a volume charge. As the holes are drawn out of the bombarded region a sheet of negative charge is left behind. Owing to the small electron mobility this space charge is likely to persist throughout most of the hole transit and reduces the applied field by V_0/d. A contribution to this space charge layer, particularly at lower temperatures, will arise from deeper electron traps presumably more numerous in the surface region than in the bulk.

The reason for the decrease of μ with specimen thickness is not clear. It is unlikely to be a fundamental property of the specimens, but may be connected with the measuring technique. For a thin specimen the duration of the excitation

pulse is no longer short compared with t_t for all V. This affects the sharpness of the pulse and could introduce considerable systematic errors in μ. Also, if the presence of a surface barrier has any effect upon the measurements, this should be more pronounced in thin specimens, where the barrier region may be an appreciable fraction of the specimen thickness.

It is of particular interest to compare the values of μ and ϵ found here for vitreous Se with the corresponding values obtained by Plessner (1951 a) and Henkels (1951 a) for single crystals of hexagonal Se grown from the vapour phase and the melt respectively. The values given in the table were obtained from conductivity, Hall effect and thermoelectric power measurements, and refer to conduction in the direction of the Se chains (c-axis) at room temperature.

	Hexagonal Se, single crystals		Amorphous Se
	Plessner	Henkels	Spear
ϵ (ev)	$0{\cdot}13 \pm 0{\cdot}02$	0·15	$0{\cdot}14 \pm 0{\cdot}01$
μ ($cm^2\ sec^{-1}\ v^{-1}$)	0·14	0·13	$0{\cdot}13 - 0{\cdot}14$

Both authors find an essentially temperature independent carrier density and agree that the measured activation energy must be associated with the mobility.

The close agreement of the ϵ values suggests the view that the centres controlling the hole mobility in amorphous and hexagonal Se are in fact identical. The agreement of the mobility values is surprising, as Hall effect and thermoelectric power measurements should lead to a microscopic mobility, far larger than μ. It seems unlikely that the agreement is fortuitous and it is conceivable that in the presence of a high density of shallow traps the Hall mobility value approaches μ. It is difficult, however, to give a convincing argument in support of this suggestion. Microcrystalline specimens possess essentially the same properties as the single crystals; the values of μ and ϵ agree approximately with those of the table but have been shown to depend on the crystallization temperature (Plessner 1951 b, Henkels 1951 b).

The properties of Se have generally been explained in terms of internal potential barriers which result from its basic structure (e.g. Moss 1959, Plessner 1951 a). In particular, for the microcrystalline form it has been suggested that such barriers are situated at the boundaries between ordered domains (2–20 μ in size), the boundary region consisting largely of amorphous material (Henisch and François 1951, Krebs 1951). It seems unlikely that barriers of this type could have much effect on the charge transport in the thin specimens used here or in single crystals. In fact, Plessner (1951 a) estimates that if the temperature dependence of μ were attributed to potential barriers of 0·13 ev height, then a total of more than 10% of the crystal would have to consist of the boundary material. No such irregularities could be detected in his single crystals.

The close agreement in the ϵ values suggests that an explanation of the nature of the acceptor centres must be sought in structural properties and defects which are common to both the hexagonal and amorphous forms. By the nature of amorphous Se such common properties can only be found in regions far smaller than the above microcrystalline grain sizes, in which some degree of short range order exists. The results of a number of recent x-ray studies of vitreous Se are of interest in this connection (e.g. Krebs and Schultze-Gebhardt 1955, Richter, Kulcke and Specht 1952, Richter and Herre 1958). The authors agree that the

first peak of the atomic distribution curves represents the Se–Se bond, but differ in the further interpretation of their results. Krebs believes that the ends of the chains, between 100 and 1000 atoms long, will tend to join and lead to an essentially random arrangement of large ring molecules. On the other hand, Richter and Herre have shown that the short range order depends in its detail on the method of preparation. For the specimens used here, prepared by evaporation on to a substrate somewhat above room temperature, their interpretation indicates a short range order similar to that of the hexagonal lattice, which extends to a distance of 5 to 10 Å from the reference atom. A hole created in a Se bond by a bombarding electron should drift along a chain in an ordered volume of about $4\pi/3 \times 10^{-21}\,\mathrm{cm}^3$. Near the boundary of this region the periodicity along the chain will break down—presumably through incorrect bond angles. If structural faults of this kind are identified with the shallow trapping centres of equation (1), then $N_t \simeq 2 \times 10^{20}\,\mathrm{cm}^{-3}$.

Alternatively it might be assumed that trapping occurs predominantly at the unsaturated chain ends (Billig 1952, Hyman 1956). Taking an average chain length of 500 atoms, $N_t = 2 \times 3{\cdot}3 \times 10^{22}/500 \simeq 10^{20}\,\mathrm{cm}^{-3}$. This estimate implies a process in which a generated hole drifts along the chain with comparatively little activation energy for a time τ and is trapped at a nearby chain end. (For the fields used here, a hole will drift along only a fraction of the total chain length between trapping events). On the average a thermal energy of 0·14 ev is required to transfer an electron from a neighbouring Se bond (i.e. from the valence band) into the hole trap. With $N_t \simeq 10^{20}\,\mathrm{cm}^{-3}$, equation (1) leads to $\mu_0 \simeq 60\,\mathrm{cm}^2\,\mathrm{sec}^{-1}\,\mathrm{v}^{-1}$, using $m^* = 2{\cdot}5m$, a value deduced from the Faraday effect (Moss 1959). A lattice mobility of this order might be expected for an insulating solid, although it is still far smaller than the mobility in the isomorphous element Te. The calculation indicates that in Se on the average only 1 in about 400 of the generated holes is free to move, the rest being trapped. With the commonly found value of $10^{-15}\,\mathrm{cm}^2$ for the trapping cross section, the lifetime τ of a free hole is about $10^{-12}\,\mathrm{sec}$; the average time in a shallow trap is $4 \times 10^{-9}\,\mathrm{sec}$. These values are far beyond the resolution of the measuring apparatus and thermal equilibrium between traps and valence band may be assumed at all times during transit.

The interpretation of the results leads to the general conclusion that in Se the hole conduction and its temperature dependence is controlled by the short range order within the chain itself or in close promixity to it. The long range order seems to have little or no effect. Accordingly, the increase in conductivity which is observed on converting an amorphous specimen to the hexagonal form, must be attributed to an increase in carrier density by a factor of about 10^6. Thus, unlike the mobility and its temperature dependence, the carrier concentration is largely determined by the long range order of the chains within the solid. The orgin of the charge carriers is still obscure; a possible explanation has been given in terms of quantum mechanical resonance effects (von Hippel 1948, Mooser and Pearson 1956). A model of this kind, which depends on the resonance between neighbouring bonds, should certainly be sensitive to the alignment of the chains.

It should be stressed that the interpretation of the results presented here is based, through equation (1), on the assumption of a trap controlled mobility. An alternative mechanism has been tentatively suggested by Schottky (1953). He envisages a process of defect level conduction in which a hole moves from one centre to the next without activation into the valence band.

A third possible interpretation is based on the band structure calculation by Reitz (1957), which shows that in Se and Te the valence band is formed from three overlapping p-bands derived from the atomic 4p and 5p levels respectively. Caldwell and Fan (1959) have concluded from free carrier absorption measurements that in Te interband transitions occur between two branches of the valence band separated by 0·11 ev. It is possible that the activation energy determined here is connected with similar transitions in Se. However, there is as yet no experimental evidence which could decide in favour of any one of these interpretations.

Acknowledgment

The work described in this paper was supported by the European Research Office of the U.S. Department of the Army.

References

Billig, E., 1952, *Proc. Phys. Soc.* B, **65,** 216.
Caldwell, R. S., and Fan, H. Y., 1959, *Phys. Rev.*, **114,** 664.
Henisch, H. K., and François, M., 1951, *Semiconducting Materials* (London: Butterworths Scientific Publications), p. 234.
Henkels, H. W., 1951 a, *J. Appl. Phys.*, **22,** 916.
—— 1951 b, *Ibid.*, **22,** 1265.
von Hippel, A., 1948, *J. Chem. Phys.*, **16,** 372.
Hyman, R. A., 1956, *Proc. Phys. Soc.* B, **69,** 743.
Krebs, H., 1951, *Semiconducting Materials* (London: Butterworths Scientific Publications), p. 246.
Krebs, H., and Schultze-Gebhardt, F., 1955, *Acta Cryst., Camb.*, **8,** 412.
Mooser, E., and Pearson, W. B., 1956, *Canad. J. Phys.*, **12A,** 1369.
Moss, T. S., 1959, *Optical Properties of Semiconductors* (London: Butterworths Scientific Publications), pp. 156 and 163.
Plessner, K. W., 1951 a, *Proc. Phys. Soc.* B, **64,** 671.
—— 1951 b, *Ibid.*, **64,** 681.
Reitz, J. R., 1957, *Phys. Rev.*, **105,** 1233.
Richter, H., and Herre, F., 1958, *Z. Naturf.*, **13A,** 874.
Richter, H., Kulcke, W., and Specht, H., 1952, *Z. Naturf.*, **7A,** 511.
Rose, A., 1951, *R.C.A. Rev.*, **12,** 362.
Schottky, W., 1953, *Z. Naturf.*, **8A,** 457.
Spear, W. E., 1956, *Proc. Phys. Soc.* B, **69,** 1139.
—— 1957, *Ibid.*, **70,** 669.

Note added in proof.—The recently published article by A. F. Ioffee and A. R. Regel (1960, *Progress in Semiconductors*, vol. **4**, p. 238, London: Heywood and Company) is of considerable interest in connection with this paper. The authors discuss the mechanism of charge transfer in low mobility semiconductors and emphasize the significance of the short range order in determining the properties of non-crystalline solids.

Absorption of Krypton in the Extreme Ultra-violet

By ANNE PERY-THORNE and W. R. S. GARTON
Physics Department, Imperial College, London

MS. received 19*th April* 1960, *in final form* 19*th May* 1960

Abstract. The far ultra-violet absorption spectra of the heavier inert gases are characterized by strong, diffuse lines in the region between the $^2P_{3/2}$ and $^2P_{1/2}$ series limits. These lines have large natural widths, owing to the high probability of auto-ionization of their upper levels. Their oscillator strengths have been measured in the case of krypton by photographic photometry, using a photomultiplier to calibrate the photographic plates. The f-values found, 0·04 for the strongest line and 0·10 for the sum of all the lines, are much smaller than had been expected on the basis of dispersion measurements. Rough measurements of the continuous absorption in krypton from the $^2P_{1/2}$ series limit to 500 Å have been made directly with a photomultiplier, and it is shown that absorption in this continuum, the diffuse lines and the resonance lines probably accounts for only about two-thirds of the refractive index measured in the quartz ultra-violet region.

§ 1. Introduction

The absorption of radiation by the inert gases in the extreme ultra-violet region of the spectrum has been of some interest since the work of Cuthbertson and Cuthbertson (1910), who deduced from dispersion measurements in the visible region that there should be strong absorption centres at wavelengths ranging from 1000 Å in xenon to about 500 Å in helium. Dispersion measurements were later extended into the quartz ultra-violet by Koch (1913) for helium, Cuthbertson and Cuthbertson (1932) for neon, Quarder (1924) and Larsén (1939) for argon, and Kronjäger (1936) and Koch (1949) for krypton and xenon.

According to the quantum theory of dispersion, the refractive index of a gas at a frequency ν_0 not too close to an absorption line is given to a sufficient approximation by

$$n-1=\frac{e^2N}{2\pi m}\sum_j\frac{f_j}{\nu_j^2-\nu_0^2} \qquad \ldots\ldots(1)$$

where e and m are the charge and mass of the electron, N is the number of absorbing atoms per cm^3, and f_j is the oscillator strength associated with an absorption region of frequency ν_j. Many of the above authors have fitted their dispersion measurements to one-, two-, or three-term dispersion formulae of this form. The most recent presentation is that of Koch (1949), using Larsén's results for argon and his own for krypton and xenon. If the known wavelengths of the resonance lines are taken in each case for the first two terms of a three-term dispersion formula, their oscillator strengths being assumed equal but unknown, then the third wavelength falls at 609 Å, 695 Å, and 846 Å in A, Kr, and Xe respectively. Moreover, of the f-values determined in this way, the sum for the resonance lines is in each case only about one-tenth of that for the third wavelength.

Absorption by the inert gases in the short wavelength region was first observed qualitatively by Cuthbertson (1927). In 1935 Beutler photographed the far ultra-violet absorption spectra of A, Kr and Xe and found in each case, in addition to the two photo-ionization continua extending from the $^2P_{3/2}$ ground state and the $^2P_{1/2}$ metastable state of the ion, a double series of strong, very diffuse lines between these two limits and converging to the upper of them ($^2P_{1/2}$). Beutler classified these lines as higher members of the two series $p^6\,{}^1S_0$–$p^5\,(^2P_{1/2})ms$ and $p^6\,{}^1S_0$–$p^5\,(^2P_{1/2})md$. He attributed their diffuseness to the large natural widths of the upper levels, owing to the high probability of radiationless transitions to the adjacent continuum above the $^2P_{3/2}$ limit, and their high intensity to perturbations by this continuum. Beutler did not attempt to measure the oscillator strengths of these auto-ionized lines, but, since they appeared on his exposures at lower pressures than did the continua, he suggested that they might be largely responsible for the strong absorption required by the dispersion formulae.

The apparently great strength of the so-called Beutler lines in the inert gases is a feature shared by lines in other spectra showing strong auto-ionization broadening. In Hg I, for example, the line at 1126 Å first photographed by Beutler (1933), arising from the excitation of an electron from an inner d-shell, appears to be even stronger than the singlet resonance line at 1849Å. In Tl I Marr (1954) has measured the oscillator strength of an extremely broad auto-ionized line at 1610 Å, finding $f = 0{\cdot}52$, as compared with $f = 0{\cdot}2$ for the strongest resonance line.

The oscillator strengths of such auto-ionized lines are also of interest in plasma physics. If the lines are sufficiently strong, they represent pronounced maxima in the photo-ionization cross section of the atom and hence also in the rate coefficient for radiative electron recombination corresponding to the inverse process. This coefficient can be calculated as a function of the electron temperature if the oscillator strengths of the lines are known (Massey and Bates 1942).

For these reasons we decided to measure the oscillator strengths of the Beutler lines in one of the inert gases. In principle argon would have been the best choice, because its continuous absorption coefficient has recently been measured by Po Lee and Weissler (1955), and the *f*-values of its resonance lines have been calculated by Knox (1958). One can therefore estimate the contribution of both these regions of absorption to the refractive index in the quartz ultra-violet. However, the Beutler lines in argon are not quite wide enough to be properly resolved by the one-metre vacuum spectrograph that was available for the experiment. We therefore decided to use krypton and to make in addition some rough measurements of the continuous absorption.

§ 2. Experimental Method

The Beutler lines in krypton lie between the $^2P_{3/2}$ and $^2P_{1/2}$ absorption edges at 885 Å and 845 Å respectively. Their *f*-values were found from photometry of the absorption lines photographed on the continuous background of a mildly condensed discharge in helium when krypton was admitted to the spectrograph at a few microns pressure. The lines are wide enough to be easily resolved with a one-metre normal incidence vacuum spectrograph, used in this case with a Bausch and Lomb aluminized grating, of 15 000 lines per inch, blazed for 1500 Å in the first order. The plates were calibrated by what is believed to be a novel method, involving a photomultiplier. We used as intensity marks the resonance

lines of A II at 920 A and 932 A, photographed for six different discharge currents. The relative intensities corresponding to these currents were then measured directly with a photomultiplier in place of the photographic plate. It was not possible to avoid plate calibration altogether by measuring the absorption directly with the photomultiplier because of the unsteadiness of the helium discharge. Moreover, the vacuum spectrograph could not easily have been adapted for accurate line-contouring with a photomultiplier. We did, however, use the direct method for the rough measurements of continuous absorption.

The details of the experiment were as follows. The discharge tube used to excite alternatively the A II lines or the He_2 continuum was a straight Pyrex tube, 80 cm long and 3 cm in diameter, with hollow, cylindrical, stainless steel electrodes. Its open end was connected directly to the spectrograph slit, which was about 20μ wide. The discharge was excited by an 8 kv transformer with a variable resistance in its primary circuit. For the He_2 continuum a 0·05 μF condenser and small spark gap were inserted in the secondary circuit, and the helium, purified over hot copper oxide and liquid air cooled charcoal, was used at a pressure of about 8 mm Hg. The A II lines appeared quite strongly in an uncondensed discharge run in cylinder argon at a pressure of about 0·25 mm Hg; preliminary experiments established that their intensity was constant and reasonably reproducible at a given current.

For the absorption photographs, spectrally pure krypton (99–100%, balance xenon) was admitted to the spectrograph through a Leybold needle valve, and its pressure was measured with a McLeod gauge, via a side arm and liquid air trap. In order to avoid pumping krypton too rapidly through the spectrograph, the main pump was partly throttled before the needle valve was opened. There was, of course, a considerable flow of helium through the slit from the discharge tube, so that the krypton pressure had to be measured before the discharge was started and checked again at the end of the exposure after the helium flow had been cut off. Two exposures at different pressures of krypton between 3μ and 10μ were taken on each plate, together with one exposure with no krypton. Both Ilford Q1 and Q2 plates were used, exposure times being about 15 minutes with the former and 30 seconds with the latter.

For the intensity marks, the argon lines were photographed on every plate at six different currents between 360 mA and 18 mA. Exposure times were 4 minutes and 8 seconds for the Q1 and Q2 plates respectively.

The relative intensities of the A II lines at the currents used were then measured directly with a photomultiplier in place of the plate and plateholder at the back of the spectrograph. The photomultiplier was a modified Allen type electron-multiplier of 11 stages with beryllium–copper dynodes and a gold photocathode. It had the advantage, owing to the high work function of gold, of being 'blind' to scattered light from the visible and quartz ultra-violet regions (Walker, Wainfan and Weissler 1955). The multiplier was run at 450 v per stage with the collector at earth potential, and its signal, of the order 10^{-7} to 5×10^{-9} A, was fed into a d.c. amplifier and read on a microammeter. Light from the grating entered the multiplier housing through a 20μ slit located on the Rowland circle, and the whole housing could be moved with a fine adjustment screw over a range of a few millimetres so as to set accurately on any required line. Although argon from the discharge tube streamed continuously through the spectrograph into the photomultiplier chamber, the pressure in the latter could be kept down to 3×10^{-5} mm by pumping it separately.

The plates were photometered on a Jarrell–Ash recording microphotometer. For each plate the calibration curve obtained from the intensity marks was used to reduce the trace of the absorption spectrum point by point to a true intensity curve, which was then plotted logarithmically. If I_0 and I_ν are the incident and transmitted intensities, the total absorption in each line is defined by

$$\int_{\text{line}} \alpha_\nu \, d\nu = \frac{1}{l} \frac{760}{p} \frac{T}{273} \int_{\text{line}} \ln\left(\frac{I_0}{I_\nu}\right) d\nu \qquad \ldots\ldots (2)$$

where l is the length of light path through the absorbing gas, p is its pressure in mm, T is its temperautre, and α_ν is the absorption coefficient at N.T.P. for frequency ν; it is thus proportional to the area under the absorption curve plotted as above, and this was measured with a planimeter. The frequency scale was obtained from Beutler's values for the wavelengths of the lines.

The f-value of a line is related to its total absorption by

$$\int_{\text{line}} \alpha_\nu \, d\nu = \frac{\pi e^2 N}{mc} f \qquad \ldots\ldots (3)$$

where e and m are the charge and mass of the electron and N is the number of absorbing atoms per cm^3 at N.T.P. The f-values found in this way for the Beutler lines are given in the next section.

A different technique was adopted for the measurements of absorption in the continuum. The absorption coefficient at the $^2P_{1\,2}$ series limit could be estimated from the plates used for the Beutler lines, but the calibration curves could hardly be relied on to much shorter wavelengths. We could have used, say, the Ne I resonance lines at 744 Å and 736 Å to calibrate the plates in this region, but we decided instead to try using the photomultiplier to measure the absorption directly. This has been made possible by the development of very low inductance flash-tube arrangements as sources of continuous radiation. Recent work in this laboratory (Garton, Celnick, Hessberg and Wheaton 1960) has indicated that in such tubes, where the necessary high current density is achieved by a very short flash (about 2 μsec) rather than by a constricting capillary tube,and where there is no external spark gap, the intensity is fairly reproducible over a hundred or so flashes. The other disadvantage of using the photomultiplier directly, the difficulty of accurate line-contouring, obviously does not apply to measurements in the continuum. By rotating the grating the spectrum could be scanned with an accuracy to ± 2 Å.

A flash tube similar to that described by Garton (1959) was connected to the spectrograph slit, and the energy from an 18 μF condenser bank at about 6 kV was discharged through it about once every 5 seconds. The tube was separately pumped and was fitted with an argon leak adjusted so that the discharge could be triggered at the desired voltage by a 15 kv trigger pulse.

The photomultiplier, mounted as in the previous experiment, had its last three stages decoupled by 0·02 μF condensers. A positive signal was taken from the last dynode instead of a negative one from the collector, and this was fed into a pulse amplifier of gain 10 and displayed on an oscilloscope triggered by the same pulse as the flash tube. In these rather rough experiments the signal was measured simply by noting the peak height of the pulse on the oscilloscope screen. About a dozen flashes were observed, then krypton was admitted to the spectrograph, its pressure measured, and a dozen more flashes observed. The grating was then rotated slightly to bring another wavelength region onto the photomultiplier

slit and the procedure repeated. It was not possible to scan the entire spectrum first without and then with krypton, because the flash continuum was fairly thickly overlaid with emission lines which we could not be sure of avoiding with a wavelength setting as crude as ±2 Å. With the notation of equation (2) the absorption coefficient at N.T.P. for the frequency ν is simply

$$\alpha_\nu = \frac{1}{l}\frac{760}{p}\frac{T}{273}\ln\left(\frac{I_0}{I_\nu}\right). \qquad \ldots\ldots(4)$$

The voltage on the photomultiplier was adjusted at every wavelength so that the output from the pulse amplifier was about 20 v peak, the largest signal obtainable without overloading. The oscilloscope could be read to little better than a volt, which was also about the noise level. It must be emphasized that this experiment was in the nature of a trial to see whether the method was workable; it was not expected in its present state of development to yield accurate results. Experiments are now being carried out to reduce the noise, improve the reproducibility, and develop a more refined method of recording intensities. It is worth mentioning that, although the sensitivity of the photomultiplier had fallen by a factor of between 10 and 100 over the period of months since it was activated, the signal over most of the region 900 Å to 500 Å had to be cut down deliberately (by under-running the photomultiplier) to about 200 μA to avoid overloading the amplifier. Below 500 Å the reflectance of the grating dropped sharply, and the signal became unreliably small.

§ 3. Results

3.1. *The Beutler Lines*

Figure 1 (Plate) shows the absorption spectrum of krypton in the region of the series limits at three different pressures. At the lowest pressure, the broad lines classified by Beutler (1935) as the two series $4p^6\ {}^1S_0$-$4p^5({}^2P_{1/2})md$ and $4p^6\ {}^1S_0$-$4p^5({}^2P_{1/2})ms$ can be clearly seen, although the continuum starting at the ${}^2P_{3/2}$ edge is barely visible. At higher pressures the ${}^2P_{1/2}$ edge appears, and the Beutler lines increase greatly in strength and width. The lines $4p^6$-$4p^5ms$ of the second series lie very close to the lines $4p^6$-$4p^5(m-2)d$ of the first series and are partly resolved only in the first two lines (for which $m = 8, 9$ respectively). The f-value obtained for each 'line' is thus the sum of the f-values of its two components. Figure 1 also shows a microphotometer trace of a typical exposure. Certain apparent intensity anomalies (e.g. the fact that the fourth line is weaker than the fifth) are due to overlying emission lines and can be corrected from the exposure taken on every plate with no krypton.

Table 1

Line (Å)	881·0 +879·4	869·5 +868·6	862·7 +862·4	858·5 +858·2	855·6 +855·4	853·6	852·2	851·1
f	0·0431	0·0235	0·0143	0·0086	0·0051	0·0032	0·0021	0·0013
Probable error	0·0009	0·0006	0·0004	0·0003	0·0003	0·0003	0·0002	0·0002

Sum for all lines: $f = 0{\cdot}101 \pm 0{\cdot}003$.

Table 1 gives the results obtained from 14 exposures on nine different plates at krypton pressures between 7·7μ and 3·3μ. The first six lines were measured in some exposures and the first eight in the rest. The percentage error for the sixth, seventh and eighth lines is high, but as they contribute together only about

7% to the f-value sum the result is little affected by this inaccuracy. The errors quoted are the probable errors calculated from the scatter of the results.

The f-values found are so surprisingly small that it seems worth discussing in some detail the possibility of systematic errors.

3.1.1. *Impurities of gas.*

We used British Oxygen Company 'spectrally pure' Kr, 99–100%, balance Xe. Accidental contamination of this seems highly improbable since three different krypton flasks all gave similar results. No impurity lines or bands appeared on the exposures.

3.1.2. *Faulty pressure measurements.*

We relied on the manufacturer's calibration of the Leybold McLeod gauge. Any error due to the rather long path, via a liquid oxygen trap, connecting this to the spectrograph should result in too low a krypton pressure being measured, which would lead to erroneously high f-values. The krypton entered the spectrograph near the slit and was pumped out at the middle of the opposite wall, so that it seems impossible that the pressure in a side arm could have been higher than that in the body of the spectrograph. Sizeable errors under this heading are in any case ruled out by the experiment described in § 3.1.5 below.

3.1.3. *Non-linearity of photomultiplier and amplifier.*

The response of the d.c. amplifier was checked directly. The photomultiplier had a dynode assembly identical with that widely used in particle counters, and it seemed safe to rely on its linearity at the very low currents used ($< 0{\cdot}1\ \mu$A).

3.1.4. *Errors in plate calibration.*

The A II lines used for calibration are only about 40 Å from the first Beutler line. Exposure times for the calibration and absorption photographs were within a factor 4 of one another. A possible source of error is the effect of scattered light of longer wavelength, for which a rough correction was made from the region beyond the end of the continuum. This type of error would lead to lower f-values at higher krypton pressures, whereas in fact the scatter of the results shows no correlation with the pressure; indeed, on two plates the f-values from two exposures at pressures differing by a factor of nearly two agree extremely closely. To ensure that no large systematic errors in plate calibration had been overlooked, we made a rough check by using the photomultiplier directly as follows. There is a group of A III lines between 883 Å and 871 Å which appears in the uncondensed discharge in argon and can therefore be observed with the multiplier. The absorption coefficient at these five wavelengths can thus be found from the decrease in signal with increasing pressure of krypton and compared with the photographic value. The direct measurement is not an accurate one, because the argon lines are weak and badly placed, in that they fall at wavelengths where the krypton absorption is either very small or else large but changing rapidly. At the two most reliable points, the direct method gives absorption coefficients about 20% higher than the photographic method. Although this discrepancy is greater than might be expected from the scatter of the results, the check does eliminate the possibility of systematic errors in calibration very much larger than the random errors.

3.1.5. *General*

As a final check on pressure measurements and photomultiplier technique, we made one spot measurement of the continuous absorption coefficient in argon for comparison with the results of Po Lee and Weissler (1955). This was done by setting the photomultiplier on each in turn of the two neon resonance lines, 744 Å and 736 Å (easily excited in an uncondensed discharge at a few millimetres pressure of neon), and observing the decrease in signal at increasing pressure of argon in the spectrograph. The latter was admitted by the same path as the krypton previously, and its pressure was measured in the same way. We found for the absorption coefficient at these two wavelengths $\alpha = 1120 \pm 50\,\mathrm{cm}^{-1}$, whereas Po Lee and Weissler give for this region $\alpha = 940 \pm 50\,\mathrm{cm}^{-1}$. This measure of agreement between results obtained by entirely different methods seems quite satisfactory.

3.2. *The Continuum*

The results are shown in figure 2. The possible error in each point, based on the reproducibility of the signal and the accuracy of reading the oscilloscope, is about 20%, and the curve in figure 2 passes within this distance of almost all the experimental points. Between 750 Å and 670 Å there is a gap due to a deep minimum in the intensity of the continuous spectrum. The absorption curve did in fact show an apparent dip in this region, but the photomultiplier signals were so weak that this dip can almost certainly be attributed to the effect of scattered light. As this minimum appears in the spectrum of the helium continuum as well as that of the flash tube, it is presumably caused by a dip in the reflectance of the aluminized grating. The continuum intensity drops sharply again below 500 Å, probably for the same reason. We did not attempt to measure the absorption between the 885 and 845 Å series limits because of the rapid fluctuations of intensity in the region of the Beutler lines. At wavelengths longer than 885 Å the absorption was zero, showing that the photomultiplier was unaffected by the increase in pressure in the chamber when krypton was admitted to the spectrograph. In most cases the krypton pressure was between $2\frac{1}{2}\mu$ and 5μ (causing a decrease in signal of about a half), but at a few wavelengths several readings were taken at a range of pressures from $1\frac{1}{2}\mu$ to $8\frac{1}{2}\mu$ to check the linearity of the absorption.

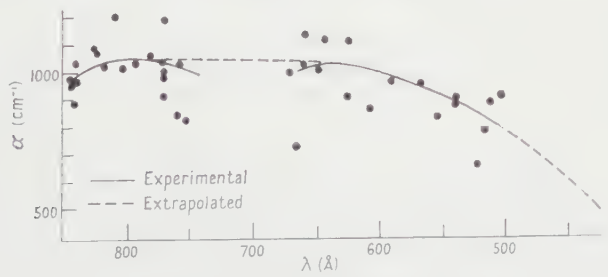

Figure 2. Coefficient of continuous absorption in Kr.
Possible error in each point $= \pm 200\,\mathrm{cm}^{-1}$.

In 13 of the exposures used to determine the f-values of the Beutler lines it was possible to estimate also the continuous absorption coefficient at the $^2P_{1/2}$ edge. The mean value is $800 \pm 50\,\mathrm{cm}^{-1}$, whereas the directly measured value

is $1120 \pm 200\,\mathrm{cm}^{-1}$. The discrepancy is thus a little larger than the probable errors, and is actually very similar to that noted between the direct and photographic measurements in the region of the Beutler lines, described in § 3.1.4 above. It is possible that scattered light of longer wavelength may be responsible, for the photomultiplier should be less sensitive to this than the photographic plates.

§ 4. Discussion

It was first suggested by Beutler (1935) that the auto-ionized lines between the $^2P_{3/2}$ and $^2P_{1/2}$ series limits in argon, krypton and xenon might be responsible for much of the far ultra-violet absorption deduced from early dispersion measurements. The most recent measurements of dispersion are those of Larsén (1939) for argon and Koch (1949) for krypton and xenon, in each case from the visible region down to 2300 Å. These authors have expressed their results as three-term dispersion formulae of the form (1), in which the first two absorption frequencies are those of the resonance lines, and the three unknowns, the f-values of the resonance lines (assumed equal) and the f-value and frequency of the third term, are found by curve-fitting. Table 2 gives their results, together with the wavelengths of the resonance lines and of the series limits between which lie the Beutler lines. The discrepancies between the observed values of the refractive index and those calculated from formulae using the constants of table 2 were in all cases small and entirely within the experimental error.

Table 2

Gas	f_1, f_2	f_3	$(f_1+f_2)/f_3$	λ_3(Å)	Series limits (Å) $^2P_{3/2}$	Series limits (Å) $^2P_{1/2}$	Resonance lines (Å)	
A	0·210	4·942	0·085	609	787	778	1067	1048
Kr	0·266	5·612	0·095	695	885	845	1236	1165
Xe	0·326	6·109	0·107	846	1022	923	1470	1296

The third wavelength found in this way may be considered as a sort of centre of gravity for the continuum together with any auto-ionized lines in the region. In comparing absorption measurements with dispersion data, it is not very satisfactory to attribute a specific f-value to the continuum, because the effect of the latter decreases rapidly with decreasing wavelength. A rough centre-of-gravity calculation from our measurements of the continuous absorption indicates that, to account for the balance of f_3 in krypton, the f-sum for the Beutler lines should be about 2·0, i.e. about 20 times larger than our measured value.

A more meaningful approach, however, is to consider the refractive index at one particular wavelength and calculate the contribution made to it by each of the known absorption regions. The wavelength chosen should be as near as possible to these regions, so we have done the calculation for Koch's shortest wavelength, 2303 Å. The contributions of the various lines are obtained from equation (1), from which we find for the sum over the Beutler lines

$$(n-1)_{2303} = 0{\cdot}11 \times 10^{-4}.$$

Unfortunately the f-values of the resonance lines are not known. We have estimated the probable value of their sum to be about 0·36 by the following

argument: the f-values for the two analogous lines in neon and argon have been calculated by Gold and Knox (1959) and Knox (1958) respectively; they find 0·133 for the sum in neon and 0·249 in argon, and a step of about the same size between argon and kyrpton would give 0·36 for krypton. Some support is lent to this extrapolation by the fact that the f-values of the resonance lines estimated from the dispersion data do show equal steps between xenon, krypton and argon (see table 2). Although the neon dispersion measurements are not accurate enough to determine the A Ne step, they are at least compatible with its being of the same size. We have also assumed that the sum of the f-values is divided between the two lines in the same way as in argon, i.e. the shorter wavelength line is about four times as strong as the longer. The resonance lines then contribute $0{\cdot}81\times10^{-4}$ to $(n-1)_{2303}$.

The formula for the continuum corresponding to (1) is

$$n-1=\frac{e^2N}{2\pi m}\int_{\nu_c}^{\infty}\frac{df}{\nu^2-\nu_0{}^2} \qquad \ldots\ldots(1\,a)$$

where ν_c is the frequency of the absorption edge. Using the relation between f-value and absorption coefficient from equation (3) gives

$$n-1=\frac{c}{2\pi^2}\int_{\nu_c}^{\infty}\frac{\alpha_\nu\,d\nu}{\nu^2-\nu_0{}^2}. \qquad \ldots\ldots(5)$$

The integration extends to infinitely short wavelengths, whereas our measurements are unreliable below 500 Å. Since, however, the term under the integral sign falls off nearly as λ^2, the errors arising from extrapolating beyond 500 A are small—in fact, only 9% of the total comes from the extrapolated region. The even smaller contribution of the continuum between the $^2P_{3/2}$ and $^2P_{1/2}$ edges has been estimated from the photographic plates.

Table 3 gives the contribution of the three absorption regions to the refractive index at 2303 A, with the corresponding figures for argon included for comparison. In the latter the measured $n-1$ value is Larsén's, and the contributions to it are evaluated from the calculations of Knox (1958) and the continuum measurements of Po Lee and Weissler (1955). Next to each contribution is given its percentage of the total measured $n-1$.

Table 3

	Krypton			Argon		
Total $(n-1)_{\text{meas}}$	$4{\cdot}8715\times10^{-4}$			$3{\cdot}0903\times10^{-4}$		
Contributions of						
(*a*) Continuum	2·55	$\times10^{-4}$	(52%)	1·62	$\times10^{-4}$	(52%)
(*b*) Beutler lines	0·11	$\times10^{-4}$	(2%)	—	—	—
(*c*) Resonance lines	0·81	$\times10^{-4}$	(17%)	0·41	$\times10^{-4}$	(14%)
Sum	3·47	$\times10^{-4}$	(71%)	2·03	$\times10^{-4}$	(66%)

It is seen that in krypton nearly one third of the measured refractive index is unaccounted for. If the contribution of the continuum were too low by 20% and that of the resonance lines by 50% (the estimated maximum errors), the discrepancy would be about one tenth of the total, of which a part may be contributed by the rest of the resonance series below $^2P_{3/2}$. Beutler considered the possibility that there might be additional auto-ionized lines arising from

excitation of the s^2 shell immediately under the p^6 shell, but his search for such lines in xenon was unsuccessful. Obviously more data are required to account satisfactorily for the dispersion values. In particular, it would be interesting to measure the f-values of the Beutler lines in argon and xenon and of the resonance lines in all three heavy inert gases. Another method of attack is to extend the dispersion measurements into the vacuum ultra-violet, an experiment we are attempting in this laboratory. Wolfsohn (1933) has in fact made a rough spot measurement of the refractive index of argon at 1850 Å, and his result differs from the value calculated from Larsén's formula by only 5%.

As regards the electron recombination coefficient, Massey and Bates (1942) have discussed the contribution to this of the process of dielectronic recombination, whereby an electron is captured into an auto-ionizing state and the excess energy disposed of by radiation. They give the following formula for the dielectronic recombination coefficient $\alpha(T)$ for electrons of temperature $T°\mathrm{K}$; if the auto-ionizing level is at $\nu\,\mathrm{cm}^{-1}$ above the ground state of the ion and can make a radiative combination of oscillator strength f and wavelength λ with a lower, singly excited level, then

$$\alpha(T)=\frac{4}{3}\times 10^{-16}\frac{g_1}{g_i}\frac{f}{\lambda^2 T^{3/2}}\exp\left(\frac{-1{\cdot}4\nu}{T}\right) \qquad \ldots\ldots(6)$$

where g_1 and g_i are the statistical weights of the auto-ionizing level and of the ground level of the ion. Garton (1956) suggested that the Beutler lines of argon might make a significant contribution to the rather high values of the recombination coefficient measured in this gas; if the first Beutler line has an f-value of order 1, as deduced from the dispersion data, $\alpha(300°)$ would be of order $10^{-10}\,\mathrm{cm}^3\,\mathrm{sec}^{-1}$. However, since the f-values of the Beutler lines in argon and krypton are likely to be similar, it seems from the results reported here that the above estimate of $\alpha(300\ )$ for argon was considerably in error—by a factor of at least 25 (Garton, Pery and Codling 1960).

On the theoretical side, no attempts appear to have been made to calculate radiative f-values from auto-ionized levels for atoms as heavy as argon and krypton. Auto-ionized lines of apparently very great strength have been photographed in the absorption spectra of many metal vapours; Marr's (1954) experimental value of $f=0{\cdot}52$ for such a line in Tl I has already been mentioned. In all these cases, however, the auto-ionized levels arise from excitation of an electron from an inner shell, so that one might anticipate on the basis of the f-sum rule a source of additional oscillator strength associated with this shell. For example, the 1126 Å line of Hg I($5d^{10}6s^2\,{}^1S_0$–$5d^9 6s^2 6p\,{}^3P_1$) might acquire its high f-value from the ten equivalent 5d electrons. In the inert gases this argument does not apply, for no new shell is broken into when exciting the Beutler lines. The f-sum rule thus provides no grounds for expecting high oscillator strengths in these lines.

Acknowledgments

We should like to thank several colleagues at Imperial College and at the Atomic Energy Research Establishment, Harwell, for their assistance. We are grateful to Professor P. M. S. Blackett, for his encouragement and, through him, to the Department of Scientific and Industrial Research for provision of

the recording microdensitometer. Much generous help has been given by Dr. R.B. Owen and Mr.D.W.S. Smout of the Atomic Energy Research Establishment in supplying the photomultipliers used. Thanks are due also to Dr. H. D. Evans, Dr. A. Folkierski and Mr. J. E. G. Wheaton, all of Imperial College, and Mr. F. R. Pryce of the Atomic Energy Research Establishment for help in electronic techniques, and to Dr. R. Latham for the loan of the concave grating.

References

Beutler, H., 1933, *Z. Phys.*, **86,** 710.
—— 1935, *Z. Phys.*, **93,** 177.
Cuthbertson, C., 1927, *Proc. Roy. Soc.* A, **114,** 650.
Cuthbertson, C., and Cuthbertson, M., 1910, *Proc. Roy. Soc.* A, **84,** 13.
—— 1932, *Proc. Roy. Soc.* A, **135,** 40.
Garton, W. R. S., 1956, *The Threshold of Space* (London: Pergamon Press), p. 157.
—— 1959, *J. Sci. Instrum.*, **36,** 11.
Garton, W. R. S., Celnick, I. W., Hessberg, H., and Wheaton, J. E. G., 1960, *Proc. 4th Int. Conf. on Ionization Phenomena in Gases* (1959), vol. I (Amsterdam: North-Holland), p. 518.
Garton, W. R. S., Pery, A., and Codling, K., 1960, *Proc. 4th Int. Conf. on Ionization Phenomena in Gases* (1959), vol. I (Amsterdam: North-Holland), p. 206.
Gold, A., and Knox, R. S., 1959, *Phys. Rev.*, **113,** 834.
Knox, R. S., 1958, *Phys. Rev.*, **110,** 375.
Koch, J., 1913, *Ark. Mat. Astrom. Fys.*, **9,** no. 6.
—— 1949, *Kungl. Fys. Sällskapets Lund Forh.*, **19,** 173.
Kronjäger, W., 1963, *Z. Phys.*, **98,** 17.
Larsén, T., 1939, *Dissertation*, Lund.
Marr, G. V., 1954, *Proc. Roy. Soc.* A, **224,** 83.
Massey, H. S. W., and Bates, D. R., 1942, *Rep. Progr. Phys.* (London: Physical Society), **9,** 62.
Po Lee, and Weissler, G. L., 1955, *Phys. Rev.*, **99,** 540.
Quarder, B., 1924, *Ann. Phys., Lpz.*, **74,** 255.
Walker, W. C., Wainfan, N., and Weissler, G. L., 1955, *J. Appl. Phys.*, **26,** 1366.
Wolfsohn, G., 1933, *Z. Phys.*, **85,** 366.

Isotope Effect in Band Spectra of Magnesium Oxide

By D. S. PEŠIĆ

Institute of Nuclear Science, B. Kidrich, Belgrade

Communicated by A. G. Gaydon; MS. received 20th June 1960

Abstract. Some studies of the electronic spectrum given by magnesium in a vacuum arc in oxygen 18, and in a mixture of ^{16}O and ^{18}O have been made. The measurements of isotope shift are given for the green and for the ultra-violet system. The isotope effect in the green system confirms the vibrational analysis of Mahanti and Lagerqvist. The bands in the ultra-violet region are again attributed to a polyatomic molecule containing magnesium and oxygen atoms. The assignment is partly supported by the isotope shift, but the molecule only contains a single oxygen atom.

§ 1. Introduction

The electronic spectrum of magnesium oxide consists of three well-known systems. Two of them, the green (5200–4800 Å) and red (6900–4700 Å), belong to the MgO molecule (see Pearse and Gaydon 1950). The third, very complex system in the ultra-violet, which has not been analysed in detail, is considered according to some new data (Pešić and Gaydon 1959) to belong to a polyatomic molecule. The spectrum can be obtained by introducing magnesium or its salts into an arc in air, but is best obtained in an arc between magnesium electrodes in oxygen at reduced pressure.

One part of the present paper, which is a continuation of our previous work (Pešić and Gaydon 1959), deals with the measurements of the bands in the ultra-violet system obtained in an $^{18}O_2$ atmosphere. The isotope effect was observed in an attempt to identify the species responsible for these bands. In addition, the vibrational and rotational isotope effect in the magnesium oxide green system has been measured.

§ 2. Experimental

The spectrum has been excited in a vacuum arc which was slightly modified from that used by Gaydon (1955). The arc, maintained by 300 volts d.c. at a current of 0·7 to 1·0 amp, was run in an atmosphere of oxygen 18† at about 10 mm Hg. Water-cooled magnesium metal electrodes were used.

Spectrograms were taken with a 3·4 m Jarrell–Ash grating spectrograph, giving a linear dispersion of 5·1 Å mm^{-1} in the first order. The exposure times, depending on the spectral region used, were from 40 seconds to 5 minutes. Ilford Zenith and HP3 plates were employed. For wavelength determinations Harrison's (1939) values for the iron spectrum were used.

† The gas contained 98·4% ^{18}O and 0·90% ^{17}O according to the manufacturers; The Weizmann Institute of Science, Rehovoth, Israel.

§ 3. Results

3.1. *Green System*

The bands of this system (strip *c*, Plate) appear readily and clearly in the vacuum arc. The small number of bands appear free from impurities in emission, and the observations with pure oxygen 18 permitted a ready measurement of isotope displacement in this system. Determination of the vibrational and rotational isotope effect has been done by the following equations:

$$\nu_{v'} - \nu_v = (\rho - 1)[\omega_e'(v' + \tfrac{1}{2}) - \omega_e''(v'' + \tfrac{1}{2})] - (\rho^2 - 1)$$
$$[\omega_e' x_e'(v' + \tfrac{1}{2})^2 - \omega_e'' x_e''(v'' + \tfrac{1}{2})^2] \qquad \ldots\ldots (1)$$

and

$$\nu_r^i - \nu_r = (\rho^2 - 1)(\nu_0 - \nu_h) \qquad \ldots\ldots (2)$$

where ν_0 is the band origin and ν_h the band head. The other constants have a common meaning. The coefficients ω_e', ω_e'', $\omega_e' x_e'$, $\omega_e'' x_e''$ are taken from Lagerqvist and Uhler's paper (1949), and together with the masses of magnesium and oxygen isotopes are given in table 1.

Table 1

$\omega_e' = 824{\cdot}1\ \text{cm}^{-1}$	$\omega_e' x_e' = 4{\cdot}7\ \text{cm}^{-1}$	$^{16}O = 16{\cdot}0000$
$\omega_e'' = 785{\cdot}1\ \text{cm}^{-1}$	$\omega_e'' x_e'' = 5{\cdot}1\ \text{cm}^{-1}$	$^{18}O = 18{\cdot}0049$
		$^{24}Mg = 23{\cdot}9924$

The results of the measurements and calculations are summarized in table 2. This table contains the values of the vibrational and rotational effects, observed wave numbers for oxygen 16 and corresponding calculated and observed wave numbers for oxygen 18 bands. It can be seen that the agreement between the observed shift and those calculated by equations is rather close, and lies within the experimental error.

Table 2. Isotope Effect in the Green Bands of MgO, in cm^{-1}

v'	v''	$\Delta\nu_0$	$\Delta\nu_r$	$\Delta\nu_0 + \Delta\nu_r$	ν_h^{16}†	ν_h^{18} calc.	ν_h^{18} obs.	ν_h^{18} obs.$-$ ν_h^{18} calc.
0	1	25·3	1·6	26·9	19204·9	19231·8	19232·0	0·2
1	2	23·3	1·5	24·8	256·3	281·1	280·5	−0·6
2	3	21·2	1·4	22·6	309·5	332·1	331·5	−0·6
0	0	−0·7	2·6	1·9	965·2	967·1	967·4	0·3
1	1	−2·0	2·4	0·4	20007·5	20007·9	20008·0	0·1
2	2	−3·5	2·3	−1·2	050·8	049·6	049·4	−0·2
3	3	−4·9	2·1	−2·8	097·1	094·3	092·4	−1·9
1	0	−28·0	5·0	−23·0	747·6	724·6	724·9	0·3
2	1	−28·8	4·5	−24·3	783·9	759·6	759·7	0·1
3	2	−29·6	4·1	−25·5	20820·9	20795·4	20795·8	0·4

$\Delta\nu_0$ is the vibrational effect, $\Delta\nu_r$ the rotational effect.
† Bands from Mahanti's data (1932).

These bands have been attributed to the MgO molecule since the first investigations on this system (see Kayser 1910). The results obtained by measuring the isotope effect verify this assignment. Recently, in their work on the magnesium spectrum, Barrow and Crawford (1945) gave a new Deslandres' scheme of this

system, with the comment that further work is necessary. These authors proposed a scheme in which the bands 5200, 5007 and 4825 Å are the (0, 0), (1,0) and (2, 1) bands. However, our present results confirm the scheme given by Ghosh, Mahanti and Mukkerjee (1930), Mahanti (1932) and Lagerqvist (1943). According to these authors the above bands represent the first members of the (0, 1), (0, 0) and (1, 0) sequences.

3.2. *Ultra-violet System*

This system (strip *c*, Plate) in oxygen 18, has the same general appearance as the system in oxygen 16, but the bands show definite isotope shift. This effect is fairly large, but the directions of the displacement are rather irregular.

The weak band at 3640 Å shows marked displacement to the red by about 20 cm^{-1}. In the first part of the second group (3672–3680), the displacement is between 0·4 to 2·1 cm^{-1}. In the second part of this group (3720·6, 3720·9, 3721·6), which is the most intense feature of the spectrum, no shift is observed. The bands of the third group, lying in the spectral region of 3766 to 3816 Å are displaced, similarly to the second, from 0·6 to 6·8 cm^{-1}. These displacements are rather irregular, although most of the bands are shifted to the red. In some bands of this group (3864–3877), the displacement is too complex to permit a correlation with corresponding bands in oxygen 16. The bands in the fourth group, which extends to 3918 Å, are displaced to the longer wavelengths by between 21 and 26 cm^{-1}.

In table 3 are given the wavelengths of outstanding bands, wave numbers and corresponding isotope shifts.

From this table it can be seen that the displacement of the band 3640 and the group 3899–3918 Å, agrees in sign and order of magnitude with that which would be expected from the equation (1) for sequences $\Delta v = \pm 1$. Displacements of the bands from another two groups (3672–3680 and 3766–3816) are of the right magnitude for the zero sequence, suggesting the possibility of more than one system existing, if the carrier of the bands is a simple diatomic molecule.

In order to determine the number of oxygen atoms, some photographs (strip *b*, Plate) were obtained with the vacuum arc running in a mixture of about equal proportions of ^{16}O and ^{18}O. This spectrum shows only bands already obtained with pure oxygen 16 and 18, but no additional features. Absence of these bands indicates that the emitter contains only one oxygen atom. If it contained more than one atom, we would expect bands due to the molecule containing ^{16}O and ^{18}O atoms.

Observed isotope shifts with ^{18}O clearly show that oxygen is present in the emitter. Since hydrogen, nitrogen and Mg_2 may be excluded (Ghosh, Mahanti and Mukkerjee 1930, Pešić and Gaydon 1959), there is no doubt that the carrier of the bands contains only oxygen and magnesium atoms. Absence of extra bands in the spectrum obtained in a mixture of ^{16}O and ^{18}O suggests very strongly that the emitter is a molecule with only one oxygen atom.

On the basis of the present data it is impossible to give a definite decision about the nature of the emitter, but in previous work, the general complexity of bands and irregular isotope shift favour a polyatomic molecule. However, until either a vibrational or a rotational analysis have been made, the other possibility that the carrier may be a diatomic molecule remains. If so, more than one system must be involved.

Table 3. Isotope Effect in the Ultra-violet Bands

Mg_x ^{18}O		Mg_x ^{16}O†		Mg_x ^{18}O–Mg_x ^{16}O	
λ (Å)	ν (cm^{-1})	λ (Å)	ν (cm^{-1})	$\Delta\lambda$ (Å)	$\Delta\nu$ (cm^{-1})
3640·54	27460·6	3637·46	27483·9	3·08	−23·3
41·19	456·7	38·30	477·6	2·89	−20·9
41·45	453·8	38·72	474·4	2·73	−20·6
42·24	448·8	39·45	468·9	2·79	−20·1
42·52	445·7	39·97	464·9	2·55	−19·2
43·52	438·2	40·83	458·5	2·69	−20·3
45·02	426·9	42·50	445·8	2·52	−18·9
46·75	413·9	44·40	431·5	2·35	−17·6
48·80	398·5	46·64	414·7	2·16	−16·2
72·07	224·9	72·11	224·5	−0·04	0·4
74·62	205·2	74·74	204·9	−0·12	0·3
77·48	184·8	77·67	183·3	−0·19	1·5
80·64	161·4	80·92	159·4	−0·28	2·1
3720·53	26870·3	3720·60	26869·7	−0·07	0·6
20·89	867·7	20·96	867·0	−0·07	0·7
21·32	864·6	21·40	863·9	−0·08	0·7
66·39	543·1	66·10	545·1	0·29	−2·0
71·89	504·4	71·80	505·0	0·09	−0·6
72·37	501·0	72·33	501·3	0·04	−0·3
77·15	468·5	77·40	465·7	−0·25	3·2
77·65	464·0	77·81	462·9	−0·16	1·1
82·78	428·1	82·65	428·9	0·13	−0·8
83·78	421·1	84·20	418·2	−0·58	2·9
87·89	392·4	88·47	388·4	−0·42	4·0
90·13	376·8	90·96	371·0	−0·83	5·8
98·6	318	98·3	320	0·3	−2
3804·37	278·1	3804·16	279·6	0·21	−1·5
05·29	271·8	05·28	271·8	0·01	0·0
10·17	238·1	10·30	237·2	−0·13	0·9
15·43	202·0	15·70	200·1	−0·27	1.9
16·40	195·3	17·53	188·5	−1·13	6·8
64·90	25866·6				
67·47	849·4				
70·42	829·7				
73·74	807·6				
77·30	783·8				
99·31	638·3	3902·60	25616·7	−3·29	21·6
3903·38	611·6	06·82	589·0	−3·44	22·6
07·80	582·6	11·38	559·2	−3·58	23·4
12·59	551·3	16·39	526·5	−3·80	24·8
3917·92	25516·5	3921·95	25490·3	−4·03	26·2

† Bands from Pešić and Gaydon's data (1959).

Acknowledgment

I am greatly indepted to Dr. A. G. Gaydon for his constant interest and advice.

References

Barrow, R. F., and Crawford, D. V., 1945, *Proc. Phys. Soc.*, **57,** 12.
Gaydon, A. G., 1955, *Proc. Roy. Soc.* A, **231,** 437.
Ghosh, P. N., Mahanti, P. C., and Mukkerjee, B. C., 1930, *Phys. Rev.*, **35,** 1491.
Harrison, G. R., 1939, *Wavelength Tables* (New York: John Wiley).
Kayser, H., 1910, *Handbuch der Spektroskopie* (Leipzig: Hirzel), **5,** 717.
Lagerqvist, A., 1943, *Ark. Mat. Astr. Fys.*, **29A,** 1.
Lagerqvist, A., and Uhler, U., 1949, *Ark. Fys.*, **1,** 459.
Mahanti, P. C., 1932, *Phys. Rev.*, **42,** 609.
Pearse, R. W. B., and Gaydon, A. G., 1950, *The Identification of Molecular Spectra* (London: Chapman and Hall).
Pešić, D., and Gaydon, A. G., 1959, *Proc. Phys. Soc.*, **73,** 244.

Magnetic Field Interactions with Shock Ionized Argon

By H. J. PAIN and P. R. SMY
Physics Department, Imperial College, London

Communicated by R. Latham; MS. received 25th March 1960, in final form 26th May 1960

Abstract. The construction, instrumentation and calibration of a pressure-driven shock tube is described. Experiments are reported on interactions occurring between a magnetic field and ionized argon moving at shock Mach numbers 8 to 23 and the conditions for these interactions are shown to be well defined in terms of the Lundquist and magnetic Reynolds numbers.

The modifications to the fluid flow which result from these interactions are discussed in terms of magnetic body forces on the fluid and steady state flow patterns associated with different magnetic field configurations have been photographed. These show that a radially symmetric magnetic field may act as a nozzle to plasma flow, that an asymmetric field may shear the plasma flow and that when the interaction is strong enough a reflected shock wave is produced in the plasma.

§ 1. Introduction

The early work of Alfvén (1950) on the interaction between an electrically conducting fluid moving relative to a magnetic field was devoted to astrophysical problems, but the application of this phenomenon to confining high temperature plasma in thermonuclear fusion research has widened the interest in magnetohydrodynamics. The criterion for such an interaction, derived by Lundquist (1952), involves the product of the magnetic induction B and a characteristic length of interaction L. In astrophysics where B may be small, Lundquist's condition is satisfied by the large value of L. In a laboratory experiment, the small dimensions of L demand a large value of B. When the fluid is a gas, significant interactions may be observed as modifications to the fluid flow. In such cases a large value of B demands a high flow velocity and this requirement may be met in a shock tube where a slug of partially ionized gas is driven through a magnetic field at a very high velocity.

Shock tubes are of two types, pressure driven and electrically driven. Experimental work with the first type has been reported by Lin, Resler and Kantrowitz (1955), Dolder and Hide (1958) and Patrick and Brogan (1959). The latter has been developed by Fowler (1952) and Kolb (1957).

§ 2. The Shock Tube

2.1. *Description of the Shock Tube*

The shock tube which has an overall length of 29 feet is shown in figure 1. The high pressure O_2–H_2 combustion chamber (5 feet long, 4½ inches internal diameter) is separated from the low pressure gas section by a copper diaphragm which ruptures when combustion takes place. A 10% O_2–90% H_2 mixture is ignited by discharging sufficient energy from a condenser system to evaporate

a fine copper wire along the axis of the combustion chamber. Any irregularities should thus propagate a distance equal only to the radius of the high pressure chamber and their effects be reduced to a minimum.

When the diaphragm ruptures, a strong shock wave is sent through the low pressure gas at speeds (for argon) between $M=8$ and $M=23$. The shock Mach number is varied by adjusting both driver and driven gas pressures. The gas behind the shock front is heated, compressed and ionized, the degree of ionization being approximately 20 %.

The shock travels along a 17-foot length of steel tube of which 11 feet has an internal diameter of 3·3 in. and 5 feet an internal diameter of 2 in., the reduction of internal diameter occurring over a length of one foot. The shock then enters a 15 in. length of 2 in. internal diameter Pyrex glass tubing, $\frac{3}{16}$ in. wall thickness, which is followed by another 5 feet of 2 in. internal diameter steel tubing.

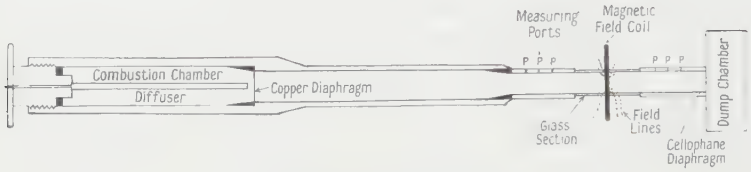

Figure 1. The shock tube, showing the combustion chamber loaded as a shell into the breech of the gun barrel main section with the copper diaphragm as a nose cap. The low pressure section is isolated between the copper and cellophane diaphragms.

This is terminated by a fine 'Cellophane' diaphragm which ruptures at static pressures slightly in excess of an atmosphere, and which separates the shock tube from a large dump chamber. The complete low pressure section is thus isolated and can be evacuated to 10^{-5} mm Hg. Impurity effects are further reduced by flushing the low pressure section with argon before each run.

The main section of the shock tube is an unrifled tank gun barrel modified to contain the high pressure chamber and part of the low pressure section. The design avoids the physical separation of high and low pressure sections when a new diaphragm is fitted. The high pressure chamber is formed by extending the breech of the gun in the shape of a hollow, flat-ended cylinder. This chamber is loaded with a steel cylindrical shell ($\frac{1}{2}$ in. wall thickness, 5 feet long) with the diaphragm as a nose.

The shell is driven home by a heavy screwed plug (12 in. long) which mates into the rear of the shell and through which is fed the high pressure gas. A perforated brass tube projects from this plug along the axis of the shell to within an inch of the diaphragm. This tube diffuses the gas mixture in the chamber before combustion and forms the return path for the current through an exploding wire stretched along its axis.

Figure 1 shows the location of the magnetic field formed by a spirally wound coil placed at the centre of the Pyrex glass section.

2.2. *Instrumentation*

The steel sections of the shock tube (other than the gun barrel) have Perspex plugs inserted in a number of ports along the tube length. For measuring shock

speeds of low Mach number these ports were used for gold film resistance thermometers after Blackman (1956). For shocks of high Mach number the light from the ionized gas operates a photomultiplier as the shock passes each plug and the output signals from these are used for shock speed measurements on calibrated oscilloscope traces and for triggering the magnetic field switch and Kerr cell camera.

The shock and the following ionized gas are photographed through the glass section at the centre of which is situated the magnetic field coil. A time-integrated photograph is obtained by leaving open a plate camera and the photomultiplier shock speed measurements are checked from the slope of an (x,t) record of the plasma flow on a drum camera film (figure 2, Plate 1). The speed of the drum camera is calibrated by photographing the light output of the spark gap which passes the current through the magnetic field coil. This light appears on the drum camera film as a series of bright streaks of equal length separated by short dark periods. Each streak corresponds to the passage of current for one half-cycle and the dark points of separation represent the extinction of light as the current reverses. The period of the current is separately calibrated by an oscilloscope.

The field current is triggered so that the shock front reaches the coil position just as the field is reaching its maximum value. The period of the field 800 μsec, is much greater than the time of interaction 20 μsec, so that the plasma sees a field of constant value.

2.3. *Calibration of the Shock Tube*

The equation relating the pressure ratio across the diaphragm P_{41} to the resulting shock Mach number M_S for a simple shock tube is given by

$$P_{41} = \frac{\gamma_1 - 1}{\gamma_1 + 1}\left[\frac{2\gamma_1 M_S^2}{(\gamma_1 - 1)} - 1\right]\left[1 - \frac{\gamma_4 - 1}{\gamma_1 + 1}\frac{M_S^2 - 1}{A_{41} M_S}\right]^{-2\gamma_4/(\gamma_4 - 1)}$$

where $\gamma_4 = C_p/C_v$ (high pressure gas), $\gamma_1 = C_p/C_v$ (low pressure gas)

and $$A_{41} = \frac{a_4}{a_1} = \frac{\text{velocity of sound (high pressure gas)}}{\text{velocity of sound (low pressure gas)}}.$$

This relationship assumes:

(i) Operation with both driver and driven gases at room temperature when diaphragm is ruptured, i.e. cold burst.
(ii) Perfect gases with constant specific heats.
(iii) Perfect diaphragm burst.
(iv) One-dimensional flow without viscosity or heat transfer.
(v) Constant area of cross section of tube.

Using the relation for P_{41}, curves for air driving air (low Mach numbers) and H_2 driving argon (high Mach numbers) are plotted, together with experimental results (figure 3) for various pressure ratios.

All calibration experiments were made with cold bursts and not by igniting O_2–H_2 mixtures.

At high Mach numbers, that is high temperatures, condition (ii) is violated. The specific heat of a monatomic gas will change with ionization and a polyatomic gas will be excited in its internal energy anodes and may also ionize. Conditions (iv) and (v) (for an area decrease) both tend to reduce the shock speed, the

attenuation becoming more pronounced at higher Mach numbers. This is shown by the increasing discrepancy between the experimental points and the theoretical curve for $M > 10$ in the hydrogen–argon curve.

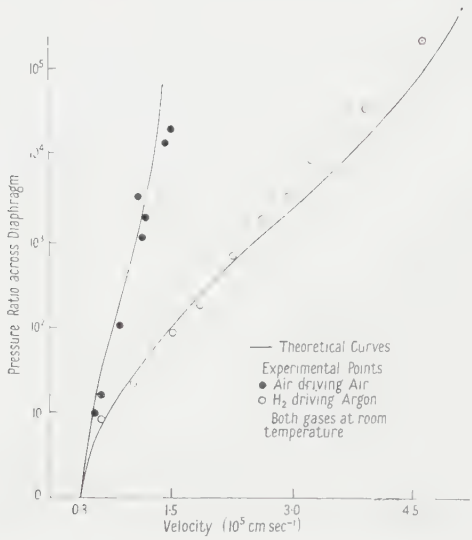

Figure 3. Plot of theoretical curves with experimental points obtained in calibrating the shock velocity against pressure ratio across the copper diaphragm at moment of rupture. Increase of pressure ratio was obtained by raising the high pressure to an upper limit of 60 atm and reducing the low pressure to a minimum of 2 mm Hg. All calibration measurements were made with cold bursts and higher shock velocities were reached by exploding O_2–H_2 mixtures in the combustion chamber.

2.4. *Diaphragms*

Correct diaphragm rupture is essential. Failure of the diaphragm to 'petal' against the tube wall removes energy from the fluid flow and increases the possibility of losing part of the diaphragm down the tube. All diaphragms used in these experiments have been taken from copper sheet. Cuts of accurately controlled depth are made with a V-shaped milling tool along two mutually perpendicular diameters. A cut along the grain of the metal gave a preferred direction of bursting and all cuts were made at an angle of 45° to this direction.

Table 1 shows the diaphragm thickness and depth of cut against cold bursting pressure. After the cuts had been milled the diaphragm was annealed to give an even tearing rate from the diaphragm centre.

In the shock tube the diaphragm was clamped between two hard steel jaws over an annular area $\frac{1}{2}$ in. wide around its circumference. These jaws were free running annular collars, the gripping faces of which were cut as a series of concentric circular teeth. In the absence of the diaphragm these teeth meshed and, when the diaphragm was clamped between them, bit into the soft copper on each side to form a series of concentric circular seals. This system was found to be gas tight to pressures up to 75 atmospheres.

Constant volume combustion theory (neglecting heat transfer) gives a 7·3-fold pressure rise for a 10% O_2–90% H_2 mixture. In practice, it was found at Luton† that this factor was reduced to 4·3.

† *Shock Tube Development Report*; Guided Weapons Division, English Electric Co., Luton, Beds., L.A. t 975.

The diaphragms used in these combustion-driven shocks have allowed for a four-fold pressure increase and have ruptured in a manner similar to those of cold bursts.

Table 1. Annealed Copper Diaphragms

Thickness (10^{-3} in.)	32	32	32	32	24	24	24	15
Depth of cut (10^{-3} in.)	11	13	15	17	11	13	15	9
Cold burst pressure (atm)	60	47	42	35	25	20	15	10

§ 3. Condition for Magnetohydrodynamic Interaction

When the plasma flow velocity u and the field B are perpendicular an e.m.f., $E=uB$ is induced in the plasma. The experimental configuration may be chosen so that this e.m.f. generates closed current loops in the plasma of current density $j=\sigma uB$, where σ is the electrical conductivity of the plasma. The interaction between j and B produces a body force per unit volume $F=\sigma uB^2$ opposing the flow and the work done by this body force over an interaction distance L is $FL=\sigma uB^2L$ which produces a pressure difference across the region of interaction.

The extent to which the flow will be disturbed is thus measured by the ratio $\sigma uB^2L/\frac{1}{2}\rho u^2$ where ρ is the plasma density. If this ratio is of the order of 1 there will be a significant change in the flow pattern and the conditions for interaction may be written as

$$\frac{2\mathscr{L}^2}{R_M}\sim 1 \qquad \ldots\ldots(1)$$

where $\mathscr{L}$ is the Lundquist number $\sigma BL(4\pi\mu/\rho)^{1/2}$ and R_M is the magnetic Reynolds number $4\pi L\mu u\sigma$ where μ is the permeability.

Values of R_M, $\mathscr{L}$ and (1) are tabulated for the experimental conditions reported here (table 2). The values of σ are those calculated by de Leeuw (1958) using the theory of Spitzer and Harm. Measurements of the electrical conductivity by the present writers (to be published) support this theory.

Table 2

$\mathscr{L}=BL\sigma\,(4\pi\mu/\rho_2)^{1/2}$, $R_M=4\pi L_2\sigma\mu u_2$, $L=1$ cm

(1)	(2)	(3)	(4)	(5)	(6)	(7)	(8)	(9)	(10)	(11)	(12)
0·2	5·33	5·5	4·7	1·53	2·88	1·44	0·72	0·33	50·3	12·6	3·2
0·5	11·8	5·1	4·8	1·03	1·97	0·99	0·55	0·31	25·1	6·3	1·6
1	20	4·6	6·4	0·79	2·01	1·00	0·50	0·36	22·5	5·6	1·4
1·3	24·5	4·4	5·94	0·71	1·7	0·85	0·43	0·33	17·5	4·4	1·1
3	46·5	3·9	5·2	0·52	1·08	0·54	0·27	0·25	9·4	2·34	0·6†
10	108	3	3·4	0·34	0·46	0·23	0·12	0·12	3·5	0·9†	0·2†
20	180	2·5	1·5	0·26	0·17	0·085	0·04	0·05	1·16	0·03†	0·01†
50	400	1·9	0·3	0·18	0·03	0·015	0·007	0·009	0·2 †	0·05†	0·025†

(1) P_1 (mm Hg); (2) $\rho_2\times10^{-6}$ (g cm^{-3}); (3) $u_2\times10^{5}$ (cm sec^{-1}); (4)$\sigma\times10^{-8}$ (e.m.u.); (5) $(4\pi/\rho_2)^{1/2}\times10^{3}$; (6) $\mathscr{L}$ for $B=4\times10^4$G; (7) $\mathscr{L}$ for $B=2\times10^4$G; (8) $\mathscr{L}$ for $B=10^4$G; (9) R_M; (10) $2\mathscr{L}^2/R_M$ for $B=4\times10^4$G; (11) $2\mathscr{L}^2/R_M$ for $B=2\times10^4$G; (12) $2\mathscr{L}^2/R_M$ for $B=10^4$G.

† Interactions were not observed experimentally.

The values of B are those at the centre of the coil. This follows the notation used by Dolder and Hide (1958). When the radial component B_r is used the values of the last three columns of table 2 are reduced by a factor of 5.

§ 4. Discussion of the Interactions between the Magnetic Field and the Plasma

The behaviour of the plasma flowing in the interaction region follows that of gas flow in a pipe with friction.

This is described by Shapiro (1951) in terms of the Fanno line, which is a curve in the enthalpy–entropy plane giving the locus of states through which the gas may pass continuously under frictional influence. Flow which is supersonic on entering the interaction region will be slowed down and the experimental configuration of Patrick and Brogan (1959) which produced a constant body force over the area of cross section of the flow reduced the flow Mach number.

The magnetic field of the circular coil used in these experiments produces a body force which has a large variation over the cross-sectional area of flow. A detailed analysis by de Leeuw (1958) of the most favourable case, where the effective coil radius is close to that of the tube, has shown that the retarding body force is negligible at the centre of the tube where the flow is almost unaffected and that its maximum value is restricted to a narrow annular region close to the tube walls.

The components of the body force per unit volume are given by $j \times B_z$ (inwards) and $j \times B_r$ (retarding) where j is the induced current density in the plasma and B_z and B_r are the axial and radial components of the field.

In the experiments reported here the effective radius of the coil is 10 cm and that of the tube is 5 cm, so that B_z is sensibly constant over the tube cross section.

Application of div $B = 0$ over a small volume gives $B_r = \frac{1}{2} r (dB_z/dz)$ where r is the radial distance from the tube axis, so that $j = \sigma u B_r$ gives an inward force per unit volume,

$$F_1 = \sigma u \frac{r}{2} \frac{dB_z}{dz} B_z, \qquad \text{i.e.} \quad \propto r.$$

The retarding body force per unit volume is then

$$F_r = \sigma u \left(\frac{r}{2} \frac{dB_z}{dz} \right)^2, \quad \text{i.e.} \quad \propto r^2.$$

The increase of these forces with radial distance from the axis results in the magnetic field configuration from a circular coil acting as a 'magnetic nozzle' and the flow patterns resulting from such an interaction are shown in figure 4 (*a*) (Plate II) to coincide with those flowing through an annular constriction placed in the tube.

In figure 4 (*a*) the value of B_z at the centre of the coil equals 20 000 G, the shock tube channel pressure equals 1 mm Hg, the shock Mach number equals 15 and the value of $2\mathscr{L}^2$ divided by R_M equals 5·6.

In figure 4 (*b*) B_z equals 40 000 G and the channel pressure equals 0·1 mm Hg. At these densities the flow is characterized by the behaviour of individual particles which will describe helical paths along the magnetic field lines. The constricting effect of the magnetic field is shown as the flow appears to follow the lines of force and to leave the tube walls.

The induced current flowing in the plasma is approximately 2000 A cm^{-2} and the magnetic pressure gradient $j \times B$, acting radially on a single turn element of the plasma radius 2 cm and thickness 1 cm is 7 atm cm^{-1}.

Figure 4 (*c*) shows the shearing flow pattern which results when the circular coil is laid flat on the top of the glass section as shown in figure 5. Most interaction experiments are designed with a field symmetry generating closed current loops in the plasma. In this asymmetric configuration the body force developed at the top of the tube must result from closed current loops formed coaxially with the circular field coil.

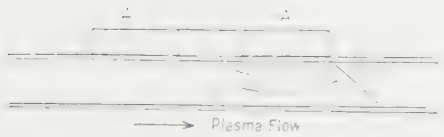

Figure 5. Explanatory diagram for the shearing flow pattern of figure 4(*c*). The coil A is placed on top of the glass section of the shock tube and the retarding magnetic body force on the plasma flowing through the field is confined to the upper part of the flow. A shear pattern results.

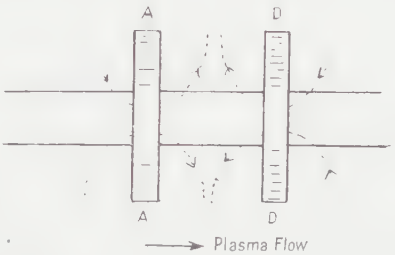

Figure 6. Glass section of shock tube showing position of coils A and D and resulting magnetic field configuration. The patterns formed by interaction between this field and the high speed plasma are shown in figure 4 (*d*) (i) and (ii).

The field strength was equal to 40 000 G, shock Mach number equals 22 and channel pressure equals 1 mm Hg.

Figure 4 (*d*) (i) shows the luminosity resulting from the plasma interaction with two similar coils arranged as a Helmholtz pair with a field configuration shown in figure 6. Heavier filtering revealed a detailed flow pattern as shown in figure 4 (*d*) (ii). Attempts to reproduce this flow pattern by scaled pairs of annular constrictions have not been successful.

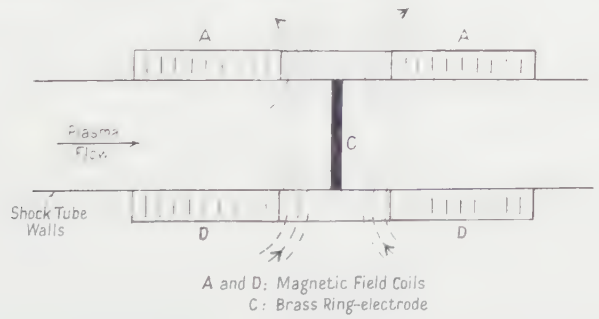

Figure 7. Glass section of the shock tube showing position of coils A and D and the resulting magnetic field configuration. Plasma flowing with velocity u through the field B develops an electric field $\mathbf{u} \times \mathbf{B}$ across the tube. Current of density $\mathbf{j}$ is generated in the plasma and flows through a circuit closed by the brass ring-electrode C which is set in the shock tube wall. The retarding magnetic body force on the plasma $\mathbf{j} \times \mathbf{B}$ is sufficient to cause a reflected shock from the interaction region and to reduce the plasma flow velocity beyond the ring-electrode as shown in figure 8.

Finally the coils were placed, in series, on either side of the glass section of the shock tube as shown in figure 7. The resulting magnetic field of 15 000 G was constant across the tube and the electric field $\mathbf{u} \times \mathbf{B}$ developed was 60 V cm^{-1}. Current was generated in a circuit closed by a brass ring-electrode set in the shock tube walls and the retarding body force $\mathbf{j} \times \mathbf{B}$ extending across the cross-sectional area of the tube was sufficient to cause a reflected shock from the interaction region and to reduce the plasma flow speed beyond the ring-electrode as shown in figure 8 (Plate I).

§ 5. Conclusion

In conclusion it may be seen that the shock tube is a convenient apparatus for the study of interactions between ionized plasma and magnetic fields. The interaction sets in when the simple theory suggests that it should, that is, when $2\mathscr{L}^2/R_M$ is of the order of unity.

Exploratory work on the effects of magnetic fields in modifying the plasma flow has shown that a single circular coil of short axial length is the equivalent of a physical constriction in the tube and that a pair of such coils in succession give an unusual luminosity pattern between the coils.

It is also interesting that reflected shocks can be produced by a transverse field if this is allowed to induce currents in the plasma.

Acknowledgments

The authors owe much to the encouragement of Professor P. M. S. Blackett and to their discussions with Dr. Latham and other members of the High Temperature Physics Group. They are indebted to the Director of Ordnance Factories (Gun Carriages) through whose courtesy they obtained the main section of the shock tube.

Mr. A. H. Chapman who has been responsible throughout for the maintenance and mechanical operation of the shock tube also developed the techniques quoted in the section on diaphragms. One of the authors (P. R. S.) has carried out this work whilst in receipt of a maintenance grant from the Department of Scientific and Industrial Research.

References

Alfvén, H., 1950, *Cosmical Electrodynamics* (Oxford: Clarendon Press).
Blackman, V., 1956, *J. Fluid Mechanics*, **1**, 61.
Dolder, K., and Hide, R., 1958, *Nature, Lond.*, **181**, 1117.
Fowler, R. G., 1952, *Phys. Rev.*, **85**, 137.
Kolb, A., 1957, *Phys. Rev.*, **107**, 345.
de Leeuw, J. H., 1958, *Interaction of a Plane Strong Shock Wave with a Steady Magnetic Field*, University of Toronto, Institute of Aerophysics. Rep. 49.
Lin, S.-G., Resler, E. L., and Kantrowitz, A., 1955, *J. Appl. Phys.*, **26**, 95.
Lundquist, S., 1952, *Ark. Fys.*, **5**, 297.
Patrick, R. M., and Brogan, T. R., 1959, *J. Fluid Mechanics*, **5**, 289.
Shapiro, A. H., 1951, *Dynamics and Thermodynamics of Compressible Fluids* (New York : Ronald Press).

Characteristic Electron Energy Loss Spectra of the Transition Metals, Ti to Cu

By J. L. ROBINS and J. B. SWAN†
Department of Physics, University of Western Australia, Nedlands, Western Australia

Communicated by C. J. B. Clews; MS. received 6th April 1960, in final form 30th May 1960

Abstract. The characteristic electron energy loss spectra of the elements of the first group of transition metals, Ti to Cu, have been obtained using the reflection technique. In the spectrum of each metal one loss peak is identified as a plasma loss, and another, except in Ti and V, as a lowered plasma loss. Two other series of loss values are associated with ionization of the M_1 and $M_{2,3}$ shells, whilst a peak observed with most metals at about 5 ev loss could be ascribed to ionization of the $M_{4,5}$ shell. Other losses have been interpreted as due to interband transitions, or as combinations or multiples of other loss values. The plasma loss values were found to agree with the theoretical values of $\hbar\omega_p$, assuming all 3d and 4s electrons to be 'free', for the first elements of the series and then to fall below the predicted values.

§ 1. Introduction

A considerable amount of experimental work has now been carried out by many workers on the characteristic energy losses suffered by electrons either on passing through thin foils or upon being scattered from the surfaces of solids (Marton, Leder and Mendlowitz 1955).

Most of the work has been done on the pure elements, and of these an emphasis has been placed on those which exhibit plasma oscillations. Such elements are characterized by having small binding energies for their valence electrons and large binding energies for their core electrons. Typical examples are Al, Mg and Be.

On the other hand there are the elements in which there is no sharp distinction between 'free' and 'bound' electrons. The transition metals, in which the electronic d band is incompletely filled, are in this class and have received much less attention both theoretically and experimentally.

Although attempts have been made to modify the theory of plasma oscillations to cover such cases, the approach is usually only qualitative. Interpretation of the loss values by associating them with interband transitions of the electrons within the solid has also been proposed with varying degrees of agreement with experiment.

The pertinent factor, however, would seem to be that most theories concerning the transition metals necessarily consider them as a series, and hence should be compared with the experimental data for all the elements in the group. The wide disagreement between the results of different workers, and often the same worker at different times, renders it unwise to combine independent measurements made under differing conditions when attempting a comparison with a theory which treats the elements as a unified series.

† Now on leave at Brookhaven National Laboratory, Upton, New York.

The first group of transition metals is the only one in which the majority of the elements are easily obtainable and convenient to handle, yet even here there is no record of a complete study of the eight elements Ti to Cu having been undertaken by any one experimenter. Indeed, the reports of Marton and Leder (1954) and Watanabe (1954, 1956) are the only two in which the results for more than three of these elements are presented as having been studied by the same worker. The metal vanadium has not previously been examined.

With this in mind, the present work on the characteristic energy losses of electrons in the eight elements, Ti, V, Cr, Mn, Fe, Co, Ni and Cu, was undertaken, using the same equipment throughout and as nearly identical conditions as possible. The apparatus has proved to be well suited for the study of elements under conditions of good bulk and surface purity.

§ 2. Theory

Marton, Leder and Mendlowitz (1955) have given a very comprehensive review of the work on the characteristic energy losses of electrons in solids up to 1955 and an outline of later work has been given in a recent paper (Powell and Swan 1959).

The plasma oscillation theory of Pines and associates (Pines and Bohm 1952, Pines 1956, Nozières and Pines 1958, 1959) appears to present a satisfactory explanation for the dominant energy loss in most materials. The magnitude of the fundamental loss is predicted in terms of $\hbar\omega_p$ where ω_p is the free electron plasma frequency and is equal to $(4\pi ne^2/m)^{1/2}$, where n is the free electron density. For elements where the valence electrons are loosely bound and the core electrons are tightly bound, the observed fundamental energy loss value should be close to $\hbar\omega_p$, if n is based on the number of valence electrons. Also the half-width of the loss peak should be small compared with $\hbar\omega_p$. This has been borne out in experiment.

The theory also predicts, however, that the observed loss values may differ from $\hbar\omega_p$ due to the core polarizability and the occurrence of interband transitions, and that these factors would also cause broadening of the loss peak.

For the transition metals, where the electronic d shell is incompletely filled, there is no sharp distinction between the 'free' conduction electrons and the 'bound' core electrons. It is therefore to be expected that the observed loss value may differ from $\hbar\omega_p$ due to the strong influence of interband transitions. Nozières and Pines predict qualitatively that in the first group of transition metals, on passing from Ti to Cu, the observed loss values will first be greater than and then become less than $\hbar\omega_p$, if the calculation is made on the assumption that all 3d and 4s electrons are 'free'. Nozières and Pines also point out the correlation between the optical properties of a solid and its characteristic energy losses. They show that the loss peaks due to plasma excitation should not appear in the optical absorption spectra at corresponding absorption energies and that a large increase in the optical transmittivity with increasing frequency should occur at $\hbar\omega_p$. This is a more accurate determination of $\hbar\omega_p$ but unfortunately reliable data in the required optical region are scant.

Ritchie (1957) predicted that the effect of the specimen boundary would cause a decrease in intensity of the plasma loss and the appearance of an additional loss, a lowered plasma loss, either at $\hbar\omega_p/\sqrt{2}$ or at $\hbar\omega_p/\sqrt{3}$, depending on whether the specimen is plane parallel-sided or of spherical grain structure. Low-lying

losses, which can be interpreted as being lowered plasma losses, have since been observed and identified in many materials which exhibit plasma losses (Powell 1960b). Such losses are very sensitive to the condition of the target surface and are affected by substrates, surface layers of oxide, contamination, etc. (Powell and Swan 1960).

Certain workers have proposed that the characteristic energy losses are predominantly or entirely due to interband transitions (Rudberg and Slater 1936, Watanabe 1954, Leder *et al.* 1956, Sternglass 1956, Gauthé 1958, Viatskin 1958). Watanabe and Leder *et al.* have compared the characteristic energy losses with x-ray absorption data. The values used in the comparison are the energy differences measured between the absorption edge (usually the K edge) and the peaks observed in the fine structure on the high energy side of the edge. Such energy differences are considered to represent the energy difference between the Fermi surface and the maxima in the density distribution of the unoccupied states above it. Gauthé refers to such energy differences as ΔE but states that the comparison should be made with a value ΔV where $\Delta V = \delta E + \Delta E$. Here δE is the energy difference between the Fermi surface and the maximum in the population density of the electronic band immediately below it. This he reasons is the initial state for the excited electrons, rather than the Fermi level itself. δE is determined from the x-ray data as the distance between an emission maximum and the corresponding absorption edge.

It has been pointed out (Ferrell 1956, Pines 1956, Nozières and Pines 1959) that the plasma oscillations may themselves be responsible for a peak in the x-ray absorption fine structure. Gauthé, however, calculates that this is highly unlikely in the cases of Ni and Cu. A similar calculation would indicate that it is also unlikely in Fe and Co.

§ 3. Experimental Procedure

The equipment used for this study has been described elsewhere (Powell, Robins and Swan 1958, Powell and Swan 1959). The reflection technique is used, whereby electrons which have been elastically and inelastically scattered through 90° at the target surface are collimated and analysed with an 127° electrostatic energy analyser. Slit widths and target position are the same as in the latter reference and the methods of recording and calibration are the same.

Targets were prepared by vacuum evaporation, *in situ*, and were examined immediately after deposition. With all the metals studied, the observed spectra changed rapidly with time immediately after deposition of a clean target surface. This rate of change was slowed down by prior evaporation of titanium or aluminium to 'getter' the chamber, and the effect was considered to be due to the formation of oxide on the target surface. Many observations were made in each case, scanning in both directions along the energy scale, and spectra were found to be reproducible when they were recorded directly after a new evaporation had been made. They are thus considered to be characteristic of the clean metals.

Spectrographically pure metals obtained from Johnson, Matthey and Co. Ltd., were used for the evaporations of all the metals, although samples of lesser purity were also used in the cases of Mn, Ni and Cu and were found to give identical results. The evaporations of Ti, V, Cr, Mn and Cu were made from multi-strand tungsten conical baskets, whilst multi-strand tungsten helical coils were used for Fe, Co and Ni. No attempt was made to measure the thickness of the

layers deposited, but they were of sufficient thickness to eliminate all effects of the substrate.

The pressure was normally less than 2×10^{-6} mm Hg, though it often rose to about ten times this value during evaporations. The target was at room temperature at all times and the carbonaceous contamination (Powell, Robins and Swan 1958) occurred so slowly that it was usually not detectable for periods of an hour or more. Throughout this work a primary electron energy of 1200 ev was used.

§ 4. Results and Discussion

The interpretation of these loss spectra, as well as subsequent comparison with theory, is made easier and more convincing by having the complete series, Ti to Cu, observed with the same instrument, and under similar conditions. Our results for the transition metals are presented in table 1. Loss values which are interpreted as having arisen from similar loss mechanisms have been tabulated in the same column and are indicated by the same symbol in figure 1, in which the complete set of loss values is shown schematically in order to emphasize the general trends which occur throughout the series.

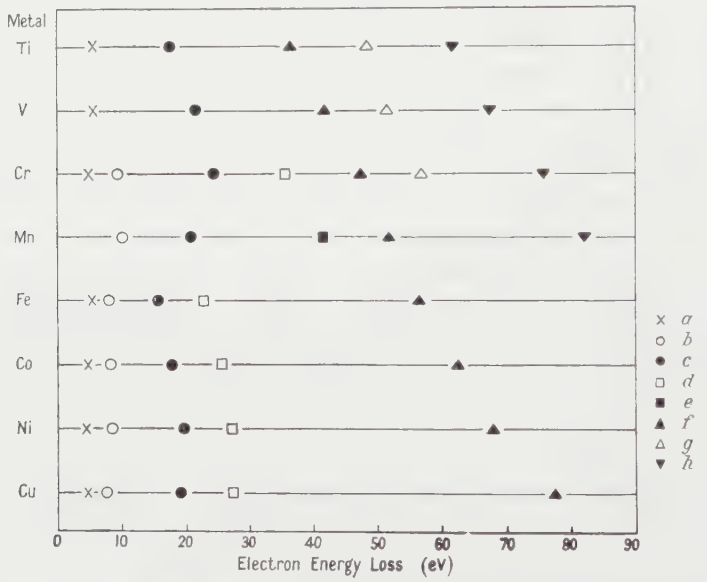

Figure 1. Schematic diagram of the characteristic energy losses observed in the transition metals, Ti to Cu. The interpretation of the losses is as follows: *a*, $M_{4,5}$ shell ionization, *b*, lowered plasma loss, *c*, plasma loss, *d*, combination or interband transition, *e*, multiple of plasma loss, *f*, $M_{2,3}$ shell ionization, *g*, unidentified, *h*, M_1 shell ionization.

The loss values quoted in table 1 are the means of measurements made on a number of different spectra taken for each element. The errors shown are the probable errors of the means. Allowance has been made for the apparent shift in the peak position where it is obvious that the background is sloping but, with such complex spectra, there may still be some error in the location of certain peaks due to this cause. The numbers in parentheses indicate the number of measurements used in the determination of the particular loss value. The complete

Table 1. Characteristic Energy Losses in the Transition Metals as found in the Present Work (in ev)

Metal	Column A	B	C	D	E	F	G	H
Ti	$5{\cdot}5 \pm 0{\cdot}4$ (19)		$17{\cdot}6 \pm 0{\cdot}3$ (20)			$36{\cdot}6 \pm 1{\cdot}0$ (16)	$48{\cdot}3 \pm 0{\cdot}5$ (17)	$61{\cdot}8 \pm 0{\cdot}5$ (17)
V	$5{\cdot}4 \pm 0{\cdot}4$ (15)		$21{\cdot}6 \pm 0{\cdot}5$ (16)			$41{\cdot}9 \pm 0{\cdot}6$ (5)	$51{\cdot}6 \pm 0{\cdot}8$ (6)	$67{\cdot}4 \pm 0{\cdot}7$ (6)
Cr	$4{\cdot}9 \pm 0{\cdot}4$ (17)	$9{\cdot}3 \pm 0{\cdot}4$ (22)	$24{\cdot}3 \pm 0{\cdot}4$ (23)	$35{\cdot}7 \pm 1{\cdot}3$ (9)		$47{\cdot}6 \pm 0{\cdot}6$ (9)	$57{\cdot}0 \pm 0{\cdot}6$ (8)	$75{\cdot}9 \pm 0{\cdot}4$ (4)
Mn		$10{\cdot}2 \pm 0{\cdot}5$ (25)	$21{\cdot}0 \pm 0{\cdot}5$ (25)		$41{\cdot}8 \pm 0{\cdot}8$ (18)	$52{\cdot}0 \pm 0{\cdot}4$ (22)		$82{\cdot}2 \pm 0{\cdot}5$ (6)
Fe	$5{\cdot}3 \pm 0{\cdot}4$ (23)	$8{\cdot}0 \pm 0{\cdot}4$ (30)	$15{\cdot}8 \pm 0{\cdot}6$ (26)	$23{\cdot}0 \pm 0{\cdot}5$ (30)		$56{\cdot}6 \pm 0{\cdot}4$ (10)		
Co	$4{\cdot}6 \pm 0{\cdot}4$ (12)	$8{\cdot}2 \pm 0{\cdot}5$ (18)	$17{\cdot}9 \pm 0{\cdot}6$ (17)	$25{\cdot}7 \pm 0{\cdot}6$ (18)		$62{\cdot}5 \pm 0{\cdot}6$ (7)		
Ni	$> 4{\cdot}3 \pm 0{\cdot}4$ (9)	$8{\cdot}3 \pm 0{\cdot}3$ (10)	$19{\cdot}5 \pm 0{\cdot}4$ (12)	$27{\cdot}1 \pm 0{\cdot}6$ (12)		$68{\cdot}0 \pm 0{\cdot}6$ (4)		
Cu	$4{\cdot}5 \pm 0{\cdot}2$ (29)	$7{\cdot}6 \pm 0{\cdot}3$ (29)	$19{\cdot}1 \pm 0{\cdot}3$ (29)	$27{\cdot}3 \pm 0{\cdot}4$ (28)		$77{\cdot}4 \pm 0{\cdot}8$ (13)		

Loss values tabulated in the same column are considered to have the same origin, as discussed in the text. The numbers in parentheses indicate the number of measurements used in the determination of the particular loss value.

spectrum was not scanned on every occasion, especially when oxidation was occurring rapidly, and this is the reason for the smaller number of observations of the peaks with greater loss values.

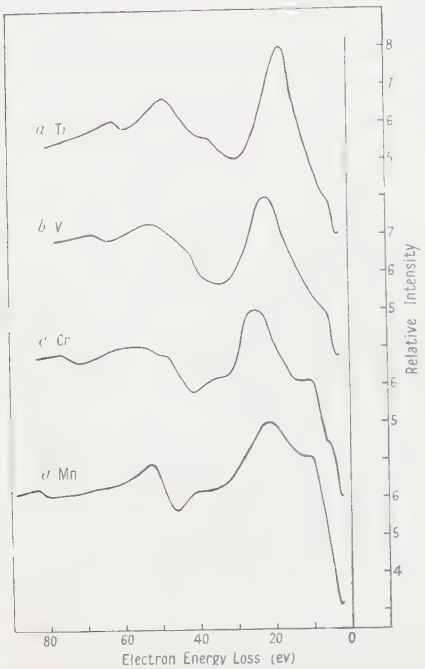

Figure 2. Characteristic energy loss spectra of Ti, V, Cr and Mn.

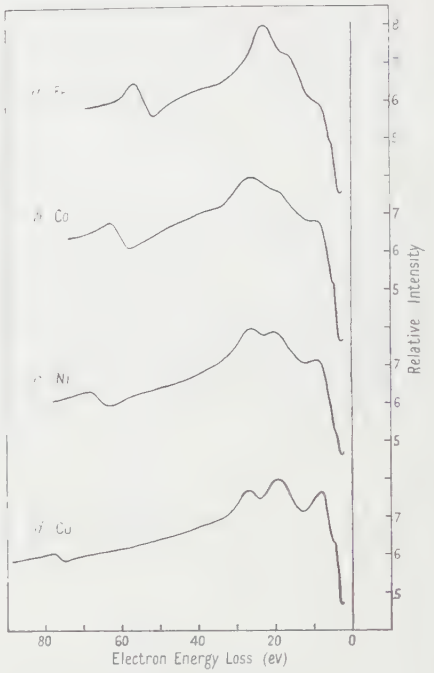

Figure 3. Characteristic energy loss spectra of Fe, Co, Ni and Cu.

The normalized characteristic energy loss spectrum for each metal is shown in figures 2 and 3. The intense peak of elastically scattered electrons, at zero energy loss, is not shown, but its width at half maximum intensity was about 1·5 ev. The intensity scale is arbitrary and has been adjusted so that the highest peak in each spectrum has an intensity of eight units.

Our interpretation of the various losses, together with the considerations leading to it, is given below. The columns referred to are those in table 1.

It was assumed that one loss value in each spectrum would be due to the excitation of a plasma oscillation (Pines 1956) and the losses in column C were interpreted as these plasma losses. These losses in Ti and V are clearly defined and their values agree well with the theoretically expected values. This is discussed in more detail later and corroborative evidence from optical experiments is also presented for Ti. The choice of the plasma peaks in Cr and Mn was governed by a consideration of the general form of the spectra in figure 2. In Cu, it is generally accepted that the loss of about 19·1 ev is the plasma loss and this has been substantiated by recent work on alloys (Powell 1960a). From this and a general consideration of the losses in this series of elements it seemed most reasonable to interpret the 15·8, 17·9 and 19·5 ev losses in Fe, Co and Ni respectively as the plasma losses even though they were not necessarily the most intense.

The loss values listed in column B are interpreted as being lowered plasma losses. The use of the reflection technique and very clean target surfaces are

conditions suited to the observation of such losses, and it is therefore reasonable to expect that they would be observed. Furthermore, the recent work on alloys mentioned above has shown that the loss of about 7·6 ev in Cu is indeed a loss of this type. No explanation can be offered as to why such a loss was not observed in either Ti or V. Also as the 9·3 ev loss in Cr seems out of place in the general pattern of the losses as presented in figure 1, its interpretation as a lowered plasma loss may be questionable.

The loss values shown in columns F and H are interpreted as being due to ionization of the electronic $M_{2,3}$ and M_1 shells respectively. Hillier and Baker (1944) who set out to observe this effect, were mainly concerned with loss values of greater magnitude but did interpret a peak at 51·3 ev in Fe as being due to M shell ionization. Our values are retabulated in table 2 together with the corresponding critical x-ray absorption energies taken from the tables of Hill, Church and Mihelich (1952), and the mean $M_{2,3}$ absorption edge energies as found by Tomboulian, Bedo and Neupert (1957) for Cr to Cu. The agreement between our values and those of Tomboulian *et al.* is seen to be quite good except for a constant difference of about 2·5 ev, allowing that our 47·6 ev value for Cr may be affected by a multiple of the plasma peak at about 48·6 ev. This constant difference may arise in the following manner. In these spectra, the so-called peak which is due to $M_{2,3}$ shell ionization should, in fact, be only a steep rise in the intensity of the background, but may appear as a peak if the background is sloping. As our measurements were made to the top of the observed peaks and as the rise is often spread over 5 or 6 ev, it is quite reasonable to suppose that our values will be slightly greater than the values of the mean $M_{2,3}$ absorption edge. The agreement between our values and those of the critical x-ray absorption energies of Hill *et al.* for both the $M_{2,3}$ and M_1 shells are reasonably good, particularly as their values are acknowledged to be only approximate. Having the results for the complete series of elements shows clearly the increase of these particular energy loss values with atomic number and lends conviction to the interpretation of these peaks.

Table 2. Comparison of the Observed Energy Loss Values quoted in columns H, F and A of Table 1 with the various M shell x-ray Absorption Energies (in ev)

Metal	Ti	V	Cr	Mn	Fe	Co	Ni	Cu
Atomic Number	22	23	24	25	26	27	28	29
Present Work (Column H)	61·8	67·4	75·9	82·2				
M_1 absorption energy (H.C.M.)	61	68	76	85				
Present Work (Column F)	36·6	41·9	47·6	52·0	56·6	62·5	68·0	77·4
$M_{2,3}$ absorption edge (T.B.N.)			43·5	49·5	54·3	59·6	65·5	76·3
$M_{2,3}$ absorption energy (H.C.M.)	35	41	42	52	56	64	73	77
Present Work (Column A)	5·5	5·4	4·9		5·3	4·6	4·3	4·5
$M_{4,5}$ energy level (HB)	4·2	5·0	2·0	6·4	5·0	6·7	7·2	4·1

The references are: (H.C.M.) Hill *et al.* 1952; (T.B.N.) Tomboulian *et al.* 1957; (HB) American Institute of Physics Handbook 1957.

The appearance of peaks due to ionization of the M_1 and $M_{2,3}$ shells leads us to consider the possibility of $M_{4,5}$ shell ionization, which would give rise to loss peaks at about 5 ev. It would thus seem reasonable to attribute the loss values listed in

column A of table 1 to ionization of the $M_{4,5}$ shell. These loss values are compared in table 2 with the energy levels of the $M_{4,5}$ shell as presented in the American Institute of Physics Handbook (1957). It should be emphasized that the comparison is intended to be indicative only, as these particular energy levels cannot be determined with any great accuracy.

The origin of the three losses recorded in column G of table 1 has not been determined. The peaks are all intense and become broader from Ti to Cr; in fact the 57·0 ev peak in Cr sometimes has the appearance of two unresolved peaks. Presumably they could arise from unidentified interband transitions.

Only one loss value appears in column E and it is a multiple of the plasma loss. The corresponding loss for Ti would be at 35·2 ev and its presence there would account for the extended slope on the low energy loss side of the 36·6 ev loss peak. The corresponding losses for V and Cr would occur at 43·2 and 48·6 ev and are possibly obscured by the 41·9 and 47·6 ev losses respectively. For Fe, Co, Ni and to a lesser extent Cu, the multiples of the plasma losses are not clearly observed although there is some structure in the spectra at the expected positions; this structure, however, was not as reproducible as the other parts of the spectra. In certain cases there also appeared to be indications of multiples of the losses tabulated in column D for these metals.

The loss values in column D correspond, within the limits of experimental error, to the combination of a plasma loss and a lowered plasma loss. Such a loss is not clearly defined in the Mn spectrum and it is not to be expected in our spectra for Ti or V where the lowered plasma loss is absent. The 23·0 ev loss for Fe and to lesser extents the 25·7, 27·1 and 27·3 ev losses of Co, Ni and Cu respectively are much more intense than would be expected so they may well arise primarily from interband transitions.

It is of interest to estimate, from x-ray K absorption data, the energy losses that might be associated with interband transitions in Fe, Co, Ni and Cu. The principle used in the calculation is the same as that used by Gauthé (1958) and has been described above. We have used the x-ray results published by Beeman and Friedman (1939) because of their completeness for these elements and because they appear to agree quite well with more recent work (Cauchois and Manesco 1950, Cauchois 1953, Sawada, Tsutsumi and Hayase 1957, Tsutsumi 1958, Bally and Benes 1959).

For Fe, one calculates from the x-ray data that $\Delta V = 22{\cdot}2$ ev, in good agreement with our observed loss at 23·0 ev. For Co, $\Delta V = 23{\cdot}6$ and 27·5 ev compared with the single broad loss at 25·7 ev and for Ni, $\Delta V = 19{\cdot}3$ and 28·1 ev compared with the observed losses at 19·5 and 27·1 ev. We have already interpreted the 19·5 ev loss as the plasma loss but it is possible that a loss due to an interband transition could coincide with it. For Cu one calculates $\Delta V = 18{\cdot}1$ and 27·5 ev compared with our observed losses at 19·1 and 27·3 ev. Again the 18·1 ev loss would have to be considered as practically coinciding with the plasma loss. The agreement, however, is sufficiently good to justify the interpretation of the losses in Fe, Co, Ni and Cu which are tabulated in column D as being primarily due to interband transitions.

Consider again the plasma losses of these transition metals. The complexity of the spectra prevents an estimation or even an intercomparison of the half-widths of these peaks. We can only note that they are broader than the plasma peaks of 'well-behaved' metals such as Al and Mg, as is predicted by theory. Regarding

their values, however, if all the 3d and 4s electrons in each element are considered as being 'free', the observed losses of 17·6 and 21·6 ev for Ti and V respectively are very close to the values of 17·7 and 22·0 ev predicted by the formula

$$\hbar\omega_p = \hbar(4\pi ne^2/m)^{1/2}.$$

The observed plasma losses of the remaining elements are less than the theoretical values of 26·1, 28·0, 32·6, 33·2, 35·5 and 35·8 ev for Cr to Cu respectively. This is not in complete agreement with the predictions of Pines (1956) and Nozières and Pines (1958) who expect the observed values to be higher than the theoretical values for Ti and V, and then to fall below them as one proceeds through the transition group. Indeed, if one accepts for Cr their theoretical value of 24 ev, which appears to include some allowance for core polarization, the agreement between the theoretical and our observed values is good for Ti, V and Cr. More theoretical work of a quantitative nature, however, is needed on this aspect of the characteristic energy losses of electrons in solids.

It has recently been suggested by Powell (1960b) that the effective free electron concentration might be calculated from the lowered plasma loss, denoted by ΔE_{II}. Taking $\Delta E_{II} = \hbar\omega_p/\sqrt{2}$ and assuming that the losses in column B of table 1 are lowered plasma losses, one obtains 1·5, 1·9, 1·1, 1·1, 1·1 and 1·0 as the number of free electrons in the elements Cr, Mn, Fe, Co, Ni and Cu respectively. Although this gives the expected value of one free electron for Cu, the validity of this procedure has still to be substantiated and these values should be treated with caution.

§ 5. Comparison with Previous Work

The amount of work previously carried out on the energy losses of electrons in these transition metals is not great, and there has been considerable disagreement between the results presented by various workers. We have, therefore, collected all the characteristic energy loss values previously published for each element and present them together with our own for inter-comparison.

Titanium. The only other workers who have studied the characteristic energy loss spectrum of Ti appear to be Marton and Leder (1954) and Watanabe (1956). Their results together with our own are shown in table 3. The agreement is poor, possibly due to the rapid rate of oxidation experienced with films of Ti. As previously mentioned, the spectrum changes during oxidation and we observe the most prominent peaks in the altered spectrum to be at 11·4, 25·1 and 48·3 ev loss.

Table 3. Characteristic Energy Losses in Titanium found in the Present Work and by Other Authors (in ev)

Present Work	5·5		17·6	36·6	48·3	61·8
Marton and Leder (1954)		11·4	21·4		42·9	
Watanabe (1956)	6·5	13	24		50	

It is interesting to note that Rustgi (1959, private communication) has observed the onset of transmission in a Ti foil to occur at 18·0 ev, in close agreement with our 17·6 ev loss which we interpret as the plasma loss.

Vanadium. No previous investigation of the energy losses in V has been published and our results for this metal are included in table 1.

Chromium. The energy losses observed in Cr by other workers, together with our own results, are shown in table 4. The agreement is not good between any of these sets of loss values.

Table 4. Characteristic Energy Losses in Chromium found in the Present Work and by Other Authors (in ev)

Present Work	4·9	9·3	24·3	35·7	47·6	57·0	75·9
Marton and Leder (1954)		9·7	21·8		45·0		
Watanabe (1954)			26			54	
Fert and Pradal (1958)			28			58	85

Manganese. Table 5 contains the energy losses observed in Mn by other workers and ourselves. The agreement here is quite good although we have observed more loss peaks.

Table 5. Characteristic Energy Losses in Manganese found in the Present Work and by Other Authors (in ev)

Present Work	10·2	21·0	41·8	52·0	82·2
Marton and Leder (1954)	9·9	22·1			
Fert and Pradal (1959)		22·5			

Iron. The electron energy losses in Fe as measured by previous workers and ourselves are shown in table 6. As discussed before, we interpret the 15·6 ev loss as the plasma loss, although the 23·0 ev loss peaks appear more intense (see figure 3, curve *a*). This latter loss has been considered by previous workers to be the plasma loss, presumably because of its intensity, and indeed it seems to have obscured the 15·8 ev loss peak in the work of Kleinn (1954) and Watanabe (1956). It is interesting to note also that after the spectrum has changed, due presumably to oxidation of the target surface, the 15·8 ev loss peak disappears and a strong peak at 22·9 ev is dominant.

Table 6. Characteristic Energy Losses in Iron found in the Present Work and by Other Authors (in ev)

Present Work	5·3	8·0	15·8	23·0			56·6	
Kleinn (1954)		7		21·5	36·5		56·9	
Marton and Leder (1954)			15·8	19·4			56·1	
Watanabe (1956)				23·2		49		62

Cobalt. The previously reported energy losses in Co, together with our observed values, are given in table 7. Marton and Leder (1954) do not observe the 25·7 ev loss peak, whilst Watanabe (1956) may not have resolved the 17·9 and 25·7 ev peaks.

Table 7. Characteristic Energy Losses in Cobalt found in the Present Work and by Other Authors (in ev)

Present Work	4·6	8·2	17·9	25·7	62·5
Marton and Leder (1954)	5·7		18·3		
Watanabe (1965)			22·9		63·3

Nickel. Many workers have investigated Ni, as is shown in table 8. It would appear quite possible that, apart from the work by Gauthé (1958) and ourselves, the 19·5 and 26·4 ev losses have not been resolved, as the other results all show a peak at about 23 ev loss. Our '> 4·3 ev' loss is tabulated thus, as only a change of slope occurs at this point and the location of the peak could be at a greater loss value.

Table 8. Characteristic Energy Losses in Nickel found in the Present Work and by Other Authors (in ev)

Present Work	>4·3	8·3		19·5		26·4					68·0
Lang (1948)			15		24·2			47·5			
Möllenstedt (1949)					22·6						65
Kleinn (1954)	5·4				21·8						
Marton and Leder (1954)	5·8	9·4	13·2	17·6	23·4						
Watanabe (1954)	6·5		12		22·5			45			
Simpson *et al.* (1956)					23						
Gauthe (1958)				20·6		26·5	32·6	42	52		

Copper. Copper has been extensively investigated and the results are collected in table 9. In a few of our spectra there was some indication of a slight peak at about 9·5 ev. There is general agreement that the plasma loss is about 19 or 20 ev, though certain workers do not seem to have resolved the peaks at approximately 19 and 27 ev. The losses tabulated for Simpson, McCraw and Marton (1956) and Pradal and Saporte (1958) are estimated from their published diagrams. The latter workers report observing a loss at about 360 ev in Cr, Mn, Ni, Cu and other materials but do not mention other loss values except for Cu.

Table 9. Characteristic Energy Losses in Copper found in the Present Work and by Other Authors (in ev)

Present Work		4·5	7·7		19·2		27·3					77·4
Rudberg (1930)	3·4		6·9	12·3		25·5		34·5				
Rudberg (1936)		4·2	7·3									
Lang (1948)					19·1							
Reichertz and Farnsworth (1949)	3·0		6·0	12·3	20·0							
Möllenstedt (1949)					20·4							
Kleinn (1954)	3·1	4·3	6·4		21							
Marton and Leder (1954)			6·9	11·3	19·6							
Watanabe (1954)			7		19·5							
Blackstock *et al.* (1955)						22·6						
Simpson *et al.* (1956)						24						
Gauthé (1956)			7·3		17·4	22·7	27·8		40	49	60	
Gauthé (1958)			7·3		18·7	23·7	28·4		41	49		
Fert and Pradal (1958)						25				49		
Pradal and Saporte (1958)		5			20							
Powell (1960 b)		4·4	7·2		19·9		27·1					

§ 6. Conclusions

The characteristic electron energy loss spectra of the elements of the first group of transition metals, Ti to Cu, have been obtained using the reflection technique and 1200 ev primary electrons. Care was taken to use clean target surfaces for the analyses.

Two series of losses observed in these metals are associated with ionization of the electronic M_1 and $M_{2,3}$ shells, whilst it is suggested that a third group might be associated with $M_{4,5}$ shell ionization. The remaining losses are interpreted as plasma losses, lowered plasma losses, losses associated with interband transitions or losses due to combinations or multiples of primary events. It is found possible to correlate certain interband transition loss values with x-ray absorption data.

When compared with the values of $\hbar\omega_p$, as calculated from the unmodified plasma excitation theory assuming all the 3d and 4s electrons to be 'free', the observed plasma loss values agree for Ti and V but fall below the predicted values for the other metals in the series. This is presumably due to core polarization and the influence of interband transitions.

However, further theoretical work, preferably quantitative, is needed on the characteristic energy losses of electrons in the transition metals, and it is hoped that the results presented here will stimulate such further studies.

Acknowledgments

The authors wish to thank Professor C. J. Birkett Clews for his continued interest and advice. We are also grateful to Dr. O. P. Rustgi for communicating his results prior to publication. The research was financed by the Research Grants Committee of the University of Western Australia, and one of us (J.L.R.) gratefully acknowledges the tenure of a General Motors–Holden Postgraduate Research Fellowship.

References

Amer. Inst. Phys. Handb., 1957 (New York: McGraw-Hill).
Bally, D., and Benes, L., 1959, *C.R. Acad. Sci., Paris*, **248,** 2327.
Beeman, W. W., and Friedman, H., 1939, *Phys. Rev.*, **56,** 392.
Blackstock, A. W., Ritchie, R. H., and Birkhoff, R. D., 1955, *Phys. Rev.*, **100,** 1078.
Cauchois, Y., 1953, *Phil. Mag.*, **44,** 173.
Cauchois, Y., and Manesco, I., 1950, *J. Chimie Physique*, **47,** 892.
Ferrell, R. A., 1956, *Rev. Mod. Phys.*, **28,** 308.
Fert, C., and Pradal, F., 1958, *C.R. Acad. Sci., Paris*, **246,** 252.
—— 1959, *Ibid.*, **248,** 666.
Gauthé, B., 1956, *C.R. Acad. Sci., Paris*, **242,** 2634.
—— 1958, *Ann. Phys., Paris*, **3,** 915.
Hill, R. D., Church, E. L., and Mihelich, J. W., 1952, *Rev. Sci. Instrum.*, **23,** 523.
Hillier, J., and Baker, R. F., 1944, *J. Appl. Phys.*, **15,** 663.
Kleinn, W., 1954, *Optik, Stuttgart*, **11,** 226.
Lang, W., 1948, *Optik, Stuttgart*, **3,** 233.
Leder, L. B., Mendlowitz, H., and Marton, L., 1956, *Phys. Rev.*, **101,** 1460.
Marton, L., and Leder, L. B., 1954, *Phys. Rev.*, **94,** 203.
Marton, L., Leder, L. B., and Mendlowitz, H., 1955, *Advances in Electronics and Electron Physics* (New York: Academic Press), Vol. 7, p. 183.
Möllenstedt, G., 1949, *Optik, Stuttgart*, **5,** 499.
Nozières, P., and Pines, D., 1958, *Phys. Rev.*, **109,** 1062.
—— 1959, *Ibid.*, **113,** 1254.
Pines, D., 1956, *Rev. Mod. Phys.*, **28,** 184.
Pines, D., and Bohm, D., 1952, *Phys. Rev.*, **85,** 338.
Powell, C. J., 1960 a, *Aust. J. Phys.*, **13,** 145.
—— 1960 b, *Proc. Phys. Soc.*, **76,** 593.
Powell, C. J., Robins, J. L., and Swan, J. B., 1958, *Phys. Rev.*, **110,** 657.
Powell, C. J., and Swan, J. B., 1959, *Phys. Rev.*, **115,** 869.
—— 1960, *Ibid.*, **118,** 640.

PRADAL, F., and SAPORTE, R., 1958, *C.R. Acad. Sci., Paris.*, **246,** 2880.
REICHERTZ, P., and FARNSWORTH, H. E., 1949, *Phys. Rev.*, **75,** 1902.
RITCHIE, R. H., 1957, *Phys. Rev.*, **106,** 874.
RUDBERG, E., 1930, *Proc. Roy. Soc.* A, **127,** 111.
—— 1936, *Phys. Rev.*, **50,** 138.
RUDBERG, E., and SLATER, J. C., 1936, *Phys. Rev.*, **50,** 150.
SAWADA, M., TSUTSUMI, K., and HAYASE, A., 1957, *J. Phys. Soc. Japan*, **12,** 628.
SIMPSON, J. A., MCCRAW, T. F., and MARTON, L., 1956, *Phys. Rev.*, **104,** 64.
STERNGLASS, E. J., 1956, *Nature, Lond.*, **178,** 1387.
TOMBOULIAN, D. H., BEDO, D. E., and NEUPERT, W. M., 1957, *J. Phys. Chem. Solids*, **3,** 282.
TSUTSUMI, K., 1958, *J. Phys. Soc. Japan*, **13,** 586.
VIATSKIN, A. IA., 1958, *Soviet Physics, Technical Physics*, **3,** 2252.
WATANABE, H., 1954, *J. Phys. Soc. Japan*, **9,** 920.
—— 1956, *J. Electronmicroscopy*, **4,** 24.

Wave-theoretic and Ray-theoretic Contrast Transmission Functions

By E. H. LINFOOT

University of Cambridge

MS. received 9th February 1960, in final form 26th April 1960

Abstract. Optical designers have always had reason to be interested in the question: how well can the practical performance of optical systems be predicted from calculations based on geometrical optics? A large number of experimental investigations have indicated that the scalar wave theory (Huyghens–Kirchhoff diffraction theory) can predict the intensity distribution in the image of a point object well enough for the purposes of instrumental optics. Thus a natural approach to the above question is to consider how well ray-theoretic evaluations of image quality agree with those based on the scalar wave theory. In those favourable cases where the agreement is good, that is to say where the effects of diffraction can be disregarded without introducing unacceptably large evaluation errors, geometrical optics can be expected to provide an adequate basis for practical optical design. The problem of delimiting the favourable cases then arises.

Some results bearing on this problem are obtained in the present paper. In §2 it is shown how, by the use of distribution functions, the contrast transmission properties of ray-theoretic images can be discussed in a way which overcomes the well-known difficulty connected with infinite ray-densities. A sharpened form of a result of Hopkins and Miyamoto is obtained (equation (2.18)) and used to discuss the sense in which the wave-theoretic image of an extended object by a small-field monochromat with given geometrical aberrations approaches the ray-theoretic image as the wavelength $\lambda \to 0$.

In §3 the relations between wave-theoretic and ray-theoretic quality evaluations of photographic images are considered. The importance of the relation between photographic spread and optical spread to the above question is clarified, and it is shown that if emulsion spread is held fixed while the aberrations are multiplied by a constant factor A, wave-theoretic and corresponding ray-theoretic photographic quality evaluations need not approach equality as $A \to \infty$; they will do so, however, if the emulsion spread is also multiplied by A.

In §4, computed quality evaluations are examined for model photographic systems with 1, 2, 4 and 8 wavelengths of fourth-power aberration, working at focal ratios 2, 4, 8, 16 over a range of focal settings in each case. Three wave-theoretic evaluations (3.9) are considered, together with the corresponding ray approximations (3.12). It appears that, over this range of special cases, the ray theoretic evaluation (3.13) can safely be used at focal ratios $F \leqslant 4$ and the error of the ray approximation (3.12) depends much more strongly on the focal ratio F than on the amount of fourth-power aberration.

§ 1. Introduction

The relations between the ray-theoretic and the wave-theoretic images of a bright point by an optical system are of both theoretical and practical interest. On the theoretical side we should like to know in precisely what sense it can be said that, as the wavelength λ tends to zero, the light distribution in the diffraction image approaches that in the ray-theoretic image as a limiting configuration. On the practical side we should like to know in what circumstances it is permissible to use the ray-theoretic image in place of the diffraction image in evaluations of visual and photographic image quality. The second question is closely bound up with that of the validity of image evaluation based on spot diagrams.

These two questions have recently been discussed by Miyamoto (1958 a, b, 1959) in three interesting and suggestive papers, from which it appears that they can be treated in a simpler way, and can receive more or less satisfactory answers in general terms, if we formulate them from the start in terms of contrast transfer functions (ct-functions). Accordingly, we first ask: *In what sense is it true that, as $\lambda \to 0$, the ct-function of a system with fixed geometrical aberrations approaches the so-called ray-theoretic ct-function*† (Fourier transform of the geometrical light-distribution)?

Miyamoto (1958 a) gave a discussion of this question which is complete in all essentials, but his handling of the error terms is not quite precise enough for the purposes of the present paper. We therefore include in § 2 a more exact version of his argument, leading to the sharper result: *As $\lambda \to 0$, the wave-theoretic ct-function of a system with fixed geometrical aberrations approaches its ray-theoretic ct-function uniformly in every finite region of the spatial frequency plane.*

This result calls to mind an observation of Hopkins (1957) to the effect that the wave-theoretic ct-function approximates to the ray-theoretic ct-function when the aberrations are large and the reduced spatial frequency s is small. However, the content of the present result is slightly different; it allows us to answer the first question as follows: *In the image of an extended object by a small-field system with given geometrical aberrations, the Fourier transforms of the wave-theoretic and ray-theoretic intensity distributions are nearly equal when λ is small; as $\lambda \to 0$ their difference tends to zero uniformly in every finite region of the spatial frequency plane.*

To the second question above we give the more specific formulation: *In what circumstances do the quality evaluations Strehl definition, structural resolution, etc. of an aerial or photographic image agree with those of the corresponding ray-theoretic image obtained by convoluting the ray-density distribution with the photographic spread function?*

It is clear on general grounds (and can be confirmed by an inspection of the particular cases analysed in figures 4, 5 and 6) that the extent of the agreement between wave-theoretic and ray-theoretic quality evaluations of a photographic image depends not only on the size of the aberrations but on the relation between the optical and photographic image-spreads. Evidently the agreement will always be good when photographic spread is large compared with optical

† Ray-theoretic ct-functions have received attention from a number of investigators, notably Hotchkiss, Washer, and Rosberry (1951), Lindberg (1955), Hopkins (1955, 1957), Sayanagi (1956), De (1955) Lukosz (1958 a, b, c), Bromilow (1958), Marathay (1959). See also Linfoot (1960 a).

spread. It is easy to verify† that in the other extreme case, where photographic spread is small compared with optical spread, the agreement is not always good even when the aberrations are large. Even in the simple case of primary spherical aberration combined with variation of focal setting, the wave-theoretic and ray-theoretic evaluations of the Strehl definition may be wildly discordant in the aerial image‡, whatever the size of the aberrations, and it follows that the same is true in images with sufficiently small photographic spread. Thus there is no possibility of formulating, in terms only of the size of the aberrations, sufficient conditions for the approximate equality of wave-theoretic and ray-theoretic Strehl definition either for aerial or for photographic images. Similar conclusions hold for the other quality evaluations mentioned in § 3. It follows rather easily, however, from the result about wave-theoretic and ray-theoretic ct-functions established in § 2, that the *wave-theoretic and the ray-theoretic quality evaluations of a photographic system of given aperture approach equality if the wave-aberrations of the system and the angular photographic spread are multiplied by the same sufficiently large factor*. Physically, multiplication of the angular photographic spread by a constant factor corresponds either to scaling down the image by reducing the focal length or to using a coarser-grained emulsion. We call a photographic system 'matched' when the optical and photographic spreads are comparable. In 'matched' systems, therefore, it is safe to use the ray-theoretic evaluation in place of the wave-theoretic evaluation provided the wave-aberration is sufficiently large §.

The above general result, proved in § 3, does not give any numerical estimate of the size of the wave-aberration above which the ray-theoretic quality evaluation becomes usable in a 'matched' photographic system. A numerical estimate only becomes possible when both the aberration type and the matching criterion between optical and photographic spread functions are specified in some way. Equation (2.17) provides a means of obtaining such an estimate in terms of the numerical aperture of the system, the third-order partial derivatives of the aberration function $\phi(\xi, \eta)$, and the photographic spread. But the estimate obtained in this way is unnecessarily large in many practical cases. It seems that we are likely to obtain a truer picture of the situation by examining selected special cases computationally. To do this systematically for the many different types of aberration met with in fast camera lenses would hardly be practicable with currently available electronic computers. But even an examination of the special case of primary spherical aberration is of some interest in view of the remarks made above. In § 4 wave-theoretic quality evaluations of model photographic images with primary spherical aberration are compared with ray-theoretic approximations over the focal range from paraxial to maginal focus in selected special cases, and some numerical conclusions are drawn about the extent of the agreement between wave-theoretic and ray-theoretic evaluations of images of this type.

† For example, by considering smooth wave-aberrations very near to one of the singular cases defined in § 2.

‡ In a system with wave aberration $\phi(\xi, \eta) = Ar^4 + ABr^2$, where $r^2 = (\xi^2 + \eta^2)/\sin^2\alpha$ and the constant $A \neq 0$, the central intensity of the ray-theoretic aerial image is infinite for $-2 \leqslant B \leqslant 0$, finite for $B < -2$ or $B > 0$.

§ Compare Miyamoto (1959), p. 61.

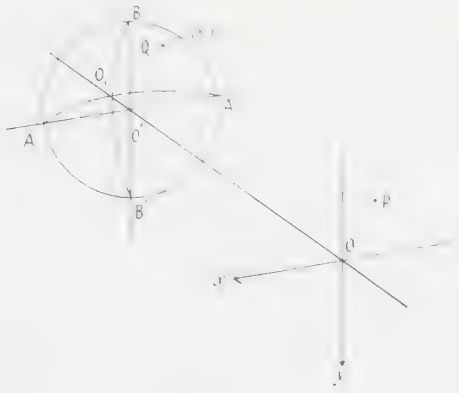

Figure 1.

§ 2. Wave-theoretic and Ray-theoretic ct-functions

In figure 1 ABA′B′ represents the exit pupil of a centred optical system with smooth aberrations of arbitrary form; (x', y') are Cartesian coordinates in the plane image surface. We denote by (u, v) the spatial frequencies relative to (x', y') in this surface. (ξ, η) are angular coordinates in the 'spherical exit pupil' centred on O′ and passing through AA′BB′O. That is to say, if Q is a point in this surface its angular coordinates (ξ, η) are defined by the equations

$$\xi = \cos \mathrm{QO'X'}, \quad \eta = \cos \mathrm{QO'Y'}.$$

In the case which mainly interests us here, that of unvignetted systems with a circular stop, the clear aperture is specified by an inequality $\xi^2 + \eta^2 < \sin^2 \alpha$, where $\sin \alpha$ is the numerical aperture of the system. It is convenient, however, to consider at the same time systems in which the clear aperture is not necessarily circular, but may, for example, be rectangular or annular in shape, or may suffer from edge-vignetting. We denote by $\mathscr{A}$ the (ξ, η) region corresponding to the clear aperture. In an unvignetted F/5 system with circular stop, imaging a point near the optic axis, $\mathscr{A}$ is represented sufficiently well by a circle $\xi^2 + \eta^2 < \frac{1}{100}$ in the (ξ, η) plane. Speaking more exactly, $\mathscr{A}$ is mapped on to this circle when the angular variables (ξ, η) are given a second interpretation as Cartesian coordinates in a mathematical (ξ, η) plane introduced for the purpose.

We denote by $\phi(\xi, \eta)$ the so-called geometrical wave-aberration in the spherical exit pupil centred on O′, and by ϕ_1, ϕ_2; ϕ_{11}, ϕ_{12}, ϕ_{22}; ϕ_{111}, ... the partial derivatives $\partial\phi/\partial\xi$, $\partial\phi/\partial\eta$; $\partial^2\phi/\partial\xi^2$, $\partial^2\phi/\partial\xi\partial\eta$, $\partial^2\phi/\partial\eta^2$; $\partial^3\phi/\partial\xi^3$, ... We denote by $w(x', y'; \lambda)$ the normalized light-intensity at the point (x', y') of the diffraction image in light of wavelength λ. The normalization is chosen so that

$$\int\int_{-\infty}^{\infty} w(x', y'; \lambda)\, dx'\, dy' = 1. \qquad \ldots\ldots (2.1)$$

In a small-field isoplanat the ct-function $\tau(u, v; \lambda)$ is related to $w(x', y'; \lambda)$ and to $\phi(\xi, \eta)$ by the approximate equations

$$\begin{aligned}\tau(u, v; \lambda) &= \int\int_{-\infty}^{\infty} w(x, y; \lambda) \exp\left[-2\pi i(ux' + vy')\right] dx'\, dy' \\ &= |\mathscr{A}|^{-1} \int\int_{S_{\lambda u,\, \lambda v}} \exp\left\{\frac{-2\pi i}{\lambda}\left[\phi\left(\xi + \frac{\lambda u}{2}, \eta + \frac{\lambda v}{2}\right)\right.\right. \\ &\qquad \left.\left. - \phi\left(\xi - \frac{\lambda u}{2}, \eta - \frac{\lambda v}{2}\right)\right]\right\} d\xi\, d\eta, \qquad \ldots\ldots (2.2)\end{aligned}$$

where the domain of integration

$$S_{\lambda u,\,\lambda v}=[\mathscr{A}+(\tfrac{1}{2}\lambda u,\,\tfrac{1}{2}\lambda v)]\times[\mathscr{A}-(\tfrac{1}{2}\lambda u,\,\tfrac{1}{2}\lambda v)]\subset\mathscr{A},\dagger \quad \ldots\ldots(2.3)$$

while $|\mathscr{A}|$ denotes the area of the region $\mathscr{A}$ in the (ξ,η) plane. When $\xi^2+\eta^2<\frac{1}{100}$ throughout $\mathscr{A}$, the errors in this approximation are negligible for practical purposes. Making use of the inequality

$$|e^{iX}-1|\leqslant|X| \qquad (-\infty<X<\infty)$$

and applying the mean value theorem, we obtain from (2.2) the equation

$$\tau=|\mathscr{A}|^{-1}\iint_{S_{\lambda u,\,\lambda v}}\exp\{-2\pi i(u\phi_1+v\phi_2)\}\,d\xi\,d\eta+\theta\frac{\pi\sqrt{2}}{12}K_3\lambda^2\omega^3, \quad \ldots\ldots(2.4)$$

in which θ denotes a number between -1 and $+1$, $\omega=\sqrt{(u^2+v^2)}$ is the line frequency corresponding to the spatial frequency (u,v) and K_3 is the greatest of the upper bounds in $\mathscr{A}$ of the continuous functions

$$|\phi_{111}(\xi,\eta)|, \quad |\phi_{112}(\xi,\eta)|, \quad |\phi_{122}(\xi,\eta)|, \quad |\phi_{222}(\xi,\eta)|. \quad \ldots\ldots(2.5)$$

(2.4) is a more precise form of a result of Hopkins (1957) and Miyamoto (1957, 1958 a). When $\lambda\to0$ the (ξ,η) domain $S_{\lambda u,\,\lambda v}$ takes the limiting form $\mathscr{A}$ and the first term on the right of (2.4) tends to the limit $t(u,v)$, where

$$t(u,v)=|\mathscr{A}|^{-1}\iint_{\mathscr{A}}\exp\{-2\pi i(u\phi_1+v\phi_2)\}\,d\xi\,d\eta \quad \ldots\ldots(2.6)$$

is the so-called geometrical ct-function of the optical system.

In those cases where the normalized ray-density $\rho(x,y)$ in the geometrical image is finite at every point, $t(u,v)$ satisfies the equation

$$t(u,v)=\int\int_{-\infty}^{\infty}\exp[-2\pi i(ux'+vy')]\rho(x,y)\,dx'\,dy'. \quad \ldots\ldots(2.7)$$

The normalization

$$\int\int_{-\infty}^{\infty}\rho(x',y')\,dx'\,dy'=1 \quad \ldots\ldots(2.8)$$

ensures that

$$t(0,0)=1, \quad \ldots\ldots(2.9)$$

just as the normalization (2.1) ensures that

$$\tau(0,0;\lambda)=1 \quad \ldots\ldots(2.10)$$

for every λ.

The condition that $\rho(x',y')$ is everywhere finite seldom holds in a practical case. In particular it is not satisfied by folded images of the usual kinds. However, equations (2.6) and (2.7) still hold for these images. It can be shown that they fail only in the 'singular' cases where there is a set of points (x',y') of two-dimensional measure zero which contains a finite proportion of the total illumination in the geometrical image. A correctly focused, aberration-free image is the simplest example of such a singular case.

To cover the singular cases together with the others, it is necessary to use a more sophisticated mathematical technique. In place of the ray-density function $\rho(x',y')$ we introduce the *distribution function* $P(x',y')$, defined by the equation

$$P(x',y')=|\mathscr{A}|^{-1}\iint_{\mathscr{A}}d\xi\,d\eta, \quad \ldots\ldots(2.11)$$

† $A+(\frac{1}{2}\lambda u,\,\frac{1}{2}\lambda v)$ means the region A displaced by the amount $(\frac{1}{2}\lambda u,\,\frac{1}{2}\lambda v)$; $\times$ denotes the 'product' (intersection) of the two regions in square brackets; $\subset$ means 'is included in'.

in which the integral on the right is taken over those points (ξ, η) of $\mathscr{A}$ at which

$$\phi_1(\xi, \eta) \leqslant x', \qquad \phi_2(\xi, \eta) \leqslant y'. \qquad \ldots\ldots (2.12)$$

Evidently $P(x_0', y_0')$ is the fraction of the total light in the geometrical image which is contained in the part $x' \leqslant x_0'$, $y' \leqslant y_0'$ of the image surface. $P(x', y')$ is an increasing $(\geqslant)$ function of x' and y', which satisfies the equation

$$\frac{\partial^2 P(x', y')}{\partial x' \partial y'} = \rho(x', y') \qquad \ldots\ldots (2.13)$$

wherever a finite ray density $\rho(x', y')$ exists. Elsewhere, $P(x', y')$ need not be differentiable nor even continuous. We call $P(x', y')$ the *distribution function of the geometrical image*. Distribution functions of this kind are familiar in modern probability theory.†

The geometrical ct-function $t(u, v)$ is defined in terms of $P(x', y')$ by the equation

$$t(u, v) = \int\int_{-\infty}^{\infty} \exp\left[-2\pi i(ux' + vy')\right] d^2P(x', y'); \qquad \ldots\ldots (2.14)$$

when the image is non-singular, the Stieltjes integral on the right reduces to the more elementary integral (2.7). It is easy to show that in all cases the function $t(u, v)$ defined by (2.14) satisfies equation (2.6).

Returning to (2.4) and making use of (2.6), we have

$$\tau(u, v; \lambda) - t(u, v) = -|\mathscr{A}|^{-1} \int\int_{\mathscr{A} - S_{\lambda u,\, \lambda v}} \exp\{-2\pi i(u\phi_1 + v\phi_2)\}\, d\xi\, d\eta + \theta \frac{\pi\sqrt{2}}{12} K_3 \lambda^2 \omega^3, \qquad \ldots\ldots (2.15)$$

where $|\theta| \leqslant 1$. Whence

$$|\tau(u, v; \lambda) - t(u, v)| \leqslant \frac{|\mathscr{A} - S_{\lambda u,\, \lambda v}|}{|\mathscr{A}|} + \frac{\pi\sqrt{2}}{12} K_3 \lambda^2 \omega^3. \qquad \ldots\ldots (2.16)$$

Now the first term on the right of (2.16) is less than $K'\lambda\omega$, where the constant K' depends only on the size and shape of the clear aperture $\mathscr{A}$; when $\mathscr{A}$ is a circle $\xi^2 + \eta^2 < \sin^2\alpha$, the value of K' is $2\,\mathrm{cosec}\,\alpha/\pi$. Thus

$$|\tau(u, v; \lambda) - t(u, v)| \leqslant K'\lambda\omega + \tfrac{3}{8} K_3 \lambda^2 \omega^3. \qquad \ldots\ldots (2.17)$$

It is interesting to note that the right hand side of each of the last two inequalities remains unchanged when the (x, y) origin in the image is shifted, and also when the focal setting is varied, provided both changes are small enough to alter the distortion function $\phi(\xi, \eta)$ by not more than, say, 20λ. For, a small shift of (x, y) origin in the image plane together with a small change in focal setting can be represented, to the order of approximation here in question, by adding a term of the form $\alpha\xi + \beta\eta + \gamma(\xi^2 + \eta^2)$ to the aberration function ϕ, where α, β, γ are constants, and this leaves K_3 unaltered.

From (2.17) we draw the conclusion: If the wave-aberration function $\phi(\xi, \eta)$ possesses bounded partial derivatives ϕ_{111}, ϕ_{112}, ϕ_{122}, ϕ_{222}, then in any bounded (u, v) region D of the spatial frequency plane, the ct-function $\tau(u, v; \lambda)$ tends *uniformly* to $t(u, v)$ as $\lambda \to 0$; that is to say

$$\max_D |\tau(u, v; \lambda) - t(u, v)| \to 0 \qquad \ldots\ldots (2.18)$$

with negligible inaccuracy as $\lambda \to 0$.

† See, for example, Cramèr (1937).

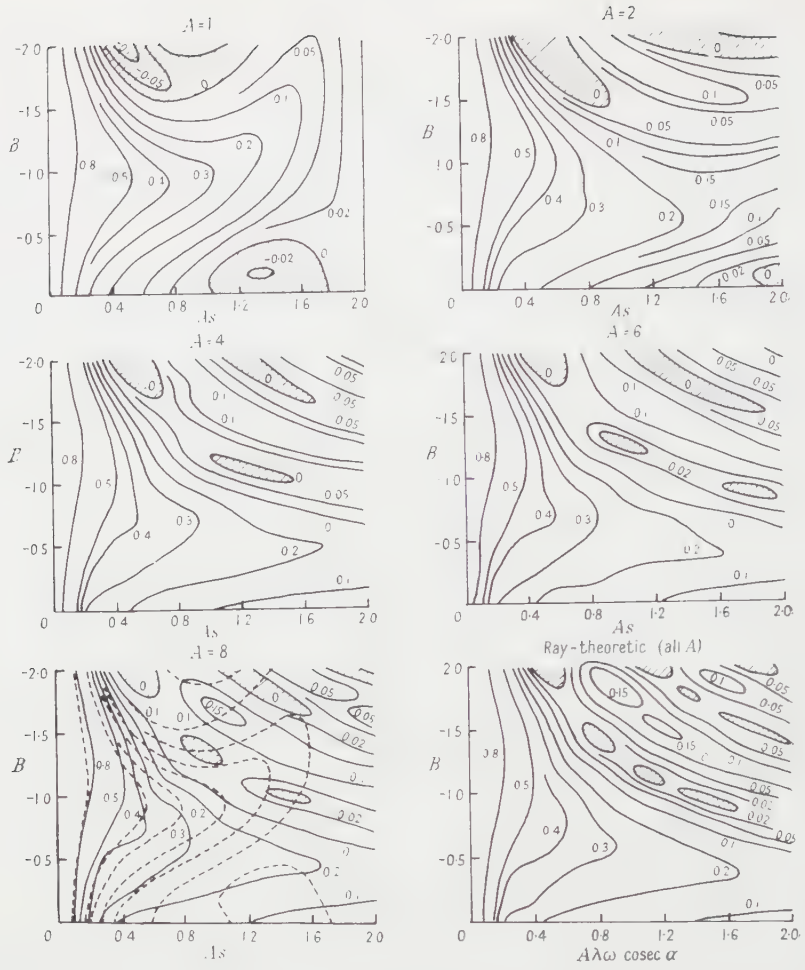

Figure 2. Contrast transmission of monochromats with primary spherical aberration $\phi(r) = A\lambda(r^4 + Br^2)$ (see text). In each diagram the abscissa represents the spatial frequency $\omega = (s \sin \alpha)/\lambda$ multiplied by a scaling factor $A\lambda$ cosec α; the ordinate is the parameter B which specifies the focal setting. Sin α is the numerical aperture of the system; $A\lambda$ is the amount of fourth-power aberration. Along each horizontal line B = constant, the values of the contrast transmission, read off from the numbered curves, give the ct-function of the system at the corresponding focal setting; wave-theoretic in the first five diagrams, ray-theoretic in the sixth. In the shaded areas there is contrast reversal (spurious resolution). The differences between the run of the curves in the first five diagrams and in the sixth show the effect of diffraction in modifying the contrast transmission in each case. At the Rayleigh limit ($A = 1$, $B = -1$) this effect is large; with four wavelengths of fourth-power aberration ($A = 4$) it is already rather small. It tends to zero as $A \to \infty$. The dotted curves in the fifth diagram ($A = 8$) reproduce those of the first diagram ($A = 1$) for comparison.

Figure 2 shows the manner in which τ approaches t, as $\lambda \to 0$, in the special case of an image with primary spherical aberration, formed by a small-field isoplanat with circular exit pupil. For a system with an amount $a = A\lambda$ of fourth-power aberration, the wave distortion in the exit pupil is given by the equation

$$\phi(r) = A\lambda(r^4 + Br^2), \qquad r^2 = (\xi^2 + \eta^2)\,\mathrm{cosec}^2\,\alpha,$$

where the parameter B gives the focal setting, while the polar variable r runs from 0 at the centre of the exit pupil to 1 at its edge. The value $B=0$ corresponds to the paraxial focal setting, $B=-2$ to the marginal focus. $B=-1$ to the so-called mid-focus.

The first five diagrams in figure 2 each show the values of τ, and the sixth the values of t, for a range of values of the line frequency ω and of the focal setting parameter B. In each figure the abscissa is taken as $a\omega \operatorname{cosec}\alpha = A\lambda\omega \operatorname{cosec}\alpha = As$, where s is the reduced spatial frequency (Hopkins 1957) and the ordinates B cover the range from paraxial to marginal focus. In the first five diagrams, the values of τ are displayed, by means of the numbered curves, for systems with λ, 2λ, 4λ, 6λ and 8λ respectively of fourth-power aberration. Along each horizontal line $B=$ constant the values of τ give the contrast transmission at the corresponding focal setting, for line frequencies $\omega \leqslant (2\sin\alpha)/A\lambda$ in the image surface. In the fifth diagram ($A=8$) the dotted curves reproduce those of the first diagram ($A=1$) for comparison. The sixth diagram displays the values of t in the same way; for given B, the ray-theoretic contrast transmission t depends on ω only through the product $A\lambda\omega \operatorname{cosec}\alpha$. A less detailed t-diagram was given by Sayanagi (1956); it covers the cases $-1{\cdot}6<B<-0{\cdot}6$, $0<A\lambda\omega \operatorname{cosec}\alpha<1{\cdot}6$.

From these six diagrams, which show quantitatively the 'diminishing effects of diffraction' as $\lambda\to 0$, it appears that, over the range of spatial frequencies $\omega \leqslant 1/aF$ and over the range of focal settings $-2\leqslant B\leqslant 0$, the wave-theoretic ct-function τ differs only slightly from the ray-theoretic approximation t when $a\geqslant 4\lambda$; when $a=\lambda$ or 2λ the differences are considerable.†

It is tempting to draw the inference that, in the practical evaluation of image quality in photographic systems with at least four wavelengths of primary spherical aberration, the ray-theoretic approximation can safely be used in place of the more accurate scalar wave model. Such a conclusion is by no means always correct, however, as will be seen in § 4.

Small-field systems. So far we have considered only the imaging of a single isoplanatism patch, but the discussion need not be so restricted. In any practical system, the wave-aberration function $\phi(\xi,\eta)$ changes its form when the object point changes its position, but the partial derivatives ϕ_{111}, ϕ_{112}, ϕ_{122}, ϕ_{222} are bounded in $\mathscr{A}$, uniformly over the working field F. The conclusion (2.18) can then be shown to hold uniformly for object points anywhere in the field of a small-field system, provided that (x',y') are replaced by 'local coordinates' (x'',y'') with origin at the centre of curvature of the spherical reference surface from which the wave-aberrations are measured‡, and that $\tau(u,v;\lambda)$, $t(u,v)$ are understood to denote the corresponding local ct-functions §

† Bromilow (1958) has discussed the relations between t and τ in systems with primary and with combined primary and secondary spherical aberration. Their relations in defocused aberration-free systems were examined by Hopkins (1955); in astigmatic systems at middle focus by De (1955); in comatic systems by Marathay (1959).

‡ It is often convenient to take this centre at the principal point of the geometrical image patch (see Linfoot 1958).

§ The notation is that of two previous papers (Linfoot 1958, 1959). Here $x'=x$, $y'=y$ are the coordinates of the point (x', y') in the image surface 'matched' against (x, y) in the object surface, and $x''=x'-x$, $y''=y'-y$, $w_{xy}(x'', y'';\ \lambda)=w(x', y';\ x, y;\ \lambda)$. In (2.20) $P(x', y';\ ix, y)$ is the distribution function defined below and the integral on the right is a Stieltjes integral.

$$\tau(u,v;x,y;\lambda)=\int\int_{-\infty}^{\infty}\exp\left[-2\pi i(ux''+vy'')\right]w_{xy}(x'',y'';\lambda)\,dx''\,dy''$$

$$=\exp\left[2\pi i(ux+vy)\right]\int\int_{-\infty}^{\infty}\exp\left[-2\pi i(ux'+vy')\right]w(x',y';x,y;\lambda)\,dx'\,dy' \quad \ldots\ldots (2.19)$$

and $$t(u,v;x,y)=\int\int_{-\infty}^{\infty}\exp\left[-2\pi i(ux''+vy'')\right]d^2{}_{x'y'}P(x',y';x,y)$$

$$=\exp\left[2\pi i(ux+vy)\right]\int\int_{-\infty}^{\infty}\exp\left[-2\pi i(ux'+vy')\right]$$

$$\times\, d^2{}_{x'y'}P(x',y';x,y). \quad \ldots\ldots (2.20)$$

The proof presents no new difficulty and is omitted for the sake of shortness. Large-field systems are outside the scope of the present paper.

The extended result provides, for small-field systems, an answer to the old question: In what sense is it true that, as $\lambda\to 0$, the diffraction image of an incoherently illuminated extended object by a system with prescribed ray-aberrations approximates to its geometrical image by the system? (The diffraction image here means the intensity distribution predicted by the scalar wave theory with the usual approximations.) After the above discussion, the following answer can be given: *As $\lambda\to 0$, the Fourier transform of the intensity distribution in the diffraction image of an extended object wholly contained in the working field of a small-field system tends to that of the light distribution in the ray-theoretic image; it does so uniformly in every finite region of the spatial frequency plane.*

Here the system need not be isoplanatic, the ray-theoretic images of point objects may be singular in the sense defined above, and the object–intensity distribution may be singular in the sense that a finite proportion of the total light may originate in a set of object points of two-dimensional measure zero.

We first prove the result on the assumptions that the object has a finite surface brightness $\sigma(x,y)$ at every point (x,y) and that the ray density is everywhere finite in the image of a luminous point situated anywhere in F. The extension to the general case will then be made with the help of distribution functions.

On the assumptions just stated, the object brightness $\sigma(x,y)$ is everywhere finite and is zero whenever the point (x,y) lies outside the working field F in the object-surface. The normalized intensity $I(x',y';\lambda)$ at the point (x',y') in the image of $\sigma(x,y)$ is given by the equation

$$I(x',y';\lambda)=\int\int_{F}\sigma(x,y)w(x',y';x,y;\lambda)\,dx\,dy, \quad \ldots\ldots (2.21)$$

where $w(x',y';x,y;\lambda)$ is the normalized intensity at (x',y') in the image of an object point situated at (x,y). Then the Fourier transform

$$F[I]=\int\int_{-\infty}^{\infty}\exp\left[-2\pi i(ux'+vy')\right]I(x',y';\lambda)\,dx'\,dy'$$

$$=\int\int_{-\infty}^{\infty}dx'\,dy'\exp\left[-2\pi i(ux'+vy')\right]\int\int_{F}\sigma(x,y)w(x',y';x,y;\lambda)\,dx\,dy$$

$$=\int\int_{F}\left(\int\int_{-\infty}^{\infty}w(x',y';x,y;\lambda)\exp\left[-2\pi i(ux'+vy')\right]dx'\,dy'\right)\sigma(x,y)\,dx\,dy$$

$$=\int\int_{F}\exp\left[-2\pi i(ux+vy)\right]\tau(u,v;x,y;\lambda)\sigma(x,y)\,dx\,dy, \quad \ldots\ldots (2.22)$$

where $\tau(u,v;x,y;\lambda)$ is the local ct-function (2.19) corresponding to the object point (x,y). Similarly, the normalized ray density $\hat{I}(x',y')$ in the ray-theoretic image of $\sigma(x,y)$ is given by the equation

$$\hat{I}(x',y')=\int\int_F \sigma(x,y)\rho(x',y';x,y)\,dx\,dy, \qquad \ldots\ldots(2.23)$$

where $\rho(x',y';x,y)$ is the normalized ray density at (x',y') in the geometrical image of the object point (x,y). The equation (2.20) which defines $t(u,v;x,y)$ assumes in this case the more elementary form

$$\exp[-2\pi i(ux+vy)]t(u,v;x,y)$$
$$=\int\int_{-\infty}^{\infty} \exp[-2\pi i(ux'+vy')]\rho(x',y';x,y)\,dx'\,dy', \quad \ldots\ldots(2.24)$$

and we obtain, by the same procedure as before, the result

$$F[\hat{I}]=\int\int_{-\infty}^{\infty} \exp[-2\pi i(ux'+vy')]\hat{I}(x',y')\,dx'\,dy'$$
$$=\int\int_F \exp[-2\pi i(ux+vy)]t(x',y';x,y)\sigma(x,y)\,dx\,dy. \qquad \ldots\ldots(2.25)$$

Let D be any finite region of the (u,v) plane. Then by (2.22) and (2.25) we have, for all (u,v) in D,

$$|F[I]-F[\hat{I}]|=\left|\int\int_F \exp[-2\pi i(ux+vy)](\tau-t)\sigma(x,y)\,dx\,dy\right|$$
$$\leqslant \int\int_F |\tau-t|\sigma(x,y)\,dx\,dy$$
$$\leqslant \left(\max_{(u,v)\text{ in }D,\,(x,y)\text{ in }F}|\tau-t|\right)\int\int_F \sigma(x,y)\,dx\,dy$$
$$=L\max_{D,F}|\tau-t|, \qquad \ldots\ldots(2.26)$$

where L is the total luminosity of the object. By (2.17), the second factor in (2.26) tends to zero as $\lambda\to 0$, since ϕ_{111}, ϕ_{112}, ϕ_{122}, ϕ_{222} are uniformly bounded over the aperture as (x,y) ranges over F. Thus, if L is held constant $F[I]-F[\hat{I}]\to 0$ as $\lambda\to 0$, which is the required result.

To extend this result to the general case where the light-flux distribution in the object and the ray-theoretic image of a point object may be singular, and it is not assumed that a finite light-flux density $\sigma(x,y)$ exists at all points of F, nor that a finite ray density $\rho(x',y';x,y)$ always exists, it is necessary to describe the object and the image by means of distribution functions. We define $S(x,y)$ as the total light flux issuing from those object points (X,Y) for which $X\leqslant x$, $Y\leqslant y$. Similarly, we describe the ray-theoretic image of the object point (x,y) by means of a distribution function $P(x',y';x,y)$, defined as the fraction of the total light in those points (X',Y') of the ray-theoretic image of the object point (x,y) for which $X'\leqslant x'$, $Y'\leqslant y'$.

Then the normalized distribution function of the ray-theoretic image of the extended object is

$$\hat{J}(x',y')=\int\int_F P(x',y';x,y)\,d^2{}_{xy}S(x,y) \qquad \ldots\ldots(2.27)$$

and the Fourier transform of the (possibly singular) light configuration in this image is, by definition,

$$F[\hat{I}] = \int\int_{-\infty}^{\infty} \exp\,[-2\pi i(ux'+vy')d^2{}_{x'y'}\hat{J}(x',y'). \quad \ldots\ldots (2.28)$$

(If, for example, the object consists of a cluster of isolated, equally bright points (x_m, y_m), $m=1, 2, \ldots n$ and the system is aberration-free except for distortion, the last equation gives

$$F[\hat{I}] = \frac{L}{n}\sum_{m=1}^{n} \exp\,[-2\pi i(ux_m'+vy_m')], \quad \ldots\ldots (2.29)$$

where (x_m', y_m') is the image of (x_m, y_m) and L is the total luminosity of the object.)

From (2.27) and (2.28) we have

$$\begin{aligned} F[\hat{I}] &= \int\int_{-\infty}^{\infty} \exp\,[-2\pi i(ux'+vy')]d^2{}_{x'y'}\left(\int\int_F P(x',y';x,y)d^2{}_{xy}S(x,y)\right) \\ &= \left(\int\int_{-\infty}^{\infty} \exp\,[-2\pi i(ux'+vy')]\int\int_F\right)d^2{}_{x'y'}P(x',y';x,y)d^2{}_{xy}S(x,y) \\ &= \int\int_F\left(\int\int_{-\infty}^{\infty} \exp\,[-2\pi i(ux'+vy')]d^2{}_{x'y'}P(x',y';x,y)\right)d^2{}_{xy}S(x,y) \\ &= \int\int_F \exp\,[-2\pi i(ux+vy)]t(u,v;x,y)d^2{}_{xy}S(x,y), \quad \ldots\ldots (2.30) \end{aligned}$$

by (2.20).

The wave-theoretic image is a little easier to deal with, because $w(x',y';x,y)$ is always finite. We have

$$I(x',y';x,y;\lambda) = \int\int_F w(x',y';x,y;\lambda)d^2{}_{xy}S(x,y), \quad \ldots\ldots (2.31)$$

$$\begin{aligned} F[I] &= \int\int_{-\infty}^{\infty} \exp\,[-2\pi i(ux'+vy')]I(x',y';x,y;\lambda)\,dx'\,dy' \\ &= \int\int_{-\infty}^{\infty} dx'\,dy' \exp\,[-2\pi i(ux'+vy')]\int\int_F w(x',y';x,y;\lambda)d^2{}_{xy}S(x,y) \\ &= \int\int_F\left(\int\int_{-\infty}^{\infty} \exp\,[-2\pi i(ux'+vy')]\,w(x',y';x,y;\lambda)\,dx'\,dy'\right)d^2{}_{xy}S(x,y) \\ &= \int\int_F \exp\,[-2\pi i(ux+vy)]\tau(u,v;x,y;\lambda)d^2{}_{xy}S(x,y), \quad \ldots\ldots (2.32) \end{aligned}$$

where $\tau(u,v;x,y;\lambda)$ is the local ct-function (2.19).

From (2.31) and (2.32) it follows that

$$\begin{aligned} |F[I]-F[\hat{I}]| &= \left|\int\int_F \exp\,[-2\pi i(ux+vy)](\tau-t)d^2{}_{xy}S(x,y)\right| \\ &\leqslant \int\int_F |\tau-t|\,d^2{}_{xy}S(x,y) \\ &\leqslant \left(\max_{(u,v)\text{ in }D,\ (x,y)\text{ in }F}|\tau-t|\right)\int\int_F d^2{}_{xy}S(x,y) \\ &= L\max_{D,F}|\tau-t|, \quad \ldots\ldots (2.33) \end{aligned}$$

where L is the total luminosity of the object. (2.33) is identical in form with (2.26), and the conclusion now follows as before.

§ 3. Wave-theoretic and Ray-theoretic Quality Evaluations

3.1. *Wave-theoretic Evaluations*

From the well-known relation

$$w(x'',y'';\lambda)=\int\int_{-\infty}^{\infty}\exp\left[2\pi i(ux''+vy'')\right]\tau(u,v;\lambda)\,du\,dv \quad \ldots\ldots(3.1)$$

between the local ct-function τ and the local optical spread function w it follows that *any local quality evaluation which can be expressed in terms of w can be expressed in terms of* τ.

For example, in coma-free images with a bright central intensity peak, formed by centred systems with circular aperture, the brightest point of the diffraction image is at the principal point P_1 of the geometrical image patch. If we take this point as the origin of the local coordinates (x'',y''), the local ct-function τ is always real and the *Strehl definition* V of the system is given in terms of τ by the equations

$$V=\int\int_{-\infty}^{\infty}\tau(u,v;\lambda)\,du\,dv\Big/\int\int_{-\infty}^{\infty}\tau_0(u,v;\lambda)\,du\,dv \quad \ldots\ldots(3.2)$$

$$=\frac{\lambda^2}{\pi\sin^2\alpha}\int\int_{-\infty}^{\infty}\tau(u,v;\lambda)\,du\,dv, \quad \ldots\ldots(3.3)$$

where τ_0 denotes the ct-function in the special case $\phi(\xi,\eta)=0$ (aberration-free system) and $\sin\alpha$ is the numerical aperture.

Equations (3.2) and (3.3) remain valid when the diffraction image of a point object is no longer biaxially symmetrical about its point of greatest intensity, provided that the (x'',y'') origin is taken at the latter point instead of at P_1.

An analogous local quality evaluation for photographic systems is the *photographic Strehl definition*

$$V_1=\frac{\lambda^2}{\pi\sin^2\alpha}\int\int_{-\infty}^{\infty}\tau\tau_1\,du\,dv, \quad \ldots\ldots(3.4)$$

in which $\tau_1=\tau_1(u,v;\lambda)$ is the Fourier transform of the photographic spread function. Since $\tau=0$ outside the spatial frequency pass-band $\mathcal{F}$ of the system, namely the region

$$u^2+v^2<(1/F\lambda)^2$$

in the spatial frequency plane, equation (3.4) can be written

$$V_1=4\underset{\mathcal{F}}{\text{mean}}\,(\tau\tau_1). \quad \ldots\ldots(3.5)$$

Other physically meaningful quality evaluations which have been formulated (Schade 1952, Fellgett 1953, Fellgett and Linfoot 1955, Linfoot 1956, 1958) in terms of ct-functions are

$$2\underset{\mathcal{F}}{\text{mean}}\,(1-|1-\tau\tau_1|^2) \quad \text{(r.m.s. fidelity)}, \quad \ldots\ldots(3.6)$$

$$8{\cdot}72\underset{\mathcal{F}}{\text{mean}}\,(|\tau\tau_1|^2) \quad \text{(structural resolution)}, \quad \ldots\ldots(3.7)$$

$$10{\cdot}60\underset{\mathcal{F}}{\text{mean}}\ln\{1+|\tau\tau_1|^2R\} \quad \text{(information density)}, \quad \ldots\ldots(3.8)$$

the last of which measures the statistical mean information density (bits per Airy disc) at signal-to-noise ratio R in the photographic images of a low-contrast random object set.

Each of the evaluations (3.5)–(3.8) is of the form

$$\underset{\mathscr{F}}{\text{mean}}\ \Phi(\tau\tau_1), \qquad \ldots\ldots(3.9)$$

where Φ is a continuous function of its argument $\tau\tau_1$ and is zero when $\tau\tau_1=0$. Thus each evaluation is a τ_1-weighted functional mean of τ over the pass-band $\mathscr{F}$ of the optical system. The corresponding evaluations of the aerial image can be included in this formulation as the special case $\tau_1\equiv 1$. Since τ is everywhere zero outside $\mathscr{F}$, the expression (3.9) can be written in the form

$$\frac{\lambda^2}{\pi\sin^2\alpha}\int\int_{-\infty}^{\infty}\Phi(\tau\tau_1)\,du\,dv; \qquad \ldots\ldots(3.10)$$

the four evaluations (3.5)–(3.8) correspond respectively to the special choices

$$\Phi(z)=4z, \quad 2(1-|1-z|^2), \quad 8{\cdot}72|z|^2, \quad 10{\cdot}60\ln\{1+|z|^2R\} \qquad \ldots\ldots(3.11)$$

of the function Φ.

3.2. *Ray-theoretic Evaluations*

Corresponding ray-theoretic evaluations are obtained on replacing τ by t in (3.9) or (3.10), where t is the ray-theoretic ct-function (2.7). The two resulting evaluations

$$\underset{\mathscr{F}}{\text{mean}}\ \Phi(t\tau_1) \qquad \ldots\ldots(3.12)$$

and

$$\frac{\lambda^2}{\pi\sin^2\alpha}\int\int_{-\infty}^{\infty}\Phi(t\tau_1)\,du\,dv \qquad \ldots\ldots(3.13)$$

are not strictly equivalent because t does not vanish everywhere outside $\mathscr{F}$. To use the former amounts to using t as an approximation to τ in $\mathscr{F}$; to use the latter amounts to using the ray-theoretic spread function $\rho(x',y')$ as an approximation to the wave-theoretic spread function $w(x',y')$. In many practical cases, the photographic acceptance factor τ_1 is so small outside $\mathscr{F}$ that the integral of $\Phi(t\tau_1)$ over all spatial frequencies outside $\mathscr{F}$ is negligible in comparison with the integral over $\mathscr{F}$†. In these cases it is of no practical consequence which of the approximations (3.12) and (3.13) is used. It is convenient, nevertheless, to distinguish between them by calling (3.12) the *ray approximation* to (3.9) and (3.13) the *ray-theoretic evaluation* corresponding to (3.9).

The ray-theoretic evaluations (3.13) are of interest because of their connection with the much debated question whether there exist realistic‡ image-evaluation procedures based on geometrical optics. Such procedures presuppose that the differences between the intensity distributions in the ray-theoretic and wave-theoretic images are harmlessly small for the purposes of image-quality evaluation. As already noted in § 1, this supposition is sometimes unrealistic even for images with rather large aberrations. In many of the more successful practical optical designs, the image of a luminous point object consists of a bright, compact core surrounded by a faint extended halo or 'flare'. General considerations given elsewhere (Linfoot 1960b) and supported by computed

† If, for example, $w_1=2\pi\mu^2\exp[-2\mu(x^2+y^2)]$, $\tau_1=\mu^3(\mu^2+u^2+v^2)^{-3/2}$ and we suppose $\mu\leqslant 0{\cdot}1/F\lambda$, then in the case $\Phi(t\tau_1)=4t\tau_1$, $t\equiv 1$ (ray-theoretic photographic Strehl definition of an aberration-free system) the values of (3.11) and (3.12) differ by less than $0{\cdot}8\%$.

‡ By a realistic evaluation of an optical system is here meant one which, in principle, enables the designer to predict the opinion of the user.

special cases indicate that in systems forming such core-and-halo images the quality of the aerial image of an extended object depends chiefly on the structure of the cores, which is powerfully influenced by diffraction. When image spread in the receiving surface is appreciable, these diffraction effects play a less critical part.† In particular, this is true in photographic systems in which the emulsion is 'matched' to the lens, in the sense that the photographic spread is comparable with the effective radius of an image core. Much less important are the diffraction effects in those mismatched systems in which emulsion spread is large compared with the effective radius of an image core. In these last systems, at least, realistic image evaluations based on spot diagrams should be possible.

From the above remarks, it appears that we cannot expect to be able to set up evaluation procedures based on geometrical optics which will be satisfactory in all cases. We can expect to be able to do so only in those cases where the wave-theoretic and ray-theoretic images, modified in the photographic case by emulsion spread, are sufficiently similar to yield approximately the same evaluation when, with some physically reasonable choice of Φ, (3.9) is applied to the one and (3.12) to the other. It seems that the real problem is to delimit these cases. A general result bearing on this problem is proved in § 3.3.

3.3. *Relations between Wave-theoretic and Ray-theoretic Evaluations*

Suppose now that the contrast transfer function τ_1 of the receiving surface never exceeds 1 and satisfies the condition

$$\int\int_{-\infty}^{\infty} |\tau_1(u,v)|\,du\,dv < \infty. \qquad \ldots\ldots (3.14)$$

This condition is satisfied in particular by the τ_1 function

$$[1+(2\pi\sigma)^2(u^2+v^2)]^{-3/2} \qquad \ldots\ldots (3.15)$$

which, as noted by Sayanagi (1957), provides a fairly satisfactory simplified model of a thin receiving surface with turbidity. The values $\sigma = 3{\cdot}4\,\mu$, $\sigma = 1{\cdot}6\,\mu$ give moderately good agreement between (3.15) and the contrast transfer functions of the emulsions Tri-X and Panatomic-X, as measured near $\lambda = 5500$A by Lamberts (1959), over the ranges 0–75 and 0–150 lines/mm respectively. Much closer agreement with these experimental values can be obtained by using, in place of (3.15), an approximation of the form

$$A_1[1+(2\pi\sigma_1)^2(u^2+v^2)]^{-3/2} + A_2[1+(2\pi\sigma_2)^2(u^2+v^2)]^{-3/2}, \qquad \ldots\ldots (3.16)$$

which also satisfies (3.14).

We first observe that *if* (3.14) *holds and* $\phi(\xi,\eta)$ *is given, then as* $\lambda \to 0$

$$\int\int_{-\infty}^{\infty} \Phi(\tau\tau_1)\,du\,dv \to \int\int_{-\infty}^{\infty} \Phi(t\tau_1)\,du\,dv \qquad \ldots\ldots (3.17)$$

in each of the special cases (3.11). For, since $|\tau|$, $|t|$ and $|\tau_1|$ never exceed unity, it is easy to show that

$$|\Phi(\tau\tau_1) - \Phi(t\tau_1)| < B|\tau_1|\,|\tau - t|, \qquad \ldots\ldots (3.18)$$

† Miyamoto (1957, 1958 a) makes some valuable comments in this connection.

where $B=4,\ 4\sqrt{5},\ 17\cdot44,\ 21\cdot20R$ respectively in the four cases (3.11). Then

$$\left|\iint_{-\infty}^{\infty}\Phi(\tau\tau_1)\,du\,dv-\iint_{\mathscr{A}}^{\infty}\Phi(t\tau_1)\,du\,dv\right|\leqslant\iint_{-\infty}^{\infty}|\Phi(\tau\tau_1)-\Phi(t\tau_1)|\,du\,dv$$
$$\leqslant B\iint_{-\infty}^{\infty}|\tau-t|\,|\tau_1|\,du\,dv$$
$$\leqslant B\max_{D}|\tau-t|\iint_{D}|\tau_1|\,du\,dv+2B\iint_{C(D)}|\tau_1|\,du\,dv,\quad(3.19)$$

where D stands for the region $u^2+v^2<\rho_1^2$, $C(D)$ for the region $u^2+v^2\geqslant\rho_1^2$ and the constant ρ_1 is at our disposal. Given $\epsilon>0$, we can, by (3.14), choose ρ_1 so large that the second term of (3.19) is less than $\frac{1}{2}\epsilon$ and then, by (2.18), we can choose λ_0 so small that for all $\lambda\leqslant\lambda_0$ the first term of (3.19) is less than $\frac{1}{2}\epsilon$. This proves (3.17).

Let $\tau(u,v;\phi;\lambda)$, $t(u,v;\phi)$ denote the values of $\tau(u,v)$ and $t(u,v)$ respectively, for given wave-aberration function $\phi(\xi,\eta)$ and given wavelength λ. Then for any positive A

$$\tau(u,v;A\phi;\lambda)=\tau(Au,Av;\phi;\lambda/A)\quad\ldots\ldots(3.20)$$

and

$$t(u,v;A\phi)=t(Au,Av;\phi),\quad\ldots\ldots(3.21)$$

by (2.2) and (2.6). Therefore

$$\iint_{-\infty}^{\infty}\Phi(\tau(u,v;A\phi;\lambda)\tau_1(Au,Av))\,du\,dv$$
$$=\iint_{-\infty}^{\infty}\Phi(\tau(Au,Av;\phi;\lambda/A)\tau_1(Au,Av))\,du\,dv$$
$$=\frac{1}{A^2}\iint_{-\infty}^{\infty}\Phi(\tau(u,v;\phi;\lambda/A)\tau_1(u,v))\,du\,dv,$$

by a simple change of variable, whence

$$A^2\iint_{-\infty}^{\infty}\Phi(\tau(u,v;A\phi;\lambda)\tau_1(Au,Av))\,du\,dv$$
$$=\iint_{-\infty}^{\infty}\Phi(\tau(u,v;\phi;\lambda')\tau_1(u,v))\,du\,dv,\quad\ldots\ldots(3.22)$$

where $\lambda'=\lambda/A$. As $A\to\infty$ the integral on the right tends, by (3.17), to the limit

$$\iint_{\mathscr{A}}^{\infty}\Phi(t(u,v;\phi)\tau_1(u,v))\,du\,dv=A^2\iint_{-\infty}^{\infty}\Phi(t(u,v;A\phi)\tau_1(Au,Av))\,du\,dv;$$

the last equality follows easily from (3.22). Thus *the wave-theoretic evaluation*

$$\frac{\lambda^2}{\pi\sin^2\alpha}\iint_{-\infty}^{\infty}\Phi(\tau(u,v;A\phi;\lambda)\tau_1(Au,Av)\,du\,dv$$

of the system in which both aberrations and angular photographic spread have been increased by the same factor A tends, as A increases, to equality with the corresponding ray-theoretic evaluation, which is $1/A^2$ times the ray-theoretic evaluation of the original system.

A similar result is true of the ray approximation (3.12). For by (3.21)

$$A^2\iint_{\mathscr{F}}\Phi(t(u,v;A\phi)\tau_1(Au,Av))\,du\,dv$$
$$=A^2\iint_{\mathscr{F}}\Phi(t(Au,Av;\phi)\tau_1(Au,Av))\,du\,dv$$
$$=\iint_{A\mathscr{F}}\Phi(t(u,v;\phi)\tau_1(u,v))\,du\,dv$$
$$\to\iint_{\mathscr{A}}^{\infty}\Phi(t\tau_1)\,du\,dv,\quad\ldots\ldots(3.23)$$

as $A\to\infty$, by (3.14), (3.18), and the inequality $|t|\leqslant1$.

In particular, the wave-theoretic evaluation (3.9), the ray approximation (3.12), and the ray-theoretic evaluation (3.13) of 'matched' systems in which both wave aberrations and angular photographic spread are multiplied by the same factor A all tend to equality as $A\to\infty$, provided (3.14) is satisfied. They need not tend to equality if the photographic spread is held constant as A increases. This may be seen by considering the 'singular' case of an isoplanat in which the wave aberration $\phi(\xi,\eta)$ is zero throughout a circular central region $\xi^2+\eta^2<1/1600$ of an F/2·5 aperture, and turns off parabolically outside this central region in accordance with the equation

$$\phi(\xi,\eta)=25A\lambda\left(\sqrt{(\xi^2+\eta^2)}-\frac{1}{40}\right)^2 \qquad \left(\frac{1}{1600}<\xi^2+\eta^2<\frac{1}{25}\right).$$

Suppose the image is received on an ordinary fast emulsion with effective spread-radius of order 10μ. When $A\ll 1$, the photographic Strehl definition V_1 is nearly the same on wave theory and on ray theory, since optical spread is here small compared with emulsion spread. Let $(V_1)_0$ denote its value for very small A. When $A\gg 1$ the ray-theoretic value of V_1 is very near to $(25/1600)^2(V_1)_0$, and the wave-theoretic value something like half of this, since the core of the aerial diffraction image now approximates to an F/20 Airy disc.

§ 4. Photographic Quality Evaluations of Systems with Primary Spherical Abberation

From the remarks made at the end of the last section, it seems clear that in trying to formulate practically useful conditions which will ensure that the ray-theoretic evaluation (3.13) of a photographic system, or the ray approximation (3.12), can safely be used in place of the evaluation (3.9) we should not consider the optical aberrations alone, but should consider these aberrations in relation to the photographic image spread. In particular, it is clear that, even if the aberration function ϕ is restricted to the class of polynomials, no general results exist of the type: the evaluations (3.13) or (3.12) can be used in place of (3.9) whenever the wave aberration is sufficiently large. It may, however, be possible to formulate useful practical rules of the above type when the form of the aberrations is more radically restricted in some way corresponding to the needs of the practical lens designer and when the lens is matched to the emulsion in some well-defined sense. For example, if in order to fix ideas we define a matched system as one in which

$$\tfrac{1}{2}<\left(\iint_{\mathscr{F}}|\tau|^2\,du\,dv\right)\Big/\left(\iint_{\mathscr{F}}|\tau_1|^2\,du\,dv\right)<2 \qquad \ldots\ldots(4.1)$$

and suppose that the seventh-order aberrations are the highest which are large enough to affect the image quality appreciably, then it should be possible to formulate working rules of the desired type for matched systems.

We do not attempt this difficult task in the present paper, but conclude by describing the results of a preliminary exploration of the relations between three wave-theoretic evaluations (3.9) and the corresponding ray approximations (3.12) in model photographic monochromats with selected amounts of primary spherical aberration. The systems are assumed to be working at a selected set of focal ratios (F/2, F/4, F/8 and F/16), and to be imaging low-contrast objects on to an emulsion with the acceptance factor τ_1 shown in figure 3 ('model emulsion 10'

of the paper by Black and Linfoot (1957))†. τ_1 is taken as zero at all line frequencies greater than 300 lines/mm. The half-width of the corresponding emulsion-spread function is about $20\,\mu$.

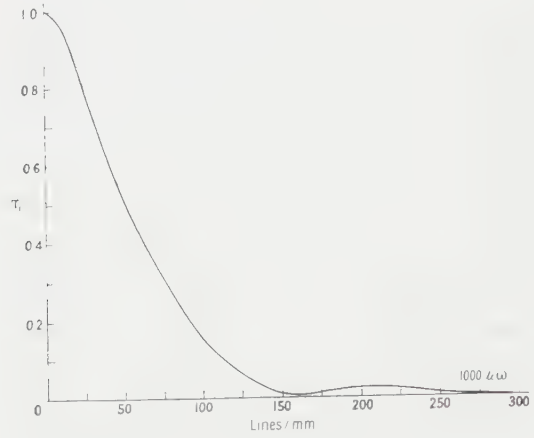

Figure 3. Acceptance factor τ_1 of a model photographic emulsion (' emulsion 10 ').

In the sixteen special cases considered, the wave aberration $\phi(r)$ is given by the equations

$$\phi(r) = A\lambda(r^4 + Br^2) \qquad (A = 1, 2, 4, 8), \qquad \ldots\ldots (4.2)$$

where the polar variable r runs from 0 at the centre of the aperture to 1 at its edge and $\lambda = 500\,\mathrm{m}\mu$ is the wavelength of the quasi-monochromatic light. Thus A measures the amount of fourth-power aberration in wavelengths and B is a parameter which specifies the focal setting. At the paraxial focus $B = 0$; at the marginal focus $B = -2$. The value $B = -1$ corresponds to the so-called mid-focus, which is by common consent the best practical focal setting in systems with very small amounts of primary spherical aberration.

In figures 4, 5 and 6 are displayed three wave-theoretic quality evaluations (solid curves) and the corresponding ray approximations (dotted curves), each in the above-mentioned sixteen cases, over the range of focal settings from paraxial focus ($B = 0$) to marginal focus ($B = -2$). The evaluations selected are photographic Strehl definition (figure 4), photographic structural resolution (figure 5), and statistical mean information density in the images of a low-contrast random object set at signal-to-noise ratio 100 (figure 6).‡ This value of the signal-to-noise ratio corresponds to fairly ' clean ' imaging.

Each figure consists of four diagrams, and curves relating to a single value of A are displayed on the same diagram. In each diagram, the abscissa represents the value of B, which specifies the focal setting, and the ordinate the quality evaluation at that focal setting. The abscissa of the highest point of each solid curve gives the ' best ' focal setting, according to the evaluation named in the figure, of a system working with model emulsion 10 at the focal ratio marked

† In § 5 of this paper, F/2 should read F/4 throughout; on p. 538, line 3, the values 20 and 5 megabits per cm^{-2} should read 3·5 and 1 respectively; and on p. 539, bottom line, $\pm 10\mu$ should read $\pm 32\mu$.

‡ In the sense defined in Fellgett and Linfoot (1955).

on the curve. The closeness of the agreement between the 'best' focal settings according to the three different evaluations considered is rather remarkable in view of their different physical meanings.

Only one model emulsion has been considered, but it is easy to verify that the effect on the quality evaluation (3.9) of halving the focal ratio is the same as that of doubling the photographic image spread. Thus, to read off the photographic Strehl definition, at any focal setting between marginal and paraxial focus, of a system with four wavelengths of primary spherical aberration, working at F 4 with an emulsion of spread twice that of model emulsion 10, we need only refer to the solid curve marked F/2 in the third diagram of figure 4.

As already mentioned, the dotted curves in figures 4, 5 and 6 display the ray approximations to the wave-theoretic evaluations. These are indistinguishable from the corresponding ray-theoretic evaluations whenever τ_1 is negligibly small†

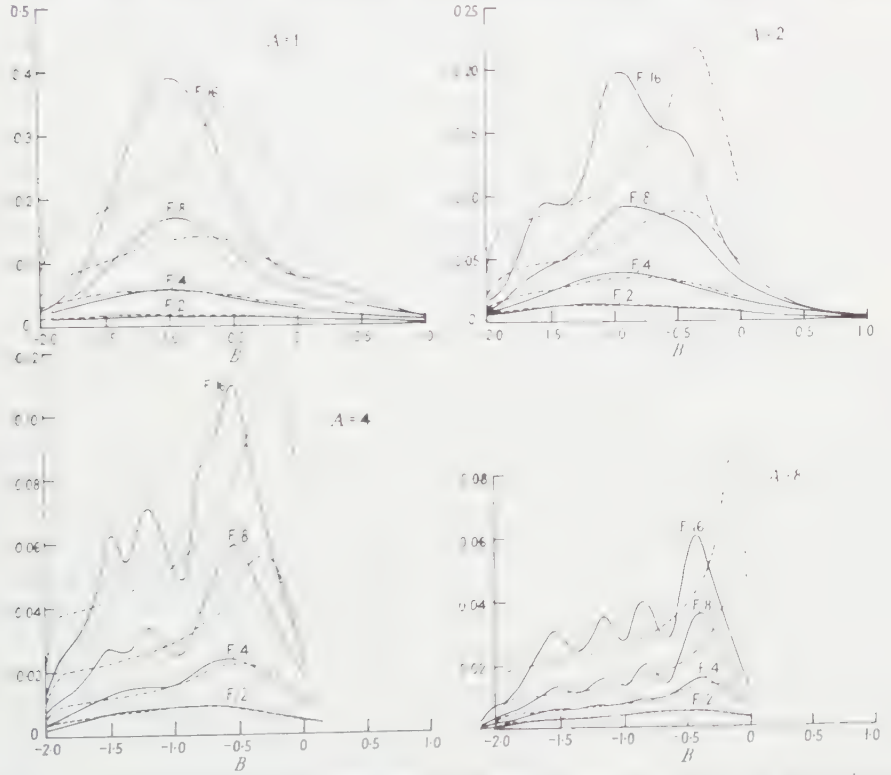

Figure 4. Photographic Strehl definition (3.4) (solid curves) and its ray approximation (3.12) (dotted curves) in monochromats with primary spherical aberration $\phi(r) = A\lambda(r^4 + Br^2)$ (see text), working with 'model emulsion 10' at selected focal ratios. In each diagram, the abscissa B specifies the focal setting; at paraxial focus $B = 0$, at marginal focus $B = -2$. The value of A gives the number of wavelengths of fourth-power aberration. At the focal ratios F 2, F 4 the ray approximation (3.12) agrees with the ray-theoretic evaluation (3.13). Thus ray- theoretic and wave-theoretic evaluations agree well in these eight cases. At F/8 the wave-theoretic evaluation and its ray approximation (3.12) begin to diverge.

† More explicitly, so small that $\left(\iint_{-\infty}^{\sigma} - \iint_{\mathscr{F}}\right) \Phi(t\tau_1)\, du\, dv$ is negligible in comparison with $\iint_{\mathscr{F}} \Phi(t\tau_1)\, du\, dv$.

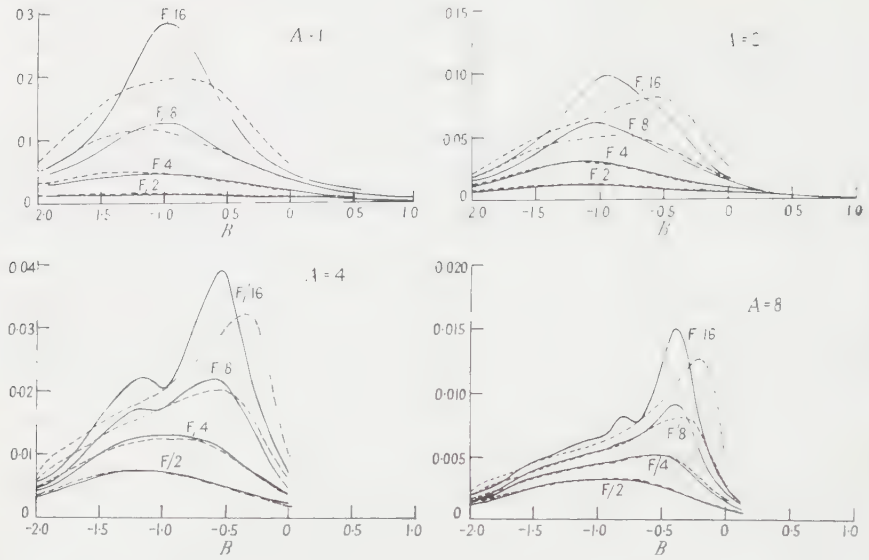

Figure 5. Photographic structural resolution (3.7) (solid curves) and its ray approximation (3.12) (dotted curves) for the sixteen special cases represented in figure 4. In each diagram B specifies the focal setting; at paraxial focus $B=0$, at marginal focus $B=-2$. At the focal ratios F/2, F/4 the ray approximation (3.12) agrees with the ray-theoretic evaluation (3.13); at F/8 the difference between them is very small. Thus ray-theoretic and wave-theoretic evaluations agree closely at F/2 and F/4, but begin to diverge at F/8. If the emulsion spread were half as great, the divergence would begin at F/4.

everywhere outside the spatial-frequency pass-band $\mathscr{F}$ of the optical system. This pass-band consists of the spatial frequencies (u, v) for which the associated line frequency $\omega = \sqrt{(u^2+v^2)}$ does not exceed (2000/F) lines/mm, where F is the focal ratio. Since τ_1 has been taken to be zero at all line frequencies greater than 300 lines/mm, it follows that at F/2 and F/4 the ray approximation curves and the ray-theoretic evaluation curves are identical for this model emulsion, whatever the aberrations. They are almost indistinguishable at F/8, for the aberrations here considered. Inspection of figures 4, 5 and 6 shows that at F/2 and F/4 the ray approximations agree rather closely with the wave-theoretic evaluations; at F/8 and F/16, on the other hand, the differences are considerable. Contrary to what might have been expected on general grounds, the closeness of the agreement between wave-theoretic evaluation and ray approximation shows no obvious correlation, over the range of cases and of focal settings examined, with the size of the aberration. It seems to depend mainly on the focal ratio. Moreover it is highly sensitive, in the F/8 and F/16 systems, to changes of focal setting.

From the computed special cases it seems reasonable to draw the conclusions that (i) a ray-theoretic treatment can provide an adequate basis for the practical quality evaluation of photographic systems with up to eight wavelengths of primary spherical aberration, working at focal ratios $F \leqslant 4$ with model emulsion 10; (ii) at longer focal ratios than F/4 the quality evaluation of these systems should take account of diffraction, and this is particularly necessary in the neighbourhood of best focus.

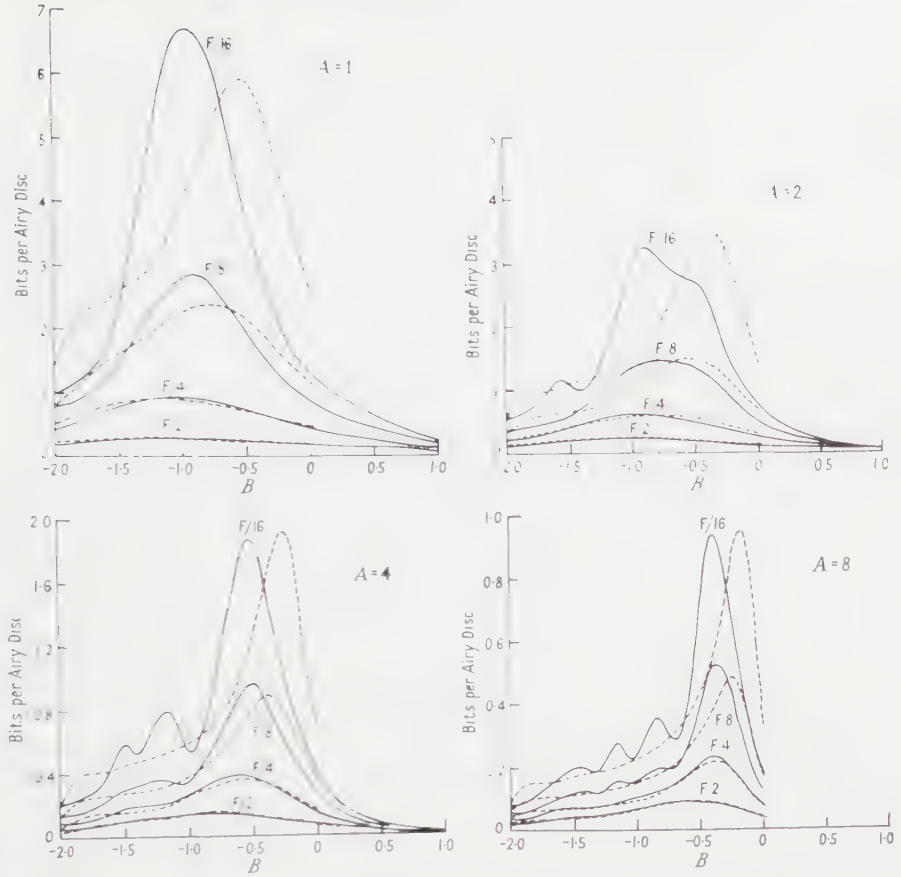

Figure 6. Information density (3.8) (solid curves) and its ray approximation (3.12) (dotted curves) for the sixteen model photographic systems of figures 4 and 5, imaging a low-contrast random object set at a signal-to-noise ratio 100 (see text). A and B have the same meanings as in figures 4 and 5. At the focal ratios F/2, F/4 the ray approximation (3.12) agrees with the ray-theoretic evaluation (3.13); at F/8 the difference between them is very small. Thus ray-theoretic and wave-theoretic evaluations agree closely at F/2 and F/4, but begin to diverge at F/8. If the emulsion spread were half as great, the divergence would begin at F/4.

These conclusions gain in interest when the changing relations between optical spread and emulsion spread in the different cases are also kept in mind. We can pick out the matched systems in a rough and ready way by comparing visually the general run of $\tau(s)$ with that of $\tau_1(\omega)$ and remembering that $s = 2F\lambda\omega$, or by using (4.1). For images near best focus, the optical and photographic spreads are fairly well matched according to (4.1) at focal ratios near F/12 when $A = 1$, near F/8 when $A = 2$, near F/4 when $A = 4$, and near F/2 when $A = 8$.

The fact that the ray approximations are, for each value of F, about equally good whether $A = 1$, 2, 4 or 8 becomes intelligible on observing that photographic spread predominates over optical spread in just those cases where the effects of diffraction are relatively more important, namely those in which A is small.

The results just described suggest the conjecture that ray approximations may be adequate for the evaluation of photographic systems with primary spherical aberration whenever the product of the linear aperture of the system, measured

in wavelengths, and the angular emulsion spread (suitably defined) exceeds a certain value K depending only on the error tolerance adopted and the choice of evaluation. But at present this conjecture cannot be regarded as anything more than a question in need of further investigation.

Acknowledgments

My grateful thanks are due to the Cambridge University Mathematical Laboratory for carrying out the heavy computations on which figures 2, 4, 5 and 6 are based, to Dr. A. M. Goodbody for several hundred independently computed τ-values, and to Miss G. E. Hayman for help with the diagrams.

References

Black, G., and Linfoot, E. H., 1957, *Proc. Roy. Soc.* A, **239,** 522.
Bromilow, N. S., 1958, *Proc. Phys. Soc.*, **71,** 231.
Cramer, H., 1937, *Random Variables and Probability Distributions* (Cambridge: University Press), chap. III.
De, M., 1955, *Proc. Roy. Soc.* A, **233,** 91.
Fellgett, P. B., 1953, *J. Opt. Soc. Amer.*, **43,** 271.
Fellgett, P. B., and Linfoot, E. H., 1955, *Phil. Trans. Roy. Soc.* A, **247,** 369.
Hopkins, H. H., 1955, *Proc. Roy. Soc.* A, **231,** 91.
—— 1957, *Proc. Phys. Soc.* B, **70,** 1162.
Hotchkiss, R. N., Washer, F. E., and Rosberry, F. W., 1951, *J. Opt. Soc. Amer.*, **41,** 600.
Lamberts, R. L., 1959, *J. Opt. Soc. Amer.*, **49,** 1165.
Lindberg, P. J., 1955, *Optica Acta*, **1,** 80.
Linfoot, E. H., 1956, *J. Opt. Soc. Amer.*, **46,** 740.
—— 1958, *Optica Acta*, **5,** 1.
—— 1959, *Proceedings of the* 1958 *Summer School, Imperial College, London*, p. 90.
—— 1960 a, *Optica Acta*, **6,** 387.
—— 1960 b, *Optica Acta*, **7,** 65.
Lukosz, W., 1958 a, *Thesis*, Brunswick.
—— 1958 b, *Optica Acta*, **5,** 29.
—— 1958 c, *Optik*, **15,** 635.
Marathay, A. S., 1959, *Proc. Phys. Soc.*, **74,** 721.
Miyamoto, K., 1957, *J. Appl. Phys.* (*Japan*), **26,** 421 (in Japanese).
—— 1958 a, *J. Opt. Soc. Amer.*, **48,** 57.
—— 1958 b, *Ibid.*, **48,** 567.
—— 1959, *Ibid.*, **49,** 35.
Sayanagi, K., 1956, *J. Appl. Phys.* (*Japan*), **25,** 449 (in Japanese).
—— 1957, *J. Opt. Soc. Amer.*, **47,** 566.
Schade, O., H., 1952, *J. Soc. Mot. Pict. Telev. Engrs*, **58,** 182.

The Field of an Electric Current in General Relativity

By W. B. BONNOR

Department of Mathematics, Queen Elizabeth College, University of London

MS. received 18*th May* 1960

Abstract. The amount of gravitational mass contributed by electromagnetic energy is not clear from previous investigations. In the case of the exterior field of a charged sphere, the charge appears not to contribute at all to the gravitational mass, but other electrostatic and magnetostatic fields give different results.

The field of a circular wire carrying a steady current is investigated by the theory of relativity. An exact solution is obtained for a wire without mass, but this contains a singular surface without physical significance. An approximate solution without this singularity is then obtained, and this shows that the energy of the magnetic field generated by the current contributes to the gravitational mass of the system. The order of magnitude of the effect is discussed with a view to its experimental detection.

§ 1. Introduction

In the general theory of relativity the field equations for regions containing electromagnetic fields but no matter are

$$R_{ik} = -8\pi E_{ik}, \qquad \ldots\ldots (1.1)$$

$$4\pi E_k^{\,i} = -F^{ia}F_{ka} - \tfrac{1}{4}\delta_k^{\,i}F^{ab}F_{ab}, \qquad \ldots\ldots (1.2)$$

where R_{ik} is the Ricci tensor and F_{ik} the electromagnetic field tensor. Maxwell's equations in generally covariant form may be written

$$F_{ik} = \kappa_{i,k} - \kappa_{k,i}, \qquad \ldots\ldots (1.3)$$

$$\mathfrak{F}^{ik}{}_{,k} = 4\pi \mathfrak{J}^i, \qquad \ldots\ldots (1.4)$$

where a comma denotes ordinary differentiation, and Gothic letters represent tensor densities; κ_i is the four-potential, and $\mathfrak{J}^i$ is the charge-and-current density.

The static, spherically symmetric, exterior solution of these equations is given by the metric

$$ds^2 = -\gamma^{-1}dr^2 - r^2d\theta^2 - r^2\sin^2\theta d\phi^2 + \gamma dt^2 \qquad \ldots\ldots (1.5)$$

where

$$\gamma = 1 - \frac{2m}{r} + \frac{e^2}{r^2}; \qquad \ldots\ldots (1.6)$$

the electromagnetic field tensor has the single component

$$F_{41} = e/r^2, \qquad \ldots\ldots (1.7)$$

corresponding to a radial electric field.

In the usual interpretation, (1.5)–(1.7) represent the field outside a spherically symmetric body of mass m and charge e. In this solution m and e are independent constants, and we are not prevented from putting $m = 0$. The charge e appears not to contribute to the gravitational mass in the ordinary sense, since e does not appear in the r^{-1} term in (1.6).

On the other hand, examples have previously been given (Bonnor 1953, 1954) of static fields in which the electromagnetic energy appears to give rise to gravitational fields like those produced by ordinary masses. Moreover, in a recent work Witten (1960), has studied static, cylindrically symmetric solutions of equations (1.1)–(1.4), and has found that the parameters describing the electromagnetic fields are related to the masses of the systems concerned. For example, he finds that in the solution representing an infinite straight wire carrying a current, the mass of the wire cannot be put equal to zero without abolishing the current. Witten's solutions, and also those of my own earlier papers, are difficult to interpret because they are not flat at infinity.

There is a definite reason why it seems to me important to investigate this question further, quite apart from the general desire to understand the part played by electromagnetic energy in gravitation. Mass in gravitation theory occurs in a number of ways—for example, as inertial mass, 'active' gravitational mass, 'passive' gravitational mass and as invariant mass (the density of which is given by the trace of the energy tensor, and which vanishes for electromagnetic fields). The relations between these masses are not properly understood, but we believe that two of them—inertial mass and passive gravitational mass—can be compared with great accuracy by the Eötvös experiment. If it should appear from the theory that for electromagnetic energy these two masses are different, a repetition of this experiment might offer the possibility of a clarification of the whole situation.

In this paper are described solutions of equations (1.1)–(1.4) corresponding to the exterior field of a circular loop of wire carrying a steady current. After some preliminaries in §§ 2–4, an exact solution is obtained in § 5, but this corresponds to a wire without gravitational mass and contains a spurious singularity. In §7 an approximate solution is obtained without the singularity, and in this there appears a gravitational mass arising from the magnetic field of the current.

§ 2. The Field Equations

We assume that the field is static and has symmetry about an axis of rotation Oz, and take for the metric

$$ds^2 = -e^{\lambda}(dz^2+dr^2) - e^{\nu}d\phi^2 + e^{\rho}dt^2 \qquad \ldots\ldots (2.1)$$

where λ, ν and ρ are functions of z and r only. Labelling the coordinates $z=x_1$, $r=x_2$, $\phi=x_3$, $t=x_4$ we suppose that the only non-vanishing components of the electro-magnetic field tensor are $F_{13}=-F_{31}$ and $F_{23}=-F_{32}$.

The metric (2.1) allows further simplification. Two of the field equations (1.1) are

$$R_{33} \equiv \tfrac{1}{4}e^{\nu-\lambda}(2\nu_{11}+2\nu_{22}+\nu_1^2+\nu_2^2+\nu_1\rho_1+\nu_2\rho_2) = -\tfrac{1}{2}e^{\nu}F^{ab}F_{ab},$$

$$R_{44} \equiv -\tfrac{1}{4}e^{\rho-\lambda}(2\rho_{11}+2\rho_{22}+\rho_1^2+\rho_2^2+\nu_1\rho_1+\nu_2\rho_2) = -\tfrac{1}{2}e^{\rho}F^{ab}F_{ab},$$

where a suffix 1 or 2 after a Greek letter means differentiation with respect to z or r. From these we obtain

$$2(\nu_{11}+\rho_{11})+2(\nu_{22}+\rho_{22})+(\nu_1+\rho_1)^2+(\nu_2+\rho_2)^2=0,$$

whence

$$\frac{\partial^2}{\partial z^2}e^{(\nu+\rho)/2}+\frac{\partial^2}{\partial r^2}e^{(\nu+\rho)/2}=0.$$

From this it follows (Weyl 1917) that we may choose

$$e^{(\lambda-\rho)/2}=r$$

without specializing the metric (2.1). The latter then becomes

$$ds^2=-e^{\lambda}(dz^2+dr^2)-e^{-\rho}r^2d\phi^2+e^{\rho}dt^2. \qquad \ldots\ldots(2.2)$$

Using the metric (2.2), and a vector potential with the single component κ_3 (hereafter denoted by α), we find for the complete gravitational and magnetic equations in space-time free of sources

$$R_{11}\equiv \tfrac{1}{2}(\lambda_{11}+\lambda_{22}+r^{-1}\lambda_2+\rho_1^2)=e^{\rho}r^{-2}(\alpha_2^2-\alpha_1^2), \qquad \ldots\ldots(2.3)$$

$$R_{22}\equiv \tfrac{1}{2}(\lambda_{11}+\lambda_{22}-r^{-1}\lambda_2-2r^{-1}\rho_2+\rho_2^2)=e^{\rho}r^{-2}(\alpha_1^2-\alpha_2^2), \qquad \ldots\ldots(2.4)$$

$$R_{33}\equiv -\tfrac{1}{2}r^2e^{-\rho-\lambda}(\rho_{11}+\rho_{22}+r^{-1}\rho_2)=-e^{-\lambda}(\alpha_1^2+\alpha_2^2), \qquad \ldots\ldots(2.5)$$

$$R_{44}\equiv -\tfrac{1}{2}e^{\rho-\lambda}(\rho_{11}+\rho_{22}+r^{-1}\rho_2)=-e^{2\rho-\lambda}r^{-2}(\alpha_1^2+\alpha_2^2), \qquad \ldots\ldots(2.6)$$

$$R_{12}\equiv \tfrac{1}{2}(\rho_1\rho_2-r^{-1}\rho_1-r^{-1}\lambda_1)=2e^{\rho}r^{-2}\alpha_1\alpha_2, \qquad \ldots\ldots(2.7)$$

$$\mathfrak{F}^{34}{}_{,k}\equiv e^{\rho}r^{-1}(\alpha_{11}+\alpha_{22}-r^{-1}\alpha_2+\alpha_1\rho_1+\alpha_2\rho_2)=0. \qquad \ldots\ldots(2.8)$$

This system is easily shown to be equivalent to the four equations

$$\nabla^2\rho=2e^{\rho}r^{-2}(\alpha_1^2+\alpha_2^2), \qquad \ldots\ldots(2.9)$$

$$\nabla^2\alpha-2r^{-1}\alpha_2=-(\alpha_1\rho_1+\alpha_2\rho_2), \qquad \ldots\ldots(2.10)$$

$$\lambda_1=-\rho_1+r\rho_1\rho_2+4e^{\rho}r^{-1}\alpha_1\alpha_2, \qquad \ldots\ldots(2.11)$$

$$\lambda_2=-\rho_2+\tfrac{1}{2}r(\rho_2^2-\rho_1^2)+2e^{\rho}r^{-1}(\alpha_2^2-\alpha_1^2), \qquad \ldots\ldots(2.12)$$

where

$$\nabla^2\equiv\frac{\partial^2}{\partial z^2}+\frac{\partial^2}{\partial r^2}+\frac{1}{r}\frac{\partial}{\partial r}$$

is the Laplacian in cylindrical polar coordinates. Equations (2.11) and (2.12) are easily shown to be consistent provided (2.9) and (2.10) are satisfied. The complete solution is generated by the functions ρ and α obtained from (2.9) and (2.10) for, given these, λ is determined to within an arbitrary constant by (2.11) and (2.12).

§ 3. A Class of Exact Solutions

In this section is presented a class of exact solutions which was previously given in a slightly different form (Bonnor 1954).

In the special case in which

$$\alpha_1\rho_1+\alpha_2\rho_2=0 \qquad \ldots\ldots(3.1)$$

we may introduce a harmonic function ψ such that

$$\alpha_1=r\psi_2, \qquad \alpha_2=-r\psi_1; \qquad \ldots\ldots(3.2)$$

ρ is then a function of ψ because of (3.1), and the complete solution of (2.9) (2.12) for the metric (2.2) is

$$e^{\rho}=A^2\sec^2(A\psi+B), \qquad \ldots\ldots(3.3)$$

$$F_{31}=r\frac{\partial\psi}{\partial r},\quad F_{32}=-r\frac{\partial\psi}{\partial z},\quad F_{12}=F_{4\beta}=0,\quad(\beta=1,2,3), \qquad \ldots\ldots(3.4)$$

$$\nabla^2\psi=0, \qquad \ldots\ldots(3.5)$$

$$\lambda_1=-\rho_1-4rA^2\psi_1\psi_2, \qquad \ldots\ldots(3.6)$$

$$\lambda_2=-\rho_2+2rA^2(\psi_1^2-\psi_2^2), \qquad \ldots\ldots(3.7)$$

where A and B are arbitrary constants. Equations (3.6) and (3.7) are compatible if ψ satisfies (3.5).

The solution is generated by a single function ψ, which plays a part similar to the magnetic scalar potential of the Maxwell theory, the field components being given in terms of it by the usual relations (3.4).

§ 4. The Classical Field of a Loop of Current

Let the loop have the form of a circle in the plane $z=0$ centre O, radius a, and suppose it to carry a steady current j (relativistic units). The magnetic scalar potential ψ is multivalued, but we can remove the multivaluedness by considering the magnetic shell equivalent to the current. Let this be the disc

$$z=0, \qquad r\leqslant a; \qquad \ldots\ldots (4.1)$$

then the potential at any point is proportional to the solid angle subtended by the disc. For a point on Oz we may take (Jeans 1927, page 431, with modifications)

$$\left.\begin{aligned} \psi &= 2\pi j[1-z(a^2+z^2)^{-1/2}], \qquad z>0, \\ \psi &= 2\pi j[-1-z(a^2+z^2)^{-1/2}], \qquad z<0, \end{aligned}\right\} \ldots\ldots (4.2)$$

when the positive value of the square root is to be chosen. The space may now be regarded as simply connected, but there is a discontinuity in ψ on crossing the disc.

In the usual way (4.2) may be used to obtain the potential at points off the z axis; using spherical polar coordinates R, θ,ϕ with O as origin, we find, (Jeans 1927)

$$\psi = 2\pi j\left[\pm 1-\frac{R}{a}P_1+\frac{R^3}{2a^3}P_3-\ldots+(-1)^{n+1}\frac{1.3.\ldots.2n-1}{2.4\ldots 2n}\left(\frac{R}{a}\right)^{2n+1}P_{2n+1}+\ldots\right] \qquad \ldots\ldots (4.3)$$

for $R<a$, the positive or negative sign being chosen according as

$$0\leqslant\theta<\tfrac{1}{2}\pi \quad \text{or} \quad \tfrac{1}{2}\pi<\theta\leqslant\pi;$$

$P_n(\cos\theta)$ are the Legendre polynomials. For $R>a$, we obtain

$$\psi = 2\pi j\left[\tfrac{1}{2}\left(\frac{a}{R}\right)^2P_1-\tfrac{3}{8}\left(\frac{a}{R}\right)^4P_3+\ldots+(-1)^{n+1}\frac{1.3.\ldots.2n-1}{2.4\ldots 2n}\left(\frac{a}{R}\right)^{2n}P_{2n-1}+\ldots\right]. \qquad \ldots\ldots (4.4)$$

§ 5. The Relativistic Field of a Loop of Current

The values of ψ given in the previous section are to be substituted into (3.3), (3.4), (3.6) and (3.7). We first verify that the metric (2.2) then tends to flatness as R, given by $(z^2+r^2)^{1/2}$, tends to infinity. From (3.3) we have

$$e^{\rho}=A^2\sec^2 B\,(\cos A\psi-\tan B\sin A\psi)^{-2}, \qquad \ldots\ldots (5.1)$$

so provided that A is finite and non-zero and provided that B is not an odd integral multiple of $\frac{1}{2}\pi$, we shall have

$$e^{\rho}\sim \text{const.}+O(R^{-2}) \qquad \ldots\ldots (5.2)$$

for large R, since (4.4) shows that $\psi\sim O(R^{-2})$. It is clear from (3.6) and (3.7) that e^{λ} will tend to a similar value. Hence (2.2) tends to flatness at great distance from the loop.

It follows now from (3.4) that the magnetic field will have at great distance the correct classical value, since the components of F_{ik} are formed in the ordinary way from the classical potential. We therefore conclude that at great distance from the source the magnetic field would be recognized by an observer as that of a current loop.

We now put

$$A^2 \sec^2 B = 1 \qquad \ldots\ldots (5.3)$$

and expand e^ρ, given by (5.1), in powers of R^{-1}. This gives

$$e^\rho = 1 + 2\pi j a^2 A R^{-2} \tan B \cos\theta + O(R^{-4}), \qquad \ldots\ldots (5.4)$$

where $\cos\theta = z/R$. The second term on the right of (5.4), which contains $\cos\theta/R^2$, corresponds to the gravitational field of mass dipoles, and implies the existence of negative mass in the source. This must be ruled out on physical grounds, so we put $B = 0$. From (5.3) it then follows that we may take $A = 1$, and (5.1) now gives

$$e^\rho = \sec^2\psi. \qquad \ldots\ldots (5.5)$$

Since λ can be found in terms of ρ from (3.6) and (3.7), it follows that (4.3), (4.4) and (5.5) determine the desired solution.

§ 6. Examination of the Solution

It will be seen from (5.4) that e^ρ contains no term in R^{-1}, and so the gravitational mass of the current wire does not appear in the solution. It therefore appears that our solution corresponds to the magnetic field of a loop of current with zero mass. To investigate further the nature of the solution we consider now the singularities of the field.

It follows from (5.5) that e^ρ becomes infinite when $\psi = \frac{1}{2}(2n+1)\pi$. Since ψ ranges from an infinite value on the wire to zero at infinity, it follows that e^ρ will take on an infinite number of such singular values. However, singularities of this type in e^ρ will not occur in the range

$$0 \leqslant |\psi| < \tfrac{1}{2}\pi, \qquad \ldots\ldots (6.1)$$

and it turns out that this range corresponds to the whole of space, except for a very small region close to the wire.

To see this, take the expressions (4.3) and (4.4) for ψ, and consider the series in the square brackets: one finds by putting every coefficient of R^n equal to $+1$ (or -1):

$$|\psi| \leqslant 2\pi j \left(1 + \frac{aR}{a^2 - R^2}\right), \quad R < a,$$

$$|\psi| < \frac{\pi j a^2}{R^2 - a^2}, \quad R > a.$$

Remembering that in the relativistic units being used here j is extremely small for any current obtainable in the laboratory ($1\,\text{A} = 3 \times 10^{-26}$ relativistic units), it follows that ψ satisfies (6.1) except for a region very close indeed to the wire. In fact in any conceivable experimental situation the singularities at $\psi = \frac{1}{2}(2n+1)\pi$ lie *inside* the material of the wire, where of course a different solution of the field equations must be used. These singularities resemble the singularity at $R = 2m$ in the Schwarzschild solution, which cannot in fact exist because matter cannot be sufficiently compressed to realize it. We therefore confine attention to that part of the field in which (6.1) is satisfied.

A singularity in e^ρ of a different type occurs on the equivalent magnetic shell corresponding to the current loop, namely on the surface (4.1). From (4.3) it follows that, on crossing this surface from negative to positive values of z, ψ

changes from $-2\pi j$ to $+2\pi j$. This does not imply a discontinuity in e^{ρ} itself because by (5.5) it is an even function of ψ. The derivative of g_{44} with respect to z is, however, discontinuous on (4.1) since

$$\frac{\partial g_{44}}{\partial z} = 2\psi_1 \tan\psi \sec^2\psi \qquad \ldots\ldots (6.2)$$

changes by

$$4(\psi_1)_0 \tan 2\pi j \sec^2 2\pi j \qquad \ldots\ldots (6.3)$$

as (4.1) is crossed from the negative to the positive side; $(\psi_1)_0$ is the value of $\partial\psi/\partial z$ on (4.1), and it is a function of r.

The solution therefore has a singularity on the surface (4.1.). This singularity evidently corresponds to no feature of the actual physical situation which the solution is supposed to represent, since in fact the only singularity should be on wire itself, viz. on $z=0$, $r=a$. We therefore ask how the singularity could be removed to make the solution conform with reality.

For many applications to static fields one may take $\log\sqrt{g_{44}}$ as a representation of the Newtonian gravitational potential χ. If we do this, with g_{44} given by (5.5), we find that χ is continuous on crossing the surface (4.1), but

$$\frac{\partial\chi}{\partial z} = \frac{\partial}{\partial z}(\tfrac{1}{2}\rho)$$

is discontinuous. Therefore *the Newtonian interpretation of the discontinuity* (6.3) *is that* (4.1) *corresponds to a surface distribution of mass.* This distribution does not show up in the field at infinity, for by (5.4) e^{ρ} has no term of order R^{-1} for large R.

The difficulty can be overcome if we can add to our solution a source of mass on the surface (4.1) of appropriate density to cancel out that represented by the discontinuity (6.3). *This will remove the singularity and at the same time give a term of order R^{-1} at infinity: and the solution will then represent a current wire, without a spurious singular surface, but having a mass which depends on the current.*

Unfortunately it has not been possible to carry out this programme using exact solutions. The solution of §3 is not the most general solution of the axially symmetric magnetostatic problem, and it may perhaps be worth while to point out why it cannot be applied to overcome the difficulty. The solution contains one source function ψ satisfying (3.5), which one uses to insert the appropriate magnetic source. Examination of g_{44}, given by (3.3), then shows that the only mass source which can be inserted into the solution is one which, at great distance, gives rise to a gravitational potential proportional to ψ. Thus if one uses ψ to represent a sheet of magnetic dipoles, the corresponding mass source would be one of mass dipoles. This source is actually represented by the second term on the right of (5.4), and since it is of no physical interest, it was abolished by putting $B=0$. Thus it is not possible to use the solution of §3 to represent a current wire with mass.

In the next section it is shown how the problem can be dealt with by a method of approximation.

§ 7. An Approximate Solution of the Equations

To find an approximate solution without the singular surface (4.1) we revert to equations (2.9)–(2.12), and suppose that ρ, α and λ can be expanded in power series in the current j and the mass m of the wire which carries it. Having regard

to the way in which ρ, α and λ enter equations (2.9)–(2.12), we see that the expansions will be of the form

$$\left.\begin{aligned}\alpha &= \sum_{p=0}^{\infty}\sum_{s=1}^{\infty} m^p j^s \alpha^{(ps)},\\ \rho &= m\rho^{(10)} + \sum_{p=0}^{\infty}\sum_{s=1}^{\infty} m^p j^{2s}\rho^{(ps)},\\ \lambda &= m\lambda^{(10)} + \sum_{p=0}^{\infty}\sum_{s=1}^{\infty} m^p j^{2s}\lambda^{(ps)}.\end{aligned}\right\} \quad \ldots\ldots (7.1)$$

From (2.9) the function $\rho^{(10)}$ satisfies

$$\nabla^2\rho^{(10)} = 0, \quad \ldots\ldots (7.2)$$

and the solution of this to be chosen is the Newtonian gravitational potential of the circular wire. This can be written down, and the corresponding value of $\lambda^{(10)}$ is then obtainable from (2.11) and (2.12); however, since $\rho^{(10)}$ and $\lambda^{(10)}$ will not be needed in what follows they will not be given here.

The lowest term in the expansion of α is given by

$$\nabla^2\alpha^{(01)} - 2r^{-1}\alpha_2^{(01)} = 0, \quad \ldots\ldots (7.3)$$

and here we must choose the solution corresponding to the magnetic field of the current j. Equation (7.3) is formally the same as (2.10) with the condition (3.1) imposed, so we may put

$$j\alpha^{(01)}{}_1 = r\psi_2, \qquad j\alpha_2{}^{(01)} = -r\psi_1 \quad \ldots\ldots (7.4)$$

as in (3.2), and use for ψ the scalar potential of the current loop, namely (4.3) and (4.4). The magnetic field components up to the (01) approximation are then given by (3.4).

We now proceed to calculate $\rho^{(02)}$; the equation for this, following from (2.9) and (7.1), is

$$\nabla^2\rho^{(02)} = 2r^{-2}(\alpha_1{}^{(01)\,2} + \alpha_2{}^{(01)\,2})$$

and using (7.4) we obtain

$$\nabla^2\rho^{(02)} = 2j^{-2}(\psi_1{}^2 + \psi_2{}^2). \quad \ldots\ldots (7.5)$$

A solution of this is

$$\rho^{(02)*} = j^{-2}\psi^2, \quad \ldots\ldots (7.6)$$

and this is the approximate solution corresponding to the exact solution (5.5). If we adopt (7.6) we find, as in (6.2), that $\partial\rho^{(02)*}/\partial z$ has a discontinuity on the surface (4.1). Let us denote the magnitude of this discontinuity by $4\pi\sigma^*(r)$, thus

$$\left(\frac{\partial\rho^{(02)*}}{\partial z}\right)_+ - \left(\frac{\partial\rho^{(02)*}}{\partial z}\right)_- \equiv 4\pi\sigma^*(r) = 8\pi j^{-1}(\psi_1)_0, \quad \ldots\ldots (7.7)$$

where $+$ and $-$ refer to the sides of (4.1) on which z is positive and negative respectively, and where, as before, $(\psi_1)_0$ denotes the value of $\partial\psi/\partial z$, as a function of r, on the surface (4.1).

As explained in §6, this singularity has no physical meaning, and we will remove it by adding another function to $\rho^{(02)*}$. From (7.5) it follows that to $\rho^{(02)*}$ we may add any harmonic function. Let us therefore add a term

$$\rho^{(02)**} = \int_\Sigma \frac{\sigma^{**}(r^*)\partial S^*}{|\mathbf{r}-\mathbf{r}^*|}, \quad \ldots\ldots (7.8)$$

where Σ denotes the surface (4.1), $\mathbf{r}$ is the position vector of a field point, $\mathbf{r}'$ is the position vector of a point on Σ, and $\sigma^{**}(r^*)$ is a function to be specified shortly.

We know from ordinary potential theory that $\partial\rho^{(02)**}/\partial z$ will be discontinuous in crossing Σ; in fact

$$\left(\frac{\partial\rho^{(02)**}}{\partial z}\right)_+ - \left(\frac{\partial\rho^{(02)**}}{\partial z}\right)_- = -4\pi\sigma^{**}(r^*). \qquad \ldots\ldots(7.9)$$

If now we put

$$\sigma^{**}(r) = \sigma^*(r) \qquad \ldots\ldots(7.10)$$

and take as the complete solution of (7.5)

$$\rho^{(02)} \equiv \rho^{(02)*} + \rho^{(02)**} = j^{-2}\psi^2 + \int_\Sigma \frac{\sigma^*(r^*)dS^*}{|\mathbf{r}-\mathbf{r}^*|}, \qquad \ldots\ldots(7.11)$$

it follows from (7.7), (7.9) and (7.10) that $\rho^{(02)}$ will be continuous on crossing Σ, and the singularity will have been removed.

The integral in (7.11) will show up at great distance as the gravitational potential of a mass which must be attributed to the presence of the current. To find this mass, we recall that at great distances $\frac{1}{2}\rho^{(02)} \sim \chi$, where χ is the Newtonian potential. Hence the mass concerned is

$$M = -\tfrac{1}{2}j^2\int_\Sigma \sigma^*(r^*)dS^*, \qquad \ldots\ldots(7.12)$$

and we can evaluate the integral by using (7.7):

$$M = -\tfrac{1}{2}\int_\Sigma 2j(\psi_1)_0 dS^* = -j\int_0^a\int_0^{2\pi}(\psi_1)_0 r^* d\phi dr^*.$$

Finally using (7.4), we have

$$M = 2\pi j^2[\alpha^{(01)}]_0^a = 2\pi j^2\alpha^{(01)}(a), \qquad \ldots\ldots(7.13)$$

where $\alpha^{(01)}(a)$ denotes the value of $\alpha^{(01)}$ on the wire itself, since $\alpha^{(01)}$ vanishes at the origin.

Our approximation method has given us α up to the (01) approximation (by (7.4)), and ρ up to the (02) approximation (by (7.11)). By expanding (3.6) and (3.7) in powers of j we could in principle find λ up to the (02) approximation. One can verify that $\lambda^{(02)}$ is singular only on the wire itself, and beyond this no interest attaches to $\lambda^{(02)}$ from our point of view. We assume that in higher approximations any spurious singularities in $\rho^{(rs)}$ can be removed by a procedure similar to that above, accumulating meanwhile additional increments of mass, such as (7.13).

To compare (7.13) with the energy of the magnetic field due to the current, we must note that the vector potential $\mathbf{A}$ of elementary theory is given in terms of $\alpha^{(01)}$ by

$$rA_3 = j\alpha^{(01)}, \qquad \ldots\ldots(7.14)$$

and that the magnetic energy is

$$W = \tfrac{1}{2}j\int \mathbf{A}.\mathbf{ds} \qquad \ldots\ldots(7.15)$$

the integral being taken round the wire. Comparing (7.13) with (7.15), and using (7.14), we see that

$$M = 2W. \qquad \ldots\ldots(7.16)$$

The gravitational mass is therefore twice the magnetic energy. If the wire is regarded as having zero cross section, $\alpha^{(01)}$, M and W are infinite, but as we saw in § 6, it is not permissible to neglect the cross section of the wire.

§ 8. Conclusion

It has been shown that to obtain a physically reasonable solution, within general relativity, for the field of a loop of steady current, it is necessary to endow the wire with a gravitational mass which corresponds to the energy of the magnetic field created. The result is surprising in that, as explained in §1, no such mass appears in the solution for a point charge, at least if one considers only the exterior solution. Otherwise, it is physically reasonable that the energy of the magnetic field should exert gravitation and therefore lead to a gravitational mass term.

The factor two in (7.16) is not entirely unexpected since factors like this are known to occur in relating electromagnetic to mechanical energy (see, for example, Papapetrou 1947). It presumably arises from the fact that non-Maxwellian stresses are present in addition to purely electromagnetic ones, and these contribute to the gravitational mass.

The gravitational effect of the current is not very far below the limit of experimental detection. For (7.16) we may write

$$M = Lj^2,$$

where L is the self-inductance of the wire. Taking $L = 10^3$ cm and $j = 10^6$ A, we find, paying due regard to the units, a value of $1{\cdot}1 \times 10^{-8}$ g for M. A rather thick wire would be needed to carry such a current, of mass, say, 100 g. Hence the mass of the magnetic field would be about 1 part in 10^{10} of the mass of the wire.

References

Bonnor, W. B., 1953, *Proc. Phys. Soc.*, **66**, 145.

—— 1954, *Ibid.*, **67**, 225.

Jeans, J. H., 1927, *The Mathematical Theory of Electricity and Magnetism* (Cambridge: University Press).

Papapetrou, A., 1947, *Proc. Roy. Irish Acad.*, **51 A**, 191.

Weyl, H., 1917, *Ann. Phys., Lpz.*, **54**, 117.

Witten, L., 1960, *Centre Belge de Recherches Mathématiques, Colloque sur la Théorie de la Relativité*, p. 59.

Infra-red Investigation of the Acceptor Levels Formed by Copper in Germanium

By D. L. GREENAWAY†
Physics Research Laboratory, University of Reading

Communicated by R. W. Ditchburn; MS. received 4th June 1959, in revised form 7th June 1960

Abstract. Infra-red absorption measurements from 1 to 34 μ have been made on germanium containing varying amounts of antimony and copper at temperatures down to 20°K. The results indicate that the three acceptor levels introduced by copper into germanium can be identified by their effect on the low temperature absorption spectra of suitably doped samples. The appearance of the levels is in good agreement with the existing theory, and in addition to this, an excited state of the shallow acceptor level has been identified which has not been previously reported.

§ 1. Introduction

Elements which have an s^1 electronic configuration (e.g. copper and gold) can act as triple acceptors in germanium. These impurities, if present substitutionally, can accept at first one, then a second, and finally a third electron as the Fermi level of the material is raised. Thus their acceptor action is determined by the tendency to complete the tetrahedral bonding arrangement with the four nearest neighbour germanium atoms. The positions of the acceptor levels formed by both copper and gold in germanium have been determined electrically (from measurement of Hall effect etc.) by Woodbury and Tyler (1957), but little work has been done on the effect of these acceptor impurities on the optical absorption spectra. Copper has been chosen in preference to gold for this research owing to its very high diffusion coefficient, and the consequent ease in preparing copper doped specimens. It is shown in this paper that the three acceptor levels formed by copper in germanium can be identified by an examination of the infra-red absorption spectra of suitably doped samples. According to the results of Woodbury and Tyler, the levels are situated at 0·04 ev and 0·32 ev from the valence band and 0·26 ev from the conduction band. These energies correspond to wavelengths of 31, 3·9 and 2·5 μ respectively, and are thus accessible using a spectrometer equipped with caesium bromide and rocksalt prisms.

§ 2. Previous Work

In 1952 Fuller and Struthers showed that copper was responsible for the introduction of some of the acceptors into heat-treated germanium. In the same year Slichter and Kolb associated the electrical properties of heat-treated and quenched germanium (thermium) with the very rapid diffusion of copper

† Now at Standard Telecommunication Laboratories, Harlow, Essex.

into germanium. Morin and Maita (1953) using Hall effect conductivity measurements located an acceptor level at 0·04 ev from the valence band, and also inferred the presence of an electron trap deeper in the forbidden gap. The inference was substantiated by Rank and Cronemeyer (1953) in a paper on the infra-red absorption of thermiated germanium, but no specific impurity was postulated. Photoconductivity measurements by Burstein *et al.* (1954) and Kaiser and Fan (1954), identified the 0·04 ev level and also suggested a deeper level at about 0·3 ev from the valence band. Optical absorption measurements by the latter workers located the shallow acceptor level at 0·055 ev above the valence band, and a deeper level at about 0·25 ev above the valence band. The conclusive electrical identification of the three copper acceptor levels was made by Woodbury and Tyler (1957). They studied the Hall effect and mobility of both copper and gold-doped germanium, using a method of systematic double doping, i.e. presence of a known concentration of donor in addition to the copper, to fill up the acceptor levels from which excitation was not required. Woodbury and Tyler located two levels below the centre of the forbidden gap, and a third level above the centre of the gap, i.e. at 0·04 ev and 0·32 ev above the valence band, and at 0·26 ev below the conduction band.

§ 3. Preparation of Compensated Specimens and Experimental Procedure

The germanium used was grown by Standard Telecommunication Laboratories, Harlow. Single crystals were pulled from a melt of zone-refined intrinsic material (resistivity $>40\,\Omega$ cm) in a silica crucible. Antimony was introduced by adding the appropriate amount of antimony–germanium alloy to the melt, and programming the growth to give the required concentration gradient. The concentration of unwanted electrically active impurities was less than 10^{14} cm^{-3}. To investigate the two deeper acceptor levels two crystals (PP155 and DS4) were grown (each some $2\frac{1}{2}$ in. long) containing approximately linear concentration gradients of antimony (7×10^{15} to 14×10^{15} carriers per cm^3 in PP155, and 13×10^{15} to 6×10^{17} carriers per cm^3 in DS4, determined from room temperature Hall effect measurement). The ingots were sawn into half-inch square cross section bars, and each bar cut into eight slices 0·25 in. thick. Several of the specimens were optically polished and the absorption measured in the 1–15 μ region at room temperature and at 80 K. Before diffusion, specimens were plated with a visible layer of copper from a pyrophosphate solution and sealed in evacuated silica tubes. A copper concentration of $4{\cdot}5\times10^{15}$ carriers per cm^3 was then introduced into the specimens by diffusion for 46 hours at 717 ± 1°C to obtain samples in which either empty double acceptor states, empty triple acceptor states, or no acceptor states at all were present. The diffusion was carried out in a large resistance furnace and specimens were quenched by dropping them into oil.

To investigate the lowest acceptor level, copper was diffused into nearly intrinsic germanium for a period of eight hours at 800 ± 5°C in a small hydrogen-flushed resistance furnace.

Absorption spectra of the samples were obtained with a Perkin Elmer 12B single-beam spectrometer modified for double-pass operation, and equipped with rocksalt and caesium bromide prisms. The resolution was 0·05 μ at 4 μ, and rather better at 30 μ. A Golay pneumatic detector was used and the amplified

output displayed with a Brown recorder. Specimens, placed at a beam focus between the exit slit of the spectrometer and the Golay cell, were mounted in an all glass cryostat fitted with KRS5 windows. This cryostat is a simplified version of one used in Bristol University (Pappalardo 1957); the exchange gas system has been omitted, the specimens being inserted in a rectangular slot in a hollow copper cold finger. Specimens are held in position by two short rectangular copper tubes inserted from each end of the slot. Figure 1 shows the cold finger together with the bottom section of the cryostat. The complete spectrometer, enclosed in an airtight case, was flushed continuously with a stream of dry air which provided protection for the prisms and also considerably decreased the absorptions due to atmospheric water vapour.

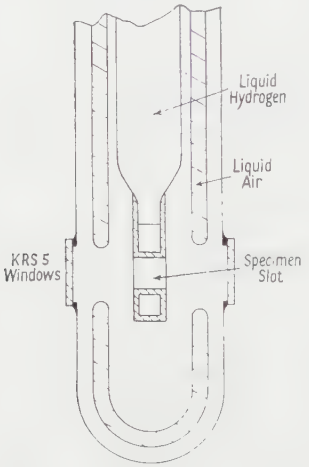

Figure 1. Lower section of the glass cryostat. The specimen is surrounded by the coolant on four sides.

Corresponding optical sample	Compensation (N = concentration)	Type	Activation energy (ev)
PP155 (1)	$2N\text{Cu} > N\text{Sb} > N\text{Cu}$	p	$0{\cdot}30 \pm 0{\cdot}02$
PP155 (2)	$2N\text{Cu} > N\text{Sb} > N\text{Cu}$	p	$0{\cdot}33 \pm 0{\cdot}02$
PP155 (5)	$3N\text{Cu} > N\text{Sb} > 2N\text{Cu}$	n	$0{\cdot}24 \pm 0{\cdot}02$
PP155 (7)	$3N\text{Cu} > N\text{Sb} > 2N\text{Cu}$	n	$0{\cdot}24 \pm 0{\cdot}02$
DS4 (2)	$N\text{Sb} \simeq 3N\text{Cu}$	n	low but indeterminate
DS4 (6)	$N\text{Sb} \gg 3N\text{Cu}$	n	low but indeterminate

To check the diffusion and quenching techniques and the compensation of specimens, and also to provide some verification of the results of previous workers, the activation energy of each of the two deep acceptor levels was determined from the variation of Hall effect with temperature; the specimens used were companion samples to the optical specimens from the copper doped ingots PP155 and DS4. The temperature was varied from 180°–290°K, and a correction for the $T^{3/2}$ dependence of the density of states applied to all Hall effect values. The results obtained are given in the table, which also contains the correspondence between the Hall effect specimens and the optical samples referred to in § 4. These results locate the deep levels at 0·32 ev above the top of the valence band, and 0·24 ev below the bottom of the conduction band; they represent good

agreement with the values given by Woodbury and Tyler. The last two results shown in the table for specimens with heavy antimony doping, indicate that at temperatures down to 180 K, as would be expected, the antimony donor level situated at approximately 0·01 ev below the conduction band is still fully ionized.

§ 4. Optical Results—The Deep Lying Acceptor Levels

In the near infra-red, absorption spectra at 80 and 20 K of specimens before copper doping gave similar results. All spectra showed an absorption coefficient of less than 0·3 cm^{-1} in the 2–7 μ region. Measurements extended to 15 μ for several specimens showed no features other than a slight increase in absorption at long wavelengths due to the effect of free carriers. Figure 2 shows the behaviour at 80 K of one undoped specimen (i.e. before copper diffusion) and six copper doped specimens each containing a substitutional copper concentration of $4{\cdot}5 \times 10^{15}$ carriers per cm^3 and varying antimony concentrations. Compared with the spectra of undoped specimens, there is a difference in the shape between the absorption edge and about 4 μ, probably due to the two deep acceptor levels.

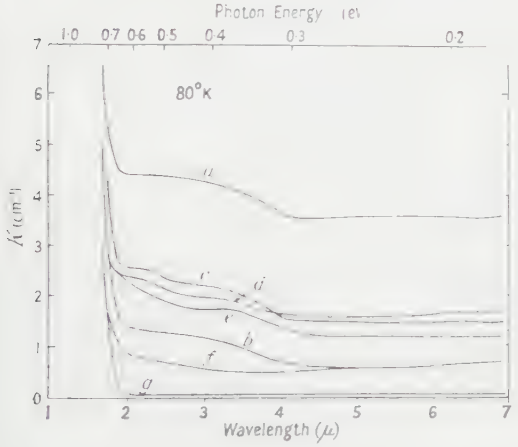

Figure 2. Spectra of six antimony–copper doped germanium specimens at 80°K: *a*, PP155 (1); *b*, PP155 (2); *c*, PP1155 (5); *d*, PP155 (7); *e*, DS4 (2); *f*, DS4 (6). Curve *g* shows an antimony doped specimen.

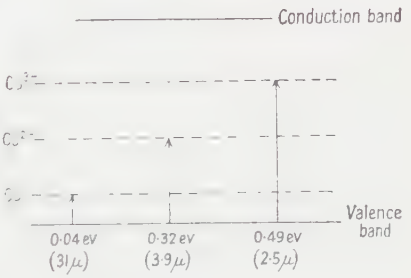

Figure 3.

The acceptor levels should manifest themselves as absorption thresholds, i.e. increases in the absorption coefficient at wavelengths shorter than either 3·9 or 2·5 μ for suitably compensated specimens. The energy scheme for the acceptor levels and the optical transitions is shown in figure 3. Specimens PP155 (1) and (2), in which $2N\,Cu > N\,Sb > N\,Cu$ show an increase in absorption starting at 4 μ and levelling out at about 3 μ. PP155 (5) and (7), in which $3N\,Cu > N\,Sb > 2N\,Cu$, show a second increase which starts at 2·5 μ and levels out just before the band edge. DS4 (2) still shows evidence of the two levels ($N\,Sb \simeq 3N\,Cu$), but for DS4 (6) in which $N\,Sb \gg 3N\,Cu$, there is little evidence of the levels. The acceptor steps are by no means clearly defined, and indicate considerable thermal broadening. Spectra taken at room

temperature show none of the above features except a gradual increase in absorption starting at about 5 μ and continuing until the band edge. Figure 4 shows the spectra of four of the above specimens remeasured at 20°K. The acceptor steps are much more clearly defined; in PP155 (1), (5) and (7), there is evidence of both the levels, but the 3·9 μ (0·32 ev) level of DS4 (2) has been completely filled and only the 2·5 μ excitation is visible. Also the magnitude of the absorption caused by the 0·32 ev acceptor level appears to decrease with the filling of the level. The size of this step is 1·0 cm^{-1} for PP155 (1), 0·7 cm^{-1} for PP155 (5), 0·6 cm^{-1} for PP155 (7), and zero for DS4 (2). The presence of

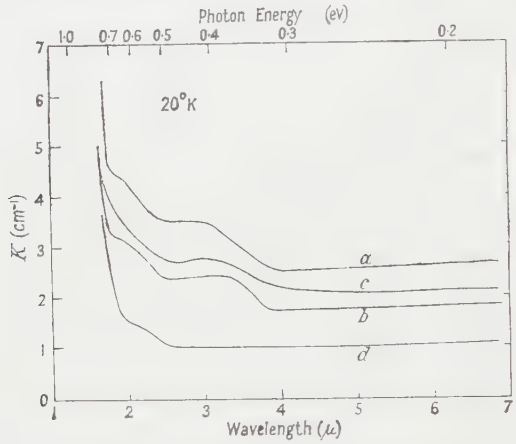

Figure 4. Spectra of four antimony–copper doped specimens at 20°K: *a*, PP155 (1); *b*, PP155 (5); *c*, PP155 (7) and *d*, DS4 (2).

both levels in spectra of the same specimen would seem to indicate microscopic inhomogeneity giving rise to more than one degree of compensation in each sample. Calculation of the expected magnitude of the deep lying acceptor absorptions has not yet been made, and hence comparison of theoretical and experimental results has been limited to those obtained in the next section for the 0·04 ev acceptor level. There is also the possibility of excitations out of filled acceptor levels into the conduction band, giving rise to further absorptions. The above results imply that these transitions, if they are present, are very weak, and are dominated by the transitions from the valence band into the acceptor states.

§ 5. Optical Results—Shallow Acceptor Level

Optical investigation of this level must be done using p-type copper doped material at temperatures low enough for the majority of the acceptor states to be un-ionized. Absorption curves for undoped high resistivity germanium at three temperatures in the 1–34 μ region (figure 5) show the strong masking effect of the lattice absorption bands in the 18–30 μ region; it is thus necessary to subtract the lattice contribution from all absorption curves of copper doped specimens. Figures 6 and 7 show the absorption spectra of copper doped germanium (containing $9{\cdot}6 \times 10^{15}$ carriers per cm^3) at room temperature, 80°K and 20°K; these results are replotted in figures 8 and 9 after subtracting the lattice absorption contribution (taken from figure 5) at the appropriate temperature. In figure 8 (*a*)

it can be seen that the room temperature curves have a very similar shape, the difference in magnitude being due to the presence of free holes in the copper doped material. Quite different behaviour is seen at low temperatures however (figure 8 (*b*) and figure 9); a sharp band has appeared at 31 μ (0·04 ev) followed by an absorption edge which rises to a maximum between 24 and 26 μ and falls

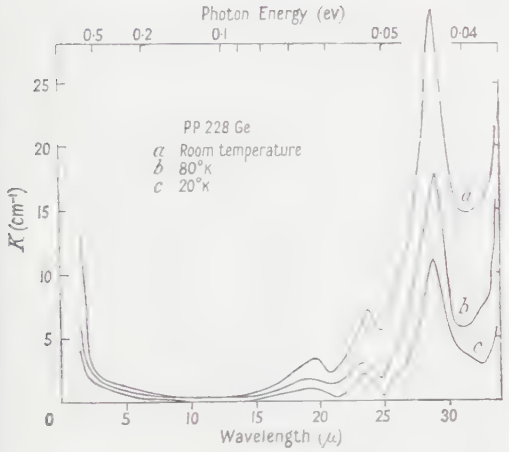

Figure 5. Spectra of high resistivity germanium showing the effect of temperature on the lattice absorption bands in the 15–30 μ region.

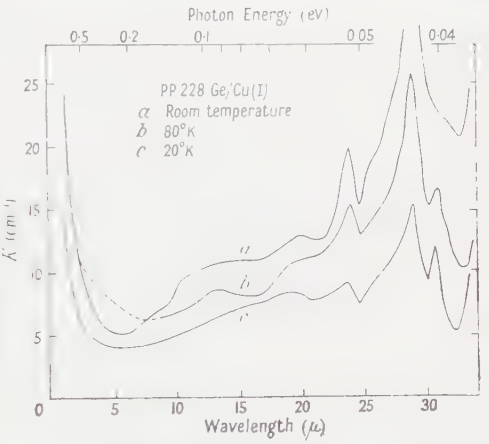

Figure 6. Spectra of PP228 Ge/Cu (I) at room temperature, 80°K and 20°K.

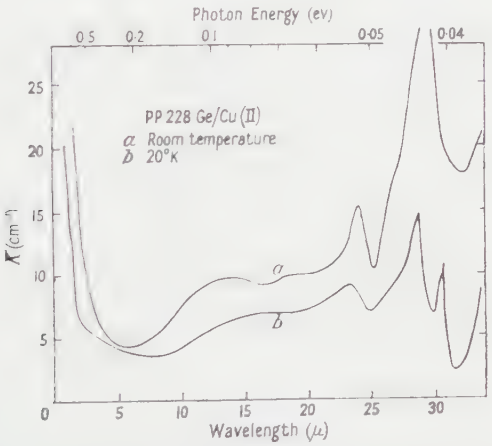

Figure 7. Spectra of PP228 Ge/Cu (II) at room temperature and 20°K.

off gradually towards shorter wavelengths. It would appear that the 31 μ band is due to an excited state of the shallow copper acceptor level. Analogy with spectra of Group III acceptors in silicon (Burstein and Egli 1956) indicates that any other excited states would lie beyond the useful range of the caesium bromide prism. Results obtained with silicon also show that as the activation energy for an acceptor increases, the excited states become much less evident, and the absorption threshold much less clearly defined. The shape of the absorption due to the two deep copper levels is therefore quite reasonable.

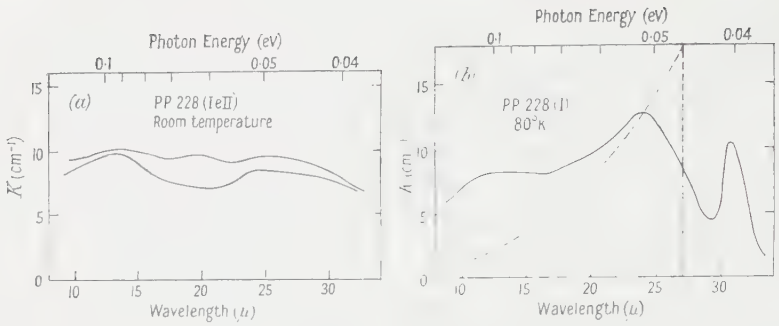

Figure 8. Shows the result of subtracting the lattice absorption (figure 5) at room temperature and 80°K from the spectra shown in figures 6 and 7.

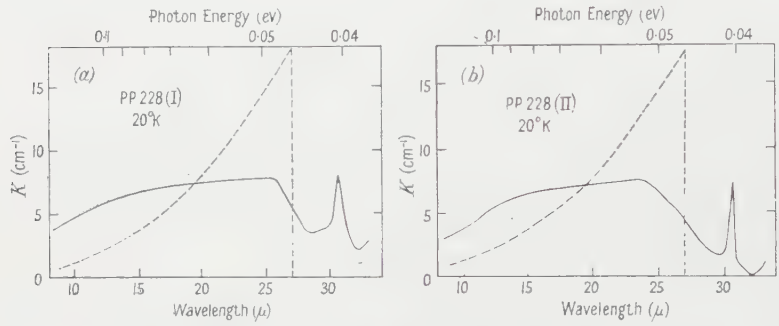

Figure 9. Shows the result of subtracting the lattice absorption (figure 5) at 20°K from the spectra shown in figures 6 and 7.

It is possible to calculate the expected absorption for the shallow acceptor level from a consideration of the photoelectric effect of a hydrogenic-type impurity in a semiconductor. From the treatment given by Heitler, it can be shown that the absorption cross section for a K-shell electron in free space is

$$\sigma = \frac{256\pi\hbar^3}{3e^2cm^2}\left(\frac{\nu_i}{\nu}\right)^{7/2} f(\zeta) \qquad \ldots\ldots(1)$$

where

$$f(\zeta) = 2\pi\left(\frac{\nu_i}{\nu}\right)^{1/2}\frac{\exp\left(-4\zeta\cot^{-1}\zeta\right)}{1-\exp\left(-2\pi\zeta\right)} \quad \text{and} \quad \zeta = \left(\frac{\nu_i}{\nu-\nu_i}\right)^{1/2}.$$

ν is the frequency of the incident radiation and ν_i the frequency of the absorption threshold. The factor $f(\zeta)$ represents the influence of the ion on the wave function of the emitted electrons. (1) can be applied to photoelectric emission in a semiconductor if e^2 is replaced by e^2/n^2 (n = refractive index of the semiconductor), m by m^* the effective mass, and c by c/n. It can then be shown that σ is given by

$$\sigma = \frac{256\pi\hbar^3}{3e^2cm^2}\left(\frac{1}{n}\frac{m}{m^*}\frac{E_H}{E_I}\right)\left(\frac{\nu_i}{\nu}\right)^{7/2} f(\zeta) \qquad \ldots\ldots(2)$$

where E_H is the ionization energy of hydrogen and E_I the ionization energy of

the localized state. For values of $\nu \gg \nu_i$, $f(\zeta) \to 1$, but in the neighbourhood of the absorption threshold $\nu \to \nu_i$, $\zeta \to \infty$, and $f(\zeta) \to 2\pi(\exp -4)(\nu_i/\nu)^{1/2}$. Thus near to the absorption threshold (0·046 ev) for the copper acceptor level

$$\sigma = \frac{K}{N} = \frac{512\pi^2\hbar^3}{3e^2cm^2} \exp(-4) \left(\frac{1}{n}\right)\left(\frac{m}{m^*}\right)\left(\frac{E_H}{E_I}\right)\left(\frac{\nu_i}{\nu}\right)^4 \quad \ldots\ldots(3)$$

where K is the optical absorption coefficient and N the concentration of acceptors Hence

$$\frac{K}{N} = \frac{6{\cdot}303 \times 10^{-18}}{n}\left(\frac{m}{m^*}\right)\left(\frac{E_H}{E_I}\right)\left(\frac{\nu_i}{\nu}\right)^4. \quad \ldots\ldots(4)$$

It should be noted here that Fan (1956) wrongly quotes (4), and gives $(\nu_i/\nu)^{8/3}$ as his expression for the cross section near to the absorption threshold.

If the following values are taken: $E_I = 0{\cdot}046$ ev (from figure 9), $E_H = 13{\cdot}6$ ev, $m/m^* = 4$ and $n = 4$ then the absorption cross section at the wavelength threshold is $K/N = 1{\cdot}86 \times 10^{-15}$ cm^2. From figure 9, $K = 8$ cm^{-1}, and from resistivity measurements $N = 9{\cdot}6 \times 10^{15}$ carriers per cm^3, thus $K/N = 0{\cdot}8 \times 10^{-15}$ cm^2. This represents reasonable agreement with the theoretical value. A note of caution should be added here on the use of Heitler's models (1954) to calculate σ, as the ionization energy used (0·046 ev) differs by a factor of 4 from that given by the model. There may thus be some error in the calculated absorption cross section of $1{\cdot}86 \times 10^{-15}$ cm^2. The experimental result is in very good agreement with the cross section obtained by Kaiser and Fan (1954) of $0{\cdot}9 \times 10^{-15}$ cm^2. The shape of the acceptor absorption has also been calculated from (2) and the broken curves in figure 8 (*b*) and figure 9 show the theoretical shape in the region of absorption threshold. Comparison between theoretical and experimental curves indicates that at 20 K some of the acceptors are still ionized, and a small amount of free hole absorption is present. Kaiser and Fan (1954) showed that at 4 K nearly all the acceptor states are empty; thus it would be expected that remeasurement of the spectra shown in figure 9 at liquid helium temperature would give better correlation with the theoretical curve.

§ 6. Conclusions

The results indicate that the acceptor levels formed by copper in germanium can be identified from their effect on the absorption spectra, and also show the presence of an excited state of the 0·04 ev level. These results suggest that further work could be done on the copper acceptor levels using a spectrometer of higher resolution to investigate any excited states of the deep levels, and a range extending further into the infra-red to locate possible excited states of the shallow acceptor level. The possibility also arises of the optical identification of the three acceptor levels and the one donor level formed by gold in germanium (see Johnson and Levenstein 1960). These suggested measurements should preferably all be made at liquid helium temperature.

Acknowledgments

I wish to express my thanks to Professor R. W. Ditchburn for supervising this research, to Dr. A. B. Lidiard and Dr. P. C. Banbury for helpful discussions, and to Standard Telecommunication Laboratories, Harlow, for providing a grant for the research.

References

Burstein, E., Davisson, J. W., Bell, E. E., Turner, W. J., and Lipson, H. G., 1954, *Phys. Rev.*, **93,** 65.
Burstein, E., and Egli, P. H., 1956, *Naval Research Labs. Report* (*Washington*), No. 4595.
Fan, H. Y., 1956, *Rep. Progr. Phys.* (London: Physical Society), **19,** 121.
—— 1960, *Phys. Rev. Letters*, **5,** 195.
Fuller, C. S., and Struthers, J. D., 1952, *Phys. Rev.*, **87,** 526.
Heitler, W., 1954, *Quantum Theory of Radiation*, 3rd edition (Oxford: University Press), p. 208.
Johnson, L., and Levenstein, H., 1960, *Phys. Rev.*, **117,** 1191.
Kaiser, W., and Fan, H. Y., 1954, *Phys. Rev.*, **93,** 977.
Morin, F. J., and Maita, J. P., 1953, *Phys. Rev.*, **90,** 337A.
Pappalardo, P., 1957, *Phil. Mag.*, **2,** 1397.
Rank, D. H., and Cronemeyer, D. C., 1953, *Phys. Rev.*, **90,** 202.
Slichter, W. P., and Kolb, E. P., 1952, *Phys. Rev.*, **87,** 527.
Woodbury, H. H., and Tyler, W. W., 1957, *Phys. Rev.*, **105,** 84.

Note added in Proof.—Recently published results (Fan 1960) confirm the existence of several excited states of the 0·04 ev copper level. Measurements at 4°K locate the most intense of these at 0·404 ev (30·7μ), in excellent agreement with the above results.

The Discontinuities in the Solutions of the Transport Equation and the Variational Principle

By R. ENGLMAN

Department of Physics, Israel Institute of Technology, Haifa

MS. received 21*st March* 1960, *in final form* 13*th June* 1960

Abstract. A corrected proof is given of the result of García-Moliner and Simons obtained in 1957 showing the equivalence of the variational formulation and the transport (Boltzmann) equation in the case of an applied magnetic field and effective crystal boundaries. The proof in the paper takes into account the existence of a hyper-surface (in phase-space) of discontinuities of the distribution function.

§ 1. Introduction

A few years ago García-Moliner and Simons (1957) extended the variational formulation of transport theory to the inclusion of the effects of a magnetic field or of the vicinities of crystal boundaries (see also Tauber 1958). It might have been thought that the variational method will prove very useful for calculations of cyclotron resonance, where just these effects are operative. It seems a pity that the method has not been put to use (or to the test) so far, notwithstanding the difficulties in the way of exact calculations (Azbel and Kaner 1956, Mattis and Dresselhaus 1958).

In the first-mentioned paper there are two Appendixes, A and B, on which the thesis of that paper rests. Examining these appendixes for cases where both the metal boundaries and magnetic fields play a role, we find that they both contain one error each. We shall discuss these in § 3 of this work. More important, however, is the fact (brought out in § 4) that the two errors exactly cancel each other, leaving the final result of the authors intact. After this happy conclusion, the re-establishment of *status quo ante*, any further comments may appear superfluous. There will emerge, however, in the course of the discussion a number of points relating to the surfaces of discontinuities (in phase-space) of the solution of the Boltzmann equation. It is the opinion of the writer, supported among others by written and oral communications, that this aspect of the distribution function has not been sufficiently considered and that attention might profitably be focused on it.

A concrete example of the general situation is first given (in the following section) to pave the way for more general treatment. The notation of García-Moliner and Simons will be used.

§ 2. A Simple Case

2.1

Consider a straight metallic wire with a circular cross section. This is shown in the figure. Constant and uniform electric and magnetic fields are applied, both normal to the plane of the paper. The conductivity of a metal of

this geometry was obtained by Chambers (1950) by considering the trajectory of an arbitrary electron. For our purposes we are concerned with the trajectory of a limited class of electrons only: those which, in the course of their helical paths, just fail to hit the boundary.

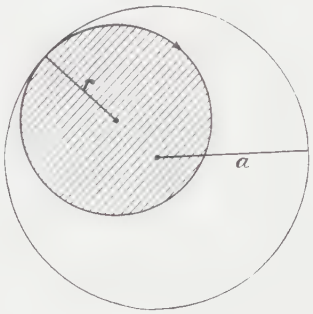

In the figure we have drawn the projection of such a trajectory, due to electrons whose direction of motion makes an angle θ with the magnetic field. Then the radius of the projection of the trajectory

$$r = \frac{mvc}{eH} \sin\theta = r_0(v) \sin\theta$$

for electrons with velocity v. Standard notation is used.

The importance of the circle drawn is that the electrons (with v, θ) will be scattered by the boundary when just outside the circle, but will escape scattering when inside it. Now boundary scattering will necessarily reduce the ordering of the electronic distribution. In this the boundary plays the same role as other scattering centres (impurities, phonons, etc.) within the solid which are responsible for the relaxation mechanism. Where the boundary differs is that, in terms of the phenomenological transport theory, an electron will be scattered by an impurity, say, with some probability, whereas, since it cannot escape from the metal, it will be scattered at and by the boundary with absolute certainty. It follows, therefore, that the electronic distributions in, and outside, the circle will in general be very different. In other words, the circle shown is a curve of discontinuity in the distribution function for the electron of the type (v, θ) considered.

(Occasionally, as in some of the cases reviewed by Sondheimer (1952), perfectly specular scattering at the boundary has been considered; this would not cause any discontinuity in the distribution function, neither would it enhance the disorder. For the reasons given, this particular type of scattering cannot be physically quite correct, though for the problems in which it has been invoked, it may form a valid and useful approximation.)

2.2

It is not difficult to show that all the circles satisfy the equation

$$R^2 + 2r_0(v) \sin\theta \, [a - R \sin(\varpi - \phi)] - a^2 = 0. \qquad \ldots\ldots (1)$$

The electronic coordinate systems are in real space the cylindrical (R, ϕ, z) and in velocity space the spherical one (v, θ, ϖ); a is the radius of the wire.

Equivalently, equation (1) represents the hyper-surface of the discontinuities in the distribution function in phase-space.

§ 3. The Variational Formulation

3.1

The transport equation to be solved for $\Phi(\mathbf{R}, \mathbf{k})$ is written by García-Moliner and Simons (their eqns 2.5–2.8) as

$$L(\Phi) + M\Phi + B\Phi = X \qquad \ldots\ldots (2)$$

where

$$M = \frac{e}{\hbar c}\frac{\partial f^0}{\partial E_{\mathbf{k}}}(\mathbf{v} \times \mathbf{H}) \cdot \nabla_{\mathbf{k}},$$

$$X = \mathbf{v} \cdot \nabla_{\mathbf{R}} f^0 + \frac{e}{\hbar}\mathcal{E} \cdot \nabla_{\mathbf{k}} f^0,$$

$$B = \left(\frac{\partial f^0}{\partial E_{\mathbf{k}}}\right)\mathbf{v} \cdot \nabla_{\mathbf{R}},$$

$$L(\Phi) = \int P(\mathbf{k}, \mathbf{k}')\,[\Phi(\mathbf{R}, \mathbf{k}) - \Phi(\mathbf{R}, \mathbf{k}')]\,d\mathbf{k}'$$

$$= \Phi(\mathbf{R}, \mathbf{k})\,Q(\mathbf{k}) - \int P(\mathbf{k}, \mathbf{k}')\,\Phi(\mathbf{R}, \mathbf{k}')\,d\mathbf{k}' \qquad \ldots\ldots (3)$$

is the collision integral for the carriers. If the problem demands it (cf. cyclotron resonance), the partial time derivative of Φ may also be incorporated in this term. The other symbols in the equation carry their conventional meaning.

The transport equation is to be solved subject to the integral relation at the boundaries

$$\Phi(\mathbf{k}) = \int G(\mathbf{k}, \mathbf{k}')\,\Phi(\mathbf{k}')\,d\mathbf{k}'. \qquad \ldots\ldots (4)$$

This integral gives the distribution of the scattered particles in terms of the distribution of all incident particles.

The variational integral is next considered (eqn 5.2). The brackets denote integration over phase-space.

$$E(\Phi) \equiv \langle \Phi_-, L(\Phi_+) \rangle + \langle \Phi_-, M\Phi_+ \rangle + \langle \Phi_-, B\Phi_+ \rangle - 2\langle \Phi_-, X \rangle. \qquad \ldots\ldots (5)$$

The definition of Φ_- in terms of the solution Φ_+ of the original transport equation (2) is:

$$\Phi_-(\mathbf{R}, \mathbf{k}, \mathbf{H}) \equiv \Phi_+(\mathbf{R}, -\mathbf{k}, -\mathbf{H}).$$

(The extension of this definition to cyclotron resonance, where a time dependence also enters, is straightforward.)

The variation formulation yields the transport equation (2) on putting the first variation of $E(\Phi)$ equal to zero. Our concern is only with the second and third terms in $E(\Phi)$, so let us see whether or not the corresponding terms in (2) can be regained from the variational principle. Considering the variation of the second term we find

$$\langle \delta\Phi_-, M\Phi_+ \rangle + \langle \Phi_-, M\delta\Phi_+ \rangle = \langle \delta\Phi_-, M\Phi_+ \rangle - \langle \Phi_+, M\delta\Phi_- \rangle.$$

The equation holds good since, by the argument given by García-Moliner and Simons, the bracket suffers a change in sign (since M is an operator odd in $\mathbf{H}$) on changing the signs of both $\mathbf{k}$ and $\mathbf{H}$.

To proceed to our goal we should have to show that

$$\langle \Phi_+, M\delta\Phi_- \rangle + \langle \delta\Phi_-, M\Phi_+ \rangle = 0.$$

We shall in fact show that this result of the authors is *not* in general true, neither is the formula with B in place of M. On the other hand the same formula with

$M+B$ replacing M does indeed hold good. This conclusion is however not trivial and we shall have to prove it (§ 4).

3.2

Writing out the brackets in full, we find that

$$\langle \Phi_+^+, M\delta\Phi_-^- \rangle + \langle \delta\Phi_-^-, M\Phi_+^+ \rangle = \int\int d\mathbf{R}\, d\mathbf{k} \left\{ \Phi_+^+ \frac{e}{\hbar c} \frac{\partial f^0}{\partial E_\mathbf{k}} \mathbf{v}\times\mathbf{H} \,.\, \nabla_\mathbf{k} \delta\Phi_-^- + \delta\Phi_-^- \frac{e}{\hbar c} \frac{\partial f^0}{\partial E_\mathbf{k}} \mathbf{v}\times\mathbf{H} \,.\, \nabla_\mathbf{k} \Phi_+^+ \right\}$$

$$= \frac{e}{\hbar c} \int\int d\mathbf{R}\, d\mathbf{k}\, \nabla_\mathbf{k} \,.\, \left[\mathbf{v}\times\mathbf{H} \left(\frac{\partial f^0}{\partial E_\mathbf{k}} \right) \Phi_+^+ \delta\Phi_-^- \right]. \qquad \ldots\ldots (6)$$

This integral *would* be zero if the expression in the square bracket were to vanish on the boundary and if it *were* continuous throughout the region of integration. But with an applied magnetic field the distribution function will in general be discontinuous. In such circumstances the integral considered, far from being zero, will give an integral, over the whole surface of discontinuity (in $\mathbf{kR}$-space), of the discontinuities. Analogous arguments apply of course to the integral involving B as an operator.

§ 4. The Surfaces of Discontinuity

4.1

We inquire now what is the nature of the surface of discontinuity of the distribution function?

Let this surface be written as

$$S(\mathbf{R}, \mathbf{k}) = 0.$$

We shall now show that

$$(M+B)\, S(\mathbf{R}, \mathbf{k}) = 0$$

on the surface itself. (It can be verified that this is actually true for (1).)

It is best to start by showing that the discontinuities of Φ indeed form a *surface* in phase-space. We argue first of all that the discontinuities will be the loci (in phase-space) of collision-free trajectories of the carriers. To see this we consider equation (3). The first term on the right-hand side gives the probability per unit time of carriers being scattered out of their position $\mathbf{R}, \mathbf{k}$; this term cannot shift the position of the discontinuity in phase-space, it can only affect the magnitude of the jump. The second term in (3) gives the rate of scatter *into* a particular position: it is necessarily continuous, being an integral of the function $\Phi(\mathbf{R}, \mathbf{k})$ ($P(\mathbf{k}, \mathbf{k}')$ is supposed continuous) and cannot therefore influence the location of the discontinuities. It follows then that the collisions are irrelevant as to where the discontinuities are.

We consider now those carriers which just graze the physical boundary of the solid at some point. Such carriers mark the discontinuity of the distribution function at these boundary points and, by the foregoing, the subsequent collision-free trajectories will coincide with the discontinuities inside the solid. Now the contact of the grazing carriers with the boundary requires four parameters ($u_1 u_2 u_3 u_4$). Of these, two give the physical boundary surface of the solid; two more will give the starting values of the carrier velocity. (Only two parameters are necessary since, for grazing contact, the normal component of the velocity is zero.)

The points of the discontinuities in phase-space will therefore be given by

$$\mathbf{R} = \mathbf{R}(t, u_1, u_2, u_3, u_4),$$
$$\mathbf{k} = \mathbf{k}(t, u_1, u_2, u_3, u_4),$$

where the additional parameter t will describe the time of flight, say.

The elimination of the five parameters between the six quantities gives the equation for the hyper-surface of discontinuities, say,

$$S(\mathbf{R}, \mathbf{k}) = 0.$$

The total time derivative of S is also zero on $S=0$.

$$0 = \frac{d}{dt} S = (\dot{\mathbf{k}} \cdot \nabla_{\mathbf{k}} - \dot{\mathbf{R}} \cdot \nabla_{\mathbf{R}}) S = (M+B)S,$$

if we neglect terms of higher order than linear in the electric field. This is the result we strove to obtain.

4.2

It is easy to show now that

$$I \equiv \langle \delta\Phi^-, (M+B)\Phi^+ \rangle + \langle \Phi^+, (M+B)\delta\Phi^- \rangle = 0.$$

Proceeding as in § 3 we obtain

$$I \equiv \int\int d\mathbf{R}\, d\mathbf{k}\, (M+B)[\Phi_+ \delta\Phi^-].$$

Now the discontinuities of Φ^+, the surface $S_+ = 0$, satisfy $(M+B)S_+ = 0$. Since Φ^- differs from Φ^+ by interchanges which change the sign of $M+B$ as a whole, therefore the surface of discontinuities ($S_- = 0$) of Φ^- also satisfies

$$(M+B)S_- = 0.$$

This means that the linear differential operator $M+B$ always refers to a variation in a direction tangential to the surfaces of discontinuities of the product $\Phi \delta\Phi$, or, in other words, if S_+ or S_- be one of the curvilinear coordinates then $M-B$ may be exactly written as the derivative operator with respect to *another* of the set of coordinates. Consequently, the surface integral to which I may be transformed does not involve integration over the surface of discontinuities and will vanish as the boundary surface of **k**-space tends to infinity.†

This provides the justification of $E(\Phi)$ as the variational functional.

Acknowledgment

The value of discussions with Mr. G. Kalman is gratefully acknowledged.

References

Azbel, M. Ya., and Kaner, E. A., 1956, *J. Exp. Theor. Phys.*, **30**, 811.
Chambers, R. G., 1950, *Proc. Roy. Soc.* A, **202**, 378.
García-Moliner, F., and Simons, S., 1957, *Proc. Camb. Phil. Soc.*, **53**, 848.
Mattis, D. C., and Dresselhaus, G., 1958, *Phys. Rev.*, **111**, 402.
Sondheimer, E. H., 1952, *Phil. Mag. Suppl.*, **1**, 1.
Tauber, G. E., 1958, *Canad. J. Phys.*, **36**, 1308.

† We have here assumed that in an arbitrary variation of Φ, the surface of discontinuity is to stay fixed. Since this latter depends only on the geometry and the applied field, this assumption is strictly legitimate. What the violation of this assumption in a practical calculation means, is not our business to investigate here.

Some (t, p) Reactions in Light Nuclei

By A. A. JAFFE, F. de S. BARROS, P. D. FORSYTH, J. MUTO, I. J. TAYLOR and S. RAMAVATARAM

The Physical Laboratories, University of Manchester

MS. received 4*th May* 1960, *in final form* 9*th June* 1960

Abstract. The (t, p) reactions induced in the target nuclei ^{10}B, ^{12}C, ^{16}O and ^{27}Al have been investigated at an incident triton energy of 5·5 MeV. The angular distributions of the observed proton groups have been compared with a theory of double stripping and good agreement has been obtained with the theoretical predictions for transfers of 0, 1, 2 and (more tentatively) 3 units of orbital angular momentum.

A new level in ^{12}B at an excitation of 4·297 MeV is reported. Spin and parity assignments have been made for the levels of ^{14}C at excitations of 6·582 MeV (1^-), 6·725 MeV (probably 3^-), a hitherto unreported level at 7·009 MeV (0^+) and at 7·335 MeV (probably 2^-). The existence of levels in ^{18}O at 3·634 and 4·448 MeV has been confirmed and the spins and parities have been determined to be 0^+ and 3^- respectively. The spin and parity of the state in ^{18}O at 3·915 MeV excitation have also been determined as 2^+.

The behaviour of the $^{16}O(t, p)^{18}O$ reaction leading to the ground and first four excited states of ^{18}O has been found to be consistent with the ^{18}O configurations predicted by the intermediate coupling theory.

The atomic mass excess of ^{29}Al has been found to be $-9·647 \pm 0·015$ MeV and the excitations of forty-two new levels of ^{29}Al have been measured.

§ 1. Introduction

Published information about ^3He induced reactions is now steadily accumulating (e.g. Hinds and Middleton 1959 a, b, Forsyth *et al.* 1960, Taylor *et al.* 1960) and previous work on these reactions has recently been reviewed by Bromley and Almqvist (1960). Relatively little information has previously been available, however, about mass-3 reactions induced by tritium except in the lightest nuclei and at very low bombarding energies (cf. Ajzenberg-Selove and Lauritsen 1959).

The mechanism of tritium induced reactions is of considerable interest and, as will be seen, they can also become a useful tool in nuclear spectroscopy. Many nuclear states may be reached by them that have not previously been observed or studied in detail because of the absence of suitable alternative reactions; the (t, p) process described here may be particularly valuable in this respect since it is governed by exceptionally stringent selection rules. In the course of these experiments the (t, d) and (t, α) reactions on several of the target nuclei have also been investigated, and the results will be treated separately in subsequent papers.

§ 2. Experimental Techniques

Tritium ions were accelerated in the Manchester University Van de Graaff generator. Initially, 4 cm^3 of tritium (supplied by the Atomic Energy Research Establishment, Harwell) was mixed with 200 cm^3 of helium and beams of up to 0·4 μA of tritons were obtained on the target spot. This mixture provided about 25 hours running time. The gas pumped from the accelerator was collected and purified by absorption in activated uranium turnings at 150° C (Allen and Almqvist 1953). The remaining gas in contact with the uranium was presumed to be fairly pure helium but it possibly contained some tritium. A further 200 cm^3 of helium and 4 cm^3 of tritium were then added to this residual gas together with the tritium recovered by heating the uranium to 400° C. This second mixture provided a tritium beam for more than 70 hours and was still not completely exhausted. Unfortunately, the beam current at the target could not then be increased above 0·1 μA and was usually much less. Contamination of the beam with ^{3}He ions was estimated as less than 0·05%, though up to about 0·5% of singly ionized HD molecules was present especially in the second run.

The targets were evaporated on to backings of thin carbon foil. The thickness of the backings and targets were measured by an alpha-particle gauge and an accuracy to ~ 15% in the cross sections appears to be justified by the consistency of the results obtained from the same reactions in several targets of different thicknesses (for example, ^{12}C (t, p_0)^{14}C). The targets consisted of natural boron, carbon, silicon dioxide and aluminium respectively. The reaction products were analysed with a broad range magnetic spectrograph which has been described previously (Barros *et al.* 1959). In the case of the boron and carbon targets two different settings of the spectrograph field were required to cover the desired range of energies of the outgoing particles. The spectrograph was recalibrated with α-particles from ^{210}Po and ThC′ immediately before these experiments.

§ 3. Results

The peak differential cross sections for the observed (t, p) reactions leading to discrete final states were found to be, on average, lower than those of either the (t, d) or (t, α) reactions produced in the same targets.

^{10}B(t, p)^{12}B.

The ground state Q-value for the ^{10}B(t, p)^{12}B reaction was found to be 6·346 ± 0·006 Mev. States of ^{12}B were found at excitations of (i) 0·955, (ii) 1·673, (iii) 2·627, (iv) 2·73, (v) 3·393, (vi) 3·754, (vii) 4·297, (viii) 4·514, (ix) 5·00, (x) 5·612 and (xi) 5·724 Mev. With the exception of the fourth and ninth excited states the accuracy of the measured excitations is within ± 0·008 Mev. The level at 4·297 Mev has not been previously reported.

The fourth excited state group was observed only at the larger angles with an extremely low cross section of about 40 μb sterad^{-1}. The ninth excited state group was observed at 40° only; the measured excitation agrees with that previously reported but it is of low intensity and particularly difficult to observe because of its width, which was found to be very approximately Γ = 40 kev.

The widths of several other groups could be measured directly provided they were greater than about 20 kev. Thus, the widths of the levels at 3·754, 4·514 and 5·61 Mev were found to be Γ = 45, 50, and 145 kev respectively. The measured width of the level at 4·514 Mev, which is identified with that previously reported at 4·54 ± 0·02 Mev, is much smaller than that derived from observation of the resonances of the ^{11}B(n, n)^{11}B reaction (Bockelman *et al.* 1951).

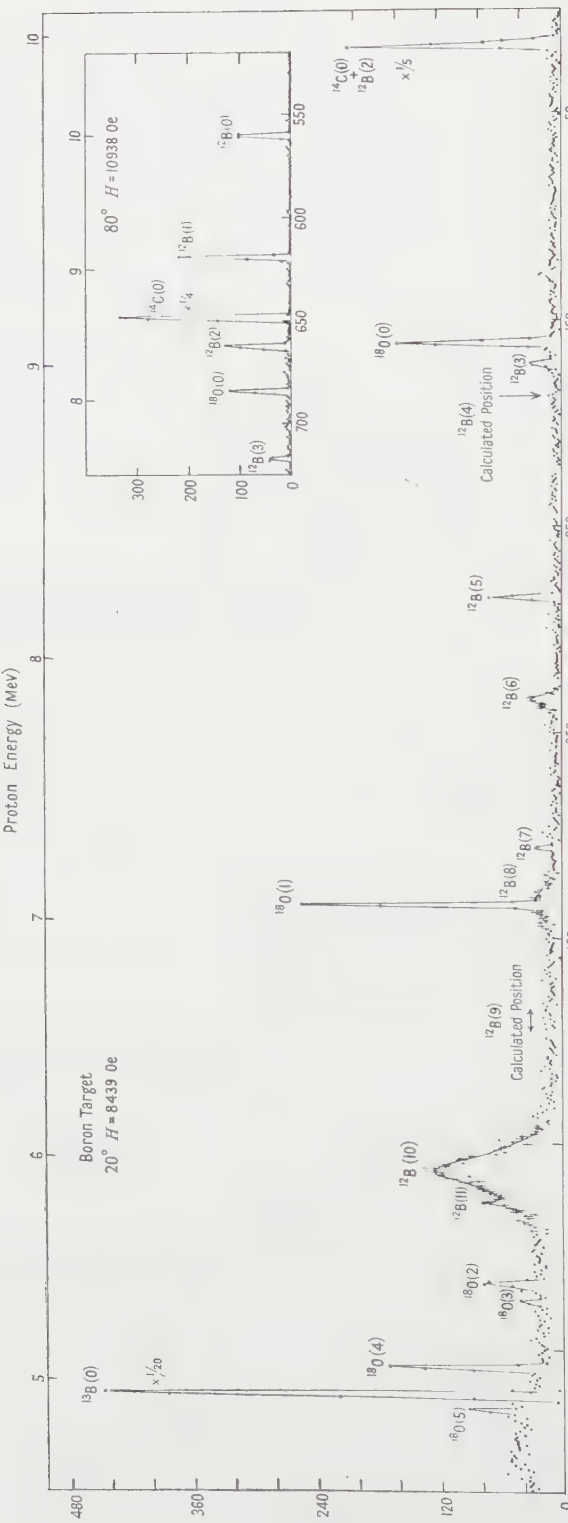

Figure 1. The proton spectrum (at an angle of 20° to the incident beams) from a natural boron target bombarded with 5·5 Mev tritons. The inset shows part of the proton spectrum obtained with the higher field setting.

Our result is obtained from the spectra at two angles where the proton group leading to this level was clear of the intense proton group from the $^{16}O(t, p)^{18}O$ reaction (which overlapped with it at some angles as it does, for example, in the 20° spectrum shown in figure 1). The effect of overlap with a large group would, of course, tend to *increase* the observed width. A proton continuum, attributed to the $^{10}B(t, pn)^{11}B$ reaction was present increasing in intensity with decreasing proton energy down to the lower limit of observation. ^{12}B is unstable against neutron emission at excitations above 3·36 Mev. The continuum does not vary rapidly in intensity with the angle of observation.

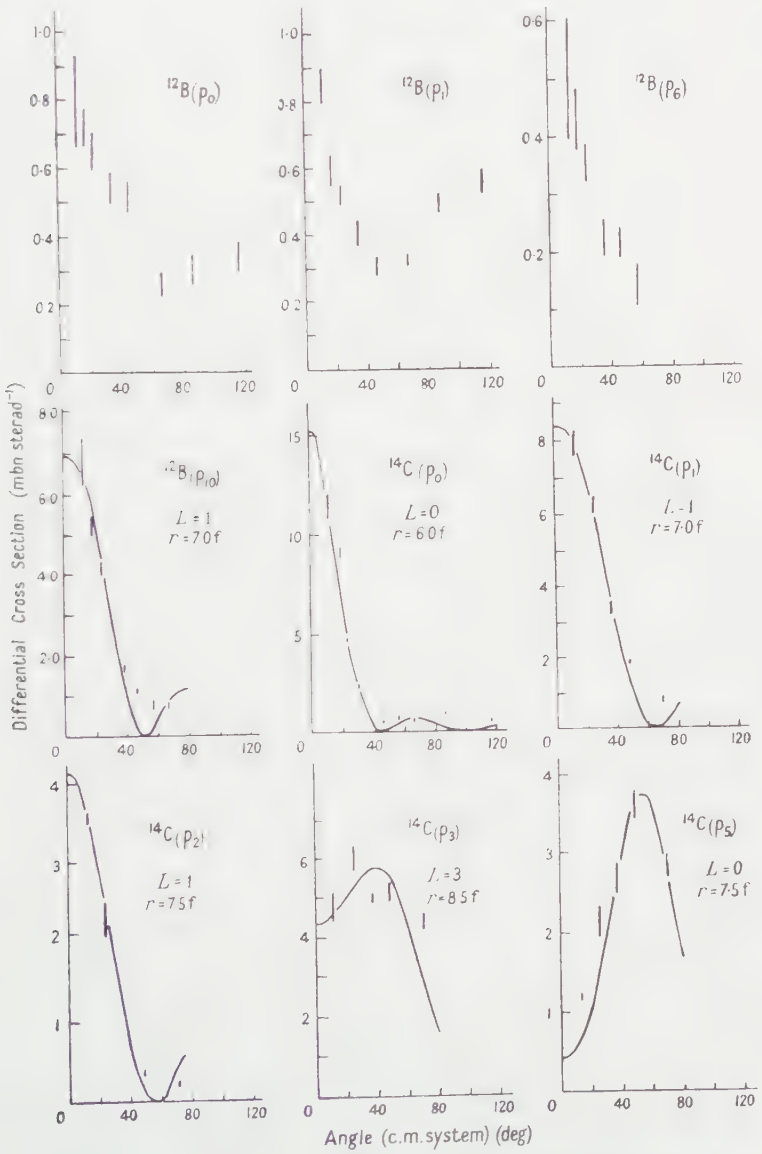

Figure 2. Angular distributions of some of the proton groups from the reactions $^{10}B(t, p)^{12}B$ and $^{12}C(t, p)^{14}C$. The curves shown are the calculated values of $j_L^2(kr)$.

The peak differential cross section of the $^{11}B(t, p_0)^{13}B$ reaction which has been described in a previous publication (Muto, Barros and Jaffe 1960) is very much larger than that of any from the $^{10}B(t, p)^{12}B$ reaction.

Angular distributions for the p_0, p_1, p_6 and p_{10} groups of the $^{10}B(t, p)$ reaction are shown in figure 2. The p_4, p_9 and p_{11} groups were too weak to yield reliable angular distributions and the p_2 group overlaps with the strong $^{12}C(t, p_0)$ group at angles below 40°. The maximum observed differential cross section for the p_2 group was 0·70 mbn sterad^{-1} (at 40°). The p_8 group overlaps at lower angles with that from $^{16}O(t, p_1)^{18}O$ but its cross section is approximately constant in the range of from 30° to 70° in the centre-of-mass system at about 0·25 mbn sterad^{-1}. The p_3 and p_5 groups are essentially isotropic in the range from 20° to 70° and they have differential cross sections of 0·20 and 0·45 mbn sterad^{-1} respectively, the p_7 group does not show a stripping pattern and reaches a maximum differential cross section of only 0·17 mbn sterad^{-1}.

$^{12}C(t, p)^{14}C$.

A proton spectrum from the $^{12}C(t, p)$ reaction at an angle of observation of 30° and at the lower field setting is shown in figure 3. The ground state proton group was observed in a series of exposures at higher magnetic fields. At the lower field settings a further six proton groups were observed, corresponding to excited states in ^{14}C at (i) 6·090, (ii) 6·582, (iii) 6·725, (iv) 6·893, (v) 7·009 and (vi) 7·335 MeV to within ± 0·010 MeV. The level at 7·009 MeV has not, apparently, been reported previously but the remainder are in good agreement with the accepted values.

The differential cross sections of the proton groups leading to the seven states of ^{14}C have been measured at a number of angles and the angular distributions are shown in figure 2, with the exception of the weak and relatively isotropic p_4 and p_6 groups, which have peak differential cross sections of only 0·4 and 0·3 mbn sterad^{-1} respectively.

$^{16}O(t, p)^{18}O$.

A proton spectrum obtained from the silicon dioxide target is shown in figure 4. No attempt has yet been made to analyse all the proton groups leading to levels of ^{30}Si which correspond to excitations in the approximate range of 7 MeV to 12 MeV. Levels in ^{18}O were observed corresponding to the ground state and to excitations of (i) 1·979, (ii) 3·552, (iii) 3·634, (iv) 3·915, and (v) 4·448 MeV (± 0·005 MeV). The levels at 3·634 and 4·448 MeV appear to correspond to those recently observed by Jarmie (private communication).

$^{27}Al(t, p)$.

The $^{27}Al(t, p)^{29}Al$ reaction was observed at nine angles in the range from 10° to 90° in the laboratory system. The proton spectra have been scanned across the whole width of the exposed plate at five angles (15°, 30°, 50°, 60° and 90°) but only partially at the remaining four angles. The 50° spectrum is shown in figure 5. Proton groups corresponding to transitions to the ground state and forty-two excited states of ^{29}Al were identified by the variation of energy of the protons with angle. The chance that any of the weak proton groups in the spectrum, although showing the correct angular energy variation, might be due to the $^{27}Al(^3He, p)^{29}Si$ resulting from ^3He contamination of the beam, seems negligible. This conclusion is based on intensity considerations (using values of

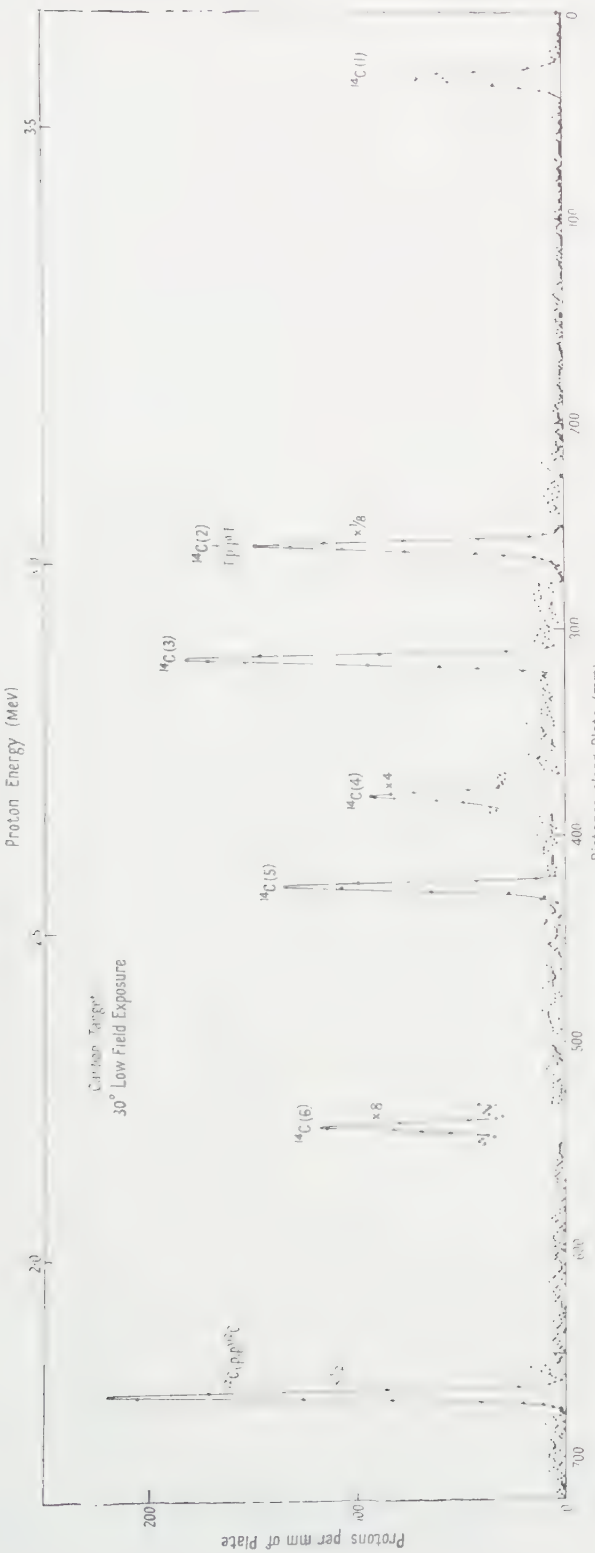

Figure 3. The proton spectrum (at an angle of 30° to the incident beam) from the carbon target bombarded with 5·5 MeV tritons.

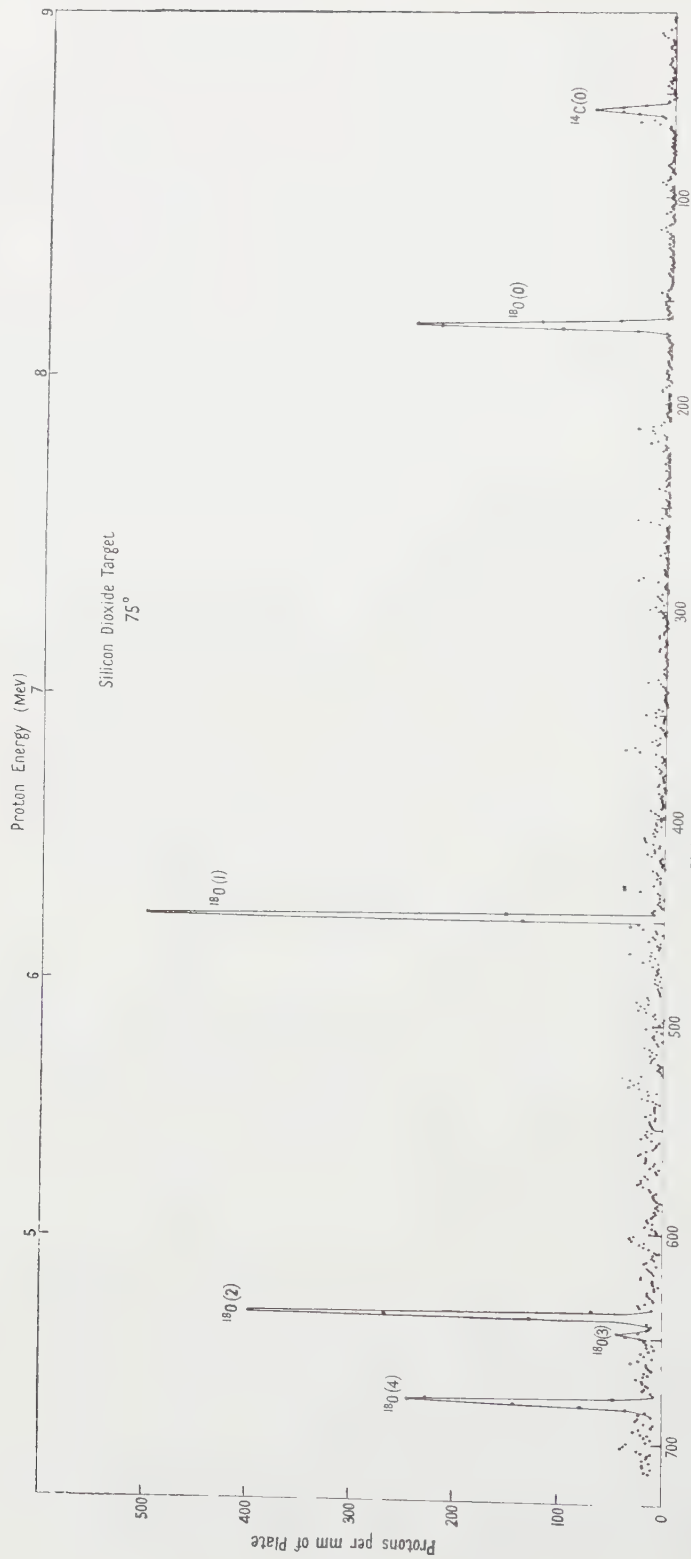

Figure 4. The proton spectrum (at an angle of 75° to the incident beam) from the silicon dioxide target bombarded with 5·5 Mev tritons. The group corresponding to the fifth excited state of ^{18}O is too low in energy to be observed on this spectrum; it is present however, on the spectrum shown in figure 1 originating from the oxygen present as an impurity on the boron target.

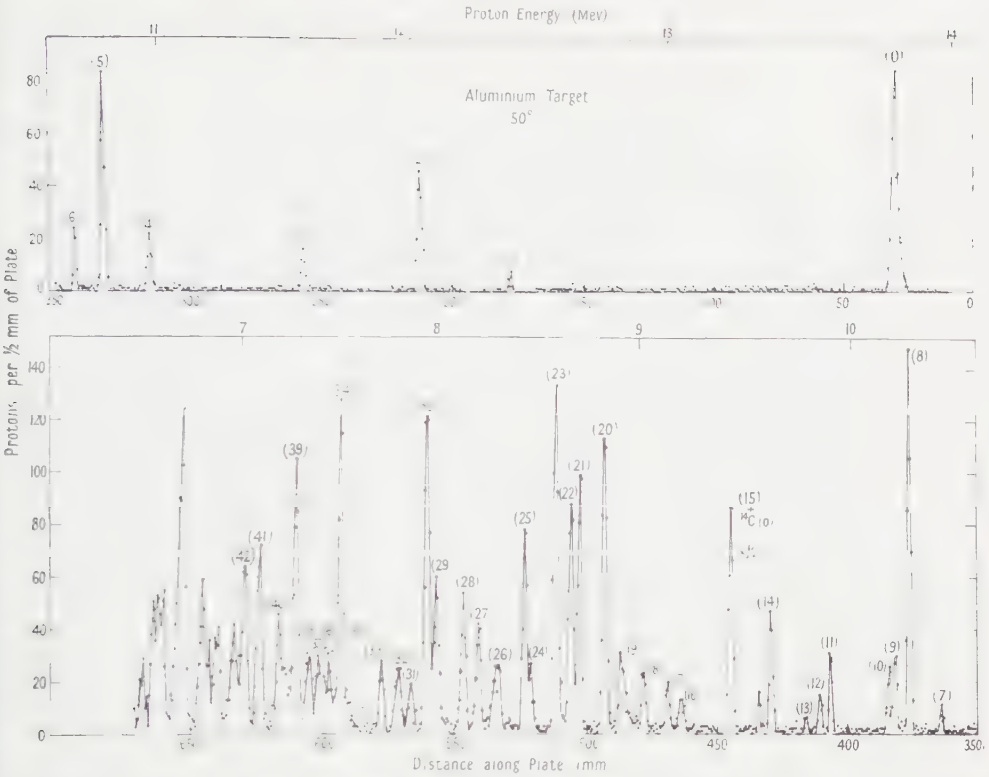

Figure 5. The 50° proton spectrum from the ^{27}Al target bombarded with 5·5 Mev tritons.

the ^{27}Al(^{3}He, p)^{29}Si cross sections which we had observed in previous experiments) and on a search for any groups at positions calculated for known levels in ^{29}Si. It thus appears certain, for example, that the weak p_1 group does not arise in this way. The energy resolution is 15–20 kev depending slightly on the position

Excitations of Levels of ^{29}Al

Level number	Excitation (Mev)	Level number	Excitation (Mev)	Level number	Excitation (Mev)
1	1·406	15	4·411 (4)	29	5·869
2	1·762	16	4·646 (3)[a]	30	5·916
3	2·334	17	4·716 (4)	31	6·002
4	2·875	18	4·846	32	6·063
5	3·071	19	4·939[a]	33	6·152 (4)
6	3·191	20	5·024	34	6·358
7	3·434	21	5·154	35	6·412 (4)
8	3·584	22	5·190	36	6·449 (3)
9	3·646 (4)	23	5·267	37	6·469 (3)
10	3·676 (4)	24	5·395 (3)	38	6·517
11	3·941	25	5·424	39	6·588
12	3·993	26	5·561[a]	40	6·674
13	4·064 (4)	27	5·654	41	6·758
14	4·228 (4)	28	5·732	42	6·840 (4)

Most of the levels were observed at five different angles, if not, the numbers in parenthesis indicate the number of angles at which they were identified.

[a] Levels suspected of having multiplet structure.

along the plate. The measured excitations of the levels of ^{29}Al are given in the table. These excitations were derived, in most cases, from observations at five angles, except in the region of the strong proton group from the ^{12}C(t, p_0) reaction which interfered with part of the spectrum (usually obscuring only one group from ^{29}Al). The relative position of this ^{12}C(t, p_0) group varies rapidly with angle. Some weaker groups at the lower energy end of the spectrum were also observed at fewer than five angles, as indicated in the table.

The beam energy was accurately determined at four angles of observation from the reaction ^{12}C(t, p_0)^{14}C, and from the relatively intense ^{27}Al(t, d_0)^{28}Al reaction. It was also derived from the energies of elastically scattered deuterons present in the beam as HD molecules. Good agreement was obtained, between the values of the beam energy derived in the above way using the accepted Q-values for the reactions.

The ground state Q-value for the ^{27}Al(t, p) reaction was then found to be $8{\cdot}678 \pm 0{\cdot}006$ MeV, a value which differs by about 300 kev from that obtained using the accepted mass excess for ^{29}Al ($-9{\cdot}35 \pm 0{\cdot}1$ MeV, Endt and Braams 1957). An accurate value of the atomic mass excesses of ^{29}Al may be found from our results using the known mass excesses for ^{27}Al ($-9{\cdot}219 \pm 0{\cdot}010$ MeV) and for the triton and proton (15·835 and 7·585 MeV respectively). Thus, the atomic mass excess of ^{29}Al was found to be $-9{\cdot}647 \pm 0{\cdot}015$ MeV.

The angular distributions of two of the many proton groups from this reaction are shown in figure 6. The angular distributions of the remaining groups require

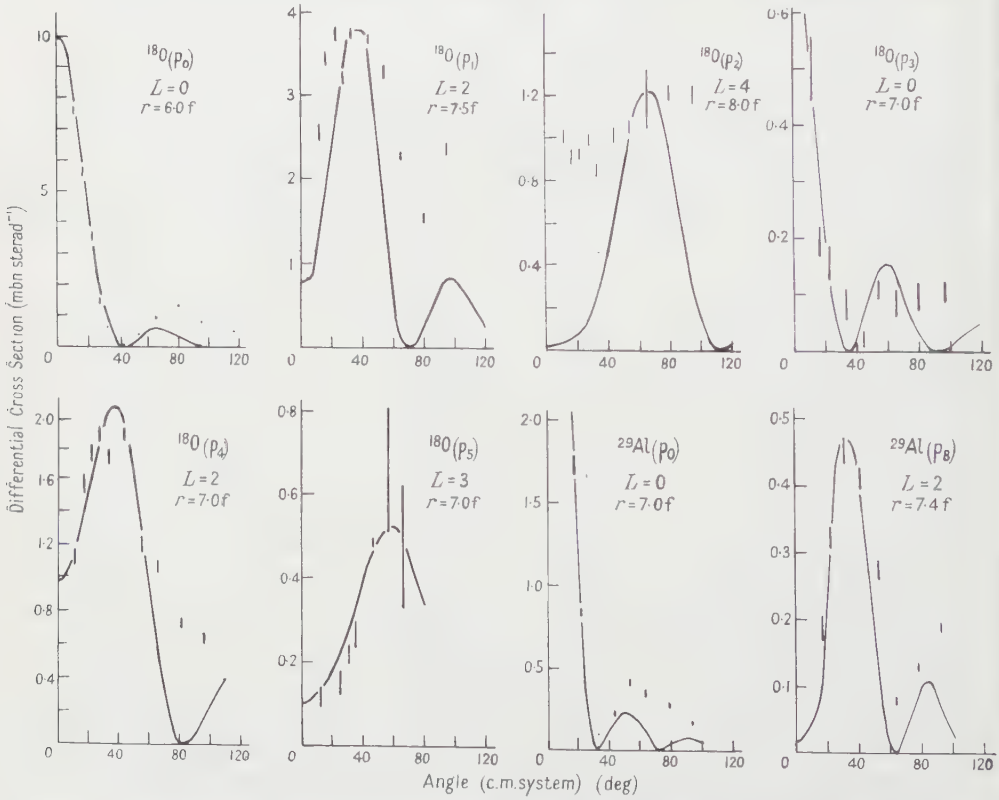

Figure 6. Angular distributions of some of the proton groups from the reactions ^{16}O(t, p)^{16}O and ^{27}Al(t, p)^{29}Al. The curves are the calculated values of $j_L{}^2(kr)$.

further analysis; but they appear in general to vary in intensity less rapidly with angle than the two shown.

§ 4. Discussion of Results

4.1. *Theory*

Recently Newns (1960) has developed a theory of double stripping using a method similar to that used by Bhatia *et al.* (1952) in the treatment of deuteron stripping. This theory may be applied to both (^{3}He ,p) and (t, p) reactions and the form of the angular distribution is essentially given by $\sum_L \alpha_L j_L^2(kr)$, where L is the total angular momentum transferred in the process. The selection rules which determine L are $\mathbf{J}_f = \mathbf{J}_i + \mathbf{L} + \mathbf{S}$; where S is the combined spin of the two captured nucleons. L must take even values if the initial and final states have the same parity and odd values if they have different parity. $L = \mathbf{l}_1 + \mathbf{l}_2$ where l_1 and l_2 are the orbital angular momenta of the two captured nucleons. For (^{3}He, p) reactions S may be 0 or 1 but in the case of (t, p) reactions S is restricted to 0 only. Thus, for the (t, p) reaction the selection rules are exceptionally restrictive compared with either (d, p) or (^{3}He, p) reactions. If the spin of either the initial or final states is zero, then at the most one value of L is possible and, if found, it uniquely determines the spin of the other state. A zero value of L indicates that the initial and final states have the same spins and parities. In contrast with the (d, p) or (^{3}He, p) reactions, some (t, p) stripping transitions would be completely forbidden, for example, between states one of which had zero spin and positive parity and the other even spin and negative parity. In transitions in which more than one L value is allowed, the relative values of the coefficients α_L depend on the configurations of the states involved.

4.2. *Transition to Ground States*

Particularly simple angular distributions with relatively large peak differential cross sections have been observed in the ground state transitions of ^{12}C(t, p)^{14}C, ^{16}O(t, p)^{18}O, ^{27}Al(t, p)^{29}Al (figures 2 and 6) and in the case of the previously published result for ^{11}B(t, p)^{13}B (Muto, Barros and Jaffe 1960). In all the above transitions a strong $L = 0$ transfer is indicated: this is the only value of L allowed by the selection rules for the transitions ^{12}C $\rightarrow$ ^{14}C and ^{16}O $\rightarrow$ ^{18}O using the known initial and final spins and parities (0^+ in both cases). The ground states of ^{27}Al and ^{29}Al have spin and parity $\frac{5}{2}^+$ (Endt and Braams 1957) and the results may be regarded as confirmation of this assignment for ^{29}Al. However, additional L values of 2 and 4 would be allowed by the selection rules in this case. The ^{11}B(t, p)^{13}B transition ($\frac{3}{2}^- \rightarrow \frac{3}{2}^-$) also has an additional allowed L value of 2.

The distinctive angular distributions and relatively large cross section which have been observed in these four ground state transitions suggest that the final nuclei (^{13}B, ^{14}C, ^{18}O, and ^{29}Al) have configurations consisting of a core composed of the target nucleus which is essentially undisturbed by the addition of the two neutrons stripped off the triton. The predominance of the $L = 0$ transfer which is observed in these transitions indicates that the orbital angular momenta of the two neutrons added to form the final nucleus (l_1, l_2) must be equal (and antiparallel, if they are greater than zero).

The ^{16}O(t, p)^{18}O angular distribution has been referred to in a previous publication (Jaffe, Taylor and Forsyth 1960); by comparing it with the known

angular distributions of the protons from the $^{16}O(^3He, p)^{18}F$ reaction the 1·044 MeV excited state of ^{18}F has been identified as the first $T=1$ state of that nucleus. In the (t, p) angular distribution the observed differential cross section falls to a strikingly low first minimum which is only 1/200 of the peak value. This indicates that direct reaction mechanisms are probably the only type which contribute significantly to the cross section. The second maximum is larger than that predicted by the square of the Bessel function $j_0^2(kr)$ and the discrepancy with the fit of this second maximum with theory would be even greater if the theoretical curve was multiplied by the form factor proposed by Newns. The size of the second maximum may be caused by partial absorption of the outgoing protons by interactions neglected in the Newns theory of double stripping; such effects have recently been reviewed in terms of a semi-classical model by Austern (1960).

In contrast to the ground state transitions discussed above, the $^{10}B(t, p)^{12}B$ angular distribution could not be fitted with the theory and the peak differential cross section is small; it is doubtful if double stripping contributes significantly to this reaction. This result may be a consequence of the relative configurations of the ^{10}B and ^{12}B ground states or alternatively to deficiencies in the theory. Macfarlane and French (1959), however, have been able to interpret the results of some (d, p) stripping data reasonably well in terms of *jj* coupling configurations of $(p_{3/2})^6$ and $(p_{3/2})^7 p_{1\,2}$ for ^{10}B and ^{12}B respectively, and on this assumption (t, p) stripping might be expected with $l_1=l_2=1$; $L=2$. This mechanism is not observed. Similar difficulties are also found for the $^{10}B(t, p)$ reaction leading to most of the excited states of ^{12}B.

4.3. *Transitions to Excited States*

$^{10}B(t, p)^{12}B$.

The $^{10}B(t, p)$ reaction is especially difficult to interpret because of the relatively complicated configuration of the target nucleus and the fact that the spins and parities of the first five excited states have not previously been determined by alternative methods. The measured differential cross sections leading to all the observed excited states except that at 5·612 MeV(p_{10}) are small and the angular distributions are not characteristic of double stripping. The p_{10} group, however, is strong and has an angular distribution which can be fitted with a curve for $L=1$, indicating that the level has negative parity (figure 2). The configuration of this level is perhaps relatively simply related to the ^{10}B ground state and may correspond to a ^{10}B core with two additional neutrons, one added to the p shell and the other entering either a 2s or 1d state.

$^{12}C(t, p)^{14}C$.

The first and second excited state groups of the $^{12}C(t, p)$ reaction have angular distributions which can both be fitted with theoretical curves having $L=1$ (figure 2). This value of L is the only one allowed for the transition to the first excited state which has the known spin and parity 1^-. The spin and parity of the second excited state of ^{14}C is determined unambiguously as 1^- from the observed angular distribution. The fifth excited state at 7·009 MeV, which has not previously been reported, can be fitted with a theoretical curve having $L=0$. Because of the low Q-value ($-2{\cdot}375$ MeV), the maximum of the experimental curve corresponds to the relatively low second maximum of the spherical Bessel function of zero order. Hence, this transition must be considered to be a relatively strong one. The

selection rules determine a spin and parity of 0^+ for this new level. This state could be identified with the state having the configuration $(p_{3/2})^{-2}$ having spin parity and isobaric spin 0^+; 1 discussed by Inglis (1953). It seems unlikely, however, that such a configuration would be strongly formed by $^{12}C(t, p)^{14}C$ double stripping since, assuming strong *jj* coupling for ^{12}C, considerable rearrangement of the ^{12}C nucleus would be required. Also, intermediate coupling calculations (Wilmore 1960, private communication) suggest that the lowest 0^- excited state of ^{14}C arising from the p^{10} configuration would have an excitation of at least 12 MeV. The observed result therefore suggests that the 7·009 MeV level is predominantly a $p^8d^2 + p^8(2s)^2$ configuration. Formation of the state by strong (t, p) stripping on ^{12}C would then be expected.

The $^{12}C(t, p_4)$ differential cross section is very small; if the spin and tentative parity assignment of 0^- is correct, (t, p) stripping is forbidden. The $^{12}C(t, p_6)$ group is also weak and almost isotropic; a spin of either 2 or 3 has been assigned to this level and it is known to have negative parity from the $^{13}C(d, p)^{14}C$ stripping reaction. A spin and parity of 2^- for this state would forbid (t, p) stripping and explain the observed result.

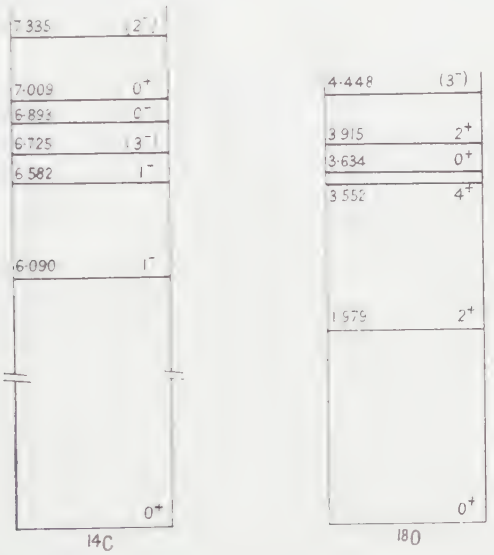

Figure 7. The level schemes of the nuclei ^{14}C and ^{18}O, summarizing the spin and parity assignments including data derived from the present results.

The p_3 group has been very tentatively fitted with a theoretical curve having $L = 3$, though a somewhat large radius has been used. The differential cross section is relatively large and stripping appears to be allowed. The spin and parity of the third excited state has previously been assumed to be either 2^- or 3^-; since (t, p) stripping on ^{12}C to this level would be forbidden if its spin and parity were 2^-, the large observed cross section and the shape of the angular distribution appears to indicate that 3^- is the most likely alternative. Improved angular distribution data over an extended range of angles are required, however, to confirm this result. The information obtained about the levels of ^{14}C and ^{18}O (see below) is summarized, together with the previously available data, in figure 7. States of spin and parity 3^- have been discussed in terms of collective octupole vibrations by Lane and Pendlebury (1959).

$^{16}O(t, p)^{18}O$.

The angular distributions of the p_1 and p_4 groups agree quite well with $j_2^2(kr)$ using $r = 7{\cdot}5$f and 7·0f respectively. The previously unknown spin and parity of the fourth excited state is therefore determined unambiguously by the selection rules as 2^+. An identical result is also obtained for the first excited state, already known to be 2^+. The peak differential cross sections for the transitions to the two states are roughly similar. The first excited state is expected to have configuration which is predominantly singlet ($^1D^{(dd)} + {}^1D^{(ds)}$) with an admixture of the triplet configurations $^3P^{(dd)}$, $^3F^{(dd)}$ and $^3D^{(ds)}$ as is also the fourth excited state.† (t, p) stripping should proceed to both these excited states to an extent depending on the proportion of the singlet states present in the configuration. Hence the fairly good $L = 2$ transfers and the roughly similar cross sections which are observed are in good agreement with the above assignments.

The spin and parity of the third excited state at 3·634 Mev is also determined by the observed angular distribution and is found to be 0^+. The peak differential cross section for the (t, p) reaction leading to this state is only one-fourteenth as large as that to the 0^+ ground state. The ground state configuration is very predominantly $^1S^{(dd)}$ whereas that of the 3·634 Mev state is chiefly $^1S^{(ss)}$. For the (t, p) stripping reaction the transition to the ground state which should proceed with $l_1 = l_2 = 2$ should be enhanced relative to that of the third excited state ($l_1 = l_2 = 0$) by a factor of five from purely statistical factors contained in the stripping theory. There is also a difference in the Q-values for these two transitions and in fact the products of the squares of the spherical Bessel functions $j_0^2(kr)$ (with the appropriate arguments) and the statistical factors are found to be quite closely proportional to the observed cross sections.

The known spin and parity of 4^+ of the second excited state of ^{18}O unambiguously predicts an $L = 4$ angular momentum transfer for formation of this state by double stripping of the triton. The differential cross section of up to 1·2 mbn sterad $^{-1}$ which is observed is somewhat larger than that of the weakest transitions discussed here, but there is no agreement between the angular distribution and the theoretical predictions. The double stripping theory of Newns, in its complete form, contains a series of terms in the expression for the angular distribution the first of which corresponds to the capture of two nucleons at the same point of the nuclear surface. The remaining terms are neglected when the single Bessel function is used. The terms of this series were computed, taking $l_1 = l_2 = 2$, $L = 4$, corresponding to the capture of two neutrons into d states to form the 4^+ level of ^{18}O. The summation of the series up to $n = 3$ was computed and it was found that the effect on the shape of the theoretical curve is negligible, so that the disagreement between the observed distribution and the theory cannot be accounted for by the neglect of such terms. However, the configuration of this 4^+ state is predominantly triplet ($^3F^{(dd)}$) though quite a large admixture of the singlet $^1G^{(dd)}$ should be present. In view of the fact that (t, p) stripping to the triplet configuration is forbidden and transitions involving large values of L should, in any case, be relatively weak, the absence of clear evidence of a stripping process is perhaps not surprising.

† The quoted configurations for the levels of ^{18}O are based on the intermediate coupling calculations of Elliott and Flowers (1955) which have recently been recomputed by D. Wilmore using a revised exchange mixture. The new spins and parities determined in this investigation are entirely consistent with the predictions of the theory.

The final group from the $^{16}O(t, p)^{18}O$ reaction is that leading to the fifth excited state at 4·448 MeV. The protons from this group were sufficiently energetic to fall within the observed spectra only at the smaller angles, though the relative cross sections at 40°, 50° and 60° could be obtained approximately from the boron exposures where ^{16}O was present as an impurity. The observations indicate an $L = 3$ transfer to this state and the spin and parity 3⁻ may be tentatively assigned to the level.

$^{27}Al(t, p)^{29}Al$.

Insufficient information is available about the levels of ^{29}Si at energies high enough to compare any levels of isobaric spin $T = \frac{3}{2}$ with the observed levels of ^{29}Al. The ground state spin and parity of ^{27}Al is $\frac{5}{2}^+$. The observed $L = 0$ stripping transfer to the ground state of ^{29}Al indicates that it may be formed by the simple addition of two neutrons with antiparallel spins and most probably these both enter the 2s shell. The angular distribution of the p_8 group also indicates some simple relationship between the configuration of this level and that of the ground state of ^{27}Al and that this level has positive parity. The relationship between the remaining levels observed in ^{29}Al and the ^{27}Al ground state is apparently more complicated.

§ 5. Conclusions

For all the observed (t, p) reactions in which reasonably large peak differential cross sections occur (i.e. $> \sim 1{\cdot}5$ mbn sterad^{-1}) angular distributions in agreement with the theory of double stripping have been obtained. Good agreement with theory is apparent in several cases involving orbital angular momentum transfers $L = 0$, 1, 2 and (more tentatively) $L = 3$. In all cases where the spins and parities of both the initial and final states were known from other data the expected value of L was obtained in the (t, p) reaction. The validity of the theoretical selection rules for (t, p) stripping has been established and the results suggest that where (t, p) stripping is forbidden, only relatively small differential cross sections (of less than $\sim 0{\cdot}5$ mbn sterad^{-1}) may be expected. Verification of the selection rules confirms that the two neutrons can only be stripped from the triton with antiparallel spins. The probability of (t, p) stripping may also be reduced because of unfavourable configurations of states of the initial or final nucleus (as for the $^{10}B(t, p)$ reaction). In such cases, failure of the angular distribution of the outgoing protons to conform with the predictions of the theory is observed, but such transitions have only small cross sections ($\sim 0{\cdot}5$ mbn sterad^{-1}).

Comparison of the observations with the theory can usually best be made using it in its simplest form (Newns 1960). There is evidence that inclusion of the proposed form factor would tend to reduce excessively the predicted relative cross section at the larger angles; also, our calculations have shown that the inclusion of the higher order terms of the more complete theory of Newns would not significantly change the predicted shape of the angular distribution (though the effect on the absolute cross section may not be negligible).

Acknowledgments

The authors wish to thank Professor B. H. Flowers, Dr. H. C. Newns and Mr. D. Wilmore for their helpful discussions concerning this paper.

References

Ajzenberg-Selove, F., and Lauritsen, T., 1959, *Nucl. Phys.*, **11,** 1.

Allen, K. W., and Almqvist, E., 1953, *Rev. Sci. Instrum.*, **24,** 70.

Austern, N., 1960, *Fast Neutron Physics*, Vol. 2 (New York: Interscience).

Barros, F. de S., Forsyth, P. D., Jaffe, A. A., and Taylor, I. J., 1959, *Proc. Phys. Soc.*, **73,** 793.

Bhatia, A. B., Huang, K., Huby, R., and Newns, H. C., 1952, *Phil. Mag.*, **45,** 485.

Bockelmann, C. K., Miller, D. W., Adair, R. K., and Barschall, H. H., 1951, *Phys. Rev.*, **84,** 69.

Bromley, D. A., and Almqvist, E., 1960, *Rep. Progr. Phys.*, **23,** 544 (London: Physical Society).

Elliott, J. P., and Flowers, B. H., 1955, *Proc. Roy. Soc.* A, **232,** 561.

Endt, P. M., and Braams, C. M., 1957, *Rev. Mod. Phys.*, **29,** 683.

Forsyth, P. D., Barros, F. de S., Jaffe, A. A., Taylor, I. J., and Ramavataram, S., 1960, *Proc. Phys. Soc.*, **75,** 291.

Hinds, S., and Middleton, R., 1959 a, *Proc. Phys. Soc.*, **74,** 762.

—— 1959 b, *Ibid.*, **74,** 775.

Inglis, D. R., 1953, *Rev. Mod. Phys.*, **25,** 390.

Jaffe, A. A., Taylor, I. J., and Forsyth, P. D., 1960, *Proc. Phys. Soc.*, **75,** 940.

Macfarlane, M. H., and French, J. B., 1959, *Rev. Mod. Phys.* **32,** 567.

Muto, J., Barros, F. de S., and Jaffe, A. A., 1960, *Proc. Phys. Soc.*, **75,** 929.

Lane, A. M., and Pendlebury, E. P., 1959, *Nucl. Phys.*, **15,** 39.

Newns, H. C., 1960, *Proc. Phys. Soc.*, **76,** 489.

Taylor, I. J., Barros, F. de S., Forsyth, P. D., Jaffe, A. A., and Ramavataram, S. 1960, *Proc. Phys. Soc.*, **75,** 772.

Gamma Radiation following Resonant Proton Capture by Chlorine

By J. C. LISLE† and P. F. D. SHAW

Clarendon Laboratory, Oxford

MS. received 10*th May* 1960, *in final form* 1*st June* 1960

Abstract. Eleven resonances have been observed in the yield of gamma radiation produced by the bombardment of chlorine with protons of energies between 500 and 1000 kev. These have been assigned to their parent isotopes either by the use of isotopically enriched targets or from the gamma rays emitted.

The decay schemes of six capture states of ^{36}A have been studied in detail and interpreted in terms of bound states at 1·97, 4·17, 4·45, 4·94, 5·85 and 6·85 Mev. Angular distribution measurements have confirmed that the spin of the 4·17 Mev level is 3; from the modes of decay, tentative spin and parity values have been assigned to some of the other levels.

§ 1. Introduction

Resonances in the yield of the Cl(p,γ)A reaction have been observed by Broström, Madsen and Madsen (1951) for proton bombarding energies between 500 and 2150 kev. In the range 500 to 1000 kev they ascribed resonances at 858 and 888 kev to radiative capture by ^{35}Cl. Towle, Berenbaum and Matthews (1957), using single counter and coincidence techniques, studied the γ-rays from resonances due to ^{36}A for incident proton energies of 855, 1484, 1510 and 1580 kev and proposed decay schemes involving bound states of ^{36}A at 1·95, 4·10 and possibly 4·90 Mev. The level at 1·95 Mev had been observed previously by Sperduto and Buechner (1955) from a study of the reaction ^{39}K(p,α)^{36}A. Angular distributions and angular correlations of the γ-rays from the 855 kev resonance (Berenbaum and Matthews 1957) indicated that the levels at 1·95 and 4·10 Mev were 2^+ and 3^- respectively.

^{38}A is known to possess excited states at 2·15 and 3·75 Mev with spins and parities 2 and 3 respectively (Endt and Braams 1957). Other levels have been found by Towle, Berenbaum and Matthews (1957) at 5·0 and 6·7 Mev from a study of the γ-rays from resonances in the ^{37}Cl(p,γ)^{38}A reaction at 1070, 1135, 1533 and 1725 kev bombarding energy.

§ 2. Experimental Methods

The proton beam was obtained from a 1·2 Mev Cockcroft Walton generator after separation from molecular ions by magnetic deflection. The voltmeter of the generator was calibrated by using the ^{19}F(p,$\alpha\gamma$)^{16}O resonances at 669, 831 and 873·5 kev. The proton beam was collimated by two $\frac{3}{16}$ in. diameter tantalum diaphragms 6 inches apart, so that all the beam hit the target which consisted

† Now at the Atomic Energy Research Establishment, Harwell, Didcot, Berks.

of evaporated barium chloride films supported on copper foil. Fluorine contamination was minimized by polishing the backing mechanically and by the use of 'specpure' barium chloride recrystallized from de-ionized water. Such targets withstood a power dissipation of 50 watts with little deterioration.

Excitation curves and single counter spectra were investigated with a scintillation counter which consisted of a 4 in. × 4 in. NaI(Tl) crystal (manufactured by the Harshaw Chemical Co.) mounted on an E.M.I. 6099A photomultiplier. The background count was reduced by 2 in. lead shielding. After amplification, the pulses from the photomultiplier were fed into a 75-channel pulse height analyser made by Sunvic Controls Ltd. The resolution of the spectrometer for the 0·662 Mev ^{137}Cs gamma ray was 9%.

The relative intensities of the gamma rays from a given resonance were obtained from spectra taken with the crystal 4 inches from the target; measurements were made at 0° and 90° with respect to the incident beam in order to reduce the effect of possible anisotropy of the γ-rays emitted. The ratio of the area under the full energy peak to that of the total was determined experimentally for the spectra of γ-rays of energy (Mev) 0·662 (^{137}Cs), 1·28 (^{22}Na), 2·14 (^{11}B(p, p′)^{11}B), 2·37 (^{12}C(p, γ)^{13}N), 2·62 (ThC″), 3·57 (^{9}Be(p, $\alpha\gamma$)^{6}Li), 4·43 (^{15}N(p, $\alpha\gamma$)^{12}C), 6·14 (^{19}F(p, $\alpha\gamma$)^{16}O), and 8·06 (^{13}C(p, γ)^{14}N). By using the total efficiency curves of Wolicki, Jastrow and Brooks (1956) a graph of the ratio of the full energy peak area to the intensity was plotted against the gamma-ray energy; similar graphs were constructed for the single and double escape peaks so that the relative intensities of gamma rays in a spectrum could be determined by using conventional subtraction techniques. The errors placed on relative intensity measurements were based on the scatter of points about the smoothed calibration curves; although they have no absolute significance, they serve to indicate approximately the relative magnitude of the errors due to cumulative subtractions.

The three-crystal pair spectrometer was of conventional design (Butler 1958), the centre crystal being a 1 in. × 1 in. cylinder, and the side crystals being 2 in. × 2 in. cylinders. The resolution for a 4·43 Mev γ-ray was 8·5%.

Coincidence measurements were made using two 4 in. × 4 in. NaI(Tl) spectrometers. The pulses from the first of these were fed to a single-channel pulse height analyser, the output of which opened a gate, of resolving time 2·5 μsec, which allowed the amplified pulses from the second crystal to pass to the multichannel analyser.

Angular distribution measurements were made with three 2 in. × 2 in. NaI(Tl) crystals mounted on a vertical ring so that the front surfaces of the crystals were 4 inches from the target which was situated on the centre of the ring. Two counters were held on either side of the beam at an angle of 145° so that their combined count was independent, to the first order of approximation, of movement of the beam. These counters were used to normalize the intensity of gamma rays recorded by a third counter whose angle relative to the beam was variable. Errors due to beam movement were reduced by performing short runs in which the third counter was moved alternately from one side of the beam to the other. The alignment of the system was checked by measuring the angular distribution of the 8·06 Mev gamma ray from the 550 kev resonance of the reaction ^{13}C(p, γ)^{14}N which is known to possess an anisotropy of only 1% (Broude *et al.* 1957); a small correction factor (< 2%) due to imperfect centring, was obtained and used to correct the measurements.

§ 3. Excitation Curves

By measuring the yield of gamma rays of energy greater than 1·28 Mev as a function of the beam energy, resonances from a natural chlorine target were found at 725, 736, 744, 769, 819, 824, 847, 861, 883, 890 and 896 kev; the uncertainty in beam energy in each measurements was ±5 kev, and the width of every resonance was less than 5 kev. Use of enriched isotopes showed that the resonances at 736, 819, 861 and 896 kev were due to ^{35}Cl, those at 725, 744, 769, 824 and 847 kev being attributed to ^{37}Cl. No assignments could be made for the resonances at 883 and 890 kev using enriched isotopes owing to the resonance at 873·5 kev from the reaction ^{19}F(p, $\alpha\gamma$)^{16}O, but the gamma-ray spectra, discussed later, have shown that both these resonances are associated with ^{35}Cl.

§ 4. Gamma Ray Spectra

4.1. 736 *and* 896 *keV Resonances*

The gamma rays observed from the 896 kev resonance, together with their relative intensities are given in table 1. Weak evidence for gamma rays of energy 1·00, 1·70, 2·20 and 3·50 Mev was also obtained; these might be associated with a cascade which is observed more strongly in other resonances to be discussed later.

Table 1

E_γ (Mev)	Relative intensity	E_γ (Mev)	Relative intensity
896 kev resonance		736 kev resonance	
7·35 ± 0·10	10·0 ± 0·8	9·20 ± 0·10	10·0 ± 0·5
4·90 ± 0·05	4·5 ± 0·4	7·20 ± 0·10	13·0 ± 1·0
4·45 ± 0·05	1·5 ± 0·5	4·75 ± 0·05	4·0 ± 0·5
2·50 ± 0·05	4·0 ± 0·5	4·45 ± 0·05	3·0 ± 1·0
1·97 ± 0·02	14·0 ± 1·5	2·50 ± 0·05	3·0 ± 0·6
		2·20 ± 0·03	—
		1·97 ± 0·02	16·0 ± 1·5
		0·77 ± 0·01	2·0 ± 1·0
861 kev resonance		819 kev resonance	
7·35 ± 0·10	2·2 ± 0·1	4·8 ± 0·1	2·2 ± 0·1
5·17 ± 0·05	20·0 ± 1·5	4·4 ± 0·1	0·8 ± 0·2
4·40 ± 0·05	6·3 ± 0·9	4·0 ± 0·1	1·5 ± 0·2
4·00 ± 0·10	1·5 ± 0·4	3·40 ± 0·05	3·3 ± 0·4
3·50 ± 0·05	4·0 ± 1·0	2·47 ± 0·03	10·2 ± 0·8
2·50 ± 0·05	6·2 ± 1·7	2·20 ± 0·03	8·3 ± 0·7
2·20 ± 0·03	26·0 ± 2·5	1·97 ± 0·02	12·8 ± 1·1
1·97 ± 0·02	28·0 ± 3·0	1·70 ± 0·05	4·1 ± 1·1
1·70 ± 0·05	6·1 ± 2·6	1·00 ± 0·01	4·9 ± 0·6
1·00 ± 0·02	3·7 ± 1·6	0·77 ± 0·01	3·3 ± 0·6
0·77 ± 0·01	7·7 ± 1·2		

The 1·97 and 7·35 Mev gamma rays were coincident, and are consistent with a cascade passing through the 1·98 Mev level. The value of the excitation energy of the capture state (9·32 Mev) agrees with the value (9·38 Mev) obtained from the known Q-value of the reaction (Endt and Braams 1957).

The 2·50 Mev gamma ray was coincident with either the 4·45 or the 4·90 Mev radiations which were themselves mutually coincident. This evidence, together

with that from the relative intensities, is consistent with a level at 4·45 MeV which is fed by the 4·90 MeV gamma ray and which decays either to the ground state, or to the 1·98 MeV level by emission of a 2·47 MeV gamma ray.

The gamma rays produced from the 736 kev resonance are given in table 1. The calculated excitation of ^{36}A for this resonance is 9·23 MeV and the 9·20 and 7·20 MeV gamma rays can be interpreted respectively as transitions to the ground and first excited states. The presence of 4·75, 4·40 and 2·50 MeV gamma rays suggests the existence of the same cascade as that found in the 896 kev resonance, and the change in energy of the 4·90 MeV quanta, found in the 896 kev resonance, to 4·75 MeV provides good evidence that these gamma rays are primary.

The 2·20 and 0·77 MeV gamma rays in the 736 kev resonance are characteristic of another cascade which features more strongly in the 861 kev resonance. This cascade is shown in figure 1 by broken lines. After allowance has been made for the intensity of a 4·3 MeV gamma ray appearing in this cascade, the ratio of the intensities of the 4·45 MeV to the 2·5 MeV gamma rays produced in the decay of the 4·45 MeV level is approximately 0·33, and compares reasonably with the ratio (0·38) found for the 896 kev resonance.

No coincidence measurements were feasible for the 736 kev resonance because of its low intensity.

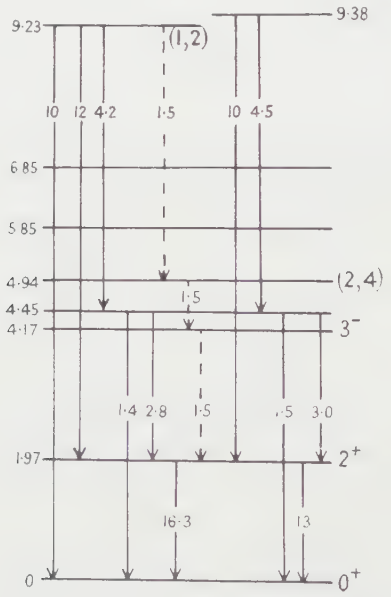

Figure 1. Decay scheme of ^{36}A; 736 and 896 kev resonances.

4.2. 861 *keV Resonance*

The gamma rays observed using a single counter are also shown in table 1. In order to confirm the interpretation placed on the complicated series of peaks between 2 and 6 MeV, this region was also examined by using a three-crystal pair spectrometer; in addition to those listed, a weak gamma ray of energy 4·2 MeV was also observed. These results agree broadly with those of Towle *et al.* (1957) except that the latter did not record gamma rays of energy 2·50, 1·70 and 1·00 MeV,

and also no gamma ray of energy 3·0 MeV was observed in the present experiments; the intensity of the latter, if present, was less than 30% of that of the 0·77 MeV gamma ray.

Coincidence measurements confirmed the 5·17–2·20–1·97 MeV and the 5·17–4·17 MeV cascades found by Towle *et al.*; these are consistent with the population of a level at 4·17 MeV which decays by emission of a 4·17 MeV gamma ray or by a 2·20–1·97 MeV cascade, to the ground state. The relative intensities of these two modes of decay are approximately 1 : 10 respectively.

The coincidence of the 4·40, 2·20, 1·97 and 0·77 MeV radiation confirms the presence of a level at 4·94 MeV proposed by Towle *et al.* No evidence was found for the 3·0 MeV gamma ray reported by these authors.

Owing to the complexity of the spectrum it was not possible to make any conclusions regarding the 1·00 and 2·50 MeV gamma rays observed in this resonance, but it was established that the 3·50, 1·70, 2·20 and 1·97 MeV radiations were mutually coincident. The decay scheme for this resonance is shown in figure 2; the transitions corresponding to the 4·0, 3·50, 2·50, 1·70 and 1·00 MeV gamma rays are discussed in the following section.

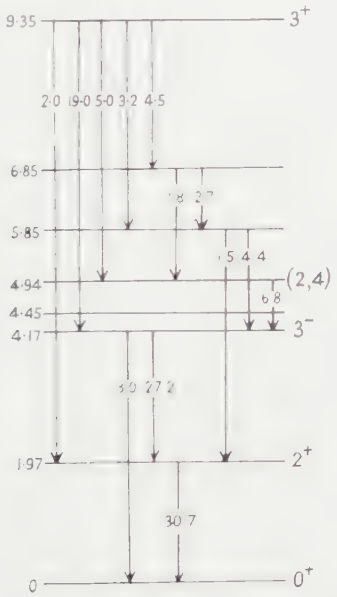

Figure 2. Decay scheme of ^{36}A; 861 kev resonance.

4.3. 819 *keV Resonance*

In table 1 are also listed the gamma rays and the relative intensities found. No 4·17 MeV gamma ray was observed, but the results from the 861 kev resonance showed that this must be present with an intensity of approximately 10% of that of the 2·20 MeV radiation.

The 3·40, 1·70, 2·20 and 1·97 MeV radiations were coincident and were consistent with a cascade passing through the 4·17 MeV level, the primary gamma ray being either that of energy 3·40 or 1·70 MeV. Coincidences were also found between the 2·47, 1·00, 1·70, 2·20 and 1·97 MeV gamma rays so that it appears that the level responsible for the emission of the 3·40 MeV gamma ray may also decay

by the emission of a 2·47–1·00 MeV gamma-ray cascade. Intensity considerations preclude the possibility that the 1·70 MeV radiation is primary, so that the capture state must decay by the emission of a 3·40 MeV gamma ray to the level at 5·85 MeV. A careful comparison of the energy of the 2·5 MeV radiation in this and the 861 keV resonance showed that there was a small energy shift corresponding to the change in excitation of the capture state, so that the 2·5 MeV gamma ray is probably primary and leads to a level at 6·85 MeV. The 1·00, 1·97 and 4·0 MeV gamma rays were mutually coincident and the latter probably corresponds to a transition from the 5·85 MeV level to that at 1·97 MeV.

The 0·77 MeV radiation was coincident with the 1·97, 2·20 and 2·47 MeV gamma rays but not with those of energy 1·00, 1·70, 3·50 and 4·00 MeV. Since the 0·77 MeV gamma ray is associated with the decay of the level at 4·94 MeV (see § 4.2), the latter must be populated by a transition, or a cascade, from the 6·85 MeV level. The energy difference between these levels is 1·90 MeV; no gamma rays could be found whose energy sum was equal to this, but it was concluded that a 1·9 MeV gamma ray might exist and that it was not observed owing to the proximity of the 1·97 MeV gamma ray. Examination of single-counter spectra under large expansion failed to show any broadening of the peak at 1·97 MeV when compared with that from the 896 keV resonance. However, the 1·97 MeV peak in the spectrum coincident with the 0·77 MeV gamma ray showed both an enhancement and a broadening when compared with that in the 1·00 MeV coincidence spectrum, the widths of the 2·20 and 2·47 MeV peaks remaining exactly the same in both spectra. A similar broadening was found when the spectra coincident with the 2·20 and 1·70 MeV radiations were compared, the width being greater in the former case; the other peaks in these spectra remained the same, thus eliminating the possibility of instrumental drift. In all cases the broadening was consistent with that expected had a gamma ray of energy less than 1·97 MeV been present, and a transition from the 6·85 to the 4·94 MeV levels may be inferred.

The 4·8 and 4·4 MeV radiations were too weak to study by coincidence methods, but it is possible that they are associated with a cascade through the 4·45 MeV level discussed earlier; in this case, part of the observed intensity of the 2·47 MeV radiation would be required to allow for the decay of this level to that at 1·97 MeV. The complete decay scheme, with tentative transitions denoted by broken lines is shown in figure 3. It should be noted that the intensities required to populate and de-excite the 5·85 MeV level are not in good agreement.

4.4. 883 *and* 890 *keV Resonances*

The principal features of the 883 keV resonance were a ground state transition and one to the first excited state having an intensity of approximately 15% that of the ground state transition. There was weak evidence for a cascade proceeding through the 5·85 MeV level.

The spectrum from the 890 keV resonance only showed gamma rays of energy 7·53 and 1·97 MeV corresponding to a transition to the first excited state. An upper limit of 5% was placed on a direct ground state transition.

4.5. ^{38}A *Resonances*

Very little information has been obtained from the ^{38}A resonances owing to their weak intensities which precluded coincidence measurements.

The principal characteristics of the 724 and 744 kev resonances were gamma rays of energy 2·15 and 1·6 Mev corresponding to the de-excitation of the first and second excited states. The lack of any clearly resolved gamma rays of higher energy implies that the decay scheme is complex.

The main features of the 769 kev resonance were gamma rays of energy 8·75, 7·15, 2·15 and 1·6 Mev which indicated transitions through the first and second excited states. The spectrum from the 847 kev resonance was similar, except that no 7·15 Mev gamma ray was observed. In both resonances a 4·0 Mev gamma ray was prominent, but no other gamma rays could be assigned as its cascade partners.

The energies of the principal gamma rays from the 824 kev resonance were 10·90, 8·75 and 2·15 Mev, indicating transitions to the ground and first excited states. The presence of 1·60 Mev radiation showed that the second excited state was also populated.

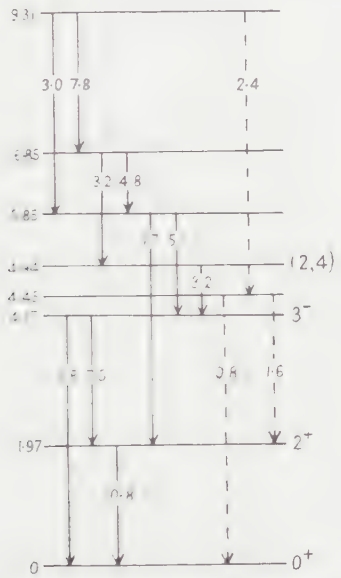

Figure 3. Decay scheme of ^{36}A; 819 kev resonance.

§ 5. Angular Distribution Measurements

5.1. 736 *keV Resonance*

The capture state of the 736 kev resonance decays predominantly to the ground and first excited states of ^{36}A (figure 1). The ground state is known to be 0^-, and from the systematics of even–even nuclei, the first excited state will most probably be 2^-. If it is assumed that the transitions to these are dipole or electric quadrupole, the capture state must be 1^+, 1^- or 2^+.

Owing to the weak intensity of the resonance it was not possible to determine the angular distributions of the 9·2 or 7·25 Mev gamma rays with accuracy and their relative distribution was therefore measured and found to be

$$W_{9\cdot2}/W_{7\cdot25}=1-(0\cdot06\pm0\cdot02)P_2.$$

This result was consistent with a 1^- state produced by p-wave interaction, if a value of t^2 (the ratio of the intensity in channel spin 1 to that in channel spin 2)

equal to 13·7 was chosen; this value of t^2 can be greatly reduced by a small contribution from f-wave excitation. Alternatively the 1^+ or 2^+ states, resulting from the capture of s-waves with a small ($< 1\%$) admixture of d-wave could also account for the observed distribution. No final conclusions regarding the capture state can therefore be made.

5.2. 861 *keV Resonance*

The angular distributions of the 7·35, 5·15, 4·40, 2·20 and 1·97 MeV gamma rays were measured and corrected for the finite angle subtended by the movable counter. The distribution of the 7·35 MeV gamma ray was made at 0°, 45° and 90° only because of its weak intensity. The accuracy of the final result for this gamma ray is poor owing to the accumulation of fluorine impurity in the target and the consequent increase of background radiation.

To reduce the number of theoretical distributions to be compared with those found, the following assumptions were made:

(i) The 1·97 MeV level has spin and parity 2^+.

(ii) The spin of the 4·17 MeV level cannot exceed 4, since a transition from this level to the ground state of spin zero was observed in coincidence with the primary gamma ray feeding this level, using a resolving time of 2·5 μsec.

(iii) The principal contribution to the orbital angular momentum cannot be greater than f-wave. Towle *et al.* have observed that the quantity $\omega\Gamma_p\Gamma_\gamma/(\Gamma_p+\Gamma_\gamma)$, where ω is a statistical weighting factor, is 1·2 ev. For g-wave, and higher orbital momentum interactions, this quantity would need to be at least an order of magnitude smaller to be consistent with the Wigner limit.

(iv) The 5·15 MeV gamma ray must be dipole or electric quadrupole, since for magnetic quadrupole and higher multipolarities the observed width would again be too great.

In the analysis of the angular distributions, the possibility of an admixture of electric quadrupole radiation was always considered in cases where magnetic dipole transitions were allowed. Allowance was also made for interference effects between the primary in-going proton wave and waves carrying two more units of angular momentum.

Table 2

Gamma-ray energy (MeV)	Angular distribution	
	Observed	Theoretical
7·35	$1+(0{\cdot}01\pm0{\cdot}10)P_2$	$1-0{\cdot}22P_2+0{\cdot}45\delta P_2+\delta^2(1+0{\cdot}08P_2-0{\cdot}11P_4)$
5·15	$1+(0{\cdot}28\pm0{\cdot}01)P_2$	$1+0{\cdot}26P_2$
4·45	$1-(0{\cdot}26\pm0{\cdot}06)P_2+(0{\cdot}04\pm0{\cdot}06)P_4$	$1-0{\cdot}09P_2-0{\cdot}90\delta P_2+\delta^2(1-0{\cdot}19P_2+0{\cdot}03P_4)$
2·20	$1-(0{\cdot}19\pm0{\cdot}01)P_2$	$1-0{\cdot}16P_2$
1·97	$1+(0{\cdot}21\pm0{\cdot}01)P_2$	$1+0{\cdot}23P_2+0{\cdot}01P_4$

δ is the E2/M1 mixing ratio

The measured angular distributions are shown in the second column of table 2. The interpretation of the angular distributions of the 1·97 and 2·20 MeV gamma rays has been made by assuming that the 4·17 MeV level is fed predominantly by

the 5·15 MeV gamma ray; theoretical distributions of the succeeding gamma rays were rejected only if their signs were different from those observed experimentally, and little attention was paid to the magnitude of the anisotropy coefficients which might be modified by the weaker cascades feeding the 4·17 MeV level.

The 5·15, 2·20 and 1·97 MeV gamma-ray angular distributions are most easily satisfied with a 4·17 MeV level of spin 3 and a capture state of spin and parity 2^-, 3^-, 3^+ or 4^-. However the observed anisotropy of the 7·35 MeV gamma ray is too small to satisfy the cases involving a capture state of 2^-, 3^- or 4^-. A spin value of 2 for the 4·17 MeV level with a capture state of 3^+ gave agreement which, although by no means good, was just acceptable in view of the alternative modes of feeding the 4·17 MeV level. The observed decay scheme, involving a much stronger transition to the 4·17 MeV level than to the first excited state, favours the assignment of spin 3 to this level.

The 4·17 MeV level is therefore assigned a spin of 3, and the capture state is most probably a 3^+ level. The best theoretical angular distributions for this case are obtained with a value of the channel spin parameter of unity and with pure d-wave excitation and are shown in the third column of table 2. The E2 to M1 mixing parameter for the 7·35 MeV transition has been left undetermined in the table.

From its mode of decay, it is possible that the 4·94 MeV level could be of spin 4 with even parity. The measured angular distribution was consistent with this if a value of δ (the E2 to M1 mixing parameter) of $+0{\cdot}2$ was assumed (using the sign convention of Sharp *et al.* 1954). However, a spin value of 2 was also consistent with this distribution and the assignment of 4^+ is therefore tentative.

§ 6. Discussion

While the analysis of angular distributions gives no definite information about parities, save that of the capture state, the fact that the experimental data could be satisfied without introducing any quadrupole term into the 5·15 and 2·20 MeV transitions suggests that these may both be electric dipole. In this case the 4·17 MeV level is an odd parity state analogous to the 3·73 MeV second excited state of ^{38}A. Lane and Pendlebury (1960) have recently discussed the existence of 3^- states of a collective nature in even–even nuclei, and the excitation of the present level appears to follow the trend of others in this mass region.

If the 4·17 MeV level is 3^-, certain anomalous features in the decay scheme of ^{36}A may be explained on the assumption that isotopic spin selection rules are still valid in this mass region. Wilkinson (1956) has predicted that the first level of unit isotopic spin will be at 6·06 MeV, lower levels having $T=0$. The electric dipole transition between the 4·17 and 2·20 MeV levels should therefore be forbidden. The intensity of the E3 cross-over transition from the 4·17 MeV level to the ground state is 10% of the E1 transition, which is therefore strongly retarded. This can be partly accounted for by an enhancement of the E3 transition owing to its collective nature. If the speed of the E3 transitions in ^{16}O and ^{40}Ca are taken as typical (Lane and Pendlebury 1960), a value of $|M^2|$ of 10 for such transitions appears reasonable; comparison with the observed intensities gives a value of $|M^2|$ of 10^{-5} for the E1 transition, a nuclear radius of $1{\cdot}2A^{1/3}$ fermi being assumed. Comparison with the best values of $|M^2|$ for allowed E1 transitions (Wilkinson 1957) indicates that the width is reduced by a factor of the order of 10^{-3} and that the inhibition is at least as great as any reported for the lightest nuclei. Such an

explanation would be consistent with the absence of a similar E3 transition in ^{38}A (Myers and Wattenburg 1949) where isotopic spin selection rules are inoperative.

Barrier considerations make it improbable that the spin of the capture state of the 819 kev resonance exceeds 4, and direct transitions to the low lying levels should occur readily. The absence of such transitions and the predominant population of levels of high excitation might also be explained by the operation of isotopic spin selection rules. The assignment of the 5·86 Mev level as the first state with $T=1$ is in agreement with the predictions of Wilkinson (1956), and possibly provides further confirmation of his observation that the first $T=1$ level in alpha-like nuclei often has a lower excitation than that calculated. By analogy with ^{36}Cl, this level should have spin and parity 2^+. Such an assignment is consistent with the decay of this level and with its mode of population providing that the capture state has $T=0$ and spin 1, 2 or 3 with odd parity. However such an interpretation gives rise to considerable difficulty in choosing any spin, parity and isotopic spin quantum numbers for the 6·85 Mev level which are consistent with its observed modes of excitation and decay.

The ratio of the excitations of the 4·45 and 1·97 Mev levels is approximately 2·2, and is consistent with the interpretation that the two levels are the first and second excited states of a vibrational spectrum (Scharff-Goldhaber and Weneser 1955). Further, the 4·94 Mev state may be the 4^- member of the vibrational second excited band, but the modes of decay of these states are not in good accord with such an interpretation.

Acknowledgments

We are grateful to Professor D. H. Wilkinson for a number of helpful discussions, and to Dr. R. E. Meads for his help and kindness on several occasions. One of us (J.C.L.) is indebted to the Ministry of Education for a maintenance grant.

The separated targets were supplied by the Atomic Energy Research Establishment, Harwell.

References

Berenbaum, R., and Matthews, J. H., 1957, *Proc. Phys. Soc.* A, **70,** 445.
Broström, K. J., Madsen, B. S., and Madsen, C. B., 1951, *Phys. Rev.*, **83,** 1265.
Broude, C., Green, L. L., Singh, J. J., and Willmott, J. C., 1957, *Phil. Mag.*, **2,** 1006.
Butler, J., 1958, *Thesis*, Oxford University.
Endt, P. M., and Braams, C. M., 1957, *Rev. Mod. Phys.*, **29,** 683.
Lane, A. M., and Pendlebury, E. D., 1960, *Nucl. Phys.*, **15,** 39.
Myers, V., and Wattenburg, A., 1949, *Phys. Rev.*, **75,** 992.
Scharff-Goldhaber, G., and Weneser, J., 1955, *Phys. Rev.*, **98,** 212.
Sharp, W. T., Kennedy, J. M., Sears, B. J., and Hoyle, M. G., 1954, Atomic Energy Report No. CRT-556.
Sperduto, A., and Buechner, W. W., 1955, M.I.T. Laboratory for Nuclear Science, Progress Report 30th November, 1955.
Towle, J. H., Berenbaum, R., and Matthews, J. H., 1957, *Proc. Phys. Soc.* A, **70,** 84.
Wilkinson, D. H., 1956, *Phil. Mag.*, **1,** 1031.
—— 1957, *Proceedings of the Rehovoth Conference on Nuclear Structure* (Amsterdam: North-Holland).
Wolicki, E. A., Jastrow, R., and Brooks, F., 1956, N.R.L. Report 4833.

Lattice Absorption Bands in Indium Antimonide

By S. J. FRAY, F. A. JOHNSON and R. H. JONES
Royal Radar Establishment, Great Malvern, Worcs.

MS. received 2nd June 1960, in final form 5th July 1960

Abstract. A series of detailed measurements of the absorption spectrum of high quality single crystals of n-type indium antimonide has been made in the wavelength range 15 to 130 μ, and over the temperature range 4·2 to 90°K.

Some new absorption bands have been found, and an explanation is offered for the positions and temperature dependence of all the principle absorption peaks in terms of multiple phonon interactions involving phonons with energies corresponding to temperatures of 259, 224, 169 and 62°K.

§ 1. Introduction

The lattice absorption bands of indium antimonide were investigated by Spitzer and Fan (1955) in the wavelength range 5 to 115 μ; they found four bands at 28·2, 30, 52 and 95 μ respectively. These bands arise from the direct interaction of infra-red radiation with phonons in the crystal lattice. The strongest of such interactions in indium antimonide is the absorption of a photon and the emission of a single long wavelength optical phonon. Spitzer and Fan have clearly demonstrated that the very strong band at 52 μ in indium antimonide is due to this process. The remaining absorption bands which are weaker arise from multiple-phonon interactions, but no detailed interpretation of these has yet been offered.

Lax and Burstein (1955), and more recently Mashkevich and Tolpygo (1957), investigated theoretically the polarization induced in atoms when they are displaced from their equilibrium positions during elastic vibrations. In diamond type crystals with filled valence bands, the electric moment M can be expressed as a power series in the atomic displacement by an equation of the form

$$M = \sum_{\alpha} A^{\alpha} + \sum_{\alpha,i} x_i^{\alpha} B_i^{\alpha} + \sum_{\substack{\alpha,\beta \\ i,j}} x_i^{\alpha} C_{ij}^{\alpha\beta} x_j^{\beta} + \ldots\ldots$$

where x_i^{α} is the displacement of the atom of type α in the ith unit cell, and A^{α}, B^{β}, and $C^{\alpha\beta}$ are in general tensors of the 1st, 2nd and 3rd rank respectively. The constant term does not give rise to any optical processes, but the remaining terms lead to interactions between photons and phonons. In particular, the linear term results in single-phonon interactions and the quadratic term results in two-phonon interactions. In all these interactions, the energy E' and the wave vector $\mathbf{k}'$ of the photon must be conserved, thus

$$E' = \sum_{p} \pm E_p$$

$$\mathbf{k}' + n\mathbf{K} = \sum_{p} \pm \mathbf{k}_p$$

where E_p and $\mathbf{k}_p$ are the energy and wave vector of the pth phonon (positive for emission and negative for absorption), $\mathbf{K}$ is any reciprocal lattice vector, and n is any integer, positive or negative including zero. Since the wave vectors of photons are very much smaller than the wave vectors of phonons, the second equation can be written as

$$n\mathbf{K} = \sum_p \pm \mathbf{k}_p.$$

The particular forms these equations take for one-, two- and three-phonon interactions are set out in the first two columns of table 1.

Table 1

Energy dependence	Wave vector dependence	Temperature dependence
	Single-phonon interactions	
$E_1 = E'$	$\mathbf{k}_1 = 0$	$(1+F_1)-F_1$
	Two-phonon interactions	
$E_1+E_2=E'$	$\mathbf{k}_1+\mathbf{k}_2=0$	$(1+F_1)(1+F_2)-F_1F_2$
$E_1-E_2=E'$	$\mathbf{k}_1-\mathbf{k}_2=0$	$(1+F_1)F_2-F_1(1+F_2)$
	Three-phonon interactions	
$E_1+E_2+E_3=E'$	$\mathbf{k}_1+\mathbf{k}_2+\mathbf{k}_3=0,\pm\mathbf{K}$	$(1+F_1)(1+F_2)(1+F_3)-F_1F_2F_3$
$E_1+E_2-E_3=E'$	$\mathbf{k}_1+\mathbf{k}_2-\mathbf{k}_3=0,\pm\mathbf{K}$	$(1+F_1)(1+F_2)F_3-F_1F_2(1+F_3)$
$E_1-E_2-E_3=E'$	$\mathbf{k}_1-\mathbf{k}_2-\mathbf{k}_3=0,\pm\mathbf{K}$	$(1+F_1)F_2F_3-F_1(1+F_2)(1+F_3)$

E' = photon energy; E_1, E_2 = phonon energies;
$\mathbf{k}_1$, $\mathbf{k}_2$ = phonon wave vectors; $\mathbf{K}$ = reciprocal lattice vector;
$F_1 = 1/[\exp(E_1/kT)-1]$.

Each of these interactions has its own characteristic temperature dependence. The net absorption is equal to the difference between the forward process—the absorption of a photon and the emission and absorption of phonons—and the reverse process—the induced emission of a photon and the absorption and emission of phonons. For every phonon emitted there is a temperature dependent factor $1+F$, where $F=1/[\exp(E/kT)-1]$, and for every phonon absorbed there is a temperature dependent factor F associated with the interaction. The specific form of the temperature dependence of one-, two- and three-phonon interactions is set out in column three of table 1. At the lowest temperatures only those interactions involving the emission of phonons (summation bands) will be observed. The remaining interactions involving the absorption of one or more phonons (difference bands) will not become appreciable until the temperature becomes comparable with E/k for the absorbed phonon.

The equations in table 1 indicate that multiple-phonon interactions will result in band spectra, since there would, in general, be a range of phonon energies and wave vectors which could satisfy the appropriate equations. The main contribution from a particular branch of the vibration spectrum will be from the region where the density of states for this branch is a maximum. Since this occurs when the energy is varying least rapidly with wave vector, one would expect the greater part of the contribution from this branch to be concentrated within a relatively narrow energy range. It follows that the more sharply defined the maxima in the density of states, the more sharply defined will be the resulting absorption maxima, and the more nearly will the

energies of the phonons producing the peak absorption become characteristic of the particular branches involved. It also follows that if the energies of the phonons producing an absorption peak are characteristic of the branches involved, then the temperature dependence of this peak will also be characteristic of the phonon branches.

In general the maxima in the density of states tend to occur for wave vectors nearer the edge of the reduced zone, and thus one would expect the characteristic phonon energies associated with lattice absorption peaks to be close to the energies of phonons near the edge of the reduced zone.

Recently an analysis of the lattice absorption bands of silicon in terms of characteristic phonon energies has been published (Johnson 1959), and although these characteristic energies were completely at variance with the values of phonon energies deduced from the fine structure in the absorption edge (Macfarlane *et al.* 1958), they were subsequently confirmed by the neutron scattering results of Brockhouse (1959). In particular the energies for the fundamental Raman frequencies agree to within 0·3%. In order to attempt a similar analysis for indium antimonide it was necessary to make a careful redetermination of the positions and temperature dependences of the lattice bands of this material.

§ 2. Experimental

In order to cover a sufficiently wide wavelength range, the measurements were made with three different spectrometers. For the first set of measurements two indium antimonide specimens approximately 4·5 mm and 1·5 mm thick were cut from a single crystal of n-type material (carrier concentration approximately $5 \times 10^{14}\,\mathrm{cm}^{-3}$) and mechanically polished. The transmission coefficients of these specimens were measured as a function of wavelength over the range 15 to 31 μ, and over the temperature range 20 to 90°K. The measurements were made with a double monochromator using KBr and CsBr prisms for the appropriate parts of the spectrum. The method has been described previously (Johnson 1959) and the curves shown in figures 1 and 2 are the best values obtained from approximately 100 000 readings taken during the course of the experiment.

For the second set of measurements a specimen approximately 1·1 mm thick was cut from a single crystal of n-type material (carrier concentration approximately $2{\cdot}5 \times 10^{13}\,\mathrm{cm}^{-3}$) and mechanically polished. Its transmission coefficient was measured as a function of wavelength over the range 24 to 78 μ, and over the temperature range 20 to 291 K. These measurements were made with a Leiss monochromator fitted with a brass echelette grating as the main dispersing element in an arrangement similar to that described by Fray and Oliver (1959). This grating was ruled with 10 lines per mm, and blazed for 80 μ in the first order; it was used in first order in the range 40 to 78 μ, and in second order in the range 24 to 40 μ. The details of this spectrometer and its associated optical system will be described by one of us (R. H. J.) elsewhere.

For the third set of measurements, two specimens approximately 4·5 mm and 1·2 mm thick were cut from a single crystal of n-type material (carrier concentration approximately $4 \times 10^{14}\,\mathrm{cm}^{-3}$) and mechanically polished. The shape of their transmission curves was measured at 4·2 K over the wavelength range 90 to 130 μ. These measurements were made with the spectrometer and

photodetector described by Fray and Oliver (1959). The brass echelette grating used, was ruled with 7·16 lines per mm, and blazed for 140 μ in the first order.

The indium antimonide specimens were placed in the helium Dewar directly in front of the photodetector, and could be moved into or out of the optical path as required. Although this arrangement is very convenient experimentally, it suffers from the disadvantage that the specimen filters out some of the background radiation falling on the photodetector, thereby altering its sensitivity. It follows that this equipment is suitable for determining relative transmission curves only.

§ 3. Results

The results obtained with the first spectrometer in the range 15 to 31 μ are shown as absorption coefficient, plotted against wave number in figures 1 and 2. In figure 1 only the 90°K curve is shown. The 77°K and 20°K curves were very similar, but the extreme weakness of the bands prevented the accurate determination of the temperature variation. When measuring weak absorption bands the relative accuracy of points on a given curve is usually much greater than their absolute accuracy, since the latter depends on the reflection correction used. Figure 2 shows the two strong bands between 26 and 31 μ. Here the 90°K curve is shown complete, and the 77 and 20°K curves are shown where these differ appreciably from the 90°K curve. In addition, the 20°K curve has been displaced towards *smaller* wave numbers by 1·0 cm^{-1} in order to bring the three curves into alignment.

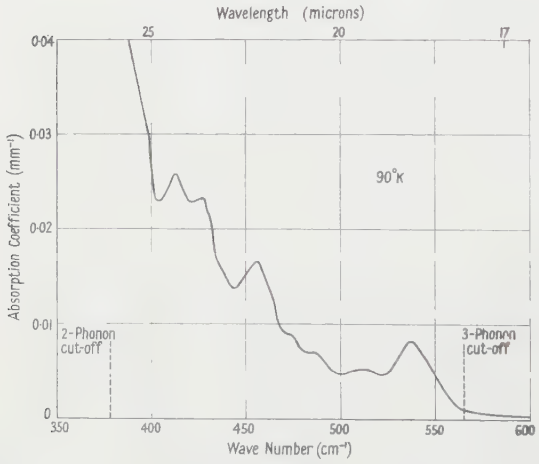

Figure 1. Absorption coefficients for indium antimonide in the range 600 to 350 cm^{-1}.

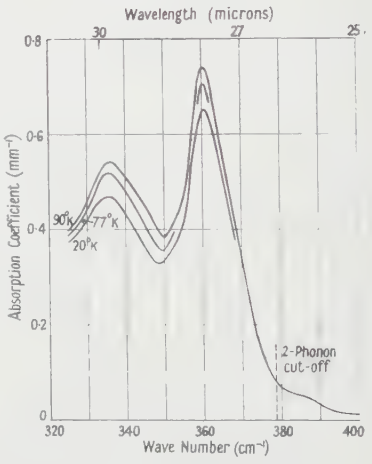

Figure 2. Percentage transmissions for indium antimonide in the range 400 to 320 cm^{-1}.

The results obtained with the second spectrometer in the range 24 to 78 μ are shown as percentage transmission of a 1·11 mm sample plotted against wave number in figure 3. At room temperature the transmission is zero between 128 and 230 cm^{-1} and at higher wave numbers the transmission is shown by the 291°K curve. No attempt was made to calculate the absorption coefficient

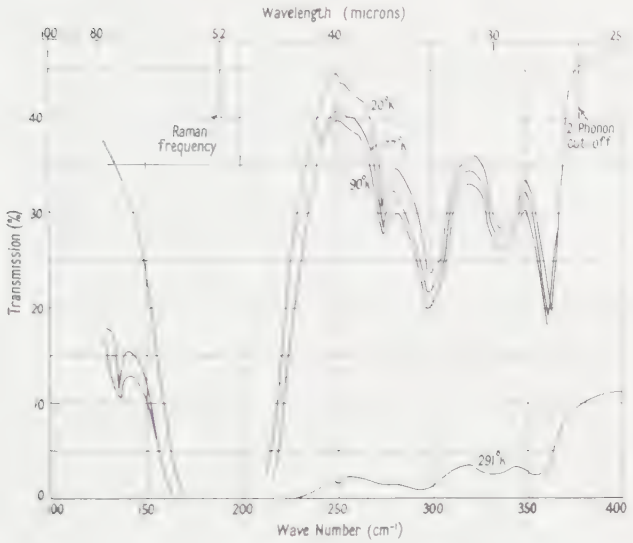

Figure 3. Absorption coefficients for indium antimonide in the range 400 to 100 cm^{-1}.

in this range because of the difficulty of estimating the reflection correction to be applied near the strong reflection band at 52 μ.

The results obtained with the third spectrometer in the range 90 to 130 μ are shown as the transmission in arbitrary units of the 4·5 mm sample only, plotted against wave number in figure 4. The curve shown is the mean of five

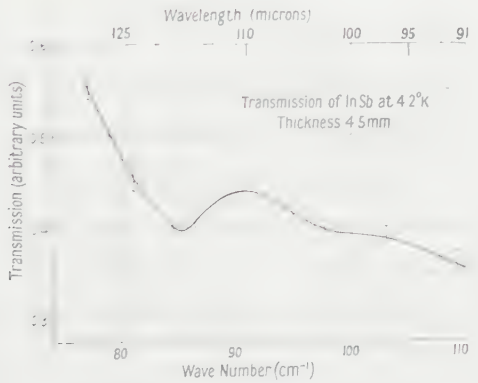

Figure 4. Transmission of indium antimonide in the range 110 to 80 cm^{-1}.

separate determinations, and the maximum deviations from the mean curve are indicated by the short vertical lines on the curve. The results obtained with the 1·2 mm sample were very similar except, of course, that the absorption band centred on 85·5 cm^{-1} was very much weaker, and was not significantly greater than the uncertainty of the individual points. This result indicates that the 85·5 cm^{-1} band cannot be due to the absorption of stray second-order radiation in the 52 μ band. The band shown by Spitzer and Fan at 95 μ was not found.

An examination of the temperature dependence of the bands in figures 1 to 3 shows that, with the exception of the band at 136 cm^{-1} all the bands are summation bands. Since the fundamental Raman frequency corresponds approximately to 190 cm^{-1} (52 μ), one would expect all two-phonon summation bands to lie below 380 cm^{-1}, and all three-phonon summation bands to lie below 570 cm^{-1}. Thus the very weak bands shown in figure 1 are probably three-phonon summation bands and the stronger bands shown in figures 2, 3 and 4, two-phonon bands—except of course the single-phonon band at 190 cm^{-1}. The relative strengths of the two sets of bands lend support to this view. A more detailed interpretation of the individual bands will now be given.

§ 4. Discussion

One would expect the highest energy phonon band at 538 cm^{-1} to be a summation band of the three highest energy phonons, to which we shall give the arbitrary label TO. The corresponding two-phonon bands at 360·5 cm^{-1} should be a summation band of two TO phonons. This would require the characteristic temperature of the TO phonons to be 258°K in the first case, and 259°K in the second. For the two-phonon band an independent check is provided by the temperature dependence which should be given by the expression $(1+F_1)^2-F_1^2$, where $F_1=1/[\exp(259/T)-1]$. The relevant information is set out in table 2, and it will be seen that there is good agreement between the calculated and observed values.

The probable assignment of the remaining bands is shown in table 2 along with the calculated and observed temperature dependences. It will be seen that again the agreement between the observed and calculated temperature dependence is good.

We shall now consider the polarizations which can probably be assigned to the four different characteristic phonons. The zinc-blende lattice of indium antimonide is very similar to the diamond lattice of silicon apart from the absence of spatial inversion symmetry. Thus one would expect that, as in silicon, the two transverse optic branches (and the two transverse acoustic branches) would be degenerate in the symmetry direction 111 and 100, but unlike silicon, there would be an energy gap in all directions between the longitudinal optic and acoustic branches in indium antimonide. Further, on the basis of the classical dispersion theory of ionic crystals (Born and Huang 1954), one would expect that, if the bonding in indium antimonide is partially ionic, then the longitudinal optic branch will have a higher energy at $\mathbf{k}=0$ than the transverse optic branches, the difference being dependent on the effective ionic charge.

The maxima in the density of states for the transverse optic and transverse acoustic branches will be closely associated with one or other of the two symmetry directions because of the degeneracy in these directions, and this in turn would account for the fact that only four different phonons are found. We therefore conclude that the two lower energy phonons are acoustic and the two higher energy phonons are optic phonons, and in addition the 169°K phonon is longitudinal acoustic, and the 62°K phonon is transverse acoustic. The assignment of the polarizations of the two optic phonons is less straightforward. In a purely homopolar crystal such as silicon the longitudinal optic branch lies below the transverse optic branch except at $\mathbf{k}=0$, where the three optic

Table 2. Assignment of Absorption Peaks and Comparison of Theoretical and Experimental Values for Temperature Dependence

(1)		(2)			(3)	(4)		
ν(cm^{-1})	$h\nu/k$ (°K)	20°K	77°K	90°K		20°K	77°K	90°K
538	775		—		TO+TO+TO 258+258+258	1	1·17	1·19
513	738		—		TO+TO+LO 258+258+222	1	1·14	1·23
488	702		—		TO+LO+LO 258+222+222	1	1·17	1·27
475	684		—		TO+TO+LA 258+258+168	1	1·21	1·33
456	656		—		LO+LO+LO 219+219+219	1	1·20	1·31
					or TO−LO+LA 258+222+176	1	1·23	1·35
426	614		—		LO+LO+LA 222+222+170	1	1·26	1·41
413	594		—		TO+LA+LA 258+168+168	1	1·32	1·49
360·5	519	1	1·08	1·13	TO+TO 259+259	1	1·07	1·12
336	484	1	1·10	1·15	TO+LO 259+225	1	1·09	1·15
297	428	1	1·14	1·25	TO+LA 259+169	1	1·16	1·24
274	394	1	1·17	1.26	LO+LA 225+169	1	1·18	1·27
136	196	0	0·8	1	TO−TA 259−63	0·06	0·83	1
85·5	123				TA+TA 62+62			

(1) Position ; (2) relative intensity (observed) ; (3) suggested assignment and characteristic temperatures ; (4) corresponding relative intensity (calculated). T = transverse, L = longitudinal, O = optic, A = acoustic. Three-phonon cut-off 815°K = 3 × 272°K ; two-phonon cut-off 544°K = 2 × 272°K.

branches become degenerate, while in an ionic crystal such as sodium chloride, the longitudinal optic branch lies entirely above the transverse optic branch. Now the situation in indium antimonide must be intermediate between these two extremes, and it would be reasonable to assume that the longitudinal optic branch lies above the transverse optic branch at $\mathbf{k}=0$, but falls below it at the zone boundary. If this is the case then the 259°K phonon is transverse optic, and the 225°K phonon is longitudinal optic. Further, since the two transverse optic branches are degenerate in the symmetry directions, the maximum in the density of states for these branches will be greater than the maximum for the longitudinal optic branches, and thus one would expect the intensity of the lattice band due to three transverse optic phonons to be stronger than that due to two transverse and one longitudinal optic phonon. This is clearly seen to be the case in figure 2.

The final point we shall consider is the values at $\mathbf{k}=0$ of the frequencies of the longitudinal (ω_l) and transverse (ω_t) optic branches. Assuming that these frequencies are higher than those at the zone boundary, one would expect that the absorption on the high-energy side of purely optical phonon bands would tend to zero at frequencies given by the appropriate combination of ω_l and ω_t. For example, one would expect the band due to two transverse optic phonons to have a high-frequency limit $2\omega_t$, while the band due to a transverse and longitudinal optic phonon would have a high-frequency limit of $(\omega_l+\omega_t)$. In practice, because the experimental curve is the sum of these various contributions, extrapolations are only possible for the highest energy two- and three-phonon bands. The high-frequency limits of the 360·5 and 538 cm^{-1} bands are 378 and 566 cm^{-1} respectively. As these bands are attributed to two and three transverse optic phonons respectively, one concludes that the fundamental Raman frequency ω_t, is equivalent to 189 cm^{-1} between 77 and 90°K. Further, if ω_l is greater than ω_t, then the bands at 336 and 513 cm^{-1} should have a higher limiting frequency than the two bands just discussed. This should show up as a change in slope and it will be seen that there is a change in slope on the high-frequency side of both the 360·5 and 538 cm^{-1} bands very near the high-frequency limits just discussed. If this change in slope is due to a frequency difference ω_l and ω_t, then one can estimate roughly the maximum value of this difference consistent with the experimental curves, and in both cases this maximum frequency difference is found to be equivalent to 8·0 cm^{-1}. This result would indicate that the maximum value for ω_l is 197 cm^{-1}, and that $(\omega_l/\omega_t)=1{\cdot}04$.

The internal consistency of the results shown in table 2 is very satisfactory and we shall now consider what external evidence there is for their correctness. The relatively very low energy of the transverse acoustic branch would suggest that a pronounced anomaly should be found in the specific heat curve at low temperatures. By making a simple comparison with the calculation of the specific heat of germanium from neutron scattering results (Johnson and Lock 1958, Phillips 1959) one concludes that the Debye temperature curve for indium antimonide should show a pronounced minimum at 12·5°K. Phillips has quoted some unpublished results of Keesom and Pearlman indicating that such a minimum is found at approximately 12°K.

The value estimated for the Raman frequency (ω_t) can be compared with values deduced from reflection measurements. If the classical dispersion

theory for ionic crystals is applicable, then the dielectric constant is related to ω_1 and ω_t by the equations

$$\epsilon(\omega) = \epsilon_\infty + \frac{\epsilon_0 - \epsilon_\infty}{1 - (\omega/\omega_t)^2 - i(\omega/\omega_t)(\gamma/\omega_t)}$$

and

$$\epsilon_0/\epsilon_\infty = (\omega_1/\omega_t)^2$$

where $\epsilon(\omega)$ is the dielectric constant at the frequency ω, ϵ_0 and ϵ_∞ are the low-frequency (static) and high-frequency (infra-red) dielectric constants, and $(\gamma\ \omega_t)$ is an arbitrarily introduced damping constant. Spitzer and Fan found that at 78°K the maximum reflectivity occurred at 52 μ and that $\epsilon_0 = \epsilon_\infty$ within the limits of experimental error. They concluded from this that the maximum value for $\epsilon_0 - \epsilon_\infty$ was 1·5, and from the shape of the reflection curve they found that γ/ω_t was approximately 0·04. For small damping constants Havelock (1924) has shown that the frequency of the maximum reflectivity (ω_m) is simply related to the Raman frequency by the equation

$$(\omega_m/\omega_t)^2 = 1 + (\epsilon_0 - \epsilon_\infty)/(6\epsilon_\infty - 4).$$

Now for indium antimonide ϵ_∞ is approximately 15·2 and using Spitzer and Fan's results we find that ω_t is equivalent to 190·5 cm^{-1} and that $\omega_1/\omega_t = 1{\cdot}05$. This value is only a little higher than the value of 189 cm^{-1} found in this investigation. More recently Yoshinaga and Oetjen (1956) have measured the reflectivity at 238 °K and find the maximum reflectivity to occur at 54·6 μ which would indicate that ω_t was equivalent to 181·5 cm^{-1} at this higher temperature. Picus *et al.* (1959) using Yoshinaga and Oetjen's values conclude that ω_t is equivalent to 174 cm^{-1} and that $\omega_1/\omega_t = 1{\cdot}05$, but the method they used to arrive at these results is not given in detail.

The results obtained in this analysis can be compared with the results found by Johnson for silicon by normalizing both sets to unit Raman frequency. When this is done one obtains the following results:

	ω_t	TO	LO	LA	TA
Si	1	0·946	0·810	0·653	0·272
InSb	1	0·953	0·823	0·622	0·228.

It will be seen that for indium antimonide the optical frequencies are relatively slightly higher, and the acoustic frequencies lower than the corresponding values for silicon. This is consistent with the fact that indium antimonide, unlike silicon, has a complete energy gap between the optic and acoustic branches of the vibration spectrum.

Acknowledgments

It is a pleasure to acknowledge the advice and assistance of many of our colleagues in this laboratory, in particular we would like to thank Dr. T. P. McLean and Dr. D. J. Howarth for some very useful discussions concerning the symmetry properties of zinc-blende lattices and Dr. D. H. Parkinson for encouragement and help. We would also like to make a generous acknowledgement to the staff of our Engineering Unit who made the two gratings used in this investigation.

This paper is published by permission of the Controller, H.M. Stationery Office.

References

Born, M., and Huang, K., 1954, *Dynamical Theory of Crystal Lattices* (Oxford: University Press).
Brockhouse, B. N., 1959, *Phys. Rev. Letters*, **2,** 256.
Fray, S. J., and Oliver, J. F. C., 1959, *J. Sci. Instrum.*, **36,** 195.
Havelock, T. H., 1924, *Proc. Roy. Soc.* A, **105,** 488.
Johnson, F. A., 1959, *Proc. Phys. Soc.*, **73,** 265.
Johnson, F. A., and Lock, J. M., 1958, *Proc. Phys. Soc.*, **72,** 914.
Lax, M., and Burstein, E., 1955, *Phys. Rev.*, **97,** 39.
Macfarlane, G. G., McLean, T. P., Quarrington, J. E., and Roberts, V., 1958, *Phys. Rev.*, **111,** 1245.
Mashkevich, V. S., and Tolpygo, K. B., 1957, *Soviet Phys., J.E.T.P.*, **5,** 435.
Phillips, J. C., 1959, *Phys, Rev.*, **113,** 147.
Picus, G., Burstein, E., Henvis, B. W., and Hass, M., 1959, *J. Chem. Phys. Solids*, **8,** 282.
Spitzer, W., and Fan, H. Y., 1955, *Phys. Rev.*, **99,** 1891.
Yoshinaga, H., and Oetjen, R. A., 1956, *Phys. Rev.*, **101,** 526.

Form Factors of the Nucleus ^{6}Li

By DAPHNE F. JACKSON

Department of Physics, Battersea College of Technology, London

Communicated by L. R. B. Elton; MS. received 22nd March 1960, in final form 18th May 1960

Abstract. The experimental results for the elastic scattering of high energy electrons from ^{6}Li have been fitted using a charge distribution derived from a smoothed finite potential $V(r) = -V_0 + \frac{1}{2}Kr^2$, $r < r_0$ and $V(r) = -Ae^{-\mu r}$, $r > r_0$, which has identical parameters for s- and p-nucleons. An r.m.s. radius of $2{\cdot}72 \pm 0{\cdot}08$ fermi and a central nuclear density of $0{\cdot}14 \pm 0{\cdot}01$ particles per cubic fermi are obtained. The form factors for inelastic scattering are calculated for three models which fit the elastic scattering and it appears that the inelastic scattering is much more sensitive to choice of parameters. The total energy of the ^{6}Li nucleus is calculated on the independent particle model, including a correction for the spurious energy of the centre of mass.

§ 1. Introduction

The experimental cross sections for elastic scattering of high energy electrons from most p-shell nuclei may be fitted very well using nuclear charge distributions derived from independent particle wave functions with an infinite oscillator potential. The results of several workers have been summarized by Hofstadter (1957) and a more recent survey has been carried out by Meyer-Berkhout, Ford and Green (1959). For ^{6}Li, however, Burleson and Hofstadter (1958) have shown such a fit is not possible unless the s- and p-protons are assumed to move in different oscillator potentials. Similar calculations for inelastic scattering using oscillator wave functions have been carried out by Morpurgo (1956) for ^{12}C, by Tassie (1956) for ^{9}Be and by Cazzola and Foglia (1958) for ^{6}Li and ^{14}N. We shall look for a modification of the oscillator potential with identical parameters for both s- and p-nucleons, which will give rise to a charge distribution to fit the ^{6}Li results for elastic scattering. The modifications considered affect principally the p-nucleon wave function and since this alone determines the form factor for inelastic scattering, the inelastic case will also be considered. As we are starting from a potential, i.e. solving the wave equation to obtain the wave functions and the charge distribution, the energy levels in this potential can be found at the same time, and the total energy of the ^{6}Li nucleus may be calculated.

§ 2. Elastic Scattering

The nuclear form factor $F(q)$ for elastic scattering is defined as the ratio of the experimental scattering amplitude to the point charge amplitude,

$$F(q) = f(\theta)_{\text{exp}}/f(\theta)_{\text{point}} \qquad |F(q)|^2 = \left(\frac{d\sigma}{d\Omega}\right)_{\text{exp}} \Big/ \left(\frac{d\sigma}{d\Omega}\right)_{\text{point}}$$

where the momentum transfer q is given by $q=2k\sin\frac{1}{2}\theta=2E\sin\frac{1}{2}\theta/\hbar c$ and E is the kinetic energy of the incident electrons, in the centre-of-mass system. Since the electron energies being considered are extremely relativistic and Z is small, Born's approximation is valid and the form factor becomes

$$F(q)=\frac{4\pi}{q}\int_0^\infty r\rho(r)\sin qr\,dr$$

for a spherically symmetric potential $V(r)$. The charge density distribution in the ground state is $Ze\rho(r)$ and the normalization is such that the integral of $\rho(r)$ over the nuclear volume is unity.

The infinite oscillator potential has the form $V(r)=-V_0+\frac{1}{2}Kr^2$ with $\frac{1}{2}K=\frac{1}{2}M\omega^2$, where M is the nucleon mass, V_0 a suitable well depth and $\hbar\omega$ is the energy interval between the energy levels of the oscillator; $\hbar\omega$ is related to a length parameter a by the relation $a^2=\hbar/M\omega$. The density distribution for a p-shell nucleus becomes

$$\rho(r)=\frac{2}{Z\pi^{3/2}a^3}\exp\left(-\frac{r^2}{a^2}\right)\left[1+\frac{(Z-2)r^2}{3a^2}\right]$$

and the form factor is (Amaldi, Fidecaro and Mariani 1950)

$$F(q)=\left[1-\frac{(Z-2)q^2a^2}{6Z}\right]\exp\left(-\frac{q^2a^2}{4}\right).$$

The corrections to this elastic form factor to allow for the finite size of the proton and the centre-of-mass motion in the shell model are given by Tassie and Barker (1958). The essential result is that the length parameter a^2 is altered to $(1-1/A)a^2+a_p{}^2$ in the exponential factor of $F(q)$ only, where $\frac{3}{2}a_p{}^2$ is the mean square radius of the proton. This correction assumes a Gaussian distribution for the proton and is applicable only to oscillator wave functions. In particular for ^{6}Li,

$$F(q)=\left(1-\frac{q^2a^2}{18}\right)\exp\left(-\frac{q^2a_c{}^2}{4}\right)$$

where

$$a_c{}^2=\tfrac{5}{6}a^2+a_p{}^2.$$

Elton† has shown that the ^{6}Li results can be fitted with the modified oscillator distribution

$$\rho(r)=\tfrac{2}{3}\pi^{-3/2}\left[\frac{1}{a^3}\exp\left(-\frac{r^2}{a^2}\right)+\frac{r^2}{3b^5}\exp\left(-\frac{r^2}{b^2}\right)\right]$$

with $a=1{\cdot}72$ fermi and $b=2{\cdot}24$ fermi. This is equivalent to considering the p-proton in a more extended potential well than the s-protons. Burleson and Hofstadter take $a=2{\cdot}65$ f, $b=1{\cdot}07$ f and Meyer-Berkhout *et al.* (1959) interpret this distribution with $a>b$ as corresponding to Z protons in a potential more square in shape than the oscillator potential. With a modified oscillator distribution the corrected expression for the form factor is

$$F(q)=\tfrac{2}{3}\exp\left(-\frac{q^2a_c{}^2}{4}\right)+\tfrac{1}{3}\left(1-\frac{b^2q^2}{6}\right)\exp\left(-\frac{q^2b_c{}^2}{4}\right)$$

where $b_c{}^2$ obeys a similar relation to that for $a_c{}^2$. Elton has shown that for the parameters $a=1{\cdot}72$ f, $b=2{\cdot}24$ f the correction to a is small (figure 1). The correction to b is slightly more important but the effect on the total form factor

† Physical Society Conference, Oxford, 1958.

is small. We shall assume that this is also true for the elastic scattering calculations which follow. We see from figure 1 that this cancellation of the corrections is peculiar to the very light nuclei, otherwise the finite size effect dominates the correction.

The infinite oscillator potential is mathematically convenient but the form of this potential at large distances is quite different from the shape we would expect for a physically reasonable nuclear potential. This difference should not have much effect on tightly bound states but will affect loosely bound states high up in the well. This is exactly the case for ^{6}Li where the separation energy of the last proton S_p is only 4·5 Mev. We therefore modify the infinite oscillator potential so that $V(r)\to 0$ as $r\to\infty$, which should give rise to a more extended p-proton distribution.

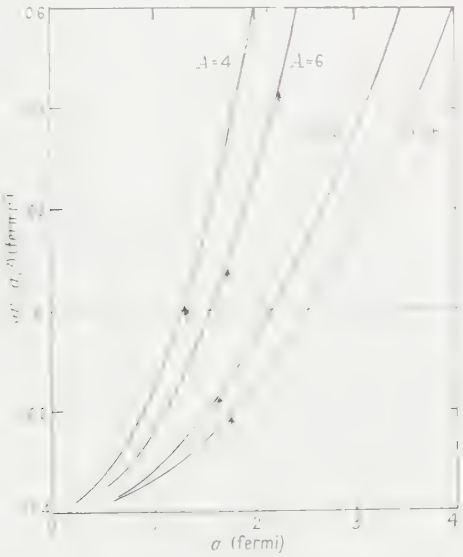

Figure 1. The correction to the length parameter a. $F(q)$ is altered by the factor $\exp[q^2(a^2-a_c^2)/4]$ so that if $a^2-a_c^2$ is positive $F(q)$ is increased and if $a^2-a_c^2$ is negative $F(q)$ is decreased. The arrows indicate the values of a for ^{4}He, ^{12}C, ^{16}O given by Hofstadter (1957) and the modified oscillator parameters of Elton for ^{6}Li.

The first step is simply to take a finite oscillator potential,

$$V(r)=-V_0+\tfrac{1}{2}Kr^2, \qquad r<r_0 \qquad \text{and } V(r)=0,\ r>r_0$$

where V_0 is adjusted so that the 1P energy level is equal to $-S_p$. For a length parameter $a=1{\cdot}7$ f, r_0 becomes 3·97 f and the p-proton density for $r<r_0$ is $\rho_p(r)\simeq Dr^2\exp(-r^2/b^2)$ with $D=0{\cdot}0021$ and $b=1{\cdot}79$ f. The contribution to the density distribution from the solution of the wave equation for $r>r_0$ is negligible. The p-wave components of the form factor for the finite oscillator are very little different from the corresponding infinite oscillator values.

It is evident that the change in potential beyond r_0 has little effect on the wave functions. Since the potential is finite it does give rise to a more extended distribution in the sense that it allows a 'spilling out' from the well beyond r_0, but cutting off the potential at r_0 has the effect of lowering the energy levels in

the well by amounts ΔE_0, ΔE_1 for $l=0, 1$ respectively. This means that the levels are now in a narrower part of the well compared with the corresponding levels for the infinite potential and this has exactly the opposite effect on the density distribution.

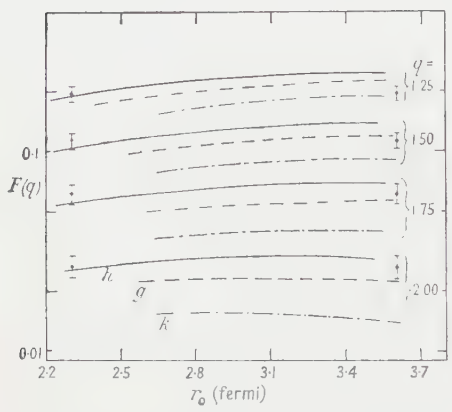

Figure 2. Elastic form factors calculated with the smoothed finite oscillator potential compared with the experimental results of Burleson and Hofstadter. Curve h corresponds to the length parameter $a=1{\cdot}64$ f, g to $a=1{\cdot}70$ f and k to $a=1{\cdot}79$ f.

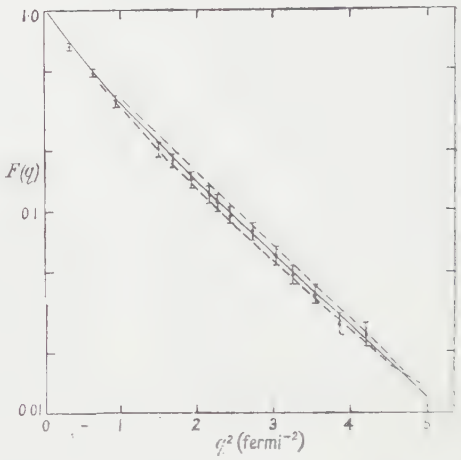

Figure 3. Elastic form factors from the smoothed finite oscillator potential for $a=1{\cdot}64$ f. The full line corresponds to $r_0=2{\cdot}50$ f and the broken lines to $r_0=2{\cdot}75$ f (above) and $r_0=2{\cdot}30$ f (below). The first three experimental points are those of Streib at 187 MeV (taken from Meyer-Berkhout, Ford and Green 1959).

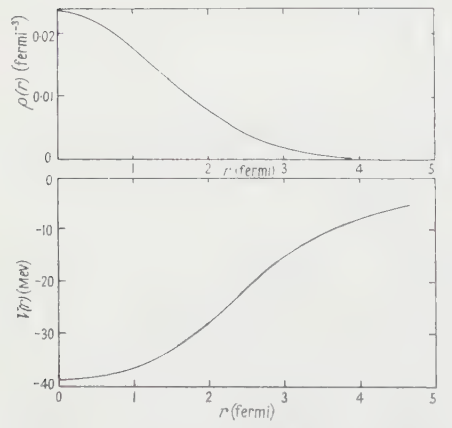

Figure 4. The smoothed finite oscillator potential $V(r)$ with $a=1{\cdot}64$ f, $r_0=2{\cdot}50$ f and the corresponding density distribution $\rho(r)$.

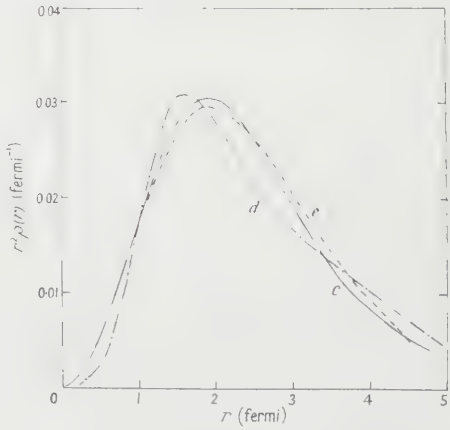

Figure 5. Total radial distributions $r^2\rho(r)$ which fit the elastic scattering data. Curve c corresponds to the smoothed finite oscillator parameters $a=1{\cdot}64$ f, $r_0=2{\cdot}50$ f. Curves d, e correspond to the modified oscillator parameters of Hofstadter ($a=2{\cdot}65$ f, $b=1{\cdot}07$ f) and Elton ($a=1{\cdot}72$ f, $b=2{\cdot}24$ f) respectively.

Now we require the first effect above and to do this we cut off the oscillator at a smaller value of r and add an exponential tail

$$V(r) = -V_0 + \tfrac{1}{2}Kr^2, \qquad r < r_0,$$
$$V(r) = -Ae^{-\mu r}, \qquad r > r_0.$$

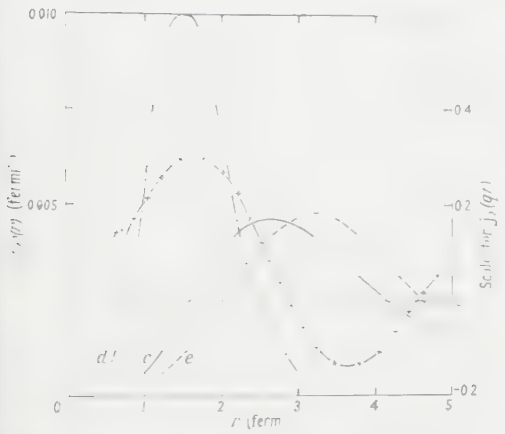

Figure 6. The p-wave components of the total distributions in figure 5. The notation *c*, *d*, *e*, applies as in figure 5 and curve *f* is the Bessel function $j_2(qr)$ for $q = 2$.

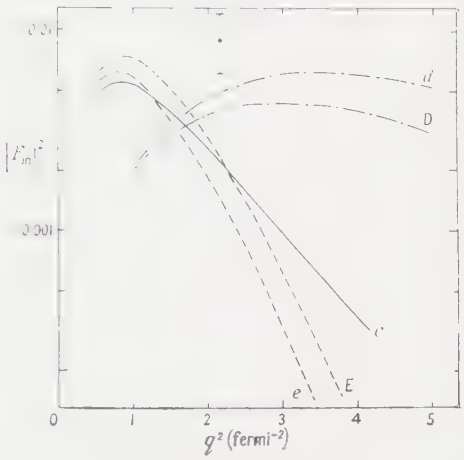

Figure 7. Inelastic form factors. *c*, *d*, *e*, apply as in figures 5 and 6. The correction for finite size etc. is applied to the modified oscillator results *d*, *e*, giving corrected curves D, E respectively.

This potential will be referred to as the smoothed finite oscillator. The parameters A, μ are determined by the requirement that $V(r)$ and its derivative should be continuous at r_0, which gives

$$\mu = Kr_0/(V_0 - \tfrac{1}{2}Kr_0^2)$$

and

$$A = (V_0 - \tfrac{1}{2}Kr_0^2)\exp\left[Kr_0^2/(V_0 - \tfrac{1}{2}Kr_0^2)\right].$$

As before V_0 is fixed so that $E_1 = -S_p$.

The radial wave equation with an exponential potential gives an analytic solution only when $l = 0$ (Rosenfeld 1948). In this case the solution for $r > r_0$ is

$$R(r) = Cr^{-1}J_p(be^{-\mu r/2})$$

where

$$b^2 = 8AM/\mu^2\hbar^2, \qquad p^2 = -8ME_0/\mu^2\hbar^2$$

and E_0 is the 1S energy level. The solution for $r < r_0$ is

$$R(r) = B\exp\left(-\frac{r^2}{2a^2}\right){}_1F_1\left(c, \frac{3}{2}, \frac{r^2}{a^2}\right)$$

with $c = \Delta E_0/2\hbar\omega$. With this potential the 2S level is not bound as would be expected since a change in potential beyond r_0 will have little effect on states with zero orbital angular momentum. In order to obtain an accurate solution for $l = 1$ and cover a range of parameters the calculation was programmed for the London University Ferranti Mercury computer. Density distributions and form factors were obtained for a range of r_0 values with $a = 1{\cdot}64$, $1{\cdot}70$ and $1{\cdot}79$ f.

In figure 2 the computed form factors are compared with the experimental results of Burleson and Hofstadter. There is no fit at all for $a=1{\cdot}79\,\mathrm{f}$; $a=1{\cdot}70\,\mathrm{f}$ gives a reasonable fit with $r_0=2{\cdot}8\pm0{\cdot}2\,\mathrm{f}$ although $F(q)$ is too small at large q values, and for $a=1{\cdot}64\,\mathrm{f}$ there is good agreement with $r_0=2{\cdot}4\pm0{\cdot}2\,\mathrm{f}$. Results for $a=1{\cdot}64\,\mathrm{f}$ are shown in detail in figure 3. The total density distribution for $a=1{\cdot}64\,\mathrm{f}$, $r_0=2{\cdot}50\,\mathrm{f}$ is shown in figure 4 with the corresponding potential. This density is negligible beyond about 4 fermi, as was also the case for the finite oscillator potential, although the smoothed oscillator potential has a much longer tail. This distribution gives an r.m.s. radius of $2{\cdot}72\,\mathrm{f}$, a p-shell radius of $3{\cdot}53\,\mathrm{f}$ and a central density of $\rho_{\max}=0{\cdot}023\pm0{\cdot}002\,\mathrm{f}^{-3}$ which, if it is assumed that protons and neutrons have the same distribution in ^{6}Li, corresponds to a nuclear mass density of $0{\cdot}14\pm0{\cdot}01$ particles/f^3. All these values agree well with those found by Meyer-Berkhout *et al.* The total radial distribution $r^2\rho(r)$ for the parameters $r_0=2{\cdot}50\,\mathrm{f}$, $a=1{\cdot}64\,\mathrm{f}$ is compared in figure 5 with the modified oscillator distributions of Elton and Hofstadter, and the p-wave components of the same distributions in figure 6.

A smoothed oscillator potential which was proportional to an inverse power of r beyond r_0 has also been considered. For the same value of r_0 this potential was little different from the exponential form already discussed and the corresponding form factors were almost identical.

§ 3. Inelastic Scattering

^{6}Li has a first excited state ($J=3^+$, $T=0$) at $2{\cdot}18\,\mathrm{Mev}$ above the ground state ($J=1^+$, $T=0$). The ground state configuration is $1s^21p$ for both protons and neutrons, so that in LS coupling $J=1$, $L=0$, $S=1$ and the excited state will be given by re-coupling the p-nucleons to $L=2$. The transition density is defined as

$$\rho_{0\mathrm{f}}{}^{MM'}(r)=\frac{1}{Z}\sum_{i=1}^{Z}\left[\int \Psi_0{}^{M*}\Psi_{\mathrm{f}}{}^{M'}\,d\tau_1\ldots d\tau_{i-1}d\tau_{i+1}\ldots d\tau_A\right]_{r_i=r}$$

where Ψ_0, Ψ_{f} are the ground and excited state wave functions respectively and M, M' are the M_J quantum numbers. The inelastic form factor is defined as

$$|F_{\mathrm{in}}|^2=(2J+1)^{-1}\sum_{M}\sum_{M'}|F_{\mathrm{in}}{}^{MM'}|^2$$

where J belongs to the ground state and

$$F_{\mathrm{in}}=\int \rho_{0\mathrm{f}}{}^{MM'}(r)e^{i\mathbf{q}\cdot\mathbf{r}}\,d\tau.$$

In the individual particle model the ground state wave function is given by

$$\Psi_0=\sum_{M}C(LSJ;\ M_LM_S)\phi_L{}^{M_L}\chi_S{}^{M_S}$$

where we have written down the p-nucleon part only, C is the appropriate Clebsch–Gordan coefficient and $\chi_S{}^{M_S}$ is a triplet spin function. $\phi_L{}^{M_L}$ is a linear combination of individual wave functions of the form

$$\phi_L{}^{M_L}=\sum_{M_L}C(l_{\mathrm{p}}l_{\mathrm{n}}L;\ m_{\mathrm{p}}m_{\mathrm{n}})\phi_{l_{\mathrm{p}}}{}^{m_{\mathrm{p}}}\phi_{l_{\mathrm{n}}}{}^{m_{\mathrm{n}}}$$

where

$$\phi_{l_{\mathrm{p}}}{}^{m_{\mathrm{p}}}=R_1(r_1)Y_{l_{\mathrm{p}}}{}^{m_{\mathrm{p}}}(\theta_1,\phi_1),\quad \phi_{l_{\mathrm{n}}}{}^{m_{\mathrm{n}}}=R_1(r_2)Y_{l_{\mathrm{n}}}{}^{m_{\mathrm{n}}}(\theta_2,\phi_2).$$

The excited state wave function can be written down in a similar way. Due to the normalization of the individual wave functions, the transition density depends

only on the form of the radial wave function for the p-proton. If this is an oscillator function $R_1^2(r) = A^2 r^2 \exp(-r^2/a^2)$ the inelastic form factor is given by Cazzola and Foglia as

$$|F_{in}|^2 = \frac{7}{270}\frac{q^4 a^4}{Z^2}\exp(-\tfrac{1}{2}q^2a^2).$$

If we differentiate this expression with respect to q, the condition for a maximum is $q^2a^2 = 4$ and this gives a maximum value for $|F_{in}|^2$ of $62{\cdot}5 \times 10^{-4}$ which is independent of q and a.

In the elastic scattering calculation the radial wave functions corresponding to the smoothed finite oscillator potential were tabulated in the form

$$P_l^2(r) = r^2 R_l^2(r).$$

In this case the inelastic form factor becomes

$$|F_{in}|^2 = \frac{7}{270}\frac{36}{Z^2}\left|\int_0^\infty j_2(qr)P_1^2(r)\,dr\right|^2$$

where the radial integral must now be evaluated numerically. The momentum transfer **q** is taken along the z axis so that e^{iqz} may be expanded in spherical harmonics. At large q values, there is considerable difference between $|F_{in}|^2$ calculated with the smoothed finite oscillator and with the modified oscillator forms of Elton and Hofstadter (figure 7). Now, the inelastic form factor is proportional to

$$\int_0^\infty j_2(qr)r^2\rho_p(r)\,dr$$

and we see from figure 6 that the effect of the spherical Bessel function is such that a small difference in the positions of the maxima of the density distributions will greatly affect the negative contribution to the integral and hence the magnitude of the form factor. A separation of 0·5 f between the maxima of curves *e* and *c* in figure 6 causes the values of $|F_{in}|^2$ at $q = 2$ to differ by a factor of 10. Since the elastic form factors involve the total proton density and the p-wave contributes only one third of this, they will not be very sensitive to such small changes in p-proton distribution, whereas the inelastic form factors are clearly much more sensitive to such changes.

At present the only published result for inelastic scattering with a discrete energy loss from ^6Li is a ratio of inelastic to elastic cross section for a laboratory angle of 40° and 426 Mev incident electrons (private communication by Burleson, quoted by Meyer-Berkhout *et al.*). With the definitions of charge density, transition density, inelastic and elastic form factors chosen, both the inelastic and the elastic differential cross sections are given by

$$d\sigma = \left(\frac{Ze^2}{2E}\right)^2 \frac{\cos^2\tfrac{1}{2}\theta}{\sin^4\tfrac{1}{2}\theta}|F|^2\,d\Omega$$

provided the angle θ is not near 0° or 180° and the excitation energy is small compared with the incident electron energy E (Morpurgo 1956). Then we may write $d\sigma_{in}/d\sigma_{el} = |F_{in}|^2/|F_{el}|^2$ and the ratios at $\theta = 40°$, $q = 1{\cdot}47$ f^{-1} are given in table 1. The values in the second line are those obtained when the correction for finite proton size, etc. are applied to $|F_{in}|^2$.

Table 1

Experiment	Modified oscillator $b=2{\cdot}24$ f	Modified oscillator $b=1{\cdot}07$ f	Smoothed finite oscillator $a=1{\cdot}64$ f $r_0=2{\cdot}50$
$0{\cdot}6\pm25\%$	0·10 0·16	0·34 0·27	0·15

Even if the inelastic form factor had its maximum value $|F_{\text{in}}|^2\simeq0{\cdot}006$ at $q=1{\cdot}47$, the ratio would be 0·41 and thus still outside the experimental error. The discrepancy probably arises from neglect of correlations between the p-nucleons in the independent particle model derivation of the inelastic form factor. The probability of re-coupling these nucleons to another state in the same shell will be dependent on the form of the coupling between the spin and orbital angular momenta of the nucleons. Clearly this coupling effect will be important only in the inelastic case. In particular, consideration of intermediate coupling might lead to markedly different transition probabilities (Lane and Radicati 1954). Similar conclusions have been reached by Morpurgo (1956) for ^{12}C and by Tassie (1956) for ^{9}Be. In the case of ^{12}C, Morpurgo found that the theoretical LS coupling values differed from the experimental results by a factor of 2·5.

§ 4. Total Energy of ^{6}Li

The basic assumption of the independent particle model, that each nucleon in the nucleus moves independently in a field which is the average effect of all interactions with the other nucleons, leads to a total wave function Ψ which is a product of individual wave functions ψ_i suitably anti-symmetrized with respect to complete exchange of any two nucleons. In addition, the sum of the interactions on the ith nucleon due to all other nucleons, assuming these interactions act in pairs, is represented by a potential which depends only on the coordinates of the nucleon itself, i.e. $\Sigma_j V_{ij}=V_i$. Then the total energy is

$$\begin{aligned}E&=\Big\langle\prod_{i=1}^{A}\psi_i\Big|\sum_{i=1}^{A}T_i+\tfrac{1}{2}\sum_{i=1}^{A}V_i\Big|\prod_{i=1}^{A}\psi_i\Big\rangle\\&=\sum E_i-\tfrac{1}{2}\sum\langle V_i\rangle\end{aligned}$$

where $\langle V_i\rangle$ stands for $\langle\psi_i|V_i|\psi_i\rangle$ and E_i is the energy of the ith nucleon in the independent particle model. Strictly we should be using that linear combination of products $\Pi\psi_i$ which gives the correctly anti-symmetrized wave function Ψ, but as we are considering expectation values of single particle operators, no exchange terms can arise.

In the shell model the coordinates are referred to an arbitrary fixed origin (the centre of the potential well) instead of the centre of mass of the system. This means that the shell model Hamiltonian describes an additional collective motion in which the centre of mass fluctuates about the origin of the coordinate system. In the special case of the infinite oscillator potential $V=-V_0+\frac{1}{2}Kr^2$ the total anti-symmetrized wave function factorizes into two parts, one of which depends on the relative coordinates of the nucleons and the other on the

centre-of-mass coordinate R, where $R=A^{-1}\Sigma r_i$ and r_i is the shell model coordinate of the ith nucleon (Elliott and Skyrme 1955, Peierls 1959). The second factor has the form $\exp(-AR^2/2a^2)$ and is the wave function of a mass AM, moving in a 1s-state in an oscillator which has the single particle parameter K replaced by AK. This represents the centre-of-mass motion, the energy of which is $\frac{3}{2}\hbar(AK/AM)^{1/2}=\frac{3}{2}\hbar\omega$ where ω is the same quantity as for the single particle motions. This centre-of-mass energy must be subtracted from the shell model energy to give the internal energy of the nucleus (Lipkin 1959), i.e.

$$\begin{aligned} E_{\text{int}} &= E-\tfrac{3}{2}\hbar\omega \\ &= \Sigma E_i-\tfrac{1}{2}\Sigma\langle V_i\rangle-\tfrac{3}{2}\hbar\omega. \end{aligned}$$

The energy of the centre-of-mass motion in the smoothed finite oscillator potential will not be exactly $\frac{3}{2}\hbar\omega$. However, the height of the 1s level above the well depth in this potential V_0+E_s differs by only a small amount from the same quantity in an infinite oscillator well with the same parameter a. For $a=1{\cdot}64$ f, $r_0=2{\cdot}50$ f the difference is 1 Mev. Since in the infinite well, $\frac{3}{2}\hbar\omega=V_0+E_s$ we take as the energy of the centre of mass in the smoothed finite oscillator potential the corresponding value of V_0+E_s. Calculated values in Mev are given in table 2. From these values we conclude that for the smoothed finite oscillator potential with $a=1{\cdot}64$ f, $r_0=2{\cdot}50$ f the expectation values of kinetic energy in the s- and p-states are $\langle T_s\rangle=9{\cdot}4$ Mev, $\langle T_p\rangle=12{\cdot}0$ Mev. Since it is generally accepted that the shell model potentials for different states depend on these energies the potentials in which the s- and p-nucleons move are apparently quite similar and the assumption of the same potential for both is reasonably justified.

Table 2

	V_0	E_s	E_p	ΣE_i	$\langle V_s\rangle$	$\langle V_p\rangle$	E	E_{int}
Infinite oscillator $a=1{\cdot}64$ fermi	43·1	−19·9	−4·5	−88·6	−31·5	−23·8	−1·9	−25·1
Smoothed finite oscillator $a=1{\cdot}64$ fermi, $r_0=2{\cdot}50$ fermi	39·0	−16·8	−4·5	−76·2	−26·2	−16·5	−7·3	−29·5

We now have a calculated total energy for ^{6}Li of −29 Mev compared with the experimental value of −32·0 Mev. In addition there is a small positive contribution to the calculated value from the Coulomb repulsion of the protons of approximately 2 Mev. Part of the discrepancy between the calculated and experimental results is due to neglect of re-arrangement energy. If one nucleon is removed from the nucleus but nothing else is changed the remaining nucleons will be left in a state which is not an equilibrium state of the system and the formula for the well depth should include an additional energy term which represents the energy change due to re-arrangement of the residual nucleons to the equilibrium state. In general, the LS coupling scheme is more appropriate to light nuclei than jj coupling, which means that the residual two-body interactions should not be neglected. For ^{6}Li the interaction between the p-nucleons will be important and can be expected to contribute several Mev to the binding energy.

Acknowledgments

The author would like to express her very sincere thanks to Dr. L. R. B. Elton for many helpful suggestions and guidance of the work; also to Dr. M. J. M. Bernal for advice and a copy of his integration programme. Thanks are also due to Battersea College of Technology for a Research Assistantship, to the National Institute for Research in Nuclear Science for support and to the University of London Computer Unit for machine time.

References

Amaldi, E., Fidecaro, G., and Mariani, F., 1950, *Nuovo Cim.*, **7,** 553.
Burleson, G., and Hofstadter, R., 1958, *Phys. Rev.*, **112,** 1282.
Cazzola, P., and Foglia, C., 1958, *Nuovo Cim.*, **10,** 913.
Elliott, J. P., and Skyrme, T. H. R., 1955, *Proc. Roy. Soc.* A, **232,** 561.
Hofstadter, R., 1957, *Ann. Rev. Nucl. Sci.*, **7**.
Lane, A. M., and Radicati, L. A., 1954, *Proc. Phys. Soc.* A, **67,** 167.
Lipkin, H. J., 1959, *The Many Body Problem* (London: Methuen), p. 335.
Meyer-Berkhout, U., Ford, K. W., and Green, A. E. S., 1959, *Ann. Phys.*, **8,** 119.
Morpurgo, G., 1956, *Nuovo Cim.*, **3,** 430.
Peierls, R. E., 1959, *Lectures in Theoretical Physics*, Vol. I (London: Interscience), p. 292.
Rosenfeld, L., 1948, *Nuclear Forces* (Amsterdam: North-Holland).
Tassie, L. J., 1956, *Proc. Phys. Soc.* A, **69,** 205.
Tassie, L. J., and Barker, F. C., 1958, *Phys. Rev.*, **111,** 940.

Note added in proof.—W. C. Barber, F. Berthold, G. Fricke and F. E. Gudden (private communication) have recently obtained experimental values for the ratio of elastic to inelastic scattering to the first excited level for two other values of q. Their results are compared below with those obtained theoretically.

q	Experiment	Modified	Oscillator	Smoothed Finite Oscillator
		$b=2{\cdot}24$ f	$b=1{\cdot}07$ f	$a=1{\cdot}64$ f $r_0=2{\cdot}50$ f
0·36	$2{\cdot}9\times10^{-3}$ +100% −50%	$1{\cdot}3\times10^{-3}$	$0{\cdot}9\times10^{-4}$	$0{\cdot}9\times10^{-3}$
0·39	$2{\cdot}6\times10^{-3}$ +100% −50%	$1{\cdot}8\times10^{-3}$	$1{\cdot}3\times10^{-4}$	$1{\cdot}4\times10^{-3}$

Anisotropy in Ionospheric Diffraction and its Effect on Drift Measurement

By R. B. BANERJI
University of New Brunswick, Fredericton, N.B., Canada

MS. received 2nd March 1960, in final form 2nd June 1960

Abstract. An attempt was made by the author a few years ago to combine the geometrical approach of Pütter and the statistical approach of Briggs and Spencer to the problem of ionosphere drift measurement. The combination gave rise to a method of wind measurement which was nearly as simple as that of Pütter and yet vigorous enough to eliminate the effect of random changes in the ground diffraction pattern. However, the method could not be proved valid when the ground pattern was statistically anisotropic. The present paper develops a method involving the use of five statistical parameters and a few simple algebraic formulae, which takes into account the effects of random motion as well as anisotropy. The intuitive clarity of the geometrical picture is, however, unfortunately lost.

§ 1. Introduction

The method of measuring ionospheric winds pioneered by Mitra (1949) has been reconsidered by Ratcliffe (1954) in view of the random nature of the diffraction pattern on the ground caused by ionospheric irregularities. His work led to the concept of 'lines of maxima'. This concept was exploited independently by Pütter (1955) to show that in the absence of any random changes in the ground diffraction pattern the lag between maxima in two pairs of receivers will be perfectly correlated, i.e. the plot of one lag against the other would be a straight line. It can be easily shown that this result will be unaffected by an anisotropy in the ground pattern. These analyses have shown that, while the validity of the Mitra method remains unaltered if the ground pattern is isotropic, the effect of anisotropy is such as to make the direction as well as magnitude of the drift computed by the Mitra method drastically different from the true value. On the other hand, Briggs and Spencer (1955), extending Ratcliffe's work, showed that in the presence of random changes the Mitra method would yield values for the drift magnitude much higher than the true value—so much so that an infinite drift velocity might be obtained when drift was entirely absent.

The rectilinear plot of lags in one pair of receivers against another is related in a very simple manner to the magnitude and direction of the drift and leads to a method for the evaluation of drift which involves very little computational labour. Moreover, the evaluation leads to the correct value even when the ground pattern is anisotropic when there is no random change. Using Briggs and Spencer's results, the author has demonstrated (Banerji 1958a) that in

the presence of random motion the direction of drift can be obtained with equal ease by drawing the mean straight line through the plot if the ground pattern is isotropic. However, the magnitude of the drift obtained from the mean straight line has to be corrected for by using the coefficient of correlation between the two lags. It still remained to be seen whether this geometrical method remained valid if anisotropy and random changes in the ground pattern were simultaneously effective.

The considerations in the next section will show that this is not the case.

We are, therefore, forced to an analytic method following Briggs and Spencer. The mean lags in the two receivers $\bar{t}_1, \bar{t}_2$, as well as the standard deviations $\sigma_{t_1}, \sigma_{t_2}$, have been evaluated by these authors as functions of the drift velocity V, the direction of drift θ and the rate of random change V_c of the ground pattern. By the evaluation of the four quantities $\bar{t}_1$, $\bar{t}_2$, σ_{t_1} and σ_{t_2} from the data, their relationships can be used for the evaluation of V, θ and V_c in the isotropic case.

However, in the presence of anisotropy, two additional unknowns appear in their equations, namely ϕ the tilt of the autocorrelation ellipse and K the ratio of the major to minor axis. This necessitated the evaluation of another statistical parameter. Briggs and Spencer suggested the correlation coefficient ρ between t_1 and t_2 as such a parameter. However, this coefficient was not given by them as a function of the five unknowns mentioned earlier.

In our previous paper we have already had occasion to evaluate the correlation coefficient as a function of V, θ, and V_c. The same techniques used in that work have been found effective in the anisotropic case. In § 2 we shall proceed to evaluate the correlation coefficient as a function of the five ionospheric unknowns. In § 3 we shall demonstrate that our results do not lead to a simple geometrical relationship between the (t_1, t_2) plot and the ionospheric unknowns. In § 4 we develop a few simple analytic formulae expressing V, θ, V_c, ϕ and K as functions of $\bar{t}_1$, $\bar{t}_2$, σ_{t_1}, σ_{t_2}, and ρ. In the concluding section, § 5, we shall have occasion to compare the value of V and θ obtained by this method in a specific case with those obtained by the previous geometrical method.

§ 2. The Distribution of Lags in the Anisotropic Case

Following Briggs and Spencer and our previous paper, we shall consider the signal strength as a function of space and time to be represented by a contour of signal strength in a three-dimensional (x, y, t) space, plotted with respect to a coordinate system moving with the drift. Due to the presence of anisotropy as well as irregular temporal changes of the pattern (our moving coordinate system having removed effects of regular temporal changes), this three-dimensional pattern has asymmetric statistical properties. If we plot the correlation between the signal strength at two points separated by a certain distance and time interval (as found by averaging over all pairs of points with this separation) we shall obtain the contours of equal correlations of signal strength as ellipsoids, one of its axes lying along the t axis. Let the major axis on the (x, y) plane make an angle ϕ with the x axis and be K times the minor axis. The anisotropy in this plane will therefore be absent in a coordinate system (x', y', t) where

$$\left.\begin{aligned} Kx' &= x\cos\phi + y\sin\phi \\ y' &= -x\sin\phi + y\cos\phi. \end{aligned}\right\} \qquad \ldots\ldots(1)$$

The wind vector (V, θ) in the old system will be transformed into (V', θ') in the new system, where

$$V' \cos\theta' = (V/K)\cos(\theta - \phi), \quad V' \sin\theta' = V \sin(\theta - \phi). \quad \ldots\ldots(2)$$

If the receivers are at $(0,0)$, $(\xi_0, 0)$, $(0, \eta_0)$, their position in the new coordinate system will be $(0,0)$, (ξ_1, η_1), (ξ_2, η_2) where

$$\xi_1 = (\xi_0 \cos\phi)/K, \quad \eta_1 = -\xi_0 \sin\phi \quad \ldots\ldots(3)$$

and

$$\xi_2 = (\eta_0 \sin\phi)/K, \quad \eta_2 = \eta_0 \cos\phi. \quad \ldots\ldots(4)$$

The only anisotropy remaining now will be in the t direction. This is removed by multiplying this coordinate by a fictitious velocity V_c which will form a measure of the random changes in the pattern.

In this new, $(X', Y', V_c t)$, system drifting with the ionosphere, the receivers will appear to move opposite to V' and their motion can be taken to be in a direction making an angle $(\pi + \theta')$ with X' axis and an angle δ to the (x', y') plane where

$$\tan\delta = V_c/V'. \quad \ldots\ldots(5)$$

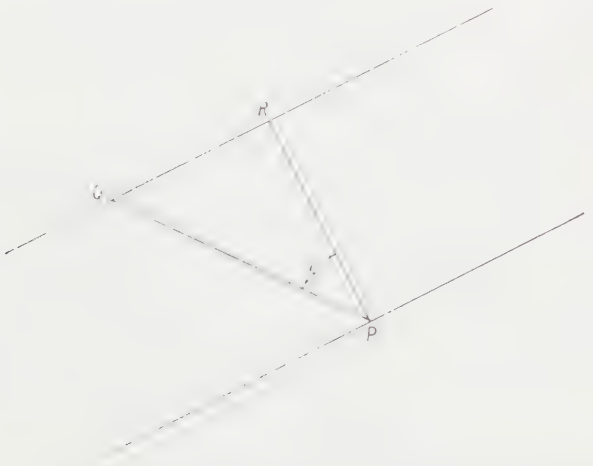

Figure 1. Relative positions of maxima in two correlated time series.

These lines will cut the three-dimensional signal strength pattern to form three random time series, the correlation between two points on them being smallest when one is on the perpendicular drawn through the other point to these lines.

Briggs and Page (1955) have analysed empirically the lag between maxima in correlated time series, which is obtained by cutting a three-dimensional time series by two lines, as in figure 1. According to their results, if there is a maximum at P in one time series, the probability is highest that there will be a maximum at R on the other. The probability of a maximum at an arbitrary point Q is given in terms of the angle ψ as

$$P(\psi) \propto \exp(-\tan^2\psi/0{\cdot}74). \quad \ldots\ldots(6)$$

Longuet-Higgins (1957) has analysed the distribution of $\tan\psi$ theoretically, leading to a distribution of which Briggs and Page's formula is an approximation.

In what follows we shall continue to use Briggs and Page's formula for its mathematical simplicity.

Let us now consider figure 2.

A and B are the initial positions of two of the receivers and O that of the third one. If there is a maximum at O, i.e. at the third receiver at time $t=0$, the most probable times $\bar{t}_1$ and $\bar{t}_2$ for a maximum at each of the two other receivers correspond to the points P and Q, the feet of the perpendiculars from O on AA′ and BB′. Concentrating on Q we have

$$\mathrm{BQ}\sin\delta = V_c\bar{t}_2, \quad \mathrm{BQ} = \mathrm{OB}\ \cos\zeta. \qquad \ldots\ldots(7)$$

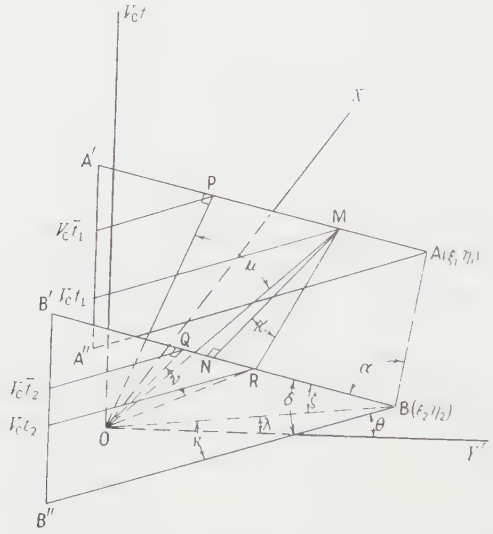

Figure 2. Geometry of the diffraction maxima in space and time.

Taking direction cosines of OB and BB′ along BB″ and perpendicular to BB″ on the $X'Y'$ plane and along the t axis we have $\cos\zeta = \cos\delta\cos\kappa$. However $\kappa = \lambda - \theta'$ where $\cos\lambda = \xi_2/\mathrm{OB}$ and $\sin\lambda = \eta_2/\mathrm{OB}$ whence

$$\mathrm{BQ} = \mathrm{OB}\cos\delta\,(\cos\lambda\cos\theta' + \sin\lambda\sin\theta')$$

and, from (7) and (5)

$$V_c\bar{t}_2 = \frac{V_c/V'}{1+V_c^2/V'^2}\,(\xi_2\cos\theta' + \eta_2\sin\theta') \qquad \ldots\ldots(8)$$

and, expressing V' and θ' (equation (2)) in terms of V and θ, the actual velocity vector, and putting values for ξ_2 and η_2 (equation (4)) in terms of η_0 we have

$$\left.\begin{aligned}\frac{\bar{t}_2}{\eta_0} &= V\,\frac{K^{-2}\sin\phi\cos(\theta-\phi) - \cos\phi\sin(\theta-\phi)}{V_c^2 + V^2\{K^{-2}\cos^2(\theta-\phi) + \sin^2(\theta-\phi)\}}\\ \text{and similarly}\quad \frac{\bar{t}_1}{\xi_0} &= V\,\frac{K^{-2}\cos\phi\cos(\theta-\phi) - \sin\phi\sin(\theta-\phi)}{V_c^2 + V^2\{K^{-2}\cos^2(\theta-\phi) + \sin^2(\theta-\phi)\}}.\end{aligned}\right\} \qquad \ldots\ldots(9)$$

Having obtained the mean values of the lags in terms of the receiver positions, velocity of drift, V_c and the shape of the anisotropic correlation ellipse, we proceed with the distribution of the actual lags. Let us turn to figure 2 once more and consider the probability of a maximum occurring at the point R.

According to Briggs and Page's analysis the tangent of the angle $\nu = \mathrm{QOR}$ is normally distributed. We have to evaluate this angle in terms of t_2, the lag between the maximum at O and R.

We have

$$V_c(t_2 - \bar{t}_2) = \mathrm{QR}\sin\delta$$

$$\tan\nu = \mathrm{QR}/\mathrm{OQ}$$

$$\mathrm{OQ}^2 = \mathrm{OB}^2 - \mathrm{BQ}^2$$

$$= \mathrm{OB}^2 - \mathrm{OB}^2\cos^2\delta\left(\cos\theta\frac{\xi_2}{\mathrm{OB}} + \sin\theta\frac{\eta_2}{\mathrm{OB}}\right)^2$$

whence

$$\tan^2\nu = \frac{V_c^2(t_2-\bar{t}_2)^2}{\sin^2\delta(\xi_2^2+\eta_2^2) - \cos^2\delta(\xi_2\cos\theta' + \eta_2\sin\theta')}$$

whence, putting values of δ, ξ_2, η_2, θ' and V' and remembering

$$P(\nu)\propto\exp(-\tan^2\nu/0{\cdot}74)$$

we have

$$\sigma_{t_2}^2 = \frac{0{\cdot}74}{2}\eta_0^2\frac{K^{-2}\sin^2\phi + \cos^2\phi}{V_c^2 + V^2\{K^{-2}\cos^2(\theta-\phi) + \sin^2(\theta-\phi)\}}$$

and similarly

$$\sigma_{t_1}^2 = \frac{0{\cdot}74}{2}\xi_0^2\frac{K^{-2}\cos^2\phi - \sin^2\phi}{V_c^2 + V^2\{K^{-2}\cos^2(\theta-\phi) + \sin^2(\theta-\phi)\}}. \quad \left.\right\} \ldots\ldots(10)$$

Equations (9) and (10) are identical, except for a change of symbols, with those of Briggs and Spencer and are reproduced here only for completeness.

We shall attack the problem of correlation in a manner similar to our previous work, i.e. by considering initially the distribution of $t_2 - t_1$. To this end we shall concentrate on the angle χ in figure 2.

We have

$$\tan^2\chi = \mathrm{NR}^2/\mathrm{MN}^2$$

where

$$\mathrm{MN} = \mathrm{AB}\sin\alpha$$

$$\mathrm{NR} = \mathrm{QR} - \mathrm{QN} = \mathrm{QR} - \mathrm{PM}$$

$$= V_0\{(t_1-\bar{t}_1) - (t_2-\bar{t}_2)\}/\sin\delta.$$

Now, expressing $\cos\alpha$ in terms of the direction cosines of AB and BB′ we have

$$\cos\alpha = \cos\delta\left[\cos\theta'\frac{\xi_2-\xi_1}{\mathrm{AB}} + \sin\theta'\frac{\eta_2-\eta_1}{\mathrm{AB}}\right]$$

whence

$$(\mathrm{MN})^2 = (\mathrm{AB})^2 - \cos^2\delta[(\xi_2-\xi_1)\cos\theta' + (\eta_2-\eta_1)\sin\theta'].$$

Remembering $\mathrm{AB}^2 = (\xi_2-\xi_1)^2 + (\eta_2-\eta_1)^2$ and putting values of ξ_1, ξ_2, η_1, η_2 and δ in terms of original coordinates and parameters we obtain, using equation (6), as the standard deviation of $(t_2-t_1)-(\bar{t}_2-\bar{t}_1)$

$$\frac{0{\cdot}74}{2}\frac{\xi_0^2\{K^{-2}\cos^2\phi + \sin^2\phi\} + \eta_0^2\{K^{-2}\sin^2\phi + \cos^2\phi\} + 2\xi_0\eta_0\sin\phi\cos\phi\{1-K^{-2}\}}{V_c^2 + V^2\{K^{-2}\cos^2(\theta-\phi) + \sin^2(\theta-\phi)\}}$$
$$-(\bar{t}_2-\bar{t}_1). \quad \ldots\ldots(11)$$

If we now compare this with the expression for the standard deviation of the difference between two correlated normal deviates, i.e. with

$$\sigma_{t_1}^2 - 2\sigma_{t_1}\sigma_{t_2} + \sigma_{t_2}^2 \qquad \ldots\ldots(12)$$

we obtain for the correlation coefficient between t_1 and t_2

$$\rho = -\frac{1}{\sigma_{t_1}\sigma_{t_2}}\left[\bar{t}_1\bar{t}_2 + \frac{\xi_0\eta_0 \sin\phi\cos\phi\{1-K^{-2}\}}{V_c^2 - V^2\{K^{-2}\cos^2(\theta-\phi)+\sin^2(\theta-\phi)\}}\right]. \qquad \ldots\ldots(13)$$

We therefore have the following expressions for the parameters of the joint distribution between t_1 and t_2

$$\left.\begin{aligned}
\frac{\bar{t}_1}{\xi_0} &= \frac{1}{V}\frac{K^{-2}\cos\phi\cos(\theta-\phi)-\sin\phi\sin(\theta-\phi)}{V_c^2/V^2+K^{-2}\cos^2(\theta-\phi)+\sin^2(\theta-\phi)}\\
\frac{\bar{t}_2}{\eta_0} &= \frac{1}{V}\frac{K^{-2}\sin\phi\cos(\theta-\phi)+\cos\phi\sin(\theta-\phi)}{V_c^2/V^2+K^{-2}\cos^2(\theta-\phi)+\sin^2(\theta-\phi)}\\
\frac{2}{0{\cdot}74}\frac{\sigma_{t_2}^2}{\eta_0^2} &= \frac{1}{V^2}\frac{K^{-2}\sin^2\phi+\cos^2\phi}{V_c^2/V^2+K^{-2}\cos^2(\theta-\phi)+\sin^2(\theta-\phi)}\\
\frac{2}{0{\cdot}74}\frac{\sigma_{t_1}^2}{\xi_0^2} &= \frac{1}{V^2}\frac{K^{-2}\cos^2\phi+\sin^2\phi}{V_c^2/V^2+K^{-2}\cos^2(\theta-\phi)+\sin^2(\theta-\phi)}\\
-\rho &= \left[\frac{\bar{t}_1\bar{t}_2}{\xi_0\eta_0}+\frac{1}{V^2}\frac{\sin\phi\cos\phi(K^{-2}-1)}{V_c^2/V^2+K^{-2}\cos^2(\theta-\phi)+\sin^2(\theta-\phi)}\right]\Big/\frac{\sigma_{t_1}\sigma_{t_2}}{\xi_0\eta_0}.
\end{aligned}\right\} \qquad \ldots\ldots(14)$$

From this we can deduce the position of the major axis of the distribution ellipse as in our previous paper. Unfortunately, however, this does not come out to be independent of ϕ as in the case of Pütter's analysis of pure drift cases. We shall describe in the next section the results of certain efforts we made towards obtaining an idea of how the distribution ellipse behaves in the anisotropic case. To our mind, this section fulfils very little useful purpose except bringing home the conviction that any effort at geometrical analysis is beset with great difficulties. In § 4, therefore, we shall proceed to an entirely analytical method of analysis.

§ 3. The Orientation of the Distribution Ellipse

In this section we shall, for ease of manipulation, consider the plot, not of t_1 and t_2, but that of $X = Vt_1/\xi_0$ and $Y = vt_2/\eta_0$. This will not subtract from the practical usefulness of the resulting formulae (if an application is found) since ξ_0 and η_0 are known and the factor V is merely a scale factor which does not affect angles.

3.1. *The Slope of the Major Axis of the Distribution Ellipse*

It has been pointed out in our previous work that the angle ϵ made by the axes of the distribution ellipse to the axes is given by

$$\tan 2\epsilon = 2\rho\frac{\sigma_x\sigma_y}{\sigma_x^2\sigma_y^2}. \qquad \ldots\ldots(15)$$

This would yield two values of ϵ, one for each axis.

Remembering that

$$\sigma_x = \frac{V}{\xi_0}\sigma_{t_1} \quad \text{and} \quad \sigma_y = \frac{V}{\eta_0}\sigma_{t_2}$$

$$\bar{x} = \frac{\bar{t}_1 V}{\xi_0}\,; \quad \bar{y} = \frac{\bar{t}_2 V}{\eta_0},$$

we obtain, after some work,

$$\tan 2\epsilon = \frac{K^{-2}\sin 2\theta - (V_c^2/V^2)(K^{-2}-1)\sin 2\phi}{K^{-2}\cos 2\theta - (V_c^2/V^2)(K^{-2}-1)\cos 2\phi}. \qquad \ldots\ldots (16)$$

For either $V_c = 0$ or $K = 1$ this resolves to $\tan 2\theta$ so that the minor axis indicates the direction of drift in both the turbulence-free anisotropic case as well as the isotropic case with turbulence. This is in accordance with Pütter's results as well as our previous result. However, when both the effects are present, the ellipse tilts away from its convenient position and we have not been able to find out any way of separating the two effects.

It may also be of interest to see how the position of the centre of the ellipse i.e. the means $\bar{X}$ and $\bar{Y}$, shift as a result of anisotropy. For this purpose we first evaluated the position of the mean in the isotropic and anisotropic case and found the slope of the line joining them. It may be pointed out that this line cannot actually be drawn in practice and is useful only in the way of clarifying ideas.

3.2. *The Line Joining the Isotropic and Anisotropic Means*

The values of $\bar{X}$ and $\bar{Y}$ in the anisotropic case $K = 1$ are $\cos\theta/(V_c^2/V^2+1)$ and $\sin\theta/(V_c^2/V^2+1)$ respectively. Hence the line joining this point to the actual mean has slope

$$\frac{\bar{Y} - \sin\theta/(V_c^2/V^2+1)}{\bar{X} - \cos\theta/(V_c^2/V^2+1)}$$

which reduces to

$$\frac{(V_c^2/V^2)\sin\phi - \cos\theta\sin(\theta-\phi)}{(V_c^2/V^2)\cos\phi + \sin\theta\sin(\theta-\phi)}. \qquad \ldots\ldots (17)$$

This slope is independent of anisotropy. This independence has some significance in the case of $V_c = 0$ where this slope is $-\cot\theta$ so that the mean moves along the anisotropic major axis. However, since the major axis passes through the mean anyway, this is really not new information.

3.3. *The Line Joining the Origin to the Mean*

It will be recalled that in the anisotropic case with or without random changes—the line joining the mean to the origin was perpendicular to the major axis. However, in the anisotropic case this relation does not hold. Generally this line has a slope given by

$$\frac{K^{-2}\sin\phi\cos(\theta-\phi) + \cos\phi\sin(\theta-\phi)}{K^{-2}\cos\phi\cos(\theta-\phi) - \sin\phi\sin(\theta-\phi)} \qquad \ldots\ldots (18)$$

which is independent of V_c.

It seems that the position of the major axis is no longer a very convenient parameter for wind measurement. The line joining the mean to origin has a somewhat simpler expression for slope but even this involves three parameters of the pattern at the same time. It is doubtful whether any easily realizable geometrical property of the distribution ellipse will be found which will be as directly related to the motion as the Pütter line is in the case of pure drift. At best we can eliminate variables between the measured parameters of the distribution. This we shall proceed to do in the next section.

§ 4. An Analytical Approach to Wind Evaluation by the Lag Method

The method we are about to suggest depends on formulae (14). For convenience of discussion (and later, of manipulation), we shall call the left-hand sides of these equations A, B, C, D and $-E$ respectively.

It can be shown that

$$\frac{E\sqrt{(CD)}+AB}{C-D}=\frac{-\sin\phi\cos\phi}{\cos^2\phi-\sin^2\phi}=-\tfrac{1}{2}\tan 2\phi \qquad \ldots\ldots(19)$$

which immediately yields one of the five parameters of the pattern. The value of ϕ so obtained can then be used for later work. We also obtain

$$\frac{C+D}{C-D}=\frac{1}{\cos 2\phi}\frac{1+K^{-2}}{1-K^{-2}}$$

or putting $\cos 2\phi(C+D)/(C-D)=P$ we have

$$\frac{1}{K^2}=\frac{P-1}{P+1} \qquad \ldots\ldots(20)$$

obtaining another parameter of the ellipse.

From the first two equations of (14) we obtain after some work

$$\tan(\theta-\phi)=\frac{1}{K^2}\frac{\cos\phi-(A/B)\sin\phi}{\sin\phi+(A/B)\cos\phi}. \qquad \ldots\ldots(21)$$

Since ϕ and K have already been calculated, this gives us θ, the direction of drift.

We shall also introduce the following symbols at this stage for convenience

$$\left.\begin{aligned} L&=\frac{1}{K^2}(\cos\phi\cos(\theta-\phi))-\sin\phi\sin(\theta-\phi)\\ N&=\frac{1}{K^2}\cos^2(\theta-\phi)+\sin^2(\theta-\phi). \end{aligned}\right\} \qquad \ldots\ldots(22)$$

It will be noticed that all of these can be calculated at this stage. We obtain in terms of these

$$\frac{1}{V}=\frac{CL/A}{K^{-2}\sin^2\phi+\cos^2\phi} \qquad \ldots\ldots(23)$$

$$\frac{V_c^2}{V^2}=\frac{L}{AV}-N. \qquad \ldots\ldots(24)$$

The procedure outlined below on the basis of these equations is comparable in length to the six-point correlation method of Yerg (1955); however, two of the five parameters to be calculated are means and involve much smaller labour than autocorrelations.

A possible procedure for calculation is given below.

1. Calculate $\quad \bar{t}_1,\ \bar{t}_2,\ \sigma_{t_1}^2,\ \sigma_{t_2}^2,\ \rho.$

2. Calculate

$A=\bar{t}_1/\xi_0,\ B=\bar{t}_2/\eta_0;\ C=(2/0{\cdot}74)\ (\sigma_{t_2}^2/\eta_0^2),\ D=(2/0{\cdot}74)\ (\sigma_{t_1}^2/\xi_0^2);\ \rho=E.$

3. Calculate $\quad \tfrac{1}{2}\tan^{-1}\dfrac{E\sqrt{(CD)}+AB}{D-C}=\phi.$

4. Calculate $\quad \cos 2\phi\dfrac{C+D}{C-D}=P.$

5. Calculate $$\frac{P-1}{P+1}=\frac{1}{K^2}.$$

6. Calculate $$\phi+\tan^{-1}\frac{1}{K^2}\frac{\cos\phi-(A/B)\sin\phi}{\sin\phi+(A/B)\cos\phi}=\theta.$$

7. Calculate

$$L=K^{-2}\cos\phi\cos(\theta-\phi)-\sin\phi\sin(\theta-\phi)$$
$$M=K^{-2}\sin^2\phi+\cos^2\phi$$
$$N=K^{-2}\cos^2(\theta-\phi)+\sin^2(\theta-\phi).$$

8. Calculate $$V=\frac{A}{C}\frac{M}{L}.$$

9. Calculate $$V_c^2=\frac{VL}{A}-NV^2.$$

§ 5. Conclusion

Up to the present three basic approaches to wind measurement by spaced receivers have been suggested. Mitra's method of lag analysis was the first to be proposed. This method was refined to take account of the random shape of the diffraction pattern by Pütter and to take account of the random motion of the pattern by Banerji. Both these latter methods suggested a graphical analysis of the data which was very quick and convenient. However, the simple graphical approach seems to be ineffective when there is significant random motion in the anisotropic case and a purely statistical technique has to be used. This technique, which we have developed in this paper, can be taken as a development of the work of Briggs and Spencer.

Briggs, Phillips and Shinn's (1950) autocorrelation analysis method, which is rather laborious, has the advantage that some of the basic assumptions can be tested in the course of the analysis. The method is primarily applicable to isotropic cases. The errors introduced in the method by anisotropy have been discussed by Phillips and Spencer (1955), and their methods can be used for deducing the correct velocity geometrically in the anisotropic case.

Yerg's recently suggested numerical analytical method (1959) has brought a new approach to the field and can be considered a third basic method of wind measurement.

We have had previous occasion to point out the basic identity of the models used in the lag and the autocorrelation methods. If there is any essential difference between these methods it is in their sensitivity to statistical errors. To our mind, it is highly desirable that the limits of error of each method be calculated and compared. This has so far only been done (Banerji 1958b) for the Yerg (1955) six-point method.

Sales (1956) has analysed a series of data by several methods and compared the wind velocities obtained by different methods. This might be a fitting place to record that we have used his (t_1, t_2) plot once more to calculate the velocity by the method proposed here. Our results indicate a velocity of 79 m sec^{-1} inclined at $-67°$ to the X axis. Our previous calculations, assuming isotropy, yielded 63 m sec^{-1} at $-39°$.

It will be noticed that the anisotropy (if neglected) introduces a definite veering of the apparent wind direction towards the minor axis. This is in

accordance with the relationship deduced by us (Banerji 1956) regarding the relationship of the true and apparent velocity as dependent on the anisotropy.

§ 6. Acknowledgments

The major part of the work reported here—the shape of the distribution ellipse and the slopes of the (t_1, t_2) plot—were carried out in the Indian Statistical Institute. My indebtedness to Mr. Samar K. Mitra for making time available for the purpose is hereby gratefully recorded.

The method of analysis suggested in § 4 was developed and applied to Sale's data at the University of New Brunswick. I am very grateful to Dean J. O. Dineen for having made time available for this work.

References

Banerji, R. B., 1956, *Scientific Report* No. 81; Ionosphere Research Laboratory, The Pennsylvania State University.

—— 1958 a, *J. Atmos. Terr. Phys.*, **12**, 248.

—— 1958 b, *Proceedings of the International Symposium on Statistical Methods in Radio Propagation, Los Angeles* (New York: Pergamon Press).

Briggs, B. H., and Page, E. S., 1955, *The Physics of the Ionosphere* (London: Physical Society), p. 119.

Briggs, B. H., Phillips, G. J., and Shinn, D. H., 1950, *Proc. Phys. Soc.* B, **63**, 106.

Briggs, B. H., and Spencer, M., 1955, *The Physics of the Ionosphere* (London: Physical Society), p. 123.

Longuet-Higgins, M. S., 1957, *Proc. Phys. Soc.* B, **70**, 559.

Mitra, S. N., 1949, *Proc. Instn Elect. Engrs*, Pt. III, **96**, 441.

Phillips, G. J., and Spencer, M., 1955, *Proc. Phys. Soc.* B, **58**, 481.

Pütter, P. St., 1955, *The Physics of the Ionosphere* (London: Physical Society), p. 191.

Ratcliffe, J. A., 1954, *J. Atmos. Terr. Phys.*, **5**, 173.

Sales, G., 1956, *Scientific Report* No. 88, Ionosphere Research Laboratory, The Pennsylvania State University.

Yerg, D. G., 1955, *J. Geophys. Res.*, **60**, 173.

—— 1959, *Ibid.*, **64**, 27.

The Specific Heats of Two Polymorphic Forms of Manganous Sulphide, and the Inferred Possibility of Antiferromagnetic Ordering in Stacking Faults†

By W. S. CARTER‡

Research and Development Department, Central Electricity Generating Board, Friars House, Blackfriars Road, London, S.E.1

MS. received 3rd March 1960, and in revised form 6th April 1960

Abstract. The results of the measurement of the specific heats in the range 76° K to 250° K of two samples of manganous sulphide are reported. The samples used crystallized in the zincblende and wurtzite structures and are the same as were used in the magnetic susceptibility measurements reported previously. The large anomaly in the specific heat of sample 1 confirms the onset of antiferromagnetic ordering in the zincblende structure at 100°K. The absence of a similar large anomaly in specimen 2 above 76°K shows that the wurtzite structure remains unordered at this temperature, but there is a small anomaly at 110°K. A study of the x-ray powder photographs, and the calculation of Madelung's constant for several possible types of stacking faults, show that this anomaly in the specific heat is consistent with magnetic ordering within stacking faults.

The possibility that the presence of ordered stacking faults may depress and smooth out the Néel temperature of the rest of the sample is also considered, and is suggested as a possible explanation for the absence of a Néel temperature above 76°K in specimen 2 whilst a specimen composed entirely of the wurtzite structure was shown to order above this temperature by Corliss *et al.*

§ 1. Introduction

In a previous paper (Carter and Stevens 1956), the results of susceptibility measurements made on the zincblende and wurtzite modifications of manganese suphide were reported.

As mentioned previously, this compound is of interest from the point of view of antiferromagnetism because it can exist in any of three crystalline structures below a temperature of about 500°K.

The best known, or green, modification has a sodium chloride structure in which the atoms are octahedrally co-ordinated and the Mn–S distance is 2·606 A. The zincblende and wurtzite modifications are cubic and hexagonal respectively and are related to each other in the same way as the cubic close packed structure is related to the hexagonal close packed. In these two structures the atoms are tetrahedrally co-ordinated with practically the same Mn–S distance, i.e. 2·425 Å and 2·427 Å respectively.

† The work reported here formed part of a Ph.D. Thesis submitted to Nottingham University 1957.

‡ Now at International Computers and Tabulators, Ltd., Gunnels Wood Road, Stevenage, Herts

The geometry of the octahedral co-ordination of the sodium chloride structure is favourable to a dominant antiferromagnetic super-exchange interaction between manganese atoms which are next nearest neighbours, and this probably involves an interaction between the $(3z^2-r^2)/r^2$ and $(x^2-y^2)/r^2$ 3d orbitals of the manganese atoms and the 3p orbitals of the sulphur atoms as suggested by Nesbet (1955) and Pratt (1955).

In the zincblende and wurtzite modifications the basic antiferromagnetic interaction is between the four manganese atoms of each tetrahedron which has a sulphur atom at its centroid. These tetrahedra are the fundamental unit of these structures, and the energetically most favourable arrangement is for two manganese atoms to have their spins pointing east, whilst the other two have west directed spins. When an ordered arrangement for the whole lattice is built up on this basis it is found, in both the wurtzite and zincblende cases, that each manganese atom has eight of its twelve nearest neighbour manganese atoms with spins aligned antiparallel, and four aligned parallel to its own.

By contrast with the sodium chloride structure, the tetrahedral co-ordination geometrically favours a super-exchange interaction via the xy/r^2, yz/r^2 and zx/r^2 3d orbitals, but the 3p sulphur orbitals are not directed to give a maximum overlap. This may be partially compensated for by a hybridization of 3p and 4s states.

In the above mentioned measurements the susceptibility of sample 1 (composed mainly of the zincblende structure) showed an anomaly at 100°K, which was assumed to be due to the onset of antiferromagnetic ordering. In contrast, the susceptibility of sample 2 (composed mainly of the wurtzite structure) showed no anomaly above 76°K.

Using the assumptions that both the nearest and the next nearest neighbour interactions are antiferromagnetic in nature, and that the interactions between nearest neighbours is much larger than that between next nearest neighbours, it was shown that the antiferromagnetic ordered arrangement represented in figure 1 (*a*) could be predicted for the zincblende structure. This arrangement corresponds to that known as improved ordering of the first kind (Anderson 1950).

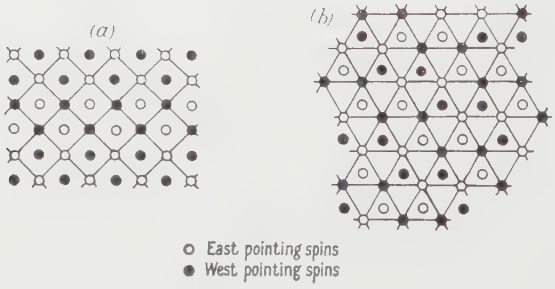

Figure 1. (*a*) represents the ordered arrangement found in the zincblende structure. Here only the manganese atom sites are shown. The black and white circles represent atoms with east and west pointing spins respectively. In this diagram the sites on the mesh lines represent the arrangement in alternate (100) planes, and the other sites show the arrangement in intermediate planes (i.e. the atoms form ferromagnetic chains in the ‹110› direction normal to the plane of the paper). (*b*) represents the ordered arrangement found in the wurtzite structure. Here the sites on the mesh lines represent the arrangement of alternate hexagonal planes and the others show the arrangement in the intermediate manganese planes. In this case ferromagnetic chains are formed in the *c* direction.

The same assumptions did not enable us to predict an ordered arrangement for the wurtzite modification, though it was realized later that the arrangement represented by figure 1 (*b*) does in fact follow from the above argument.

The neutron diffraction experiments of Corliss, Elliott and Hastings (1956) showed that both structures have an ordered antiferromagnetic arrangement at low temperatures, and that these are as expected on the above arguments. Corliss *et al.* also made susceptibility measurements, but at such wide temperature intervals that no sharp transitions, corresponding to Néel temperatures, were found. At high temperatures our measurements are in good agreement with those of Corliss *et al.* but in the vicinity of the Néel temperature there is some divergence. However both measurements agree in showing that the Néel temperature for the wurtzite modification is below that for the zincblende type.

The purpose of this paper is to report the results of measurements of the specific heats of the two modifications, made on the same samples as were used in the susceptibility work.

§ 2. Specific Heat Measurements

The apparatus was constructed according to the well-established practice of having a copper calorimeter, with an electric heater, surrounded by a shield, which was suspended in a vessel which formed part of a high vacuum system. The powder specimen was sealed in the calorimeter with an atmosphere of hydrogen, and the specific heat measurements were made by heating the calorimeter over successive intervals of 1° or 2° from 80°K to 250°K. During the measurements the shield temperature was automatically kept within 1° or 2° of that of the calorimeter. The time of heating was fixed at 90 seconds by a decatron controlled circuit, which was activated by the 50 c/s mains.

The heat input was calculated from potentiometric measurements of the p.d. across, and the current through, the calorimeter heater. The current and voltage, as well as the time of heating, were considered to be accurate to better than 0·1%. The rise in temperature was measured in terms of the change in e.m.f. produced by the thermocouple. The cold junction of this thermocouple was placed in a Dewar flask of liquid nitrogen so that the most sensitive range of the potentiometer could be used when the calorimeter temperature was in the vicinity of the boiling point of liquid nitrogen. As the change of e.m.f. due to a temperature of 1° or 2° could be measured to about 1% it was expected that the thermal capacity could be obtained to this degree of accuracy, as errors in the other measurements were small enough to be ignored. Unfortunately, the temperature rise could not be measured with the accuracy anticipated because of large fluctuations in the output of the thermocouple, even when the calorimeter was at a steady temperature. These were partially reduced by lagging all the connections external to the vacuum system with cotton wool. The remaining fluctuations appeared to originate at the cold junction and limited the measurement of thermal capacity to an accuracy to 5%.

Despite the rather large error involved in making each measurement of the specific heat, the trend of the specific heat curve could be obtained with more certainty by making several series of observations over the same temperature range. Had more time been available the apparatus could have been improved by using a platinum resistance thermometer in conjunction with an appropriate bridge circuit to make the temperature measurements.

Figures 2 and 3 are the result of the best of four or five series of measurements in the range 80°K to 240 K. Figure 2 shows the variation of the specific heat with temperature of specimen 1, which it was estimated consisted of 3·5 parts of the zincblende structure to 1 part of the wurtzite structure. This curve shows a large anomaly at 100 K, which corresponds to the Néel temperature as estimated by susceptibility measurements made on the sample. There seems to be little doubt that this sudden increase in specific heat as the temperature is lowered corresponds to the onset of antiferromagnetic ordering in the zincblende structure.

The specific heat of specimen 2, which it was estimated contained four parts of the wurtzite structure to one part of the zincblende modification, is shown in figure 3, and has a small anomaly at 110°K. Though this anomaly is only a little larger than the experimental spread of results it is thought to correspond to a genuine anomaly, as it appeared at the same temperature in each series of measurements. It is possible that this small excess specific heat is associated with ordering in the fraction of the sample which crystallized in the zincblende structure. However, as this anomaly appears at 10 K above the Néel temperature of specimen 1, it seems likely that it can be associated with antiferromagnetic ordering within stacking faults.

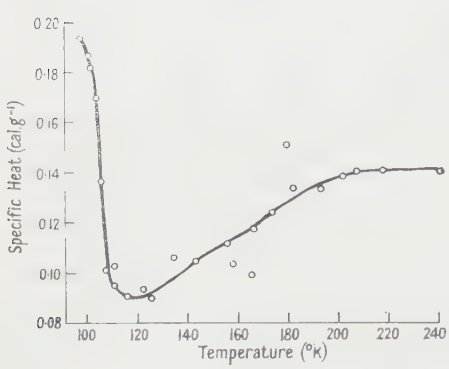

Figure 2. Specific heat plotted against temperature of sample 1, which is mostly zincblende.

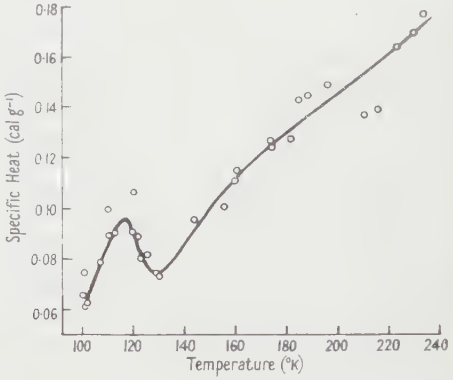

Figure 3. Specific heat plotted against temperature of sample 2, which is mostly wurtzite.

§ 3. Possibility of Ordering within Stacking Faults

The occurrence of stacking faults has been examined by Edwards, Lipson and Wilson (1942, 1943) in the case of hexagonal cobalt; and by Jagodizinski and Laves (1948) in a single crystal of zinc sulphide.

The results of the x-ray investigation of a single crystal of hexagonal cobalt showed that all the spots on an oscillation photograph are elongated along one of two lines, which correspond to the c direction in reciprocal space, with the exception of such reflections as 0001 (i.e. those due to the hexagonal planes) which remain sharp. This elongation of the spots, which is due to the presence of stacking faults, shows up in a powder photograph as a broadening of the lines, but in this case the line for which $\frac{1}{3}(h-k)$ is an integer and l is even (i.e. those which coincide with cubic reflections) are also sharp because they are elongated along Debye–Sherrer lines.

Examination of the x-ray powder photograph of specimen 2 indicates that the above mentioned lines are sharper than the others, and this is more noticeable for lines which correspond to large Bragg angles. From this it can be concluded that stacking faults must exist in specimen 2, though it is impossible to estimate their proportional contribution to the total amount of cubic phase present.

The nature of these stacking faults is more easily described if the crystals are thought of as though they were composed of a sulphur lattice, with the manganese atoms entering the appropriate tetrahedral sites as interstitial components. When thought of in this way two distinct types of fault can be envisaged. The first type arises as a fault in the sulphur lattice which is copied by the manganese lattice. This gives the following cases:

$$\text{AaBbCcAaBbCc}\ \boxed{\text{AaBbAaBb}}\ \text{CcAaBbCc} \quad \ldots\ldots(1)$$

and $$\text{AaBbCcAaBbCc A}\ \boxed{\text{bB}}\ \text{aAbBcCaAbBcC} \quad \ldots\ldots(2)$$

in the cubic structure, and

$$\text{AaBbAaBb}\ \boxed{\text{A}^{\alpha}\text{a}^{\beta}\text{B}^{\gamma}\text{b}^{\delta}\text{C}^{\epsilon}\text{c}^{\mu}}\ \text{BbCcBbCcBbCc} \quad \ldots\ldots(3a)$$

$$\text{AaBbAaBb}\ \boxed{\text{Aa Bb Cc}}\ \text{BbAaBbAa} \quad \ldots\ldots(3b)$$

$$\text{AaBbAaBbAaBb}\ \boxed{\text{AaBcCb}}\ \text{BcCbBcCbBc} \quad \ldots\ldots(4a)$$

$$\text{AaBbAaBbAaBb}\ \boxed{\text{AaBcCb}}\ \text{BaAbBaAbBa} \quad \ldots\ldots(4b)$$

in the hexagonal modification. Here the capitals refer to the hexagonal layers of sulphur atoms, and the lower case letters to the layers of manganese atoms.

Considering the cubic case first: In (1) there are four manganese layers whose relative positions are the same as in the hexagonal lattice. In case (2) there is an odd manganese layer which separates two portions of the crystal in which the relative stacking arrangement of manganese layers is displaced with respect to each other. This case also contains the arrangement c A b which does not occur in either of the parent lattices but would be characteristic of an inverse nickel arsenide structure. In cases $(3a, b)$ and $(4a, b)$ there are three layers of manganese atoms which have the same arrangement as found in the cubic lattice. Cases $(4a, b)$ also have the arrangement a B c, which is equivalent to the c A b found in case (2).

The other type of fault that can be postulated is that of a misarrangement of the manganese stacking order whilst the sulphur lattice remains regular. This gives the following cases:

$$\text{AaBbCcAaB}\ \boxed{\text{bCcAbBc}}\ \text{CaAbBcCaAbBcC} \quad \ldots\ldots(5)$$

for the cubic case, and

$$\text{AaBbAaBb A}^{\pi}\ \boxed{\text{a}^{\rho}\text{B}^{\sigma}\text{a}^{\rho}}\ \text{A}^{\pi}\ \text{bBaAbBaAbB} \quad \ldots\ldots(6)$$

for the hexagonal case.

Case (5) gives a manganese lattice which contains four planes of the hexagonal structure and is, from the point of view of the manganese atoms, the same as case (1). This case also contains the arrangement c A b as found in case (2).

In case (6) the arrangement a B a which is characteristic of the normal nickel arsenide structure is found.

The probability of each of these faults occurring will largely depend on the ratio of the Madelung constant of the fault to that of the parent lattice. The Madelung constants were only calculated for faults of types (3) and (6), because the wurtzite structure was of more interest from the immediate point of view. Faults of type $(4a, b)$ were considered as unlikely to occur as they contained the arrangement c A b, which is characteristic of the unknown nickel arsenide structure.

The Madelung constants were calculated by the method proposed by Frank (1950), and details are given in Appendix 1. As a check, the Madelung constants for the normal zincblende and wurtzite structures were calculated first. These were found to be $M_a = 2{\cdot}67(1)$ and $M_a = 2{\cdot}67(5)$ which compare well with the values $M_a = 2{\cdot}675$ and $M_a = 2{\cdot}680$ ($M_d = 1{\cdot}6381$, and $M_d = 1{\cdot}641$) given by Seitz (1940). For the calculation it was assumed that the lattice was composed of monovalent ions.

In the case of both faults of type (3) values of $M_a = 2{\cdot}67(5)$, $M_a = 2{\cdot}68(1)$, $M_a = 2{\cdot}67(2)$; and $M_a = 2{\cdot}67(5)$, $M_a = 2{\cdot}67(1)$, $M_a = 2{\cdot}67(1)$, were found for the planes indexed α, β, γ; and δ, ϵ and μ respectively. The values obtained for fault type (6) were $M_a = +10{\cdot}1$, $M_a = -3{\cdot}92$, $M_a = 21{\cdot}88$ for the planes indexed ρ, π, σ when the spacing was fixed so that the distance between sulphur planes remained constant across the fault. The values $M_a = 13{\cdot}51$, $M_a = -3{\cdot}72$, $M_a = 3{\cdot}51$ were obtained for these three planes when the spacing of the planes in the fault was adjusted to correspond to that which might be predicted for manganous sulphide if it crystallized in the nickel arsenide structure.

The constant value of M_a obtained for faults of type $(3a, b)$ which also corresponded to the value obtained for the parent crystal was taken as indicating that these faults are quite likely to occur. On the other hand, the oscillating value obtained for the planes in fault type (6) was taken as indicating that this fault is not favoured electrostatically and is therefore unlikely to occur.

When considered from the magnetic point of view it would appear that the four manganese planes of fault types (1) and (5) could order independently of the rest of the lattice, and that the ordered arrangement would be compatible with the ordering in the neighbouring cubic planes. However there is no reason to suppose that ordering within these faults is likely to occur at a higher temperature than it does for the rest of the crystal. The question of independent ordering does not arise in the case of fault type (2), as the odd layer of manganese atoms only serves to separate two portions of cubic crystal whose stacking arrangements are displaced with respect to each other.

Faults of type $(3a)$ and $(3b)$ and $(4a)$ and $(4b)$ in the hexagonal structure contain three manganese planes which conform to the cubic structure, and if the same assumptions as were applied to determine the ordering of the hexagonal structure are also applied here it seems reasonable to suppose that these faults may order independently of the rest of the crystal (especially when it is realized that a manganese atom of the central plane is unaware of the fact that it is not in an infinite zincblende lattice, as long as nearest and next nearest neighbour

interactions only are considered). However, each manganese atom of the outer planes has three of its nearest and three of its next nearest neighbours in the rest of the crystal. Fault type (6) may be supposed to order so that each of the manganese planes forms a ferromagnetic sheet but with the direction of magnetization of these planes arranged antiparallel to each other. This would then correspond to the ordered arrangement found in CrSb.

From the above discussion and calculation of Madelung's constant, it can be concluded that faults of type (3 *a*) and (3 *b*) only are likely to occur in the wurtzite structure and that these faults are capable of ordering independently of the rest of the crystal. Though no definite estimate can be made of their Néel temperatures, it is reasonable to assume that they would be virtually the same as that of the zincblende structure.

By comparing the respective areas under the anomalies in the specific heat curves of specimens 1 and 2 it was estimated that that of specimen 2 was due to antiferromagnetic ordering occurring in 10% to 20% of the sample. Because this occurs at 110°K, which is 10°K above that of specimen 1, it is suggested that this anomaly should be associated with antiferromagnetic ordering within stacking faults of types (3 *a*) and (3 *b*) rather than ordering in separate crystals of zincblende structure. This assumption then implies that the cubic phase identified in the x-ray photograph of the specimen, which was estimated at 25%, must be considered as being composed entirely of stacking faults.

If both these values are taken as estimates of the proportion of stacking faults in specimen 2, though rather approximate, they are consistent with the average value of a stacking fault in every 14 planes, which was given by Edwards, Lipson and Wilson (1942) for hexagonal cobalt.

If 10% to 20% of the sample comprises stacking faults of types (3 *a*) and (3 *b*) then, on the average, there are 10 to 30 manganese planes between each consecutive pair of faults. Since this number is small, especially when compared with the number of hexagonal planes in a crystal entirely composed of the wurtzite structure, the stacking faults may influence the temperature at which the intervening planes order.

When the temperature is reduced sufficiently for these regions to order, the ordering already present in the stacking faults will act as nuclei, and each region will be influenced by the ordered arrangement of the two stacking faults which define its boundaries.

As the probability of these arrangements being compatible is one in twelve (see Appendix 2) most of these regions will have to accommodate a magnetic ordering fault and the reduction in internal energy will not be as large as it will be in a region where the ordering is compatible.

The effect, in any one region, will be to depress the Néel temperature by an amount that will be a function of the number of planes in the region. Because of the statistical variation of the number of planes in these regions the effect on a large sample will cause a smoothing out of the Néel temperature as well as depressing the mean value.

It is not possible to say how large this effect should be, or even if it is significant, but it is interesting to note that this could explain why one sample used by Corliss *et al.* which was entirely composed of the wurtzite structure ordered above 76°K, whereas no ordering was detected in sample 2 apart from that found in the stacking faults.

§ 4. Conclusion

The specific heat measurements help to confirm that antiferromagnetic ordering occurs at 100°K in the zincblende structure, and that ordering is not apparent above 80°K for the wurtzite structure. However the work of Corliss, Elliott and Hastings has shown that both structures order when the temperature is reduced sufficiently.

The small anomaly in the specific heat of specimen 2, which occurs at 110°K, cannot be explained with certainty, but it has been shown that it is possibly due to antiferromagnetic ordering within stacking faults, and this in turn suggests that the structure of specimen 2 (and probably that of specimen 1 as well) is largely composed of stacking faults, rather than being composed of a mixture of the two types of crystals.

Acknowledgments

The author wishes to thank Professor L. F. Bates for the use of his laboratory and for his constant interest in the work. Professor K. W. H. Stevens must also be thanked for the initial suggestion of ordering within stacking faults, and for his continued interest and help.

APPENDIX 1

The calculation of the Madelung constant for the zincblende and wurtzite structures as well as for the stacking faults, were performed by applying the method suggested by Frank (1950) to these lattices.

In the results of these calculations the value of M quoted (which is given in terms of the unit distance a in the hexagonal plane) corresponds to a crystal composed of monovalent ions. The divalent nature of the ions in the compound manganous sulphide (assuming it is entirely ionic in nature) was ignored as we are only interested here in the relative values of the Madelung constants.

For this method each charge e is replaced by two charge distributions A and B, about the same lattice site. Charge distribution A consists of a charge $-e$ at the lattice point and n charges of $+e/n$ each, at a distance r from the lattice point and arranged so that it coincides with their electric 'centre of gravity'. Charge distribution B consists of n charges of $-e/n$ which coincide with the n charges of value $+e/n$ of distribution A. The two distributions are equivalent to the original charge, but if the resultant potentials are summed over the lattice separately, distribution A is a high order multipole whose effect very rapidly diminishes with distance. In the case of the wurtzite structure the calculation was made by considering the hexagonal prism, represented in figure 4, of height $2c$ and extending over 19 atoms in a 'B' plane. The potential at the central site was calculated by considering the effect of the charges within the prism directly, and dividing the charges of the rest of the lattice into distributions A and B, where the fractional charges were taken as $-e/4$ and placed tetrahedrally about their associated site so that they were at the bond centres. The potential resulting from the multipoles of distribution A was ignored and the charges of distribution B due to neighbouring hexagonal planes cancelled out except at the edge of the hexagonal prism. The resultant potential was then found by adding the potential due to the charges within the prism and the fractional charges at the edges of the prism, which are shown in figure 4.

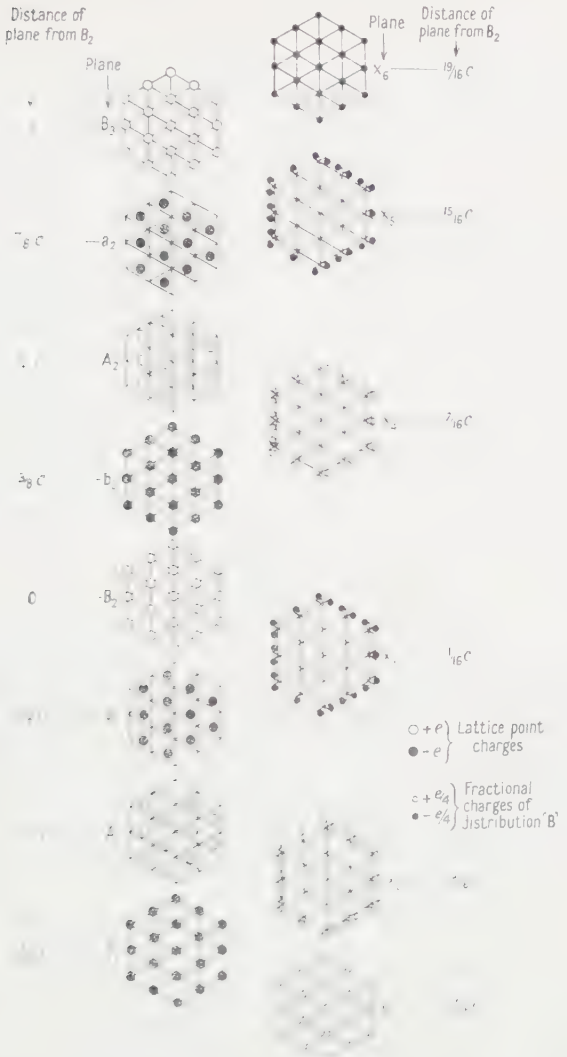

Figure 4 represents the charge distribution used to calculate the electrostatic potential at the central site of plane B2. The left-hand side shows the charges within a prism of height $2c$, and the potential due to these charges is calculated directly. The right-hand side shows the result of summing charges of distribution B over the rest of the lattice, and the potential due to these charges is used to represent the effect of the remainder of the lattice.

In the calculation of fault type (6) the fractional charges that appear in distributions A and B had to be given the value $e/6$ and placed three on each side of the plane containing the lattice site in question. In order to obtain the cancellation of charges in distribution B, it was found necessary to place these fractional charges at a greater distance from the lattice point as the distance from the central plane to the plane considered increased. This means that neglecting the multipole moments of distribution A is no longer such a good approximation, and may even invalidate the use of the method in this case. The difficulty of applying Frank's method to this type of fault is a reflection of the fact that the atoms within the central (or B) plane of the fault have six-fold

co-ordination so that the atoms of the neighbouring (A) planes have to satisfy six-fold co-ordination on one side of their plane, whilst they are tetrahedrally co-ordinated on the other side. This fact alone probably provides sufficient reason to reject the possibility of the occurrence of this type of fault.

APPENDIX 2

If two regions, such as stacking faults, of one of these crystals are already ordered then the probability of the ordering being compatible is the same as that of making a tracing of figure 1 (*b*) register on the original diagram so that circles of the same shade correspond, when the only restriction imposed is that the mesh lines should register.

It is readily seen that there are four different sites in each hexagonal plane so that the probability of exact registration is one in four if the tracing is not rotated, but if it can be rotated then it may be put down in one of three orientations. Out of these three orientations there is only one in which the pattern can register, so that the total probability is reduced to one in twelve.

References

Anderson, P. W., 1950, *Phys. Rev.*, **79**, 350.
Carter, W. S., and Stevens, K. W. H., 1956, *Proc. Phys. Soc.* B, **69**, 1006.
Corliss, L., Elliott, N., and Hastings, J., 1956, *Phys. Rev.*, **104**, 924.
Edwards, O. S., Lipson, H., and Wilson, A. J. C., 1942, *Proc. Roy. Soc.* A, **180**, 268.
—— 1943, *J. Inst. Metals*, **69**, 177.
Frank, F. C., 1950, *Phil. Mag.*, **41**, 1287.
Jagodizinski, H., and Laves, F., 1948, *Schweiz. Min. Petrogr. Mitt.*, **28**, 456.
Nesbet, R. K., 1955, *Prog. Rep.* (*Jan.*) *M.I.T. Solid State Group.*
Pratt, G. W., Jr., 1955, *Phys. Rev.*, **97**, 926.
Seitz, F., 1940, *The Modern Theory of Solids* (New York: McGraw-Hill).

Paramagnetic Resonance Absorption in Bromine and Chlorine

By J. S. M. HARVEY, R. A. KAMPER and K. R. LEA
The Clarendon Laboratory, Oxford

Communicated by B. Bleaney; MS. received 10th June 1960

Abstract. The microwave Zeeman spectra of atomic chlorine and bromine have been observed. From measurements on several lines in the spectrum of the $^2P_{3/2}$ ground level, the electronic g-factors are found to be

$$g_J(\mathrm{Br}) = 1{\cdot}333921 \pm (5 \times 10^{-6})$$
$$g_J(\mathrm{Cl}) = 1{\cdot}333927_5 \pm (3 \times 10^{-6}).$$

An estimate of relativistic and diamagnetic corrections to the g-factors, based on self-consistent field wave functions, is in satisfactory agreement with the experimental results. A comparison is made with the g-factors of fluorine and iodine.

§ 1. Introduction

Paramagnetic resonance has been observed in free atoms of bromine and chlorine, and measurements have been made with a precision of a few parts per million.

The ground electronic configurations of these elements consist of closed shells, together with an outermost incomplete p shell containing five electrons. The only Russell–Saunders spectral term which can be formed from this configuration is a ^2P, the ground state being $^2P_{3/2}$. Bromine possesses two stable isotopes, of masses 79 and 81, which occur naturally in the ratio 50·5 : 49·5; chlorine also has two stable isotopes, of masses 35 and 37, which occur in the ratio 75·5 : 24·5. Each isotope of each element has a nuclear spin of 3/2, and therefore gives rise to $2J(2I+1)=12$ transitions of the form $\Delta M_J = \pm 1$, $\Delta M_I = 0$, all of which were observed experimentally. Six bromine and six chlorine lines were selected for accurate measurement, and some six runs were made on each line.

In magnetic fields of the order of a few kilogauss the energy of the Zeeman splitting in an atom is considerably greater than that of the hyperfine interaction. We have therefore used values of the hyperfine structure constants obtained in low fields by atomic beam methods to interpret our results, which then yield accurate values for the electronic g-factors.

The interest in the g-factors lies in their departure from the value predicted by the Landé formula. If the electronic wave functions are sufficiently well known, an experimental result can be interpreted to give a value for the spin magnetic moment of the electron. In the present work this is not the case, and the experimental results serve as much as a test of the precision of the available wave functions as of the validity of the underlying theory. It is also interesting to compare the g-values of all the halogens; this is done in the last part of this paper.

§ 2. Experimental

The experiments were performed with the paramagnetic resonance spectrometer of Bowers, Kamper and Knight (1957) which was slightly modified. The free atoms of bromine and chlorine were produced by an 80 Mc/s electrodeless

discharge, power at this frequency being coupled into a tuned circuit located above the cavity resonator. A quartz tube containing the low pressure gas passed straight through the coil of the tuned circuit into the cylindrical cavity resonator, along its axis. At the far end the tube was led out through a hole in the base of the cavity and connected to a condensing trap and fast pumping system. The flow of gas was maintained by vacuum distillation, the bromine (or chlorine) evaporating from a reservoir at $-70°$c, flowing through the discharge tube and condensing in the cold trap which was maintained at $-180°$c. Signal-to-noise ratios obtained for the bromine and chlorine lines averaged about 15 or 20:1, indicating about 1% dissociation of the molecular vapour inside the cavity.

§ 3. Results

We interpreted our measurements on the basis of the following Hamiltonian, which is based on that of Abragam and Pryce (1951):

$$\begin{aligned}\mathscr{H} = {} & \xi(\mathbf{L}.\mathbf{S}) + \beta\mathbf{H}.(\mathbf{L}+g_s\mathbf{S}) - g_I\beta_N(\mathbf{H}.\mathbf{I}) \\ & + 2g_I\beta\beta_N\langle r^{-3}\rangle\{(\mathbf{L}.\mathbf{I}) + \tfrac{2}{5}L(L+1)(\mathbf{S}.\mathbf{I}) - \tfrac{3}{5}(\mathbf{L}.\mathbf{S})(\mathbf{L}.\mathbf{I}) - \tfrac{3}{5}(\mathbf{L}.\mathbf{I})(\mathbf{L}.\mathbf{S})\} \\ & - \frac{e^2Q\langle r^{-3}\rangle}{5I(2I-1)}\{3(\mathbf{L}.\mathbf{I})^2 + \tfrac{3}{2}(\mathbf{L}.\mathbf{I}) - L(L+1)I(I+1)\}\end{aligned}$$

in the conventional notation. The first term has eigenvectors characterized by values of J, the total electronic angular momentum. It gives rise to the fine structure splitting (3685 cm^{-1} in bromine and 881 cm^{-1} in chlorine) and is more than three orders of magnitude greater than any of the others. The whole Hamiltonian was therefore diagonalized with respect to J using second-order perturbation theory. The secular problem within the $J=3/2$ manifold was then solved numerically, using the Ferranti MERCURY computer at the Oxford University Computing Laboratory. The hyperfine structure interaction constants in the $^2P_{3/2}$ level had previously been measured by the method of atomic beams by King and Jaccarino (1954) for bromine, and by Holloway, Aubrey and King (1956) for chlorine. The nuclear gyromagnetic ratios for bromine and chlorine were also known from the work of Sherriff and Williams (1951) and Ting and Williams (1953) respectively. Our results confirm the atomic beam values of the hyperfine structure constants to within 0·01 Mc s, and yield the following values for the electronic g-factors, expressed in terms of the gyromagnetic ratio of the proton, g_p:

$$g_J(\mathrm{Br};\ {}^2P_{3/2})/g_p = 438{\cdot}5026 \pm 0{\cdot}0013$$
$$g_J(\mathrm{Cl};\ {}^2P_{3/2})/g_p = 438{\cdot}5048 \pm 0{\cdot}0007.$$

The error quoted represents twice the root mean square deviation of the six results from their mean. Combining these with the current theoretical value for the spectroscopic splitting factor of a free electron ($g_s = 2{\cdot}0023192$), and the experimental result of Koenig, Prodell and Kusch (1952) for g_p/g_s, the electronic g-factors may be written:

$$g_J(\mathrm{Br};\ {}^2P_{3/2}) = 1{\cdot}333921\ \pm (5\times10^{-6})$$
$$g_J(\mathrm{Cl};\ {}^2P_{3/2}) = 1{\cdot}333927_5 \pm (3\times10^{-6}).$$

Independent measurements.

The g-value given above for bromine is the only one of this precision known to us.

The result for chlorine is not in agreement with the value of $1{\cdot}33379 \pm (7 \times 10^{-5})$ obtained by Wolga (1959) in a paramagnetic resonance experiment. It is, however, consistent with the result recently announced by Beltran-Lopez and Robinson (1960), who find $g_J = 1{\cdot}333916 \pm (15 \times 10^{-6})$. The theoretical g-value (see § 4) agrees with the higher values.

§ 4. Discussion

Electronic g-factors of the Halogens

The foregoing studies of bromine and chlorine complete a series of precise experimental measurements of the electronic g-factors of the halogens from fluorine to iodine. These other g-values are:

$g_J(\mathrm{F};\ {}^2\mathrm{P}_{3\,2}) = 1{\cdot}333861\ \pm (2 \times 10^{-6})$ (Radford, Hughes and Beltran-Lopez 1960)†
$g_J(\mathrm{I};\ {}^2\mathrm{P}_{3\,2}) = 1{\cdot}333995\ \pm (4 \times 10^{-6})$ (Bowers, Kamper and Lustig 1957).

On the basis of pure Russell–Saunders coupling and including the theoretical value for the spectroscopic splitting factor of a free electron, the Landé formula predicts a g-value of $1{\cdot}334106_4$ for a ${}^2\mathrm{P}_{3\,2}$ level. Abragam and Van Vleck (1953) showed how various relativistic and diamagnetic corrections to the g-value could be calculated, provided the radial wave functions are known. The effect of an external magnetic field may be included in the Hamiltonian for an atom by taking all the velocity-dependent terms and replacing the linear momentum $\mathbf{p}$ by $\mathbf{p} + (e/c)\mathbf{A}$, where $\mathbf{A}$ is the vector potential. (In a non-relativistic approach the spin magnetic moment must be introduced separately, but it does not lead to any extra corrections to the Landé formula of the kind we are seeking.) When this is done to the spin–orbit, spin–other-orbit and orbit–orbit interactions it leads to small terms which are linear in H and hence must contribute to the g-value of the atom. Also, the mass m of the electron in the formula for the Bohr magneton should be replaced by its relativistic value $m(1 - v^2/c^2)^{-1/2}$. This relativistic correction and that generated from the spin–orbit coupling together form the Breit Margenau correction which may be obtained by a proper relativistic treatment of a single electron in a central field. The other two terms give the effect of the diamagnetism of the inner electrons on the spin and orbital spectroscopic splitting factors respectively.

We have followed Abragam and Van Vleck's method for calculating theoretical g-values for the halogens. These are shown in the table where the contributions of the different correction terms are separated. For fluorine, the self-consistent field wave functions of Brown (1933) were used. This calculation has already been reported by Radford, Hughes and Beltran-Lopez (1960). Two sets of wave functions were available for chlorine: one from a self-consistent field calculation by Hartree, Kronig and Petersen (1934) and the other from a variational co-detor calculation by Boys and Price (1954). The latter were slightly simplified for the calculation of the diamagnetic corrections. The error introduced in the predicted g-value should not be greater than one or two parts per million. Arnot and McLauchlan (1934) have calculated a self-consistent field wave function for bromine. Calculations using the self-consistent field wave functions are subject to a small uncertainty, depending on the method of interpolating the wave functions between the tabulated values, which is magnified in the case of one of the

† We are indebted to Professor V. W. Hughes for communicating his results in advance of publication.

Halogen g-factor Corrections

Wave function	Fluorine		Chlorine			Bromine		Iodine
	Slater	Brown	Slater	Boys	Hartree	Slater	Arnot	Slater
Correction (ppm)								
Breit–Margenau	−144	−127	−41	−84	−85	−31	−84	−24
Spin–other-orbit	−29	−20	−12	−14	−13	−10	−14	−9
Orbit–orbit	−40	−35	−28	−29	−28	−36	−35	−36
Total	−213	−182	−81	−127	−126	−77	−133	−69
Predicted g-value	1·333823	1·333864	1·334000	1·333936	1·333938	1·334005	1·333929	1·334015
Observed g-value	1·333861		1·333928			1·333921		1·333995
Deviation (ppm)	−28	2	54	6	8	63	6	15

corrections (see below) because the major contribution to it comes from a small region of space near the origin. The only wave functions available in a suitable form for iodine were the approximate screened hydrogenic ones of Slater (1930). These were tested by calculating the g-values of all the other halogens in the hope of being able to judge the amount and direction of their error in iodine.

It can be seen from the table that the g-values of fluorine, chlorine and bromine are all predicted to within a few parts per million on the basis of the more elaborate wave functions. The residual deviations are within the limits of accuracy of the theory, in which exchange integrals were ignored. Kambe and Van Vleck (1954) showed that in oxygen the exchange integrals accounted for a proportion of the order of 10 parts per million of the g-value, so that the uncertainty introduced by leaving them out makes it unprofitable to attach any significance to such small discrepancies. The experimental results show an overall trend to larger g-values with increasing atomic number, except that the g-value for chlorine is a little higher than that for bromine. This anomaly is reflected in the theoretical predictions, which show that although the Breit–Margenau and spin–other-orbit corrections are almost identical for the two elements, the orbit–orbit correction is appreciably smaller in chlorine. This latter correction has an almost constant value of 35 parts per million in the other halogens.

The Slater wave functions appear to give reasonable agreement with the others for the diamagnetic corrections but give rather poor values for the Breit–Margenau term. This term depends on $\langle T \rangle$, the mean value of the kinetic energy of the outermost p electrons, which is very sensitive to the electron density near the origin. A comparison with the values predicted for this term by self-consistent field wave functions shows that the Slater wave functions over-estimate $\langle T \rangle$ in fluorine, predict only half its value in chlorine and little more than a third in bromine. A smooth extrapolation suggests that the value of $\langle T \rangle$ predicted for iodine may be too small by a factor of about 3. If we multiply the Breit–Margenau term by 3, the new g-value predicted for iodine falls some 35 parts per million below the experimental result. This discrepancy is significantly greater than, and of opposite sign to, those found with the self-consistent field wave functions in the other halogens. It strongly suggests the occurrence of a small breakdown of Russell–Saunders coupling in the ground level of the iodine atom. Such a breakdown is more probable in iodine than in the other halogens because of the greater spin–orbit interaction in iodine and the closer proximity to the ground level of the excited states which it must admix. The admixture of other terms required to make this change in the g-value is less than one part in 2000 (amplitude squared), so Russell–Saunders coupling is still a fair approximation for most spectroscopic purposes. An admixture of this size is quite plausible in order of magnitude, but a proper theoretical prediction is impossible without reasonable wave functions for the excited states.

Acknowledgments

The authors are grateful to Professor B. Bleaney for his interest and encouragement, to Dr. C. D. Lustig and Mr. L. J. Arundel for their generous assistance, to the Board of Admiralty for a grant towards equipment, and to the Oxford University Computing Laboratory for use of its facilities. J. S. M. H. is indebted to the Shell Petroleum Company for a Scholarship; R. A. K. to Imperial Chemical Industries for a Research Fellowship; and K. R. L. to the Department of Scientific and Industrial Research for a maintenance grant.

References

Abragam, A., and Pryce, M. H. L., 1951, *Proc. Roy. Soc.* A, **205,** 135.

Abragam, A., and Van Vleck, J. H., 1953, *Phys. Rev.*, **92,** 1448.

Arnot, F. L., and McLauchlan, J. C., 1934, *Proc. Roy. Soc.* A, **146,** 662.

Beltran-Lopez, V., and Robinson, H. G., 1960, *Bull. Amer. Phys. Soc.*, Ser. II, **5,** 273.

Bowers, K. D., Kamper, R. A., and Knight, R. B. D., 1957, *J. Sci. Instrum.*, **34,** 49.

Bowers, K. D., Kamper, R. A., and Lustig, C. D., 1957, *Proc. Phys. Soc.* B, **70,** 1176.

Boys, S. F., and Price, V. E., 1954, *Phil. Trans. Roy. Soc.* A, **246,** 451.

Brown, F. W., 1933, *Phys. Rev.*, **44,** 214.

Hartree, D. R., Kronig, R. de L., and Petersen, H., 1934, *Physica*, **1,** 895.

Holloway, J. H., Aubrey, B. B., and King, J. G., 1956, *Quarterly Progress Report, Research Laboratory of Electronics, Massachusetts Institute of Technology*, April 15, p. 35.

Kambe, K., and Van Vleck, J. H., 1954, *Phys. Rev.*, **96,** 66 (see also Innes, F. R., and Ufford C. W., 1958, *Phys. Rev.*, **111,** 194).

King, J. G., and Jaccarino, V., 1954, *Phys. Rev.*, **94,** 1610.

Koenig, S. H., Prodell, A. G., and Kusch, P., 1952, *Phys. Rev.*, **88,** 191.

Radford, H. E., Hughes, V. W., and Beltran-Lopez, V., 1960, *Bull. Amer. Phys. Soc.*, Ser. II, **5,** 272, and private communication.

Sherriff, R. E., and Williams, D., 1951, *Phys. Rev.*, **82,** 651.

Slater, J. C., 1930, *Phys. Rev.*, **36,** 57.

Ting, Y., and Williams, D., 1953, *Phys. Rev.*, **89,** 595.

Wolga, G. J., 1959, *Quarterly Progress Report, Research Laboratory of Electronics, Massachusetts Institute of Technology*, April 15, p. 45.

RESEARCH NOTES

Electric Conduction in Antiferromagnetics

By G. L. SEWELL
Mathematical Institute, University of Liverpool

MS. received 24th June 1960, in final form 10th August 1960

In a previous note by Fröhlich and the author (1959), it was pointed out that there are two theoretically-possible mechanisms which can lead to a very low mobility μ in a semiconductor. Our alternative is that the conduction takes place in an energy band rendered very narrow by the electron–lattice interaction (cf. Sewell 1958). However, there are circumstances where the band model becomes invalid, namely when the electron–phonon coupling is so strong that the electrons move from ion to ion more easily by means of phonon-activated processes than by tunnel effect; and in such cases, electric conduction may be regarded as a diffusion process in which the electrons jump from ion to ion through the agency of the phonons. The theory of the jump mobility may be based on a model in which an electron can move along a line L of cations spaced at intervals of a. Assuming that jumps between non-nearest neighbours of L occur with negligible probability, it suffices to consider procesess in which an electron jumps from a cation A to one of its nearest neighbours on L. We shall denote these neighbours by A_- and A_+; and we shall let $P_\pm$ denote the probabilities per unit time that an electron jumps from A to $A_\pm$ when an electric field F is applied in the direction of AA_-. The mean electronic velocity in the direction of F is thus $a(P_+ - P_-)$, so that the mobility is given by the relation

$$\mu F = a(P_- - P_+). \qquad \ldots\ldots (1)$$

It is important to note that the only processes which yield contributions to $P_\pm$ are phonon-activated ones, since the requirement of energy conservation ensures that an electron cannot migrate by tunnel effect from A to $A_\pm$ in the presence of the applied field.

A characteristic feature of the jumping mechanism is that it does not lead to a Hall effect. This is because a single jump is a process in which an electron starts from a state of zero velocity at one ion and finishes in a similar state at another ion. Thus, as the electron jumps along L from A to $A_\pm$, the Lorentz force due to an applied magnetic field transmits no velocity to it in the direction perpendicular to L, and therefore no Hall effect is produced.

The object of the present paper is to provide a simple qualitative explanation, based on the above ideas, for the anomalous electrical properties observed in impure specimens of the antiferromagnetic oxides NiO and α-Fe_2O_3 (Morin 1954). The main facts to be explained are that, in these materials, the electron mobilities are very small ($\ll 1\,cm^2\,sec^{-1}\,v^{-1}$), increase with T and possess activation energies of the order of 0·1 ev; and also that no Hall effect has been detected. It should be pointed out that, in Morin's experiments, both the conductivity σ and the density of conduction electrons n were measured, so that the activation

energy in μ could be separated from that in σ. The density n, which was measured by observing the Seebeck effect, was simply the density of extra d-electrons introduced by the impurities.

We shall base our theoretical explanation of these properties on the hypothesis that conduction takes place by jumping. This hypothesis appears to be justified by the fact that no Hall effect has been observed in the materials concerned.

In setting up our theory, we must first note that a special situation arises when conduction takes place by jumping in an antiferromagnetic compound. For, as pointed out by Heikes (1955), the atomic d-states on different cations overlap very little in such materials, so that the only significant processes in which an electron can move from cation to cation are indirect ones involving the participation of anions. Thus, Heikes was able to show that, if L is a line along which an electron can move, the nearest-neighbouring cations of L are strongly coupled by superexchange, so that their spins are antiparallel in the perfectly ordered state. It should be pointed out that, though Heikes's arguments were originally employed in connection with electronic motion by tunnel effect, they are nevertheless applicable to cases when the electrons move by phonon-activated jumps, as in our theory.

A further restriction in the jumping motion arises from the fact that an electron will have less energy when bound to an ion I_1, with spin parallel to its own than when bound to an ion I_2 with antiparallel spin. An energy ϵ will therefore be required to transfer the electron from I_1 to I_2. This energy will clearly be of the order of the mutual potential energy of a pair of electrons in an ion, i.e. $\gtrsim 1$ ev. Therefore, since any jumping processes involving ions of antiparallel spin will require an activation energy ϵ, it follows that such processes cannot contribute significantly to μ at the temperatures ($\lesssim 1000°$K) that we are considering. (These are the temperatures at which Morin's experiments were performed.) Consequently, at such temperatures, an electron moves in localized states based on ions of parallel spin.

Let us now consider the motion of an electron along a line L in the presence of an applied electric field, according to the model specified at the beginning of the note. The electron may move by jumping from A to A_+. However, a jump from A to A_+, say, can only be accomplished if both of these ions have spins parallel to that of the electron. Now, as shown above, the spins of these ions are antiparallel in the perfectly ordered state. Consequently, at temperature T, an energy E will be required to render the spins of these ions parallel when the electron is at A; and consequently the transition rate P_+ for jumping from A to A_+ contains a factor $\exp(-E/kT)$. Since the transition rate P_- will likewise contain this factor, it follows from equation (1) that an activation energy E is required for conduction by jumping in an antiferromagnetic.

Thus, according to our theory, μ contains an activation energy E, which is simply the energy required to align the spins of a pair of neighbouring cations coupled by superexchange so that a conduction electron can jump from one to the other. This energy E is temperature-dependent and does not vanish above the Néel point T_N since some local order persists above that temperature. At temperatures very much lower than T_N, E is of the order of kT_N, though it is not equal to that energy because of the presence of the conduction electron. This certainly means that, in NiO and α-Fe_2O_3, E is of the same order of magnitude as the activation energy observed in μ.

Acknowledgments

The author would like to express his thanks to Professor H. Fröhlich, and Dr. H. Matsuda, for a number of helpful discussions.

References

Fröhlich, H., and Sewell, G. L., 1959, *Proc. Phys. Soc.*, **74**, 643.
Heikes, R. R., 1955, *Phys. Rev.*, **99**, 1232.
Morin, F. J., 1954, *Phys. Rev.*, **93**, 1195, 1199.
Sewell, G. L., 1958, *Phil. Mag.*, **3**, 1361.

The Elastic Scattering of ^{3}He by ^{3}He

By B. H. Bransden and R. A. H. Hamilton
University of Glasgow

MS. received 24*th June* 1960

Collisions, both elastic and inelastic, between the lightest nuclei have been investigated intensively, for a considerable period, both experimentally and theoretically. At low incident energies attempts at calculating cross sections have met with two major difficulties. The approximations that are easily applied, such as the impulse approximation and Born's approximation, are invalid and it is only recently that the details of the nuclear potential are becoming clear. To meet the first of these difficulties wave functions of resonating group form may be used. Calculations using the variation method support the view that even when no allowance is made for target deformation, such wave functions give a good description of the system over a considerable energy range (see, for example, a review by Massey 1960).

Calculations with a realistic nuclear potential have so far not been possible (although this remains the ultimate aim and work is in progress towards this end) and many calculations have been made employing an 'equivalent' central potential between nucleons of the form

$$\mathscr{V}(ij) = V(r_{ij})\{w + mM_{ij} + bB_{ij} + hH_{ij}\}$$
$$V(r) = A\exp(-\lambda r^2); \quad A = -45\ \text{Mev},\ \lambda = 0{\cdot}2669\ \text{f}^{-2}, \qquad \ldots\ldots(1)$$

where M, B, H are the Majorana, Bartlett and Heisenberg exchange operators and w, m, b, h are constants which determine the exchange nature of the potential. Among the systems investigated with this potential have been the elastic scattering of nucleons by deuterons, ^{3}H, ^{3}He and ^{4}He. This work has been recently reviewed (Bransden 1960, Burke 1960, Massey 1960). In these and other examples the experimental results agree quite closely with the theoretical predictions and it is interesting to examine the domain of applicability of the model by applying it to further systems.

In this note the elastic scattering cross section of ^{3}He by ^{3}He is calculated with the potential (1) and the wave function

$$\bar{\Psi} = (1 - P_{56} - P_{13} - P_{14} - P_{23} - P_{24})\,\sigma_s(125\,;\,346)\,\chi(125)\,\chi(1346)\,F_s(125-346) \qquad \ldots\ldots(2)$$

and

$$F_s(125-346) = (-1)^s F_s(346-125)$$

where 1, 2, 3, 4 are protons and 5, 6 neutrons and P_{ij} is the exchange operator and where χ is the internal wave function of ^{3}He, approximated by

$$\chi = N \exp -\mu \Sigma_{ij} r_{ij}^2 \quad (\mu = 0{\cdot}1404\,\mathrm{f}^{-2}),$$

σ_s is the spin function appropriate to the singlet or triplet state and $F_s(\mathbf{r})$ is a wave function describing the relative motion of the colliding nuclei. By inserting (2) into the Schrödinger equation, integro-differential equations for the radial

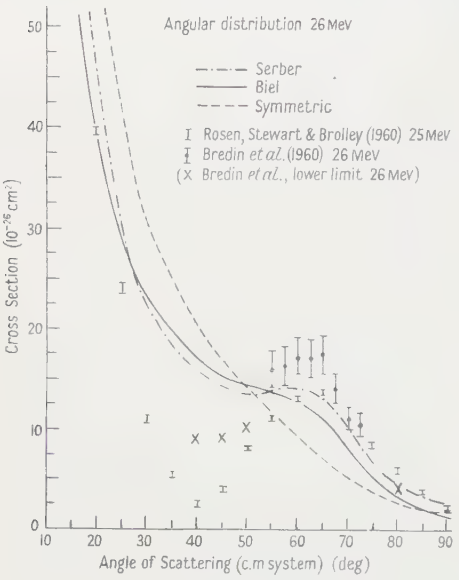

Figure 1

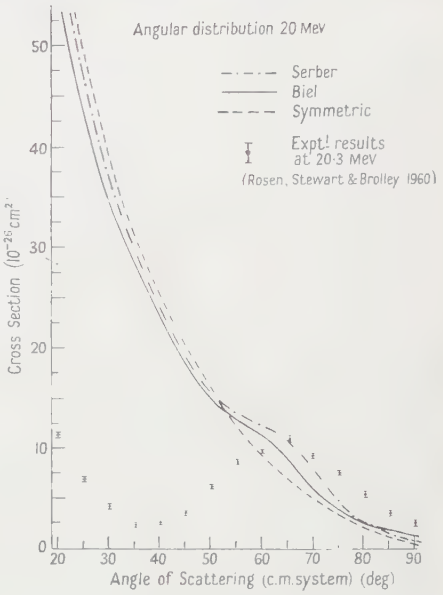

Figure 2

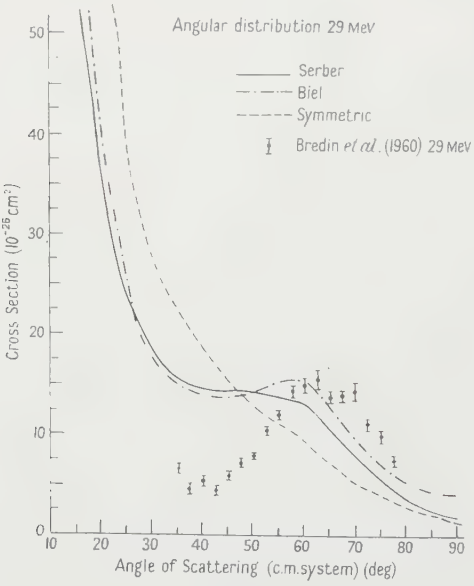

Figure 3

Figures 1–3. Angular distributions in the centre-of-mass system for ^{3}He of 20, 26 and 29 Mev laboratory energies elastically scattered by ^{3}He.

functions $f_l(r)$ in a harmonic expansion of $F_s(\mathbf{r})$ may be obtained. This technique has been described in detail several times before and need not be repeated here (cf. Massey 1953, Bransden, Robertson and Swan 1956).

Numerical solutions of the appropriate equations have been obtained for laboratory incident energies of 20, 26 and 29 Mev, for potentials having exchange properties of the Serber, symmetrical and Biel (70% Serber + 30% symmetric) types and the results are shown in figures 1 to 3. The experimental results shown are those of Rosen, Stewart and Brolley (1960) at 20 and 25 Mev and of Bredin *et al.* (1960) at 26 and 29 Mev.

From the figures it is evident that although the cross section at large angles is in reasonable agreement with experiment, the deep minimum observed in the experimental cross section at 35–40° is not reproduced. It may be concluded that for the ^{3}He – ^{3}He system the model fails. This may be contrasted with ^{4}He elastic scattering by ^{4}He (Butcher and McNamee 1959) for which system good agreement was found, with the same model. Two effects may contribute to the differences between the systems. The alpha particle is very tightly bound compared with ^{3}He, and the alpha group correspondingly more stable during the collision, also as ^{3}He is a spin $\frac{1}{2}$ particle, the $l=0$ partial wave is associated only with the singlet state and the $l=1$ (triplet) state is relatively much more important. The opposite is true for ^{4}He + ^{4}He, the odd angular momentum states being completely excluded. As it is likely that the $l=0$ phase shift is not very model dependent (approximating to hard sphere scattering), it is seen that for ^{3}He + ^{3}He the model dependent terms are emphasized.

Acknowledgments

We are indebted to Dr. H. H. Robertson for permission to use several programmes prepared by him and also to Dr. J. E. Brolley, Jr. and Dr. J. S. C. McKee for communicating to us the results of their respective groups, before publication.

References

Bransden, B. H., 1960, *Nuclear Forces and the Few Body Problems* (London : Pergamon Press).
Bransden, B. H., Robertson, H. H., and Swan, P., 1956, *Proc. Phys. Soc.* A., **69**, 877.
Bredin, D., England, J. B. A., Evans, D., McKee, J. S. C., March, P. V., Mosinger, E. M., and Toner, W. T., 1960, *Proc. Roy. Soc.* A, **258**, 202.
Burke, P. G., 1960, *Nuclear Forces and the Few Body Problem* (London : Pergamon Press).
Butcher, A. C., and McNamee, J. M., 1959, *Proc. Phys. Soc.*, **74**, 529.
Massey, H. S. W. 1953, *Progr. Nucl. Phys.*, **3**, 235,
—— 1960, *Nuclear Forces and the Few Body Problem* (London : Pergamon Press).
Rosen, L., Stewart, L., and Brolley, J. E., Jr., 1960, *Phys Rev.*, in the press.

The Knight Shift in Alloys

By W. G. Henry

Division of Applied Chemistry, National Research Council, Ottawa 2, Canada.

MS. received 19*th May* 1960, *in revised form* 25*th July* 1960

§ 1. Introduction

Blandin and Daniel (1959) presented an explanation of the Knight shift in silver alloys based on a finding by Friedel (1958) that the charge density about a solute atom has a component which oscillates with a decreasing

amplitude as the distance from the solute increases. The mean density of the charge in the matrix is calculated on the assumption that exactly Z units of electronic charge are accumulated around the solute atom, where Z is the excess valency. Their calculated shifts per unit of concentration of solute for the solvent agree well with the observed shifts. They do not attempt, however, to calculate the shift for the solute and in fact the assumption that exactly Z units of charge are accumulated at the solute would appear, on the basis of the present work, to preclude this possibility.

In the present note a different picture of the charge distribution in an alloy is described. It is pointed out that it is reasonable to expect excess charge, the excess being proportional to Z, over and above the excess valency Z, to accumulate at polyvalent solute sites with a corresponding decrease in charge at the monovalent solvent sites. Thus it is suggested that there is associated with each solute site $Z+1+q$ electrons, where q is the excess charge. On this basis, the order of magnitude of the Knight shift and its Z dependence for the solvent may be estimated. A reason may be given for the shift of the solute resonance to lower frequencies.

The rigorous interpretation of the present approach suggests that the shift should be linear with concentration even at infinite dilution.

§ 2. Charge Distribution in Alloys

The problem of the distribution of charge at a solute atom has been considered, in connection with calculations of the heats of solution of alloys, by Huang (1948), Arafa (1949), Varley (1954) and Henry (1958, to be referred to as I). The agreement between the investigations, regarding the sign and the order of magnitude of the accumulation of excess charge over and above the excess valency Z, is good. In almost all cases it is found that charge accumulates at either the solvent or solute sites in excess of the excess valency Z. The amount of charge which accumulates depends on the difference in the attractive potential of the two constituents. The differences in the amounts calculated by the different investigators, depend in general on the degree of self-consistency and on the method of estimating the relative potentials.

Huang, who studied the copper–gold system by a self-consistent Thomas–Fermi method, assumed that the difference in the attractive potentials was equal to the difference in the Sommerfeld potentials of the valence electrons in the pure metals. For monovalent metals the Sommerfeld potential is approximately equal to the negative value of the sum of the absolute values of the sublimation energy, the first ionization energy and the mean kinetic energy. For monovalent metals with equal volumes the difference in Sommerfeld potential is equal to the difference in the mean energy of the valence electrons in the pure metals. Varley, who used a two-band model, used this same approximation for monovalent–monovalent systems and extended the idea to monovalent–polyvalent systems. In I, where an approximately self-consistent one-band model was used, this same idea was used for monovalent–monovalent systems and no attempt was made to be specific regarding the relative potential for monovalent–polyvalent systems. Arafa who made a quantum mechanical study of the copper–silver system, used the Hartree self-consistent field potentials for copper and silver.

Huang found a charge accumulation of about 0·5 unit round a gold atom in a silver lattice. Varley found 0·18 unit and in I, 0·18 unit was found for the accumulation at a gold site in a silver lattice. Arafa found a charge accumulation of 0·32 unit round a copper ion in a silver lattice and a diminution of 0·29 unit round a silver ion in a copper lattice. Arafa states that if a higher approximation had been examined, a different change, presumably smaller, in the charge distribution would have been obtained. Varley, who calculated the charge transfer at a concentration of one half, found a zero charge transfer in the copper–silver system. In I, an accumulation of 0·11 unit and a diminution of 0·10 unit, in qualitative agreement with Arafa, was found. If the difference in the mean energy of the electrons in copper and silver is taken as a measure of the difference in attractive potentials, a zero charge accumulation would be predicted. It thus appears that gold in silver attracts more charge than copper in silver and that in the copper–silver system the accumulation of charge may be slight.

In I a relatively simple expression was derived for the excess charge q; it is

$$q = V_p \overline{W}_A^0 \qquad \ldots\ldots(1)$$

where $\overline{W}_A^0$ is the mean energy of the electrons of the solvent and V_p is the self-consistent perturbing potential which is proportional to the relative attractive potentials of the two species. The excess charge q as given by equation (1) was calculated from an approximation to the first-order perturbed wave function suggested by Lennard–Jones (1930). The approximation to ψ_k is given by

$$\psi_k = \psi_k^0 (1 - H_{kk}'/W_k^0) + H'/W_k^0 \qquad \ldots\ldots(2)$$

where H' is the perturbation; $H_{kk}' = \int \psi_k^{0*} H' \psi_k^0 \, d\tau$ and W_k^0 is the energy associated with the unperturbed state. In the present work $H' = V_p$. The approximation is independent of the form of the wave function. The form of ψ_k indicates that the accumulated charge comes uniformly from the lattice; that each wave function contributes to the localized charge, and that the more energetic electrons contribute least. Arafa also concluded that the charge comes uniformly from the lattice.

In I the nature of the relative potential or perturbation for polyvalent solutes was not discussed in any detail. It is to be expected however that the attractive potential will increase in the series: silver, cadmium, indium, tin and antimony. Slater's (1930) method of calculating the effective nuclear charge $N - s$, where N is the atomic number and s an empirical screening constant, yields for the singly charged ions of this series: 3·70, 4·35, 5·00, 5·65, and 6·30 units respectively. The differences in the effective nuclear charges for the polyvalent solutes with respect to silver are 0·65, 1·30, 1·95, and 2·60 respectively. The differences and hence V_p are in the ratio 1 : 2 : 3 : 4 and thus it is to be expected that the excess charge q, as given by (1), accumulated at the solute sites will also be approximately in the ratio of 1 : 2 : 3 : 4. Slater's method predicts identical effective nuclear charges for the singly charged, noble metal ions and hence no charge accumulation. The more detailed treatments described earlier show that this is not exactly true. It seems safe to conclude, however, that the charge accumulations in monovalent monovalent systems are less than in monovalent–polyvalent systems.

§ 3. Knight Shift in Alloys

The Knight shift is a measure of the change in the field at the nucleus due to the magnetization of the conduction electrons. It has been suggested by Townes, Herring and Knight (1950) that the shift may be represented by

$$\Delta H/H = (8\pi/3)\chi_p M\langle|\psi_F(0)|^2\rangle_{av} \qquad \ldots\ldots(3)$$

where χ_p is the spin paramagnetism of the conduction electrons per gramme; M is the weight of a gramme atom, and $\langle|\psi_F(0)|^2\rangle_{av}$ is the probability density at the nucleus, of a given species, for all electronic states on the Fermi surface. It is assumed in what follows that the variation in ψ_p is negligible in comparison with variations in $\langle|\psi_F(0)|^2\rangle_{av}$. The form of the approximate wave function, equation (2), indicates that the probability of all states is increased at a solute which has a greater attractive potential than the solvent. It is suggested that this is the essential reason for the concentration dependence of the Knight shift of silver in the silver–copper and the silver–gold systems (Rowland 1960, private communication), and in the silver–cadmium, silver–indium, silver–tin and silver–antimony systems reported by Rowland (Blandin and Daniel 1959).

The excess charge q would appear to be a measure of the change in probability of all states at a site. The shift for the solvent, assuming ψ_p is constant, may be written in terms of q as

$$\Delta H/H = \text{const}\,[1-qx/(1-x)] \qquad \ldots\ldots(4)$$

where x is the mole fraction of solute; q is the excess charge accumulated at the solute at infinite dilution, and $[1-qx/(1-x)]$ is the charge density at a solvent site. The rate of change of $\Delta H/H$ with respect to the mole fraction is thus proportional to q at small concentrations. Rowland (1960, private communication) reports that the rate of change of the silver shift is much greater on the addition of gold than on the addition of copper and less than for any polyvalent solute. This is in accord with the relative magnitudes of the charge accumulation discussed earlier.

Blandin and Daniel, when discussing the alloys of silver with the elements following it in the periodic table, let $K = \Delta H/H$. The expression $-\Delta K/xK$ may be expressed in terms of q, by making use of (4); the result is

$$-\Delta K/xK \simeq q. \qquad \ldots\ldots(5)$$

In § 2, it was pointed out that it was to be expected that q for the series of solutes; cadmium, indium, tin and antimony, would be approximately in the ratio of 1:2:3:4. Equation (5) suggests, therefore, that $-\Delta K/xK$ for this series of solutes should be in the ratio of 1:2:3:4. Blandin and Daniel have determined $-\Delta K/xK$ from the data of Drain (1959) for the silver–cadmium system and from the data of Rowland (Blandin and Daniel 1959) for the silver–cadmium, silver–indium, silver–tin, and silver–antimony systems. For the four systems $-\Delta K/xK$ is: 0·34–0·4, 0·7, 1·1 and 1·2 respectively. It is seen that they are approximately in the ratio of 1:2:3:4. The implied absolute values of q are not unreasonable in view of the values found for monovalent–monovalent systems.

Regarding the cadmium shift at infinite dilution (Drain 1959), it should be noted that the shift for cadmium in silver is greater than in pure cadmium. This is in agreement with the present suggestion that charge is accumulated at the cadmium site. To explain the decrease in the cadmium shift with increasing concentration,

it is only necessary to make the reasonable suggestion that the amount of charge accumulated at a cadmium site per cadmium atom decreases as the concentration increases because of the increasing opposition of the silver atoms to the withdrawals of charge and the competition of other cadmium ions.

References

Arafa, M. K. I., 1949, *Proc. Phys. Soc.*, **62**, 238.
Blandin, A., and Daniel, E., 1959, *Phys. Chem. Solids*, **10**, 126.
Drain, L. E., 1959, *Phil. Mag.*, **4**, 484.
Friedel, J., 1958, *Nuovo Cim.*, **2**, 287.
Henry, W. G., 1958, *Canad. J. Phys.*, **36**, 611.
Huang, K., 1948, *Proc. Phys. Soc.*, **60**, 161.
Lennard-Jones, J. E., 1930, *Proc. Roy. Soc.* A, **129**, 598.
Slater, J. C., 1930, *Phys. Rev.*, **36**, 57
Townes, C. H., Herring, C., and Knight, W. D., 1950, *Phys. Rev.*, **77**, 852.
Varley, J. H. C., 1954, *Phil. Mag.*, **45**, 887.

The Identification of Precipitate Particles in Single Crystals of Silicon by Reflection Electron Diffraction

By R. C. Newman

Research Laboratory, Associated Electrical Industries,
Aldermaston Court, Aldermaston, Berks.

MS. received 14*th July* 1960, *in final form* 22*nd August* 1960

It has been shown that impurities diffuse to and precipitate at dislocations and other crystal defects in silicon containing aluminium during annealing at temperatures between 1000° and 1250°c (Bullough *et al.* 1959 a, b, 1960). The size of the precipitates was found to be much greater than could be accounted for from the known quantity of aluminium present and its known diffusion coefficient, and hence the presence of other electrically inactive impurities was indicated. The only impurities likely to have been present with a sufficiently high concentration of about 10^{15} atoms per cm^3 or greater were oxygen and carbon (Kaiser and Keck 1957, Papazian and Wolsky 1956). The precipitation of oxygen on dislocations has been demonstrated previously by Lederhandler and Patel (1957) who used infra-red spectrographic techniques, and provides a ready explanation for the co-precipitation of aluminium due to the high bond energy between aluminium and oxygen (Bullough *et al.* 1959 a, Fuller 1959). It has now been found that precipitates can form in silicon grown with an oxygen concentration of less than 10^{17} atoms per cm^3 (see Gasson 1959) and which do not contain aluminium; hence it seemed that carbon might also be involved in the precipitation process. This would be in accord with a previous suggestion that part of the carbon in the β-silicon carbide layer formed at external surfaces, during similar annealing, originated from the bulk silicon (Newman and Wakefield 1958). A technique is now described whereby the precipitate particles can be examined directly by reflection electron diffraction. From the observed patterns it has been possible to make some deductions concerning the crystal structure and hence the chemical composition of the particles.

In order to examine internal precipitate particles, it is necessary to etch the crystal with an etchant that does not attack these particles, but leaves them free of the matrix material. A suitable etchant has not yet been found which satisfies the latter condition when undoped silicon or silicon doped with aluminium only is used; that is, the silicon around the precipitate particles is found to etch more slowly than in other regions and the particles remain embedded in a relatively thick coating of silicon. This difficulty does not occur, however, if silicon containing both aluminium and an n-type impurity such as phosphorus is used: aluminium is incorporated into the precipitate particles, thus leading to adjacent regions which are electrically n-type, while the main bulk of the crystal remains p-type, assuming that the aluminium was originally in excess (Bullough *et al.* 1960). Etchants such as mixtures of hydrofluoric and nitric acids attack the n-type regions of the crystal preferentially, compared with the p-type regions, due to the built-in electric field across the junctions, and it is found that the precipitate particles can be exposed without a coating of silicon.

In order to obtain a sufficiently high density of particles on the surface, crystals with a moderately high grown-in dislocation density of up to 3×10^4 lines per cm^2 were used, since the precipitates form preferentially at these sites. When the annealing temperature is below about 1150 c, a cloud of precipitate particles is formed in the n-type region immediately surrounding each dislocation. These particles are also exposed by the etching, and up to twenty to thirty particles, of diameter between 0·3 and 0·7 μ, are frequently observed. Some particles at random sites away from dislocations are also exposed. Such a total density of particles smeared out over the surface would be equivalent to a layer of about 12 Å in mean thickness, and hence should be detectable by electron diffraction (see Newman and Pashley 1955, Grünbaum, Newman and Pashley 1958).

The surface preparation of samples prior to examination was of the utmost importance, since their surfaces were covered with silicon carbide after the heat treatment (Newman and Wakefield 1958). Samples were therefore etched first in a mixture of 50% hydrofluoric and 50% nitric acids to remove this layer. They were then ground down with diamond powder and alcohol and re-etched in fresh etchant contained in cleaned dishes; these two steps were repeated to ensure that all effects due to the original surface had been removed.

A typical reflection diffraction pattern obtained after this procedure from a sample heated at 1132° c for 64 hours is shown in the figure (Plate). The elongated spots are due to the etched silicon which has a locally smooth surface; the removal of surface damage due to grinding is apparent from the appearance of the strong Kikuchi line pattern. In addition, it is seen that there is a second spot pattern due to a substance which is basically face-centred cubic with $a_0 = 4{\cdot}37 \pm 0{\cdot}03$ Å (the silicon spot pattern was used as a lattice spacing reference pattern), and oriented parallel to the silicon substrate. There was sometimes evidence for twinning and well-defined {111} facets in this material, and some randomly oriented particles were always present, as indicated by the ring pattern. It seems reasonable to identify this material as β-silicon carbide which has a zinc-blende structure with $a_0 = 4{\cdot}348$ Å. This type of pattern has been obtained from samples heated at various temperatures between 1000° and 1200°c, and is found to be the strongest on samples heated to about 1100°c. This is to be expected since the size of the precipitates is a maximum at about this temperature (Bullough *et al.* 1960). The fraction of material in a parallel orientation decreases

as the temperature is reduced, and thus shows a similar behaviour with temperature as the silicon carbide deposits formed on external surfaces (Newman and Wakefield 1958). A diffraction pattern due to silicon only was found after grinding and etching unheated samples and samples heated to temperatures above 1250 c, consistent with previous observations that no appreciable precipitation occurs at these higher temperatures. This proves that the extra pattern described above could not have arisen from contamination in the etchants or from the surface deposits of silicon carbide, since these were also formed on the samples heated in the higher temperature range.

The general absence of a diffraction pattern from the precipitated aluminium is not unexpected, since the quantity which can precipitate has been shown to be between two and three orders smaller than the observed size of the particles. However, in a few cases, a further very weak square array of spots was observed at the [001] azimuth. These could be interpreted as due to a face-centred cubic type lattice oriented parallel to the silicon with $a_0 = 3{\cdot}96 \pm 0{\cdot}04$ Å. A plausible explanation is that these spots were due to γ-aluminium oxide, which has a cubic spinel type structure with an $a_0 = 7{\cdot}895$ Å, i.e. approximately double the experimental value given above. The strongest reflections for this structure, i.e. (400), (440) etc., coincide with the observed spots, and hence we may *tentatively* identify this very weak pattern with γ-aluminium oxide. (Metallic aluminium with an $a_0 = 4{\cdot}04$ Å is unlikely to be present in a non-chemically combined form.) There was no evidence for the presence of any silicon oxide particles. It cannot be concluded, however, that such precipitate particles were not present, since they would almost certainly have been dissolved in the etchant, whereas neither silicon carbide nor aluminium oxide is soluble. It should again be noted that there was no evidence for a thin coherent oxide film over the silicon surface produced by the etching (Holmes and Newman 1959).

It is concluded that the crystal structure of a large fraction of the precipitate particles, formed in silicon during annealing, is consistent with that of β-silicon carbide. A second structure has also been found in a few cases which could be attributed to γ-aluminium oxide. It must be stressed that, in general, the identification of chemical compounds from diffraction patterns where no information is obtained about the relative intensities of the various reflections, as in the present work, is not entirely satisfactory. It is hoped later to examine the precipitate particles using an x-ray microanalyser to ascertain which elements are present directly (see, for example, Mulvey 1959). The associations of silicon and carbon to form silicon carbide and aluminium and oxygen to form aluminium oxide are, however, reasonable chemical reactions as deduced from the thermodynamic properties of these materials, and, moreover, all of these elements were present in the silicon samples used. Some further properties of carbon in silicon, as determined from experiments using ^{14}C, and a more detailed discussion of the observed precipitation phenomena will be given in a later publication.

Acknowledgments

Thanks are due to Dr. T. E. Allibone, Director of the Laboratory, and to the Admiralty, for permission to publish this paper.

References

Bullough, R., Newman, R. C., and Wakefield, J., 1959 a, *Proc. Instn Elect. Engrs* B, **106**, Suppl. no. 15, 277.

Bullough, R., Newman, R. C., Wakefield, J., and Willis, J. B., 1959 b, *Nature, Lond.*, **183**, 34.
—— 1960, *J. Appl. Phys.*, **31**, 707.
Fuller, C. S., 1959, *Chem. Rev.*, **59**, 65.
Gasson, D. B., 1959, *Proc. Instn Elect. Engrs* B, **106**, Suppl. no. 17, 854.
Grünbaum, E., Newman, R. C., and Pashley, D. W., 1958, *Phil. Mag.*, **3**, 1337.
Holmes, P. J., and Newman, R. C., 1959, *Proc. Instn Elect. Engrs* B, **106**, Suppl. no. 15, 287.
Kaiser, W., and Keck, P. H., 1957, *J. Appl. Phys.*, **28**, 882.
Lederhandler, S., and Patel, J. R., 1957, *Phys. Rev.*, **108**, 239.
Mulvey, T., 1959, *J. Sci. Instrum.*, **36**, 350.
Newman, R. C., and Pashley, D. W., 1955, *Phil. Mag.*, **46**, 927.
Newman, R. C., and Wakefield, J., 1958, *Proc. International Conference on Solid State Physics in Electronics and Telecommunications, Brussels* (editors: Désirant, M., and Michiels, J. L.) (London, New York: Academic Press), p. 318.
Papazian, H. A., and Wolsky, S. P., 1956, *J. Appl. Phys.*, **27**, 1561.

The Infra-red Absorption Spectra of Potassium Manganicyanide and Vanadium Corundum

By G. D. Jones† and W. A. Runciman

Physics Department, University of Canterbury, Christchurch, New Zealand

MS. received 27th June 1960

The spectra were recorded in the range 7000–12 000 A using the glass optics of a Hilger large quartz and glass spectrograph. The Kodak IZ plates cover this spectral range and were sensitized in 4% ammonia solution, rinsed in methanol and dried.

The crystal samples were immersed in liquid nitrogen contained in a glass Dewar with a transparent tip. The light from a projection lamp was incident normal to the axis of the samples and polarization spectra, hereafter denoted π and σ, obtained by passing the transmitted light through a Nicol prism set with its E-vector direction parallel and perpendicular respectively to the crystal axis. The E-vector direction of the Nicol prism was initially determined by noting the orientation of the prism when set to extinguish light reflected off a glass plate at the Brewster angle.

The potassium manganicyanide crystals used were prepared by the method described by Fernelius (1946). They are dark-red needles whose symmetry has been reported by Gottfried and Nagelschmidt (1930) to be orthorhombic. However, the atomic arrangement has not been established (Wyckoff 1951) and some doubt exists regarding the symmetry and space group of the crystals. The crystal axis was taken to coincide with the needle axis in the determinations of the polarization spectra.

Earlier work on the absorption spectrum of potassium manganicyanide (Samuel and Despande 1932, Szego and Ostinelli 1930) has been confined to determinations of the spectrum of the solution at room temperature.

† Now at Clarendon Laboratory, Oxford.

For the crystals at liquid nitrogen temperature there is a detailed line spectrum in the region of 10 500 Å. At least four lines are visible on the photographic plates and all show partial polarization. The figure gives their approximate relative intensities, spacings and polarizations. Their wavelengths are difficult to measure as the lines are weak and somewhat diffuse. To the nearest 10 Å they are: 10 410; 10 470; 10 570 and 10 850 Å.

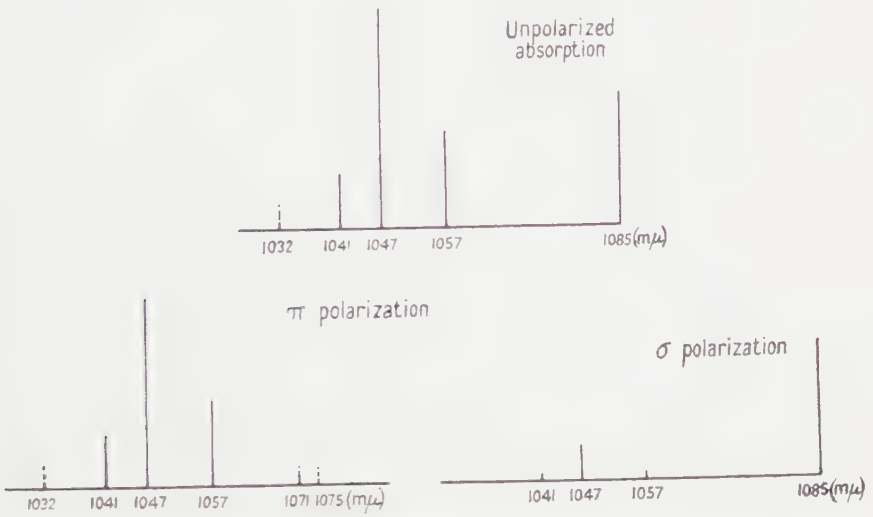

Diagram of the *approximate* relative intensities, spacings and polarizations of the lines present in the absorption spectrum of potassium manganicyanide.

These values were obtained by use of the Hartmann formula:

$$\lambda = \lambda_0 + \frac{c}{d - d_0}$$

in which the constants λ_0, c and d_0 were determined by use of the mercury lines at 10 140 and 11 287 Å and of a sodium line at 8195 Å as calibration lines.

Although only four lines are positively identified there appear to be one or two more lines present (shown broken in the figure), but these are still doubtful.

In some respects, it is unfortunate that lines occur close to the limit of response of the Kodak I Z plates as it is quite likely that there are lines further in the infra-red. The variation of the sensitivity of different batches of Kodak I Z plates makes attempts to extend the range by large overexposure difficult.

For interpretation of the line spectra, the starting point is the Tanabe–Sugano diagrams, and these apply to d^n compounds possessing cubic symmetry. Potassium manganicyanide is a 'strong-field' d^4 compound and the corresponding diagram (Tanabe and Sugano 1954) shows the existence of two possible line transitions, namely $^3T_1 \rightarrow {}^1E$ and $^3T_1 \rightarrow {}^1T_2$ which give rise to two lines at wavelengths of approximately 12 500 and 14 500 A respectively, if one assumes the B parameter to have the free-ion value of 965 cm^{-1}. The detection of lines in potassium manganicyanide crystals in the same spectral region is certainly satisfactory, especially when one considers the assumption of cubic symmetry for our compound and also the fact that B values for trivalent ions are appreciably

lower than the 'free-ion' values. If, instead, we redetermine the B value by fitting the $^3T_1 \rightarrow {}^1E$ transition to the 10 500 Å lines, we get $B = 810\,cm^{-1}$ and $\beta = B\,(complex)/B\,(free\text{-}ion) = 0{\cdot}84$. These values are in only fair agreement with Jørgensen's table of B values given as the parameters f, g, h and k (Jørgensen 1958). For, from our value of β, we get $k = 0{\cdot}42$ for the Mn III ion and this may be compared with the values of $k = 0{\cdot}24$, $0{\cdot}21$ and $0{\cdot}30$ for Fe III, Cr III and Co III, respectively, given by Jørgensen. The absorption band peak in the solution at 3230 Å ($31\,000\,cm^{-1}$) gives $g = 18\,000\,cm^{-1}$ for Mn III, which is consistent with the values (Fe III, $14\,400\,cm^{-1}$; Cr III, $17\,400\,cm^{-1}$ and Co III, $19\,000\,cm^{-1}$) for other transition ions.

At present, the theoretical explanation of the observed spectra seems a formidable problem because of the low symmetry of the crystals. Furthermore, the possible existence of other lines either too weak to detect or beyond 11 000 Å prevents any more than tentative deductions to be made from the observed line pattern.

The absorption spectrum of vanadium corundum has already been studied by Pryce and Runciman (1958). We can now report that the infra-red line at $9660\,cm^{-1}$ is largely π polarized. This is in agreement with the energy level scheme, for d^2 in a trigonal field, of Pryce and Runciman. From this same diagram one would expect the other two infra-red lines, only one of which is yet reported, to be both mainly σ polarized. This prediction still has to be verified as the line at $8770\,cm^{-1}$ is too weak and too far into the infra-red for a positive identification to be made.

References

Fernelius, W. C., 1946, *Inorganic Syntheses*, Volume 2 (New York : McGraw-Hill), p. 213.

Gottfried, C., and Nagelschmidt, J. C., 1930, *Z. Krist.*, **73,** 357.

Jørgensen, C. K., 1958, *Proc. Symp. Coordination Compounds* (Rome, September 1957) and *Faraday Soc. Discussions*, **26,** 110.

Pryce, M. H. L., and Runciman, W. A., 1958, *Faraday Soc. Discussions*, **26,** 34.

Samuel, R., and Despande, A. R. R., 1932, *Z. Phys.*, **80,** 395.

Szego, L., and Ostinelli, P., 1930, *Gazz. Chim. Ital.*, **60,** 946.

Tanabe, Y., and Sugano, S., 1954, *J. Phys. Soc. Japan*, **9,** 766.

Wyckoff, P. W. G., 1951, *Crystal Structures*, Vol. 2 (New York: Interscience).

The Lifetime of the He^- Ion

By D. R. SWEETMAN

Atomic Weapons Research Establishment, Aldermaston, Berks.

MS. received 23*rd August* 1960

The He^- ion was first identified by Hiby (1939) as a weak trace in a mass spectrograph. Confirmation of its existence was not forthcoming for many years but Holøien and Midtdal (1955) showed on theoretical grounds that the $(1s\,2s\,2p)^4P$ state was not subject to auto-ionization and was therefore expected to be metastable with a lifetime long enough to account for the observations of Hiby.

More recently information on the formation of He^- ions has been obtained from ion source investigations (e.g. Windham, Joseph and Weinman 1958) and the cross section for their formation on electron capture by positive ions has been measured by Dukel'skii, Afrosimov and Federenko (1956), Jorgensen (1958) and others.

As far as is known, no measurements of the He^- lifetime have been made. Recent attempts to accelerate He^- particles to high energies in a tandem Van de Graaff machine have met with difficulties and the suggestion has been made that the lifetime may be sufficiently short to result in loss of particles along the flight path. Reported in this paper are measurements we have made which set a lower limit on the lifetime and which indicate the size of the loss cross sections for interaction with gas molecules.

The figure is a diagram of the apparatus used. A beam of He^+ ions, of intensity a few microamperes, was accelerated to 1 MeV in a Van de Graaff machine. After magnetic analysis it was passed down a tube, of length about 2 metres, the pressure in which was held at 0·6 microns Hg of air. Some of the beam was converted to the He^- state in this tube and this was separated from the other charge states by a 4° bending magnet. The separated beam then passed down a drift tube, 60 cm long, evacuated to better than 10^{-6} mm Hg.

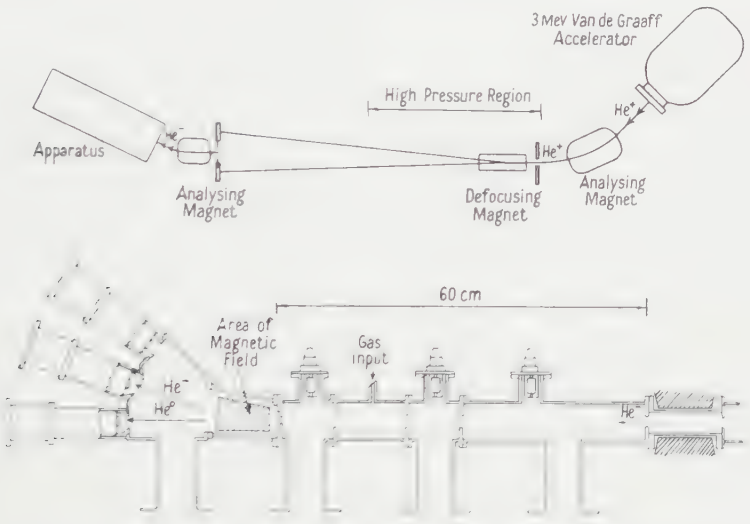

At the far end of the drift tube the beam was analysed by magnetic separation and the individual particles were counted using CsI crystal counters, so that both the energy of and e/m for the particles could be determined. This part of the apparatus has been described previously (Sweetman 1959, 1960).

The experiment consisted, essentially, of counting simultaneously the He^0 particles produced by the decay of the He^- beam in the 60 cm length of drift tube and the He^- beam itself. The ratio $R = He^0/(He^0 + He^-)$ is then related to the lifetime τ by the expression $R = 1 - \exp(-L/v\tau)$ where L is the drift tube length and v is the velocity of the particles.

The beam was identified by the magnetic field settings and by the pulse height in the crystal. The He^- particles gave the same pulse height and appeared

at the same (but reversed) magnetic setting, as the He^- beam and were therefore clearly separated from the reaction products of possible contaminants of the original beam such as D_2^+ or H_2D^+. An He^- count rate of approximately 1000 per second was obtained. Under these conditions, the ratio $He^0/(He^- + He^0)$ determined from the average of several runs was $7{\cdot}75 \times 10^{-3}$. This small He^0 beam could have been produced by (*a*) dissociation of the He^- by residual gas, (*b*) dissociation by beam defining stops in the system, and (*c*) natural decay of the He^-. Process (*b*) is estimated to be insignificant. With the residual gas pressure obtained, process (*a*) is sufficient to account for the He^0 beam observed and we can set therefore only a maximum limit to the natural decay rate and a minimum value to the lifetime. The minimum lifetime (obtained assuming all the He^0 beam is due to process (*c*)), is $1{\cdot}0 \times 10^{-5}$ second.

We have measured also the cross section for the reaction $He^- \rightarrow He^0$ on interaction with helium gas. This was obtained by varying the pressure of helium in a gas cell inserted in the 60 cm flight path and observing the change of $He^0/(He^- + He^0)$ ratio with pressure. The detailed technique has been described previously (Sweetman 1960). The cross section measured was $2{\cdot}13 \pm 0{\cdot}20 \times 10^{-16}$ cm^2 per molecule at 1·09 Mev energy.

The beams of He^- ions in a tandem Van de Graaff machine are appreciably attenuated if the He^- lifetime is short compared with the flight time in the machine, which is of the order of 5×10^{-7} second. The measured lifetime of 10^{-5} second would give negligible attenuation. The effect of residual gas in a tandem Van de Graaff machine may be estimated from the value of the electron loss cross section we have measured. On general theoretical and experimental grounds, the cross section per atom would be expected to vary as ZE^{-1} (where Z is the atomic number of the target gas and E is the particle energy). Using such a dependence, and assuming the residual gas to be nitrogen, we calculate that the gas pressure in such a machine must be reduced to below 3×10^{-5} mm Hg for the particle loss to be less than 20%. Such a vacuum is well within present technological capabilities.

Acknowledgments

The author is greatly indebted to Mr. R. E. Bradford, for his help in constructing the apparatus and taking the results, and to Dr. K. W. Allen for his stimulating interest in the work.

References

Dukel'skii, V. M., Afrosimov, V. V., and Federenko, N. V., 1956, *Zh. Eksper. Teor. Fiz.*, **30,** 792 (English translation, *Soviet Physics, J.E.T.P.*, **3,** 764).

Hiby, J. W., 1939, *Ann. Phys., Lpz.*, **34,** 473.

Holøien, E., and Midtdal, J., 1955, *Proc. Phys. Soc.* A, **68,** 815.

Jorgensen, T., 1958, *Proceedings of Conference on the Penetration of Charged Particles in Matter, Gatlinburg, Tennessee.*

Sweetman, D. R., 1959, *Phys. Rev. Letters*, **3,** 425.

—— 1960, *Proc. Roy. Soc.* A, **256,** 416.

Windham, P. M., Joseph, P. J., and Weinman, J. A., 1958, *Phys. Rev.*, **109,** 1193.

LETTERS TO THE EDITOR

Hot Carriers in Germanium

In a semiconductor, if excess charge carriers are excited by radiation, the mean energy of the carriers may be considerably greater than that corresponding to the lattice temperature (Honig and Levitt 1960). We have investigated the properties of hot carriers excited in germanium at low temperatures by measurement of the resistivity ρ and the Hall coefficient R, from which the Hall mobility $\mu = R/\rho$ is obtained. It is known that μ, if determined by lattice scattering only, should be inversely proportional to the lattice temperature T_L and will also depend on the energy of the carriers whereas, if determined by ionized impurity scattering only, μ should be independent of T_L and depend only on the carrier energy.

The results obtained for μ as a function of T_L for a specimen of p-type copper doped germanium ($N_A = 1{\cdot}3 \times 10^{16}$ per cm^3, $N_D \simeq 10^{15}$ per cm^3 with all shallow states compensated) are shown in figure 1. Curve *a* was obtained with no incident

Figure 1

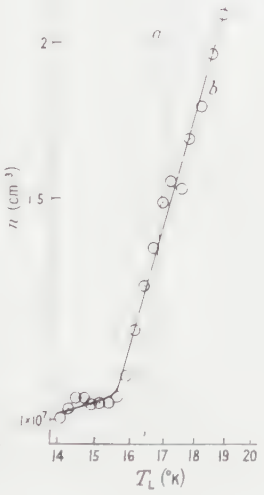

Figure 2

Figure 1. Variation of mobility with temperature: *a*, with no incident radiation; *b*, with room temperature radiation.

Figure 2. Variation with temperature of: *a*, carrier density with no incident radiation n_C; *b*, excess carrier density with room temperature radiation n_H.

radiation and down to 17·5 K, where impurity conduction becomes important, μ is proportional to $T_L^{3/2}$ as expected when ionized impurity scattering is predominant. Curve *b* was obtained when the specimen was illuminated with black body radiation from room temperature. It seems probable that the increase of μ with decrease of T_L is due to the fact that, at these temperatures, carriers lose energy mainly by interaction with phonons, so that the mean carrier energy increases as T_L decreases. At lower temperatures the mobility reaches a constant limit and, between 4·2 and 1·8 K, is found to be independent of T_L.

In fact no variation with temperature of the mobility of carriers excited by room temperature radiation has been observed over this temperature range in copper doped or high purity n-type (shallow impurity) germanium specimens. A possible explanation of this result is that the carrier energy is now independent of T_L because interaction with phonons is no longer the predominant process for loss of energy.

Interesting results were obtained with a high purity n-type specimen ($N_D = 6 \times 10^{12}$ per cm^3, $N_A = 1{\cdot}6 \times 10^{12}$ per cm^3). At 4·2°K, when illuminated with room temperature radiation, the mobility was $1{\cdot}2 \times 10^6$cm^2 v^{-1} sec^{-1} and was constant between 4·2 and 1·8°K. When illuminated with intrinsic radiation ($\lambda < 1{\cdot}8$ microns) the mobility was 3×10^6 cm^2 v^{-1} sec^{-1} at 4·2°K, and 7×10^6 cm^2 v^{-1} sec^{-1} at 1·8°K. We think the explanation of these results is that, with only room temperature radiation, μ is limited by ionized impurity scattering but, with intrinsic radiation, there is a reduction in the number of ionized impurities due to trapping of hole–electron pairs generated by the radiation, so that the mobility is now limited by lattice scattering. If this is correct, the increase of μ with reduction of T_L can be attributed to the reduction of lattice scattering. The hypothesis that radiation reduces the number of ionized impurities is supported by the observation that, for low illumination, the increase of mobility with increasing intensity of radiation is approximately proportional to the increase of carrier density.

The very high mobility observed with intrinsic illumination is in good agreement with the relaxation time deduced from cyclotron resonance experiments when carriers are excited by radiation (Fletcher, Yager and Merritt 1955).

From the experiments reported with the copper doped specimen illuminated with room temperature radiation, it is possible to obtain information about the cross section σ for capture of holes by ionized impurities. It is observed (figure 2) that the excess carrier density n_H varies approximately as T_L^4 between 20 and 16°K at which temperature the number of carriers excited by radiation (n_H) begins to exceed appreciably those thermally excited in the dark (n_C). Since σ is inversely proportional to n_H, σ is proportional to T^{-4} over this range. This should be compared with the experimental result of Koenig (1959) and the theory of Lax (1959) (temperature dependence of $T^{-3{\cdot}5}$ and T^{-4} respectively). This agreement appears to indicate that the carriers which are captured (i.e. those with low energy) are in approximate equilibrium with the lattice.

The Clarendon Laboratory,
Oxford.
2nd September 1960.

B. V. Rollin.
J. M. Rowell.

Fletcher, R. C., Yager, W. A., and Merritt, F. R., 1955, *Phys. Rev.*, **100,** 747.
Honig, A., and Levitt, R., 1960, *Phys. Rev. Letters*, **5,** 93.
Koenig, S. H., 1959, *J. Phys. Chem. Solids*, **8,** 227.
Lax, M., 1959, *J. Phys. Chem. Solids*, **8,** 66.

CORRIGENDUM

The Spin–Orbit Potential in Proton–Proton Scattering, by D. W. L. Sprung and J. B. Willis (*Proc. Phys. Soc.*, 1960, **76,** 539.)

In equations 1(*a*) and 1(*b*) and following text ψ^{2+} should read ψ^{++}.

REVIEWS OF BOOKS

Electronics, by A. T. Starr. 2nd Edition. Pp. viii + 429. (London: Pitman, 1959.) 35*s*.

The first edition of *Electronics* appeared in 1954 soon after the old Telecommunications course in London University had been split into Telecommunications and Electronics. The need for a second edition was primarily due to the need to deal with the rapid developments in the field of semiconductors. In addition, the author has taken the opportunity to add a very brief mention of the klystron and travelling-wave tube, though the magnetron is still omitted.

Not the least value of the textbook to the undergraduate student is the author's close familiarity with the University requirements. No one who works through the many examples, some new to this edition, should have difficulty in satisfying the examiners, and when that hurdle is past the book, especially the 58 pages of appendices (chiefly mathematics) will still be found useful.

Physicists, however, will undoubtedly experience some shocks, which are the more serious because they will probably pass unnoticed by the engineering undergraduate. It is not altogether surprising that the first equation in the book should give the mass of the electron in kilogrammes, but it is disappointing to find the m.k.s. system dropped forthwith only to reappear spasmodically. Fortunately the erroneous material on the energy levels in atoms will probably be ignored by the young engineer, and though it occurs in the first few pages it is no true augury for the value of the volume. R. L. F. BOYD.

The Theory of Space Time and Gravitation, by V. Fock. Translated by N. Kemmer. Pp. xviii + 411. (New York, London, Paris, Los Angeles: Pergamon Press, 1959.) 100*s*.

The first four chapters of this book are an account of the theory of special relativity that shows the workmanship of a master's hand but that, at the same time, will be recognized as being on the whole a fairly standard treatment.

The rest of the book is an exposition of what most of us call the theory of general relativity but which Professor Fock prefers to call Einstein's theory of gravitation. This part does differ from other treatments and in the following respects, amongst others: (*a*) In nearly the whole of the work, Fock deals with systems such that the associated space time tends to that of special relativity ' at infinity '. This is his way of handling boundary conditions and of ensuring uniqueness in his results. It is an effective way of dealing with an aspect to which Einstein and most of his successors have given insufficient attention. (*b*) Fock gives a special place to what he calls ' harmonic coordinates ' which are, roughly, the analogues of the usual inertial coordinates of special relativity. Although these prove to be very convenient, I have not understood why Fock regards their employment as being of basic significance. (*c*) Most of the latter part of the book deals with the derivation of the equations of motion of a body from the field-relations. Here Fock treats the mass-tensor (or ' matter '-tensor) as having essential significance, whereas Einstein regarded it as a makeshift device that ought to be avoided in this part of the theory.

To put the position briefly, the theory of gravitation is not yet a unique, well-defined theory. Fock has given what is probably the most thoroughly developed theory so far published. He gives powerful reasons for his views, although he explicitly recognizes the possibility of others. His book, so ably translated by Professor Kemmer, will have a great influence both as a source of new knowledge and as a challenge to others to produce as thorough-going accounts of their own contributions. It is an addition to the literature of first-rate importance. W. H. MCCREA.

Methods of Experimental Physics, Vol. 6, Part A, *Solid State Physics*. Edited by K. LARK-HOROVITZ and V. A. JOHNSON. Pp. xvi+466. (New York, London: Academic Press, 1959.) $11.80.

Once upon a time the properties of solids tended to be studied in compartments isolated by techniques—'A' knew about low temperatures, 'B' was the optics man, 'C' did work with magnets, 'D' studied creep and so on . . . Nowadays a solid state physicist has to be prepared to turn his hand to anything.

There is no doubt that the only way of learning techniques is by using them. However, it is very desirable to benefit from the experience of others and the present volume provides a collection of such experience covering some of the experimental methods involved in the preparation, structure and mechanical and thermal properties of solids. The 'preparation' chapter includes articles on purification techniques, single crystal growing and the preparation of thin films and surfaces—including etching. X-ray and electron diffraction methods are discussed in the 'structure' chapter.

In all, there are twenty-one essays, mostly by different authors, together with an introduction about errors of measurement and a seven-page summary of the theory of the solid state. The essays are of varying lengths and the balance achieved between the principles of the methods and the purely experimental techniques varies considerably. But the book is none the worse for that. The x-ray diffraction section is concise and to the point, and while only sixteen out of the thirty-six pages by Professor Amelinckx are concerned with detecting and counting dislocations, many research students will find that the twenty pages of theoretical discussion form a very useful summary. There is a technically useful article on the production of thin films, although to understand it completely one needs to know how a Japanese fan operates. The 'mechanical' chapter includes a helpful little discussion about high precision density determinations.

Most authors provide plenty of references. An exception to this is the article on agglomeration which has a blanketed reference to five textbooks and a published bibliography. The man who wants to sinter something will not find that this article is of much assistance, nor will his understanding of sintering be improved much by reading "The temperature of initiation of self agglomeration of a powder consequently bears a fundamental relationship to the predominant bond type and strengths." The final chapter dealing with high pressure techniques provides an experimentally useful summary, although the authors have omitted to discuss the joint use of high pressures and high temperatures.

Most people will find something useful in this book and research students, particularly, will find it invaluable. E. W. J. MITCHELL.

Tantalum and Niobium, by G. L. Miller. Pp. xxii+767. (London: Butterworths Scientific Publications; New York: Academic Press, 1959.) 120*s*. $21.00.

This volume forms one of a series of monographs on the metallurgy of the rarer metals. Dr. Miller is an excellent choice in this case since he has a wide knowledge of the metallurgy of tantalum and niobium, both in its scientific and industrial aspects.

The purpose of the book is to assemble and arrange all the available chemical and metallurgical information on the science and technology of these two metals. After introductory chapters on the history, occurrence and use of the metals, there are long chapters related to processing; these cover all the stages to finished products, and deal both with production practices and the underlying scientific principles. This material is well-organized and is broken down into extraction from ores, separation of the two metals and their reduction, methods of consolidation to massive material and its fabrication into useful shapes. This is followed by chapters on physical and mechanical properties, corrosion behaviour, binary alloys and on refractory compounds; the chapter on alloys is particularly thorough. There are appendices on chemical analysis, metallographic techniques and thermodynamic data for some compounds.

The book runs to over 750 pages and the treatment is equally painstaking and comprehensive over every aspect covered. This is made even more useful by an exhaustive bibliography at the end of each chapter, very carefully cross-referenced in the text and by excellent subject and author indices and a detailed table of contents. Anyone seeking factual information will readily find it here, lucidly set out and with a complete guide to original sources.

The book reveals, almost incidentally, a fascinating transition from traditional chemico-metallurgy to the most up-to-date and complex techniques, which are rapidly revolutionizing the technology of these metals. This underlines the only real regret one can have about this book, that the author did not provide the reader with as much critical analysis and judgment as might be desired; this is the case both in the comparison of processes and in the appraisal of data presumably obtained on material which is unsatisfactory by present standards. The commendable desire to make the collated information available quickly no doubt accounts for this.

The book is clearly and accurately printed, the only error noticed being the insertion of an incorrect figure (10.60). Unfortunately, the binding is unsatisfactory both for the excellence of the book and its price (£6).

Dr. Miller is to be congratulated on what will undoubtedly become a standard work; it is to be hoped that in future editions further critical comment, which he is so well fitted to provide, will be added. L. GRAINGER.

Einführung in die Physik der Leiterwerkstoffe, by K. M. Koch and R. Reinbach. Pp. vii+255. (Vienna: Franz Deuticke, 1960.) 222 Austrian sh.

Engineers nowadays have to be physicists, and electrical engineers have to be solid-state physicists. The book under review is intended to help in building the requisite bridges between science and technology. Its central chapter presents a useful descriptive review of the physical properties of technically important conducting materials—copper, aluminium, zinc, iron, various associated alloys, and materials with specialized uses as resistors, heating

elements, resistance thermometers and thermoelectric circuit elements. These technical matters are given a scientific framework in four chapters of introduction, and one of conclusion, which contain an elementary treatment of the relevant aspects of modern solid-state physics. Unfortunately the theory of the conduction process forms a complex branch of the electron theory of metals and is difficult to popularize intelligibly without becoming superficial. In the account given here there is, apart from a few minor errors of interpretation, a general tendency to quote detailed formulae applicable to models of doubtful validity, when a more general discussion of the physical basis of the phenomena in question might have been more illuminating. But the authors have successfully avoided the major pitfalls and can be said to have made a creditable attempt at a difficult task of exposition and synthesis. E. H. SONDHEIMER.

Structure Reports: Supplementary Volume and Cumulative Index for 1940–1950, Vol. 14, general editor: A. J. C. WILSON. Pp. vii+215. (Utrecht: N. V. A. Oosthoek's Uitgevers Mij—Published for the International Union of Crystallography, 1959.)

Volume 14 is mainly concerned with cumulative indexes for the volumes covering the period 1940 to 1950 (Volumes 8–14). The cumulative indexes provided are as follows: Metals, Subject, Formula, Compounds and Author. The Subject Index includes all substances referred to in the Reports except metals, group headings, e.g. organic compounds, geographical names giving mineral localities, and some physical properties such as expansion coefficient. A few corrigenda to be applied to the volumes 8 to 13 are also included. A.C.S.

Structure Reports for 1952, Vol. 16, general editor: A. J. C. WILSON. Pp. viii+651. (Utrecht: N. V. A. Oosthoek's Uitgevers Mij—Published for the International Union of Crystallography, 1959.)

The Structure Report Volume 16 follows the same pattern as previous volumes in the series and covers the year 1952. The Subject Index has been slightly modified as a result of the experience gained in the preparation of the cumulative indexes contained in Volume 14. A.C.S.

Elements of Wave Mechanics, by N. F. MOTT. Pp. ix+156. (London: Cambridge University Press, 1958.) 15*s*.

Elements of Wave Mechanics, was first published in 1951 to replace the author's earlier 1930 *An Outline of Wave Mechanics*. The present edition is an offset-litho reproduction of this 1951 edition, and is one in the new series of Students' Edition textbooks recently introduced by Cambridge University Press. This neat and inexpensive edition will be much welcomed by students. A.C.S.

Confluent Hypergeometric Functions, by L. J. SLATER. Pp. ix+247. (London: Cambridge University Press, 1960.) 65*s*.

The confluent hypergeometric functions are Kummer's function and the Whittaker functions which the physicist frequently meets in the solution of partial differential equations. The first part of the book gives a full discussion of the main properties of the functions and of the analysis necessary to develop their asymptotic expansions. In the second part are three appendices giving tables of the function ${}_1F_1(a; b; x)$ over the ranges most useful to the computer. These tables are stated to be the most complete yet to be published. A.C.S.

Electronic Computers: Principles and Applications, by T. E. Ivall. Pp. viii + 263. (London: Iliffe and Sons; New York: Philosophical Library, 1960.) 25*s*.

This is a second edition of a book first published in 1956. Developments have been so rapid that much of the new edition is modified and three new chapters have been added dealing with analogue computer circuits, programming of digital computers and a discussion of computers of the future.

The fundamental approach is, as in the first edition of the book, intended as a non-mathematical introduction to the principles and applications of computers, and is designed to appeal to technicians, engineers and students with some knowledge of electronic or electrical engineering. A.C.S.

Theory of A.C. Circuits, by S. Fisch and J. L. Potter. Pp. xii + 453. (London: Macmillan, 1959.) 35*s*.

In writing a book on such a topic as this for which there is already a wealth of literature, the authors should be convinced of their ability to throw considerable new light on a well studied subject. Apart from a few minor instances the book gives little evidence of any new approaches and in at least one case reverts to an outmoded explanation; the quantity j is defined as $\sqrt{(-1)}$ and not as an operator rotating through 90° as is now generally accepted. This is merely an instance of the general trend throughout the book whereby the engineering phenomena are subjugated to the mathematical analyses.

Despite the preceding rather condemnatory remarks the book is well presented and covers the field of a.c. circuit analysis applied to lumped circuits with commendable clarity. In attempting to be comprehensive, chapters dealing with Laplace transform and circuit synthesis have been included. The former is very well developed from Fourier analysis via the Fourier integral and transform and gives an admirable introduction to the subject; it does, however, limit the discussion to the use of Laplace transform as a mathematical tool. The chapter on synthesis is naturally so restricted that it is only possible to deal with the four simplest canonical reactance forms. Nevertheless the significance of even these could have been enhanced by a more comprehensive survey of the analysis of frequency dependent networks earlier in the book. The more elementary topics are dealt with in a very detailed manner at times bordering on the pedestrian; a student who would require explanation at this level would find some of the later parts of the book too sophisticated. It will therefore take its place among the large number of standard texts on circuit theory from which the student must make his selection. R. A. KING.

Luminescence Cristalline, by D. Curie. Pp. x + 209. (Paris: Dumond Monographs, 1960.) 14.50 n fr.

The monograph is one of a series intended as up-to-date introductions to specialized scientific topics. The author is an established research worker in his field and the text represents his lectures to students which form part of a wider grounding in solid state physics given in the University of Paris. Much of the subject matter is concerned with emission processes, but there is brief treatment of effects such as thermal and optical stimulation of luminescence and modes of energy transfer in phosphors. The brevity of the volume restricts its critical approach. For example, exciton theory is presented without mention of current doubts as to the significance, if any, of excitons in sulphide phosphors.

The bibliography is restricted to review articles in general. However, the book is a useful contribution to the teaching of the subject and will help many postgraduate students entering the field. G. F. J. GARLICK.

Paramagnetic Resonance in Solids, by W. Low. *Solid State Physics, Supplement* 2, edited by F. SEITZ and D. TURNBULL. Pp. viii + 212. (New York, London: Academic Press, 1960.) $7.50.

Paramagnetic resonance spectroscopy now finds a wide application in the field of solid state physics. A particular aspect of the study, namely paramagnetic resonance of transition group ions, has been extensively investigated and because of the rapid accumulation of data has already been the subject of a series of review articles in *Reports on Progress in Physics*. Professor Low has been prolific in the field and his book is mainly concerned with this subject. The second chapter deals with the effects of crystalline electric fields of different symmetries on the energy levels of transition group ions and with the spin Hamiltonian. Tables of matrix elements of crystal field operators are collected here and examples given of the manner in which they are used to calculate the splitting of degenerate orbital levels by crystal fields. The following chapter gives a detailed discussion of measurements on individual magnetic ions. It is pointed out that a knowledge of the optical spectrum of a magnetic ion is usually necessary for a full understanding of the paramagnetic resonance spectrum and examples are given of cases where optical and microwave measurements in the same crystal have been profitably combined. Both these chapters contain a large number of references to original papers and are the most extensive and useful review of transition ions now available. The following chapters dealing with relaxation times, colour centres and experimental techniques are less specialized and not so well developed and do not add greatly to the usefulness of the book. W. HAYES.

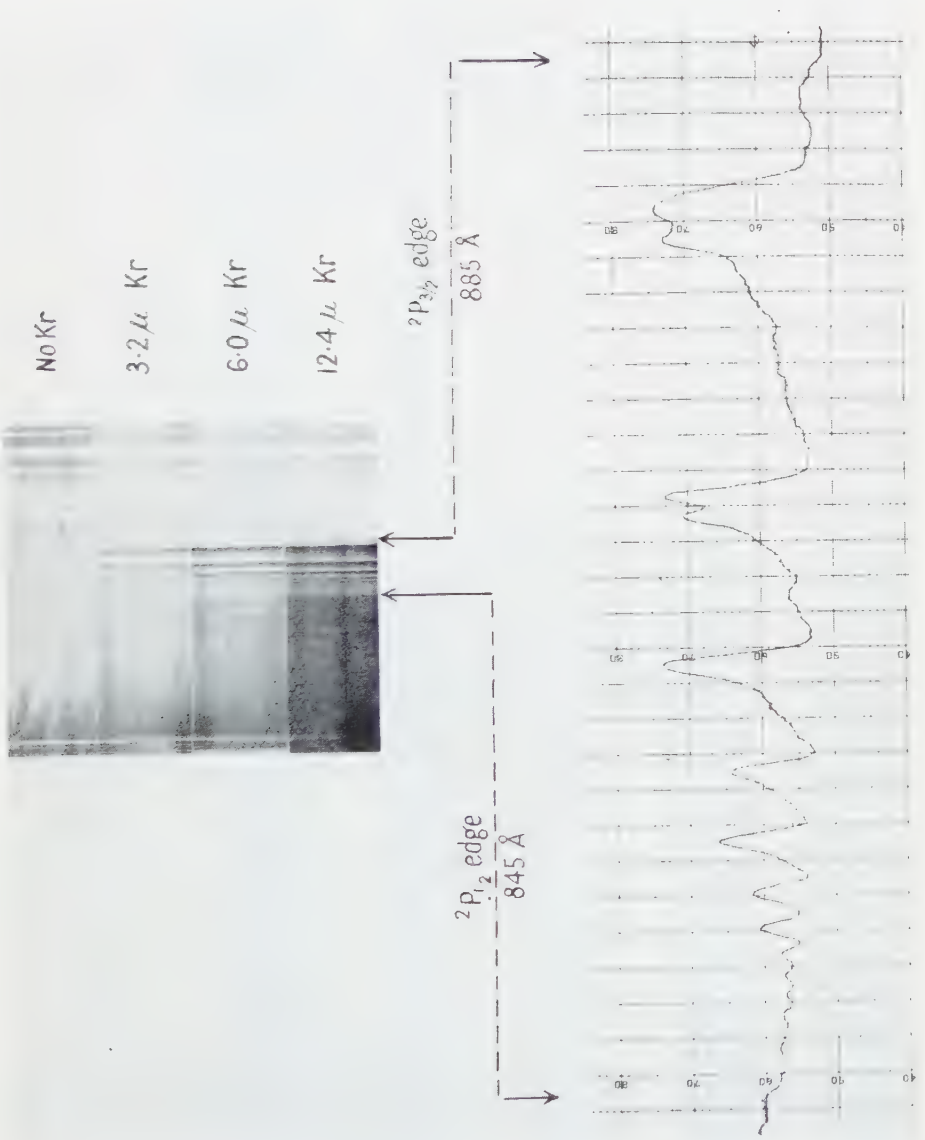

Figure 1. Absorption spectrum of Kr.

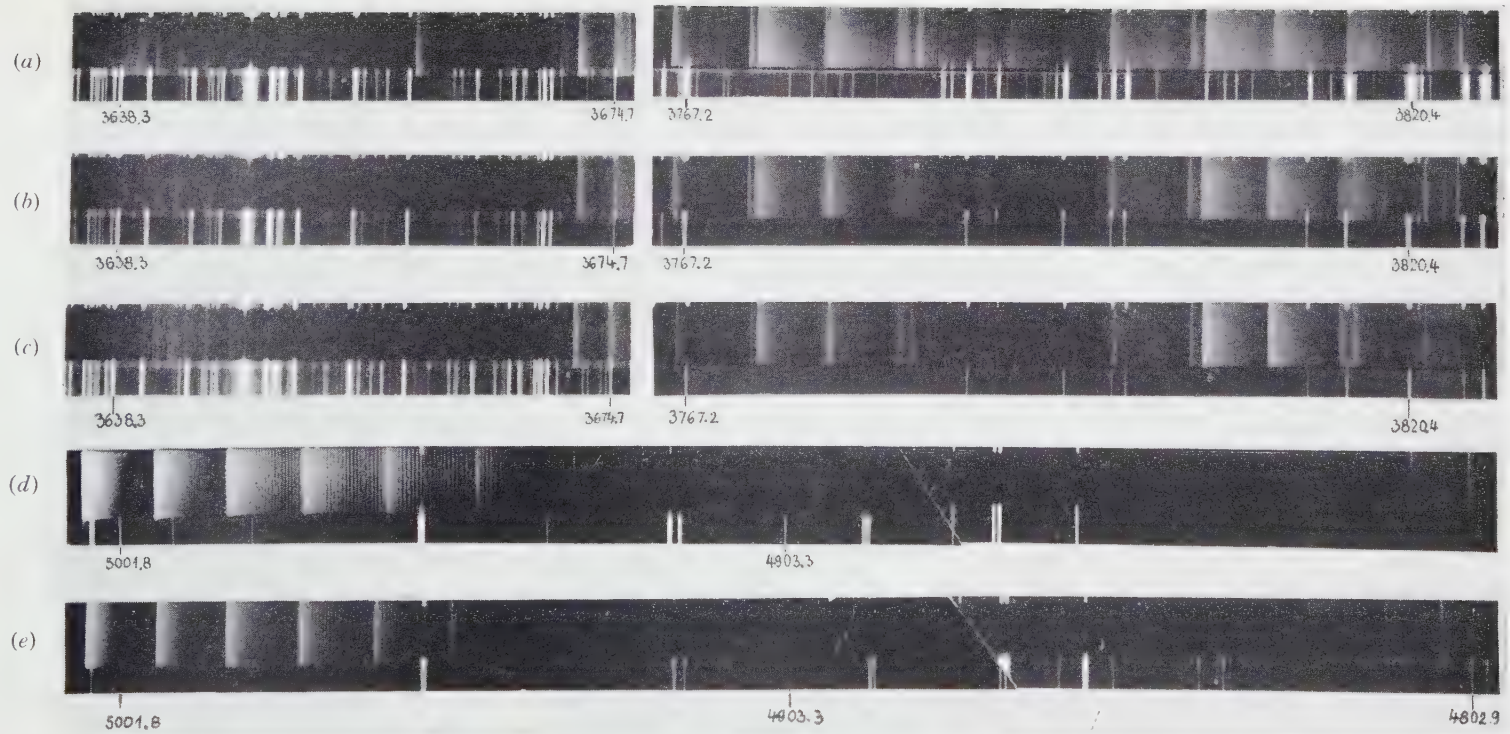

a, Ultra-violet system in $^{16}O_2$; *b*, ultra-violet system in a mixture of $^{16}O_2$ and $^{18}O_2$; *c*, ultra-violet system in $^{18}O_2$; *d*, green system of $Mg^{16}O$; *e*, green system of $Mg^{18}O$. Iron arc spectra are shown below the main spectra.

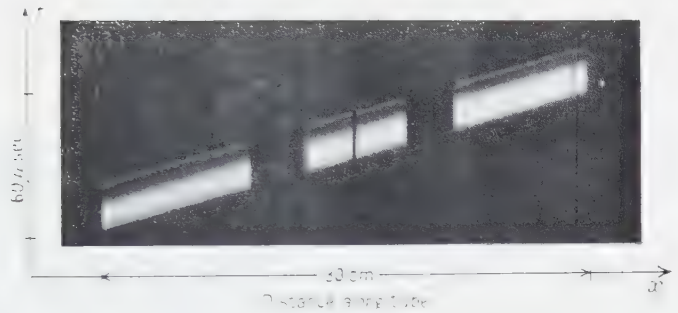

Figure 2. Drum camera record of ionized argon shock front moving through the glass section of the shock tube at Mach 15. The speed is measured from the slope of the trace in the (x, t) plane and checks the speed recorded by photomultipliers.

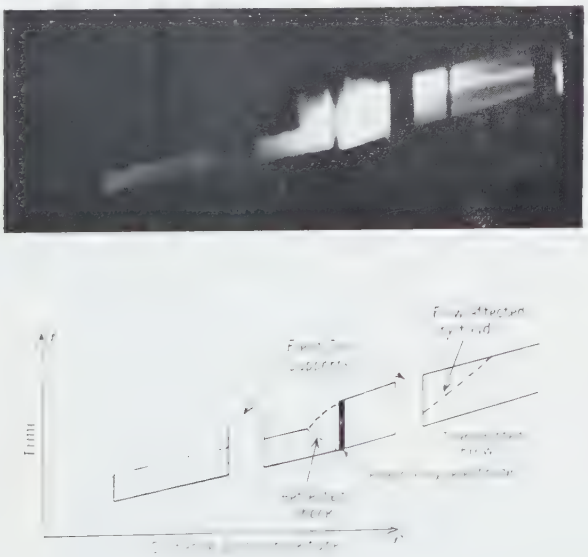

Figure 8. Drum camera record of plasma interaction described in figure 7. The highly luminous region displays the shock reflected at the brass electrode position and the effect of the interaction on transmitted flow speed. The luminous contours of the plate are indicated in the explanatory diagram.

Figure 4. (*a*) The top photograph shows plasma flowing through the glass section of the shock tube and the field coil, in the absence of a magnetic field. When the field value is 20 000 G the flow is modified as shown in the centre photograph. The effect of the field is to form a 'magnetic nozzle' and a similar flow may be seen in the bottom photograph where the magnetic field has been replaced by an annular nozzle made of araldite. (*b*) shows the constricting effect of the magnetic field when the flow appears to leave the shock tube walls and follows the lines of force. Here the field value is 40 000 G and the plasma density is such that the individual particles describe helical paths along the magnetic field lines. (*c*) shows a shear flow pattern which forms when the plasma interacts with a magnetic field which is confined to the upper part of the tube. The field coil position is shown in figure 5 (*d*) (i).

Plate II

Diffraction pattern from etched silicon after heat treatment at 1132°C. Streaked spots due to silicon and sharp spots and rings due to precipitate particles. (100) surface; [011] azimuth.

PROCEEDINGS OF THE PHYSICAL SOCIETY

1960—VOL. 76

SUBJECT INDEX

PAGE

Abrasion of graphite, surface re-orientation, friction and wear 513
Absorption of krypton in extreme ultra-violet 833
Absorption, optical, in semiconductors, treatment of impurity scattering in (R) . . 574
Absorption, *see also under* Lattice absorption, Nuclear resonance, Optical absorption
Acoustic resonant frequencies of gases in tubes, effect of attenuation (R) . . . 772
Acoustic sources, underwater explosions 233
Afterglows, oxygen, ion charge exchange reactions in 137
Air showers, extensive, investigation using Cerenkov detectors 1
Alkali halide molecules, Pauling's theory (R) 794
Alloys, cubic, nuclear quadrupole coupling with conduction electrons in . . . 526
Alloys, Knight shift in (R) 989
Alloys, Ni–Fe, internal ferromagnetic resonance and magnetostatic modes . . . 273
Alloys, Si–Fe, magnetothermal effects 282
Alloys, Si–Fe sheet, ' cube-textured ': domain patterns 754
Aluminium, anodized, absorption of water vapour by, electrical effects . . . 721
Anisotropy, magnetocrystalline, and magnetic resonance in ytterbium iron garnet (L) . 308
Antiferromagnetics, electric conduction in (R) 985
Antiferromagnetism, stacking faults and specific heats of polymorphous manganous sulphide 969
Arc, low-pressure, pinch effect in (R) 409
Argon, and argon mixtures, specific heats 732
Argon ions and atoms, charge exchange (R) 416
Argon, shock ionized, magnetic field interactions 849
Argon and xenon, phase equilibria in condensed mixtures 180
Atomic spectra, SCEPTRE III as source 17
Atoms, stopping powers (R) 422

Band spectra of magnesium oxide, isotope effect 844
Band system, B'–B, of N_2 rotational analysis of 5–1 band 337
Barium titanate, cubic–hexagonal transition, investigation 763
Bismuth, monocrystalline and liquid, electrical resistivity (L) 163
Bismuth telluride, infra-red Faraday rotation and free carrier absorption in . . 169
Bismuth telluride, thermal conductivity and thermoelectric power at low temperatures 113
Breakdown mechanism and measurement of ionization and attachment coefficients in humid air 223
Brillouin zone, correct enumeration of vibration frequencies (R) 777

Carrier accumulation and electroluminescence (R) 782
Carrier transport effect, reversed, in germanium 465
Cathodoluminescence spectra of natural diamonds, radiation induced changes in . 688
Cerenkov detectors, for investigation of extensive air showers 1
Charge exchange between argon ions and atoms (R) 416
Charge exchange, *see also under* Exchange
Charged particles moving through plasma without magnetic field, electrodynamics . 657
Classical mechanics, perturbations in 33
Collisions, slow electron, with hydrogen atoms, numerical solution of exchange equations 532

PAGE

Compression waves in plasma in static magnetic field . . . . . corr. 808
Conducting sheet in strong magnetic field, waves in 329
Conductivity, *see under* Electrical conductivity, Ionic conductivity, Thermal conductivity
Cosmic ray showers, extensive, singly scattered delayed electrons in 449
Counters, scintillation, large area, performance 745
Cross section, inelastic collision, estimation from electron mobility measurements (L) . 439
Cross section, relativistic, for K shell ionization by electrons 623
Cross section, total and absorption, for high energy pions (R) 577
Crystals, ionic, field dependent electron mobility in 261
Crystals, single, $BaTiO_3$, electrical conductivity 93
Crystals, single, manganese–zinc fluoride, optical absorption near Néel temperature . 355
Crystals, single, of PbSe grown from vapour, Hall coefficient and electrical conductivity measurements (R) 783
Crystals, single, of Si, identification of precipitate particles by reflection electron diffraction (R) 993

Debye characteristic temperature of solids (R) 295
Deuterons, direct inelastic scattering 185
Deuterons, 19·6 MeV, elastic and inelastic scattering by Mg 149
Deuterons, *see also under* Scattering
Diamond, centres formed by nitrogen in (R) 787
Diamond, natural, radiation induced changes in cathodoluminescence spectra . . 688
Diamond, particle excited luminescence in 670
Diffraction, *see under* Ionosphere
Dipole moments, and calculations on ionic character and hybridization for AsF_3 and $AsCl_3$ 267
Domain patterns on ' cube-textured ' Si–Fe sheet 754
Domain widths, optimum, in Si–Fe, measurements (R) 567
Domains, magnetic interaction (R) 160
Dysprosium, paramagnetic resonance spectrum in cubic field of CaF_2 (L) . . . 307

Ehrenberg–Franks experiment on penetration of electrons into luminescent material (L) 437
Elastic and viscous properties, of thixotropic fluids, measurements 127
Electric conduction in antiferromagnetics (R) 985
Electric strength of KCl and NaCl, influence of ionic conductivity 817
Electrical conductivity of $BaTiO_3$, single crystals 93
Electrical conductivity, non-ohmic, in Ba_2TiO_3 and CdS theory of space charge limited currents 497
Electrical resistivity of monocrystalline and liquid bismuth (L) 163
Electroluminescence due to carrier accumulation (R) 782
Electron capture, orbital, measurement, in ^{131}Cs 349
Electron diffraction, reflection, for identification of precipitate particles in single crystals of Si (R) 993
Electron diffraction for study of abrasion of graphite 513
Electron energy loss spectra, characteristic, of transition metals, Ti to Cu . . . 857
Electron, K, wave functions by variational principle 641
Electron mobility, field dependent, in ionic crystals 261
Electron mobility in hydrogen, calculated (R) 779
Electron mobility measurements for estimation of inelastic collision cross sections (L) . 439
Electron mobility, polar scattering in III–V compounds (R) 414
Electron–photon cascades, stochastic problem 650
Electron temperature, measurement in high-temperature plasmas . . . corr. 168
Electrons, singly scattered shower, delay 449
Electrons, slow, transmission through thin films 705
Energy levels of ^{24}Mg and ^{32}Si 553
Energy levels of ^{29}P, ^{33}Cl and ^{41}Sc from (d, n) reactions 56
Energy losses, characteristic, of fast electrons in metals, phenomenological theory . 481
Energy losses, electron, characteristic, in various elements, origin 593
Equilibrium distribution of N atoms on N sites (L) 580

PAGE

Exchange equations for slow electron collisions with hydrogen atoms, numerical solution 532
Exchange reactions, ion charge, in oxygen afterglows 137
Explosions, underwater, as acoustic sources 233

Ferrimagnetic resonance experiments, wall effect in 99
Ferromagnetic resonance, internal, and magnetostatic modes in Ni–Fe alloys . . 273
Films, thin, *see under* Thin films
Fluids, thixotropic, measurements of elastic and viscous properties 127
Fluorides, uranium-activated, luminescence (R) 158
Form factors of nucleus ^{6}Li 949
Fourier images IV: phase grating 378
Friction, internal, in Ge and Si I: electron and impurity relaxation 385
Friction, internal, in Ge and Si II: oxygen movement and dislocation damping . . 398

Gamma emission, recoillness, of $^{119}Sn^{m}$, thermal red shift (L) 165
Gamma radiation following resonant proton capture by Cl 929
Gas mixtures, binary, viscosity and thermal conductivity 104
Gases in tubes, effect of attenuation on acoustic resonant frequencies (R) . . . 772
Germanium, hot carriers (L) 1001
Germanium, infra-red investigation of acceptor levels formed by Cu 900
Germanium, interband photoconductivity in (R) 565
Germanium, reversed carrier transport effect 465
Germanium and silicon, internal friction in I: electron and impurity relaxation . . 385
Germanium and silicon, internal friction in II: oxygen movement and dislocation damping 398
Graphite, surface re-orientation, friction and wear in unidirectional abrasion . . 513

Helium, and argon, liquid, interpretation of ion mobility measurements in . . 36
Helium, elastic scattering of ^{3}He by ^{3}He (R) 987
Helium, Lamb shift in 49
Helium, lifetime of He^{-} ion (R) 998
Helium, liquid, Knight shift of nuclear magnetic resonance (R) 301
Helium, nitrogen and neon, high energy photodisintegration under 65
Hole mobility in selenium 826
Humid air, ionization in, and breakdown mechanism 223
Hydrogen, atomic, catalytic magnetization (L) 806
Hydrogen, atomic, scattering of electrons and positrons from s-state 559
Hydrogen, electron mobility in, calculated (R) 779
Hydrogen ions, optical excitation of N_2 by 217
Hyperfine structure of U and Am lines in 1·6–2·1 micron region (R) 569

Indium antimonide, lattice absorption bands in 939
Inert gases, *see under* Argon, Helium
Infra-red absorption spectra of potassium manganicyanide and vanadium corundum (R) 996
Infra-red Faraday rotation and free carrier absorption in Bi_2Te_3 169
Infra-red investigation of acceptor levels formed by Cu in Ge 900
Ion mobility measurements in argon and helium liquids, interpretation . . . 36
Ionic character and hybridization of AsF_3 and $AsCl_3$ fom dipole moments . . 267
Ionic conductivity, influence on electric strength of KCl and NaCl 817
Ionization and attachment coefficients in CO_2, measurement in uniform fields . . 369
Ionization in humid air and breakdown mechanism 223
Ionization, K-shell, by electrons, relativistic theory 623
Ionosphere, anisotropy in diffraction and effect on drift 959
Ionospheric disturbances, sudden, observations 79
Ions, heavy, method of measuring range in solids (L) 438
Isotope effect in band spectra of magnesium oxide 844

PAGE

Knight shift in alloys (R) 989
Knight shift of nuclear magnetic resonance in liquid He (R) 301
Krypton, absorption in extreme ultra-violet 833

Lamb shift in helium 49
Lattice absorption bands in indium antimonide 939
Lead selenide single crystals grown from vapour, Hall coefficient and electrical conductivity measurements (R) 783
Lifetime of He^- ion (R) 998
Light beams, partially polarized, correlation between photons (R) 424
Lithium, form factors of nucleus ^6Li 949
Low temperatures, resistance anisotropy at 458
Low temperatures, second dislocation relaxation peak in Al (R) 412
Low temperatures, thermal conductivity and thermoelectric power of Bi_2Te_3 . . 113
Luminescence in diamond, particle excited 670
Luminescence of uranium-activated fluorides (R). 158
Luminescent material, Ehrenberg–Franks experiment on penetration of electrons into (L) 437

Magnesium oxide, band spectra, isotope effect 844
Magnetic field interactions with shock ionized argon 849
Magnetic interaction domains (R) 160
Magnetic resonance and magnetocrystalline anisotropy in ytterbium iron garnet (L) 308
Magnetization, catalytic, of atomic hydrogen (L) 806
Magnetostriction of lithium–chromium ferrite near compensation point (R) . . 411
Magnetostriction, saturation, constants for Ni in temperature range $-196°$ to 365°C . 502
Magnetothermal effects in Si–Fe alloys 282
Metals, characteristic energy losses of fast electrons in, phenomenological theory . 481
Metals, noble and transition, soft x-ray emission spectra (R) 791

Nickel, saturation, magnetostriction constants in temperature range $-196°$ to 365°C . 502
Nitrogen, centres formed by, in diamond (R) 787
Nuclear emulsion material, asymmetry in scattering of 90–140 MeV polarized protons from (R) 427
Nuclear magnetic resonance, Knight shift, in liquid He (R) 301
Nuclear resonance absorption of ultrasound in KI and KBr (R) 776
Nuclei, light, (t, p) reactions in 914
Nucleons, *see under* Stripping

Optical absorption in manganese–zinc fluoride single crystals near Néel temperature . 355
Optical excitation of N_2 by 0·5 to 1·5 MeV hydrogenic ions 217
Optics, wave-theoretic and ray-theoretic contrast transmission functions . . . 870

Paramagnetic material, cylinder of, stability in magnetic field (L) 800
Paramagnetic resonance absorption in Br and Cl 979
Paramagnetic resonance spectrum of dysprosium in cubic field of CaF_2 (L) . . 307
Pauling's theory of alkali halide molecules (R) 794
Perturbations in classical mechanics 33
Phase equilibria in condensed mixtures of argon and xenon 180
Phases, scattering, variational principle for 206
Photoconductivity, impurity, in n-type InSb (L) 802
Photoconductivity, interband, in Ge (R) 565
Photodisintegration, high energy, of helium, nitrogen and neon 65
Photons, correlation in partially polarized light beams (R) 424
Photoproduction of charged pions from deuterium (R) 430
Pinch effect in low-pressure arc (R) 409
Pinched plasma, stable, Joule heating. 250
Pions, charged, photoproduction from deuterium (R) 430
Pions, high energy, total and absorption cross section (R) 577

PAGE
Plasma, high-temperature, measurement of electron temperature in . . . corr. 168
Plasma, stable pinched, Joule heating 250
Plasma, in static magnetic field, compression waves in . . . . . corr. 808
Plasma without magnetic field, electrodynamics of charged particle moving through . 657
Polar scattering in III–V compounds (R) 414
Polarization of particles in electron–photon cascades, stochastic problem . . . 650
Polymorphism of thallium hallides 507
Potassium manganicyanide and vanadium corundum, infra-red absorption spectrum (R) 996
Proton capture, resonant, by Cl, γ-radiation following 929

Quadrupole coupling with conduction electrons in cubic alloys 526

Radiation, resonance and fluorescence in ^{152}Sm, multipolarity and character . . 759
Radiative transitions in ^{8}Be 737
Radium C′, half-value period (R) 299
Reaction ^{27}Al(^{3}He, d)^{28}Si 545
Reactions, (d, n), energy levels of ^{29}P, ^{33}Cl and ^{41}Sc from 56
Reactions, (t, p) in light nuclei 914
Red-shift, thermal, of recoilless emission of ^{119}Sn^{m} (L) 165
Relativistic K electron wave functions by variational principle 641
Relativistic theory of K ionization by electrons 623
Relativity, general, field of electric current in 891
Relaxation, second dislocation peak in Al at low temperatures (R) 412
Relaxation times, spin–lattice, in ruby at 34·6 Gc/s 697
Relaxation, ultrasonic in triethylamine 321
Resistance anisotropy at low temperatures 458
Resonance, *see under* Ferrimagnetic resonance, Ferromagnetic resonance, Nuclear magnetic resonance, Paramagnetic resonance
Ruby, spin–lattice relaxation times at 34·6 Gc/s 697

Scattering, elastic, of ^{3}He by ^{3}He (R) 987
Scattering, elastic and inelastic, of 19·6 MeV deuterons by Mg 149
Scattering, elastic and inelastic, of electrons and positrons from s-states of atomic hydrogen 559
Scattering, inelastic, direct, of deuterons 185
Scattering, inelastic, of 12 MeV neutrons in carbon, spin–orbit effects 611
Scattering phases, variational principle for 206
Scattering of GeV pions and nucleons by deuterons, shadow effect 346
Scattering of 90–140 MeV polarized protons from nuclear emulsion material, asymmetry (R) 427
Scattering, proton–proton, spin–orbit potential in . . . . 539, corr. 1002
Sceptre III, as source of spectra of highly ionized atoms 17
Selection rules for spin–orbit matrix elements for configuration f^{n} (R) . . . 419
Selenium, hole mobility 826
Semiconductors, treatment of impurity scattering in optical absorption (R) . . 574
Semiconductors, *see also under* Bismuth telluride, Carrier, Germanium
Silicon and germanium, internal friction in I: electron and impurity relaxation . . 385
Silicon and germanium, internal friction in II: oxygen movement and dislocation damping 398
Solids, Debye characteristic temperature (R) 295
Solids, ranges of heavy ions in, method for measuring (L) 438
Sound, transmission through wake 25
Space charge limited currents, theory 497
Specific heats of polymorphous forms of manganous sulphide and antiferromagnetic ordering in stacking faults 969
Specific heats of solid argon and equimolar argon–krypton mixture 732
Spectra, emission, soft X-ray, of transition and noble metals (R) 791
Spectra, energy loss, in various elements 593
Spectra, *see also under* Atomic spectra, Band spectra, Cathodoluminescence, various types of resonance

PAGE

Spectroscopy, hyperfine structure of U and Am lines in 1·6–2·1 micron region (R) . 569
Spin–orbit effects in inelastic scattering of 12 MeV neutrons in carbon . . . 611
Spin–orbit matrix elements for configuration f^n, selection rules (R) 419
Stability of infinite gravitating cylinder of paramagnetic material in magnetic field (L) . 800
Stopping power of atoms (R) 422
Stopping power theory, relativistic K shell (R) 433
Stripping of two nucleons 489
Switching properties of tetramethylammonium-trichloromercurate . . . 797

Tetramethylammonium-trichloromercurate, switching properties (R) . . . 797
Thallium halides, polymorphism 507
Thermal conductivity and thermoelectric power of Bi_2Te_3 at low temperatures . . 113
Thermal conductivity and viscosity of binary gas mixtures 104
Thin films, transmission of slow electrons through 705
Transition metals, Ti to Cu, characteristic electron energy loss spectra . . . 857
Transport equation and variational principle, discontinuities in solutions . . . 909
Triethylamine, ultrasonic relaxation 321

Ultrasonic relaxation in triethylamine 321
Ultrasound, nuclear resonance absorption in KI and KBr (R) 776
Ultra-violet, extreme, absorption of krypton 833
Underwater explosions as acoustic sources 233

Vanadium corundum, infra-red absorption spectra of potassium manganicyanide (R) . 996
Vapour–liquid system, behaviour above and below critical point (R) 303
Variational principle for scattering phases 206
Vibration frequencies in Brillouin zone, correct enumeration (R) 777
Viscosity and thermal conductivity of binary gas mixtures 104
Viscous and elastic properties of thixotropic fluids, measurements 127

Water vapour, adsorption by anodized aluminium, electrical effects 721
Waves, Alfvén 329

X-rays, soft, emission spectra of transition and noble metals (R) 791

Ytterbium iron garnet, magnetic resonance and magneto-crystalline anisotropy in (L) . 308

INDEX TO AUTHORS (WITH TITLES)

PAGE

Allan, H. R., Beamish, R. F., Bryant, D. A., Kasha, H., and Wills, R. D. : Investigation of extensive air showers, using Cerenkov detectors 1
Anderson, J. C. : Internal ferromagnetic resonance and magnetostatic modes in nickel–iron alloys . . . . . 273, corr. 808
Asaad, W. N. : Relativistic K electron wave functions by variational principle. . 641
Austin, I. G. : Infra-red Faraday rotation and free carrier absorption in Bi_2Te_3 . 169

Banerji, R. B. : Anistropy in ionospheric diffraction and its effect on drift measurement 959
Barnaby, C. F., and Barton, J. C. : Performance of large area scintillation counters 745
Barnes, J. F., and Tredgold, R. H. : Field dependent electron mobility in ionic crystals 261
Barros, F. de S., with Jaffe, A. A., Forsyth, P. D., Muto, J., Taylor, I. J., and Ramavataram, S. : Some (t, p) reactions in light nuclei 914
Barton, J. C., with Barnaby, C. F. : Performance of large area scintillation counters 745
Bates, L. F., and Carey, R.: Domain patterns on ' cube-textured ' silicon–iron sheet 754
Batty, C. J. : Total and absorption cross section for high energy pions (R) . . 577
Beamish, R. F., with Allan, H. R., Bryant, D. A., Kasha, H., and Wills, R. D. : Investigation of extensive air showers, using Cerenkov detectors . . . 1
Beer, R., and Bovey, L. : Hyperfine structure of some uranium and americium lines in 1·6–2·1 micron region (R) 569
Bhalla, M. S., and Craggs, J. D. : Measurement of ionization and attachment coefficients in carbon dioxide in uniform fields 369
Billington, E. W. : Some measurements of elastic and viscous properties of thixotropic fluids 127
Birss, R. R., and Lee, E. W. : Saturation magnetostriction constants of nickel within temperature range -196° to 365°C 502
Birss, R. R., with Lee, E. W. : Magnetostriction of lithium–chromium ferrite in neighbourhood of its compensation point (R) 411
Bonnor, W. B. : Field of electric current in general relativity 891
Booker, C. J. L., and Wood, J. L. : Further electrical effects of adsorption of water vapour by anodized aluminium 721
Bovey, L., with Beer, R. : Hyperfine structure of some uranium and americium lines in 1·6–2·1 micron region (R) 569
Boyle, A. J. F., Bunbury, D. St. P., Edwards, C., and Hall, H. E. : Thermal red shift of recoilless γ-emission of $^{119}Sn^m$ (L) 165
Bransden, B. H., and Hamilton, R. A. H., : Elastic scattering of ^3He by ^3He (R) . 987
Branwood, A., and Tredgold, R. H. : Electrical conductivity of barium titanate single crystals 93
Bromley, D. A., with Reeves, E. M., and Nicholls, R. W. : Optical excitation of N_2 by 0·5 to 1·5 MeV hydrogenic ions 217
Bryant, D. A., with Allan, H. R., Beamish, R. F., Kasha, H., and Wills, R. D. : Investigation of extensive air showers, using Cerenkov detectors . . . 1
Bunbury, D. St. P., with Boyle, A. J. F., Edwards, C., and Hall, H. E. : Thermal red shift of recoilless γ-emission of $^{119}Sn^m$ (L) 165

Carey, R. : Measurements of optimum domain widths in silicon–iron (R) . . 567
Carey, R., with Bates, L. F. : Domain patterns on ' cube-textured ' silicon–iron sheet 754
Carroll, P. K., and Rubalcava, H. E. : Rotational analysis of 5–1 band of B'-B system of N_2 337
Carter, W. S. : Specific heats of two polymorphic forms of manganous sulphide, and inferred possibility of antiferromagnetic ordering in stacking faults. . . 969
Cooper, R., Higgin, R. M., and Smith, W. A. : Influence of ionic conductivity on electric strength of KCl and NaCl 817

PAGE

Cowley, J. M., and Moodie, A. F. : Fourier images IV : phase grating . . 378
Craggs, J. D., with Bhalla, M. S. : Measurement of ionization and attachment coefficients in carbon dioxide in uniform fields 369
Craggs, J. D., with Prasad, A. N. : Measurement of ionization and attachment coefficients in humid air in uniform fields and mechanism of breakdown . . 223
Craik, D. J., and Isaac, E. D. : Magnetic interaction domains (R). . . . 160
Curry, C., and McNeill, D. J. : Soft x-ray emission spectra of some transition and noble metals (R) 791

Dalgarno, A. : Stopping powers of atoms (R) 422
Dalgarno, A., and Stewart, A. L. : Lamb shift of helium 49
Dayal, B., and Singh, S. P. : Correct enumeration of vibration frequencies in Brillouin zone (R) 777
Dean, P. J., Kennedy, P. J., and Ralph, J. E. : Particle excited luminescence in diamond 670
Dejon, B., and Smith, K. : Shadow effect in scattering of Gev pion and nucleons by deuterons 346
Dickinson, P. H. G., and Sayers, J. : Ion charge exchange reactions in oxygen afterglows 137
Doniach, S. : Catalytic magnetization of atomic hydrogen ? (L) 806
Donovan, B. : Note on treatment of impurity scattering in optical absorption in semiconductors (R) 574

Eccles, P. J. : Singly scattered delayed electrons in extensive cosmic ray air showers 449
Edwards, C., with Boyle, A. J. F., Bunbury, D. St. P., and Hall, H. E. : Thermal red shift of recoilless γ-emission of $^{119}Sn^{m}$ (L) 165
Elliott, R. J. : Speculation on centres formed by nitrogen in diamond (R) . . 787
Emeleus, K. G., with Johnston, A. R. : Note on pinch effect in low-pressure arc (R) 409
Englman, R. : Discontinuities in solutions of transport equation and variational principle 909

Fatuzzo, E. : Switching properties of tetramethylammonium-trichloromercurate (R) 797
Figgins, B. F. : Specific heats of solid argon and equimolar argon–krypton mixture 732
Finlayson, D. M., Robertson, I. S., Smith, T., and Stevenson, R. W. H. : Optical absorption in manganese–zinc fluoride single crystals near Néel temperature . 355
Flynn, C. P., and Seymour, E. F. W. : Knight shift of nuclear magnetic resonance in liquid indium (R) 301
Flynn, C. P., and Seymour, E. F. W. : Nuclear quadrupole coupling with conduction electrons in cubic alloys 526
Forsyth, P. D., with Jaffe, A. A., Barros, F. de S., Muto, J., Taylor, I. J., and Ramavataram, S. : Some (t, p) reactions in light nuclei 914
Fray, S. J., Johnson, F. A., and Jones, R. H. : Lattice absorption bands in indium antimonide 939

Garrido, L. M. : Perturbations in classical mechanics 33
Garton, W. R. S., and Pery-Thorne, Anne: Absorption of krypton in extreme ultra-violet 833
Gergely, Gy. : On Ehrenberg–Franks experiment relating to penetration of electrons into luminescent material (L) 437
Glaister, R. M., and Kay, H. F. : Investigation of cubic–hexagonal transition in barium titanate 763
Grant, I. S. : Radiative transitions in ^{8}Be 737
Greenaway, D. L. : Infra-red investigation of acceptor levels formed by copper in germanium 900
Greenlees, G. W., and Lowe, J. : Elastic and inelastic scattering of 19·6 Mev deuterons by Mg 149
Guggenheim, E. A. : Equilibrium distribution of N atoms on N sites (or in N cells) (L) 580

PAGE

Haines, M. G. : Joule heating of stable pinched plasma 250
Hall, H. E., with Boyle, A. J. F., Bunbury, D. St. P., and Edwards, C. : Thermal red shift of recoilless γ-emission of $^{119}Sn^{m}$ (L) 165
Hamilton, R. A. H., with Bransden, B. H. : Elastic scattering of ^{3}He by ^{3}He (R) . 987
Harvey, J. S. M., Kamper, R. A., and Lea, K. R. : Paramagnetic resonance absorption in bromine and chlorine 979
Hawkins, T. D. H., with Moss, T. S. : Interband photoconductivity in germanium (R) 565
Heasell, E. L., with Padmanabhan, R. A. : Ultrasonic relaxation in triethylamine . 321
Heastie, R., and Lefebvre, C. : Phase equilibria in condensed mixtures of argon and xenon 180
Henisch, H. K., and Marathe, B. R. : Note on electroluminescence due to carrier accumulation (R) 782
Henry, W. G. : Knight shift in alloys (R) 989
Heylen, A. E. D. : Calculated electron mobility in hydrogen (R) 779
Higgin, R. M., with Cooper, R., and Smith, W. A. : Influence of ionic conductivity on electric strength of KCl and NaCl 817
Hilsum, C. : Polar scattering in III–V conpounds (R) 414
Hinds, S., and Middleton, R. : Energy levels of ^{24}Mg and ^{32}Si 553
Hinds, S., and Middleton, R. : Study of $^{27}Al(^{3}He, d)^{28}Si$ reaction 545
Hughes, T. P., with Kaufman, A. S., and Williams, R. V. : SCEPTRE III—Intense source of spectra of highly ionized atoms 17
Hurle, D. T. J., and Weintroub, S. : Electrical resistivity of monocrystalline and liquid bismuth (L) 163

Isaac, E. D., with Craik, D. J. : Magnetic interaction domains (R) 160

Jackson, Daphne F. : Form factors of the nucleus ^{6}Li 949
Jaffe, A. A., Barros, F. de S., Forsyth, P. D., Muto, J., Taylor, I. J., and Ramavataram, S.: Some (t, p) reactions in light nuclei 914
John, T. L. : Numerical solution of exchange equations for slow electron collisions with hydrogen atoms 532
Johnson, F. A., with Fray, S. J., and Jones, R. H. : Lattice absorption bands in indium antimonide 939
Johnston, A. R., and Emeleus, K. G. : Note on pinch effect in low-pressure arc (R) 409
Jones, G. D., and Runciman, W. A. : Infra-red absorption spectra of potassium manganicyanide and vanadium corundum (R) 996
Jones, R. H. : Hall coefficient and electrical conductivity measurements on lead selenide single crystals grown from vapour (R) 783
Jones, R. H., with Fray, S. J., and Johnson, F. A. : Lattice absorption bands in indium antimonide 939
Joshi, B. R., and Lewis, G. M. : On measurement of orbital electron capture with particular reference to ^{131}Cs 349
Joshi, S. K., and Mitra, S. S. : Debye characteristic temperature of solids (R) . 295
Joshi, S. K., with Verma, G. S. : Nuclear resonance absorption of ultrasound in KI and KBr (R) 776

Kamper, R. A., with Harvey, J. S. M., and Lea, K. R. : Paramagnetic resonance absorption in bromine and chlorine 979
Karmohapatro, S. B. : Charge exchange between argon ions and atoms (R) . . 416
Kasha, H., with Allan, H. R., Beamish, R. F., Bryant, D. A., and Wills, R. D. : Investigation of extensive air showers, using Cerenkov detectors 1
Kaufman, A. S., Hughes, T. P., and Williams, R. V. : SCEPTRE III—Intense source of spectra of highly ionized atoms 17
Kaufman, S. (A. S.), with Williams, R. V.: Measurement of electron temperature in high temperature plasmas . . . . . corr. 168
Kay, H. F., with Glaister, R. M. : Investigation of cubic–hexagonal transition in barium titanate 763
Kennedy, P. J., with Dean, P. J., and Ralph, J. E. : Particle excited luminescence in diamond 670

PAGE

Khan, I. H. : On polymorphism of thallium halides 507
Klemperer, O., and Thetford, A., (with a note by F. Lenz) : Transmission of slow electrons through thin films 705

Lalovic, B., with Reid, J. M. : High energy photodisintegration of helium, nitrogen and neon 65
Lea, K. R., with Harvey, J. S. M., and Kamper, R. A. : Paramagnetic resonance absorption in bromine and chlorine 979
Lee, E. W., and Birss, R. R. : Magnetostriction of lithium–chromium ferrite in neighbourhood of its compensation point (R) 411
Lee, E. W., with Birss, R. R. : Saturation magnetostriction constants of nickel within temperature range $-196°$ to $365°$c 502
Lefebvre, C., with Heastie, R. : Phase equilibria in condensed mixtures of argon and xenon 180
Lenz, F., with Klemperer, O., and Thetford, A. : Transmission of slow electrons through thin films 705
Lewis, G. M., with Joshi, B. R. : On measurement of orbital electron capture with particular reference to ^{131}Cs 349
Linfoot, E. H. : Wave-theoretic and ray-theoretic contrast transmission functions . 870
Lisle, J. C., and Shaw, P. F. D. : Gamma radiation following resonant proton capture by chlorine 929
Low, W. : Paramagnetic resonance spectrum of dysprosium in cubic field of calcium fluoride (L) 307
Lowe, J., with Greenlees, G. W. : Elastic and inelastic scattering of 19·6 Mev deuterons by Mg 149
Lys, J. E. A., and Runciman, W. A. : Luminescence of uranium-activated fluorides (R) 158

McLellan, A. G. : Selection rules for spin–orbit matrix elements for configuration f^n (R) 419
McNeill, D. J., with Curry, C. : Soft x-ray emission spectra of some transition and noble metals (R) 791
Macefield, B. E. F., and Towle, J. H. : Energy levels of ^{29}P, ^{33}Cl and ^{41}Sc from (d, n) reactions 56
Majumdar, S. K. : Electrodynamics of a charged particle moving through a plasma without magnetic field 657
Marathe, B. R., and Henisch, H. K. : Note on electroluminescence due to carrier accumulation (R) 782
Meijer, P. H. E. : Note on behaviour of vapour–liquid system above and below critical point (R) 303
Middleton, R., with Hinds, S. : Energy levels of ^{24}Mg and ^{32}Si 553
Middleton, R., with Hinds, S. : Study of ^{27}Al(^{3}He, d)^{28}Si reaction. 545
Miller, W. F., with Smith, K., and Mumford, A. J. P. : Elastic and inelastic scattering of electrons and positrons from s-states of atomic hydrogen . . 559
Mitra, S. S., with Joshi, S. K. : Debye characteristic temperature of solids (R) . 295
Moodie, A. F., with Cowley, J. M. : Fourier images IV : phase grating. . . . 378
Morriss, R. W. : Observations of sudden ionospheric disturbances 79
Moss, T. S., and Hawkins, T. D. H. : Interband photoconductivity in germanium (R) 565
Mumford, A. J. P., with Smith, K., and Miller, W. F. : Elastic and inelastic scattering of electrons and positrons from s-states of atomic hydrogen 559
Murty, G. S., with Nayyar, N. K. : Stability of infinite gravitating cylinder of paramagnetic material in presence of magnetic field (L). 800
Muto, J., with Jaffe, A. A., Barros, F. de S., Forsyth, P. D., Taylor, I. J., and Ramavataram, S. : Some (t, p) reactions in light nuclei 914

el-Nadi, M., and Wafik, M. : Direct inelastic scattering of deuterons 185
Nash, W. B., and Standley, K. J. : Wall effect in ferrimagnetic resonance experiments 99
Nayyar, N. K., and Murty, G. S. : Stability of infinite gravitating cylinder of paramagnetic material in presence of magnetic field (L). 800

PAGE

Newman, R. C. : Identification of precipitate particles in single crystals of silicon by reflection electron diffraction (R) 993
Newns, H. C. : On stripping of two nucleons 489
Nicholls, R. W., with Reeves, E. M., and Bromley, D. A. : Optical excitation of N_2 by 0·5 to 1·5 MeV hydrogenic ions 217

Ogilvie, K. W. : Half-value period of radium C′ (R) 299

Pace, J. H., Sampson, D. F., and Thorp, J. S. : Spin–lattice relaxation times in ruby at 34·6 Gc/s 697
Padmanabhan, R. A., and Heasell, E. L. : Ultrasonic relaxation in triethylamine . 321
Pain, H. J., and Smy, P. R. : Magnetic field interactions with shock ionized argon . 849
Pearson, R. F., and Teale, R. W. : Magnetic resonance and magnetocrystalline anisotropy in ytterbium iron garnet (L) 308
Percival, I. C. : Variational principle for scattering phases 206
Percival, I. C. : Waves in conducting sheet situated in strong magnetic field . . 329
Perlman, H. S. : Relativistic K shell stopping power theory (R) 433
Perlman, H. S. : Relativistic theory of K ionization by electrons 623
Pery-Thorne, Anne, and Garton, W. R. S. : Absorption of krypton in the extreme ultra-violet 833
Pésić, D. S. : Isotope effect in band spectra of magnesium oxide 844
Porat, D. I., and Ramavataram, K. : Proposed method for measuring ranges of heavy ions in solids (L) 438
Porgess, P. V. K., and Wilman, H. : Surface re-orientation, friction and wear, in unidirectional abrasion of graphite 513
Powell, C. J. : Origin of characteristic electron energy losses in ten elements . . 593
Prasad, A. N., and Craggs, J. D. : Measurement of ionization and attachment coefficients in humid air in uniform fields and mechanism of breakdown . . 223
Prior, A. C. : Reversed carrier transport effect in germanium 465
Putley, E. H. : Impurity photoconductivity in n-type InSb (L) 802

Ralph, J. E. : Radiation induced changes in cathodoluminescence spectra of natural diamonds 688
Ralph, J. E., with Dean, P. J., and Kennedy, P. J. : Particle excited luminescence in diamond 670
Ramavataram, K., with Porat, D. I. : Proposed method for measuring ranges of heavy ions in solids (L) 438
Ramavataram, S., with Jaffe, A. A., Barros, F. de S., Forsyth, P. D., Muto, J., and Taylor, I. J. : Some (t, p) reactions in light nuclei 914
Ranganathan, N. R., and Vasudevan, R. : Stochastic problem of electron–photon cascades including polarization 650
Reeves, E. M., Nicholls, R. W., and Bromley, D. A. : Optical excitation of N_2 by 0·5 to 1·5 MeV hydrogenic ions 217
Reid, J. M., and Lalovic, B. : High energy photodisintegration of helium, nitrogen and neon 65
Rhys-Roberts, C., and Tredgold, R. H. : Note on theory of space charge limited currents 497
Richardson, E. G. : Transmission of sound through wake 25
Robertson, I. S., with Finlayson, D. M., Smith, T., and Stevenson, R. W. H. : Optical absorption in manganese–zinc fluoride single crystals near Néel temperature 355
Robins, J. L., and Swan, J. B. : Characteristic electron energy loss spectra of the transition metals, Ti to Cu 857
Robson, B. A., and Robson, D. : Spin–orbit effects in inelastic scattering of 12 MeV neutrons in carbon 611
Robson, D., with Robson, B. A. : Spin–orbit effects in inelastic scattering of 12 MeV neutrons in carbon 611
Rollin, B. V., and Rowell, J. M. : Hot carriers in germanium (L) 1001

PAGE

Rowell, J. M., with Rollin, B. V. : Hot carriers in germanium (L) 1001
Rubalcava, H. E., with Carroll, P. K. : Rotational analysis of 5–1 band of the B′–B system of N_2 337
Runciman, W. A., and Jones, G. D. : Infra-red absorption spectra of potassium manganicyanide and vanadium corundum (R) 996
Runciman, W. A., with Lys, J. E. A. : Luminescence of uranium-activated fluorides (R) 158
Rutherglen, J. G. : Asymmetry in scattering of 90–140 MeV polarized protons from nuclear emulsion material 427
Rutherglen, J. G., and Walker, J. K. : Photoproduction of charged pions from deuterium (R) 430

Sampson, D. F., with Pace, J. H., and Thorp, J. S. : Spin–lattice relaxation times in ruby at 34·6 Gc/s 697
Saunders, N. H., and Tebble, R. S. : Magnetothermal effects in silicon–iron alloys . 282
Sayers, J., with Dickinson, P. H. G. : Ion charge exchange reactions in oxygen afterglows 137
Sewell, G. L. : Electric conduction in antiferromagnetics (R) 985
Seymour, E. F. W., with Flynn, C. P. : Knight shift of the nuclear magnetic resonance in liquid indium (R) 301
Seymour, E. F. W., with Flynn, C. P. : Nuclear quadrupole coupling with conduction electrons in cubic alloys 526
Shaw, P. F. D., and Lisle, J. C. : Gamma radiation following resonant proton capture by chlorine 929
Shukla, R. C., with Varshni, Y. P. : On Pauling's theory of alkali halide molecules (R) 794
Simons, S. : Resistance anisotropy at low temperatures 458
Singh, S. P., with Dayal, B. : Correct enumeration of vibration frequencies in Brillouin zone (R) 777
Smith, K., with Dejon, B. : Shadow effect in scattering of GeV pions and nucleons by deuterons 346
Smith, K., Miller, W. F., and Mumford, A. J. P. : Elastic and inelastic scattering of electrons and positrons from s-states of atomic hydrogen 559
Smith, T., with Finlayson, D. M., Robertson, I. S., and Stevenson, R. W. H. : Optical absorption in manganese–zinc fluoride single crystals near Néel temperature 355
Smith, W. A., with Cooper, R., and Higgin, R. M. : Influence of ionic conductivity on electric strength of KCl and NaCl 817
Smy, P. R., with Pain, H. J. : Magnetic field interactions with shock ionized argon 849
Sobhanadri, J. : Calculations on ionic character and hybridization from dipole moments for AsF_3 and $AsCl_3$ 267
Sodha, M. S. : Estimation of inelastic collision cross section from electron mobility measurements (L) 439
Sood, B. S. : Multipolarity and character of 961 kev resonance and 840 kev fluorescence radiation in ^{152}Sm 759
Southgate, P. D. : Internal friction in germanium and silicon I : electron and impurity relaxation 385
Southgate, P. D. : Internal friction in germanium and silicon II : oxygen movement and dislocation damping 398
Spear, W. E. : Hole mobility in selenium 826
Sprung, D. W. L., and Willis, J. B. : Spin–orbit potential in proton–proton scattering . . . . . 539, corr. 1002
Standley, K. J., with Nash, W. B. : Wall effect in ferrimagnetic resonance experiments 99
Stevenson, R. W. H., with Finlayson, D. M., Roberston, I. S., and Smith, T. : Optical absorption in manganese–zinc fluoride single crystals near Néel temperature . 355
Stewart, A. L., with Dalgarno, A. : Lamb shift of helium 49
Swan, D. W. : Interpretation of ion mobility measurements in argon and helium liquids 36
Swan, J. B., with Robins, J. L. : Characteristic electron energy loss spectra of transition metals, Ti to Cu 857
Sweetman, D. R. : Lifetime of He^- ion (R) 998

PAGE

Taylor, I. J., with Jaffe, A. A., Barros, F. de S., Forsyth, P. D., Muto, J., and Ramavataram, S. : Some (t, p) reactions in light nuclei 914
Teale, R. W., with Pearson, R. F. : Magnetic resonance and magnetocrystalline anisotropy in ytterbium iron garnet (L) 308
Tebble, R. S., with Saunders, N. H. : Magnetothermal effects in silicon–iron alloys 282
Thetford, A., with Klemperer, O., (with a note by F. Lenz) : Transmission of slow electrons through thin films 705
Thornton, E. : Viscosity and thermal conductivity of binary gas mixtures : xenon–kypton, xenon–argon, xenon–neon and xenon–helium 104
Thorp, J. S., with Pace, J. H., and Sampson, D. F. : Spin–lattice relaxation times in ruby at 34·6 Gc/s 697
Towle, J. H., with Macefield, B. E. F. : Energy levels of ^{29}P, ^{33}Cl and ^{41}Sc from (d, n) reactions 56
Tredgold, R. H., with Barnes, J. F. : Field dependent electron mobility in ionic crystals 261
Tredgold, R. H., with Branwood, A. : Electrical conductivity of barium titanate single crystals 93
Tredgold, R. H., with Rhys-Roberts, C. : Note on theory of space charge limited currents 497

Varshni, Y. P., and Shukla, R. C. : On Pauling's theory of alkali halide molecules (R) 794
Vasudevan, R., with Ranganathan, N. R. : Stochastic problem of electron–photon cascades including polarization 650
Verma, G. S. : Second dislocation relaxation peak in aluminium at low temperatures (R) 412
Verma, G. S., and Joshi, S. K. : Nuclear resonance absorption of ultrasound in KI and KBr (R) 776

Wafik, M., with el-Nadi, M. : Direct inelastic scattering of deuterons 185
Walker, J. K., with Rutherglen, J. G. : Photoproduction of charged pions from deuterium (R) 430
Walker, P. A. : Thermal conductivity and thermoelectric power of bismuth telluride at low temperatures 113
Weintroub, S., with Hurle, D. T. J. : Electrical resistivity of monocrystalline and liquid bismuth (L) 163
Weston, D. E. : Underwater explosions as acoustic sources 233
Williams, R. V., and Kaufman, S. (A. S.) : Measurement of electron temperature in high temperature plasmas . . . . . corr. 168
Williams, R. V., with Kaufman, A. S., and Hughes, T. P. : SCEPTRE III—Intense source of spectra of highly ionized atoms 17
Willis, J. B., with Sprung, D. W. L. : Spin–orbit potential in proton–proton scattering 539, corr. 1002
Wills, R. D., with Allan, H. R., Beamish, R. F., Bryant, D. A., and Kasha, H. : Investigation of extensive air showers, using Cerenkov detectors 1
Wilman, H., with Porgess, P. V. K. : Surface re-orientation, friction and wear, in unidirectional abrasion of graphite 513
Wilson, C. B. : Phenomenological theory of characteristic energy losses of fast electrons in metals 481
Wintle, H. J. : Effect of attenuation on acoustic resonant frequencies of gases in tubes (R) 772
Wolf, E. : Correlation between photons in partially polarized light beams (R) . . 424
Wood, J. L., with Booker, C. J. L. : Further electrical effects of adsorption of water vapour by anodized aluminium 721

INDEX TO REVIEWS OF BOOKS

PAGE

Andrade, E. N. da C.: *An approach to modern physics* 447

Band, William: *Introduction to mathematical physics* 444
Bellman, Richard: *Introduction to matrix analysis* 591
Bishop, Amasa S.: *Project Sherwood : The U.S. program in controlled fusion* . . 584
Bockris, J. O'M., White, J. L., and Mackenzie, J. D. (Eds): *Physico-chemical measurements at high temperatures* 815
de Broglie, Louis: *La spectrographie infrarouge et les grandeurs moléculaires* . . 446

Claus, W. D., (Ed.): *Radiation biology and medicine* 313
Colloques Internationaux du Centre National de la Recherche Scientifique: *Acoustique musicale* 442
Cot, D.: *Éléments des calculs d'interpolation* 588
Curie, D.: *Luminescence cristalline* 1007

Dewitt, Cécile, (Ed.): *The many body problem. Report of the summer school of theoretical physics, Les Houches*, 1958 812
Dugas, René: *La théorie physique au sens de Boltzmann et ses prolongements modernes* 447

Elliot, A., and Home Dickson, J.: *Laboratory instruments*, 2nd edn. 811
Elton, L. R. B.: *Introductory nuclear theory* 448
Estermann, I., (Ed.): *Methods of experimental physics.* Vol. 1. *Classical methods* 318

Fisch, S., and Potter, J. L.: *Theory of a.c. circuits* 1007
Flügge, S., (Ed.): *Handbuch der Physik.* Vol. 111/2. *Principles of thermodynamics and statistics* 584
Flügge, S., (Ed.): *Handbuch der Physik.* Vol. 38/2. *Neutrons and related gamma ray problems* 315
Flügge, S., and Truesdell, C., (Eds) : *Handbuch der Physik.* Vol. VIII/I. *Fluid dynamics* 814
Fock, V., (Translated by N. Kemmer): *The theory of space time and gravitation* . 1003
Frisch, O. R., (Ed.): *Progress in nuclear physics.* Vol. 7 314

Goldstein, H.: *Fundamental aspects of reactor shielding* 320
Gugenberger, P., (Ed.): *Proceedings of the international conference on nuclear physics, Paris*, 1958 445

Hamer, W. J., (Ed.): *The structure of electrolytic solutions* 809
Hamilton, J.: *Theory of elementary particles* 311
Heisenberg, W.: *Physics and philosophy* 316
Herzfeld, K. F., and Litovitz, T. A.: *Absorption and dispersion of ultrasonic waves* 445

Irving, J., and Mullineux, N.: *Mathematics in physics and engineering* . . . 319
Ivall, T. E.: *Electronic computers: principles and applications* 1007

Jaswon, M. A.: *Studies in crystal physics* 590

Koch, K. M., and Reinbach, R.: *Einführung in die Physik der Leiterwerkstoffe* . . 1005

PAGE

Landau, L. D., and Lifshitz, E. M. (Translated from the Russian by J. B. Sykes and W. H. Reid): *Fluid mechanics* 586
Landau, L. D., and Smorodinsky, Ya.: *Lectures on nuclear theory* 585
Lark-Horovitz, K., and Johnson, V. A., (Eds): *Methods of experimental physics*, Vol. 6, Part A. *Solid state physics* 1004
Leontovich, M. A., (Ed.): *Plasma physics and the problem of controlled thermonuclear reactions*. Vol. 3 591
Low, W.: *Paramagnetic resonance in solids* 1008

Macke, W.: *Wellen, Ein Lehrbuch der theoretischen Physik* 809
Makarov, E. S., (Translated from the Russian by E. B. Uvarov): *Crystal chemistry of simple compounds of uranium, thorium, plutonium, neptunium* 445
Martin, J. H., (Ed.): *Radiation biology* 810
Marton, L., (Ed.): *Advances in electronics and electron physics*. Vol. 10 . . . 582
Marton, L., (Ed.): *Advances in electronics and electron physics*. Vol. 11 . . . 583
Matossi, F.: *Der Raman Effekt*. 168
Messiah, A.: *Mécanique quantique*. Vol. 2 586
Miller, G. L.: *Tantalum and niobium* 1005
Mott, N. F.: *Elements of wave mechanics* 1006

Nightingale, A.: *Physics and electronics in physical medicine* 811

Pauli, W. (Translated by G. Field): *Theory of relativity* 312
Pearson, Carl E.: *Theoretical elasticity* 312
Preuss, H.: *Die Methoden der Molekülphysik und ihre Anwendungsbereiche* . . 315

Robinson, R. A., and Stokes, R. H.: *Electrolytic solutions* 809
Rocard, Y.: *Principles of electricity and magnetism* 589
Rochlin, R. S., and Schultz, W. W.: *Radioisotopes for industry* 442

Saratovkin, D. D. (Translated from the Russian by J. E. S. Bradley): *Dendritic crystallization* 317
Schönhuber, M. J.: *Quecksilber-Niederdruck-Gasentladungen*. 588
Sciama, D. W.: *The unity of the universe* 592
Segrè, E., (Ed.): *Experimental nuclear physics*. Vol. 3 443
Segrè, E., and Schiff, L. I., (Eds): *Annual review of nuclear science*. Vol. 9 . . 813
Slater, L. J.: *Confluent hypergeometric functions* 1006
Smith, R. A.: *Semiconductors* 587
Somerville, J. M.: *The electric arc* 589
Starr, A. T.: *Electronics*, 2nd Edn 1003
Stasiw, O.: *Elektronen- und Ionenprozesse in Ionenkristallen* 317
Stumpff, K.: *Himmelsmechanik*. Vol. 1 590

Watkins, Dean A.: *Topics in electromagnetic theory* 313
Wilson, A. J. C., (Ed.): *Structure reports for* 1952. Vol. 16 1006
Wilson, A. J. C., (Ed.): *Structure reports: supplementary volume and cumulative index for* 1940-50. Vol. 14 1006
Wolf, K. L.: *Physik und Chemie der Grenzflächen*, II: *Die Phänomene in Besonderen* 582

Printed in England
Taylor & Francis, Ltd., Red Lion Court, Fleet Street, London, E.C.4